AD-A264 206

ARO 29669.2-PH-CF

quantum chemistry

International Journal of

ψ

DTIC
SELECTE
MAY 5 1993
S   C   D

QUANTUM CHEMISTRY

SYMPOSIUM NO. 26, 1992

②

Proceedings of the
International Symposium on

Atomic, Molecular, and Condensed Matter Theory and Computational Methods

Held at the Ponce de Leon Conference Center
St. Augustine, Florida, March 14-21, 1992

Editor in Chief: Per-Olov Löwdin
Special Editors: N. Yngve Öhrn
John R. Sabin
Michael C. Zerner

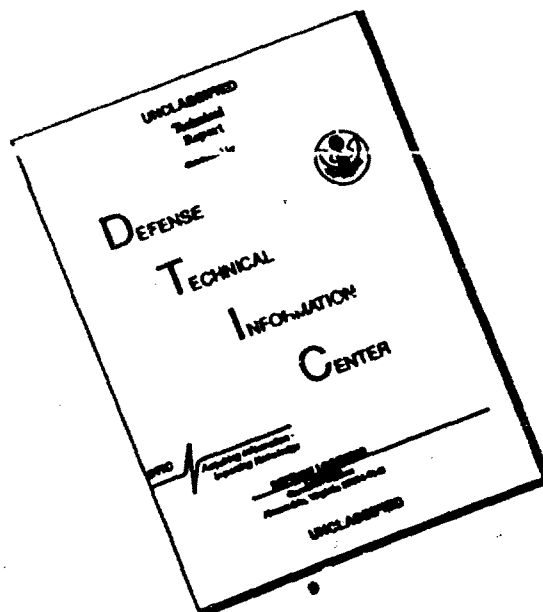An Interscience* Publication
published by JOHN WILEY & SONS

New York • Chichester • Brisbane • Toronto • Singapore

ISSN 0360-8832

DISTRIBUTION STATEMENT A

Approved for public release
Distribution Unlimited

DISCLAIMER NOTICE

THIS DOCUMENT IS BEST QUALITY AVAILABLE. THE COPY FURNISHED TO DTIC CONTAINED A SIGNIFICANT NUMBER OF PAGES WHICH DO NOT REPRODUCE LEGIBLY.

REPORT DOCUMENTATION PAGE

Form Approved
OMB No 0704-0188

Public reporting burden for this collection of information is estimated to average 1 hour per response, including the time for reviewing instructions, searching existing data sources, gathering and maintaining the data needed, and completing and reviewing the collection of information. Send comments regarding this burden estimate or any other aspect of this collection of information, including suggestions for reducing this burden to Washington Headquarters Services, Directorate for Information Operations and Reports, 1215 Jefferson Davis Highway, Suite 1204, Arlington, VA 22202-4302, and to the Office of Management and Budget, Paperwork Reduction Project (0704-0188), Washington, DC 20503

1. AGENCY USE ONLY (Leave blank)	2. REPORT DATE	3. REPORT TYPE AND DATES COVERED
	Feb 93	Final 6 Apr 92-5 Jan 93

4. TITLE AND SUBTITLE	5. FUNDING NUMBERS
32nd Sanibel Symposium	DAAL03-92-G-0214

6. AUTHOR(S)

Rodney J. Bartlett

7. PERFORMING ORGANIZATION NAME(S) AND ADDRESS(ES)	8. PERFORMING ORGANIZATION REPORT NUMBER
University of Florida Gainesville, Florida 32611	

9. SPONSORING/MONITORING AGENCY NAME(S) AND ADDRESS(ES)	10. SPONSORING/MONITORING AGENCY REPORT NUMBER
U. S. Army Research Office P. O. Box 12211 Research Triangle Park, NC 27709-2211	ARO 29669.2-PH-CF

11. SUPPLEMENTARY NOTES

The view, opinions and/or findings contained in this report are those of the author(s) and should not be construed as an official Department of the Army position, policy, or decision, unless so designated by other documentation.

12a. DISTRIBUTION/AVAILABILITY STATEMENT	12b. DISTRIBUTION CODE
Approved for public release; distribution unlimited.	

13. ABSTRACT (Maximum 200 words)

The 32nd annual Sanibel Symposium was held March 14 to 21, 1992.

The format of the symposium adopted for the past 2 years was followed again this year providing a compact 8-day schedule with an integrated program of quantum biology, quantum chemistry, and condensed matter physics. The topics of the sessions covered by these proceedings include Thirty-five Years of Progress in Electronic Structure Theory, Density Matrices and Other Revelations of 1955, Non-Born-Oppenheimer Methods, Atomic and Molecular Phenomena in Astrophysics, Photo-induced Phenomena, Reactive Molecular Collisions, Quantum Monte Carlo, Density-Functional Theory, Thin Films and Surfaces.

A special session on Theoretical Inorganic Chemistry was held in memory of Arnold Karo, one of the real "old-timers" at Sanibel.

All the articles have been subjected to the ordinary refereeing procedures of the The International Journal of Quantum Chemistry The articles presented in the sessions on quantum biology and associated poster sessions are published in a separate volume of the The International Journal of Quantum Chemistry

14. SUBJECT TERMS		15. NUMBER OF PAGES
Quantum Chemistry, Condensed Matter Theory, Symposium		896
		16. PRICE CODE

17. SECURITY CLASSIFICATION OF REPORT	18. SECURITY CLASSIFICATION OF THIS PAGE	19. SECURITY CLASSIFICATION OF ABSTRACT	20. LIMITATION OF ABSTRACT
UNCLASSIFIED	UNCLASSIFIED	UNCLASSIFIED	UL

NSN 7540-01-280-5500

Standard Form 298 (Rev 2-89)
Prescribed by ANSI Std 239-18
298-102

DTIC QUALITY INSPECTED 5

*Proceedings of the
International Symposium on*
Atomic, Molecular, and Condensed Matter Theory and Computational Methods

Held at St. Augustine, Florida, March 14–21, 1992

Editor-in-Chief: Per-Olov Löwdin
Special Editors: N. Yngve Öhrn, John R. Sabin, and
Michael C. Zerner

93-09606

93 5 04 147

Contents

CONTENTS   v

CONTENTS

Introduction

The 32nd annual Sanibel Symposium, organized by the faculty of the Quantum Theory Project of the University of Florida, was held March 14 to 21, 1992 at the Ponce de Leon Conference Center located at the north gate of the city of St. Augustine, Florida. About 330 participants gathered for 8 days of lectures and discussions in a program that paid special tribute to the scientific contributions of Professor Per-Olov Löwdin of the University of Florida in his celebrated three articles on density matrices, natural spin orbitals, the Hartree–Fock approximation, and its extensions, published back-to-back in The Physical Review **97** (1955). The daily schedule was packed with plenary sessions in the morning, and late afternoon, and with poster presentations in the evenings, often lasting until midnight.

The format of the symposium adopted for the past 2 years was followed again this year providing a compact 8-day schedule with an integrated program of quantum biology, quantum chemistry, and condensed matter physics. The topics of the sessions covered by these proceedings include Thirty-five Years of Progress in Electronic Structure Theory, Density Matrices and Other Revelations of 1955, Non-Born–Oppenheimer Methods, Atomic and Molecular Phenomena in Astrophysics, Photo-induced Phenomena, Reactive Molecular Collisions, Quantum Monte Carlo, Density-Functional Theory, Thin Films and Surfaces.

A special session on Theoretical Inorganic Chemistry was held in memory of Arnold Karo, one of the real "old-timers" at Sanibel.

All the articles have been subjected to the ordinary refereeing procedures of the *The International Journal of Quantum Chemistry*. The articles presented in the sessions on quantum biology and associated poster sessions are published in a separate volume of the *The International Journal of Quantum Chemistry*.

1992 Sanibel Symposia List of Participants

WILLIAM ADAMS
Rutgers University
Department of Chemistry
P.O. Box 939
Piscataway, NJ 08855-0939

HANS AGREN
University of Linkoeping
Department of Physics
Linkoeping, S 58183
Sweden

GERRARD AISSING
University of Florida
Quantum Theory Project
372 WM Hall
Gainesville, Fl 32611

ARIE AIZMAN
Universidad Tenica Federico Santa Maria
Departamento de Quimica
Casilla 110-V
Valparaiso,
Chile

STEVE ALEXANDER
University of Florida
Department of Physics
Gainesville, FL 32611

JAMES B. ANDERSON
Pennsylvania State University
Department of Chemistry
152 Davey Lab
University Park, PA 16802

JAN ANDZELM
BIOSYM Technologies, Inc.
10065 Barnes Canyon Road
San Diego, CA 92121-2777

IBIS APONTE-AVELLANET
University of Puerto Rico
Departmento of Physics
Facundo Bueso Bldg.
Rio Piedras, Puerto Rico 00931

ROBERT ASHER
University of Florida
Department of Chemistry
109 Leigh Hall
Gainesville, FL 32611

MICHAEL BAER
SOREQ Nuclear Research Center
Physics & Applied Mathematics
Yavne, 70600
Israel

KELD BAK
Aarhus University
Department of Chemistry Langelandscade 140
Aarhus C, DK-8000
Denmark

DIRK BAKOWIES
Bergische Universitat GH Wuppertal
Theoretische Chemie
Gaussstr. 20
Wuppertal-1, W-5600
Germany

ANNA BALKOVA
University of Florida
Quantum Theory Project
370 WM Hall
Gainesville, Fl 32611

K. L. BALUJA
Florida A&M University
Department of Physics
Tallahassee, FL 32307

ALAN BANDY
Drexel University
Department of Chemistry
3200 Chestnut Street
Philadelphia, PA 19104

RODNEY BARTLETT
University of Florida
Quantum Theory Project
381 WM Hall
Gainesville, FL 32611

INDER BATRA
IBM
Almaden Research Center
650 Harry Road, K62/802
San Jose, CA 95120

SULLIVAN BECK
University of Florida
Department of Chemistry
Gainesville, FL 32611

DARIO BEKSIC
University of Florida
Quantum Theory Project
Physics Department
Gainesville, FL 32611

RAJIV D. BENDALE
University of Florida
Quantum Theory Project
378 WM Hall
Gainesville, FL 32601

HERMAN BERENDSEN
University of Groningen
Physical Chemistry Dept.
Nyenborgh 16
Groningen, AG 9747
The Netherlands

GORAN BERGSON
Uppsala University
Department of Chemistry
Thunbergsvagen 5, PO Box 531
Uppsala, S-75121
Sweden

MARGARITA I. BERNAL
Universidad Nacional Autonoma de Mexico
Instituto de Fisica
AP Postal 139-B
Cuernavaca, Morelos 62190
Mexico

DAVID BERNHOLDT
University of Florida
Quantum Theory Project
345 WM Hall
Gainesville, FL 32611

MANUEL BERRONDO
Brigham Young University
Department of Physics
296-ESC
Provo, UT 84602

DAVID BEVERIDGE
Wesleyan University
Department of Chemistry
Lawn Avenue
Middletown, CT 06457

F. MATHIAS BICKELHAUPT
Universiteit Van Amsterdam
Inst. Voor Massaspectrometrie
Nieuwe Achtergracht 129
Amsterdam, WS 1018
The Netherlands

DAVID BISHOP
University of Ottawa
Chemistry Department
Ottawa, ON K1N 6N5
Canada

FRANK BLANEY
Smithkline Beecham Medicinal Research Centre
Computational Chemistry
The Pinnacles
Harlow, Essex CM19 5AD
England

JEAN BLAUDEAU
Ohio State University
Department of Chemistry
140 W 18th Avenue
Columbus, OH 43120

JONATHAN BOETTGER
Los Alamos National Laboratory
Group T-1, MS B221
Los Alamos, NM 78545

JAMES BOGGS
National Science Foundation
401 South 12th Street
Apartment 1604
Arlington, VA 22202

EDWARD BOUDREAUX
University of New Orleans
Department of Chemistry
Lakefront
New Orleans, LA 70148

MARCUS BREWSTER
University of Florida
Pharmatec, Inc.
P.O. Box 730
Alachua, FL 32615

TORE BRINCK
University of New Orleans
Department of Chemistry
New Orleans, LA 70148

EWA BROCKAWIK
Universite de Montreal
Department of Chemistry
C.P. 6128, Succ. A
Montreal, Quebec H3C 3J7
Canada

RIA BROER
University of Groningen
Department of Chemical Physics
Nijenborgh 4
Groningen, AG 9747
The Netherlands

BERNARD BROOKS
National Institute of Health
Bldg. 12A, Room 2055
Bethesda, MD 20892

JENNIFER BROWN
University of Florida
Department of Chemistry
416 Leigh Hall
Gainesville, FL 32611-2046

JORGE A. BRUNO
Universidad de Buenos Aires
Quimica Inorg. Analitica y
Qca. Fisica
Captial Federa, 1428
Argentina

JEAN-LOUIS CALAIS
University of Uppsala
Quantum Chemistry Department
Box 518
Uppsala, S-75120
Sweden

JAMES CALDWELL
University of California
Department of Pharmaceutical Chemistry,
Box 0446
San Francisco, CA 94143-0446

CRISTIAN CARDENAS-LAILHACUR
University of Florida
Quantum Theory Project
212 Leigh Hall
Gainesville, FL 32611

PETR CARSKY
University of Colorado
Department of Chemistry
Campus Box 215
Boulder, CO 80309-0215

DAVID CASE
The Scripps Research Institute
Dept. of Molecular Biology
10666 N. Torrey Pines Road
La Jolla, CA 92037

EDUARDO A. CASTRO
INIFTA
Division Quimica Teorica
Suc. 4, C.C. 16
La Plata, Buenos Aires 1900
Argentina

DAVID CEPERLEY
University of Illinois
Department of Physics
1110 W. Green Street
Urbana, IL 61801

MONIQUE CHACON
University of Florida
Quantum Theory Project
348 WM Hall
Gainesville, FL 32611

MATT CHALLACOMBE
Florida State University
Department of Chemistry
Tallahassee, FL 32306-3006

PAUL W. CHUN
University of Florida Department of
Biochemistry & Molecular Biology,
Box 100245
J. Hillis Miller Health Center
Gainesville, FL 32610

JERSY CIOSLOWSKI
Florida State University
Department of Chemistry
Tallahassee, FL 32306-3006

JIRI CIZEK
University of Waterloo
Dept. of Applied Mathematics
Waterloo, Ontario N21 3G1
Canada

ROBERT COLDWELL
University of Florida
Department of Physics
Williamson Hall
Gainesville, FL 32611

JACK COLLINS
Molecular Research Institute
845 Page Mill Road
Palo Alto, CA 94304

DONALD COMEAU
University of Florida
Quantum Theory Project
371 WM Hall
Gainesville, FL 32611

JOHN CONNOLLY
University of Missouri
Department of Chemistry
5100 Rockhill Road
Kansas City, MO 64110-2499

MICHAEL CONRAD
Wayne State University
Computer Science Department
Detroit, MI 48202

RENATO R. CONTRERAS
University of Chile
Department of Chemistry
Casilla 653-STGO
Santiago,
Chile

BERNARD COOPER
West Virginia University
Department of Physics
Morgantown, WV 26505

RICHARD CROSSLEY
University of York
Department of Mathematics
York, YO1 5DD
United Kingdom

PETER CSAVINSZKY
University of Maine
Department of Physics
Orono, ME 04469

THOMAS CUNDARI
Memphis State University
Department of Chemistry
Smith Chemistry Building
Memphis, TN 38152

HERBERT F.M. DA COSTA
University of Florida
Quantum Project Theory
372 WM Hall
Gainesville, FL 32611

ALEXANDER DALGARNO
Harvard-Smithsonian Center for Astrophysics
60 Garden Street
Cambridge, MA 02138

ERNEST DAVIDSON
Indiana University
Department of Chemistry
Bloomington, IN 47405

ROBIN DAVIES
University of Wales
Pharmacy Dept., Redwood Bldg.
King Edward VII Avenue
Cardiff, Wales CF1 3XF
United Kingdom

EDGAR E. DAZA C.
Universidad Nacional de Colombia
Theoretical Chemistry Group
Calle 53 No. 28-16, Apto. 501
Santafe, Bogota
Colombia

JANET DEL BENE
Youngstown State University
Department of Chemistry
Youngstown, OH 44555

MICHAEL DELEUZE
Facultes Universitaires Notre-Dame de la Paix
Departement de Chimie
Rue de Bruxelles, 61
Namur, B-5000
Belgium

JOSEPH DELHALLE
Facultes Universitaries Notre-Dame de la Paix
Departement de Chimie
Rue de Bruxelles, 61
Namur, B-5000
Belgium

AGNES DERECSKEI-KOVACS
University of Texas
Department of Chemistry
P.O. Box 19605
Arlington, TX 76019

ERIK DEUMENS
University of Florida
Quantum Theory Project
359 WM Hall
Gainesville, FL 32611

MICHAEL DEWAR
University of Florida
Department of Chemistry
Gainesville, FL 32611

AGUSTiN DIZ
University of Florida
Quantum Theory Project
345 WM Hall
Gainesville, FL 32611

PING DU
Molecular Research Institute
845 Page Mill Road
Palo Alto, CA 94304

MICHEL DUPUIS
IBM
MLM/MS 428
Neighborhood Road
Kingston, NY 12401

DANIEL EDWARDS
University of Idaho
Department of Chemistry
Moscow, ID 83843

ADOLFO G. EGUILUZ
Montana State University
Department of Physics
AJM Johnson Hall
Bozeman, MT 59717

RON ELBER
University of Illinois
Department of Chemistry
P.O. Box 4348
Chicago, IL 60680

ERIK ENGDAHL
Hebrew University
Department of Physical Chemistry
Jerusalem, 91904
Israel

LEOPOLDO ESQUIVEL
University of Costa Rica
Escuela de Fisica
San Jose, 2060
Costa Rica

GUILLERMINA ESTIU
University of Florida
Quantum Theory Project
380 WM Hall
Gainesville, FL 32611

BABAK ETEMADI
Florida A&M University
Physics Department
Tallahassee, FL 32307

ADALBERTO FAZZIO
Universidade de Sao Paulo
Instituto de Fisica
Cidade Universitaria
Sao Paulo, SP 01498
Brazil

FRANCISCO FERNANDEZ
INIFTA
DQT
Suc. 4, CC 16
La Plata, 1900
Argentina

KIM FERRIS
Pacific Northwest Labs
P.O. Box 999
Richland, WA 99352

MICHAELA FLOCK
Technische Universitat Graz
Institut fur Phsikal Chemie
Graz, A-8010
Austria

PAUL FRIEDMAN
Pratt Institute
Department of Chemistry
Brooklyn NY 11205

MAXIMO GARCIA-SUCRE
IVIC and UCV
Centro de Fisica
Apartado 21827
Caracas, 1020A
Venezuela

DAVID GARMER
Mount Sinai School of Medicine
Physiology & Biophysics
1 Gustave Levy Place
New York, NY 10029-6574

JACK GAY
GM Research Labs
Physics Department
3C500 Mound Road
Warren, MI 48090-9055

PETER GILL
Carnegie Mellon University
Department of Chemistry
4400 Forbes Avenue
Pittsburgh, PA 15213

ERIC GISLASON
University of Illinois
Chemistry Department
Box 4348
Chicago, IL 60680

ALEXANDRU GLONDEANU
Institute of Physics and Technology of Materials
Department of Atomic Physics
Bucharest, Magurale MG-6
Romania

DANIEL GLOSSMAN
University of Valladolid
Departamento Fisica Teorica
Valladolid, E 47011
Spain

NICK GONZALES
University of Utah
Department of Chemistry
Salt Lake City, UT 84112-1194

CARLOS GONZALEZ
Carnegie Mellon University
Department of Chemistry
4400 Forbes Avenue
Pittsburgh, PA 15213

LIONEL GOODMAN
Rutgers University
Department of Chemistry
New Brunswick, NJ 08903

MARK GORDON
North Dakota State University
Department of Chemistry
Fargo, ND 58105

ANTE GRAOVAC
The R. Boskovic Institute
Dept. of Phys. Chem.
Bijenicka C.54
Zagreb, Croatia YU-41001
Yugoslavia

NOHAD GRESH
Center for Advanced Research in Biotechnology
9600 Gudelsky Drive
Rockville, MD 20850

PETER GRIBI
Universitat Stuttgart
Inst. f. Theoret. Physik
Pfaffenwaldring 57
Stuttgart, 80 D-7000
Germany

LAWRENCE GRIFFEN
Texas A&M University
Marine Sciences Dept.
P.O. Box 1675
Galveston, TX 77553

ARNOLD HAGLER
BIOSYM Technologies, Inc.
10065 Barnes Canyon Road
San Diego, CA 92121

MARK HAGMANN
Florida International University
Electrical & Computer
Engineering Department
Miami, FL 33199

FRANK HARRIS
University of Utah
Department of Chemistry
Henry Eyring Bldg.
Salt Lake City, UT 84112

BERND HARTKE
UCLA
Dept. of Chemistry & Biochem.
405 Hilgard Avenue
Los Angeles, CA 90024-1569

TIM HAVEL
Harvard Medical School
Department of BCMP
240 Longwood Avenue
Boston, MA 02115

JOHN HEAD
University of Hawaii
Department of Chemistry
2545 The Mall
Honolulu, HI 96822

ERIC HERBST
Ohio State University
Department of Physics
174 W. 18th Avenue
Columbus, OH 43210

HIROAKI HIROSE
University of Florida
Quantum Theory Project
WM Hall, Rm. 379
Gainesville, FL 32611

KENDALL HOUK
University of California
Dept. of Chemistry & Biochem.
405 Hilgard Avenue
Los Angeles, CA 90024-1569

MING-JU HUANG
University of Florida J. Hillis Miller
  Health Center
College of Pharmacy
P.O. Box 100497
Gainesville, FL 32611

YASUJUKI ISHIKAWA
University of Puerto Rico
Department of Chemistry
P.O. Box 23346
San Juan, Puerto Rico 00931

SAUL JACCHIERI
Universidade Federal de Minas Gerais
Depto. de Biochemistry
Campus da Pampulha
Belo Horizonte, MG 32170
Brasil

ASHOK JAIN
Florida A&M University
Physics Department
Tallahassee, FL 32307

HANS JORGEN AA. JENSEN
Odense University
Department of Chemistry
Campusvej 55
Odense M, DK-5230
Denmark

MU SHIK JHON
Korea Advanced Institute of Science
  and Technology
Department of Chemistry
P.O. Box 150, Cheong Ryang Ri
Seoul,
Korea

BENNY JOHNSON
Carnegie Mellon University
Department of Chemistry
4400 Fifth Avenue
Pittsburgh, PA 15213

WALTER R. JOHNSON
University of Notre Dame
Department of Chemistry
College of Science
Notre Dame, IN 46556

HERBERT JONES
Florida A&M University
Department of Physics
Tallahassee, FL 32307

WILLIAM L. JORGENSEN
Yale University
Department of Chemistry
New Haven, CT 06511-6299

GUAN-ZHI JU
Indiana University
Department of Chemistry
Bloomington, IN 47405

ANDRE JUFFER
University of Groningen
Physical Chemistry Dept.
Nijenborgh 16
Groningen, AG 9747
The Netherlands

MICHAEL KASHA
Florida State University
Institute of Molecular
Biophysics, B-165
Tallahassee, FL 32306-3015

VITALY KHUTORSKY
Weizmann Institute of Science
Chemical Physics Department
Rehovot, 76 100
Israel

JAMES KING
U.S. Army Chemical RD&E Center
SMCCR-RSC-O
Edgewood Area
Aberdeen Proving Gr., MD 21010-5423

KATE KIRBY
Harvard-Smithsonian Center for Astrophysics
60 Garden Street
Cambridge, MA 02138

BERNARD KIRTMAN
University of California
Department of Chemistry
Santa Barbara, CA 93106

LEO KLASINC
Louisiana State University
Department of Chemistry
Baton Rouge, LA 70803

DOUGLAS KLEIN
Texas A&M University
MARS
Galveston, TX 77553-1675

RACHEL KLEVIT
University of Washington
Department of Biochemistry
SJ-70
Seattle, WA 98195

HERBERT KLOTZ
Air Products & Chemicals, Inc.
7201 Hamilton Blvd.
Allentown, PA 18195-1501

JOHN KNEISLER
University of North Carolina
Department of Chemistry
Chapel Hill, NC 27599-3290

MANFRED KOTZIAN
Techn. Universitat Munchen
Lehrstuhl f. Theoretische
Chemie, Lichtenbergstr. 4
Garching, 8046
Germany

MORRIS KRAUSS
National Institute of Standards Technology
Biotechnology Division
Rm. B256, Bldg. 221
Gaithersburg, MD 20899

KARSTEN KROGH-JESPERSEN
Rutgers University
Department of Chemistry
P.O. Box 939
Piscataway, NJ 08854

STANISLAW KUCHARSKI
University of Florida
Quantum Theory Project
371 WM Hall
Gainesville, FL 32611

HENRY KURTZ
Memphis State University
Department of Chemistry
Memphis, TX 38125

JOZEF S. KWIATKOWSKI
Jackson State University
Department of Chemistry
Jackson, MI 39217

JANOS LADIK
University of Erlangen
Institute for Theoretical
Chemistry, Mistelweg 5
Erlangen, 8520
Germany

BILL LAIDIG
Proector & Gamble Company
Miami Valley Laboratories
P.O. Box 398707
Cincinnati, OH 45329-8707

EVERITT LARSON
Brigham Young University
Physics & Astronomy
296 Eyring Science Center
Provo, UT 84602

JEAN-MICHEL LAUNAY
Observatoire de Paris-Meudon
Department of Atomic &
Molecular Astrophysics
Meudon, 92195
France

CARMEN LAVIN
Universidad de Valladolid
Quimica Fisica
Valladolid, 47005
Spain

PIERRE LEBRETON
The University of Illinois
Department of Chemistry
Box 4348
Chicago, IL 60680

CLAUDE LEFORESTIER
Universite Paris-Sud
Lab. Chimie Theorique
Batiment 490
Orsay, 91405
France

CHRISTOPHOROV LEONID
Ukrainian Academy of Sciences
Inst. of Theoretical Physics
Metrologicheskaya Str. 14 b
Kiev, Ukraine 252143
USSR

JERZY LESZCZYNSKI
Jackson State University
Department of Chemistry
1400 Lynch Street
Jackson, MS 39217

ANTHONY LEWANDOWSKI
Oklahoma State University
Department of Physics
145 Physical Sciences II
Stillwater, OK 74078

JAN LINDERBERG
Aarhus University
Department of Chemistry
Aarhus, C, DK-8000
Denmark

GILDA LOEW
Molecular Research Institute
845 Page Mill Road
Palo Alto, CA 94304

PER-OLOV LOWDIN
University of Florida
Quantum Theory Project
365 WM Hall
Gainesville, FL 32611

CHENGBE LUI
Shandong University
Department of Chemistry
22 Shanda South Road
Jinan, 250100
China

ISTVAN LUKOVITS
Hungarian Academy of Science
Ctrl. Res. Inst. for Chemistry
P.O. Box 17
Budapest, H-1525
Hungary

KARL LUTH
Southern Illinois University
Chemistry Department
Carbondale, IL 62901

FRANCISCO MACHADO
Indiana University
Department of Chemistry
Bloomington, IN 47405

NORMAN MARCH
Oxford University
Theoretical Chemistry Dept.
5, South Parks Road
Oxford, OX1 3UB
England

TODD MARSHALL
Oklahoma State University
Department of Physics
145 Physical Sciences II
Stillwater, OK 74078

IMMACULADA MARTIN
Universidad de Valladolid
Quimica Fisica
Valladolid, 47005
Spain

MANUEL MARTIN
Universidad de Autonoma de Puebla
F.C. Fis-Mat.
Apartado Postal J-48
Puebla, Puebla 72570
Mexico

JOSE MARTINEZ-MAGADAN
Instituto Mexicano del Petroleo
SGIA, A.P. 14-805
Eje Cen. Lazaro Cardenas 152
Mexico, DF 07730
Mexico

DENNIS MARYNICK
University of Texas
Department of Chemistry
Arlington, TX 76019-0065

RENEE MATTIE
University of Florida
Quantum Theory Project
345 WM Hall
Gainesville, FL 32611

ISTVAN MAYER
Hungarian Academy of Sciences
Central Research Institute for
 Chemistry, P.O. Box 17
Budapest, H-1525
Hungary

SEAN MCGLYNN
Louisiana State University
Department of Chemistry
Choppin Hall
Baton Rouge, LA 70803-1804

VINCENT MCKOY
California Institute of Technology
Department of Chemistry
Pasadena, CA 91125

EMILE MEDVEDEV
Academy of Sciences of the USSR
Institute of Chemical Physics
Chernogolovka, Moscow 142432
USSR

DAVID A. MICHA
University of Florida
Quantum Theory Project
366 Williamson Hall
Gainesville, FL 32611

H. HARVEY MICHELS
United Technologies Research Center
Applied Physics Department
Silver Lane
East Hartford, CT 06108

WILLIAM H. MILLER
University of California
Department of Chemistry
Berkeley, CA 94720

STACEY MIXON
Florida State University
Department of Chemistry
Tallahassee, FL 32306-8281

JOSE R. MOHALLEM
Universidade Federal de Minas Gerais
Departamento de Fisica
P.O. Box 702
Belo Horizonte, MG 30161
Brasil

EDUARDO MOLA
Universidad de La Plata
INIFTA
Casilla de Correo 314
La Plata, 1900
Argentina

HENDRIK J. MONKHORST
University of Florida
Quantum Theory Project
361 WM Hall
Gainesville, FL 32611

JESUS MORALES
Instituto Mexicano Del Petroleo
Molecular Physics Dept.
Eje Central Lazaro, Car. 152
Mexico, DF 07730
Mexico

JORGE MORALES
University of Florida
Quantum Theory Project
212 Leigh Hall
Gainesville, FL 32611

JOHN MORGAN
University of Delaware
Department of Physics
Newark, DE 19716

KEIJI MOROKUMA
Institute of Molecular Science
Myodaiji
Okazaki, 444
Japan

JOAQUIM DA MOTTA NETO
University of Florida
Department of Chemistry
212 Leigh Hall
Gainesville, FL 32611

MAX MUIR
University of Florida
Department of Chemistry
415 Leigh Hall
Gainesville, FL 32611-2046

BENGT NAGEL
Royal Institute of Technology
Dept. of Theoretical Physics
Stockholm, S-100 44
Sweden

HIROSHI NAKATSUJI
Kyoto University
Department of Synthetic
Chemistry
Kyoto, 606
Japan

ROMAN NALEWAJSKI
Jagiellonian University
Theoretical Chemistry Dept.
R. Ingardena 3
Cracow, 30-060
Poland

ASIRI NANAYAKKARA
Florida State University
Super-Computer Computations
Research Institute
Tallahassee, FL 32306

WILLEM NIEUWPOORT
University of Groningen
Lab. of Chemical Physics
Nijenborgh 16
Groningen, AG 9747
The Netherlands

MARCEL NOOIJEN
Vrije Universiteit
Theoretical Chemistry
De Boelelaan 1083
Amsterdam, HV 1081
The Netherlands

DAVID NORDFORS
Physikalisch-Chemisches Inst.
Theoretische Chemie
Im Neuenheimer Feld 253
Heidelberg, D-6900
Germany

JAMES NORRIS
Argonne National Lab.
Department of Chemistry
9700 S. Cass Avenue
Argonne, IL 60439

JIM NOVOTNY
Bristol-Myers Squibb Research Institute
Rt. 206 & Province Line Road
Princeton, NJ 08543-4000

NILS YNGVE OHRN
University of Florida
Quantum Theory Project
363 WM Hall
Gainesville, FL 32611

VINCENT ORTIZ
University of New Mexico
Chemistry Department
Albuquerque, NM 87131

VLADIMIR OSHEROV
Academy of Sciences of the USSR
Institute of Chemical Physics
Chernogolovka, Moscow 142432
USSR

ROMAN OSMAN
Mount Sinai School of Medicine
Physiol. & Biophysics Dept.
#1218
New York, NY 10029

NEIL S. OSTLUND
Hypercube, Inc.
#7-419 Phillip Street
Waterloo, Ontario N2L 3X2
Canada

GIANFRANCO PACCHIONI
University of Milano
Dept. of Inorganic Chemistry
Via Venezian 21
Milan, 20133
Italy

GEORGE R. PACK
University of Illinois
Biomedical Sciences Department
1601 Parkwood Avenue
Rockford, IL 61107

JOSEF PALDUS
University of Waterloo
Dept. of Applied Mathematics
M&C Bldg.
Waterloo, Ontario N2L 3G1
Canada

ROCIO PALMA
Escuela Politecnica Nacional
Depto. de Fisica
Aptdo. 17-01-2759
Quito, Ecuador

DAO KAI PAN
East China Normal University
Chemistry Department
3662 Zhongsan North Road
Shanghai, 200062
China

WILLIAM A. PARKINSON
Southeastern Louisiana University
Department of Chemistry and Physics
Hammond, LA 70402

NINA PASTOR
Universidad Nacional Autonoma Mexico
Instituto de Fisica
AP Postal 139-B
Cuernavaca, Morelos 62190
Mexico

RUBEN PAUNCZ
TECHNION-Israel Institute of Technology
Department of Chemistry
Technion City, Haifa 32000
Israel

S. AJITH PERERA
University of Florida
Quantum Theory Project
345 WM Hall
Gainesville, FL 32611

WILLIS PERSON
University of Florida
Department of Chemistry
CLB 309
Gainesville, FL 32611

MONTE PETTITT
University of Houston
Department of Chemistry
4800 Calhoun
Houston, TX 77204-5641

BARRY T. PICKUP
University of Sheffield
Department of Chemistry
Sheffield, S3 7HF
United Kingdom

PETER POLITZER
University of New Orleans
Department of Chemistry
New Orleans, LA 70148

EMIL POP
Pharmetec, Inc.
P.O. Box 730
Alachua, FL 32615

JOHN POPLE
Carnegie Mellon University
Department of Chemistry
4400 Fifth Avenue
Pittsburgh, PA 15213

CRIAG PORTER
University of Florida
Department of Chemistry
415 Leigh Hall
Gainesville, FL 32611

RONALD POSHUSTA
Washington State University
Chemistry Department
Pullman, WA 99164-4630

MICHAEL PROBST
Innsbruck University
Department of Chemistry
Innrain 52a
Innsbruck, A-6020
Austria

JAMES RABINOWITZ
U.S. Environmental Protection Agency
MD-68
Health Effects Research Lab.
Research Triangle Pk., NC 27711

MICHAEL RAMEK
Techn. Universitat Graz
Institut F. Physikal. Chemie
Graz, A-8010
Austria

MARK RASOLT
Oak Ridge National Lab
Solid State Division
Oak Ridge, TN 37831

JOSE RECAMIER
Universidad Nactional Autonoma de Mexico
Instituto de Fisica
Apdo Postal 139-B
Cuernavaca, Morelos 62191
Mexico

BRIAN R. REID
University of Washington
Chemistry Department, BG-10
Seattle, WA 98195

PETER REYNOLDS
Office of Naval Research
Physics Division, Code 1112
800 N. Quincy Street
Arlington, VA 22217

ANN RICHARD
U.S. Environmental Protection Agency
MD-68
Research Tri. Pk., NC 27711

NIGEL RICHARDS
University of Florida
Department of Chemistry
418 Leigh Hall
Gainesville, FL 32611

MAGNUS RITTBY
Texas Christian University
Department of Physics
Box 32915
Fort Worth, TX 76129

MARK ROBERSON
The University of Utah
Department of Chemistry
Salt Lake City, UT 84112-1194

KEITH RUNGE
University of Florida
Quantum Theory Project
345 WM Hall
Gainesville, FL 32611

JOANNA SADLEJ
University of Idaho
Department of Chemistry
Moscow, ID 83843

VIRAHT SAHNI
Booklyn College of CUNY
Department of Physics
Bedford Avenue & Avenue H
Brooklyn, NY 11210

DENNIS SALAHUB
Universite de Montreal
Department of Chemistry
C.P. 6128, Succ. A
Montreal, Quebec H3C 3J7
Canada

STEPHAN P.A. SAUER
Odense Universitet
Kemsik Institut
Campusvej 55
Odense M, DK-5230
Denmark

V. R. SAUNDERS
SERC Daresbury Lab
Daresbury, Warrington WA4 4AD
United Kingdom

HENRY SCHAEFER
University of Georgia
Center for Computational
Quantum Chemistry, Chem. Bldg.
Athens, GA 30602

STEVE SCHEINER
Southern Illinois University
Department of Chemistry
Carbondale, IL 62901

HAROLD A. SCHERAGA
Cornell University
Department of Chemistry
Baker Laboratory
Ithaca, NY 14853-1301

H. BERNHARD SCHLEGEL
Wayne State University
365, Chemistry Department
Detroit, MI 48202

PETER SCHMIDT
Office of Naval Research
Chemistry Division
800 N. Quincy Street
Arlington, VA 22217-5000

DIETER SCHUCH
J.W. Goethe Universitat
Inst. F. Physikal u. Theoret.
Chemie. Niederurseler Hang
Frankfurt, Main 50 6000
Germany

PETER SCHULMEYER
Universitat Stuttgart
Inst. F. Theor. Phys.
Pfaffenwaldring 57
Stuttgart, 80 D-7000
Germany

DIANE SCOTT
Drexel University
Department of Chemistry
3200 Chestnut Street
Philadelphia, PA 19104

HIDEO SEKINO
University of Florida
Quantum Theory Project
Rm. 370 WM Hall
Gainesville, FL 32611

JORGE SEMINARIO
University of New Orleans
Department of Chemistry
New Orleans, LA 70148

MOSHE SHAPIRO
The Weizmann Institute
Chemical Physics Department
Rehovot, 76100
Israel

ISAIAH SHAVITT
Ohio State University
Department of Chemistry
120 W. 18th Ave.
Columbus, OH 43210-1173

HARRISON SHULL
Naval Postgraduate School
Code 01
Monterey, CA 93943

OKTAY SINANOGLU
Yale University
Sterling Chemistry Laboratory
P.O. Box 6666
New Haven, CT 06511

YVES G. SMEYERS
Consejo Superior de Investigaciones Cientificas
Inst. De Estructura de la Mat.
Quimica Teorica, Serrano, 123
Madrid, 28006
Spain

VEDENE SMITH
Queen's University
Department of Chemistry
Kingston, Ontario K7L 3N6
Canada

EDWARD SOLOMON
Stanford University
Department of Chemistry
Stanford, CA 94305

SHAUN SOMMERER
Penn State University,
Division of Science,
Engineering and Technology
Erie, PA 16563

RICHARD SQUIRE
Marshall University
Department of Chemistry
901 W. DuPont Avenue
Belle, WV 25015

JOHN STANTON
University of Florida
Quantum Theory Project
367 WM Hall
Gainesville, FL 32611

CLIFF STODDEN
Embry-Riddle Aeronautical University
Math & Physical Science Dept.
Daytona Beach, FL 32114

PETER SZALAY
University of Florida
Quantum Theory Project
371 WM Hall
Gainesville, FL 32611

MARIAN SZCZESNIAK
University of Florida
Chemistry Department
CLB 309
Gainesville, FL 32611

HUGH TAYLOR
University of Florida
Quantum Theory Project
376 WM Hall
Gainesville, FL 32611

AJIT J. THAKKAR
University of New Brunswick
Chemistry Department
Fredericton, NB E3B 6E2
Canada

COLIN THOMSON
University of St. Andrews
Department of Chemistry
North Haugh
St. Andrews, Fife KY169ST
Scotland

SAMUEL B. TRICKEY
University of Florida
Quantum Theory Project
364 WM Hall
Gainesville, FL 32611

MIROSLAV URBAN
Comenius University
Physical Chemistry Department
Mlynska Dolina
Bratis'ava, 84215
Czechoslovakia

PIET VAN DUIJNEN
University of Groningen
Chemistry Department
Nyenborgh 4
Groningen, AG 9747
The Netherland

PIET VAN LEUVEN
University of Antwerp
Theoretical & Math. Physics
Groenenborgerlaan 171
Antwerp, B2020
Belgium

ROBERT VERGENZ
University of North Florida
Department of Natural Sciences
Jacksonville, FL 32216

ALEXEI N. VESELKOV
Sevastopol Instrumental Development Institute
Department of Physics
Kulakova Str. 38-24
Sevastopol, 335000
USSR

OLIVIER VISSER
University of Groningen
Lab. of Chemical Physics
Nijnborgh 4
Groningen, AG 9747
The Netherlands

ANDREY VOLOSOV
Colorado State University
Department of Biochemistry
Fort Collins, Co 80523

JOHN WATTS
University of Florida
Quantum Theory Project
377 WM Hall
Gainesville, FL 32611

BRIAN WEINER
Penn State University
Physics Department
College Place
DuBois, PA 15807

HAREL WEINSTEIN
Mount Sinai School of Medicine
Dept. of Physiology & Biophys.
Box #1218, 5th Ave. & 100th St.
New York, NY 10029

STEPHEN WHITE
University of California
Physiology & Biophysics
Irvine, CA 92717

TIMOTHY WILSON
Oklahoma State University
Department of Physics
145 PSII
Stillwater, OK 74078

PETER WINKLER
University of Nevada
Department of Physics, 220
Reno, NV 89577-0058

KRZYSZTOF WOLINSKI
University of Arkansas
Department of Chemistry
Fayetteville, AR 72701

DAVID WOON
Batelle Pacific Northwest Lab
P.O. Box 999
K2-18
Richland, WA 99352

JIN ZHONG WU
University of Florida
Quantum Theory Project
368 WM Hall
Gainesville, FL 32611

DAVID YARKONY
Johns Hopkins University
Department of Chemistry
34th & Charles Street
Baltimore, MD 21218

DARRIN YORK
National Institute of Environmental Health
 Sciences
Bldg. 101; B-302
Research Tri. Pk., NC 27709

JENWEI YU
University of Florida
Quantum Theory Project
380 WM Hall
Gainesville, FL 32611

JIANGUO YU
University of Florida
Department of Chemistry
Gainesville, FL 32611

MICHAEL C. ZERNER
University of Florida
Quantum Theory Project
382 WM Hall
Gainesville, FL 32611

ZHONGXIANG ZHOU
University of North Carolina
Department of Chemistry
Chapel Hill, NC 27599-3290

Memorial Session
in Honor of
Arnold Karo

This session is dedicated to the memory of Arnold Karo who died last year, at the age of 63, after a year-long battle with lymphoma. Arnold was a theoretical chemist/solid-state physicist with the Lawrence Livermore Laboratory. He received his Ph.D. from MIT in 1953 and, after a brief service with the U.S. Army Chemical corps, he joined John Slater's group at MIT as a postdoctoral fellow, where he worked on lattice dynamics of crystalline materials. Arnold began his long association with L^3 in 1958 where he continued his work on crystalline materials, including the first detailed calculations relating structural features of experimental spectra to calculated critical features of the phonon densities of states. Many of us knew Arnold from this period of time. He was one of the old-timers at Sanibel and was one of the special people included in John Slater's famous Sanibel solid state theory group meetings that were traditionally held on the beach on Wednesday afternoon. In recent years, Arnold carried out fundamental studies on chemical laser systems and plasma properties of negative ion beams. This work was in support of the controlled nuclear fusion efforts at L^3. This memorial should not end without mention of Arnold Karo, the person. He could simply and best be described as the perfect gentleman. We have all lost a good friend.

H. Harvey Michels

Total Energies and Energy Gradients in Electron Propagator Theory

J. V. ORTIZ

*Department of Chemistry, University of New Mexico, Albuquerque, New Mexico, 87131 and
Quantum Theory Project, Departments of Physics and Chemistry, University of Florida,
Gainesville, Florida 32611-2085*

Abstract

From the second-order self-energy of electron propagator theory, one can obtain total energies for the initial, N-electron state and the final, $N \pm 1$-electron states. Recent derivations and computational studies have demonstrated the feasibility of calculating effective first-order density matrices corresponding to the electron-binding energies. One-electron properties and energy gradients of the final states are thereby made accessible. Applications to the ground and excited states of CaCN and to C_3^- illustrate the capabilities of this method. © 1992 John Wiley & Sons, Inc.

Introduction

Electron propagator theory has been applied in quantum chemistry chiefly to the calculation of vertical ionization energies and electron affinities [1-7]. Calculations of ground-state total energies and one-electron properties have been considerably less frequent in the literature [8-13]. Because electron propagator theory is a direct method, one in which an energy difference is evaluated without recourse to individual state energies or wavefunctions, it is, in principle, applicable to final states of any energy. The prospect of using electron propagator theory to optimize molecular geometries is therefore an attractive alternative to many correlated methods that concentrate chiefly on ground states. A recent derivation of gradients for the second-order self-energy has shown the feasibility of this approach [14]. These derivatives are combined with derivatives of the reference state total energy described by second-order many-body perturbation theory [15-17] to yield derivatives of final state potential energy surfaces. In addition, effective density matrices that describe the density difference between the initial and final states enable calculation of final-state properties when combined with initial-state density matrices.

It is possible to demonstrate that the potential energy surfaces for the initial state and the final states in this level of electron propagator theory have a common origin: the second-order self-energy. Using this description of electron correlation, one can obtain the second-order many-body perturbation theory expression for the initial state total energy. Electron-binding energies calculated with this self-energy therefore yield a unified treatment of total energies for the N-electron initial state

and the $N \pm 1$-electron final states. This unified treatment also affords one-electron properties for each state.

Superoperator Formulation of Electron Propagator Theory

Using superoperator notation [4,18], the electron propagator matrix, $G(E)$, is expressed as

$$G(E) = (a|(E\hat{I} - \hat{H})^{-1}a) .$$

Simple electron annihilation operators with spin-orbital labels constitute the vector a, whose length is the dimension of the spin-orbital basis. The identity superoperator, $\hat{I}$, defined by

$$\hat{I}X = X ,$$

and the Hamiltonian superoperator, $\hat{H}$, defined by

$$\hat{H}X = [X, H] ,$$

operate on simple electron field operators or on products of field operators that change the number of electrons by one. With the following choice of superoperator metric,

$$(Y|Z) = \langle 0|[Y^{+}, Z]_{+}|0\rangle ,$$

where $|0\rangle$ is an N-electron reference state, one obtains the participation of all field operators that pertain to $N \pm 1$-electron states. Note that no distinction is made between particle and hole subspaces, for all manipulations occur in Fock space.

To avoid explicit consideration of the superoperator resolvent, $(E\hat{I} - \hat{H})^{-1}$, an inner projection is employed:

$$G(E) = (a|h)(h|(E\hat{I} - \hat{H})h)^{-1}(h|a) ,$$

where the vector, h, contains all field operators on which the superoperators act. Partitioning of the last equation follows from orthonormalizing two subspaces, a and f. The ensuing block structure of $G(E)$, where

$$G(E) = [(a|a) \quad (a|f)]\begin{bmatrix} (a|(E\hat{I} - \hat{H})a) & (a|(E\hat{I} - \hat{H})f) \\ (f|(E\hat{I} - \hat{H})a) & (f|(E\hat{I} - \hat{H})f) \end{bmatrix}^{-1}\begin{bmatrix} (a|a) \\ (f|a) \end{bmatrix} ,$$

thereby simplifies to

$$[1 \quad 0]\begin{bmatrix} E1 - (a|\hat{H}a) & -(a|\hat{H}f) \\ -(f|\hat{H}a) & E1 - (f|\hat{H}f) \end{bmatrix}^{-1}\begin{bmatrix} 1 \\ 0 \end{bmatrix} .$$

Two separate strategies have been employed at this point. The first departs from the observation that only the upper left block of the inverse matrix is needed. This yields

$$G(E) = [E1 - (a|\hat{H}a) - (a|\hat{H}f)[E1 - (f|\hat{H}f)]^{-1}(f|\hat{H}a)]^{-1} .$$

A more convenient form leads to an alternative statement of the Dyson equation.

$$G^{-1}(E) = E1 - (a|\hat{H}a) - (a|\hat{H}f)$$

$$\times [E1 - (f|\hat{H}f)]^{-1}(f|\hat{H}a) = G_0^{-1}(E) - \Sigma(E)$$

where all terms not pertaining to the uncorrelated, Koopmans's theorem description of electron-binding energies are contained in the last term, the self-energy matrix. Poles occur when the determinant of $G^{-1}(E)$ vanishes; this is equivalent to searching for E_{pole} such that

$$[(a|\hat{H}a) + (a|\hat{H}f)[E_{pole}1 - (f|\hat{H}f)]^{-1}(f|\hat{H}a)]C = CE_{pole} .$$

In the second approach, one seeks the eigenvalues of the superoperator Hamiltonian matrix,

$$\begin{bmatrix} (a|\hat{H}a) & (a|\hat{H}f) \\ (f|\hat{H}a) & (f|\hat{H}f) \end{bmatrix} .$$

Insertion of these eigenvalues into the partitioned form of $G(E)$, discussed above, leads to the inversion of a matrix with a zero eigenvalue; in other words, this insertion is sufficient to produce a pole. Provided that the same superoperator Hamiltonian matrix elements are used, the two approaches are equivalent.

Derivatives of Electron-Binding Energies

Having solved for a pole of the electron propagator, E_{pole}, one can inquire into its derivatives with respect to changes in the one-electron part of the many-electron Hamiltonian. Such changes may correspond to external fields or to the field produced by the nuclei arranged in a given way. Suppose that the Dyson equation approach to discovering poles has been adopted, where

$$E_{pole} = C^\dagger(\varepsilon + \Sigma(E))|_{E=E_{pole}}C .$$

Defining the superscript, α, to denote differentiation with respect to a perturbation, one obtains

$$E_{pole}^\alpha = C^{\dagger\alpha}(\varepsilon + \Sigma(E))|_{E=E_{pole}}C + C^\dagger(\varepsilon + \Sigma(E))|_{E=E_{pole}}C^\alpha$$

$$+ C^\dagger\left(\varepsilon^\alpha + \Sigma^\alpha(E)\Big|_{E=E_{pole}} + E_{pole}^\alpha \frac{\partial\Sigma(E)}{\partial E}\Big|_{E=E_{pole}}\right)C .$$

Note that in the last of the three terms there are three portions that pertain to orbital energy derivatives, derivatives of the self-energy, where the E parameter is held constant, and derivatives of the self-energy employing the chain rule. This equation can be rearranged to

$$E_{pole}^\alpha\left(1 - C^\dagger \frac{\partial\Sigma(E)}{\partial E}\Big|_{E=E_{pole}} C\right)$$

$$= C^{\dagger\alpha}CE_{pole} + C^\dagger C^\alpha E_{pole} + C^\dagger(\varepsilon^\alpha + \Sigma^\alpha(E))|_{E=E_{pole}}C.$$

The left side of the previous equation is E_{pole}^α divided by the pole strength, P, while the first two terms on the right side vanish because

$$(C^{\dagger}C)^{\alpha} = 0.$$

Therefore,

$$E^{\alpha}_{\text{pole}} = PC^{\dagger}(\varepsilon^{\alpha} + \Sigma^{\alpha}(E)|_{E\cdot E_{\text{pole}}})C.$$

Both P and C are generated in the process of finding the pole; only explicit differentiation of the orbital energies and the self-energy matrix elements is required to obtain E^{α}_{pole}.

A similar conclusion follows from the second approach to finding poles. Denoting the entire superoperator Hamiltonian matrix as $\hat{H}$, one may express the poles as solutions of the eigenvalue problem

$$\hat{H}t = tE_{\text{pole}}.$$

Differentiation leads to

$$\hat{H}^{\alpha}t + \hat{H}t^{\alpha} = t^{\alpha}E_{\text{pole}} + tE^{\alpha}_{\text{pole}}.$$

After multiplying both sides by $t^{\dagger}$, one finds that

$$E^{\alpha}_{\text{pole}} = t^{\dagger}\hat{H}^{\alpha}t.$$

Having found a pole by this approach, one must evaluate derivatives of the superoperator Hamiltonian matrix in order to calculate E^{α}_{pole}.

Connections between the two approaches are facilitated by partitioning the eigenvectors t into their a and f portions:

$$t = [t_a \quad t_f].$$

For a given pole, the Feynman–Dyson amplitudes, C, suffice to determine the eigenvectors, t, through the following relationships,

$$t_a = \sqrt{P}C$$

$$t_f = \sqrt{P}[E_{\text{pole}}\mathbf{1} - (f\,|\,\hat{H}\,f)]^{-1}(f\,|\,\hat{H}a)C.$$

Second-Order Expression

The second-order self-energy derives from an f operator manifold consisting of products of three simple field operators. Only the Hartree–Fock (HF) contribution to the superoperator reference state is needed. Operators with two-particle and one-hole indices or with two-hole and one-particle indices are needed to produce all second-order terms. Letting i, j, k, l be occupied spin-orbital indices, a, b, c, d, be virtual indices, and p, q, r, s be general indices, one can express the superoperator matrix elements in terms of canonical orbital energies and transformed electron repulsion integrals. The zeroth-order elements of $(a|\hat{H}a)$,

$$H_{pq} = \delta_{pq}\varepsilon_p,$$

the first-order elements of $(a|\hat{H}f)$,

$$H_{p,ab} = \langle pi \| ab \rangle, \qquad a < b$$

$$H_{p,aij} = \langle pa \| ij \rangle, \qquad i < j.$$

and zeroth-order elements of $(f | \hat{H} f)$,

$$H_{iab,jcd} = (\varepsilon_a + \varepsilon_b - \varepsilon_i)\delta_{ij}\delta_{ac}\delta_{bd}$$

$$H_{aij,bkl} = (\varepsilon_i + \varepsilon_j - \varepsilon_a)\delta_{ab}\delta_{ik}\delta_{jl}.$$

suffice to obtain second-order poles in either of the approaches discussed above. Higher order expressions result from retaining additional terms generated by correlated reference state averages.

From the above expressions for E_{pole}^{α}, one obtains

$$E_{\text{pole}}^{\alpha} = \sum_{pq} t_p^* H_{pq}^{\alpha} t_q + \sum_p t_p^* \sum_{ia<b} H_{p,iab}^{\alpha} t_{iab} + \sum_p t_p^* \sum_{ai<j} H_{p,aij}^{\alpha} t_{aij}$$

$$+ \sum_{ia<b} t_{iab}^* \sum_p H_{iab,p}^{\alpha} t_p + \sum_{ai<j} t_{aij}^* \sum_p H_{aij,p}^{\alpha} t_p + \sum_{ia<b} t_{iab}^* \sum_{jc<d} H_{iab,jcd}^{\alpha} t_{jcd}$$

$$+ \sum_{ai<j} t_{aij}^* \sum_{bk<l} H_{aij,bkl}^{\alpha} t_{bkl}.$$

In second order,

$$t_p = \sqrt{P} C_p$$

and

$$t_{iab} = \sqrt{P}[E_{\text{pole}} + \varepsilon_i - \varepsilon_a - \varepsilon_b]^{-1} \sum_p \langle ab \| pi \rangle C_p$$

$$t_{aij} = \sqrt{P}[E_{\text{pole}} + \varepsilon_a - \varepsilon_i - \varepsilon_j]^{-1} \sum_p \langle ij \| pa \rangle C_p.$$

Therefore,

$$E_{\text{pole}}^{\alpha} = P \sum_{pq} C_p^* C_q \left\{ H_{pq}^{\alpha} + \sum_{ia<b} \left(\frac{H_{p,iab}^{\alpha} H_{iab,q}}{E_{\text{pole}} + \varepsilon_i - \varepsilon_a - \varepsilon_b} + \frac{H_{p,iab} H_{iab,q}^{\alpha}}{E_{\text{pole}} + \varepsilon_i - \varepsilon_a - \varepsilon_b} \right. \right.$$

$$+ \frac{H_{p,iab}}{E_{\text{pole}} + \varepsilon_i - \varepsilon_a - \varepsilon_b} H_{iab,iab}^{\alpha}$$

$$\left. \times \frac{H_{iab,q}}{E_{\text{pole}} + \varepsilon_i - \varepsilon_a - \varepsilon_b} \right)$$

$$+ \sum_{ai<j} \left(\frac{H_{p,aij}^{\alpha} H_{aij,q}}{E_{\text{pole}} + \varepsilon_a - \varepsilon_i - \varepsilon_j} + \frac{H_{p,aij} H_{aij,q}^{\alpha}}{E_{\text{pole}} + \varepsilon_a - \varepsilon_i - \varepsilon_j} \right.$$

$$\left. \left. + \frac{H_{p,aij}}{E_{\text{pole}} + \varepsilon_a - \varepsilon_i - \varepsilon_j} H_{aij,aij}^{\alpha} \frac{H_{aij,q}}{E_{\text{pole}} + \varepsilon_a - \varepsilon_i - \varepsilon_j} \right) \right\}.$$

Similar expressions will arise for more complicated forms of the self-energy matrix or the superoperator Hamiltonian matrix [14].

Reference State Total Energies

When added to or subtracted from a reference state total energy, electron-binding energies yield final state total energies. A reference state total energy expression derived from the same self-energy expression employed for the electron-binding energies would provide a reasonable choice for the purpose of optimizing geometries on final state potential energy surfaces. The ground state total energy is related to the electron propagator through a contour integral that encloses the ionization energy poles [1,2]:

$$\langle H \rangle = \frac{1}{2} \, \text{Tr} \, \frac{1}{2\pi i} \int_c (\mathbf{h} + E\mathbf{1}) \mathbf{G}(E) dE .$$

In the above expression, $\mathbf{h}$ is the matrix of the one-electron part of the electronic Hamiltonian. Insertion of $\mathbf{G}_0(E)$, where

$$\mathbf{G}_0(E) = (E\mathbf{1} - \varepsilon)^{-1} ,$$

in this equation results in the HF expectation value, that is, the energy expression is correct through first order in the fluctuation potential. Closed forms for correlated energies have been sought through an alternative form of the Dyson equation,

$$\mathbf{G}(E) = \mathbf{G}_0(E) + \mathbf{G}_0(E)\boldsymbol{\Sigma}(E)\mathbf{G}(E) ,$$

which, in iterated form,

$$\mathbf{G}(E) = \mathbf{G}_0(E) + \mathbf{G}_0(E)\boldsymbol{\Sigma}(E)\mathbf{G}_0(E) + \mathbf{G}_0(E)\boldsymbol{\Sigma}(E)\mathbf{G}_0(E)\boldsymbol{\Sigma}(E)\mathbf{G}_0(E) + \cdots ,$$

provides terms of various orders for a given choice of $\boldsymbol{\Sigma}(E)$. A consistent counting of orders in the fluctuation potential discloses that the matrix, $\mathbf{h}$, introduces terms of zeroth and first order when it is rewritten in terms of the Fock matrix and the Coulomb-exchange potential matrix:

$$\mathbf{h} = \mathbf{f} - \mathbf{v} .$$

By consolidating terms of the same order, it is possible to identify two separate contributions to the total energy expression through order n [12]:

$$E^{(n)} = \frac{1}{2} \, \text{Tr} \, \frac{1}{2\pi i} \int_c (\mathbf{f} + E\mathbf{1}) \mathbf{G}^{(n)}(E) dE - \frac{1}{2} \, \text{Tr} \, \frac{1}{2\pi i} \int_c \mathbf{v} \mathbf{G}^{(n-1)}(E) dE$$

Second-order many-body perturbation theory can be recovered by inserting the second-order expression

$$\mathbf{G}^{(2)}(E) = \mathbf{G}_0(E) + \mathbf{G}_0(E)\boldsymbol{\Sigma}^{(2)}(E)\mathbf{G}_0(E)$$

into the first term on the left side of the previous equation [2]; the other term is zero because $\mathbf{G}^{(1)}(E)$ vanishes.

TABLE I.   CaCN bond lengths (Å) and total energies (au).

Isomer	State	Ca-X	C-N	Total energy
CaCN	X$^2\Sigma^+$	2.365	1.206	−768.7801299
	A$^2\Pi$	2.357	1.205	−768.6941171
	B$^2\Sigma^+$	2.332	1.207	−768.6924186
CaNC	X$^2\Sigma^+$	2.221	1.203	−768.7768773
	A$^2\Pi$	2.220	1.203	−768.6892728
	B$^2\Sigma^+$	2.210	1.203	−768.6844680

Only the second-order self-energy matrix is needed to produce reasonable approximations for the total energies of the reference state and the final states in electron propagator theory. Second-order many-body perturbation theory total energies for the N-electron reference state may be supplemented by second-order self-energy results from electron propagator theory to produce final state total energies for states with $N \pm 1$ electrons.

Applications

Reference state total energies and gradients at the second-order level are calculated with GAUSSIAN 90 [19]. Electron-binding energies and their gradients are calculated with a modified version of EPT90 [20]. Detailed formulas for the second-order electron propagator gradients have been derived and presented in spin-orbital form elsewhere [14].

Calcium Cyanide Ground and Excited States

Using the closed-shell cation, CaCN$^+$, as a reference. it is possible to study the ground and excited states of CaCN by adding various electron affinities to the reference state potential energy surface. This molecule is an interesting test case for the present methods for several reasons. First, there is a low-lying excited state with the same symmetry as the ground state. Second, there is the possibility of linkage

TABLE II.   CaCN harmonic frequencies (cm^{-1}).

Isomer	State	$\sigma_{Ca-X\ stretch}$	$\sigma_{C-N\ stretch}$	π
CaCN	X$^2\Sigma^+$	364	1969	143
	A$^2\Pi$	369	1973	144
	B$^2\Sigma^+$	375	1961	127
CaNC	X$^2\Sigma^+$	415	2052	89
	A$^2\Pi$	416	2057	87
	B$^2\Sigma^+$	412	2056	25i

TABLE III.   CaCN dipole moments (D).

Isomer	State	Dipole moment
CaCN	$X^2\Sigma^+$	6.485
	$A^2\Pi$	6.402
	$B^2\Sigma^+$	6.516
CaNC	$X^2\Sigma^+$	6.474
	$A^2\Pi$	6.362
	$B^2\Sigma^+$	6.845

isomerism for all states, that is, it is possible that there are minima with CaCN and CaNC geometries [21]. Finally, there are questions surrounding the origin of emission bands that lie to the red of the lowest absorption frequencies [22,23].

A $5s,3p,2d$ basis for Ca, obtained from a previous study [24], is combined with a $3s,2p,1d$ description for C and N [25]. All molecular orbitals are retained in the post-HF calculations. The default convergence criteria employed for geometry optimizations in GAUSSIAN 90 are retained: a maximum force of 0.00045, a maximum root mean square force of 0.0003, a maximum displacement of 0.0018, and a maximum root mean square displacement of 0.0012. Final state geometries and total energies, calculated as the sum of the CaCN$^+$ second-order total energy and the second-order electron propagator electron affinity, are listed in Table I. The Ca–X distance pertains to the nucleus loser to Ca in each isomer. Optimizations on the A$^2\Pi$ states performed with and without a symmetry axis converge to identical results. Evaluation of finite differences of final state gradients permits the determination of harmonic frequencies, which are listed in Table II. For the A$^2\Pi$ states, the lower symmetry calculations are performed for the $^2A'$ state that arises from the degenerate state in $C_{\infty v}$ symmetry. Most of the stationary points are minima, although some of the harmonic frequencies are very small. One of the optimized geometries has an imaginary bending frequency. A definitive study of the relative energies of the stationary points and their curvatures must await, at the very least, a testing of basis-set effects. Because the expressions for the gradients of the cationic reference state total energies and of the electron affinities include effective density

TABLE IV. $^2B_2$ C_3 properties.

Property	CCSD	CCSDT	EPT
Total energy (au)	-113.300286	-113.328883	-113.330573
Bond length (Å)	1.337	1.350	1.337
Bond angle (degrees)	68.3	68.0	68.6
ω_1 a_1 (cm^{-1})	1668	1601	1677
ω_2 a_1 (cm^{-1})	687	638	720
ω_3 b_2 (cm^{-1})	1215	1194	1287

TABLE V. $^2\Sigma_u^+$ C$_3^+$ properties.

Property	CCSD	CCSDT	EPT
Total energy (au)	−113.279310	−113.321152	−113.326453
Bond length (Å)	1.314	1.327	1.322
$\omega_1\ \sigma_g$			1168
$\omega_2\ \pi_u$			260
$\omega_3\ \sigma_u$	2500i	451i	2032i
Energy relative to $^2B_2$ (kcal/mol)	13.2	4.9	2.6

matrices for one-electron properties, the sum of the reference state's effective density and that of the electron affinity provides a density matrix that describes the final state's electronic distribution. Dipole moments calculated with this information are listed in Table III.

C$_3^+$ Minima and Transition States

Potential energy surfaces for C_3^+ have been extensively studied with a variety of theoretical techniques [26–28]. Among the difficulties encountered by previous workers are multiple unrestricted HF solutions with sharply contrasting amounts of spin contamination for the $^2B_2$ ground state of the C_{2v} isomer. This finding prompted a recent work in which coupled cluster energies calculated with unrestricted HF and restricted, open-shell HF reference states were compared with results from a quasi-restricted HF reference state. The latter approach bears some resemblance to the present electron propagator method, for orbitals optimized for the closed-shell molecule C_3 are employed. The same $4s,2p,1d$ basis used in the coupled cluster work is used in these calculations [26]. Tables IV and V compare the present methods to two methods based on an unrestricted HF reference configuration, coupled cluster singles and doubles and coupled cluster singles, doubles, and triples. The total energies for the electron propagator results are lower because no orbitals have been discarded from the correlated calculations. Structures, harmonic frequencies, and relative energies display close agreement with the coupled cluster results. It is worth noting that coupled cluster singles and doubles calculations with open-shell HF or quasi-restricted HF reference states yield results that are very close to their unrestricted HF counterparts in Table IV.

Conclusions

From the second-order self-energy of the electron propagator, it is possible to derive a general description of the N-electron ground state and final states with $N \pm 1$ electrons. For the ground state, one must take care that orders in the fluctuation potential are consistently treated; the simplest correlated example leads to the second-order total energy of many-body perturbation theory. Procedures for evaluating derivatives of this total energy with respect to changes in the one-electron part of

the Hamiltonian are well known. Evaluation of derivatives of electron-binding energies from the electron propagator has been implemented recently. Only derivatives of the superoperator Hamiltonian matrix are needed. Difference density matrices emanate from the derivation, enabling the calculation not only of final state gradients, but one-electron properties as well. In the case where a closed-shell HF calculation defines the reference propagator, no spin contamination is introduced in the final state doublets. Applications to cases where ionization energies and electron affinities are calculated in order to study the species of interest have shown the versatility of this approach. One of the most attractive aspects of the energy dependence of the self-energy matrix is reinforced here, for optimizations on excited states of a given symmetry can now be undertaken routinely.

Acknowledgments

Bibliography

[1] J. Linderberg and Y. Öhrn, *Propagators in Quantum Chemistry* (Academic, New York, 1973).
[2] B. Pickup and O. Goscinski, Molec. Phys. **26**, 1013 (1973).
[3] L. S. Cederbaum and W. Domcke, Adv. Chem. Phys. **26**, 206 (1977).
[4] Y. Öhrn and G. Born, Adv. Quant. Chem. **13**, 1 (1981).
[5] M. F. Herman, K. F. Freed, and D. Yeager, Adv. Chem. Phys. **48**, 1 (1981).
[6] W. von Niessen, J. Schirmer, and L. S. Cederbaum, Comput. Phys. Rep. **1**, 57 (1984).
[7] J. Simons, Theor. Chem. Adv. Perspectives **3**, 1 (1978).
[8] J. D. Doll and W. P. Reinhardt, J. Chem. Phys. **57**, 1169 (1972).
[9] P. W. Langhoff and A. J. Hernandez, Chem. Phys. Lett. **49**, 361 (1977).
[10] V. Carravetta and R. Moccia, Molec. Phys. **35**, 129 (1978).
[11] J. Schirmer and G. Angonoa, J. Chem. Phys. **91**, 1754 (1989).
[12] L. J. Holleboom and J. Snijders, J. Chem. Phys. **93**, 5826 (1990).
[13] M. Jaszunski, B. T. Pickup, and R. McWeeny, Chem. Phys. Lett. **90**, 167 (1982).
[14] J. Cioslowski and J. V. Ortiz, J. Chem. Phys. (to appear).
[15] R. J. Bartlett, Ann. Rev. Phys. Chem. **32**, 359 (1981).
[16] E. A. Salter, G. W. Trucks, and R. J. Bartlett, Chem. Phys. Lett. **141**, 61 (1987).
[17] J. A. Pople, R. Krishnan, H. B. Schlegel, and J. S. Binkley, Int. J. Quant. Chem., Quant. Chem. Symp. **13**, 225 (1979).
[18] O. Goscinski and B. Lukman, Chem. Phys. Lett. **7**, 573 (1970).
[19] M. J. Frisch, M. Head-Gordon, G. W. Trucks, J. B. Foresman, H. B. Schlegel, K. Ragavachari, M. Robb, J. S. Binkley, C. Gonzalaz, D. J. Defrees, D. J. Fox, R. A. Whiteside, R. Seeger, C. F. Melius, J. Baker, R. L. Martin, L. R. Kahn, J. J. P. Stewart, S. Topiol, and J. A. Pople, GAUSSIAN 90 (Revision F) (Gaussian, Inc., Pittsburgh, PA, 1990).
[20] J. V. Ortiz, EPT90, an *ab initio* electron propagator program: J. V. Ortiz, Int. J. Quant. Chem., Quant. Chem. Symp. **23**, 321 (1989).
[21] C. W. Bauschlicher, S. R. Langhoff, and H. Partridge, Chem. Phys. Lett. **115**, 124 (1985).
[22] M. Douay and P. F. Bernath, Chem. Phys. Lett. **174**, 230 (1990).
[23] C. J. Whitham, B. Soep, J. P. Visticot, and A. Keller, J. Chem. Phys. **93**, 991 (1990).

[24] J. V. Ortiz, J. Chem. Phys. **92**, 6728 (1990).
[25] T. H. Dunning and P. J. Hay, in *Methods of Electronic Structure Theory*, H. F. Schaefer, Ed. (Plenum Press, New York, 1977). C and N d exponents are 0.6 and 0.864, respectively.
[26] J. D. Watts, J. F. Stanton, and R. J. Bartlett, J. Chem. Phys. **94**, 4320 (1991).
[27] K. Ragavachari, Chem. Phys. Lett. **171**, 249 (1990).
[28] R. S. Grev, I. L. Alberts, and H. F. Schaefer, J. Phys. Chem. **94**, 3379, 8744 (1990).

The Perturbed Electron Propagator Approach to Molecular Response Properties

B. T. PICKUP

Department of Chemistry, University Sheffield, United Kingdom S3 7HF

Abstract

A new method is presented for the calculation and analysis of static linear and nonlinear response properties. The method involves the use of a perturbed electron propagator formalism, and is a correlated generalization of standard scf-level coupled Hartree-Fock (or RPA) schemes. © 1992 John Wiley & Sons, Inc.

Introduction

The theory and calculation of the response of a molecular system to an external applied field [1] has developed into an important research area in modern quantum chemistry [2,3], since it embraces a vast area of research, from applied subjects such as nonlinear optics [4] and material design, through to the theory of inter-molecular forces. A recent review of a wide range of molecular properties is given by Fowler [5]. The theory and computational methods [8,9] for both static and frequency-dependent molecular response properties have been refined over many years by many authors. The commonest methods of calculation involve scf-level response properties via so-called coupled Hartree-Fock (CPHF) approaches (in either AO or MO basis sets) [10], or the equivalent random-phase approximation (RPA) [11], which also gives direct access to the polarization propagator [6,7], and hence, to excitatioi, energies of low-lying electronic excited states, transition amplitudes, and also frequency dependent polarizabilities. Algorithms for computations exist inside most of the major *ab initio* codes such as GAUSSIAN XX, CADPAC, HONDO, SYSMO, etc. The theory for computations, including the higher order effects or correlation (e.g., MCSCF approaches), has also been detailed [12], although published calculations are as yet uncommon because of the cost. Polarization prop-agator codes are also conventional, but in the guise of the RPA method, which is accurate through first-order in terms of correlation. The higher order (in terms of correlation) versions of this (SOPPA, and its coupled cluster variant [8]) are com-putationally expensive, and are unviable for all but the smallest molecules, such as saturated first row hydrides. The theory for quadratic response is also worked out at the scf and MCSCF levels [12], although the correlated versions are not yet fully implemented. Indeed, accurate near-basis limit calculations of quadratic response are rare, even at the scf level.

The aim of this work is to present a new approach to linear and nonlinear (initially quadratic) static response tensors by exploiting the power and elegance of the electron propagator (EP) approach [13,14] for correlated calculations of the one-electron density. The EP is well known for accurate computations of molecular ionization and attachment energies. These emerge directly out of a system of eigenvalue equations based upon the EP equations of motion [15]. The method is well-known and established, but there is no obvious connection with response tensors. It is true, however, that a numerically simple contour integration over a special contour, the renowned Coulson contour [16], directly produces also the correlated *ground state* one-electron density [19], and hence, any one-electron property expectation value. The present work arose by trying to generalize an analysis of CPHF linear response tensors produced by Grant and Pickup [17]. This latter uses a breakdown of the SCF first order perturbed one density into direct and induced terms, and hence, produces an appealing picture of response in terms of polarization, back polarization, and self-interaction of the perturbed density. The basic idea of the present work is to study the effect of an external applied field upon the EP, and hence, to obtain the *correlated* perturbed density through Coulson contour integration. There has been an early attempt at a Green's function formulation of the linear response problem [18], though only in the SCF approximation.

The perturbed electron propagator is described in detail in the next section. The third section gives the form of the dynamic perturbed self energy at second order in correlation, while the section after details the analysis of Grant and Pickup for the correlated case. The fifth section outlines possible calculations, while the following one describes the results of pilot calculations on a series of small molecules. The last section briefly describes the use of the method for quadratic response.

The Perturbed Electron Propagator

Let us consider a static (time-independent) one-electron perturbation

$$h^{(1)} = \sum_{pq} h^{(1)}_{pq} a^\dagger_p a_q \tag{1}$$

in terms of an orthonormal spinorbital basis. This one-electron perturbation can represent the effect of an externally applied electric or magnetic field, or even a perturbation arising from the displacement of a nucleus [3]. In general, we must acknowledge that a field may have a set of components, so that we must decompose the operator

$$h^{(1)} = \sum_\pi V_\pi F_\pi \tag{2}$$

into a sum over components labeled by the index π. The factors, F_π, are variable-strength factors. We can express the expectation value of the operator in (1) as

$$\langle h^{(1)} \rangle = \langle \Psi^N_0 | h^{(1)} | \Psi^N_0 \rangle = \sum_{pq} h^{(1)}_{pq} \langle a^\dagger_p a_q \rangle = \text{tr } \mathbf{h}^{(1)} \rho_1 \tag{3}$$

where the one-density is defined in the normalization of McWeeny [2]. We now introduce the (causal) electron propagator matrix [20] defined in terms of its spectral resolution as

$$G_{1qp} = \langle\langle a_p^\dagger; a_q \rangle\rangle_\omega = \sum_a \left\{ \frac{\langle \Psi_0^N | a_q | \Psi_a^{N+1} \rangle \langle \Psi_a^{N+1} | a_p^\dagger | \Psi_0^N \rangle}{\omega + E_0^N - E_a^{N+1} + i\epsilon} \right\}$$

$$+ \sum_i \left\{ \frac{\langle \Psi_0^N | a_p^\dagger | \Psi_i^{N-1} \rangle \langle \Psi_i^{N-1} | a_q | \Psi_0^N \rangle}{\omega - E_0^N + E_i^{N-1} - i\epsilon} \right\} \quad (4)$$

The one-density matrix can be derived firstly from the electron propagator via the contour integration over the Coulson contour, $\mathcal{C}$

$$\mathcal{C} \{ G_{1qp} \} = \frac{1}{2\pi i} \int_c d\omega\, G_{1qp}(\omega) = \sum_i \langle \Psi_0^N | a_p^\dagger | \Psi_i^{N-1} \rangle$$

$$\times \langle \Psi_i^{N-1} | a_q | \Psi_0^N \rangle = \langle a_p^\dagger a_q \rangle = \rho_{1qp} \quad (5)$$

where the $\mathcal{C}$-operator is a shorthand notation for the integration over the Coulson contour encircling the ionization poles, and we have used the $(N-1)$-electron completeness relation to provide the final two identities.

We now return to the subject of response theory, considering that all the definitions above apply to a perturbed system in which the operator representing the external field (1), has been added to the Hamiltonian. We are interested in expanding the expectation value (3) in powers of the perturbation

$$\langle h^{(1)} \rangle = \langle h^{(1)} \rangle^{(0)} + \langle h^{(1)} \rangle^{(1)} + \langle h^{(1)} \rangle^{(2)} + \cdots \quad (6)$$

where the term $\langle h^{(1)} \rangle^{(n)}$ represents the nth-order response of the system to the field. In terms of the density the nth order change in the expectation value is

$$\langle h^{(1)} \rangle^{(n)} = \text{tr}\, h^{(1)} \rho_1^{(n)} = \text{tr}\, \mathcal{C} \{ h^{(1)} G_1^{(n)} \} \quad (7)$$

The electron propagator matrix satisfies the equation [13,14]

$$G_1 = (\omega 1 - F(\rho_1^{HF}) - \Sigma(\omega))^{-1} \quad (8)$$

where the Fock matrix *in the presence of the perturbing field*

$$F(\rho_1^{HF}) = h^{(0)} + h^{(1)} + J(\rho_1^{HF}) - K(\rho_1^{HF}) \quad (9)$$

is expressed in terms of the perturbed HF density, which, assuming we use a basis of MOs (defined in the presence of the field) implies

$$\rho_{1pq}^{HF} = \delta_{pq} n_p \quad (10)$$

with

$$n_p = \begin{cases} 1 & p \in \text{occ} \\ 0 & p \in \text{virt} \end{cases} \quad (11)$$

The two-electron part of (9) is commonly denoted by the G matrix

$$G_{pq}(\rho_1^{HF}) = J_{pq}(\rho_1^{HF}) - K_{pq}(\rho_1^{HF}) = \sum_{rs} \langle pr\|qs\rangle \rho_{1sr}^{HF} \qquad (12)$$

which is distinguished from the electron propagator by the lack of suffix "1." The self energy matrix in (8) contains all the effects of correlation, and can be divided into two terms

$$\Sigma(\omega) = \Sigma(\infty) + M(\omega) \qquad (13)$$

The first term on the left hand side of (13) is the frequency-independent (so-called "constant") term,

$$\Sigma_{pq}(\infty) = \sum_{rs} \langle pr\|qs\rangle [\rho_{1sr} - \rho_{1sr}^{HF}] \qquad (14)$$

which can be obtained in the limit as $\omega \rightarrow \infty$, since the dynamic self-energy, M, is zero in this limit. Using arguments based upon the energy uncertainty principle, we can interpret the constant part of the self energy as representing the instantaneous response of a correlated many electron system to the presence of a hole or a particle. The dynamic self energy, on the other hand, is dependent upon the frequency and contains all relaxation and reorganization effects which are on a long time scale. It is normal in the electron propagator formalism to expand the dynamic self energy in a perturbation theory defined in terms of the correlation potential. In this way we can define second- and higher-order electron propagators. It is vital to distinguish this perturbation expansion in terms of the fluctuation potential from the entirely separate one we intend to make for the applied external field.

It is convenient to include the constant part of the self energy with the Fock operator to give

$$G_1 = (\omega 1 - F(\rho_1) - M(\omega))^{-1} \qquad (15)$$

The Fock operator above is defined in terms of the exact perturbed one-density.

We now make a perturbation expansion of the propagator in powers of the external applied field using

$$G_1 = G_1^{(0)} + G_1^{(1)} + G_1^{(2)} + \cdots \qquad (16)$$

which is achieved via

$$F(\rho_1) = F(\rho_1)^{(0)} + F(\rho_1)^{(1)} + F(\rho_1)^{(2)} + \cdots$$

$$M = M^{(0)} + M^{(1)} + M^{(2)} + \cdots \qquad (17)$$

and an expansion of the inverse. We can now identify the perturbed Green's functions by expansion of (15) as

$$G_1^{(0)} = (\omega 1 - F^{(0)} - M^{(0)})^{-1}$$

$$G_1^{(1)} = G_1^{(0)}(F^{(1)} + M^{(1)})G_1^{(0)}$$

$$G_1^{(2)} = G_1^{(0)}[F^{(2)} + M^{(2)} + (F^{(1)} + M^{(1)})G_1^{(0)}(F^{(1)} + M^{(1)})]G_1^{(0)}$$

$$\vdots \tag{18}$$

The perturbed Fock operators are

$$F(\rho_1)^{(0)} = h^{(0)} + G(\rho_1^{(0)})$$

$$F(\rho_1)^{(1)} = h^{(1)} + G(\rho_1^{(1)})$$

$$F(\rho_1)^{(n)} = G(\rho_1^{(n)}) \qquad n \geq 2 \tag{19}$$

An expression for the first-order dynamic self energy is derived in the next section. We can identify the individual terms in the expansion of the inverse as

$$G_1 = (\omega 1 - F^{(0)} - M^{(0)} - F^{(1)} - M^{(1)} - F^{(2)} - M^{(2)} - \cdots)^{-1} \tag{20}$$

The densities appearing in the above equations are correlated densities defined through Coulson integration as

$$\rho_1^{(n)} = \mathcal{C}\{G_1^{(n)}\} \tag{21}$$

We shall now analyze the linear response via the first-order coupled equations arising from eqs. (18) and (20):

$$\rho_1^{(1)} = \mathcal{C}\{G_1^{(0)}(F^{(1)} + M^{(1)})G_1^{(0)}\} \tag{22}$$

It is of some interest to investigate (22) in the HF limit, in which we put

$$G_1^{(0)} \to (\omega 1 - \varepsilon)^{-1}$$

$$M^{(1)} \to 0 \tag{23}$$

where the matrix ε is a diagonal matrix of SCF orbital energies, since we are working in a canonical HF basis. In eq. (23) we have assumed that the basis set with respect to which the propagator matrices are defined is a canonical HF basis, in which case the zeroth order propagator is expressed entirely in terms of the diagonal matrix of Koopmans' orbital energies. It follows that

$$\rho_{1qp}^{(1)} = \frac{1}{2\pi i} \int_c d\omega \frac{F_{qp}^{(1)}}{(\omega - \varepsilon_p)(\omega - \varepsilon_q)} \tag{24}$$

for two general MO indices, p and q. Using the notation, $i, j \in$ occ and $a, b \in$ virt, and noting that only ionization poles (occupied Koopmans's orbital energies in the present context) are included in the Coulson contour, it is easy to show that

$$\frac{1}{2\pi i} \int_c d\omega \frac{1}{(\omega - \varepsilon_i)(\omega - \varepsilon_j)} = 0$$

$$\frac{1}{2\pi i} \int_c d\omega \frac{1}{(\omega - \varepsilon_a)(\omega - \varepsilon_b)} = 0$$

$$\frac{1}{2\pi i} \int_c d\omega \frac{1}{(\omega - \varepsilon_i)(\omega - \varepsilon_a)} = \frac{1}{\varepsilon_i - \varepsilon_a} \tag{25}$$

so that the only nonzero blocks of (24) are

$$
\rho^{(1)}_{1ia} = \frac{F^{(1)}_{ia}}{\varepsilon_i - \varepsilon_a} \; ; \; \rho^{(1)}_{1ai} = \frac{F^{(1)}_{ai}}{\varepsilon_i - \varepsilon_a}
\tag{26}
$$

which are just the well-known first-order perturbed SCF equations (or CPHF) in the MO basis.

We now consider eq. (22) in the case where we have formally exact Green's functions. We shall first analyze the equations assuming that the perturbed dynamic self-energy $M^{(1)} \to 0$. Using the spectral resolution of the propagator (4), and defining the poles

$$
E_i = E_0^N - E_i^{N-1} \; ; \qquad E_a = E_a^{N+1} - E_0^N
\tag{27}
$$

and the Dyson spinorbitals

$$
g_i(x) = \sum_p \psi_p(x) h_{pi} = \sum_p \psi_p(x) \langle \Psi_i^{N-1} | a_p | \Psi_0^N \rangle
$$

$$
f_a(x) = \sum_p \psi_p(x) h_{pa} = \sum_p \psi_p(x) \langle \Psi_0^N | a_p | \Psi_a^{N+1} \rangle
\tag{28}
$$

Using eqs. (27) and (28) in (4) and (22) gives the first-order coupled perturbed electron propagator equations (1-CPEP) in the following form

$$
\rho^{(1)}_{1qp} = \sum_{ia} \frac{F^{(1)}_{ia} b_{qi} b^*_{pa} + F^{(1)}_{ai} b_{qa} b^*_{pi}}{E_i - E_a}
\tag{29}
$$

where the matrix elements

$$
F^{(1)}_{ia} = \langle g_i | F^{(1)} | f_a \rangle ; \qquad F^{(1)}_{ai} = \langle f_a | F^{(1)} | g_i \rangle
\tag{30}
$$

are expressed using Dyson spinorbitals rather than the plain MO matrix elements found in coupled HF. Indeed using the expression for the one-density function,

$$
\rho_1(x, x') = \sum_{pq} \psi_q(x) \psi_p(x')^* \rho_{1qp} ,
\tag{31}
$$

it is easily seen that eq. (29) is just a Dyson orbital expansion of the first-order perturbed one-density

$$
\rho_1^{(1)}(x, x') = \sum_{ia} \frac{F^{(1)}_{ia} g_i(x) f_a(x')^* + F^{(1)}_{ai} f_a(x) g_i(x')^*}{E_i - E_a}
\tag{32}
$$

It should be noted that the Dyson spinorbitals form an unnormalized, nonorthogonal, and linearly dependent set of spinorbitals [21].

It is obvious that the 1-CPEP equations are identical in structure to the CPHF equations, but using correlated poles and amplitudes instead of Koopmans's orbital energies and MO coefficients. We have, of course, neglected the perturbed self-energy, $M^{(1)}$, a defect which we now remedy.

The Perturbed Dynamic Self Energy

The dynamic self energy can be expressed through second-order in terms of the correlation potential as

$$M_{pq}(\omega) = M_{pq}^{\text{hole}}(\omega) + M_{pq}^{\text{particle}}(\omega) \tag{33}$$

where the hole contribution

$$M_{pq}^{\text{hole}}(\omega) = \frac{1}{2} \sum_{ija} \frac{\langle pa \| ij \rangle \langle ij \| qa \rangle}{\omega - \varepsilon_i - \varepsilon_j + \varepsilon_a} \tag{34}$$

and the particle part

$$M_{pq}^{\text{particle}}(\omega) = \frac{1}{2} \sum_{abi} \frac{\langle pi \| ab \rangle \langle ab \| qi \rangle}{\omega - \varepsilon_a - \varepsilon_b + \varepsilon_i} \tag{35}$$

We adhere throughout to the convention that orbitals labeled $i, j, k, \ldots$, refer to occupied molecular spinorbitals, while $a, b, c, \ldots$, are virtuals, and $p, q, \ldots$, are general in nature. The antisymmetrized two-electron integrals are defined as

$$\langle pi \| ab \rangle = \langle pi | ab \rangle - \langle pi | ba \rangle \tag{36}$$

The formulae shown refer to the basis of canonical spin molecular orbitals in terms of which the HF reference determinant is specified. We now consider that a perturbation of the form (1, 2) has been applied with an arbitrary set of infinitesimal strength factors, F_x. In this instance, the orbitals are perturbed by the infinitesimal field. We shall signify these perturbed orbitals by placing primes on the orbital indices. We write the perturbed self energy as

$$M_{pq}(\omega)' = M_{pq}^{\text{hole}}(\omega)' + M_{pq}^{\text{particle}}(\omega)' \tag{37}$$

with

$$M_{pq}^{\text{hole}}(\omega)' = \frac{1}{2} \sum_{ija} \frac{\langle pa' \| i'j' \rangle \langle i'j' \| qa' \rangle}{\omega - \varepsilon_i' - \varepsilon_j' + \varepsilon_a'}$$

$$M_{pq}^{\text{particle}}(\omega)' = \frac{1}{2} \sum_{abi} \frac{\langle pi' \| a'b' \rangle \langle a'b' \| qi' \rangle}{\omega - \varepsilon_a' - \varepsilon_b' + \varepsilon_i'} \tag{38}$$

One subtlety in connection with (38) is that the indices, p, q, the matrix indices, are unprimed. The perturbed orbitals are orthonormal as are the unprimed ones, and are therefore a unitary transformation of the unperturbed ones. It follows that we are free to express the matrix indices in any basis we choose. We choose the unperturbed basis. We are not free to choose the basis in terms of which the i, j, a and a, b, i summations are expressed. This latter basis must be in terms of orbitals which make the *perturbed* Fock operator diagonal, i.e., a perturbed canonical basis. We can expand these perturbed canonical spinorbitals through first order as

$$|p'\rangle \rightarrow |p\rangle + |p^{(1)}\rangle = |p\rangle + \sum_{q \ne p} |q\rangle \frac{F_{qp}^{(1)}}{\varepsilon_p - \varepsilon_q} \tag{39}$$

where the unperturbed (field free) orbitals and orbital energies are indicated without the superscript (i.e., $\varepsilon_p^{(0)} = \varepsilon_p$, and $|q\rangle = |q^{(0)}\rangle$). The perturbation expression for the orbital energies is

$$\varepsilon_p' \rightarrow \varepsilon_p + \varepsilon_p^{(1)} = \varepsilon_p + F_{pp}^{(1)} \tag{40}$$

Substitution of (39, 40) into (38), followed by an expansion through first order gives

$$
\begin{aligned}
M_{pq}^{(1)\text{hole}}(\omega) = &\ \frac{1}{2} \sum_{ija} \frac{\langle pa\|ij\rangle(F_{ii}^{(1)} + F_{jj}^{(1)} - F_{aa}^{(1)})\langle ij\|qa\rangle}{(\omega - \varepsilon_i - \varepsilon_j + \varepsilon_a)^2} \\
&+ \frac{1}{2} \sum_{ija} \sum_{r \ne a} \frac{F_{ar}^{(1)}\langle pr\|ij\rangle\langle ij\|qa\rangle + \langle pa\|ij\rangle\langle ij\|qr\rangle F_{ra}^{(1)}}{(\varepsilon_a - \varepsilon_r)(\omega - \varepsilon_i - \varepsilon_j + \varepsilon_a)} \\
&+ \sum_{ija} \sum_{r \ne i} \frac{F_{ir}^{(1)}\langle pa\|ij\rangle\langle rj\|qa\rangle + \langle pa\|rj\rangle\langle ij\|qa\rangle F_{ri}^{(1)}}{(\varepsilon_i - \varepsilon_r)(\omega - \varepsilon_i - \varepsilon_j + \varepsilon_a)}
\end{aligned} \tag{41}
$$

This expression contains three terms, the first arising from the expansion of the orbital energies in the primed denominators, while the remaining two are from orbital perturbations of the primed numerators. The first term varies as $O(1/\omega^2)$, while the others have one constant (i.e., frequency independent) denominator. These constant denominators contain differences between particle (or hole) and *general* spinorbitals. We usually expect many-body perturbation theory expressions to involve only differences between occupied (hole) and virtual (particle) subspaces. The summations in the second terms over r can be broken up into sums over occupied and virtual spaces. After some magical but mindless manipulations, the final expression for the first-order perturbed hole contribution to the dynamic self energy is

$$
\begin{aligned}
M_{pq}^{(1)\text{hole}}(\omega) = &\ \sum_{ijka} \frac{\langle pa\|ij\rangle F_{ik}^{(1)}\langle kj\|qa\rangle}{(\omega - \varepsilon_i - \varepsilon_j + \varepsilon_a)(\omega - \varepsilon_k - \varepsilon_j + \varepsilon_a)} \\
&- \frac{1}{2} \sum_{ijab} \frac{\langle ij\|qa\rangle F_{ab}^{(1)}\langle pb\|ij\rangle}{(\omega - \varepsilon_i - \varepsilon_j + \varepsilon_a)(\omega - \varepsilon_i - \varepsilon_j + \varepsilon_b)} \\
&+ \sum_{ijab} \frac{F_{ib}^{(1)}\langle pa\|ij\rangle\langle bj\|qa\rangle + \langle pa\|bj\rangle\langle ij\|qa\rangle F_{bi}^{(1)}}{(\varepsilon_i - \varepsilon_b)(\omega - \varepsilon_i - \varepsilon_j + \varepsilon_a)} \\
&- \frac{1}{2} \sum_{ijak} \frac{F_{ak}^{(1)}\langle pk\|ij\rangle\langle ij\|qa\rangle + \langle pa\|ij\rangle\langle ij\|qk\rangle F_{ka}^{(1)}}{(\varepsilon_k - \varepsilon_a)(\omega - \varepsilon_i - \varepsilon_j + \varepsilon_a)}
\end{aligned} \tag{42}
$$

The reduction of the particle part of the first-order perturbed dynamic self energy is carried out in the same way to give

$$M_{pq}^{(1)particle}(\omega) = \sum_{iab} \frac{\langle pi|ab\rangle F_{ia}^{(1)}\langle ab|qi\rangle}{(\omega - \epsilon_a - \epsilon_b + \epsilon_i)(\omega - \epsilon_a - \epsilon_b + \epsilon_i)}$$

$$-\frac{1}{2}\sum_{iab}\frac{\langle ab|qi\rangle F_{ia}^{(1)}\langle pi|ab\rangle}{(\omega - \epsilon_a - \epsilon_b + \epsilon_i)(\omega - \epsilon_a - \epsilon_b + \epsilon_i)}$$

$$-\sum_{iab}\frac{\langle pi|jb\rangle\langle ab|qi\rangle F_{M}^{(1)} + F_{a}^{(1)}\langle pi|ab\rangle\langle jb|qi\rangle}{(\epsilon_i - \epsilon_a)(\omega - \epsilon_a - \epsilon_b + \epsilon_i)}$$

$$+\frac{1}{2}\sum_{iab}\frac{F_{ia}^{(1)}\langle pi|ab\rangle\langle ab|qi\rangle + \langle pi|ab\rangle\langle ab|qi\rangle F_{a}^{(1)}}{(\epsilon_i - \epsilon_a)(\omega - \epsilon_a - \epsilon_b + \epsilon_i)} \qquad (43)$$

It should be noticed that the first-order dynamic self energy contains terms strictly first order in the applied field, which involve the two-electron interaction through the perturbed Fock operator, $F^{(1)}$. If these terms are to be accounted for exactly in the CPHP procedure, then we must include the dynamic self energy in the iteration scheme.

We now define the total first-order perturbed one-density via (22) as

$$\rho_1^{(1)} = \rho_1^{(1)stat} + \rho_1^{(1)dyn} \qquad (44)$$

where the static correlated one-density arises purely from the Fock operator portion of (22), and the dynamic self-energy contribution to the perturbed one-density comes from the *dynamic* self energy

$$\rho_1^{(1)dyn} = C\{G_1^{(0)}M^{(1)}G_1^{(0)}\} \qquad (45)$$

which contains a product of three frequency-dependent contributions.

The dynamic coupling scheme is implemented at second-order in the correlation potential using eq. (45), together with (42) and (43), in the form

$$\rho_{1pq}^{(1)dyn} = \sum_{rs} C\{G_{1pr}^{(0)}M_{rs}^{(1)}G_{1sq}^{(0)}\} = \sum_{rs}\Delta_{pqrs}F_{rs}^{(1)} \qquad (46)$$

where the precise form of the matrix elements, Δ, actually depends upon the occupancy of the spinorbitals p, q, s, r. The precise form of the matrix elements has been derived by the author through second order in correlation. It is easy also to see that (46) is the correct form through all orders in correlation, although this statement needs diagrammatic analysis for its proof.

Analysis of Linear Response Properties

We now consider the generalization of the analysis of the linear response which has been described by Grant and Pickup [17] for SCF-level linear response properties. Using eqs. (7), (45), and (46), and the cyclic invariance of the trace operation, we deduce that

$$\langle h^{(1)}\rangle^{(1)} = \text{tr } C\{G_1^{(0)}h^{(0)}G_1^{(0)}F^{(1)}\} + \text{tr } h^{(1)}\rho_1^{(1)dyn} \qquad (47)$$

We can now proceed by elimination of

$$G_1^{(0)} h^{(1)} G_1^{(0)}$$

from (47), using (22), to give

$$\text{tr } \mathcal{C} \{ G_1^{(0)} h^{(1)} G_1^{(0)} F^{(1)} \} = \text{tr } \mathcal{C} \{ (G_1^{(0)} h^{(1)})^2 \} + \text{tr } \rho_1^{(1)} G(\rho_1^{(1)})$$
$$- \text{tr } \mathcal{C} \{ G_1^{(0)} [G(\rho_1^{(1)}) + M^{(1)}] G_1^{(0)} \} G(\rho_1^{(1)}) \quad (48)$$

We can recognize inside the equation above that the $M^{(1)}$ term can be rewritten in terms of the matrix Δ in (46) to give

$$\langle h^{(1)} \rangle^{(1)} = \text{tr } \mathcal{C} \{ (G_1^{(0)} h^{(1)})^2 \} + \text{tr } \rho_1^{(1)} G(\rho_1^{(1)}) - \text{tr } \mathcal{C} \{ (G_1^{(0)} G(\rho_1^{(1)}))^2 \}$$
$$+ \text{tr } h^{(1)} \rho_1^{(1)dyn} - \text{tr } \rho_1^{(1)dyn} G(\rho_1^{(1)}) \quad (49)$$

The final two terms of (49) are reduced by substitution of (46) to give the final expression

$$\langle h^{(1)} \rangle^{(1)} = \text{tr } \mathcal{C} \{ (G_1^{(0)} h^{(1)})^2 - (G_1^{(0)} G(\rho_1^{(1)}))^2 \} + \text{tr } \rho_1^{(1)} G(\rho_1^{(1)})$$
$$+ \sum_{pqrs} \{ h_{pq}^{(1)} \Delta_{qp,sr} h_{rs}^{(1)} - G_{pq}(\rho_1^{(1)}) \Delta_{qp,sr} G_{rs}(\rho_1^{(1)}) \} \quad (50)$$

The five terms in (50) can be interpreted in the following manner:

1. The static direct term, $E^{(2)stat\,dir}$, is the interaction between a one-electron field and a system of correlated interacting electrons which are frozen into the zero-field form:

2. The static back polarization, $E^{(2)stat\,back}$, is the response of the system arising solely from the field induced by the total (static plus dynamic) perturbed electron density;

3. The third term, $E^{(2)stat\,int}$, the static interaction, is the self-interaction (Coulomb minus exchange) of the perturbed one-density;

4. The fourth contribution, $E^{(2)dyn\,dir}$, is the dynamic analog of the direct static response; and

5. The final term, the dynamic back polarization, $E^{(2)dyn\,back}$, is the dynamic analog of the static back polarization.

In the HF limit, the last two terms, which are purely correlation effects, are absent. The first three contributions reduce to the terms described by Grant and Pickup.

It is instructive to write expressions for the first two parts of (50) in the Dyson orbital basis. Using the spectral resolution of the electron propagator as before, we derive

$$E^{(2)dir} = \sum_{ia} \frac{|\langle g_i | h^{(1)} | f_a \rangle|^2}{E_i - E_a}$$

$$E^{(2)back} = \sum_{ia} \frac{|\langle g_i | G(\rho_1^{(1)}) | f_a \rangle|^2}{E_i - E_a}. \quad (51)$$

The three static contributions to the correlated linear response are all contributions arising from instantaneous interactions. The hole and particle Dyson orbitals ap-

pearing in eq. (51) are just the correlated versions of the HF MOs. They describe holes and particles which, in the static equations, can interact with the applied field, $h^{(1)}$, and in the average field, $G(p_1^{(1)})$, induced by the perturbed density, but the hole and particle orbitals are not mutually polarized. These latter effects are accounted for by the dynamic contributions.

Algorithms for CPEP Calculations

The CPEP approach can be implemented in at least two different forms. The first, the analytic method, is to carry out all Coulson integrals *exactly*, using the approximate calculated spectral expansions (i.e., using poles and Dyson orbitals explicitly) computed using standard implementations of the EP method. Once these are known, the Coulson integrals can be carried out exactly as in (25), and they lead to equations such as (29), which involves sums over Dyson orbital matrix elements and differences in hole and particle pole energies. The analytic approach requires the computation of all poles which contribute significantly to the response. There are basically two kinds of poles in the EP equations. These are best discussed in terms of the pole strength, defined as the norm of the Dyson orbitals, viz.

$$P_i = \langle g_i | g_i \rangle; \qquad P_a = \langle f_a | f_a \rangle, \tag{52}$$

respectively, for the hole (ionization) and particle (attachment) processes. The two types of poles are those with pole strengths close to unity, and those with small pole strengths. We shall term these primary and shake events, respectively. The primary poles are those linked to Koopmans's theorem, in the sense that the respective states are dominated by configurations in which a hole (or particle) is added to the HF sea. These are the poles close to the Koopmans's orbital energies in the outer valence and core regions of the photoelectron (ionization) spectrum. Similar comments apply to the attachment spectrum, with the reservation that discrete HF states may not exist for anions, i.e., we may merely be producing discretizations of the continuum in this case. The shake events are all the nonprimary states dominated by configurations involving simultaneous orbital removal (or addition) and excitation. These events tend to have small pole strengths, the intensity having been borrowed from the primary poles. There are large numbers of these shake poles even in small basis calculations, and it is well known that in the inner valence region (for instance, involving ionization of $2s$-like electrons in first-row atoms) of the ionization spectrum, the orbital picture tends to break down because of the large numbers of shake poles interacting strongly with the primary poles. A similar phenomenon occurs in the attachment spectrum. If we examine eq. (29) for the perturbed density, we see a spectral expansion in terms of all particle and hole poles, and the question arises as to which are important in deciding the polarizability, and which are not. This consideration is affected by two factors, the first being quantities in numerator, and the second the energy differences in the denominator. In comparison with the CPHF cases, where only (Koopmans's) primary poles are present in the sum, on introduction of correlation there are many more terms, but the norms of the Dyson orbitals are all reduced. This latter effect may

tend to reduce the polarizability. The "band gap" implied by the difference E_i – E_a, however, tends to be decreased by the effects of correlation, a factor tending to enhance the perturbed density. The resultant polarizability arises from the net effect of both of these trends and may be lower or higher than the CPHF values depending on the case. The effect of the dynamic terms is unknown at this time, but is likely to be very important.

There are basically two methods used for computing Dyson orbitals and poles. The first is the Dyson equation approach, in which the zero eigenvalues of the matrix inverse of eq. (8) are computed. This method produces selected poles and Dyson orbitals iteratively. It is not a useful technique for obtaining *all poles* as required in principle by the analytic method described above. An alternative method is the "large matrix" method [22] derived from the algebraic superoperator of Pickup and Goscinski [15]. This method exists in the form of a suite of programs, SHEEP (the Sheffield Electron Propagator Program) [23]. SHEEP can iteratively diagonalize an operator $\bar{\sigma}$ equation containing information about primary and shake ionization and attachment poles, or for small cases (in which individual symmetry blocks have dimensions of less than 1000), it can do in core diagonalization of selected symmetry blocks of the superoperator Hamiltonian matrix. The test calculations given in this study are all based upon this latter option and, for this reason, we do not claim to have produced a viable algorithm. The alternative method to the analytic one is to carry out Coulson integrals using quadrature. Hence, one bases the coupled equations on the form (22), rather than (29). We can define the quantity

$$\Gamma_{pq,sr} = \mathcal{C} \{ \mathbf{G}^{(0)}_{1pr} \mathbf{G}^{(0)}_{1sq} \} \tag{53}$$

from which it follows (neglecting dynamic correlation) that

$$\rho^{(1)}_{1pq} = \sum_{rs} \Gamma_{pq,sr} F^{(1)}_{rs} \tag{54}$$

Inclusion of dynamic correlation leads to

$$\rho^{(1)}_{1pq} = \sum_{rs} (\Gamma_{pq,sr} + \Delta_{pq,sr}) F^{(1)}_{rs} . \tag{55}$$

The Γ and Δ quantities are both matrices labeled by four indices. They can both be efficiently computed using numerical quadrature in the complex plane in the traditional manner [19]. This quadrature requires only the construction of the matrix $\mathbf{G}^{(0)}_1(iz_k)$ at specific frequencies $\omega = iz_k$ along the imaginary axis, the integration points being derived from a transformed Gauss–Legendre formula. The construction of this quantity at second order in correlation is rather trivial, since we need a linear process

$$\Gamma_{pq,sr} = \frac{1}{\pi} \sum_k A_k \operatorname{Re} \{ \mathbf{G}^{(0)}_{1pr}(iz_k) \mathbf{G}^{(0)}_{1sq}(iz_k) \} \tag{56}$$

A similar procedure can be worked out for the quantity Δ. Both quantities can be computed only once and stored in core, or in a file, depending on the storage

available. The Γ and Δ quantities do not depend in any way upon the nature of the perturbation. Eq. (55) is not the most efficient way to organize the CPEP iterative loops. It is better to form the two subsidiary quantities

$$A_{pq}^{(1)} = \sum_{rs} (\Gamma_{pq,sr} + \Delta_{pq,sr}) h_{rs}^{(1)} \tag{57}$$

and

$$B_{pq,ut} = \sum_{rs} (\Gamma_{pq,sr} + \Delta_{pq,sr}) \langle ru \| st \rangle \tag{58}$$

in terms of which (56) can be rearranged as

$$p_{1pq}^{(1)} = A_{pq}^{(1)} + \sum_{tu} B_{pq,ut} p_{1tu}^{(1)} \tag{59}$$

The main cost is obviously in the procedure is the initial calculation of the quantities Γ and Δ. The former is not very expensive provided one can (as seems likely) throw away shake processes with very large energies. In addition, it is not necessary to use fully transformed two-electron integrals for the construction of Γ. The iterations implied by (59) are actually no more expensive than CPHF iterations, and can be considered as a "dressed" (correlated) version of CPHF. The four-indexed quantity, B, is independent of the field, so that it can be used time and time again to obtain response to different external fields (or nuclear perturbations). The matrix, $A^{(1)}$, does depend on the perturbation, and must be formed in a zeroth iteration for each different kind of field. The CPEP procedure, whether in analytic or numerical (56) forms, can be carried out with or without the Δ terms arising from dynamic correlation. We refer to the two possibilities as static and dynamic CPEP, respectively.

Calculations

The trial calculations were carried out with the H_2O, HF, and N_2 molecules in a STO 6-31G basis set. The algorithm used was the static analytic one described in the last section. The algorithm for the unperturbed IP calculation was that of Baker and Pickup [22], in which the superoperator matrix comprised 533, 341, and 1404 operators respectively, 13, 11, and 18 of which correspond to Koopmans's primary processes. The individual symmetry blocks of the C_{2v} (and D_{2h} for N_2) point group were separately diagonalized using a standard Householder method, and the poles and Dyson orbitals were stored on the propagator dumpfile. A separate CPEP program has been written to perform the iterative procedure. The algorithm uses symmetry to cut down the time spent in the construction of the polar sums. The program does not yet include dynamic self-energy effects. The method is able to handle perturbations from any external field, including multipolar electrostatic, as well as magnetic cases. We have not included an option to handle nuclear derivatives, although this is an obvious and relatively trivial extension of the method. Results for H_2O are shown in Table I, and for HF in Table II. It is unfortunate that it was not possible to do calculations using extended basis sets as in Grant and Pickup [17]. This is because of the large matrix diagonalizations required. Matrix sizes

TABLE I. CPHF and CPHP calculations of the dipole polarizabilities of water (in au) using a STO 631G basis. $O = 104.45°$, $R = 1.8104$ au. The z-axis is the C_2 axis, and the molecule is in the xz-plane.

Method	Static direct	Interaction	Static back	Full	Component
CPHF	4.8127	2.8899	-1.0491	6.6536	xx
	0.9839	0.6585	-0.2486	1.3938	yy
	3.2914	1.8967	0.7733	4.4148	zz
CPHP, 2nd order	5.3113	3.1380	-1.1568	7.2925	xx
	1.1255	0.9551	0.4231	1.6575	yy
	3.6742	2.3343	0.9980	5.0106	zz
CPHP, full H33	5.2591	3.0846	-1.1360	7.2077	xx
	1.1187	0.9314	-0.4085	1.6416	yy
	3.6374	2.2790	0.9699	4.9466	zz
CPHP, 3rd order	5.0851	2.8180	-1.0115	6.8916	xx
	1.0829	0.7798	-0.3153	1.5474	yy
	3.5003	1.9990	-0.8218	4.6775	zz

increase rapidly with the orbital basis, since the number of hole and particle poles rise like n^2m and m^2n, respectively, where n and m are the numbers of occupied and virtual orbitals in the basis. Larger basis calculations await the numerical approach outlined in the last section, although we already have some tentative indications that fairly accurate polarizabilities can be obtained excluding the highest orbitals from the four-index transformation. This point needs further study. The 631G basis set we have used does not describe response effects (to dipolar perturbations) very well, since it does not have the necessary diffuse and polarization functions. The basis set is particularly deficient for out-of-plane directions, and this

TABLE II. CPHF And CPHP calculations of the dipole polarizabilities (in au) of hydrogen fluoride using a STO 631G basis. $R = 1.7719$ au. The molecule is oriented down the x-axis.

Method	Static direct	Interaction	Static back	Full	Component
CPHF	3.0791	1.7071	-0.6622	4.1240	xx
	0.4619	0.2908	-0.1017	0.6510	yy
	0.4619	0.2908	0.1017	0.6510	zz
CPHP, 2nd order	3.3927	1.8399	-0.7166	4.5159	xx
	0.5292	0.3953	0.1584	0.7661	yy
	0.5292	0.3953	-0.1584	0.7661	zz
CPHP, full H33	3.3550	1.8004	-0.6995	4.4559	xx
	0.5241	0.3834	-0.1516	0.7559	yy
	0.5241	0.3834	0.1516	0.7559	zz
CPHP, 3rd order	3.2357	1.6408	-0.6255	4.2509	xx
	0.5040	0.3264	0.1193	0.7110	yy
	0.5040	0.3264	-0.1193	0.7110	zz

results in polarizabilities which are too asymmetric. The other main effect of a small basis is that the interaction component is too large. This comes about because of the artificial compression of the perturbed density, i.e., the only variational freedom is in terms of relatively contracted orbitals, so that perturbed electron density is confined to a relatively small volume. In the basis limit, the perturbed density would be much more delocalized, and this markedly decreases the interaction from the values seen here. Overall, this effect pushes the direct static contribution to the total polarizability down to the 70 region from the value expected in an extended basis of ~90. The effect of correlation is to raise the total polarizability for all components of both of these molecules. The increases are largest in the second-order EP calculations, amounting to 13.5 along the C_2 axis of H_2O, and 9.8 down the C_∞ axis of HF. The increase across the H_2O molecule is 9.6. The largest percentage increases due to correlation are seen in the out-of-plane (perpendicular to the bond in the HF case) directions, namely 18.9 for H_2O, and 17.7 for HF. In absolute terms, about 80 of the increase in second-order polarizability comes from the direct term both in the bond direction for HF, and across the molecule for H_2O. In the C_2 direction for H_2O this figure is down to 64. Less than 60 of the increase perpendicular to the bond in HF, and out of plane for H_2O, comes from the direct term. Correlated calculations of dipolar polarizabilities have been carried out by Sadlej for HF and H_2O, using the finite field approach, in conjunction with MP4 [24]. The basis set used was a medium-sized basis, specially developed by Sadlej, and which produces excellent polarizabilities. For this reason we cannot compare directly with our own work. Sadlej's correlation corrections tend to be somewhat larger than ours. This is probably partly a basis set effect, but may also arise because our results do not include the effects of dynamic correlation. MP4 is, of course, correct to fourth order in a perturbation theory developed in terms of the correlation potential. The CPEP method also includes fourth-order terms, since "second order," in an electron propagator sense, implies corrections to the *self energy* in second order. By virtue of eq. (8), there are correlation corrections included in the eventual perturbed density which are summed up through infinite order. CPEP also includes correlations in a self-consistent way by virtue of its iterative nature. The au. or believes, therefore, that it is at least potentially a superior approach to methods such as Sadlej's, provided that it can be efficiently carried out in appropriate basis sets. The pattern of results for these two saturated molecules is best explained by looking at the changes in pole strength and polar energies on introducing correlation. Table III shows orbital energies, pole energies, and pole strengths for H_2O calculated in the second-order EP approximation. The 13 primary poles and the four largest shake poles are shown (out of the total of 520 shake poles) in order of increasing energy for the Green's function results. One notices immediately that the changes from Koopmans's theorem to correlated poles are largest for the ionization poles $1a_1$ to $1b_1$. The percentage changes on correlation for the $1b_2$, $3a_1$, $1b_1$, $4a_1$, and $2b_2$ poles are 6.4, 15, 20, 6.9, and 5.4, respectively. The largest relative changes, therefore, occur for the $3a_1$ and $1b_1$ poles. The y, x, and z perturbations implied by a homogeneous (dipolar) field have B_1, B_2, and A_1 symmetry, respectively. There are no MOs in a 631G basis transforming

TABLE III.   SCF orbital energies and EP2 pole energies (in au.) and pole strengths for the H_2O molecule using a STO 631G basis. The geometry and orientation are as in Table I.

Designation	Orbital energy	Pole energy	Pole strength
$1a_1$	−20.5606	−19.8426	0.7703
$2a_1$	−1.3560	−1.2518	0.6865
$2a_1$ shake		−1.1931	0.2062
$1b_2$	−0.7096	0.6644	0.9384
$3a_1$	−0.5605	−0.4751	0.9200
$1b_1$	−0.5014	−0.3996	0.9150
$4a_1$	0.2036	0.1896	0.9817
$2b_2$	0.2997	0.2835	0.9760
$3b_2$	1.0570	1.0158	0.8860
$5a_1$	1.1866	1.0905	0.8514
$2b_1$ shake		1.0993	0.3360
$2b_1$	1.1644	1.1051	0.5985
$6a_1$ shake		1.1589	0.2800
$6a_1$	1.2157	1.1656	0.6073
$4b_2$	1.3792	1.2429	0.6423
$4b_2$ shake		1.3419	0.2533
$7a_1$	1.6963	1.6171	0.8748

as A_2, so that for the y-perturbation, the hole-particle excitations produced by the perturbation involve $a_1 \to b_1$, and vice versa. The lowest excitations will provide the highest contributions to the polarizability and, in this case, these are $1b_1 \to 4a_1$, and $3a_1 \to 2b_1$. The former is the lowest excitation, and the 20% lowering of the $1b_1$ on correlation provides the most important increase in polarizability on correlation. The $2b_1$ attachment pole has an important shake component which steals intensity from the main pole. In this case, the marked reduction in pole strength probably overcomes any gain in polarizability implied by the energy shifts due to correlation. The x perturbation has, as its most important excitation contributions, $3a_1 \to 2b_2$ and $1b_2 \to 4a_1$. These are higher energy excitations than those found for y, so the shifts in poles after correlation have much less effect on the polarizability. The z-perturbation has slightly more effective excitation contributions, with $3a_1 \to 4a_1$ being the most important. It is well known that second-order EP calculations overestimate the correlation shifts in Koopmans' ionization poles, an effect which is corrected in higher order. This shows up as a reduced polarizability for the higher order Green's function calculations.

The results for nitrogen are given in Table IV. They show quite a different pattern to the other two molecules. N_2 has already been noted as anomalous by Grant and Pickup [17], since it has a static back component in the bond (x-) direction which far outweighs the interaction term. The effect of correlation this time, is to reduce the total polarizability, but the reduction is smaller for the higher order Green's function calculations. The perpendicular polarizability components behave more like those for saturated molecules.

TABLE IV. CPHF And CPEP calculations of the dipole polarizabilities (in au) of N_2 using a STO-63lG basis, R = 2.074 au. The molecule is oriented down the x-axis.

Method	Static direct	Interaction	Static back	Full	Component
CPHF	17.4668	0.1251	3.4578	14.1341	xx
	3.9238	1.2121	0.2617	4.8742	yy
	3.9238	1.2121	0.2617	4.8742	zz
CPEP, 2nd order	16.2160	0.2111	2.9762	13.4508	xx
	4.1302	1.2735	0.2869	5.1168	yy
	4.1302	1.2735	0.2869	5.1168	zz
CPEP, full H33	16.5237	0.1678	3.0766	13.6149	xx
	4.1439	1.2773	0.2881	5.1331	yy
	4.1439	1.2773	0.2881	5.1331	zz
CPEP, 3rd order	16.9312	0.0979	3.1525	13.8766	xx
	4.0934	1.2109	0.2643	5.0400	yy
	4.0934	1.2109	0.2643	5.0400	zz

Quadratic Response

In CPHF theory, the quadratic response can be calculated using only information from the first-order perturbed density. The CPEP version of the theory can be derived straightforwardly using the formalism outlined previously. It is obvious that terms arise in the second-order perturbed propagator which depend upon $F^{(2)}$, the second-order perturbed Fock operator, and also the second-order dynamic self-energy, $M^{(2)}$. It is not obvious that these second-order terms can be removed from the equations. We have been able to prove that this is so, however [25]. Neglecting the dynamic terms, it is very easy to show that

$$\langle h^{(1)} \rangle^{(2)} = \left\{ \sum_{iab} \frac{F_{ia}^{(1)} F_{ab}^{(1)} F_{bi}^{(1)}}{(E_i - E_a)(E_i - E_b)} - \sum_{ija} \frac{F_{ia}^{(1)} F_{ij}^{(1)} F_{ja}^{(1)}}{(E_i - E_a)(E_j - E_a)} \right\} \quad (60)$$

The construction of quadratic response tensors is, therefore, relatively straightforward once the first-order equations are solved.

Acknowledgments

Bibliography

[1] A. D. Buckingham, Adv. Chem. Phys. 12, 107–142 (1967).
[2] R. McWeeny, Methods of Molecular Quantum Mechanics (Academic, London, 1989).

[3] B. T. Pickup, in *Methods in Computational Chemistry* (vol. 6) S. J. Wilson, Ed. (to appear).

[4] D. S. Chemla and J. Zyss, Eds., *Nonlinear Optical Properties of Organic Molecules and Crystals*, (vols. 1 and 2). (Academic, New York, 1987).

[5] P. W. Fowler, Ann. Rep. Chem. Soc. C84, 3–42 (1987).

[6] J. Linderberg and Y. Öhrn, *Propagators in Quantum Chemistry* (Academic, New York, 1973).

[7] P. Jørgensen and J. Simons. *Secon Quantisation-Based Methods in Quantum Chemistry* (Academic, New York, 1981).

[8] J. Oddershede, Adv. Chem. Phys. 69, 201–239 (1987).

[9] C. E. Dykstra, S.-Y. Liu, and D. J. Malik, Adv. Chem. Phys. 75, 37–111 (1989).

[10] G. H. F. Diercksen and R. McWeeny, J. Chem. Phys. 44, 3554 (1966); R. McWeeny and G. H. F. Diercksen, J. Chem. Phys. 49, 4852 (1968).

[11] D. J. Thouless, *Quantum Mechanics of Many Body Systems* (Academic, New York, 1961); Nucl. Phys. 21, 225 (1960); Nucl. Phys. 22, 78 (1961).

[12] J. Olsen and P. Jørgensen. J. Chem. Phys. 82, 3235–3264 (1985).

[13] G. Y. Csanak, H. S. Taylor, and R. Yaris, Adv. Atom. Molec. Phys. 7, 287–361 (1971).

[14] L. S. Cederbaum and W. Domcke, Adv. Chem. Phys. 36, 205–344 (1977).

[15] B. T. Pickup and O. Goscinski, Molec. Phys. 26, 1013–1035 (1973).

[16] C. A. Coulson and M. S. Longuet-Higgins, Proc. Camb. Phil. Soc. 36, 201 (1940).

[17] A. J. Grant and B. T. Pickup, Chem. Phys. Lett. 174, 523–530 (1990).

[18] H. K. McDowell and R. N. Porter, J. Chem. Phys. 65, 4210–4217 (1976).

[19] L. J. Holleboom, J. G. Snijders, E. J. Baerends, and M. A. Buijse, J. Chem. Phys. 89, 3638 (1988).

[20] D. N. Zubarev, Usp. Fiz. Nauk. (English trans.) 71, 71–116 (1960); Sov. Phys. Usp. 3, 320–324 (1960).

[21] O. Goscinski and P. Lindner, J. Math. Phys. 11, 1313–1317 (1970).

[22] J. Baker and B. T. Pickup, Chem. Phys. Lett. 76, 537 (1980); Molec. Phys. 49, 651 (1983).

[23] B. T. Pickup, J. Baker, and D. H. Mosley, *The Sheffield Electron Propagator Package*, University of Sheffield (1976–92).

[24] A. J. Sadlej, Coll. Czech. Chem. Commun. 53, 1995 (1988).

[25] B. T. Pickup (to appear).

Second-Order Green's Function Simulations of the Valence XPS Spectra of Unsaturated Hydrocarbons

M. DELEUZE, P. HORECZKY, and J. DELHALLE

Laboratoire de Chimie Théorique Appliquée, Facultés Universitaires Notre Dame de la Paix Rue de Bruxelles 61, B-5000 Namur, Belgium

B. T. PICKUP

Department of Chemistry, the University, Sheffield S3 7HF, United Kingdom

Abstract

The second-order self-energy is expressed in terms of the the zeroth-order polarization propagator. The polarizability dependence of the many-body features in the ionization spectra is assessed by means of second-order Green's function simulation of the XPS valence spectra of the 1,3-hexadiene, 1,4-hexadiene 1,5-hexadiene, 1,3-cyclohexadiene, 1,4-cyclohexadiene molecules, the open forms being considered in several conformations. Variations in the one-particle and many-body features determining the shape of the spectra are also interpreted in terms of the molecular primary and secondary structures. © 1992 John Wiley & Sons, Inc.

Introduction

Extensive work on valence-shell photoelectron (PE) spectra of saturated hydrocarbons has been successfully conducted [1,2] on the assumption that there is a one-to-one correspondence between the main bands in the PE spectrum and the molecular orbitals; most of the spectra of the saturated alkane molecules have been theoretically interpreted on the basis of the one-particle Hartree–Fock (HF) model and the Koopmans approximation. Despite the neglect of correlation and relaxation effects in the description of the ionization process, significant information on the primary and secondary structure of oligomeric and polymeric systems have been obtained, through the interplay of theory and experiment, from XPS valence spectra. However, in a recent study conducted on model folds of crystalline polyethylene, it has been shown that inclusion of relaxation and correlation effects can be important when the search for signature of conformational changes in valence XPS spectra comes to the tricky question of photoionization intensity [3].

On the other hand, for ionization out of the valence orbitals of unsaturated hydrocarbons, there are several experimental [4–7] and theoretical [8–10] investigations available which indicate strong correlation and reorganization effects in the form of a shift of the ionization potentials by several eV and even a reordering of the effective electron energy levels compared to the HF approximation. In the more extreme situations, as for instance the ionization of an electron from an inner-valence orbital, important interactions between excited

configurations in the ionized system can occur, resulting in a complete "break-down of the molecular orbital picture" [11–15] for the ionization process: the intensity is spread out over several lines of comparable intensity, and the distinction between the main and the "shake-up" lines is no longer possible. Even in the case of a partial conservation of the one-particle picture, one should then at least take into account the dispersion of the main photoionization intensities in shake-up and scattering processes to obtain reliable simulation of the inner-valence XPS spectra, this energy region being the one that provides the most specific information on the molecular structure. However, reliable calculations of ionization potentials and spectral intensities are difficult in the valence energy region, the number of excited states that have to be taken into account to ensure definite conclusions being generally very high. In addition, the energies and interaction elements may be strongly basis set dependent.

Particularly well-adapted to the description of interacting particle systems, the one-particle Many-Body Green's Function method (MBGF; also referred to as the one-particle propagator method) has been shown to yield reliable simulation of ionization spectra for a large variety of molecules [16]. In this contribution, the second-order MBGF method is applied to the simulation of the XPS spectra of similar molecules differing essentially in their degree of conjugation. Because of the decreasing quality of the molecular orbital picture for the ionization process, structural information will be difficult to obtain from the ionization spectra of the most conjugated compounds. The aim of this investigation is to study the relationship between structural aspects (cyclization, isomerization, and conformation) and the one-particle and many-body features in the ionization spectra.

Outline of Theory

The one-particle propagator (Green's function) is closely related to the photo-electron spectrum. In time space representation, the one-particle propagator, defined as,

$$G_{ij}(t_2, t_1) = i^{-1} \langle \Psi_0^N | T_{ii} \{ a_i(t_2), a_j^\dagger(t_1) \} | \Psi_0^N \rangle \tag{1}$$

describes the probability amplitude of propagation, depending on the time ordering (t_1, t_2), of an extra-particle (or a hole) from the HF spin-orbital $\chi_i(\chi_j)$ to the HF spin-orbital $\chi_j(\chi_i)$, because of dynamic correlation effects. In this expression, $|\Psi_0^N\rangle$ is the exact ground state wavefunction and T_{ii} is the Wick chronological operator. The creation and annihilation operators are expressed in the Heisenberg representation. The propagation of a hole being equivalent, from the point of view of charge transportation, to the propagation of an electron backward in time, these processes can be diagrammatically represented, using the Feynman convention, as in Figure 1(a).

In the Green's function method, Hartree–Fock energies and wavefunction are taken as a zeroth-order solution for a perturbation expansion. In the background of the noninteracting HF ground state wavefunction, either hole or particle cannot be scattered to other states, and the one-particle HF propagator is diagonal with
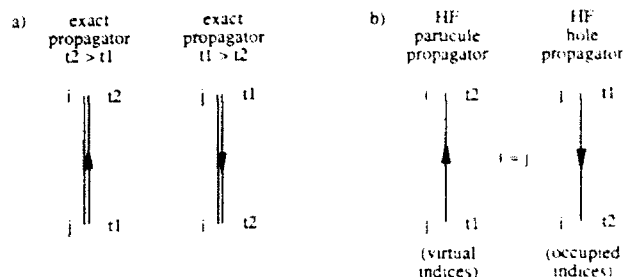
Figure 1. Exact and HF propagators.
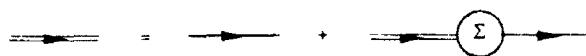
Figure 2. The diagrammatic Dyson equation.
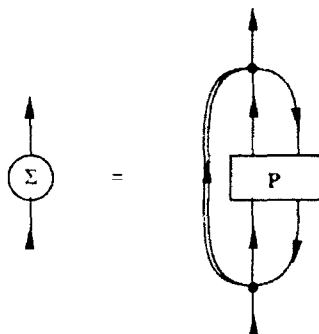
Figure 3. Partial expansion of the self-energy using the polarization propagator, P.
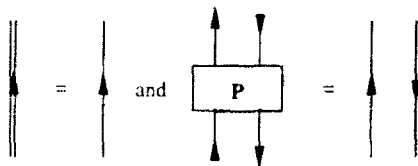
Figure 4. Propagators involved in the second-order expansion of the self-energy.

respect to the i and j indices. The diagrammatic representation of the propagation of a HF particle or hole is provided in Figure 1(b).

Turning to the frequency representation, the spectral resolution of the exact Green's function can be cast in the basis of the HF spin-orbitals as [17–21]:

$$G_{ii}(\omega) = \sum_m \frac{\langle \Psi_0^N | a_i^\dagger | \Psi_m^{N-1} \rangle \langle \Psi_m^{N-1} | a_i | \Psi_0^N \rangle}{\omega - (E_0^N - E_m^{N-1}) - i0^+}$$

$$+ \sum_p \frac{\langle \Psi_0^N | a_i | \Psi_p^{N+1} \rangle \langle \Psi_p^{N+1} | a_i^\dagger | \Psi_0^N \rangle}{\omega - (E_p^{N+1} - E_0^N) + i0^+} \qquad (2)$$

where the sums over m and p run over all the states of the $N-1$ and $N+1$ particle system. From Eq. (2), it is obvious that $G(\omega)$ has poles at the (changed of sign) exact vertical ionization and vertical electron attachment energies: the MBGF theory provides a powerful approach to many-particle systems while retaining the one-particle picture associated to the HF theory.

Carrying infinite summation through a renormalization [22] procedure, the exact one-particle propagator can be expanded, in terms of the HF propagators, using the diagrammatic perturbation expansion scheme provided in Figure 2, known as the diagrammatic equivalent of the Dyson equation [23]. Interactions of the particle or hole considered with the remaining electrons or holes in the system are introduced through a nonlocal time-dependent effective potential: the irreducible self-energy Σ [24].

Turning to the frequency representation, this diagrammatic equation has the algebraic equivalent:

$$\mathbf{G}(\omega) = \mathbf{G}^0(\omega) + \mathbf{G}^0(\omega)\Sigma(\omega)\mathbf{G}(\omega) \qquad (3)$$

with the HF propagator matrix calculated as:

$$G_{ii}^0(\omega) = \frac{\delta_{ij}}{\omega - \varepsilon_i \pm i0^+} \left\{ \begin{array}{l} + \text{ if } i \text{ virtual index} \\ - \text{ if } i \text{ occupied index} \end{array} \right\} \qquad (4)$$

Its poles provide the Koopmans' value for the ionization and electron attachment energies obtained, after inversion of sign, as the energies ε_i of the occupied and virtual spin-orbitals.

The poles of the one-particle propagator matrix can be obtained solving iteratively the equation:

$$\det[\omega - \varepsilon - \Sigma(\omega)] = 0 \qquad (5)$$

Using the Hugenholtz convention, Σ is written, to the nth-order in the correlation perturbation expansion, as the sum of all the time-ordered, topologically different and strongly connected diagrams built up from n point vertices (each of them standing for an antisymmetrized bielectron interaction element $\langle ij | | kl \rangle$) and ($2n - 1$) zeroth-order propagator lines [22]. For further discussion, it is interesting to mention the partial diagrammatic expansion [25] of the self-energy in terms of the exact polarization propagator $\mathbf{P}$ [26], this expansion being provided in Figure 3.

Applying the standard rules to write down the algebraic equivalent of the self-energy diagrams, the above expansion can be expressed as:

$$\Sigma_{pq}(\omega) = \frac{1}{2} \sum_{klm} \sum_{k'l'm'} \langle pk||lm \rangle [G_{mm'}(\omega) \circ P_{kl,l'k'}(\omega)] \langle l'm' || qk' \rangle \qquad (6)$$

in which the correlation product is defined by:

$$A(\omega)OB(\omega) = \frac{i}{2\pi} \int_{-\infty}^{+\infty} A(\omega')B(\omega' - \omega) \, d\omega' \tag{7}$$

In this expression, $P(\omega)$, in the frequency representation, is the spectral resolution [26] of the polarization propagator:

$$P_{ij,kl}(\omega) = \sum_{m \neq 0} \left[\frac{\langle \Psi_0^N | a_i^+ a_j | \Psi_m^N \rangle \langle \Psi_m^N | a_k^+ a_l | \Psi_m^N \rangle}{\omega + E_0^N - E_m^N + i0^+} \right.$$
$$\left. - \frac{\langle \Psi_0^N | a_k^+ a_l | \Psi_m^N \rangle \langle \Psi_m^N | a_i^+ a_j | \Psi_m^N \rangle}{\omega - E_0^N + E_m^N - i0^+} \right] \tag{8}$$

where the sum over m runs this time over all the excited states of the N-particle system. This frequency dependent function is obtained as the Fourier transform of:

$$P_{ij,kl}(t_2, t_1) = i^{-1} \langle \Psi_0^N | T_W \{ a_i^+(t_2) a_j(t_2), a_k^+(t_1) a_l(t_1) \} | \Psi_0^N \rangle \tag{9}$$

the former time-dependent function providing the probability amplitude of propagation, in the background of the interacting system, of a particle-conserving perturbation, this time.

Taking (Fig. 4), in the above expansion, the zeroth-order HF one-particle propagator as an approximation for $G(\omega)$, and the HF zeroth-order polarization propagator

$$P_{ij,kl}^{(0)}(\omega) = \frac{\pm \delta_{jk} \delta_{il}}{\omega + \varepsilon_i - \varepsilon_j \pm i0^+} \begin{cases} + \text{ if } i \text{ occupied and } j \text{ virtual indices} \\ - \text{ if } i \text{ virtual and } j \text{ occupied indices} \end{cases} \tag{10}$$

as an approximation for $P(\omega)$, and considering all time orders, it is easy, performing the integration (7) in the complex ω-plane, to derive from Eq. (6) the second-order expansion [11,27] of the self-energy:

$$\Sigma_{pq}^{(2)}(\omega) = \frac{1}{2} \sum_{ars} \frac{\langle pa \| rs \rangle \langle rs \| qa \rangle}{\omega + \varepsilon_a - \varepsilon_r - \varepsilon_s} + \frac{1}{2} \sum_{abr} \frac{\langle pr \| ab \rangle \langle ab \| qr \rangle}{\omega + \varepsilon_r - \varepsilon_a - \varepsilon_b} \tag{11}$$

where the sums over a and b run over all the occupied (hole indices) HF spin-orbitals while the sums over r and s run over all the unoccupied (particle indices) HF spin-orbitals. In the approximation of a diagonal Green's function matrix (also referred to as the quasi-particle approximation), the two components of the second-order self-energy describe, to that particular order in the interaction elements, the energy contribution to the ionization potential of the dynamic polarization response of the electron system to, respectively, the destruction of the particle and the creation of the hole resulting from the ionization out of one of the occupied molecular spin-orbitals.

The components of the electric dipole frequency dependent polarizability tensor are related to $P(\omega)$:

$$\alpha_{\beta\gamma}(\omega) = -\sum_{ijkl} \langle i | \vec{r}_{\beta} | j \rangle \langle k | \vec{r}_{\gamma} | l \rangle P_{ij,kl}(\omega) \tag{12}$$

Using, as previously, the zeroth-order HF polarization propagator as an approximation for $P(\omega)$, one can derive from Eq. (12) the well-known Sum-Over-State (SOS) formulation of the static (frequency independent) polarizability tensor:

$$\alpha_{\beta\gamma}^{(0)}(0) = 2 \sum_{ar} \frac{\langle a | \vec{r}_{\beta} | r \rangle \langle r | \vec{r}_{\gamma} | a \rangle}{\varepsilon_r - \varepsilon_a} \tag{13}$$

Pole strength [15,22] related to the ionization of an electron in the spin-orbital X_c can be calculated, in the quasi-particle approximation as:

$$\Gamma_c = \left[1 - \left(\frac{\partial \Sigma_{cc}(\omega)}{\partial \omega} \right)_{\omega = \omega_c} \right]^{-1} \tag{14}$$

Defined as the residue of $1/(\omega - \Sigma_{cc}(\omega))$ taken at the pole ω_c, it can be equated [28] to the fraction of the photoemission intensity associated with a monoelectronic process, the remaining fraction $[1 - \Gamma_c]$ being the intensity borrowed in shake-up or scattering processes resulting from correlation and relaxation effects. In a one-electron description, the self-energy would have no energy dependence, and the pole strength would be 1 for all ionization potentials. In a real interacting system, pole strengths larger than 0.9 can be referred to a quasi-monoelectronic process, while pole strengths smaller than 0.9 are indicative of a breakdown of the molecular orbital picture. Heavy breakdowns in the inner valence region are likely to occur when the molecule possesses many low-lying energy states.

From Eqs. (6) and (12), it appears that the magnitude of the correlation and relaxation effects on the ionization potentials, and of the breakdown of the molecular orbital picture throughout the overall ionization spectra, can be ultimately related, at least on a qualitative point of view, to the polarizability of the molecular system. As other factors, such as the degree of localization [29,30] or the inner-character of the ionized molecular orbitals, also influence the magnitude of the many-body features in the ionization spectra, such a dependence might not be precisely assessed. One has at least to recall that establishing such a dependence implies the comparison between the dynamic polarization response of the molecular electronic system to the internal perturbation that results from the ionization process, and the static polarization response of this system to an external electric field.

Model Systems and Methodology

In this contribution, the MBGF method is applied, using the second-order expansion for the self-energy, to the isomeric series: 1,3-hexadiene, 1,4-hexadiene, 1,5-hexadiene; and the related nearly isoelectronic cyclic molecules: 1,3-cyclohexadiene, 1,4-cyclohexadiene. The XPS spectra, for the linear molecules presented in this series, are simulated by taking different conformers as model systems. The 1,3-hexadiene will be taken in its trans-trans-trans (TTT) and cis-trans-trans (CTT) conformations. The 1.4-hexadiene molecule will be considered in its envelope (E), trans-cis-trans (TCT), and trans-trans-trans (TTT) conformations. The 1,5-hexadiene

molecule will be taken in its cis-trans-cis (CTC), cis-trans-trans (CTT), trans-trans-trans (TTT), envelope (E), and trans-cis-trans (TCT) conformations. The corresponding molecular structures are presented in Figure 5, each compound in this series being labeled using the alphabetical order a to l.

The calculations have been carried out using, at the ab initio level, the GAUSSIAN 82 series of programs [31]. The requested convergence on the density matrix was fixed to 10⁻⁸ and the integral cutoff was fixed to 10⁻¹⁰ hartree. The use of the extended 3-21G basis sets was imposed by the storage of the large number of integrals needed for the HF–MBGF2 calculations.

Assuming the planarity of the hydrogen and the carbon atoms involved in the vinyl groups, all the remaining geometrical parameters of the molecular systems mentioned have been optimized (Table I) at the SCF level. Among the linear systems considered here, the most stable isomer is the conjugated 1,3-hexadiene molecule [Figs. 5(a) and 5(b)]. Because of the increasing interruption of the conjugation from the insertion of a methylene, —CH₂—, or ethylene, —CH₂—CH₂—, group in between the two double bonds, the next stable isomer is the 1,4-hexadiene molecule [Figs. 5(c) to 5(e)], and the most unstable the 1,5-hexadiene molecule [Figs. 5(f) to 5(j)]. In each series of conformers, citing the different molecular structures by order of increasing instability reflects decreasing direct (in the 1,3-hexadiene series) or through-space (in the 1,4- and 1,5-hexadiene series) π-interactions resulting from the larger separation of the C—C double bonds. In the 1,5-hexadiene series, it is interesting to mention the strong destabilization of the structure with the rotation of the vinyl groups in an eclipsed conformation [Figs. 5(i) and 5(j)] with respect to the central single C₃—C₄ bond. At least, the conjugated 1,3-cyclohexadiene compound presenting [Fig. 5(k)] a destabilizing butane-like fragment in an eclipsed conformation, while the 1,4-cyclohexadiene molecule allowing a double π-methylenic conjugation between the double bonds, the large similarity of the energies for the two isomers results from a delicate balance between steric and conjugation effects.

Photoionization intensities are computed using the Gelius model [32] for molecular cross sections, the relative atomic photoionization cross sections used for C_{2s}, C_{2p}, and H_{1s} being 100, 7.69, 0.00, respectively (in the valence region, core atomic functions do not participate significantly). In the case of the spectra obtained through a Green's function approach, the Gelius intensities are multiplied by the pole strength Γ_i. Simulated XPS spectra are constructed from a superposition of peaks centered at the Koopmans, or MBGF2 values for electron binding energies. The peak-shape is represented by a standard linear combination of one lorentzian and one gaussian, both having the same height and width (1.5 eV) over the energy range considered, the peak-height being scaled according to the intensity previously computed. The basis set dependence of the trends obtained by comparing the variation of relative photoionization intensities in the investigated series of molecules have been tested performing the same calculations within the minimal basis set STO-3G. Although the STO-3G and 3-21G basis set can lead to rather different spectra, both basis sets provide qualitatively similar trends in the variation of the sharpness and heights of peaks with the molecular structure.
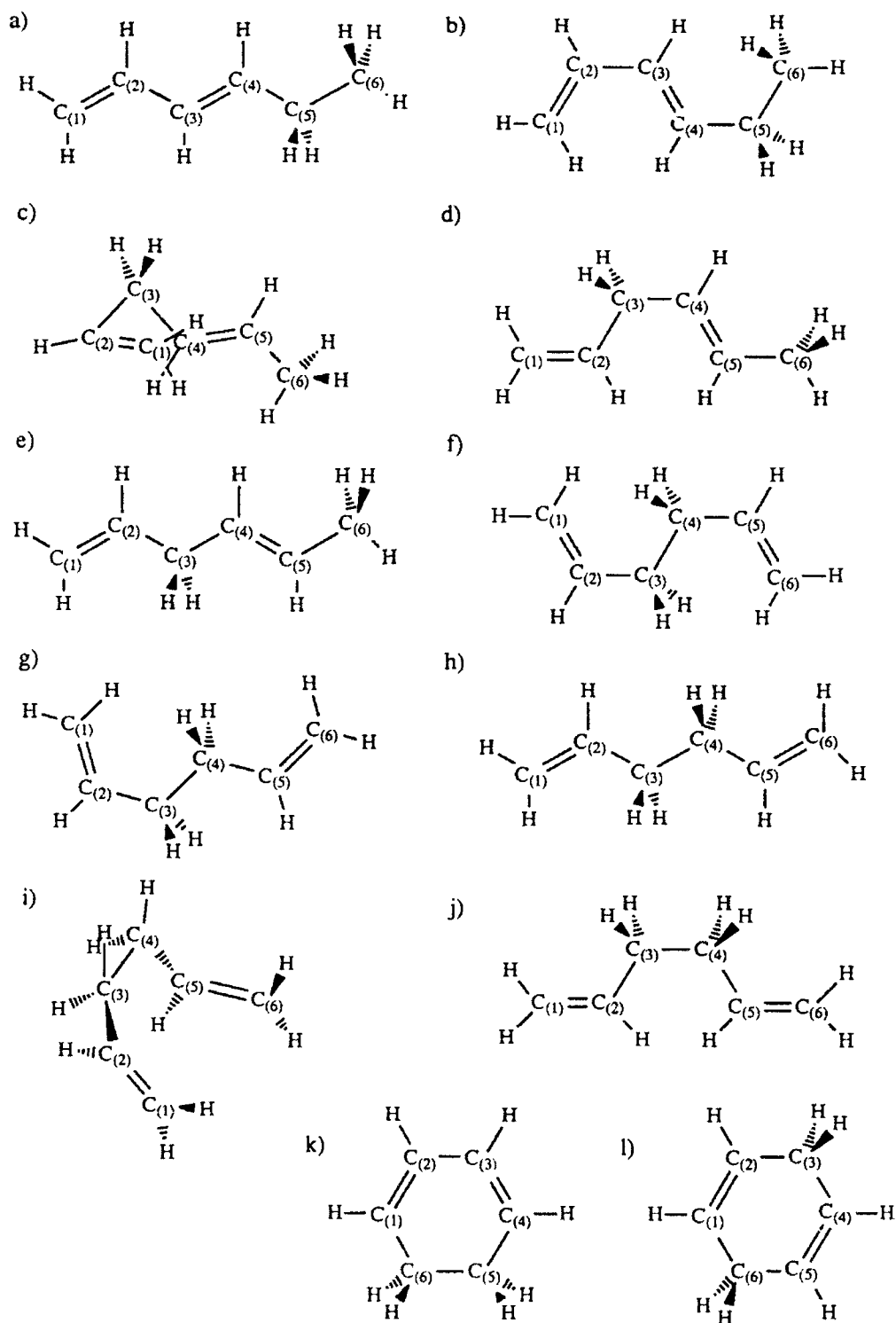
Figure 5. Selected molecular structures in the hexadiene and cyclohexadiene series of compounds.

Table I. Geometrical parameters of the carbon backbone for the selected compounds.

Molecule/energy (a.u.)	Bond lengths (Å)	Bond angles (°)	Torsion angles (°)
a) 1,3-hexadiene TTT E(RHF) = -231.698301	C1-C2 = 1.3208 C2-C3 = 1.4661 C3-C4 = 1.3216 C4-C5 = 1.5186 C5-C6 = 1.5416	C1-C2-C3 = 124.261 C2-C3-C4 = 123.884 C3-C4-C5 = 124.646 C4-C5-C6 = 112.132	
b) 1,3-hexadiene CTT E(RHF) = -231.692638	C1-C2 = 1.3207 C2-C3 = 1.4771 C3-C4 = 1.3209 C4-C5 = 1.5203 C5-C6 = 1.5416	C1-C2-C3 = 127.181 C2-C3-C4 = 126.696 C3-C4-C5 = 124.151 C4-C5-C6 = 112.181	
c) 1,4-hexadiene E E(RHF) = -231.694327	C1-C2 = 1.3154 C2-C3 = 1.5144 C3-C4 = 1.5147 C4-C5 = 1.3159 C5-C6 = 1.5098	C1-C2-C3 = 124.782 C2-C3-C4 = 111.209 C3-C4-C5 = 124.689 C4-C5-C6 = 124.718	C1-C2-C3-C4 = -120.876 C2-C3-C4-C5 = 118.348 C3-C4-C5-C6 = (180.000)
d) 1,4-hexadiene TCT E(RHF) = -231.685515	C1-C2 = 1.3163 C2-C3 = 1.5185 C3-C4 = 1.5167 C4-C5 = 1.3160 C5-C6 = 1.5207	C1-C2-C3 = 123.561 C2-C3-C4 = 116.935 C3-C4-C5 = 128.537 C4-C5-C6 = 123.412	
e) 1,4-hexadiene TTT E(RHF) = -231.685234	C1-C2 = 1.3156 C2-C3 = 1.5217 C3-C4 = 1.5223 C4-C5 = 1.3160 C5-C6 = 1.5198	C1-C2-C3 = 124.492 C2-C3-C4 = 113.290 C3-C4-C5 = 124.448 C4-C5-C6 = 124.209	
f) 1,5-hexadiene CTC E(RHF) = -231.689071	C1-C2 = 1.3165 C2-C3 = 1.5141 C3-C4 = 1.5347	C1-C2-C3 = 127.107 C2-C3-C4 = 114.787	
g) 1,5-hexadiene CTT E(RHF) = -231.687334	C1-C2 = 1.3165 C2-C3 = 1.5126 C3-C4 = 1.5387 C4-C5 = 1.5208 C5-C6 = 1.3159	C1-C2-C3 = 126.789 C2-C3-C4 = 115.141 C3-C4-C5 = 111.930 C4-C5-C6 = 124.560	
h) 1,5-hexadiene TTT E(RHF) = -231.685396	C1-C2 = 1.3160 C2-C3 = 1.5194 C3-C4 = 1.5428	C1-C2-C3 = 124.612 C2-C3-C4 = 112.364	
i) 1,5-hexadiene E E(RHF) = -231.682995	C1-C2 = 1.3157 C2-C3 = 1.5102 C3-C4 = 1.5767	C1-C2-C3 = 124.413 C2-C3-C4 = 114.729	C1-C2-C3-C4 = -115.743 C2-C3-C4-C5 = (0.000)
j) 1,5-hexadiene TCT E(RHF) = -231.672384	C1-C2 = 1.3169 C2-C3 = 1.5225 C3-C4 = 1.5718	C1-C2-C3 = 123.066 C2-C3-C4 = 119.169	
k) 1,3-cyclohexadiene E(RHF) = -230.539671	C1-C2 = 1.3185 C2-C3 = 1.4734 C4-C5 = 1.5161 C5-C6 = 1.5648	C1-C2-C3 = 121.504 C3-C4-C5 = 123.391 C4-C5-C6 = 115.107	
l) 1,4-cyclohexadiene E(RHF) = -230.54382	C1-C2 = 1.3158 C2-C3 = 1.5110	C1-C2-C3 = 123.785 C2-C3-C4 = 112.431	

Again because of computing constraints, the MBGF2 calculations achieved within the extended 3-21G basis set have been performed at the quasi-particle (QP) level of approximation. Only the main ionization processes have been considered. The second-order self-energy expansion is known to be quantitatively deficient, and no

more than a qualitative simulation of the XPS spectra can be expected from these calculations. However, as this approximation provides a simple but rather complete description of the physics involved in the main ionization process, one should be confident in the conclusions that can be drawn from our simulations.

Molecular Structure Dependence of the One-Particle and Many-Body Features in the Ionization Spectra

The photoelectron spectra of the selected compounds, in the series of the hexadiene (and cyclohexadiene) molecules, are displayed, using the same labeling order, at the Koopmans and MBGF2/QP levels of approximation, together with the corresponding MBGF2/QP poles presented as spike spectra, from Figures 6(a) to 6(l). They all reflect the classification of the valence molecular orbitals of a C_nH_{2n-2} (C_nH_{2n-4}) molecule into n molecular orbitals of $(C_{2s} + H_{1s})$ character in the inner valence region, and $2n - 1$ $(2n - 2)$ molecular orbitals of $(C_{2p} + H_{1s})$ character in the outer valence region. Considering the very different C_{2s} and C_{2p} photoelectric atomic cross section, the relative intensities from the inner and outer valence region do not reflect directly their corresponding electronic population. Because of the low XPS photoionization cross sections of outer molecular orbitals, the most specific information on the molecular structure is likely to be obtained from the inner-valence region.

The simulated spectra differ significantly from one system to another, confirming the earlier proposition that the valence region of the XPS valence spectra can be usefully analyzed in terms of primary and secondary molecular structures. As there are many factors (cyclization, isomerization, conformation) leading to such dissimilarity, this observation calls for more systematic and detailed investigation.

Cyclization

Most of the simulated spectra for the open linear hexadiene molecules considered here [Figs. 6(a) to 6(j)] show the characteristic accumulation of one-particle levels in pairs at the edges of the inner-valence regions, these unresolved pairs of levels resulting in the extremely sharp and broad peaks bordering the C_{2s} valence bands. In the outer valence region, the electron levels are so densely packed that a precise assignment of peaks in terms of molecular orbital levels is not possible in an experimental spectrum. Considering the overall energy distribution of the electronic states, the inner-valence spectra simulated at the Koopmans level of approximation are qualitatively similar to the corresponding spectrum of the n-hexane molecule [33], the most striking difference coming from the gap between the C_{2s} and C_{2p} valence bands, and the shape of the C_{2p} valence band.

The inner-valence electron levels are better resolved [Figs. 6(k) and 6(l)] in the case of the cyclohexadiene molecules. The electron levels are either nearly degenerate, or separated by rather large and similar energy intervals, these structures being characteristic of medium sized highly symmetric cyclic molecules. In the outer valence region also, the electron levels fall into well-resolved structures. Considering again qualitatively the overall distribution of electron levels, the cyclic

molecules considered here provide spectra closely related to the corresponding spectra of the cyclohexane molecule in condensed phase [34].

Isomerization and Conjugation

To compare the isomerization fingerprint in the XPS spectra of the open 1,3-hexadiene, 1,4-hexadiene, and 1,5-hexadiene molecule series, we consider each of these molecules taken in its more spatially extended TTT conformation. Their corresponding spectra [respectively, Figs. 6(a), 6(e), and 6(h)] show slight differences in the gap between the C_{2s} and C_{2p} regions, in the ionization energy of the highest (π) molecular orbital, and the energy splitting of the two π outermost levels. These quantities decrease as the conjugation between the C—C double bonds is progressively interrupted by the insertion of methylenic and ethylenic spacers. In relationship to the large variation in the amplitude of π-conjugation or through-space interactions, the most striking effect of the isomerization is observed in the outer valence spectra. On the other hand, the carbon backbone and the general bonding or antibonding pattern of the molecular orbitals of (C_{2s} + H_{1s}) character being almost unchanged, only slight but continuous variations are observed in the inner valence region when comparing, at the Koopmans level of approximation, the spectra of the 1,3-, 1,4-, and 1,5-TTT-hexadiene isomers.

The spectra obtained at this level of approximation for the 1,3- and 1,4-cyclohexadiene molecules also only display slight variations in the relative positions of peaks and photoionization intensities in the inner valence region, because of the large resolution of the C_{2s} HF levels, and almost because the general topology of the carbon backbone remains also nearly unchanged. As in the case of the linear hexadiene molecules, the ionization energy of the highest (π) molecular orbital and the energy splitting between the π levels decrease strongly with the loss of conjugation between the double bonds, leading to a more significant change in the shape of the outer valence band. In a UPS spectra, because of the enhancement of the photoionization cross sections in the outer valence region, the effects of isomerization on the π levels would lead to much more striking features than in our simulated XPS spectra.

Going beyond the Koopmans approximation, the MBGF2/QP calculations show considerable differences between the spectra from one isomer to another with the introduction of the many-body effects in the description of the ionization process. Both MBGF2 spectra show an important contraction of the energy scale compared to the HF results, the relaxation effects being exacerbated as long as we move from the top to the bottom of the valence bands [35]. The outermost π levels are affected during the ionization by much more weaker many-body effects than the σ levels. In connection with the increasing relaxation effects, we observe (Table II) a decreasing pole strength and hence validity of the molecular orbital picture in the region of the larger electron binding energies. We observe a much stronger breakdown of the molecular orbital picture in the inner valence spectra of the fully conjugated dienic molecules [Figs. 6(a), 6(b), and 6(k)], the magnitude of this breakdown decreasing (Table II) in the spectra corresponding to methylenic and then ethylenic structures, as expected from the loss of "internal" polarizability with
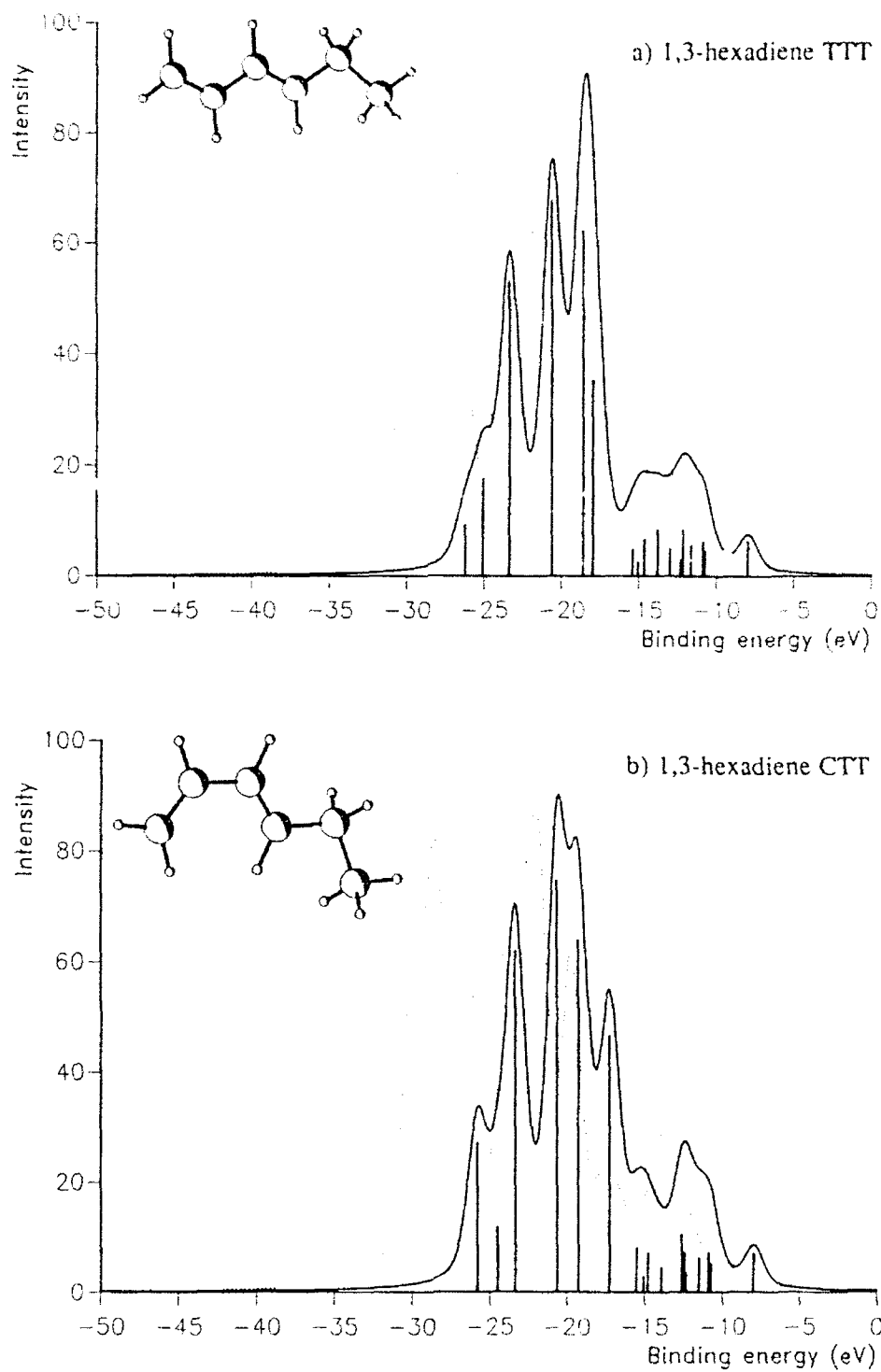
c) 1,4-hexadiene E

d) 1,4-hexadiene TCT

Figure 6. (Continued)

Figure 6. (Continued)

g) 1,5-hexadiene CTT

h) 1,5-hexadiene TTT

Figure 6.   (Continued)

Figure 6. (Continued)

k) 1,3-cyclohexadiene

l) 1,4-cyclohexadiene
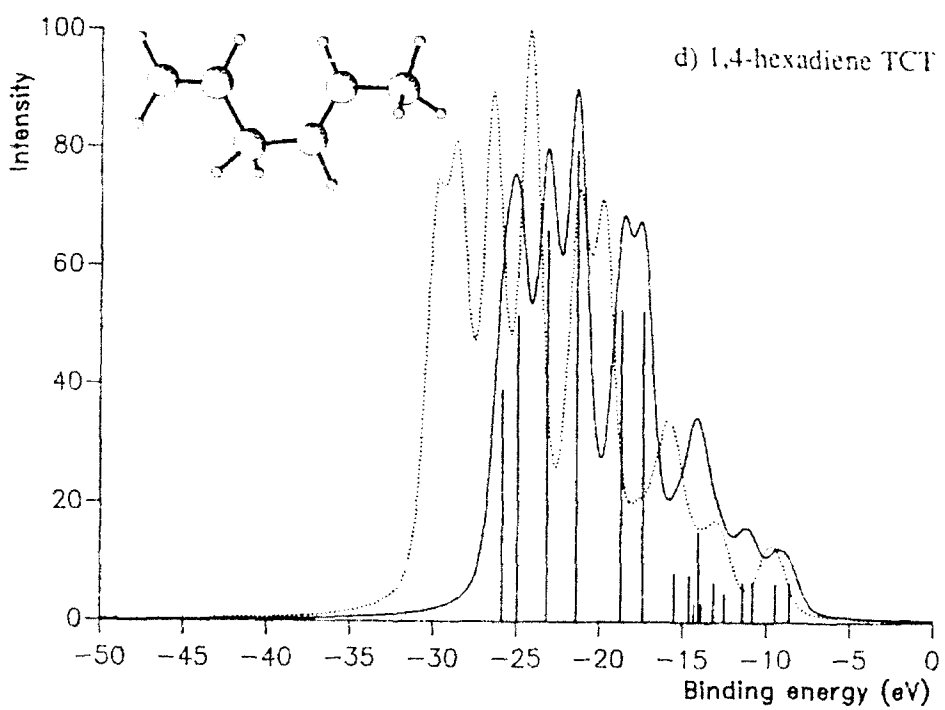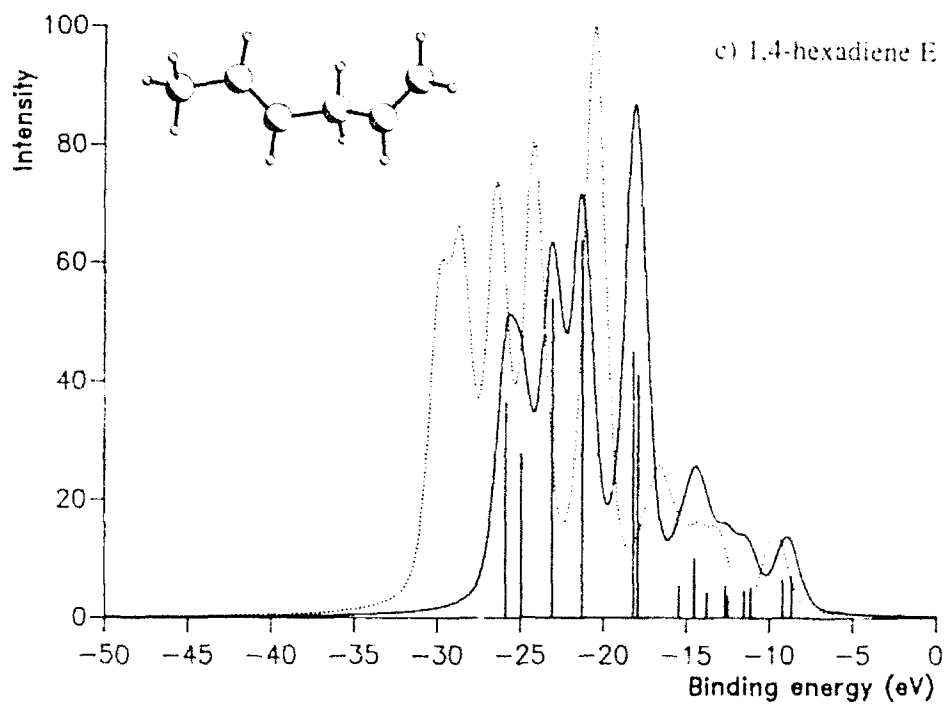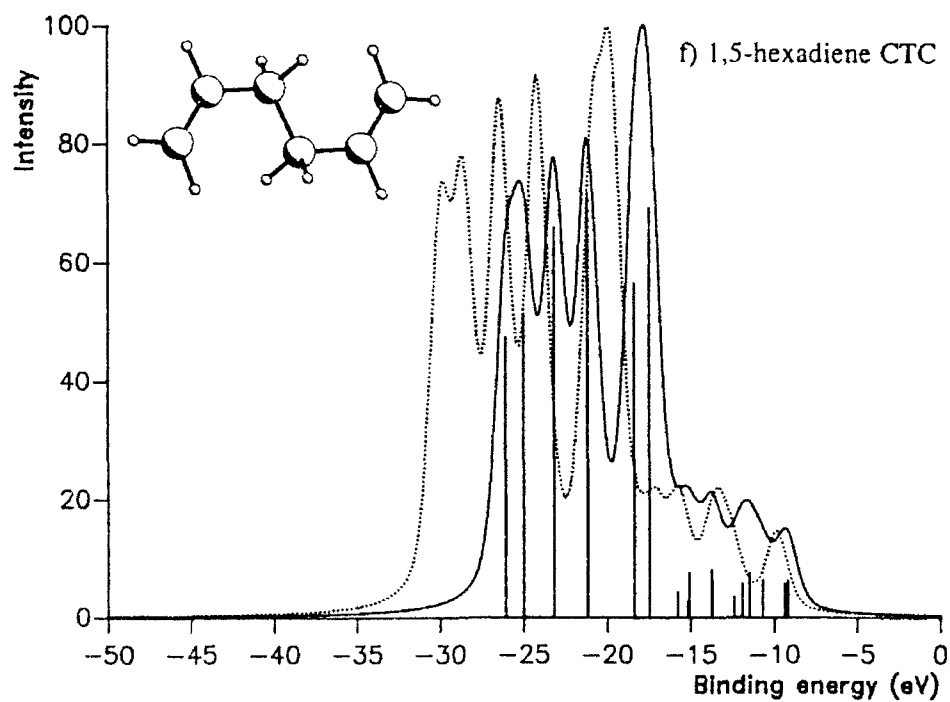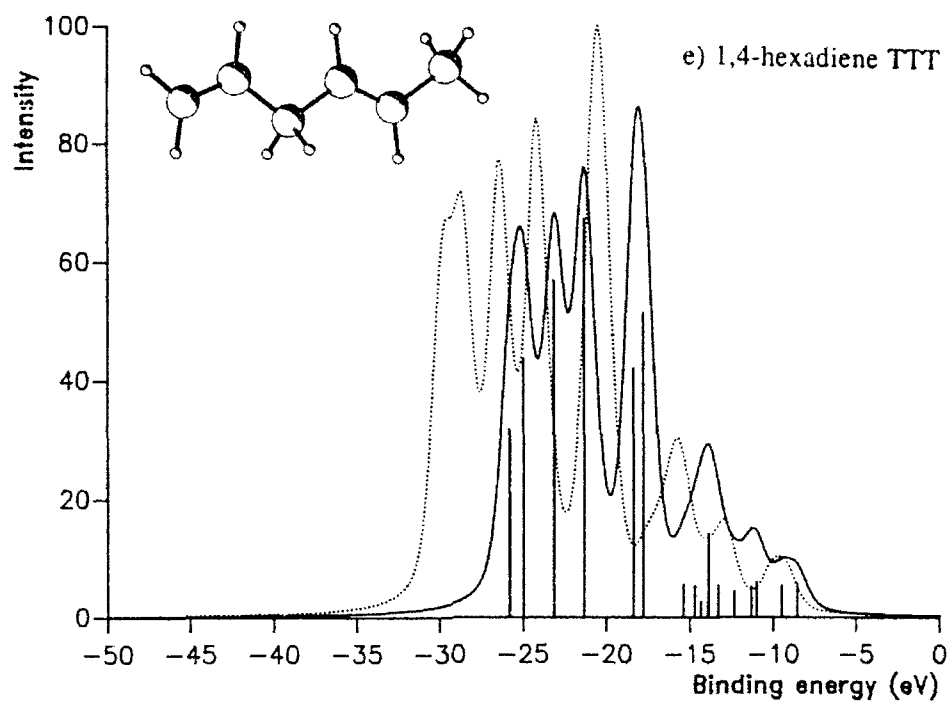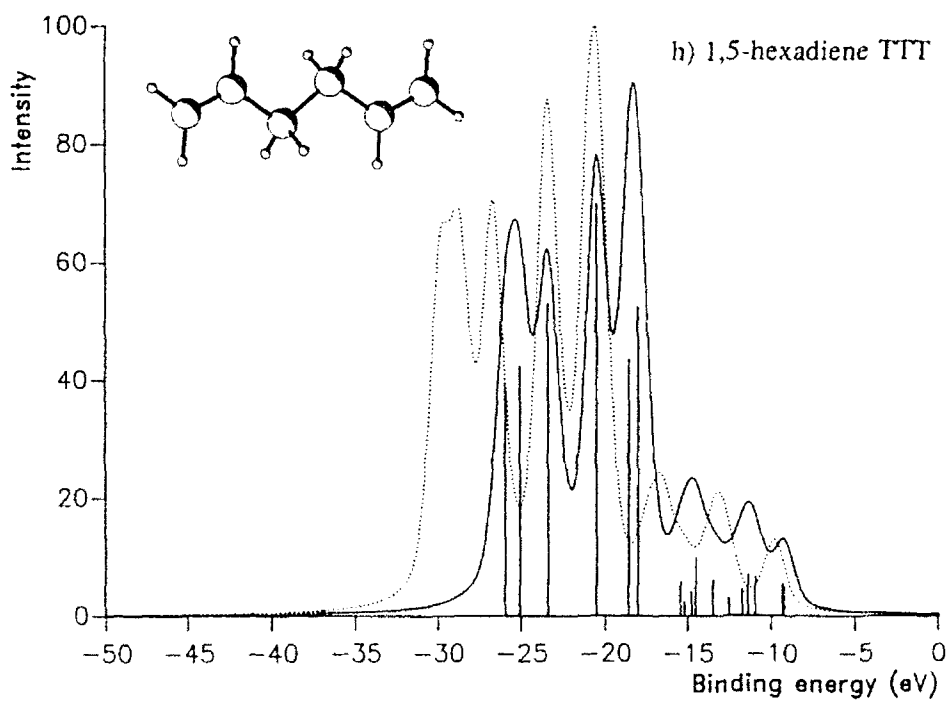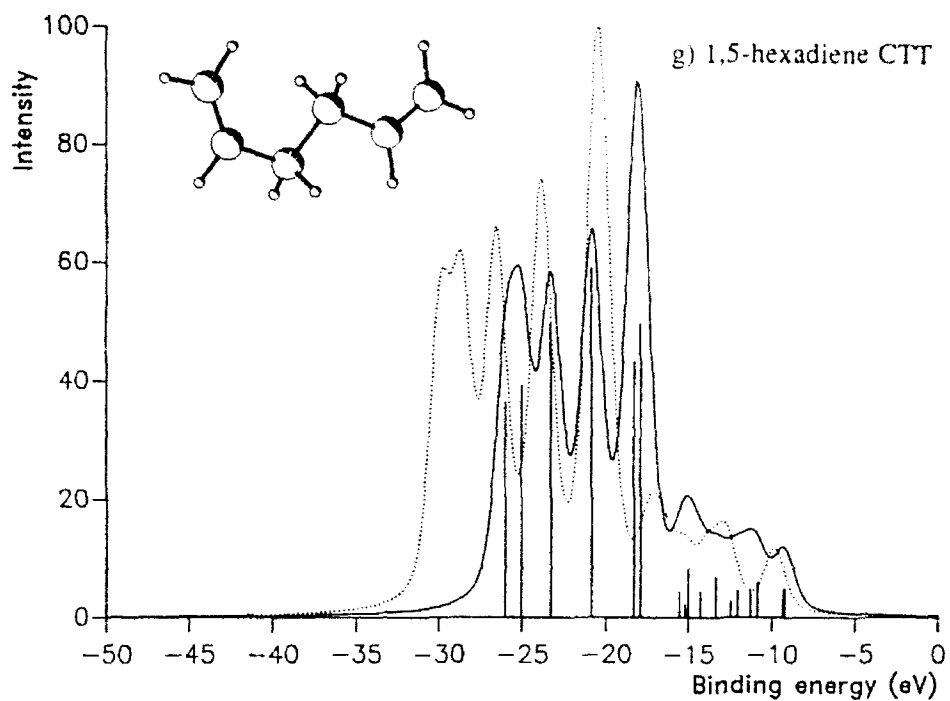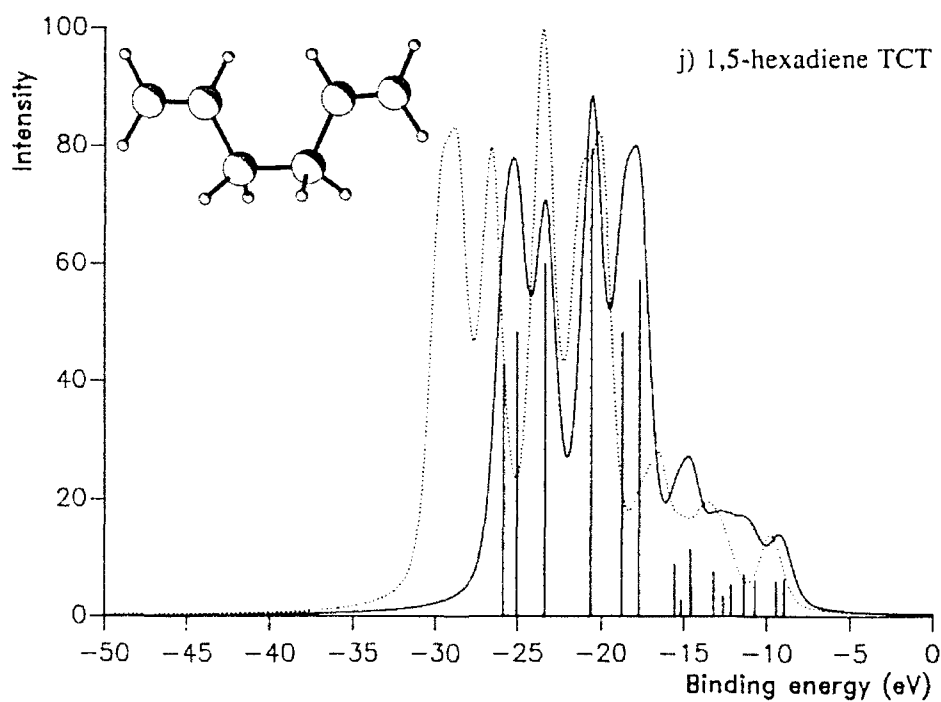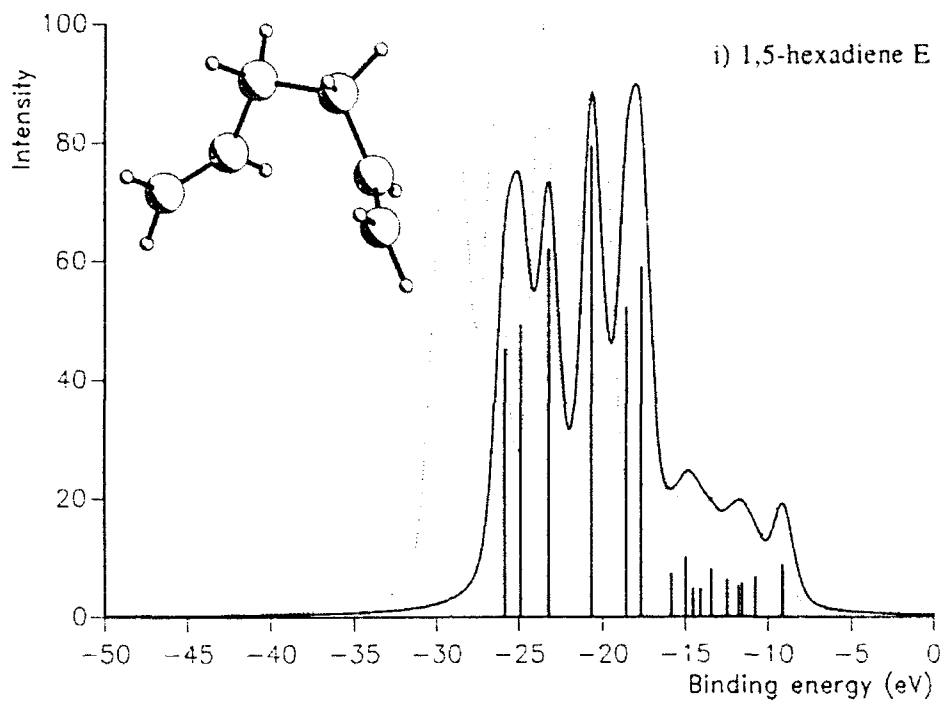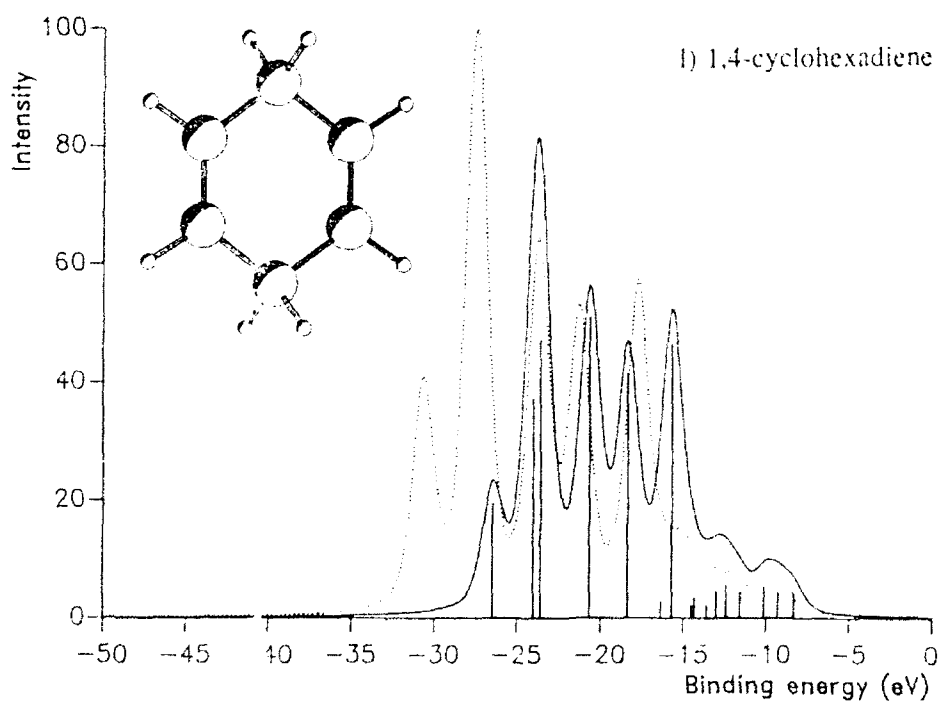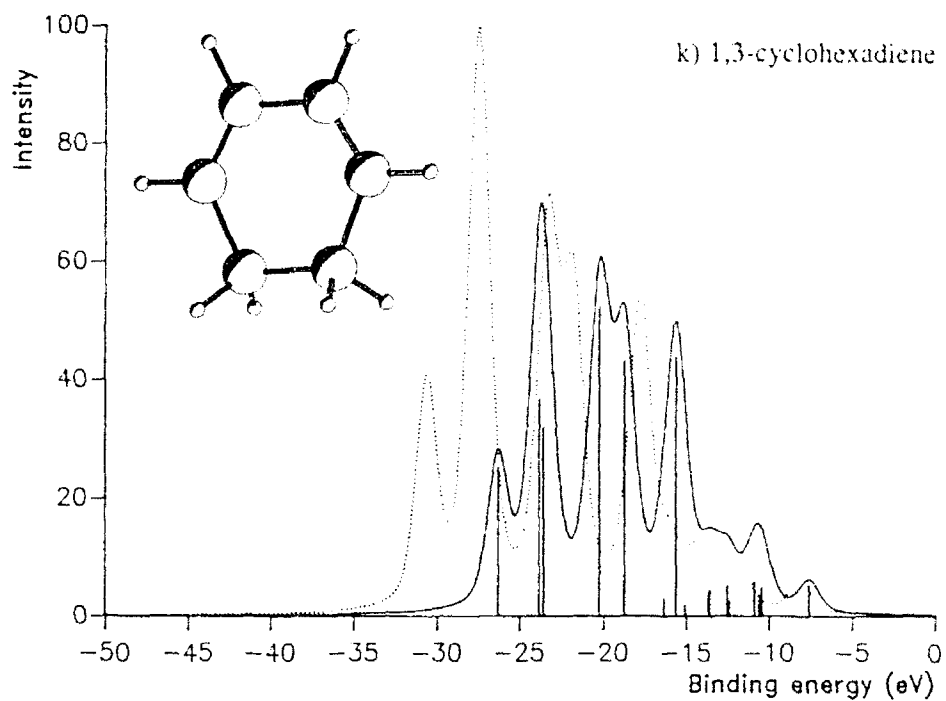
Figure 6. (Continued)

TABLE II.   Many-body features in the inner valence spectra of the selected unsaturated hydrocarbons.

Molecule/ polarizability (a.u.)	MO	IP(HF)-(eV)	IP(GF2)-(eV)	ΔIP (eV)	Γ_s
a) 1,3-hexadiene TTT	1	29.975	26.232	3.742	0.194
α = 49.61	2	28.574	25.075	3.499	0.301
	3	26.754	23.370	3.384	0.832
	4	23.477	20.615	2.862	0.857
	5	21.287	18.597	2.690	0.865
	6	20.517	17.962	2.555	0.964
b) 1,3-hexadiene CTT	1	29.924	25.796	−4.128	0.489
α = 47.78	2	28.497	24.474	−4.023	0.179
	3	26.622	23.342	−3.280	0.845
	4	23.523	20.618	−2.905	0.856
	5	21.917	19.250	−2.666	0.869
	6	19.729	17.248	−2.480	0.870
c) 1,4-hexadiene E	1	29.902	25.914	−3.989	0.772
α = 47.33	2	28.582	24.946	−3.636	0.533
	3	26.415	23.097	−3.318	0.828
	4	24.171	21.275	−2.896	0.866
	5	20.631	18.202	−2.429	0.876
	6	20.435	17.921	−2.514	0.872
d) 1,4-hexadiene TCT	1	29.864	25.842	−4.022	0.670
α = 46.34	2	28.533	24.911	−3.623	0.813
	3	26.422	23.135	−3.287	0.838
	4	24.177	21.351	−2.823	0.871
	5	21.284	18.670	−2.614	0.868
	6	19.734	17.363	−2.371	0.878
e) 1,4-hexadiene TTT	1	29.826	25.790	−4.026	0.640
α = 45.95	2	28.594	24.962	−3.633	0.805
	3	26.388	23.119	−3.269	0.835
	4	24.145	21.302	−2.084	0.870
	5	20.794	18.359	−2.436	0.876
	6	20.260	17.770	−2.490	0.874
f) 1,5-hexadiene CTC	1	29.966	29.061	−3.905	0.797
α = 46.96	2	28.586	24.990	3.596	0.828
	3	26.423	23.172	−3.251	0.851
	4	24.178	21.166	−3.012	0.860
	5	20.871	18.371	−2.500	0.874
	6	19.718	19.473	−2.245	0.887
g) 1,5-hexadiene CTT	1	29.921	26.007	−3.914	0.789
α = 46.53	2	28.620	25.027	−3.593	0.821
	3	26.556	23.289	−3.267	0.850
	4	23.832	20.867	−2.965	0.861
	5	20.728	18.304	−2.424	0.877
	6	20.243	17.886	−2.356	0.881
h) 1,5-hexadiene TTT	1	29.867	25.946	−3.922	0.777
α = 46.07	2	28.658	25.065	−3.592	0.815
	3	26.681	23.400	−3.281	0.848
	4	23.414	20.500	2.914	0.863
	5	20.974	18.569	−2.405	0.880
	6	20.372	17.995	−2.377	0.878

TABLE II. (Continued)

Molecule/ polarizability (a.u.)	MO	IP(HF)-(eV)	IP(GF2)-(eV)	ΔIP (eV)	Γ
i) 1,5-hexadiene F	1	29.794	25.850	3.944	0.790
α = 46.87	2	28.522	25.212	3.310	0.799
	3	26.498	23.212	3.285	0.843
	4	23.603	20.636	2.967	0.860
	5	21.075	18.550	2.524	0.874
	6	19.967	17.647	2.319	0.881
j) 1,5-hexadiene TCT	1	29.744	25.853	3.891	0.799
α = 45.75	2	28.647	25.032	3.614	0.813
	3	26.614	23.364	3.250	0.848
	4	23.515	20.612	2.903	0.862
	5	21.283	18.739	2.544	0.872
	6	20.038	17.699	2.338	0.880
k) 1,3-cyclohexadiene	1	30.616	26.301	4.315	0.664
α = 45.87	2	27.606	23.815	3.791	0.763
	3	27.341	23.561	3.780	0.615
	4	23.290	20.242	3.048	0.846
	5	21.805	18.741	3.064	0.851
	6	18.786	16.339	2.447	0.869
l) 1,4-cyclohexadiene	1	30.681	26.477	4.204	0.520
α = 45.84	2	27.681	24.012	3.670	0.830
	3	27.322	23.575	3.748	0.825
	4	23.715	20.678	3.037	0.856
	5	21.306	18.376	2.930	0.859
	6	18.746	16.367	2.379	0.874

the increasing interruption of the π-conjugation. For the 1,3-hexadiene molecule in its more stable conformation, the breakdown of the molecular orbital picture [Fig. 6(a)] for the ionization process of the first two molecular orbitals is virtually complete, a result that recently has been confirmed by an experimental investigation on the closely related butadiene system [36]. For such systems, a very large fraction of the main photoionization intensity is dispersed to a rich satellite structure of shake-up lines, rendering delicate the interpretation of their XPS spectra.

Conformation

Because of large variations in the amplitude of interactions between the conjugated double bonds, considerable differences are induced by conformational changes both in the inner and the outer regions of the XPS spectra simulated [Figs. 6(a), 6(b)] for the selected forms (TTT, CTT) in the 1,3-hexadiene series. In the inner valence region, the two highest occupied molecular orbitals, exhibiting four and five nodes along the carbon backbone, are strongly stabilized or destabilized with the enhancement of, respectively, the bonding or antibonding contributions in the CTT form. The resulting splitting of the corresponding energy levels at the low energy edge of the C_{2s} valence band lead to the largest variation observed in the convoluted relative photoionization intensities. Moreover, at the MBGF2/QP level of approx-

imation, a weaker (but still heavy) breakdown of the molecular orbital picture in the bottom of the inner valence band is predicted (Table II) for the CTT conformer. This can indirectly be related to a small but significant reduction of the molecular electric polarizability with the cis-orientation of the double bonds. The variation in the amplitude of the many-body effects leads to observable variations at the high energy edge of the C_{2s} band.

As we run along the series of the 1,4-hexadiene conformers [Figs. 6(c) to 6(e)], systems which provide strong methylenic and through-space π-interactions between the double $C_1 — C_2$ and $C_4 — C_5$ bonds, significant variations are also observed both in the inner and outer valence regions. The spectra simulated [Figs. 6(c), 6(e)] for the E and TTT conformers are very similar, reflecting a large resemblance in the molecular structures. Indeed, from the point of view of intramolecular interactions, the E conformer differs essentially from the TTT conformer only by a gauche instead of *anti* orientation of the substituents with respect to the $C_2 — C_3$, and $C_3 — C_4$ single bonds. Considering [Fig. 6(d)] the spectrum obtained for the TCT conformer, the most obvious variation also comes from the peak at the low energy edge of the C_{2s} band. The energy separation between the two electron levels from which this peak results through convolution increases strongly, reflecting large variations in the bonding or antibonding pattern for the molecular orbitals of $(C_{2s} + H_{1s})$ character resulting from the *cis*-orientation of C_2 and C_5 with respect to the $C_3 — C_4$ central single bond. In these series, significant variations in the magnitude of the many-body effects are also observed from one conformer to another. Our calculations show important many-body effects in the form of a strong breakdown of the orbital picture at the bottom of the inner valence band, the importance of this breakdown decreasing again with the methylenic conjugation and the π-interactions of the $C = C$ double bonds from the E to the TC and then the TT conformers.

On the other hand, the vinyl groups interact much more weakly in the 1,5-hexadiene series of conformers, and significant variations can only be observed in the shape of the inner valence spectra. Considering the conformers (CTC, CTT, TTT) which provide an *anti* orientation for the vinyl substituents with respect to the central $C_3 — C_4$ single bond, slight but continuous variations can be observed [Figs. 6(f), 6(g), and 6(h)] in their inner valence spectra. With the E, and TCT conformers, once again, the most striking variation [Fig. 6(i), 6(j)] comes from the bordering peak at the low energy side of the C_{2s} region, and the splitting of the electron levels from which it results is reflecting the severe destabilization of the molecular system with the rotation of the vinyl substituents in an eclipsed orientation with respect to the central $C_3 — C_4$ single bond. Despite the influence of the two extreme vinyl groups, leading to rather important many-body effects on the ionization potential and a small breakdown of the molecular orbital picture throughout the inner valence energy range, the Koopmans and MBGF-2 spectra are qualitatively similar.

Polarizability Dependence of the Many-Body Features in the Inner Valence Ionization Spectra

In recent articles [29,30] we have pointed out a dependence of the relaxation and correlation contributions on the ionization potential with the size of oligomeric

systems or the delocalization of molecular orbital, both factors influencing also the electric polarizability.

The heavy breakdown of the molecular orbital picture predicted in the inner valence ionization spectra of large conjugated molecules can be explained in terms of a low molecular symmetry group and the presence of a high density of excited configurations in the low energy region. The observed trends reflect the analogy between the mechanisms underlying the internal response of the molecular system to the ionization of one of its electrons, and to the response to an external electric field: small excitation energies to a large number of states favor both strong final dynamic correlation effects on the ionization process and large molecular electron polarizabilities. From such considerations, it is interesting to attempt to establish a correlation (Fig. 7) between the fraction of photoionization intensity dispersed from the main inner valence lines to satellite structures with the static spatially averaged polarizability obtained from a SOS calculation. Despite the variations in the volume and shape of the molecular electron cloud, despite the changes in the relative orientation of bonds, the observed trend in this figure is a consistent enhancement of the probability to observe shake-up lines with the polarizability of the most conjugated 1,3-; and 1,4-hexadiene molecular systems. In the 1,5-hexadiene series, on the other hand, these average probabilities do not provide such a variation with the molecular polarizability, a result that can be explained if we assume the additivity of the dynamic internal polarization effects due to the most polarizable double bonds interacting weakly, such an additivity for the static polarizability to an external field being complicated by difference in relative bonding orientation.

Conclusions and Outlook for the Future

The quality of the molecular orbital picture for the ionization process has been shown to decrease strongly with the degree of π-conjugation in unsaturated hydro-
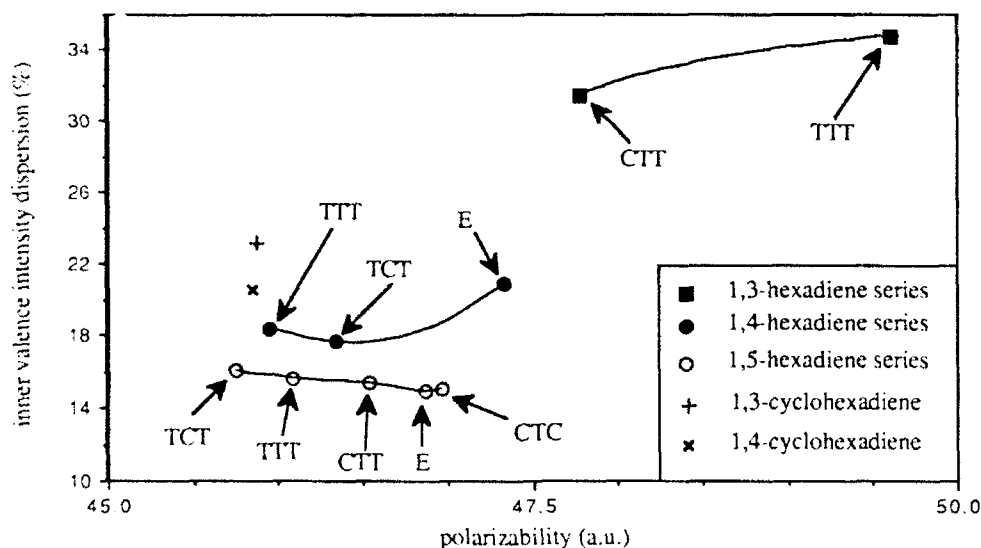
Figure 7   Average fraction of inner valence photoionization intensity dispersed to shake-up processes versus the molecular electric polarizability.

carbons, in indirect relationship with the molecular polarizability, making the interpretation of the XPS spectra of highly conjugated compounds difficult. To obtain reliable information on structural questions from the ionization spectra, the inclusion of relaxation and correlation contributions is important to describe, even at a qualitative level, the effects resulting from variations in the primary and secondary molecular structure.

In the particular case of the hexadiene series of conformers and isomers considered here, the most specific information on the molecular conformation can be obtained from the inner valence region. Changes induced by isomerization in the outer valence spectra obtained with Koopmans and second order MBGF calculations are quite comparable. However, important differences arise between the two levels of description of the relative photoionization intensities in the inner valence region, stressing the need for many-body effects to interpret that region of the XPS spectra.

To obtain more reliable and quantitative simulations, Green's function calculations have to be achieved going beyond the quasi-particle approach and using a more sophisticated scheme for the expansion of the self-energy, such as the two-particle-hole Tamm–Dankoff–Approximation. This should result in an enhancement of the trends observed in the many-body features occurring in the spectra of the compounds considered. Photoionization cross sections should also be computed by means of a nonparametric approach, and larger basis sets should be considered.

Acknowledgments

Bibliography

[1] J. J. Pireaux and R. Caudano, Phys. Rev. B 14, 2133 (1977).
[2] J. J. Pireaux, S. Svensson, E. Basilier, P.-Å. Malmqvist, U. Gelius, R. Caudano, and K. Siegbahn, Phys. Rev. A, 14, 2133 (1976).
[3] J. Delhalle and M. Deleuze, J. Mol. Struct. (Theochem.) and references therein (in press).
[4] A. W. Pots and T. A. Williams, J. Electron Spectrosc. 3, 3 (1974).
[5] A. Berndtsson, E. Basilier, U. Gelius, J. Hedman, M. Klasson, R. Nilsson, C. Nordling, and S. Svensson, Phys. Scr. 12, 235 (1975).
[6] M. S. Sanna and D. A. Shirley, J. Electron Spectrosc. 8, 255 (1976).
[7] W. R. Salaneck, H. R. Thomas, R. W. Bigelow, C. B. Duke, E. W. Plummer, A. J. Heeger, and A. G. MacDiarmid, J. Chem. Phys. 72, 3674 (1980).
[8] L. S. Cederbaum, Mol. Phys. 28, 479 (1974).
[9] P. S. Bagus and E.-K. Viinikka, Phys. Rev. A 15, 1486 (1977).
[10] L. S. Cederbaum, W. Domcke, J. Schirmer, W. Von Niessen, G. H. F. Diercksen, and W. P. Kraemer, J. Chem. Phys. 69, 1591 (1978).

[11] L. S. Cederbaum, G. Hohlneicher, and W. Von Niessen, Chem. Phys. Lett. **18**, 503 (1973).

[12] L. S. Cederbaum, Chem. Phys. Lett. **25**, 562 (1974).

[13] J. Schirmer, W. Domcke, L. S. Cederbaum, and W. Von Niessen, J. Phys. B **11**, 1901 (1978).

[14] W. Domcke, L. S. Cederbaum, and W. Von Niessen, Chem. Phys. **40**, 171 (1979).

[15] L. S. Cederbaum, W. Domcke, J. Schirmer, and W. Von Niessen, Adv. Chem. Phys. **65**, 115 (1986).

[16] W. Von Niessen, J. Schirmer, and L. S. Cederbaum, Comput. Phys Rep **1**, 57 (1984) and references therein.

[17] J. Baker, Chem. Phys. Lett. **101**, 136 (1983).

[18] J. Baker, Chem. Phys. **79**, 117 (1983).

[19] J. Baker, J. Chem. Phys. **80**, 2693 (1984).

[20] J. Baker, Int. J. Quantum Chem. **37**, 145 (1985).

[21] A. L. Fetter and J. P. Walecka, *Quantum Theory of Many-Particle System* (McGraw-Hill, New York, 1971).

[22] G. Y. Csanak, and H. S. Taylor, Adv. At. Mol. Phys. **7**, 287 (1971).

[23] F. J. Dyson, Phys. Rev. **75**, 436 (1949); **75**, 1736 (1949).

[24] J. C. Inkson, *Many-Body Theory of Solids* (Plenum, New York, 1984).

[25] R. Mc Weeny and B. T. Pickup, Rep. Progr. Phys. **43**, 1065 (1980).

[26] J. Oddershede, P. Jorgenen, and D. L. Yeager, Comput. Phys. Rep. **2**, 35 (1984).

[27] B. T. Pickup and O. Goscinski, Mol. Phys. **26**, 1013 (1973).

[28] L. S. Cederbaum, Theor. Chim. Acta **31**, 239 (1973).

[29] M. Deleuze, J. Delhalle, and J.-M. André, Int. J. Quantum Chem. **41**, 243 (1992).

[30] M. Deleuze, J. Delhalle, and B. T. Pickup, Theor. Chim. Acta **82**, 309 (1992).

[31] J. S. Binkley, M. J. Frish, D. J. DeFrees, K. Raghavachari, R. A. Whiteside, H. B. Schlegel, E. M. Fluder, and J. A. Pople, GAUSSIAN 82, Carnegie-Mellon University, Pittsburgh, PA, 1982 (implemented for the IBM 9377 and FPS 564 by J. G. Fripiat).

[32] U. Gelius, J. Electron Spect. Relat. Phenom. **5**, 985 (1974).

[33] J. J. Pireaux and R. Caudano, Phys. Rev. B **15**, 2242 (1977).

[34] J. J. Pireaux, J. Riga, R. Caudano, J. J. Verbist, J. K. Delhalle, S. Delhalle, J.-M. André, and Y. Gobillon, Phys. Scr. **16**, 329 (1977).

[35] M. Deleuze, J. Delhalle, and B. T. Pickup, "Second-order Green's Function Study of Valence Band Formation of Linear Alkanes," J. Electron Spectrosc. Rel. Phenom. (accepted for publication).

[36] M. P. Keane, A. Naves de Brito, N. Correia, S. Svensson, L. Karlsson, B. Wannberg, U. Gelius, S. Lunell, W. R. Salaneck, M. Lödlung, B. B. Swanson, and A. G. MacDiarmid, University of Uppsala, Institute of Physics, Report No. UUIP-1282, 1991.

Coupled Cluster Approach to the Single-Particle Green's Function

MARCEL NOOIJEN and JAAP G SNIJDERS

*Department of Theoretical Chemistry, Vrije Universiteit, de Boelelaan 1083,
1081 HV Amsterdam, The Netherlands*

Abstract

Diagrammatic and Coupled Cluster techniques are used to develop an approach to the single-particle Green's function G which concentrates on G directly rather than first approximating the irreducible self-energy and then solving Dyson's equation. As a consequence the ionization and attachment parts of the Green's function satisfy completely decoupled sets of equations. The proposed Coupled Cluster Green's Function method (CCGF) is intimately connected to both Coupled Cluster Linear Response Theory (CCLRT) and the Normal Coupled Cluster Method (NCCM). These relations are discussed in detail. © 1992 John Wiley & Sons, Inc.

Introduction

The single-particle Green's function is a powerful tool to calculate ionization and electron attachment spectra of molecular and atomic systems [1–9]. Vertical ionization potentials and electron affinities derive from the pole positions of the frequency dependent single-particle Green's function, while the spectral intensities are related to the corresponding residues. In the field of quantum chemistry various approaches, such as those based on Dyson's equation [1–4], the superoperator resolvent [5,8] or equation of motion techniques [9], exist to approximate the single-particle Green's function. If perturbation theory is used to arrive at the detailed form of the working equations these methods are all closely related or equivalent [6,7]. The methods based on Dyson's equation employ an irreducible self-energy $\Sigma(\omega)$ that can be represented by a series of perturbation diagrams. The single-particle Green's function, $G(\omega)$, is then obtained from Dyson's equation

$$G(\omega) = G_0(\omega) + G_0(\omega)\Sigma(\omega)G(\omega) = G_0(\omega) + G_0(\omega)\Sigma(\omega)G_0(\omega)$$

$$+ G_0(\omega)\Sigma(\omega)G_0(\omega)\Sigma(\omega)G_0(\omega) + \cdots .$$

By solving Dyson's equation using some diagrammatic approximation to the irreducible self-energy one implicitly performs a partial infinite summation of perturbation diagrams contributing to $G(\omega)$.

In order to obtain acceptable results approximations have to be used that preserve the analytical structure of the irreducible self-energy. The ω-dependent part of the irreducible self-energy has a spectral representation that is given as a sum over simple poles [4]. These poles lie partly in the ionization part of the spectrum and

partly in the attachment part. Because of the desired structure of the approximate
irreducible self-energy one cannot employ a simple order by order perturbation
expansion of the irreducible self-energy beyond second order. In higher order ap-
proximation schemes (2ph-TDA [2], ADC [4]) the irreducible self-energy is therefore
defined by a partial infinite series of diagrams. In such schemes there is one equation
that determines the ionization part of Σ and one equation for the attachment part.
These equations are completely decoupled and by solving them one is implicitly
summing a partial infinite series of diagrams that contribute to the respective parts
of the irreducible self-energy. Both parts of the irreducible self-energy are essential
for an adequate description of ionization and electron attachment processes. The
coupling between the two parts of Σ is achieved through Dyson's equation that
subsequently has to be solved to obtain the single-particle Green's function. This
way both ionization potentials and electron affinities are obtained from a single
equation and this may be considered the main characteristic of current Green's
function methods as applied to calculate quantities of spectroscopic interest.

Because of the similarity of the diagrammatic perturbation series for G and Σ
the question arises if one could not define separate equations for the ionization and
the attachment part of G directly instead of Σ and skip Dyson's equation altogether.
Such a scheme can only be useful if both parts of the irreducible self-energy are
present in either resulting part of G. This is the starting point for the present in-
vestigation.

To arrive at decoupled equations for the respective parts of the single particle
Green's function we start from the connected diagram perturbation series for $G(\omega)$.
The decoupling of the ionization from the attachment part of $G(\omega)$ is trivially
achieved by considering only those time-ordered diagrams in which the (external)
annihilation operator acts before the creation operator. The corresponding frequency
dependent diagrams constitute the perturbation series for the ionization part of
$G(\omega)$. Analyzing this perturbation series and taking it apart we identify a number
of ω-dependent connected excitation operators and define them in terms of their
diagrammatic perturbation series. Then, using essentially the techniques of Coupled
Cluster theory [10–15], diagrammatic equations are presented that define these
operators in a recursive way. In the final step the diagrammatic perturbation series
that determines $G(\omega)$ is reconstructed in terms of the ω-dependent cluster operators.
The diagrammatic approach advocated here is potentially exact. Approximations
are introduced by neglecting connected excitation operators from a certain excitation
level onwards. The truncated diagrammatic equations then determine a partial
infinite set of perturbation diagrams, which defines the approximation to the single-
particle Green's function.

Having established the diagrammatics of the Coupled Cluster Green's function
(CCGF) approach we proceed to translate the diagrammatic equations into algebra.
From the algebraic equations it will transpire that the CCGF approach is intrinsically
related to Coupled Cluster Linear Response Theory, CCLRT, [16–23], also known
as CC equation of motion, CC–EOM [18,20,21]. CCLRT in turn has been shown to
be related to the Fock Space Multi-Reference Coupled Cluster method [24–26] or
open shell CC [24,25] which presently is under strong development [27–30]. The

CCLRT equations for the principal ionization potentials and electron affinities can be shown to be equivalent to the equations that derive from the one-valence sectors of Fock Space MR–CC [31,32,28].

The diagrammatic Green's function approach presented here provides an alternative derivation of the CCLRT equations and elucidates the intimate relation between Green's functions and Linear Response in the context of Coupled Cluster theory. An advantage of the present presentation is that the derivation follows very natural lines once the perturbative diagrammatic content of the ω-dependent connected excitation operators is established. In a previous derivation of CCLRT choices that were made in the process were mentioned explicitly [20,21]. Also the connection with Green's function methods remains clear due to the diagrammatic point of view. On the other hand algebraic methods show clearly how the equations can be cast in a tractable computational scheme and allow an easy interpretation of the equations. For this latter purpose the equation of motion derivation of CCLRT [18,20,21] is particularly useful. We will consider the EOM derivation and elaborate on these equations in relation to CCGF in order to arrive at equations for Feynman–Dyson transition amplitudes and consequently ground-state properties that derive from the Coupled Cluster Green's function. At this point contact is made with the Normal Coupled Cluster Method (NCCM), [33,34] which allows evaluation of ground-state expectation values in a CC framework. The CCGF can then be regarded as the Fourier transform of a time-dependent expectation value within the NCCM formalism.

The Single-Particle Green's Function

We assume a finite dimensional Fock space, that is defined through a suitable set of orthonormal spin orbitals and if we refer to "exact" results this applies to the finite vector space considered. The system of interest consists of a number of positively charged nuclei at fixed positions, and N electrons. The Fock space Hamiltonian is given by

$$H = V_{NN} + \sum_{p,q} h_{pq}\hat{a}_p^\dagger\hat{a}_q + \frac{1}{2}\sum_{p,q,r,s} V_{pqrs}\hat{a}_p^\dagger\hat{a}_q^\dagger\hat{a}_s\hat{a}_r \tag{1}$$

V_{NN} is the nuclear repulsion term, h_{pq} denotes the sum of the matrix elements of the kinetic energy and nuclear attraction operators, while V_{pqrs} are two electron integrals in "1212" notation. $\hat{a}_p^\dagger$ and $\hat{a}_q$ are creation and annihilation operators with respect to the one-particle basis functions.

The single-particle Green's function (or matrix) is defined by [1,35]

$$G_{pq}(t, t') = -i\langle \Psi_0| T\{\hat{a}_p(t)\hat{a}_q^\dagger(t')\} |\Psi_0\rangle . \tag{2}$$

Here $|\Psi_0\rangle$ is the exact, normalized groundstate of the N-particle system under consideration. $\hat{a}_p(t)$, $\hat{a}_q^\dagger(t')$ denote annihilation and creation operators in the Heisenberg picture and $T\{\cdots\}$ is the Wick time-ordering operator. The components of the frequency dependent single-particle Green's function.

$$G(\omega) = \int_{-t}^{t} d(t - t')e^{i\omega(t-t')}G(t, t') ,$$ (3)

expressed in their spectral representation read

$$G_{pq}(\omega) = \sum_{\mu} \frac{\langle \Psi_0 | \hat{a}_p | \Psi_\mu^{(N+1)} \rangle \langle \Psi_\mu^{(N+1)} | \hat{a}_q^\dagger | \Psi_0 \rangle}{\omega - (E_\mu^{(N+1)} - E_0)}$$

$$+ \sum_{\nu} \frac{\langle \Psi_0 | \hat{a}_q^\dagger | \Psi_\nu^{(N-1)} \rangle \langle \Psi_\nu^{(N-1)} | \hat{a}_p | \Psi_0 \rangle}{\omega - (E_0 - E_\nu^{(N-1)})} .$$ (4)

where we suppressed the usual convergence factors $\pm i\eta$, which are unimportant in this work. Vertical ionization energies and electron affinities are derived from the pole-positions of $G(\omega)$, while the Feynman–Dyson transition amplitudes $\langle \Psi_\nu^{(N-1)} | \hat{a}_p | \Psi_0 \rangle$, and so forth can be obtained from the corresponding residues. The single-particle Green's function also contains detailed information concerning the groundstate. Both the one-particle reduced density matrix and the total ground-state energy can be obtained by taking appropriate contour integrals that enclose the ionization potentials [35].

To arrive at a perturbation expansion for the single-particle Green's function, the Hamiltonian is partitioned as

$$\hat{H} = \hat{H}_0 + \hat{V}$$

$$\hat{H}_0 = E^{(0)} + \sum_p \varepsilon_p N(\hat{a}_p^\dagger \hat{a}_p), \text{ with } E^{(0)} = \langle \Phi_0 | \hat{H} | \Phi_0 \rangle$$

$$\hat{V} = \frac{1}{2} \sum_{p,q,r,s} V_{pqrs} N(\hat{a}_p^\dagger \hat{a}_r \hat{a}_q^\dagger \hat{a}_s) .$$ (5)

where we assume a representation in canonical Hartree–Fock orbitals. The operators we use are always written in normal order with respect to $|\Phi_0\rangle$, the Hartree–Fock determinant. The use of Hartree–Fock orbitals ensures that the one particle perturbation in normal order vanishes identically, and this reduces considerably the number of perturbative contributions (diagrams) that have to be taken into account.

The perturbation expansion of the single-particle Green's function is treated in many textbooks, (for example, Ref. [35]), and the result can concisely be written as

$$G_{pq}(t, t') = \frac{\langle \Phi_0 | T\{ \hat{U}(\infty, -\infty)\hat{a}_p(t)\hat{a}_q^\dagger(t') \} | \Phi_0 \rangle}{\langle \Phi_0 | \hat{U}(\infty, -\infty) | \Phi_0 \rangle} .$$ (6)

which after invoking the Linked Cluster Theorem reads

$$G_{pq}(t, t') = \langle \Phi_0 | T\{ \hat{a}_p(t)\hat{a}_q^\dagger(t')\hat{U}(\infty, -\infty) \} | \Phi_0 \rangle_{\text{connected}} .$$ (7)

All operators are now given in the interaction representation. The perturbation expansion of G derives from the perturbation expansion of the evolution operator, expressed formally as

$$U(t, t') = T\left\{\exp\left[-i\int_{t'}^{t} V(t_1)\,dt_1\right]\right\}.\qquad(8)$$

Equation (7) is represented diagrammatically by the sum over all topologically distinct, closed, connected diagrams, that besides interactions (represented by wiggly lines) contain two external points labeled p and q. We represent these external points by crosses connected by a dashed line that runs from p to q. Typical examples of contributing diagrams are given in Figure 1. Each nth order Feynman diagram (containing n interactions) gives rise to $(n + 2)!$ different time-orderings or Goldstone diagrams [36]. Time runs upwards in these diagrams. The diagrams can be divided in two distinct classes, according to the time ordering of the external points. If $t > t'$ then $a_q^\dagger(t')$ acts before $a_p(t)$ and the diagram contributes to the attachment part of $G_{pq}(t, t')$. The dashed line points downwards. If $t < t'$ then $a_p(t)$ acts first and the diagram contributes to the ionization part. These diagrams are characterized by a dashed line that points upwards. This partitioning of diagrams remains valid if the internal time integrations and the Fourier transform of $G_{pq}(t, t')$ are performed. It follows that the ionization part of $G_{pq}(\omega)$ is given by the sum over all time-ordered diagrams where the dashed line points upwards.

The diagrams are evaluated according to the usual rules, as given for example in Cederbaum and Domcke [1]. With regard to this article the most important rule concerns the energy denominators: With each level (between each two interactions, between an interaction and an external point, etc.) there is associated an energy denominator which reads

$$\sum_i \varepsilon_i - \sum_a \varepsilon_a(\pm\omega)\qquad(9)$$

The sum over i runs over all hole-lines (directed downwards), that are present at this level. The sum over a runs likewise over all particle lines (directed upwards). The ω-contribution is present if the dashed (or ω-) line cuts the level considered, entering with a minus sign if the line points upward, with a plus sign otherwise. Another important rule says that a minus sign should be added for each hole-line, and for each closed loop in the diagram. In this connection it should be mentioned that the dashed ω-line is not treated as a real line in the algebraic evaluation of
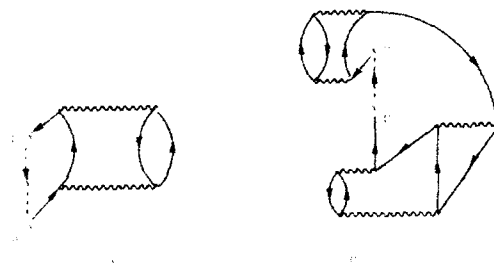
Figure 1. Perturbation diagrams that contribute to $G_{pq}(\omega)$. (a) second-order contribution to the attachment part of G; (b) fifth-order contribution to the ionization part.

these diagrams in the sense that it cannot make a loop closed, it does not contribute to the number of hole lines, nor does it influence the degree of connectedness of a diagram. The dashed line is merely a help to the eye to facilitate the evaluation of the diagram, in particular the ω-dependence of the denominators. We will see shortly, however, that the dashed line plays a crucial role in this work.

Derivation of the Coupled Cluster Approach to the Single-Particle Green's Function

Cluster Expansion of the Single-Particle Green's Function

Diagrammatics. From now on we restrict ourselves to the ionization part of the single-particle Green's function, $G_{pq}^{II}(\omega)$, that is represented by those perturbation diagrams contributing to $G(\omega)$ in which the ω-line points upwards. The derivation for the attachment part would be completely analogous. Let us first sketch briefly what we intend to do. To analyze the diagram series that determines $G(\omega)$ we consider an arbitrary diagram and cut off a number of its top levels (interactions or external points). What remains is a diagram that has free, open lines emerging at the top. Such a diagram corresponds to an operator [10–14]. Different types of operators will be distinguished, depending on the presence and the position of the dashed ω-line and each operator is defined as the sum over all perturbation diagrams of a particular form. As in Coupled Cluster theory all operators we use consist of connected diagrams only.

In the next step we show how one can write down diagrammatic equations that determine the newly defined operators in terms of these very operators, that is, recursively. Iterating these equations generates the complete diagrammatic perturbation series for each operator. The single-particle Green's function is written in terms of these operators, analogous to the correlation energy in Coupled Cluster theory.

In this section the identifications we make are purely diagrammatical and we will not give a physical interpretation of the associated operators. In the following sections the resulting diagrammatics is translated into algebra, which is discussed in detail subsequently and the connections with CCLRT and NCCM are made.

To arrive at the desired operators we proceed as follows. Take an arbitrary diagram contributing to $G(\omega)$ and mentally cut it across a horizontal line between two successive vertices. Now consider only the part (diagram) below the horizontal cut. This part consists in general of a number of mutually disconnected parts, which are internally connected, open from above (there are free lines emerging at the top of each disconnected part), and closed from below (there are no free lines at the bottom of the disconnected parts). Of course the part of the diagram below the hypothetical horizontal may also consist of only one connected part.

A few remarks on nomenclature are appropriate here (Cf. Lindgren [11]). A disconnected (internally connected) part is just one piece in the diagram. Free lines only occur at the top of a diagram (due to our stripping off the top part of the diagram) and they correspond to creation or annihilation operators, that generate excitations out of the reference state $|\Phi_0\rangle$. Free lines directed downward and going

Figure 2. Diagrammatic representation of ω-independent connected (Coupled Cluster) operators $\hat{T}$.

into the diagram create a hole in $|\Phi_0\rangle$ (operator $\hat{a}_i$), free lines directed upward and leaving the diagram create a particle (operator $\hat{a}_a^{\dagger}$). Here and in the sequel we will refer to holes through the labels $i, j, k, \ldots$, to particles with $a, b, c, \ldots$, while p, q, r, s are used for arbitrary spin orbitals. Lines that are not free but run from one vertex to another are called *internal*. The term *open* means that the diagram contains free lines and corresponds to an operator (of particle-rank higher than zero). A closed diagram is a diagram without free lines and corresponds to a constant. $G(\omega)$, the quantity of interest consists of closed diagrams only. We note that the external points, represented by crosses, and indicating the particular matrix-element of $G(\omega)$ that is involved, are not free lines associated with an operator.

Now let us classify the disconnected parts that are obtained by applying the hypothetical horizontal cut. A disconnected part may or may not contain the dashed ω-line. If it does not contain the dashed line it has diagramatically the same form as a contribution to a connected cluster operator familiar from the Coupled Cluster formalism. These are the first type of building blocks. The cluster operators are given by the sum over all possible, topologically distinct connected diagrams with one ($\hat{T}_1$), two ($\hat{T}_2$), and so forth, pairs of free lines emerging at the top of the diagram, where each pair consists of a particle and a hole line [10–14]. Diagrammatically the various $\hat{T}$-operators are given in Figure 2, where the rectangular boxes symbolize a sum over all possible connected "paths" leading to the free lines as indicated.

The second possibility is that the disconnected part does contain the dashed line. Here we distinguish two subcases.

(a) The ω-line emerges at the top of the disconnected part. At this point one of the external indices of $G_{pq}(\omega)$ is specified (p if the ω-line runs upwards). The diagram is a contribution to a new type of operator, denoted as $\hat{S}^{(p)}(\omega)$. Analogous to the $\hat{T}$-operators we have $\hat{S}_1^{(p)}(\omega)$, $\hat{S}_2^{(p)}(\omega)$, and so forth, symbolized by a box with 1, 2, and so forth, pairs of lines emerging at the top, where one of the pairs contains the dashed line (see Fig. 3). These diagrams correspond to h, $2hp$, and so forth.
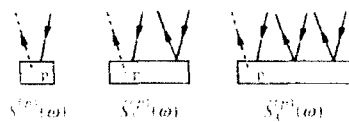
Figure 3. Diagrammatic representation of ω-dependent connected operators $\hat{S}^{(p)}(\omega)$, that generate $(N-1)$ particle states when operating on $|\Phi_0\rangle$. The dashed line is external.
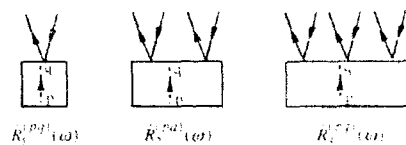
Figure 4. Diagrammatic representation of ω-dependent connected operators $R^{(pq)}(\omega)$. The dashed line is internal.

ionization/excitation operators assuming that the ω-line is directed upwards. The box symbolizes again the sum over all connected perturbation diagrams leading to the emergence of the free lines as indicated.

(b) The ω-line is an internal line. At this point both external points (i.e., the matrix element considered) of $G_{pq}(\omega)$ are specified and we denote the associated operator as $\hat{R}^{(pq)}(\omega)$, distinguishing single, double, and so forth, excitation operators. The corresponding diagrams are given in Figure 4. The box symbolizes the sum over all "connected" perturbation diagrams with an internal ω-line, with free lines at the top of the diagram as indicated. (The term *connected* has a slightly different meaning here as will be explained below).

A general diagram contributing to $G_{pq}(\omega)$ is given in Figure 5. By successively drawing hypothetical horizontal lines between interactions one obtains mutually disconnected parts that are internally connected and which are all of one of the above forms $\hat{T}$, $\hat{S}^{(p)}(\omega)$, or $\hat{R}^{(pq)}(\omega)$. It will be clear that any disconnected part constructed in the above way can always be classified as a contribution to one and only one of the above operators. In Figure 5 it is also illustrated how both the ionization and the attachment part of the irreducible self-energy enter the ionization part of G which is known to be essential for an adequate description of ionization processes. The diagram in Figure 5 is reducible as it falls apart if one cuts the line that is present at the level of the single $\hat{S}_1^{(p)}(\omega)$ operator. The part below this cut contains a fourth-order contribution to the ionization part of Σ, while in the part above the $\hat{S}_1^{(p)}(\omega)$ level one identifies a third-order contribution to the attachment
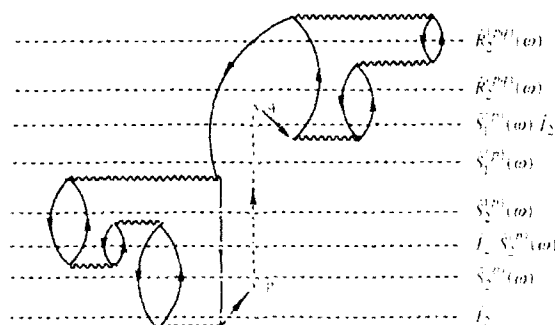
Figure 5. A general (seventh-order) diagram contributing to $G_{pq}(\omega)$. Hypothetical horizontal lines are drawn, and the parts below these horizontal cuts are identified as contributions to operators $\hat{T}$, $\hat{S}^{(p)}(\omega)$, or $\hat{R}^{(pq)}(\omega)$ of definite excitation level.
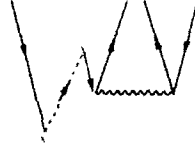
Figure 6. First-order contribution to $\hat{R}^{(p\wedge)}(\omega)$. We define this diagram to be connected, treating the dashed line as an ordinary line in this respect.

part of Σ. The attachment part of Σ enters in our CC description through nonlinear terms like $\hat{S}_1^{(p)}(\omega)\hat{T}_2$ and inclusion of these terms is hence a crucial ingredient of the CCGF approach.

The perturbation diagrams that contribute to the operators $\hat{T}$, $\hat{S}^{(p)}(\omega)$, or $\hat{R}^{(pq)}(\omega)$ can be evaluated algebraically combining the rules for ω-independent operators that are given for example in Lindgren [11], with the familiar rules for the ω-dependence of the denominators [1]. There are some subtleties, however, in connection with the operator $\hat{R}^{(pq)}(\omega)$ that we will address now.

(i) Consider the diagram given in Figure 6. This diagram consists of two disconnected parts, but by adding interactions and closing the diagram, such that it becomes a diagram that contributes to $G(\omega)$, these parts will always get connected. The parts cannot be closed separately because each of these parts contains an odd number of free lines. This notion is completely general. Diagrams like Figure 6 occur if we apply the hypothetical horizontal cut, and we include such contributions in the definition of the operator $\hat{R}^{(pq)}(\omega)$. It follows that if we extend the notion of connectedness by treating the ω-line as an ordinary line that may connect two disconnected parts, the operator $\hat{R}^{(pq)}(\omega)$ is given by the sum over all open connected diagrams with an internal ω-line.

(ii) Consider next the diagrams in Figure 7. Both diagrams contribute to $\hat{R}_1^{(pq)}(\omega)$. If we add an extra interaction to this operator, as in Figure 8, we close a loop in Figure 8(a), but not in 8(b). So the algebraic rules for propagating the operator $\hat{R}^{(pq)}(\omega)$ are not unambiguously defined. We resolve this ambiguity by adding one extra rule to evaluate the diagrams. The ω-line is treated just like an ordinary line in the sense that we assign a minus sign also to those loops that contain the ω-line. On the other hand we add an extra minus sign to any diagram
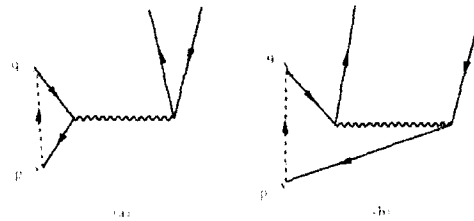
Figure 7. First-order contributions to $\hat{R}^{(pq)}(\omega)$. (a) The dashed line is part of a closed loop; (b) The dashed line is part of an open line connecting the free lines at the top.
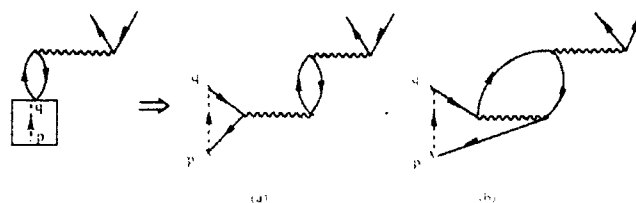
Figure 8.   The rules for propagating the operator $\hat{R}^{(pq)}(\omega)$ are not unambiguously defined.
In Fig. 8(a) a loop is closed, in Fig. 8(b) no loop is closed.

that contains the ω-line as an internal line. Since the perturbation series for $G(\omega)$ only contains closed diagrams where the ω-line is both internal and part of a (non-existent) loop the extra minus signs correctly compensate each other. This extra rule resolves the ambiguity noted in Figure 8 as now a loop is closed in both cases. Also the diagrams in Figure 7 differ in sign using the new rule, which is correct as diagram 7(b) is an exchange diagram of Figure 7(a).

Summarizing we treat the ω-line as an ordinary line in the sense that it may close a loop, and it may connect two disconnected parts. If the ω-line is internal an additional minus sign is included in the algebraic expression corresponding to the diagram.

The perturbative diagrammatic definition of the operators allows us to write down diagrammatic equations for the operators directly. This can be understood if we strip off the topmost interaction (or external point) of an arbitrary diagram contributing to a particular operator and analyze the remainder. This remainder of course consists again of contributions to the previously defined operators. To derive the diagrammatic equations we proceed in the reverse way. A particular operator can be formed by connecting a number (possibly zero) of building blocks (operators) to the topmost interaction element (or external point) such that the total diagram has the structure of the particular operator under consideration. As each building block symbolizes a sum over *all* perturbation diagrams of a particular form the equations are exact if all possibilities of constructing the operator are exhausted. This means that for N-electron systems up to N-fold connected excitation operators of the various types have to be included. The equations have a recursive character because a building block beneath the topmost interaction may be of the same type as the operator under consideration. The factorization theorem (Frantz and Mills [37]) ensures that automatically all relative time orderings between different disconnected parts are taken into account by the above procedure. Hence iterating the diagrammatic equations generates the complete perturbation series for each operator.

In practice the equations have to be decoupled by neglecting high-level connected excitation operators and iteration of the diagrammatic equations then generates a partial infinite set of perturbation diagrams.

To avoid the plethora of terms that is usually obtained if diagrams are drawn in full detail, we only indicate which diagrams contribute. This is sufficient for the definition and understanding of the equations. Detailed algebraic expressions

(working equations) can be obtained by expanding the diagrammatic equations and evaluating the resulting diagrams according to the rules.

To draw the diagrams we make use of the operator $C = e^T$, the wave operator in Coupled Cluster theory. C is as usual partitioned in operators generating single, double, and so forth, excitations out of $|\Phi_0\rangle$. The C operators are represented by shaded boxes with pairs of particle hole lines emerging at the top and they are easily expressed in T-operators diagrammatically (Fig. 9).

A second (and related) reduction in the number of diagrams is obtained if the lines in the diagrams are not explicitly connected, but only the structure of the contributing diagrams is indicated. In the diagrams we consider there are free lines emerging at the top of the diagram (one line may be dashed) that indicate the excitation level of the operator (which may be zero if the diagram is closed from above). There is an energy denominator associated with the free lines and this is indicated by a dashed horizontal line in the diagrams. Beneath the free lines is the top vertex which is considered to be a two-particle interaction in normal order with respect to $|\Phi_0\rangle$, or an external point. Beneath the vertex there may be 0, 1, or 2 operators. At most one of the operators contains the dashed line and corresponds to an $\hat{S}^{(p)}(\omega)$, or $\hat{R}^{(pq)}(\omega)$ operator. Also there may be a C-type operator, which can be expanded in T-operators if desired. The expansion of the C-operator in T-operators is crucial in the ultimate evaluation of the diagrams as they determine whether the diagrams are connected. The total number of *connected* operators beneath the interaction is at most four. In the diagram the lines are not yet connected to the interaction, nor identified with free lines at the top and we use the subscript C to indicate that only connected diagrams are to be included.

Figures 10 to 12 represent the diagrammatic equations that determine the operators $\hat{T}$, $\hat{S}^{(p)}(\omega)$, and $\hat{R}^{(pq)}(\omega)$ up to two-fold excitation level. The diagrammatic equations have a hierarchical structure and have to be solved in succession. Figure 10 represents the Coupled Cluster equations and contains $\hat{T}$-operators only. The equation for $\hat{S}^{(p)}(\omega)$ contains both $\hat{T}$- and $\hat{S}^{(p)}(\omega)$-operators. Hence to solve for $\hat{S}^{(p)}(\omega)$ requires knowledge of $\hat{T}$. $\hat{R}^{(pq)}(\omega)$ (Fig. 12) depends on $\hat{T}$ and $\hat{S}^{(p)}(\omega)$,
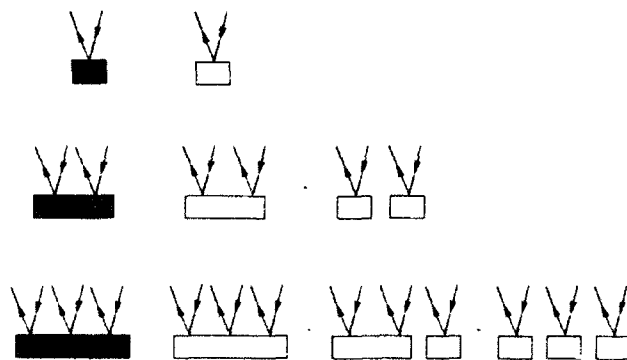
Figure 9. Diagrammatic representation of the relation $C = e^T$. C_1, C_2, and C_3 are represented by shaded boxes.
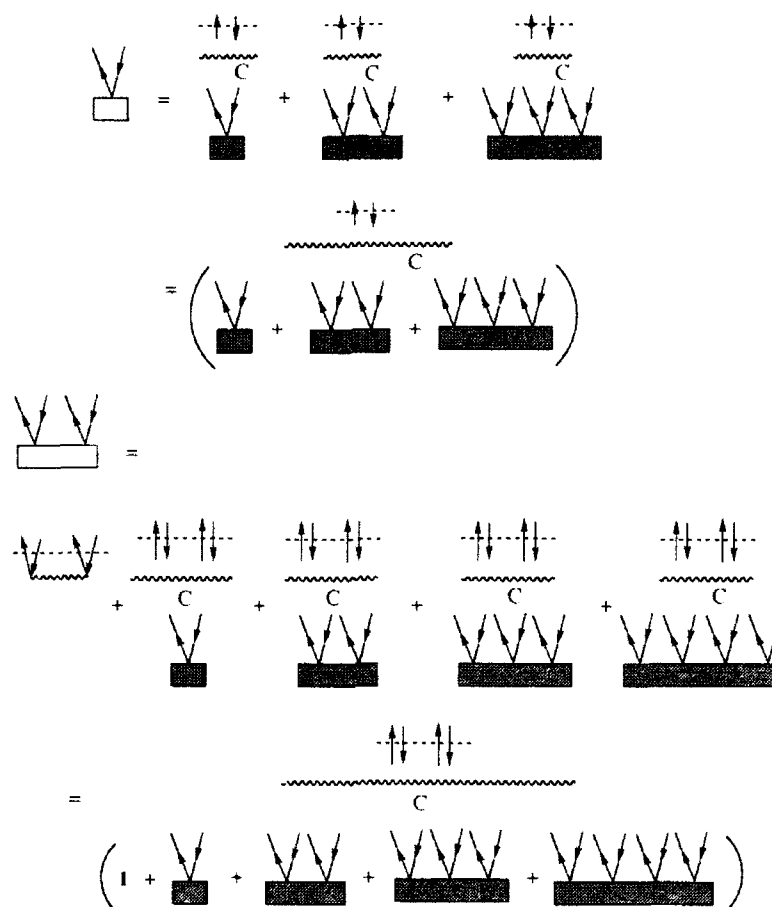
Figure 10.   Compact representation of diagrammatic recursion relations for $\hat{T}$. An interaction with a C attached to it denotes the sum over all topologically distinct connected diagrams of the indicated form. (a) equation for $\hat{T}_1$. (b) equation for $\hat{T}_2$.

so this equation can be solved only after the equations that determine $\hat{T}$ and $\hat{S}^{(p)}(\omega)$ have been solved.

The equations for the different components of an operator [e.g., $\hat{T}_1$, Fig. 10(a), and $\hat{T}_2$, Fig. 10(b)] are strongly coupled. Such equations are always treated together and they are considered one equation in the following sections.

In Figure 13 (the ionization part of) $\mathbf{G}_{pq}(\omega)$ is constructed in terms of the above building blocks $\hat{T}$, $\hat{S}^{(p)}(\omega)$, $\hat{R}^{(pq)}(\omega)$, and $\hat{a}_q^\dagger$. This equation for $\mathbf{G}_{pq}(\omega)$ is derived in the same manner as the operator equations. Strip off the topmost vertex (interaction or external point) of an arbitrary diagram contributing to $\mathbf{G}_{pq}(\omega)$ and analyze the remainder. The various contributions are easily classified as given in Figure 13.

In Figure 14 it is illustrated how the equations can be expanded in detailed diagrams that can be evaluated with the usual diagram rules [1,10–14].

Figure 11. Diagrammatic recursion relations for $\tilde{S}^{(p)}(\omega)$. (a) Equation for $\tilde{S}_1^{(p)}(\omega)$. The first two diagrams correspond to the initialization of $S_1^{(p)}(\omega)$, where the dashed line emerges from the external point. The other diagrams denote the propagation of $S^{(p)}(\omega)$-operators to $S_1^{(p)}(\omega)$. (b) Equation for $\tilde{S}_2^{(p)}(\omega)$. The first term corresponds to initialization, the others to propagation.

Figures 10 to 13 constitute the diagrammatic representation of the Coupled Cluster approach to the single-particle Green's function. We end our discussion of the diagrammatics of the CCGF with an account of the Coupled Cluster aspects of the approach.

(i) The operators we use are all connected.

(ii) In the diagrammatic definition of the operators, the free lines emerge at the top of the diagrams. All interaction lines occur beneath the endpoints of the operator lines, and consequently all operator lines end at the same level. Hence, if a certain perturbation diagram is included in the definition of an operator it does not mean that every different time-ordering of this diagram is included in the perturbation series for this operator as well. We stress that there is a choice here. One might alternatively conceive of an approach where operators are defined in terms of Feyn-
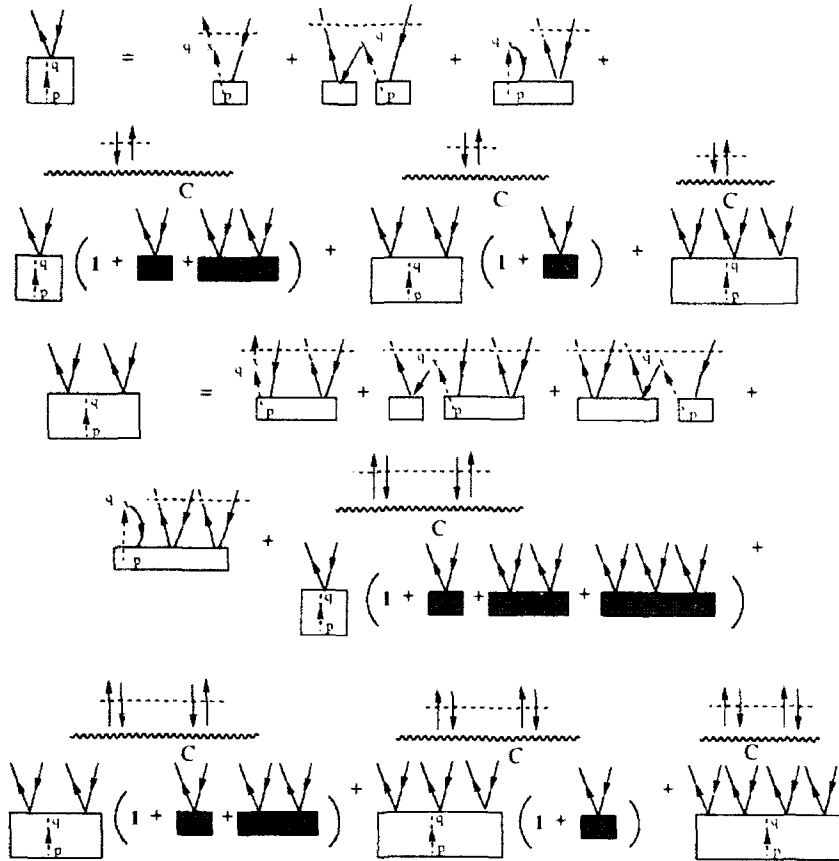
Figure 12. Diagrammatic recursion relation for operator $\hat{R}^{(pq)}(\omega)$. (a) Equation for $\hat{R}_1^{(pq)}(\omega)$. In the first three diagrams the ω line runs into the external point, initializing the operator $\hat{R}_1^{(pq)}(\omega)$. The other diagrams correspond to propagation. (b) Equation for $\hat{R}_2^{(pq)}(\omega)$. Contributions 1–4: initialization. Contributions 5–8: propagation.

man diagrams, with no restriction on the time-orderings included. This would be in line with the original time-dependent perturbation theory and the concept of Green's functions. However, the use of time-ordered diagrams is essential to decouple the ionization and attachment parts of the Green's function. It also allows us to concentrate on the topmost vertex to generate rather simple diagrammatic

$G_{pq}(\omega) \quad = $

Figure 13. The construction of $G_{pq}(\omega)$ in terms of $\hat{a}_q^\dagger$, $\hat{S}^{(p)}(\omega)$, $\hat{R}^{(pq)}(\omega)$, and $\hat{T}$.
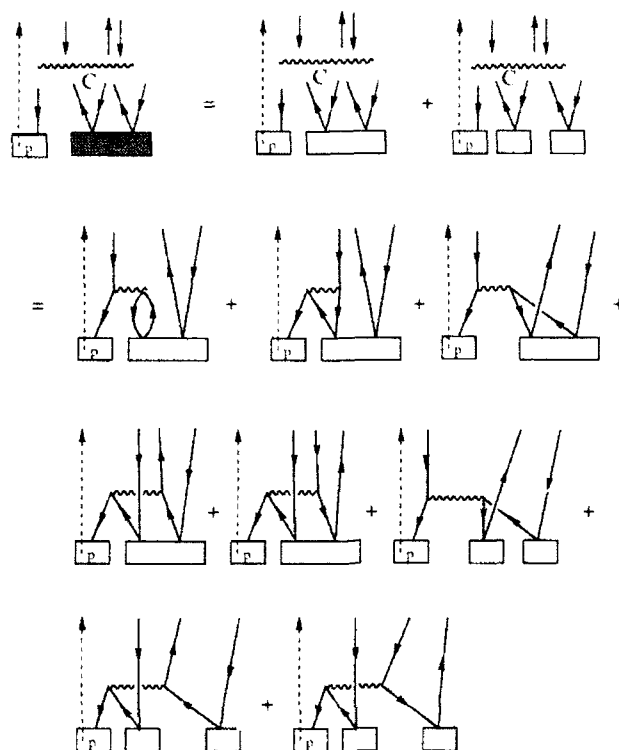
Figure 14. Example of expansion of one of the compact diagrams contributing to $\hat{S}_2^{(p)}(\omega)$. Using nondegenerate (not antisymmetric) vertices for both the interaction and $\hat{T}$-operator, this single diagram corresponds to eight distinct contributions.

recursion relations. The restriction on time-orderings included gains relevance if approximations are introduced. For example a diagram that contains a contribution (in the sense of Fig. 5) from $\hat{T}_2 \cdot \hat{S}_2^{(p)}(\omega)$ might contain a contribution from $\hat{S}_3^{(p)}(\omega)$ in another time-ordering of the diagram. This diagram containing an $\hat{S}_3^{(p)}(\omega)$-contribution might then be excluded from the partial infinite perturbation series that defines the approximation to $G_{pq}(\omega)$.

(iii) Although perturbation theory is the starting point for our approach the final equations are independent of the partitioning of the Hamiltonian in a zeroth-order order and perturbed part. This will be evident once the algebra of the equations is discussed.

The above notions are characteristic for the Coupled Cluster nature of our approach.

The diagrammatic equations that determine the Coupled Cluster operator $\hat{T}$ (Fig. 10) are usually presented in a different way. In the perturbative type of diagrams we use there is an energy denominator associated with the lines above each interaction (if any) and all interaction elements correspond to $\hat{V}$ (instead of $\hat{H}$). We stress that it is precisely the use of these perturbative type diagrams, together with

their Feynman-like interpretation, that permits us to write down the diagrammatic equations directly. No algebraic equation is needed to define the diagram series. Nowadays the common route to Coupled Cluster theory derives from algebra. It is straightforward to show how the perturbative approach follows from the conventional Coupled Cluster equation. We will briefly reflect on the relations between the diagrammatic Coupled Cluster equations and their algebraic counterparts. This also serves to introduce some convenient notation.

We use capitals I and A to denote ordered strings of hole and particle labels, respectively.

$$I = \{i_1, i_2, \ldots, i_k\}, \quad i_1 < i_2 < \cdots < i_k$$

$$A = \{a_1, a_2, \ldots, a_k\}, \quad a_1 < a_2 < \cdots < a_k . \tag{10}$$

The strings I and A are nonempty and have equal length. The cluster operator is written

$$\hat{T} = \sum_{I,A} \hat{T}_I^A = \sum_{I,A} t_I^A \hat{\Omega}_I^A , \tag{11}$$

where $\hat{\Omega}_I^A$ is a string of quasi-particle (or q-) creation operators.

$$\hat{\Omega}_I^A = (\hat{a}_{a_1}^\dagger \hat{a}_{i_1} \hat{a}_{a_2}^\dagger \hat{a}_{i_2} \cdots \hat{a}_{a_k}^\dagger \hat{a}_{i_k}) , \tag{12}$$

which generates excitations out of $|\Phi_0\rangle$:

$$\hat{\Omega}_I^A |\Phi_0\rangle = |\Phi_I^A\rangle . \tag{13}$$

The amplitude corresponding to this excitation operator is given by t_I^A. Of course the operator $\hat{T}$ is usually truncated, for example, to one and twofold excitation operators. This is not essential in the theory and we will not further specify the sum over I and A. The projection used below is on the manifold of states $\{|\Phi_I^A\rangle\}$ that have a nonzero overlap with the state $\hat{T}|\Phi_0\rangle$. The Coupled Cluster equations read

$$\hat{H}e^{\hat{T}}|\Phi_0\rangle = E_0 e^{\hat{T}}|\Phi_0\rangle \implies \langle\Phi_I^A| e^{-\hat{T}}\hat{H}e^{\hat{T}}|\Phi_0\rangle = 0 \iff$$

$$\langle\Phi_I^A| e^{-\hat{T}}\hat{H}_0 e^{\hat{T}} + e^{-\hat{T}}\hat{V}e^{\hat{T}}|\Phi_0\rangle = 0 \iff$$

$$-\langle\Phi_I^A|[\hat{H}_0, \hat{T}]|\Phi_0\rangle = \langle\Phi_I^A| e^{-\hat{T}}\hat{V}e^{\hat{T}}|\Phi_0\rangle \iff$$

$$(E_I - E_A)t_I^A = \langle\Phi_I^A|\{\hat{V}e^{\hat{T}}\}_c|\Phi_0\rangle . \tag{14}$$

Here $E_I - E_A = \sum_{i\in I}\varepsilon_i - \sum_{a\in A}\varepsilon_a$. The equations can also be given at an operator level as

$$\hat{T}_I^A = \frac{1}{E_I - E_A}\{\hat{V}e^{\hat{T}}\}_{c,I}^A , \tag{15}$$

where in the connected product $\{\hat{V}e^{\hat{T}}\}_{c,I}^A$ only those terms contribute that correspond to the substitution operator $\hat{\Omega}_I^A$. This operator form is precisely the content of the diagrammatic equations given in Figure 10. The energy denominator associated with the free lines at the top of the diagrams is explicit in Eq. (15). In this

derivation we used the familiar substitution $e^{-T}Ve^{T} = \{Ve^{T}\}_c$ which derives from the application of Wick's theorem. see, for example. Ref. [38].

Algebraics of the operator $\hat{S}^{(p)}(\omega)$. Analogous to the operator $\hat{T}$. the operator $\hat{S}^{(p)}(\omega)$ is written as

$$\hat{S}^{(p)}(\omega) = \sum_{I_+,A} \hat{S}^{(p)A}_{I_+}(\omega) = \sum_{I_+,A} s^{(p)A}_{I_+}(\omega)\hat{\Omega}^A_{I_+} , \tag{16}$$

where I_+ is an ordered string of hole labels (of length ≥ 1) and A an ordered string of particle labels (possibly of length zero). The length of I_+ exceeds the length of A by one, for example,

$$\hat{S}^{(p)A}_{I_+}(\omega) = s^{(p)A}_{I_+}(\omega)\hat{\Omega}^A_{I_+} = s^{(p)a_1\cdots a_k}_{i_1\cdots i_k}(\omega)N(\hat{a}^\dagger_{a_1}\hat{a}_{i_1}\cdots\hat{a}^\dagger_{a_k}\hat{a}_{i_k},\hat{a}_{i_k}) \tag{17}$$

and

$$\hat{S}^{(p)A}_{I_+}(\omega)|\Phi_0\rangle = s^{(p)A}_{I_+}(\omega)\hat{\Omega}^A_{I_+}|\Phi_0\rangle = s^{(p)A}_{I_+}(\omega)|\Phi^A_{I_+}\rangle . \tag{18}$$

If the operator $\hat{S}^{(p)}(\omega)$ is expanded up to N-fold excitations (the excitation level being defined through the length of the string I_+) the set of states $\{|\Phi^A_{I_+}\rangle\}$ is complete in the $(N-1)$-particle Hilbert space.

The diagrammatic equation given in Figure 11. that defines $\hat{S}^{(p)}(\omega)$ recursively can be directly translated into

$$\hat{S}^{(p)A}_{I_+}(\omega) = \frac{1}{-\omega + E_{I_+} - E_A}\left(\{[V\hat{S}^{(p)}(\omega)]_c e^T\}^A_{c,I_+} + \{\hat{a}_p e^T\}^A_{c,I_+}\right) \tag{19}$$

The energy denominator is made explicit. The first term on the right-hand side corresponds to the "propagation" of $\hat{S}^{(p)}(\omega)$: connect $\hat{S}^{(p)}(\omega)$ to a V interaction and possibly connect $\hat{T}$ operators to the interaction, too, such that the free lines generate the ionization/excitation $I_+ \rightarrow A$. The second term generates the "initialization" of $\hat{S}^{(p)}(\omega)$, the diagrams in Figure 11 where the ω-line emerges directly from the external point p.

Equation (19) can be rewritten by bringing the denominator to the other side and writing it as a commutator of $\hat{S}^{(p)A}_{I_+}(\omega)$ with $\hat{H}_0$. Then we let both sides of the equation operate on $|\Phi_0\rangle$. This does not change the content of the equation as $\hat{S}^{(p)}(\omega)$ contains only q-creation operators. In the next step we sum over the various $\hat{S}^{(p)}(\omega)$-components and project against $\langle\Phi^A_{I_+}|$. This leads to

$$\langle\Phi^A_{I_+}| -\omega\hat{S}^{(p)}(\omega) - [\hat{H}_0, \hat{S}^{(p)}(\omega)]|\Phi_0\rangle$$

$$= \langle\Phi^A_{I_+}|e^{-T}([V, \hat{S}^{(p)}(\omega)] + \hat{a}_p)e^T|\Phi_0\rangle \tag{20}$$

Here we also used that each component of $\hat{S}^{(p)}(\omega)$ consists of q-creation operators only, and the fact that V contains an even number of construction operators to replace the connected products with commutators on the right-hand side.

If one uses next that $[\hat{H}_0, \hat{S}^{(p)}(\omega)]$ contains q-creation operators only and hence commutes with $\hat{T}$ one may write

$$\langle \Phi_{I_+}^A | (-\omega \hat{S}^{(P)}(\omega) - e^{-i}[\hat{H}, \hat{S}^{(P)}(\omega)]e^{i}) | \Phi_0 \rangle = \langle \Phi_{I_+}^A | e^{-i}\hat{a}_p e^{i} | \Phi_0 \rangle \qquad (21)$$

where $\hat{H}_0$ and $\hat{V}$ are recollected.

After expanding $\hat{S}^{(P)}(\omega) = \Sigma_{J_+,B} s^{(P)B}_J(\omega)\hat{\Omega}^B_J$, Eq. (21) reads

$$\sum_{J_+,B} \langle \Phi_{I_+}^A | e^{-i}(-\omega\hat{\Omega}^B_J - [\hat{H}, \hat{\Omega}^B_J])e^{i} | \Phi_0 \rangle s^{(P)B}_J(\omega)$$

$$= \langle \Phi_{I_+}^A | (e^{-i}\hat{a}_p e^{i}) | \Phi_0 \rangle \qquad (22)$$

Define the matrix A with elements

$$\langle \Phi_{I_+}^A | e^{-i}[\hat{H}, \Omega^B_J]e^{i} | \Phi_0 \rangle \qquad (23)$$

and the vectors $b^{(P)}$ with components

$$\langle \Phi_{I_+}^A | e^{-i}\hat{a}_p e^{i} | \Phi_0 \rangle . \qquad (24)$$

Equation (22) for the coefficients $s^{(P)}(\omega)$ then transforms into

$$(-\omega 1 - A)s^{(P)}(\omega) = b^{(P)} \qquad (25)$$

which can be solved by diagonalizing A: $A = UAU^{-1}$ leads to

$$U(-\omega 1 - \Lambda)U^{-1}s^{(P)}(\omega) = b^{(P)} \qquad (26)$$

or

$$s^{(P)}(\omega) = U(-\omega 1 - \Lambda)^{-1}U^{-1}b^{(P)} . \qquad (27)$$

This equation deserves further analysis. The most salient feature of the matrix A is that it is nonsymmetric. This implies that the matrix U is nonunitary: $U^{-1} \neq U^\dagger$. The right eigenvectors of A are accumulated in U, while U^{-1} contains the left eigenvectors. The eigenvalue spectrum is the same for both types of eigenvectors.

The matrix A has previously been derived in the context of Coupled Cluster Linear Response Theory (CCLRT) [16–23] in a number of alternative ways and below we review the equation of motion type of procedure [18,20,21]. The EOM derivation leads directly to an interpretation of the quantities A, U, U^{-1}, and $U^{-1}b^{(P)}$ occurring in Eq. (27) and shows how Feynman–Dyson amplitudes can be extracted from the formalism.

Equation of motion derivation of matrix A. Let us use a shorter notation $|\Phi_\lambda\rangle$ to denote $|\Phi_{I_+}^A\rangle$ and introduce a nonorthogonal basis for the $(N - 1)$-particle Hilbert space

$$|X_\lambda\rangle = e^{T}|\Phi_\lambda\rangle = e^{T}\hat{\Omega}_\lambda|\Phi_0\rangle = \hat{\Omega}_\lambda e^{T}|\Phi_0\rangle = \hat{\Omega}_\lambda|\Psi_{CC}\rangle \qquad (28)$$

together with the bra states

$$\langle \tilde{X}_\kappa | = \langle \Phi_\kappa | e^{-T} , \qquad (29)$$

which are dual to the states $|X_\lambda\rangle$ in the sense that

$$\langle \tilde{X}_\kappa | X_\lambda \rangle = \langle \Phi_\kappa | e^{-T}e^{T} | \Phi_\lambda \rangle = \langle \Phi_\kappa | \Phi_\lambda \rangle = \delta_{\kappa\lambda} \qquad (30)$$

and

$$\sum_\lambda |X_\lambda\rangle\langle \check{X}_\lambda| = \sum_\lambda e^T |\Phi_\lambda\rangle\langle \Phi_\lambda| e^{-T} = 1^{(N-1)} \tag{31}$$

The set of states $\{|X_\lambda\rangle\}$ is complete if the set of states $\{|\Phi_\lambda\rangle\}$ is, because the operator e^T is nonsingular. If the set of states $\{|X_\lambda\rangle\}$ is taken to be incomplete, Eq. (31) denotes a nonorthogonal projector on the space spanned by $\{|X_\lambda\rangle\}$. The idempotency of the projection operator follows directly from the bi-orthonormality relation (30).

Next one tries to find $(N - 1)$-particle eigenstates $|\Psi_\nu^{(N-1)}\rangle$ by expanding

$$|\Psi_\nu^{(N-1)}\rangle = \sum_\lambda |X_\lambda\rangle\langle \check{X}_\lambda|\Psi_\nu^{(N-1)}\rangle \equiv \sum_\lambda |X_\lambda\rangle c_{\lambda\nu}$$

$$= \sum_\lambda c_{\lambda\nu}\hat{\Omega}_\lambda e^T |\Phi_0\rangle \equiv \hat{O}_\nu |\Psi_{CC}\rangle \tag{32}$$

In this last expression one recognizes the equation of motion ansatz. Using that $e^T|\Phi_0\rangle = |\Psi_{CC}\rangle$ is the exact groundstate, the eigenvalue equation for state $|\Psi_\nu^{(N-1)}\rangle$ can be written

$$\left[\hat{H}, \sum_\lambda c_{\lambda\nu}\hat{\Omega}_\lambda\right]e^T|\Phi_0\rangle = (E_\nu - E_0)\sum_\lambda c_{\lambda\nu}|X_\lambda\rangle . \tag{33}$$

Projecting against $\langle \check{X}_\kappa| = \langle \Phi_\kappa|e^{-T}$ one finds

$$\sum_\lambda \langle \Phi_\kappa|e^{-T}[\hat{H}, \hat{\Omega}_\lambda]e^T|\Phi_0\rangle c_{\lambda\nu} = (E_\nu - E_0)c_{\kappa\nu} \tag{34}$$

that is,

$$\mathbf{A}\mathbf{c}_\nu = \Delta E_\nu \mathbf{c}_\nu \tag{35}$$

It follows that the expansion coefficients c_ν of $|\Psi_\nu^{(N-1)}\rangle$ in the nonorthogonal basis $\{|X_\lambda\rangle\}$ are obtained as the right eigenvectors of the matrix $\mathbf{A}$. The eigenvalues of $\mathbf{A}$ correspond to the energy differences $E_\nu - E_0$, that is, ionization potentials.

This equation is also used to determine energy differences in case $e^T|\Phi_0\rangle$ is not an exact eigenstate of $\hat{H}$. In that case the eigenvalue equation for $|\Psi_\nu^{(N-1)}\rangle$ and Eq. (33) are not equivalent. The use of the ansatz $|\Psi_\nu^{(N-1)}\rangle = \hat{O}_\nu|\Psi_0\rangle$ and the use of the commutator to arrive at the equation that determines the energy difference directly is characteristic for the equation of motion method. Other assumptions in the above derivation are particular of the method and various alternatives are found in the literature [20,21].

(i) The choice of the operator $\hat{O}_\nu$, which consists of q-creation operators only.

(ii) The Coupled Cluster form of the (approximate) ground-state wave function.

(iii) The projection on the states $\langle \check{X}_\kappa|$ to cast Eq. (33) in a computationally tractable form. A consequence of using this projection is the absence of an overlap matrix on the right-hand side of Eq. (35).

(iv) The operator $\hat{O}_\nu$ is not required to satisfy the killer condition $\langle \Psi_0|\hat{O}_\nu = 0$ which occurs frequently in equation of motion type of approaches. This is related

to the parametrization of the operator $\hat{O}_\nu$ (point i). The equation $\hat{O}_\lambda|\Psi_0\rangle = |\Psi_\nu^{(N-1)}\rangle$ determines the operator $\hat{O}_\nu$ completely and there is no freedom left to satisfy an additional killer condition [39].

We note that the above specifications arise naturally in our procedure starting from the diagrammatic perturbation series for $G(\omega)$.

We now continue our analysis of the matrix A by defining bra-states, which are required to be $(N-1)$-particle eigenstates of $\hat{H}$

$$\langle \check{\Psi}_\nu^{(N-1)}| = \sum_\kappa \langle \check{\Psi}_\nu^{(N-1)}|X_\kappa\rangle\langle \check{X}_\kappa| = \sum_\kappa d_{\nu\kappa}\langle \check{X}_\kappa| = \sum_\kappa d_{\nu\kappa}\langle \Phi_\kappa|e^{-T} \quad (36)$$

The coefficients d_ν are determined such that

$$\sum_\kappa d_{\nu\kappa}\langle \check{X}_\kappa|\hat{H}|X_\lambda\rangle = E_\nu d_{\nu\lambda} \quad (37)$$

or to get energy differences

$$\sum_\kappa d_{\nu\kappa}\langle \Phi_\kappa|e^{-T}[\hat{H}, \hat{\Omega}_\lambda]e^T|\Phi_0\rangle = d_{\nu\lambda}(E_\nu - E_0) \quad (38)$$

that is, $d_\nu A = d_\nu \Delta E_\nu$. The expansion coefficients d_ν are determined as the left eigenvectors of the nonsymmetric matrix A.

As the vectors d_ν and c_ν are the left and right eigenvectors of A they form a bi-orthogonal set, and they can be chosen to form a bi-orthonormal set:

$$d_\nu \cdot c_\mu = \delta_{\nu\mu} \quad (39)$$

Similar results hold for the states $|\Psi_\nu^{(N-1)}\rangle$ and $\langle \check{\Psi}_\mu^{(N-1)}|$:

$$\langle \check{\Psi}_\mu^{(N-1)}|\Psi_\nu^{(N-1)}\rangle = \sum_{\kappa,\lambda} d_{\mu\kappa}\langle \check{X}_\kappa|X_\lambda\rangle c_{\lambda\nu} = \delta_{\mu\nu} \quad (40)$$

Also

$$\sum_\nu |\Psi_\nu^{(N-1)}\rangle\langle \check{\Psi}_\nu^{(N-1)}| = \sum_{\lambda,\kappa,\nu} |X_\lambda\rangle c_{\lambda\nu} d_{\nu\kappa}\langle \check{X}_\kappa|$$

$$= \sum_{\lambda,\kappa} |X_\lambda\rangle\delta_{\lambda\kappa}\langle \check{X}_\kappa| = \sum_\lambda |X_\lambda\rangle\langle \check{X}_\lambda| = 1^{(N-1)}. \quad (41)$$

The above results remain valid if one uses a restricted set of states $\{|X_\lambda\rangle\}$ and its dual basis $\{\langle \check{X}_\kappa|\}$. $1^{(N-1)}$ is then a nonorthogonal projector on the space spanned by $\{|X_\lambda\rangle\}$ or a resolution of the identity within this space.

Let us now return to the interpretation of the operator $\hat{S}^{(P)}(\omega)$ and insert the above resolution of the identity into Eq. (22)

$$\sum_{J,\nu,B} \langle \Phi_{I_\nu}^A|e^{-T} \sum_\nu |\Psi_\nu^{(N-1)}\rangle\langle \check{\Psi}_\nu^{(N-1)}|(-\omega\hat{\Omega}_{J_\nu}^B - [\hat{H}, \hat{\Omega}_{J_\nu}^B])e^T|\Phi_0\rangle s^{(P)B}_{J_\nu}(\omega)$$

$$= \langle \Phi_{I_\nu}^A|(e^{-T}\hat{a}_\rho e^T)|\Phi_0\rangle \quad (42)$$

or

$$\sum_{J,B} \sum_{\nu} \langle \Phi_{I}^{A} | e^{-\tau} | \Psi_{\nu}^{(N-1)} \rangle (-\omega - E_{\nu}^{(N-1)} + E_0) \langle \check{\Psi}_{\nu}^{(N-1)} | e^{\tau} | \Phi_{J}^{B} \rangle s^{(p)H}(\omega)$$

$$= \langle \Phi^{A} | (e^{-\tau} \hat{a}_p e^{\tau}) | \Phi_0 \rangle$$

(43)

Comparing with Eq. (26) we identify

$$\Lambda_{\nu\mu} = (E_{\nu}^{(N-1)} - E_0)\delta_{\nu\mu}$$ (44)

$$U_{\kappa\nu} = \langle \hat{X}_{\kappa} | \Psi_{\nu}^{(N-1)} \rangle = c_{\kappa\nu}$$ (45)

and

$$U_{\nu\lambda}^{-1} = \langle \check{\Psi}_{\nu}^{(N-1)} | X_{\lambda} \rangle = d_{\nu\lambda} .$$ (46)

From these identities and the definition of $b^{(p)}$ [Eq. 24] it follows

$$U^{-1}b^{(p)} = \sum_{I,A} \langle \check{\Psi}_{\nu}^{(N-1)} | e^{\tau} | \Phi_{I}^{A} \rangle \langle \Phi_{I}^{A} | e^{-\tau} \hat{a}_p e^{\tau} | \Phi_0 \rangle = \langle \check{\Psi}_{\nu}^{(N-1)} | \hat{a}_p | \Psi_{cc} \rangle$$ (47)

and using Eq. (27)

$$\hat{S}^{(p)}(\omega) | \Phi_0 \rangle = \sum_{\nu} \sum_{I,A} | \Phi_{I}^{A} \rangle \langle \Phi_{I}^{A} | e^{-\tau} | \Psi^{(\nu-1)}$$

$$\times (-\omega - E_{\nu}^{(N-1)} + E_0)^{-1} \langle \check{\Psi}_{\nu}^{(N-1)} | \hat{a}_p | \Psi_{cc} \rangle$$ (48)

hence

$$e^{\tau} \hat{S}^{(p)}(\omega) | \Phi_0 \rangle = \hat{S}^{(p)}(\omega) | \Psi_{cc} \rangle = \sum_{\nu} \frac{| \Psi_{\nu}^{(N-1)} \rangle \langle \check{\Psi}_{\nu}^{(N-1)} | \hat{a}_p | \Psi_{cc} \rangle}{-\omega - (E_{\nu}^{(N-1)} - E_0)}$$ (49)

which is used later on.

If $\hat{T}$ is expanded up to N-fold excitations and the manifold of states $\{|\Phi_\lambda\rangle\}$ is taken to be complete the equations are exact. In this case $|\Psi_{\nu}^{(N-1)}\rangle$ and $\langle \check{\Psi}_{\mu}^{(N-1)} |$ are both exact ($N-1$)-particle eigenstates, which may still differ, however, in their normalization (only the overlap of these states is specified, not their individual normalizations). In actual applications one will use a restricted set of states, or equivalently a restricted set of operators $\hat{\Omega}_\lambda$. We note a few interesting observations. Let us consider the concrete case of using a $\{h, 2hp\}$ manifold:

$$\{\hat{\Omega}_\lambda\} = \{\{\hat{a}_i\}, \{\hat{a}_i\hat{a}_j\hat{a}_h^\dagger\}\} .$$ (50)

(i) The character of the states $|\Psi_{\nu}^{(N-1)}\rangle$ and $\langle \check{\Psi}_{\nu}^{(N-1)}|$ is vastly different. Due to the presence of e^{τ} the states $|\Psi_{\nu}^{(N-1)}\rangle$ contain up to N-fold excitations with respect to $|\Phi_0\rangle$. With respect to $\langle \Phi_\kappa |$, $e^{-\tau}$ acts as a deexcitation operator and the states $\langle \check{\Psi}_{\nu}^{(N-1)}|$ can all be expanded in terms of $(h, 2hp)$ bra-states $\langle \Phi_\kappa |$.

(ii) The set of states $\{|\Psi_{\mu}^{(N-1)}\rangle\}$ do not, in general, form an orthogonal basis:

$$\langle \Psi_{\mu}^{(N-1)} | \Psi_{\nu}^{(N-1)} \rangle \neq 0, \mu \neq \nu ,$$ (51)

where $\langle \Psi_{\mu}^{(N-1)} |$ is the adjoint of $|\Psi_{\nu}^{(N-1)}\rangle$. This also implies that the operator $\sum_{\nu} |\Psi_{\nu}^{(N-1)}\rangle \langle \Psi_{\nu}^{(N-1)}|$ lacks the requirement of idempotency and hence cannot be

considered a projection operator. The orthogonality of approximate states with different eigenvalues might seem to be a very desirable property, but one may put a question mark here. If one would project the exact eigenstates on a certain truncated manifold, the projected eigenstates would not be orthogonal, although in a least-squares sense this represents the best possible approximation of the eigenstates within the manifold.

(iii) From the analysis sofar one might expect that the ionization part of $G(\omega)$ can be constructed from the information that can be extracted from the equation for $\hat{S}^{(p)}(\omega)$ alone:

$$
G_{pq}^{IP}(\omega) = \sum_{\nu} \frac{(\langle \tilde{\Psi}_{\nu}^{(N-1)} | \hat{a}_q | \Psi_{CC} \rangle)^* \langle \tilde{\Psi}_{\nu}^{(N-1)} | \hat{a}_p | \Psi_{CC} \rangle}{\omega - (E_0 - E_{\nu}^{(N-1)})}
$$

$$
= \sum_{\nu} \frac{\langle \Psi_{CC} | \hat{a}_q^{\dagger} | \tilde{\Psi}_{\nu}^{(N-1)} \rangle \langle \tilde{\Psi}_{\nu}^{(N-1)} | \hat{a}_p | \Psi_{CC} \rangle}{\omega - (E_0 - E_{\nu}^{(N-1)})} . \qquad (52)
$$

According to the above expression $G^{IP}(\omega)$ is obtained in intermediate normalization, but this is easily corrected by introducing a normalizing factor. The fact, however, that the operator $\sum_{\nu} | \tilde{\Psi}_{\nu}^{(N-1)} \rangle \langle \tilde{\Psi}_{\nu}^{(N-1)} |$ does not represent a projection renders the above formula useless in practice. (This was born out in numerical experiments in which Eq. (52) was utilized to calculate the residues of the single-particle Green's function.) Therefore we continue our analysis and show in the next section how one can build up the remaining part of G.

Algebraics of the operator $\hat{R}^{(pq)}(\omega)$ and the construction of $G_{pq}(\omega)$. The operator $\hat{R}^{(pq)}(\omega)$ is written

$$
\hat{R}^{(pq)}(\omega) = \sum_{J,B} \hat{R}^{(pq)B}_J(\omega) = \sum_{J,B} r^{(pq)B}_J(\omega) \hat{\Omega}^B_J \qquad (53)
$$

J and B denote ordered strings of hole and particle labels, respectively, of equal length, so $\hat{\Omega}^B_J | \Phi_0 \rangle = | \Phi^B_J \rangle$ refers to an N-particle state. The diagrammatic equation in Figure 12 that defines $\hat{R}^{(pq)}(\omega)$ corresponds algebraically to

$$
\hat{R}^{(pq)}(\omega)^B_J = \frac{1}{(E_J - E_B)} (\{\{ \hat{V} \hat{R}^{(pq)}(\omega)\} e^{\hat{T}}\}_{C,J}^B - \{(\hat{a}_q^{\dagger} \hat{S}^{(p)}(\omega)) e^{\hat{T}}\}_{C,J}^B) \qquad (54)
$$

The first term on the right-hand side corresponds to the propagation of $\hat{R}^{(pq)}(\omega)$: Connect $\hat{R}^{(pq)}(\omega)$ to a $\hat{V}$-interaction and possibly connect extra $\hat{T}$-operators, such that the lines emerging at the top of the diagram generate precisely the excitation $J \to B$. The second term generates the initialization of $\hat{R}^{(pq)}(\omega)$ where the ω-line disappears again in the external point labeled q. There are two subtleties however. Firstly $\hat{S}^{(p)}(\omega)$ is not necessarily connected to $\hat{a}_q^{\dagger}$ by a real line. It may be connected to $\hat{a}_q^{\dagger}$ by the dashed line only. An example of such a diagrammatic contribution is given in Figure 6 as was discussed previously. On the other hand if a cluster operator $\hat{T}$ is present it will always be connected to $\hat{a}_q^{\dagger}$. Secondly, there is a minus sign in Eq. (54). The algebraic expression then agrees with the direct evaluation of the diagrams using the rules as discussed in connection with Figures 7 and 8.

Equation (54) can be cast in matrix form following essentially the same steps as in rewriting the equation for $\hat{S}^{(p)}(\omega)$.

$$-\langle \Phi_i^j | e^{-T} [\hat{H}, \hat{R}^{(pq)}(\omega)] e^T | \Phi_0 \rangle = -\langle \Phi_i^j | e^{-T} \hat{a}_q^\dagger \hat{S}^{(p)}(\omega) e^T | \Phi_0 \rangle \quad (55)$$

or

$$-\sum_{J,B} \underbrace{\langle \Phi_i^j | e^{-T} [\hat{H}, \hat{\Omega}_J^B] e^T | \Phi_0 \rangle}_{B} \, r^{(pq)B}_J(\omega) = \underbrace{-\langle \Phi_i^j | e^{-T} \hat{a}_q^\dagger e^{-T} \hat{S}^{(p)}(\omega) | \Phi_0 \rangle}_{c^{(pq)}_J(\omega)} . \quad (56)$$

$c^{(pq)}(\omega)$ can also be written as

$$c^{(pq)}_J(\omega) = \sum_\nu \frac{\langle \Phi_i^j | e^{-T} \hat{a}_q^\dagger | \Psi_\nu^{(N-1)} \rangle \langle \Psi_\nu^{(N-1)} | \hat{a}_p | \Psi_0 \rangle}{\omega - (E_0 - E_\nu^{(N-1)})} \quad (57)$$

using Eq. (49).

The equation for $r^{(pq)}(\omega)$ hence reads

$$-B r^{(pq)}(\omega) = c^{(pq)}(\omega) \quad (58)$$

that is,

$$r^{(pq)}(\omega) = -B^{-1} c^{(pq)}(\omega) . \quad (59)$$

using the newly defined matrix B and the ω-dependent vectors $c^{(pq)}(\omega)$.

These equations hardly present a practicle means of calculating the coefficients $r^{(pq)}(\omega)$. For each element (pq) and for each pole of $r^{(pq)}(\omega)$ one would have to solve a large system of linear equations. We will arrive at a suitable method, however, if we continue to construct $G(\omega)$. The final diagrammatic equation in Figure (13) translates algebraically into

$$G_{pq}^{IP}(\omega) = \{ \hat{V} \hat{R}^{(pq)}(\omega) e^T \}_{f.c.} - \{ a_q^\dagger \hat{S}^{(p)}(\omega) \}_{f.c.} \quad (60)$$

where $f.c.$ stands for *fully contracted*, that is, no construction operators remain uncontracted. The resulting expression is a number. The minus sign in the second term agrees with the direct evaluation of the diagrams under consideration. The equation is rewritten

$$G_{pq}^{IP}(\omega) = \langle \Phi_0 | \hat{V} \hat{R}^{(pq)}(\omega) e^T | \Phi_0 \rangle - \langle \Phi_0 | a_q^\dagger \hat{S}^{(p)}(\omega) | \Phi_0 \rangle \quad (61)$$

as only fully contracted terms survive in expectation values of the reference determinant. Hence

$$G_{pq}^{IP}(\omega) = \sum_{J,B} \underbrace{\langle \Phi_0 | \hat{V} \hat{\Omega}_J^B e^T | \Phi_0 \rangle}_{f_J^B} \, r^{(pq)B}_J(\omega) - \langle \Phi_0 | a_q^\dagger \hat{S}^{(p)}(\omega) | \Phi_0 \rangle . \quad (62)$$

Substituting Eq. (59) for $r^{(pq)}(\omega)$ one finds

$$G_{pq}^{IP}(\omega) = -f B^{-1} c^{(pq)}(\omega) - \langle \Phi_0 | a_q^\dagger \hat{S}^{(p)}(\omega) e^T | \Phi_0 \rangle \quad (63)$$

where we also used that one can insert e^T in the second term without altering this expression as $\hat{a}_q^\dagger$ has to be contracted to $\hat{S}^{(p)}(\omega)$ and only the constant term in e^T leads to a nonvanishing contribution.

Now define coefficients z through

$$z = -\mathbf{f}\mathbf{B}^{-1} \tag{64}$$

or

$$z\mathbf{B} + \mathbf{f} = 0 \tag{65}$$

The z-coefficients can easily be solved for. They are the solution of an ω-independent, nonsymmetric system of linear equations. The crucial difference with Eq. (59) is that now one has to solve only one such equation.

Using the coefficients z and the expressions for $c^{(pq)}(\omega)$ [Eq. (57)] and $e^T \hat{S}^{(p)}(\omega)|\Phi_0\rangle$ [Eq. (49)] one finds from Eq. (63)

$$G_{pq}^{IP}(\omega) = \sum_\nu \frac{\left(\langle\Phi_0| + \sum_{J,B} z_J^B\langle\Phi_J^B|e^{-T}\right)\hat{a}_q^\dagger|\Psi_\nu^{(N-1)}\rangle\langle\Psi_\nu^{(N-1)}|\hat{a}_p|\Psi_{CC}\rangle}{\omega - (E_0 - E_\nu^{(N-1)})}$$

$$= \sum_\nu \frac{\langle\check{\Psi}_{CC}|\hat{a}_q^\dagger|\Psi_\nu^{(N-1)}\rangle\langle\Psi_\nu^{(N-1)}|\hat{a}_p|\Psi_{CC}\rangle}{\omega - (E_0 - E_\nu^{(N-1)})}, \tag{66}$$

where $\langle\check{\Psi}_{CC}|$ is defined by the expression between parentheses,

$$\langle\check{\Psi}_{CC}| = \langle\Phi_0| + \sum_{I,A} z_I^A\langle\Phi_I^A|e^{-T}. \tag{67}$$

Equation (66) clearly resembles the spectral resolution of the ionization part of $G(\omega)$.

The approximate ground-state bra $\langle\check{\Psi}_{CC}|$ is by now well established in the CC literature [33,34]. It was introduced by Arponen in the framework of the Normal Coupled Cluster method (NCCM) [33]. An important feature of $\langle\check{\Psi}_{CC}|$ is that it has an overlap of unity with the CC ket $|\Psi_{CC}\rangle$, irrespective of the parameters z and t

$$\langle\check{\Psi}_{CC}|\Psi_{CC}\rangle = \langle\Phi_0|e^T|\Phi_0\rangle + \sum_{J,B} z_J^B\langle\Phi_J^B|\Phi_0\rangle = 1 \tag{68}$$

It follows that the optimal values for the parameters z and t can be obtained from a bivariational principle [33]: the requirement that $\langle\check{\Psi}_{CC}|\hat{H}|\Psi_{CC}\rangle$ be stable under a variation of either the parameters z or t leads to the conventional CC equations for the parameters t and to the equations for the parameters z, as given in Eq. (65). The variational principle implies the existence of a Hellmann–Feynman theorem, which means that expectation values of an operator $\hat{O}$ can be obtained as

$$\langle\hat{O}\rangle = \langle\check{\Psi}_{CC}|\hat{O}|\Psi_{CC}\rangle. \tag{69}$$

Hence the NCCM furnished the solution of a longstanding problem in Coupled Cluster theory.

A second feature of the NCCM bra state $\langle \tilde{\Psi}_{CC} |$, which is of great practical importance, is its simplicity. Due to the fact that the components of $\tilde{I}$ act as de-excitation operators when operating to the left, the state $\langle \tilde{\Psi}_{CC} |$ lies completely in the linear space spanned by $\{ \langle \Phi_0 |, \langle \Phi_I^A | \}$ used in the definition of $\langle \tilde{\Psi}_{CC} |$. This means that expectation values of the form (69) can be calculated with relative ease. The same holds for the transition moments that occur in the Coupled Cluster Green's function [Eq. (66)]. Due to the simplicity of the bra's the expressions for the transition amplitudes can be calculated in practice.

The state $\langle \tilde{\Psi}_{CC} |$ is also used to calculate Coupled Cluster energy gradients [40–44]. Similar manipulations as described above were used to reduce the number of linear equations to be solved when calculating the gradient [40–44]. The procedure goes back to Handy and Schaefer [40] who used it when solving for the orbital rotation part of the gradient. Adamowicz et al. [41] similarly showed it to be a convenient short cut to calculate the CC energy gradient and the procedure is now known as the Z-vector method [42]. Koch et al. [44] regarded the z-coefficients as Lagrangian multipliers and derived their equations from a variational principle. The use of a variational principle is clearly very useful when calculating energy derivatives. Explicit working equations for the coefficients z have been given [42–44] that allow for an efficient solution on a computer. Finally Koch and Jørgensen started from the bi-orthonormal formulation in their recent work on Coupled Cluster response functions [22,23]. The matrix **B** [Eq. (56)], which has a similar structure as the matrix **A** [Eq. (23)] is used in CCLRT to calculate excitation energies [16–23].

Returning to Eq. (66) consider the calculation of

$$\langle \tilde{\Psi}_{CC} | \hat{a}_q^\dagger | \Psi_r^{(N-1)} \rangle = \sum_{I,A} \langle \tilde{\Psi}_{CC} | \hat{a}_q^\dagger e^T | \Phi_I^A \rangle \langle \Phi_I^A | e^{-T} | \Psi_r^{(N-1)} \rangle \equiv e^{(q)} U . \quad (70)$$

where the vector $e^{(q)}$ is given by

$$e^{(q)} = \langle \tilde{\Psi}_{CC} | \hat{a}_q^\dagger e^T | \Phi_I^A \rangle = \langle \Phi_0 | \hat{a}_q^\dagger e^T | \Phi_I^A \rangle + \sum_{J,B} z_J^B \langle \Phi_J^B | e^{-T} \hat{a}_q^\dagger e^T | \Phi_I^A \rangle$$

$$= \langle \Phi_0 | \hat{a}_q^\dagger | \Phi_I^A \rangle + \sum_{J,B} z_J^B \langle \Phi_J^B | \hat{a}_q^\dagger + [\hat{a}_q^\dagger, \hat{T}] | \Phi_I^A \rangle . \quad (71)$$

It follows that $G_{pq}(\omega)$ is then given by

$$G_{pq}(\omega) = e^{(q)} U (\omega + \Lambda)^{-1} U^{-1} b = e^{(q)} (\omega + A)^{-1} b^{(p)} \quad (72)$$

where the former expression is in direct correspondence with Eq. (66).

It was mentioned before that certain properties that derive from the ground-state wavefunction can be obtained by calculating contour integrals over $G(\omega)$ that enclose the ionization potentials. Equation (72) allows us to calculate these contour integrals analytically. The one-particle density matrix can be calculated as

$$\frac{1}{2\pi i} \oint_{IP} G_{pq}(\omega) d\omega = p_{pq} = e^{(q)} U U^{-1} b^{(p)} = e^{(q)} \cdot b^{(p)} . \quad (73)$$

To calculate the total energy from the Green's function one also needs

$$\frac{1}{2\pi i} \oint_{LP} \omega G_{pq}(\omega)d\omega = e^{(q)}U(-\Lambda)U^{-1}b^{(p)} = -e^{(q)}\cdot Ab^{(p)}. \tag{74}$$

It follows that to calculate these quantities in our formalism one does not need to know the pole structure of $G(\omega)$ explicitly.

Approximations

The equations considered sofar are exact for N-electron systems if all connected operators are expanded up to N-fold excitation level (assuming a finite dimensional Fock space, defined through a finite set of one particle basis functions). By solving these equations one is hence implicitly summing the connected diagram perturbation series through all orders. In actual applications the equations are decoupled by neglecting connected excitation operators from a certain excitation level onwards. A managable and hopefully adequate set of operators arises from

$$\hat{T} = \hat{T}_1 + \hat{T}_2$$
$$\hat{S}^{(p)}(\omega) = \hat{S}_1^{(p)}(\omega) + \hat{S}_2^{(p)}(\omega)$$
$$\hat{R}^{(pq)}(\omega) = \hat{R}_1^{(pq)}(\omega) + \hat{R}_2^{(pq)}(\omega) \tag{75}$$

that is, all operators are expanded up to twofold excitation level. For this approach the acronym CCGF-SD is used. By solving the CCGF-SD equations one is implicitly summing a partial but infinite set of perturbation diagrams. Given an arbitrary perturbation diagram contributing to $G(\omega)$ it is fairly easy to determine whether or not this diagram is included in the partial CCGF-SD series, by applying the test described below.

Mentally cut the diagram at a certain level (between two successive interactions, or between an external point and an interaction, etc.). In the part below the horizontal cut, each of the resulting disconnected parts (internally connected) should have at most four free lines emerging at the top. The dashed line is to be treated on an equal footing with the other lines here. The diagram is included in the CCGF-SD series if it satisfies the above test at each level. This follows directly from the diagrammatic definition of the approach (Figures 10–13), if one discards the contributions that contain connected operators of excitation level higher than two.

The fact that the Coupled Cluster approximation to the single-particle Green's function corresponds to a well-defined partial infinite series of connected perturbation diagrams implies that the method is size-consistent. Size consistency is important (a kind of necessary condition nowadays) but it does by no means imply that one will also get sensible results out of a calculation. The aim in this kind of diagram summation should be to sum over the important diagrams in a balanced way. It is not so clear if the diagram series implied by CCGF-SD indeed constitutes such a balanced series. The CCGF-SD approach to the single-particle Green's function is quite similar to the CCSD approach to the correlation energy however, and this

is known to give quite satisfactory results for a large number of systems. This serves as an indication that the approach presented here will lead to adequate results.

Conclusions

The diagrammatic approach we employed to arrive at equations that allow evaluation of the single-particle Green's function is quite general. In a similar way one may (re-)derive equations that determine for example expectation values (leading to the NCCM equations [33,34]), the polarization propagator (leading to the CCLRT equations for excitation energies [16–23] and the corresponding transition amplitudes), higher order response properties (Cf. Monkhorst [19]), and so forth. The starting point is always the diagrammatic perturbation series for the quantity of interest. If a diagram contributing to the series is taken apart as in this article, by applying a complete horizontal cut between two successive vertices and one considers the connected parts beneath the cut as perturbative contributions to operators of a particular type (compare our T, $S^{(n)}(\omega)$ and $R^{(m)}(\omega)$ operators) one will be lead to a Normal Coupled Cluster type of approach [33,34]. It is interesting to note that the only choice made is the way that one takes the diagrams apart; the identification of the building blocks in terms of their perturbative diagrammatic content. The subsequent establishment of diagrammatic recursion relations for the operators and the translation of the diagrammatic equations into algebraic equations is merely a matter of technique.

Although the diagrammatics is quite sufficient to establish the CCGF approach and diagrams are also very useful in deriving the detailed working equations, the algebraic equations presented in the third section greatly help to clarify the general structure of the approach. The algebra also establishes the intimate relation between CCGF, CCLRT, and NCCM. Indeed the diagrammatic approach advocated here may be regarded as a powerful alternative to derive current extensions of Coupled Cluster Theory which are characterized not only by the use of the exponential ansatz for the wave operator but also by the use of bi-orthogonal sets of bra's and kets of very different character. A striking example of the biorthogonal formulation is encountered in the final expression for the single-particle Green's function [Eq. (66)], where only the *products* of the Feynman–Dyson transition amplitudes represent meaningful quantities.

We end our discussion with an overview of the main features of the Coupled Cluster Green's function method.

(1) The decoupling of the equations for the ionization and the attachment energies greatly reduces the dimension of the problem compared to many other approaches to the single-particle Green's function. The CCGF-SD method for ionization energies leads to an eigenvalue problem in the $h - 2hp$ space. The decoupling of the $(N - 1)$- and $(N + 1)$-particle problems is also satisfying from a conceptual point of view. In contrast to most other approaches to the Green's function well-defined states are recovered in the CCGF formalism.

(2) The method is potentially exact. Inclusion of up to N-fold excitation/ionization operators will lead to exact results for N-electron systems. This is useful

both in analyzing the method and in implementing/debugging the corresponding computer code (we know for example which results we should get for two-electron systems).

(3) The method is size consistent. It shares this property with any method that derives from a connected diagram expansion of the single-particle Green's function.

(4) Unlike many other Green's function methods CCGF does not depend on a partitioning of the Hamiltonian in a zeroth order and a perturbed part. We have only used perturbation theory to derive the method. In general the results do depend on the division of the orbital space in holes and particles, that is, on the reference state employed.

(5) Ground-state properties that derive from the CC Green's function are closely related to properties obtained in the NCCM framework. The precise relationship will be discussed in a forthcoming article.

(6) The eigenvalue problem that has to be solved to obtain ionization potentials is nonhermitean, with the possibility that one might obtain complex eigenvalues, or even the matrix may not be diagonalizable. Also the one particle density matrix and the residue corresponding to a pole of $G(\omega)$ is nonhermitean. The degree of nonhermiticity may serve, however, as an indication of the quality of a calculation.

(7) The method uses a single determinant as a reference state. This limits the applicability of the method to systems that can reasonably be described in terms of a single determinant, analogous to the CCSD approach. On the other hand, this also facilitates the actual application of the method.

Acknowledgments

Bibliography

[1] L. S. Cederbaum and W. Domcke, Adv. Chem. Phys. 36, 205 (1977).

[2] J. Schirmer and L. S. Cederbaum, J. Phys. B11, 1889 (1977).

[3] O. Walter and J. Schirmer, J. Phys. B14, 3805 (1981).

[4] J. Schirmer, L. S. Cederbaum, and C. Walter, Phys. Rev. A28, 1237 (1983).

[5] O. Goscinski and B. Lukman, Chem. Phys. Lett. 7, 573 (1970); B. T. Pickup and O. Goscinski, Mol. Phys. 26, 1013 (1973).

[6] G. Born and Y. Öhrn, Chem. Phys. Lett. 61, 307 (1979).

[7] Y. Öhrn and G. Born, Adv. Quantum Chem. 13, 1 (1981).

[8] J. A. Nichols, D. L. Yeager, and P. Jørgensen, J. Chem. Phys. 80, 293 (1984); J. T. Golab and D. L. Yeager, J. Chem. Phys. 87, 2925 (1987).

[9] J. Baker, Chem. Phys. 79, 117 (1983).

[10] J. Cizek, J. Chem. Phys. 45, 4256, (1966); J. Paldus and J. Cizek, Adv. Quantum Chem. 9, 105 (1975).

[11] I. Lindgren, J. Phys. B7, 2441 (1974); I. Lindgren, Int. J. Quantum Chem., Quantum Chem. Symp. 12, 33 (1978).

[12] V. Kvasnicka, V. Laurinc, and S. Biskupic, Phys. Rep. 90, 159 (1982).

[13] M. R. Hoffman and H. F. Schaefer, Adv. Quantum Chem. **18**, 207 (1986).

[14] S. A. Kucharski and R. J. Bartlett, Adv. Quantum Chem. **18**, 281 (1986).

[15] R. J. Bartlett, J. Phys. Chem. **93**, 1697 (1989).

[16] D. Mukherjee and P. K. Mukherjee, Chem. Phys. **39**, 325 (1979).

[17] S. Ghosh, D. Mukherjee, and S. Bhattacharyya, Mol. Phys. **43**, 173 (1981).

[18] S. Ghosh, D. Mukherjee, and S. Bhattacharyya, Chem. Phys. **72**, 161 (1982).

[19] H. Monkhorst, Int. J. Quantum Chem., Quantum Chem. Symp. **11**, 421 (1977); E. Dalgaard and H. J. Monkhorst, Phys. Rev. A**28**, 1217 (1983).

[20] H. Sekino and R. J. Bartlett, Int. J. Quantum Chem., Quantum Chem. Symp. **18**, 255 (1984).

[21] J. Geertsen, M. Rittby, and R. J. Bartlett, Chem. Phys. Lett. **164**, 57 (1989).

[22] H. Koch and P. Jørgensen, J. Chem. Phys. **93**, 3333 (1990).

[23] H. Koch, H. J. Aa Jensen, P. Jørgensen, and T. Helgaker, J. Chem. Phys. **93**, 3345 (1990).

[24] M. Haque and D. Mukherjee, J. Chem. Phys. **80**, 5058 (1984).

[25] S. Pal, M. Rittby, R. J. Bartlett, D. Sinha, and D. Mukherjee, Chem. Phys. Lett. **137**, 273 (1987); J. Chem. Phys. **88**, 4357 (1988).

[26] L. Stolarczyk and H. J. Monkhorst, Phys. Rev. A**32**, 725, 743 (1985); **37**, 1908, 1926 (1988).

[27] U. Kaldor, Theor. Chim. Acta **80**, 427 (1991).

[28] D. Mukhopadhyay, S. Mukhopadhyay, R. Chauduri, and D. Mukherjee, Theor. Chim. Acta **80**, 441 (1991).

[29] C. M. L. Rittby and R. J. Bartlett, Theor. Chim. Acta **80**, 469 (1991).

[30] M. Barysz, H. J. Monkhorst, and L. Z. Stolarczyk, Theor. Chim. Acta **80**, 483 (1991).

[31] D. Sinha, S. K. Mukhophadhyay, R. Chaudhuri, and D. Mukherjee, Chem. Phys. Lett. **154**, 544 (1989).

[32] L. Meissner and R. J. Bartlett, J. Chem. Phys. **94**, 6670 (1991).

[33] J. Arponen, Ann. Physics **151**, 311 (1982).

[34] R. F. Bishop and J. S. Arponen, Int. J. Quant. Chem. S**24**, 197 (1990); R. F. Bishop, Theor. Chim. Acta **80**, 95 (1991); J. Arponen, ibid. 149.

[35] A. L. Fetter and J. D. Walecka, Quantum theory of many-particle systems (McGraw-Hill, New York, 1971).

[36] J. Goldstone, Proc. Phys. Soc. London, Sect. A**239**, 267 (1957).

[37] L. M. Frantz and R. L. Mills, Nucl. Phys. **15**, 16 (1968).

[38] F. E. Harris, B. Jeziorski, and H. J. Monkhorst, Phys. Rev. A**23**, 1632 (1980).

[39] E. Dalgaard, Int. J. Quantum Chem. **15**, 169 (1979).

[40] N. C. Handy and H. F. Schaefer, III, J. Chem. Phys. **81**, 5031 (1984).

[41] L. Adamowicz, W. D. Laidig, and R. J. Bartlett, Int. J. Quantum Chem., Quantum Chem. Symp. **18**, 245 (1984).

[42] A. C. Scheiner, G. E. Scuseria, J. E. Rice, T. J. Lee, and H. F. Schaefer, III, J. Chem. Phys. **87**, 5361 (1987).

[43] E. A. Salter, G. W. Trucks, and R. J. Bartlett, J. Chem. Phys. **90**, 1752 (1988).

[44] H. Koch, H. J. Aa. Jensen, P. Jørgensen, T. Helgaker, G. E. Scuseria, and H. F. Schaefer, J. Chem. Phys. **92**, 4924 (1990).

Alternative Ansätze in Coupled-Cluster Theory. IV. Comparison for the Two Electron Problem and the Role of Exclusion Principle Violating (EPV) Terms*

PÉTER G. SZALAY⁺ and RODNEY J. BARTLETT

Quantum Theory Project, University of Florida, Gainesville, Florida 32611-2085

Abstract

The two-electron problem is investigated using exponentially parametrized wave functions for various different coupled-cluster (CC) methods, including regular, expectation value, symmetrized expectation value (i.e., unitary), extended, and quadratic configuration interaction (CI) variants. All are viewed as arising from alternative energy functionals. This pedagogical evaluation demonstrates the differences in these methods, including the role of EPV terms. © 1992 John Wiley & Sons, Inc.

Introduction

To ensure the extensive property [1,2], many body methods (unlike CI) use an exponential parameterization of the wave function

$$\Psi = e^{T}|0\rangle \tag{1}$$

where T is the cluster operator for n electrons

$$T = T_1 + T_2 + T_3 + \cdots T_n$$

$$T_n = \frac{1}{(n!)^2} \sum_{ijk \ldots abc} t_{ijk\cdots}^{abc\cdots} \{a^{\dagger}ib^{\dagger}jc^{\dagger}k \cdots\} \tag{2}$$

with $i, j, k, \cdots$ indices indicating spin orbital and operator labels for orbitals occupied in $|0\rangle$, while $a, b, c, \cdots$ correspond to orbital and operator labels unoccupied in $|0\rangle$. Orbitals are orthonormal and normal ordering is denoted by $\{\ \}$. We assume real amplitudes in T_n.

The normal-ordered Hamiltonian defined by

$$H_N = H - \langle 0|H|0 \rangle = \sum_{pq} f_{pq}\{p^{\dagger}q\}$$

$$+ \frac{1}{4} \sum_{p,q,r,s} \langle pq\|rs\rangle \{p^{\dagger}q^{\dagger}sr\} = f_N + W_N \tag{3}$$

---

is composed of Fock matrix elements, f_{pq}, and antisymmetrized two-electron integrals, $\langle pq\|rs\rangle$.

With a wave function of the form (1), the expectation value of H_N can be written as

$$\Delta E = \frac{\langle 0|e^{T^\dagger}H_N e^T|0\rangle}{\langle 0|e^{T^\dagger}e^T|0\rangle} = \langle 0|(e^{T^\dagger}H_N e^T)_c|0\rangle \qquad (4)$$

The right-hand side of the equation indicates that the energy can be written as a sum of connected terms only as was shown by Čížek [3]. Cancellation of the denominator introduces the so-called EPV terms (see later); therefore, the energy expression (4) and the associated stationary equations are infinite [3] for any number of electrons (i.e. even if $T_n = 0$ for some n). Thus, variational determination of the parameters of the wave function is not straightforward.

Alternatively, the traditional coupled-cluster method [4] is built upon projections of the Schrödinger equation:

$$e^{-T}H_N e^T|0\rangle = \Delta E|0\rangle$$

Using properties of the normal-ordered operators, T and H_N, this can be written as:

$$(H_N e^T)_c|0\rangle = \Delta E|0\rangle$$

where the subscript c denotes that connected diagrams only are included. To determine the coefficients, this equation is projected against excited determinants, for example:

$$\langle D_i^a|(H_N e^T)_c|0\rangle = 0$$

$$\langle D_{ij}^{ab}|(H_N e^T)_c|0\rangle = 0$$

$$\vdots \qquad\qquad (5)$$

Projecting against the reference function we get the energy:

$$\Delta E = \langle 0|(H_N e^T)_c|0\rangle$$

Bartlett, et al. [5-7] introduced a de-excitation operator, Λ, to make it possible to evaluate analytical derivatives with CC and MBPT wave functions, without requiring an explicit determination of the derivative wave functions. From another viewpoint, this means we can associate an energy functional [8] with CC theory in the form:

$$\Delta E = \langle 0|(1 + \Lambda)(H_N e^T)_c|0\rangle \qquad (6)$$

where Λ is a de-excitation operator. Because this functional is linear in Λ, the stationary equations provide the usual decoupled equations for T in the form given above. Stationarity of T will define the Λ equations.

Another variant on CC theory is offered by the so-called QCI [9] method. Assuming canonical Hartree-Fock orbitals the equations are:

$$\langle D_i^{ab} | H_N (C_1 + C_2 + C_1 C_2) | 0 \rangle = c^{ab} \Delta E$$

$$\langle D_{ij}^{ab} | H_N (1 + C_1 + C_2 + \tfrac{1}{2} C_1^2) | 0 \rangle = c_{ij}^{ab} \Delta E \qquad (\cdot)$$

and the correlation energy is:

$$\Delta E = \langle 0 | H_N C_2 | 0 \rangle$$

where the QCI coefficients, $C_2 = T_2 + T_1^2/2$ (i.e., $c_{ij}^{ab} = t_{ij}^{ab} + t_i^a t_j^b - t_i^b t_j^a$) and $C_1 = T_1$. The above equations are closely related to the traditional form of the CC method described above, being a truncation of $\exp(T)$. However, this particular truncation is still exact for two electrons. We can also construct a QCI functional analogous to Eq. (6) by invoking the same truncation of $\exp(T)$, which is:

$$\Delta E = \langle 0 | [H_N C_2 + \Lambda_1 (H_N (C_1 + C_2 + C_1 C_2))$$

$$+ \Lambda_2 (H_N (1 + C_1 + C_2 + \tfrac{1}{2} C_1^2) | 0 \rangle$$

Realizing that the CC functional (6) has an exponential ket state and a CI type bra state, it can be generalized using an exponential function also for the bra state:

$$\Delta E = \langle 0 | e^\Lambda (H_N e^T)_c | 0 \rangle$$

Unlike the Λ in Eq. (6), which can have disconnected parts, Λ can be restricted to a connected form with e^Λ introducing appropriate disconnected products. This functional defines the extended CC (ECC) method of Arponen et al. [8,10]. Now, unlike that of the CC method, this functional is not linear in Λ, and therefore, the stationary equations provide coupled equations for the variables Λ and T:

$$\langle D_{ij}^{ab} | e^\Lambda (H_N e^T)_c | 0 \rangle_c = 0$$

$$\langle 0 | e^\Lambda (H_N e^T)_c | D_{ij}^{ab} \rangle_c = 0$$

This functional has some desirable formal properties, as it ensures that both T and Λ are fully connected; however, such coupled equations can be computationally inconvenient.

The ECC method is already closely related to the expectation value of the energy (4). As mentioned before, the normal CC expectation value, Eq. (4) provides an infinite expansion. Therefore in application truncation is necessary. In the XCC (expectation value CC) method [11], we used the order of the terms defined by perturbation arguments to truncate the expression. Recently, we investigated the structure of the stationary equations of the untruncated infinite functional [12]:

$$\langle D_a | e^{T^\dagger} H_N e^T | 0 \rangle = 0 \qquad (8)$$

$$\langle 0 | e^{T^\dagger} H_N e^T | D_a \rangle = 0 \qquad (9)$$

for $a = 1, 2 \cdots n_c$. We use D_a to symbolize excited determinants. As we have proven elsewhere [12] the set of equations defined by Eqs. (8) and (9) becomes exactly the following set of equations:

$$\langle D_a | e^{T^+}(H_N e^T)_c | 0 \rangle_c = 0 \tag{10}$$

$$\langle 0 | (e^{T^+} H_N)_c e^T | D_a \rangle_c = 0 \tag{11}$$

The very important consequence of the above form of the amplitude equations is that the number of terms in them is finite because only four operators can be connected to H_N (because it contains no more than two electron operators). Then, the energy with the converged amplitudes can also be written in closed form:

$$\Delta E = \langle 0 | e^{T^+}(H_N e^T)_c | 0 \rangle_c$$

The advantage of the XCC method over ECC is that only one set of equations (for real amplitudes) has to be solved to determine T and to calculate the energy. On the other hand, as we also showed in ref. 12 no simplified energy functional exists; i.e., for the calculation of energy derivatives the original form of the ΔE functional (4) has to be used.

An approximate functional can be defined, however, which is finite. In refs. 11 and 12 we choose the following form:

$$\Delta E = \tfrac{1}{2}[\langle 0 | e^{T^+}(H_N e^T)_c | 0 \rangle_c + \langle 0 | (e^{T^+} H_N)_c e^T | 0 \rangle_c] \tag{12}$$

because it is symmetric in T and T^+, and only one set of equations (for T or for T^+) has to be solved, even for a gradient calculation. The method described by this functional is equivalent to the SXCC (symmetric XCC) method, which is equivalent to unitary (UCC(n)) for low n-orders [11]. Since this method ensures the satisfaction of the generalized Hellmann–Feynman theorem, it may be readily used to evaluate analytical gradients and other properties, as demonstrated elsewhere [11,13,14]. Stationary conditions (amplitude equations) for this functional are:

$$\tfrac{1}{2}\langle D_a | e^T(H_N e^T)_c | 0 \rangle_c + \tfrac{1}{2}\langle D_a | (e^{T^+} H_N)_c e^T | 0 \rangle_c = 0 \tag{13}$$

$$\tfrac{1}{2}\langle 0 | (e^{T^+} H_N)_c e^T | D_a \rangle_c + \tfrac{1}{2}\langle 0 | e^{T^+}(H_N e^T)_c | D_a \rangle_c = 0 \tag{14}$$

Both the functional and the amplitude equations are finite unlike the original ones. One has to remember, however, that functional (12) is only an approximation of the original functional (4) [12].

In this article we compare the above methods for the special case of the two-electron problem. This is not a precise derivation of these methods, but rather a pedagogical evaluation. This simple example, however, is very useful for understanding the structure of these coupled-cluster ansätze. Except for the SXCC, all methods are exact for two electrons, therefore, the same results will be obtained from them. However, even though the final results are the same, the differences of the actual form of equations defined by the different methods provides a deeper understanding of their structure. Below, we discuss the role and properties of EPV (Exclusion Principle Violating) terms. The different ways these methods handle these terms provides the principal difference in alternative coupled-cluster ansätze.

For a more transparent analysis we use diagrammatic language in this article. The detailed discussion of this formalism is given in ref. 15. Here we give the basic definitions only.

The normal ordered Hamiltonian is described by six, undirected diagram forms,

$$\mathbf{H_N} = f \cdot x + f \cdot f + \wedge f + \vee f + \wedge \wedge + \vee \vee$$

where the first term is f_{ii} and the remainder arise from H_N. The cluster operators, T_1 and T_2, are described by the diagrams.

$$\underline{\vee}$$

$$\underline{\vee}\underline{\vee}$$

while the hermitian conjugate of them is denoted by the upside-down form. These are also their normal product forms.

Origin and Properties of EPV Terms

EPV (exclusion principle violating) terms play an essential role in many-body perturbation theory. Complete cancellation of the renormalization part of the energy expression of perturbation theory in any order introduces such EPV terms [16]. A similar process can be used to cancel the denominator of an expectation value energy expression as in Eq. (4) [3].

Schematically this process can be demonstrated by a simple model in which only double excitations are allowed, i.e., $T = T_2$; the numerator of the energy expression according to Eq. (4) is

$$\text{⬭} \cdot \text{⬭} + \cdot \text{⬭} \text{⬭} \cdot + \cdot \text{⬭} \text{⬭} \cdot$$
$$= (\text{⬭} \cdot \text{⬭} +)(1 + \text{⬭} \cdot \text{⬭} \text{⬭} +) \tag{15}$$

The diagrams are drawn without regard to EPV terms, as the summations in the first and second terms are independent from the viewpoint of intermediate determinantal states. This means labels in the first and second term can be the same, which would mean allowing excitation from or to the same spin orbitals. The denominator in our example has the form:

$$1 + \text{⬭} + \text{⬭} \text{⬭} + \tag{16}$$

so that, after cancellation, the energy expression is

$$\triangle E = \text{⬭} \cdot \text{⬭} + \tag{17}$$

The above example was chosen to describe the structure of this cancellation in a simple way. The price we pay for this cancellation is that for even two electron terms like the second in Eqn. (17) that arise from $Q_2 H T_2^2 / 2$, which would formally correspond to quadruple excitations, have to be included.

The general case follows now. In this we strongly refer to the proof of theorem 1 of ref. 12. There we have:

$$\Delta E = \frac{\langle 0 | e^{T^\dagger} H_N e^T | 0 \rangle}{\langle 0 | e^{T^\dagger} e^T | 0 \rangle} = \frac{\langle 0 | (e^{T^\dagger} H_N e^T)_c e^{T^\dagger} e^T | 0 \rangle}{\langle 0 | e^{T^\dagger} e^T | 0 \rangle} \tag{18}$$

The cancellation by the denominator can be performed only if the summations in T's [see eq. (2)] in $(e^{T^\dagger} H_N e^T)_c$ and in $e^{T^\dagger} e^T$ are independent. This means that already on the left-hand side of the above equation the summation in T's and $T^\dagger$'s

should be independent. This requires the inclusion of the EPV terms. The sum of all such EPV terms, linked and unlinked, is zero, and any diagram of $H_N e^T$ which has two or more open lines with the same index vanishes according to lemma 3 of ref. 12. The sum of all diagrams that one can create by closing these open diagrams by pieces of e^T is still zero. In that way we introduce connected and unlinked diagrams also. In the next step we can cancel by the denominator, and we obtain:

$$\Delta E = \langle 0|(e^{-T}H_N e^T)_c|0\rangle$$

This connected expression contains the connected EPV terms.

EPV terms do not introduce nonphysical contributions to the energy as is clear from the above derivation. We simply added zero to the energy expression in order to be able to perform the cancellation. Therefore, the result is exact. For that reason, we prefer the name "conjoint" [17] rather than EPV for the remaining linked terms. On the other hand, the the latter name is very much used in the literature.

We now introduce the basic technique for dealing with those terms. We will need this technique for later developments as well. Consider the $Q_3 H T_3^2/2$ term—which contribute to the T_2 amplitude equation— for two electrons. In this case there are only two different spin-orbital hole-line labels. The five possible diagrams for this term are given in Fig. 1. The last one is unlinked, the other four are the usual connected diagrams (see, e.g., ref. 15). We would like to show that the sum of all five terms is zero in line with the above discussion. If two lines have the same label then the end of these lines (where they are pointing) can be changed. This process is described in Figure 1. Note that the sign of the diagram may change by this because the number of loops is different after interchanging the lines. Similarly, one has to consider that the factor in the algebraic expression associated with a diagram can change during this process. The rules can be summarized as follows:

1. Interchange lines with the same label.

Figure 1.

2. Sign is determined according to the change in the number of loops.
3. (a) Multiply by a factor of 2 if there is a new equivalence (vertex or line);
   (b) multiply by a factor of 1/2 if a new permutation is possible or the equivalence of vertices is destroyed after step 1 is done.

Alternatively to steps 3(a) and 3(b) the factor can be determined in the following way:

3. Multiply by 2 if the original diagrams are not symmetric but the one obtained by step 1 is, divide by 2 in the opposite case; the factor is 1 otherwise.

The above rules, as every rule on diagrams, are based on the manipulation of second quantized operators. Thus, for example, rule 2 can be understood as a consequence of the fact that changing the order of the operators causes the sign to change.

As we see from Figure 1 the sum of all five diagrams is zero; the first two connected diagrams cancel the unlinked one. This means that the unlinked diagram can equally well be written in a connected way.

The third and fourth diagrams of Figure 1 cancel each other, thus they are not needed for the cancellation of the unlinked diagram. This property of EPV parts is well known, and has been used to define approximate CC methods (see later) [18–21], as well as being integral to the older CEPA methods [22,23].

The Two-Electron Problem With Brueckner Orbitals

The easiest way to analyze the two-electron problem formally is to assume the use of Brueckner orbitals [24,25]. In this case, $T_1 = 0$, so $T = T_2$ and the energy expectation value can be written as

$$\Delta E = \frac{\langle 0|(1 + T_2^\dagger)H_N(1 + T_2)|0\rangle}{\langle 0|(1 + T_2^\dagger)(1 + T_2)|0\rangle}$$

$$= \frac{\text{◯◯} \cdot \text{◯◯} \cdot \text{◯◯} \cdot \text{◯◯} \cdot \times}{1 \cdot \text{◯◯}} \tag{19}$$

since all higher products of e^{T_2} vanish.[1] The derivative of ΔE with respect to $T_2^\dagger$ may be written in diagrammatic language as

$$\frac{(1 \cdot \text{◯◯})(\vee\vee \cdot \vee\vee \cdot \vee\vee \times)}{(1 \cdot \text{◯◯})^2}$$

$$\frac{(\text{◯◯} \cdot \text{◯◯} \cdot \text{◯◯} \cdot \text{◯◯} \times)\vee\vee}{(1 \cdot \text{◯◯})^2} \tag{20}$$

According to the variational principle the parameters of T_2 (or $T_2^\dagger$) can be determined by requiring, for example, $(\partial \Delta E/\partial T_2^\dagger) = 0$. From this we obtain

---

[1] In this section we do not introduce the EPV terms at the beginning, but instead, later, to get another idea of their origin.

$$(1 \cdot \boxminus)(\lor \lor + \underline{\lor}\lor + \lor\underline{\lor} \cdot \times) - $$
$$(\boxdot \cdot \boxdot \cdot \boxminus \cdot \boxminus \cdot \times) \underline{\lor}\lor - 0 \qquad (21)$$

or using the definition of ΔE:

$$\lor\lor + \underline{\lor}\lor + \lor\underline{\lor} \cdot \times - \triangle E \cdot \underline{\lor}\lor \qquad (22)$$

The latter is the diagrammatic form of the CID equation and exact for the two-electron problem. We, on the other hand, attempt to get the CCD equation by manipulating the former one. After rewriting it, we obtain

$$(1 \cdot \boxminus)(\lor\lor + \underline{\lor}\lor + \lor\underline{\lor} \cdot \times - \boxdot \underline{\lor}\lor) \cdot$$
$$\boxminus \boxdot \underline{\lor}\lor - (\boxdot \cdot \boxminus \cdot \boxminus \cdot \times) \underline{\lor}\lor - 0 \qquad (23)$$

Using the definition

$$\boxed{\underline{\lor}\lor} = \lor\lor + \underline{\lor}\lor + \lor\underline{\lor} \cdot \times - \boxdot \underline{\lor}\lor \qquad (24)$$

this can be written as:

$$(1 \cdot \boxminus)(\boxed{\underline{\lor}\lor}) - \boxed{} \underline{\lor}\lor - 0 \qquad (25)$$

This equation has the form of a homogeneous equation in $\boxed{}$. Note that, in the second term, $\boxed{}$ is contracted to $\wedge$, that is, we sum over all labels. To ensure the stationary condition (23), the following equation has to be solved:

$$\lor\lor + \underline{\lor}\lor + \lor\underline{\lor} \cdot \times - \boxdot \underline{\lor}\lor - 0 \qquad (26)$$

The last term is an unlinked EPV term. Now we can use the results of the previous chapter and replace the unlinked term with linked ones. As can be seen from Figure 1, $(\frac{1}{2} W T_2^2)_L = -(\frac{1}{2} W T_2^2)_{UL}$. Here the subscripts UL and L mean unlinked (last diagram) and linked (first to fourth diagrams), respectively. Using this, we arrive at the fully connected (linked) CCD equation, which applies for any number of electrons, as well,

$$W_N + W_N T_2 + f_d T_2 + \tfrac{1}{2} W_N T_2^2 = 0 \qquad (27)$$

f_d is the diagonal part of f_{pq}.

Trivially, QCID (i.e., QCISD with $C_1 = T_1 = 0$) is equivalent to CCD. Furthermore, the above equation is the XCCD [12] and ECCD [8,10] T_2 equation for two electrons. Note that the general equation of these two latter methods (see Introduction) includes additional terms which vanish for two electrons.

Other methods can be derived also. From Figure 1 it is clear that to replace the unlinked term we do not need all four linked diagrams, hence, the last two cancel each other. Therefore, including only the first two terms the method is still right for two electrons and leads to the ACCD = ACP-D45 = ACP of Dykstra and Paldus [18–21]. Moreover all the CEPA methods [22,23] calculate only the EPV part of diagrams one and two of Figure 1. Therefore, unlike ACCD, for more than two electrons, they are not invariant under virtual–virtual or occupied–occupied orbital rotations.

Returning to the two-electron problem, the stationary energy can be written as

$$\triangle E = \boxed{\ } + \frac{\boxed{\ } + \boxed{\ } + \boxed{\ } - \times - \boxed{\ }\,\boxed{\ }}{1 + \boxed{\ }} = \boxed{\ } \qquad (28)$$

if the stationary condition (26) is satisfied.

Finally we are going to determine the functional of the various methods. Eq. (19) is clearly the CID functional with $T_2 = C_2$. Rewriting (19), we get

$$\triangle E = \boxed{\ } + \frac{\boxed{\ } + \boxed{\ } + \boxed{\ } \cdot \times - \boxed{\ }\,\boxed{\ }}{1 + \boxed{\ }} =$$

$$= \boxed{\ } + \frac{\boxed{\ }}{1 + \boxed{\ }} \qquad (29)$$

where c is the strictly connected form of c as described above.

Introducing the new variable, Λ_2,

$$\bigwedge = \frac{\bigwedge}{1 + \boxed{\ }} \qquad (30)$$

the functional becomes

$$\triangle E = \boxed{\ } + \boxed{\ } \qquad (31)$$

This is the functional form of CCD, QCID, and ECCD methods for two electrons. It also holds in the many-electron case for CCD and QCID. Clearly, differentiating it according to Λ_2 leads to Eq. (27).

In the two-electron case it is not necessary to solve an equation for Λ_2 because of its relationship with $T_2^\dagger$. This is not valid, however, if the number of electrons exceeds the excitation rank in T. In this case, eq. (30) is only a better initial guess for the Λ_2 amplitudes than the usual $\Lambda_2 = T_2^\dagger$.

The functional for the XCC method can be obtained from Eq. (19) by full expansion of the denominator:

$$\triangle E = \boxed{\ } + \boxed{\ } + \boxed{\ } + \boxed{\ } \cdot \times - \boxed{\ }\,\boxed{\ } -$$
$$- \boxed{\ }\,\boxed{\ } - \boxed{\ }\,\boxed{\ } - \boxed{\ } \cdot \times \boxed{\ } +$$
$$+ \boxed{\ }\,\boxed{\ }\,\boxed{\ } + \; -$$
$$- \boxed{\ } + \boxed{\ } - \boxed{\ }\,\boxed{\ } + \boxed{\ }\,\boxed{\ }\,\boxed{\ } - \qquad (32)$$

which is infinite. Differentiating according to $T_2^\dagger$, we get for the stationary equation:

$$\boxed{\ } - \boxed{\ }\,\boxed{\ } - \bigvee\bigvee\boxed{\ } + \boxed{\ }\,\boxed{\ }\,\boxed{\ } + \; = 0 \qquad (33)$$

The solution is clearly the same as from Eq. (26).

The Two Electron Problem With Singles and Doubles

In this case, $T = T_1 + T_2$, $f_{pq} = G_p \delta_{pq}$, and the energy functional has the form:

$$\triangle E = \frac{\langle 0| e^{T_1^\dagger + T_2^\dagger} H_N e^{T_1 + T_2}|0\rangle}{\langle 0| e^{T_1^\dagger + T_2^\dagger} e^{T_1 + T_2}|0\rangle} = \frac{\text{Numerator}}{\text{Denominator}}$$

DENOMINATOR =

$$-1 + \square + \square\square + \square\square + \square\square + \square\square + \widehat{\square\square}$$

NUMERATOR =

$$-\square\cdot x + \square + \square^{\square} + \square^{\square} + \square_{\square} + \square_{\square} + \square\square + \square\square +$$

$$+\square\square + \square\square + \square\square + \square\square + \square\square + \square\square + \widehat{\square} + \square\square\cdot x +$$

$$+\square\square\cdot x + \square\square\cdot x + \square\square\cdot x + \widehat{\square}\cdot x + \square\square + \widehat{\square} +$$

$$+\square\square + \square\square$$

(34)

The stationary conditions are $(\partial \Delta E / \partial T_2^\dagger) = 0$ and $(\partial \Delta E / \partial T_1^\dagger) = 0$, which lead to the following equations:

$$\text{DENOMINATOR} \cdot (\vee + \vee\vee + \vee\vee + \vee\vee + \vee\vee\cdot x +$$

$$+\vee\vee + \vee\vee\cdot x) - \text{NUMERATOR} (\vee\vee + \vee\vee) = 0$$

$$\text{DENOMINATOR} \cdot (\vee\cdot x + \vee + \vee^{\square} + \square^{\vee} + \vee_{\square} +$$

(35)

$$+\vee_{\square} + \vee\square + \vee\square + \vee\square + \vee\square + \vee\square\,\vee\vee + \vee\vee +$$

$$+\vee\square\cdot x + \square\vee\cdot x + \vee\square\cdot x + \square\vee\cdot x + \vee\vee\cdot x +$$

$$+\vee\vee\cdot x + \vee\square + \square\vee + \vee\vee) - \text{NUMERATOR} \cdot$$

$$(\vee + \vee\square + \vee\square + \vee\vee) = 0$$

The CCSD Method

For this method we define the following one- and two-particle variables:

$$\underset{\square}{\vee\vee} = \vee^{\vee} + \vee\vee + \vee\vee + \vee\vee + \vee\vee\cdot x + \vee\vee\cdot x +$$

$$+\vee\vee - (\square\square + \square\square)(\vee\vee + \vee\vee)$$

(36)

$$\underset{\square}{\vee} = \vee\cdot x + \vee + \vee_{\square} + \vee_{\square} - (\square\square + \square\square)\vee$$

and with this it is transparent that we have again a homogeneous system of equations:

$$\text{DENOMINATOR} \cdot (\underset{\square}{\vee} + \underset{\square}{\vee\square}) -$$

$$- (\underset{\square}{\square\square} + \underset{\square}{\square\square} + \underset{\square}{\square})(\vee + \vee\square + \vee\square + \vee\vee) = 0$$

(37)

$$\text{DENOMINATOR} \cdot \underset{\square}{\vee\vee} -$$

$$- (\underset{\square}{\square\square} + \underset{\square}{\square\square} + \underset{\square}{\square})(\vee\vee + \vee\vee) = 0$$

As before, linear independence requires that

$$\underset{\square}{\vee\vee} = 0$$

$$\underset{\square}{\vee} = 0$$

(38)

The two-particle variable has unlinked EPV and disconnected terms, while the one-particle variable has only unlinked EPV terms. One can remove the disconnected terms of the T_2 equation using the following identity, which is a consequence of the T_1 equation, which is embedded into the T_2 equation:

$$\underline{V}\cdot\underline{V}\times+\underline{V}\,\underline{V}-(\underline{V}_a+\underline{V}_a)\underline{V}+2\underline{V}\,\underline{V}\,(\underline{0}\,\underline{0}\cdot\underline{0}\,\underline{0}) \qquad (39)$$

Recognizing this the two-particle variable becomes:

$$\boxed{}=\underline{V}^{\,v}+\underline{V}.\underline{V}+\underline{V}.\underline{V}+\underline{V}\,\underline{V}+\underline{V}.\underline{V}\times\underline{V}\,\underline{V}_a-$$
$$-\underline{V}\,\underline{V}_a-(\underline{0}\,\underline{0}+\underline{0}\,\underline{0})\underline{V}.\underline{V}+(\underline{0}\,\underline{0}+\underline{0}\,\underline{0})\underline{V}\,\underline{V} \qquad (40)$$

and now all unlinked terms are of EPV type. Again, we can arrange them into connected EPV terms using the above rules:

$$(H_N T_2 T_1)_c = -(H_N T_2 T_1)_{cl}$$

$$\left(\frac{1}{3!}H_N T_1^3\right)_c = -\left(\frac{1}{3!}H_N T_1^3\right)_{cl}$$

$$\left(\frac{1}{2}H_N T_2^2\right)_c = -\left(\frac{1}{2}H_N T_2^2\right)_{cl}$$

$$\left(\frac{1}{4!}H_N T_1^4\right)_c = -\left(\frac{1}{4!}H_N T_1^4\right)_{cl}$$

$$\left(\frac{1}{2!}H_N T_2 T_1^2\right)_c = \underline{0}\,\underline{0}\,\underline{V}\,\underline{V}-\underline{V}\,\underline{V}\,\underline{0}\,\underline{0}$$

As a further demonstration, the $\frac{1}{2}H_N T_2 T_1^2$ case is given in Figure 2. The two-particle variable is now fully connected:

$$= +1\ \ \underline{0}\,\underline{0}\ \underline{V}\ \underline{V}$$

$$= +1\ \ \underline{V}\,\underline{V}\ \underline{0}\,\underline{0}$$

$$= -2\ \ \underline{V}\,\underline{V}\ \underline{0}\,\underline{0}$$

$$= -1\ \ \underline{V}\,\underline{0}\ \underline{0}\ \underline{V}$$

$$= +1\ \ \underline{V}\,\underline{0}\ \underline{0}\ \underline{V}$$

$$\left(\tfrac{1}{2}W T_2 T_1^2\right)_L = \underline{0}\,\underline{0}\ \underline{V}\ \underline{V}-\underline{V}\,\underline{V}\ \underline{0}\,\underline{0}$$

Figure 2.

$$\Box = W_N T_1 + W_N + W_N T_2 + W_N \frac{T_2^2}{2} + f_d T_2 + W_N T_1 T_2$$

$$+ W_N \frac{T_1^3}{3!} + W_N \frac{T_2^2}{2} + W_N T_2 \frac{T_1^2}{2} + W_N \frac{T_1^4}{4!} \qquad (41)$$

and the equation to solve reads:

$$W_N T_1 + W_N + W_N T_2 + W_N \frac{T_2^2}{2} + f_d T_2 + W_N T_1 T_2$$

$$+ W_N \frac{T_1^3}{3!} + W_N \frac{T_2^2}{2} + W_N T_2 \frac{T_1^2}{2} + W_N \frac{T_1^4}{4!} = 0 \qquad (42)$$

which is the CCSD T_2 equation for any number of electrons.

In the same way. we can replace the unlinked EPV terms of the T_1 equation using

$$(W_N T_2 T_1)_c = -(W_N T_2 T_1)_{UL}$$

$$\left(W_N \frac{T_1^3}{3!} \right)_c = -\left(W_N \frac{T_1^3}{3!} \right)_{UL}$$

For a demonstration see Figure 3. The fully connected one-particle variable then becomes:

$$\Box = f_d T_1 + W_N T_1 + W_N T_2 + W_N \frac{T_1^2}{2} + W_N T_2 T_1 + W_N \frac{T_1^3}{3!} \qquad (43)$$

which leads exactly to the CCSD T_1 equation of the many-electron system:

$$f_d T_1 + W_N T_1 + W_N T_2 + W_N \frac{T_1^2}{2} + W_N T_2 T_1 + W_N \frac{T_1^3}{3!} = 0 \qquad (44)$$

Using the fact that satisfying these equations means. for two electrons. the fulfillment of the original homogeneous equation. the energy can be simplified to

$$\triangle E = \text{(IIIIII)} + \text{(IIIIII)} \qquad (45)$$

Figure 3.

which again is the CCSD energy expression. The fact that we arrived at the CCSD equations and energy expression shows that the method is exact for two electrons.

Finally, we determine the CCSD functional. Using the definition of Eq. (36) the energy functional of Eq. (34) can be rewritten as:

$$\triangle E \cdot \text{(diagram)} \cdot \text{(diagram)} \cdot \frac{\text{(diagram)} \cdot \text{(diagram)} \cdot \text{(diagram)}}{\text{DENOMINATOR}} \cdot$$

$$\cdot \text{(diagram)} \cdot \text{(diagram)} \cdot \frac{\text{(diagram)} \cdot \text{(diagram)}}{} \tag{46}$$

where, in the last step, Λ was introduced as:

$$\overline{\Lambda} \cdot \frac{\Lambda}{\text{DENOMINATOR}}$$

$$\overline{\Lambda\Lambda} \cdot \frac{\Lambda\Lambda \cdot \Lambda \Lambda}{\text{DENOMINATOR}} \tag{47}$$

This definition of Λ shows, that it is "CI"-like, i.e., Λ contains disconnected parts. At this point the two- and one-particle variables in the functional include unlinked terms. As we have seen above, it is possible to write them in connected form [see steps from Eqs. (39)–(43)]. Therefore, the final form of the functional is

$$\triangle E \cdot \text{(diagram)} \cdot \text{(diagram)} \cdot \text{(diagram)} \cdot \text{(diagram)} \tag{48}$$

The derivative, according to Λ, leads to the CCSD eqs. (42) and (44).

The QCISD Method

We define the same one- and two-particle variables as for the CCSD method with eq. (36), and follow the same steps through Eq. (40). Then, we do not cancel the disconnected diagrams of the two-particle variable, but instead introduce a new, disconnected variable. In diagrammatic language

$$\text{(diagram)} \cdot \text{(diagram)} \cdot \text{(diagram)} \tag{49}$$

or algebraically,

$$c_{ij}^{ab} = t_{ij}^{ab} + t_i^a t_j^b - t_i^b t_j^a$$

The permutation of the indices on the T_1 amplitudes is required to maintain full antisymmetry. This new variable corresponds to the CI coefficient. Introduction of the new variable means using $C_2 = T_2 + \frac{1}{2}T_1^2$ in the operator basis. We now obtain,

$$\text{(diagram)} \cdot \text{(diagram)} \times \cdot \text{(diagram)} \cdot \text{(diagram)} \quad (\text{(diagram)}) \text{(diagram)}$$

$$\text{(diagram)} \cdot \text{(diagram)} \cdot \text{(diagram)} \cdot \text{(diagram)} \cdot \text{(diagram)} \times - (\text{(diagram)})(\text{(diagram)}) \tag{50}$$

One should, of course, check whether the replacement is justified for all terms. This can be done at the diagrammatic level, and this process is shown in Figure 4 for the $Q_1 W_N T_2$ term and for the energy.

The next step is, as in the CCSD case, the replacement of the unlinked EPV terms by the linked one. The only difference to the former case is that now we use C_2 rather than T_2. The one- and two-particle connected variables are then

$$\tau \cdot W_N T_1 + f_N T_1 + W_N C_2 + W_N C_2 T_1 \tag{51}$$

$$\tau_2 \cdot W_N T_1 + W_N + W_N C_2 + f_N C_2 + \frac{1}{2} W_N C_2^2 \tag{52}$$

Figure 4.

Therefore, the amplitude equations are:

$$W_N T_1 + f_d T_1 + W_N C_2 + W_N C_2 T_1 = 0 \tag{53}$$

$$W_N T_1 + W_N + W_N C_2 + f_d C_2 + \tfrac{1}{2} W_N C_2^2 = 0 \tag{54}$$

and the energy expression is:

$$\Delta E = W_N C_2 \tag{55}$$

These equations and energy expression are the QCISD equations [9] for any number of electrons and, as it follows from above, they are exact for two electrons. One should note here that the QCI Eqs. (53) and (54) and CCSD Eqs. (42) and (44) are equivalent for two electrons only. In this case, all steps of our derivations are exact and, therefore, the differences are hidden. Inclusion of the connected EPV terms with the variable T (CCSD method) or C (QCI method), which are tetraexcited contributions in the many-electron case, is essentially different. The relationship of CCSD and QCISD has been discussed in detail by Paldus et al. [26,27] and Pople et al. [28,29].

Using similar steps as for the CCSD method the functional can be written:

$$\Delta E = \text{(diagram)} \tag{56}$$

The XCC Method

We now define the one- and two-particle variables differently:

$$\text{(diagram)} \tag{57}$$

Note the difference with Eq. (36): the new one-electron variable contains pieces of the two-electron variable contracted by $T_1^\dagger$. On the other hand, the two-particle variable is exactly the same as for CCSD. With those, the T_1 and T_2 equations become:

$$\text{DENOMINATOR} \cdot \boxed{} \cdot$$

$$-\left(\boxed{} + \boxed{} + \boxed{}\right)\left(\vee + \vee \bar{\partial} + \vee \bar{\partial} + \vee\vee\right) = 0 \tag{58}$$

$$\text{DENOMINATOR} \cdot \boxed{}$$

$$-\left(\boxed{} + \boxed{} + \boxed{}\right)\left(\vee\vee + \vee\vee\right) = 0$$

Again, the homogeneous equation has only the trivial solution, therefore, the new variable should vanish. Now, contrary to the CCSD case, the T_1 equation has unlinked terms, which are not EPV type. One should cancel them. We use the CCSD T_1 Eq. (44). This is justified because we are looking for exact results for two electrons and, in this case, the CCSD T_1 equation satisfies this condition. We use the following equalities:

$$\vee + \times + \vee + = \vee_\partial + \vee_\partial + (\partial_\partial + \partial\partial)\vee$$

$$\vee(\partial + \times + \partial) + \vee(\partial_\partial + \partial_\partial) + (\partial_\partial + \partial\partial)\partial\vee$$

$$\partial(\vee + \times + \vee) + \partial(\vee_\partial + \vee_\partial) + (\partial_\partial + \partial\partial)\vee\partial \tag{59}$$

$$\vee\vee + \times + \vee\vee + \times + \vee\vee + \vee\vee_\partial + \vee\vee_\partial + (\partial_\partial + \partial\partial)\vee\vee$$

With this:

$$\boxed{} = \vee + \times + \vee + \vee + \partial + \vee_\partial + \vee_\partial +$$
$$+ \vee\partial + \vee\partial + \times + \vee\partial + \vee\partial + \vee\partial + \vee\partial + \vee\partial +$$
$$+ \vee\vee + \vee\vee + (\partial_\partial + \partial\partial)(\vee + \vee\partial) + \vee_\partial + \tag{60}$$
$$+ \partial\vee_\partial + \vee\partial_\partial + \partial\vee_\partial + \vee\vee_\partial + \vee\vee_\partial +$$
$$+ (\partial_\partial + \partial\partial)\partial\vee$$

After replacing the unlinked EPV terms with the linked ones, we obtain,

$$= f_{ai}T_1 + H_N T_1 + T_1^\dagger H_N T_1 + H_N T_2 + \frac{1}{2}H_N T_1^2 + T_1^\dagger H_N + T_1^\dagger f_{ai}T_2$$

$$+ T_1^\dagger H_N T_2 + \frac{1}{2}T_1^\dagger (H_N T_1^2) + H_N T_1 T_2 + \frac{1}{3!}H_N T_1^3$$

$$+ \frac{1}{2}T_1^\dagger (H_N T_2 T_1^\dagger) + \frac{1}{2}T_1^\dagger (H_N T_2)$$

$$+ \frac{1}{4!}T_1^\dagger (H_N T_1^4) + T_1^\dagger (H_N T_2 T_1) + \frac{1}{3!}T_1^\dagger (H_N T_1^3) \tag{61}$$

Because the two-particle variable of Eq. (57) is the same as in the CCSD case above, the connected two-particle variable is the same as for CCSD:

$$\sigma\sigma = W_N T_1 + W_N + W_N T_2 + W_N \frac{T_1^2}{2} + f_d T_2 + W_N T_1 T_2$$

$$+ W_N \frac{T_1^3}{3!} + W_N \frac{T_2^2}{2} + W_N T_2 \frac{T_1^2}{2} + W_N \frac{T_1^4}{4!} \tag{62}$$

[compare Eq. (42)]. The equations to solve are then

$$\begin{array}{c} \boxtimes = 0 \\ \boxtimes = 0 \end{array} \tag{63}$$

At this point, one should note that the one-particle variable of Eq. (61) can be turned into that for CCSD (43): all terms containing $T_1^\dagger$ add up to zero because of the T_2 equation. This, of course, must be true, because both equations must be exact for two electrons. They give, however, different results if we apply them to problems with more than two electrons. In this case, as we will see below, other terms appear in the T_2 equations, therefore, these terms do not cancel each other. They introduce higher excitation effects (see later). The energy expression is the same as for the CCSD method but for only the two-electron case.

Now we are going to show that the above equations are really XCC type equations, i.e., they are the same as Eq. (10) for two electrons. The XCCSD equations, according to Eq. (10), have the structure:

$$Q_1 \Bigg(f_d T_1 + W_N T_1 + T_1^\dagger W_N T_1 + W_N T_2 + \frac{1}{2} W_N T_1^2 + T_1^\dagger W_N + T_1^\dagger f_d T_2$$

$$+ T_1^\dagger W_N T_2 + \frac{1}{2} T_1^\dagger (W_N T_1^2)_c + W_N T_1 T_2 + \frac{1}{3!} W_N T_1^3 + \frac{1}{2} T_1^\dagger (W_N T_2 T_1^2)_c$$

$$+ \frac{1}{2} T_1^\dagger (W_N T_2^2)_c + \frac{1}{4!} T_1^\dagger (W_N T_1^4)_c + T_1^\dagger (W_N T_2 T_1)_c + \frac{1}{3!} T_1^\dagger (W_N T_1^3)_c$$

$$+ T_2^\dagger (\cdots) + T_1^{\dagger 2} (\cdots) \Bigg) = 0$$

and

$$Q_2 \Bigg(W_N T_1 + W_N + W_N T_2 + W_N \frac{T_1^2}{2} + f_d T_2 + W_N T_1 T_2$$

$$+ W_N \frac{T_1^3}{3!} + W_N \frac{T_2^2}{2} + W_N T_2 \frac{T_1^2}{2} + W_N \frac{T_1^4}{4!}$$

$$+ T_1^\dagger (\cdots) + T_1^{\dagger 2} (\cdots) + T_2^\dagger (\cdots) \Bigg) = 0$$

All the terms denoted by $(\cdots)$ are EPV terms with more than two open hole lines. Therefore, they are zero according to lemma 3 of ref. 12, and for two electrons the XCC equations are exactly the same as the above. The conclusion is that the XCC method is right for two electrons. However, in practice, some truncation of

the finite equations is necessary [11]. If we want it to be right for two electrons also in this case, the first part should be retained completely and only the terms denoted by (···) can be truncated.

The vanishing of terms for two electrons denoted by (···) suggest that these terms represent higher excitation effects. This is in line with the findings of refs. 11 and 30–32, where terms like these were used to include higher excitation effects into the CCSD calculations.

As in the Brueckner orbital case, the XCC functional is infinite. Using the definition of Eq. (57), the original functional (34) can be written as

$$\triangle E \cdot \boxed{}\boxed{} \cdot \boxed{} \boxed{} \cdot \frac{}{\text{DENOMINATOR}} \tag{64}$$

[compare to eq. (46)]. Using the above results, it can be rewritten into a fully connected form,

$$\triangle E = \boxed{}\boxed{} \cdot \boxed{}\boxed{} \cdot \frac{}{\text{DENOMINATOR}} \tag{65}$$

Now we expand the denominator completely:

$$\triangle E \cdot \boxed{}\boxed{} \cdot \boxed{}\boxed{} \cdot ()(1 \cdot \text{DENOMINATOR} \cdot \tag{66}$$
$$\cdot \text{DENOMINATOR}^2 -)$$

After replacing the unlinked EPV terms it can be written as being fully connected. Making it stationary according to T^+ we get an equation which is satisfied if Eq. (63) is satisfied.

The ECCSD Method

For this method we start at Eq. (65). We define Λ differently as in Eq. (47):

$$\boxed{} = \frac{\boxed{}}{\text{DENOMINATOR}}$$
$$\boxed{} = \frac{\boxed{}}{\text{DENOMINATOR}} \tag{67}$$

i.e., it is not CI-like. This leads to

$$\triangle E \cdot \boxed{}\boxed{} \cdot \boxed{}\boxed{} \cdot \boxed{} \cdot \boxed{} \tag{68}$$

This is now very similar to the ECC functional. One has to remember, however, the definition of the one-particle variable [see Eq. (61)]; there are some terms having T_1^+ in them. In the ECC case they should be Λ_1. The derivative of (68) according to Λ leads to the Eqs. (63). We have seen above that, at least for the two-electron case, the terms including T_1^+ in the one-particle variable add up to zero. Therefore, replacing T_1^+ by Λ_1 does not change the amplitude equations. The modified one-particle variable is instead,

$$\lambda = f_d T_1 + H_N T_1 + \Lambda_1 H_N T_1 + H_N T_2 + \frac{1}{2} H_N T_1^2 + \Lambda_1 H_N + \Lambda_1 f_d T_2$$
$$+ \Lambda_1 H_N T_2 + \frac{1}{2} \Lambda_1 (H_N T_1^2) + H_N T_1 T_2 + \frac{1}{3!} H_N T_1^3$$

$$+ \frac{1}{2} \Lambda_1 (W_N' T_2 T_1^2)_c + \frac{1}{2} \Lambda_1 (W_N' T_2^2)_c$$

$$+ \frac{1}{4!} \Lambda_1 (W_N' T_1^4)_c + \Lambda_1 (W_N' T_2 T_1)_c + \frac{1}{3!} \Lambda_1 (W_N' T_1^3)_c \tag{69}$$

and the functional becomes

$$\triangle E = \overline{\text{CD}} + \overline{\text{CD}} + \frac{\overline{\text{C}}}{\text{Ch}} + \overline{\text{Ch}}$$

which is now the ECC functional.[2] If there are more then two electrons then the replacement of $T_1^\dagger$ by Λ_1 is not justified because the cancellation of $T_1^\dagger$ containing terms does not appear. In fact, it causes a scaling of these terms (which represents higher order contributions) by the denominator. This eventually may cause an unbalanced description.

SXCC Method

The amplitude equation of the SXCC method is described by Eq. (13). As mentioned in the introduction, and shown in ref. 12, this method is not exact, i.e., including all possible excitations in T the method is not equivalent to full CI. Therefore, it is not correct for two electrons. Even if we know that already, it is interesting to understand the origin of this deficiency to try to estimate its error.

We know from the previous section that the first term in Eq. (13) is zero for two electrons (the XCC functional is exact). Therefore, we now investigate the second term

$$\langle D_a | ((e^{T'} H_N)_c e^{T'})_c | 0 \rangle \tag{70}$$

only. It should vanish in the case of an exact theory.

For the sake of easier understanding we first return to the Brueckner orbital case. We have to modify the two-electron variable defined by Eq. (24) to a form given by (70). To that end we now do not replace the last term by the corresponding connected expression, because the term (70) does not contain it. We rather use the following identity:

$$\overline{\text{CD}} = \overline{\text{CD}} \tag{71}$$

This follows from the definition of T [Eq. (2)] and the symmetry of the functional and amplitude equations. Now the unlinked EPV term is

$$-\overline{\text{CD}} \, \bigvee \tag{72}$$

and the question is whether we can replace it by the corresponding connected one:

$$-\overline{\text{CD}} \, \bigvee \; = \; (T_2^\dagger \, WT_2)_L \tag{73}$$

---

[2] Transformation to the double connected structure [8,10] is not discussed here because it would need a notation which would not be consistent with the present one, but the transformation is exact [8].

According to Figure 5,

$$\text{...} = T^\dagger WT \quad \text{...} \tag{74}$$

i.e., the simple replacement introduces the further nonzero unlinked terms. We need only the second and sixth term of Figure 5 to replace the unlinked term. Thus, the exact amplitude equation can be written as:

$$W_N + W_N T_2 + t_2 T_2 + (T^\dagger W_N T_2)_{2,6} = 0 \tag{75}$$

where subscript 2, 6 means the second and sixth diagrams of Figure 5. This equation is correct for two electrons, but unfortunately, not compatible with the form of (70). In other words, not all derivatives of the energy functional (12) are included in the exact amplitude equation. Therefore, in order to have the functional we have to include all the terms of Figure 5 and, in addition, we have to add some terms which cancel the second term of Eq. (74).

Using Eq. (26) we can write:

$$\text{...} = 0 \tag{76}$$

Figure 5

Replacing these unlinked EPV terms by linked ones, and inserting into Eq. (75), we get:

$$W_N + W_N T_2 + f_d T_2 + T_2^\dagger W_N T_2 + \tfrac{1}{2}((T_2^\dagger f_d) T_2^2),$$

$$+ \tfrac{1}{2}((T_2^\dagger W_N) T_2^2)_r + \tfrac{1}{4}((T_2^{\dagger 2} W_N) T_2^2)_r = 0$$

Here subscript r means that only specific diagrams have to be included. Therefore, once again, we do not have the whole derivative of the diagrams of the energy expression. It is worth mentioning that this equation has exactly those higher-order terms which prevented us in ref. 12 from showing that the $\langle D_a|((e^{T^\dagger} H_N)_c e^T)_c|0\rangle = 0$ equation is exact.

The rule we see here is that the sum of all connected EPV terms is equal to the sum of all unlinked EPV terms (see also Origin and Properties of EPV Terms). The exact equation of the two-electron problem does not include all unlinked EPV terms, therefore, a subset of the connected terms are needed to cancel them. Hence, the inclusion of specific diagrams into the amplitude equation is not compatible with a finite functional.

Now we return to the $T = T_1 + T_2$ case. We start with Eq. (60) for the T_1 amplitudes. Beside Eq. (71) we also use a similar identity,

$$\underline{\Omega}\,\Omega - \overline{\Omega}\,\overline{\Omega} \tag{77}$$

Replacing the unlinked terms with the connected ones and remembering the rule obtained above we have:

$$\begin{aligned}
\mathbf{x} &= f_d T_1 + W_N T_1 + T_1^\dagger W_N T_1 + W_N T_2 + \tfrac{1}{2} W_N T_1^2 + T_1^\dagger W_N + T_1^\dagger W_N T_2 \\
&\quad + T_1^\dagger W_N T_2 + \tfrac{1}{2} T_1^\dagger W_N T_1^2 + T_1^\dagger W_N T_2 T_1 + \tfrac{1}{2} T_1^\dagger W_N T_1^2 \\
&\quad + T_2^\dagger W_N T_1 + T_1^\dagger T_2^\dagger W_N T_2 + T_1^{\dagger 2} W_N T_1 + \tfrac{1}{3} T_1^{\dagger} W_N T_2 \\
&\quad + \tfrac{1}{2} T_1^\dagger T_2^\dagger W_N T_1^2 + \tfrac{1}{6} T_1^{\dagger} W_N T_1^2 \\
&\quad + \quad \text{(diagrams)}
\end{aligned} \tag{78}$$

For the T_2 equation, from Eq. (40) we obtain,

TABLE I.   Total energy of the H_2 molecule at 1 A.

Method	Total energy	
	DZ	DZP
Full CI	1.12671267	1.13962789
SXCC (4')[a]	1.12671873	1.13963528

[a] This method is a truncated form of the SXCC method [11] according to fourth-order, using both T_1 and T_2 as first-order quantities.

$$\omega = H_N T_1 + H_N + H_N T_2 + \tfrac{1}{2} H_N T_1^2 + \tfrac{1}{2} T_2 + H_N T_1 T_2 + \tfrac{1}{2} H_N T_2^2$$
$$+ T_1 \tfrac{1}{2} H_N T_2^2 + \tfrac{1}{2} T_2^\dagger H_N T_1^2 + \tfrac{1}{2} T_1^\dagger H_N T_2 + \tfrac{1}{2} T_1^\dagger H_N T_1^2$$
$$+ \qquad \qquad \qquad \qquad \qquad \qquad \qquad \qquad \qquad \qquad \quad (79)$$

As in the simplest case, the T_2 CCSD Eq. (42) can be used to replace unlinked terms. This process again introduces specific higher-order terms so that the exact equation is not compatible with the form (70).

The conclusion of this section is that even for two electrons it is not possible to have a simplified symmetric functional in an exact method. The error is represented by higher-order terms only, which are small and whose magnitude can be estimated by perturbation theory arguments. Table I shows that a truncated form of SXCC gives an energy very close to the full CI energy for two electrons.

Conclusion

In this study, the two-electron problem has been investigated using an exponentially parametized energy functional. The exact stationary equations can be shown to become the CCSD, QCISD, ECCSD, and XCCSD equations, because these methods are exact for two electrons. The different forms of the various equations illuminates some of the connection between CCSD and QCISD, and also how higher excitation effects are introduced for more then two electrons in the ECCSD and XCCSD methods.

The SXCCSD method was found not to be correct for two electrons, although it fails only because of some higher-order terms. This small difference may not affect the method for practical calculations. One should also note that, in practice, the finite but rather long equations of the ECCSD method probably need to be truncated, making other methods computationally competitive with ECC because they are symmetric in the T and in the $T^\dagger$ parameters. For SXCC, it very easy to evaluate properties as the generalized Hellmann–Feynman theorem is satisfied [11,13]. All other methods require the determination of both T and Λ to determine properties (see, e.g., refs. 7,33,34, and 35).

Bibliography

[1] R. J. Bartlett and G. D. Purvis, Int. J. Quant. Chem. 14, 561 (1978).
[2] R. J. Bartlett and G. D. Purvis, Phys. Scr. 21, 251 (1980).
[3] J. Čížek, Adv. Chem. Phys. 14, 35 (1969).
[4] R. J. Bartlett, J. Phys. Chem. 93, 1697 (1989), and references therein.
[5] R. J. Bartlett, in Geometrical Derivatives of Energy Surfaces and Molecular Properties, P. Jørgensen and J. Simons, Eds. (Reidel, Dordrecht, The Netherlands, 1986) p. 35.
[6] J. Adamowicz, W. D. Laidig, and R. J. Bartlett, Int. J. Quant. Chem. Symp. 18, 245 (1984).
[7] E. A. Salter, G. W. Trucks, and R. J. Bartlett, J. Chem. Phys. 90, 1752 (1989).
[8] J. Arponen, Ann. Phys. 151, 311 (1983).
[9] J. A. Pople, M. Head-Gordon, and K. Raghavachari, J. Chem. Phys. 87, 5968 (1987).
[10] J. S. Arponen, R. F. Bishop, and E. Pajanne, Phys. Rev. A 36, 2519 (1987).
[11] R. J. Bartlett, S. A. Kucharski, J. Noga, J. D. Watts, and G. W. Trucks, Lecture Notes in Chem. 52, 125 (1989).

[12] P. G. Szalay and R. J. Bartlett, J. Chem. Phys. (to appear).
[13] R. J. Bartlett, S. A. Kucharski, and J. Noga, Chem. Phys. Lett. 155, 133 (1989).
[14] J. D. Watts, G. W. Trucks, and R. J. Bartlett, Chem. Phys. Lett. 164, 502 (1989).
[15] S. A. Kucharski and R. J. Bartlett, Adv. Quant. Chem. 18, 281 (1986).
[16] M. Urban, I. Hubač, V. Kellö, and J. Noga, J. Chem. Phys. 72, 3378 (1980).
[17] R. J. Bartlett and G. D. Purvis, Int. J. Quant. Chem. 14, 561 (1978).
[18] R. A. Chiles and C. E. Dykstra, Chem. Phys. Lett. 80, 69 (1981).
[19] S. M. Bachrach, R. A. Chiles, and C. E. Dykstra, J. Chem. Phys. 75, 2270 (1981).
[20] K. Jankowski and J. Paldus, Int. J. Quant. Chem. 18, 1243 (1980).
[21] B. G. Adams, K. Jankowski, and J. Paldus, Phys. Rev. A24, 2330 (1981).
[22] W. Meyer, Int. J. Quant. Chem. Symp. 5, 341 (1971).
[23] A. C. Hurley, *Electron Correlation in Small Molecules* (Academic Press, London, 1976).
[24] K. Brueckner, A. M. Lockett, and B. Rotenberg, Phys. Rev. 121, 255 (1961), and references therein.
[25] P.-O. Löwdin, J. Math. Phys. 3, 1171 (1962).
[26] J. Paldus, J. Čížek, and B. Jeziorski, J. Chem. Phys. 90, 4356 (1989).
[27] J. Paldus, J. Čížek, and B. Jeziorski, J. Chem. Phys. 93, 1485 (1990).
[28] J. A. Pople, M. Head-Gordon, and K. Raghavachari, J. Chem. Phys. 90, 4635 (1989).
[29] K. Raghavachari, M. Head-Gordon, and J. A. Pople, J. Chem. Phys. 93, 1486 (1990).
[30] R. J. Bartlett, J. D. Watts, S. A. Kucharski, and J. Noga, Chem. Phys. Lett. 165, 513 (1990).
[31] J. Noga, S. A. Kucharski, and R. J. Bartlett, J. Chem. Phys. 90, 3399 (1989).
[32] S. A. Kucharski and R. J. Bartlett, Chem. Phys. Lett. 158, 550 (1989).
[33] J. F. Stanton, J. Gauss, and R. J. Bartlett, J. Chem. Phys. 94, 4084 (1991).
[34] J. Gauss, J. F. Stanton, and R. J. Bartlett, J. Chem. Phys. 95, 2623 (1991).
[35] W. J. Lauderdale, J. F. Stanton, J. D. Watts, J. Gauss, and R. J. Bartlett, Chem. Phys. Lett. 182, 207 (1991).

Coupled-Cluster Method for an Incomplete Model Space

STANISLAW A. KUCHARSKI* and RODNEY J. BARTLETT†

Quantum Theory Project, University of Florida, Gainesville, Florida 32611

Abstract

The coupled-cluster method with multidimensional reference space is studied in the case of the incomplete active space (IAS). The latter was chosen as a subspace of the Hilbert space corresponding to a fixed number of valence particles. Two different approaches for the normalization condition are analyzed. When not imposing intermediate normalization, the cancellation of disconnected terms is proven, ensuring that extensive energies are obtained. © 1992 John Wiley & Sons, Inc.

Introduction

The selection of the reference space is a crucial problem in the multireference generalization of the many-body perturbation (MBPT) and coupled-cluster (CC) theories. The most convenient approach to this problem would be an inclusion of a very limited number of functions, possibly those which strongly interact and are close in energy. The model space formed in this manner is usually incomplete. To make it complete would usually require taking into account many more functions, not important from the viewpoint of the physics in the problem. This also enlarges the size of the model space, and it brings about the problem of intruder states [1–3]. The first is impractical and the second often fatal. It should then be concluded that a reasonable answer to the problem would be an adoption of an incomplete model space. This complicates the theory somewhat [4–6].

MBPT for an incomplete model space was first considered by Hose and Kaldor [7] where the disconnected terms occur and a general method for their generation is suggested. The detailed analysis of the additional terms due to incompleteness is given in Ref. [2]. The main question connected with the occurrence of the disconnected terms pertains to the (size) extensivity property [8]. This feature is considered to be a prime virtue of MBPT/CC methods as compared to the CI-based methods. The coupled-cluster formulation corresponding to the Hose–Kaldor MBPT approach was presented by Jeziorski and Monkhorst [5]. The CC equation given there for an incomplete model space leads to disconnected terms in agreement with conclusions reached by Hose and Kaldor.

---

* Permanent address: Institute of Chemistry, Silesian University, Szkolna 9, 40-006 Katowice, Poland.
† To whom correspondence should be addressed.

The problem of extensivity of the different approaches was addressed by Shepard [9], who arrived at the conclusion that the presence of disconnected terms destroys the correct scaling of the energy with a system's size. That statement had weakened the importance of the incomplete model space approaches.

A new aspect of the problem was presented in the studies by Mukherjee [10] and Mukherjee and Lindgren [11]. In their approach, they exploit the previously introduced idea of the universal wave operator [12–14] defined, not only for the given n-valence Hilbert space, but also for all other m-valence ($m < n$) spaces, i.e., for the entire Fock space. They call this method a Fock-space approach to distinguish it from the Hilbert space approaches, e.g., realized by Jeziorski and Monkhorst. The conclusions drawn in Ref. [11] state that the incomplete model space may also generate an effective Hamiltonian of connected nature, provided the wave operator is a valence universal Fock space operator and once the intermediate normalization typical of the Bloch approach is abandoned.

Another Fock-space approach to the CC theory was developed by Stolarczyk and Monkhorst [15]. Here the active space was expanded to include the whole spectrum and, consequently, the model space lost its usual meaning. That would require an alternative definition of the effective Hamiltonian as a quasiparticle conserving operator.

The aim of the present study is to give a thorough discussion of the terms appearing in the expansion of the effective Hamiltonian and in the CC equations for the incomplete model case. Particular attention will be paid to the role of the intermediate normalization condition in the generation of the unlinked diagrams in the effective Hamiltonian expansion.

General Coupled-Cluster Equations for Multidimensional Reference State

The basic equation in the derivation of the CC equation is a generalized Bloch equation [16,17]:

$$H\Omega P = \Omega PH^{\text{eff}}P \qquad (1)$$

When operating on the Bloch equation with the model space projector, P, we obtain an expression for the effective Hamiltonian H^{eff}

$$H^{\text{eff}} = PH\Omega P - P\chi PH^{\text{eff}}P \qquad (2)$$

where $\Omega = P + \chi$.

Acting on Eq. (1) with operator Q, i.e., the orthogonal space projector, we obtain a general form of the CC equations:

$$QH\Omega P - Q\chi PH^{\text{eff}}P = 0 \qquad (3)$$

Further analysis of Eqs. (2) and (3) requires a specification of the wave operator. Two main forms of the wave operator will be considered in the present study. The first one, based on Jeziorski–Monkhorst (JM) [5], will be termed a Hilbert space, ket-dependent exponential ansatz; whereas the second, corresponding to the Mu-

kherjee–Lindgren (ML) formulation [12–14], will be termed the universal (or Fock space) wave operator approach.

Description of the Method

The approximations introduced into the coupled-cluster method usually rely on the truncation of the cluster expansion. In order to avoid excessive proliferation of terms we adopt the method denoted in the literature as CCSD for the single reference [18] or MRCCSD for the multireference case [6], in which the cluster operator, T, is approximated as

$$T(K) = T_1(K) + T_2(K) \tag{4}$$

i.e., only single and double replacement amplitudes are included with respect to each (i.e. K) reference state. The detailed form of the T_1 and T_2 operators depends on the type of wave operator assumed and will be specified later.

As far as the reference function is concerned, the two-dimensional model space is selected, spanned by the functions Φ_0 and $\Phi_{\mu\nu}^{\alpha\beta}$, i.e., the simplest case of the incomplete space.

Hilbert Space Exponential Ansatz

The explicit form of the wave operator, Ω, may be expressed as

$$\Omega = \sum_K e^{T(K)+S(K)} P_K \tag{5}$$

where

$$T(K) = \sum_L T_L(K) \tag{6}$$

and

$$T_L(K) = (L!)^{-2} \sum{}' t_{i_1 \cdots i_2}^{a_1 \cdots a_2}(K) a_1^+ \cdots a_2^+ i_2 \cdots i_1 \tag{7}$$

The prime in the last summation reminds us that those components of $T_L(K)$, which produce excitations within the model space, are excluded from the summation. $S(K)$ is an additional operator, which depends on the choice of the normalization condition.

In order to employ diagrammatic techniques in further derivation, the reference function which would play the role of the Fermi vacuum should be selected. The natural choice would be to assume also a ket-dependent Fermi vacuum, which means that the particle and hole states will be redefined for each column of the effective Hamiltonian matrix. This also means that the diagrammatic expansion of the diagonal element of the effective Hamiltonian matrix will be expressed in terms of closed diagrams, i.e., those appearing in the energy expansion for closed-shell theory.

In order to proceed, the normalization condition should be specified. In the following subsections two options will be considered with the intermediate normalization imposed or abandoned.

Intermediate Normalization Imposed

The intermediate normalization condition assumed in this subsection may be expressed as

$$P\Omega = P \tag{8}$$

This equality only holds for the specific form of the $S(K)$ operator:

$$S(K) = [t^\alpha_\mu(K)t^\beta_\nu(K) - t^\alpha_\nu(K)t^\beta_\mu(K)]\alpha^\dagger\mu\beta^\dagger\nu \tag{9}$$

With these assumptions the effective Hamiltonian operator of Eq. (2) takes the form

$$H^{\text{eff}} = P H \Omega P \tag{10}$$

$$H^{\text{eff}}_{00} = \langle \Phi_0 | He^{T(0)} | \Phi_0 \rangle \tag{10a}$$

$$H^{\text{eff}}_{10} = [\Phi^{\alpha\alpha}_{\mu\nu} | He^{T(0)} | \Phi_0 \rangle \tag{10b}$$

In order to obtain specific diagrammatic expressions for the diagonal and off-diagonal element of the above operator, standard techniques based on Wick's theorem are employed. The diagonal element, H^{eff}_{KK}, takes the form, as previously mentioned, analogous to the energy expression in the closed-shell theory [see Fig. 1(a)].

The off-diagonal element, $H^{\text{eff}}_{JK} = W^{\alpha\beta}_{\mu\nu}$, graphically denoted as ⇒ (double arrows refer to the active levels) is given in Figure 1(b). The symbols, $\mathbf{V}$ and $\mathbf{V}^{-1}$, represent the sets of diagrams occurring in the expansion of the effective Hamiltonian for the complete model space (CMS) approach and are given in Ref. [19]. The difference between the diagrammatic expansion of the $W^{\alpha\beta}_{\mu\nu}$ element for the CMS and the present treatment is represented by the last four diagrams in Figure 1(b), all being disconnected. Thus, the off-diagonal elements contain disconnected diagrams, absent in the CMS theory. The origin of those terms may be attached to the fact that the T_1 operator is allowed to carry active labels only.

The coupled-cluster equations are given in Eqs. (11) and (12), and their diagrammatic versions in Figure 2(a and b) for T_1 and T_2 amplitudes, respectively.
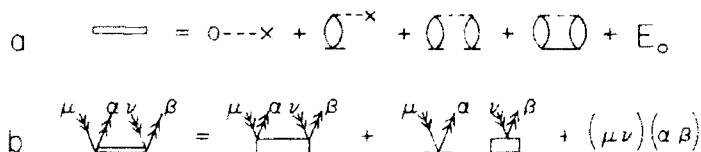
Figure 1. Diagrams contributing to the diagonal (a) and off-diagonal (b) element of the effective Hamiltonian. Hilbert space type wave operator with intermediate normalization assumed. $(\mu\nu)(\alpha\beta)$ means permute indices in last diagram in the two possible ways.

$$\langle \Phi_i^a(K)|(E_0^0 - H_0)e^{T(K)}|\Phi_K \rangle$$

$$= \langle \Phi_i^a(K)|Te^{T(K)}|\Phi_K \rangle - \sum_l \langle \Phi_i^a(K)|(e^T - 1)|\Phi_l \rangle\langle \Phi_l|H^{eff}|\Phi_K \rangle \quad (11)$$

$$\langle \Phi_{ij}^{ab}(K)|(E_0^0 - H_0)e^{T(K)}|\Phi_K \rangle$$

$$= \langle \Phi_{ij}^{ab}(K)|Te^{T(K)}|\Phi_K \rangle - \sum_l \langle \Phi_{ij}^{ab}(K)|(e^T - 1)|\Phi_l \rangle\langle \Phi_l|H^{eff}|\Phi_K \rangle \quad (12)$$

The general structure of the CC equations is analogous to that of the CMS case [19], i.e., no explicitly unlinked terms contribute. The T_1 equations are set up now also for the t_a^i amplitudes, i.e., those engaging active labels only. This is a consequence of the incompleteness of the model space. The latter fact also affects, to some extent, the renormalization diagrams which are now slightly modified.

In the T_2 equation two types of terms contribute: connected and disconnected. This means that the explicitly unlinked terms are fully canceled. The connected terms may be divided into two parts: (principal term graphically denoted as ", ", which is identical to that occurring in the CMS case and close to the diagrams obtained for the closed-shell theory; and the renormalization term, denoted as ", ", which is somewhat modified with respect to Ref. [19] and which is entirely absent in the closed-shell theory [18]. The terms written in Figure 2(b) as disconnected diagrams are, in fact, of a connected nature when their order-by-order structure is examined. In full analogy with the complete model space, they may be called apparent disconnected terms.

The full set of renormalization diagrams, i.e., those represented in Figure 2 by symbols ", " and ", " is given in Ref. [19].

It should be mentioned here that although the CC equations are formally of a connected nature, they also implicitly generate unlinked terms. This is caused by the fact that the $H_{\mu\nu}^{eff}$ element of the H^{eff} involves some disconnected contributions [see Fig. 1(b)]. Substituting the $H_{\mu\nu}^{eff}$ disconnected component for the $H_{\mu\nu}^{eff}$ element in the CC equation will create a number of unlinked diagrams. This should be kept in mind when dealing with the CC method based on the wave operator considered in this subsection, as applied to an incomplete active space.

Figure 2. Diagrammatic equations for the single (a) and double (b) excitation amplitudes, for Hilbert space formulation of the CC theory with intermediate normalization assumed. $(ij)(ab)$ indicates the inclusion of the last diagram subject to permutting the labels as specified.

Intermediate Normalization Abandoned

The departure from the intermediate normalization may be written as

$$P\Omega \neq P \tag{13}$$

This happens when we set the $S(K)$ operator equal to zero. As a consequence, the second term on the right hand side (rhs) of Eq. (2), known as a renormalization term, does not disappear. The diagonal element of the H^{eff} operator, e.g., for the reference, Φ_0, may be expressed as

$$H_{00}^{\text{eff}} = \langle \Phi_0 | He^{T(0)} | \Phi_0 \rangle - \langle \Phi_0 | X | \Phi_{\mu\nu}^{\alpha\beta} \rangle \langle \Phi_{\mu\nu}^{\alpha\beta} | H^{\text{eff}} | \Phi_0 \rangle \tag{14}$$

since the other reference function, Φ_0, does not contribute to the renormalization term. The diagrams appearing in the expansion of H_{00}^{eff} are presented in Figure 3(a). We observe the presence of the additional term as compared to the case described in the previous subsection. This term is due to the renormalization component of Eq. (2) or, in other words, due to the fact that the X operator can reproduce the component of the model function. The off-diagonal element of H^{eff} may be expressed as

$$H_{10}^{\text{eff}} = \langle \Phi_{\mu\nu}^{\alpha\beta} | He^{T(0)} | \Phi_0 \rangle - \langle \Phi_{\mu\nu}^{\alpha\beta} | X | \Phi_0 \rangle \langle \Phi_0 | H^{\text{eff}} | \Phi_0 \rangle \tag{15}$$

where we took advantage of the equality $\langle \Phi_{\mu\nu}^{\alpha\beta} | X | \Phi_{\mu\nu}^{\alpha\beta} \rangle = 0$.

There is a basic difference between expressions (10b) and (15). In the former, the unlinked diagrams do not appear when applying Wick's theorem, since the operator, $e^{T(0)+S(0)}$, cannot generate the function $\Phi_{\mu\nu}^{\alpha\beta}$. The elimination of the $S(K)$ operator from the exponent allows us to create the function $\Phi_{\mu\nu}^{\alpha\beta}$ when operating with $e^{T(0)}$ on Φ_0 and this has the consequence of creating unlinked diagrams from the term $\langle \Phi_{\mu\nu}^{\alpha\beta} | He^{T(0)} | \Phi_0 \rangle$. The unlinked terms are also generated by the second term of Eq. (15) and these cancel all those coming from the first term. The full mutual cancellation is not possible, however, due to the term in brackets in Figure 3(a). The structure of the noncanceled diagrams points out its connected nature. In fact, this is an EPV diagram shown as the last term in Figure 3(b).

The disconnected terms are now generated by the terms:

$$\langle \Phi_{\mu\nu}^{\alpha\beta} | H_0 e^{T(0)} | \Phi_0 \rangle \langle \Phi_{\mu\nu}^{\alpha\beta} | Ve^{T(0)} | \Phi_0 \rangle \tag{16}$$
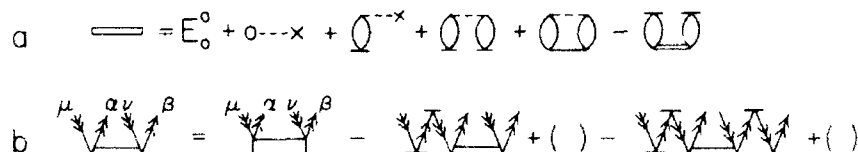
Figure 3.   Diagrams contributing to the diagonal (a) and off-diagonal (b) element of the effective Hamiltonian. Within the Hilbert space formalism without intermediate normalization assumed. (   ) denotes permutation of the nonequivalent lines.

and also by the renormalization part of Eq. (11). Exploiting the CC equation for the t_2^a amplitude, we observe the partial cancellation of the disconnected diagrams. The surviving term [the second term in Fig. 3(b)] is actually a connected EPV diagram. Thus, in this approach, only connected terms contribute to the off-diagonal effective Hamiltonian element.

The CC equations derived for the present form of the wave operator are identical to those presented in Figure 2. The cancellation of the unlinked terms in the current case is a little more complicated. This is due to the fact that $\langle \Phi_u | He^{T_{\mathrm{eff}}} | \Phi_v \rangle$ is no longer equal to H_{uv}^{eff}. Writing the T_1 in the general form [Eq. (11)], we observe that the cancellation of the unlinked terms occurs between the first and second term. This is also true for the CMS and wave operator described in the previous subsection. Here only partial cancellation takes place between them with the term $\cdots \square$ (with plus sign) surviving. The absence of the intermediate normalization makes the term $\langle \Phi_0 | X(1) | \Phi_0 \rangle$ nonvanishing and, as a result, the last term of Eq. (11) generates the diagram $\cdots \square$ (minus sign), making the cancellation of the unlinked terms complete.

Fock Space, Universal Wave Operator Approach

In this section we will discuss briefly the formulation of the same problem within the Fock space scheme.

The formulation of the Fock space CC theory relies on the wave operator defined as

$$\Omega = \{e^T\} P \tag{17}$$

where $\{\ \}$ denotes the normal product of the second quantized operators. The cluster operator is, as usual, separated into components corresponding to the single, double, etc., excitations

$$T = T_1 + T_2 + \cdots \tag{18}$$

where

$$T_k = \frac{1}{k!^2} \sum t_{i_1 \cdots i_k}^{a_1 \cdots a_k} a_1^\dagger \cdots a_k^\dagger i_k \cdots i_1 \tag{19}$$

The summation over a_l runs over particle and active levels, and summation over $\bar{i}_l$ goes over hole and active levels. This means that active labels occur both as the creation and annihilation operators. Owing to this property there are possible operators which are formally classified as double, triple, etc., excitations, but effectively generate the single excitation function Φ_i^a, e.g., t_i^a, t_{iu}^{au}, t_{iuv}^{auv}, etc. and the same is true for higher clusters.

The number of unknown amplitudes, defined according to Eq. (19), far exceeds the number of equations. In order to solve the problem we need to include into the model space also lower ranked sectors, containing different numbers of electrons. The standard way of constructing the Fock space operator is to proceed in an hierarchical manner, starting with the $S^{(0,0)}$ sector (Φ_0) and after solving the CC

equations go to the sectors $S^{(1,0)}$ and $S^{(0,1)}$ with one extra and one less electron and solve the CC equations until finally ending with the $S^{(2,2)}$ sector, which corresponds to doubly excited configurations relative to $\Phi_0(\Phi_{\mu\nu}^{ij})$. Now with all single and doubly excited configurations included in the orthogonal space, with respect to the additional reference states, the required number of cluster equations may be formulated. This allows the universal waveoperator to be unambiguously determined.

The second approach which could be employed here is to adopt the core as a vacuum, which means the $S^{(0,0)}$ sector is now the doubly ionized configuration and we will consider, also, the $S^{(1,0)}$ sector corresponding to four singly ionized configurations and finally the $S^{(2,0)}$ sector which would include four determinants in the complete case, or the two Φ_0 and $\Phi_{\mu\nu}^{ij}$ in the current example.

It was shown in Refs. [10,11,20] that the connected form of the effective Hamiltonian and the CC equations may be ensured by retaining the above operators in the expansion or, in other words, by dropping the intermediate normalization.

Thus, in the present case, we also end up with the connected structure of the involved quantities. However, the complexity of the problem is greater in some respects, although computational considerations are such that Fock space calculations represent only a fraction of the time of the ground state CC solution [23].

Conclusions

It was shown on the example of the two-dimensional model space that the presence of the disconnected diagrams in the effective Hamiltonian cluster expansion may be attributed to the intermediate normalization condition. Departure from that condition eliminates disconnected terms.

The disconnected diagrams, present in the effective Hamiltonian expansion, are the source of the unlinked contributions when iterating the CC equations.

The important observation is that the connected expansion of the effective Hamiltonian may be obtained for the Jeziorski–Monkhorst wave operator, i.e., an operator defined for an incomplete n-valence Hilbert space [4,6]. The necessity of the inclusion of the lower rank components of the Fock space approach is very inconvenient from the computational point of view, particularly for problems where full potential energy surfaces, as opposed to energy differences, are derived [20,21]. It also confuses the usual meaning of "excitation," as "spectator" amplitudes like $t_{i\mu}^{ab\mu}$ are part of "double" excitation amplitudes. The number of equations which should be considered is larger than that in the Hilbert-space approach.

One may anticipate that the later formulation of the multireference coupled-cluster theory will be easier to implement and more useful in actual applications. Elsewhere, this is explicitly shown for the two-configuration, open-shell singlet case [22], the bête noire of single-reference CC approaches.

Acknowledgment

Bibliography

[1] T. H. Schucan and H. A. Weidenmüller, Ann. Phys. 76, 483 (1973); U. Kaldor, Phys. Rev. A 38, 6013 (1988).

[2] S. A. Kucharski and R. J. Bartlett, Int. J. Quant. Chem. Symp. 22, 383 (1988).

[3] S. Zarrabian and R. J. Bartlett, Chem. Phys. Lett. 153, 133 (1988); S. Zarrabian, W. D. Laidig. and R. J. Bartlett, Phys. Rev. A. 41, 4711 (1990).

[4] L. Meissner, S. A. Kucharski, and R. J. Bartlett, J. Chem. Phys. 91, 6187 (1989); L. Meissner and R. J. Bartlett, J. Chem. Phys. 92, 561 (1990).

[5] B. Jeziorski and H. J. Monkhorst, Phys. Rev. A 24, 1668 (1981).

[6] A. Balkova, S. A. Kucharski, L. Meissner, and R. J. Bartlett, J. Chem. Phys. 95, 4311 (1991).

[7] G. Hose and U. Kaldor, J. Phys. B 12, 3827 (1979).

[8] R. J. Bartlett, J. Phys. Chem. 93, 1697 (1989); Ann. Rev. Phys. Chem. 32, 359 (1981).

[9] M. Shepard, J. Chem. Phys. 83, 624 (1985).

[10] D. Mukherjee, Chem. Phys. Lett. 125, 207 (1986).

[11] I. Lindgren and D. Mukherjee, Phys. Rep. 151, 931 (1987).

[12] D. Mukherjee, R. K. Moitra, and A. Mukhopadhyay, Molec. Phys. 30, 1861 (1975).

[13] I. Lindgren, Int. J. Quant. Chem. S 12, 33 (1984).

[14] M. A. Haque and D. Mukherjee, J. Chem. Phys. 80, 5058 (1984).

[15] L. Z. Stolarczyk and H. J. Monkhorst, Phys. Rev. A 32, 725, 743 (1985).

[16] B. H. Brandow, Rev. Mod. Phys. 39, 771 (1967).

[17] I. Lindgren, J. Phys. B 7, 2441 (1974).

[18] G. D. Purvis, III and R. J. Bartlett, J. Chem. Phys. 76, 1910 (1982).

[19] S. A. Kucharski and R. J. Bartlett, J. Chem. Phys. 95, 8227 (1991).

[20] M. Rittby, S. Pal, and R. J. Bartlett, J. Chem. Phys. 90, 3214 (1989).

[21] C. M. L. Rittby and R. J. Bartlett, Theoret. Chim. Acta 80, 469 (1991), and references therein.

[22] A. Balkova and R. J. Bartlett, Chem. Phys. Lett. 193, 364 (1992).

[23] J. Stanton, R. J. Bartlett and C. M. L. Rittby, J. Chem. Phys., in press.

Moment-Method Perturbation Theory for the Hydrogen Atom in Parallel Electric and Magnetic Fields and in Inhomogeneous Electric Fields

FRANCISCO M. FERNÁNDEZ

QUINOR, Facultad de Ciencias Exactas, Universidad Nacional de La Plata, Calle 47 y 115, Casilla de Correo 962, 1900 La Plata, Argentina

Abstract

The problems posed by the hydrogen atom in parallel electric and magnetic fields and in inhomogeneous electric fields are treated simultaneously by means of perturbation theory. The application of this approach is facilitated by the transformation of the Schrödinger equation into a recurrence relation for the moments of the wavefunction which does not appear explicitly in the calculation. Two infinite sets of states are considered as illustrative examples, one of them can be treated as nondegenerate, and the other requires perturbation theory for degenerate states. Closed-form expressions for the perturbation corrections to the energy are obtained in terms of the hydrogenic principal quantum number. The present calculation extends and generalizes previously published results. © 1992 John Wiley & Sons, Inc.

Introduction

Perturbation theory without wavefunction is one of the simplest and most efficient ways of deriving analytic expressions for the energy eigenvalues of relatively simple quantum-mechanical systems. One version of this approach which comes from the combination of perturbation theory with the hypervirial and Hellmann–Feynman theorems leads to closed-form expressions for the energy coefficients of arbitrary states in terms of the zeroth-order energy [1,2]. This method only applies to separable problems, because only in such cases one can obtain the required recurrence relations for the expectation values of properly selected operators. On the other hand, the combination of perturbation theory and the moment method applies to a wider variety of problems, and has been intensively used in the study of the hydrogen atom in magnetic [3–6] and magnetic and electric [7] fields. The first applications of this method were restricted to nondegenerate states and states not coupled by the fields. The latter can be treated as if they were nondegenerate thus facilitating the application of the approach. Recently, the moment method was shown to also be useful in the application of perturbation theory for degenerate states to the Zeeman and Stark effects in hydrogen [8,9].

The purpose of this study is the application of the moment-method perturbation theory to the hydrogen atom in parallel magnetic and electric fields and in inhomogeneous electric fields. A previous application of this method to the former

system consisted of a numerical calculation for states that can be treated as non-degenerate [7]. Here are derived analytic expressions for the energies of these states and also of a class of states coupled by the perturbation. The physical problems are outlined in the next section; the recurrence relations for the moments are derived in the section following; examples of nondegenerate and generate states are treated in the subsequent two sections, respectively; and, finally, results are discussed.

The Models

First consider a spinless hydrogen atom under the combined action of a uniform static magnetic field **B** and a homogeneous electric field **E** both along the z axis. Choosing an axially symmetric gauge for which the vector potential **A** is related to the magnetic field induction **B** by $A = \frac{1}{2} B \times r$, then the interaction between the atom and the fields is

$$\frac{1}{2}(\omega_c \cdot L) + \frac{1}{8}(\omega_c \times r)^2 + eE \cdot r ,\qquad (1)$$

where **r** is the position of the electron of charge $-e$, **L** is the angular momentum operator, and ω_c is the cyclotron angular velocity of the electron $\omega_c = e/mc B$. In this last equation, m is the mass of the electron and c the velocity of light. The first term in eq. (1) is proportional to L_z, which commutes with the total Hamiltonian operator because of the cylindrical symmetry of the system. Therefore, L_z is a constant of the motion and without loss of generality that term can be omitted during the calculation, and its contribution added at the end.

In atomic units, the energy and length are multiples of e^2/a_0 and $a_0 = \hbar^2/(me^2)$, respectively, and the Hamiltonian operator reads

$$H = H_o + \lambda[ar^2(1 - \cos^2 \theta) + br \cos \theta] ,\qquad (2)$$

where $H_o = -\nabla^2/2 - 1/r$ describes the hydrogen atom in absence of fields, $a = B^2 a_0^3/[8(mc)^2]$ and $b = 6a_0^2/e$. Here, B and 6 are, respectively, the magnetic and electric field intensities, and the perturbation parameter, λ, is set equal to unity at the end of the calculation.

For the hydrogen atom in an inhomogeneous electric field along the z axis, taking into account only the dipole and quadrupole contributions to the classical interaction energy between the atom and the field [10], one has to add

$$e6(0)z + \frac{e}{6}\frac{\partial 6}{\partial z}(0)(3z^2 - r^2) ,\qquad (3)$$

to the Hamiltonian operator for the isolated atom. Therefore, the total Hamiltonian operator in atomic units reads

$$H = H_o + \lambda[ar^2(1 - 3\cos^2 \theta) + br \cos \theta] ,\qquad (4)$$

in which $a = -(a_0^3/6e)(\partial 6/\partial z)(z = 0)$ and $b = a_0^2 6(0)/e$.

One can treat both problems simultaneously by means of the Hamiltonian operator

$$H = H_0 + \lambda[ar^2(1 - \sigma \cos^2 \theta) + br \cos \theta],$$ (5)

which reduces to either (2) or (4) when $\sigma = 1$ or $\sigma = 3$, respectively.

Moment-Method Perturbation Theory

If Ψ is an eigenfunction of H, with eigenvalue E and F, belongs to the domain of H, then $\langle (H - E)F|\Psi \rangle = \langle F|(H - E)\Psi \rangle = 0$. In particular, if F is of the form,

$$F_{i,j,n,m} = \sin^i \theta \cos^j \theta r^n e^{-\alpha r} e^{im\phi}, \qquad i, j, n = 0, 1, \ldots, m = 0, \pm 1, \ldots \qquad (6)$$

then

$$HF_{i,j,n,m} = -\frac{1}{2} \beta^2 F_{i,j,n,m} + [\beta(n+1) - 1]F_{i,j,n-1,m}$$

$$+ \frac{1}{2} [(i+j)(i+j+1) - n(n+1)]F_{i,j,n-2,m}$$

$$+ \frac{m^2 - i^2}{2} F_{i-2,j,n-2,m} - \frac{1}{2} j(j-1)F_{i,j-2,n-2,m}$$

$$+ \lambda(aF_{i,j,n+2,m} - \sigma a F_{i,j+2,n+2,m} + bF_{i,j+1,n+1,m}). \qquad (7)$$

The second term on the right-hand side of this equation vanishes when $n = N - 1$ if $\beta = 1/N$, $N = 1, 2, \ldots$. Another choice that simplifies this recurrence relation is $i = |m|$ because, in that case, the subscript i remains unchanged and equal to a good quantum number. Under these conditions the moments

$$I_{j,n} = \langle F_{|m|,j,n,m}|\Psi \rangle, \qquad (8)$$

satisfy the recurrence relation

$$\frac{n+1-N}{N} I_{j,n-1} + \frac{1}{2} [(|m|+j)(|m|+j+1) - n(n+1)]I_{j,n-2}$$

$$- \frac{1}{2} j(j-1)I_{j-2,n-2} - \Delta E I_{j,n} + \lambda(a I_{j,n+2} - \sigma a I_{j+2,n+2} + b I_{j+1,n+1}) = 0. \qquad (9)$$

in which ΔE is the energy shift $E + 1/(2N^2)$. In principle, this recurrence relation completely determines the energy and the moments the same way the Schrödinger equation does for the energy and the wavefunction. Hence, numerical calculation of the energy and moments from their recurrence relation is possible, as shown by Blankenbecler et al. for anharmonic oscillators [11]. Here the recurrence relation (9) is treated by means of perturbation theory: an approach which requires an appropriate expression for the energy shift in terms of the moments. This point is illustrated in the examples that follow.

Nondegenerate States

The only nondegenerate state of the spinless hydrogen atom is the ground state. In addition to it there are some degenerate states that can be treated as nondegenerate

because the perturbation operator does not connect them to other states with the same energy. One such class of states is discussed here.

The first three terms in the recurrence relation (9) vanish simultaneously when $j = J$, $n = N - 1$ and $|m| = N - J - 1$, J being either 0 or 1. When $J = 0$, the recurrence relation reduces to $\Delta E I_{0,N-1} = \lambda(a I_{0,N-1} - \sigma a I_{2,N-1} + b I_{1,N})$. In order to obtain perturbation corrections for an arbitrary value of N it is convenient to redefine subscript n as $N - 1 + i$ and the moments as $A_{j,i} = I_{j,N-1+i}$. The recurrence relation is linear in the moments so that one of them can be chosen arbitrarily, and the energy is independent of this choice that plays the role of a normalization condition. In the present case, $A_{0,0} = 1$ leads to a particularly simple expression for the energy shift: $\Delta E = \lambda(a A_{0,2} - \sigma a A_{2,2} + b A_{1,1})$.

The perturbation expansions for the energy shift and moments,

$$\Delta E = \sum_{p=1}^{'} E_p \lambda^p, \quad A_{j,i} = \sum_{p=0}^{'} A_{j,i}^{(p)} \lambda^p , \tag{10}$$

lead to the following expression for the energy coefficients:

$$E_p = a A_{0,2}^{(p-1)} - \sigma a A_{2,2}^{(p-1)} + b A_{1,1}^{(p-1)}, \quad p > 0 . \tag{11}$$

According to eq. (9) the perturbation corrections to the moments satisfy the recurrence relation:

$$A_{j,i}^{(q)} = \frac{N}{i+1}\left\{ \frac{1}{2}[(N+i)(N+i+1) - (j+N-1)(j+N)]A_{j,i-1}^{(q)} \right.$$

$$+ \frac{1}{2}j(j-1)A_{j-2,i-1}^{(q)} + \sum_{s=1}^{c} E_s A_{j,i+1}^{(q-s)}$$

$$+ \left. \lambda[\sigma a A_{j+2,i+3}^{(q-1)} - a A_{j,i+3}^{(q-1)} - b A_{j+1,i+2}^{(q-1)}] \right\} . \tag{12}$$

The starting point of the hierarchical calculation of the perturbation corrections from this equation is given by

$$A_{0,0}^{(p)} = \delta_{p0} . \tag{13}$$

which follows from the normalization condition. In order to obtain E_p, one has to proceed according to the nested loops: $q = 0, 1, \ldots, p$, $j = 0, 1, \ldots, 2(p - q)$, and $i = 0, 1, \ldots, 3(p - q) - 1$. Because only one expression for the energy suffices to carry out the calculation one can treat this class of states as nondegenerate.

Degenerate States

The choice, $J = 1$, selects a class of states with $|m| = N - 2$, $N = 2, 3, \ldots$. In this case it is convenient to define the subscript i according to $n = N - 2 + i$ so that the moments $A_{j,i} = I_{j,N-2+i}$ satisfy the recurrence relation

$$iA_{i,j} = N\left\{\frac{1}{2}[(N + i - 1)(N + i) - (N + j - 2)(N + j - 1)]A_{i,j-1}\right.$$

$$+ \frac{1}{2}j(j - 1)A_{i,j-1} + \Delta E A_{i,j-1}$$

$$\left. + \lambda(\sigma a A_{i-2,j-1} - a A_{i,j-3} - b A_{i-1,j-2})\right\}.\qquad(14)$$

When $i = 0$ and $j = 1$, this recurrence relation gives an expression for the energy shift in terms of the moments:

$$\Delta E A_{1,1} = \lambda(a A_{1,3} - \sigma a A_{3,3} + b A_{2,2}).\qquad(15)$$

Straightforward application of perturbation theory, as in the previous section, shows that the recurrence relation (14) and eq. (15) are insufficient to solve the problem, because the perturbation corrections to the moments and energy depend on those for $A_{0,0}$ and $A_{1,1}$. The reason is that these states are connected by the perturbation and have to be treated explicitly as degenerate.

To obtain additional equations, $j = i = 0$ in the recurrence relation (14), which becomes

$$(N - 1)A_{0,-1} + \Delta E A_{0,1} + \lambda[\sigma a A_{2,3} - a A_{0,3} - b A_{1,2}] = 0.\qquad(16)$$

whereas, when $j = 0$ and $i = -1$, one obtains

$$A_{0,-1} = -N[\Delta E A_{0,0} + \lambda(\sigma a A_{2,2} - a A_{0,2} - b A_{1,1})].\qquad(17)$$

Substitution of eq. (17) into eq. (16) yields a second expression for the energy shift:

$$\Delta E[A_{0,1} - N(N - 1)A_{0,0}]$$
$$+ \lambda\{\sigma a[A_{2,3} - N(N - 1)A_{2,2}] - a[A_{0,3} - N(N - 1)A_{0,2}]$$
$$- b[A_{1,2} - N(N - 1)A_{1,1}]\} = 0.\qquad(18)$$

The normalization condition, $A_{1,1} = 1$, leads to a particularly simple expression for the energy shift

$$\Delta E = \lambda(a A_{1,3} - \sigma a A_{3,3} + b A_{2,2}).\qquad(19)$$

which, when substituted into (18), gives

$$[A_{0,1} - N(N - 1)A_{0,0}](a A_{1,3} - \sigma a A_{3,3} + b A_{2,2})$$
$$+ \sigma a[A_{2,3} - N(N - 1)A_{2,2}] - a[A_{0,3} - N(N - 1)A_{0,2}]$$
$$- b[A_{1,2} - N(N - 1)A_{1,1}] = 0.\qquad(20)$$

According to eq. (19), the perturbation corrections to the energy are given by

$$E_p = a A_{1,3}^{(p-1)} - \sigma a A_{3,3}^{(p-1)} + b A_{2,2}^{(p-1)}.\qquad(21)$$

and those for the moments are obtained hierarchically by means of

$$A_{i,j}^{(q)} = \frac{\lambda}{i}\left\{\frac{1}{2}[(N + j - 1)(N + i) - (N + j - 2)(N + j - 1)]A_{i,j}^{(q)}\right.$$

$$+ \frac{1}{2}j(j - 1)A_{i-2,j-1}^{(q)} + \sum_{s=1}^{q} E_s A_{i,j}^{(q-s)}$$

$$\left. + \sigma a A_{i-2,j+3}^{(q-1)} - a A_{i,j+3}^{(q-1)} - b A_{i+1,j+2}^{(q-1)}\right\}, \tag{22}$$

starting from

$$A_{1,1}^{(p)} = \delta_{p0}, \tag{23}$$

which comes from the normalization condition. These equations yield the perturbation corrections to the energy and to all the moments in terms of those for $A_{0,0}$ which are determined by eq. (20) that play the role of the secular determinant in standard perturbation theory [12]. For instance, after writing all the moments of order zero in terms of $A_{0,0}^{(0)}$, by means of the recurrence relation (22), eq. (20) for $\lambda = 0$ becomes

$$N^5\left[aN(2N + 1) + \frac{3}{2}b\right]A_{0,0}^{(0)2}$$

$$+ aN^4\left[\frac{5}{2} - N\left(N + \frac{9}{2}\right) + \sigma(1 - N)\right]A_{0,0}^{(0)} - \frac{3}{2}Nb = 0. \tag{24}$$

The two roots of this equation, which are both real, give the splitting of the pair of degenerate states considered for each value of N. Expanding eq. (20) in λ-power series, and expressing all the perturbation corrections in terms of those for $A_{0,0}$, shows that the resulting equation is linear in the corrections $A_{0,0}^{(p)}$ with $p > 0$, which one can obtain in terms of corrections of lesser order already evaluated in previous steps. Explicit expressions in the simpler case of the Stark effect in hydrogen ($a = 0$) are shown [8], but here it seems preferable to use a symbolic processor to solve for $A_{0,0}^{(p)}$ in every step, thus avoiding mistakes.

Results and Discussion

Throughout this communication, the states have been labeled by means of three numbers that occur naturally in the recurrence relation for the moments N, $|m|$, and J. The projection of the angular momentum along the z axis is a constant of motion with value mh, $m = 0, \pm1, \cdots$ and the energy depends on $|m|$ which appears explicitly in that recurrence relation. The number, N, is the principal quantum number of the isolated atom so that the zeroth-order energy is $E_0 = -1/(2N^2)$ in atomic units. For low fields, it is customary to designate the states by means of the hydrogenic quantum numbers. According to this convention it remains to introduce the angular momentum quantum number $l = 0, 1, \ldots$ Close inspection of the expressions for the energy derived above shows that $l = |m| = N - 1$ for the states treated in the Nondegenerate States section, because they are nodeless

when $\lambda = 0$. On the other hand, for the pair of degenerate states, considered in the Degenerate States section, one has $l = N - 1$ for one of them and $l = N - 2$ for the other, both having $m = N - 2$. This conclusion follows from the coefficients of ΔE in eqs. (15) and (18) which reveal that, for $\lambda = 0$, one of the states is nodeless, whereas the other has exactly one radial zero. For example, when $N = 2$, the pair of unperturbed states are $2p$ and $2s$. Thus present approach agrees with standard perturbation theory that leads to a 2×2 secular determinant with nonvanishing off-diagonal matrix elements for such states. The splitting of the energy level due to the admixture of these states is entirely due to the term bz, because the terms proportional to a have zero off-diagonal matrix elements.

The moment method leads to remarkably simple recurrence relations which are suitable for both numerical and analytic calculations. Here the interest is in analytic expressions because they allow a clearer interpretation of the physical phenomenon. Even with the help of the moment method, an analytic calculation of order larger than the second would be extremely tedious without the assistance of a symbolic processor such as Maple or Reduce. The former is used to obtain the results in Tables I–IV. Table I shows the first four perturbation corrections to the energy of the states with $l = |m| = N - 1$ of the hydrogen atom in parallel electric and magnetic fields ($\sigma = 1$). These results agree completely with the analytic calculation of Lambin et al. [13], with the numerical calculation of Johnson et al. [14] for the ground state, and with the numerical calculation of Fernández and Castro [7] for excited states. On the other hand, the coefficient of $b^2 z^2$ in the analytic ground-state energy obtained by Turbiner [15] through the logarithmic perturbation theory must be wrong. Table II shows the perturbation corrections to the energies of the pair of states with $|m| = N - 2$, $l = N - 1$, and $l = N - 2$ for the same system. Because the energy coefficients become increasingly complicated functions of N, as the perturbation order increases, only the first perturbation correction for arbitrary N and the first three corrections for $N = 2$ are shown. Notice that the splitting of the pair of degenerate states is given by the sign of the square root in $E_2^{(1)}$. This

TABLE I. Perturbation corrections to the energies of the states with $l = m = N - 1$ for the hydrogen atom in parallel electric and magnetic fields.

$E_1 = aN^2(N+1)$

$E_2 = \dfrac{1}{24}N^4(N+1)[a^2N^2(48N^2 + 108N + 56) + b^2(12N + 15)]$

$E_3 = \dfrac{1}{72}aN^6(N+1)[a^2N^2(86N^4 + 4356N^3 + 8192N^2 + 6800N + 2112) + b^2(216N^2 + 675N + 540)]$

$E_4 = \dfrac{1}{17280}N^8(N+1)[a^4N^4(1797120N^4 + 14819760N^3 + 51601120N^2 + 97164600N + 104392224N + 60637248N + 14826240) + a^2b^2N^2(518400N^3 + 3009960N^2 + 6480480N + 5896800N + 1834560) + b^4(25920N^3 + 125955N^2 + 209250N + 118800)]$

TABLE II. Perturbation corrections to the energy of the states with $|m| = N - 2$, $l = N - 1$ and $l = N - 2$ for the hydrogen atom in parallel electric and magnetic fields. Here $A = A_{0,0}^{(0)}$.

$$E_1 = aN^2(N^2 - 1) + \frac{3}{2} bN^3 A$$

$$A = \{a[2N^3 + 11N^2 - 7N] \pm [a^2N^2(4N^4 + 44N^3 + 93N^4 - 154N + 49) + 24abN(2N + 1)$$
$$+ 36b^2]^{1/2}\}/[2N^2(4aN^2 + 2aN + 3b)]$$

$$N = 2$$

$$E_1 = 12a + 12bA$$

$$E_2 = -2688a^2 - 4416abA + b^2(2688A^2 - 294b^2) - 12b[a^2(-256768A^2 + 131584A) + ab(-73856A^2$$
$$+ 160000A^3 - 14496A + 3336) + b^2(21120A^3 - 1656A)]/(96bA + 640aA - 184a)$$

$$E_3 = \frac{4}{5} [a^6(-33016371200 + 344518656000A - 1198325760000A^2 + 1389363200000A^3)$$
$$+ a^5b(170714931200A^4 + 1345363834880A^3 - 784635667456A^2 + 101330065920A)$$
$$+ a^4b^2(-81341644800A^5 + 130628736000A^4 + 340686297600A^3 + 5184082608A$$
$$- 117119362560A^2 - 265992240) + a^3b^3(7818240000A^6 - 89171389440A^5 + 42978037248A^4$$
$$+ 40913244480A^3 - 9372717024A^2 + 1043037120A + 12091680) + a^2b^4(2564352000A^6$$
$$- 23014775808A^5 + 2995896960A^4 + 4861565568A^3 - 74329560A - 1004842080A^2$$
$$- 9250020) + ab^5(630374400A^6 - 1854524160A^5 - 481610880A^4 + 378855360A^3$$
$$+ 36243720A^2 - 9690705A) + b^6(63244800A^6 - 30922560A^4 + 2528010A^2)]/[12bA + a(80A$$
$$- 23)]^3$$

$$A = \frac{1}{4(20a + 3b)} [23a \pm (529a^2 + 60ab + 9b^2)^{1/2}]$$

splitting is caused entirely by the electric field in agreement with the prediction of standard perturbation theory. Thus far, no independent calculation of these perturbation corrections has been reported so the present results are compared with those for the Stark ($a = 0$) and Zeeman ($b = 0$) effects in hydrogen obtained by

TABLE III. Energy coefficients for the states with $l = |m| = N - 1$ of hydrogen in an inhomogeneous electric field.

$$E_1 = b\xi N^2 2(N^2 - 1)$$

$$E_2 = -\frac{1}{8} b^2N^4(N + 1)[\xi^2N^2(16N^3 + 20N^2 + 28N + 56) + 4N + 5]$$

$$E_3 = \frac{1}{4} b^3\xi N^8(N + 1)[\xi^2N^2(48N^5 + 168N^4 + 240N^3 + 36N^2 - 748N - 968 + 4N^3 - 22N^2 - 102N$$
$$- 93]$$

$$E_4 = -\frac{1}{640} b^4N^{10}(N + 1)[\xi^4N^4(66560N^7 + 415120N^6 + 1167840N^5 + 1936800N^4 + 2486528N^3$$
$$+ 6005776N^2 + 13623520N + 11373440) + \xi^2N^2(8960N^5 + 33160N^4 + 166160N^3 + 810400N^2$$
$$+ 1665800N + 1165840) + 960N^3 + 4665N^2 + 7750N + 4400]$$

TABLE IV Energy coefficients for the states with $|m| = N - 2, l = N - 1$ and $l = N - 2$ of hydrogen in an inhomogeneous electric field. Here $A = f_{00}^{(0)}$.

$$E_1 = \frac{1}{2} h N^2 [g(2N^2 - 6N - 8) + 3NA]$$

$$A = \{\xi N(2N^2 + 15N - 11) \pm [\xi^2 N^2(4N^4 + 60N^3 + 181N^2 - 330N + 121) + 24\xi N(2N + 1 + 36)]^{1/2}\} / \{2N^2[2\xi N(2N + 1) + 3]\}$$

$$N = 2$$

$$E_1 = 12h(A - 2\xi)$$

$$E_2 = -6h^2[\xi^3(209920A - 70848) + \xi^2(81408A - 76416A^2) + \xi(4160A^2 - 5664A + 296A - 1101) + 174A - 96A^3]/[\xi(80A - 27\xi) + 12A]$$

$$E_3 = \frac{12}{5} h^3[\xi^6(214453370880 - 19062521856000A + 56481546240000A^2 - 5578424320000A^3) + \xi^5 A(-328738487040 + 2010785780736A - 3602664284160A^2 + 13172367360000A^3) + \xi^4(6731274960 - 387592153392A + 176941359360A^2 - 339210828800A^3 - 1383042355520A^4 + 382432051200A^5) + \xi^3(-41577480 - 5841953280A + 23069407104A^2 - 28333392000A^3 - 114458431488A^3 + 1475927193600A^5 + 2606080000A^6) + \xi^2(490590 - 29085480A + 1681773600A^2 - 2116040832A^3 - 9384504960A^4 + 16603978752A^5 + 854784000A^6) + \xi A(-3792015 + 120812400A - 69958080A^2 - 160536960A^3 + 4079808000A^4 + 210124800A^5) + A^2(842670 - 10307520A^2 + 21081600A^4)]/[\xi(-27 + 80A) + 12A]^3$$

$$A = [25\xi \pm (625\xi^2 + 60\xi + 9)^{1/2}]/[4(20\xi + 3)]$$

the same method but a different symbolic processor (MUMATH) and contrasted with results from various sources [8,9].

Table III shows the perturbation corrections to the energy of the states with $l = |m| = N - 1$ of the hydrogen atom in an inhomogeneous electric field ($\sigma = 3$). Because the whole perturbation vanishes as the electric field is turned off it is convenient to write $a = b\xi$. To compare present results with those obtained by Bednář [16] by means of the Lie algebraic method one has to substitute $\alpha/3$ for ξ and F for h. The first-order corrections agree, but there is a slight discrepancy between the second-order ones, which may be attributed to the long and tedious hand calculation followed by Bednář. Table IV shows the perturbation corrections to the energies of the pair of states with $|m| = N - 2$, $l = N - 1$ and $l = N - 2$. For the same reason given before only the first perturbation correction is shown for arbitrary N and the first three energy coefficients for $N = 2$. The author is not aware of published results for these states to which he can compare present energy coefficients, but they must be correct since they come from the same program that produced the results for the other problem.

The moment method provides a systematic and simple way of applying perturbation theory to various problems of physical interest. One obtains the perturbation corrections hierarchically from recurrence relations which are suitable for both analytic and numerical calculation. Their treatment by means of symbolic processors is straightforward, so that one easily derives analytic expressions of relatively large

order which commonly facilitates the understanding of physical aspects of the problem.

Moment-method perturbation theory is preferable to logarithmic perturbation theory [15] because the latter becomes much more tedious in the process of treating states with nodes. Furthermore, it seems that this method has not yet been applied to degenerate states. If one is only interested in the energy the moment method is more convenient, because of its greater simplicity, than the Lie algebraic approach [16,17]. The latter is certainly the most powerful method to derive analytic expressions for all the relevant dynamical variables in the system. However, in the calculation of such properties by means of perturbation theory, the moment method is still useful for providing a rapid and independent test of the energy coefficients.

Bibliography

[1] F. M. Fernández and E. A. Castro, *Hypervirial Theorems, Lecture Notes in Chemistry* (Springer-Verlag, Berlin, 1987), vol. 43.

[2] G. A. Arteca, F. M. Fernández, and E. A. Castro, *Large Order Perturbation Theory and Summation Methods in Quantum Mechanics, Lectures Notes in Chemistry* (Springer-Verlag, Berlin, 1990), vol. 53.

[3] F. M. Fernández and E. A. Castro, Int. J. Quantum Chem. **26**, 497 (1984).

[4] G. A. Arteca, F. M. Fernández, A. M. Mesón, and E. A. Castro, Physica **128A**, 253 (1984).

[5] F. M. Fernández, J. F. Ogilvie, and R. H. Tipping, J. Phys. **A20**, 3777 (1987).

[6] E. J. Austin, Int. J. Quantum Chem. **18S**, 449 (1984).

[7] F. M. Fernández and E. A. Castro, Int. J. Quantum Chem. **28**, 603 (1985).

[8] F. M. Fernández, J. Phys. **A25**, 495 (1992).

[9] F. M. Fernández and J. A. Morales, Phys. Rev. **A** (to appear).

[10] J. D. Jackson, *Classical Electrodynamics* (2nd ed.) (Wiley, Singapore, 1990).

[11] R. Blankenbecler, T. DeGrand, and R. L. Sugar, Phys. Rev. **D21**, 1055 (1980).

[12] A. Dalgarno, in *Quantum Theory, Elements*, D. R. Bates, Ed. (Academic, New York, 1961), vol. I.

[13] P. Lambin, J. C. Van Hay, and E. Kartheuser, Am. J. Phys. **46**, 1144 (1978).

[14] B. R. Johnson, K. F. Scheibner, and D. Farrelly, Phys. Rev. Lett. **51**, 2280 (1983).

[15] A. V. Turbiner, Sov. Phys. JETP Lett. **33**, 173 (1981).

[16] M. Bednář, Ann. Phys. NY **75**, 305 (1973).

[17] B. G. Adams, J. Čížek, and J. Paldus, Adv. Quantum Chem. **19**, 1 (1988).

Relativistic Many-Body Perturbation Theory Using the Discrete Basis Expansion Method: Analysis of Relativistic Pair Correlation Energies of the Xe Atom

YASUYUKI ISHIKAWA

*Department of Chemistry and The Chemical Physics Program, University of Puerto Rico
P.O. Box 23346, UPR Station, San Juan, Puerto Rico 00931-3346*

Abstract

Relativistic pair correlation energies of Xe were computed by employing a partial-wave expansion up to order $l_{p,n}$ = 5. The Dirac–Fock (DF), SCF, and many-body perturbation calculations were performed by employing analytic basis sets of well-tempered GAUSSIAN-type functions. A detailed study of the pair correlation energies in Xe is done in order to analyze the nature of relativistic and correlation effects in this heavy-atom system. © 1992 John Wiley & Sons, Inc.

Introduction

The relativistic many-body theory has been the subject of active research interest during the last decade. This is due to the increasing awareness of the importance of relativity in describing the electronic structure of heavy-atom systems, and due to the inadequacy of the physical model that neglects relativity or treats it as a small perturbation. It is necessary to forfeit the Schrödinger equation in favor of the Dirac equation to describe the electronic structure of heavy-atom systems.

In the last few years, the relativistic many-body perturbation theory (MBPT), which accounts for both relativistic and electron correlation effects, was developed by a number of groups [1–9]. The relativistic MBPT algorithm, based on an expansion in analytic basis functions [4–9], has the advantage in that it provides the compact representation of the complete Dirac spectrum, and greatly facilitates the evaluation of the many-body diagrams using finite summations [6]. Furthermore, by invoking the finite basis set expansion in terms of GAUSSIAN spinors (G-spinors), the relativistic many-body methods can be applied to molecular electronic structure problems in a straightforward way [10,11]. Applications of the relativistic many-body calculations, however, have been limited to lighter systems, because the applications to many electron systems require large integral storage space and computation time.

In a series of studies [5,7,12,13], we have developed matrix Dirac–Fock (DF), self-consistent field (SCF), and relativistic MBPT calculations using analytic basis expansion in terms of G-spinors in order to account for both relativistic and electron correlation effects in heavy-atom systems. The analytic basis expansion in terms

of G-spinors has yielded accurate results for highly ionized systems, and shows none of the signs of the near-linear dependency problems reported with S-spinor basis sets [4]. In a recent study [13], we also developed a way to reduce the computational burden in relativistic MBPT calculations on Kr and Xe by using contracted G-spinor basis sets that retain both accuracy and flexibility in the core and the valence region. The feasibility of a practical relativistic MBPT on heavy atoms is examined by benchmark electronic structure calculations on the ground state Xe atom by using the contracted G-spinor basis sets. The Xe atom possesses 54 electrons, and is one of the heaviest atoms to which nonrelativistic and relativistic MBPT calculations employing analytic basis functions that has ever been applied.

In the relativistic MBPT study on the xenon atom [13], we have obtained the relativistic second-order energy to be −2.7403 au. Its nonadditive contribution [13], due to the interference between relativistic and correlation effects, was found to be −0.0326 au. Although the electron correlation energy and the nonadditive contribution are small in magnitude in comparison with the total DF energy of Xe, they may constitute a significant fraction of the valence-shell energy. Because of the large number of electrons involved, it is very likely that we will be able to take only the valence-shell correlation energy into account in *ab initio* fully relativistic many-body calculations on heavy-atom-containing molecules. Thus, it is important to investigate what fraction of the correlation energy, as well as of the nonadditive contribution in a heavy-atom system, is due to its valence shell correlation energy. If a significant fraction of the nonadditive contribution comes from the valence shell, then the relativistic and correlation effects are no longer additive in the valence shell.

In the present study, relativistic pair correlation energies of Xe are computed by using a recently proposed contracted G-spinor basis set that is capable of reproducing over 99% of the relativistic correlation energies computed by using the large uncontracted G-spinor basis set [13]. The computed second-order pair energies are partitioned into the core, core-valence, and valence shell contributions, in order to study the nature of electron correlation energy in the valence shell of the heavy-atom system. The objective of the present study is to perform a detailed analysis of the relativistic correlation energies of Xe, in order to provide a benchmark for heavy-atom systems.

Methods

The N-electron Hamiltonian for our relativistic MBPT calculations is the so-called relativistic "no-pair" Dirac–Coulomb (DC) Hamiltonian [14, 15],

$$H_+ = \Sigma_i h_D(i) + \mathcal{L}_+ (\tfrac{1}{2}\Sigma_{i,j} 1/r_{ij}) \mathcal{L}_+ \tag{1}$$

where $\mathcal{L}_+ = L_+(1) \cdot L_+(2) \cdots L_+(N)$, and $L_+(i)$ is the projection operator onto the space spanned by the positive-energy eigenfunctions, $\{\phi_{n\kappa}^+\}$ of the radial DF operator, F_κ [16].

$$F_\kappa \phi_{n\kappa}^+(r) = \varepsilon_{n\kappa} \phi_{n\kappa}^+(r) \tag{2}$$

TABLE 1. Orbital energies and total
DF energy of Xe (in au).

Orbital	Orbital energies[a]
$1s_{1/2}$	-1277.256
$2s_{1/2}$	-202.4646
$2p_{1/2}$	-189.6769
$2p_{3/2}$	-177.7045
$3s_{1/2}$	-43.01016
$3p_{1/2}$	-37.65910
$3p_{3/2}$	-35.32504
$3d_{3/2}$	-26.02319
$3d_{5/2}$	-25.53694
$4s_{1/2}$	-8.429622
$4p_{1/2}$	-6.452115
$4p_{3/2}$	-5.982547
$4d_{3/2}$	-2.711115
$4d_{5/2}$	-2.633551
$5s_{1/2}$	-1.009964
$5p_{1/2}$	-0.4923594
$5p_{3/2}$	-0.4396173
E_{DF}[a,b]	-7446.88356
E_{HF}[c]	-7232.07173

[a] Computed by using well-tempered $21s19p13d$ G-spinor basis set.

[b] Total Dirac-Fock-Coulomb SCF energy.

[c] Nonrelativistic limit computed by using $c = 10^4$.

where

$$F_\kappa = \begin{pmatrix} V^{LL} & c\Pi_\kappa + V^{LS} \\ c\Pi_\kappa + V^{SL} & V^{SS} - 2c^2 \end{pmatrix} \tag{3}$$

and

$$\phi_{n\kappa}^+(r) = \begin{pmatrix} P_{n\kappa}(r) \\ Q_{n\kappa}(r) \end{pmatrix} \tag{4}$$

The radial functions, $P_{n\kappa}(r)$ and $Q_{n\kappa}(r)$, are referred to as the large and small components, respectively. $P_{n\kappa}(r)$ and $Q_{n\kappa}(r)$ may be expanded in sets of analytic basis functions [4-8,16].

In q-number theory, the negative-energy states are taken to be filled in the true vacuum state, and the relativistic many-body perturbation theory is conveniently described within the particle-hole second-quantized formalism in which the occupied positive-energy states as well as the negative energy continuum are taken to be below the Fermi level [6,7].

TABLE II. Pair correlation energies of Xe (in milli-hartrees).

	Pair energy		
Pair	$c = 137.0370$	$c = 10^4$	Diff.
Valence			
$5p5p$	−73.63	−73.81	+0.18
$5p5s$	−26.72	−25.35	−1.37
$5s5s$	−5.89	−5.78	−0.11
Core-valence			
$5p4d$	−138.39	−134.24	−4.15
$5p3d$	−13.15	−12.50	−0.65
$5p4p$	−17.73	−17.20	−0.53
$5p3p$	−3.56	−3.54	−0.02
$5p2p$	−1.23	−1.16	−0.07
$5p4s$	−3.09	−3.21	+0.12
$5p3s$	−0.80	−0.85	+0.05
$5p2s$	−0.28	−0.28	0.00
$5p1s$	−0.11	−0.10	−0.01
$5s4d$	−49.61	−43.75	−5.86
$5s3d$	−6.26	−5.29	−0.97
$5s4p$	−10.81	−9.86	−0.95
$5s3p$	−1.80	−1.59	−0.21
$5s2p$	−0.50	−0.42	−0.08
$5s4s$	−1.59	−1.52	−0.07
$5s3s$	−0.35	−0.34	−0.01
$5s2s$	−0.11	−0.10	−0.01
$5s1s$	−0.04	−0.03	−0.01
Core			
$4d4d$	−409.53	−409.75	+0.22
$4d3d$	−171.72	−172.86	+1.14
$4d4p$	−187.64	−184.91	−2.73
$4d3p$	−48.42	−50.96	+2.54
$4d2p$	−16.90	−17.33	+0.43
$4d4s$	−46.22	−46.10	−0.12
$4d3s$	−11.08	−12.41	+1.33
$4d2s$	−3.85	−4.19	+0.34
$4d1s$	−0.16	−0.19	+0.03
$3d3d$	−383.96	−382.72	−1.24
$3d4p$	−81.98	−77.41	−4.57
$3d3p$	−200.96	−200.92	−0.04
$3d2p$	−121.20	−124.01	+2.81
$3d4s$	−27.40	−23.79	−3.61
$3d3s$	−50.62	−49.59	−1.03
$3d2s$	−28.38	−31.20	+2.82
$3d1s$	−1.09	−1.26	+0.17
$4p4p$	−53.93	−53.23	−0.70
$4p3p$	−31.87	−31.33	−0.54
$4p2p$	−12.31	−11.69	−0.62
$4p4s$	−26.67	−25.67	−1.00

TABLE II. (Continued)

Pair	Pair energy		
	$c = 137.0370$	$c = 10^4$	Diff.
4p3s	7.50	7.85	+0.35
4p2s	2.84	2.79	0.05
4p1s	1.14	1.09	0.05
3p3p	56.51	55.87	0.64
3p2p	58.74	56.24	2.50
3p4s	10.51	9.46	1.05
3p3s	27.34	27.13	0.21
3p2s	13.25	13.07	0.18
3p1s	5.96	5.72	0.24
2p2p	135.57	131.82	3.75
2p4s	3.54	3.06	0.48
2p3s	13.16	11.61	1.55
2p2s	45.82	43.98	1.84
2p1s	31.65	31.08	0.57
4s4s	4.70	4.56	0.14
4s3s	2.48	2.46	0.02
4s2s	0.78	0.74	0.04
4s1s	0.28	0.24	0.04
3s3s	4.57	4.55	0.02
3s2s	3.46	3.27	0.19
3s1s	1.29	1.11	0.18
2s2s	7.70	7.43	0.27
2s1s	6.04	5.28	0.76
1s1s	23.93	24.77	+0.84

In a series of studies [5,7,12,13,17,18], we have performed matrix Dirac–Fock–Coulomb (DFC) and Dirac–Fock–Breit (DFB) SCF calculations on many-electron systems with a finite nucleus model. In these studies, we have emphasized alteration of the boundary conditions such that GAUSSIANs become the best form for basis functions. Representing the nucleus as a finite body of uniform proton charge accomplishes that feat [17]. With this representation of the potential, for example, the exact $s_{1/2}$ solutions of the Dirac equation near the origin, we have

$$P(r)/r = 1 + g_2 r^2 + g_4 r^4 + \cdots \tag{5}$$

$$Q(r)/r = f_1 r + f_3 r^3 + \cdots \tag{6}$$

so that, for α arbitrary parameters [17],

$$P(r) = r + g_2 r^3 + \cdots \approx r \exp(-\alpha r^2) \tag{7}$$

$$Q(r) = f_1 r^2 + f_3 r^4 + \cdots \approx Nr^2 \exp(-\alpha r^2). \tag{8}$$

Thus, in the finite nuclear model, the GAUSSIAN functions of an integer power of r are appropriate basis functions because imposition of the finite nuclear boundary results in a solution which is GAUSSIAN at the origin [17].
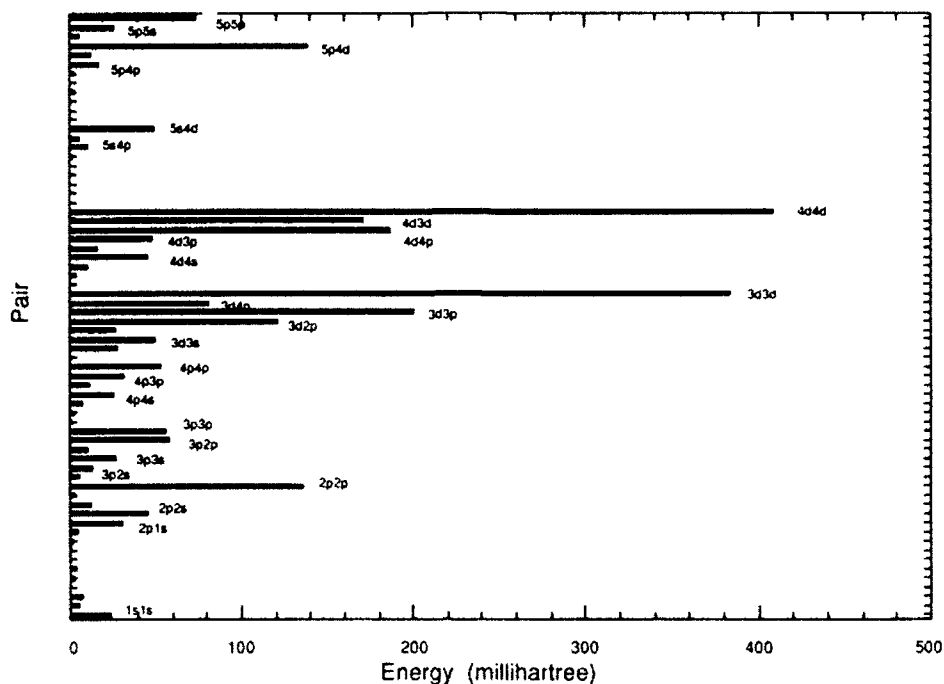
Figure 1. Partial wave analysis of the pair correlation energies (sign reversed) for the ground state of Xe.

The G-spinors that satisfy the boundary conditions associated with the finite nucleus automatically satisfy the condition of the so-called "kinetic balance" for a finite value of c. The kinetically balanced G-spinor basis sets are precisely the form given in eqs. (7) and (8). This is a consequence of the fact that the exponent of r in the GAUSSIAN functions does not depend on the speed of light. In this sense, the G-spinors are chosen to satisfy the condition of kinetic balance and relativistic boundary conditions associated with a finite nucleus.

TABLE III. Core, core-valence, and valence contributions of pair and nonadditive energies (in milli-hartrees).

	Pair energy	Nonadditive energy
Core	−2384.64	−17.87
Core-valence	−249.41	−13.43
Valence	−106.24	−1.30
Total[a]	−2740.29	−32.60

[a] Ref. 13.

In a recent study [13], we have performed relativistic DFC SCF and MBPT calculations on ground-state xenon with the well-tempered GAUSSIAN basis of Huzinaga and Klobukowski [19,20] in a contracted and an uncontracted form. In the present study, we have used the same well-tempered GAUSSIAN basis sets. The DFC SCF calculations were done by using the uncontracted $21s19p12d$ basis set. Basis functions in the $21s$, $19p$, and $12d$ primitive sets were contracted to generate the $[14s13p10d]$ contracted set for MBPT calculations. The contracted set was derived by grouping the functions of highest exponents (see Table 2 of ref. 13). The pair correlation energy calculations were performed by employing a partial-wave expansion up to order $L_{max} = 5$ ($14s13p10d7f6g5h$ basis set). The Xe nucleus was represented as a sphere of uniform proton charge distribution. The atomic mass used in the calculations was 131.30 amu. The speed of light used was 137.0370 au. To simulate the nonrelativistic limit, a value of c of 10^4 was used.

The virtual orbitals used in the study were calculated in the field of the nucleus and of all the electrons (V^N potential). Goldstone diagrams have been summed to compute the second-order pair correlation energies. Diagrammatic summation was done within the subspace of the positive energy branch, i.e., in the no-pair approximation [14, 15].

The DC Hamiltonian used in the present study is approximate. In the DC Hamiltonian, one-electron interactions are treated relativistically as a sum of Dirac one-electron Hamiltonians, whereas the two-electron interaction is treated nonrelativistically as the instantaneous Coulomb repulsion. However, the energy shift induced by the low-frequency Breit interaction in the SCF and correlated calculations is known to be significant for inner-shell orbitals of heavy systems [8, 18]. The effects of relativity on the valence spinors, however, are almost entirely accounted for by the DC Hamiltonian used in the present study.

Results and Discussion

Table I displays the total DFC energy, E_{DFC}, as well as the orbital energies of Xe computed by using an uncontracted $21s19p13d$ G-spinor basis sets. This total DFC energy is 0.017 au higher than the total DFC energy, -7446.9010 au computed by using numerical finite difference DF program [21]. We have computed the nonrelativistic limit, E_{HF}, by taking $c = 10^4$ in our DFC SCF calculations. This gave -7232.07173 au. The relativistic energy lowering, which is the difference between the total DFC SCF energy, E_{DFC}, and the nonrelativistic limit, E_{HF}, is 214.81 au.

A number of quasirelativistic effective core potential calculations [22-24] have been performed on diatomic Xe_2 and XeCl. In these calculations, the $5s$ and $5p$ orbitals of Xe are taken to be the valence orbitals. All the remaining orbitals are treated as the core orbitals, and they are replaced by a set of effective core potentials for valence-only calculations.

In the present study, we also treat the $5s$ and $5p$ orbitals as the valence orbitals and the remaining as the core orbitals. Then the total of 66 second-order pair correlation energies for ground state Xe may be partitioned into the valence, core-valence, and core contributions. Table II gives the second-order pair correlation

energies partitioned in this manner. In the table, the relativistic pair energies computed by using $c = 137.0370$ are given in the second column. The nonrelativistic pair energies obtained by setting $c = 10^4$ are tabulated in the third column. In the fourth column, the nonadditive contributions, i.e., the difference between the relativistic and the nonrelativistic pair correlation energies, are given.

The partial-wave analysis of the second-order pair correlation energies given in Table II are schematically presented in Figure 1. Here, the magnitude of the relativistic second-order pair energies for the ground state of Xe are presented as a bar graph. From Figure 1, one can clearly see that the dominant correlation contribution comes from the $4d4d$ and $3d3d$ pairs as well as those that involve $4d$ and $3d$ orbitals (e.g., $4d4p$, $4d3d$, $3d4p$, $3d3p$, etc.). This may easily be understood because the $4d$ and $3d$ shells each possess 10 electrons, and the dynamical correlations among these electrons are not well accounted for in the DFC SCF step.

The valence, core-valence, and core contributions of the relativistic pair correlations, as well as the nonadditive energies, are tabulated in Table III. The valence and the core-valence contribution of the pair energy are, respectively, 3.9% and 9.1% of the overall second-order energy of Xe. The valence contribution of the nonadditive energy, -1.3 milli-hartrees, accounts for only 4% of the overall nonadditive energy, and only 1.2% of the valence pair correlation energy. This strongly indicates that relativity and correlation effects are additive in the valence shell of Xe.

Table II shows that a number of core pair energies are of comparable magnitude but with opposite sign. Because of the large cancellation of the nonadditive energies in the core shell, the overall nonadditive energy of the system remains small. Furthermore, the core contribution of the nonadditive energy accounts for only 55% of the total nonadditive energy. Because there is no such cancellation, the core-valence contribution of the nonadditive energy accounts for a large fraction (41%) of the total nonadditive energy.

Acknowledgments

Bibliography

[1] W. R. Johnson and J. Sapirstein, Phys. Rev. Lett. 57, 1126 (1986).
[2] W. R. Johnson, S. A. Blundell, and J. Sapirstein, Phys. Rev. A37, 307 (1988); 41, 1689 (1990).
[3] S. Salomonson and P. Oster. Phys. Rev. A40, 5548 (1989).
[4] H. M. Quiney, I. P. Grant, and S. Wilson, Phys. Scr. 36, 460 (1987).
[5] Y. Ishikawa, H. Sekino, and R. C. Binning Jr., Chem. Phys. Lett. 160, 206 (1989).
[6] H. M. Quiney, I. P. Grant, and S. Wilson, in Many-Body Methods in Quantum Chemistry, Lecture Notes in Chemistry 52, U. Kaldor, Ed. (Springer, Berlin, 1989).
[7] Y. Ishikawa, Phys. Rev. A42, 1142 (1990).
[8] H. M. Quiney, I. P. Grant, and S. Wilson, J. Phys. B23, L271 (1990).

[9] A. Rutkowski. J. Phys. **B19**, 3443 (1986); A. Rutkowski and W.H.E. Schwarz, Theoret. Chim. Acta **76**, 391 (1990).

[10] P. J. C. Aerts and W. C. Nieuwpoort, Chem. Phys. Lett. **113**, 165 (1985); D. Hegarty and P. J. C. Aerts. Phys. Scr. **36**, 432 (1987).

[11] K. G. Dyall, P. R. Taylor, K. Faegri Jr., and H. Partridge. J. Chem. Phys. **95**, 2583 (1991).

[12] Y. Ishikawa. H. Sekino, and R. C. Binning, Jr., Chem. Phys. Lett. **165**, 237 (1990).

[13] Y. Ishikawa, Can. J. Chem. (in press); Y. Ishikawa, Chem. Phys. Lett. **179**, 291 (1991).

[14] J. Sucher, in *Relativistic Effects in Atoms, Molecules, and Solids. Proceedings of the NATO Advanced Study Institute.* G. L. Malli, Ed. (Plenum, New York, 1983).

[15] M. H. Mittleman. Phys. Rev. **A24**, 1167 (1981).

[16] Y.-K. Kim, Phys. Rev. **154**, 17 (1967).

[17] Y. Ishikawa and H. M. Quiney. Intern. J. Quantum Chem. **S21**, 523 (1987); Y. Ishikawa, R. Baretty, and R. C. Binning Jr., Chem. Phys. Lett. **121**, 130 (1985).

[18] Y. Ishikawa, H. M. Quiney, and G. L. Malli, Phys. Rev. **A43**, 3270 (1991).

[19] S. Huzinaga and M. Klobukowski, J. Mol. Struct. Theochem. **167**, 1 (1988); S. Huzinaga. M. Klobukowski, and H. Tatewaki, Can. J. Chem. **63**, 1812 (1985).

[20] O. Matsuoka and S. Huzinaga, Chem. Phys. Lett. **140**, 567 (1987); S. Okada and O. Matsuoka. J. Chem. Phys. **91**, 4193 (1989).

[21] I. P. Grant, B. J. McKenzie, P. H. Norrington, D. F. Mayers, and N. C. Pyper, Comp. Phys. Commun. **21**, 207 (1980).

[22] W. R. Wadt, P. J. Hay, and L. R. Kahn, J. Chem. Phys. **68**, 1752 (1978); W. C. Ermler, Y.-S. Lee, K. S. Pitzer, and N. Winter, J. Chem. Phys. **69**, 976 (1978).

[23] J. Andzelm, S. Huzinaga, M. Klobukowski, and E. Radzio, Mol. Phys. **52**, 1495 (1984).

[24] M. Krauss and W. J. Stevens, Ann. Rev. Phys. Chem. **35**, 357 (1984).

Nonorthogonality and the MO Energy Level Patterns of Molecules Deduced Directly from Structural Formulas by the New VIF Method as Compared with Machine Computations*

OKTAY SINANOĞLU

Sterling Chemistry Laboratory, Yale University, P.O. Box 6666, New Haven, Connecticut 06511

Abstract

The MO energy level patterns of molecules deduced directly from the pictures of molecules (VIF method) are shown to implicitly include the overlap integrals between highly nonorthogonal AO's and to be invariant under crucial nonunitary transformations. Further, machine-computed MO levels are found to readily yield chemically interpretable information such as the nonbonding MO levels and the nature of the HOMO and LUMO once the proper invariant quantity found here is subtracted out from the numerical energies. The resulting EHT, Gaussian STO-3G, . . . type computed MO energy level patterns then show correspondence with the VIF-pictorially deduced level patterns obtained without point group symmetries. © 1992 John Wiley & Sons, Inc.

This article is a contribution to the bridging of the gap between the pictorial, electronic language of chemistry needed by practicing experimental or synthetic chemists and the numerical results obtained by machine computations.

Conceptual and necessarily pictorial theory of valency based more and more on the molecular orbital (MO) formulation teaches us to think in terms of bonding, nonbonding, and antibonding MO energy levels. Computations on the other hand yield a set of MO energy level values the lowest ones negative, a few of the highest ones being positive numbers. Can these numbers be readily interpreted and be put into correspondence with conceptual notions without going into a full, detailed analysis of MO coefficients and/or extensive use of point group symmetries as most molecules are not symmetrical anyway?

Computational methods starting with Extended Hückel Theory (EHT) [1] and going on up to Gaussian 90/92 [2] options RHF STO–3G and higher, fully include in the calculation of MO energy levels, the overlap integrals $S_{\mu\nu}$ between the valence shell atomic orbitals (AO) of different centers these being highly nonorthogonal.

The qualitative features of a molecule's MO energy levels pattern are given by three level pattern indices LPI $= \{ n_+, n_o, n_- \}$, the three integers being the numbers

---

of bonding (+), nonbonding (o), and antibonding (−) levels. It has been shown that [3] these integers already so useful for qualitative chemical reasoning are also fundamental invariants [4] when isomeric sets of molecules (and their MO hamiltonians h) are transformed into other isomeric molecules yielding thermic and kinetic reaction selection rules more general than any based on quantum numbers and point group symmetries. Such chemical transformations can be carried out pictorially [3] by simple-to-use pictorial rules applied to the VIF (valency interaction formula) pictures of molecules which look like amplified structural formulas (SF). While SF depicts the electron density (electron pair bonds, lone pairs) in the ground state of a molecule, the VIF depicts an effective one-electron MO hamiltonian, h. The VIF therefore yields more electronic information, such as HOMO–LUMO reactivity, than the SF. Further, SF has difficulty in dealing with nonclassical, nonoctet rule structures, while VIF applies equally well to any electron-deficient, organometallic, or unstable, transient species.

With the pictorial VIF rules one may also deduce the LPI directly from a picture of the molecule [3].

Nonorthogonality of AO's, the MO Hamiltonian, and the VIF

We start with the abstract, basis-frame independent MO equation.

$$(h - EI)|\psi\rangle = 0 \tag{1}$$

According to the principle of linear covariance [4], Eq. (1) can be written in a linearly covariant form which then looks the same in any orthonormal (O.N.) or nonorthonormal basis frame for the valence shell vector space V_n of dim $= n$. We use

$$I = |e^\mu\rangle\langle e_\mu| \tag{2}$$

and

$$\langle e^\mu|e_v\rangle = \delta^\mu_{.v} \tag{3}$$

with $\{|e_\mu\rangle\}$ a valency basis set for V_n, in general non-O.N. The I is inserted in several places in Eq. (1) to get the form

$$(h_{\mu v} - ES_{\mu v})c^v = 0 \tag{4}$$

covariant with respect to the most general group, $L(n)$, (linear group over V_n). The covariance principle used has been deduced and shown by this author [3,4] to be a major consequence of the *superposition principle*, the primary postulate of quantum mechanics.

Upper and lower indices balance out and are summed over 1 to n. Lower indices we take to indicate covariant components, upper ones contravariant.

$$h_{\mu v} = \langle e_\mu|h|e_v\rangle; \quad h_{\mu\mu} = \alpha_{\mu\mu}; \quad h_{\mu v} = \beta_{\mu v}; \quad (\mu \neq v) \tag{5}$$

$$S_{\mu v} = \langle e_\mu|e_v\rangle \tag{6}$$

The primary calculated (or semiempirical) quantities are taken to be the covariant ones. Eqs. (5) and (6). Indices are raised using the metric tensor

$$\Delta^{rr} = S^{rr} \tag{7}$$

where

$$\Delta^{rr}\Delta_{r\sigma} = \delta^{r}_{\sigma}$$

Thus in matrix form

$$\{\Delta_{r\rho}\} = \underline{S} \tag{8}$$

the usual overlap matrix, and

$$\{\Delta^{rr}\} = \underline{S}^{-1} \tag{9}$$

its inverse. In most molecular problems $\underline{S}$ is nonsingular ($|S| \neq 0$) except in some cases of far-UV spectroscopy interest where a "Δ-catastrophe" and its resolution were previously mentioned [5]. The

$$\{h_{\mu\nu}\} = \underline{h} \tag{10}$$

is the usual $\{\alpha_{\mu\mu}, \beta_{\mu\nu}\}$-Extended Hückel (EHT) matrix if non-O.N. AO's are the particular basis set chosen and the EHT approximations are used on h.

More generally h may be a closer approximation to the Hartree–Fock–Roothaan hamiltonian in which case α's and β's may include major pieces of electron–electron repulsions $J_{\mu\mu}$, $J_{\mu\nu}$ as in the Pariser–Parr–Pople method [6] for II-systems, and CNDO [7] more generally. Even pieces of the all-external correlations $\varepsilon_{\mu\mu}$, $\varepsilon_{\mu\nu}$ may be included as done using the many-electron theory (MET) of this writer [8].

By linear covariance [4], however, the same form of the Eq. (4) now applies to any other basis frame. For example in the MO-basis (necessarily O.N.), $h_{\mu\nu}$ becomes diagonal, as does $S_{\mu\nu} \rightarrow I_{\mu\nu} = I^{\mu\nu} = \delta^{\mu}_{\nu}$, the Kroenecher delta.

There are also newly discovered unusual non-O.N. basis sets in which $\{h_{\mu\nu}\}$ becomes the same matrix as the h of another molecule. These topics are treated in a previous set of articles [4] giving the foundations of chemical transformations theory and its VIF pictorial implementations [3].

Convenient starting points for MO calculations are $\{h_{\mu\nu}, S_{\mu\nu}\}$ taken in the non-O.N. valence shell AO's basis set (as in EHT, MNDO [9], RHF STO–3G).

The MO energy levels $\{E_i\}$ with $i \in \{1$ to $n\}$ come out very similar in any approximate method of calculation in the case of the lower negative eigenvalues, but differ widely in magnitude for the few highest and positive E_i. These levels are measured relative to the "total zero" reference, that of all electrons and nuclei separated out to infinity.

Given a certain basis set (such as that of EHT or of STO–3G), all other bases obtained by linear transformations $\{T\}$ on that (initially non-O.N.) set, leave the $(IPI)^h$ of h, Eq. (5), invariant. Thus the numbers $\{n^h_+, n^h_0, n^h_-\}$ are conserved since $T \subset L(n)$, the linear group, and h transforms adjointly

$$\underline{h}' = \underline{T}^+ \underline{h} \underline{T} \tag{10'}$$

as seen from $h'_{\mu\nu} = T_{\mu}^{\cdot\tau} T_{\nu}^{\cdot\rho} h_{\tau\rho}$ (covariant to covariant tensor transformation). The eigenvalues $\{ E_i \}$ themselves are of course not preserved unless the transformation is from an O.N. to another O.N. basis in which case $\underline{T}$ is unitary. In general $\underline{T}$ is nonunitary.

The conservation of the MO-level pattern of h (true with or without the consideration of $S_{\mu\nu}$ in Eq. (4), see below) with the $\{ E_i \}$ relative to the "total zero," and this (LPI)^h are not however particularly useful for qualitative chemical reasoning on the behavior of that molecule. We need to shift the zero of the energy and look at the E_i relative to separated atoms (and their free atom AO's), to assess the bonding, nonbonding, . . . quality of each MO level. To do this, *one* of the $\alpha_{\mu\mu}$'s is substracted out from the diagonal elements of $\{ h_{\mu\nu} \}$. A convenient one is that of a most frequently occurring suitable AO, for example, that of carbon for the pyridine pi-system (for sigma systems see Ref. [3]). As alternatives, one may substract α, the average of all the $\alpha_{\mu\mu}$ in h. Taking the substracted one as the standard (std) α, one has from the abstract form, Eq. (1),

$$\bar{h} = h - \alpha I$$

and

$$(\bar{h} - \bar{E}I)|\Psi\rangle = 0$$

with

$$\bar{E} = E - \alpha \tag{11}$$

This $\bar{h}$ was used initially in Hückel's pi-HMO with the large overlaps $S_{\mu\nu}$ neglected, but here the α-substraction is done now on the abstract form for any molecule sigma and pi, and as we will see below, without neglecting the overlaps.

Starting for the general case, with the abstract Eq. (11), we now apply the *non-O.N. unity trick*, Eq. (2) for any basis frame and get

$$[(\bar{h})_{\mu\nu} - \bar{E}S_{\mu\nu}]c^\nu = 0 \tag{12}$$

where however $\bar{h} = h - \alpha I$ has become

$$(\bar{h})_{\mu\nu} = h_{\mu\nu} - \alpha S_{\mu\nu} \tag{13}$$

The std non-O.N. AO basis set is such that each AO is normalized to unity, those on the same atom are orthogonal, on different centers they are not. Thus

$$(\bar{h})_{\mu\mu} = \alpha_{\mu\mu} - \alpha \tag{14}$$

$$(\bar{h})_{\mu\nu} = \beta_{\mu\nu} - \alpha S_{\mu\nu}; \quad (\mu \neq \nu) \tag{15}$$

If all $\alpha_{\mu\mu}$'s are nearly equal to α (std α), then

$$\bar{h}_{\mu\mu} \approx 0 \tag{16}$$

but if only some of the $\alpha_{\mu\mu}$'s $= \alpha$ (std), there will arise some nonzero $\bar{h}_{\mu\mu}$'s.

The original VIF's were drawn (even for sigma systems), based seemingly on

$$[(\bar{h})^{a}_{\mu\mu} - \bar{E}^{a}\delta_{\mu\nu}]c^{a} = 0 \tag{17}$$

where $(\bar{h})^{a}_{\mu\mu} = \alpha_{\mu\mu} - \alpha$

but $(\bar{h})^{a}_{\mu\nu} = \beta_{\mu\nu}$ $\}$ (18)

$(\mu \neq \nu)$

To make it dimensionless $\{(\bar{h})^{a}_{\mu\nu}\}$ is divided by a std β. Then we have the correspondence

$$\{(\bar{h}^{a})_{\mu\nu}\} \sim \text{VIF}$$

Thus, for example, for an almost linear H_3

VIF:
(19)
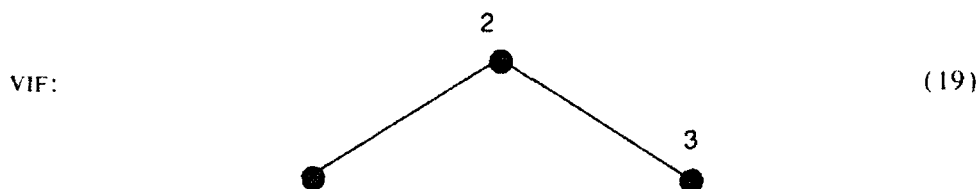
where each dot = a *valency point*, VP, and each line is a symmetrized dyad $|e_\mu\rangle\langle e_\iota|$ with the coefficient giving the line strength $\kappa_{\mu\nu} = \beta_{\mu\nu}/\beta$. All $(\bar{h}_{\mu\mu})^{a} = 0$, so there are no AO (i.e., VP) self-energy loops $|e_\mu\rangle\langle e_\mu|$ in this VIF.

In the initial VIF [3,4] papers it was stated that nevertheless VIF includes overlaps due to the principle of linear covariance, but proof was not given which is given now in several steps.

Step 1. The VIF is actually drawn for $(\bar{h})_{\mu\nu}$ of Eqs. (13–15), where, for example, for the H_3 species $(\alpha_{\mu\mu} - \alpha)/\beta = 0$, and line strengths are $\kappa_{\mu\nu} = (\beta_{\mu\nu} - \alpha S_{\mu\nu})/\bar{\beta}$ with the std $\bar{\beta} = \beta - \alpha S$ using a std overlap value S. In the starting VIF's nonnearest neighbor (non-n.n.) lines are neglected as in Eq. (19). This neglect is not essential. The effect on the LPI of the inclusion of further interactions can also be examined with the VIF-rules. For example if we take the n.n. $\overline{12}$ and $\overline{23}$ as equal and their strengths as β, then their $\kappa = 1$ (if no κ is written on a line in the VIF that line strength is implied to be $\kappa = 1$), but $\overline{13}$ line will have a weaker strength $\kappa < 1$ as in

VIF:
(19')
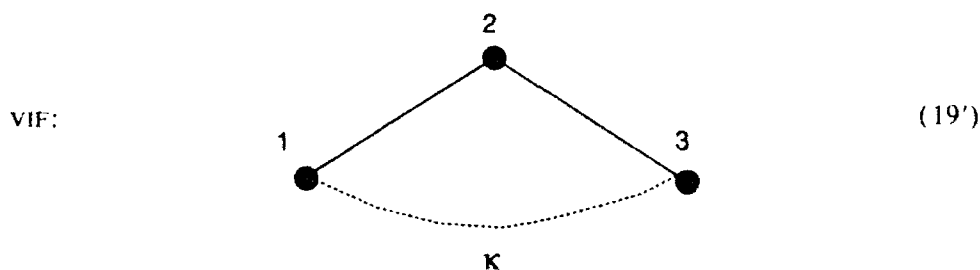
[This change would also allow one to examine how the LPI of linear H₃ evolves into that of an equilateral triangular H₃ if one were to vary κ continuously and apply the VIF-rules].

The VIF's drawn for $\bar{h}_{\mu\iota}$ and $(\bar{h})_{\mu\iota}^{o}$ are the same and yield the same LPI. This constitutes the first step of the proof that inclusion of overlaps does not affect the VIF theory going from Eq. (18) to Eqs. (14) and (15).

Step 2. The MO levels $\{\bar{E}_i\}$ of Eq. (12) with overlaps in the second term, and the eigenvalues $\{\bar{E}_i^{o}\}$ of Eq. (17) are different. Even though Step 1 above showed the *structural covariance* under $L(n)$, of $(\bar{h})_{\mu\iota}$ $\underline{se}(\bar{h})_{\mu\iota}^{o}$ so that when simply diagonalized as individual matrices they should yield the same LPI of their diagonalized elements, the presence of $S_{\mu\iota}$ rather than $\delta_{\mu\iota}$ in the full equations Eq. (12), need be considered.

We show now that the LPI from h alone remains the same when the MO levels are to be calculated from $\underline{h} - E\underline{S}$.

The overlap matrix occurring explicitly in Eq. (12') below can be eliminated in a number of ways.

$$(\bar{\underline{h}} - \bar{E}\underline{S})\underline{c}^v = 0$$

where

$$\underline{c}^v \equiv \{c^v\}$$

while

$$\underline{c}^. = \{c_v\}$$

and

$$c^v = \Delta^{vp}c_p$$

or in matrix form

$$\underline{c}^. = \underline{S}^{-1}\underline{c}. \tag{12'}$$

The $\underline{S}$ matrix is turned into the unit matrix $\underline{I}$ by any number of transformations from the non-O.N. basis to *some* O.N. one. Any such transformation is nonunitary.

(a) The method used computationally in the EHT FORTRAN programs is to find the transformation matrix corresponding to the act of Schmidt-orthogonalization procedure (this matrix *which is not unitary* may be derived in the general case by writing, then solving recursion relations).

(b) Another way is Löwdin's [11] "square root" $S^{-1/2}$ device which yields the OAO (symmetrically orthogonalized AO's) basis. Equations (20) show this method.

Multiply Eq. (12') from the left with $\underline{S}^{-1/2}$. Inserting $S^{-1/2}S^{+1/2}$ after the last bracket, one gets

$$(\underline{S}^{-1/2}\bar{\underline{h}}\underline{S}^{-1/2} - \bar{E}\underline{S}^{-1/2}\underline{S}\underline{S}^{-1/2})\underline{S}^{+1/2}\underline{c}^. = 0 \ .$$

$$(\bar{\underline{h}} - \bar{E}\underline{I})\underline{c} = 0$$

where

$$\varsigma = S^{-1} \varsigma' \quad S^{-1} \varsigma \tag{20}$$

(c) Still another way is: first diagonalize S obtaining its eigenvalues $\{s_i\}$ and its eigenvector columns which make up the diagonalizing unitary transform U.

$$S_{Diag.} = U^{\dagger} S U \tag{21}$$

where $U^{\dagger} = U^{-1}$ and

$$S_{Diag.} = \begin{pmatrix} s_1 & & & \\ & s_2 & & 0 \\ & & \ddots & \\ 0 & & & s_n \end{pmatrix}$$

Next apply the nonunitary transform

$$B = \begin{pmatrix} s_1^{-1/2} & & & 0 \\ & s_2^{-1/2} & & \\ & & \ddots & \\ 0 & & & s_n^{-1/2} \end{pmatrix}$$

yielding

$$I = B^{\dagger} U^{\dagger} S U B \tag{21m}$$

The full nonunitary transform is

$$I = \chi^{\dagger} S \chi \tag{21n}$$

with $\chi = U B$.

In all of the methods above (and other possible ones). the nonunitary χ used to transform the symmetric S, act as an *adjoint transformation*. Eq. (21n). The same χ is now applied to the h, also self-adjoint. again in an *adjoint transformation* yielding another self-adioint matrix h, nondiagonal.

$$\bar{h} = \chi^{\dagger} h \chi \tag{21k}$$

so the eigenvalue equation becomes

$$(\bar{h} - \bar{E}_i I)\varsigma = 0 \tag{21p}$$

with $\varsigma = \chi^{-1} \varsigma'$.

All the χ-transforms in methods (a) to (c) are nonsingular and they are elements of the general linear group $L(n)$. Thus they preserve the MO-level pattern indices. LPI of h. that is.

$$\bar{h} \stackrel{lpi}{=} h. \tag{21q}$$

In this case (unlike in Step 1). the $\{\bar{E}_i\}$ MO levels are also numerically the same whether calculated from Eq. (21p) or from Eq. (12') with S explicit as in EHT.

Note however that even in OAO basis Eqs. (20), (21), it is the original non-O.N. basis α that is subtracted out from the $\{E_i\}$ to get the chemically meaningful $\{\bar{E}_i\}$ relative to separated atoms.

$$\bar{\underline{h}} = \underline{h}^{OAO} - \alpha\underline{1}$$

and

$$\bar{E}_i = E_i - \alpha. \tag{22}$$

One would have thought on the basis of the original OAO justification [11,12] of the pi-HMO theory [10] vis-a-vis dropping of overlaps, that α_{OAO} would be subtracted from the E_i and the h^{OAO}. As we see this is not true. The starting non-O.N. AO basis' α is taken out. Just as well, since α_{OAO} values greatly vary for the same atom in different locations (even in H_3) and they are difficult to calculate.

The proof for the invariance of the VIF method vis-a-vis overlaps is still not complete. The two pictorial VIF rules applied to the initial VIF in any combination and succession amount to generating various basis set transformations $\underline{T}$ on the same molecule *or* to transforming molecules into other molecules in the same equivalence class with all such $\underline{T} \in L(n)$. As most of these $\underline{T}$ are nonunitary, at each step of the VIF manipulations new overlap integrals will arise in the transformed versions of Eq. (12). That the LPI remains invariant under all such nonunitary transformations is proved in Step 3.

Step 3. Let us demonstrate the problem with a simple example. Take a square configuration of H_4 or the isomorphic system, the pi-system of cyclobutadiene. Divided out by the single $\beta_{\mu\nu} = \beta$, and the single $\alpha = \alpha_{\mu\mu}$ taken out

$$\underline{h}^o = \underline{h} - \alpha\underline{1} \sim \text{VIF}^o \tag{23}$$
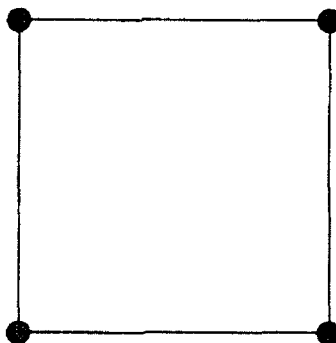
VIF^o

where there are no loops at each VP as α has been taken out making the reference zero of energy at $\alpha \rightarrow$ ref. zero.

The line strengths are $\beta_{\mu\nu}/\beta = 1$. However Step 1 showed that the VIF and the LPI that will result are the same with $\beta_{\mu\nu} \rightarrow (\beta_{\mu\nu} - \alpha S_{\mu\nu}) = (\beta - \alpha S) = \bar{\beta}$; $\kappa = \bar{\beta}_{\mu\nu}/\bar{\beta} = 1$ and VIF$^o \sim$ VIF ($\sim$ isomorphic).

The VIF is "reduced" by the VIF-rules to get iso-LPI structures as well as the LPI itself (for the details cf. Ref. [4]) as follows:

$$(24)$$

$$= \left\{ \begin{array}{l} n_+ = n_- = 1 \\ n_0 = 2 \end{array} \right\}$$

with the MO level pattern:

$$(24')$$
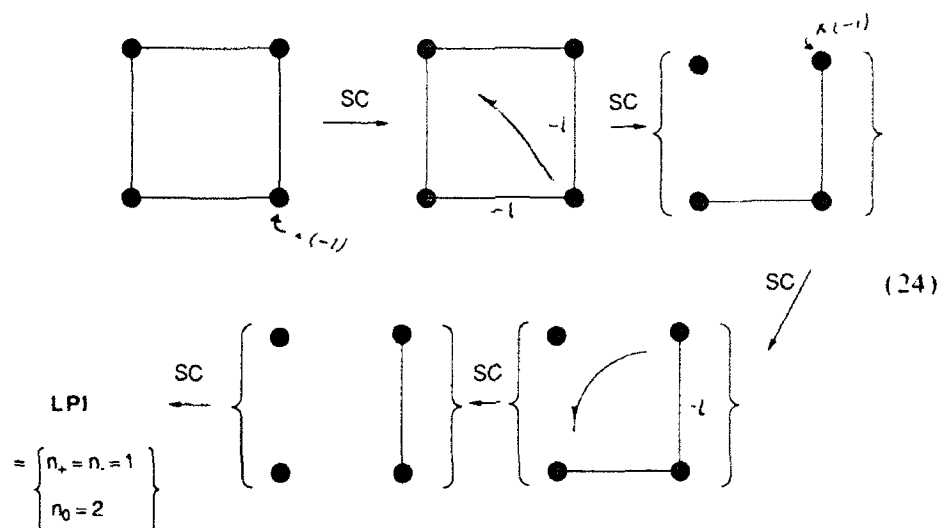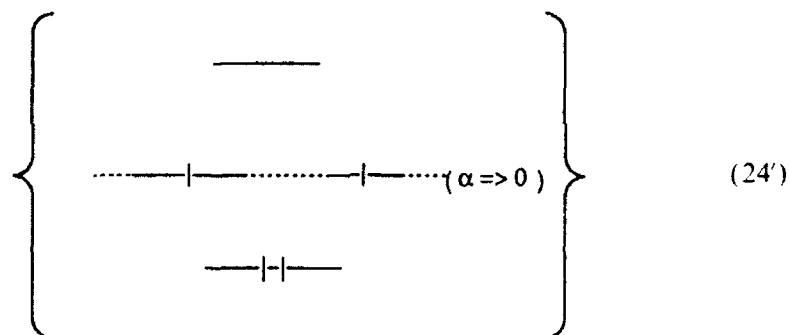
The two nonbonding levels are found. Assigning the four electrons for the neutral species, we see the antiaromaticity for the cyclobutadiene pi-case, or the unstable nature of a square H_4 (or the high activation barrier in a reaction like $H_2 + D_2 \rightarrow$ 2HD with a square activated complex). (In this example the LPI could also be obtained of course, with the Frost–Musulin mnemonic, cf, e.g., Ref. [10], which is applicable only to single rings. VIF however gives such results for any polycyclics, branched, bridged, side-chained hydrocarbons [13]).

Principle of linear covariance allows us to interpret each step in Eq. (24) either in the MO-basis (thus MO LPI is read off directly from the last picture (No. of free dots = no. of nonbonding overall MO's), or in a localized orbital LO basis. In the latter reading of Eq. (24), for the H_4 case, ones sees the reactions

$$H_4 \overset{sc}{\rightarrow} H_3 \text{ (linear)} + H \overset{sc}{\rightarrow} H_2 + H + H \tag{25}$$
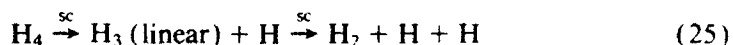
to be "allowed" having the same LPI's and in the same L-equivalence class (thereby called *structurally covariant* (sc) [4]).

Each picture in Eq. (24) corresponds to a $\{ \bar{h}_{\mu\nu} \}$ written in a new basis-set frame,

transformations from one to the next in general being nonunitary thereby generating new overlap matrices in the full equation $(\bar{h}_{\mu\nu} - \bar{E}S_{\mu\nu})c^i = 0$.

During the reactions, Eq. (25), MO composite levels $\{\bar{E}_i\}$ change, but the level patterns, LPI remain the same. This is proved as

$$\bar{h}_{\mu\nu} \rightarrow \bar{h}_{\mu'\nu'} \rightarrow \bar{h}_{\mu''\nu''} \rightarrow \cdots \tag{26}$$

Each basis and hamiltonian transformation occurs by an $T \in L(n)$ and an adjoint transform, for example,

$$\bar{h}' = T^{\dagger}\bar{h}T \tag{27}$$

in each step of Eq. (24). By the fundamental theorem [3,4], these h's all have the same LPI. Further for each step, as new overlaps arise, the nonunitary transform χ shows the S term does not affect the LPI as in Eqs. (20, 21).

$$(\bar{h}' - \bar{E}S') \rightarrow (\chi^{+}\bar{h}'\chi - \bar{E}I)$$

$$\tilde{h}' \overset{sc}{=} \bar{h}' \overset{sc}{=} \bar{h} \overset{sc}{=} \bar{h}'' \tag{28}$$

(q.e.d.)

This completes the three-steps proof and we state the proved theorem.

Theorem on the Conservation of MO Energy Level Patterns Under the Effect of Overlaps

Theorem

The VIF picture of a molecule (or reacting isomeric assembly) drawn without regard to the large non-O.N. AO basis overlaps yields the same MO level pattern, LPI = $\{n_+, n_o, n_-\}$, numbers of bonding, nonbonding, and antibonding MO levels (relative to a chosen free atom AO self-energy) as if the overlaps were included in a full $(h - ES)$ calculation. The chemical VIF-rules transformations or the VIF pictorial changes in deducing LPI, while they imply nonunitary transformations (among non-O.N. bases) leading to new overlaps still retain the same LPI. (Proof was given above.)

Remark. The simplest and qualitatively most useful VIF's for blackboard type chemical deductions are drawn with nearest neighbor or proximity h elements only (with the corresponding overlaps in S, implied). Next nearest neighbor terms in h or any other terms of h may be drawn in more elaborate VIF's to explore the effects on the LPI, if any, of such refinements. A computer EHT calculation (or, e.g., STO-3G) normally includes all $\beta_{\mu\nu}$'s and $S_{\mu\nu}$'s. To compare such an EHT $\{E_i\}$ pattern after subtracting out the chosen α from each $E_i \rightarrow \bar{E}_i = E_i - \alpha$, with the LPI predicted by a certain VIF, the $S_{\mu\nu}(\beta_{\mu\nu})$ terms omitted in that VIF can be deleted in the EHT calculation using the input option L2 = .TRUE. in the program [1].

Some Numerical Examples

(1) Allyl pi-system or H_3(linear)

$$\text{(29)}$$

$$\text{LPI} = \{\ n_+ = n_- = 1;\ n_c = 1\ \}$$
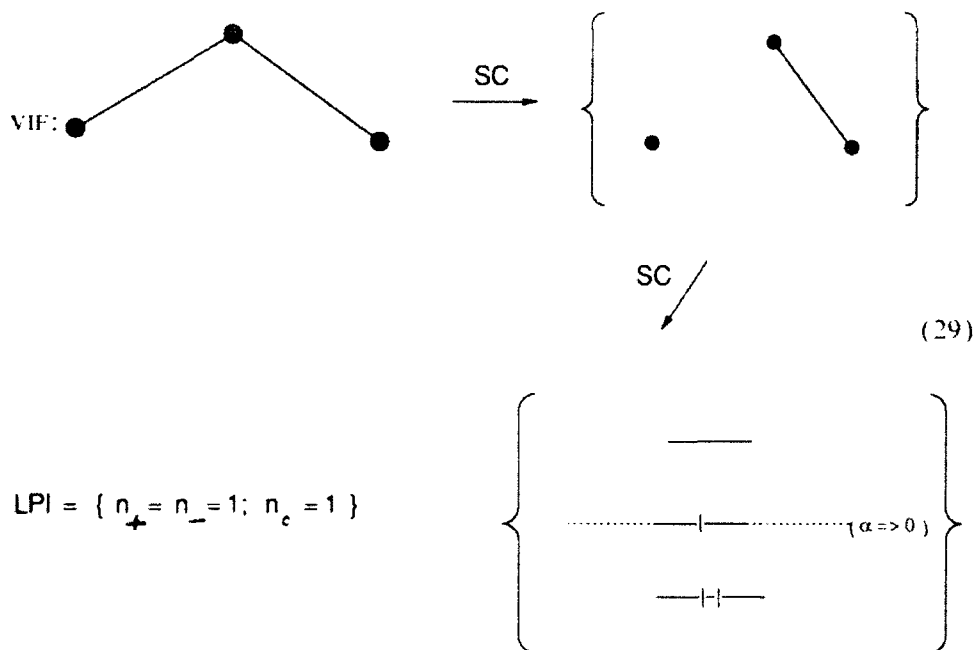
This n.n. VIF omits the overlap between atoms 1 and 3. It shows clearly the presence of one nonbonding level. That level is invariant if the $\overline{12}$ or $\overline{13}$ or both are changed by any amount as seen with the VIF rule 1 (κ-rule):

$$\text{(30)}$$

(same LPI)
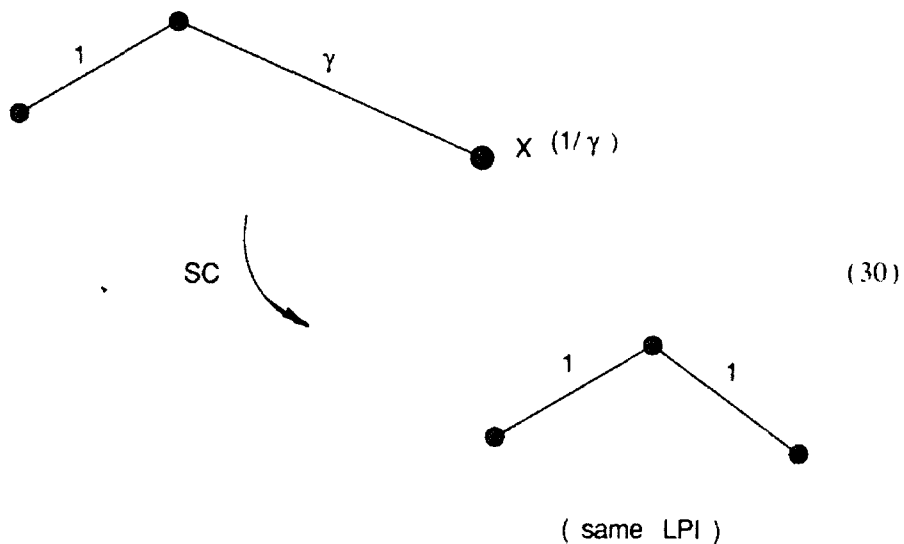
Thus the $H_2 + D \rightarrow H + HD$ reaction along a collinear path is LPI preserving, hence "allowed" with a small activation barrier ($H_3^\ddagger$ linear or nearly so) indicated relative to a β ($\approx (-1/2)D_e$ of H_2).

TABLE I. Comparison of MO energy level patterns by the pictorial VIF with those from numerical EHT[a] and EHTD[b] calculations. Linear H_3 complex H1 — H2 — H3 with $R(12) = R(23) = 0.85$ Å; α_H = -13.6 eV. All E_i in electron volts (eV).

i = MO level # (highest energy to lowest)	EHT[a] $\bar{E}_i = E_i - \alpha_H$	EHTD[b] $\bar{E}_i^D = E_i^D - \alpha_H$	VIF direct level pattern, LPI[c]
(1)	+25.72	+39.72	$n = 1$
(2)	+2.07	0.00	$n_o = 1$
(3)	-4.79	-4.52	$n_- = 1$

[a] The $E(i)$ MO levels from full EHT calculation (Ref. [1]). The $\alpha_H = -13.6$ is the invariant-subtraction yielding $\bar{E}_i$.

[b] The $E^D(i)$ MO levels from EHTD, that is, EHT with non-n.n. overlaps S_{13} deleted in the input. The $(E_i^D - \alpha_h) = \bar{E}_i^D$ level pattern coincides with the pictorial VIF result.[c]

[c] Pictorially deduced [Eq. (29)] level pattern indices LPI = $\{n_+, n_o, n_-\}$, the *structural covariant* invariants, also #'s of bonding (+), nonbonding (o), and antibonding ($-$) MO's which agree with numerical calculation after the proper (covariant) subtraction.

A complete VIF, VIF_I includes the $\overline{13}$ overlap (or $\bar{\beta}_{13}$) line:

$$VIF_I: \tag{31}$$
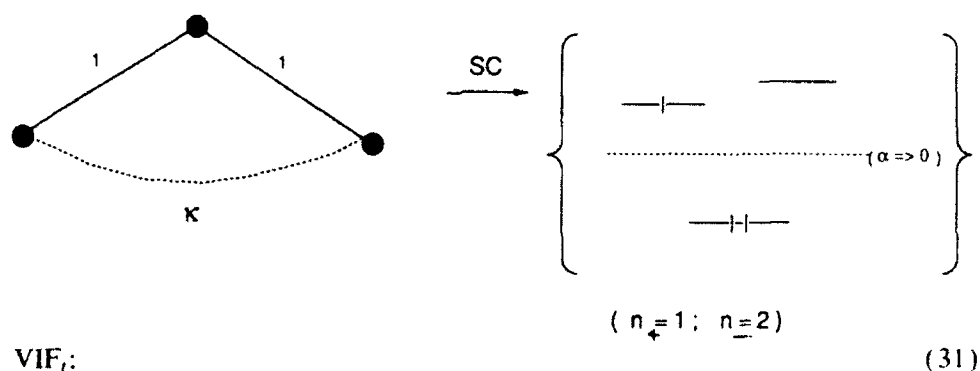
The nonbonding MO level is expected to move up a little (dependent on magnitude of $\kappa < 1$).

The same picture shows what happens when linear H_3 is bent into a triangle. The nonbonding HOMO moves up becoming slightly antibonding.

Tables I and II show two EHT calculations, for linear H_3, one with all overlaps, another with $\overline{13}$ overlap deleted (EHTD). The $\alpha = -13.6$ eV substracted E_i shows the same LPI's as the corresponding VIF's.

(2) Cyclobutadiene pi-system or square H_4.

VIF :
(n. n.)

(cf. Eq. (24))

and

(32)

VIF$_f$:

LPI$_f$ = { n_+ = 1 ; n_- = 3 ; n_0 = 0 }
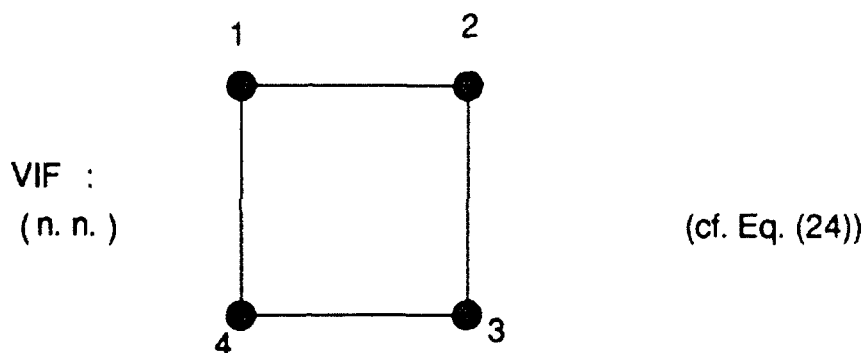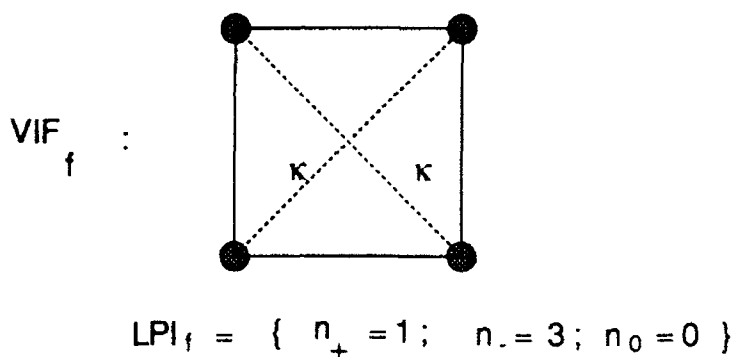
With the weaker ($\kappa < 1$) overlap (and $\bar{\beta}_{\mu\nu}$) lines $\overline{13}$ and $\overline{24}$ included, the LPI changes from the n.n. only, that is, square, such that n_0 = 2 nonbonding levels become slightly antibonding.

The same happens if the square H$_4$ is distorted to become slightly tetrahedral (squeeze $\overline{24}$, lift up 3 out of plane). [One caution, however: the bonding level in the quantitative sense, could go considerably lower affecting stability in the opposite way of the HOMO].

Table III shows the EHT computations for each of the two VIF's and the E_i's with $\alpha = -13.6$ eV removed. The $\{E_i\}$ level patterns coincide with those of the pictorial VIF deductions.

These examples further demonstrate how VIF implicitly takes into account the overlaps in ($h - ES$).

TABLE II. MO level patterns obtained by the pictorial VIF rules compared with numerical EHT/EHTD calculations. Along linear H_3 reaction surface H1 — H2 — H3 at $R(\overline{12}) = 0.81$ Å and $R(\overline{23}) = 1.27$ Å (i.e., along $H_2 + H$). The $\alpha_H = -13.6$ eV. (All energies in electron volts).

i = MO level # (highest energy to lowest)	EHT^a $\bar{E}_i = E_i = \alpha_H$	EHTD^b $\bar{E}_i^D = E_i^D - \alpha_H$	VIF^c pictorially deduced LPI
(1)	+16.33	+18.85	$n_- = 1$
(2)	+0.78	0.00	$n_o = 1$
(3)	-4.15	-4.01	$n_+ = 1$

^{a} The $E(i)$ MO levels from full EHT calculation (Ref. [1]). The $\alpha_H = -13.6$ is the invariant-subtraction yielding E_i.

^{b} The $E^D(i)$ MO levels from EHTD, that is, EHT with non-n.n. overlaps S_{ij} deleteted in the input. The $(E_i^D - \alpha_H) = E_i^D$ level pattern coincides with the pictorial VIF result.^{c}

^{c} Pictorially deduced [Eq. (29)] level pattern indices LPI = $\{n_+, n_o, n_-\}$, the *structural covariant* invariants, also #'s of bonding (+), nonbonding (o), and antibonding (−) MO's which agree with numerical calculation after the proper (covariant) subtraction.

^{d} At $R(\overline{23}) = 1.5 R(\overline{12})$;VIF relative line strength $(\kappa\overline{23}) = S_{23}/S_{12} = 0.574$ [cf. Eq. (30) showing $\kappa = \gamma$].

Conclusion

This article has shown how the MO energy levels obtained from computer MO theory computations (such as EHT, but applicable with care also to MNDO, and *ab initio* e.g., STO-3G) may be converted to MO energy level patterns from which important qualitative deductions based on bonding, nonbonding, and antibonding

TABLE III. MO level patterns for a square H_4 complex with $R = 1.00$ Å. EHT^a and EHTD^b calculation (the latter with only the non-n.n. overlaps deleted) after the invariant-subtraction of $\alpha_H = -13.6$ eV coincide with the pictorially deduced VIF level pattern. LPI = $\{n_+, n_o, n_-\}$ which implicitly includes the overlaps. All energies in eV.

i = MO level # (highest energy to lowest)	EHT^a $\bar{E}_i = E_i - \alpha_H$	EHTD^b $\bar{E}_i^D = E_i^D - \alpha_H$	VIF^c pictorially deduced LPI
(1)	+21.1	+153.2	$n_+ = 1$
(2)	+3.65	0.0	$n_o = 2$
(3)	+3.65	0.0	
(4)	-5.57	-4.94	$n_- = 1$

^{a} EHT calcuation with PROGRAM FORTICON8 (Ref. [1]).

^{b} EHTD calculation with only the $S(\overline{13})$ and $S(\overline{14})$ overlaps deleted as nonnearest neighbors. The α_H is invariant-subtracted.

^{c} VIF pictorially deduces [Eq. (24)] the MO level pattern, numbers of bonding, nonbonding, antibonding levels relative to $1s_H$ energy, α_H.

MO level types become possible. Correspondence with the MO level patterns deduced directly from the VIF pictures drawn from structural formulas or ORTEP diagrams using the pictorial "blackboard" type VIF-rules is established, this article giving the proof that, for one thing, VIF implicitly includes overlaps. VIF-method has a considerable advantage in that many reactions, distortion, rearrangement pathways can be readily and visually examined. Many seemingly different molecules also become relatable to each other getting classified into fundamental classes, each class with a given MO level pattern. In addition, now VIF selected molecules or paths maybe made more quantitative, relationship to computation having been demonstrated. High-level machine computations may be carried out once certain reaction paths or species are readily chosen on the basis of pictorial VIF-rules.

Bibliography

[1] R. Hoffmann, J. Chem. Phys. **39**, 1397 (1963); (Program, FORTICON8, QCPE 344).

[2] W. J. Hehre, L. Radom, P. V. R. Schleyer, and J. A. Pople, *Ab Initio Molecular Orbital Theory* (Wiley, New York, 1986); Gaussian 92, M. J. Frisch et al. (Gaussian, Inc., Pittsburgh, PA, 1992).

[3] O. Sinanoglu, Theo. Chim. Acta **68**, 251 (1985); Chem. Phys. Lett. **103**, 315 (1984); earlier refs. therein and further lit. refs. in [13].

[4] O. Sinanoglu, Theo. Chim. Acta **65**, 243, 233, 249, 255, and 267 (1984).

[5] O. Sinanoglu, in *Chem. Spectr. and Photochem. in the Vacuum Ultraviolet*, C. Sandorfy, P. J. Ausloos, and M. Robin. Eds. (Dordrecht, D. Reidel, 1974).

[6] R. Pariser and R. G. Parr, J. Chem. Phys. **21**, 466, 767 (1953).

[7] J. A. Pople, D. P. Santry, and G. A. Segai, J. Chem. Phys. **43**, S129 (1965).

[8] (a) O. Sinanoglu, Adv. Chem. Phys. **XIV**, 237 (1969); (b) O. Sinanoglu and M. K. Orloff, in *Modern Quantum Chemistry*. Vol. I. O. Sinanoglu, Ed. (Academic Press, New York, 1965), p. 221.

[9] M. J. S. Dewar and W. Thiel, J. Am. Chem. Soc. **99**, 4899 (1977); (Program MNDO, QCPE 353).

[10] A. Streitweiser, Jr., *Molecular Orbital Theory for Organic Chemists* (Wiley, New York, 1961).

[11] P. O. Löwdin, J. Chem. Phys. **18**, 365 (1950).

[12] R. G. Parr, J. Chem. Phys. **33**, 1184 (1960).

[13] O. Sinanoglu, Tetrahedron Letts. **29**, 889 (1988); Int. J. Quantum Chem. S22, 143 (1988); J. Math. Chem. **2**, 117–136 (1988); *ibid.* **2**, 137–154 (1988).

Energy Levels for a Quartic Oscillator Using Algebraic Techniques

JOSÉ RÉCAMIER A.

Laboratorio de Cuernavaca, Instituto de Física, Universidad Nacional Autónoma de México, Apartado Postal 139-B, 62191 Cuernavaca, Morelos, México

ROCÍO JÁUREGUI R.

Instituto de Física, Universidad Nacional Autónoma de México, Apartado Postal 20364, 01000, México D. F., México

Abstract

In this work use is made of algebraic techniques developed for the evaluation of Vibration–Translation energy transfer in atom–diatom collisions to obtain the energy eigenvalues of the one-dimensional quartic oscillator. We have found that even our zero order approximation results are very close to the exact ones and when second-order perturbation theory is used, they improve even for high values of the anharmonicity parameter. © 1992 John Wiley & Sons, Inc.

Introduction

The one-dimensional harmonic oscillator potential has been used extensively in nuclear physics, high-energy physics, solid-state physics, and in atomic and molecular physics [1]. Among this model's many favorable characteristics, is that it is a rather simple model and allows testing of different levels of approximations against exact results. On the other hand, the evaluation of accurate energy levels of a quantum mechanical anharmonic oscillator has received renewed interest since it can be seen as a field theory in one dimension and it has become the testing ground for new methods in quantum field theory [2]. Different techniques have been applied to that end, optimized variational method [3], variational and coupled cluster calculations [4], and matrix diagonalization techniques [5] to name a few. Rayleigh-Schrödinger perturbation theory has proved to give good results when the nature of the unperturbed Hamiltonian is changed to that of a squared harmonic oscillator Hamiltonian with an adjustable frequency [6].

In atomic and molecular physics, in those cases where heteronuclear diatomics are involved, the harmonic oscillator model has severe limitations since the presence of anharmonicities cannot be included, nor can one study rearrangement collisions because the potential supports an infinite number of vibrational bound states. For homonuclear diatomics, when the collision energy is large compared with the energy level spacing of the vibrational states of the molecule, anharmonic terms play an important role, this is also the case for heteronuclear diatomics where the anharmonic terms are important even for low-lying transitions and low collision energies. Some time ago, a study of the 0 → 1 vibrational transition in anharmonic oscillators

was made, including quadratic and cubic terms in the potential function [7], more recently, the one-dimensional anharmonic oscillator including quadratic, cubic, and quartic terms in the potential function was used for the evaluation of vibrational transition probabilities in collisions between an atom and a diatomic molecule [8,9]. The anharmonicity parameters were fitted to adjust a Morse oscillator. The results obtained with this model could be compared favorably with exact quantum results [10] in a large energy range and for several transitions.

In this work, we evaluate the energy spectra of a quartic oscillator using an extension of the algebraic method developed for the study of TV energy transfer. We apply a sequence of Bogoliubov transformations to the Hamiltonian in order to obtain a set of transformed basis functions such that, after each iteration, they contain information from the quartic part of the potential in the previous iteration. In the next section we describe the method, then we obtain the energy eigenvalues for different anharmonicity constants λ within two simple approximations. The first consists in the evaluation of the eigenenergies for the transformed diagonal Hamiltonian and the second, in the use of second-order perturbation theory to treat that part of the transformed Hamiltonian which is not diagonal in the transformed basis. We compare our approximations with exact numerical results [4,13] and we also show the behavior of the coefficients of the Hamiltonian as a function of the iteration number.

Theory

Consider the one-dimensional anharmonic oscillator Hamiltonian

$$\mathcal{H} = \frac{1}{2} p^2 + \frac{1}{2} x^2 + \lambda x^4 , \tag{1}$$

now we express the displacement operator x in terms of boson creation and anhilation operators a, a^+

$$x = \frac{1}{\sqrt{2}} (a + a^+) , \tag{2}$$

then we get

$$\mathcal{H} = \mathcal{H}_{ho}$$

$$+ \frac{\lambda}{4} (a^4 + 4a^+ a^3 + 6a^2 + 6a^{+2} a^2 + 12a^+ a + 6a^{+2} + 4a^{+3} a + a^{+4} + 3) , \tag{3}$$

with $\mathcal{H}_{ho} = (a^+ a + 1/2)$ and we have written the Hamiltonian in normal order. Now we decompose the Hamiltonian as the sum of two parts.

$$\mathcal{H} = \mathcal{H}_0^{(1)} + \mathcal{H}_1^{(1)} \tag{4}$$

where

$$\mathcal{H}_0^{(1)} = \mathcal{H}_{h_0} + \frac{\lambda}{4}(6a^2 + 12a^+a + 6a^{+2} + 3) = \sum_{0 \cdot i + j \cdot 2} G_{ij}a^{+i}a^j \qquad (5)$$

forms a closed set under the operation of commutation. and $\mathcal{H}_1^{(1)} = \mathcal{H} - \mathcal{H}_0^{(1)}$.

The Hamiltonian $\mathcal{H}_0^{(1)}$ is a bilinear form in the operators $a.a^+$, so it is convenient to apply a generalized Bogoliubov transformation to obtain a new set of operators $a^{(1)}$, $a^{(1)^*}$ such that the Hamiltonian $\mathcal{H}_0^{(1)}$ is diagonal in the new basis [8,9]. The transformation is canonical and thus must preserve the commutation relations between the boson operators. Consequently, we get the condition that the determinant of the transformation must be equal to one. The required transformation has the form [11] ($i = 0$ for the first time we apply the transformation)

$$a^{(i+1)} = t_1^{(i)}a^{(i)} + t_2^{(i)}a^{(i)^*} \qquad (6)$$

$$a^{(i+1)^*} = t_2^{(i)}a^{(i)} + t_1^{(i)}a^{(i)^*} \qquad (7)$$

and the transformation coefficients are given by:

$$t_1^{(1)} = \left(1 + \frac{G_{02}^2}{G_{00} - G_{00}^{(1)}}\right)^{1/2} \qquad (8)$$

$$t_2^{(1)} = \frac{t_1^{(1)}G_{02}^2}{G_{00} - G_{00}^{(1)}}, \qquad (9)$$

$$G_{00}^{(1)} = \frac{1}{2}\left(-G_{11} + 2G_{00} + \sqrt{G_{11}^2 - 4G_{02}^2}\right). \qquad (10)$$

$$G_{11}^{(1)} - G_{00}^{(1)} = \frac{1}{2}\left(G_{11} - 2G_{00} + \sqrt{G_{11}^2 - 4G_{02}^2}\right). \qquad (11)$$

and the transformed Hamiltonian has been expressed as

$$\mathcal{H}_0^{(1)'} = G_{11}^{(1)}a^{(1)^+}a^{(1)} + G_{00}^{(1)}. \qquad (12)$$

When we apply the transformation to $\mathcal{H}_1^{(1)}$, we get a new Hamiltonian which contains the same set of operators as the original one with coefficients dependent upon the $t_j^{(i)}$. The Hamiltonian we obtain after k transformations has the form

$$\mathcal{H}^{(k)} = \sum_{0 \cdot i + j \cdot 4} G_{ij}^{(k)}a^{(k)^+}a^{(k)j}. \qquad (13)$$

and, since it is hermitean we have the restriction $G_{ij}^{(k)*} = G_{ji}^{(k)}$. In the case of a quartic oscillator, the coefficients $G_{ij}^{(k)}$ are real and we have the condition $G_{ij}^{(k)} = G_{ji}^{(k)}$. The series of transformations mentioned above is done as many times as necessary until the matrix of the transformation is as close as we want to the identity matrix, indicating that we have minimized the anharmonic part of the oscillator. As will be seen in the next section, the sequence of transformations has a very fast convergence.

In Figure 1 we show the behavior of the coefficient $G_{11}^{(k)}$ as a function of the
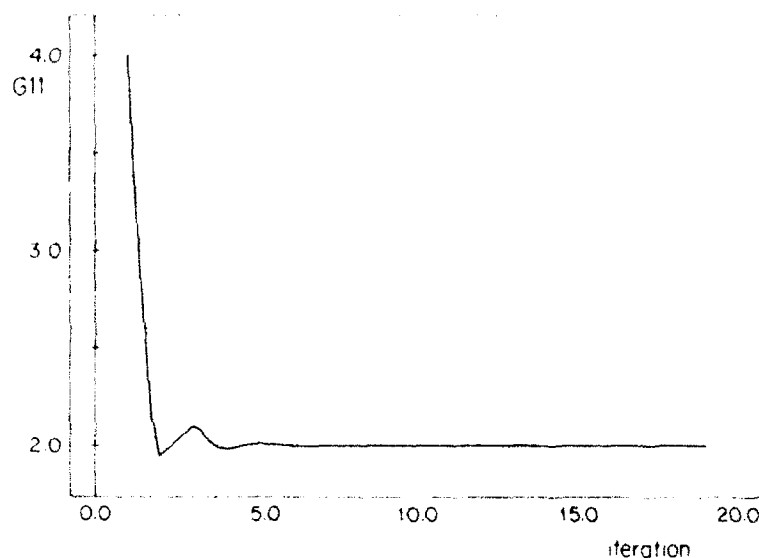
Figure 1.   Behaviour of the coefficient of $a^\dagger a$ as a function of the iteration number for a
fixed value of the anharmonicity parameter $\lambda = 1$.

number of iterations performed for $\lambda = 1$. Notice that after a few transformations
(say 5 or 6). $G_{11}^{(k)}$ attains a fixed value. corresponding to the frequency that a
harmonic oscillator should have in order to represent the anharmonic oscillator.
It is a characteristic value associated to the potential function as a whole. not only
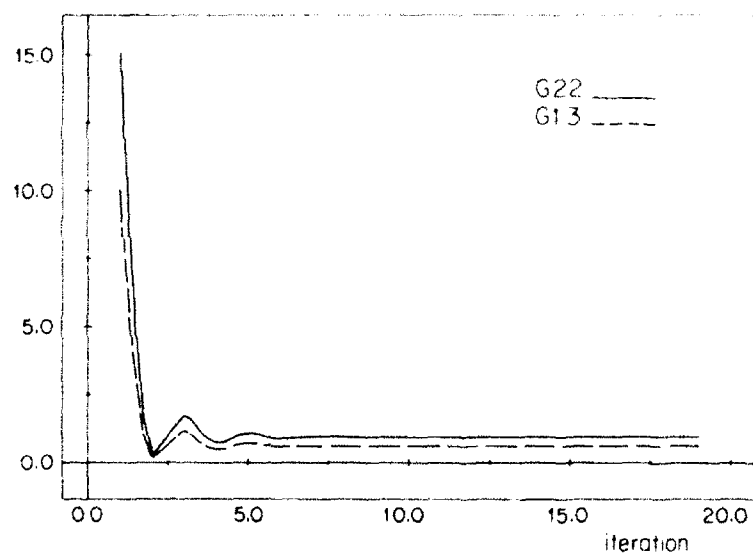
Figure 2.   Behaviour of the coefficients $G_{22}^{(k)}$ (full line) and $G_{13}^{(k)}$ (broken line) as a function
of the number of iterations for a fixed value of $\lambda = 10$.

near the minimum. The final frequency for the oscillator is smaller than the original one indicating that the corresponding harmonic oscillator should be softer than the anharmonic one. All the $G_i^{(k)}$ show a similar behavior for all the values of λ we have tested, they change significantly from their initial values during the first few iterations and after that, they all attain fixed values, generally different from zero. As an example in Figure 2 we show $G_{11}^{(k)}$ and $G_{22}^{(k)}$ for $\lambda = 10$. Notice that the asymptotic values of the $G_{ii}^{(k)}$ are smaller than originally, an indication that one can try to apply perturbation theory to this transformed Hamiltonian and hopefully obtain improved results.

Energy Eigenvalues

With the boson operators we obtained after k transformations, we evaluated the energy spectrum of the corresponding diagonal Hamiltonian $\hat{\mathcal{H}}_D^{(k)} = \sum_{i=0,1,2} G_{ii}^{(k)} a^{(k)\dagger} a^{(k)i}$. We show in Table I this *zeroth* order approximation after 10 transformations, the results obtained when we use second-order perturbation theory [12] after the same 10 transformations, and the exact results of Hsue and Chern [13] for the ground and the first four excited states of a quartic oscillator with $\lambda = 1$.

It can be seen that the zero-order approximation gives very reasonable results when compared with the exact, not only for the ground but also for the excited states. The percentage difference

$$\Delta_{E_0} = 100 \times \frac{E_0^{(10)} - E_{ex}}{E_{ex}} \tag{14}$$

being a few percent at most. When we apply second-order perturbation theory to the transformed oscillator, we improve the results significantly and it is interesting to notice that this is so even for the excited states where simple perturbation theory is known to fail badly. Notice that the percentage difference

$$\Delta_{E_p} = 100 \times \frac{|E_p^{(10)} - E_{ex}|}{E_{ex}} \tag{15}$$

is in this case less than 3% in the worst case, that is, for $n = 4$.

TABLE I. Energy eigenvalues for a quartic oscillator ($\lambda = 1.0$).

n	$E_0^{(10)}$	$E_p^{(10)}$	E_{ex}	ΔE_0	ΔE_p
0	.81250	.80410	.80377	1.1	.04
1	2.8125	2.7223	2.73789	2.7	.6
2	5.5625	5.0994	5.17929	7.4	1.5
3	9.0625	7.7537	7.94240	14.1	2.4
4	13.3125	10.6485	10.9636	21.4	2.9

Table II shows the results obtained with perturbation theory (after 10 transformations) as a function of λ for the ground and first four excited states of the oscillator and compare these with exact results [13]. Notice that perturbation theory can be safely applied for the whole range of values of the anharmonicity parameter $.1 \leq \lambda \leq 1000.0$. We also show the percentage difference Δ_{E_p} defined above.

Finally, Table III shows the convergence behavior of the ground state energy eigenvalue in the *zeroth* approximation $E_0^{(k)}$, when we have applied second-order perturbation theory to the transformed Hamiltonian $E_p^{(k)}$, and the value of the perturbation correction $\Delta_p^{(k)}$ for different values of λ. For $\lambda = 1.0$, the eigenvalue changes drastically during the first few iterations but, after about 4 or 5, the unperturbed results hardly change and the contribution due to the perturbation approaches a fixed value. When we increase the strength of the anharmonicity to $\lambda = 10.0$, we have to make more transformations before attaining convergence:

TABLE II.   Energy eigenvalues for a quartic oscillator.

n	E_{ex}	$E_p^{(10)}$	ΔE_p	λ^a
0	.55915	.55920	.009	.10
1	1.76950	1.76776	.10	.10
2	3.13862	3.12814	.33	.10
3	4.62888	4.59831	.66	.10
4	6.22030	6.15759	1.01	.10
0	.80377	.80500	.15	1.0
1	2.73789	2.72226	.57	1.0
2	5.17929	5.09939	1.54	1.0
3	7.94240	7.75367	2.38	1.0
4	10.9636	10.6485	2.87	1.0
0	1.50497	1.50974	.32	10.0
1	5.32161	5.27491	.88	10.0
2	10.3471	10.1191	2.2	10.0
3	16.0901	15.5876	3.12	10.0
4	22.4088	21.6278	3.49	10.0
0	3.13138	3.14361	.39	100.0
1	11.1872	11.0832	.93	100.0
2	21.9069	21.3937	2.34	100.0
3	34.1825	33.0599	3.28	100.0
4	47.7072	45.9808	3.62	100.0
0	6.69422	6.72184	.41	1000.0
1	23.9722	23.7488	.93	1000.0
2	47.0173	45.9061	2.36	1000.0
3	73.4191	70.9864	3.31	1000.0
4	102.516	98.7767	3.65	1000.0
0	11.4308	11.4753	.39	5000.0
1	40.9517	40.5462	.33	5000.0
2	80.3430	78.3904	2.43	5000.0
3	125.475	121.262	3.36	5000.0
4	175.218	168.816	3.65	5000.0

^{a} For $\lambda = 5000$, E_{ex} was taken from Ref. 15.

TABLE III. Energy eigenvalues for a quartic oscillator.

k	$E_0^{(0)}$	$E_P^{(1)}$	$E_P^{(2)}$	$E_P^{(2)}$ E_{ex}
$\lambda = 1.0$				
0	1.2500	.79679	.45321	.0070
1	.86307	.80239	.06068	.0014
2	.81974	.80137	.01837	.0024
3	.81350	.80567	.00782	.0019
4	.81264	.80465	-.00780	.0009
5	.81252	.80512	-.00740	.0014
6	.81250	.80495	.00755	.0012
7	.81250	.80502	.00748	.0013
8	.81250	.80499	.00751	.0012
9	.81250	.80500	.00750	.0012
$\lambda = 10.0$				
0	8.0000	2.6153	5.3847	1.1103
1	2.1075	1.5098	.59776	0.0048
2	1.6853	1.4674	-.21796	0.0376
3	1.5607	1.5116	-.04908	0.0066
4	1.5381	1.5040	-.03408	0.0010
5	1.5327	1.5114	.02134	0.0064
6	1.5316	1.5087	.02283	0.0037
7	1.5313	1.5102	.02116	0.0052
8	1.5313	1.5095	-.02172	0.0045
9	1.5313	1.5098	.02141	0.0048

however, the importance of the perturbation term decreases significantly during the first few transformations. Notice also that the ground-state energy obtained after convergence is not necessarily the closest to the exact value; this indicates that we are modelling the whole of the potential function, not only the region near the minimum. For example, for $\lambda = 1.0$, the result obtained with second-order perturbation theory after four iterations differs from the exact in 0.0009, less than .11%, while the difference between the second-order perturbation results after nine iterations and the exact is .0012. The same kind of behavior occurs for $\lambda = 10.0$ where again, the closest result is obtained after four iterations. One could also make the transformations state dependent and thus obtain enhanced energy for a given state. If one requires more accuracy that can be obtained with a variational calculation which uses the transformed states as a basis [14].

Conclusions

We have shown an algebraic method to evaluate the energy eigenvalues of a quartic oscillator. After transforming the quartic oscillator's Hamiltonian, we can safely use perturbation theory. The results we have obtained even before the use of perturbation theory are close to the exact in a large range of values of the anharmonicity parameter and the use of second-order perturbation theory improves

the results significantly. The same happens for the excited states of the oscillator. The extension of the method to the double well and to the anharmonic oscillator with cubic and quartic terms present is under study as well as the implementation of a variational calculation using as a basis the k-transformed states and will be published elsewhere [14].

Acknowledgment

Bibliography

[1] M. Moshinsky, *The Harmonic Osillator in Modern Physics: From Atoms to Quarks* (Gordon and Breach, New York, 1969).

[2] C. M. Bender and T. T. Wu, Phys. Rev. **184**, 1231 (1969).

[3] A. Okopińska, Phys. Rev. D36, 1273 (1987).

[4] R. F. Bishop and M. F. Flynn, Phys. Rev. A38, 2211 (1988).

[5] R. Balsa, M. Plo, J. G. Esteve, and A. F. Pacheco, Phys. Rev. D28, 1945 (1983).

[6] R. Fanelli and R. E. Struzynski, Am. J. Phys. **51**, 561 (1983); P. M. Stevenson, Phys. Rev. D23, 2916 (1981); R. Seznec and J. Zinn-Justin, J. Math. Phys. **20**, 1398 (1979).

[7] H. K. Shin, J. Phys. Chem. 77, 2657 (1973).

[8] J. Récamier, Int. J. Quantum Chem. S24, 655 (1990); J. Récamier, AIP Conf. Proc. 225, 309 (1990).

[9] J. Récamier and J. Ortega, Mol. Phys. 73, 635 (1991).

[10] A. P. Clark and A. S. Dickinson, J. Phys. B: Atom. Molec. Phys. 6, 164 (1973).

[11] Y. Tikochinsky, J. Math. Phys. **19**, 270 (1978).

[12] L. I. Schiff, *Quantum Mechanics* (McGraw-Hill, Tokyo, 1968).

[13] C. S. Hsue and J. L. Chern, Phys. Rev. D29, 643 (1984).

[14] R. Jáuregui and J. Récamier (to appear, Phys. Rev. A).

[15] N. Aquino, M. S. thesis, UNAM (1992).

Studies in the Paired Orbital Method. IV. Orthogonal Transformations in the Virtual Space

RUBEN PAUNCZ

Department of Chemistry, Technion Israel Institute of Technology, Haifa, Israel 32000

Abstract

The paired orbital method deals with the problem how to obtain the best pairing scheme in the different orbitals for the different spins (DODS) method. Once one has found those virtual orbitals which are the best pairs of the occupied orbitals. one can use the same formalism for the energy expression as used earlier in the alternant molecular orbital (AMO) method. Starting from the canonical orbitals, one performs orthogonal transformations in the virtual space until the minimum of the total energy is obtained. An illustrative calculation on the water molecule for three internuclear distances shows that the method yields 25–60% of the energy improvement obtained by a full configuration interaction method. The percentage of improvement increases with the increase of the internuclear distance. © 1992 John Wiley & Sons, Inc.

Introduction

In the theoretical treatment of atoms and molecules, the self-consistent field method (SCF) is an excellent starting point. The wavefunction is given in the form of a single determinant in which n orbitals are doubly occupied. For the sake of simplicity we shall restrict our treatment to the case where the number of electrons is even ($N = 2n$). The orbitals are determined from the minimization of the total energy of this wavefunction. In most of the applications, the orbitals are given as linear combinations of given basic orbitals, and let us denote the number of basic orbitals by M. The corresponding variational equations for the best coefficients have been derived by Roothaan [1] and Hall[2]. After solving the equations one obtains n orbitals which are doubly occupied and, in addition, $n_v = M - n$ orbitals, which do not have immediate physical significance. The latter are called *virtual* orbitals.

The SCF solution gives good results for the total energy, bond lengths, and some other properties of the molecules. The small error in the total energy (0.5%) is still too large when we would like to calculate transition energies, dissociation energies, and so on. It is necessary to go beyond the SCF method. The difference between the SCF energy and the best energy obtained in the given basis using the nonrelativistic Hamiltonian is called the *correlation energy*. Several methods have been suggested to treat the electronic correlation problem. One should remember that

the single determinantal approach already takes into account, to some extent, the correlation between electrons with parallel spins because the wavefunction is antisymmetric, and therefore, the probability of finding two electrons with the same spin in the neighborhood of the same point is zero. The single determinant does not describe properly the correlation between electrons with antiparallel spins.

Löwdin [3] suggested a simple method for the improvement of the one determinantal representation. One should relax the restriction that each of the n orbitals occurs twice in the wavefunction. One can assign different sets of orbitals to be associated with α and β spins. The method is called *different orbitals for different spins* (DODS). The single determinant constructed in this way is not a pure spin eigenfunction, but a definite spin state is obtained using the projection operator of Löwdin [4]. This method is also called the spin-projected extended Hartree–Fock (HF) method. An excellent review is given by Mayer [5]. In a recent article, K adakov [6] derived equations for obtaining the best orbitals in this scheme.

A simple variant of the DODS method is the *alternant molecular orbital method* (AMO) suggested by Löwdin [7]. The basis of the method and its early developments are given in a book by Pauncz [8]. The AMO method was quite successful for alternant conjugated systems.

The paired orbital method (PO) is also a variant of the different orbitals for the DODS approach. It can be considered as a generalization of the AMO method. The wavefunction is formally similar to the one used in the AMO method, and the corresponding energy expression is identical with one derived by Pauncz et al. [9] and de Heer and Pauncz [10]. The difference between the two approaches is in the selection of the orbital pairs. In the case of AMO, Löwdin's suggestion was very successful because it used the special properties of alternant conjugated systems in which occupied and virtual orbitals are paired according to the Coulson–Rushbroke theorem [11]. The PO method seeks the answer to the question of how to obtain the best pairing of the occupied and virtual orbitals for a general system.

Pauncz et al. [12] have given an algorithm for the determination of orbital pairs in a general system using the idea that these orbitals should be close to each other spatially. The sum of coulomb integrals between the corresponding orbitals was maximized. The method was tested for the case of water molecule. Harrison and Handy [13] performed a full configuration interaction calculation for this case so one can compare the result with the best possible treatment in the given basis. The PO method, using five nonlinear parameters, recovered about 20% of the correlation energy obtained with the full CI treatment (256,473 configurations). Pauncz [14] has derived the expressions for the derivatives of the energy with respect to the nonlinear parameters, and he proved that the SCF energy is a maximum with respect to the nonlinear parameters in the PO method. The structure of the PO wavefunction and its relation to a limited configuration interaction method was investigated by Pauncz [15]. Refs. [12], [14], and [15] will be referred as I, II, and III, respectively.

The aim of the present approach is to obtain the orbitals by minimizing the total energy instead of maximizing the sum of coulomb integrals between the corresponding orbitals. Orthogonal transformation among the virtual orbitals will be

performed to achieve this goal. First, we shall discuss the structure of the PO wave-function and the energy expression, and then consider in detail the method of orthogonal transformations in the virtual space.

The Paired Orbital Wavefunction and the Energy Expression

The wavefunction used in the PO method is of the following form:

$$\Psi = N\mathcal{A}\Phi\mathcal{O}_S\alpha(1)\cdots\alpha(n)\beta(n + 1)\cdots\beta(2n) \qquad (1)$$

where $\mathcal{A}$ is the antisymmetrizer, N is a normalization constant, and $\mathcal{O}_S$ is the spin projection operator. We shall consider the singlet state only ($S = 0$). Φ is a spatial (freeon) wavefunction which is a product of one-electron orbitals:

$$\Phi = u_1(1)\cdots u_n(n)v_1(n + 1)\cdots v_n(2n) \qquad (2)$$

In the PO (and in the AMO) method, the u_i's and v_i's form a set of orthogonal one-electron orbitals in the following way:

$$u_i = a_i\psi_i + b_i\psi_{i'}$$
$$v_i = a_i\psi_i - b_i\psi_{i'} \qquad (3)$$

where $a_i = \cos\theta_i$ and $b_i = \sin\theta_i$, ψ_i ($i = 1,\ldots,n$) is a doubly occupied orbital in the single determinantal SCF wavefunction, and $\psi_{i'}$ is a virtual orbital with which it is paired.

Let us introduce the overlap integral between u_i and v_i:

$$\langle u_i|v_i\rangle = \lambda_i = \cos 2\theta_i \qquad (4)$$

There are three important functions of the λ_i which appear in the energy expression:

$$\Lambda_q = \sum_{k=0}^{n-q}(-1)^k C(S, k + q)S_k(x_1,\ldots,x_n). \qquad (q = 0, 1, 2) \qquad (5)$$

where $x_i = \lambda_i^2$, $C(S, k)$ are the spin projection (Sanibel) coefficients [16]. For the singlet state they are given as follows:

$$C(0, k) = (-1)^k\binom{n}{k}\Big/(n + 1) \qquad (6)$$

and $S_k(x_1,\ldots,x_n)$ (abbreviated as S_k) is the kth symmetric sum formed from the $x_1,\ldots,x_n$:

$$S_0 = 1,$$

$$S_1 = \sum_{i=1}^{n} x_i,$$

$$S_2 = \sum_{i<j}^{n} x_i x_j,$$

$$\cdots$$

$$S_n = x_1\cdots x_n \qquad (7)$$

Λ_0 is the normalization integral:

$$\Lambda_0 = \langle \Psi_0 | \Psi_0 \rangle \tag{8}$$

Let us divide the energy expression into two parts. The first one corresponds to the one-electron operators in the Hamiltonian (kinetic energy and nuclear-electron attraction), the second one to the two-electron operators (electron-electron repulsion). The one-electron part is:

$$E_1 = E_{1a} + E_{1b}/\Lambda_0$$

$$= \sum_{i=1}^{n} w_i - \Lambda_0^{-1} \Delta w_i \lambda_i \frac{\partial}{\partial x_i} (\Lambda_1 + \Lambda_0) \tag{9}$$

Here

$$w_i = h_i + h_{i'}, \qquad \Delta w_i = h_i - h_{i'} \tag{10}$$

and

$$h_i = \int \psi_i^* h \psi_i \, dv, \qquad h_{i'} = \int \psi_{i'}^* h \psi_{i'} \tag{11}$$

that is, they are diagonal elements of the one-electron Hamiltonian over the occupied orbitals and their virtual pairs, respectively.

The two-electron part reads as follows:

$$E_2 = (E_{2a} + E_{2b} + E_{2c})\Lambda_0^{-1} \tag{12}$$

where

$$E_{2a} = \sum_{i=1}^{n} [A_{ii}\gamma_{ii} + A_{i'i'}\gamma_{i'i'} - B_i\gamma_{ii'} - C_i\delta_{ii'}]$$

$$E_{2b} = \sum_{i<j}^{n} [\Gamma(i,j) - \Delta(i,j)]$$

$$E_{2c} = -\sum_{i<j}^{n} Z(i,j) . \tag{13}$$

$$A_{ii} = (1/4)(1 + \lambda_i)^2 \frac{\partial}{\partial x_i} (\Lambda_1 + \Lambda_0).$$

$$A_{i'i'} = (1/4)(1 - \lambda_i)^2 \frac{\partial}{\partial x_i} (\Lambda_1 + \Lambda_0).$$

$$B_i = (1/2)(1 - \lambda_i^2) \frac{\partial}{\partial x_i} (\lambda_1 - \lambda_0).$$

$$C_i = (1 - \lambda_i^2) \frac{\partial}{\partial x_i} \Lambda_1 \tag{14}$$

$\Gamma(i, j)$, $\Delta(i, j)$, and $Z(i, j)$ are defined as follows:

$$\Gamma(i, j) = \Gamma_{ii}\gamma_{ii} + \Gamma_{ii'}\gamma_{ii'} + \Gamma_{i'j}\gamma_{i'j} + \Gamma_{i'j'}\gamma_{i'j'}.$$

$$\Delta(i, j) = \Delta_{ii}\delta_{ii} + \Delta_{ii'}\delta_{ii'} + \Delta_{i'j}\delta_{i'j} + \Delta_{i'j'}\delta_{i'j'}.$$

$$Z(i, j) = Z_{ii}\zeta_{ii} + Z_{ii'}\zeta_{ii'} \tag{15}$$

The basic two-electron integrals, γ_{ij}, δ_{ij}, and ζ_{ij}, are respectively the coulomb, exchange, and a new kind of integral which is characteristic of the AMO and PO methods:

$$\gamma_{ij} = (ii|jj) \qquad \delta_{ij} = (ij|ji), \qquad \zeta_{ij} = (ij|j'i')$$

$$(ij|kl) = \iint \psi_i^*(1)\psi_j^*(1)(1/r_{12})\psi_k(2)\psi_l(2)\,dv_1\,dv_2 . \tag{16}$$

The $\lambda(\theta)$-dependent factors in eqs. (15) are given as follows:

$$\Gamma_{ij} = (1 + \lambda_i)(1 + \lambda_j)(a + b(\lambda_i + \lambda_j) + c\lambda_i\lambda_j),$$

$$\Delta_{ij} = (1 + \lambda_i)(1 + \lambda_j)(a + b[2(\lambda_i + \lambda_j) - 1 - \lambda_i\lambda_j] + c\lambda_i\lambda_j)/2 . \tag{17}$$

$$Z_{ij} = \sin 2\theta_i \sin 2\theta_j(a + b) - (1/4)\sin 4\theta_i \sin 4\theta_j(b + c)$$

$$Z_{ij'} = \sin 2\theta_i \sin 2\theta_j(a + b) + (1/4)\sin 4\theta_i \sin 4\theta_j(b + c) \tag{18}$$

where

$$a = \frac{\partial^2}{\partial x_i \partial x_j} \Lambda_2, \qquad b = \frac{\partial^2}{\partial x_i \partial x_j} \Lambda_1, \qquad c = \frac{\partial^2}{\partial x_i \partial x_j} \Lambda_0 . \tag{19}$$

From the expressions in eqs. (17) one obtains the corresponding factors involving i' and/or j' by reversing the sign of the λ_i and/or λ_j.

Orthogonal Transformations in the Virtual Space

The main problem in the PO method is how to choose the paired orbitals [eq. (3)]. We shall leave the occupied orbitals unchanged, these orbitals have been determined from the SCF procedure. they minimize the energy of the single determinant with doubly occupied orbitals. For a concrete example, let us choose the water molecule in a double-zeta basis. The number of basis orbitals, $M = 14$; the number of occupied orbitals, $n = 5$; the dimension of the virtual space, $n_v = 9$. We are looking for a set of molecular orbitals in the virtual space which are the pairs of the occupied orbitals. The original occupied and virtual orbitals form an orthonormal set, and we want to preserve this property, so we are looking for an orthogonal transformation in the virtual space which will provide the 5 virtual orbitals.

$$\psi_{i'} = \sum_{r=6}^{14} \psi_r c_{ri}, \qquad = \sum_{k=1}^{9} v_k d_{ki} \ (i = 1, 5) \tag{20}$$

TABLE 1.   Symmetries of the canonical orbitals in the water molecule.

Occupied	$1a_1$	$2a_1$	$3b_2$	$4a_1$	$5b_1$				
Virtual	$6a_1$	$7b_2$	$8b_1$	$9a_1$	$10b_2$	$11a_1$	$12b_2$	$13a_1$	$14a_1$

The D matrix has n_v rows and n columns. From the orthogonality of the n columns, and from the normalization conditions, follows that the number of independent parameters. $n_p = n_v n - (n + n(n - 1)/2) = n(2n_v - (n + 1))/2$. In the case of the water molecule we have 30 independent parameters.

The first 8 parameters determine a 9-dimensional unit vector:

$$d_{11} = \cos(p_1) \tag{21}$$

$$d_{21} = \sin(p_1) \cos(p_2)$$

$$d_{31} = \sin(p_1) \sin(p_2) \cos(p_3)$$

$$\cdots$$

$$d_{81} = \sin(p_1) \sin(p_2) \cdots \sin(p_7) \cos(p_8)$$

$$d_{91} = \sin(p_1) \sin(p_2) \cdots \sin(p_7) \sin(p_8)$$

The next 7 parameters determine 8 elements of the second column, starting from the *second* element and using the same algorithm as given in eq. (21). The first element is determined from the orthogonality of the second column to the first one, and finally, the second column is normalized. One can continue this algorithm, which is essentially a Schmidt orthogonalization procedure. It is an essential point in this procedure that, if all the parameters are zeros, then we obtain 9 columns in which the diagonal elements are equal to one and the rest are zeros.

Beside the 30 parameters which determine the 5 orbital pairs, we have 5 more variational parameters (θ_i, $i = 1,5$, if all the θ's are zero then we have a single determinant with doubly occupied orbitals). The total energy is a function of the 30 + 5 variational parameters. Using the energy expression given in section 2, one can minimize the total energy by the variation of the nonlinear parameters. In the calculation we used the DUMCGF program of the IMSL library, this is a minimization program using a conjugate gradient algorithm and a finite-difference gradient.

The procedure outlined so far deals with the case if the molecular orbitals do not belong to certain irreducible representations of the symmetry group of the molecule. This is the case when we use localized molecular orbitals which correspond to inner shells, bonds, and lone pairs. These type of orbitals have been used in the calculations reported in I.

The calculation needs less variational parameters if we use canonical orbitals which belong to the different irreducible representations of the symmetry group

TABLE II.   Paired orbital calculations for the water molecule.

	R_e	$1.5R_e$	$2R_e$
SCF	−76.009838	−75.803529	−75.595180
FCI	−76.157866	−76.014521	−75.905247
ΔE(FCI)	−0.148028	−0.210992	−0.310063
ΔE(PO)	−0.040704	−0.083576	−0.191607
c_i^2	27.5	39.6	61.8

All energies in atomic units.

(In the case of water molecule the group is C_{2v}). In this case, the occupied orbital and its pair should belong to the same irreducible representation. Table I shows the symmetries of the canonical orbitals.

Inspection of Table I shows that there are 3 orbitals of symmetry a_1 among the occupied orbitals and 5 orbitals of the same symmetry among the virtuals. That means that we have to form 3 paired orbitals as a linear combination of the 5 virtuals, all belonging to the a_1 symmetry. There is only one orbital among the occupied and 3 orbitals in the virtual set which belong to symmetry b_2, and finally, one orbital both in the occupied and in the virtual set which belongs to b_1. We have to form three orthonormal vectors of length 5 (symmetry a_1) and one vector of length 3 (symmetry b_2). The number of parameters determining these vectors using the same algorithm presented above is $9 + 2 = 11$.

Results and Discussion

Illustrative calculations have been performed for the water molecule. Here we are able to compare the results with the best possible result obtainable in the same basis. Harrison and Handy [13] have performed full CI (FCI) calculations for three bond distances. The calculations refer to the C_{2v} symmetry at the O — H distances: R_e, $1.5R_e$ and $2R_e$. There are 256,473 configurations.

The results of the calculations using the canonical orbitals are given in Table II. Table III contains the θ_i values for the optimum orbitals.

TABLE III.   The θ_i values for optimum orbitals.

	θ_1	θ_2	θ_3	θ_4	θ_5
$1R_e$	0.00124	0.16014	0.25203	0.21120	0.18852
$1.5R_e$	−0.03126	0.01968	0.42355	0.42497	0.07295
$2R_e$	0.00041	−0.00037	−0.58337	0.59572	−0.04474
Sym.	a_1	a_1	b_2	a_1	b_1

Comparing the results with those obtained in I we see a substantial improvement in the quality of the approximation. In the earlier calculation, where the paired orbitals were determined by maximizing the sum of the interelectronic repulsion between paired orbitals, we obtained only about 20% of the energy improvement of the FCI. In the present treatment where we optimize the total energy of the PO wavefunction the results are much better and the percentage of the energy improvement increases with increasing internuclear distance. The number of parameters determining the orbitals is 11. It was a quite surprising result that when localized orbitals were used instead of the canonical ones, the results were quite close to the results obtained with the canonical orbitals, but slightly inferior. This is surprising because, in the latter calculations, 30 parameters have been varied for optimizing the orbitals.

On the one hand, the results are satisfying, as we obtain using 11 + 5 nonlinear variational parameters 27–60% of the energy improvement obtained by the FCI (256,473 linear parameters), and the wavefunction has a relatively simple meaning as contrasted with the sum of 256,473 configurations; on the other hand, this is still far from the accuracy one can obtain with alternative methods (e.g., coupled cluster method). We have to remember that our solution is still not the best PHF solution. Löwdin [17] pointed out that we do not have to retain the occupied orbitals as unchanged; by forming the paired orbitals, we can use orthogonal transformations in the full basis (in our case 14 orbitals). There is still another approach in which one uses general spin-orbitals. See Takatsuka et al. [18] and Mayer and Löwdin [19]. We emphasize that, in our treatment, the pairing theorem [20] was used consistently as an essential part of the theory. The problem of how to obtain the best PHF solution by a practical algorithm is still an open question.

Acknowledgment

The author expresses his gratitude to Professor Per-Olov Löwdin for his interest in this work and for his inspiration and scientific advice.

Bibliography

[1] C. C. J. Roothaan, Rev. Mod. Phys. 23, 69 (1951).
[2] G. G. Hall, Proc. Roy. Soc. A208, 328 (1951).
[3] P.-O. Löwdin, Phys. Rev. 97, 1509 (1955).
[4] P.-O. Löwdin, Calcul des Fonctions d'Onde Moléculaires, Centre Nat. de la Rech. Sci., Paris, 82, 23 (1958).
[5] I. Mayer, Adv. Quantum Chem. 12, 189 (1980).
[6] P. Karadakov, Int. J. Quantum Chem. 30, 239 (1986).
[7] P.-O. Löwdin, Symposium on Molecular Physics (Maruzen Co., Tokyo. 1954). p. 13.
[8] R. Pauncz, The Alternant Molecular Orbital Method (Saunders, Philadelphia, 1957).
[9] R. Pauncz, J. de Heer, and P.-O. Löwdin, J. Chem. Phys. 36, 2247 (1962).
[10] J. de Heer and R. Pauncz, J. Chem. Phys. 39, 2314 (1963).
[11] C. A. Coulson and G. S. Rushbroke, Proc. Cambridge Phil. Soc. 36, 193 (1940).
[12] R. Pauncz, B. Kirtman, and W. E. Palke, Int. J. Quantum Chem. 21S, 533 (1987).

[13] R. J. Harrison and N. C. Handy. Chem. Phys. Lett. 95, 386 (1983).

[14] R. Paunez. Theor. Chim. Acta 73, 383 (1988).

[15] R. Paunez. Structure of Small Molecules and Ions. R. Naaman and Z. Vager. Eds. (Plenum. New York 1988). p. 237.

[16] R. Manne. Theor. Chim. Acta 6, 116 (1966).

[17] P.-O. Löwdin (private communication).

[18] K. Takatsuka. S. Nagase. K. Yamagouchi. and T. Fueno. J. Chem. Phys. 67, 2527 (1977).

[19] I. Mayer and P.-O. Löwdin. Adv. Quantum Chem. (to appear).

[20] (a) P.-O. Löwdin, J. Appl. Phys. 33 (Suppl.), 251 (1962); (b) A. T. Amos and G. G. Hall. Proc. Roy soc. A263, 483 (1961); (c) P. Karadakov. Int. J. Quantum Chem. 27, 699 (1985); (d) I. Mayer. Int. J. Quantum Chem. 29, 31 (1986). (e) P.-O. Löwdin. Israel J. Chem. (31, 297 (1991).

Alternative Approach to the Factorization Method

J. MORALES,* G. ARREAGA, and J. J. PEÑA

Instituto Mexicano del Petróleo, Subdirección General de Investigación Aplicada, Apartado Postal 14-805, 07730, México, D.F., México

J. LÓPEZ-BONILLA

Universidad Autónoma Metropolitana, CBI-Área de Física, Azcapotzalco, Ave Sn Pablo 180, 02200 México, D.F., México

Abstract

A procedure to obtain the operational solutions of second order differential equations related with Sturm–Liouville problems is presented. The method is based on the commutation relation between the ladder operators themselves, with a certain structure, and the position and momentum operators. Even though the creation and annihilation operators, derived by the proposed approach, factorize as expected the corresponding differential equation, the method does not use, as original premise factoring, the differential relation under consideration. That is, the displayed procedure is quite different, simple, and direct when compared with other procedures such as the factorization method of Infeld and Hull. To illustrate the above, the usefulness of the proposed procedure is shown by finding the ladder operators associated to the quantum numbers n and l for various potential wave functions. © 1992 John Wiley & Sons, Inc.

Introduction

Since von Neumann introduced the operator algebra theory in 1929 [1], it has played an important role in diverse fields of mathematical physics. Probably the most important improvement brought about by the algebraic procedures has been the factorization method of Infeld and Hull [2,3], which permits one to obtain ladder operators for Sturm–Liouville problems. For many years, the operational methods have shown their usefulness in quantum mechanics problems, mostly in the algebraic calculation of matrix elements where the factorization method has been used along with other mathematical techniques such as the hypervirial theorem [4] and parameter differentiation [5] method.

Recently Morales et al. [6] have proposed an alternative approach to obtain ladder operators for potential wavefunctions from the algebraic representation of the orthogonal polynomials with which the wavefunction is directly involved. Also, that method was used to obtain, algebraically, generalized recurrence relations and closed-form expressions for multipole matrix elements of hydrogen-like wavefunctions [7]. However, in spite of its simplicity and usefulness, it seems at first glance that such a procedure necessarily needs the previous knowledge of the wavefunction

---

*Also at Universidad Autónoma Metropolitana (Azc-CBI), Mexico.

under consideration, which is contrary to the virtue of the usual factorization method. This occurs because their procedure was applied to solve, operationally, differential equations of orthogonal polynomials. Thus, in order to overcome that apparent deficiency, in the present work we consider the operational solutions of the Schrödinger equation for various potential wavefunctions by means of an alternative procedure to the usual factorization method. That objective is achieved by finding two kinds of ladder operators: those shifting the n quantum number and the ones acting on the l orbital number, or equivalent numbers, for the Coulomb, Morse, and Pöschl–Teller equations.

Alternative Approach to the Factorization Method

As stated above, in order to include the most general case of second order differential equations containing first order derivatives, let us consider the relationship

$$\alpha(x) f_n'' + \beta(x, n) f_n' + \xi(x, n) f_n = 0 \tag{1}$$

into its operational form

$$\hat{H}_n f_n = 0 \tag{2}$$

which is appropriate for obtaining its algebraic solutions. In that case, by assuming the existence of the ladder operators $\varphi_n^\pm$ such that

$$\varphi_n^\pm f_n = f_{n\pm 1} \tag{3}$$

Eq. (2) transforms to

$$[\varphi_n^\pm, \hat{H}_n] + \hat{H}_n \varphi_n^\pm = 0 \tag{4}$$

where it should be noted that the f_n functions were dropped in order to leave the operators alone. At this point, by defining

$$\beta(x, n) = \beta(x, n \pm 1) + \beta^\pm(x, n) \tag{5a}$$

and

$$\xi(x, n) = \xi(x, n \pm 1) + \xi^\pm(x, n) \tag{5b}$$

one obtains

$$[\varphi_n^\pm, \hat{H}_n] = -\left(\beta^\pm(x, n)\frac{d}{dx} + \xi^\pm(x, n)\right)\varphi_n^\pm \tag{6}$$

where we have used the identity $\hat{H}_{n\pm 1} f_{n\pm 1} = 0$. Thus, by commuting $\varphi_n^\pm$ and $\beta^\pm(x, n)d/dx$ in the above equation, and reordering it, we get finally

$$\left[\varphi_n^\pm, \hat{H}_n - \beta^\pm(x, n)\frac{d}{dx}\right] = -\varphi_n^\pm \beta^\pm(x, n)\frac{d}{dx} - \xi^\pm(x, n)\varphi_n^\pm \tag{7}$$

In order to solve this relationship for $\varphi_n^\pm$, it is necessary to propose some structure for the ladder operator solutions. For example, if these are considered to be linear according to

$$\varphi_n^{\pm} = a^{\pm}(x, n) + b^{\pm}(x, n) \frac{d}{dx}. \tag{8}$$

Eq. (7) becomes

$$-\alpha(x) \frac{d^2 a^{\pm}(x, n)}{dx^2} - \beta(x, n \pm 1) \frac{da^{\pm}(x, n)}{dx} + b^{\pm}(x, n) \frac{d\xi(x, n)}{dx}$$

$$+ \left[b^{\pm}(x, n) \frac{d\beta(x, n \pm 1)}{dx} - \alpha(x) \left(2 \frac{da^{\pm}(x, n)}{dx} + \frac{d^2 b^{\pm}(x, n)}{dx^2} \right) \right.$$

$$\left. - \beta(x, n \pm 1) \frac{db^{\pm}(x, n)}{dx} \right] \frac{d}{dx}$$

$$+ \left(b^{\pm}(x, n) \frac{d\alpha(x)}{dx} - 2\alpha(x) \frac{db^{\pm}(x, n)}{dx} \right) \frac{d^2}{dx^2} = -\xi^{\pm}(x, n) a^{\pm}(x, n)$$

$$- \left[\beta^{\pm}(x, n) a^{\pm}(x, n) + b^{\pm}(x, n) \left(\xi^{\pm}(x, n) + \frac{d\beta^{\pm}(x, n)}{dx} \right) \right] \frac{d}{dx}$$

$$- (\beta^{\pm}(x, n) b^{\pm}(x, n)) \frac{d^2}{dx^2}. \tag{9}$$

Thus, matching term by term in the above relation one gets the differential equations system

$$\alpha(x) \frac{d^2 a^{\pm}(x, n)}{dx^2} + \beta(x, n \pm 1) \frac{da^{\pm}}{dx} - b^{\pm}(x, n) \frac{d\xi(x, n)}{dx}$$

$$- \xi^{\pm}(x, n) a^{\pm}(x, n) = 0 \tag{10a}$$

$$-\beta^{\pm}(x, n) a^{\pm}(x, n) + 2\alpha(x) \frac{da^{\pm}(x, n)}{dx} + \alpha(x) \frac{d^2 b^{\pm}(x, n)}{dx^2}$$

$$- b^{\pm}(x, n) \left(\xi^{\pm}(x, n) + \frac{d\beta(x, n)}{dx} \right) + \beta(x, n \pm 1) \frac{db^{\pm}(x, n)}{dx} = 0 \tag{10b}$$

$$2\alpha(x) \frac{db^{\pm}(x, n)}{dx} - \left(\frac{d\alpha(x)}{dx} + \beta^{\pm}(x, n) \right) b^{\pm}(x, n) = 0 \tag{10c}$$

which can be easily solved. In fact, $b^{\pm}(x, n)$ comes from Eq. (10c) as

$$b^{\pm}(x, n) = A^{\pm} \exp\left(\int \frac{1}{2\alpha(x)} \left(\frac{d\alpha(x)}{dx} + \beta^{\pm}(x, n) \right) dx \right) \tag{11}$$

On the other hand, in order to avoid the apparent redundance that comes from Eqs. (10a) and (10b), the latter is rewritten as

$$\frac{da^{\pm}(x, n)}{dx} = P^{\pm}(x, n) + Q^{\pm}(x, n) a^{\pm}(x, n) \tag{12}$$

where

$$Q^{\pm}(x, n) = \frac{\beta^{\mp}(x, n)}{2\alpha(x)}$$ (13)

and

$$P^{\pm}(x, n) = -\frac{1}{2}\frac{d^2 b^{\mp}(x, n)}{dx^2} + \frac{b^{\mp}(x, n)}{2\alpha(x)}\left(\frac{d\beta(x, n)}{dx} + \xi^{\mp}(x, n)\right)$$
$$- \frac{\beta(x, n \pm 1)}{2\alpha(x)}\frac{db^{\mp}(x, n)}{dx}.$$ (14)

Thus, the $a^{\pm}(x, n)$ solutions are straightforwardly obtained by using Eq. (12) into Eq. (10a) by means of

$$a^{\pm}(x, n)\left[\alpha(x)\left(\frac{dQ^{\pm}(x, n)}{dx} + (Q^{\pm}(x, n))^2\right) + Q^{\mp}(x, n)\beta(x, n \pm 1) - \xi^{\mp}(x, n)\right]$$

$$= b^{\pm}(x, n)\frac{d\xi(x, n)}{dx} - P^{\pm}(x, n)(\alpha(x)Q^{\pm}(x, n) + \beta(x, n \pm 1))$$

$$- \alpha(x)\frac{dP^{\pm}(x, n)}{dx}.$$ (15)

That is, the $\varphi_n^{\pm}$ ladder operators specified by Eq. (8) are then given from Eqs. (11) and (15).

Applications

In this section we are going to consider the algebraic treatment of the Schrödinger equation for the Coulomb, Morse, and Pöschl–Teller potential wavefunctions by assuming $A^{\pm} = \mp 1$ hereafter.

Algebraic Approach to the Coulomb Potential Wavefunctions

For the hydrogen atom potential, the differential equation containing first order derivative is given by [8]:

$$\hat{C}_{n,l}R_{n,l}(x) = 0$$ (16)

with

$$\hat{C}_{n,l} = \frac{d^2}{dx^2} + \frac{2}{x}\frac{d}{dx} - \left(\frac{1}{4} - \frac{n}{x} + \frac{l(l + 1)}{x^2}\right)$$ (17)

where $x = \sigma r$ with $\sigma^2 = -8mE/\hbar^2$ and $n = 2mZe^2/\sigma\hbar^2$. There are two cases to be considered: ladder operators $\varphi_{n,l}^{\pm}$ moving l and the ones acting over n according to the properties

$$\varphi_l^{\pm} R_{n,l}(x) = R_{n,l\pm 1}(x)$$ (18a)

and

$$\varphi_n^+ R_{n,l}(x) = R_{n+1,l}(x).$$ (18b)

In the first situation, $\beta^+(x, l) = 0$ and $\xi^+(x, l) = \pm2(l + 1/2 \pm 1/2)/x^2$, for which $Q^+(x, l) = 0$ and $P^+(x, l) = \mp(l \mp 1/2 + 1/2)/x^2$. It follows that,

$$b^+(x, l) = \mp1 \quad \text{and} \quad a^+(x, l) = -\frac{n}{2(l + 1/2 \pm 1/2)} + \frac{l + 1/2 \mp 1/2}{x}$$

That is, the φ_l^+ ladder operators, shifting l, are then given by

$$\varphi_l^+ = -\frac{n}{2(l + 1)} + \frac{l}{x} - \frac{d}{dx}$$ (19a)

and

$$\varphi_l^- = -\frac{n}{2l} + \frac{l + 1}{x} + \frac{d}{dx}$$ (19b)

that are equivalent to the ladder operators published by Salburg [9].

We are going to consider the second case. In order to find the corresponding $\varphi_n^\pm$ creation and annihilation operators, without loss of generality, Eq. (16) is multiplied by x^2 from left to right. In that case, $\beta^+(x, n) = 0$ and $\xi^+(x, n) = \mp x$ for which $Q^+(x, n) = 0$ and $P^+(x, n) = 1/2$. That is, $b^+(x, n) = \mp x$ and $a^+(x, n) = x/2 - n \mp 1$. Straightforwardly, the $\varphi_n^\pm$ raising and lowering operators are then

$$\varphi_n^+ = \frac{x}{2} - n - 1 - x\frac{d}{dx}$$ (20a)

and

$$\varphi_n^- = -\frac{x}{2} - n + 1 + x\frac{d}{dx}$$ (20b)

are previously obtained by Badawi et al. [10]. It should be noted that both ladder operators, $\varphi_{n,l}^\pm$, factorize the corresponding differential equation by means of

$$\left(\varphi_{l-1}^+\varphi_l^- + \frac{1}{4} - \frac{n^2}{4l^2}\right)R_{n,l}(x) = 0$$ (21a)

$$(\varphi_{n-1}^+\varphi_n^- + l(l + 1) - n(n - 1))R_{n,l}(x) = 0$$ (21b)

and conversely, from $\varphi_{n+1,l+1}^-\varphi_{n,l}^+$ as expected.

Algebraic Approach to the Morse Potential Wavefunctions

The Schrödinger equation for this potential, according to Infeld and Hull [3], is given by

$$\hat{M}_{s,n}R_{s,n}(x) = 0$$ (22)

with

$$\hat{M}_{s,n} = \frac{d^2}{dx^2} + \left(\left(s + \frac{1}{2}\right)e^x - \frac{1}{4}e^{2x} - n^2\right)$$ (23)

where the variable changes $x = -a(r - r_0) + \log[(8MD)^{1/2}/(ah)]$, $s + \frac{1}{2} = (2MD)^{1/2}/(ah)$, $n^2 = -2ME/(a^2h^2)$, and $s - n = 0, 1, 2 \cdots$ let us recover the original Morse differential equation as well as the corresponding energy spectra.

It should be noted that we have used a differential equation that does not contain a first order derivative, that is, $\beta(x) = 0$ and $Q^\pm(x, s, n) = 0$. Then, similar to the above case, two types of ladder operators will be considered: $\theta^\pm_{s,n}$, acting on s and n, respectively, according to equivalent properties of Eqs. (18).

For those creation and annihilation operators, $\theta^\pm_s$, s related, one has $b^\pm(x, s) = \mp 1$, $\xi^\pm(x, s) = \mp e^x$, and $P^\pm(x, s) = \frac{1}{2}e^x$ leading to $a^\pm(x, s) = \frac{1}{2}e^x - (s + \frac{1}{2} \pm \frac{1}{2})$. That is, the corresponding ladder operators are

$$\theta^+_s = \frac{1}{2}e^x - (s + 1) - \frac{d}{dx}$$ (24a)

and

$$\theta^-_s = \frac{1}{2}e^x - s + \frac{d}{dx}$$ (24b)

as reported by Infeld and Hull [3]. The $\theta^\pm_n$ case is worked out as before. That is, by making

$$e^{-2x}\hat{M}_{s,n}R_{s,n}(x) = 0,$$ (25)

one gets $\alpha(x) = e^{-2x}$, $\xi^\pm(x, n) = (\pm 2n + 1)e^{-2x}$ and $P^\pm(x, n) = -ne^{-x}$. Consequently, $a^\pm(x, n) = ne^{-x} - (s + 1/2)/(2n \pm 1)$ and $b^\pm(x, n) = \mp e^{-x}$. Therefore, the corresponding ladder operators shifting n are then given by

$$\theta^\pm_n = ne^{-x} - \frac{s + 1/2}{2n \pm 1} \mp e^{-x}\frac{d}{dx}$$ (26)

as obtained by Huffaker and Dwivedi [11], after multiple variable changes, in order to use factorization type F. Finally, the Morse potential equation is factorized according to

$$(\theta^+_{s-1}\theta^-_s + n^2 - s^2)R_{s,n}(x) = 0$$ (27a)

$$\left(\theta^+_{n-1}\theta^-_n + \frac{1}{4} - \left(\frac{s + 1/2}{2n - 1}\right)^2\right)R_{s,n}(x) = 0$$ (27b)

and, conversely, from $\theta^-_{s+1,n+1}\theta^+_{s,n}$ as expected.

Algebraic Approach to the Pöschl–Teller Potential Wavefunctions

The Pöschl–Teller (PT) equation is

$$\widehat{PT}_{m,n}R_{m,n}(x) = 0$$ (28)

with

$$\hat{PT}_{m,n} = \frac{d^2}{dx^2} - \left(\frac{\rho^2(m+g)(m+g+1)}{\sin^2 \rho x} + \frac{\rho^2(m-g)(m-g+1)}{\cos^2 \rho x} \right) + E_n.$$

(29)

where $x = r - r_0$ and $E_n = 4\rho^2(m+n+1)^2$. Similar to the Morse potential case, Eq. (28) does not contain a first order derivative for which $\beta(x) = 0$, and $Q^{\mp}(x, m, n) = 0$. In consequence, for the $\eta_m^{\pm}$, creation and annihilation operators, with equivalent properties to those given in Eqs. (18), $b^{\mp}(x, m) = \mp 1$ and

$$\xi^{\pm}(x, m) = \pm 2\rho^2 \left(\frac{m+g+1/2 \pm 1/2}{\sin^2 \rho x} + \frac{m-g+1/2 \pm 1/2}{\cos^2 \rho x} \right)$$

and

$$P^{\pm}(x, m) = -\rho^2 \left(\frac{m+g+1/2 \pm 1/2}{\sin^2 \rho x} + \frac{m-g+1/2 \pm 1/2}{\cos^2 \rho x} \right).$$

That is,

$$a^{\pm}(x, m) = \rho(m+g+1/2 \pm 1/2) \cot \rho x - \rho(m-g+1/2 \pm 1/2) \tan \rho x$$

in order to obtain straightforwardly

$$\eta_m^{\pm} = \rho(m+g+1/2 \pm 1/2) \cos \rho x - \rho(m-g+1/2 \pm 1/2) \tan \rho x \mp \frac{d}{dx}$$

(30)

in good agreement with Barut et al. [12]. Therefore, one can factor the PT equation by means of

$$(\eta_{m-1}^{+} \eta_m^{-} + 4\rho^2 m^2 - E_n) R_{m,n}(x) = 0$$

(31a)

$$(\eta_{m+1}^{-} \eta_m^{+} + 4\rho^2 (m-1)^2 - E_n) R_{m,n}(x) = 0$$

(31b)

depending on the choice of $\eta_{m\mp1}^{\pm} \eta_m^{\mp}$.

Finally, in order to get the $\eta_n^{\pm}$ ladder operators acting over n, Eq. (28) is transformed to

$$\sin^2 \rho x \cos^2 \rho x \hat{PT}_{m,n} R_{m,n}(x) = 0.$$

(32)

In that case, $\beta^{\pm}(x, n) = 0$ and $\xi^{\pm}(x, n) = \mp 8\rho^2(m+n+1 \pm \frac{1}{2}) \sin^2 \rho x \cos^2 \rho x$ for which $Q^{\pm}(x, n) = 0$ and $P^{\pm}(x, n) = 4\rho^2(m+n+1) \sin \rho x \cos \rho x$. That is, $b^{\pm}(x, n) = \mp \sin \rho x \cos \rho x$ and

$$a^{\pm}(x, n) = -\frac{\rho}{2} \left(\frac{(m+g)(m+g+1) - (m-g)(m-g+1)}{2(m+n+1 \pm \frac{1}{2})} \right.$$

$$\left. + 2(m+n+1)(\cos^2 \rho x - \sin^2 \rho x) \right).$$

Thus, as the above cases, the $\eta_n^\pm$ ladder operators are then given by

$$\eta_n^\pm = -\frac{\rho}{2}\left(\frac{(m+g)(m+g+1)-(m-g)(m-g+1)}{2(m+n+1\pm\frac{1}{2})}\right.$$
$$\left.+2(m+n+1)(\cos^2 \rho x - \sin^2 \rho x)\right) \mp \sin \rho x \cos \rho x \frac{d}{dx}. \quad (33)$$

It is interesting to point out that the latter creation and annihilation operators, as far as we know, have not been published elsewhere. However, due to the fact that $\eta_n^\pm$ factorize Eq. (32) through

$$\left[\eta_{n+1}^-\eta_n^+ - \frac{\rho^2}{4}\left(\left(\frac{(m+g)(m+g+1)-(m-g)(m-g+1)}{2(m+n+3/2)}\right)^2\right.\right.$$
$$-2(m+g)(m+g+1)+4(m+n+1)(m+n+2)$$
$$\left.\left.-2(m-g)(m-g+1)\right)\right]R_{m,n}(x) = 0 \qquad (34a)$$

and

$$\left[\eta_{n-1}^+\eta_n^- - \frac{\rho^2}{4}\left(\left(\frac{(m+g)(m+g+1)-(m-g)(m-g+1)}{2(m+n+1/2)}\right)^2\right.\right.$$
$$+4(m+n+1)(m+n)-2(m+g)(m+g+1)$$
$$\left.\left.-2(m-g)(m-g+1)\right)\right]R_{m,n}(x) = 0, \qquad (34b)$$

these ladder operators also could be obtained using the standard factorization method.

Concluding Remarks

In the present work, an alternative procedure to the usual factorization method has been proposed. That approach is generalized in the sense that it can be also applied directly to second order differential equations containing first order derivatives. That is, although it is always possible to eliminate the first order derivative, by a change of variable or a change in the function, the proposed method avoids such kinds of unnecessary transformations. The method is simplified because it is reduced to solve the commutation relation between the operator related with the differential equation and a trial structure for the ladder operators under consideration. As exemplified, for creation and annihilation operators with linear structure on the derivative, the method applied to various useful potential wavefunctions gives rise, adequately, to previously accomplished equivalent results. Advantageously, the proposed procedure also permits determination of the two kinds of ladder operators that characterize any potential wavefunction by means of a single multiplicative factor in the original differential equation. Although finding such a multiplicative factor is not trivial, the price to pay is comparatively inexpensive vis à vis more cumbersome procedures that require the transformation of the equation

according to a structure *ad hoc* to the different classes and types specified by the factorization method. Thus, our approach is quite simple and direct when compared with other published methods. Also, it can be easily extended to obtain the algebraic representation of other potential wavefunctions as well as nonlinear structures for ladder operators.

Bibliography

[1] J. von Neumann, Math. Ann. **102**, 370 (1929).
[2] L. Infeld, Phys. Rev. **59**, 737 (1941).
[3] L. Infeld and E. Hull, Rev. Mod Phys. **23**, 21 (1951).
[4] J. O. Hirschfelder, J. Chem. Phys. **33**, 1462 (1960).
[5] R. M. Wilcox, J. Math. Phys. **8**, 962 (1967).
[6] J. Morales, J. J. Peña, M. Sánchez, and J. López-Bonilla, Int. J. Quant. Chem. S **25**, 155 (1991).
[7] J. Morales, J. J. Peña, and J. López-Bonilla, Phys. Rev. A, **45**, 4259 (1992).
[8] G. Arfken, *Mathematical Methods for Physicists* (Academic, London, 1970).
[9] Z. W. Salsburg, Am. J. Phys. **33**, 36 (1965).
[10] M. Badawi, N. Bessis, G. Bessis, and G. Hadinger, Phys. Rev. A **8**, 727 (1973).
[11] J. N. Huffaker and P. H. Dwivedi, J. Math. Phys. **16**, 862 (1975).
[12] A. O. Barut, A. Inomata, and R. Wilson, J. Phys. A Math. Gen. **20**, 4075, 4083 (1987).

Some Comments on
The Electrostatic Potential of a Molecule

EVERETT G. LARSON, MINGSHENG LI, and GUY C. LARSON

Department of Physics and Astronomy, Brigham Young University, Provo, Utah 84604

Abstract

In this article we discuss several principles and tools which should expedite description of the electrostatic potentials and electrostatic interactions of molecules, and show that these also lead to some rather remarkable results in the theory of the irreducible representations of the full rotation group $SO(3)$. First, by representing a molecule's charge-density matrix over a basis of atomic-like orbitals (on the various atoms), we observe that outside its charge distribution the molecule's electrostatic potential is *exactly* the same as if that charge distribution were merely a sum (and in the case of a finite orbital basis, this is a *finite* sum) of point multipoles on each of the atomic centers and line multipoles on the line segments joining each of those atomic centers. Possible methods of approximating the field of these line charges and line multipoles, as if they were due to point charges and point multipoles, are discussed. The calculation of the interaction of point multipoles of high order, as is necessary for this procedure to successfully calculate the interaction of arbitrarily oriented molecules, motivates our second topic. Here we present a differential operator which, when acting on the 3-dimensional delta function, produces the source density for a scalar field that is exactly an (l,m) multipole field. Using the Hermitian adjoint of this operator, we express the interaction of this (l,m) multipole with an external scalar field as the result of this differential operator acting on that external field at the location of this multipole source. Irreducible representation matrices of the full rotation group are then used, together with these relations, to simplify the interaction of two arbitrarily oriented multipoles of any orders. Finally, we use the representation of the Condon and Shortley "raising and lowering" relations on eigenstates of the z-component of angular momentum, in an orientation that is not aligned with its fundamental basis states, to generate recursion relations that allow simple calculations of the irreducible representation matrices of the full rotation group, $SO(3)$, and the special unitary group, $SU(2)$. From these recursion relations we display some useful symmetry properties of our parameterization of these matrices, that allow the entire matrix to be very simply generated from an explicit calculation of only about $1/8$ of its elements. © 1992 John Wiley & Sons, Inc.

Introduction

This article presents a number of concepts [1–28] which should prove useful in the efficient calculation of molecular electrostatic potentials and their associated intermolecular forces and intermolecular interaction energies.

The electrostatic potential of a molecule has been shown to be very useful in calculating the forces of this molecule, at medium-to-long distances, upon other molecules [29]. Forces at this range are very important in determining the kinematics of a molecule [2,29–33,59], which become important in many aspects of molecular physics, including biochemistry [2,7,31–42,59]. The knowledge of the electric field and the charge density [7,35–45,59] of such an electrostatic potential

is also useful in determining the chemical reactivity at the reactive sites of a molecule [7,31–46,59], which is very important in predicting drug activity [7,31–39,59].

Simple representations of the electrostatic potential of a molecule, in terms of point charges at the centers of the atoms [2,31–50], while providing simply calculated values[1] for the field, are not of high-quality; and different methods for computing these charges lead to different values for them [2,37,38,45–50]. Allowing for point multipoles, either on the atoms[7,37,38,42,51–53] or on the bonds [7,42,49,51], improves the numerical accuracy of the calculated potentials [37,38,51]; but generally diminishes the stability of the mathematical representation [38,51]; and experience has shown that, for the model to be stable and accurate (especially *globally* accurate), it must also include charges [7] (or preferably, charges and multipoles [7,51,42][2]) on the "bond axes" between the atoms.

Yet, how should we determine the proper positions and values of the charges and charge multipoles to be used? How can we most simply calculate the interaction energies of these electrostatic potentials? And, are there any auxiliary mathematical functions or relations that will expedite these calculations? In the course of this article we present information that we hope will be helpful in obtaining appropriate answers to these questions.

First, we present a parameterization of the electrostatic potential that is uniquely determined by the density matrix over the atomic-like orbitals that are the primitive basis orbitals for the molecular wavefunction. For Slater-type orbitals (STOs) [21,54,46,47,30,34,], such a description leads to an electrostatic potential which, for field points outside of a volume (of appropriate shape) which is large enough to [essentially[3]] contain the charge distribution, is [almost[3]] exactly represented by point charges and point multipoles, on the atomic centers, together with line charges and line multipoles on the line segments (i.e., bond lines) connecting each pair of atoms [3–9,54,55]. It is the field of the point multipoles on the atomic centers and the line charges along the bond lines which, when represented by charges on the atomic centers, leads to inconsistency and instability in the calculated values of the atomic charges used to represent the molecular electrostatic potential [38,42,29].[4] However, a representation of these line charges and line multipoles by point charges and point multipoles at suitably chosen points along the bond line [29] is adequate:

---

[1] Simple methods based solely on point charges invoke a calculation algorithm that leads to numerically unsatisfactory field values at far distances, since these field values are obtained as tiny differences of large, nearly equal numbers; also, because of the long range of the field of a point charge, all source points are needed to calculate the value of the field at any field point [51].

[2] Where more than one reference occurs in the same citation, we have endevored to have the references most relevant to that topic listed first.

[3] Here we are dealing with an asymptotic relationship that is exponentially convergent and is computationally useful for distances beyond about two bond lengths [7,42,46].

[4] For Gaussian-type orbitals (GTOs), the line charges and line multipoles become replaced by many point charges and point multipoles distributed along the bond lines [7,11,42,54–56]. A more efficient parameterization of the potential of the set of point charges and point multipoles along a given bond line may be a much smaller set of line charges and line multipoles, which parameterization is likely also much less affected by a change to a quite different (but still valid) choice of basis GTOs than is the set of point charges and point multipoles along the bond line.

and we show how such an optimally chosen set of point charges and point multipoles may be obtained.

Next, we show how we can use this representation of the molecular potential to calculate interaction energies* of a molecule with an external potential and with other molecules. Such calculations are expedited by a knowledge [8-10] of the source charge densities of the "solid spherical harmonic" point multipole potentials, and by a simple algorithm for quickly computing matrices of each irreducible representation "carried by" these spherical harmonics under the full rotation group SO(3).

We introduce a basis for such rapid computational algorithms for the irreducible representation matrices of SO(3) [and SU(2)] by invoking the Condon and Shortley "raising and lowering relations" [13,15-17,22] on spherical harmonics [13,14-17,22] in a Cartesian coordinate frame aligned in an arbitrary orientation [11,17,16,13] with respect to the frame of the originally chosen spherical harmonic basis. This procedure yields recursion relations among the matrix elements of any chosen irreducible representation, which are useful for constructing compact analytical formulas for each of these elements, and particularly suited for generating their numerical values for any given rotation. From this we also obtain a new three-term recursion relation [16] for generating all of the spherical harmonics of a given l-value from the $m = l$ spherical harmonic, without differentiation. Finally, using the symmetry properties of the recursion relations among the matrix elements of an irreducible representation, we derive some symmetry properties [16,13,58] of these irreducible representation matrices that allow the algebraic expressions for all of the elements to be obtained from explicit knowledge of slightly more than 1/8 of them.

The Electrostatic Potential of a Molecule Outside of Its Charge Distribution

The electrostatic potential, $V(\vec{r})$, due to the electronic* charge density of a molecule, may be written as [12]

$$V(\vec{r}_1) = \int \frac{\rho(\vec{r}_2)}{r_{12}} d^3\vec{r}_2 \qquad (1)$$

where the charge density $\rho(\vec{r})$ may be expressed as a bilinear form over the atomic orbital basis $\{\chi_J^i\}$ as follows [2-6]:

---

* Such calculations of the interaction energies neglect the effects of polarization [29,52-53] (unless the input information has already taken that into account), but nevertheless are valid in the weak field limit, providing that the source of the external potential (which here may be the charge density of one molecule) does not significantly penetrate the appropriate volume around the other molecule

* Here we are primarily concerned with representing the charge density of the electrons, and we are adopting the sign convention in which the electronic charge density is negative and the electronic charge density matrix is negative definite. Of course, the negative electronic charge density must be complemented by the positive charges on the nuclei, reducing the ultimate range of the total potential for neutral molecules to at most that of a dipole [1]

$$\rho(\vec{r}) = \sum_{\mu \in A} \sum_{\nu \in B} \chi_\mu^A(\vec{r}) P_{\mu\nu} (\chi_\nu^B(\vec{r}))^* \tag{2}$$

Here, A and B each label atoms, μ labels an atomic orbital on atom A, and ν labels an atomic orbital on atom B. The expansion coefficients $\{P_{\mu\nu}\}$ form the electronic charge density matrix of the molecule in this basis of atomic orbitals. The charge density, $\rho(\vec{r})$, may be decomposed into a sum of intra-atomic parts $\{\rho_{at}^A(\vec{r})\}$ and pairwise interatomic parts $\{\rho_{ov}^{A,B}(\vec{r})\}$ as follows

$$\rho(\vec{r}) = \sum_A \rho_{at}^A(\vec{r}) + \sum_A \sum_{B>A} \rho_{ov}^{A,B}(\vec{r}) \tag{3}$$

with [3-5]

$$\rho_{at}^A(\vec{r}) = \sum_{\mu \in A} \sum_{\mu' \in A} \chi_\mu^A(\vec{r}) P_{\mu\mu'}(\chi_{\mu'}^A(\vec{r}))^*$$

$$\rho_{ov}^{A,B} = \sum_{\mu \in A} \sum_{\nu \in B} [\chi_\mu^A(\vec{r}) P_{\mu\nu}(\chi_\nu^B(\vec{r}))^* + \chi_\nu^B(\vec{r}) P_{\nu\mu}(\chi_\mu^A(\vec{r}))^*]$$

$$= 2 \operatorname{Re}\left\{ \sum_{\mu \in A} \sum_{\nu \in B} \chi_\mu^A(\vec{r}) P_{\mu\nu}(\chi_\nu^B(\vec{r}))^* \right\} \tag{4}$$

Note that the intra-atomic piece, $\rho_{at}^A(\vec{r})$, is expressed solely in terms of the orbitals on atom A, whereas the interatomic piece, $\rho_{ov}^{A,B}(\vec{r})$, is expressed using terms involving one atomic orbital on A, and another atomic orbital on B. Thus, $\rho_{at}^A(\vec{r})$ represents an atomic charge density on atom A, and $\rho_{ov}^{A,B}(\vec{r})$ represents the "overlap charge" connecting atoms A and B. We shall find that, for field points everywhere outside of a sphere[7] (centered on the appropriate atom) large enough to contain[8] that part of the charge distribution, each intra-atomic charge-density term, $\rho_{at}^A(\vec{r})$, produces an electrostatic potential that is exactly expressible in terms of a point charge and a (small) finite number of point multipoles centered on atom A [7]. However, the interatomic part, $\rho_{ov}^{A,B}(\vec{r})$, produces an electrostatic potential that is best expressible in terms of a line charge and a (small) finite number of line multipoles along the line segment joining the centers of atoms A and B [3-5,8-11,7].

The Atom-Centered Charge Density and Its Electrostatic Potential

The electrostatic potential, V_{at}^A, due to the charge density, $\rho^A(\vec{r})$, that involves only the atomic orbitals on atom A, may be written

$$V_{at}^A(\vec{r}_1) = \int \frac{\rho_{at}^A(\vec{r}_2)}{r_{12}} d^3\vec{r}_2$$

$$= \int \frac{\rho_{at}^A(\vec{r}_2)}{r_{12}} (r_2)^2 dr_2 \sin\theta_2 d\theta_2 d\varphi_2 \tag{5}$$

---

[7] Note that for $\rho_{ov}^{A,B}(\vec{r})$, this region generalizes to a prolate ellipsoid (i.e., the region formed by spinning an ellipse about its major axis) with foci on A and B.

[8] See footnotes 9 and 3.

and we may represent $1/r_{12}$ by [12-16,11]

$$\frac{1}{r_{12}} = \sum_{l=0}^{\infty} \frac{4\pi}{2l+1} \frac{(r_<)^l}{(r_>)^{l+1}} \sum_{m=-l}^{l} Y_{lm}(\theta_1,\varphi_1)(Y_{lm}(\theta_2,\varphi_2))^* \qquad (6)$$

where the $\{Y_{lm}(\theta,\varphi)\}$ are the standard spherical harmonics [12-17]. Substituting Eq. (6) into Eq. (5), we find that for[9] $r_1 > \max(r_2)$—i.e., for $\vec{r}_1$ outside of the smallest sphere (centered at A) containing[10] the charge distribution—this yields an expansion of the atomic charge potential $V_{at}^A(\vec{r}_1)$ in the form

$$V_{at}^A(\vec{r}_1) = \sum_{l=0}^{\infty} \frac{1}{(r_1)^{l+1}} \sum_{m=-l}^{l} q_{l,m} \frac{4\pi}{2l+1} Y_{lm}(\theta_1,\varphi_1) \qquad (7)$$

We recognize this as a point multipole expansion [7,12,14] of this electrostatic potential about the center of atom A, with $q_{l,m}$ as the value of the (l,m)-multipole moment.

The Interatomic Overlap Charge Density and Its Electrostatic Potential

The electrostatic potential, $V_{ov}^{A,B}$, due to the interatomic overlap charge density, $\rho_{ov}^{A,B}(\vec{r})$, of the pair of atoms, A and B, may be written [18,3-5]

$$V_{ov}^{A,B}(\vec{r}_1) = \int \frac{\rho_{ov}^{A,B}(\vec{r}_2)}{r_{12}} d^3\vec{r}_2$$

$$= \int \frac{\rho_{ov}^{A,B}(\vec{r}_2)}{r_{12}} \frac{R^3}{8} (\xi_2^2 - \eta_2^2) d\xi_2 d\eta_2 d\varphi_2 \qquad (8)$$

where $\xi \equiv (r_A + r_B)/R$, $\eta \equiv (r_A - r_B)/R$, and φ [the azimuthal angle about the bond axis] are prolate ellipsoidal[11] coordinates [3-5,18,19], $(1 \le \xi < \infty$, $-1 \le \eta \le 1, 0 \le \varphi < 2\pi)$, and R is the internuclear distance. We can represent $1/r_{12}$ by[12] the Neumann expansion [18,3,5]

$$\frac{1}{r_{12}} = \frac{2}{R} \sum_{m=-\infty}^{\infty} \sum_{l=|m|}^{\infty} (-1)^m (2l+1)\left(\frac{(l-|m|)!}{(l+|m|)!}\right)^2$$

$$\times P_l^{|m|}(\xi_<) Q_l^{|m|}(\xi_>) P_l^{|m|}(\eta_1) P_l^{|m|}(\eta_2) e^{im(\varphi_1-\varphi_2)} \qquad (9)$$

For $\xi_1 > \max(\xi_2)$—i.e., for $\vec{r}_1$ outside of the smallest ellipsoid (with foci A and B)

---

[9] What we mean here by $\max(r_2)$ is the lowest permissible value of the upper limit of r_2 to which the integral in Eq. (5) needs to be taken (to obtain the desired accuracy of the result). How exactly we interpret this influences how exactly we can interpret many of our subsequent statements [e.g., Eq. (7)] concerning $V_{at}^A(\vec{r})$ and $\rho_{at}^A(\vec{r})$.

[10] See footnotes 9 and 3.

[11] We prefer the term "prolate ellipsoidal" to the more indefinite term "prolate spheroidal" used by Abramowitz and Stegun [19] and several other authors.

[12] We are using the Abramowitz and Stegun [12,19,20] definitions of the P_l^m and Q_l^m functions, which, for argument $(-1 \le u \le 1)$, differ by a factor of $(-1)^m$ from the standard definitions used by many other authors [13-15].

containing[11] the charge distribution—this yields an expansion of the overlap charge potential $V_{ov}^{AB}(\vec{r}_1)$ in the form

$$V_{ov}^{AB}(\vec{r}_1) = \sum_{m} \sum_{l \geq |m|} a_{lm} P_l^{|m|}(\eta_1) Q_l^{|m|}(\xi_1) e^{im\varphi_1} \tag{10}$$

The part of this potential belonging to a given m-value has, as its source, the singular volume charge density [8,9,3,1]

$$\rho_m(\vec{r}) = \lambda_m(\eta)(-)^m \left(\frac{\partial}{\partial x} + i\,\text{sgn}(m) \frac{\partial}{\partial y} \right)^{|m|} [\delta(x)\delta(y)] \tag{11}$$

where the δ's are Dirac delta functions and $\lambda_m(\eta)$ is (by definition) the line (m,m)-pole density[14] [i.e., the (m,m)-multipole moment per unit length] at the point on the bond axis (the z-axis) parametrized by ($\xi = 1$, $-1 \leq \eta \leq 1$) with

$$\lambda_m(\eta) = \frac{(-R)^{|m|}}{2^{|m|+1}} (1 - \eta^2)^{|m|/2} \sum_{l \geq |m|} a_{lm} P_l^{|m|}(\eta) \tag{12}$$

where a_{lm} is the same coefficient as that which appears in Eq. (10).

Thus, outside of the charge distribution, the electrostatic potential due to the (distributed) charge density of a molecule may be represented as if it were produced by the following sources:

1. Point charges and point multipoles on each atom. (These represent the intra-atomic terms in the charge density [18,3–5].)

2. Line charges and line multipoles along each of the line segments joining two nuclei. (These represent the interatomic terms (i.e., the "overlap" terms) in the charge density [18,3–5].)

For a given finite atomic orbital basis, the intra-atomic terms in the charge density lead to a potential that, outside the charge distribution, is expressible in terms of a point charge and a (small) finite number of point multipoles on each atom [7]. For this same basis, the interatomic terms in the charge density lead to a potential that, outside of the charge distribution, is exactly expressible as that due to line charges and line multipoles of order less than or equal to some (small) finite m_{max} [5]. This point charge, point multipole, line charge, line multipole representation of the potential is uniquely determined by the representation of the charge density as a bilinear form over the given atomic orbital basis [2–5,51]. Any valid simpler representation [29,51] of the potential is appropriately obtainable as a canonical reduction of the potential due to these point and line sources.

Possible ways to reduce the above representation[15]:

---

[11] See footnotes 9 and 3.

[14] For STO bases, or any basis with the correct asymptotic behavior at the nucleus and at infinity, λ_m is a continuous function of η. However, for a Gaussian orbital basis, this "line-multipole density" becomes a set of point multipoles, "strewn" over the line segment joining atoms A and B [7,11,42,54–57], so that $\lambda_m(\eta)$ becomes a linear combination of delta functions.

[15] Gaussian orbitals do not produce a line-charge or line multipoles but, rather, produce point charges and point multipoles along the "bond" line [7,11,42,54–57]. Still, reduction of their number, in these ways, may be appropriate.

1. Replace the line charge and line multipole potentials for the pair of atoms A and B (from the corresponding interatomic terms in the charge density) by a point multipole expansion about e.g. the center of the line segment joining the nuclei of atoms A and B (i.e., about the center of the "bond") [7.29]. (This is mathematically simple and fairly rapidly converging for most field points of interest.)

2. "Sever" the line charge and line multipole densities joining atoms A and B at e.g. the point equidistant from these atoms, and express the potential of each of these two "pieces" as a point multipole expansion about its corresponding atom [7.29]. (This leads to a canonical representation of the total electrostatic potential solely in terms of point multipoles centered on each atom [7.29]. However, it is less rapidly converging than the procedure outlined in (1) above, and the calculated values of the "atomic" charges and multipoles can be overly sensitive to small changes in the wavefunction [7.29] if the bond is asymmetrical and there is a large absolute value of the effective line charge density at or in the vicinity of the midpoint of the "bond".)

3. Replace the line charge density joining atoms A and B by a point charge (at the center of charge) and its complement [7.29]. This complement thus contains no monopole component and no dipole component. It therefore can be replaced by an $m = 0$ point quadrupole (aligned along the bond line) and its complement, with the quadrupole centered at the particular point on the bond line such that its complement contains no poles of order less than or equal to that of an octopole. One may represent this latter complement by a point hexadekapole centered at the point such that its complement contains no pole of order less than or equal to 32; and the procedure may be continued, with all generated point multipoles lying on the bond line and being aligned in the direction of the bond line. Analogous procedures are possible for each line multipole density joining atoms A and B. (This should be the most rapidly convergent method of these that we have suggested.)

Methods (1) and (3) are appropriate when atoms A and B are close neighbors, since they require fewer terms for a given accuracy of the field values. When atoms A and B are far apart, the line source being represented is of very small magnitude, so method (2) may be preferred, since it does not place charges and multipoles anywhere except on the atomic centers.

Point Multipole Potentials, Their Source Charge Distributions, and Their Interaction Energies

The above description for the electrostatic potential of a molecule, in terms of point charges and point multipoles on the atomic centers and line charges and line multipoles along the "bond" axes, is accurate and compact, leading to simple evaluations of the potential in the region outside of the sources. However, the interaction energy of two line multipoles of arbitrary orientation is presently awkward to calculate. Thus, for the purpose of calculating interaction energies of molecules, it is presently appropriate to re-express the molecular electrostatic potential of at least one of the two interacting molecules solely in terms of point charges and point multipoles centered on appropriate centers, in a manner akin to the reductions

suggested in the previous section. When this is accomplished. the interaction energy of two molecules may be calculated using a procedure based upon the following discussion.[16]

The Charge Distribution of a Point Multipole Potential

The electrostatic potential of a charge distribution $\rho(\vec{r})$ may be written [12,1,5]

$$\psi(\vec{r}) = \int G(\vec{r}, \vec{r}')\rho(\vec{r}')d^3\vec{r}' \qquad (13)$$

where the Green's function. $G(\vec{r}, \vec{r}')$. has the representation [12-16]

$$G(\vec{r}, \vec{r}') = \frac{1}{|\vec{r} - \vec{r}'|}$$

$$= \sum_{l=0}^{\infty} \sum_{m=-l}^{l} \frac{4\pi}{2l + 1} Y_{l,m}(\theta, \varphi) \frac{(r_<)^l}{(r_>)^{l+1}} (Y_{l,m}(\theta', \varphi'))^* \qquad (14)$$

From this, one can show that one source charge distribution that will produce the potential [11]

$$\psi_m^{(l)}(\vec{r}) = \sqrt{\frac{4\pi}{2l + 1}} Y_{l,m}(\theta, \varphi) \frac{1}{r^{l+1}} \qquad (15)$$

may be written [8,9]

$$\rho_m^{(l)}(\vec{r}) = \mathcal{L}_m^{(l)}\delta^3(\vec{r} - \vec{a}) \qquad (16)$$

where

$$\mathcal{L}_m^{(l)}$$

$$= \begin{cases} (-)^l \sqrt{\dfrac{1}{(l - m)!(l + m)!}} \left(\dfrac{\partial}{\partial z}\right)^{l-m}\left[-\dfrac{\partial}{\partial x} - i\dfrac{\partial}{\partial y}\right]^m & \text{for } 0 \leq m \leq l; \\[3ex] (-)^l \sqrt{\dfrac{1}{(l - |m|)!(l + |m|)!}} \left(\dfrac{\partial}{\partial z}\right)^{l-|m|}\left[\dfrac{\partial}{\partial x} - i\dfrac{\partial}{\partial y}\right]^{|m|} & \text{for } -l \leq m \leq 0 \end{cases}$$

$$(17)$$

We note that $(\mathcal{L}_m^{(l)})^\dagger$. the Hermitian adjoint of the operator $\mathcal{L}_m^{(l)}$. may be written

---

[16] Follow the appropriate footnotes in this discussion to be appraised of some of the relevant applications of this approach. as well as its limitations.

$(\mathcal{L}_m^{(l)})^+$

$$= \left\{ \begin{array}{ll} \dfrac{1}{(l-m)!(l+m)!}\left(\dfrac{\partial}{\partial z}\right)^{l-m}\left[-\dfrac{\partial}{\partial x}+i\dfrac{\partial}{\partial y}\right]^m & \text{for } 0 \le m \le l; \\[4mm] \dfrac{1}{(l-|m|)!(l+|m|)!}\left(\dfrac{\partial}{\partial z}\right)^{l-|m|}\left[\dfrac{\partial}{\partial x}+i\dfrac{\partial}{\partial y}\right]^{|m|} & \text{for } -l \le m \le 0 \end{array}\right.$$

(18)

Expressions for the generating operators for the source charge distributions of the corresponding "nonorthogonal" Cartesian multipole potentials are of an even simpler form [8].[17]

The Interaction Energy of a Point Multipole With an External Potential

The (complex) energy of interaction of the (complex) multipole potential $\psi_m^{(l)}(\vec{r})$ [produced by the point source charge density $\rho_m^{(l)}(\vec{r})$] and a (complex) external potential $\Phi(\vec{r})$ may be written [29]

$$E^{(\psi_m^{(l)},\Phi)} \equiv \int (\rho_m^{(l)}(\vec{r}))^*\Phi(\vec{r})d^3r$$

$$= \int (\mathcal{L}_m^{(l)}\delta^3(\vec{r}-\vec{o}))^*\Phi(\vec{r})d^3r$$

$$= \int \delta^3(\vec{r}-\vec{o})(\mathcal{L}_m^{(l)})^+\Phi(\vec{r})d^3r$$

$$= ((\mathcal{L}_m^{(l)})^+\Phi(\vec{r}))_{\vec{r}=\vec{o}} \tag{19}$$

(In any physical situation, the total interaction energy will, of course, be real.)

It is easy to show that if we translate the potential $\psi_m^{(l)}(\vec{r})$ from the origin $\vec{r}=\vec{o}$ to the origin $\vec{r}=\vec{r}_0$, $\delta^3(\vec{r}-\vec{o})$ becomes replaced by $\delta^3(\vec{r}-\vec{r}_0)$ and we have the generalization [15]

$$E^{(\psi_m^{(l)},\Phi)} = ((\mathcal{L}_m^{(l)})^+\Phi(\vec{r}))_{\vec{r}=\vec{r}_0} \tag{20}$$

Also, providing the orientation of the Cartesian axes with respect to the axes of definition of the polar angles (θ, φ) is preserved, our differential operators may be expressed in terms of spherical coordinates with respect to any origin[18] as [15]

$$\frac{\partial}{\partial z} = \cos\theta\frac{\partial}{\partial r} - \frac{\sin\theta}{r}\frac{\partial}{\partial\theta}$$

$$-\frac{\partial}{\partial x}+i\frac{\partial}{\partial y} = -e^{i\varphi}\sin\theta\frac{\partial}{\partial r} - e^{i\varphi}\frac{\cos\theta}{r}\frac{\partial}{\partial\theta} + \frac{ie^{i\varphi}}{r\sin\theta}\frac{\partial}{\partial\varphi}$$

$$\frac{\partial}{\partial x}+i\frac{\partial}{\partial y} = e^{i\varphi}\sin\theta\frac{\partial}{\partial r} + e^{i\varphi}\frac{\cos\theta}{r}\frac{\partial}{\partial\theta} + \frac{ie^{i\varphi}}{r\sin\theta}\frac{\partial}{\partial\varphi} \tag{21}$$

---

[17] Such "nonorthogonal" Cartesian multipole potentials occur in the far-field representations [57,56,42] of the fields of charge distributions arising from molecular charge densities represented in terms of Cartesian Gaussian orbitals [57,56,42].

[18] Transformation to other coordinate systems, such as prolate ellipsoidal [19,18] (known in these references as "prolate spheroidal"), is also straightforward and can expedite such things as the calculation of the interaction energy of our point multipole with a line multipole.

Simplifications occur if the Cartesian axes defining the spherical coordinate system for the potential $\Phi(\vec{r})$ are parallel[19] to the Cartesian axes defining the spherical coordinate system for the multipole potential $\psi_m^l(\vec{r})$, for then we may choose the spherical coordinate system representing our differential operators to be the spherical coordinate system natural to our potential $\Phi(\vec{r})$.

To illustrate this, we might choose $\Phi(\vec{r})$ to be an untranslated point multipole potential $\Psi_{m'}^{(l')}(\vec{r})$, and let $(r_o, \theta_o, \varphi_o)$ be the spherical coordinates of $\vec{r}_o$ [the center of the translated $\psi_m^{(l)}(\vec{r})$, potential] in the coordinate system natural to $\Phi(\vec{r})$. In this case, the mathematical representation of the interaction energy, derived from the above procedure, is exemplified by the following expressions,[20] valid for $l = l' = 2$ with $m = m' = \pm 2$ and $-m = m' = \pm 2$, respectively.

$$(E^{(\psi_m^{(l)}, \Psi_m^{(l')})})_{l'\,l''\,2}^{m\;m'\cdots} = \frac{9 + 20\cos 2\theta_o + 35\cos 4\theta_o}{64 r_o^5} \tag{22a}$$

$$(E^{(\psi_m^{(l)}, \Psi_m^{(l')})})_{l'\,l''\,2}^{m\;m'} = \frac{35 e^{\pm i 4\varphi_o}\sin^4\theta_o}{8 r_o^5} \tag{22b}$$

[where the $\pm$ signs are correlated in Eq. (22b)].

When the interacting potential, $\Phi(\vec{r})$, does not have its Cartesian axes aligned parallel to those of the multipole potential $\psi_m^{(l)}(\vec{r})$, it may be appropriate that we express $\psi_m^{(l)}(\vec{r})$ in terms of potentials aligned to the coordinate system of $\Phi(\vec{r})$ via the relations [17,16,13,11]

$$\psi_m^{(l)}(\vec{r}) = \sum_{m'\,l} \psi_{m'}^{u(l)}(\vec{r}) D_{m',m}^{(l)}(\hat{R}) \tag{23}$$

[The corresponding source charge densities, $\rho_m^{(l)}(\vec{r})$ and $\{\rho_{m'}^{u(l)}(\vec{r})\}$, are related in exactly the same way.] Here $\{\psi_{m'}^{u(l)}(\vec{r})\}$ is the set of multipole potentials whose Cartesian axes are aligned parallel to those of $\Phi(\vec{r})$. $\hat{R}$ is the operator which rotates the Cartesian axes of $\Phi(\vec{r})$ to be parallel with those of $\psi_m^{(l)}(\vec{r})$, and $D^{(l)}(\hat{R})$ is the irreducible representation matrix, of the full rotation group, appropriate to this rotation. | This is the same irreducible representation matrix for which the substitution of $Y_{lm}(\theta, \varphi)$ for $\psi_m^{(l)}(\vec{r})$ and $Y_{lm'}(\theta', \varphi')$ for $\psi_{m'}^{u(l)}(\vec{r})$ in Eq. (23) yields a true relation. [Here (θ, φ) and (θ', φ') are the spherical polar angles with respect to the Cartesian axes of $\psi_m^{(l)}\vec{r}$ and of $\Phi(\vec{r})$, respectively.] | Because their natural Cartesian coordinate systems are mutually parallel, the interaction energies between each member of the basis set of potentials, $\{\psi_{m'}^{u(l)}(\vec{r})\}$, and the external potential, $\Phi(\vec{r})$,

[19] Such "parallel axis" representations are very common in the representation of the atomic orbital basis of molecules, and propagate to the representation of the charge distributions appearing in the two-electron integrals of the $1/r_{12}$ interaction. Thus, this simplification is valid and relevant to the multipole interaction representation of these integrals under conditions in which the interpenetration of the two relevant charge regions may be neglected [3–5].

[20] We have obtained expressions for all (l, m, l', m') with l and l' in the range 0 through 5, using the symbolic manipulation facility of the *Mathematica* program [25]. Some of these results are reported elsewhere [24].

may be easily calculated in the (θ', φ') coordinate system, using our former procedure. This feature expedites the evaluation of the interaction energy between $\psi_m^{(l)}(\vec{r})$ and $\Phi(\vec{r})$ (whose natural coordinate systems are here not mutually parallel) via the principle of linear superposition.

It is also often convenient to represent the orientation of the axes of each of the potentials, $\psi_m^{(l)}(\vec{r})$ and $\Phi(\vec{r})$, with respect to a laboratory coordinate system,[21] via the rotation operators, $\hat{R}^{(\psi_m^{(l)})}$ and $\hat{R}^{(\Phi)}$, which rotate the laboratory coordinate system, about its origin, into the coordinate system parallel to that of $\psi_m^{(l)}$, and of Φ, respectively [17,16,13,11]. Now, consider Φ itself to be a point multipole potential, $\Psi_m^{(l')}$, with its own orientation for its Cartesian axes, and let $\hat{R}^{(+)}$ be the operator that rotates the laboratory coordinate system (about its origin) such as to make its new z-axis parallel to the line through the centers of $\psi_m^{(l)}$ and $\Psi_m^{(l')}$. Then we may define the sets of potentials $\{\hat{\psi}_m^{(l)}\}$ and $\{\hat{\Psi}_m^{(l')}\}$, having the same centers as $\psi_m^{(l)}$ and $\Psi_m^{(l')}$, respectively, but aligned with their common z-axis through the centers of $\psi_m^{(l)}$ and $\Psi_m^{(l')}$, as follows:

$$\hat{\psi}_m^{(l)}(\vec{r}) = \hat{R}^{(+)}(\hat{R}^{(\psi_m^{(l)})})^{-1}\psi_m^{(l)}(\vec{r}) = \sum_{m''}^{l} \psi_{m''}^{(l)}(\vec{r})D_{m'',m}^{(l)}(\hat{R}^{(+)}(\hat{R}^{(\psi_m^{(l)})})^{-1}) \quad (24a)$$

$$\hat{\Psi}_m^{(l')}(\vec{r}) = \hat{R}^{(+)}(\hat{R}^{(\Psi_m^{(l')})})^{-1}\Psi_m^{(l')}(\vec{r})$$

$$= \sum_{m''}^{l} \Psi_{m''}^{(l')}(\vec{r})D_{m'',m'}^{(l)}(\hat{R}^{(+)}(\hat{R}^{(\Psi_m^{(l')})})^{-1}) \quad (24b)$$

Let $\mathcal{E}_{m,m'}^{(l,l')}(r_{12})$ be the interaction energy between the aligned multipoles, $\hat{\psi}_m^{(l)}(\vec{r})$ and $\hat{\Psi}_m^{(l')}(\vec{r})$. It is easy to show that

$$\mathcal{E}_{m,m'}^{(l,l')}(r_{12}) \equiv \int (\hat{\rho}_m^{(l)}(\vec{r}))^*\hat{\Psi}_{m'}^{(l')}(\vec{r})d^3\vec{r}$$

$$= \mathcal{E}_{m,m'}^{(l,l')}(r_{12})\delta_{m,m'} \quad (25a)$$

and we have just recently succeeded in proving[22] that

$$\mathcal{E}_{m,m'}^{(l,l')}(r_{12}) = (-)^{l+m}\left[\frac{(l'+l)!}{\sqrt{(l'-m)!(l'+m)!(l-m)!(l+m)!}}\right]\left(\frac{1}{r_{12}}\right)^{l+l'+1} \quad (25b)$$

Here, r_{12} is the distance between the multipoles, and l_l is the l-value of the potential centered at the point having the larger value of the z-coordinate in the coordinate system obtained by rotating the laboratory coordinate system about its origin by the operator $\hat{R}^{(+)}$. These interaction energies are zero unless $m' = m$, making the

[21] This is particularly relevant if one is following the classical dynamical interaction of molecules, represented (in part) by such electrostatic multipoles, in a laboratory coordinate system.

[22] After one of us (M.L.) had verified this by explicit evaluation via Eqs. (18)-(21) [through their analogs of Eqs. (22), with $\theta_{12} = 0$] for all integer l and l' values in the range 0 through 5 (and their allowed values of m), another (G.C.L.) managed to finally prove it for all integer l and l' (and their allowed m).

rectangular matrix, $\mathcal{E}^{(l,l')}(r_{12})$, defined below, zero except for its diagonal, symmetrically placed, maximal square submatrix.

Let $\mathcal{E}^{(l,l')}(r_{12})$ be the $(2l + 1)$ by $(2l' + 1)$ matrix whose (m,m') element is $\mathcal{E}^{(l,l')}_{m,m'}(r_{12})$, and let $\mathbf{D}^{(l)}(R)$ be the $(2l + 1)$ by $(2l + 1)$ matrix whose (m'',m) element is $D^{(l)}_{m'',m}(R)$. Then, it is easy to show that the interaction energy between the original point multipole, $\psi^{(l)}_m(\vec{r})$, and the point multipole, $\Psi^{(l')}_{m'}(\vec{r})$, is given by[23]

$$E^{(\psi^{(l)}_m, \Psi^{(l')}_{m'})}(r_{12})$$

$$= [(\mathbf{D}^{(l)}(R^{(\psi^{(l)}_m)}))^{\dagger}\mathbf{D}^{(l)}(R^{(\dagger)})\mathcal{E}^{(l,l')}(r_{12})(\mathbf{D}^{(l')}(R^{(\dagger)}))^{\dagger}\mathbf{D}^{(l')}(R^{(\Psi^{(l')}_{m'})})]_{m,m'} \quad (26)$$

The $\mathcal{E}$ matrices are simply calculated using Eq. (25). All of the heavy orientational information is contained in the $\mathbf{D}$ matrices. Symbolic programming [23] can algebraically simplify the final expression and make it reasonably easy to compute for values of l and l' less than or equal to 6. Most quantum chemical calculations can be virtually exactly managed with l values less than or equal to 4, so this represents a feasible route toward calculating the interaction energies of molecules of moderate size. However, satisfactory implementation of this procedure, for the evaluation of intermolecular forces in a dynamical setting, requires evaluating spatial derivatives of such interaction energies for many different intermolecular conformations. This is often best expedited by simple and rapid numerical calculation of the $\mathbf{D}$ matrices (and their derivatives) for many different orientations. The foundations of a method for accomplishing such calculations of these $\mathbf{D}$ matrices are presented in the following sections.

Angular Momentum Operators, Rotations, Euler Angles, Spherical Harmonics, Pauli Spinors, and the Irreducible Representations of the Full Rotation Group [Also of SU(2)]

Starting with the quantum mechanical definition of the position operator, $\vec{r} = \vec{r}$, and the momentum operator, $\vec{p} = (\hbar/i)\vec{\nabla}$, the quantum mechanical angular momentum operator, $\vec{L}$, is derived to be: [15,17]

$$\vec{L} = \vec{r} \times \vec{p} = \frac{\hbar}{i}(\vec{r} \times \vec{\nabla}) \quad (27)$$

(Hereafter we shall take $\hbar = 1$.) From the commutation relations between the components of $\vec{r}$ and the components of $\vec{p}$ one derives the commutation relations among the components of $\vec{L}$ that may be summarized as $\vec{L} \times \vec{L} = i\vec{L}$. From these commutation relations on $\vec{L}$ one may derive the Condon and Shortley relations [22,17,15,13]:

[23] The careful reader will note that the left-hand side of Eq. (26) [upon substituting the definition from Eq. (19)] explicitly shows the necessary transformation properties required by the laws of physics (e.g., it is invariant under any global rotation or translation), whereas the right-hand side is expressed in terms of coordinate-dependent parameters and, therefore, does not display these transformation properties explicitly. (However, the reader is invited to test that it does in fact transform correctly. As an example, we point out that interchanging ψ^{l}_m and $\Psi^{l'}_{m'}$, which is equivalent to the transformation $(l \leftrightarrow l')(m \leftrightarrow m')$, transforms each side of Eq. (26) into its complex conjugate.

$$\hat{L}_z | l, m \rangle = m | l, m \rangle \tag{28a}$$

$$\hat{L}_\pm | l, m \rangle = \sqrt{l(l + 1) - m(m \pm 1)} | l, m \pm 1 \rangle \tag{28b,c}$$

Here $\hat{L}_\pm = \hat{L}_x \pm \hat{L}_y$, and $\{ | l, m \rangle \}$ is any set of states or functions that satisfy these relations (e.g., the set of spherical harmonics $\{ Y_{l,m}(\theta, \varphi) \}$ belonging to a given l-value).

Whereas uniqueness of the scalar wavefunction requires l to be a nonnegative integer, the formal algebra that derives the Condon and Shortley relations requires only that $2l$ be a nonnegative integer. When we allow for the possibility that "l" is a half-integer, we denote $\hat{L}$ as $\hat{J}$ and l as j to remind us that, when j is a half-integer, every component of $\hat{J}$ has no single-valued scalar eigenfunctions [23]. The Condon and Shortley relations are uniquely determined by the algebra, to within multiplicative phase factors on the results of $\hat{L}_\pm$, from which the corresponding unimodular phase factors on the results of $\hat{L}_\pm$ are determined [17]. The Condon and Shortley convention sets all of these phase factors equal to unity [17].

Now the $\hat{R}(\phi, \hat{n})$ rotation operator for a counterclockwise rotation by an angle ϕ about an axis labeled by its unit vector, $\hat{n}$, when acting on an entity ψ upon which $\hat{J}$ can operate, may be represented [17] as

$$\hat{R}(\phi, \hat{n}) | \psi \rangle = \exp(-i\phi \hat{n} \cdot \hat{J}) | \psi \rangle \tag{29}$$

From this and the Condon and Shortley relations, we derive that [17]

$$\hat{R}(\phi, \hat{n}) | v_\uparrow, v_\downarrow \rangle = | v_\uparrow, v_\downarrow \rangle \begin{bmatrix} a & b \\ -b^* & a^* \end{bmatrix} \tag{30}$$

where $a = \cos(\phi/2) - in_z \sin(\phi/2)$ and $b = -(n_y + in_x) \sin(\phi/2)$.

Here $\{ v_\uparrow, v_\downarrow \}$ are the Pauli spinors (often denoted by $\{ \alpha, \beta \}$), and the matrix involving $\{ a, b, -b^*, a^* \}$ is the corresponding element of the special unitary group, SU(2). The elements $\{ a, b, -b^*, a^* \}$ play a dominant role in describing the irreducible representations of SU(2) and SO(3) (the full rotation group), and may be expressed as shown above [17], or in any of several other ways that parametrize the rotations [17,11,13].

In particular, Rotations may also be parameterized by the Euler angles $\{ \alpha, \beta, \gamma \}$, which have each of the following two interpretations.

Body-fixed interpretation [11,58]: (1) Rotate the system counterclockwise about the body-fixed z-axis by the angle α. (2) Then, rotate the system counterclockwise about the present orientation of the body-fixed y-axis by angle β. (3) Finally, rotate the system counterclockwise about the present orientation of the body-fixed z-axis by the angle γ.

Space-fixed interpretation [17,58]: (1) Rotate the system counterclockwise about the space-fixed z-axis by γ. (2) Then, rotate the system counterclockwise about the space-fixed y-axis by β. (3) Finally, rotate the system counterclockwise about the space-fixed z-axis by α.

In either of these representations, the above-introduced parameters, a and b, take on the values [17]:

$$a = e^{-i(\alpha/2)}\cos\frac{\beta}{2}e^{-i(\gamma/2)}, \quad b = e^{-i(\alpha/2)}\left(-\sin\frac{\beta}{2}\right)e^{i(\gamma/2)} \qquad (31a,b)$$

We now consider the normalized spherical harmonics $\{Y_{l,m}(\theta, \varphi)\}$ [17,15,13,22]. For any given l, the set $\{Y_{l,m}(\theta, \varphi)|m = -l, -l+1, \cdots l-1, l\}$ may be obtained [17,15,13,22] by the repeated action of $\hat{L}_-$ acting on $Y_{l,l}(\theta, \varphi) = C_l(\sin \theta)^l e^{il\varphi}$, choosing the magnitude of the constant C_l by the requirement of normalization, and the phase of C_l by the requirement that $Y_{l,0}(\theta, \varphi) = A_l P_l(\cos \theta)$, where A_l is a positive constant. It is easy to show [17,15,13,22] that this set forms a basis for an irreducible representation of the full rotation group, and we may write $\mathbf{Y}^{(l)}(\theta, \varphi)$ as shorthand for the row array [28] formed by the set of spherical harmonics belonging to this l-value. Thus,

$$\mathbf{Y}^{(l)}(\theta, \varphi) \equiv (Y_{l,l}(\theta, \varphi), Y_{l,l-1}(\theta, \varphi) \cdots Y_{l,-l+1}(\theta, \varphi), Y_{l,-l}(\theta, \varphi)) \qquad (32)$$

which allows us to write

$$Y'_{l,m}(\theta, \varphi) \equiv \hat{R}(\phi, \hat{n})Y_{l,m}(\theta, \varphi) = \sum_{m'=-l}^{l} Y_{l,m'}(\theta, \varphi)D^{(l)}_{m',m}(\phi, \hat{n}) \qquad (33a)$$

in the form [28]

$$\mathbf{Y}'^{(l)}(\theta, \varphi) \equiv \hat{R}(\phi, \hat{n})\mathbf{Y}^{(l)}(\theta, \varphi) = \mathbf{Y}^{(l)}(\theta, \varphi)\mathbf{D}^{(l)}(\phi, \hat{n}) \qquad (33b)$$

where $\mathbf{D}^{(l)}(\phi, \hat{n})$ is the irreducible representation matrix [16,17] associated with the basis $\mathbf{Y}^{(l)}(\theta, \varphi)$ and the rotation operator $\hat{R}(\phi, \hat{n})$ in the full rotation group $SO(3)$. [Here we need to distinguish between ϕ as an angle of rotation and φ as the spherical azimuthal angle.] It is easy to show that the basis vectors [17]

$$\hat{\mathbf{e}}^{(1)} \equiv (\hat{e}_+, \hat{e}_0, \hat{e}_-) = (\hat{e}_x, \hat{e}_y, \hat{e}_z)\begin{bmatrix} -\dfrac{1}{\sqrt{2}} & 0 & \dfrac{1}{\sqrt{2}} \\[2mm] -\dfrac{i}{\sqrt{2}} & 0 & -\dfrac{i}{\sqrt{2}} \\[2mm] 0 & 1 & 0 \end{bmatrix} \qquad (34)$$

(where $\hat{e}_x, \hat{e}_y, \hat{e}_z$ are the unit vectors along the Cartesian axes) have the property that [17]

$$\hat{R}(\phi, \hat{n})\hat{\mathbf{e}}^{(1)} = \hat{\mathbf{e}}^{(1)}\mathbf{D}^{(1)}(\phi, \hat{n}) \qquad (35a)$$

where also [17]

$$\hat{R}(\phi, \hat{n})\mathbf{Y}^{(1)}(\theta, \varphi) = \mathbf{Y}^{(1)}(\theta, \varphi)\mathbf{D}^{(1)}(\phi, \hat{n}) \qquad (35b)$$

Thus, $\hat{\mathbf{e}}^{(1)}$ transforms according to the same irreducible representation, $\mathbf{D}^{(1)}$, of the full rotation group, as does the set of spherical harmonics belonging to $l = 1$. This irreducible representation may be written in terms of the parameters $\{a, b, a^*, -b^*\}$ as [17]

$$
\mathbf{D}^{(1)}(\phi, \hat{n}) \quad
\begin{bmatrix}
a^2 & \sqrt{2}ab & b^2 \\
\sqrt{2}a(-b^*) & aa^* + b(-b^*) & \sqrt{2}a^*b \\
(-b^*)^2 & \sqrt{2}a^*(-b^*) & (a^*)^2
\end{bmatrix}
\tag{36}
$$

It is easy to show that under rotation, the Cartesian components $(\hat{L}_x, \hat{L}_y, \hat{L}_z)$ of the vector angular momentum operator $\hat{L}$ transform in the same way as the unit vectors $(\hat{e}_x, \hat{e}_y, \hat{e}_z)$. Because of the relationship of $(\hat{e}_x, \hat{e}_y, \hat{e}_z)$ to $(\hat{e}_-, \hat{e}_0, \hat{e}_+)$ this means that [17,13]

$$
\left[-\frac{1}{\sqrt{2}} \hat{L}_+, \hat{L}_z, \frac{1}{\sqrt{2}} \hat{L}_- \right] = \hat{R}(\phi, \hat{n}) \left[-\frac{1}{\sqrt{2}} \hat{L}_+, \hat{L}_z, \frac{1}{\sqrt{2}} \hat{L}_- \right] (\hat{R}(\phi, \hat{n}))^{-1}
$$

$$
\left[-\frac{1}{\sqrt{2}} \hat{L}_+, \hat{L}_z, \frac{1}{\sqrt{2}} \hat{L}_- \right] \mathbf{D}^{(1)}(\phi, \hat{n})
\tag{37}
$$

Now the Condon and Shortley relations [Eqs. (28)], when used in conjunction with the spherical harmonics, $\{ Y_{l,m}(\theta, \varphi) \}$, give

$$
\hat{L}_z Y_{l,m}(\theta, \varphi) = m Y_{l,m}(\theta, \varphi)
\tag{38a}
$$

$$
\hat{L}_\pm Y_{l,m}(\theta, \varphi) = \sqrt{l(l+1) - m(m \pm 1)}\, Y_{l,m\pm 1}(\theta, \varphi)
\tag{38b,c}
$$

Using our definitions of the $\{ Y_{l,m} \}$ given in Eqs. (33), together with our definitions of $\{ \hat{L}_+, \hat{L}_z, \hat{L}_- \}$ given in Eq. (37), the invariance of the "laws of physics" (here, the Condon and Shortley relations) to the orientation of our reference frame requires that also [16,13]

$$
\hat{L}'_z Y_{l,m}(\theta, \varphi) = m Y_{l,m}(\theta, \varphi)
\tag{39a}
$$

$$
\hat{L}'_\pm Y_{l,m}(\theta, \varphi) = \sqrt{l(l+1) - m(m \pm 1)}\, Y_{l,m\pm 1}(\theta, \varphi)
\tag{39b,c}
$$

Writing

$$
\hat{L}'_+ = \alpha \hat{L}_+ + \beta \hat{L}_z + \gamma \hat{L}_-
\tag{40a}
$$

$$
\hat{L}'_z = \alpha_0 \hat{L}_+ + \beta_0 \hat{L}_z + \gamma_0 \hat{L}_-
\tag{40b}
$$

$$
\hat{L}'_- = \alpha \hat{L}_+ + \beta \hat{L}_z + \gamma \hat{L}_-
\tag{40c}
$$

we may read the "values" of the (α, β, γ) coefficients from the definitions of $(\hat{L}'_+, \hat{L}'_z, \hat{L}'_-)$ and the matrix elements of $\mathbf{D}^{(1)}(\phi, \hat{n})$.

The Condon and Shortley relation for $\hat{L}'_z$ [Eq. (39a)] may be written as

$$
(\alpha_0 \hat{L}_+ + \beta_0 \hat{L}_z + \gamma_0 \hat{L}_-) \sum_{m'=-l}^{l} Y_{l,m'}(\theta, \varphi) D^{(l)}_{m',m}(\phi, \hat{n})
$$

$$
= m \sum_{m'=-l}^{l} Y_{l,m'}(\theta, \varphi) D^{(l)}_{m',m}(\phi, \hat{n})
\tag{41}
$$

which, upon substituting the entities on the right-hand side of Eqs. (38) for the products shown on the left-hand side of Eqs. (38), as they appear in Eq. (41), and then comparing the coefficients of the $\{ Y_{l,m'} \}$ on each side of the equation, yields

$$\alpha_0\sqrt{l(l+1) - m'(m'-1)}\,D_{m'-1,m}^{(l)} + \beta_0 m' D_{m',m}^{(l)}$$

$$+ \gamma_0\sqrt{l(l+1) - m'(m'+1)}\,D_{m'+1,m}^{(l)} = m D_{m',m}^{(l)} \qquad (42)$$

with

$$\alpha_0 = -ab, \ \beta_0 = (aa^* + b(-b^*)), \ \gamma_0 = a^*(-b^*)$$

This equation allows one to obtain the element $D_{n,m}^{(l)}$ (for any row n in column m) from the elements ($D_{n+1,m}^{(l)}$ and $D_{n+2,m}^{(l)}$) or from the elements ($D_{n-1,m}^{(l)}$ and $D_{n-2,m}^{(l)}$) or (except for $n = m = 0$) from the elements ($D_{n+1,m}^{(l)}$ and $D_{n-1,m}^{(l)}$), [all of these elements belonging to the same column m of $\mathbf{D}^{(l)}$]. As implied by the coefficients, in using these relations, one may take the elements whose indices lie outside of the range of the matrix to be zero. By this means every element in column m of $\mathbf{D}^{(l)}$ may be generated from either $D_{l,m}^{(l)}$ or $D_{-l,m}^{(l)}$. The Condon and Shortley relation for $L'_\pm$ may be written as

$$(\alpha_\pm \hat{L}_+ + \beta_\pm \hat{L}_z + \gamma_\pm \hat{L}_-) \sum_{m'=-l}^{l} Y_{l,m'}(\theta, \varphi) D_{m',m}^{(l)}(\phi, \hat{n})$$

$$= \sqrt{l(l+1) - m(m \pm 1)} \sum_{m'=-l}^{l} Y_{l,m'}(\theta, \varphi) D_{m',m\pm1}^{(l)}(\phi, \hat{n}) \qquad (43)$$

which, upon substituting the entities on the right-hand side of Eqs. (38) for the products shown on the left-hand side of Eqs. (38), as they appear in Eqs. (43), and then comparing the coefficients of the $\{Y_{l,m'}\}$ on each side of the equation, yields

$$\alpha_\pm\sqrt{l(l+1) - m'(m'-1)}\,D_{m'-1,m}^{(l)} + \beta_\pm m' D_{m',m}^{(l)}$$

$$+ \gamma_\pm\sqrt{l(l+1) - m'(m'+1)}\,D_{m'+1,m}^{(l)} = \sqrt{l(l+1) - m(m \pm 1)}\,D_{m',m\pm1}^{(l)} \qquad (44)$$

with

$$\alpha_+ = a^2, \ \beta_+ = -2a(-b^*), \ \gamma_+ = -(-b^*)^2$$

$$\alpha_- = -b^2, \ \beta_- = 2a^*b, \ \gamma_- = (a^*)^2$$

The $\hat{L}'_+$ relation [with $(\alpha_+, \beta_+, \gamma_+)$] allows element $D_{n,m+1}^{(l)}$ to be obtained from the elements $\{D_{n+1,m}^{(l)}, D_{n,m}^{(l)}, D_{n-1,m}^{(l)}\}$, thereby generating an element in the column $m + 1$ from its three closest neighboring elements of column m. The $\hat{L}'_-$ relation [with $(\alpha_-, \beta_-, \gamma_-)$] allows element $D_{n,m-1}^{(l)}$ to be obtained from the elements $\{D_{n+1,m}^{(l)}, D_{n,m}^{(l)}, D_{n-1,m}^{(l)}\}$, thereby generating an element in the column $m - 1$ from its three closest neighboring elements of column m. Thus, using each of the $\{\hat{L}'_z, \hat{L}'_+, \hat{L}'_-\}$ relations one may obtain every element of the $\mathbf{D}^{(l)}$ matrix by any element on its perimeter. In particular, using only the relations $\{\hat{L}'_z, \hat{L}'_-\}$, one may generate every element of $\mathbf{D}^{(l)}$ from the element $D_{l,l}^{(l)} = a^{2l}$.

As will be shown in the next section, the symmetry of the $\mathbf{D}^{(l)}$ matrix requires also that the following relations hold. These relations are images of the $\{\hat{L}'_z, \hat{L}'_+, \hat{L}'_-\}$ relations under the symmetry operation of simultaneously reflecting both the matrix $\mathbf{D}^{(l)}$ and the matrix $\mathbf{D}^{(1)}$, each about its main diagonal.

The image of Eq. (42) under this symmetry operation is:

$$\alpha'_0 \sqrt{l(l+1) - m'(m'-1)} D^{(l)}_{m,m'-1} + \beta'_0 m' D^{(l)}_{m,m'}$$
$$+ \gamma'_0 \sqrt{l(l+1) - m'(m'+1)} D^{(l)}_{m,m'+1} = m D^{(l)}_{m,m'} \tag{45}$$

with

$$\alpha'_0 = -a(-b^*), \quad \beta'_0 = (aa^* + (-b^*)b), \quad \gamma'_0 = a^* b$$

This relation[24] does for the rows of the matrix $D^{(l)}$ what the relation given in Eq. (42) does for the columns of $D^{(l)}$.

The image of Eqs. (44) under this symmetry operation is:

$$\alpha'_- \sqrt{l(l+1) - m'(m'-1)} D^{(l)}_{m,m'-1} + \beta'_- m' D^{(l)}_{m,m'}$$
$$+ \gamma'_- \sqrt{l(l+1) - m'(m'+1)} D^{(l)}_{m,m'+1} = \sqrt{l(l+1) - m(m \pm 1)} D^{(l)}_{m \pm 1, m'} \tag{46}$$

with

$$\alpha'_- = a^2, \quad \beta'_- = -2ab, \quad \gamma'_- = -b^2$$

$$\alpha'_+ = -(-b^*)^2, \quad \beta'_+ = 2a^*(-b^*), \quad \gamma'_+ = (a^*)^2$$

These relations do for the rows of the matrix $D^{(l)}$ what the relations given in Eqs. (44) do for the columns of the matrix $D^{(l)}$.

The Relationship of Column m = 0 of $D^{(l)}$ With the Spherical Harmonics

The so-called "addition theorem" for spherical harmonics may be written [15,14]:

$$P_l(\cos \tilde{\gamma}) = \frac{4\pi}{2l+1} \sum_{m=-l}^{l} Y_{l,m}(\theta, \varphi)(Y_{l,m}(\theta', \varphi'))^* \tag{47}$$

where $\tilde{\gamma}$ is the angle between a vector from the origin, pointing toward (θ, φ) and a vector, from the origin, pointing toward (θ', φ'). Now, for any φ'',

$$P_l(\cos \tilde{\gamma}) = \sqrt{\frac{4\pi}{2l+1}} Y_{l,0}(\tilde{\gamma}, \varphi'')$$

and

$$Y_{l,0}(\tilde{\gamma}, \varphi'') = \hat{R}(\alpha, \beta, \gamma) Y_{l,0}(\theta, \varphi) \tag{48}$$

where the Euler angles (α, β, γ) are such as to define a rotation $\hat{R}(\alpha, \beta, \gamma)$ that will carry the original z-axis into the direction of (θ', φ'). This may be accomplished by choosing $\alpha = \varphi', \beta = \theta', \gamma$ arbitrary. Thus, we may now rewrite the "addition theorem"

---

[24] A reduction of Eq. (45) for a rotation about the y-axis is given as Eq. (3.84) of Ref. 16.

$$\tilde{R}(\alpha, \beta, \gamma) Y_{l,0}(\theta, \varphi) = \sum_{m=-l}^{l} Y_{l,m}(\theta, \varphi) \left[\frac{4\pi}{2l+1} Y_{l,m}(\theta', \varphi') \right]^* \qquad (49)$$

Since the coefficient of $Y_{l,m}(\theta, \varphi)$ in this equation is, by definition, $D_{m,0}^{(l)}(\alpha, \beta, \gamma)$ we have [13]

$$D_{m,0}^{(l)}(\alpha, \beta, \gamma) = \frac{4\pi}{2l+1} [Y_{l,m}(\beta, \alpha)]^* \qquad (50)$$

Also, since [15]

$$Y_{l,l}(\theta, \varphi) = (-1)^l \frac{\sqrt{(2l)!}}{2^l (l!)} \sqrt{\frac{2l+1}{4\pi}} (\sin \theta)^l e^{il\varphi} \qquad (51)$$

then [17]

$$D_{l,0}^{(l)}(\alpha, \beta, \gamma) = (-1)^l \frac{\sqrt{(2l)!}}{2^l (l!)} (\sin \beta)^l e^{-il\alpha} \qquad (52)$$

but, from Eq. (31):

$$e^{-i\alpha} \sin \beta = -2ab \qquad (53)$$

so

$$D_{l,0}^{(l)} = \frac{\sqrt{(2l)!}}{(l!)} (ab)^l \qquad (54)$$

This is the same result as is obtainable from stepping down m-wise [using Eq. (44)] from $(D_{l,m}^{(l)})_{m=l} = a^{2l}$, which is the $D_{l,l}^{(l)}$ value obtained [17] from a known which the $m = l$ function is $(v_+)^{2l}$, where v_+ is the Pauli spinor α. The starting [15] with $Y_{l,0}(\theta, \varphi) = A_l P_l(\cos \theta)$, with A_l a positive normalization constant, and generating the rest of the spherical harmonics via the action of the Condon and Shortley $\hat{L}_\pm$ operators upon $Y_{l,0}$, establishes, via the connection of $D_{m,0}^{l}$ to $Y_{l,m}^*$ [as given in Eq. (50)], exactly the same irreducible representation matrix as is obtained from our recursion procedure based upon Eqs. (42) and (44)-(46) (or the traditional SU(2)-based procedure [16,17]), starting from $D_{ll}^{(l)} = a^{2l}$. Our recursion procedure is capable of generating $\mathbf{D}^{(l)}$ matrices for all j-values (including the half-integral ones). Recognizing the proportionality [Eq. (50)] between $D_{m,0}^{(l)}(\alpha, \beta, \gamma)$ and $(Y_{lm}(\beta, \alpha))^*$, we may use the $\hat{L}_\pm$ relation [as expressed in Eqs. (39a), (40b), (41), and (42)] to derive the following recursion relation for spherical harmonics[26]:

---

[25] Completion of the $\mathbf{D}^{(l)}$ matrix from this starting point may proceed by using this column $m = 0$ of $\mathbf{D}^{(l)}$ and the recursion relations [given in Eqs. (44)], to obtain the adjacent columns, then iterating with these relations to generate the remaining columns of the matrix. This requires a knowledge of the coefficients $(\alpha_\pm, \beta_\pm, \gamma_\pm)$ which are directly obtainable from either the matrix $\mathbf{D}^1$ or the primitive SU(2) matrix. For consistency, all elements of $\mathbf{D}^l$ and $\mathbf{D}^1$ should here be represented in terms of the Euler angles (α, β, γ) with $\alpha = \varphi, \beta = \theta$. [Note that the $m = 0$ column of $\mathbf{D}^l(\alpha, \beta, \gamma)$ does not depend upon the Euler angle γ.]

[26] With care, this relation is also derivable from some well-known properties and recursion relations [19, using Eq. (8.3.1) in Eqs. (8.5.1), (8.5.2), and (8.5.4)] on the $\{P_l^m(\cos \theta)\}$. Nevertheless, a search of the available literature failed to reveal any citing of this relation [Eq. (55)].

$$Y_{l,m-1}(\theta, \varphi) = \frac{(1)}{\sqrt{l(l+1) - m(m-1)}}$$

$$\times [2m \cot \theta e^{-i\varphi} Y_{l,m}(\theta, \varphi) + \sqrt{l(l+1) - m(m+1)} e^{-i\varphi} Y_{l,m+1}(\theta, \varphi)] \quad (55)$$

One may generate the entire set of spherical harmonics by stepping down m-wise from

$$(Y_{l,m}(\theta,\varphi))_{m=l} \equiv Y_{l,l}(\theta, \varphi) = (-1)^l \frac{\sqrt{(2l)!}}{2^l(l!)} \sqrt{\frac{2l+1}{4\pi}} (\sin \theta)^l e^{il\varphi} \quad (56)$$

using this relation.[27] Because Eq. (55) does not involve differentiation,[28] it is especially well adapted to generating numerical[27] values (at fixed θ and φ) for all of the spherical harmonics belonging to the same l-value.

Symmetry Properties of the Irreducible Representation Matrices of the Full Rotation Group, SO(3), and of the Special Unitary Group, SU(2)

Because the spherical harmonics $\{Y_{l,m}(\beta, \alpha)\}$ are expressible solely in terms of the factors $\{\cos \beta, \sin \beta, e^{i\alpha}, e^{-i\alpha}\}$, and cannot involve irreducible factors such as $\{e^{-i(\alpha/2)}, e^{+i(\alpha/2)}, \cos(\beta/2), \sin(\beta/2), e^{-i(\alpha/2)}, e^{+i(\alpha/2)}\}$, the elements of column $m = 0$ of $\mathbf{D}^{(l)}$ (which are expressible in terms of the $\{Y_{l,m}(\beta, \alpha)\}$) are invariant to the transformation $(a \Leftrightarrow b)(-b^* \Leftrightarrow a^*)$, such as is induced by reflecting the primitive SU(2) matrix $\mathbf{D}^{(1/2)}(\vec{R}) = \begin{bmatrix} a & b \\ -b^* & a^* \end{bmatrix}$ about its vertical midline. The symmetry[29] of the operators L'_+ and L'_-, which, via Eq. (44), generate the $m > 0$ and $m < 0$ columns, respectively, of $\mathbf{D}^{(l)}$ from the $m = 0$ column,[30] show that the element $D^{(l)}_{m,-m_0}$ (the image, under reflection about the vertical midline, of the element $D^{(l)}_{m,m_0}$) may be obtained from the element $D^{(l)}_{m,m_0}$ by the transformation $(a \Leftrightarrow b)(-b^* \Leftrightarrow a^*)$ of the primitive elements $\{a, b, -b^*, a^*\}$ appearing in the expression for the element $D^{(l)}_{m,m_0}$. This shows that the matrix elements of $\mathbf{D}^{(l)}(\vec{R})$, related to each other by reflection about the vertical midline, display the same

---

[27] Analytical performance of this procedure is always possible. However, in the above form, it may have numerical difficulties (i.e., it may lack sufficient precision) when $\sin \theta$ is very tiny. (Of course, we should expect this, because when $\sin \theta$ is truly zero, all of the Y_{lm} except Y_{l0} are exactly zero.) To avoid this problem, it may be preferable to rewrite Eq. (55) directly in terms of $P_l^{(m)}(\cos \theta) = (d^m/d(\cos \theta)^m)P_l(\cos \theta) = (-\sin \theta)^{-m}P_l^m(\cos \theta)$, which are numerically more stable than the $\{Y_{lm}(\theta, \varphi)\}$ near $\sin \theta = 0$.

[28] Unlike the standard procedure for generating the Y_{lm} through the action of the linear differential [16,13,17] operator L_-.

[29] To show this symmetry, it is appropriate to insert the factor 1 in the form $(a)(a^*) + (b)(-b^*)$ on the right-hand side of Eqs. (44).

[30] This symmetry may be also seen by starting with the $m = \pm l$ columns and, symmetrically, stepping toward the center column from these [after first examining the symmetrical relationship of the generation of the $m = l$ column from $D^{(l)}_{ll} = a^{2l}$ and the $m = -l$ column from $D^{(l)}_{l,-l} = b^{2l}$, using Eq. (42)] and observing that this generation procedure ascribes the proper vertical reflection interchange symmetries to the elements of these columns.

TABLE I. The irreducible representation matrix, $D^{(2)}$, of the full rotation group, $SO(3)$, expressed in terms of the elements $\{a, b, -b^*, a^*\}$ of the primitive $SU(2)$ matrix.

	$m = 2$	$m = 1$	$m = 0$	$m = -1$	$m = -2$
$m' = 2$	a^4	$2a^3b$	$\sqrt{6}a^2b^2$	$2ab^3$	b^4
$m' = 1$	$2a^3(-b^*)$	$a^2(aa^* - 3bb^*)$	$\sqrt{6}ab[aa^* + bb^*]$	$b[b(a^*)^2 + ...]$	$2b^3a^*$
$m' = 0$	$\sqrt{6}a^2(-b^*)^2$	$\sqrt{6}a(-b^*)[aa^* + bb^*]$	$(aa^* + bb^*)^2 - 2aa^*bb^*$	$\sqrt{6}a^*b^*[bb^* - a^*a]$	$\sqrt{6}b^2(a^*)^2$
$m' = -1$	$2a(-b^*)^3$	$(-b^*)^2(-b^*b + 3a^*a)$	$\sqrt{6}(-b^*)a^*[-bb^* + a^*a]$	$a^*[a^*(a^*a + 3b^*b]$	$2(b^*)(a^*)^3$
$m' = -2$	$(-b^*)^4$	$2(-b^*)^3a^*$	$\sqrt{6}(b^*)^2(a^*)^2$	$2(b^*)(a^*)^3$	$(a^*)^4$

interchanges of the elements $\{a, b, -b^*, a^*\}$ as are obtained by reflecting the primitive $SU(2)$ matrix $D^{(1/2)}(\hat{R}) = \begin{bmatrix} a & b \\ -b^* & a^* \end{bmatrix}$ about its vertical midline.[31]

Also, because of the homomorphism between the irreducible representation matrices $\{D^{(l)}(\hat{R})\}$ and the rotation operators $\{\hat{R}\}$, together with the homomorphism between the rotation operators and the primitive $SU(2)$ matrices $\left\{\begin{bmatrix} a & b \\ -b^* & a^* \end{bmatrix}\right\}$, and the fact that all of these entities are unitary, we have the following[32]

$$\left[D^{(l)}\left(\hat{R}\begin{pmatrix} a & b \\ -b^* & a^* \end{pmatrix}\right)\right]_{m,m'}$$

$$= \left[\left(\left\{D^{(l)}\left(\hat{R}\begin{pmatrix} a & b \\ -b^* & a^* \end{pmatrix}\right)\right\}^{-1}\right)^*\right]_{m',m} = \left[\left\{D^{(l)}\left(\hat{R}^{-1}\begin{pmatrix} a & b \\ -b^* & a^* \end{pmatrix}\right)\right\}^*\right]_{m',m}$$

$$= \left[\left\{D^{(l)}\left(\hat{R}\begin{pmatrix} a^* & -b \\ b^* & a \end{pmatrix}\right)\right\}^*\right]_{m',m} = \left[D^{(l)}\left(\hat{R}\begin{pmatrix} a & -b^* \\ b & a^* \end{pmatrix}\right)\right]_{m',m} \quad (57)$$

Thus, $[D^{(l)}(\hat{R})]_{m',m}$ is obtained from $[D^{(l)}(\hat{R})]_{m,m'}$ by the interchange $(b \Leftrightarrow -b^*)$ in the expression for $[D^{(l)}(\hat{R})]_{m',m}$ in terms of the parameters $\{a, b, -b^*, a^*\}$. This shows that the matrix elements of $D^{(l)}(\hat{R})$, related to each other by reflection about the main diagonal, display the same interchanges of the elements $\{a, b, -b^*, a^*\}$ as are obtained by reflecting the primitive $SU(2)$ matrix $D^{(1/2)}(\hat{R}) = \begin{bmatrix} a & b \\ -b^* & a^* \end{bmatrix}$ about its main diagonal.

---

[31] Here, the elements $\{a, b, -b^*, a^*\}$ must be treated as being totally independent, since this symmetry property is lost when the algebraic expressions for the elements of the $D^{(l)}$ matrix are reduced [13,16,11], such as by expressing $\{a, b, -b^*, a^*\}$ in terms of the Euler angles (α, β, γ) and then algebraically reducing these expressions using the trigonometric identities.

[32] Here, $[D^{(l)}(\hat{R}(s))]_{m',m}$ denotes the (m', m) element of the irreducible representation matrix $D^{(l)}$ for that operator $\hat{R}$ whose primitive $SU(2)$ matrix is [s]. Also, $\hat{R}^{-1}(s)$ is the inverse of the operator $\hat{R}(s)$.

By combining the reflection about the vertical midline with the reflection about the main diagonal, we can show that[33]

$$D^{(j)}_{m',m}\begin{pmatrix} a & b \\ -b^* & a^* \end{pmatrix} = D^{(j)}_{m',m}\begin{pmatrix} b & a \\ a^* & -b^* \end{pmatrix} \text{ (reflection about vertical midline)}$$

$$D^{(j)}_{m',m}\begin{pmatrix} a & b \\ -b^* & a^* \end{pmatrix} = D^{(j)}_{m',m}\begin{pmatrix} a & -b^* \\ b & a^* \end{pmatrix} \text{ (reflection about main diagonal)}$$

$$D^{(j)}_{m',m}\begin{pmatrix} a & b \\ -b^* & a^* \end{pmatrix} = D^{(j)}_{m',m}\begin{pmatrix} -b^* & a^* \\ a & b \end{pmatrix} \text{ (reflection about horizontal midline)}$$

$$D^{(j)}_{m',m}\begin{pmatrix} a & b \\ -b^* & a^* \end{pmatrix} = D^{(j)}_{m',m}\begin{pmatrix} a^* & b \\ -b^* & a \end{pmatrix} \text{ (reflection about cross diagonal)}$$

These symmetries are illustrated by the matrix $D^{(1)}$ shown in Eq. (36) and the matrix $D^{(2)}$ shown in Table I. Using these symmetries, we can reduce the number of matrix elements that need to be explicitly calculated to a fraction only modestly greater than $\frac{1}{8}$ of the total number of elements in the matrix $D^{(j)}$. The $(\hat{L}_z, \hat{L}', \hat{L}')$ rotations given above, together with the above symmetry properties, are equally valid for $(\hat{J}_z, \hat{J}', \hat{J}')$ (with the substitution of j for l), and half-integral values of j. Thus, this procedure also generates the irreducible representation matrices $D^{(j)}(\hat{R})$, for all values of j, for the special unitary group $SU(2)$.

Although not widely known, these symmetries have also been observed by certain other authors [16,58]. Whereas in Ref. 58 these symmetries are described in their Euler angle representation, in Ref. 16 they are described by means of an analysis of the range of the index k in the traditional representation of the elements of the matrix $D^{(j)}$, namely [16,13,17]:

$$\left[D^{(j)}\left(\hat{R}\begin{pmatrix} a & b \\ -b^* & a^* \end{pmatrix}\right)\right]_{m'm} = \sqrt{(j+m')!(j-m')!(j+m)!(j-m)!}$$

$$\times \sum_k \frac{a^{j+m-k}(a^*)^{j-m'-k}b^{m'-m+k}(-b^*)^k}{(j+m-k)!(j-m'-k)!(m'-m+k)!k!} \tag{58}$$

These authors have used these symmetries to display some otherwise-hidden symmetries of the Wigner symbols [16,26]. We believe that these symmetries are at least equally transparent in our approach. We also believe that the recursion relations given in Eqs. (42) and (44)–(46) offer some distinct advantages [over the explicit expression of Eq. (58)] for obtaining complete columns (or complete rows) of a D matrix either in parametric[34] form (as functions of $\{a, b, -b^*, a^*\}$) or the

[33] As a shorthand, we are omitting the intermediate "function," $\hat{R}$, and writing $D^{(j)}(\hat{R}(s))$ simply as $D^{(j)}(s)$.

[34] For parametric calculations, it seems best to multiply the right-hand sides of Eqs. (42) and (44)–(46) by unity, in the form $(aa^* - b(-b^*))$, to bring all coefficients to the same degree in the parameters $\{a, b, -b^*, a^*\}$.

parameters that define them) or in numerical form. For parametric calculations, both procedures are enhanced by the use of a symbolic manipulation program such as *Mathematica* [25], and both benefit by the use of the symmetry properties discussed above. However, the recursion relations produce the more efficient algorithm. This is especially true for large values of j, where often several k-values are needed and the evaluation and processing of the factorials can become a burden. For numerical calculations, it is very easy to construct, from the recursion relations, efficient algorithms that are also optimally numerically accurate. Whereas numerical calculations using the explicit expression of Eq. (58) may be organized to be accurate and moderately efficient, numerical algorithms based upon the recursion relations presented here have a distinct computational advantage.[35]

Conclusions

In this work, we described some concepts which should prove to be relevant to algorithms for the efficient calculation of molecular electrostatic potentials and their associated intermolecular forces and interaction energies. Our approach is very similar, in spirit, to that of Srebrenik, et al. [42], in that we find an expression for the solution to Poisson's equation for the region outside of the charge distribution, using, as input, the density matrix over the orbital basis. We explicitly emphasized the representation in terms of point charges and point multipoles whose potentials are expressed as "solid spherical harmonics" specified either in terms of their mutual orientation or in terms of each of their arbitrary orientations with respect to a laboratory frame.[36] The mathematical foundations for a complete quantum mechanical description of a molecule whose atomic orbitals have their orientations described in this manner have been given earlier by Harris [11]. Whereas the specifics of our results are expressed from this perspective, the general methodology is hopefully also relevant to the description based upon a global Cartesian coordinate system, with Cartesian Gaussian orbitals centered on each of the atoms of the complete system, as the reference basis [57,56,31]. Using the source charge densities for the Cartesian point multipole potentials, many of the two-electron integrals of the Coulomb interaction may be simply calculated as point-multipole interactions [57]. For the interactions of two separate molecules, each in its separate Cartesian coordinate system [57,56,31], some of the methods described here for dealing with multipoles of arbitrary mutual orientation may also be useful.

Our expressions for the multipole interaction energy rest upon a knowledge of the source charge densities of the "solid spherical harmonic" multipole potentials; and their effective implementation requires either a "parallel axis" orientation of the potentials, or an efficient way of calculating the matrices of the irreducible

---

[35] The authors of Ref. 16 present, as their Eq. (3.84), a very restricted version of our Eq. (45), and state that it has ". . . been found to be particularly useful in numerical calculations . . ." Used together, our set of six such relations [Eqs. (42) and (44)–(46)] should be even more effective.

[36] Such a parameterization is especially relevant to a "rigid molecule" [52] representation of molecular dynamics, in which the electrostatic interactions can play a very important role and lead to the time-dependent mutual orientations of the interacting molecules.

representations (of the full rotation group) "carried by" the spherical harmonics. Such an efficient algorithm can be based upon the recursion relations (among the elements of these matrices) presented here, which may be implemented to generate the reduced algebraic formulas for these elements, or to very efficiently calculate their numerical values, from the formula or numerical value of only one element on the perimeter of the matrix.

Our procedure for representing the electrostatic potential of a molecule in terms of point multipoles on each of the atoms and line multipoles on each of the "bond" axes is uniquely determined by the representation of the electronic charge density matrix in terms of its basis of atomic orbitals, with orbitals on each atom. One weakness of this procedure is the dependence of the values of the atomic point multipoles and "bond" line multipoles on the partitioning of this orbital basis among the various atoms of the molecule. An extreme of this dependence may be illustrated by a one-center orbital expansion (which, although grossly inefficient, is possible), which would yield a point multipole expansion of the electrostatic potential of the molecule about that center. Such a point multipole expansion would be valid only outside of a sphere that would "enclose" the charge distribution of the entire molecule, and it would serve only a very small fraction of our needs. Fortunately, experienced quantum chemists have learned how to optimally partition the atomic orbital basis of a molecule among the various atoms, and it is their work which gives stability to our calculated values for the atomic point multipoles and bond line multipoles and contributes greatly to the integrity of our method.

Acknowledgments

Bibliography

[1] R. H. Good, Jr. and T. J. Nelson, *Classical Theory of Electric and Magnetic Fields* (Academic Press, New York, 1971), pp. 104–105.

[2] R. J. Woods, M. Khalil, W. Pell, S. H. Moffat, and V. H. Smith, J. Comput. Chem. **11**, 297–310 (1990).

[3] M. Berrondo, S. W. Eggleston, and E. G. Larson, Int. J. Quantum Chem. **36**, 749–764 (1989).

[4] M. Berrondo and E. G. Larson, Int. J. Quantum Chem. Quantum Biol. Symp. **16**, 343–344 (1989)

[5] M. Li, Charge Density and Electrostatic Potential in Molecules. Master's thesis, Department of Physics and Atronomy, Brigham Young University, Provo, UT (April 1992).

[6] B. H. Besler, K. M. Merz, and P. A. Kollman, J. Comput. Chem. 11, 431-439 (1990).

[7] J. S. Murray, M. E. Grice, P. Politzer, and J. R. Rabinowitz, J. Comput. Chem. 11, 112-120 (1990).

[8] G. C. Larson and S. W. Eggleston (unpublished research, 1986). To be submitted for publication, 1992.

[9] S. W. Eggleston, *The Physical Nature and Applications of the Singular Associated Legendre Functions*. Master's thesis, Department of Physics and Astronomy, Brigham Young University, Provo, UT (December 1986).

[10] S. W. Eggleston, *Applications of Singular Associated Legendre Functions to Electromagnetics and to Acoustics* Ph.D. dissertation, Department of Physics and Astronomy, Brigham Young University, Provo, UT (December 1988).

[11] F. E. Harris, Rev. Mod. Phys. 35, 558-569 (1963).

[12] J. D. Jackson, *Classical Electrodynamics* (Wiley, New York, 1975), pp. 38-49, 98-102, 136-143.

[13] A. Messiah, *Quantum Mechanics* (Interscience Publishers, New York, 1961, 1963) vols. I and II, pp. 492-497, 522, 575, 1068-1075, especially Eqs. (C.49) on p. 1069.

[14] J. Mathews and R. L. Walker, *Mathematical Methods of Physics* (W. A. Benjamin, Menlo Park, CA, 1970), pp. 167-178.

[15] S. Hassani, *Foundations of Mathematical Physics* (Allyn & Bacon, Boston, 1991) sections 5.2, 8.4.

[16] L. C. Biedenharn and J. D. Louck, in *Angular Momentum in Quantum Physics* (Vol. 8 of *Encyclopedia of Mathematics*), G. Rota, Ed. (Addison-Wesley, Reading, MA, 1981), pp. 7-179 and 250-256, especially Eqs. (3.84) and (3.85) on p. 53 and Eqs. (C-5) on p. 251.

[17] S. L. Altmann, *Rotations, Quaternions, and Double Groups* (Clarendon Press, Oxford, 1986) especially pp. 67, 69, 75, 85, 94-98, 224.

[18] J. C. Slater, *Quantum Theory of Molecules and Solids—Electronic Structure of Molecules* (vol. 1), McGraw-Hill, New York, 1963 especially pp. 264-267.

[19] M. Abramowitz and I. A. Stegun, Eds., *Handbook of Mathematical Functions*. (Dover Publications, New York, 1972) chapters 8 and 21, especially Eqs. (8.6.6), (8.6.7), (8.6.18), (8.6.19), and (21.2.2).

[20] I. S. Gradshteyn and I. M. Ryzhik, *Table of Integrals, Series, and Products* (Academic Press, New York, 1980) Eqs. 8.752.1-5, p. 1008.

[21] H. W. Jones, J. Comput. Chem. 12, 1217-1222 (1991).

[22] E. U. Condon and G. H. Shortley, *The Theory of Atomic Spectra* (Macmillan, New York, 1935), especially Eqs. (3), (17), and (22), pp. 48, 52-54.

[23] J. M. Blatt and V. F. Weisskopf, *Theoretical Nuclear Physics* (Wiley, New York, 1952), pp. 785-789.

[24] G. C. Larson, M. Li, and E. G. Larson, Submitted to *Encyclia* (Thomas F. Rogers, Ed.), Utah Academy of Arts, Sciences and Letters, (May 1990).

[25] S. Wolfram, *Mathematica—A System for Doing Mathematics by Computer* (2nd ed.). (Addison-Wesley, New York, 1988), pp. 87-104, 570-638.

[26] E. P. Wigner, *Group Theory and its Application to the Quantum Mechanics of Atomic Spectra* (vol. 5 of *Pure and Applied Physics*), (Academic, New York, 1959) pp. 153-170, especially p. 167.

[27] M. Carmeli and S. Malin, *Representations of the Rotation and Lorentz Groups* (vol. 16 of *Lecture Notes in Pure and Applied Mathematics*) (Marcel Dekker, New York, 1976), chapters 1-8, especially pp. 36-37.

[28] P.-O. Löwdin, Rev. Mod. Phys. 39, 259-287 (1967).

[29] C. E. Dykstra, J. Comput. Chem. 9, 476-487 (1988).

[30] M. Orozco and F. J. Luque, J. Comput. Chem. 11, 909-923 (1990).

[31] Y. Shiratori and S. Nakagawa, J. Comput. Chem. 12, 717-730 (1991).

[32] P. Cieplak and P. Kollman, J. Comput. Chem. 12, 1232-1236 (1991).

[33] R. J. Zauhar and R. S. Morgan, J. Comput. Chem. 9, 171-187 (1988).

[34] A. Chung-Phillips, J. Comput. Chem. 10, 17-34 (1989).

[35] S. M. Bachrach, J. Comput. Chem. 10, 392-406 (1989).

[36] M. K. Gilson, K. A. Sharp, and B. H. Honig, J. Comput. Chem. 4, 327-335, 1987.

[37] S. L. Price, R. J. Harrison, and M. F. Guest, J. Comput. Chem. **10**, 552–567 (1989).

[38] S. L. Price, C. H. Faerman, and C. W. Murray, J. Comput. Chem. **12**, 1187–1197 (1991).

[39] G. A. Arteca, A. Hernández-Laguna, J. J. Rández, Y. G. Smeyers, and P. G. Mezey, J. Comput. Chem. **12**, 705–716, 1991.

[40] H. Bruning and D. Feil, J. Comput. Chem. **12**, 1–8 (1991).

[41] G. A. Arteca, N. D. Grant, and P. D. Mezey, J. Comput. Chem. **12**, 1198–1210 (1991).

[42] S. Srebrenik, H. Weinstein, and R. Pauncz, Chem. Phys. Lett. **20**, 419–423 (1973).

[43] R. J. Boyd and L.-C. Wang, J. Comput. Chem. **10**, 367–375 (1989).

[44] R. Glaser, J. Comput. Chem. **10**, 118–135 (1989).

[45] G. G. Ferenczy, C. A. Reynolds, and W. G. Richards, J. Comput. Chem. **11**, 159–169 (1990).

[46] J. C. Culberson and C. Zerner, Chem. Phys. Lett. **122**, 436–441 (1985).

[47] J. M. Gruschus and A. Kuki, J. Comput. Chem. **11**, 978–993 (1990).

[48] G. G. Ferenczy, J. Comput. Chem. **12**, 913–917 (1991).

[49] L.-G. Hammarström, T. Liljefors, and J. Gasteiger, J. Comput. Chem. **9**, 424–440 (1988).

[50] C. M. Breneman and K. B. Wiberg, J. Comput. Chem. **11**, 361–373 (1990).

[51] D. E. Williams, J. Comput. Chem. **9**, 743–745 (1988).

[52] U. Dinur, J. Comput. Chem. **12**, 469–486 (1991).

[53] U. Dinur, J. Comput. Chem. **12**, 91–105 (1991).

[54] X. Jiancheng and J. Shouping, Int. J. Quantum Chem. **39**, 123–130 (1991).

[55] A. Fortunelli and O. Salvetti, J. Comput. Chem. **12**, 36–41 (1991).

[56] P. M. W. Gill and J. A. Pople, Int. J. Quantum Chem. **40**, 753–772 (1991).

[57] P. M. W. Gill, B. G. Johnson, and J. A. Pople, Int. J. Quantum Chem. **40**, 745–752 (1991).

[58] D. A. Varshalovich, A. N. Moskalev, and V. K. Chersonskii, *Quantum Theory of Angular Momentum* (in Russian), Nauka, Leningrad, 1975, chapter 4, especially Table 4.1 and sections 4.1–4.4 & 4.17.

[59] A. Pullman, B. Pullman, and R. Lavery, Theochem. **10**, 85, (1983).

Complex Regional Virial Relations in Molecules

M. GARCÍA-SUCRE*

Departamento de Química e Física Molecular, Instituto de Física e Química de Sao Carlos,
Universidade de Sao Paulo, Cx. Postal 369, 13560, Sao Carlos SP, Brazil

Abstract

We extend the validity of the virial theorem for complex scaling to the case in which a molecule is partitioned in different regions fulfilling certain prescribed conditions. There is a parallelism between our results for complex scaling and those of the literature for real scaling. Therefore, we extend regional virial relations useful to the treatment of bound states to the case of metastable states. © 1992 John Wiley & Sons, Inc.

Introduction

If the electronic density of a molecule in a stationary state is partitioned in several regions separated by "zero one-particle density flux" surfaces, the virial-type relations are found to be valid in each of these regions with a high degree of approximation [1,2]. On the other hand, the use of real-scaled molecular coodinates with fixed nuclei, produces a formally different variational condition for these relations [3]. The importance of this difference has been discussed recently using a very simple model wave function for homonuclear and heteronuclear diatomic molecules with fixed nuclei [4].

Moreover, using a real scaling technique, a general condition fulfilled by the regional virial relations for a molecule in a stationary state with nuclei quantum mechanically described, has been found [5]. Here we extend these results to the case of a molecule in a metastable state [6-8].

According to our results, we can classify the molecular virial-type relation in the following way: there is a first type that we may call global, which is obtained when all the coordinates, quantum mechanically described, are multiplied by a real scaling factor and the physical space of the molecule is not partitioned [9-12]. These virial relations are the more usual ones, and have been of great utility in the description of the global properties of molecules in stationary states [13]. A second type is obtained in the same way as in the preceding case, except that now, the scaling factor is complex instead of real [14-16]. This type has also proved of great utility in the calculation of resonances in molecular systems [16-18]. Recently, a third type has been obtained using a scaling procedure in which only some of the co-

ordinates, quantum mechanically described, are modified by a scaling factor: real for the description of stationary states [19], and complex for metastable states [20]. In these two cases, a restricted number of the system variables is included in the virial-type relations obtained, yielding more detailed information about the relation between kinetic and potential energies of the particles than that provided by the global virial relations [19,20]. In contrast with these two cases, in the present study, we consider the physical space of the molecule partitioned, while complex scaling factors modify all the coordinates of the system that are quantum mechanically described.

Complex Regional Virial Relations

Let us consider a molecule described by the Schrödinger equation:

$$H(\eta)|\Psi(\eta)\rangle = E(\eta)|\Psi(\eta)\rangle \tag{1}$$

where $H(\eta)$ is the resulting Hamiltonian, after all coordinates had been modified by the complex factor $\eta = e^{i\alpha}$. Assume that $|\Psi(\eta = 1)\rangle$ describes a metastable state of the molecule such that for angles Θs fulfilling $\Theta^c < \Theta < \pi/2$, where $0 < \Theta^c \ll \pi/2$, the ket $|\Psi(\eta)\rangle$ becomes normalizable (for an introductory view of the complex scaling method, see, for instance, Ref. 21). Assuming that $H(\eta = 1)$ is real, the extremum principle can be written under the form [14]:

$$E(\eta) = \frac{\langle \Psi(\eta^*)|H(\eta)|\Psi(\eta)\rangle}{\langle \Psi(\eta^*)|\Psi(\eta)\rangle} \tag{2}$$

and we have the equalities $H^*(\eta) = H(\eta^*)$, $E^*(\eta) = E(\eta^*)$, and $\Psi^*(\eta) = \Psi(\eta^*)$, where $H(\eta)$ is, in general, non–self-adjoint; and, $E(\eta)$ may be complex (for a study on the change of spectra associated with complex scaling transformation see Refs. 21 and 22).

Let us now define the quantity

$$E^{R_i}(\eta) \equiv \frac{\langle \Psi(\eta^*)|H(\eta)|\Psi(\eta)\rangle_{R_i}}{\langle \Psi(\eta^*)|\Psi(\eta)\rangle_{R_i}} \tag{3}$$

where the subscript, R_i, in the right-hand side of Eq. (3) means that the coordinates of the particle i are integrated only in the region R_i.

The restricted region, R_i, may be associated to either an electron or a nucleus in the case that both kinds of particles are quantum mechanically described. On the other hand, when the nuclei are considered to occupy successive fixed positions, the region R_i can be associated to electrons only. Here, we will consider the case in which electrons and nuclei are quantum mechanically described. In general, the region, R_i, depends on the scaling parameter η. Taking into account this dependence, and the fact that in the present problem the Hamiltonian also depends on η, we have

$$\frac{\partial E^{R_i}}{\partial \eta} = \left[\left\langle \frac{\partial \Psi(\eta^*)}{\partial \eta} \bigg| H - E^{R_i} \big| \Psi(\eta) \right\rangle_{R_i} \right.$$

$$+ \left\langle \Psi(\eta^*) | H - E^{R_i} \big| \frac{\partial \Psi(\eta)}{\partial \eta} \right\rangle_{R_i} + \left\langle \Psi(\eta^*) \bigg| \frac{\partial H}{\partial \eta} \bigg| \Psi(\eta) \right\rangle_{R_i}$$

$$+ \int_{S_i^{(\eta)}} ds_i \frac{\partial S_i}{\partial \eta} \left\langle \Psi(\eta^*) | H - E^{R_i} \big| \Psi(\eta) \right\rangle_{R_i} \bigg] \bigg/ \left\langle \Psi(\eta^*) | \Psi(\eta) \right\rangle_{R_i} \quad (4)$$

where $S_i(\eta)$, appearing in the last term of Eq. (4), is the surface surrounding the region, $R_i(\eta)$. Now, from Eqs. (1) and (3), one immediately finds $E(\eta) = E_i^R(\eta)$, which implies that the first and the last terms in Eq. (4) equal zero. On the other hand, the third term in Eq. (4) yields:

$$\frac{\left\langle \Psi(\eta^*) | \partial H / \partial \eta | \Psi(\eta) \right\rangle_{R_i}}{\left\langle \Psi(\eta^*) | \Psi(\eta) \right\rangle_{R_i}} = -\frac{1}{\eta} (2 T^{R_i}(\eta) + V^{R_i}(\eta)) \quad (5)$$

where $T_i^R(\eta)$ and $V_i^R(\eta)$ are, respectively, the mean kinetic and potential energies which contribute to the energy, $E_i^R(\eta)$, according to Eq. (3). Therefore, from Eqs. (4) and (5), and the condition of stationarity of the energy, E_i^R, with respect to the scaling parameter, η, one obtains

$$2T^{R_i}(\eta) + V^{R_i}(\eta) = \eta \left\langle \Psi(\eta^*) | H - E^{R_i} \bigg| \frac{\partial \Psi(\eta)}{\partial \eta} \right\rangle_{R_i} \bigg/ \left\langle \Psi(\eta^*) | \Psi(\eta) \right\rangle_{R_i}. \quad (6)$$

Thus,

$$\left\langle \Psi(\eta^*) | H - E^{R_i} \bigg| \frac{\partial \Psi(\eta)}{\partial \eta} \right\rangle_{R_i} = 0 \quad (7)$$

will be the condition for the complex regional virial relation

$$2T^{R_i}(\eta) = -V^{R_i}(\eta) \quad (8)$$

Equation (7) reduces to the condition of the real scaling case in the limit $\eta \to 1$ [5]. Even in this situation, Eq. (7) is not an identity for any R_i, but a relation only fulfilled by certain regions, R_i, because of the non-Hermitian character of H, which arises from the fact that for the particule, i, the space of integration is truncated [5]. Another source of non-Hermiticity arises in our case of complex scaling from the fact that the Hamiltonian, $H(\eta)$, is itself a non-self-adjoint operator when $0 < \Theta < \pi/2$.

The condition for the boundary of the region, R_i, given in Eq. (7), has to have the same form as the condition for approximate wave functions in order to be compatible with the regional virial relations associated to real scaling [3]. This condition has been derived in Ref. 3 for the fixed nuclei case and, by following the same steps detailed in Ref. 5, it can be generalized to the case in which the nuclei are quantum mechanically described. In both the case of virial relations for approximate wave functions [3], and our case, the energy E_i^R may be complex.

Moreover, adding a term equal to zero to Eq. (7), we obtain

$$\left\langle \Psi(\eta^*)|H - E^{R_i}| \frac{\partial\Psi(\eta)}{\partial\eta} \right\rangle_{R_i} + \left\langle \frac{\partial\Psi(\eta^*)}{\partial\eta} |H - E^{R_i}|\Psi(\eta) \right\rangle_{R_i} = 0 \qquad (9)$$

which can be interpreted as a Hurley-type condition [13,23] for the fulfillment of a Hellmann–Freynman type relation, which will follow from Eqs. (4) and (9):

$$\frac{\partial E^{R_i}}{\partial\eta} = \left\langle \Psi(\eta^*) \left| \frac{\partial H}{\partial\eta} \right| \Psi(\eta) \right\rangle_{R_i} \qquad (10)$$

Similar to the case of real scaling [3], we can also write the complex scaling relations in the form given in Eqs. (3)–(8), but now for approximate wave functions. Given an approximate wave function, the condition, $\partial E_i^R/\partial\eta = 0$, will determine an optimal value, η_0, for η. Then, a relation of the same form as Eq. (9) for $\eta = \eta_0$, i.e.,

$$\left\langle \Psi(\eta^*)|H - E^{R_i}| \frac{\partial\Psi(\eta)}{\partial\eta} \right\rangle_{R_i}\bigg|_{\eta=\eta_0} + \left\langle \frac{\partial\Psi(\eta^*)}{\partial\eta} |H - E^{R_i}|\Psi(\eta) \right\rangle_{R_i}\bigg|_{\eta=\eta_0} = 0 \qquad (11)$$

will determine the region, $R_\eta = R_\eta^0$, for which the virial relation, $2T^{R0}(\eta_0) = -V^{R0}(\eta_0)$, holds, according to Eqs. (5), (10), and (11) and the stationarity condition, $\partial E^{R_i}/\partial\eta = 0$.

Conclusions

Experimentally, it is found that ionization or dissociation processes in a relatively large molecule can be frequently interpreted as occurring locally, in a small part of a molecule. The region, R_i, determined by Eq. (11), is a precise criterion to select such localized regions where the process, responsible for the nonbonding character of the molecular state, actually occurs. For instance the method of the θ-trajectory of the complex energy [21], which is based in the virial theorem, could be applied to the fragment of the molecule enclosed by a region, R_i, fulfilling Eq. (11).

Given an approximate wave function for a bound state, it is well known that the global virial relations associated to real scalings hold, independently of the quality of the wave function considered, provided that this wave function is optimized variationally with respect to the real scaling parameter [12]. This property implies that the fulfillment of virial relations cannot be invoked as a criterion to test the quality of a given wave function [12].

When one introduces the partition of the physical space, the fulfillment of regional virial relations requires both the stationarity of E_i^R with respect to η and that the partition of the physical space be such that Eq. (11) holds. Thus, in this case, although the stationarity of E_i^R with respect to η can be obtained for a low-quality wave function, the corresponding partition of the physical space induced by Eq. (11) may be a criterion for the quality of the approximate wave function used. This argument applies to both real regional virial relations [3,5] and to the complex

regional virial relations considered here. For instance, a partition incompatible with the symmetry or other well-known structural features of the molecule will serve as a criterion to discard a given approximate wave function.

Acknowledgments

Bibliography

[1] R. F. W. Bader, P. M. Beddall, and P. E. Cade, J. Am. Chem. Soc. 93, 3095 (1971).
[2] R. F. W. Bader, S. Srebrenik, and T. T. Ngyen-Dang, J. Chem. Phys. 68, 3680 (1978).
[3] A. Mazziotti, R. G. Parr, and G. Simons, J. Chem. Phys. 59, 939 (1973).
[4] V. Mujica, M. Garcia-Sucre, and Y. Aray, J. Mol. Struct. (Theochem.) (to appear).
[5] M. Garcia-Sucre and V. Mujica, Int. J. Quantum Chem. Symp. 24, 375 (1990).
[6] J. Nuttal, Phys. Rev. 160, 1459 (1967).
[7] J. Aguilar and J. M. Combes, Comm. Math. Phys. 22, 269 (1971).
[8] E. Balslev and J. M. Combes, Comm. Math. Phys. 22, 280 (1971).
[9] E. Hylleraas, Z. Phys. 54, 855 (1930).
[10] Y. Fock, Z. Phys. 63, 855 (1930).
[11] J. C. Slater, J. Chem. Phys. 1, 687 (1933).
[12] P. O. Lodwin, J. Mol. Spectrosc. 3, 46 (1959).
[13] S. T. Epstein, *The Force Concept in Chemistry*, B. M. Deb, Ed. (Van Nostrand, New York, 1981), p. 1.
[14] E. Brandas and P. Froelich, Phys. Rev. A16, 2207 (1977).
[15] E. Yaris and P. Winkler, J. Phys. B Atom. Molec. Phys. 11, 1475 (1978).
[16] N. Moiseyev, P. R. Certain, and F. Weinhold, Int. J. Quantum Chem. 14, 727 (1978).
[17] Proceedings of the 1978 Sanibel Workshop on Complex Scaling, Int. J. Quantum Chem. 14, 343 (1978).
[18] S. I. Chu, Int. J. Quantum Chem. Symp. 20, 129 (1986), and references cited therein.
[19] M. Garcia-Sucre, J. Molec. Struct. (Theochem.) 210, 85 (1990).
[20] M. Garcia-Sucre, Int. J. Quantum. Chem. 43, 209 (1992).
[21] W. P. Reinhardt, Ann. Rev. Phys. Chem. 33, 223 (1982).
[22] P. O. Lowdin, Adv. Quant. Chem. 19, 87 (1988).
[23] A. C. Hurley, Proc. R. Soc. (Lond.) A226, 170 (1954).

Calculating Atomic and Molecular Properties Using Variational Monte Carlo Methods

S. A. ALEXANDER,* R. L. COLDWELL,* and GERRARD AISSING[†]

Department of Physics, University of Florida, Gainesville, Florida 32611

AJIT J. THAKKAR

Department of Chemistry, University of New Brunswick, Fredericton, NB E3B 6E2, Canada

Abstract

We compute a number of properties for the $1\,^1S$, $2\,^1S$, and $2\,^3S$ states of helium as well as the ground states of H_2 and H_3^+ using Variational Monte Carlo. These are in good agreement with previous calculations (where available). Electric-response constants for the ground states of helium, H_2 and H_3^+ are computed as derivatives of the total energy. The method used to calculate these quantities is discussed in detail. © 1992 John Wiley & Sons, Inc.

Introduction

Variational Monte Carlo is a method of computing the expectation value of an operator (such as the Hamiltonian) and a trial wavefunction, Ψ_t, using Monte Carlo integration [1–14]. Typically the adjustable parameters in Ψ_t are chosen so as to minimize some combination of the total energy and its variance. In Ref. [14] we computed a number of Hylleraas-type wavefunctions by minimizing the variance functional

$$\sigma^2 = \sum_i \left[(H\Psi_i - E_{in}\Psi_i)^2 \Psi_i^2 / w_i^2 \right] \Big/ \left\{ \sum_i [\Psi_i^2 / w_i] \right\}^2 \tag{1}$$

where $\Psi_i = \Psi_t(x_i)$ and where

$$H = -\frac{1}{2} \sum_a \nabla_a^2 - \sum_{a,A} \frac{Z_a}{r_{aA}} + \sum_{a<b} \frac{1}{r_{ab}} + \sum_{A<B} \frac{Z_A Z_B}{r_{AB}} \tag{2}$$

is the molecular Hamiltonian (A,B denote nuclei; a,b denote electrons). Unless otherwise indicated, all values in this article are given in atomic units. In Eq. (1) the weight function, $w_i = w(x_i)$, is the relative probability of choosing the ith configuration, x_i, and exactly compensates for not having chosen it randomly. The constant E_{in} is fixed at a value close to the desired state in order to start the opti-

---

* Also at Institute for Astrophysics and Planetary Exploration, One Progress Blvd., Box 33, Alachua, Fl. 32615.

† Also at Quantum Theory Project, University of Florida, Gainesville, Fl. 32611.

mization in the proper region. With these wavefunctions we were able to accurately determine the total energy

$$\langle H \rangle = \sum_i [\Psi_i H \Psi_i / w_i] \Big/ \sum_i [\Psi_i^2 / w_i] \tag{3}$$

of several simple systems. Once a trial wavefunction has been optimized, however, a number of properties of physical interest can be computed using exactly the same techniques which were developed to evaluate the total energy. In fact, the expectation value

$$\langle A \rangle = \sum_i [\Psi_i A \Psi_i / w_i] \Big/ \sum_i [\Psi_i^2 / w_i] \tag{4}$$

and variance

$$\sigma_A^2 = \sum_i [(A\Psi_i - \langle A \rangle \Psi_i)^2 \Psi_i^2 / w_i^2] \Big/ \left(\sum_i [\Psi_i^2 / w_i] \right)^2 \tag{5}$$

of simple operators (A) which act only on a single, previously-optimized wavefunction can be evaluated at the same time as the total energy and with little additional cost. Because all integrals are done numerically, Variational Monte Carlo enables relatively complicated expectation values to be evaluated easily. Unlike analytic calculations, explicitly correlated wavefunctions present no more of a problem than traditional wavefunction forms. When the Biased Selection Method [4–9,11,14] is used to compute the Monte Carlo integration points, the value and error of an expectation value converges independently of the weight function for a sufficiently large number of configurations. There is no time step bias. Unlike Diffusion Monte Carlo [15–19], Variational Monte Carlo is only capable of calculating properties involving the trial wavefunction; expectation values involving the exact wavefunction cannot be made. In practice, however, Diffusion Monte Carlo most naturally calculates mixed expectation values involving both the exact and the trial wavefunction.

In this article we show that a number of properties can be accurately computed using Variational Monte Carlo methods. Besides being of general physical interest, these properties provide an important check on the accuracy of the Biased Selection Method. Because our trial wavefunctions were computed by minimizing the deviations in $H\Psi/\Psi$, an accurate value for the expectation value of the Hamiltonian does not automatically mean that other properties are sampled correctly. In the next section we consider several expectation values of a number of simple atomic and molecular systems. Both ground and excited states are examined. The third section describes our calculations of the dipole polarizability and the second dipole hyperpolarizabilities for the ground states of helium, H_2, and H_3^+. Since electric-response constants are derivatives of the total energy, their evaluation is considered in some detail.

Simple Properties

The Hylleraas-like trial wavefunctions we computed in Ref. [14] for various states of the helium atom have the form

$$\Psi_t = (1 \pm P_{12}) \sum_k a_k \{ e^{-\alpha r_1 - \alpha r_2} r_{12}^{b_k} (r_1 - r_2)^{c_k} (r_1 + r_2)^{d_k} \} \tag{6}$$

where P_{12} is the operator which interchanges the coordinates of the two electrons ($+1$ for singlets, -1 for triplets); α, β, and a_k are the parameters to be optimized with the minimization functional; and b_k, c_k, and d_k are predetermined integer constants. For comparison we also optimized a set of trial wavefunctions based on Slater-type geminals (see, for example, Refs. [20–22])

$$\Psi_t = (1 \pm P_{12}) \sum_k a_k z_1^{b_k} (3 z_1^2 - r_1^2)^{c_k} e^{-\alpha r_1 - \beta r_2} \tag{7}$$

The predetermined constants b_k and c_k allow the wavefunction to be distorted in the z direction; a flexibility which will be needed in the fourth section to study electric-response properties.

Table I shows that both a 50-term Hylleraas expansion and a set of 8s Slater functions ($b_k = c_k = 0$) produce a number of helium ground ($1\,^1S$) state properties

TABLE I. Selected properties (in a.u.) of the helium 1^1S state.

Property	Hylleraas[a]	Slater[b]	Literature[c]
c_f[d]	0.010	0.010	
E	2.90371(1)	2.903724(5)	2.903724375
$p^2 = p_1^2 + p_2^2$	5.8151(6)	5.8105(3)	5.80744
$r = r_1 + r_2$	1.856(1)	1.8558(5)	1.8589446
$r^{-1} = r_1^{-1} + r_2^{-1}$	3.381(4)	3.380(2)	3.3766336
$r^2 = r_1^2 + r_2^2$	2.375(2)	2.375(1)	2.386966
$r^{-2} = r_1^{-2} + r_2^{-2}$	12.02(9)	12.05(5)	12.0348
r_{12}	1.4185(9)	1.4189(5)	1.422070
r_{12}^{-1}	0.948(1)	0.9477(6)	0.945818
r_{12}^2	2.501(3)	2.504(1)	2.516439
r_{12}^{-2}	1.49(4)	1.49(2)	1.46477
$\nabla_1 \cdot \nabla_2$	−0.157(2)	−0.157(1)	0.1590
p^4	54(2)	53.3(5)	54.08802
$2\langle \delta(r_1) \rangle$	3.631(4)	3.621(2)	3.620854
$\langle \delta(r_{12}) \rangle$	0.1070(2)	0.1066(1)	0.106345

[a] Evaluated using 1,024,000 configurations.
[b] Evaluated using 4,096,000 configurations.
[c] Reference [24].
[d] Error per configuration in the total energy.

which are in good agreement with the literature [20,23,24]. A few quantities. however, differ from the "exact" results by several standard deviations. The Hylleraas and Slater wavefunctions give values for $\langle p^2 \rangle$ which are $(0.13 \pm 0.01)\%$ and $(0.053 \pm 0.005)\%$ larger than the exact result. This behavior is consistent with these wavefunctions being optimized to slightly too high a value near the origin (where $p^2 \sim 1/r$). It also indicates that we do not exactly satisfy the virial theorem. To do so would require a scale change in the expectation values. While this would correct the virial theorem. it would also increase the statistical error in the energy. The values for $\langle r^2 \rangle$ and $\langle r_{12}^2 \rangle$ are about 0.5% too low which shows that the trial wavefunctions drop a little too fast at large r. These small discrepancies are due to the fact that variance minimization does not completely optimize the edge of any wavefunction and to inadequacies in our sampling technique. This last problem can probably be corrected by minimizing over more than the 4000 configurations used in these calculations and by changing the form of the guiding function so as to place more Monte Carlo integration points just beyond the edge of the wavefunction.

In Ref. [16] Caffarel and Claverie computed values of $E = -2.904(1)$ and $\langle r^2 \rangle = 2.37(2)$ for the helium ground state using Diffusion Monte Carlo. This calculation was performed with 400 trajectories and 40,000 time steps for each trajectory. that is, a set of 16 million configurations Since the statistical error in each property behaves like $c_i/\sqrt{N}$ (where N is the number of configurations). c_i is a constant whose value depends on the method used to generate each configuration, on the method used to estimate the property, and on the quality of the trial wavefunction (especially in the case of the total energy). This error per configuration is 400 times smaller in our energy and almost 80 times smaller in our evaluation of $\langle r^2 \rangle$. Although our Variational Monte Carlo results converge to expectation values of the trial wavefunction rather than the exact result. Table I shows that for this system these expectation values are well within 1% of the exact result and can be calculated using a much smaller number of configurations.

Table II shows that the properties of the triplet ground (2^3S) state of helium are in generally good agreement with the literature [21,24,25]. It should be pointed out that the 34-term Hylleraas expansion which we use has an energy limit of -2.1752253 [14]. In contrast. the set of 8s functions which constitutes the Slater wavefunction produces a total energy which is much closer to the "exact" result. Both trial wavefunctions have an error per configuration for the total energy which is over three times better than that of the singlet ground state. This is because the antisymmetry of the (2^3S) state makes the wavefunction small when r_{12} is small. Like the calculations in Table I. a few expectation values differ from the results in the literature by several standard deviations. The quantity $\langle p^2 \rangle$ differs by $(0.08 \pm 0.01)\%$ when computed with the Hylleraas wavefunction and by $(-0.11 \pm 0.01)\%$ when computed with the Slater wavefunction. The results for $\langle r_{12}^2 \rangle$ show a similar behavior: differences of $(-0.17 \pm 0.01)\%$ and $(0.10 \pm 0.02)\%$, respectively.

Unlike the wavefunctions used in Tables I and II. the trial wavefunctions for the first excited singlet (2^1S) state of helium were not optimized in an explicitly variational manner. Instead they were found by simply minimizing the variance. Eq.

TABLE II. Selected properties (in a.u.) of the helium 2^1S state

Property	Hylleraas[a]	Slater[a]	Literature
c_i[b]	0.003	0.003	
E	2.175206(3)	2.175218(3)	2.175229378[c]
$p^2 \quad p_1^2 + p_2^2$	4.3542(5)	4.3459(5)	4.3504586[c]
$r \quad r_1 + r_2$	5.069(2)	5.118(2)	5.1009254[d]
$r^{-1} \quad r_1^{-1} + r_2^{-1}$	2.317(3)	2.314(3)	2.3093283[d]
$r^2 \quad r_1^2 + r_2^2$	22.55(2)	23.16(2)	22.92864[d]
$r^{-2} \quad r_1^{-2} + r_2^{-2}$	8.42(9)	8.41(9)	8.340900[d]
r_{12}	4.417(2)	4.464(2)	4.447535[d]
r_{12}^{-1}	0.2695(1)	0.2674(1)	0.26819787[d]
r_{12}^2	22.66(2)	23.27(4)	23.04620[d]
r_{12}^{-2}	0.0896(1)	0.088(1)	0.0889060[d]
$\nabla_1 \cdot \nabla_2$	−0.0071(6)	0.0070(6)	0.007442[c]
p_1^4	42(1)	41.5(8)	41.8355406[c]
$2 \delta(r_1)$	2.638(4)	2.636(4)	2.64071[c]
$\delta(r_{12})$	0.0	0.0	0.0

[a] Evaluated using 1,024,000 configurations.
[b] Error per configuration in the total energy.
[c] Reference [25].
[d] Reference [24].

(1), with $E_{ni} = -2.145$. Orthogonality with the ground state was checked *a posteriori* using the Rayleigh–Ritz method described in Ref. [14] and found to be very good. In Table III we show that the properties of the (2^1S) state are in generally good agreement with the literature [21,25,26]. The Hylleraas wavefunction consists of a 50-term expansion while the Slater wavefunction is again constructed from 8s functions. The values of c_i for the total energy show that for this system the quality of Slater wavefunction is much better than the Hylleraas. In fact, only two properties for the Slater wavefunction differ by more than 4σ from the accepted values: $\langle p^2 \rangle$ by $(-0.080 \pm 0.014)\%$ and $\langle \delta(r_{12}) \rangle$ by $(-1.06 \pm 0.23)\%$. These two values suggest that this wavefunction is spread out a little too much (in fact the smallest exponent in Eq. (7) was optimized to 0.452).

For the H_2 ground state at the internuclear distance 1.4 a.u., the Hylleraas wavefunction in Ref. [14] has the form

$$\Psi_t = (1 + P_{12}) \sum_{k=1}^{126} a_k \{ e^{-\alpha r_{1A} - \beta r_{2B}} r_{12}^{b_k} (r_{1A} - r_{1B})^{c_k}$$

$$\times (r_{1A} + r_{1B})^{d_k} (r_{2A} - r_{2B})^{e_k} (r_{2A} + r_{2B})^{h_k} \} \quad (8)$$

TABLE III   Selected properties (in a.u.) of the helium $2\,^3S$ state

Property	Hylleraas[a]	Slater[a]	Literature
c_i[b]	0.009	0.004	
E	2.145907(9)	2.145963(4)	2.145974(4)[c]
p^2 $p_1^2 + p_2^2$	4.2812(6)	4.2885(6)	4.291948[c]
r $r_1 + r_2$	5.883(3)	5.951(3)	5.94612[c]
r^{-1} $r_1^{-1} + r_2^{-1}$	2.268(3)	2.270(3)	2.2708155[d]
r^2 $r_1^2 + r_2^2$	31.16(3)	32.23(4)	32.1782[c]
r^{-2} $r_1^{-2} + r_2^{-2}$	8.20(9)	8.23(9)	8.293566[d]
r_{12}	5.208(3)	5.276(3)	5.26969[c]
r_{12}^{-1}	0.2496(2)	0.2492(2)	0.24968338[d]
r_{12}^2	31.30(3)	32.37(4)	32.302[c]
r_{12}^{-2}	0.142(2)	0.145(2)	0.143743[d]
$\nabla_1 \cdot \nabla_2$	0.0099(6)	-0.0096(6)	0.009503[c]
p^4	40.2(9)	40.6(9)	41.118667[c]
$2 \cdot \delta(r_1)$	2.613(4)	2.619(4)	2.618894[c]
$\delta(r_{12})$	0.00831(1)	0.00856(2)	0.0086521[c]

[a] Evaluated using 1,024,000 configurations.
[b] Error per configuration in the total energy.
[c] Reference [25].
[d] Reference [21].

where A and B are nuclear positions. Although the Slater wavefunction in Eq. (7) is for atomic systems, one generalization of this expression to molecular systems is

$$\Psi_t = (1 + P_{12}) \sum_k a_k x_{1A}^{b_k} y_{1A}^{c_k} z_{1A}^{d_k} e^{-\alpha_k r_{1A} - \beta_k r_{2B} - \gamma_k r_{12}} \qquad (9)$$

These basis functions are added on whatever combination of atoms (A and B both situated on the same atom; A and B situated on different atoms) will produce the minimum variance. In Table IV we compare the properties computed with these trial wavefunctions with the literature [27–32]. Our Slater wavefunction was optimized with a set of 9s functions and $7p_z$ functions (since the internuclear axis is taken to be in the z direction) and yields a slightly worse c_i than the Hylleraas form. As a result, many of the properties computed with this Slater wavefunction are also less accurate. This inaccuracy is partially masked by the fact that the form of the Slater wavefunction (because it has fewer basis functions) enables us to calculate expectation values with more configurations than the Hylleraas wavefunction in the same amount of CPU time. The only significantly incorrect value for the Hylleraas wavefunction, $\langle \delta(r_{12}) \rangle$, is off by $(-0.15 \pm 0.04)\%$. Because the electron–electron correlation is less important in this system than it is in helium [14], properties which are functions of r_{12} are also more accurate.

Table IV. Selected properties (in a.u.) of the H_2 ground state. $R = 1.4$ a.u. along the z axis

Property	Hylleraas[a]	Slater[b]	Literature
c_I^c	0.015	0.020	
E	1.17444(3)	1.17438(2)	1.1744699[d]
$p^2 = p_1^2 + p_2^2$	2.350(1)	2.3460(7)	2.35007[d]
$p_z^2 = p_{z_1}^2 + p_{z_2}^2$	0.870(1)	0.868(1)	0.838[e]
$p_x^2 = p_{x_1}^2 + p_{x_2}^2$	0.611(1)	0.608(1)	0.577[e]
r_{12}	2.168(2)	2.174(1)	2.1689528[c]
r_{12}^2	5.629(9)	5.675(5)	5.6323895[d]
r_{12}^{-1}	0.5882(9)	0.586(4)	0.58736591[d]
r_{14}	1.548(2)	1.550(8)	1.5488034[d]
r_{14}^2	3.031(6)	3.050(3)	3.0363543[d]
r_{14}^{-1}	0.910(2)	0.912(1)	0.91278856[d]
$r_{14}r_{1B}$	2.700(5)	2.720(3)	2.7039128[d]
$r_{14}r_{24}$	2.323(3)	2.328(2)	2.3214145[d]
$r_{14}r_{2B}$	2.381(3)	2.393(2)	2.3848370[d]
z_1z_2	-0.160(2)	0.1625(8)	0.15963461[d]
x_1x_2	0.055(1)	0.0574(6)	0.0551102913[d]
$z^2 = \frac{1}{2}(z_1^2 + z_2^2)$	1.017(2)	1.030(1)	1.0229686[d]
$x^2 = \frac{1}{2}(x_1^2 + x_2^2)$	0.764(2)	0.7657(9)	0.76169285[d]
$r^2 = \frac{1}{2}(r_1^2 + r_2^2)$	2.543(4)	2.562(2)	2.5463543[d]
Q_2^f	0.473(5)	0.450(3)	0.4568443[g]
Q_4^h	0.27(4)	0.26(2)	0.2826[i]
$\nabla_1 \cdot \nabla_2$	-0.102(2)	0.1019(8)	0.1008602[i]
$2p_1^4$	13.0(4)	13.2(2)	13.2490[i]
$\delta(\mathbf{r}_{14})$	0.459(1)	0.4600(5)	0.46015[j]
$\delta(\mathbf{r}_{12})$	0.01669(6)	0.01684(3)	0.016938[j]

[a] Evaluated using 256,000 configurations.
[b] Evaluated using 1,024,000 configurations.
[c] Error per configuration in the total energy.
[d] Reference [28].
[e] SCF values from Ref. [32].
[f] The electric quadrupole moment for H_2 is defined as

$$Q_2 = R^2/2 + \langle x_1^2 + x_2^2 - z_1^2 - z_2^2 \rangle$$

[g] Reference [30].
[h] The electric hexadecapole moment for H_2 is defined as

$$Q_4 = R^4/8 + \langle x_1^4 + x_2^4 + z_1^4 + z_2^4 - 6(x_1^2 z_1^2 + x_2^2 z_2^2) \rangle$$

[i] Reference [29].
[j] Reference [27].

Earlier Diffusion Monte Carlo studies have computed several properties of this system. Because they sample both the trial wavefunction and the exact eigenfunction, their results should, in principle, be equal to the exact values within the statistical error. In Ref. [18] Barnett et al. calculated values of $1.026(3)$ for $\langle z^2 \rangle$ and $2.549(6)$ for $\langle r^2 \rangle$ but did not list the number of configurations used to produce these results. Caffarel and Claverie [16] computed values of $-1.175(2)$ for the total energy, $0.587(3)$ for $\langle r_{12}^{-1} \rangle$, $2.169(9)$ for $\langle r_{12} \rangle$, $5.63(5)$ for $\langle r_{12}^2 \rangle$, $1.550(6)$ for $\langle r_{1A} \rangle$, $0.908(4)$ for $\langle r_{1A}^{-1} \rangle$, $3.04(2)$ for $\langle r_{1A}^2 \rangle$, $2.71(2)$ for $\langle r_{1A}r_{1B} \rangle$, $2.33(2)$ for $\langle r_{1A}r_{2A} \rangle$, $2.39(2)$ for $\langle r_{1A}r_{2B} \rangle$, $-0.156(6)$ for $\langle z_1 z_2 \rangle$, $-0.055(4)$ for $\langle x_1 x_2 \rangle$, $1.02(2)$ for $\langle z^2 \rangle$, $0.76(2)$ for $\langle x^2 \rangle$, and $2.55(4)$ for $\langle r^2 \rangle$. These properties were evaluated over a set of $50,000,000$ configurations in contrast to the $256,000$ configurations our Hylleraas results used.

At its equilibrium configuration the ground state of the H_3^+ ion has D_{3h} symmetry and a bond distance of 1.65 a.u. For this reason we chose our Hylleraas trial wavefunction to have the form [14]

$$\Psi_t = (1 + P_{12}) \sum_{k=1}^{120} a_k \{ e^{-ar_{1A}-dr_{2B}} r_{12}^{h_k}(r_{1A} - r_{1B})^{c_k}(r_{1A} + r_{1B})^{d_k}$$

$$\times (r_{2A} - r_{2B})^{e_k}(r_{2A} + r_{2B})^{f_k}(r_{1C} - r_{2C})^{g_k}(r_{1C} + r_{2C})^{h_k}$$

$$+ [A \leftrightarrow C] + [B \leftrightarrow C] \} \qquad (10)$$

where A, B, and C are the positions of the three nuclei. Using the same form as in Eq. (9), we have also optimized a Slater wavefunction for this system. When the H_3^+ ion is placed in the xy plane, a set of 18s functions, $8p_x$ functions, and $9p_y$ functions produces a reasonable wavefunction. In Table V we compare the properties computed with these trial wavefunctions. For this system we could find no published properties except for the energy. This value has been recently computed to be -1.3438279 [33] and -1.3438220 [34] using explicitly correlated basis functions and $-1.343835(1)$ using Diffusion Monte Carlo [35]. The values of c_i indicates that the Hylleraas values should be much more accurate than those calculated with the Slater trial wavefunction (with a systematic error less than the difference between the two calculations).

All of the properties computed in Tables I to V were determined using Eq. (4). Thus they require only that the wavefunction or its derivatives be evaluated (both of which are known). For the function p^2 we used the well-known relation

$$\int d\tau \Psi_t p^2 \Psi_t = -\int d\tau \Psi_t \nabla^2 \Psi_t \qquad (11)$$

and for p_1^4 we used [36]

$$\int d\tau \Psi_t p_1^4 \Psi_t = \int d\tau (\nabla_1^2 \Psi_t)^2 \qquad (12)$$

The delta functions were computed simply as

TABLE V. Selected properties (in a.u.) of the H_3 ground state. The system is in an equilateral triangle configuration in the xy plane with $R = 1.65$ a.u.

Property	Hylleraas[a]	Slater[b]
c_i[c]	0.025	0.202
E	-1.3437(1)	-1.3410(4)
$p^2 = p_1^2 + p_2^2$	2.69(1)	2.705(6)
$p_x^2 = p_{x_1}^2 + p_{x_2}^2$	0.792(4)	0.804(2)
$p_z^2 = p_{z_1}^2 + p_{z_2}^2$	1.104(6)	1.098(3)
r_{12}	1.99(1)	1.984(5)
r_{12}^2	4.61(2)	4.60(1)
r_{12}^{-1}	0.652(3)	0.625(2)
r_{14}	1.572(8)	1.569(4)
r_{14}^2	2.97(2)	2.955(8)
r_{14}^{-1}	0.856(5)	0.857(2)
$r_{14}r_{1B}$	2.59(1)	2.583(7)
$r_{14}r_{24}$	2.42(1)	2.402(6)
$r_{14}r_{2B}$	2.49(1)	2.469(6)
$x_1 x_2$	-0.108(3)	0.106(1)
$z_1 z_2$	-0.034(2)	0.036(1)
$x^2 = \frac{1}{2}(x_1^2 + x_2^2)$	0.760(4)	0.752(2)
$z^2 = \frac{1}{2}(z_1^2 + z_2^2)$	0.541(4)	0.539(2)
$r^2 = \frac{1}{2}(r_1^2 + r_2^2)$	2.06(1)	2.046(5)
$\nabla_1 \cdot \nabla_2$	-0.115(4)	-0.121(2)
p^4	7.7(1)	8.3(3)
$\langle \delta(r_{14}) \rangle$	0.363(2)	0.3866(8)
$\langle \delta(r_{12}) \rangle$	0.0185(1)	0.0270(5)

[a] Evaluated using 64,000 configurations.
[b] Evaluated using 256,000 configurations.
[c] Error per configuration in the total energy.

$$\langle \delta(\mathbf{r}_1) \rangle = \int d\mathbf{r}_1 d\mathbf{r}_2 \Psi_t(r_1,r_2,r_{12}) \delta(\mathbf{r}_1) \Psi_t(r_1,r_2,r_{12})$$

$$= \int d\mathbf{r}_2 \Psi_t(r_1 = 0, r_2, r_2)^2 \qquad (13)$$

and

$$\langle \delta(\mathbf{r}_{12}) \rangle = \int d\mathbf{r}_1 d\mathbf{r}_2 \Psi_t(r_1,r_2,r_{12}) \delta(\mathbf{r}_{12}) \Psi_t(r_1,r_2,r_{12})$$

$$= \int d\mathbf{r}_2 \Psi_t(r_1 = r_2, r_2, 0)^2 \qquad (14)$$

In both Eqs. (13) and (14) the Monte Carlo integration is only over the r_2 electron and the weight of the configuration must be changed so as to reflect the fact that r_1 is no longer chosen randomly.

Electric-Response Properties

When an atomic or molecular system is placed in an electric field, F, the Hamiltonian becomes

$$H(F) = H(F = 0) - \sum_i \mathbf{F} * \mathbf{r}_i \tag{15}$$

where r_i is the position of the ith electron. The total energy of a neutral S-state atom or a symmetric molecule upon introduction of a static, axially symmetric, homogeneous field F is thus

$$E(F) = E(F = 0) - \frac{1}{2} \alpha_{ab} F_a F_b - \frac{1}{24} \gamma_{abcd} F_a F_b F_c F_d - \cdots \tag{16}$$

where we have assumed an implicit summation over repeated indices and the subscripts run over the Cartesian coordinates (x,y,z). In Eq. (16) α is the dipole polarizability tensor of the system and γ is the second dipole hyperpolarizability tensor. For S-state atoms α and γ have only one independent component so we drop these subscripts for helium.

To calculate the electric-response constants for helium we set the electric field to lie along the z Cartesian axis. Since the Hamiltonian now has a directional preference, the trial wavefunction must be flexible enough to respond to this change. Our Hylleraas wavefunctions do not allow one coordinate to be selectively preferred but our Slater wavefunctions do. In the presence of small electric fields ($F = 0.02$ and $F = 0.04$), Slater wavefunctions were constructed from 9s functions, $3p_z$ functions ($b_k = 1$, $c_k = 0$), and $1d_{zz}$ function ($b_k = 0$, $c_k = 1$). Table VI shows that this

TABLE VI. Convergence of the energy, polarizability, and hyperpolarizability (in a.u.) of helium. N is the number of configurations.

N	$E(F = 0)$	$E(F = 0.02)$	$E(F = 0.04)$
16,000	-2.9038(1)	-2.9040(1)	2.9048(1)
64,000	-2.90383(4)	-2.90411(4)	-2.90494(5)
256,000	-2.90374(2)	-2.90401(2)	-2.90484(2)

N	$\dfrac{2\langle E(F = 0.02)\rangle - 2\langle E(F = 0)\rangle}{F^2}$	$\dfrac{2\langle E(F = 0.02)\rangle - E(F=0)\rangle}{F^2}$	$\dfrac{\langle 2E(F = 0.04)\rangle - 8E(F = 0.02) + 6E(F = 0)\rangle}{F^4}$
16,000	1.3(7)	1.33(4)	609(770)
64,000	1.4(3)	1.38(2)	74(415)
256,000	1.4(1)	1.371(9)	182(201)
Literature [40, 41]		1.383192	41.9

basis gives roughly the same statistical error as our $F = 0.0$ result. With these trial wavefunctions, we computed the polarizability and the hyperpolarizability for helium as derivatives of the energy

$$\left. \frac{\partial^2 E}{\partial F^2} \right|_{F=0} = -\alpha = \frac{E(F) - 2E(F=0) + E(-F)}{F^2} \tag{17}$$

and

$$\left. \frac{\partial^4 E}{\partial F^4} \right|_{F=0} = -\gamma = \frac{E(2F) - 4E(F) + 6E(F=0) - 4E(-F) + E(-2F)}{F^4} \tag{18}$$

These derivatives can be numerically computed in a number of ways. We experimented with several formulas (see, for example, Ref. [37]) and found little difference between them. Once a particular formula has been chosen, the most direct way of computing the derivative is to simply evaluate the total energy of this system at $F = 0.0$, 0.02, and 0.04 and then subtract the appropriate numbers. Table VI shows that this approach gives reasonable results but with a fairly large variance. Since a large part of the statistical error in these expectation values should be the same if the value of the electric field is sufficiently small (i.e., only a minor perturbation), a much more accurate approach is to compute the differences directly. This technique has been used to determine the dipole moment of LiH [38], molecular derivatives [17], and differences in potential energy surfaces [7,12,39]. When applied to our calculation of the polarizability, this method decreases the variance by about a factor of 15 and gives a result which is in much better agreement with the accepted value of 1.383192 [40,41]. When applied to the calculation of the second dipole hyperpolarizability, however, we see that the resulting statistical error completely obscures the computed value. The reason for this may be that the optimized error in the trial wavefunction is too large to detect the influence of this constant, 41.9 [41], in the total energy. In a Variational Monte Carlo calculation the effect of the electric field on the total energy has to be larger than the statistical error in the trial wavefunction in order to influence the optimization of the adjustable parameters. If the strength of the field is too large, however, then the composition of the wavefunction will change significantly and the various expectation values used to calculate the derivatives will no longer be strongly correlated. In fact, the formulas we have chosen may themselves become inaccurate because of contributions from higher-order terms. While we have tried to strike a balance between these two limits, a closer investigation of this problem is clearly in order.

If the Hellmann–Feynman theorem [42] is satisfied, then electric response properties can also be obtained from the induced dipole moment. In most traditional calculations this automatically occurs because the parameters in the wavefunction are optimized so as to minimize the total energy. Since our Variational Monte Carlo procedure adjusts the parameters in the trial wavefunctions so as to minimize the variance, the Hellmann–Feynman theorem will not be explicitly satisfied. For S-state atoms the dipole moment alternative to Eq. (16) is

$$\mu_a(F) = \alpha_{ab}F_b + \frac{1}{6}\gamma_{abcd}F_bF_cF_d + \cdots \tag{19}$$

where, for example,

$$\mu_z(F) = \langle \Psi(F) \sum_i z_i \Psi(F) \rangle \tag{20}$$

Again for simplicity we drop the subscripts and obtain the expressions

$$\left.\frac{\partial\mu}{\partial F}\right|_{F=0} = \alpha = \frac{\mu(F) - \mu(F=0)}{F} \tag{21}$$

and

$$\left.\frac{\partial^3\mu}{\partial F^3}\right|_{F=0} = \gamma = \frac{\mu(2F) - 2\mu(F) + 2\mu(-F) - \mu(-2F)}{2F^3} \tag{22}$$

Although $\mu(F=0)$ is zero for the systems considered here, we found that computing this operator as part of Eq. (21) reduces the size of the statistical fluctuations. Table

TABLE VII. Ground state polarizabilities (in a.u.) of various systems. N is the number of configurations.

System	N	Dipole[a] [Eq. (21)]	Energy [Eq. (17)]	Literature
He (α)	16,000	1.41(2)	1.33(4)	
	64,000	1.41(1)	1.38(2)	
	256,000	1.418(6)	1.371(9)	1.383[b]
H$_2$ (α_z)	16,000	5.57(6)	6.1(6)	
	64,000	5.57(3)	6.2(3)	
	256,000	5.57(1)	6.3(2)	6.380[c]
H$_2$ (α_{xx})	16,000	4.15(5)	3.7(8)	
	64,000	4.06(3)	4.6(4)	
	256,000	4.11(1)	4.4(2)	4.578[c]
H$_3$ (α_{xx})	16,000	3.48(4)	2.8(2)	
	64,000	3.44(2)	3.3(1)	
	256,000	3.44(1)	3.4(4)	3.4768[d]
H$_3$ (α_{yy})	16,000	3.46(4)	3.1(2)	
	64,000	3.47(2)	3.4(1)	
	256,000	3.47(1)	3.5(3)	3.4768[d]
H$_3$ (α_{zz})	16,000	2.14(3)	1.4(2)	
	64,000	2.16(2)	1.6(1)	
	256,000	2.169(8)	2.0(3)	2.0778[d]

[a] These numbers do not agree with those computed using energy derivatives because our wavefunctions do not satisfy the Hellmann–Feynman theorem.

[b] References [40, 41].

[c] Reference [43].

[d] Reference [44].

VII shows that this calculation produces a smaller statistical error than Eq. (17) (over an order of magnitude in most systems) but not the correct result. Clearly our calculations do not sufficiently satisfy the Hellmann–Feynman theorem to justify using Eq. (19) despite the fact that all our trial wavefunctions are reasonably accurate otherwise. Although not shown, the calculation of the second dipole hyperpolarizability using Eq. (22) is again inconclusive.

For the H_2 ground state polarizability calculations we used field strengths of $F = 0.01$ and $F = 0.02$. When the field was placed parallel to the molecular axis (i.e., along the z direction), we simply needed to reoptimize our field-free wavefunction in order to obtain an adequate trial wavefunction, that is, one whose variance is comparable to the field-free value. When the field was placed perpendicular to the molecular axis (i.e., along the x direction), we had to reoptimize our field-free wavefunction and add $2p_x$ functions. These trial wavefunctions produced polarizabilities which are in good agreement with those in the literature [43]. Not surprisingly, the statistical errors for this system are larger than those in helium since the Slater wavefunction is of poorer quality.

For the H_3^+ ground state we used a field strength of $F = 0.03$ for the polarizability calculations since the error per configuration for this system is 10 times larger than in H_2. When the field was placed along the x axis or the y axis, we simply needed to reoptimize our field-free wavefunction in order to obtain an adequate trial wavefunction. When the field was placed along the z axis (perpendicular to the plane of the molecule) we had to reoptimize our field-free wavefunction and add $6p_z$ functions. These trial wavefunctions produced polarizabilities which are in good agreement with some unpublished RPA results by Sauer and Oddershede [44].

Conclusions

Variational Monte Carlo enables a wide variety of properties to be computed in a straightforward manner. Since the wavefunction and its derivatives must be computed in order to evaluate the total energy, many other expectation values can be determined at the same time and with little additional cost. Although all the calculations presented here have been done with wavefunctions which were optimized using the variance functional, we examined the influence of other minimization functionals [14] and found only slight changes in the values of these properties. In general, most of the properties computed here agree to 1% or better (two or three significant figures) with those values determined by more traditional methods. This success verifies the accuracy of the Biased Selection Method. For the H_3^+ molecular ion, our calculations provide the first look at the properties of this system.

The difference between our Hylleraas and Slater calculations show the effect that changes in the trial wavefunction can have on the accuracy of different expectation values. These two forms also illustrate the tradeoff one must frequently make between the complexity of a wavefunction and its computational cost. Because the Slater-geminal form contains a large number of nonlinear parameters per basis function, it usually takes much longer to optimize than the Hylleraas form (which contains almost only linear parameters). Once these parameters are optimized

however, the computational time needed to evaluate a trial wavefunction over a large number of configurations scales as the number of basis functions. For this reason a compact Slater-geminal form is usually preferable to a large Hylleraas expansion for most purposes. Although all the properties computed in this article were evaluated using wavefunctions optimized by Monte Carlo techniques, wavefunctions computed by more traditional methods could also have been used. This might be done, for example, to quickly estimate some expectation value which would otherwise be difficult to evaluate analytically.

To obtain even more accurate expectation values, better trial wavefunctions and guiding functions will be needed. In this article we computed all properties over the same set of configurations. Although the guiding function which generated these configurations was chosen to produce accurate energies, our calculations show that it also gives good results for most expectation values. Some properties, however, (e.g., p^4) are large (or small) in quite different regions than the total energy and might be more accurately computed with a guiding function which places more (or less) configurations in these regions.

Previous work has shown that the selection of a good wavefunction is essential to the calculation of accurate electric-response properties [45–47]. Because of its ability to easily evaluate a wide variety of wavefunctions (including those containing interelectronic coordinates), Variational Monte Carlo should be a powerful method with which to calculate these properties. While all our polarizabilities agree with those computed by traditional methods (within the statistical error), Table VII shows that the statistical error of these results do not always drop by the expected factor of $c_L/\sqrt{N}$. This suggests that the guiding functions we use for these systems are reasonable for calculating simple properties but not for calculating some derivatives. Future work in this area must first concentrate on finding better guiding functions and wavefunctions. Also needed, however, are algorithmic changes which will lower the statistical error of taking the difference of two or more quantities. One possibility might be to optimize the change between the field and field-free solutions directly. Certainly any technique which enables the polarizabilities to be calculated more accurately will also enable higher derivatives, such as the hyperpolarizabilities, to be ultimately computed.

Acknowledgments

Bibliography

[1] A. A. Frost, J. Chem. Phys. 10, 240 (1942).

[2] A. A. Frost, R. E. Kellogg, and E. C. Curtis, Rev. Mod. Phys. 32, 313 (1960).

[3] H. Conroy, J. Chem. Phys. 41, 1327, 1331, 1336, 1341 (1964).

[4] R. L. Coldwell, Int. J. Quantum Chem. S11, 215 (1977).

[5] R. L. Coldwell and R. E. Lowther, Int. J. Quantum Chem. S12, 329 (1978).

[6] R. L. Coldwell, Int. J. Quantum Chem. S13, 705 (1979).

[7] R. E. Lowther and R. L. Coldwell, Phys. Rev. A22, 14 (1980).

[8] K. A. Wilson and R. L. Coldwell, J. Comput. Phys. 61, 483 (1985).

[9] M. C. Huang, R. L. Coldwell, and M. Katoot, Nucl. Phys. B309, 733 (1988).

[10] C. J. Umrigar, K. G. Wilson, and J. W. Wilkins, Phys. Rev. Lett. 60, 1719 (1988).

[11] S. A. Alexander and R. L. Coldwell, Int. J. Quantum Chem. S23, 169 (1989).

[12] C. J. Umrigar, Int. J. of Quantum Chem. S23, 217 (1989).

[13] Z. Sun, S. Y. Huang, R. N. Barnett, and W. A. Lester, Jr., J. Chem. Phys. 93, 3326 (1990).

[14] S. A. Alexander, R. L. Coldwell, H. J. Monkhorst, and J. M. Morgan, III, J. Chem. Phys. 95, 6622 (1991).

[15] P. J. Reynolds, R. N. Barnett, B. L. Hammond R. M. Grimes, W. A. Lester, Jr., Int. J. Quantum Chem. 29, 589 (1986).

[16] M. Caffarel and P. Claverie, J. Chem. Phys. 88, 1100 (1988).

[17] J. Vrbik, D. A. Legare, and S. M. Rothstein, J. Chem. Phys. 92, 1221 (1990).

[18] R. N. Barnett, P. J. Reynolds, and W. A. Lester, Jr., J. Comput. Phys. 96, 258 (1991).

[19] B. L. Hammond, M. M. Soto, R. N. Barnett, and W. A. Lester, Jr., J. Mol. Struct. 234, 525 (1991).

[20] A. J. Thakkar and V. H. Smith, Jr., Phys. Rev. A15, 1 (1977).

[21] A. J. Thakkar and V. H. Smith, Jr., Phys. Rev. A15, 16 (1977).

[22] S. A. Alexander and H. J. Monkhorst, Phys. Rev. A38, 26 (1988).

[23] C. L. Perkeris, Phys. Rev. 112, 1649 (1958).

[24] C. L. Pekeris, Phys. Rev. 115, 1216 (1959).

[25] C. L. Pekeris, Phys. Rev. 126, 1470 (1962).

[26] C. L. Pekeris, Phys. Rev. 127, 509 (1962).

[27] W. Kolos and L. Wolniewicz, J. Chem. Phys. 41, 3663 (1964).

[28] W. Kolos and L. Wolniewicz, J. Chem. Phys. 43, 2429 (1965).

[29] G. Karl, J. D. Poll, and L. Wolniewicz, Can. J. Phys. 53, 1781 (1975).

[30] J. D. Poll and L. Wolniewicz, J. Chem. Phys. 68, 3053 (1978).

[31] B. Jeziorski and K. Szalewicz, Phys. Rev. A19, 2360 (1979).

[32] B. S. Sharma and A. J. Thakkar, Int. J. Quantum Chem. 29, 323 (1986).

[33] D. Frye, G. C. Lie, and E. Clementi, J. Chem. Phys. 91, 2369 (1989).

[34] S. A. Alexander, H. J. Monkhorst, R. Roeland, and K. Szalewicz, J. Chem. Phys. 93, 4230 (1990).

[35] J. B. Anderson, J. Chem. Phys. 96, 3702 (1992).

[36] H. A. Bethe and E. E. Salpeter, Quantum Mechanics of Two-Electron Atoms (Springer, Berlin, 1957).

[37] R. J. Bartlett and G. D. Purvis III, Phys. Rev. A20, 1313 (1979).

[38] B. H. Wells, Chem. Phys. Lett. 115, 89 (1985).

[39] C. A. Traynor and J. B. Anderson, Chem. Phys. Lett. 147, 389 (1988).

[40] A. J. Thakkar, J. Chem. Phys. 75, 4496 (1981).

[41] D. M. Bishop and B. Lam, Phys. Rev. A57, 464 (1988).

[42] S. T. Epstein, The Variation Method in Quantum Mechanics (Academic, New York, 1974).

[43] D. M. Bishop and L. M. Cheung, J. Chem. Phys. 72, 5125 (1980).

[44] Stephan Sauer and Jens Oddershede (unpublished results).

[45] A. Dalgarno, Adv. Phys. 11, 281 (1962).

[46] A. D. Buckingham, Adv. Chem. Phys. 12, 107 (1967).

[47] M. Urban, I. Cernusak, V. Kello, and J. Noga, in Methods in Computational Chemistry, Stephen Wilson, Ed. (Plenum, New York, 1987), Vol. 2.

Localization of Wavefunctions From Extended Systems Using Orbital Occupation Numbers

JOHN D. HEAD and SUSIL J. SILVA

Department of Chemistry, University of Hawaii, Honolulu, Hawaii 96822

Abstract

An algorithm is presented which produces localized cluster region orbitals which may be useful in embedded cluster calculations. The orbital occupation number matrix, n, for a trial set of functions is evaluated using the density matrix computed from an extended system. Surprisingly, when using Hartree–Fock (HF) orbitals from finite cluster calculations, several partially occupied orbitals having n_i different from 2 and 0 are found. The localization is accomplished by applying Jacobi transformation to n, mixing surrounding functions with the cluster region, so that the final set of localized functions have $\tilde{n}_{ii}$ with either 2 or 0. Numerical examples of the algorithm are given for Li clusters simulating the Li(100) surface. © 1992 John Wiley & Sons, Inc.

Introduction

Cluster calculations in combination with the standard tools of quantum chemistry is a convenient approach to modeling local interactions on surfaces [1]. For example, *ab initio* calculations on transition metal clusters have already been helpful in rationalizing a number of surface properties. Recently, we have even found Hartree–Fock (HF) calculations on clusters composed of the free electron–like Al metal useful for proposing structures for H chemisorbed on the Al(111) surface [2]. Nevertheless, the truncation at the cluster edge is a drastic approximation to the extended substrate. It does appear that properties such as adsorbate–surface geometries and vibrational frequencies converge rapidly with cluster size while adsorbate binding energies are more problematic [3,4]. Siegbahn and co-workers have recently suggested that relatively large clusters often need to be prepared for chemisorption bonding by making an excitation to the proper bonding state [5]. On the surface, such an excited state will always be easily accessible.

An alternative to the Siegbahn et al. strategy is to use an embedded cluster approach where the potential on the edge atoms is modified to simulate the potential from the extended surface. There are a number of groups developing these procedures [6,7], with the method of Whitten et al. [8] perhaps being the simplest to implement into existing *ab initio* computer codes. The Whitten et al. method essentially localizes the delocalized functions of an extended substrate into functions spanning mainly the cluster of interest. These localized functions are then taken to form a basis set for use in the truncated calculation. Although Whitten et al.

have now successfully applied their method to several applications there still remain a number of concerns, including the localization technique, with the method [7].

In this article, we develop a better procedure for obtaining the localized cluster region orbitals. We start by using the results from a HF calculation on the extended periodic substrate, performed by using the CRYSTAL program developed by Pisani et al. [9], instead of the very large finite cluster results which Whitten et al. use. The CRYSTAL program allows one to use the same basis sets in both the extended substrate and the cluster calculations. From the density matrix computed by the CRYSTAL program we obtain occupation numbers for orbitals located in the cluster region. The cluster orbital occupation numbers are obtained in a manner similar to a Davidson population analysis [10]. In such a population analysis one might expect the occupied HF orbitals from a finite cluster when measured against the extended substrate density matrix to have an orbital occupation number of 2. In the results section we show this does not always happen, illustrating another feature to be considered when using cluster models to simulate extended systems. In the next section, we describe how the cluster region orbital populations are computed. We then present an algorithm which transforms the cluster region orbitals into a new set of functions having occupations numbers of either 2 or 0. These transformed functions are like the Whitten et al. localized functions, and they have tails which connect the cluster to the surroundings. Examples of generating these transformed functions are given in the second part of the Results section. We expect these new functions to be useful in an embedded cluster procedure which will only require minor modifications of existing *ab initio* computer packages.

Method

In this section, we present an algorithm which generates a set of localized functions $\{\bar{\phi}_i^c\}$ with orbital occupation numbers of either 2 or 0 with respect to the density matrix computed in an extended substrate calculation. The functions are localized in a manner similar to the linear combination of basis functions one obtains in a cluster calculation. We start with cluster orbitals, ϕ_i^c, which have the form

$$\phi_i^c = \sum_\mu X_\mu c_{\mu i} \qquad (1)$$

where X_μ are the basis functions centered on the atoms composing the cluster. The cluster we pick initially is somewhat arbitrary, but then we can similarly define surrounding functions ϕ_i^s which have X_μ on the surrounding atoms of the extended substrate but outside of the cluster region.

The occupation number for a cluster function is computed according to

$$n_{ij} = C_i^\dagger SP^X SC_j \qquad (2)$$

where P^X is the density matrix from the extended substrate calculation spanning the same basis function types X_μ, as used in the cluster region, and S is the matrix of the basis functions overlaps. Davidson has described how the n matrix can be used in a population analysis [10]. The diagonal element, n_{ii}, is the occupation number of the cluster function ϕ_i^c, and should obey the inequality

$$0 \le n_{ii} \le 2. \tag{3}$$

However, the occupation number can only be used to assign electrons to a definite cluster orbital when the $\{\phi_i^c\}$ set is orthonormal. Presently, we Schmidt orthogonalize the ϕ_i^c, starting with the basis functions at the center of the cluster and working outward, but we expect other orthogonalization schemes to produce equivalent results. HF Orbitals from finite cluster calculations also automatically satisfy the orthogonality requirement on $\{\phi_i^c\}$. In the first part of the Results section we discuss the n_{ii} computed when using finite cluster HF orbitals. When the $\{\phi_i^c\}$ is augmented by additional functions from the surroundings set, then these new functions are also Schmidt orthogonalized to the existing cluster functions.

The localized cluster functions $\tilde{\phi}_i^c$ with $\tilde{n}_{ii}$ either 0 or 2 are produced by performing Jacobi-like unitary transformations which mix a cluster region orbital with an orthonormal surroundings function

$$\tilde{\phi}_i^c = \phi_i^c \cos\theta + \phi_j^s \sin\theta \tag{4}$$

giving the resulting orbital occupation number

$$\tilde{n}_{ii} = n_{ii} \cos^2\theta + n_{jj} \sin^2\theta + 2n_{ij} \sin\theta \cos\theta \tag{5}$$

We use a ϕ_j^s with $n_{jj} > n_{ii}(n_{jj} < n_{ii})$ to reduce (increase) the occupation number of ϕ_i^c. The algorithm consists of the following steps:

1. Pick the orbitals to be included in the cluster region basis set and orthogonalize them to produce $\{\phi_i^c\}$.
2. Select the extra functions $\{\phi_i^f\}$ which will be allowed to mix with the $\{\phi_i^c\}$ from the surroundings set. Schmidt orthogonalize the $\{\phi_i^f\}$ to the $\{\phi_i^c\}$. The resulting ϕ_i^f correspond to the ϕ_j^s used in eq. (4).
3. Compute the orbital occupation matrix, using eq. (2), for all the ϕ_i^c and ϕ_i^f functions and perform a Jacobi diagonalization [11] on the cluster-cluster, n_{CC}, block.
4. Determine whether the final $\tilde{n}_{ii}$ should be 0 or 2. We use the scheme if

$$n_{ii} < \delta \qquad \text{then} \qquad \tilde{n}_{ii} = 0 \tag{6}$$

or if

$$n_{ii} > 2 - \delta \qquad \text{then} \qquad \tilde{n}_{ii} = 2 \tag{7}$$

where δ can be varied, but is taken as 0.5 for calculations in the Results section. When

$$\delta < n_{ii} < 2 - \delta \tag{8}$$

use perturbation theory to predict whether the cluster orbital prefers to gain or lose electrons.
5. Perform Jacobi rotations of the type given by eqs. (4) and (5) between the cluster and surrounding orbitals. This step is performed iteratively, reducing the n_{ii} of those orbitals which want $\tilde{n}_{ii} = 0$ first, and then increasing n_{ii} for the $\tilde{n}_{ii} =$

2-type orbitals. The occupation number change in a single iteration was restricted to 0.25 electrons. Convergence is achieved when no changes in the n_{ii} occur.

In the Results section, we demonstrate the utility of the above algorithm by performing monolayer cluster and slab calculations to simulate the Li(100) surface. The (100) surface consists of Li atoms arranged in an array of squares. In the calculations, we only include Li $1s$ and $2s$ orbitals via a STO-3G basis [12], but we expect the algorithm to still be applicable when using more extended basis sets. The density matrix for the extended substrate, $\mathbf{P}^X$, was computed by a CRYSTAL [9] calculation on a monolayer of Li(100) atoms. In all of the calculations we used a Li–Li distance of 3.087 Å, which was obtained by optimizing the Li monolayer lattice spacing in the CRYSTAL calculation. This 3.087-Å distance matches closely the nearest neighbor distance (3.02 Å) for bulk Li [13]. Since CRYSTAL only performs closed-shell HF calculations, all of the cluster calculations were performed on systems containing an even number of Li atoms. The different-sized clusters are made by using different numbers of shells of symmetry-equivalent atoms around the cluster center; the coordinates for each of the unique atoms are listed in Table 1. Finite-cluster HF calculations were performed on Li_8, Li_{16}, Li_{30}, and Li_{44} and the resulting n_{ii}, computed by eq. (2), are discussed in the Results section. Li_8 is the simplest cluster, it has 2 central atoms, each surrounded by all their nearest neighbor atoms. Li_{16} is obtained by adding the shell of next nearest neighbor atoms surrounding Li_8. Li_{30} and Li_{44} are built from Li_{16} by adding the next two series of neighboring atom shells. Li_{44} and the component clusters are shown in Figure 1.

When the cluster functions are being localized to produce $\tilde{n}_{ii} = 0$ or 2, we use the extra functions in the order they are listed in Table I. For example, for the ϕ_i^c from Li_8, 10 extra functions ϕ_i^f would come from the lattice positions (2.5,0), (2.5,1), and (2.5,2).

For convenience, apart from when HF orbitals are used, the initial cluster orbitals are taken as symmetry-adapted combinations. For the four symmetry-equivalent atoms at the ($\pm(i + 0.5)$, $\pm j$) lattice positions, cluster orbitals which transform as a_1, a_2, b_1, and b_2 irreducible representations in the C_{2v} point group are obtained. For the two symmetry-equivalent atoms at ($\pm(i + 0.5)$, 0), only a_1 and b_1 orbitals are obtained. All of the cluster calculations have been performed using a modified version of the GAMESS package [14].

Results

The valence orbital occupation number obtained by using closed-shell HF orbitals, in eq. (2), from the Li_8, Li_{16}, Li_{30}, and Li_{44} cluster calculations, are illustrated graphically by Figures 2–5, where n_{ii} is plotted against the HF orbital energy. The total sum of the core orbital occupation numbers, given in Table II, reflect that each core orbital, as expected, is completely occupied by two electrons. Similarly, Figures 2–5 show the low-lying valence orbitals are also essentially completely filled. However, Table II shows that the total occupation number for the valence orbitals exceeds the number of valence electrons available from the finite cluster. This extra

TABLE I. Lattice positions for the symmetry unique atoms, at increasing distance from the origin, which are used to build the different Li clusters and form the symmetry-adapted surroundings extra functions, ϕ_i^c.

Function number	Number of atoms	Lattice positions
1	2	(0.5,0)
2	6	(0.5,1)
3	8	(1.5,0)
4	12	(1.5,1)
5	16	(0.5,2)
6	20	(1.5,2)
7	22	(2.5,0)
8	26	(2.5,1)
9	30	(0.5,3)
10	34	(2.5,2)
11	38	(1.5,3)
12	40	(3.5,0)
13	44	(3.5,1)
14	48	(2.5,3)
15	52	(0.5,4)
16	56	(3.5,2)
17	60	(1.5,4)
18	62	(4.5,0)
19	66	(3.5,3)
20	70	(4.5,1)
21	74	(2.5,4)
22	78	(4.5,2)
23	82	(0.5,5)
24	86	(1.5,5)
25	90	(3.5,4)
26	94	(4.5,3)
27	96	(5.5,0)
28	100	(2.5,5)
29	104	(5.5,1)
30	108	(5.5,2)

valence population is a reflection of the orthogonalization procedure we use for the cluster functions ϕ_i^c. The ϕ_i^c have the correct orthonormality condition which enables using n_{ii} to assign orbital populations, but the ϕ_i^c still overlap with orbitals outside the cluster region resulting in contributions to n_{ii} from the surroundings. Perhaps the most interesting result from Figures 2–5 is that the high-lying occupied HF orbitals have n_{ii} significantly less than 2, while the virtual HF orbitals have n_{ii} much greater than zero. To emphasize this result, in Table II, we list the occupation numbers for the highest occupied (HOMO) and lowest unoccupied (LUMO) molecular orbitals. In a cluster calculation, one often assumes the occupied (virtual) orbitals are representative of the filled (empty)
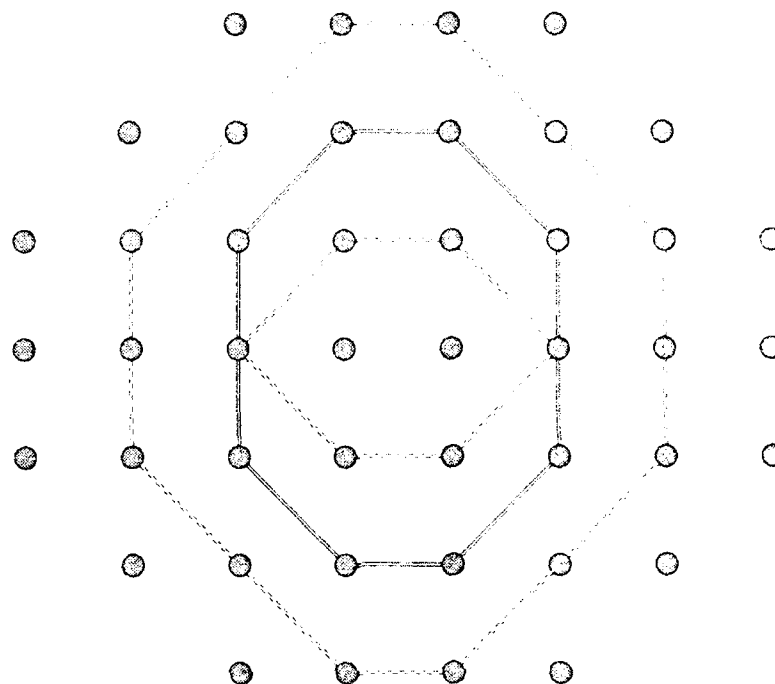
Figure 1.   The Li_{44} cluster and its components: Li_8 (central dashed lines). Li_{16} (solid lines), and Li_{30} (outer dashed lines).

Bloch functions of the extended substrate. Our results here suggest that cluster orbitals may not be as good an approximation to the extended substrate as one would like. Below we show how our localization algorithm can produce more favorable occupation numbers.

In Tables III and IV we present the results of applying our localization procedure to cluster functions ϕ_i^c from Li_8 and Li_{30}, respectively. Instead of HF orbitals, the ϕ_i^c are now symmetry-adapted combinations of the $1s$ and $2s$ STO-3G orbitals centered on the equivalent atoms sets listed in Table I. For example, the ϕ_i^c functions 9 and 10 in Table III correspond to the symmetric and antisymmetric combinations of the $2s$ orbitals at the (0.5,0) and (−0.5,0) lattice points. Similarly, ϕ_i^c functions 11, 12, 13, and 14 are the respective a_1, a_2, b_2, and b_1 symmetry adapted $2s$ functions generated from the four equivalent lattice points (±0.5,±1). The first eight Li_8 ϕ_i^c are created in the same manner using symmetry-adapted combinations of the $1s$ orbitals. The numbers of extra functions ϕ_j^t used in Tables III and IV match taking all symmetry-adapted $2s$ orbitals from the appropriate set of equivalent atoms. The first four ϕ_j^t used with Li_8 are derived from the (±1.5,±1) lattice sites; further ϕ_j^t are added in the order they are listed in Table I. Only two ϕ_j^t are added
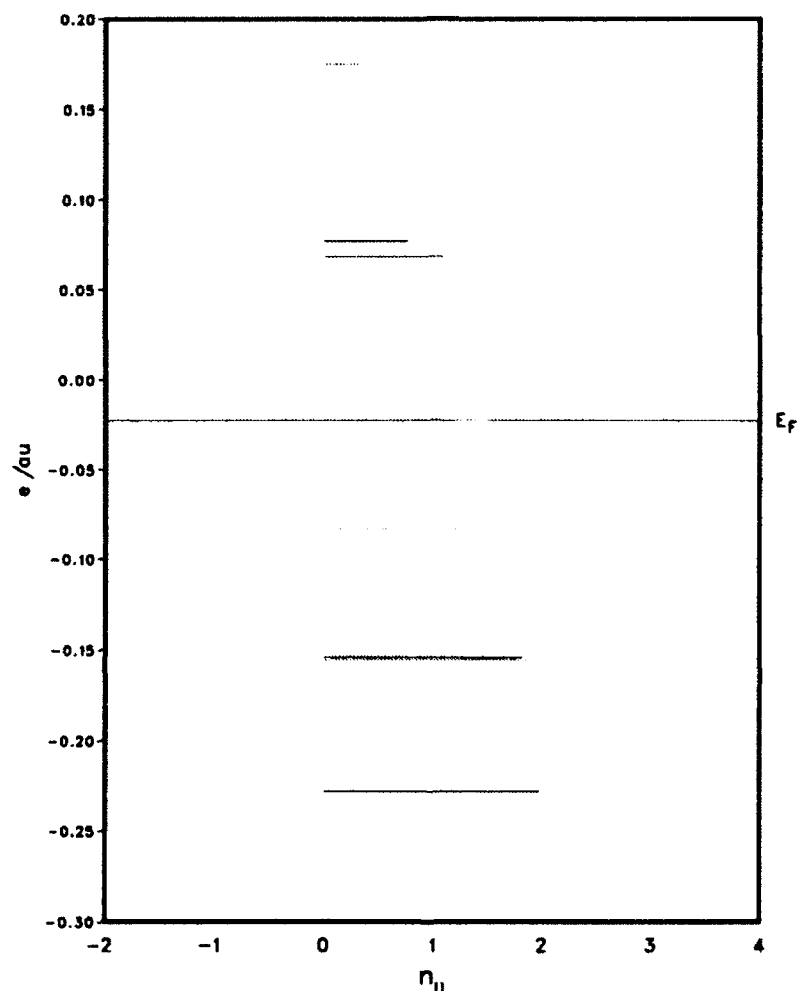
Figure 2. The occupation numbers. n_{ii}, from the HF Li_8 finite-cluster calculation versus HF orbital energy.

between 12 and 14 because these additional functions are centered on the ($\pm 2.5,0$) site. The nonorthogonality of the $1s$ and $2s$ STO-3G functions is removed when the $\{ \phi_i^C \}$ and $\{ \phi_j^L \}$ are Schmidt orthogonalized.

Since the initial ϕ_i^C are not HF orbitals we obtain initial orbital occupation numbers n'_{ii} with a broad range of values. However, the trace of the cluster-cluster block n_{CC} is still the same as that obtained with the HF orbitals, since both sets of functions span the same space. The n_{ii}^D in Tables III and IV give the occupation numbers after the Jacobi diagonalization of the cluster-cluster block, n_{CC}. In the case of Li_8 we find n_{ii}^D approaching 2 when the initial n'_{ii} are greater than ~ 1.1. Only ϕ_i^C 14
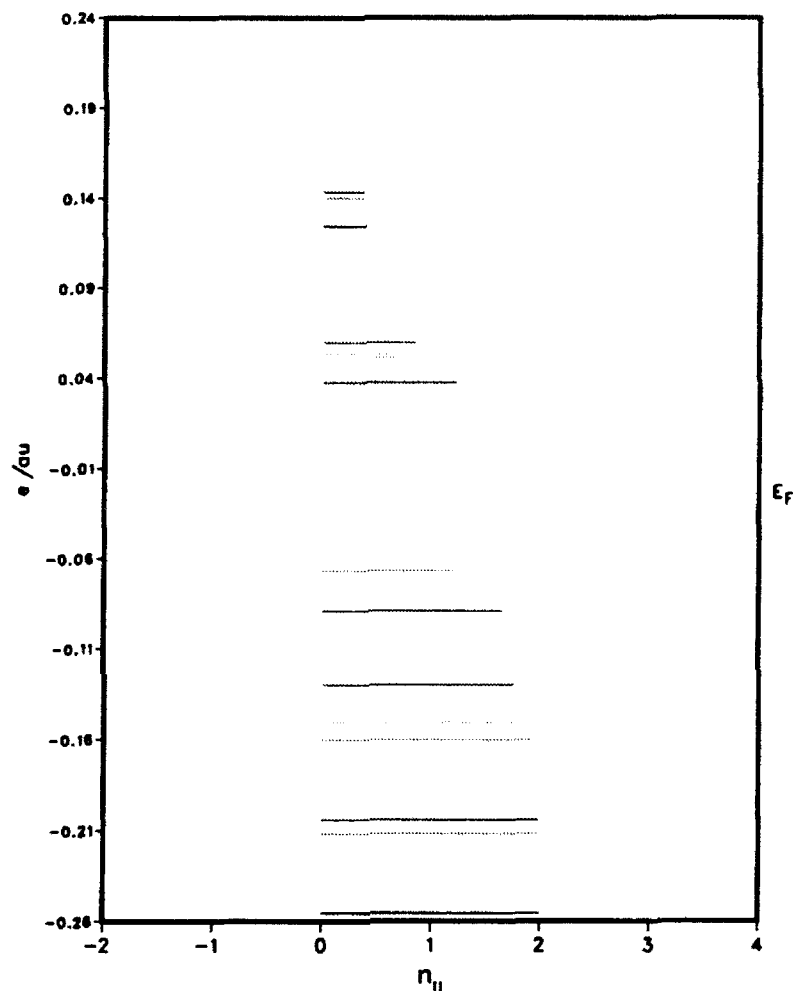
Figure 3.   The occupation numbers, n_{ii}, from the HF Li$_{10}$ finite-cluster calculation versus
HF orbital energy.

results in a n_{ii}^D approaching zero. In Table IV, the ϕ_i^C for functions 31–46 have n_{ii}^D very close to either 2 or 0. Initially, these 31–46 ϕ_i^C only span the Li$_{16}$ cluster, the remaining ϕ_i^C come from basis functions located on the Li$_{30}$ edge atoms, connected by the dashed line in Figure 1, which surround the central Li$_{16}$. Thus, we find the orbitals inside the cluster edge atoms to be either completely filled or completely empty. A similar trend is evident for the Li$_8$ calculation in Table III. However, the total occupation number for the valence orbitals of these two atoms is close to 4 rather than the 2 expected from a finite cluster calculation. Perhaps
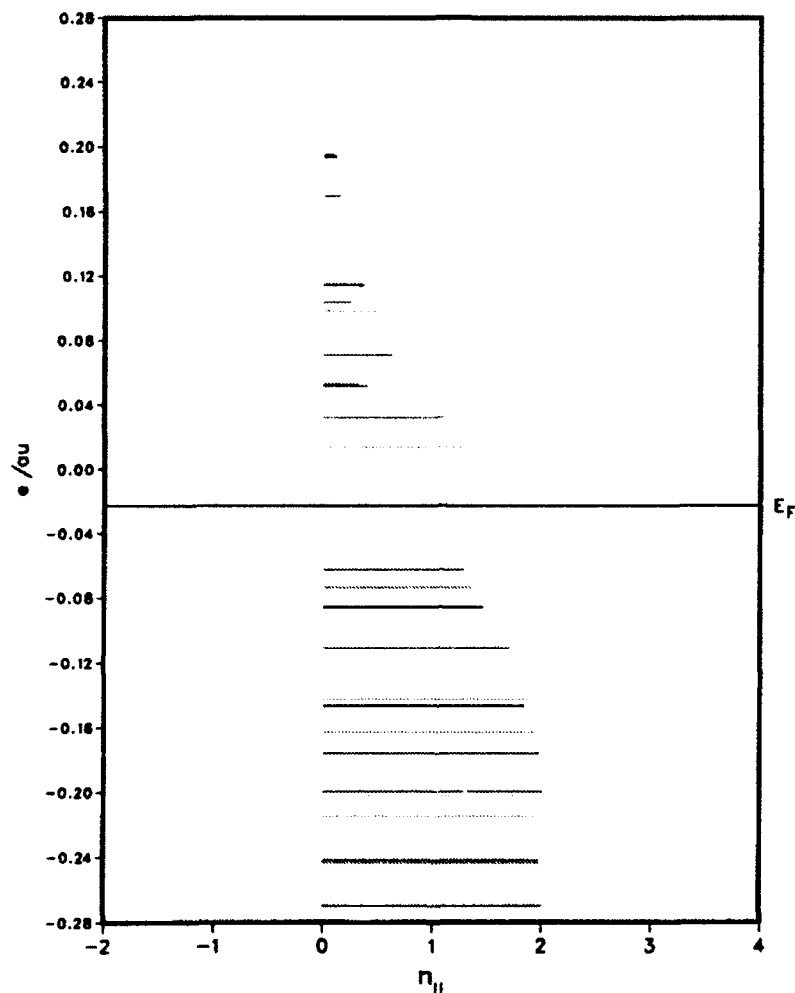
Figure 4.   The occupation numbers, n_{ii}, from the HF Li$_{30}$ finite-cluster calculation versus HF orbital energy.

surprisingly, in Table IV, the total n_{ii}^D for the inner Li$_{16}$ cluster is nearly 18, and not 16. At present we have no physical explanation for these populations.

The addition of 4 ϕ_j^F to Li$_8$ reduces the total number of cluster electrons by 0.825 electrons. Each atom in the Li$_8$ cluster has a complete shell of neighbors when there are 14 ϕ_j^F, and, at this stage, the transformed occupation numbers, $\tilde{n}_{ii}$, are fairly close to 2 and 0. Even better, $\tilde{n}_{ii}$ are obtained when 22 ϕ_j^F are used, these extra functions span the same atoms in the Li$_{30}$ cluster used as a starting point for Table IV. The $\tilde{n}_{ii}$ for Li$_8$ ϕ_j^C with 22 ϕ_j^F resemble the n_{ii}^D for functions 31–38 in Table IV. The remaining differences between the two sets of occupation numbers
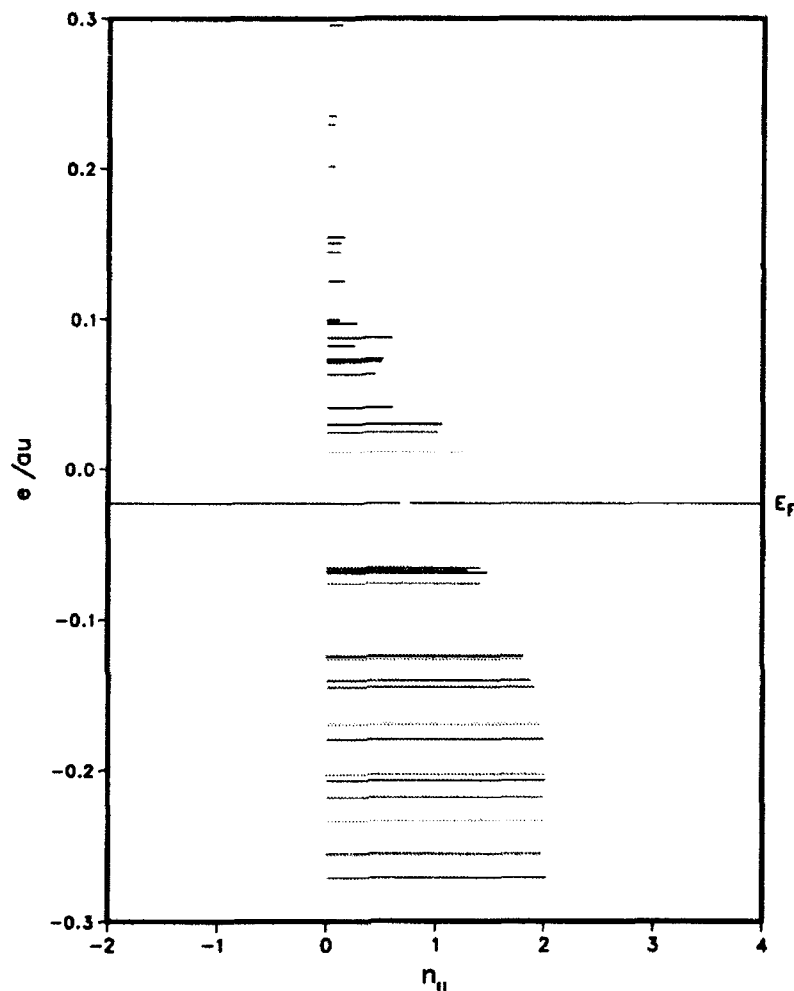
Figure 5.   The occupation numbers. n_u, from the HF Li$_{44}$ finite-cluster calculation versus
HF orbital energy.

are due to our algorithm using only a partial Jacobi diagonalization to transform the Li$_8$ $\tilde{\phi}_i^C$. The Li$_8$ ϕ_i^C are essentially converged when 22 ϕ_i^F are used, and only slight improvements in the $\tilde{n}_u$ are found when the 2s orbitals from the next-next-nearest shell of atoms are included in the localization. Having 36 ϕ_i^F extra functions corresponds to working with a Li$_{44}$ cluster.

The different numbers of ϕ_i^F listed in Table IV correspond to surrounding the Li$_{30}$ cluster with 1, 2, and 3 extra shells of Li valence functions. The first shell, with 14 ϕ_i^F, clearly improves the $\tilde{n}_u$ for the 31-46 orbitals, making the small n_u^D closer to zero. These 16 $\tilde{\phi}_i^C$ were originally derived from the inner Li$_{16}$ cluster. Indeed, some of the $\tilde{n}_u$ violate slightly the $0 \leq n_u \leq 2$ condition, but we feel this a reflection

TABLE II. Orbital occupation numbers, n_u, computed from the HF calculations on the finite clusters illustrated in Figure 1.

Cluster	n_u HOMO	n_u LUMO	Valence Σn_u	Core Σn_u
Li_8	1.369	1.064	10.306	15.999
Li_{16}	1.197	1.222	19.130	31.999
Li_{30}	1.292	1.288	34.474	59.998
Li_{44}	1.411	1.275	49.177	87.997

of the limitations on the numerical precision of our algorithm. When the second shell with 30 ϕ_f^t are allowed to mix with the ϕ_u^c, the $\tilde{n}_u$ for the Li_{30} edge atom functions 47–60 improve considerably. At this stage, there are 17 $\tilde{\phi}_i^c$ with $\tilde{n}_u$ greater than 1.95 and the other 43 $\tilde{\phi}_i^c$, with the exception of functions 50 and 59, are all close to zero. Further improvements are found using functions from a Li_{86} cluster, except for $\tilde{\phi}_i^c$ 55, which has a $\tilde{n}_u$ reduced to 1.480. The failure of orbital 55 is because two of the ϕ_f^t have n_{ff} equal to 1.557 and 1.495, thereby preventing an increase in $\tilde{n}_u$. Presently, we are performing step 5 of the localization algorithm by allowing mixing with all of the ϕ_f^t simultaneously. The problem we find with orbital 55 suggests that an improvement of step 5 might be to have a sequential mixing of the successive ϕ_f^t shells with the cluster functions. This will be investigated as the algorithm is developed further.

TABLE III. The valence orbital occupation numbers, $\tilde{n}_u$, obtained after transformation of the cluster functions, ϕ_i^c, from Li_8 using different numbers of surrounding functions, ϕ_f^t. The n_u^I are initial orbital occupations for the ϕ_i^c, and the n_u^D, are obtained after diagonalization of the n_{cc} block.

| IR ϕ_i^c | n_u^I | n_u^D | Number of ϕ_f^t | | | | | | |
			4	8	12	14	18	22	36
a_1 9	1.775	1.991	1.996	1.997	1.997	1.997	1.995	1.997	1.992
b_1 10	1.147	1.868	1.989	1.991	1.988	1.991	1.991	1.991	1.991
a_1 11	1.185	0.930	0.479	0.315	0.178	0.166	0.110	0.080	0.072
a_2 12	1.100	1.100	0.433	0.322	0.184	0.184	0.106	0.096	0.107
b_2 13	1.859	1.859	1.935	1.993	1.984	1.984	1.984	1.984	1.984
b_1 14	0.695	0.271	0.099	0.049	0.046	0.046	0.038	0.034	0.010
a_1 15	1.465	1.501	1.794	1.940	1.937	1.941	1.999	1.995	2.004
b_1 16	1.086	0.784	0.752	0.444	0.425	0.242	0.218	0.145	0.052
$\Sigma^{core} n_u$	15.990	16.001	15.998	15.999	15.999	16.000	16.002	16.000	15.999
$\Sigma^{val} n_u$	10.315	10.304	9.479	9.050	8.739	8.551	8.442	8.322	8.211
$\Sigma^{cs} n_u$	(Initial)		4.422	9.308	13.730	16.352	20.847	25.789	41.770
	(Final)		5.249	10.563	15.297	18.106	22.708	27.773	43.865

TABLE IV. The valence orbital occupation numbers, $\tilde{n}_{ii}$, obtained after transformation of the cluster functions ϕ_i^C from Li_{30} using different numbers of surrounding functions, ϕ_j^I. The n_{ii}^I are initial orbital occupations for the ϕ_i^C, and the n_{ii}^D are obtained after diagonalization of the n_{CC} block.

ϕ_i^C	n_{ii}^I	n_{ii}^D	Number of ϕ_i^I		
			14	30	56
31	1.775	1.999	2.001	2.008	2.019
32	1.148	1.996	2.025	2.012	2.025
33	1.185	0.132	0.053	-0.054	0.006
34	1.101	0.002	-0.020	0.023	-0.013
35	1.861	2.002	2.016	2.021	2.028
36	0.693	0.018	-0.022	0.024	-0.040
37	1.465	2.007	2.008	2.008	2.008
38	1.085	0.192	0.029	0.020	0.111
39	0.906	0.004	-0.020	-0.018	-0.018
40	1.114	2.007	2.011	2.019	2.026
41	1.422	1.897	1.971	1.977	1.978
42	0.738	0.015	-0.001	-0.002	-0.014
43	1.342	2.032	2.041	2.039	2.038
44	0.855	0.215	0.003	-0.013	0.003
45	1.583	1.973	2.000	2.002	2.008
46	0.868	1.958	2.000	1.977	1.997
47	1.119	1.521	1.987	2.002	2.004
48	0.938	1.391	1.977	1.956	1.990
49	1.140	0.455	0.052	-0.008	-0.036
50	0.857	0.349	0.223	0.130	-0.081
51	1.312	1.280	1.806	1.949	1.961
52	1.212	1.854	1.975	1.993	1.977
53	0.843	0.575	0.189	0.032	-0.093
54	1.231	1.740	1.877	1.998	1.962
55	1.293	1.409	1.837	1.983	1.480
56	0.775	0.630	0.073	-0.042	0.008
57	1.428	1.817	1.903	1.966	1.967
58	0.877	0.751	0.308	0.038	-0.059
59	1.493	1.052	0.616	0.343	0.143
60	0.848	1.199	1.290	1.953	1.987
$\Sigma^{core}\ n_{ii}$	59.962	60.000	59.991	59.998	60.010
$\Sigma^{val}\ n_{ii}$	34.510	34.472	34.211	34.243	33.401
$\Sigma^{ex}\ n_{ii}$	(Initial)		15.595	33.645	63.337
	(Final)		15.866	33.878	64.391

Summary

We have developed an algorithm which enables the localization of cluster functions, $\bar{\phi}_i^C$, which have orbital occupation numbers of either 2 or 0 with respect to the density matrix obtained from a calculation on an extended substrate. These ϕ_i^C initially consist of a linear combination of orbitals centered on a finite cluster of atoms. Partial Jacobi transformations of the occupation number matrix, $\mathbf{n}$, are then used to mix the cluster functions ϕ_i^C with extra orbitals, ϕ_j^E, on the surroundings

atoms to produce the required $\tilde{n}_{u}$. We are presently investigating whether these localized basis functions are suitable for use in an embedded cluster procedure.

Acknowledgment

References

[1] G. Pacchioni and P. S. Bagus, Eds., *Cluster Models for Surface and Bulk Phenomena* (Plenum, New York, 1991).

[2] J. D. Head, Chem. Phys. Lett. **190**, 417 (1992).

[3] P. S. Bagus, H. F. Schaeffer, and C. W. Bauschlicher, J. Chem. Phys. **78**, 1390 (1983).

[4] K. Herman, P. S. Bagus, and C. J. Nelin, Phy. Rev. B **35**, 4378 (1987).

[5] I. Panas, J. Schule, P. Siegbahn, and U. Whalgren, Chem. Phys. Lett. **149**, 265 (1988); I. Panas and P. E. M. Siegbahn, J. Chem. Phys. **92**, 4625 (1990); P. E. M. Siegbahn, L. G. M. Pettersson, and U. Wahlgren, J. Chem. Phys. **94**, 4024 (1991).

[6] C. Pisani, R. Dovesi, R. Nada, and L. N. Kantorovish, J. Chem. Phys. **92**, 7448 (1990); C. Dykstra and B. Kirtman, Ann. Rev. Phys. Chem. **41**, 155 (1990).

[7] P. J. Feibelman, Ann. Rev. Phys. Chem. **40**, 261 (1989).

[8] H. Yang and J. L. Whitten, in *The Challenge of d and f electrons: Theory and Computation*, D. R. Salahub and M. C. Zerner, Eds. (ACS Symposium Series, No. 394, 1989), p. 140.

[9] C. Pisani, R. Dovesi, and C. Roetti, in *Hartree-Fock Ab Initio Treatment of Crystalline Systems*, *Lecture Notes in Chemistry* (vol. 48) (Springer-Verlag, Berlin, 1988); R. Dovesi, C. Pisani, C. Roetti, M. Causa, and V. R. Saunders, *QCPE program 577* (Indiana University, Bloomington, IN, 1988).

[10] E. R. Davidson, J. Chem. Phys. **46**, 3320 (1967).

[11] W. H. Press, B. P. Flannery, S. A. Teukolsky, and W. T. Vetterling, *Numerical Recipes* (Cambridge University Press, Cambridge, UK, 1989).

[12] W. J. Hehre, R. F. Stewart, and J. A. Pople, J. Chem. Phys. **51**, 2657 (1969); W. J. Hehre, R. Ditchfield, R. F. Stewart, and J. A. Pople, J. Chem. Phys. **52**, 2769 (1970).

[13] N. W. Ashcroft and N. D. Mermin, *Solid State Physics* (Holt, Rinehart and Winston, New York, 1976).

[14] M. W. Schmidt, J. A. Boatz, K. K. Baldridge, S. Koseki, M. S. Gordon, S. T. Elbert, and B. Lam, QCPE Bull. **7**, 115 (1987).

A Comparison of Geometry Optimization with Internal, Cartesian, and Mixed Coordinates

H. BERNHARD SCHLEGEL

Department of Chemistry, Wayne State University, Detroit, Michigan 48202

Abstract

Improvements in MO programs and computer speeds have dramatically increased the size of molecules that can be optimized by MO methods. This has put a considerable strain on existing geometry optimization techniques. For a given molecular system, the performance of a geometry optimization method can vary significantly depending on the coordinates used. Nonredundant internal coordinates (e.g., Z-matrix coordinates) are easily constructed and behave well for acyclic molecules but can be quite troublesome for cyclic systems. Cartesian coordinates behave well for rigid, cyclic molecules but can be quite poor for flexible, acyclic systems. Mixed cartesian and internal coordinates have been suggested as a means of combining the best of both approaches and are particularly convenient for cyclic systems with flexible substituents. The efficiency of these different approaches is compared for a number of molecules. © 1992 John Wiley & Sons, Inc.

Introduction

Geometry optimization is one of the important steps in almost any quantum chemical study. With the advent of efficient methods for computing energy gradients for *ab initio* molecular orbital calculations [1] and the use of gradient-based optimization algorithms [2], finding equilibrium geometries has become almost routine for many simple molecules [3]. The key to the efficiency of any optimization is the choice of a suitable coordinate system. Strong coupling between coordinates, narrow gullies, and curved valleys cause serious problems for even the best optimizers [2]. Many geometry optimizations in quantum chemical calculations are carried out using nonredundant internal coordinates, for example, Z-matrix coordinates or similar definitions of internal coordinates. This is both convenient and efficient for many small molecules, since the Z-matrix is constructed from the natural coordinates of a molecule, that is, bondlengths, valence angles, and torsions about bonds. Such internal coordinates are normally not very strongly coupled, and the optimization proceeds efficiently [3,4]. However for cyclic molecules, it is very difficult to set up a nonredundant coordinate system without strong coupling [4]. There are a number of ways around this problem: cartesian coordinates, redundant internal coordinates, or a nonredundant linear combination of cartesian or redundant internal coordinates (e.g., symmetry adapted coordinates). Pulay [5] recently demonstrated that suitable combinations of redundant coordinates can be used very efficiently in geometry optimization. Generating an appropriate redundant

internal coordinate system that minimizes coupling requires some skill or a suitable program [6]. The effort in constructing such a coordinate system is rewarded by significant improvements in the efficiency of the geometry optimization [5]. The other alternative, cartesian coordinates, is routinely used in molecular mechanics [7]. Cartesian coordinates are unambiguous and easy to set up, but are moderately strongly coupled. Traditionally, cartesian coordinates have been avoided in molecular orbital calculations because it was thought they would slow down optimization significantly. Recently Hehre et al. [8] showed that with a suitable initial guess for the hessian and the geometry, cartesian coordinate-based optimization could be quite comparable to internal coordinate-based methods. Cartesian coordinates were better for cyclic and rigid molecules, but were poorer for flexible, acyclic systems. Cartesian coordinates also make constraints more difficult to impose (however, see Refs. [9]–[11]). As an alternative to pure cartesian or pure internal coordinates, Head [11] and Obara et al. [12] have suggested the use of mixed cartesian and internal coordinates. In this article we compare the efficiency of geometry optimization based on internal, cartesian, and mixed coordinates.

Methodology

All molecular orbital calculations were carried out with the GAUSSIAN 92 series of programs [13]. The Hartree–Fock level of theory was used with the STO-3G basis set [14]. Geometries were optimized with two different sets of internal coordinates, cartesian coordinates, and mixed cartesian/internal coordinates. Starting geometries were obtained by molecular mechanics minimization using MacroModel [15] and the MM2 force field [7] (the $C-H$ bonds were shortened by 0.03 Å to take into account the systematic difference between MM2 and ab initio MO computed $C-H$ bondlengths). Internal, cartesian, and mixed internal/cartesian coordinate optimizations were started from the same geometry. The initial estimates of the hessians were generated from a simple valence force field transformed to the coordinate system used in the optimization [16]. The standard optimization routine in GAUSSIAN was used for all minimizations [17].

For optimizations using mixed cartesian and internal coordinates, variable cartesian coordinates are treated analogous to variable internal coordinates. The transformations for the coordinates and gradients from cartesian to internal coordinates is

$$\delta q = B\delta x \quad \text{and} \quad g_q = (BMB')^{-1}BMg_x$$

where B is the Wilson B matrix [18]. If the Z-matrix orientation is used for the cartesian coordinates of the molecule, M is an identity matrix with the diagonal elements for $x_1, y_1, z_1, x_2, y_2, y_3$ set to zero (i.e., for those cartesian coordinates that are always zero in the Z-matrix orientation). To add a few cartesian coordinates to the internal coordinates, one simply defines the appropriate B-matrix elements for cartesian displacements (i.e., an identity matrix). This approach has been implemented in GAUSSIAN 92 [13]. The current specification of the Z-matrix geometry input already includes the possibility of defining some (or all) of the atoms

by cartesian coordinates and the remainder by internal coordinates. Unlike earlier implementations of mixed coordinate optimization [12], the present approach allows full coupling between the cartesian and internal coordinates.

For full cartesian coordinate optimization, the structure input can be via cartesian coordinates or Z-matrix internal coordinates (the cartesian variable names are generated automatically and passed to the same optimizer used for internal coordinates [17]). Even though translational and rotational invariance of the gradient should assure that the molecule does not undergo overall translation or rotation during the optimization, the hessian for cartesian coordinate optimization is adjusted so that the coordinates for overall translation or rotation have large positive force constants, effectively freezing these degrees of freedom (this is similar to the frozen coordinates that can be used in regular geometry optimizations [13]).

Results and Discussion

Table I presents a selection of some monocyclic, bicyclic, and tricyclic molecules. A number of these have been used in previous articles [5,8] to test the performance of geometry optimization methods. To assess the variability in performance of optimizations in internal coordinates, a number of molecules were optimized with two different sets of internal coordinates. Those in set (a) were constructed according to the suggestions of Ref. [4] so as to minimize the coupling between coordinates and to maintain the symmetry of the molecule during the optimization. These internal coordinates, along with the starting geometries are shown in Figure 1. The internal coordinates of set (b) were chosen in a more cavalier manner without regard to problems of strong coupling (e.g., a six-membered ring is constructed as a simple chain of six atoms). For cartesian coordinates, all $3N$ coordinates are allowed to vary. For mixed coordinates, the n atoms in the rings are described by $3n - 6$ cartesian coordinates, while the substituents are attached using internal coordinates.

TABLE I. Comparison of geometry optimization performance using internal, cartesian, and mixed interal/cartesian coordinates.

Molecule	Number of atoms	Symmetry	Number of variables	Internal (a)	Internal (b)	Cartesian	Mixed
2 fluoro furan	9	C_s	15	7	8	7	7
norbornane	19	C_{2v}	15	7	6	5	5
bicyclo[2.2.2]octane	22	D_3	11	11	25	19	14
bicyclo[3.2.1]octane	22	C_s	33	6	5	6	7
endo hydroxy bicyclopentane	14	C_1	36	8		18	9
exo hydroxy bicylopentane	14	C_1	36	10		20	11
ACTHCP	16	C_1	42	65		>81	72
1,4,5 trihydroxy anthroquinone	27	C_s	51	10		11	17
histamine H⁺	18	C_1	48	42		>100	47

2 fluoro furan
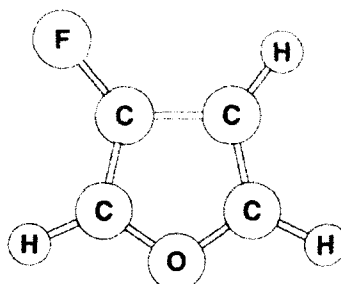
Starting geometry & internal coordinate set (a)

```
C
C 1 r1
C 1 r2 2 a2
C 2 r3 1 a3 3   0.
O 1 r4 2 a4 3   0
F 1 r5 2 a5 3 180.
H 2 r6 1 a6 3 180.
H 3 r7 1 a7 2 180
H 4 r8 2 a8 1 180.
```

Number of optimization steps

internal coordinates (a)	7
internal coordinates (b)	8
cartesian coordinates	7
mixed coordinates	7

r1=1.4558/r2=1.3375/r3=1.3395
r4=2.1286/r5=1.3336/r6=1.0721
r7=1.0724/r8=1.0726/a2=102.5826
a3=101.6686/a4= 70.3774/a5=128.8779
a6=129.0378/a7=126.9982/a8=126.7146

norbornane
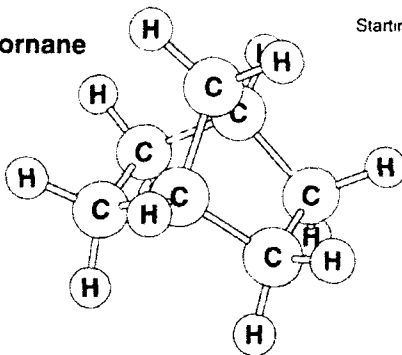
Starting geometry & internal coordinate set (a)

```
C
C 1 r1
C 1 r1 2 a1
C 2 r2 1 a2 3   d2
C 2 r2 1 a2 3  -d2
C 3 r2 1 a2 2   d2
C 3 r2 1 a2 2  -d2
H 1 r3 2 a3 3 a3  1
H 1 r3 2 a3 3 a3 -1
H 2 r4 1 a4 3 180.
H 3 r4 1 a4 2 180.
H 4 r5 2 a5 1   d5
H 4 r6 2 a6 1   d6
H 5 r5 2 a5 1  -d5
H 5 r6 2 a6 1  -d6
H 6 r5 3 a5 1   d5
H 6 r6 3 a6 1   d6
H 7 r5 3 a5 1  -d5
H 7 r6 3 a6 1  -d6
```

Number of optimization steps

internal coordinates (a)	7
internal coordinates (b)	6
cartesian coordinates	5
mixed coordinates	5

r1=1.5378/r2=1.5418/r3=1.0863
r4=1.0876/r5=1.0869/r6=1.0858
a1= 92.5394/a2=102.1580/a3=113.4070
a4=115.0850/a5=110.2372/a6=112.0658
d2=-56.4782/d5=-81.9032/d6=157.5936

Figure 1.   Structures, starting geometries, and internal coordinate set (a) for the molecules in Table 1.

The table shows that for a variety of systems internal coordinates perform as well as or better than cartesian coordinates, in agreement with Baker and Hehre [8]. Secondly, the number of steps taken by optimizations using mixed cartesian and internal coordinates is generally intermediate between pure cartesian coordinates and well-chosen internal coordinates. Since mixed coordinate systems do not require the careful crafting of good internal coordinates for rings [4], and since their performance is equal to or better than cartesian coordinates, there is some merit to using mixed coordinates.

Fluorofuran, hydroxybicyclopentane, norbornane, and 2 bicyclooctanes are fairly rigid and are well represented by the MM2 force field. Thus, relatively few steps are

Starting geometry & internal coordinate set (a)

bicyclo [3.2.1] octane


```
c 1 r1
c 1 r2 2 90
c 1 r2 2 90. 3 180
c 3 r3 1 a3 2 d3
c 4 r3 1 a3 2 -d3
c 3 r4 1 a4 2 d4
c 4 r4 1 a4 2 -d4
c 1 r5 2 a5 3 90
h 2 r6 3 a6 4 a6 -1
h 2 r7 3 a7 4 a7 1
h 3 r8 2 a8 4 d8
h 4 r8 2 a8 3 -d8
h 5 r9 3 a9 6 d9
h 5 r10 3 a10 6 d10
h 6 r9 4 a9 5 -d9
h 6 r10 4 a10 5 -d10
h 7 r11 3 a11 9 d11
h 7 r12 3 a12 9 d12
h 8 r11 4 a11 9 -d11
h 8 r12 4 a12 9 -d12
h 9 r13 7 a13 8 a13 1
h 9 r14 7 a14 8 a14 -1
```
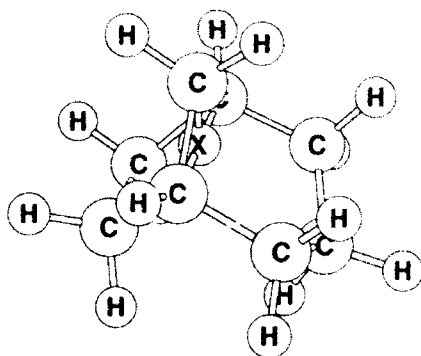
Number of optimization steps

internal coordinates (a)	6
internal coordinates (b)	5
cartesian coordinates	6
mixed coordinates	7

```
r1=0.9863/r2=1.1768/r3=1.5408
r4=1.5404/r5=2.2660/r6=1.0856
r7=1.0871/r8=1.0889/r9=1.0871
r10=1.0855/r11=1.0865/r12=1.0868
r13=1.0872/r14=1.0859/a3= 74.7408
a4= 93.5429/a5=130.0092/a6=113.4879
a7=110.7039/a8=111.4780/a9=109.6191
a10=112.0531/a11=108.8747/a12=109.9315
a13=110.3734/a14=109.2114/d3=-132.2131
d4=115.7902/d8=166.7660/d9=117.9400
d10=-123.1354/d11=-121.1057/d12=122.3794
```

bicyclo [2.2.2] octane

Starting geometry & internal coordinate set (a)


```
C
C 1 r1
C 1 r2 2 a2
C 1 r2 2 a2 3 120.
C 1 r2 2 a2 3 240.
C 2 r2 1 a2 3 d2
C 2 r2 1 a2 6 120.
C 2 r2 1 a2 6 240.
-1 1. 2 90. 3 0.
-2 1. 1 90. 6 0.
H 1 r3 9 90. 2 180.
H 2 r3 10 90. 1 180.
H 3 r4 1 a4 2 d4
H 3 r5 1 a5 2 d5
H 4 r4 1 a4 2 d4
H 4 r5 1 a5 2 d5
H 5 r4 1 a4 2 d4
H 5 r5 1 a5 2 d5
H 6 r4 2 a4 1 d4
H 6 r5 2 a5 1 d5
H 7 r4 2 a4 1 d4
H 7 r5 2 a5 1 d5
H 8 r4 2 a4 1 d4
H 8 r5 2 a5 1 d5
```
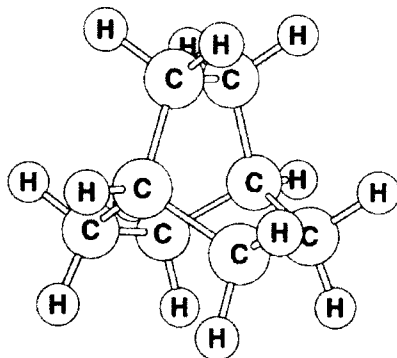
Number of optimization steps

internal coordinates (a)	11
internal coordinates (b)	25
cartesian coordinates	19
mixed coordinates	14

```
r1=2.5790/r2=1.5396/r3=1.0895
r4=1.0867/r5=1.0868/a2= 70.0910
a4=109.2484/a5=110.4824/d2=6.3053
d4=114.9771/d5=-127.9986
```

Figure 1.   (Continued)

2 hydroxy bicyclopentane
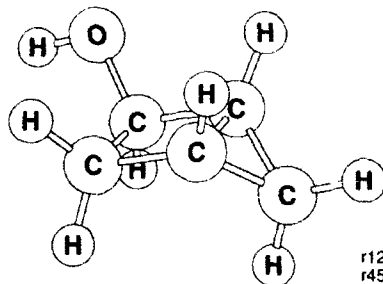
Number of optimization steps

internal coordinates (a)	10
cartesian coordinates	20
mixed coordinates	11

Starting geometry and internal coordinate set (a)

```
C
C 1 r12
C 1 r13 2 a213
C 1 r14 2 a214 3 d3214
C 4 r45 1 a145 2 d2145
O 4 r46 1 a146 2 d2146
H 1 r17 2 a217 3 d3217
H 2 r28 1 a128 3 d3128
H 3 r39 1 a139 2 d2139
H 3 r3A 1 a13A 2 d213A
H 4 r4B 1 a14B 2 d214B
H 5 r5C 4 a45C 1 d145C
H 5 r5D 4 a45D 1 d145D
H 6 r6E 4 a46E 1 d146E
```

```
r12=1.5447/r13=1.4892/r14=1.5367
r45=1.5374/r46=1.4064/r17=1.0875
r28=1.0877/r39=1.0845/r3A=1.0839
r4B=1.0877/r5C=1.0854/r5D=1.0851
r6E=0.9423/a213=58.7631/a214=89.4219
a145=90.6265/a146=111.3076/a217=109.2699
a128=109.1552/a139=116.0099/a13A=115.6587
a14B=113.6734/a45C=114.7176/a45D=113.3309
a46E=108.0277/d3214=125.1018/d2145=-0.3599
d2146=114.4321/d3217=-113.9872/d3128=114.3015
d2139=-107.2585/d213A=107.0506/d214B=-118.5685
d145C=115.4893/d145D=-113.2697/d146E=177.3806
```

ACTHCP
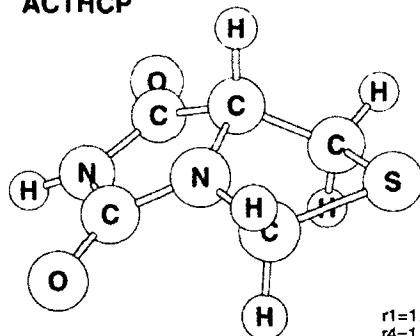
Number of optimization steps

internal coordinates (a)	65
cartesian coordinates	>81
mixed coordinates	72

Starting geometry & internal coordinate se.

```
C
N 1 r1
C 1 r2 2 a2
N 1 r3 2 a3 3 d3
C 2 r4 1 a4 3 d4
C 1 r5 2 a5 3 d5
C 2 r6 1 a6 6 d6
S 1 r7 2 a7 6 d7
H 1 r8 2 a8 3 d8
O 3 r9 1 a9 2 d9
H 4 rA 3 aA 1 dA
O 5 rB 2 aB 1 dB
H 6 rC 1 aC 2 dC
H 6 rD 1 aD 2 dD
H 7 rE 2 aE 1 dE
H 7 rF 2 aF 1 dF
```

```
r1=1.4763/r2=1.5142/r3=2.3316
r4=1.3397/r5=1.5277/r6=1.4667
r7=2.6282/r8=1.0872/r9=1.2263
rA=1.0141/rB=1.2516/rC=1.0851
rD=1.0841/rE=1.0843/rF=1.0835
a2= 99.1882/a3= 64.9195/a4=112.8177
a5=101.7456/a6=122.6016/a7= 69.6216
a8=110.1242/a9=127.3698/aA=124.2840
aB=126.5097/aC=110.4262/aD=111.8364
aE=110.9696/aF=111.1680/d3=-6.3596
d4=5.3108/d5=122.7439/d6=-34.1633
d7=29.1542/d8=-115.5422/d9=173.4622
dA=-179.3990/dB=-179.3990/dC=-75.3678
dD=163.4138/dE=123.1421/dF=-113.1194
```

Figure 1. (Continued)

required for the optimizations for any of the coordinate systems. Bicyclo [2.2.2] octane can twist about the C_3 axis and this may account for the greater number of steps taken by the cartesian based optimization. For the hydroxybicyclopentanes, optimization of the rotation of the hydroxyl groups may be more difficult in cartesian coordinates. Rigid planar molecules such as fluorofuran and trihydroxyanthroqui-

1,4,5 trihydroxy anthroquinone

Starting geometry & internal coordinate set (a)
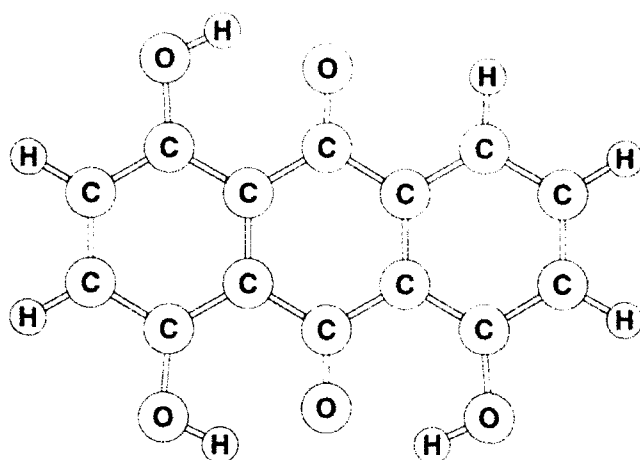

```
C
C  1 r1
C  1 r2   2 a2
C  3 r3   1 a3  2 180.
C  4 r4   3 a4  1 180
C  2 r5   1 a5  3  0.
C  6 r6   2 a6  1 180
C  7 r7   6 a7  2 180.
C  1 r8   2 a8  3 180
C  9 r9   1 a9  3 180
C 10 r10  9 a10 1 180.
C  2 r11  1 a11 3 180
C 12 r12  2 a12 1 180.
C 13 r13 12 a13 2 180
O  1 r14  3 r14 2 180
O  4 r15  3 a15 1  0.
H 16 r16  4 a16 3  0.
H  5 r17  4 a17 3 180
H  8 r18  7 a18 6 180.
O  7 r19  6 a19 2  0
H 20 r20  7 a20 6  0.
O  2 r21  6 a21 7  0
O 13 r22 12 a22 2  0
H 23 r23 13 a23 12 0.
H 14 r24 13 a24 12 180
H 11 r25 10 a25 9 180.
H 10 r26  9 a26 1  0
```

Number of optimization steps

internal coordinates (a)	10
cartesian coordinates	11
mixed coordinates	17

```
r1=2.8128/r2=1.4007/r3=1.4025/r4=1.3934
r5=1.4009/r6=1.4025/r7=1.3934/r8=1.3998
r9=1.3986/r10=1.3926/r11=1.3999/r12=1.4025
r13=1.3945/r14=1.2122/r15=1.3656/r16=0.9757
r17=1.0735/r18=1.0735/r19=1.3653/r20=0.9747
r21=1.2141/r22=1.3652/r23=0.9750/r24=1.0734
r25=1.0737/r26=1.0735/a2= 59.7891
a3=119.9130/a4=119.8322/a5= 59.7502
a6=119.9728/a7=119.8749/a8= 59.4339
a9=119.4018/a10=120.5069/a11= 59.9316
a12=120.5476/a13=119.9462/a14=120.1535
a15=123.2100/a16=112.4815/a17=119.9896
a18=119.9769/a19=123.2140/a20=112.5473
a21=120.3804/a22=123.0024/a23=112.3739
a24=119.9078/a25=120.2592/a26=121.6324
```

Figure 1. (Continued)

none optimize readily in all three coordinate systems since there are no flexible rings or internal rotors to cause problems. For trihydroxyanthroquinone, Baker and Hehre were unable to achieve convergence with internal coordinates, but the present choice of internal coordinates performed as well as cartesian coordinates. ACTHCP and protonated histamine were the most troublesome molecules in the present study. Both contain a very flexible five-membered ring that changes conformation during the course of the optimization. Baker and Hehre found a minimum for ACTHCP only with cartesian coordinates (90 cycles) [8]. In the present study, internal and mixed coordinates both converged in somewhat fewer cycles (65 and 72, respectively). Internal and mixed coordinates behaved similarly for histamine H⁺; cartesian coordinate-based optimization had difficulties adjusting the flexible hydrogen-bonded side chain and did not converge with 100 cycles.

With the reduction in computational cost and the improvements in *ab initio* MO calculations over the last decade, it is possible to contemplate optimizing the ge-

Starting geometry & internal coordinate set (a)

histamine H⁺

N
C 1 r1
C 2 r2 1 a2
C 1 r3 2 a3 3 d3
N 2 r4 1 a4 3 d4
C 2 r5 1 a5 3 d5
C 6 r6 2 a6 1 d6
N 7 r7 6 a7 2 d7
H 3 r8 2 a8 5 d8
H 5 r9 3 a9 4 d9
H 4 r10 1 a10 5 d10
H 6 r11 2 a11 7 d11
H 6 r12 2 a12 7 d12
H 7 r13 6 a13 8 d13
H 7 r14 6 a14 8 d14
H 8 r15 7 a15 6 d15
H 8 r16 7 a16 16 d16
H 8 r17 7 a17 16 d17

Number of optimization steps

internal coordinates (a)   42
cartesian coordinates   >100
mixed coordinates   47

r1=1.3572/r2=1.3770/r3=1.3240/r4=2.1863
r5=1.4995/r6=1.5363/r7=1.5050/r8=1.0704
r9=1.0495/r10=1.0708/r11=1.0854/r12=1.0851
r13=1.0846/r14=1.0849/r15=1.0450/r16=1.0437
r17=1.0450/a2=110.7216/a3=105.5982/a4=73.1915
a5=120.8022/a6=113.5238/a7=109.0633/a8=131.4886
a9=126.3666/a10=126.3072/a11=108.7003/a12=108.1367
a13=111.8514/a14=110.1194/a15=109.6284/a16=110.1589
a17=109.329/d3=-0.2008/d4=0.0839/d5=-179.6829
d6=39.6818/d7=-62.5378/d8=179.9720/d9=180.0000
d10=179.8032/d11=121.5462/d12=-122.2758/d13=120.6163
d14=-118.2480/d15=-45.3540/d16=120.9891/d17=-119.7540

Figure 1.   (Continued)

ometry for each point on a potential surface scan. Such a relaxed surface scan requires one or more coordinates to be constrained (i.e., the coordinate(s) defining the surface) while the remaining coordinates are minimized. Internal coordinates such as bond lengths and dihedral angles are often the most convenient and meaningful for surface scans. However, constraints on internal coordinates are more complicated to impose when the optimization is carried out in cartesian coordinates [9–11]. With mixed internal and cartesian coordinates, the surface coordinates can be expressed in terms of internals, whereas cartesian coordinates can be used for rings. Figure 2 shows an example of a relaxed scan for protonated histamine as a function of the two dihedral angles of the side chain. The five-membered ring is defined in terms of cartesian coordinates: internal coordinates are used for all of the substituents. The dihedral angles were stepped in 60° increments and the relaxed energies were fitted to a double fourier expansion. The surface shows a deep diagonal valley where the RNH_3^+ group forms a strong hydrogen bond to the imidazole nitrogen. The narrow, diagonal nature of the valley indicates strong coupling between the 2 dihedral angles. Provided both angles change in a concerted manner, the ring formed by he hydrogen-bonded side chain can flex above and below the plane of the imidazole without significant change in energy. This deep, narrow valley with a flat bottom probably is the reason for the slow convergence in the geometry optimization of this molecule (Table 1).

Conclusions

Coordinate systems with a mixture of internal and cartesian coordinates are useful alternatives to pure cartesians or pure internals for geometry optimization
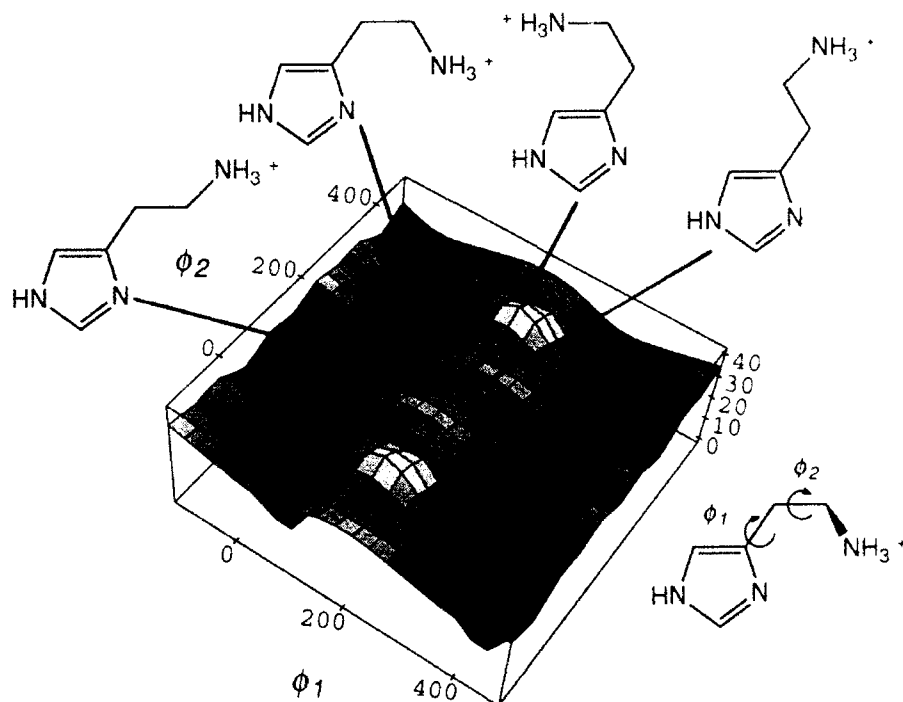
Figure 2. Potential energy surface scan for protonated histamine. The dihedral angles ϕ_1 and ϕ_2 were stepped in $60°$ intervals and all of the remaining degrees of freedom were optimized using mixed internal/cartesian coordinates.

and have been incorporated in GAUSSIAN 92. Rings can be represented more easily in cartesian coordinates: side chains can be readily described by internal coordinates. The performance of mixed coordinate optimizations is generally intermediate between cartesian and well-chosen internal coordinate systems. Well-chosen internal coordinates and mixed coordinates may require a bit more work to set up but generally performed as well as or better than cartesian coordinates for the examples considered in this study. Internal and mixed coordinates also have some advantages for relaxed potential surface scans.

Acknowledgments

Bibliography

[1] P. Pulay, Mol. Phys. 17, 197 (1979).

[2] R. Fletcher, Practical Methods of Optimization: Unconstrained Optimization (Wiley, New York, 1980); P. E. Gill, W. Murray, and M. H. Wright, Practical Optimization (Academic, London,

1981); L. E. Scales, *Introduction to Non-linear Optimization* (Macmillan, Basingstoke, 1985); J. E. Dennis and R. B. Schnabel, *Numerical Methods for Unconstrained Optimization and Nonlinear Equations* (Prentice-Hall, Englewood Cliffs, NJ, 1983).

[3] H. B. Schlegel, Adv. Chem. Phys. **67**, 249 (1987); J. D. Head and M. C. Zerner, Adv. Quantum Chem. **20**, 239 (1989).

[4] H. B. Schlegel, In *New Theoretical Concepts for Understanding Organic Reactions*, J. Bertrán, Ed. (Kluwer Academic, the Netherlands), NATO-ASI series **C267**, 33 (1989).

[5] P. Pulay and G. Fogarasi, J. Chem. Phys. **96**, 2856 (1992).

[6] P. Pulay and co-workers, *TX90* (Fayatteville, AR, 1990); P. Pulay, Theor. Chim. Acta **50**, 299 (1979).

[7] U. Burkart and N. L. Allinger, *Molecular Mechanics* ACS Monogr. **177**, (American Chemical Society, Washington, DC, 1982).

[8] J. Baker and W. J. Henre, J. Comput. Chem. **12**, 606 (1991).

[9] D. Lu, M. Zhao, and D. G. Truhlar, J. Comput. Chem. **12**, 376 (1991).

[10] J. Baker, J. Comput. Chem. **13**, 241 (1992).

[11] J. D. Head, J. Comput. Chem. **11**, 67 (1990).

[12] H. Nakano, T. Nakajima, and S. Obara, Chem. Phys. Lett. **177**, 458 (1992).

[13] M. J. Frisch, G. W. Trucks, M. Head-Gordon, P. M. W. Gill, M. W. Wong, J. B. Foresman, B. G. Johnson, H. B. Schlegel, M. A. Robb, E. S. Replogle, R. Gomperts, J. L. Andres, K. Raghavachari, J. S. Binkley, C. Gonzalez, R. L. Martin, D. J. Fox, D. J. DeFrees, J. Baker, J. J. P. Stewart, and J. A. Pople, GAUSSIAN 92 (Gaussian, Inc., Pittsburgh, PA, 1991).

[14] W. J. Hehre, R. F. Stewart, and J. A. Pople, J. Chem. Phys. **51**, 2657 (1969).

[15] W. C. Still, N. G. J. Richards, W. C. Guida, M. Lipton, R. Liskamp, G. Chang, and T. Hendrickson, *MacroModel V2.0* (Columbia University, New York, 1985).

[16] H. B. Schlegel, Theor. Chim. Acta **66**, 333 (1984).

[17] H. B. Schlegel, J. Comput. Chem. **3**, 214 (1982) with various enhancements including trust radius and RFO optimization.

[18] E. B. Wilson, J. C. Decius, and P. C. Cross, *Molecular Vibrations* (McGraw-Hill, New York, 1955).

Chemical Potential(Electronegativity)-Related Quantities in a Model Multilevel System

ROMAN F. NALEWAJSKI

R. Gumiński Department of Theoretical Chemistry. Jagiellonian University,
R. Ingardena 3, 30-060 Cracow, Poland

Abstract

Various chemical potential(electronegativity)-related quantities, given by relevant derivatives of the energy with respect to the electron occupation/density variables, are examined for the model one-dimensional system consisting of m-levels occupied by electron moving in a common one-body potential. The previously proposed hyperspherical orbitals, with the common radial factor, $\chi = \sqrt{\rho}$, where ρ is the electron density, are used to derive explicit expressions for approximations to the local, global, and orbital "chemical potentials" ("electronegativities"). Relevant Euler equations are summarized, and an illustrative example of the harmonic oscillator is discussed in more detail. © 1992 John Wiley & Sons, Inc.

Introduction

The electronic *global chemical potential* (negative of the global electronegativity), given by the derivative of the system energy with respect to its number of electrons,

$$\mu_g = -X_g = \partial E(N)/\partial N ,\qquad (1)$$

represents a key concept of the *density functional theory* (DFT) [1,2] and the related *charge sensitivity analysis* (CSA) [1,3–8], in which some of its derivatives are used. It appears as the Lagrange multiplier in the DFT variational formulation [9]:

$$\frac{\delta}{\delta\rho}\left[E_v[\rho] - \mu_g\left(\int \rho \, d\mathbf{r} - N_o \right) \right] = 0 ,\qquad (2)$$

incorporating the subsidiary condition of the specific particle number, $N_o = \int \rho_o \, d\mathbf{r}$; here ρ is the electron density and the subscript, v, indicates the fixed external potential. For the exact ground-state (equilibrium) density, ρ_o, the *local chemical potential* (electronegativity) equalizes throughout the whole electron distribution [9a]:

$$\mu_o(\mathbf{r}) = \delta E_v[\rho]/\delta\rho(\mathbf{r})|_{\rho_o} = \mu_o(\mathbf{r}') = \cdots = \mu_g .\qquad (3)$$

The properties of μ_g and the orbital electronegativity, as defined by Hinze et al. [10], have been extensively studied [1,6,9,11–13]. It has been pointed out that *electronegativity equalization* (EE) of eq. (3) cannot take place in the Hartee–Fock (HF) theory, due to the extreme orbital occupation constraints. Thus, in this ap-

proximation, only an approximate (average) global "chemical potential" level can be defined. This level has been approximated in recent studies as the energy per particle, E/N [11,12], or as the average orbital energy,

$$\bar{\mu} = \sum_{i=1}^{m} p_i \varepsilon_i ,$$ (4)

where $p_i = n_i/N$ is the ith orbital occupation probability, n_i is the occupation number, and ε_i is the orbital energy [6].

The main purpose of the present study is to examine properties of various chemical potential–related quantities, local, orbital, and global, within a well-defined and realistic multilevel model system. We shall consider m-levels occupied by electrons moving in a common one-body potential $V(x)$. This model has already been successfully used to determine $\rho = \rho[V]$ relation and to investigate properties of the so-called *Pauli potential*, $V_P(x)$, originating from the density matrix idempotency (orbital orthonormality) constraints [14–16]. It realistically models, for example, a multishell spherical atom $(x = r)$, with the one-dimensional density $\rho(x)$ then being related to the radial density [15]. A formally exact definition of such an effective one-body potential $V = V[v, \rho]$ was given by Kohn and Sham [17], though it involves a functional derivative of yet unknown exchange–correlation functional. As in the previous development, we adopt the hyperspherical orbital representation with the common radial function, $\chi = \rho^{1/2}$.

Model

Consider the m-occupied level one-dimensional system, within an independent-particle approximation, in which electrons move in a common one-body potential, $V(x)$. The canonical orbitals $\phi = (\phi_1, \ldots, \phi_m)$ must satisfy the associated one-body Schrödinger equations,

$$\phi_i'' + 2(\varepsilon_i - V)\phi_i = 0, \qquad i = 1, 2, \ldots, m .$$ (5)

As done previously [16], we adopt the hyperspherical function frame [14]; for the doubly occupied orbitals:

$$\sqrt{2}\phi = \chi\mathbf{K} ,$$ (6a)

where χ determines the *radial* function "variable" of ϕ, and the *angular* functions, $\mathbf{K}$,

$$K_1(x) = \sin f_1(x) \sin f_2(x) \cdots \sin f_{m-1}(x) ,$$

$$K_2(x) = \cos f_1(x) \sin f_2(x) \cdots \sin f_{m-1}(x) ,$$

$$K_3(x) = \qquad \cos f_2(x) \cdots \sin f_{m-1}(x) ,$$

$$\cdots\cdots\cdots\cdots\cdots\cdots\cdots\cdots\cdots\cdots\cdots\cdots\cdots\cdots\cdots\cdots\cdots\cdots\cdots\cdots$$

$$K_m(x) = \qquad\qquad\qquad\qquad \cos f_{m-1}(x) .$$ (6b)

depend upon the $(m - 1)$-angle functions $\{f_i(x)\}$ and satisfy the familiar properties of coordinates of a unit vector in the n-dimensional vector space. The corresponding Euler equations, "radial" (associated with a variation of x) and "angular" (associated with variations of $\mathbf{K}$), are summarized in Appendix A.

Chemical Potential Quantities

The energy functional [eq. (A14)] of Appendix A can be expressed as a function of fractional orbital occupations in the $N < 2m$ case, by an appropriate scaling procedure. Let us consider first the energy function of orbital occupations $\mathbf{n} = (n_1, n_2, \ldots, n_m)$, where $\sum_{i=1}^{m} n_i = N$. Rewriting eq. (6a) as

$$n_i^{1/2} \phi_i = x K_i, \qquad i = 1, 2, \cdots m, \tag{7}$$

allows one to interpret this procedure as the occupation-dependent scaling of the angular functions $\mathbf{K}(2)$ of eq. (6) into

$$K_i(\mathbf{n}) = K_i(2)(n_i/2)^{1/2}, \qquad i = 1, 2, \cdots m, \tag{8}$$

where $\mathbf{K}(2)$ refers to the doubly occupied m-levels. It can, therefore, be termed the *angular orbital occupation scaling*. It preserves a common radial factor, x, essential for the hyperspherical representation (6), and thus, ρ and its derivatives. The scaled functional of eq. (A14) now becomes the following function of orbital occupations:

$$E[\rho, \bar{\mathbf{K}}(\mathbf{n})] = \int \left(\frac{1}{4} \rho' + \sum_{i=1}^{m} n_i \phi_i^2 \varepsilon_i\right) dx \equiv \bar{E}(\mathbf{n}). \tag{9}$$

giving the *rigid* (i.e., orbitally unrelaxed) *orbital chemical potentials* (negative *rigid orbital electronegativities*),

$$\bar{\mu}_i = -\bar{X}_i = [\partial \bar{E}(\mathbf{n})/\partial n_i]_\phi = \varepsilon_i \int \phi_i^2 \, dx = \varepsilon_i, \qquad i = 1, 2, \cdots m, \tag{10}$$

equal to the respective orbital energies in accordance with our earlier conjectures [6].

In order to obtain the working function $E(N)$, we can similarly modify eq. (6a) to reflect the uniform (statistical) occupations of all m orbitals,

$$n_i = \bar{n} \equiv N/m, \qquad i = 1, 2, \cdots m. \tag{11}$$

However, such a uniform occupation scaling can now be interpreted as performed on either the angular or radial factors of the hyperspherical orbitals. First consider the angular case with $\mathbf{n} = \bar{\mathbf{n}}$, to which eqs. (7)–(9) apply. The functional $E[\rho, \mathbf{K}(\bar{\mathbf{n}})]$ now becomes a simple function of N:

$$\bar{E}(N) = \bar{E}(\mathbf{n}(N)). \tag{12}$$

leading to a measure of the global chemical potential given by the average orbital energy [eq. (4)]:

$$\tilde{\mu} = -\tilde{X} = \partial\bar{E}(N)/\partial N = \frac{1}{m}\sum_{i-1}^{m}\varepsilon_i = \frac{2}{N}\sum_{i \cdot 1}^{m}\varepsilon_i \ . \tag{13}$$

Consider now the case of the *radial scaling* due to the uniform fractional occupations of orbitals

$$\bar{n}^{1/2}\phi_i = \chi K_i, \qquad i = 1, 2, \cdots m \ , \tag{14}$$

or, by comparison with eq. (6a),

$$\chi(\bar{n}) = \chi(2)\left(\frac{N}{2m}\right)^{1/2} \ , \tag{15}$$

where, again, $\chi(2)$ is the "radial" function for the doubly occupied electron configuration. Such a radial scaling of the energy functional (A14) gives

$$\tilde{E}(N) = \frac{N}{2m} E(2) \ , \tag{16}$$

where $E(2)$ is the electronic energy for the fully occupied m-levels ($N = 2m$) for which the scaling factor in eq. (15) is equal to unity. The associated measure of the global chemical potential (electronegativity),

$$\tilde{\mu} = -\tilde{X} = \partial\tilde{E}(N)/\partial N = E(2)/2m = E/N \ , \tag{17}$$

reproduces the earlier findings by other authors [11,12].

This scaling procedure can be easily modified to account for any electron configuration, by writing the orbital occupation numbers in terms of the global number of electrons and occupation probabilities, $n_i = N p_i$, with the subsequent N-scaling being attributed to the radial part of orbitals and the p-scaling affecting the angular parts. Such a more general case is briefly summarized in Appendix B.

Let us now turn to the *local chemical potential (electronegativity)* quantities. Taking the partial functional derivative of the energy functional (A14) gives the *rigid local chemical potential*:

$$\mu(x) \equiv \left(\frac{\delta E[\rho, \mathbf{K}]}{\delta\rho(x)}\right)_{\mathbf{K}} = \sum_{i \cdot 1}^{m} K_i^2(x)\varepsilon_i \equiv \sum_{i \cdot 1}^{m} \mu_i(x) = -X(x) \ , \tag{18}$$

where

$$\mu_i(x) = \left(\frac{\delta E[\rho, \mathbf{K}]}{\delta\rho_i}\right)_{\mathbf{K}} = \varepsilon_i \ , \tag{18a}$$

Its space average gives the average global potential [eqs. (4) and (13)]:

$$\bar{\mu} = \int \mu(x)\rho(x)\, dx \Big/ \int \rho(x)\, dx \ , \tag{19}$$

so that

$$\bar{\mu} \, dN = \int \mu(x) \, d\rho(x) \, dx \, . \tag{20}$$

On the other hand, since the functional (A15) already includes the functional dependence of $K = K[\rho, V]$,

$$E[\rho, V] = E[\rho, K[\rho, V]] \, , \tag{21}$$

its functional derivative will provide the (orbitally) *relaxed local chemical potential* (*electronegativity*):

$$\mu^{\text{rel}}(x) \equiv \frac{\delta E[\rho, V]}{\delta \rho(x)} = -X^{\text{rel}}(x) \, . \tag{22}$$

The explicit form of the functional derivative (18), obtained by using the expression (A10) is:

$$\mu(x) = \frac{1}{8} \left(\frac{\rho'}{\rho} \right)^2 - \frac{1}{4} \left(\frac{\rho''}{\rho} \right) + V + V_a = V - \frac{1}{8} \left(\frac{\rho''}{\rho} \right) - \frac{1}{2\rho} \int^x \rho V' \, dt \, . \tag{18b}$$

The relaxed quantity of eq. (22) includes an additional orbital relaxation term due to the angular potential, V_a,

$$\mu^{\text{rel}}(x) = \mu(x) + \frac{\delta V_a[\rho, V]}{\delta \rho(x)} \, , \tag{22a}$$

where the functional $V_a[\rho, V]$ is defined by eq. (A10). It directly follows from this definition that

$$\frac{\delta V_a}{\delta \rho} = \frac{\delta}{\delta \rho} \left(-\frac{1}{2\rho} \int^x \rho V' \, dt \right) \equiv \frac{\delta}{\delta \rho} \, U(x) \, , \tag{23}$$

since the contribution from the remaining terms vanishes identically.

Illustrative Example: Harmonic Oscillator

Consider a linear harmonic oscillator with units in which the Hamiltonian takes the form,

$$H = \frac{1}{2} p^2 + \frac{1}{2} x^2 \, ; \tag{24}$$

we are assuming the first two states singly occupied: $\epsilon_1 = 1/2$, $\epsilon_2 = 3/2$,

$$\rho = \phi_1^2 + \phi_2^2 = \rho_1 + \rho_2 = \pi^{-1/2} \exp(-x^2)Z \, , \tag{25}$$

where $Z = 1 + 2x^2$, following the previous analysis [15].

We note that, for a single occupied level only, $\rho_1 = \phi_1^2 = \pi^{-1/2} \exp(-x^2)$, one obtains $V_a = 0$, and all chemical potential quantities assume a constant value:

$$\bar{\mu} = \bar{\mu}_1 = \mu(x) = \mu^{\text{rel}}(x) = \epsilon_1 \, . \tag{26}$$

In the case of two occupied levels with the density distribution (25)

$$V_a = Z^{-2},$$ (27)

which gives the local chemical potential function

$$\mu(x) = \frac{3}{2} - 1/Z;$$ (28)

when averaged over space this local quantity indeed generates the global chemical potential measure:

$$\bar{\mu} = \frac{1}{2}\int \mu(x)\rho(x)\,dx = \left(\frac{1}{2} + \frac{3}{2}\right)\Big/ 2 = 1.$$ (29)

It should be observed that, due to the presence of the space-dependent "switching function," $1/Z$,

$$\mu(0) = \frac{1}{2} = \varepsilon_1 \qquad \text{and} \qquad \mu(\infty) = \frac{3}{2} = \varepsilon_2.$$ (30)

The integral function, $U(x)$ of eq. (23), assumes the following form:

$$U(x) = (Z + 2)/(4Z).$$ (31)

For the purpose of calculating the orbitally relaxed potential $\mu^{rel}(x)$, $U(x)$ should be interpreted as functional of ρ and V, in order to calculate the orbital relaxation correction of eqs. (22a) and (23). This can be formally pursued by observing that [see eqs. (6) and (25)]

$$Z = \rho/\rho_1 = K_1^2,$$ (32)

whose functional dependence on ρ and V follows from the Schrödinger equation (A8).

Conclusions

The combination formulas, expressing the "chemical potential" of the whole electron distribution in terms of potentials characterizing its constituent fragments (spatial or functional), involve the relevant *Fukui function* (F) data as the weighting factors. For example:

$$\mu_g = \frac{\partial E}{\partial N} = \sum_{i=1}^{m} \frac{\partial E}{\partial n_i}\frac{\partial n_i}{\partial N} \equiv \sum_{i=1}^{m} \mu_i F_i$$ (33a)

$$= \int \frac{\delta E}{\delta\rho(x)}\cdot\frac{\partial\rho(x)}{\partial N}\,dx \equiv \int \mu(x)F(x)\,dx$$ (33b)

$$= \sum_{i=1}^{m}\int \frac{\delta E}{\delta\rho_i(x)}\frac{\partial\rho_i(x)}{\partial N}\,dx \equiv \sum_{i=1}^{m}\int \mu_i(x)F_i(x)\,dx,$$ (33c)

and similar chain-transformation formulas can formally be written for various molecular fragments, e.g., an orbital i or a fragment Y (collection of orbitals):

$$\mu_i = \left(\frac{\partial E}{\partial n_i}\right)_k = \int \frac{\delta E}{\delta \rho_i(x)} \frac{\partial \rho_i(x)}{\partial n_i} dx = \int \mu_i(x) F^{(i)}(x) dx \qquad (34a)$$

$$\mu_Y = \left(\frac{\partial E}{\partial N_Y}\right)_k = \int \frac{\delta E}{\delta \rho_Y(x)} \frac{\partial \rho_Y(x)}{\partial N_Y} dx = \int \mu_Y(x) F^{(Y)}(x) dx . \qquad (34b)$$

or a local infinitesimal "volume" element at x:

$$\mu(x) = \left(\frac{\delta E}{\delta \rho(x)}\right)_k = \sum_{i=1}^{m} \int \frac{\delta E}{\delta \rho_i(x')} \frac{\partial \rho_i(x')}{\partial \rho(x)} dx' = \sum_{i=1}^{m} \int \mu_i(x') F^{(i)}(x',x) dx' . \qquad (35)$$

The respective normalization conditions for the global F-indices, referring to constituent parts of the whole system, of eqs. (33), are:

$$\sum_{i=1}^{m} \int F_i(x) dx = \sum_{i=1}^{m} F_i = \int F(x) dx = 1 , \qquad (36)$$

while the fragment F-indices in eqs. (34) and (35) are normalized in accordance with the requirements:

$$\int F^{(i)}(x) dx = \int F^{(Y)}(x) dx = 1 , \qquad (37)$$

$$\sum_{i=1}^{m} \int dx' F^{(i)}(x,x') = 1 , \qquad (38)$$

respectively.

A comparison between the formulas of eqs. (33)–(35) and the corresponding expressions for the chemical potential quantities noted previously identifies the associated F-indices. For example, it immediately follows from eqs. (13) and (33a) that

$$F_i = \frac{1}{m} = \frac{2}{N} = \text{const.}, \qquad i = 1, 2, \cdots m , \qquad (39)$$

for the closed-shell configuration, is simply the orbital occupation probability [6]. A corresponding local F-index can be similarly identified from eqs. (19), (33b), and (A2) as

$$F(x) = \frac{\rho(x)}{N} . \qquad (40)$$

It should also be observed that, since $\mu_i(x) \sim \mu_i = \varepsilon_i$ [compare eqs. (10) and (18a)], the *local orbital electronegativity is equalized* throughout the space at the negative orbital energy level. The orbital local F-index,

$$F_i(x) = \frac{\rho_i(x)}{N} = \frac{\rho(x)K_i^2(x)}{N},$$ (41)

again measuring the orbital local occupation probability and appropriately normalized,

$$\sum_{i=1}^{m} \int F_i(x)\,dx = 1,$$ (42)

automatically satisfies eq. (33c). Finally, one similarly identifies

$$F^{(i)}(x) = \phi_i^2(x) = \rho_i(x)/n_i = \rho(x)K_i(x)/n_i,$$ (43a)

$$F^{(Y)}(x) = \rho_Y(x)/N_Y = \left[\sum_{i \in Y} \rho_i(x) \right] \Big/ \sum_{i \in Y} n_i.$$ (43b)

which automatically satisfy eqs. (34), and

$$F^{(i)}(x, x') = K_i^2(x)\,\delta(x - x')$$ (44)

fulfilling eq. (35).

Acknowledgment

Appendix A: Euler Equations in Hyperspherical Orbital Representation

Consider a general m-level, one-dimensional, independent-particle problem, defined by an external potential, $V(x)$. We assume the hyperspherical function frame of eq. (6) for a closed-shell system:

$$\sqrt{2}\phi_i(x) = \chi(x)K_i(x), \qquad i = 1, 2, \cdots m,$$ (A1)

where $\chi^2 = \rho = 2\sum_{i=1}^{m}\phi_i^2$ is the electron density. Eqs. (A1) imply that, at each point in space, the optimum "angular" functions, $K(x)$, must behave as components of the unit-vector in the m-dimensional vector space:

$$\sum_{i=1}^{m} K_i^2(x) = 1, \text{ and hence, } \sum_{i=1}^{m} K_i(x)K_i'(x) = 0.$$ (A2)

The remaining subsidiary conditions are the usual relations of the orthonormality of orbitals:

$$S_{ij} = \langle \phi_i | \phi_j \rangle = 1/2 \int x^2 K_i K_j \, dx = \delta_{ij}, \qquad i, j = 1, 2, \cdots m. \qquad (A3)$$

Therefore, the optimum orbitals correspond to the minimum of the auxiliary functional,

$$E = \int v(x) \left(\sum_{i=1}^{m} K_i^2 - 1 \right) dx - 1/2 \sum_{i,j=1}^{m} \lambda_{ij} (S_{ij} - \delta_{ij}). \qquad (A4)$$

where the energy functional is [16]:

$$E = E[x, \mathbf{K}] = \int \left\{ \frac{1}{2} (x')^2 + x^2 \left[V - \frac{1}{2} \sum_{i=1}^{m} K_i K_i'' \right] \right\} dx. \qquad (A5)$$

λ groups the Lagrange multipliers associated with the orthonormality constraints (A3), and $v(x)$ is the Lagrange multiplier function corresponding to the local constraints (A2).

The "radial" and "angular" Euler equations, obtained by taking the functional derivative of (A4) with respect to x and K_i, respectively, are:

$$-\left(\frac{x''}{x} \right) + 2 \left(V - \frac{1}{2} \sum_{i=1}^{m} K_i K_i'' \right) = \sum_{i,j=1}^{m} K_i \lambda_{ij} K_j. \qquad (A6)$$

$$K_i'' + 2 \left(\frac{x'}{x} \right) K_i' + \left(\frac{x''}{x} \right) K_i + \left(\frac{x'}{x} \right) K_i = \sum_{j=1}^{m} \lambda_{ij} K_j + \frac{2v}{x^2} K_i.$$

$$i = 1, 2, \cdots m. \qquad (A7)$$

In order to identify the Lagrange multipliers, we shall manipulate the one-body Schrödinger equations (5) which, when expressed in terms of hyperspherical functions, become:

$$K_i'' + 2 \left(\frac{x'}{x} \right) K_i' + \left(\frac{x''}{x} \right) K_i + 2(\varepsilon_i - V) K_i = 0, \qquad i = 1, 2, \cdots m. \qquad (A8)$$

Multiplying the ith Schrödinger equation by K_i, summing over all occupied orbitals, and using the property (A2), gives the angular potential [16]:

$$V_a = -\frac{1}{2} \sum_{i=1}^{m} K_i K_i'' = \frac{1}{2} \left(\frac{x''}{x} \right) + \sum_{i=1}^{m} K_i^2 \varepsilon_i - V. \qquad (A9)$$

appearing in the effective potential term of eq. (A6). As demonstrated previously [15,16], the explicit functional form, $V_a[x, V]$, resulting from the one-dimensional virial theorem, is:

$$V_a[x, V] = \frac{1}{4} \left[\left(\frac{x''}{x} \right) - \left(\frac{x'}{x} \right)^2 \right] - \frac{1}{2x^2} \int x^2 V \, dt$$

$$- \frac{1}{8} \left[\left(\frac{\rho''}{\rho} \right) - \left(\frac{\rho'}{\rho} \right)^2 \right] - \frac{1}{2\rho} \int \rho V \, dt$$

$$= V_a[\rho, V]. \qquad (A10)$$

Inserting eq. (A9) into the "radial" equation (A6) gives

$$\sum_{i,j=1}^{m} \lambda_{ij} K_i K_j = 2 \sum_{i=1}^{m} K_i^2 \varepsilon_i \,. \tag{A11}$$

Let us now multiply ith "angular" equation (A7) by K_i; subsequent summation over all occupied orbitals and using of eqs. (A2), (A9), and (A11) allows one to identify $v(x)$:

$$v = -V\chi^2 - \frac{1}{2}\chi\chi' = -V\rho - \frac{1}{4}\rho' \,. \tag{A12}$$

This expression transforms eq. (A7) into the following equation:

$$\left(\frac{\chi''}{\chi}\right) K_i + 2\left(\frac{\chi'}{\chi}\right) K_i' + K_i'' + 2\left[\frac{1}{2} \sum_{j=1}^{m} \lambda_{ij} K_j - VK_i\right] = 0 \,.$$

which becomes identical with the corresponding Schrödinger equation (A8), when

$$\lambda_{ij} = \frac{1}{2} \varepsilon_i \delta_{ij} \,, \tag{A13}$$

in accordance with eq. (A11).

We conclude this Appendix with the explicit energy functionals resulting from inserting the angular potential expressions (A9) and (A10), respectively, into eq. (A5):

$$E[\chi, \mathbf{K}] = \int \left[\frac{1}{2}(\chi\chi')' + \chi^2 \sum_{i=1}^{m} K_i^2 \varepsilon_i\right] dx$$

$$= \int \left(\frac{1}{4}\rho' + \rho \sum_{i=1}^{m} K_i^2 \varepsilon_i\right) dx = E[\rho, \mathbf{K}] \,. \tag{A14}$$

$$E[\chi, V] = \int \left[\frac{1}{2}(\chi')^2 + \frac{1}{4}(\chi\chi')' + V\chi^2 - \frac{1}{2}\int^x \chi^2 V' dt\right] dx$$

$$= \int \left[\frac{1}{8}\frac{(\rho')^2}{\rho} + \frac{1}{8}\rho'' + V\rho - \frac{1}{2}\int^x \rho V' dt\right] dx = E[\rho, V] \,. \tag{A15}$$

These functionals provide a basis for deriving in the Chemical Potential Quantities section, and in Appendix B, various derivative quantities related to the global, local, and orbital "chemical potentials" ("electronegativities"), via appropriate electron population scaling relations.

Appendix B: General Occupation Scaling

Consider a general scaling of orbitals,

$$(Np_i)^{1/2} \phi_i = \chi K_i \,, \tag{B1}$$

where p_i is the orbital occupation probability ($n_i = Np_i$). We assume that the scaled orbitals ϕ^o are known for the configuration $\mathbf{n}^o = N^o\mathbf{p}^o$ in question:

$$(N^o p_i^o)^{1/2} \phi_i^o = \chi(N^o) K_i(p_i^o) = \chi^o K_i^o, \tag{B2}$$

together with the eigenvalues, ε_i^o. The orbitals (B1) for a general configuration $\mathbf{n} = N|\mathbf{p}$ now consist of the N-scaled radial part [see eq. (15)]:

$$\chi(N) = \chi^o(N/N^o)^{1/2}, \tag{B3}$$

and the $\mathbf{p}$-scaled angular parts [see eq. (8)]:

$$K_i(\mathbf{p}) = K_i^o(p_i/p_i^o)^{1/2}, \qquad i = \text{occupied orbitals.} \tag{B4}$$

The energy function resulting from such a combined radial and angular scaling of the functional (A14) is:

$$E(N, \mathbf{p}) = (N/N^o)E[\chi(N^o), \mathbf{K(p)}]$$

$$= (N/N^o) \int \left(\frac{1}{4}(\rho^o)' + \frac{N^o}{N} \sum_{i=1}^{occ} n_i \varepsilon_i^o \right) dx \equiv E(N, \mathbf{n}). \tag{B5}$$

where the summation is over all occupied orbitals. It immediately follows from the above expression that:

$$\left(\frac{\partial E(N, \mathbf{p}^o)}{\partial N} \right)_{\mathbf{p}^o} = E(N^o, \mathbf{p}^o)/N^o, \tag{B6}$$

$$\left(\frac{\partial E(N^o, \mathbf{n})}{\partial n_i} \right)_{N^o} = \varepsilon_i^o. \tag{B7}$$

Therefore, the results of eqs. (10) and (17) remain valid for any assumed scaled electron configuration.

Bibliography

[1] R. G. Parr and W. Yang, *Density Functional Theory of Atoms and Molecules* (Oxford University Press, New York, 1989), and references therein.

[2] R. M. Dreizler and E. K. U. Gross, *Density Functional Theory. An Approach to the Quantum Many-Body Problem* (Springer-Verlag, Berlin, 1990).

[3] R. F. Nalewajski, in *Structure and Bonding. The Chemical Hardness*, K. Sen, Ed. (to appear), and references therein.

[4] R. F. Nalewajski and J. Korchowiec, J. Mol. Catal. **54**, 324 (1990).

[5] R. F. Nalewajski, (a) Acta Phys. Polon. A77, 817 (1990); (b) Int. J. Quant. Chem. **40**, 265 (1991); (c) Int. J. Quant. Chem. **42**, 243 (1992).

[6] R. F. Nalewajski and J. Mrozek, Int. J. Quantum Chem. **42** (to appear); R. F. Nalewajski, ibid, in press; Erratum, ibid, **43** (to appear);

[7] W. J. Mortier, S. K. Ghosh, and S. Shankar, J. Am. Chem. Soc. **108**, 4315 (1986); K. A. Van Genechten, W. J. Mortier, and P. Geerlings, J. Chem. Phys. **86**, 5063 (1987); B. G. Baekelandt, J. Mortier, J. L. Lievens, and R. A. Schoonheydt, J. Am. Chem. Soc. **113**, 6730 (1991).

[8] J. L. Gázquez, A. Vela, and M. Galván, Struct. Bond. **66**, 79 (1987).

[9] (a) R. G. Parr, R. A. Donnelly, M. Levy, and W. E. Palke, J. Chem. Phys. **68**, 3801 (1978);
(b) J. P. Pardew, R. G. Parr, M. Levy, and J. L. Balduz, Phys. Rev. Lett. **49**, 1691 (1982);
(c) J. Katriel, R. G. Parr, M. R. Nyden, J. Chem. Phys. **74**, 2397 (1981).

[10] J. Hinze, M. A. Whitehead, and H. H. Jaffé, J. Am. Chem. Soc. **85**, 148 (1963).

[11] T. T. Nguen-Dang, R. F. W. Bader, and H. Essén, Int. J. Quant. Chem. **22**, 1049 (1982).

[12] D. Bergmann and J. Hinze, Struct. Bond. **66**, 145 (1987), and references therein.

[13] R. A. Donnelly and R. G. Parr, J. Chem. Phys. **69**, 4431 (1978); R. A. Donnelly, J. Chem. Phys. **71**, 2874 (1979).

[14] K. A. Dawson and N. H. March, J. Chem. Phys. **81**, 5850 (1984).

[15] N. H. March and R. F. Nalewajski, Phys. Rev. A**35**, 525 (1987).

[16] R. F. Nalewajski and P. M. Kozłowski, Acta Phys. Polon. A**74**, 287 (1988).

[17] W. Kohn and J. L. Sham, Phys. Rev. A**140**, 1133 (1965).

Restricted Basis Functions for H ⁺₂ With Use of Overlap Integrals of Slater-Type Orbitals

HERBERT W. JONES and BABAK ETEMADI

Department of Physics, Florida A&M University, Tallahassee, Florida 32307

FRANKLIN B. BROWN

Science and Mathematics Division, Tallahassee Community College, Tallahassee, Florida 32304, Supercomputer Computations Research Institute, Florida State University, Tallahassee, Florida 32306

Abstract

The Löwdin α-function method, augmented by the computer-generated C matrix, is applied to the H ⁺₂ molecule. A LCAO (linear combination of atomic orbitals) method is employed using several s-orbitals with equal screening constants. Precautions are taken to avoid cancellation errors, thereby achieving convergence with increasingly higher orbitals. © 1992 John Wiley & Sons, Inc.

Introduction

We make an application of the Löwdin α-function method to the determination of the ground state energy of the hydrogen molecular ion, H ⁺₂, using a basis set of Slater-type s-orbitals with equal screening constants. Essentially, only overlap integrals are needed for this task. This kind of problem was considered by Bishop and Schneider [1] in their study of a new integral transform, namely

$$ e^{-\zeta r} \int_0^r s(n) r^n \, dn $$

where $s(n)$ is a shape function. As a preliminary, they investigated a LCAO (linear combination of atomic orbitals) using $1s2s3s4s$ STOs. Steinborn and Weniger [2] pointed out, in their study of H ⁺₂ using "B-functions," that there was probably an error in Bishop and Schneider's treatment because of numerical integration difficulties.

We have made a more detailed study using orbitals from $1s$ to $8s$ with analytic methods [3] employing FORTRAN and, independently, *Mathematica* [4]. Since a *Mathematica* program for overlap integrals with unequal screening constants has been published [5], we include here the required program for overlap integrals with equal screening constants (Table I).

α-Function and Overlap Integral

Every displaced STO may be expanded in an infinite series of spherical harmonics, the functional coefficients being designated as α-functions. Assume that a local

TABLE I.   The *Mathematica* program for overlap integrals with equal orbital exponents.

```
azeta=a*zeta:
nnp=1;hhp=0;mm=0;
nn=1;hh=0;h=hhp
    cpolynomial=Sum[d^(nn+hh+2h-2pp-2vp-2v-k-kp)*
        r^(2pp+2v+2vp+kp)*(-1)^(v+qp+p+pp+hh)*(-1)^hh*
        (2hh-2p)!*(2h-2pp)!/4^(hh+h-p-pp)/((hh-p)!*
        p!*pp!*q!*qp!*v!*vp!*(hh+mm-2p-q-v)!)*
        (nn-hh+2p+2q+2qp)!/((h-pp)!*(h-mm-2pp-qp-vp)!*
        kp!*(nn-hh+2p+2q+2qp-k-kp)!),
        {p,0,Floor[(hh+mm)/2]},{q,0,hh+mm-2p},
        {v,0,hh+mm-2p-q},{pp,0,Floor[(h-mm)/2]},
        {qp,0,h-mm-2pp},{vp,0,h-mm-2pp-qp},
        {k,0,nn-hh+2p+2q+2qp},
        {kp,0,nn-hh+2p+2q+2qp-k}];
    cmatrix=CoefficientList[cpolynomial,{d,r}];
    c=cmatrix;

    kk=2^(nnp+nn)*(-1)^mm*Sqrt[(2hh+1)*(2hhp+1)*(hh+mm)!*
        (hhp-mm)!/((2nnp)!*(2nn)!*(hhp+mm)!*(hh-mm)!)];

    se1=Sum[c[[i+1,j+1]]*((-1)^j*azeta^(j+nnp-2hhp-hh+i)/(j+nnp-hhp+1)
        -(j+nnp-hhp)!*azeta^(i-hhp-hh-1)/2^(j+nnp-hhp+1)),
        {i,0,nn+hh+hhp},{j,0,nn+hhp}];

    se2=Sum[c[[i+1,j+1]]*(-1)^i*(j+nnp-hhp)!*azeta^
        (j+nnp-2hhp-k+i-hh-1)/(j+nnp-hhp-k)!/2^(k+1),
        {i,0,nn+hh+hhp},{j,0,nn+hhp},{k,0,nnp-hhp+j}];

    overlap=kk*Exp[-azeta]*(se1+se2)
```

coordinate system (R, Θ, φ) is displaced a distance a along the z-axis. In terms of the original coordinate system (r, θ, φ) we have [6]

$$\chi = AR^{N-1}e^{-\zeta R}Y_L^M(\Theta, \phi),$$

$$\chi = \frac{A}{\zeta^{N-1}}\left[\frac{(2L+1)(L+M)!}{4\pi(L-M)!}\right]^{1/2}\sum_{l=M}^{\infty}\left[\frac{4\pi(l+M)!}{(2l+1)(l-M)!}\right]^{1/2}(-1)^M$$

$$\times \alpha_l^{N,L,M}(\zeta a, \zeta r)Y_l^M(\theta, \phi),$$

where

$$\alpha_l^{N,L,M}(\zeta a, \zeta r) = \frac{(2l+1)(l-M)!}{2(l+M)!}\sum_{i=0}^{N+L+l}\sum_{j=0}^{N+l}C_l^{N,L,M}(i,j)$$

$$\times H_{ij}(\zeta a)^{i-L-l-1}(\zeta r)^{j-l-1}$$

and

$$H_{ij} = \begin{cases} e^{-\zeta a}[(-1)^l e^{\zeta r} - e^{-\zeta r}], & r < a \\ e^{-\zeta r}[(-1)^l e^{\zeta a} - e^{-\zeta a}], & r > a \end{cases}$$

$A = (2\zeta)^{N+1/2}[(2N)!]^{-1/2}$ is the normalization factor: N, L, and M are the quantum numbers of the orbital; and ζ is the screening constant or orbital exponent. Most importantly, for our developments, the elements of the C matrix are integers.

The overlap integral is defined as

$$S = \int \chi_a^* \chi_b \, dv$$

We place χ_a at the origin and χ_b is placed at $(0, 0, a)$.

$$\chi_a = A' r^{N'-1} e^{-\zeta' r} Y_{L'}^{M'}(\theta, \varphi)$$

$$\chi_b = A R^{N-1} e^{-\zeta R} Y_L^M(\Theta, \varphi)$$

Expanding χ_b about the origin and invoking orthogonality of spherical harmonics, we get [3]:

$$S(N'L'M, NLM) = Ke^{-P} \sum_{i=0}^{N+L'+L} \sum_{j=0}^{N+L'} C_{L'}^{NLM}(i, j)$$

$$\times \left((-1)^j \frac{p^u}{t+1} - \frac{t!}{2^{t+1}} p^v + (-1)^i \sum_{k=0}^{t} \frac{t!}{(t-k)!} \frac{p^w}{2^{k+1}} \right),$$

where

$$p = \zeta a$$

$$t = j + N' - L'$$

$$u = j + N' - 2L' - L + i$$

$$v = i - L' - L - 1$$

$$w = t - k + i - L - L' - 1$$

and

$$K = 2^{N'+N}(-1)^M \left(\frac{(2L+1)(2L'+1)(L+M)!(L'-M)!}{(2N')!(2N)!(L'+M)!(L-M)!} \right)^{1/2}$$

Also, $M' = M$ and $\zeta' = \zeta$.

Table I shows the programming of this formula in *Mathematica*.

Restricted LCAO Treatment of H$_2^+$

In atomic units, the Hamiltonian for H$_2^+$ is

$$H = -\frac{1}{2}\nabla^2 - \frac{1}{r_a} - \frac{1}{r_b} + \frac{1}{a}$$

We place s-orbital trial functions $\psi_{a,b}$ at each nucleus, i.e.:

$$\psi_a = e^{-\zeta r} \sum C_N r^{N-1}$$

$$\psi_b = e^{-\zeta R} \sum C_N R^{N-1}$$

Setting $\psi = \psi_a + \psi_b$,

$$H\psi = E\psi.$$

The variational principle for this equation leads to a secular determinant for the energy (eigenvalues).

The kinetic energy between a N' STO at the origin and a N STO at a displaced distance a is [7]

$$(KE)_{ab} = -\frac{1}{2}\zeta^2 S(N', N) + \frac{2\zeta^2 N' S(N'-1, N)}{[(2N'-1)(2N')]^{1/2}}$$

$$- \frac{2\zeta^2 N'(N'-1)S(N'-2, N)}{[(2N'-3)(2N'-2)(2N'-1)(2N')]^{1/2}}$$

The matrix elements for the other parts of the Hamiltonian are standard, with the potential energy between separated orbitals expressed as overlaps [7].

Results and Conclusion

Table II shows the energy resulting from the successive addition of more and more s-orbitals to each nucleus of the H_2^+ molecule. The same orbital exponent is used in each case and it is varied from 0.5 to 3.5; these results are plotted in Fig. 1 for $n = 1, 3, 5,$ and 7. It clearly shows that, as the number of orbitals is in   .d

TABLE II.   LCAO calculations of H_2^+ with s-orbitals and an internuclear distance of 2.0 a.u.

Trial function	Orbital exponent	Energy (a.u.)	Authors
1,2s STO		$-.590450$	Bishop and Schnieder
1234s STO		$-.590502$	Bishop and Schnieder
ϕ_{21}		$-.59045$	Steinborn and Weniger
ϕ_{31}		$-.59082$	Steinborn and Weniger
8 GTO		$-.59089$	Katriel and Adam
1s STO	1.24	$-.586505$	This article
1s2s STO	1.63	$-.590450$	"
123s STO	1.96	$-.590830$	"
1234s STO	1.96	$-.590830$	"
1...5s STO	1.59	$-.590893$	"
1...6s STO	2.05	$-.590935$	"
1...7s STO	2.45	$-.590948$	"
1...8s STO	2.78	$-.590951$	"
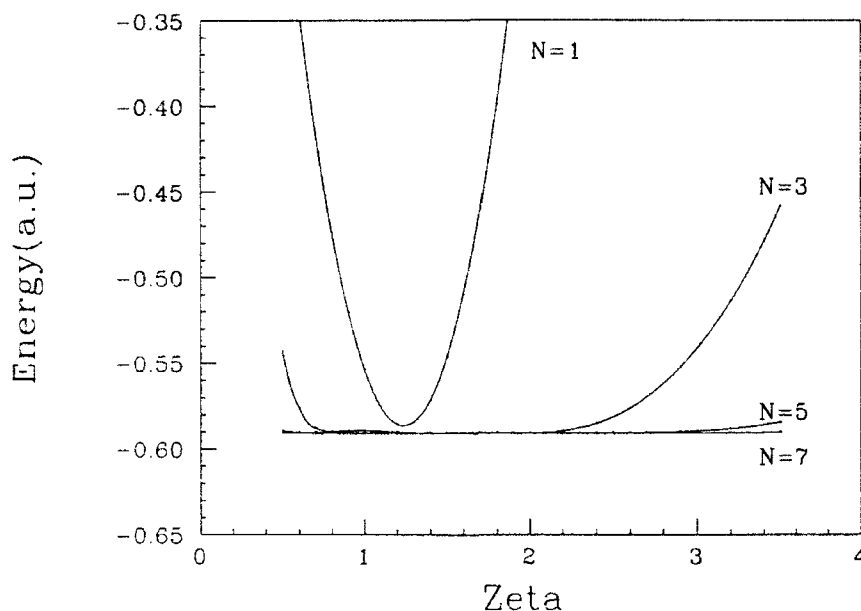
Figure 1. Energy vs. orbital exponent for $n = 1, 3, 5, 7$ (sum of n orbitals).

on each nucleus, the energy is less dependent on the precise value of the orbital exponent. Also, we note the presence of local minima in some of these curves.

Finkelstein and Horowitz [8] were the first to use $1s$ orbitals on each nucleus with an adjustable orbital exponent. Geller [9] used $1s$ and $2s$ orbitals on each nuclei with the same orbital exponent.

Referring to Table II, Bishop and Schneider [1] increased the orbitals to $4s$, but obtained an answer greater than our $1s2s3s$ value. Steinborn and Weniger, using their "B-function," spanned the $1s2s$ space with their ϕ_{21} [2] and the $1s2s3s$ space with their ϕ_{31}, obtaining values with which we agree. Katriel and Adam [10] placed eight two-parameter spherical Gaussians at each nucleus and claimed convergence to -0.59089 a.u. As expected, we achieve this result with only five STO orbitals that have only one parameter. We converge to six decimal digits, -0.590951, with eight orbitals on each center.

The implementation of the Löwdin α-function method with analytic procedures, including the use of integer arithmetic, permits us to work with high quantum numbers for s-orbitals to improve convergence.

Acknowledgments

the Florida State University Supercomputer Computations Research Institute (SCRI).

Bibliography

[1] D. M. Bishop and B. E. Schneider, Int. J. Quant. Chem. **9**, 67 (1975).
[2] E. O. Steinborn and E. J. Weniger, Int. J. Quant. Chem. Symp. **11**, 509 (1977).
[3] H. W. Jones, Int. J. Quant. Chem. **19**, 567 (1981).
[4] S. Wolfram, *Mathematica: A System for Doing Mathematics by Computer* (Addison-Wesley, Reading, MA, 1988).
[5] H. W. Jones, Int. J. Quantum Chem. **41**, 749 (1992).
[6] H. W. Jones and C. A. Weatherford, Int. J. Quant. Chem. Symp. **12**, 483 (1978).
[7] C. C. J. Roothaan, J. Chem. Phys. **19**, 1448 (1951).
[8] B. N. Finkelstein and G. E. Horowitz, Z. Phys. **48**, 118 (1928).
[9] M. Geller, Ph.D. dissertation, Northwestern University, Evanston, II., 1959.
[10] J. Katriel and G. Adam, Chem. Phys. Lett. **6**, 431 (1970).

Basis Set Quantum Chemistry and Quantum Monte Carlo: Selected Atomic and Molecular Results

M. URBAN,* RODNEY J. BARTLETT, and S. A. ALEXANDER†

Quantum Theory Project, University of Florida, Gainesville, Florida 32611

Abstract

We present results for the total energy, the first ionization potential, and the electron affinity of the Li, Be, B, C, N, O, F, Mg, Si, Ca, Fe, and Ge atoms using the coupled-cluster method with several standard basis sets, including correlation consistent, polarized, and atomic natural orbital bases. We also consider multiplet splittings in Fe and the activation barriers of the reactions, $H_3 \rightarrow H_2 + H$ and $FH_2 \rightarrow F + H_2$. These readily generated results are provided for comparison with Quantum Monte Carlo values. © 1992 John Wiley & Sons, Inc.

Introduction

In chemistry there are several requirements that a theoretical method must meet if it is to be widely applied to molecules and their potential surfaces. These include treating different molecular geometries with effectively equal accuracy and high precision; routine application to open- as well as closed-shell systems; treatment of excited as well as ground states; predictions of accurate energy differences between ions and neutral systems; and predictions of other properties like moments and polarizabilities. Powerful correlated basis set quantum chemistry methods have been developed for all of the above and are now incorporated into several readily-available, easily-applied program packages, such as ACES II [1]. Such applications permeate modern chemistry and play a role which can be scarcely overestimated. However, there are two fundamental problems which limit the accuracy of these methods. First, there is an inherent inaccuracy in any basis set (this causes about a 10%–50% error in absolute correlation energies in typical correlated calculations), while the highly nonlinear scaling of accurate correlated calculations with the number of basis functions (as n^6 or n^7) makes it effectively impossible to converge to the basis set limit. Second, for a sufficiently extended basis set, the treatment of electron correlation is inevitably inexact.

Monte Carlo methods present the prospect of eliminating both of these problems, however, in practice these calculations are more limited. In a Variational Monte

---

Carlo (VMC) calculation. for example. an analytic wavefunction (usually with explicitly correlated coordinates) is optimized and then used to calculate the energy and other expectation values [2.3]. Just as in basis set methods. the error in this method is due to the choice of wavefunction form. while Monte Carlo is only used to perform the multidimensional integration. In a Quantum Monte Carlo (QMC) calculation the Schrödinger equation is reformulated as a diffusion equation and then solved stochastically [4–11]. This method. however. suffers from errors caused by the fixed nodal structure of the importance function. As a result. these calculations cannot obtain the "exact" nonrelativistic result unless one eliminates this nodal error (by either a "released node" technique [12] or an improved weighting algorithm [13.14] both of which have only been applied to a small number of systems). Secondly. the different time scales for the core and valence electrons make it difficult for many of these methods to get accurate results for high-Z systems without introducing pseudopotentials [15–22]. damped core methods [23]. or convergence acceleration techniques [24].

In this article we present the total energies. the first ionization potentials (IPs). and the electron affinities (EAs) of several selected atoms and molecules of interest to the QMC community. Our objective is not to offer "definitive" basis set results. Instead. using a variety of standard basis sets and established "black-box" coupled cluster (CC) methods and programs. we demonstrate the accuracy obtained (and the CPU time required) for selected systems. These provide some comparative analysis of the quality of standard basis sets. We also compare our results with a number of other *ab initio* and Monte Carlo results which have been taken from the literature.

Method

The wavefunction in a coupled cluster calculation is based on the exponential ansatz [25]

$$\Psi_0 = \exp(T)\Phi_0 \qquad (1)$$

where T is expanded in terms of cluster operators

$$T = T_1 + T_2 + T_3 + \cdots \qquad (2)$$

acting on the reference state Φ_0. In a CCSD calculation [26]. Eq. (2) contains only the amplitudes from T_1 and T_2. These amplitudes are obtained from an iterative procedure which contains summations over no more than six indices (the worst step is $n_{occ}^2 n_{virt}^4$). The CCSD energy incorporates the effects from single and double excitations and from disconnected triple (i.e., $T_1 T_2$) and quadruple (i.e., $\frac{1}{2}T_2^2$) excitations. Extending CCSD to include "connected" triple excitations, that is, CCSDT [27], is much more time consuming (the worst step is $n_{occ}^3 n_{virt}^5$). To avoid this cost, noniterative methods that include T_3 effects through fourth order were developed. In a CCSD + T(CCSD) calculation [28]. the effects from connected triples are computed in a noniterative way using the converged amplitudes from a CCSD calculation. These amplitudes are placed in expressions analogous to fourth-order MBPT and

the resulting energy is then added to the CCSD energy so this adds only a single $n_{occ}^3 n_{vir}^4$ step. The CCSD(T) method [29,30] extends CCSD + T(CCSD) by adding one fifth-order term which reflects the effect of triple excitation amplitudes (as estimated noniteratively from converged CCSD amplitudes) on single excitation amplitudes. Because this term is fifth-order, its contribution to the energy is small, except in some pathological cases where it might offer a better noniterative approximation [29–32].

In most open-shell calculations we use a UHF reference. By monitoring the correlated multiplicity [33], no problems with spin contamination were encountered at the CCSD level of theory. For comparison, we also report several results using a restricted open-shell Hartree Fock reference (ROHF) coupled-cluster method that has been developed in our laboratory [34]. This method further eliminates spin contamination in UHF based CC calculations for open-shell systems. ROHF–CC requires that contributions due to off-diagonal Fock operators be included. In the ROHF CC approach the term which extends CCSD + T(CCSD) to CCSD(T) is of fourth-order. The addition of another fourth-order term, along with a necessary restriction to the use of semicanonical orbitals, defines the CCSD(T^*) method. We refer the reader to the original literature for a full discussion [34b]. We also wish to note that even more sophisticated methods have been developed and could easily be applied to most of the atomic calculations examined here. However, since their applicability to *large* molecular systems is more restricted at present, they are not routine enough to satisfy our current purposes. A general discussion of several such methods and their performance can be found in recent review papers [35]. All new results presented here have been obtained from the ACES II program [1]. For the sake of brevity we do not present separate values for CCSD + T(CCSD) unless their IPs and EAs differ from those computed with CCSD(T) by more than 0.02 eV (we used a conversion factor 1 a.u. = 27.2116 eV throughout).

Calculations

As the aim of this article is to examine the performance of coupled-cluster methods over a number of atoms, we have chosen to use mostly standard basis sets from the literature. No attempt to optimize these basis sets for the specific purpose of achieving the best EAs or IPs was made. In some cases, where general basis sets were not available, such as Fe, we have added selected diffuse functions to previously computed basis sets. A short description of each basis set is presented in footnotes to the tables. The basis sets generally employed are those of Dunning [36,37], the POL basis of Sadlej [38–42], and the ANO basis of Widmark, Malmquist, and Roos [43,44]—all of which are cataloged in ACES II.

There are several observations apparent from the atomic results presented in Tables I-XII. In those cases where the nonrelativistic energy limit is available, it is clear that the best CC calculations have errors in the total energy of less than 0.2%, but errors in the more relevant correlation energy ($E_{corr} = E_{NR} - E_{SCF}$) is as much as 60% for Li down to 20% for F. Most of the error in the correlation energy is due to an inadequate description of the $1/r_{12}$ cusp when traditional basis sets are used,

TABLE I. The lithium (^{2}S) atom.

Method	Energy (a.u.)	EA (eV)	IP (eV)	Reference
SCF	-7.4327269	-0.122	5.342	[59]
Hylleraas		0.609 (7)		[60]
Hylleraas	-7.4780601		5.3918	[61]
VMC	-7.4768 (3)			[3]
QMC	-7.47809 (24)	0.600 (27)	5.386 (8)	[10][a]
QMC		0.611 (20)	5.412 (8)	[10][b]
CISD		0.617	5.342	[43][c]
MCSCF		0.615		[62]
MCSCF			5.388	[63][d]
MBPT			5.39175 (1)	[64]
CCSD			5.39204 (8)	[65]
N.R. Limit	-7.478060326 (10)			
UHF	-7.431696	0.129	5.322	this work[e]
MBPT (2)	-7.444208	0.316	5.323	this work[e]
CCSD	-7.446338	0.605	5.323	this work[e]
CCSD (T)	-7.446342	0.608	5.323	this work[e]
UHF	-7.432733	-0.127	5.343	this work[f]
MBPT (2)	-7.447606	0.355	5.364	this work[f]
CCSD	-7.450062	0.608	5.370	this work[f]
CCSD (T)	-7.450089	0.615	5.371	this work[f]
Exp.		0.6180 (5)	5.392	[67]

[a] Damped core used.
[b] Pseudopotential used.
[c] This basis set is the uncontracted version of the one described in footnote f.
[d] Numerical basis set.
[e] POL: (10.6.4)/[5.3.2], spherical basis, Ref. [40].
[f] ANO: (14.9.4.3)/[5.4.3.2], spherical basis, Ref. [43].

especially for the inner-shell electrons (see, for example, Ref. [45]) where most of the total energy resides. The different percentages obtained reflect the percentage of valence to inner-shell electrons, explaining why F has a lower error than Li. Correlation among the valence electrons is more important to chemistry but less important to the total energy. The QMC results are generally better by tenths of a.u.'s. If we had wanted to get the best possible energy in our calculations, our basis set would have been chosen to be more like those used by Sasaki and Yoshimine [46] or by Feller and Davidson [47]. However, since the inner-shell correlation energy is largely insensitive to the addition or removal of valence electrons, the inner-shell basis set/correlation error has little effect on the first IPs or EAs.

On the other hand, the EAs are far more dependent on the choice of basis set in the valence region for the obvious reason that an anion requires a better description of the regions of space farther from the atomic nucleus. This means the basis set should contain a number of relatively diffuse functions. Note that those EAs of carbon which were computed with basis sets containing few diffuse basis functions

Table II. The beryllium (^{1}S) atom.

Method	Energy (a.u.)	IP (eV)	Reference
SCF	-14.573023	8.045	[59]
Hylleraas	-14.66654		[68]
VMC	-14.6664 (3)		[2]
QMC	-14.66718 (3)		[11]
QMC		9.34 (1)	[20]
CISD		9.292	[43][a]
MCSCF	-14.66698		[69][b]
MBPT (2)	-14.649373		[70]
CCSD	-14.666690		[71]
N.R. Limit	-14.66737 (3)		[69]
UHF	-14.571128	8.030	this work[c]
MBPT (2)	-14.607349	8.677	this work[c]
CCSD	-14.627694	9.191	this work[c]
CCSD (T)	-14.627807	9.194	this work[c]
UHF	-14.572984	8.044	this work[d]
MBPT (2)	-14.608905	8.854	this work[d]
CCSD	-14.625471	9.291	this work[d]
CCSD (T)	-14.625793	9.299	this work[d]
Exp.		9.322	[67]

[a] This basis set is the uncontracted version of the one described in footnote d.

[b] Numerical basis set.

[c] POL: (10.6.4)/[5.3.2], spherical basis, Ref. [40].

[d] ANO: (14.9.4.3)/[5.4.3.2], spherical basis, Ref. [43].

differ from the experimental value by up to 0.4 to 0.8 eV. However, in standard basis sets like the POL basis [38-42] or the ANO basis [43,44], sufficient diffuse character is included to provide reasonable EAs.

Good agreement with experiment for both the IPs and EAs is obtained with the POL basis [38-42] considering its relatively small size. Since it was developed for calculating electric dipole moments and polarizabilities the POL basis allows a good description of the outer part of the atomic (or molecular) electronic distribution and so produces better EAs than other basis sets of comparable size. Another advantage is that consistent POL basis sets are available for a number of atoms.

The ANO basis [43,44] was optimized following an averaging procedure for the correlated density matrix of the neutral atom, the atom in an external field, and the corresponding positive and negative ions. For this reason it is capable of providing good EAs and IPs for several first-row atoms, and such results are reported using CISD [43,44]. Coupled-cluster methods as shown here, further improve upon these CISD results, and we can usually obtain atomic IPs and EAs with a predictable accuracy of about 0.1 to 0.05 eV or better. For example, the IPs computed with CCSD + T(CCSD) and CCSD(T) agree with experiment to better than 0.1 eV for

TABLE III. The boron (^{2}P) atom.

Method	Energy (a.u.)	EA (eV)	IP (eV)	Reference
SCF	-24.529061	-0.268	7.932	[59]
VMC	-24.6156 (6)			[3]
CISD		0.154	8.179	[43][a]
CI	-24.6500	0.15		[46]
MRCI (SD)		0.278		[72]
MCSCF		0.2668 (30)		[73][b]
N.R. Limit	-24.65393			[74]
UHF	-24.531929	-0.463	8.036	this work[c]
CCSD (T)	-24.510829	-0.137	8.161	this work[c]
UHF	-24.532068	-0.600	8.038	this work[d]
CCSD (T)	-24.605382	-0.196	8.228	this work[d]
UHF	-24.524003	-0.300	8.047	this work[e]
MBPT (2)	-24.574888	0.143	8.180	this work[e]
CCSD	-24.599022	0.115	8.100	this work[e]
CCSD (T)	-24.600009	0.158	8.123	this work[e]
UHF	-24.533044	-0.310	8.042	this work[f]
MBPT (2)	-24.584516	0.213	8.283	this work[f]
CCSD	-24.604625	0.172	8.199	this work[f]
CCSD (T)	-24.606205	0.238	8.235	this work[f]
Exp.		0.277 (10)	8.298	[67]

[a] This basis set is the uncontracted version of the one described in footnote f.

[b] Numerical basis set.

[c] TZ2P: (10.6.3)/[5.3.2], spherical basis, Ref. [75].

[d] PVTZ: (10.5.2.1)/[4.3.2.1], spherical basis, Ref. [36].

[e] POL: (10.6.4)/[5.3.2], spherical basis, Ref. [39].

[f] ANO: (14.9.4.3)/[5.4.3.2], spherical basis, Ref. [43].

almost all of the atoms considered—an average error of less than 1%. With this same method, the EAs typically differ from experiment by 0.05 eV—an average error of about 5%, and it is only that high because of the 14% error in boron and an 8% error in oxygen. Of course, if an accuracy of 0.01 eV is required then a careful analysis of both the basis set and the method of including electron correlation is needed.

For the carbon atom we examine a number of basis sets. Obviously Cartesian basis functions (i.e., six d- and 10 f-functions) will produce a slightly better energy than spherical basis functions due to their greater flexibility. Of course, this slight improvement comes at the cost of a larger number of basis functions and a greater possibility of linear dependence problems. Although the EAs are clearly influenced by inclusion of diffuse basis functions, the extra Cartesian components have little added benefit.

In addition to more traditional *ab initio* methods, several EAs and IPs have recently been calculated using Variational Monte Carlo and Quantum Monte Carlo methods

TABLE IV. The carbon (^3P) atom.

Method	Energy (a.u.)	EA (eV)	IP (eV)	Reference
SCF	37.688619	0.549	10.787	[59]
UHF	37.693308	0.282		[31][a]
UHF	37.693342	0.449		[31][c]
RHF	37.688320	0.547		[31][c]
VMC	37.8017 (6)			[3]
QMC	37.848 (5)			[6]
QMC	37.815 (10)	1.3 (2)	11.2 (2)	[23][c]
CISD		1.133	11.158	[43][e]
CI	37.8393	1.11		[46]
MRCI (SD)		1.267		[72]
MCSCF			11.2516	[76][c]
UHF-CCSD (T)	37.812091	0.962		[31][a]
UHF-CCSD (T)	37.812213	1.207		[31][c]
RHF-CCSD (T)	37.812216	1.203		[31][c]
N.R. Limit	37.84499			[74]
UHF	37.688746	0.152	10.817	this work[f]
CCSD (T)	37.776293	0.461	10.945	this work[f]
UHF	37.692123	0.317	10.798	this work[g]
CCSD (T)	37.792934	0.865	11.103	this work[g]
UHF	37.690638	0.458	10.815	this work[h]
MBPT (2)	37.759171	1.171	11.142	this work[h]
CCSD	37.782747	1.070	11.044	this work[h]
CCSD (T)	37.784008	1.116	11.058	this work[h]
UHF	37.690324	0.463	10.822	this work[i]
MBPT (2)	37.758329	1.177	11.154	this work[i]
CCSD	37.781926	1.077	11.056	this work[i]
CCSD (T)	37.783175	1.121	11.068	this work[i]
UHF	37.690333	0.462	10.822	this work[j]
CCSD (T)	37.787743	1.170	11.137	this work[j]
UHF	37.691569	0.125	10.798	this work[k]
CCSD (T)	37.789527	0.698	11.184	this work[k]
UHF	37.693593	0.451	10.806	this work[l]
MBPT (2)	37.771189	1.273	11.279	this work[l]
CCSD	37.790951	1.154	11.183	this work[l]
CCSD (T)	37.793344	1.226	11.210	this work[l]
Exp.		1.2629 (3)	11.260	[67]

[a] PVQZ: (12.6.3.2.1)/[5.4.3.2.1], spherical basis. Ref. [31].

[b] PVQZ + sp, spherical basis. Ref. [31].

[c] The energy was computed with the standard QMC method but the EA and IP were computed with the damped core method.

[d] This basis set is the uncontracted version of the one described in footnote 1.

[e] Numerical basis set.

[f] DZ: Ref. [37] + d = 0.28, Cartesian basis.

[g] TZ2P: (10.6.3)/[5.3.2], Cartesian basis. Ref. [75].

[h] POL: (10.6.4)/[5.3.2], Cartesian basis. Ref. [38].

[i] POL: (10.6.4)/[5.3.2], spherical basis. Ref. [38.].

[j] (10.6.4.1)/[5.3.2.1], spherical basis. Same basis set as the one described in footnote i but with f = 0.761.

[k] PVTZ: (10.5.2.1)/[4.3.2.1], spherical basis. Ref. [36].

[l] ANO: (14.9.4.3)/[5.4.3.2], spherical basis. Ref. [43].

TABLE V. The nitrogen (⁴S) atom

Method	Energy (a.u.)	IP (eV)	Reference
SCF	54.400934	13.958	[59]
VMC	54.5456 (6)		[3]
QMC	54.5765 (12)		[7]
CISD		14.451	[43]ᵃ
CI	54.5835	14.51	[47]
N.R. Limit	54.5893		[74]
UHF	54.402012	13.896	this workᵇ
CCSD (T)	54.524049	14.349	this workᵇ
UHF	54.400686	13.893	this workᶜ
CCSD (T)	54.524873	14.450	this workᶜ
UHF	54.398447	13.925	this workᵈ
MBPT (2)	54.487900	14.471	this workᵈ
CCSD	54.506555	14.328	this workᵈ
CCSD (T)	54.507771	14.337	this workᵈ
UHF	54.404366	13.905	this workᵉ
MBPT (2)	54.513296	14.619	this workᵉ
CCSD	54.528693	14.478	this workᵉ
CCSD (T)	54.531443	14.502	this workᵉ
Exp.		14.534	[67]

[a] This basis set is the uncontracted version of the one described in footnote c.
[b] TZ2P: (10.6.3)/[5.3.2], spherical basis. Ref. [75].
[c] PVTZ: (10.5.2.1)/[4.3.2.1], spherical basis. Ref. [36].
[d] POL: (10.6.4)/[5.3.2], spherical basis. Ref. [38].
[e] ANO: (14.9.4.3)/[5.4.3.2], spherical basis. Ref. [43].

These are reported in the tables. There is no doubt that at least for small systems QMC can obtain highly accurate results provided that adequate computer time is available.

The Fe atom, whose IP, EA, and energy splitting has been calculated with several basis set ab initio methods as well as QMC, requires a separate discussion. Fe has a complicated open-shell structure, with interesting multiplets. Our CCSD calculation was found to be slowly convergent. An analysis of the T_1 amplitudes (and to a lesser extent T_2) showed that some values were above 0.1. The sensitivity of CCSD(T) to the inclusion of a single fifth-order contribution which arises from the effect of T_3 onto T_1 amplitudes (with all other fifth-order terms neglected [29]) is demonstrated by the significant difference in the EA of iron with the CCSD + T(CCSD) and CCSD(T) methods. It is interesting to note that CCSD + T(CCSD) agrees with the experimental EAs, IPs, and the $(d^6s^2 \rightarrow d^7s^1)$ multiplet splittings better than CCSD(T). The same holds for EAs of oxygen and fluorine. We do not want to overemphasize this point, however. Previous studies [29–32] have shown that the CCSD(T) energy is often in

TABLE VI. The oxygen (3P) atom.

Method	Energy (a.u.)	EA (eV)	IP (eV)	Reference
SCF	74.809398	0.540	11.888	[59]
VMC	75.0146 (7)			[3]
CISD		1.025	13.327	[43][c]
CI		1.287		[77]
MRCI(SD)		1.453		[72]
MCSCF			13.595	[78][c]
CCSD	75.054230	1.25		[79]
CCSD(T)	75.058621	1.42		[79]
N.R. Limit	75.067198			[74]
UHF	74.809036	0.549	12.019	this work[a]
MBPT(2)	74.928504	1.241	12.995	this work
CCSD	74.946285	1.064	13.013	this work[a]
CCSD(T)	74.948026	1.165	13.042	this work[a]
UHF	74.818648	0.577	12.033	this work[d]
MBPT(2)	74.980520	1.422	13.365	this work[d]
CCSD	74.996492	1.184	13.402	this work[d]
CCSD + T(CCSD)	75.000203	1.357	13.451	this work[d]
CCSD(T)	75.000130	1.336	13.450	this work[d]
ROHF	74.812110	0.539	11.979	this work[d]
MBPT(2)	74.980821	1.425	13.374	this work[d]
CCSD	74.996410	1.184	13.401	this work[d]
CCSD + T(CCSD)	75.000161	1.361	13.451	this work[d]
CCSD(T)	75.000127	1.338	13.450	this work[d]
CCSD(T*)	75.000134	1.338	13.450	this work[d]
Exp.		1.46111	13.618	[67]

[a] This basis set is the uncontracted version of the one described in footnote d.
[b] Numerical basis set.
[c] POL: (10,6,4)/[5,3,2], spherical basis. Ref. [38].
[d] ANO: (14,9,4,3)/[5,4,3,2], spherical basis. Ref. [43].

better agreement with higher levels of CC (e.g. CCSDT) than is CCSD + T(CCSD) because the latter method can overestimate the effect of triples. Especially for anions. however. one often encounters difficulties in converging the correlation energy and in saturating the basis set. Thus a slight overestimation of the correlation energy by CCSD + T(CCSD) might numerically compensate for basis set problems and give better agreement with experiment through error cancellation. Another possible explanation is that when large T_1 amplitudes occur. the additional term included in CCSD(T) (which is usually positive) is overestimated. For iron (and the oxygen and fluorine atoms as well) a comparison of both CCSD + T(CCSD) and CCSD(T) methods provides valuable information about the convergence of the CC wavefunction in these cases. As there are several additional fifth-order correlation corrections being neglected [29]. all should be considered in assessing the reliability of such noniterative methods. as well as other higher-order corrections.

TABLE VII. The Fluorine (^2P) atom.

Method	Energy (a.u.)	EA (eV)	IP (eV)	Reference
SCF	99.409349	1.362	15.717	[59]
VMC	99.6736 (7)			[3]
QMC	99.7178 (6)			[8]
QMC	99.7005 (21)	3.45 (11)		[4]
MBPT (2)	99.7299			[80]
MBPT (2)	99.696921	3.692		[81]a
CI	99.7166	3.12		[46]
CISD		2.976	17.133	[43]b
MRCI (SD)		3.363		[72]
CCSD	99.707610	3.185		[81]a
CCSD + T(CCSD)	99.712831	3.373		[81]a
CCSD (T)	99.719347	3.36		[56]
N.R. limit	99.7337			[74]
UHF	99.402062	1.248	15.700	this work c
MBPT (2)	99.558608	3.519	17.038	this work c
CCSD	99.571428	3.109	16.961	this work c
CCSD + T(CCSD)	99.574135	3.265	17.003	this work c
CCSD (T)	99.573746	3.210	16.995	this work c
UHF	99.415792	1.179	15.659	this work d
MBPT (2)	99.641246	3.647	17.320	this work d
CCSD	99.652411	3.147	17.213	this work d
CCSD + T(CCSD)	99.657158	3.344	17.275	this work d
CCSD (T)	99.657008	3.314	17.272	this work d
Exp.		3.401190 (4)	17.422	[67]

a Numerical basis set

b This basis set is the uncontracted version of the one described in footnote d.

c POL: (10.6.4)/[5.3.2], spherical basis, Ref. [38].

d ANO: (14.9.4.3)/[5.4.3.2], spherical basis, Ref. [43].

For the IPs and the multiplet splittings of iron our results are very similar to those Raghavachari and Trucks obtained with QCISD(T) (an approximation to CCSD(T)) [48,49]. These authors did not correlate the inner-shell electrons. In our calculations, we have correlated all electrons and performed to two calculations with frozen orbitals. A calculation with the (1s, 2s, 2p) electrons uncorrelated clearly shows that the K and L shells may be safely removed from the correlation part of the calculation. A similar calculation, however, with the (1s, 2s, 2p, 3s, 3p) electrons uncorrelated is completely inadequate especially for the EA. Removing the 3s and 3p electrons from the correlation part of the calculation produces IPS and multiplet splittings similar to those observed in earlier studies [48–50]. This suggests that the choice of pseudopotential, which is of interest in QMC and other studies, can have an important influence on the quality of results.

In addition to the basis set used by Raghavachari and Trucks, we created an extended basis set by adding more diffuse functions. No significant change in the

TABLE VIII.   The magnesium (^1S) atom.

Method	Energy (a.u.)	IP (eV)	Reference
SCF	199.61463	6.615	[59]
QMC		7.637 (26)	[15][a]
QMC		7.675 (8)	[16][a]
QMC		7.571 (32)	[17][a]
QMC		7.753 (8)	[18][a]
MBPT (2)	200.0349		[82]
CI	199.83495	7.57	[83][b]
CHF	199.606624	6.605	this work[c]
MBPT (2)	199.712949	7.305	this work[c]
CCSD	199.726417	7.555	this work[c]
CCSD (T)	199.727874	7.570	this work[c]
CHF	199.608639	6.606	this work[d]
MBPT (2)	199.930722	7.367	this work[d]
CCSD	199.943214	7.571	this work[d]
CCSD (T)	199.947222	7.608	this work[d]
Exp.		7.646	[67]

[a] Pseudopotential used.

[b] This basis set is the same one described in footnote d.

[c] POL : (13.10.4)/[7.5.2], spherical basis. Ref. [40].

[d] BAL : (12.9.12.6)/[8.6.4.2], spherical basis. Ref. [83].

IP and the multiplet splittings of the Fe atom was observed but the EA was significantly improved as would be expected. Although good basis sets for Fe are not as commonly available as for other atoms, with some effort at their determination, an accuracy of about 0.05 eV for CC methods including triples seems to be obtainable for the EAs, IPs, and multiplet splittings of this system.

In Table XIII we present several examples of total times for some of the calculations performed here. The time required for the correlation part of these calculations is large compared to the other operations only for the largest atoms considered, that is, Fe and Ge. It should be stressed, however, that all electrons were correlated in all our calculations including Fe, except as indicated for the second and third calculations on Fe, so these timings represent the worst possible case. For example, when we did not correlate the inner shell (1s, 2s, 2p) in Fe, the computer time needed for the CC part of the calculation was 40% of the all-electron calculation. Not correlating the 3s and 3p electrons reduces the CC part of the calculation by almost 90% to only 27s but the results are now greatly affected.

Unfortunately, there is only limited information available about the computer time needed for other calculations. Unpublished QMC studies of Fe using a pseudopotential which correlates only the 4s and 3d electrons required several hours on an IBM RISC 6000 [22]. These produced results, however, which are relatively far from experiment. Using a Ne pseudopotential produced much better results but required significantly more time.

TABLE IX.   The silicon (^{3}P) atom.

Method	Energy (a.u.)	EA (eV)	IP (eV)	Reference
SCF	-288.85436	0.956	7.658	[59]
QMC	-289.0 (5)	1.3 (2)	8.3 (2)	[15][a]
QMC		1.39 (3)	8.19 (3)	[18][b]
QMC		1.42 (2)	8.25 (2)	[19][b]
MRCI (SD)	-288.9623	1.30		[84]
UHF	-288.851653	0.859	7.645	this work[c]
MBPT (2)	-288.942521	1.309	7.952	this work[c]
CCSD	-288.962709	1.251	7.984	this work[c]
CCSD (T)	-288.964624	1.280	8.000	this work[c]
UHF	-288.858016	0.848	7.638	this work[d]
MBPT (2)	-288.982419	1.380	8.044	this work[d]
CCSD	-289.000609	1.316	8.069	this work[d]
CCSD (T)	-289.004355	1.375	8.108	this work[d]
Exp.		1.385 (5)	8.151	[67]

[a] Damped core used.
[b] Pseudopotential used.
[c] POL: (14.10.4)/[7.5.2], spherical basis, Ref. [41].
[d] ANO: (17.12.5.4)/[7.6.3.2], spherical basis, Ref. [44].

Because they have attracted the attention of the QMC community, and also because they are two of the few molecular systems which are amenable to accurate experimental and theoretical treatment, we report CC results for the activation barriers

TABLE X.   The calcium (^{1}S) atom.

Method	Energy (a.u.)	IP (eV)	Reference
SCF	-676.75818	5.120	[59]
QMC		5.878 (32)	[21][a]
MBPT (2)	-677.5565		[45]
MCSCF		6.156	[85][b]
RHF	-676.725485	5.121	this work[c]
UHF	-676.725485	5.100	this work[c]
MBPT (2)	-676.868157	5.802	this work[c]
CCSD	-676.881490	5.950	this work[c]
CCSD (T)	-76.884112	5.976	this work[c]
Exp.		6.113	[67]

[a] Pseudopotential used.
[b] Numerical basis set.
[c] POL: (15.13.4)/[9.7.2], Cartesian basis, Ref. [40].

Table XL. The iron (^5D) atom.

Method	Energy (a.u.)	EA (eV) $3d^7 4s^2$	IP (eV) $3d^6 4s^1$	E($^5D \to ^3F$) (eV) $3d^6 4s^2 \to 3d^7 4s^1$	Reference
SCF	-1262.4437	2.103	6.052	1.820	[59]
QMC		0.27 (8)	7.65 (5)	0.44 (5)	[22][a]
QMC			7.08 (8)	0.9 (1)	[22][b]
QCISD (T)			7.73	0.86	[48, 49][a]
CISD				1.34	[50]
MCSCF	-1262.50639		7.069		[86]
UHF	-1262.370937	-1.988	6.369	1.831	this work[d]
MBPT (2)	-1263.045976	0.228	7.506	0.205	this work[d]
CCSD	-1263.032146	-0.277	7.600	0.971	this work[d]
CCSD + T (CCSD)	-1263.048305	0.065	7.738	0.821	this work[d]
CCSD (T)	-1263.047266	0.017	7.728	0.870	this work[d]
ROHF	-1262.364742	-2.081	6.308	1.815	this work[d]
MBPT (2)	-1263.045478	0.279	7.485	0.165	this work[d]
CCSD	-1263.032079	-0.279	7.600	0.971	this work[d]
CCSD + T (CCSD)	-1263.048324	0.066	7.739	0.820	this work[e]
CCSD (T)	-1263.047269	-0.016	7.728	0.869	this work[d]
CCSD (T*)	-1263.047259	-0.017	7.728	0.869	this work[d]
UHF	-1262.379979	1.988	6.368	1.831	this work[e,f]
MBPT (2)	-1262.549399	-0.100	7.411	0.552	this work[e,f]
CCSD	-1262.560155	-0.293	7.594	1.033	this work[e,f]
CCSD + T (CCSD)	-1262.566816	0.030	7.688	0.895	this work[e,f]
CCSD (T)	-1262.566465	-0.031	7.683	0.923	this work[e,f]
UHF	-1262.370979	-1.988	6.368	1.831	this work[e,g]
MBPT (2)	-1262.893391	0.257	7.512	0.217	this work[e,g]
CCSD	-1262.884731	-0.244	7.604	0.974	this work[e,g]
CCSD + T (CCSD)	-1262.900067	0.146	7.741	0.816	this work[e,g]
CCSD (T)	-1262.899048	0.043	7.731	0.868	this work[e,g]
UHF	-1262.370979	-1.988	6.368	1.831	this work[e]
MBPT (2)	-1263.046536	0.262	7.513	0.212	this work[e]
CCSD	-1263.032458	-0.239	7.602	0.966	this work[e]
CCSD + T (CCSD)	-1263.048671	0.151	7.740	0.809	this work[e]
CCSD (T)	-1263.047628	0.049	7.730	0.861	this work[e]
Exp.		0.151 (3)	7.870	0.87[h]	[67]

[a] Pseudopotential used which includes relativistic effects—8 electrons explicitly correlated.

[b] Neon pseudopotential used which includes relativistic effects.

[c] This basis set is the same one described in footnote d.

[d] RT: (15.11.6.3)/[10.7.4.3], spherical basis. Ref. [48].

[e] RT ext.: (15.11.7.4)/[10.7.5.4], spherical basis. Same basis set as the one described in footnote d but with an extra d = 0.034 and f = 0.0945.

[f] With (1s, 2s, 2p, 3s, 3p) orbitals frozen.

[g] With (1s, 2s, 2p) orbitals frozen.

[h] The nonrelativistic value is 0.65 [48]. Most calculations here should be compared with this value. Considering the rather large difference, however, perhaps the relativistic result should be reconsidered.

TABLE XII. The germanium (^3P) atom.

Method	Energy (a.u.)	IA (eV)	IP (eV)	Reference
SCF	-2075.3597	0.952	7.434	[59]
QMC	-2073 (8)	1.3 (3)	8.0 (3)	[23]*
UHF	2075.277953	0.883	7.444	this work[c]
MBPT (2)	2076.110639	1.281	7.763	this work[b]
CCSD	-2076.054321	1.224	7.749	this work[b]
CCSD (T)	-2076.064449	1.254	7 764	this work[b]
UHF	-2075.114938	0.871	7.440	this work[c]
MBPT (2)	-2075.547394	1.299	7.848	this work[c]
CCSD	-2075.523550	1.246	7.831	this work[c]
CCSD (T)	-2075.531820	1.277	7.858	this work[c]
UHF	-2075.117400	0.872	7.433	this work[d]
CCSD (T)	-2075.537821	1.276	7.851	this work[d]
Exp.		1.233 (3)	7.899	[67]

[a] Damped core used.
[b] POL: (15.12.9.4)/[9.7.4.2], spherical basis, Ref. [42].
[c] BC: (15.12.6.1)/[10.7.3.1], spherical basis, Ref. [87].
[d] BC: (15.12.6.1)/[10.7.3.1], Cartesian basis, Ref. [87].

of the H + H_2 reaction in Table XIV and the interesting F + H_2 reaction in Table XV. Diedrich and Anderson [5] obtained an energy for the transition state of H — H — H of -1.659154(19) a.u. which is 9.61 kcal/mol above the exact value for separated H + H_2. This calculation took about 80 machine days on an IBM RISC 6000. Reducing the accuracy from 0.01 kcal/mol to 0.10 kcal/mol reduces the computational effort by a factor of 100. Using coupled-cluster methods and a [6.4.2.1] basis set (120 CGTFs) with no effort at further optimization, we obtain a CCSD + T(CCSD) energy of -1.658531 a.u. for H — H — H and an activation barrier of 9.71 kcal/mol. This required 205 s of CPU time on a CRAY-YMP most of which was spent manipulating the large number of 4-index virtual orbital integrals (ab/cd) that occur for a calculation with few electrons but a large number of basis functions. The CC part of the calculation took 12 s. Our barrier was calculated relative to the energy of H + H_2 in the same basis set (the CCSD energy of H_2 was -1.674004 a.u.) and is only slightly different from Liu's MRCI result (9.65 kcal/mol) which used a superior Slater orbital [5.3.3.2] basis (156 STOs) [51]. An ROHF reference calculation produced almost exactly the same results as that based on a UHF reference. To improve our result by the difference of 0.1 kcal/mol from the QMC result or 0.05 kcal/mol from Liu's result would take some effort. In other words, it is the error bar we accept as the price of a routine "black box" calculation.

Like the H_3 reaction, the transition barrier of F + $H_2 \rightarrow$ HF + F has been studied using a number of different methods [8.52–57]. Until a few years ago, the best *ab initio* result for the barrier fell in the range of 3 to 4 kcal/mol [58]. However, as

TABLE XIII.   Typical CPU times of the CCSD(T) calculations presented here (in seconds on a Cray YMP).[a]

ATOM	Basis set	Total	CC part
B/UHF	ANO, 46 spher.	44.2	3.6
C/UHF	POL, 24 spher.	9.5	2.0
	PVTZ, 33 spher.	17.6	1.6
	ANO, 46 spher.	30.1	5.0
N/UHF	POL, 24 spher.	10.3	1.?
	ANO, 46 spher.	47.3	5.7
F/UHF	POL, 24 spher.	7.4	2.7
	ANO, 46 spher	23.2	5.3
Mg/RHF	POL, 32 spher.	10.2	4.6
	BAU, 60 spher.	84.0	22.2
Mg/UHF	POL, 34 Cart.	28.4	15.7
Si/UHF	POL, 32 spher.	11.8	5.0
	ANO, 54 spher.	48.3	15.0
Ca/RHF	POL, 42 Cart.	27.0	17.2
Fe/UHF	RI, 72 spher.	209.7	162.6
	RI ext., 84 spher.	339.0	258.5
	RI ext., 84 spher.[b]	169.7	101.0
	RI ext., 84 spher.[c]	92.9	27.0
Ge/UHF	POL, 64 spher.	169.6	129.2

[a] All atomic calculations employ D_{2h} symmetry. Total times as well as CC times obviously depend on the number of iterations needed to reach convergence. Our SCF equations were considered converged when the maximum change in density matrix elements was less than 10^{-7}. CC equations were converged when the maximum change in amplitudes was less than 10^{-7}. Typically, CCSD calculations required 10 to 20 iterations to converge.

[b] With (1s, 2s, 2p) orbitals frozen.

[c] With (1s, 2s, 2p, 3s, 3p) orbitals frozen.

pointed out by Schaefer [58], the experimental estimates, which then ranged from 2.05 to 2.47 kcal/mol, were inconsistent with theory. Steckler et al. later estimated an experimental barrier of 1.6 kcal/mol [52a]. The first theoretical calculation that supported a low value of 2.0 to 2.5 kcal/mol was the CCSD + T(CCSD) and CCSDT-1 results of Bartlett and Rittby [35a,53]. These entirely *ab initio* values were obtained in the same basis as that of Truhlar et al. [52]. Their MR-CI result was 3.69 which was then empirically scaled to 1.6 kcal. Later, large scale MR-CI calculations of Bauschlicher et al. [55] led to a barrier of 2.89 kcal/mol, but adding the Davidson correction, which estimates the size-inextensivity error that remains in the MR-CI this value is reduced by a critical 0.75 kcal/mol, giving a value of 2.14 for the barrier, falling between the Bartlett and Rittby [35a] values. Further computed values by these authors [55b] are 1.81 and 1.85 kcal/mol at the Davidson corrected MR-CI level and averaged coupled pair functional level, respectively. Later CCSD(T) results of Scuseria [56] in an even larger [7.7.5.4.2/6.5.4.2] basis set gave 2.05 further

TABLE XIV.   Energy barrier for the H + H₂ reaction. This energy is in atomic units and the barrier height is in kcal/mol.

Method	H + H₂ energy	H₃ energy	Barrier	Reference
QMC			<9.70 (13)	[9][a]
QMC		-1.6617 (2)	9.68 (8)	[12][a]
QMC	-1.674451 (23)	-1.659154 (14)	9.61 (1)	[5][a]
CISD	-1.673977	-1.658018	10.11	[51][b]
MRCI	-1.674142	-1.658755	9.65	[51][b]
Hylleraas	-1.673776	-1.6366379	9.68	[88]
UHF	-1.633597	-1.605521	17.62	this work[b,c]
MBPT (2)	-1.666784	-1.646024	13.03	this work[b,c]
CCSD	-1.674004	-1.657992	10.05	this work[b,c]
CCSD + T(CCSD)	-1.674004	-1.658531	9.71	this work[b,c]
CCSD (T)	-1.674004	-1.658500	9.73	this work[b,c]

[a] Barrier height calculated relative to the separated H + H₂ energy.

[b] Barrier height calculated as the difference H₃ - (H + H₂).

[c] [6.4.2.1]. Cartesian basis. Constructed from Duijenvelt's 8s set contracted to 6s [89] with p and d functions from Widmark, Malmquist, and Roos [43] and Dunning's f functions [36]. The bond legnth of the linear H — H — H is 1.759 a.u.

supporting the 2.02 result of Bartlett and Rittby [35a]. The most recent MRCI + Q calculations [57] also support these results, reporting a transition barrier of 1.93 kcal/mol, but this value is plagued by an unacceptably high (26%) Davidson's correction.

To be consistent with the philosophy of this article, we repeat the F + H₂ → HF + F barrier using the standard ANO basis of Widmark et al. [43]. The results are in Table XV. We used the two optimized transition state geometries, the earlier CCSD + T(CCSD) optimized geometry of Bartlett and Rittby [35a, 53], and the CCSD(T) geometry of Scuseria [56]. Due to the flatness of the surface, the computed barriers are nearly indistinguishable, causing a difference of only 0.02 kcal/mol.

Our calculations were performed with a (14.9.4.3/8.4.3)/[5.4.3.2/4.3.2] spherical basis (92 CGTFs). The calculation at the transition state required a total of 207.3 s of CPU time on a CRAY-YMP, of which 79.0 s was spent in the CC part of the calculation. At the CCSD(T) level the F + H₂ transition barrier of 2.11 kcal/mol is in excellent agreement with the prior CC results. Our exothermicity differs by a kcal/mol from Scuseria's, despite his use of a larger basis set [56]. We find a 0.3 kcal/mol difference between our CCSD + T(CCSD) and CCSD(T) results, with the former giving the lower, value, 1.8 kcal/mole, which is close to the lowest barrier estimates. The difference between a UHF and an ROHF open-shell reference, was found to be inconsequential.

In contrast, the F + H₂ barrier height predicted by QMC is too high [8] in agreement with the older ab initio results, while the exothermicity is a little too low [8]. Some question as to whether the transition state could be bent [52b, 55a, 56, 57] (it is assumed linear in all above calculations) has been raised, also.

Table XV. Energy barrier for the F + H2 reaction and the exothermicity for F + H2 → FH + H. The energy and geometry are given in atomic units while the barrier height and the exothermicity are given in kcal/mol

Method	Geometry		FH2 energy	Barrier	Exothermicity	Reference
	F–H	F–H				
MRCI (SD)	2.81	1.46		3.69		[52]
SEC*	3.00	1.46		1.59		[52a]
UHF–CCSDT-1	2.87	1.46		2.50		[53, 35a]
QRHF–CCSDT-1	2.871	1.455		2.02		[53, 35a]
CCSD (T)	2.913	1.445		2.05	31.6	[56]
MRCI	2.95	1.45		2.46		[57]
MRCI + Q	2.95	1.45		1.93		[57]
QMC	2.57	1.48	-100.8861 (17)	3.2 (1.3)	29.7 (1.6)	[8]
UHF	2.871	1.455	-100.531402	11.24	15.0	this work[b,c]
CCSD	2.871	1.455	-100.808363	3.11	28.6	this work[b]
CCSD + T (CCSD)	2.871	1.455	-100.815111	1.80	30.8	this work[b,c]
CCSD (T)	2.871	1.455	-100.814455	2.11	30.7	this work[b,c]
ROHF	2.871	1.455	-100.524811	12.33	16.1	this work[b,c]
CCSD	2.871	1.455	-100.808246	3.13	28.7	this work[b,c]
CCSD + T (CCSD)	2.871	1.455	-100.815071	1.78	30.9	this work[b,c]
CCSD (T)	2.871	1.455	-100.814412	2.11	30.7	this work[b,c]
CCSD (T*)	2.871	1.455	-100.814407	2.11	30.7	this work[b,c]
Estimated limits for barrier				1.6		[54][d]
				1.65		[55]
Experimental exothermicity					31.7 (2)	[90]

[a] SEC—Scaled External Correlation (extrapolated result).

[b] ANO: (14.9.4.3/8.4.3)/[5.4.3.2/4.3.2]. Cartesian basis. Ref. [43]. In all present correlated calculations the inner-shell electron was dropped. Geometry of the transition state optimized by Ritthy and Bartlett [53]. The geometry optimized by Scuseria changes the barrier by less than 0.02 kcal/mol.

[c] Energy of F(^{2}P): UHF CCSD + T (CCSD) -99.644471; UHF CCSD (T) -99.644317; ROHF CCSD + T (CCSD) -99.644397; ROHF CCSD (T) -99.644265; ROHF CCSD (T*) -99.644268. Energy of H2 (R = 1.402): CCSD -1.173506. The bond length of H2 is taken from experiment; our optimized bond length coincides with this value. Energy of FH (R = 1.7329): CCSD + T (CCSD) -100.367132; CCSD (T) -100.366738. The bond length of FH is taken from experiment; our optimized bond lengths are almost identical with it: R(CCSD + T (CCSD)) = 1.734; R(CCSD(T)) = 1.733.

[d] Collinear barrier.

Note added in proof: Since the acceptance of this manuscript a MRCI study by Kendall, Dunning, and Harrison on the electron affinities of the first-row atoms (J. Chem Phys. **96**, 6796 (1992)) appeared as has a VMC study by Moskowitz and Schmidt (J. Chem. Phys. **97**, 3382 (1992)).

Acknowledgments

Bibliography

[1] Advanced Concepts in Electronic Structure (ACES II)—A product of the University of Florida Quantum Theory Project: J. F. Stanton, J. Gauss, J. D. Watts, W. J. Lauderdale, and R. J. Bartlett.

[2] C. J. Umrigar, K. G. Wilson, and J. W. Wilkins, Phys. Rev. Lett. 60, 1719 (1988).

[3] K. E. Schmidt and J. W. Moskowitz, J. Chem. Phys. 93, 4172 (1990).

[4] R. N. Barnett, P. J. Reynolds, and W. A. Lester, Jr., J. Chem. Phys. 84, 4992 (1986).

[5] D. L. Diedrich and J. B. Anderson, J. Chem. Phys. (submitted).

[6] K. E. Schmidt and J. W. Moskowitz, J. Stat. Phys. 43, 1027 (1986).

[7] P. J. Reynolds, R. N. Barnett, B. L. Hammond, and W. A. Lester, Jr., J. Stat. Phys. 43, 1017 (1986).

[8] D. R. Garmer and J. B. Anderson, J. Chem. Phys. 86, 7237 (1987); 89, 3050 (1988).

[9] R. N. Barnett, P. J. Reynolds, and W. A. Lester, Jr., J. Chem. Phys. 82, 2700 (1985).

[10] B. L. Hammond, M. M. Soto, R. N. Barnett, and W. A. Lester, Jr., J. Mol. Struct. 234, 525 (1991).

[11] C. J. Umrigar, K. J. Runge, and M. P. Nightingale, Monte Carlo Methods in Theoretical Physics, S. Caracciolo and A. Fabrocini, Eds. (Editrice, Pisa, 1991).

[12] D. M. Ceperley and B. J. Alder, J. Chem. Phys. 81, 5833 (1984).

[13] S. Zhang and M. H. Kalos, Phys. Rev. Lett. 67, 3074 (1991).

[14] J. B. Anderson, C. A. Traynor, and B. M. Boghosian, J. Chem. Phys. 95, 7418 (1991).

[15] B. L. Hammond, P. J. Reynolds, and W. A. Lester, Jr., J. Chem. Phys. 87, 1130 (1987).

[16] P. A. Christiansen and L. A. Lajohn, Chem. Phys. Lett. 146, 162 (1988).

[17] T. Yoshida and K. Iguchi, J. Chem. Phys. 88, 1032 (1988).

[18] G. D. Bachlelet, D. M. Ceperley, and M. G. B. Chiochetti, Phys. Rev. Lett. 62, 2088 (1989).

[19] L. Mitas, E. L. Shirley, and D. M. Ceperley, J. Chem. Phys. 95, 3467 (1991).

[20] P. A. Christiansen, J. Chem. Phys. 88, 4867 (1988).

[21] T. Yoshida and K. Iguchi, J. Chem. Phys. 93, 5783 (1990).

[22] L. Mitas and D. M. Ceperley (to be published).

[23] B. L. Hammond, P. J. Reynolds, and W. A. Lester, Jr., Phys. Rev. Lett. 61, 2312 (1988).

[24] See, for example, P. J. Reynolds, Int. J. Quantum Chem. S24, 679 (1990).

[25] J. Čízek, J. Chem. Phys. 45, 4256 (1966); Adv. Chem. Phys. 14, 35 (1969).

[26] G. D. Purvis and R. J. Bartlett, J. Chem. Phys. 76, 1910 (1982).

[27] J. Noga and R. J. Bartlett, J. Chem. Phys. 86, 7041 (1987).

[28] M. Urban, J. Noga, S. J. Cole, and R. J. Bartlett, J. Chem. Phys. 83, 4041 (1985).

[29] R. J. Bartlett, J. D. Watts, S. A. Kucharski, and J. Noga, Chem. Phys. Lett. 165, 513 (1990); J. D. Watts, I. Cernusak, J. Noga, R. J. Bartlett, C. W. Bauschlicher, T. J. Lee, A. P. Rendell, and P. R. Taylor, J. Chem. Phys. 93, 8875 (1990).

[30] K. Raghavachari, G. W. Trucks, J. A. Pople, and M. Head-Gordon, Chem. Phys. Lett. 157, 479 (1989).

[31] J. D. Watts and R. J. Bartlett, J. Chem. Phys. 96, 6073 (1992).

[32] J. D. Watts, J. F. Stanton, and R. J. Bartlett, Chem. Phys. Lett. 178, 471 (1991); G. E. Scuseria and T. J. Lee, J. Chem. Phys. 93, 5857 (1990).

[33] G. D. Purvis, III, H. Sekino, and R. J. Bartlett, Collect. Czech. Chem. Commun. 63, 2203 (1988).

[34] (a) M. Ritthy and R. J. Bartlett, J. Phys. Chem. 92, 303 (1988); (b) J. Gauss, J. Stanton, and R. J. Bartlett, Chem. Phys. Lett. 182, 207 (1991).

[35] (a) R. J. Bartlett, J. Phys. Chem. 93, 1697 (1989); (b) M. Urban, I. Cernusak, V. Kello, and J. Noga, Methods in Computational Chemistry, Vol. 2, Stephen Wilson, Ed. (Plenum, New York, 1987); (c) P. Piecuch, S. Zarrabian, J. Paldus, and J. Cizek, Phys. Rev. A 42, 3351, 5155 (1990).

[36] T. H. Dunning, Jr., J. Chem. Phys. 90, 1007 (1989).

[37] T. H. Dunning, Jr., J. Chem. Phys. 53, 2823 (1970).

[38] A. J. Sadlej, Collect. Czech. Chem. Commun. 53, 1995 (1988).

[39] A. J. Sadlej (private communication).

[40] A. J. Sadlej and M. Urban, J. Mol. Struct. 234, 147 (1991).

[41] A. J. Sadlej, Theo. Chim. Acta 79, 123 (1991).

[42] A. J. Sadlej, Theo. Chim. Acta 81, 45 (1991).

[43] P. O. Widmark, P. O. Malmquist, and B. O. Roos, Theo. Chim. Acta 77, 291 (1990).

[44] P. O. Widmark, P. O. Malmquist, and B. O. Roos, Theo. Chim. Acta 79, 419 (1991).

[45] V. Termath, W. Klopper, and W. Kutzelnigg, J. Chem. Phys. 94, 2002 (1991).

[46] F. Sasaki and M. Yoshimine, Phys. Rev. A 9, 17, 26 (1974).

[47] D. Feller and E. R. Davidson, J. Chem. Phys. 88, 7580 (1988).

[48] K. Raghavachari and G. W. Trucks, J. Chem. Phys. 91, 1062 (1989).

[49] K. Raghavachari and G. W. Trucks, J. Chem. Phys. 91, 2457 (1989).

[50] C. W. Bauschlicher, Jr., J. Chem. Phys. 86, 5591 (1987).

[51] B. Liu, J. Chem. Phys. 80, 581 (1984).

[52] (a) R. Steckler, D. W. Schwenke, F. B. Brown, and D. G. Truhlar, Chem. Phys. Lett. 121, 475 (1985); (b) D. W. Schwenke, R. Steckler, F. B. Brown, and D. G. Truhlar, J. Chem. Phys. 64, 2443 (1987).

[53] M. Rittby and R. J. Bartlett, Presented at the 1987 Sanibel symposia.

[54] M. J. Frisch, J. S. Binkley, and H. F. Schaefer, III, J. Chem. Phys. 81, 1882 (1984); M. J. Frisch, J. S. Binkley, H. F. Schaefer, III, and W. H. Miller, Chem. Phys. Lett. 114, 1 (1985).

[55] (a) C. W. Bauschlicher, S. P. Walch, S. R. Langhoff, P. R. Taylor, and R. L. Jaffe, J. Chem. Phys. 88, 1743 (1988); (b) C. W. Bauschlicher, P. R. Langhoff, T. J. Lee, and P. R. Taylor, J. Chem. Phys. 90, 4296 (1989).

[56] G. E. Scuseria, J. Chem. Phys. 95, 7426 (1991).

[57] P. Knowles, K. Stark, H.-J. Werner, Chem. Phys. Lett. 185, 555 (1991).

[58] H. F. Schaefer, III, J. Phys. Chem. 89, 5336 (1985).

[59] C. F. Fischer, The Hartree–Fock Method for Atoms (Wiley, New York, 1977); E. Clementi and C. Roetti, At. Nucl. Data Tables 14, 177 (1974).

[60] J. S. Sims, S. A. Hagstrom, D. Munch, and C. F. Bunge, Phys. Rev. A 13, 560 (1976).

[61] J. Pipin and D. A. Bishop, Phys. Rev. A 45, 2736 (1992).

[62] H. Agren, J. Olsen, H. J. Aa. Jensen, and P. Jorgensen, Phys. Rev. A 40, 2265 (1989).

[63] C. F. Fischer, Nucl. Instrum. Methods B 31, 265 (1988).

[64] S. A. Blundell, W. R. Johnson, Z. W. Liu, and J. Sapirstein, Phys. Rev. A 40, 2233 (1989).

[65] I. Lindgren, Phys. Rev. A 31, 1273 (1985).

[66] D. K. McKenzie and G. W. F. Drake, Phys. Rev. A 44, R6973 (1991).

[67] CRC Handbook of Chemistry and Physics, D. R. Lide, Ed. (CRC, Boca Raton, 1991).

[68] J. S. Sims and S. A. Hagstrom, Phys. Rev. A 4, 908 (1971).

[69] D. Sundholm and J. Olsen (unpublished results). Values reported in A. M. Martensson-Pendrill, S. A. Alexander, L. Adamowicz, N. Oliphant, J. Olsen, P. Oster, H. M. Quiney, S. Salomonson, and D. Sundholm, Phys. Rev. A 43, 3355 (1991).

[70] S. A. Alexander, H. J. Monkhorst, and K. Szalewicz, J. Chem. Phys. 85, 5821 (1986).

[71] S. Salomonson and P. Oster, Phys. Rev. A 41, 4670 (1990).

[72] T. Noro, M. Yoshimine, M. Sekiya, and F. Sasaki, Phys. Rev. Lett. 66, 1157 (1991).

[73] D. Sundholm and J. Olsen, Chem. Phys. Lett. 171, 53 (1990).

[74] E. R. Davidson, S. A. Hagstrom, S. J. Chakravorty, V. M. Umar, and C. F. Fischer, Phys. Rev. A 44, 7071 (1991).

[75] J. Stanton, J. Gauss, and R. J. Bartlett, unpublished. TZ2P basis available from authors.

[76] D. Sundholm and J. Olsen, Chem. Phys. Lett. 182, 497 (1991).

[77] C. W. Bauschlicher, Jr., S. R. Langhoff, H. Partridge, and P. R. Taylor, J. Chem. Phys. **85**, 3407 (1986).

[78] D. Sundholm, J. Olsen, and S. A. Alexander, J. Chem. Phys. **96**, 5229 (1992).

[79] D. L. Stout and G. E. Scuseria, J. Chem. Phys. (submitted).

[80] E. Eggarter and T. P. Eggarter, J. Phys. B **11**, 2969 (1978).

[81] L. Adamowicz and R. J. Bartlett, J. Chem. Phys. **84**, 6837 (1986).

[82] K. Jankowski, P. Malinowski, and M. Polasik, J. Phys. B **12**, 3157 (1979).

[83] C. W. Bauchlicher, Jr., B. H. Lengsfield, III, and B. Liu, J. Chem. Phys. **77**, 4084 (1982).

[84] M. Leweenz, P. Bruma, S. D. Peyerimhoff, and R. J. Bunker, J. Phys. B **16**, 4511 (1983).

[85] D. Sundholm and J. Olsen (unpublished results).

[86] C. F. Fisher and J. S. Carley, J. Phys. B **9**, 29 (1976).

[87] R. C. Binning and L. A. Curtiss, J. Comput. Chem. **11**, 1206 (1990).

[88] D. Frye, A. Preiskorn, and E. Clementi, J. Comput. Chem. **12**, 560 (1991).

[89] F. B. Van Duijneveldt, IBM Res. Rep. No. RJ 945 (1971).

[90] K. P. Huber and G. Herzberg, *Constants of Diatomic Molecules* (Van Nostrand Reinhold, New York, 1979).

Analytic Approximations to the Momentum Moments of Neutral Atoms

AJIT J. THAKKAR

*Department of Chemistry, University of New Brunswick, Fredericton,
New Brunswick, Canada E3B 6E2*

TOSHIKATSU KOGA

Department of Applied Chemistry, Muroran Institute of Technology, Muroran, Hokkaido 050, Japan

Abstract

Simple analytic approximations to the moments of electronic momentum $\langle p^k \rangle$ ($k = -2, -1, 1, 2, 3, 4$) of the neutral atoms from hydrogen through uranium are presented. These approximations are generated by using Thomas-Fermi-Dirac-Scott and hydrogenic results to guess suitable functional forms, and then fitting the latter to tabulated Hartree-Fock (HF) moments. The root mean square (rms) percent errors of our best functions for p^k with $k > 1$ are less than 0.6%. The best functions for $\langle p \rangle$ and p^{-1} have a rms percent error of less than 2%. The $\langle p^{-2} \rangle$ moments exhibit very strong shell structure, and our best function has a rms percent error as large as 12%. © 1992 John Wiley & Sons, Inc.

Introduction

Atoms are the building blocks of chemistry, and hence, the systematics of their properties are of interest to all chemists. Gross systematics, as taught in introductory courses, are often rationalized by qualitative arguments. A semiquantitative account of the systematics can often be achieved with the Thomas–Fermi (TF) and related models [1]. The TF model also gives the correct asymptotic behavior of some physical properties of an atom in the limit of a large number of electrons, N [2]. A quantitative description of atomic properties requires a theory at least as sophisticated as the Hartree–Fock (HF) model [3,4]. Tables of many physical properties of all the atoms computed by the HF method have been published [4,5]. Obviously, it would be nice to find analytic formulae as simple as those of the TF model and as accurate as the HF model. Such formulae can be obtained by using simple models to guess analytic forms that are then fitted to calculations based on sophisticated theories.

We focus on the electronic momentum moments $\langle p^k \rangle$, which are finite only [6,7] for $-3 < k < 5$. These moments are rather interesting. $\langle p^{-1} \rangle / 2$ is the peak height of the Compton profile [8]. $\pi \langle p \rangle$ is a good approximation [9,10] to the Dirac–Slater exchange energy of density functional theory [11]. $\langle p^2 \rangle / 2$ is the electronic kinetic energy. $\langle p^3 \rangle$ is roughly proportional [9,10] to the initial value of the Patterson function of x-ray crystallography [12]. $\langle p^4 \rangle$ is proportional to the

Breit–Pauli correction to the energy due to the relativistic variation of mass with velocity [13].

We use recent work [14–17] on the Thomas–Fermi–Scott description of momentum moments in atoms to guess suitable analytic forms which give $\langle p^k \rangle$ as a function of N and fit them to recent HF calculations [18–20] of these quantities. In this manner, we obtain simple formulae for $\langle p^k \rangle$ which have root mean square errors not exceeding 0.6% for $k > 1$, and less than 2% for $\langle p \rangle$ and $\langle p^{-1} \rangle$.

Method

Dmitrieva and Plindov [14,15] have used the TF model including the exchange interaction, and the Scott–Schwinger correction for strongly bound electrons [16,21], to find

$$\langle p^4 \rangle = \frac{5\pi^2}{3} N^4 - 16.60 N^{11/3}$$ (1)

$$\langle p^3 \rangle = \frac{32}{9\pi} N^3 (\ln N + 0.5578) + 1.720 N^{7/3}$$ (2)

$$\langle p^2 \rangle = 1.53749 N^{7/3} - N^2 + 0.53978 N^{5/3}$$ (3)

$$\langle p \rangle = 0.693747 N^{5/3} + 0.187 N$$ (4)

Dmitrieva and Plindov [14], and Buchwald and Englert [17] used the Thomas–Fermi–Scott model to find

$$\langle p^{-1} \rangle = 9.1759 N^{1/3} + 0.0283 N^{-1}$$ (5)

Note that eq. (5), unlike eqs. (1)–(4), does not include exchange corrections; the latter behave as $N^{-1/3}$ for $\langle p^{-1} \rangle$. The normalization condition requires that $\langle p^0 \rangle = N$.

We used eqs. (1)–(5) to guess functional forms for $\langle p^k \rangle$ and then fitted them to HF data [18–20] for all the neutral atoms from hydrogen ($N = 1$) through uranium ($N = 92$), by minimizing the root mean square percent deviation, δ_1, using Powell's conjugate direction algorithm [22]. We also record the maximum percent deviation, δ_2, and the value (N^*) of N for which it is attained. In an attempt to report our parameters to the "optimal" number [23] of significant figures, we list parameters rounded as much as possible without degrading δ_1 by 1% or more.

Results and Discussion

Our functional forms for $\langle p^4 \rangle$ are listed in Table I. It shows that eq. (1) is a decent starting point with $\delta_1 = 14\%$. Table I contains six functions that have $\delta_1 < 1\%$. We recommend the penultimate function in Table I, because it has nearly the lowest $\delta_1 = 0.55\%$, the lowest $\delta_2 = 2.1\%$, and the correct behavior in the limit of large N.

Table II lists our approximations to $\langle p^3 \rangle$. Eq. (2) is a fine starting point with $\delta_1 = 4.2\%$. Table II contains eight functions with $\delta_1 < 1\%$. The function with the lowest

TABLE I.   Analytic approximations to $\langle p^4 \rangle$: $a_0 = 5\pi^2/3 = 16.449$, $b_0 = 16.60$.

Function	Parameters	δ_1	δ_2	N^*
$a_0 N^4$	—	52.	229.	1
$a N^4$	$a = 11.0$	19.	120.	1
$a N^\alpha$	$a = 6.498, \alpha = 4.161$	4.4	30.	1
$a_0 N^4 + b_0 N^{11/3}$	—	14.	103.	1
$a_0 N^4 + b N^{11/3}$	$b = -13.3$	6.1	37.	1
$a_0 N^4 + b N^\beta$	$b = -11.59, \beta = 3.742$	0.79	2.8	1
$a N^4 + b N^\beta$	$a = 18.05, b = -13.05,$ $\beta = 3.793$	0.49	2.2	4
$a N^\alpha + b N^\beta$	$a = 12.252, \alpha = 4.0396,$ $b = -7.2774, \beta = 3.6785$	0.47	2.5	2
$a_0 N^4 + b_0 N^{11/3} + c N^{10/3}$	$c = 5.26$	1.0	4.3	4
$a_0 N^4 + b_0 N^{11/3} + c N^\gamma$	$c = 5.226, \gamma = 3.331$	1.0	4.3	4
$a_0 N^4 + b N^{11/3} + c N^{10/3}$	$b = -16.733, c = 5.4349$	0.99	4.5	4
$a_0 N^4 + b N^{11/3} + c N^\gamma$	$b = -25.613, c = 14.206,$ $\gamma = 3.581$	0.55	2.1	4
$a N^4 + b N^{11/3} + c N^{10/3}$	$a = 15.934, b = -14.556,$ $c = 3.6463$	0.60	2.7	4

TABLE II.   Analytic approximations to $\langle p^3 \rangle$: $a_0 = 32/(9\pi) = 1.1318$, $b_0 = 0.6313$, $c_0 = 1.720$.

Function	Parameters	δ_1	δ_2	N^*
$a_0 N^3 \ln N$	—	23.	100.	1
$a N^3 \ln N$	$a = 1.37$	15.	100.	1
$a N^\alpha \ln N$	$a = 2.185, \alpha = 2.874$	12.	100.	1
$a N^\alpha$	$a = 2.0234, \alpha = 3.2404$	2.8	19.	1
$a_0 N^3 \ln N + b_0 N^3$	—	10.	63.	1
$a_0 N^3 \ln N + b N^3$	$b = 0.97$	6.5	43.	1
$a_0 N^3 \ln N + b N^\beta$	$b = 1.684, \beta = 2.797$	0.77	2.1	10
$a N^3 \ln N + b N^3$	$a = 0.919, b = 1.589$	1.5	6.4	1
$a N^3 \ln N + b N^\beta$	$a = 1.174, b = 1.721, \beta = 2.733$	0.59	2.9	4
$a N^\alpha \ln N + b N^\beta$	$a = 0.45099, \alpha = 2.9139, b = 1.7007,$ $\beta = 3.2140$	0.44	2.0	4
$a_0 N^3 \ln N + b_0 N^3 + c_0 N^{7/3}$	—	4.2	38.	1
$a_0 N^3 \ln N + b_0 N^3 + c N^{7/3}$	$c = 1.26$	2.1	11.	1
$a_0 N^3 \ln N + b_0 N^3 + c N^{8/3}$	$c = 0.908$	2.3	9.3	1
$a_0 N^3 \ln N + b_0 N^3 + c N^\gamma$	$c = 1.12, \gamma = 2.51$	0.98	4.5	4
$a_0 N^3 \ln N + b N^3 + c N^{7/3}$	$b = 0.7220, c = 1.084$	1.5	6.4	1
$a_0 N^3 \ln N + b N^3 + c N^{8/3}$	$b = 0.415, c = 1.31$	0.62	3.1	4
$a N^3 \ln N + b N^3 + c N^{7/3}$	$a = 1.02, b = 1.17, c = 0.557$	0.74	3.3	4
$a_0 N^3 \ln N + b N^3 + c N^\gamma$	$b = 0.3714, c = 1.348, \gamma = 2.688$	0.61	2.9	4
$a_0 N^3 \ln N + b N^\beta + c N^\gamma$	$b = 0.0002478, \beta = 4.353, c = 1.714,$ $\gamma = 2.776$	0.50	2.5	4

TABLE III. Analytic approximations to $\langle p^2 \rangle$: $a_0 = 1.53749$, $b_0 = 1$, $c_0 = 0.53978$.

Function	Parameters	δ_1	δ_2	N^*
$a_0 N^{7/3}$	—	21.	54.	1
$a N^{7/3}$	$a = 1.275$	5.3	27.	1
$a N^\alpha$	$a = 1.054, \alpha = 2.388$	0.80	5.4	1
$a_0 N^{7/3} + b_0 N^2$	—	8.6	46.	1
$a_0 N^{7/3} + b N^2$	$b = -0.73$	3.6	19.	1
$a_0 N^{7/3} + b N^\beta$	$b = 0.536, \beta = 2.12$	0.91	5.3	2
$a N^{7/3} + b N^2$	$a = 1.4276, b = -0.45301$	1.2	6.0	2
$a N^{7/3} + b N^\beta$	$a = 2.4537, b = -1.4228, \beta = 2.2784$	0.70	4.6	2
$a_0 N^{7/3} + b_0 N^2 + c_0 N^{5/3}$	—	1.1	7.7	1
$a_0 N^{7/3} + b_0 N^2 + c N^{5/3}$	$c = 0.533$	1.1	7.0	1
$a_0 N^{7/3} + b N^2 + c N^{5/3}$	$b = -0.969, c = 0.484$	0.98	5.5	2
$a_0 N^{7/3} + b_0 N^2 + c N^\gamma$	$c = 0.5064, \gamma = 1.711$	0.93	5.5	2
$a_0 N^{7/3} + b N^2 + c N^\gamma$	$b = -1.817, c = 1.308, \gamma = 1.922$	0.77	5.0	2
$a_0 N^{7/3} + b_0 N^2 + c_0 N^{5/3} + d N^{4/3}$	$d = -0.0248$	1.0	5.7	2
$a_0 N^{7/3} + b_0 N^2 + c N^{5/3} + d N^{4/3}$	$c = 0.6478, d = -0.1544$	0.84	5.4	2
$a_0 N^{7/3} + b N^2 + c N^{5/3} + d N^{4/3}$	$b = -1.105, c = 1.041, d = -0.457$	0.67	4.2	2
$a N^{7/3} + b N^2 + c N^{5/3} + d N^{4/3}$	$a = 1.640, b = -1.782, c = 2.351,$ $d = -1.201$	0.50	2.6	2

$\delta_1 = 0.44\%$ also has the lowest $\delta_2 = 2.0\%$, but not the right asymptotic behavior. We favor the last function in the table: it gives almost as good a fit and has the right asymptotic behavior.

Table III lists our approximations to $\langle p^2 \rangle$. Eq. (3) is nearly quantitative with $\delta_1 = 1.1\%$ and $\delta_2 = 7.7\%$. Table III contains nine functions with $\delta_1 < 1\%$. The last

TABLE IV. Analytic approximations to $\langle p \rangle$: $a_0 = 0.693747$, $b_0 = 0.187$.

Function	Parameters	δ_1	δ_2	N^*
$a_0 N^{5/3}$	—	4.4	21.	2
$a N^{5/3}$	$a = 0.715$	3.2	19.	2
$a N^\alpha$	$a = 0.795, \alpha = 1.6373$	1.9	12.	2
$a_0 N^{5/3} + b_0 N$	—	1.4	7.9	2
$a_0 N^{5/3} + b N$	$b = 0.183$	1.4	8.2	2
$a N^{5/3} + b N$	$a = 0.695, b = 0.177$	1.4	8.5	2
$a_0 N^{5/3} + b N^\beta$	$b = 0.176, \beta = 1.03$	1.4	8.5	2
$a N^\alpha + b N^\beta$	$a = 0.626, \alpha = 1.6833, b = 0.241, \beta = 1.2032$	1.4	8.3	2
$a_0 N^{5/3} + b N + c N^{4/3}$	$b = 0.17, c = 0.0073$	1.4	8.5	2
$a N^{5/3} + b N + c N^{4/3}$	$a = 0.695, b = 0.173, c = 0.00352$	1.4	8.5	2
$a_0 N^{5/3} + b_0 N + c N^{1/3}$	$c = -0.013$	1.4	8.5	2
$a_0 N^{5/3} + b N + c N^{1/3}$	$b = 0.195, c = -0.0229$	1.4	8.4	2
$a_0 N^{5/3} + b_0 N + c n_m^2$	$c = -0.016, \gamma = 2.0$	1.4	8.5	2
$a_0 N^{5/3} + b N + c n_m^2$	$b = 0.296, c = -0.1124, \gamma = 2.21$	1.2	4.3	5
$a_0 N^{5/3} + b N^\beta + c n_m^2$	$b = 0.432, \beta = 0.850, c = -0.266, \gamma = 1.46$	1.2	4.3	5

function in the table has both the lowest $\delta_1 = 0.50\%$ and $\delta_2 = 2.6\%$, but not the right asymptotic behavior. We prefer the penultimate function because it gives a similar quality fit and has the right asymptotic behavior.

Table IV lists our approximations to $\langle p \rangle$. Eq. (4) is nearly quantitative with $\delta_1 = 1.4\%$ and $\delta_2 = 7.9\%$. Table IV shows that no smooth function of N alone is able to produce a better δ_1. This is so because the residual discrepancies of eq. (4) show a periodic pattern. Therefore, we tried to introduce an element of periodicity by allowing the last three functions to include a term in n_m, which is defined to be the principal quantum number of the valence shell. The special case of Pd ($N = 46$) has completely filled K, L, M, and N shells and had to be assigned $n_m = 5$ for the sake of smoothness. Similarly, $n_m = 6$ was assigned to Pt ($N = 78$). We tried very many functions containing n_m, and found the last two functions in Table IV which have a slightly improved δ_1, a substantially reduced δ_2, and the right asymptotic behavior. The penultimate function is preferable because it has one less parameter than the last function.

Fitting $\langle p^{-1} \rangle$ is more difficult. Eq. (5) is not a good starting point ($\delta_1 = 117\%$), because the HF $\langle p^{-1} \rangle$ values are strongly periodic as Figure 1 shows. Thus, it is necessary to use functions containing variables other than N, such as n_m defined above. Guided by hydrogenic formulas [14,15] for $\langle p^{-2} \rangle$, we also used as variables N_s and N_{sp}, the numbers of s and p electrons, respectively, in the valence shell, and an effective nuclear charge

$$Z_{eff} = N - N_{core} \qquad (6)$$

in which N_{core} is the number of electrons in the largest neutral rare gas atom with atomic number less than N. Table V shows a small selection of the functions we tried. It contains four functions with $\delta_1 < 2\%$. Perhaps the last function should be preferred, because it includes a TF-like $N^{1/3}$ term.
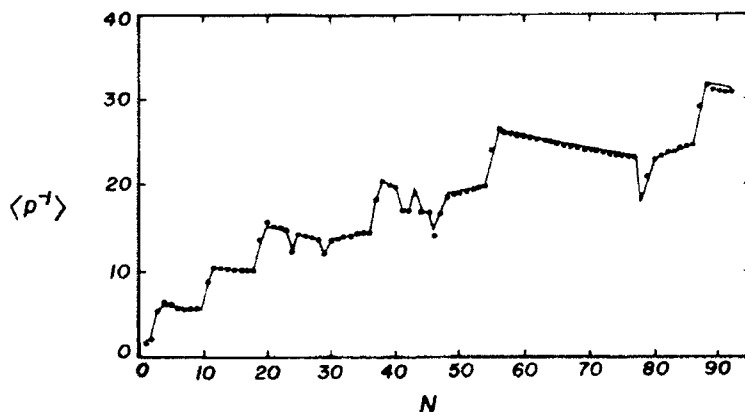
Figure 1. $\langle p^{-1} \rangle$ as a function of electron number, N, for the neutral atoms from hydrogen through uranium. The solid circles are Hartree-Fock values, and the solid line corresponds to the penultimate function in Table V.

TABLE VI.   Analytic approximations to p^{-2}.

Function (parameters)	δ_1	δ_2	N^*
$an_m^{3/2} + bN_{1s} + c/Z_{\text{eff}}$ ($a = 1.57, b = 0.661, c = -0.489$)	7.1	25.	78
$an_m^{3/2} + bN_{1s} + c/Z_{\text{eff}}$ ($a = 1.63, b = 0.540, c = 0.0518$)	7.3	26	46
$an_m^{3/2} + bn_m \cdot N_{1s}^2 + c/Z_{\text{eff}}$ ($a = 1.306, b = 0.6085, \beta = 0.9007, c = -0.07669$)	3.4	8.2	1
$an_m^{3/2} + bn_m^\beta \cdot N_{1s} + c/Z_{\text{eff}}$ ($a = 1.346, b = 0.5836, \beta = 0.9334, c = -0.08104$)	3.3	9.8	2
$an_m^{3/2} + bn_m^\beta \cdot N_{1s} + c/Z_{\text{eff}}$ ($a = 1.294, b = 0.5191, \beta = 0.9586, c = -0.01532$)	4.4	10	19
$an_m^{3/2} + bn_m \cdot N_{1s} + cN_{1p} + d/Z_{\text{eff}}$ ($a = 1.374, b = 0.5075, c = 0.1164, d = -0.1079$)	2.9	9.8	4
$an_m^{3/2} + n_m(bN_{1s} + cN_{1p}) + d/Z_{\text{eff}}$ ($a = 1.384, b = 0.5054, c = 0.05692, d = -0.1271$)	2.5	10	4
$an_m^\gamma + n_m(bN_{1s}^\beta + cN_{1p}) + d/Z_{\text{eff}}^\delta$ ($a = 1.96, \alpha = 1.33, b = 0.393, \beta = 1.25, c = 0.0455, \gamma = 1.01, d = -0.574, \delta = 0.566$)	1.7	5.9	4
$an_m^{4/3} + n_m(bN_{1s}^{5/4} + cN_{1p}) + d/Z_{\text{eff}}^{1/2}$ ($a = 1.923, b = 0.3988, c = 0.03659, d = -0.6010$)	1.9	6.7	4
$an_m^{4/3} + n_m(bN_{1s}^{5/4} + cN_{1p}) + d/Z_{\text{eff}}^{3/5}$ ($a = 1.955, b = 0.3878, c = 0.05002, d = -0.5369$)	1.8	6.4	1
$eN^{4/3} + an_m^{4/3} + n_m(bN_{1s}^{5/4} + cN_{1p}) + d/Z_{\text{eff}}^{3/5}$ ($a = 1.968, b = 0.3911, c = 0.04799, d = -0.5021, e = -0.07253$)	1.7	6.0	4

Fitting $\langle p^{-2} \rangle$ is even more difficult. The asymptotic [14,15] form $\langle p^{-2} \rangle$ = constant is no help at all. Figure 2 shows the marked periodic variation of the HF $\langle p^{-2} \rangle$ moments. We used the hydrogenic formula for $\langle p^{-2} \rangle$ as a guide to generate more
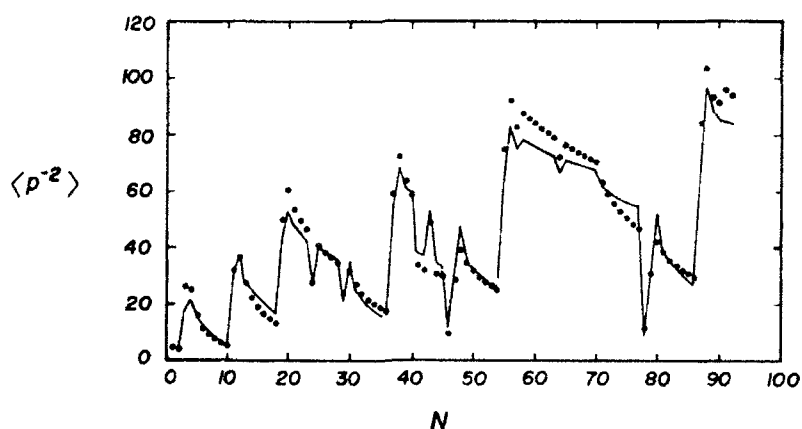
Figure 2. $\langle p^{-2} \rangle$ as a function of electron number, N, for the neutral atoms from hydrogen through uranium. The solid circles are Hartree-Fock values, and the solid line corresponds to the second function in Table VI.

TABLE VI.   Analytic approximations to $\langle p^{-1} \rangle$.

Function (parameters)	n_i		N^*
$an_m^2 + n_m(bN_s^2 + cN_p^2) + dZ_{eff}\ (a = 15946,\ a = 0.10695,\ b = 3.8345,$			
$d = 1.0767,\ c = 3.0153,\ \gamma = 0.18679,\ d = 157.85,\ \delta = 0.050413)$	13	32	78
$an_m^2 + n_m(bN_s^2 + cN_p^2 + dN_d^2) + eZ_{eff}\ (a = 14.84,\ b = 4.069,$			
$c = -2.356,\ d = -0.9007,\ e = 14.71,\ \alpha = 0.7378,\ \beta = 0.8869,$			
$\gamma = 0.2823,\ \delta = 0.2376,\ \epsilon = 0.2959)$	12	32	3
$an_m^2 + n_m^2(bN_s^2 + cN_p^2 + dN_d^2) + eZ_{eff}\ (a = 19.28,\ b = 3.090,$			
$c = -1.926,\ d = -0.6665,\ e = 17.70,\ \alpha = 0.6125,\ \beta = 1.146,$			
$\beta = 0.9527,\ \gamma = 0.2803,\ \delta = 0.2089,\ \epsilon = 0.2663)$	12	30	78
$an_m^2 + n_m(bN_s^2 + cN_p^2) + dN_d^2 + eZ_{eff}\ (a = 28.75,\ b = 4.041,$			
$c = -2.633,\ d = -3.276,\ e = -28.16,\ \alpha = 0.4724,\ \beta = 0.9493,$			
$\gamma = 0.2387,\ \delta = 0.1864,\ \epsilon = 0.2013)$	12	29	80
$an_m^2 + n_m(bN_s^2 + cN_p^2) + dN_d^2 + eZ_{eff} \cdot n_m^2\ (a = 286.86,\ b = 3.8910,$			
$c = -2.3068,\ d = -2.8910,\ e = -286.50,\ \alpha = 0.49302,\ \beta = 0.97315,$			
$\gamma = 0.27619,\ \delta = 0.13079,\ \epsilon = 0.017043,\ \phi = 0.45361)$	11	28	78

than 30 different functions containing the variables used for $\langle p^{-1} \rangle$, and the variable N_{td}, which is the number of electrons in the outermost d-subshell. Table VI lists the best of our functions but, unfortunately, none of them is a quantitative approximation.

Concluding Remarks

The root mean square percent errors of our best functions for $\langle p^k \rangle$ with $k > 1$ are less than 0.6%. The best functions for $\langle p \rangle$ and $\langle p^{-1} \rangle$ have a rms percent error of less than 2%. These rms errors are less than the errors in the HF moments due to neglect of electron correlation and relativistic effects. Thus, we think our best phenomenological approximations to $\langle p^k \rangle$ ($k = -1, 1, 2, 3, 4$) have real value. More thought needs to be devoted to finding a functional form for $\langle p^{-2} \rangle$.

Acknowledgments

Bibliography

[1] P. Gombas, Die statistische theorie des atoms und ihre anwendungen (Springer, Vienna, 1948).
[2] E. H. Lieb, Rev. Mod. Phys. 46, 353 (1976).
[3] J. C. Slater, Quantum Theory of Atomic Structure (McGraw-Hill, New York, 1960).
[4] C. Froese-Fischer, The Hartree-Fock Method for Atoms (Wiley, New York, 1977).
[5] S. Fraga, J. Karwowski, and K. M. S. Saxena, Handbook of Atomic Data (Elsevier, New York, 1976).

[6] R. Benesch and V. H. Smith, Jr., in *Wave Mechanics—The First Fifty Years*, W. C. Price, S. S. Chissick, and T. Ravensdale, Eds. (Butterworths, London, 1973), pp. 357–377.

[7] A. J. Thakkar, J. Chem. Phys. **86**, 5060 (1987).

[8] B. G. Williams, Ed., *Compton Scattering: The Investigation of Electron Momentum Distributions* (McGraw-Hill, New York, 1977).

[9] R. K. Pathak, B. S. Sharma, and A. J. Thakkar, J. Chem. Phys. **85**, 958 (1986), and earlier references cited therein.

[10] A. J. Thakkar and W. A. Pedersen, Int. J. Quantum Chem. S24, 327 (1990).

[11] R. G. Parr and W. Yang, *Density Functional Theory of Atoms and Molecules* (Oxford, New York, 1989).

[12] J. P. Glusker, B. K. Patterson, and M. Rossi, Eds., *Patterson and Pattersons* (Oxford, New York, 1986).

[13] H. A. Bethe and E. E. Salpeter, *Quantum Mechanics of One- and Two-Electron Atoms* (Springer-Verlag, Berlin, 1957).

[14] I. K. Dmitrieva and G. I. Plindov, Z. Phys. A305, 103 (1982).

[15] I. K. Dmitrieva and G. I. Plindov, J. Phys. (Paris) **44**, 333 (1983).

[16] J. Schwinger, Phys. Rev. A22, 1827 (1980).

[17] K. Buchwald and B. G. Englert, Phys. Rev. A40, 2738 (1989).

[18] S. R. Gadre, S. P. Gejji, and S. J. Chakravorty, Atom. Data Nucl. Data **28**, 477 (1983).

[19] T. Koga and Y. Yamamoto, Phys. Rev. A42, 6336 (1990).

[20] W. M. Westgate, R. P. Sagar, A. Farazdel, V. H. Smith, Jr., A. M. Simas, and A. J. Thakkar, Atom. Data Nucl. Data **48**, 213 (1991).

[21] M. S. Scott, Philos. Mag. **43**, 859 (1952).

[22] M. J. D. Powell, Comput. J. **7**, 155 (1964).

[23] J. Tellinghuisen, J. Molec. Spectrosc. **137**, 248 (1989).

Quantum Tunneling Times: A New Solution Compared to 12 Other Methods

MARK J. HAGMANN

Department of Electrical and Computer Engineering Florida International University Miami, Florida 33199

Abstract

A variety of different theoretical procedures have been used to determine tunneling times. These include (1) phase time; (2) the Stevens procedure; (3) Larmor times; (4) a complex "time"; (5) dwell time; (6) the Büttiker–Landauer time; (7) Feynman path-integrals; (8) scattering theory; (9) a stochastic formulation; (10) oscillatory perturbation of the barrier; (11) kinetic time; and (12) the semiclassical solution. Interest in tunneling times is not purely pedagogical, since correction for changes in image potential during transit is required in determining the conductance of several new high-speed semiconductor devices. A new procedure to evaluate transit time is presented, which assumes that energy fluctuations keep a tunneling particle above the barrier while transiting the classically forbidden region. For large rectangular barriers, the most probable fluctuations minimize the product of their magnitude and the transit time. This results in the semiclassical solution. For the case of very small barriers, there is a separate solution in which the transit time is indeterminate but bounded. The new solution is compared with 12 different results by others. Numerical values, limiting forms, and interpretations are presented for these various tunneling times. Difficulties in using time-domain numerical solutions to determine the transit time for a wave packet will also be described. © 1992 John Wiley & Sons, Inc.

Introduction

Quantum mechanics provides useful results regarding tunneling, such as the transmission coefficient and the transition probability per unit time, but does not describe the motion of a particle within the classically forbidden region. In particular, the duration of the transit has been the focus of much interest and controversy.

Some texts contain confusing comments on tunneling. For example, it is said that tunneling "is not governed by the conventional transit time concept" [1], or that the velocity of a tunneling particle is infinite [2]. Cohen [3] appears to have been the first to state that the transit time for tunneling is finite, and to support this claim by analysis. A variety of different theoretical procedures have been used to determine the transit time, with differing results. The main "contenders" have been listed [4] as follows: (1) phase time; (2) the Stevens procedure; (3) Larmor times; (4) a complex "time"; (5) dwell time; and (6) the Büttiker–Landauer time. Several procedures not considered [4] may be added, such as: (7) Feynman path-integrals [5]; (8) scattering theory [6]; (9) a stochastic formulation [7]; (10) os-

cillatory perturbation of the barrier [8]; (11) kinetic time [9]; and (12) the semi-classical solution [10,11].

Values of transit time have been calculated using numerical solutions for tunneling by a wave packet in the time domain [12]. Some consider this process to be "without basis," because it is not possible to identify a particular part of the transmitted packet (e.g., the peak) with its incident counterpart [13]. This uncertainty is decreased by reducing the breadth of the wave packet, but then the spread of energy is increased, which causes other errors.

Interest in tunneling times is not purely pedagogical. In devices, the charges on both sides of a barrier move in response to a particle transiting the classically forbidden region. This movement of charge, which alters the potential, is dependent upon the transit time [14]. Failure to correct for this phenomenon causes calculated values of conductance to differ from measured values by one to two orders of magnitude [15]. Recent advances in high-speed devices based on tunneling in semiconductors [16] requires a greater understanding of the tunneling process for design purposes.

Analysis

We assume tunneling occurs when the energy of a particle fluctuates sufficiently to be above the barrier while crossing the classically forbidden region. Energy is not conserved during tunneling, but the magnitude and duration of the violation are limited by the uncertainty principle.

The energy-time uncertainty relation differs from the uncertainty relation for momentum and position regarding both derivation and interpretation. It is known, however, to relate the uncertainty of energy to the mean lifetime of unstable particles [17]. Yukawa's successful prediction of the mass of the pi-meson is an example [18]. We assume the most probable value for the product of the magnitude ΔE and duration Δt of an energy fluctuation is $h/2$, where $h = 1.05443 \times 10^{-34}$ Js/radian, is Planck's constant.

Consider a particle with energy E incident upon a rectangular barrier with constant potential V, and length d, as shown in Figure 1. We assume that an energy fluctuation, ΔE, causes the particle to pass over the barrier with kinetic energy $mv^2/$
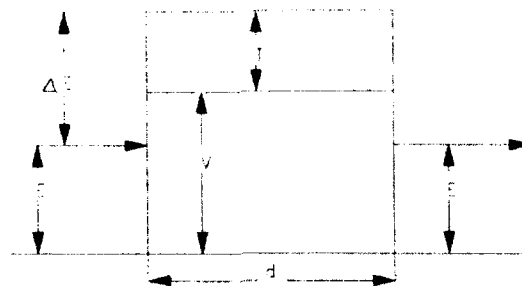
Figure 1.   Tunneling of a particle through a rectangular potential barrier.

2, where m is the mass of the particle and v is the velocity within the classically forbidden region. Thus, the magnitude of the energy fluctuation is

$$\Delta E = \frac{mv^2}{2} + (V - E) \tag{1}$$

If ΔE is not constant during an energy fluctuation, we define the effective energy-time product by

$$(\Delta E \Delta t)_{\text{eff}} = \int_0^{\Delta t} \Delta E(t)\, dt \tag{2}$$

which is equivalent to

$$(\Delta E \Delta t)_{\text{eff}} = \int_0^d \frac{\Delta E(x)\, dx}{v(x)} \tag{3}$$

From eqs. (1) and (3):

$$(\Delta E \Delta t)_{\text{eff}} = \int_0^d \left[\frac{mv(x)}{2} + \frac{(V(x) - E)}{v(x)} \right] dx \tag{4}$$

Large Barrier Case

If $(\Delta E \Delta t)_{\text{eff}} > h/2$, the most probable value for the magnitude of an energy fluctuation permitting tunneling is found by minimizing the integral in (4). Thus, v and v_m, the value which minimizes the integrand and is given by

$$v_m(x) = \left[\frac{2(V(x) - E)}{m} \right]^{1/2} \tag{5}$$

Setting v equal to v_m in (4), gives the minimum effective energy-time product as

$$(\Delta E \Delta t)_{\text{meff}} = \int_0^d [2m(V(x) - E)]^{1/2}\, dx \tag{6}$$

From eq. (5), the transit time is given by

$$t_r = \int_0^d \left[\frac{m}{2(V(x) - E)} \right]^{1/2} dx \tag{7}$$

Eq. (7) is equivalent to the classical expression for nontunneling transit time ($E > V$), except the sign of the argument of the square root is reversed. Thus, eq. (7) is referred to as the "semiclassical" solution, but is considered to be an imaginary quantity [11]. For a rectangular barrier, eq. (7) reduces to

$$t_r = d \left[\frac{m}{2(V - E)} \right]^{1/2}. \tag{8}$$
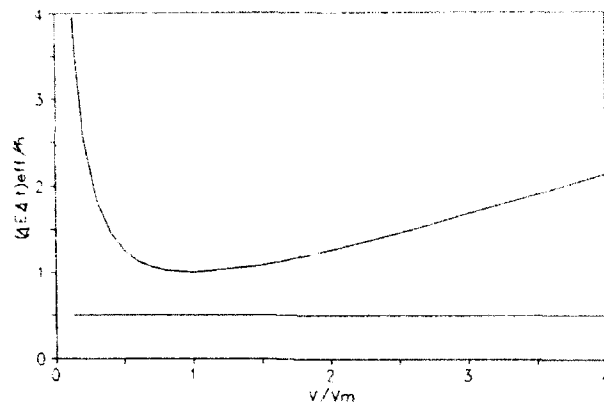
Figure 2.   Energy-time product vs. velocity for the large barrier case.

For a rectangular barrier, the integral in (6) may be evaluated to show the criterion $(\Delta E \Delta t)_{meff} > \hbar/2$ is equivalent to

$$d[2m(V - E)]^{1/2} > \frac{\hbar}{2} \tag{9}$$

Since (9) sets a lower limit on the height-length product of the barrier, we call the case for which (7)–(9) are appropriate the "large barrier" case. Figure 2 shows how $(\Delta E \Delta t)_{eff}$ depends on velocity for a "large" rectangular barrier when the velocity is constant, and the duration of the fluctuation equals the transit time. The barrier has $d[2m(V - E)]^{1/2} = \hbar$, corresponding to $d = 6.172$ Å for 7.9 eV electrons and $V = 8.0$ eV. The horizontal line represents a value of $\hbar/2$. The energy-time product has a broad minimum near $v = v_m$.
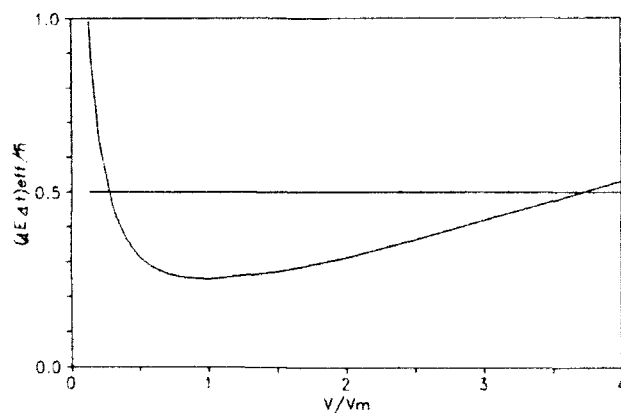
Figure 3.   Energy-time product vs. velocity for the small barrier case.

Small Barrier Case

There is also a small barrier case for which $(\Delta E \Delta t)_{\text{eff}} < \hbar/2$. Figure 3 shows how $(\Delta E \Delta t)_{\text{eff}}$ depends on velocity for a "small" rectangular barrier when the velocity is constant, and the duration of the fluctuation equals the transit time. The barrier has $d[2m(V - E)]^{1/2} = \hbar/4$, corresponding to $d = 1.543$ Å for 7.9 eV electrons and $V = 8.0$ eV. The horizontal line represents a value of $\hbar/2$. Figure 3 shows that the most probable value for energy fluctuations, $\hbar/2$, occurs for two different velocities, $v/v_{m} = 0.268$ and 3.752. Minimizing the energy-time product is not required for this case, so

$$\int_0^d \left[\frac{mv(x)}{2} + \frac{(V(x) - E)}{v(x)} \right] dx \geq \frac{\hbar}{2} \tag{10}$$

where equality pertains when the duration of the fluctuation equals the transit time. It is convenient to define

$$\alpha(x) = \frac{v(x)}{v_m(x)} \tag{11}$$

From (10) and (11)

$$\int_0^d [2m(V(x) - E)]^{1/2} \left[\frac{\alpha^2(x) + 1}{2\alpha(x)} \right] dx \geq \frac{\hbar}{2} \tag{12}$$

From (5) and (11), the transit time is given by

$$t_t = \int_0^d \left[\frac{m}{2(V(x) - E)} \right]^{1/2} \frac{dx}{\alpha(x)} \tag{13}$$

For a rectangular barrier, (12) and (13) simplify to

$$[2m(V - E)]^{1/2} \int_0^d \left[\frac{\alpha^2(x) + 1}{2\alpha(x)} \right] dx \leq \frac{\hbar}{2} \tag{14}$$

$$t_t = \left[\frac{m}{2(V - E)} \right]^{1/2} \int_0^d \frac{dx}{\alpha(x)} \tag{15}$$

For a rectangular barrier, the criterion for the small barrier case simplifies to the following inequality:

$$d[2m(V - E)]^{1/2} < \frac{\hbar}{2} \tag{16}$$

Numerical solutions of (14)–(16), assuming a piecewise-constant velocity, show that the transit time is indeterminate but bounded. Limits for the transit time occur when the velocity is constant, and the duration of a fluctuation equals the transit time for equality in (14). Thus, (14) reduces to a quadratic that is solved for α, and used with (5) and (11) to obtain the following interval for the velocity.

$$\frac{h}{2dm}\left[1 - \left[1 - \frac{8m(V - E)d^2}{h^2}\right]^{1/2}\right] \le v$$

$$\le \frac{h}{2dm}\left[1 + \left[1 - \frac{8m(V - E)d^2}{h^2}\right]^{1/2}\right] \quad (17)$$

From (15) and (17), the interval for the transit time is

$$\frac{2md^2}{h\left[1 + \left[1 - \frac{8m(V - E)d^2}{h^2}\right]^{1/2}\right]} \le t_t \le \frac{2md^2}{h\left[1 - \left[1 - \frac{8m(V - E)d^2}{h^2}\right]^{1/2}\right]} \quad (18)$$

The two limits in (18) have the semiclassical time (8) as their geometric mean, and an arithmetic mean of $h/4(V - E)$, which is the value of transit time at which the small and large barrier cases meet. For extremely small barriers (18) may be simplified to obtain

$$\frac{md^2}{h} \le t_t \le \frac{h}{2(V - E)} \quad (19)$$

Figure 4 shows the dependence of transit time on the length of a rectangular barrier calculated with (8) and (18) for 7.9 eV electrons and $V = 8.0$ eV. The large barrier case, where $d > 3.086$ Å, agrees with the semiclassical time. At shorter lengths, requiring the small barrier case, the two limits for the interval of transit times are plotted.

Figure 5 shows the dependence of transit time on energy, calculated with (8) and (18), for electrons with $V = 1.0$ eV and $d = 1.7$ Å. The large barrier case, where $E < 0.6704$ eV, agrees with the semiclassical time. For larger values of energy, requiring the small barrier case, the two limits for the interval of transit time are plotted.
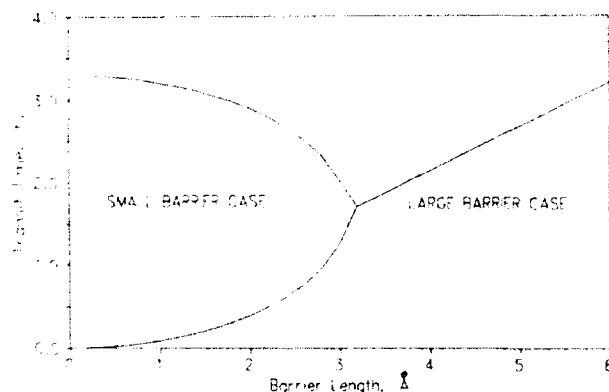
Figure 4. Transit time vs. barrier length for fixed barrier height and particle energy.
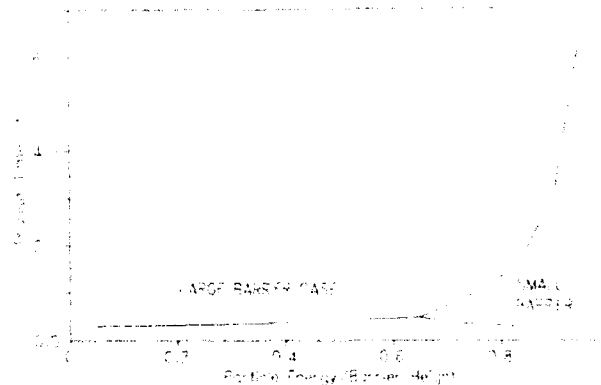
Figure 5. Transit time vs. particle energy for a barrier with fixed length and height.

Comparison With the Results of Others

Twelve different procedures used to determine tunneling times are listed in the Introduction. Of these. the Stevens procedure [6]. and one method using an oscillatory perturbation of the barrier [10]. both result in the semiclassical solution. The approach using Feynman path-integrals [5] results in the Büttiker–Landauer time, so it need not be considered separately. The scattering theory approach [6]. reduces to the phase time for a rectangular barrier. The two components of the complex time correspond to the two Larmor times, and these equal the dwell time for a rectangular barrier [4]. Thus, for a rectangular barrier. only six values of time need to be considered: (1) phase time [19]; (2) dwell time [19]; (3) Büttiker–Landauer time [20]; (4) stochastic time [7]; (5) kinetic time [9]; and (6) semiclassical time [10].

Table I gives expressions for these six tunneling times for the cases of: (1) a very small barrier $(d[2m(V - E)]^{1/2} \ll h$ and $Vd \ll h[2E/m]^{1/2})$; (2) an opaque barrier $(d[2m(V - E)]^{1/2} \gg h)$; and (3) a delta-function barrier. The latter case is defined as the limit for infinite potential and zero barrier length. with $Vd = hhc$. where h is a constant and c is the velocity of light in a vacuum [4]. Particles sufficiently close to the top of the barrier satisfy (16). regardless of the barrier height and length. but the small barrier expressions in Table I are only appropriate if both of the requirements given above are satisfied. Each of the six procedures will be considered separately.

Phase Time

It is seen in Table I that only the phase time is nonzero for a delta-function barrier. This result. considered to be nonphysical, has been explained as an effect of self-interference between the incident and reflected waves in front of the barrier [4]. It may also be seen in Table I that only the phase time and dwell time are bounded as the length of the barrier becomes large. which is also nonphysical [13].

TABLE 1   Expressions for tunneling times of different formulations for several limiting cases with rectangular barriers

	Small barrier	Large barrier	δ-function barrier
Phase time	$\dfrac{d\left[\dfrac{m}{2E}\right]^{1/2}\left[\dfrac{V+2E}{2E}\right]}{1+\dfrac{mV^2d^2}{2\hbar^2E}}$	$\dfrac{\hbar}{[E(V-E)]^{1/2}}$	$\dfrac{\hbar h\left[\dfrac{mc^2}{2E}\right]^{1/2}}{1+\dfrac{\hbar^2mc^2}{2E}}$
Dwell time	$\dfrac{d\left[\dfrac{m}{2E}\right]^{1/2}}{1+\dfrac{mV^2d^2}{2\hbar^2E}}$	$\dfrac{\hbar}{V}\left[\dfrac{E}{V-E}\right]^{1/2}$	0
Büttiker–Landauer	$\dfrac{d\left[\dfrac{m}{2E}\right]^{1/2}}{\left[1+\dfrac{mV^2d^2}{2\hbar^2E}\right]^{1/2}}$	$d\left[\dfrac{m}{2(V-E)}\right]^{1/2}$	0
Stochastic time	$\dfrac{d\left[\dfrac{m}{2E}\right]^{1/2}}{\left[1+\dfrac{mV^2d^2}{2\hbar^2E}\right]^{1/2}}$	$d\left[\dfrac{m}{2(V-E)}\right]^{1/2}$	0
Kinetic time	$d\left[\dfrac{m}{2E}\right]^{1/2}$	$\dfrac{\hbar V\exp(2d/\hbar)[2m(V-E)]^{1/2}}{16E^{1/2}(V-E)^{1/2}}$	0
Semiclassical time	$d\left[\dfrac{m}{2(V-E)}\right]^{1/2}$	$d\left[\dfrac{m}{2(V-E)}\right]^{1/2}$	0
Present solution	$\dfrac{md^2}{\hbar}<t_t<\dfrac{\hbar}{2(V-E)}$	$d\left[\dfrac{m}{2(V-E)}\right]^{1/2}$	0

Thus, phase time is not considered to represent the transit time. Numerical solutions for tunneling by a wave packet [12] give (apparent) values of transit time that approximate the phase time, but are not simply related to the transit time [4,19].

Dwell Time

The dwell time is claimed to be a measure of the time a particle spends within the classically forbidden region, averaged over all particles that are ultimately either transmitted through the barrier, or reflected by the barrier [19]. Thus, dwell time is only equal to the transit time for very small barriers, or at resonances, when the transmission coefficient is near unity [4]. The expression for opaque barriers in Table 1 shows that the dwell time is bounded as the length of the barrier becomes large, which is appropriate because it is then a measure of the time spent in the barrier region by reflected particles.

Büttiker-Landauer Time

A particle with nonzero spin in a magnetic field has a higher probability of tunneling if the spin is aligned parallel, rather than antiparallel, to the magnetic field. This preferential transmission causes an effective rotation, which exceeds that due to Larmor precession [20]. This effective rotation has been used experimentally to produce beams of polarized electrons and neutrons. The Büttiker-Landauer time [20] is a modification of the Larmor times in which the effective rotation just described is combined with the (smaller) Larmor precession to obtain the total rotation, which is used as a clock to measure the time for a particle to traverse the barrier. Several objections have been raised regarding the Büttiker-Landauer time [19,21], and a response was made to some of them [13].

Stochastic Time

A stochastic formulation of quantum mechanics has been used to calculate the time for a tunneling particle to traverse a rectangular barrier [7]. This formulation is essentially a classical interpretation in which quantum phenomena are treated as random fluctuations similar to Brownian motion [22]. Particles are assumed to be subject to a stochastic force, generated by quantum fluctuations resulting from the action of a stochastic invariant thermostat, as well as to external forces. It may be seen in Table I that the limiting forms of the stochastic time for both small and large barriers are equal those for the Büttiker-Landauer time. Our numerical studies have shown that the stochastic time is generally close to the Büttiker-Landauer time for other values of the parameters.

Kinetic Time

de Moura and de Albuquerque [9] have described what we term the "kinetic time," which they define as the ratio of the density of particles in the barrier to the total flux within that region. The kinetic time, like dwell time, is averaged over all particles in the barrier region whether they are ultimately transmitted through the barrier or reflected. Thus, the kinetic time could not equal the transit time except for very small barriers, or at resonances, when the transmission coefficient is near unity. The expression in Table I for the kinetic time for opaque barriers should be the time spent in the barrier region by reflected particles, but this expression does not equal that for the dwell time. Furthermore, this expression depends exponentially on the length of the barrier, which has no clear physical basis.

Semiclassical Time

The semiclassical time (7) has been derived by studying the sensitivity of tunneling to: (1) oscillatory perturbation of the barrier [10]; (2) modulation of the incident wave [23]; (3) temperature [24]; (4) damping [25]; and (5) dynamic corrections to the image potential [26]. The semiclassical time is also obtained by the Stevens procedure [6], and by minimizing energy fluctuations [3].

The previous paragraphs suggest that, of the 12 procedures considered, only the Büttiker–Landauer time, stochastic time, or the semiclassical time could possibly represent the transit time for tunneling. Our solution for the large barrier case is the semiclassical time, and it also agrees with the Büttiker–Landauer time and stochastic time for opaque barriers.

For the case of very small barriers, the Büttiker–Landauer and stochastic times correspond to tunneling at the incident velocity, which is quite different from the semiclassical result, and each of these times differs from the new solution. We question the validity of the semiclassical solution for the small barrier case because: (1) an opaque barrier is required for derivations of the semiclassical time [10,23,24]; and (2) the semiclassical time diverges for energies near the top of the barrier, contradicting experiments [27].

Discussion and Conclusions

We believe that indeterminacy of the transit time for the case of small barriers, which is first suggested in this article, is reasonable because of the lower limit for energy fluctuations set by the uncertainty principle. Others have suggested there is a distribution of transit times [5,28,29] but not within this context. Most examples considered by others correspond to the large barrier case. Typical parameters used for Zener tunneling, field-emission of electrons from a metal, and Josephson junction circuits, correspond to $(\Delta E \Delta t)_{...eff}/\hbar$ equal to 20, 200, and 1000, respectively [23].

Figure 6 shows the boundary between the large and small barrier cases, calculated with (9) and (16), for both protons and electrons. This figure shows that the large barrier case is generally appropriate when the length of the barrier exceeds the size of an atom, but the small barrier case may be required for problems on the scale of the nucleus.

We acknowledge that the problem analyzed in this study is idealized in that a single particle with known momentum is incident upon a one-dimensional rectan-
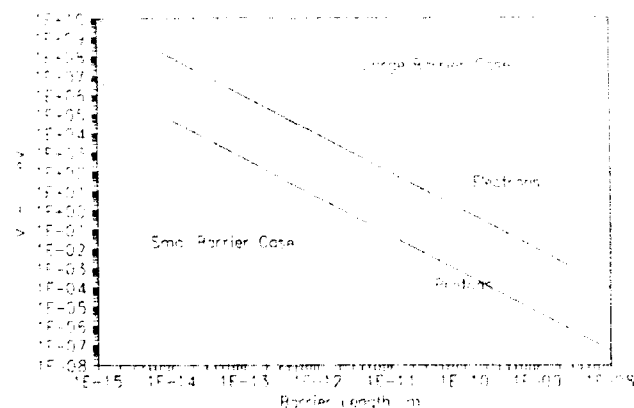
Figure 6.   Boundary between the large and small barrier cases for protons and electrons.

gular barrier. In tunneling phenomena, a particle is injected into the barrier with a variable energy and orientation, and must go from one allowed state to another, so a variety of factors affects the transit time [15,23,30].

Bibliography

[1] S. M. Sze, *Physics of Semiconductor Devices*, 2nd ed. (Wiley, New York, 1981) p. 515.

[2] E. O. Kane, in *Tunneling Phenomena in Solids*, E. Burstein and S. Lundqvist Eds. (Plenum, New York, 1969) pp. 1–11.

[3] B. L. Cohen, Am. J. Phys. **33**, 97 (1965).

[4] E. H. Hauge and J. A. Stovneng, Rev. Mod. Phys. **61**, 917 (1989).

[5] H. A. Fertig, Phys. Rev. Lett. **65**, 2321 (1990).

[6] K. M. S. V. Bandara, D. D. Coon, and H. Zhao, J. Appl. Phys. **66**, 127 (1989).

[7] A. B. Nassar, Phys. Rev. B. **38**, 683 (1988).

[8] K. Mullen, E. Ben-Jacob, Y. Gefen, and Z. Schuss, Phys. Rev. Lett. **62**, 2543 (1989).

[9] M. A. de Moura and D. F. de Albuquerque, Solid State Commun. **74**, 353 (1990).

[10] M. Büttiker and R. Landauer, Phys. Rev. Lett. **49**, 1739 (1982).

[11] E. Pollak and W. H. Miller, Phys. Rev. Lett. **53**, 115 (1984).

[12] Z.-H. Huang, P. H. Cutler, T. E. Feuchtwang, R. H. Good Jr., E. Kazes, H. Q. Nguyen, and S. K. Park, IEEE Trans. Electron Dev. **36**, 2665 (1989).

[13] M. Büttiker and R. Landauer, J. Phys. C**21**, 6207 (1988).

[14] B. N. J. Persson and A. Baratoff, Phys. Rev. B**38**, 9616 (1988).

[15] P. Gueret, E. Marclay, and H. Meier, Appl. Phys. Lett. **53**, 1617 (1988).

[16] F. Capasso, K. Mohammed, and A. Y. Cho, IEEE J. Quantum Electron. **22**, 1853 (1986).

[17] J. Rayski and J. M. Rayski Jr., in *The Uncertainty Principle and Foundations of Quantum Mechanics*, W. C. Price and S. S. Chissick, Eds. (Wiley, New York, 1977) pp. 13–20.

[18] R. B. Leighton, *Principles of Modern Physics* (McGraw-Hill, New York, 1959) pp. 616–618.

[19] S. Collins, D. Lowe, and J. R. Barker, J. Phys. C**20**, 6213 (1987).

[20] M. Büttiker, Phys. Rev. B**27**, 6178 (1983).

[21] J. A. Stovneng and E. H. Hauge, in Proceedings of the International Symposium, College Station, TX, 13–15 March 1989 (Academic Press, New York) pp. 303–310.

[22] E. Nelson, Phys. Rev. **150**, 1079 (1966).

[23] M. Büttiker and R. Landauer, IBM J. Res. Dev. **30**, 451 (1986).

[24] R. Bruinsma and P. Bak, Phys. Rev. Lett. **56**, 420 (1986).

[25] A. Schmid, Ann. Phys. **170**, 333 (1986).

[26] M. Jonson, Solid State Commun. **33**, 743 (1980).

[27] K. W. H. Stevens, J. Phys. C**16**, 3649 (1983).

[28] C. R. Leavens, Solid State Commun. **68**, 13 (1988).

[29] C. R. Leavens, Solid State Commun. **74**, 923 (1990).

[30] K. K. Thornber, T. C. McGill, and C. A. Mead, J. Appl. Phys. **38**, 2384 (1967).

Reliable Hellmann–Feynman Forces for Nuclei-Centered GTO Basis of Standard Size

REINALDO O. VIANNA, ROGÉRIO CUSTÓDIO,* HÉLIO CHACHAM,
and JOSÉ RACHID MOHALLEM

*Departamento de Física, ICEx, Universidade Federal de Minas Gerais,
C. P. 702, 30.161, Belo Horizonte, MG, Brazil*

Abstract

We use the continuous formulation for the matrix Hartree–Fock method, called the generator-coordinate-Hartree–Fock method, to rephrase a theorem of Nakatsuji et al. concerning the improvement of the Hellmann–Feynman forces calculated with nuclei-centered GTO basis functions. We show that we do not need to increase the size of the basis set in order to obtain reliable Hellmann–Feynman forces, but just use a self-consistent set so that, starting with some s-type GTOs, the p-type GTOs are a subset of the derivatives of those s-type GTOs, and so on. We illustrate this feature in calculations on small dyatomic molecules. © 1992 John Wiley & Sons, Inc.

Introduction

The Hellmann–Feynman (HF) forces for nonexact wave functions are almost always associated to floating wave functions [1], a kind of function which is not appropriate to most quantum chemical calculations. However, more than a decade ago, Nakatsuji et al. [2] proved a theorem for the improvement of the HF forces for nuclei-centered GTOs. They showed that starting with a parent standard basis set, the inclusion of all the derivatives of those basis functions related to their centers lead the Pulay corrections [3] to the HF forces to vanish. On the other hand, even if the process is stopped after getting a desired accuracy, this procedure raises the size of the basis sets in a undesirable way, which is why we think that this technique has been receiving little attention [4].

The geometry optimization of molecules in *ab initio* calculations, either with standard SCF procedure or simulated dynamics (SD) techniques [5], needs an accurate evaluation of the forces on nuclei, within the Born–Oppenheimer approximation. The analytical gradient is used for the SCF calculations, though being very expensive (the only SD calculation we know so far used floating Gaussians within the density functional theory [6]). The analytical gradient has two terms. One is the HF force, which is very easy to calculate since it does not involve two electron

terms. The other is the Pulay correction, whose calculation expends a lot of computer time. In order to have an economical way of optimizing geometry in *ab initio* calculations of large systems, which includes simultaneous optimization of energy and geometry by SD [5], we need to use reliable HF forces without the aforementioned drawback concerning Nakatsuji et al.'s method. Also, owing to the current tendency of doing *ab initio* calculations with saturated basis sets [4,7] it seems unreasonable to include all the derivatives or to have two different sets, i.e., a parent set and a derivative set. A solution is presented in this work. We rephrase the theorem of Nakatsuji et al. in the scope of the generator-coordinate-Hartree–Fock (GCHF) method. The continuous formulation drives us to new conclusions about how to choose the basis sets in order to satisfy the HF theorem. We then show that there are self-consistent sets, of almost the same size of the commonly used sets, which lead to good HF forces. We conclude with illustrative applications to the diatomic molecules H_2, LiH, CO, and F_2.

Theory

As in the applications of the GCHF method to closed-shell molecules with $2m$-electrons [7b], we start with the choice of the MO in the form

$$|\psi_a\rangle = \sum_A \sum_\sigma \int d\alpha f_{a,\mathrm{A}\sigma}(\alpha)|\phi_\sigma(\alpha, \vec{r}_1)\rangle, \quad a = 1, \cdots m \qquad (1)$$

In Eq. (1), the first summation, over A, runs over the atomic nuclei, and the second, over σ, runs over the symmetries of the basis functions (s, p, d $\cdots$); $f_{a,\mathrm{A}\sigma}(\alpha)$ are the unknown weight functions (wf) and $\phi_\sigma(\alpha, \vec{r}_1)$ the basis functions (normally GTOs) with σ-symmetry, exponent α, and centered on nucleus A. To save notation we will drop the summation over the nuclei, since it does not affect our conclusions.

Instead of starting with a complete parent basis which contains functions of various symmetries as in Nakatsuji et al. [2], we start with only s-type GTOs, that is, our MO are written as

$$|\psi_a\rangle = \int d\alpha f_a(\alpha)\phi_s(\alpha, \vec{r}_1). \qquad (2)$$

Applying the variational method, the wf will obey the integral equations

$$\int [F(\alpha, \beta) - \varepsilon_a S(\alpha, \beta)] f_a(\beta)\, d\beta = 0 \qquad (3)$$

where ε_a are the orbital energies, $S(\alpha, \beta)$ is the overlap matrix, and the Fock matrix is

$$F(\alpha, \beta) = (\alpha|h|\beta)$$
$$+ \int d\gamma \int d\delta \left[2 \sum_a f_a(\gamma) f_a(\delta) \right] [(\alpha\beta|\gamma f) - 1/2(\alpha\gamma|\beta\delta)]. \qquad (4)$$

in standard notation.

Being Ψ, the Slater determinant formed with functions (2) and R_i, the nuclear coordinates, the force on nuclei i is given by

$$F_i = -\langle \Psi | \partial \hat{H}/\partial R_i | \Psi \rangle - \left[\int d\alpha \, \Delta_s(\alpha) \right] (\partial d_i/\partial R_i) \qquad (5)$$

where d_i is the center of the GTO, and

$$\Delta(\alpha) = \int d\beta \left[2 \sum_a f_{as}(\alpha) f_{as}(\beta) \right] \left\{ 2(\alpha'|h|\beta) \right.$$

$$+ 2 \int d\gamma \int d\gamma \left[2 \sum_a f_{as}(\gamma) f_{as}(\delta) \right] [(\alpha'\beta|\gamma\delta) - 1/2(\alpha'\gamma|\beta\delta)] \bigg\}$$

$$- 2 \int d\beta \left[2 \sum_a \varepsilon_a f_{as}(\alpha) f_{as}(\beta) S(\alpha', \beta) \right]. \qquad (6)$$

In (6), α' stands for $\phi'_s(\alpha, \vec{r}_i) \equiv \partial/\partial R_i \phi_s(\alpha, \vec{r}_i)$.

For GTOs, these derivatives yield p-type functions. So, taking R_i in the Z direction for instance, we have

$$\alpha' : \frac{\partial}{\partial Z} \phi_s(\alpha, \vec{r}_i) = \phi_{p_z}(\alpha, \vec{r}_i) \qquad (7)$$

For each α, $\Delta_s(\alpha)$ is what is called AO error by Nakasuji et al. [2]. In our case, $\int d\alpha \, \Delta_s(\alpha)$ is the error associated to the hole set of s-type functions, that is, the s-type AO error.

Handling Eq. (6), in the same way of Ref. 2 we get

$$\Delta_s(\alpha) = 4 \sum_a f_{as}(\alpha) \int d\beta f_{as}(\beta) \left\{ (\alpha'|h|\beta) + \int d\gamma \int d\delta \left[2 \sum_a f_{as}(\gamma) f_{as}(\delta) \right] \right.$$

$$\times [(\alpha'\beta|\gamma\delta) - 1/2(\alpha\gamma|\beta\delta)] - \varepsilon_a S(\alpha', \beta) \bigg\}. \qquad (8)$$

This equation, with the use of (4), becomes

$$\Delta_s(\alpha) = 4 \sum_a f_{as}(\alpha) \left\{ \int d\beta f_{as}(\beta) [F(\alpha', \beta) - \varepsilon_a S(\alpha', \beta)] \right\}. \qquad (9)$$

Now, consider the MO written as a sum of terms of s and p symmetry.

$$|\psi_a\rangle = \sum_{\sigma = s,p} \int d\alpha f_{a\sigma}(\alpha) |\phi_\sigma(\alpha, \vec{r}_i)\rangle \qquad (10)$$

In this case, the Hartree–Fock equation will be

$$\sum_{\mu} \int d\beta f_{a\mu}(\beta)[F_{\sigma\mu}(\alpha, \beta) - \epsilon_a S_{\sigma\mu}(\alpha, \beta)] = 0 \tag{11}$$

$$p, \sigma = s, p$$

For $\sigma = p$, Eq. (11) has two terms which should vanish separately. One of them is what is inside the brace in Eq. (9). That is, as for GTOs

$$F_{ss}(\alpha', \beta) = F_{pp}(\alpha, \beta) \tag{12}$$

the inclusion of the p-type symmetry functions will lead to vanishing of the s-type AO error,

$$\int d\alpha \, \Delta_s(\alpha) = 0. \tag{13}$$

We can go on with this process so that the errors associated with $p, d \cdots$ functions will also vanish. The derivative of a p-type GTO is a $(d + s)$-type GTO, but as the s-types are already included in the basis we include only the d-type ones. This is a convergent process, and we can stop it as long as some convergence criterion for HF forces is reached.

In order to solve the Hartree–Fock equations of the type (11) we should discretize them in the space of the GTO exponents, therefore getting Roothan-type equations [7b]. This discretization may be guided by the wf in a process we call integral discretization [8]. This technique allows us to obtain a discrete form of the wf $f_{a l_\sigma}(\alpha)$ by plotting the linear coefficients of the GTOs against the discrete values of the exponents. α_i, chosen in a mesh. $\{\alpha_i\}$. Our development above is kept. changing integrals over α by summation over $\{\alpha_i\}$. The only additional condition is that the exponents of the $s, p, d \cdots$ GTOs must be the same, so that the discrete version of (14) is obeyed. In principle, the same number of GTOs of all symmetries should be used. This seems to be a too-strong condition, however. since we know that a l-type GTO wf gets narrower as l increases. Figure 1 illustrates these points. In order to discretize the various terms of the Hartree–Fock equations, like (11). at the same level of accuracy, we may use meshes that become smaller as l increases.

In fact, for $\sigma = p$, the two terms of (11), which must vanish separately, have $f_{as}(\alpha)$ and $f_{ap}(\alpha)$ as unknowns, respectively, the latter being narrower than the former.

Summarizing our main conclusions:

1. We do not need a parent $s, p, d \cdots$ basis and another derivative $p, d + s, f + \cdots$ basis. We need only a self-consistent basis where the p functions are the derivatives of the s functions, and so on. Derivative here means a p-function with the same exponent.
2. We do not need to include all the derivatives. The set of exponents of the p functions may be a subset of the exponents of the s functions, and so on.
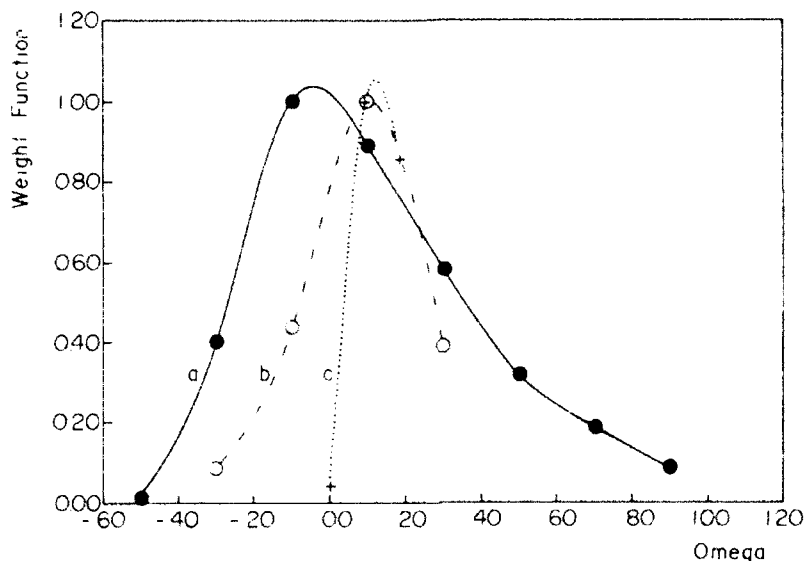
Figure 1.   The weight functions for (a) s-type, (b) p-type, and (c) d-type GTOs centered
on nuclei for the H₂ molecule.

These points permit us to use common size basis sets for the first-row atoms. This is a quite different procedure of that of Nakatsuji et al. [2] or even Custódio and Godard [4]. For instance, the total basis set parent plus derivative used in Ref. 2 for the LiH molecule has $14s$, $14p$, and $5d$ functions centered on the Li nucleus.

We have to say here that conclusion 2 above has already been introduced ad hoc in Ref. 4; that is, they use the HF force as a criterion for choosing which derivatives must be included to improve the wave function.

Applications

We have done applications of these ideas to some diatomic molecules. First, we use H₂ and LiH as test cases, to show details of the calculations, and also to compare with the results obtained by Nakatsuji's method. As in previous works [7b,8] the exponents are chosen in an evenly spaced mesh in the Ω-space,

$$\Omega_i = \Omega_{min} + i\Delta\Omega, \quad \alpha_i = \exp(6.0\Omega_i) \, [-\infty < \Omega < +\infty] \qquad (14)$$

where we have a pair of discretization parameters (Ω_{min}, $\Delta\Omega$) for each symmetry of the GTOs centered in each different nucleus. These parameters are not optimized but chosen with a sight on the wf in probe calculations.

We set, for H₂:
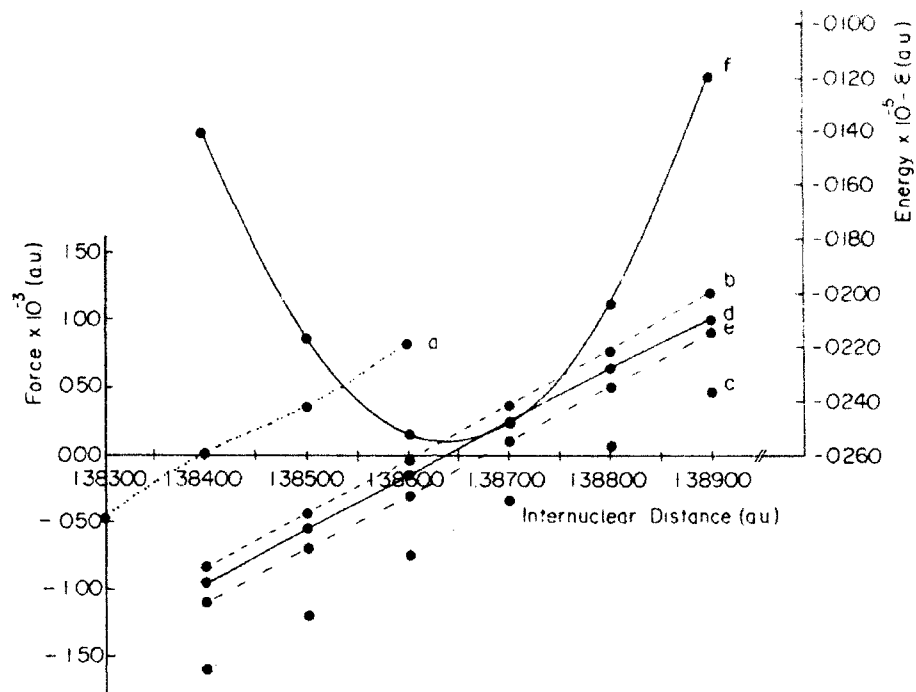
Figure 2. Forces at different internuclear distances of H_2 for (a) gradient with s-type GTOs only; (b) gradient with s- and p-type GTOs; (c) Hellmann–Feynman force with s- and p-type GTOs; (d) gradient with s-, p-, and d-type GTOs; (e) Hellmann–Feynman force with s-, p-, and d-type GTOs. (The 9s Hellmann–Feynman force is to bad to appear in this figure).

N_σ	Ω_{min}	$\Delta\Omega$
6s	-.50	.20
5p	-.30	.20
3d	-.10	.20

(Fig. 1 was not drawn with this basis but it illustrates how we choose the discretization parameters.) For LiH:

Atom	N_σ	Ω_{min}	$\Delta\Omega$
Li	9s	-.592	.216
	5p	-.376	.216
	3d	-.160	.216
H	5s	.349	.260
	3p	-.089	.260

TABLE I. Hellmann–Feynman (HF) force and Hartree–Fock ground state total energy, E, at the minimum nuclear distance, R_0, for H_2 and LiH, for the different basis sets considered

System	Basis set	R_0 (a.u.)	HF force (a.u.)	E (a.u.)
H_2	6s	1.384	+1.55 E-1	1.12786655
(This work)	6s, 5p	1.387	+1.21 E-3	1.13287085
	6s, 5p, 3d	1.388	+4.88 E-4	1.13292920
		1.40*		1.1336*
LiH	(9s, 5p, 3d)		2.28 E-4 (Li)	
(This work)	(Li)	3.026	6.25 E-4 (H)	7.98418413
	(5s, 3p)			
	(H)			
LiH	9s, 14p, 5 (s + d)	3.015	4. E-4 (Li)	7.9851
(Ref. 2)	4s, 4p^b		1.7 E-3 (H)	

* Data from literature, exact energy.

^b Number of primitives in the set (parent + derivatives) from Ref. 2. The parent set is contracted.

We have calculated the total Hartree–Fock energy and the HF force on a reduced-mass nucleus for various configurations near the minimum energy distance, R_0. We illustrate, in Figure 2 and Table I, the improvement of the HF force in H_2 as we use the (6s), (6s, 5p), and (6s, 5p, 3d) bases, respectively. This improvement is impressive, since the force decays by three orders of magnitude from the smallest to the greatest basis.

In this calculation, we noted that it is not an accurate procedure to calculate the HF force at a minimum geometry provided by another calculation or experiment, since each basis has its own minimum geometry.

Results of our calculation on LiH are also found in Table I. The minimum of the energy curve is at $R = 3.026$ a.u. and there the HF force is 8.5E-4 a.u. It vanishes at $R = 3.032$ a.u. Our result is equivalent in accuracy to those in Ref. 2, where a much greater basis set is used.

In order to show that our approach applies well to greater systems, we tested it on the CO and F_2 molecules. We found proper to start with a standard set of s-type GTOs, i.e., from the D95 basis [9], and complete it in two ways. First, taking

TABLE II. Hellmann–Feynman force (HF), electric field, G, and Hartree–Fock ground state total energy, E, at the minimum nuclear distance, R_0, for CO and F_2, for the basis sets displayed.

System	Basis set	R_0 (a.u.)	HF force (a.u.)	G (electric field a.u.)	E (a.u.)
CO	(10s, 7p, 4d, 2f)	1.103	4.59 E-2 (O)	5.74 E-3 (O)	112.776009
			2.16 E-2 (C)	3.60 E-3 (C)	
F_2	(10s, 8p, 4d, 2f)	1.327	+2.73 E-2	3.04 E-3	198.748238

the two more diffuse GTOs as if they belonged to an even-spaced set and use the corresponding increment $\Delta\Omega$ to increase the set of s functions, when it is needed. Second, introducing the derivatives as in the above calculations. In this way, we built the basis sets for C, O, and F, shown in Table II, together with the optimized equilibrium distances R_0, the total energy, the electrostatic field $\mathcal{E}$ and the HF forces. We see that the HF forces are very accurate. We could increase the basis to get the E-3 accuracy but always keeping its size smaller than that which we would get by Nakatsuji's method ($14s$, $14p$, $11d$ plus six mixed d derivatives).

The total energies reported in Tables I and II show that our self-consistent basis sets are also good for energy calculations. Therefore, the need of some basis functions to have the same exponent of others seems to be not a great restriction. In fact, the basis sets like this have already been reported [10], though not in the context of improving HF forces.

Conclusions

We presented here a way of constructing self-consistent basis sets of standard size so that the HF forces are very good approximations to the forces on the nuclei. Those basis sets can be used in place of the analytical gradient in SCF geometry optimization, with a great economy of computation. In fact, we are now using these HF forces for doing calculations with simultaneous optimization of geometry and Hartree–Fock total energy by SD, in a work in progress [5b].

Acknowledgment

Bibliography

[1] F. L. Pilar, *Elementary Quantum Chemistry* (McGraw-Hill, New York, 1968).
[2] H. Nakatsuji, K. Kanda, and T. Yonezawa, Chem. Phys. Lett. 75, 340 (1980).
[3] P. Pulay, Molec. Phys. 17, 197 (1969).
[4] R. Custódio and J. D. Goddard, J. Molec. Struc. Theochem. (to appear).
[5] (a) H. Chacham and J. R. Mohallem, Molec. Phys. 70, 391 (1990); (b) R. O. Vianna, H. Chacham, and J. R. Mohallem (to appear)
[6] M. R. Pederson, B. M. Klein, and J. Q. Broughton, Phys. Rev. B 38, 3825 (1988).
[7] (a) B. H. Wells and S. Wilson, J. Phys. B 22, 1285 (1989); (b) H. F. M. da Costa, A. B. F. da Silva, J. R. Mohallem, A. M. Simas, and M. Trsic, Chem. Phys. 154, 379 (1991).
[8] J. R. Mohallem, Z. Phys. D 3, 339 (1986).
[9] T. H. Dunning and P. J. Hay, in *Methods of Electronic Structure Theory*, H. F. Schaeffer, III, Ed. (Plenum, New York, 1977), pp. 1–27.
[10] S. Huzinaga, Comp. Phys. Rep. 2, 279 (1985).

An Investigation of the Performance of a Hybrid of Hartree-Fock and Density Functional Theory

PETER M. W. GILL, BENNY G. JOHNSON, and JOHN A. POPLE

Department of Chemistry, Carnegie Mellon University, Pittsburgh, Pennsylvania 15213

MICHAEL J. FRISCH

Lorentzian Inc., 127 Washington Avenue, North Haven, Connecticut 06473

Abstract

We explore a hybrid methodology in which the Hartree-Fock energy and density are combined with the nonlocal exchange functional of Becke (1988) and the nonlocal correlation functional of Lee, Yang and Parr (1988) to yield an estimate of the Schrödinger total energy. The resulting mean absolute deviation from a large number of experimental atomization energies, ionization potentials, electron affinities, and proton affinities is 5.86 kcal/mol. Performance comparisons are made with the recently developed G2 theory and nonconventional interpretations of the density functionals are discussed. © 1992 John Wiley & Sons, Inc.

Introduction

Systematic prediction of molecular energy by quantum mechanical methods is one of the principal objectives of theoretical chemistry. In the last few years, there has been some success in developing methods which will reproduce experimental energies, such as dissociation energies, ionization potentials, and electron affinities, to an accuracy of ±2 kcal/mol or 0.1 eV. The GAUSSIAN-1 (G1) and GAUSSIAN-2 (G2) models [1,2] achieve this by *ab initio* procedures, supplemented by a single small semiempirical parameter to allow for higher-order basis functions and higher-order correlation corrections. However, this level of accuracy is only reached at a cost that rapidly increases with the size of the system (an iterative N^4 step followed by a single N^5 step, where N scales as the molecular size). There is, therefore, interest in methods which might reach similar precision more efficiently.

Density functional theory has recently shown promise in this direction. In particular, Becke [3] has proposed an algorithm which, when applied to the same experimental data set as used in G1 theory, gives total atomization energies of neutral molecules with an average absolute error of 3.7 kcal/mol. This result compares with 1.6 kcal/mol for G1 and 1.2 kcal/mol for G2 theory, but is obtained at lower cost and is more easily extendable to larger molecules. Other density functional theories have also shown promise in this direction [4,5].

Most density functional theories attempt to express the exchange and/or correlation energies as functionals of the one-electron density $\rho(r)$ (or of the α- and β-densities $\rho_\alpha(r)$, $\rho_\beta(r)$ for open-shell systems). Exact functionals are unknown,

but some general properties have been elucidated and many explicit forms have been tried. The densities ρ_α, ρ_β are obtained usually via a self-consistent procedure, based on the potential derived from the exchange-correlation functional (Kohn-Sham equations). However, it is quite possible to apply the same energy functionals to electron densities derived by standard (HF) theory. An extensive study of this sort, using several functionals, has been published by Clementi and Chakravorty [6]. Such comparative studies should help our understanding of both the densities and functionals as well as pointing the way towards improved treatments.

Our principal objective is to apply a combination of energy functionals from the recent literature to a large set of Hartree-Fock densities. This set consists of the atoms, molecules, and ions used in the G2 study [2], where they were tested against well-known atomization energies, ionization potentials, electron affinities, and proton affinities. Here we make a parallel study, using a Hartree-Fock density and a combination of exchange-correlation functionals due to Becke [7] and Lee et al. [8]. Emphasis is on the development of a unique procedure for all species, with well-defined total energies, which may be compared directly with Schrödinger total energies, insofar as they are known. Such total energies, which are rarely reported in the current density functional literature, can then be used to calculate energy differences, directly comparable to experimental data (as is possible with G2 theory).

Method

In order to facilitate comparison with previous calculations, we shall use molecular structures and frequencies exactly as in G2 theory. All geometrical parameters are found at the MP2/6-31G(d) level and harmonic frequencies at HF/6-31G(d). These frequencies (scaled by the usual 0.893 empirical factor [9]) are used to calculate zero-point vibrational energies. Single-point Hartree-Fock calculations are then carried out with the largest basis used in G2 theory, 6-311 + G($3df,2p$) [10]. Restricted (RHF) and unrestricted Hartree-Fock (UHF) methods are used for closed and open shell systems, respectively. The electron density, ρ, may be described in conventional notation as HF/6-311 + G($3df,2p$)//MP2/6-31G(d). This is then used for density functional calculations.

In density functional theory, the total energy is written

$$E = E_I + E_V + E_J + E_{XC} \tag{1}$$

where E_I is the kinetic energy of independent electrons having the density ρ. E_V is the potential energy involving nuclei (nuclear–electron + nuclear–nuclear) and E_J is the overall coulomb repulsive energy

$$E_J = \frac{1}{2} \int\int \rho(r_1) r_{12}^{-1} \rho(r_2)\, dr_1\, dr_2 \tag{2}$$

The remaining term E_{XC} is the exchange-correlation energy, representing the energy lowering due to the fact that the complete electron–electron interaction is less than E_J, partly because this incorrectly includes the interaction of a particular electron with its own smoothed distribution, and partly because the relative motion of other electrons is correlated, not independent as implicit in Eq. (2).

In Hartree-Fock theory, the energy is calculated as the expectation value of the Hamiltonian using the optimized single-determinant wavefunction with occupied spin orbitals χ_i. This gives an energy

$$E_{HF} = E_T + E_1 + E_J + E_X \tag{3}$$

where E_X is the exchange energy

$$E_X = -\frac{1}{2} \sum_{i,j}^{occ} \int\int \chi_i(1)\chi_j(1)r_{12}^{-1}\chi_i(2)\chi_j(2) \, d\tau_1 \, d\tau_2 \tag{4}$$

integration being over cartesian and spin coordinates. This expression takes some account of the tendency of electrons of parallel spin to be kept spatially apart by virtue of the antisymmetry principle. However, as is well known, the Hartree-Fock energy E_{HF} takes no account of the correlation between electrons of antiparallel spin. The remaining part of the energy is the correlation energy E_C, which deals with α-β correlation and also the remaining α-α and β-β correlation effects not included in the exchange part of E_{HF}. E_C is difficult and frequently expensive to compute. In G2 theory, it is treated by a combination of Møller-Plesset (MP) and quadratic configuration interaction methods.

A common recommendation in density functional theory is to treat E_X and E_C together as a single correction E_{XC}, determined by a functional $E_{XC}[\rho]$. There is some point to this, since the exchange energy by itself is not clearly defined for densities other than Hartree-Fock. Nevertheless, in practice, E_{XC} often *is* split into two parts, one of which has the *appearance* of an exchange correction and the other the *appearance* of a correlation correction. However, the two do not necessarily correspond to exact exchange and correlation, in the normal meaning of these terms. Ziegler [11], for example, notes that poor results are often obtained if exact (i.e., HF) exchange energies are used in conjunction with certain functionals for correlation. Instead, it is better to use a different density functional theory (DFT) functional for exchange to go along with the correlation calculation. Since the exchange energy is well-defined (at least for ρ_{HF}), we prefer to denote this partition of E_{XC} as a division into a *parallel*-spin ($\alpha\alpha + \beta\beta$) part E_P and an *antiparallel*-spin ($\alpha\beta$) part E_A,

$$E_{XC} = E_P[\rho_\alpha] + E_P[\rho_\beta] + E_A[\rho_\alpha, \rho_\beta] \tag{5}$$

The parallel part, which is exchange-like, is the sum of an α- and a β-part, determined solely by their respective densities ρ_α and ρ_β. The antiparallel part, which is correlation-like, is a single functional $E_A[\rho_\alpha, \rho_\beta]$ which vanishes unless ρ_α and ρ_β are both nonvanishing and overlapping. A possible interpretation is that E_P takes account of both elimination of self-interaction and effects of full correlation of parallel ($\alpha\alpha + \beta\beta$) electrons (including exchange), while E_A takes into account of the remaining correlation between antiparallel ($\alpha\beta$) electrons. We shall return to this hypothesis in a later section.

We now turn to specification of the functionals. For the parallel part, we use the expression introduced by Becke in 1988 [7], and also used by Becke [3] in his recent study of atomization energies. We shall write this as

$$E_{x}^{\text{B88}} = E_{x}[\rho_{\alpha}] + E_{x}[\rho_{\beta}] \tag{6}$$

where

$$E_{x}[\rho] = -\frac{3}{2}\left(\frac{3}{4\pi}\right)^{1/3} \int \rho^{4/3}\, dr - \int \rho^{4/3}\, \frac{bx^{2}}{1 + 6bx\sinh^{-1}x}\, dr \tag{7}$$

$$x = \rho^{-4/3}|\nabla\rho| \tag{8}$$

The first term in (7) is designed to reproduce the exchange energy of a uniform electron gas. The second term introduces a correction for nonuniformity through the density gradient $\nabla\rho$, the particular analytic form being such that correct asymptotic behaviour is achieved far from the molecular centre. The parameter b is chosen by Becke as 0.0042 to fit the known exchange energies for the inert gas atoms.

The Becke functional (7) is parameterized to give good *atomic* exchange energies. However, as noted above, it may not always lead to good exchange energies for molecules. It is useful to introduce a quantity

$$\Delta E_{x}^{\text{B88}} = E_{x}^{\text{B88}} - E_{x} \tag{9}$$

which measures the "Becke 88 excess," or excess exchange energy implied by (7). As will be seen in the next section, this excess is quite large for many molecules. Since we are using a Hartree-Fock density, the values of E_{x}^{B88} and E_{x} are both computable and $\Delta E_{x}^{\text{B88}}$ is easily obtained.

It remains to add the antiparallel correlation correction $E_{c}[\rho_{\alpha}, \rho_{\beta}]$. Here we use the form introduced by Lee, Yang and Parr (LYP) [8]. This originates in an older study of $\alpha\beta$ correlation in the helium atom by Colle and Salvetti [12]. The actual form programmed is one equivalent to LYP presented by Miehlich, Savin, Stoll, and Preuss (MSSP) [13]. It is given fully by eq. (2) of this reference and need not be reproduced in full. It does have the property of vanishing if either ρ_{α} or ρ_{β} is nonexistent, so has the appearance of representing only $\alpha\beta$ correlation. We denote it by E_{c}^{LYP}.

It should be noted that both LYP and MSSP applied the LYP functional to a number of other atomic and molecular systems and sometimes obtained good results when compared with known *total* correlation energies. Since E_{c}^{LYP} does not incorporate effects of $\alpha\alpha$ or $\beta\beta$ correlation in any direct manner, the significance of this is somewhat unclear. We shall use E_{c}^{LYP} only to represent the antiparallel part.

The (Becke 88 + Lee, Yang and Parr) correlation energy is then given by

$$E_{c}^{\text{BLYP}} = \Delta E_{x}^{\text{B88}} + E_{c}^{\text{LYP}} \tag{10}$$

and the corresponding total energy E_{0}^{BLYP} is obtained by adding the HF and zero-point vibrational energies

$$E_{0}^{\text{BLYP}} = E_{\text{HF}} + E_{c}^{\text{BLYP}} + E_{\text{ZPV}} \tag{11}$$

The actual procedure is:

1. Obtain the Hartree-Fock energy E_{HF};
2. Remove the Hartree-Fock exchange energy E_X;
3. Compute E_P^{B88} and E_P^{LYP} by numerical quadrature and add to give E_P^{BLYP};
4. Compute E_{ZP} and add to give E_0^{BLYP}.

Details of the numerical integration scheme are given in the Appendix.

Results and Discussion

The BLYP procedure just described has been applied to the 152 atoms, molecules, and ions needed for comparison with the experimental G2 data set (which we have extended here to include H_2, H_2^+, He, He$^+$, Ne, Ne$^+$, Ar, and Ar$^+$) using a modified version of the GAUSSIAN 92 suite of programs [14]. The source data listed in Table I are:

1. The proper (unrestricted Hartree-Fock) exchange energy, E_X, with the large 6-311+G(3df,2p) basis;
2. The Becke-88 excess, ΔE_P^{B88}, given by Eq. (9), measuring the amount by which the Becke functional (7) gives an energy contribution additional to E_X;
3. The estimate of the total correlation energy, E_P^{BLYP}, given in this theory as the sum of ΔE_P^{B88} and the antiparallel part due to Lee, Yang and Parr;
4. The total energy, E_0^{BLYP}, obtained by adding the correlation to the Hartree-Fock energy, to give E, and then further modified by addition of the zero-point energy, as listed elsewhere [1,2].

This set of data should prove of value in assessing the role of various energy contributions; it is more comprehensive than most of the data published in the density functional literature.

We begin with information about the total energies of atoms. For small atoms, the total energy (corresponding to full solution of the Schrödinger equation) is moderately well known, either by high-level theory, or by some combination of experimental and theoretical ionization potentials. The BLYP results are compared with some such values in Table II. Agreement is generally achieved within 10 millihartrees (mh), although there is some variation. The Becke-88 functional fails to give the correct exchange energy for the hydrogen atom (-312.5 mh) by 2.8 mh, leading to a significant error of 3 mh. For the heavier atoms, such as oxygen, fluorine, and neon, there are some partly compensating errors. On the one hand, incompleteness of the orbital basis results in a Hartree-Fock energy that is too positive by about 20 mh for the neon atom (based on the HF limit of -128.5470 given by Veillard and Clementi [15]). On the other hand, the magnitude of the correlation energy is overestimated in this treatment. Here, we have -31.1 mh from ΔE_P^{B88} and -383.4 mh from E_P^{BLYP}, giving a total of -414.5 mh. The actual correlation energy of neon is close to -390 mh [16].

Table III lists the total atomization energies, ΣD_0, from the present theory, together with G2 and experimental data. This consists of the 55 molecules of the G2 set plus H_2. The mean absolute difference between BLYP and experiment is 3.94 kcal/mol, which may be compared with 1.16 kcal/mol for G2 theory. The BLYP

TABLE I. Source data.

Molecule	E_x (mh)	ΔH_f^{Bxx} (mh)	E_c^{BLYP} (mh)	E_0^{BLYP} (ht)	Molecule	E_x (mh)	ΔH_f^{Bxx} (mh)	E_c^{BLYP} (mh)	E_0^{BLYP} (ht)
H	312.5	+2.8	+2.8	0.4970					
He	1026.2	+1.0	-42.8	-2.9027	He$^+$	623.2	+5.2	+5.2	1.9929
Li	1781.0	+5.9	-47.5	7.4796	Li$^+$	1651.1	+6.2	41.4	7.2772
Be	-2666.2	+9.0	-85.5	-14.6575	Be$^+$	-2504.9	+9.5	51.6	14.3278
B	-3768.6	+9.2	-115.7	-24.6467	B$^+$	-3491.3	+10.2	96.4	24.3320
C	5074.6	+8.7	-149.6	-37.8398	C$^+$	-4745.2	+9.8	129.4	37.4224
N	-6603.5	+10.0	-181.9	54.5808	N$^+$	6212.0	+12.1	161.2	54.0488
O	-8212.3	-6.0	-262.7	75.0721	O$^+$	-7911.6	+18.3	-188.4	-74.5550
F	-10037.0	-20.3	-341.4	99.7432	F$^+$	-9670.6	+3.2	209.8	99.0946
Ne	-12098.3	-31.1	-414.5	128.9411	Ne$^+$	11656.5	-7.1	-344.6	128.3457
Na	-14017.6	-12.4	-420.8	162.2668	Na$^+$	-13902.2	8.1	-407.4	162.0717
Mg	-15991.7	-1.0	-460.5	-200.0671	Mg$^+$	-15859.7	+3.5	-423.8	-199.7877
Al	-18090.4	+8.0	-485.1	-242.3591	Al$^+$	-17892.2	+3.1	-477.7	-242.1457
Si	-20303.1	+12.2	-517.0	-289.3690	Si$^+$	-20071.1	+8.3	-506.6	-289.0779
P	-22641.0	+15.1	-551.2	-341.2604	P$^+$	-22368.4	+10.7	540.3	-340.8855
S	-25033.0	+18.3	-609.4	-398.1123	S$^+$	-24791.3	+18.2	-569.3	397.7331
Cl	-27541.1	+19.9	-669.9	-460.1471	Cl$^+$	-27262.2	+20.4	629.0	-459.6734
Ar	-30183.4	+25.9	-724.9	-527.5318	Ar$^+$	-29854.7	+25.2	-685.7	526.9571
C	-5265.3	-5.2	-176.1	-37.8833	Si	-20455.1	+9.9	-528.8	-289.4119
					P	-22766.0	+7.9	-591.9	-341.2884
O	-8387.7	-42.0	-339.4	-75.1274	S	-25194.6	+9.9	-652.4	398.1876
F	-10276.6	-60.2	-421.2	-99.8669	Cl	-27748.0	+12.1	712.4	-460.2778
H$_2$	-659.7	+3.1	-35.3	-1.1588	CN	-11757.7	-36.9	-450.4	-92.6806
LiH	-2140.2	+7.3	-81.1	-8.0642	HCN	-12013.2	-53.7	-515.9	-93.4024
BeH	-3084.3	+16.2	-91.1	-15.2387	CO	-13301.6	-62.4	-545.4	-113.3162
CH	-5423.0	+5.5	-190.4	-38.4649	HCO	-13685.4	-59.2	-564.7	-113.8419
CH$_2$ ($^3B_1$)	-5874.6	+14.8	-196.4	-39.1166	H$_2$CO	-14071.2	-49.6	-588.9	-114.4723
CH$_2$ ($^1A_1$)	-5789.6	+6.3	-226.1	-39.1020	H$_3$COH	-14843.6	-22.9	-618.3	-115.6567
CH$_3$	-6227.3	+15.7	-240.6	-39.7895	N$_2$	-13050.9	-79.8	-560.6	-109.5275
CH$_4$	-6592.4	+17.6	-276.4	-40.4460	H$_2$NNH$_2$	-14623.2	-33.2	-629.3	-111.8009
NH	-6936.7	-1.6	-236.8	-55.2100	NO	-14736.1	-83.2	-609.2	-129.9006
NH$_2$	-7286.4	-9.4	-287.2	-55.8548	O$_2$	-16291.3	115.7	-682.9	150.3423
NH$_3$	-7661.6	-13.3	-330.9	-56.5160	HOOH	-17063.7	-103.6	-739.1	-151.5425
OH	-8557.3	-24.5	-324.2	-75.7339	F$_2$	-19936.3	-138.7	-813.4	-199.5522
OH$_2$	-8930.3	-38.0	-378.2	-76.4142	CO$_2$	-21591.1	-113.1	-901.6	-188.5912
FH	-10411.9	-45.9	-408.2	-100.4547	Na$_2$	-28022.9	-27.4	-868.0	-324.5593
SiH	-20652.8	+17.5	-545.7	-289.9765	Si$_2$	-40558.6	-6.1	-1101.4	-578.8468
SiH$_2$ ($^1A_1$)	-21007.6	+22.9	-573.8	-290.5898	P$_2$	-45181.0	-16.4	-1227.8	-682.7032
SiH$_2$ ($^3B_1$)	-21053.3	+30.8	-543.5	-290.5525	S$_2$	-50051.0	+1.8	-1301.0	-796.3851
SiH$_3$	-21413.4	+39.9	-573.2	-291.1907	Cl$_2$	-55078.7	+14.3	-1398.1	-920.3803
SiH$_4$	-21780.7	+49.8	-598.6	-291.8275	NaCl	-41688.8	+8.7	-1123.5	-622.5593
PH	-22984.8	+19.7	-583.1	-341.8698	SiO	-28548.5	-55.6	-906.8	-364.7374
PH$_2$	-23328.5	+23.0	-617.2	-342.4866	PO	-30807.7	-60.7	952.0	-416.5567
PH$_3$	-23682.7	+27.6	-647.7	-343.1085	SC	-30084.0	-23.3	-869.9	-436.2151
SH	25371.7	+17.7	-647.5	-398.7414	SO	-33218.2	-54.4	-990.6	-473.3827
SH$_2$	-25720.4	+18.0	-683.2	-399.3773	ClO	-35736.7	-31.5	-1019.8	-535.3139
ClH	-27889.4	+15.6	-711.0	-460.8045	ClF	-37554.7	-52.6	-1098.2	-559.9862
Li$_2$	-3560.7	+12.2	-120.6	-14.9903	Si$_2$H$_6$	-42883.6	+89.9	-1170.4	-582.4896
LiF	-11994.2	-43.3	-461.2	-107.4382	CH$_3$Cl	-33809.1	+28.6	-953.5	-500.0574
HCCH	-10963.1	-22.4	-465.2	-77.2852	CH$_3$SH	-31641.5	+30.4	-927.4	-438.6342
H$_2$CCH$_2$	-11743.2	+5.5	-491.5	-78.5046	HOCl	-36077.7	-43.3	-1067.7	-535.9644
H$_3$CCH$_3$	-12514.1	+32.7	-518.5	-79.7048	SO$_2$	-41427.7	-125.5	-1377.1	-548.6482

TABLE I. (Continued)

Molecule	I_s (mh)	ΔE_f^{HSS} (mh)	I_s^{BLYP} (mh)	I_s^{BLYP} (th)	Molecule	I_s (mh)	ΔE_f^{HSS} (mh)	I_s^{BLYP} (mh)	I_s^{BLYP} (th)

TABLE II. Energies for neutral atoms[a].

Atom	E(HF)	E(BLYP)	E(Sch)[b]	ΔE(BLYP-Sch)
H	0.4998	0.4970	0.5000	+3.0
He	2.8599	2.9026	2.9042	+1.6
Li	7.4320	7.4796	7.4781	1.5
Be	14.5719	14.6574	14.6673	+9.9
B	24.5311	24.6467	24.6539	+7.2
C	37.6903	37.8399	37.8451	+5.2
N	54.3989	54.5809	54.5895	+8.6
O	74.8093	75.0721	75.0673	4.8
F	99.4018	99.7432	99.7313	11.9
Ne	128.5266	128.9411	128.937	4.

[a] Total energies in hartrees; differences in millihartrees.

[b] Based on Hartree-Fock and correlation estimates [15], but with the Lamb Shift correction reversed in sign as pointed out [16].

mean accuracy is quite close to that obtained by Becke [3], 3.7 kcal/mol, based on the original 55 compounds. He uses a combination of B88 and a correlation correction based on the paramatrization of the free-electron gas by Vosko et al. [17]. We shall refer to this procedure as B92.

A detailed examination of the entries in Table III shows little correlation with errors reported for B92, even though the overall performance is comparable. The BLYP binding energies are mostly too small, whereas B92 tends to overbind. A large BLYP error occurs for the CN radical, for which D_0 is 13.4 kcal/mol too low; B92 gives a value 6.1 kcal/mol too high. This radical is known to be highly spin-contaminated at the UHF level. It is therefore of interest to note that the restricted ROHF density leads to a BLYP binding of 174.0 kcal/mol, in much better agreement with experiment. Other large BLYP errors are found for C_2H_6 and Si_2H_6, the latter giving an atomization energy 17.2 kcal/mol too small. These errors are spread over seven bonds, however. B92 gives good agreement for these molecules.

TABLE III. Total atomization energies ΣD_0 (in kcal/mol).

Molecule	BLYP	G2	Expt	Molecule	BLYP	G2	Expt
H_2	103.4	104.4	103.3	HCN	304.2	302.8	301.8
LiH	55.0	56.6	56.0	CO	253.7	258.0	256.2
BeH	52.8	45.5	46.9	HCO	271.7	271.4	270.3
CH	80.4	80.5	79.9	H_2CO	355.4	359.3	357.2
$CH_2(^3B_1)$	177.5	178.6	179.6	H_3COH	474.9	482.3	480.8
$CH_2(^1A_1)$	168.3	172.0	170.6	N_2	229.6	223.8	225.1
CH_3	287.8	289.1	289.2	H_2NNH_2	408.7	404.4	405.4
CH_4	387.9	393.2	392.5	NO	155.4	150.6	150.1
NH	83.0	77.9	79.0	O_2	124.3	115.6	118.0
NH_2	175.7	170.1	170.0	HOOH	253.7	252.1	252.3
NH_3	278.7	276.5	276.7	F_2	41.3	36.6	36.9
OH	103.4	101.6	101.3	CO_2	381.0	384.6	381.9
OH_2	218.4	219.6	219.3	Na_2	16.1	19.2	16.6
FH	134.6	136.3	135.2	Si_2	68.3	73.6	74.0
$SiH_2(^1A_1)$	142.3	147.1	144.4	P_2	114.5	114.7	116.1
$SiH_2(^3B_1)$	118.9	123.8	123.4	S_2	100.7	97.4	100.7
SiH_3	207.5	213.5	214.0	Cl_2	54.0	55.8	57.2
SiH_4	295.2	304.8	302.8	NaCl	91.2	98.8	97.5
PH_2	145.7	144.9	144.7	SiO	185.9	188.8	190.5
PH_3	224.1	226.4	227.4	SC	165.0	170.5	169.5
SH_2	170.1	173.0	173.2	SO	124.4	120.8	123.5
ClH	100.7	102.6	102.2	ClO	59.4	61.2	63.3
Li_2	19.5	25.9	24.0	ClF	60.2	61.0	60.3
LiF	135.2	137.5	137.6	Si_2H_6	482.9	503.0	500.1
HCCH	383.8	387.2	388.9	CH_3Cl	363.6	372.1	371.0
H_2CCH_2	525.2	531.7	531.9	CH_3SH	435.6	445.0	445.1
H_3CCH_3	654.6	666.6	666.3	HOCl	155.7	156.8	156.3
CN	163.2	176.0	176.6	SO_2	245.8	248.9	254.0

Table IV gives ionization energies for the same G2 set plus values for the hydrogen atom and the three inert gases helium, neon and argon. The mean absolute difference between BLYP and experiment is 0.195 eV (4.49 kcal/mol), compared with 0.054 eV (1.24 kcal/mol) by the G2 procedure. We note that the majority (30 of 42) of the BLYP ionization energies are smaller than experiment. In particular, the result for the hydrogen atom is significantly too small (by 0.08 eV). This may be traced to the failure of the Becke-88 formula to give the correct exchange energy for the hydrogen atom. On the other hand, the worst error in Table IV is for carbon mono-sulfide, for which the BLYP value is 0.69 eV too large. Our results show comparable accuracy to a smaller set of ionization energies of another DFT study reported by Ziegler [11], using different functionals.

Table V lists electron affinities for the G2 dataset. The mean error for BLYP is found to be 0.137 eV (3.16 kcal/mol), compared with 0.056 eV (1.29 kcal/mol) for G2 theory. The majority (20 of 25) of the values are numerically too small. However, the result more seriously in error is the cyano radical, for which the BLYP electron affinity is 0.74 eV too high. This large error evidently is due to the poor description of the neutral radical, as already noted in the discussion of atomization energies. Our results may be compared with a DFT study of electron affinities due to Ziegler and Gutsev [18], using different functionals. They studied many of the same molecules and also found an average error of about 0.2 eV. However, for the cyano radical, they obtain an electron affinity which is too small, whereas ours is

TABLE IV — Ionization potentials (eV)

Molecule	BLYP	G2	Expt	Molecule	BLYP	G2	Expt
H	13.52	13.60	13.60	OH	12.51	12.63	12.62
He	24.76	24.84	24.59	HF	15.99	16.08	16.04
Li	5.51	5.33	5.39	SiH₄	10.79	11.01	11.00
Be₂	8.97	9.41	9.32	PH	9.98	10.09	10.15
B	8.56	8.20	8.30	PH₂	9.73	9.72	9.82
C	11.36	11.18	11.26	PH₃	9.73	9.87	9.87
N	14.48	14.48	14.54	SH	10.31	10.31	10.37
O	14.07	13.52	13.61	SH₂ (²B₁)	10.28	10.43	10.47
F	17.65	17.39	17.42	SH₂ (²A₁)	12.49	12.75	12.78
Ne	21.64	21.64	21.56	ClH	12.60	12.71	12.75
Na	5.31	4.95	5.139	HCCH	11.11	11.42	11.40
Mg	7.60	7.65	7.646	HCCH₂	10.28	10.58	10.51
Al	5.81	5.93	5.984	CO	14.28	14.01	14.01
Si	7.92	8.10	8.15	N₂ (²Σ)	15.54	15.56	15.58
P	10.20	10.44	10.49	N₂ (²Π)	16.42	16.67	16.70
S	10.32	10.20	10.36	O₂	12.40	12.17	12.07
Cl	12.89	12.85	12.97	P₂	10.16	10.54	10.53
Ar	15.64	15.69	15.76	S₂	9.27	9.28	9.36
CH₄	12.55	12.68	12.62	Cl₂	11.15	11.51	11.50
NH₃	10.08	10.19	10.18	CN	12.59	12.65	12.66
OH	13.14	12.98	13.01	CS	12.02	11.42	11.33

TABLE V.   Electron affinities (eV).

Molecule	BLYP	G2	Expt.	Molecule	BLYP	G2	Expt.
C	1.18	1.19	1.26	Si	1.17	1.35	1.385
CH	1.17	1.13	1.24	SiH	0.99	1.18	1.277
CH$_2$	0.69	0.66	0.65	SiH$_2$	0.91	0.99	1.124
CH$_3$	−0.10	0.04	0.08	SiH$_3$	1.28	1.42	1.44
CN	4.56	3.97	3.82	P	0.76	0.64	0.746
NH	0.35	0.30	0.38	PH	0.93	0.96	1.00
NH$_2$	0.62	0.77	0.74	PH$_2$	1.08	1.25	1.26
NO	0.01	−0.07	0.02	PO	0.99	1.04	1.09
O	1.50	1.40	1.46	S	2.05	2.00	2.077
OH	1.70	1.87	1.83	SH	2.19	2.30	2.314
O$_2$	0.42	0.47	0.44	S$_2$	1.51	1.66	1.663
F	3.37	3.48	3.40	Cl	3.56	3.60	3.615
				Cl$_2$	2.73	2.38	2.39

much too large. Like us, they use spin-unrestricted methods. The reasons for this anomaly are hard to pursue further as Ziegler and Gutsev do not report their detailed energy components for the separate species CN and CN⁻.

Table VI gives eight proton affinities that are compared with G2 theory and experiment. Here the performance of BLYP is quite good, the mean error of 2.11 kcal/mol being not much greater than the value of 1.04 kcal/mol obtained at the G2 level. This superior performance is not surprising, since no change in the number of electrons is involved and the electron configurations of the protonated species are closely related to those of the neutral molecules.

Combining all of the 130 experimental comparisons in Tables III to VI, we obtain an overall mean absolute error of 3.86 kcal/mol for the BLYP model. This is not much greater than the value of 3.7 kcal/mol obtained by Becke [3] for atomization energies only.

Parallel and Antiparallel Contributions

We return now to the interpretation of the separation of E_{xc} into parallel and antiparallel parts, E_P^{BXX} and E_A^{LYP}. As noted earlier, one possibility is that the parallel

TABLE VI.   Proton affinities (kcal/mol).

Molecule	BLYP	G2	Expt	Molecule	BLYP	G2	Expt
H$_2$	97.7	99.2	100.8	SiH$_4$	153.7	153.0	154.
HCCH	153.0	153.6	152.3	PH$_3$	183.2	186.2	187.1
NH$_3$	200.5	202.5	202.5	H$_2$S	166.5	167.7	168.8
H$_2$O	162.1	163.1	165.1	HCl	132.0	133.0	133.6

part represents the full exchange energy plus further energy lowering due to extra (non-Hartree-Fock) correlation energy between $\alpha\alpha$ and $\beta\beta$ pairs. Inspection of Table I. clearly shows that this cannot be correct in all cases because the Becke-88 excess ΔE_x^{B88} is sometimes *positive*, indicating an energy lowering of *less* than the exchange energy. This cannot be correct. It shows up for the hydrogen atom, where there is no electron correlation, but the Becke-88 energy fails to cancel the coulomb energy E_J, as it should. This may, of course, be a fault of the particular analytic form of the Becke-88 energy. Indeed, the constant b in Eq. (7) could be increased so that ΔE_x^{B88} is zero for the hydrogen atom; all values of ΔE_x^{B88} for other systems then become negative. However, we will not investigate modified functionals here.

Another possibility is that the partition of correlation into ΔE_x^{B88} and E_c^{LYP} gives the breakdown of *correlation binding* into parallel and antiparallel parts, even though this does not work fully for the isolated atoms. We have tested this idea by evaluating some of these binding contributions from Table I (they turn out all to be positive) and compare them with the corresponding parallel ($\alpha\alpha + \beta\beta$) and antiparallel ($\alpha\beta$) contributions from an MP2 treatment (frozen core or valence electrons only with the same basis), where the parallel–antiparallel partition is unequivocal. This comparison as displayed in Table VII shows moderate success for the simple hydrides CH_4, NH_3, OH_2, and FH. However, for the two heavy-atom molecules N_2 and F_2, the comparison is much less successful. For F_2, the satisfactory reproduction of the *total correlation binding* (as evidenced by the good dissociation energy in Table III) is ascribed mainly to the parallel (Becke-88) part rather than to the antiparallel (LYP) part. At the MP2 level, the opposite is true. Evidently, the success of the BLYP procedure cannot be fully understood along these lines; new insight is needed.

Conclusions

The following conclusions are drawn from this work:

1. The BLYP procedure described, based on existing energy functionals and using the Hartree-Fock density, is capable of giving total energies in reasonable agreement (~ 20 mh) with exact Schrödinger energies, insofar as these are known.

TABLE VII   Parallel and antiparallel binding energies (mh)

| | Parallel | | Antiparallel | |
Molecule	MP2($\alpha\alpha + \beta\beta$)	$\Delta(\Delta E_x^{B88})$	MP2($\alpha\beta$)	$\Delta(E_c^{LYP})$
CH_4	23.4	2.9	103.4	135.8
NH_3	22.8	31.4	114.1	125.9
OH_2	28.6	37.5	89.9	83.5
FH	21.5	28.3	52.0	41.3
N_2	40.1	99.6	153.1	97.0
F_2	34.7	97.9	90.5	32.8

2. Various differences of BLYP total energies reproduce good experimental data on atomization energies, ionization energies, electron affinities and proton affinities to an accuracy of about 4 kcal/mol or 0.2 eV. Even though this does not match the greater accuracy achieved by G2 theory, it is a significant achievement for a method of moderate computational cost. The use of a single, well-defined, theoretical procedure for all of these physical properties gives some coherence to the theory.

3. The partition of the electron correlation into parallel (B88) and antiparallel (LYP) parts does not always match the corresponding partition in simple Møller-Plesset theory. The significance of the individual components of BLYP (or other comparable density functional treatments) is not fully understood.

Acknowledgments

Appendix: Numerical Integration in Three Dimensions

Our preliminary method for evaluating density functionals such as (7) is closely related to that described by Becke [19] but, for various reasons, we have made a number of modifications to his scheme which we now describe.

(1) Our cell functions $P_i(r)$ are identical to Becke's for homonuclear systems. but we have *not* found it necessary to adopt the "atomic size adjustments" which Becke suggests for heteronuclear systems.

(2) We employ Gauss-Laguerre, rather than Gauss-Chebyshev, quadrature for the single-center radial subintegrations. This choice was motivated by the fact that the true electron density is known to decay exponentially at large distances from the molecule.

(3) We use 31 radial points on each center, scaled so that the 16th (middle) point lies at the maximum of the radial probability function $4\pi r^2 \varphi^2(r)$ of the valence atomic orbital $\varphi(r)$ given by Slater's well known rules [20]. For example, the 16th radial point for a hydrogen atom lies at $r = 1.0$ au and that for a carbon atom lies at $r = 16/13$ au.

(4) We use 72 angular points at each radial point. The distribution of these is given by a special set of 12 points corresponding to the vertices of a regular icosahedron inscribed in the sphere (the axes of the icosahedron follow the "standard orientation" conventions of the GAUSSIAN program), plus a general set of 60 points generated by the rotation subgroup of the icosahedral group. Such formulae, based on finite rotation subgroups of the sphere, are highly efficient in the sense that the number of surface harmonics exactly integrated by them is close to one per angular point. A clear exposition of the theory of

this approach to quadrature on the surface of a sphere can be found in the literature [21].

If the electron density $\rho(r)$ itself is integrated using this preliminary scheme, the results agree with the total number of electrons to within a few thousandths of an electron for all of the molecules studied. Furthermore, we have observed that both the B88 and LYP functional values are comparatively insensitive to further improvements in the grid. Nonetheless, further work is underway to construct even more efficient integration schemes.

Bibliography

[1] (a) J. A. Pople, M. Head-Gordon, D. J. Fox, K. Raghavachari, and L. A. Curtiss, J. Chem. Phys. 90, 5622 (1989); (b) L. A. Curtiss, C. Jones, G. W. Trucks, K. Raghavachari, and J. A. Pople, J. Chem. Phys. 93, 2537 (1990).

[2] L. A. Curtiss, K. Raghavachari, G. W. Trucks, and J. A. Pople, J. Chem. Phys. 94, 7221 (1991).

[3] A. D. Becke, J. Chem. Phys. 96, 2155 (1992).

[4] J. Andzelm and E. Wimmer, J. Chem. Phys. 96, 1280 (1992).

[5] B. Delley, J. Chem. Phys. 92, 508 (1990).

[6] E. Clementi and S. J. Chakravorty, J. Chem. Phys. 93, 2591 (1990).

[7] A. D. Becke, Phys. Rev. A38, 3098 (1988).

[8] C. Lee, W. Yang, and R. G. Parr, Phys. Rev. B37, 785 (1988).

[9] J. A. Pople, H. B. Schlegel, R. Krishnan, D. J. Defrees, J. S. Binkley, M. J. Frisch, R. A. Whiteside, R. F. Hout, and W. J. Hehre, Int. J. Quantum Chem. Symp. 15, 269 (1981).

[10] Hitherto, the 6-311+G(3df,2p) basis set has not been defined for Ne and Ar. We have therefore defined the diffuse function exponents for Ne and Ar to be 0.13 and 0.06, respectively, and the f function exponent for Ar to be 0.85.

[11] T. Ziegler, Chem. Rev. 91, 651 (1991).

[12] R. Colle and O. Salvetti, Theoret. Chim. Acta 37, 329 (1975).

[13] B. Miehlich, A. Savin, H. Stoll, and H. Preuss, Chem. Phys. Letters 157, 200 (1989).

[14] GAUSSIAN 92, M. J. Frisch, G. W. Trucks, M. Head-Gordon, P. M. W. Gill, M. W. Wong, J. B. Foresman, B. G. Johnson, H. B. Schlegel, M. A. Robb, E. S. Replogle, R. Gomperts, J. L. Andres, K. Raghavachari, J. S. Binkley, C. Gonzalez, R. L. Martin, D. J. Fox, D. J. Defrees, J. Baker, J. J. P. Stewart, and J. A. Pople, Gaussian, Inc., Pittsburgh, PA, 1992.

[15] A. Veillard and E. Clementi, J. Chem. Phys. 49, 2415 (1968).

[16] R. K. Nesbet, T. L. Barr, and E. R. Davidson, Chem. Phys. Letters 4, 203 (1969).

[17] S. H. Vosko, L. Wilk, and M. Nusair, Can. J. Phys. 58, 1200 (1980).

[18] T. Ziegler and G. L. Gutsev, J. Comput. Chem. 13, 70 (1992).

[19] A. D. Becke, J. Chem. Phys. 88, 2547 (1988).

[20] J. C. Slater, Phys. Rev. 36, 57 (1930).

[21] A. D. McLaren, Math. Comput. 17, 361 (1963).

The Gradient Expansion Approximation for Exchange: A Physical Perspective

MARLINA SLAMET and VIRAHT SAHNI

*Department of Physics, Brooklyn College of the City University of New York
Brooklyn, New York 11210 and The Graduate School and University Center of the City University
of New York, 33 West 42nd Street, New York, New York 10036*

Abstract

In recent work, we have provided a rigorous physical interpretation for the exchange energy and potential (or functional derivative) as obtained within the local-density approximation via the Harbola–Sahni formulation of many-electron theory. In this article, we analyze the gradient-expansion approximation (GEA) for these properties from the same physical perspective. The source charge distribution in this approximation is the GEA Fermi hole to $O(\nabla^4)$. This charge distribution is unphysical, so that the resulting force field and work done cannot be defined in a physically meaningful manner, and the exchange energy is singular. Thus, when viewed from the perspective of a source charge, the existence of the gradient expansions for the potential and energy is questionable. We next discuss the conventional method of employing a screened-Coulomb interaction to eliminate the singularities due to the GEA source charge, and show that it leads to inconsistent results. These inconsistencies are also intrinsic to a proof of the inequivalence of the Harbola–Sahni and Kohn–Sham exchange potentials within the GEA. Thus, although the inequivalence of these potentials has been established by other analyses, this proof is shown not to be rigorous. Finally, we demonstrate that when the physics of the GEA exchange source charge is corrected by the satisfaction of sum rules, the modified charge distribution then leads to a well-behaved local exchange potential and exchange energy density, and to a finite exchange energy. The consequences of our analysis on the gradient expansions for the correlation and exchange-correlation potential and energy are also noted. © 1992 John Wiley & Sons, Inc.

Introduction

In Hohenberg–Kohn–Sham density-functional theory [1,2], all the many-body effects, including those of the correlation contribution to the kinetic energy, are incorporated in the exchange-correlation energy functional of the density. The corresponding local many-body potential seen by the noninteracting quasiparticles is derived by application of the variational principle for the energy to be the functional derivative of this energy functional. Thus, the relationship between the energy and potential in this formalism is mathematical. The simplest and most commonly employed of the approximations to the exchange-correlation energy functional is that of the local-density approximation (LDA). In the LDA, each point of the non-uniform electronic system is treated as if it were homogeneous, but with a density corresponding to the local value at that point. Since the exchange energy per electron

for the homogeneous electron gas is known, the exchange component of the LDA energy functional of the density and its functional derivative are both known also.

The mathematical framework of density-functional theory has recently been provided a physical interpretation in the work of Harbola and Sahni [3,4]. Accordingly, the exchange-correlation potential and energy are unified physically in that both properties are described to arise from the same source charge distribution. This source charge is the Fermi–Coulomb hole which represents the effects of Pauli and Coulomb correlations between the electrons. As such, both the many-body potential and energy are derived as a consequence of the Coulomb interaction between the electron and the Fermi–Coulomb hole charge. Based on this formulation of many-electron theory, we have in recent work [5] provided a rigorous physical interpretation for the exchange (Pauli-correlated) component of the potential and energy in the LDA by identifying the corresponding source charge distribution. As a consequence, we have also explained why the functional derivative of the LDA exchange energy functional is in fact a *bona fide* potential in that it is path independent. The LDA exchange energy functional and its functional derivative are, of course, the leading terms in the *a priori* gradient-expansion approximation [1,2,6] (GEA) for these properties. The fact that the leading terms of these expansions can be rigorously interpreted indicates that it is meaningful to examine the GEA for exchange from the same physical perspective. In this article, we therefore analyze the exchange energy and potential in the GEA from the viewpoint of the Harbola–Sahni interpretation.

In the Harbola–Sahni formulation, the Fermi hole, which embodies the correlations between electrons due to the Pauli exclusion principle, constitutes the source charge distribution for the local exchange potential and the exchange energy. The Fermi hole $\rho_x(\mathbf{r}, \mathbf{r}')$ at $\mathbf{r}'$ for an electron at $\mathbf{r}$ is derived in terms of the orbitals $\phi_i(\mathbf{r})$ of the Slater determinant to be $\rho_x(\mathbf{r}, \mathbf{r}') = |\gamma(\mathbf{r}, \mathbf{r}')|^2/2\rho(\mathbf{r})$, where $\gamma(\mathbf{r}, \mathbf{r}') = \Sigma_i \phi_i^*(\mathbf{r})\phi_i(\mathbf{r}')$ is the single particle density matrix and where the density $\rho(\mathbf{r}) = \gamma(\mathbf{r}, \mathbf{r})$. The Fermi hole satisfies the physical constraints of charge neutrality $\int \rho_x(\mathbf{r}, \mathbf{r}') d\mathbf{r}' = 1$, positivity $\rho_x(\mathbf{r}, \mathbf{r}') \geq 0$, and value at electron position $\rho_x(\mathbf{r}, \mathbf{r}) = \rho(\mathbf{r})/2$. The source charge gives rise to an electric field, which is

$$\mathcal{E}_x(\mathbf{r}) = \int \rho_x(\mathbf{r}, \mathbf{r}') \frac{(\mathbf{r} - \mathbf{r}')}{|\mathbf{r} - \mathbf{r}'|^3} d\mathbf{r}' . \tag{1}$$

so that the local exchange potential $W_x(\mathbf{r})$ is the work done to bring an electron from infinity to its final position at $\mathbf{r}$ against this force field:

$$W_x(\mathbf{r}) = - \int_\infty^\mathbf{r} \mathcal{E}_x(\mathbf{r}') \cdot d\mathbf{l}' . \tag{2}$$

The exchange energy, E_x, in turn, is the energy of interaction between the electron and the source charge, and thus

$$E_x = \frac{1}{2} \int \int \frac{\rho(\mathbf{r})\rho_x(\mathbf{r}, \mathbf{r}')}{|\mathbf{r} - \mathbf{r}'|} d\mathbf{r} \, d\mathbf{r}' . \tag{3}$$

The potential, $W_x(r)$, is well-defined in that it is path-independent for symmetrical systems such as jellium metal surfaces [7] and spherically symmetric atoms [8], or open-shell atoms [9] in the central field approximation. Equivalently, for these systems, the curl of the electric field vanishes. There is as yet no rigorous proof that this is the case for nonsymmetrical density systems. However, if for such systems the curl of the field does not vanish [10], an accurate local exchange potential can be obtained [3,4,6,11] from the irrotational component of the field, since it has been shown [12] that the solenoidal component is negligible.

The GEA for exchange to $O(\nabla^2)$ was originally proposed on dimensional grounds by Herman et al [13]. The GEA exchange energy functional and its functional derivative are given as

$$E_x^{GEA}[\rho] = \int d\mathbf{r}\, \epsilon_x\{\rho(\mathbf{r})\}\rho(\mathbf{r}) + C_x \int d\mathbf{r}\, |\nabla\rho(\mathbf{r})|^2/\rho^{4/3}(\mathbf{r}) \qquad (4)$$

and

$$\mu_x^{GEA}[\rho] = \frac{\delta E_x^{GEA}[\rho]}{\delta\rho} = \frac{4}{3}\epsilon_x\{\rho(\mathbf{r})\} + C_x\left(\frac{4}{3}\frac{|\nabla\rho(\mathbf{r})|^2}{\rho^{7/3}(\mathbf{r})} - 2\frac{\nabla^2\rho(\mathbf{r})}{\rho^{4/3}(\mathbf{r})}\right). \qquad (5)$$

where $\epsilon_x = -3k_F/4\pi$ is the exchange energy per electron for the homogeneous system with $k_F(\mathbf{r}) = [3\pi^2\rho(\mathbf{r})]^{1/3}$ being the local value of the Fermi momentum. The leading terms of these expansions correspond to the LDA exchange energy functional and functional derivative. The coefficient, C_x, of the gradient correction term was originally determined variationally by these authors. In order to understand our analysis of these gradient expansions for the exchange energy and functional derivative from the unifying perspective of a source charge distribution, we first describe how the leading LDA terms are similarly explained.

Just as with the exchange energy, the single-particle density matrix and consequently the Fermi hole can also be expanded [2,14,15] in a series of the gradients of the density. This gradient expansion of the Fermi hole $\rho_x^{(i)}(\mathbf{r}, \mathbf{r}')$, where the superscript (i) refers [16] to the order of the gradient, has at present been derived [17] up to terms of $O(\nabla^3)$. An analysis of the Fermi holes of this expansion to each order up to $O(\nabla^3)$, as applied to atoms, has also been performed [18]. We refer the reader to Refs. 17 and 18 for the expressions of this expansion.

Now in the LDA for exchange, the source charge distribution [5] is $\rho_x^{(1)}(\mathbf{r}, \mathbf{r}')$, the GEA Fermi hole to $O(\nabla)$. It satisfies the constraints of charge neutrality and value at the electron position, but not that of positivity. This source charge can be decomposed into a spherically symmetric component $\rho_x^{(0)}(\mathbf{r}, \mathbf{r}')$, (the LDA Fermi hole), and a nonspherically symmetric component which is comprised of a term of $O(\nabla)$. The electric field due to this source charge distribution is $\mathcal{E}_x^{(1)}(\mathbf{r}) = -\nabla k_F(\mathbf{r})/\pi$, and therefore, the work done against this force field is the same as the leading term of eq. (5) for the functional derivative. Since the $\nabla \times \mathcal{E}_x^{(1)}(\mathbf{r}) = 0$, we understand, from a physical viewpoint, why the functional derivative in the LDA is a potential. Furthermore, it is only the nonspherically symmetric component of this source charge that contributes to the electric field and thus to the work done.

In turn, the exchange energy is the energy of interaction of the electronic density with the source charge. However, it is only the spherically symmetric component of this source charge that contributes to the energy. The resulting expression is thus the same as the LDA term of the exchange energy functional of Eq. (4). We emphasize that the orbitals employed for the determination of the LDA exchange energy are not generated by the LDA Fermi hole $\rho_x^{(0)}(r, r')$, but by the nonspherically symmetric component of the source charge distribution. Thus, the Harbola–Sahni formulation provides a rigorous physical interpretation for the exchange potential and energy in the LDA. Furthermore, the accuracy of properties derived within the LDA can now be explained by a study [5] of the source charge distribution as a function of electron position.

In the next section we analyze the potential and energy in the GEA for exchange from the physical perspective of a source charge distribution. Our analysis shows that, as a consequence of the unphysical [18] nature of the GEA source charge, the results for the force field, work done, and exchange energy are also unphysical, thereby raising the issue of the existence of the expansions for these properties. The conventional screened-Coulomb interaction method of eliminating the various singularities that arise due to the GEA source charge is discussed later in this study, and shown to lead to inconsistent results. These inconsistencies are also intrinsic to a proof by Wang et al. [17] of the inequivalence of the Harbola–Sahni potential W_x, to the Kohn–Sham exchange potential, μ_x. Thus, although the inequivalence of these potentials has been established by other analyses [3,8,17], the proof by these authors is shown not to be rigorous. We will also demonstrate that when the physics of the GEA exchange source charge distribution is corrected [19] by the satisfaction of sum rules, the modified charge distribution then gives rise to a well-behaved local exchange potential and exchange energy density, and to a finite exchange energy. Finally, we summarize our conclusions and consequences of our analysis.

The Gradient Expansion Approximation From a Source Charge Perspective

The first step in the description of the GEA for exchange to $O(\nabla^2)$ from the Harbola–Sahni perspective is the identification of the corresponding source charge distribution. Since the source charge in the LDA is the GEA Fermi hole to $O(\nabla)$, and the fact that only odd-order terms [17] contribute to the electric field and work done, implies that the source charge in this case is $\rho_x^{(3)}(r, r')$, the GEA Fermi hole to $O(\nabla^3)$. In contrast to the LDA source charge, however, this charge distribution does not satisfy the constraint of charge neutrality. In fact, the total charge of this distribution is infinite [18]. In addition, it violates the constraint of positivity by possessing growing oscillations [17,18] in the region away from the electron position. The only constraint it does satisfy is that at the electron position. To see the singular nature of the GEA source charge distribution, Figure 1 plots the cross-section in the electron-nucleus plane of $\rho_x^{(3)}(r, r')$ for the neon atom employing analytical Hartree–Fock wave functions [20]. The electron position considered, as indicated by the arrow, is at $r = 0.307$ a.u., which corresponds to the intershell minimum of the
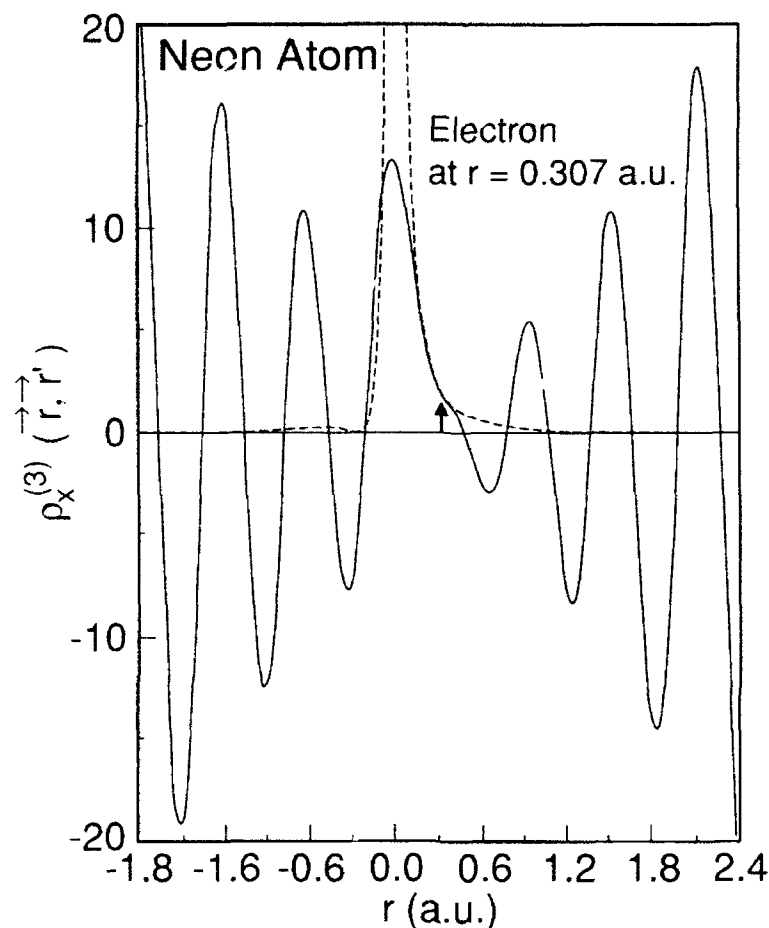
Figure 1.   The GEA source charge distribution, $\rho_x^{(3)}(\mathbf{r}, \mathbf{r}')$, as applied to the neon atom
for an electron at $r = 0.307$ a.u. The exact Fermi hole is shown (dashed line).

radial probability density. The same cross-section for the exact Fermi hole is also
plotted as the dashed curve. It is evident from the figure that, in contrast to the
exact Fermi hole which is localized about the nucleus, the GEA source charge is
spread throughout space with increasing amplitude of its oscillations which begin
even within the atom. This same behavior of the source charge occurs [18] for all
electron positions. The concept of an electric field due to such an unphysical charge
distribution is thus meaningless, and consequently, the work done is undefined.
Further, we note that it is the terms of $O(\nabla^3)$ of the source charge which cause this
to occur since, as noted earlier, the term of $O(\nabla)$ does lead to a finite electric field
and well-defined potential.

The substitution of the GEA source charge (see Fig. 1) into Eq. (3) also clearly shows that the exchange energy is singular. To see how this singularity in fact comes about, we consider the Slater potential defined as [21]:

$$
\Gamma_x(r) = \int \frac{\rho_x(r, r')}{|r - r'|} dr',
$$

(6)

which is, equivalently, the exchange energy density. As in the LDA, it is only the even-order terms of the expansion Fermi hole that contribute to the Slater potential and exchange energy. Thus, it is $\rho_x^{(2)}(r, r')$, the component of the GEA source charge to $O(\nabla^2)$, that causes the singularity, since the total charge of this distribution is infinite [18]. In Figure 2, we plot the component $\rho_x^{(2)}(r, r')$ of the source charge for the same electron position as in Figure 1. The singularity in the energy density and energy can now be seen to arise from the undamped oscillations of this component of the source charge which also extends throughout space. (Note that the charge in Fig. 2 is plotted up to 7 a.u. from the nucleus.) The singularity in the exchange energy is thus consistent with the fact that the corresponding potential is not well-defined.

The above conclusions with regard to the GEA, based on the perspective of a source charge distribution, are also consistent with those of density-functional theory.
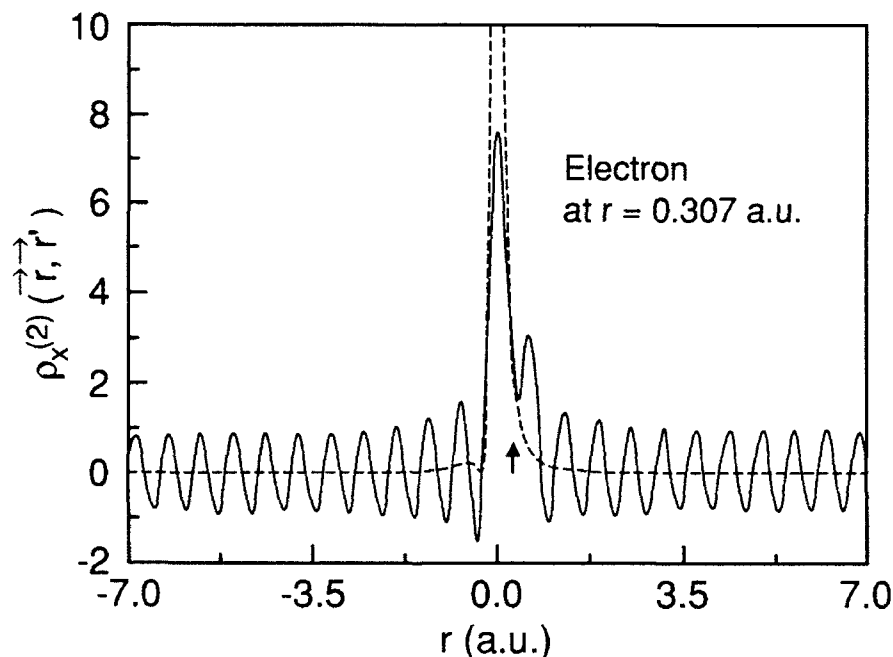
Figure 2.   The component $\rho_x^{(2)}(r, r')$ to $O(\nabla^2)$ of the GEA source charge distribution for the same electron position as in Figure 1. The exact Fermi hole is shown (dashed line).

In density-functional theory one begins with the approximate energy functional and obtains the potential as its functional derivative. The exchange energy in the GEA to $O(\nabla^2)$ is the energy of interaction between the electronic density and the gradient expansion Fermi hole $\rho_x^{(2)}(\mathbf{r}, \mathbf{r}')$ to $O(\nabla^2)$. This functional, as discussed above, is singular. Therefore, its functional derivative has no physical meaning.

If it is *assumed* that the GEA exchange energy functional of the density, as defined by eq. (4), exists, then it and its functional derivative can be employed in the self-consistent Kohn–Sham scheme. { We note that the functional derivative of Eq. (5) is singular [13] for small and large electron positions, and therefore, convergence factors have to be introduced [13] in the self-consistent procedure.} However, when viewed from the perspective of a charge which gives rise to a force field, a potential, and an energy, we see that the unphysical source charge calls into question the existence of such expansions for these properties.

Elimination of Singularities via the Screened-Coulomb Interaction

One approach [14,22] to the elimination of singularities in the properties determined within the GEA for exchange is to introduce a convergence factor or equivalently to perform calculations for the screened-Coulomb interaction $\exp(-\lambda r)/r$. This modification of the Hamiltonian eliminates the effects of the growing oscillations of the GEA source charge away from the electron. Thus, the electric field [17], work done, Slater potential [17], exchange energy [18,23], and its functional derivative [18], as derived from $\rho_x^{(3)}(\mathbf{r}, \mathbf{r}')$, are now all finite.

In the limit of bare-Coulomb interaction as the screening parameter λ vanishes, the electric field is singular [17] as $\ln \lambda$. This result is consistent with the conclusions of the previous section, in which the undefined nature of the electric field and work done for bare-Coulomb interaction was arrived at by an examination of the GEA source charge distribution itself. In other words, the limit of the electric field for screened-Coulomb interaction, as λ vanishes, is the same as the electric field obtained directly for bare-Coulomb interaction.

The behavior of the GEA exchange energy functional in the limiting procedure is, however, mathematically inconsistent. The limit of the exchange energy as λ vanishes is not the same as the energy for bare-Coulomb interaction. To see this, we note that the Slater potential $V_S^{\lambda,(3)}(\mathbf{r})$ for screened-Coulomb interaction derived from the source charge distribution $\rho_x^{(3)}(\mathbf{r}, \mathbf{r}')$ is also singular [17] as $\ln \lambda$ in the limit as λ vanishes. This result is consistent with the conclusions of the previous section in which the Slater potential for bare-Coulomb interaction was shown to be singular. However,

$$\lim_{\lambda \to 0} E_x^{\lambda,\text{GEA}}[\rho] = \lim_{\lambda \to 0} \frac{1}{2} \int \rho(\mathbf{r}) \, V_S^{\lambda,(3)}(\mathbf{r}) d\mathbf{r} \qquad (7)$$

is finite, and reduces [14,23] to Eq. (4) with coefficient $C_x = C_x^{\text{Sham}}$ corresponding to that of Sham [22]. Therefore, it is not equal to the energy of interaction between the density and the source charge, $\rho_x^{(3)}(\mathbf{r}, \mathbf{r}')$, which is singular (see previous section), nor is it equal to $(1/2) \int \rho(\mathbf{r})[\lim_{\lambda \to 0} V_S^{\lambda,(3)}(\mathbf{r})] d\mathbf{r}$, which is also singular.

Thus, we see that the method of employing a screened-Coulomb interaction to overcome the singularities leads to inconsistent results for the various properties. It also leads to an incorrect value for the coefficient C_χ. On the assumption that the GEA-exchange energy functional exists, it is now accepted that the correct [6,24] coefficient is $C_\chi = (10/7) C_\chi^{Sham}$. We note, however, that a recent temperature-dependent perturbation theory calculation [2] leads, in the zero temperature limit, to a result that is $C_\chi = (24/7) C_\chi^{Sham}$.

The inconsistencies of the screened-Coulomb approach to the elimination of the singularities in the GEA for exchange also bear on the proof of Wang et al. [17] that the work done, W_χ, is not equivalent to the Kohn–Sham potential, μ_χ, the functional derivative of the exchange energy functional. Their proof is for slowly varying densities, so it is assumed that the exchange energy can be expanded in a series of the gradients of the density. The authors then employ the fact that, whereas the electric field due to the source charge, $\rho_\chi^{(3)}(\mathbf{r}, \mathbf{r}')$, for screened-Coulomb interaction is singular, as $\ln \lambda$ in the limit as λ vanishes, the expression for the negative gradient $-\nabla \mu_\chi^{GEA}$ is finite for bare-Coulomb interaction. They conclude, therefore, that the potentials W_χ and μ_χ are inequivalent. However, as we have seen in the previous section, the potential W_χ for bare-Coulomb interaction cannot be defined for the GEA source charge. Wang et al. have in effect calculated the electric field due to an unphysical charge distribution (see Fig. 1), and consequently, correctly arrived at an unphysical result. Furthermore, the finiteness of $-\nabla \mu_\chi^{GEA}$ is based on the assumption that the GEA exchange energy functional exists. However, as also discussed previously, when considered as the energy of interaction between an electron and the source charge, the GEA exchange energy functional is singular. As such, its functional derivative is not well-behaved, and therefore has no physical meaning. Thus, when considered from a physical viewpoint, this proof of the inequivalence of W_χ to μ_χ is inconsistent. Furthermore, the fact that both the potentials, W_χ and μ_χ, are not well-defined within the GEA makes a comparison between them not meaningful.

The inequivalence of the potentials, W_χ and μ_χ, has, however, been established as follows. Presently there are two definitions of the exchange potential, μ_χ, of exchange-only density-functional theory. The first definition [25] states that it is the difference between the local effective potential which minimizes the expectation value of the Hamiltonian taken with respect to a Slater determinant of the orbitals generated by the effective potential and the Hartree potential. The effective potential and the resulting Kohn–Sham exchange potential μ_χ^{OPM} are determined by the optimized potential method (OPM) [26]. The orbitals and the density of the OPM differ [3,8,17] from those of Hartree–Fock theory, and consequently, the total ground-state energies are an upperbound to the Hartree–Fock energies. The W_χ and μ_χ^{OPM} potentials are essentially equivalent [3] throughout space except in the intershell regions of atoms, so that the total ground-state energies differ [8,9] by only a few parts per million, with the results of the W_χ potential lying above those due to the optimized potential. According to the second definition (see sections 3.4 and 6.2 of Ref. 2) there exists an (as yet unknown) energy density functional, $E^{HF}[\rho]$ (and its functional derivative μ_χ^{HF}), which achieves its minimum value at

the Hartree–Fock ground-state energy at the Hartree–Fock density. Thus, it is clear that the Harbola–Sahni potential, W_x, corresponds to neither μ^{OPM}_x nor μ^{HF}_x.

Finally, we note that the analytical expressions for the force field $\mathcal{E}_x^{WDA}(r)$ and the negative gradient $-\nabla \mu_x^{WDA}$, due to the source charge $\rho_x^{WDA}(r, r')$ for finite screening, are different. (Numerically, however, the two expressions for fixed values of the screening parameter, λ, are practically indistinguishable throughout space for atoms.) Thus, the corresponding potentials are also different. However, although for finite screening one obtains convergent results for the various properties, it is important to note that the description of the physics is still incorrect since the source charge distribution $\rho_x^{WDA}(r, r')$ still violates the constraint of charge neutrality. Furthermore, except for electron positions in the deep interior of atoms, there is elsewhere no value of the parameter λ which can ensure this constraint. Thus, all that the convergence factor does is to lead to closed-form analytical expressions, but it cannot correct the erroneous description of Pauli correlations within the GEA.

Elimination of Singularities by Modification of Source Charge

As we have seen in the previous section, the method of employing a screened-Coulomb interaction to eliminate the singularities in the GEA for exchange is inconsistent. In the bare-Coulomb interaction limit, the electric field is singular, but the exchange energy is finite—albeit with an erroneous coefficient for the gradient term. However, let us instead view the problem from the perspective of a single source charge distribution giving rise to a local potential and energy. The cause of the singularities is the GEA source charge $\rho_x^{(3)}(r, r')$ of $O(\nabla^3)$. Thus, in order to obtain finite and well-behaved results for the force field, work done, and exchange energy, it is the unphysical behavior of this source charge that must be corrected. An approach to this, for example, could be the generalized-gradient-expansion approximation (GGA) method of Perdew [15], in which the conditions of positivity and charge neutrality are imposed [19] on this distribution, thereby ensuring that it satisfies all the constraints of the exact Fermi hole. The work done and exchange energy could then be determined from this modified but more physically accurate charge distribution. This idea can, of course, be generalized to also include the GEA Fermi holes to $O(\nabla)$ and $O(\nabla^2)$, since each modified GGA Fermi hole, whether of even or odd order in ∇, can contribute to both the force field and energy.

In Figure 3(b–d), we plot the potential W_x for the neon atom, employing analytical Hartree–Fock wave functions [20] for the GGA source charge distributions to $O(\nabla)$, $O(\nabla^2)$, and $O(\nabla^3)$, respectively. For completeness, Figure 3(a) plots the potential W_x due to the GEA hole to $O(\nabla)$, which is the LDA Kohn–Sham potential. For comparison, also plotted (dashed line) is the potential W_x due to the exact Fermi hole. Observe [Fig. 3(b–d)] that, as a result of the fact that the GGA source charges to each order are physically realistic, the corresponding potentials, W_x, due to them are all well-behaved. So are the corresponding Slater potentials plotted in Figure 4(b–d). The Slater LDA potential [21] is given in Fig 4(a). The Slater potential due to the exact Fermi hole is also plotted (dashed line) in each figure for comparison. The resulting GGA-exchange energies [19] to each order in ∇ are
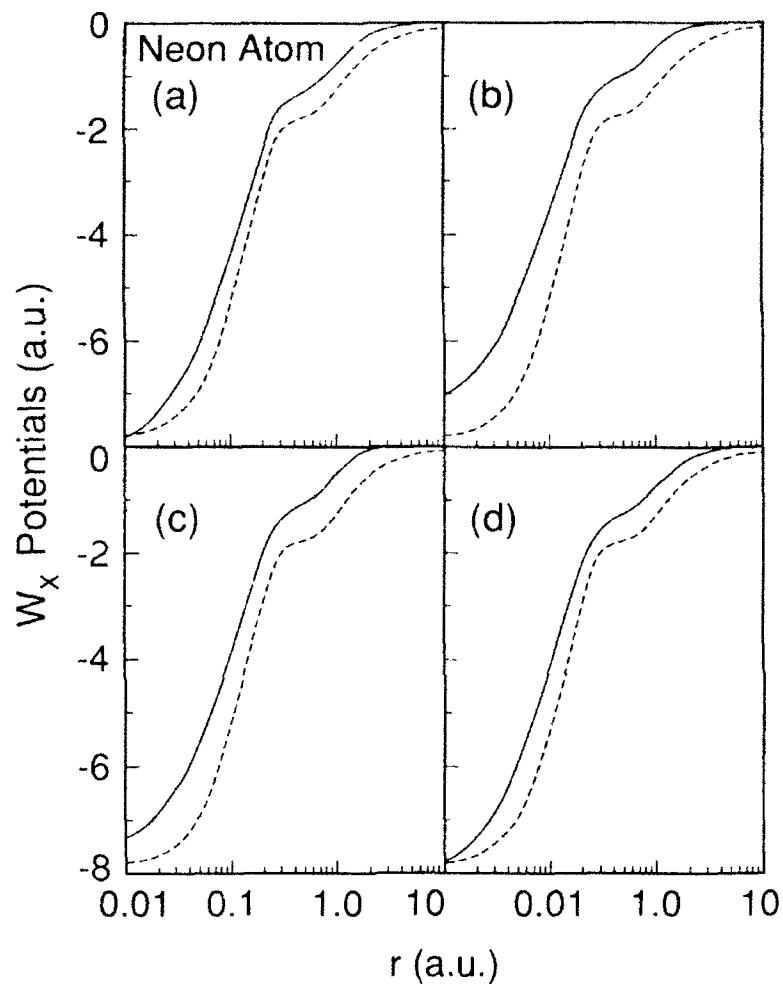
Figure 3.   The exchange potentials, W_x, for the neon atom as determined from the following approximate Fermi hole source charge distributions: (a) the GEA hole to $O(\nabla)$; and (b), (c), and (d), the GGA holes to $O(\nabla)$, $O(\nabla^2)$, and $O(\nabla^3)$. In each panel, the potential W_x due to the exact Fermi hole is plotted (dashed line).

also consequently finite and are -11.90, -12.24, and -12.47 a.u. in comparison to the exact W_x and Hartree–Fock theory values of -12.12 a.u. and -12.11 a.u., respectively. Thus, correcting the unphysical behavior of the GEA source charge leads to well-behaved W_x potentials and exchange energy densities and finite values for the exchange energy.

Conclusions

Since a rigorous physical interpretation for the LDA-exchange energy functional and its functional derivative is provided by the Harbola–Sahni formulation of many-
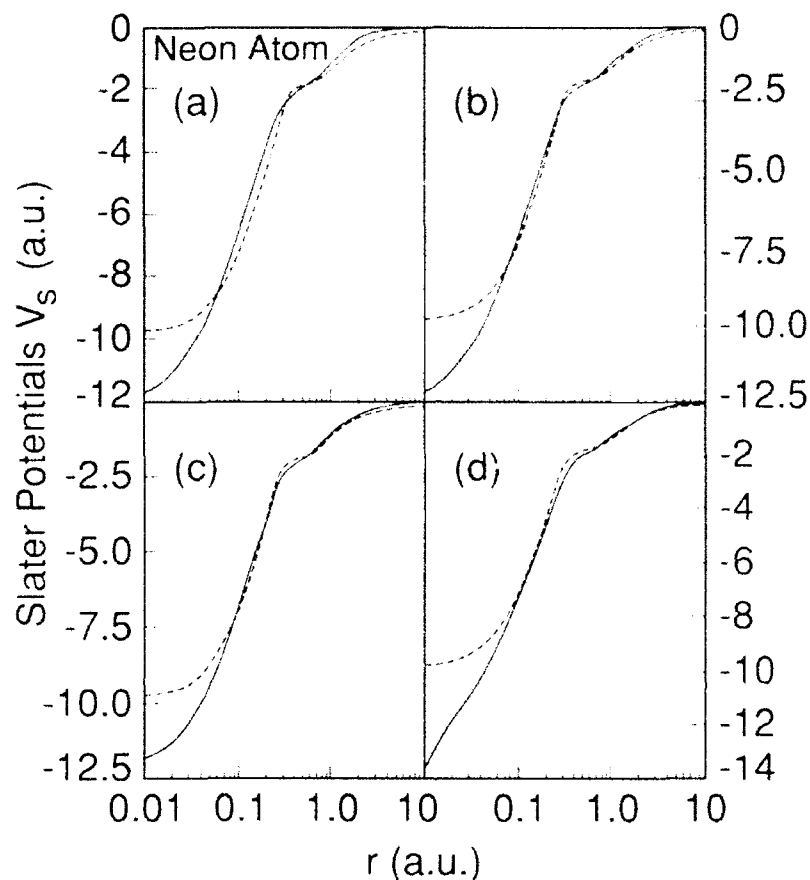
Figure 4. The Slater potentials V_s for the neon atom as determined from the following approximate Fermi hole source charge distributions: (a) the LDA hole, and (b), (c), and (d), the GGA holes to $O(\nabla)$, $O(\nabla^2)$, and $O(\nabla^3)$. In each panel, the Slater potential due to the exact Fermi hole is plotted (dashed line).

electron theory, we have examined the GGA for exchange to $O(\nabla^2)$ from the same physical perspective. In this approximation, the source charge distribution in which the correlations due to the Pauli exclusion principle are incorporated, is the GGA Fermi hole to $O(\nabla^2)$. As this charge distribution is unphysical, the work required to move an electron in its force field is undefined and the exchange energy is singular. Thus, when viewed from the perspective of a source charge, the existence of the expansions for the exchange potential and energy are questionable. The same conclusion can also be arrived at from the expression for the GGA-exchange energy functional written in terms of the Fermi hole to $O(\nabla^2)$. This functional is singular, and therefore, its functional derivative has no physical meaning. Thus, if the expansions for the exchange-correlation potential and energy are to exist, the singu-

larities in the separate expansions for exchange and correlation must cancel. More fundamentally, the unphysical components of the GEA Fermi hole source charge distribution must be canceled by those of the Coulomb hole charge.

Another consequence of viewing the GEA for exchange from a source charge perspective is that it shows the proof of the inequivalence (within this approximation) of the work, W_x, to the Kohn-Sham potential, μ_x, to be inconsistent. The proof is based on the use of an unphysical charge distribution so that the force field and work done cannot be defined in a physically meaningful manner. On the other hand, it is assumed that the energy due to this same charge is finite. These facts are physically inconsistent and thus the proof not rigorous. However, when this unphysical source charge distribution is modified, so as to make it more physically reasonable by the requirement of satisfaction of various sum rules, then the resulting force field and work done are well-defined and finite, as are the exchange energy density and exchange energy.

Acknowledgment

Bibliography

[1] P. Hohenberg and W. Kohn, Phys. Rev. 136, B864 (1964); W. Kohn and L. J. Sham, Phys. Rev. 140, A1133 (1965).
[2] R. M. Dreizler and E. K. U. Gross, Density Functional Theory (Springer-Verlag, Berlin, 1990); R. G. Parr and W. Yang, Density Functional Theory of Atoms and Molecules (Oxford University Press, Oxford, 1989).
[3] M. K. Harbola and V. Sahni, Phys. Rev. Lett. 62, 489 (1989); V. Sahni and M. K. Harbola, Int. J. Quant. Chem. Symp. 24, 569 (1990).
[4] M. K. Harbola, M. Slamet, and V. Sahni, Phys. Lett. A 157, 60 (1991).
[5] M. Slamet and V. Sahni, Phys. Rev. B 45, 4013 (1992).
[6] L. Kleinman and V. Sahni, Adv. Quant. Chem. 21, 201 (1990).
[7] M. K. Harbola and V. Sahni, Phys. Rev. B 39, 10437 (1989); V. Sahni, Surf. Sci. 213, 226 (1989)
[8] Y. Li, M. K. Harbola, J. B. Krieger, and V. Sahni, Phys. Rev. A 40, 6084 (1989).
[9] V. Sahni, Y. Li, and M. K. Harbola, Phys. Rev. A 45, 1434 (1992).
[10] H. Ou-Yang and M. Levy, Phys. Rev. A 41, 4038 (1990); M. Rasolt and D. J. W. Geldart, Phys. Rev. Lett. 65, 276 (1990); M. K. Harbola and V. Sahni, Phys. Rev. Lett. 65, 277 (1990).
[11] M. K. Harbola, Ph.D. Thesis, City University of New York, November, 1989.
[12] M. Slamet, M. K. Harbola, and V. Sahni (manuscript in preparation).
[13] F. Herman, J. P. Van Dyke, and I. B. Ortenburger, Phys. Rev. Lett. 22, 807 (1970); F. Herman, I. B. Ortenburger, and J. P. Van Dyke, Int. J. Quant. Chem. 3S, 827 (1970).
[14] E. K. U. Gross and R. M. Dreizler, Z. Phys. A 302, 103 (1981).
[15] J. P. Perdew, Phys. Rev. Lett. 55, 1665 (1985).
[16] Thus, for example: $\rho_x^{(1)}(r, r') = \rho_x^{(0)}(r, r') + $ term of $O(\nabla)$, etc.
[17] Y. Wang, J. P. Perdew, J. A. Chevary, L. D. Macdonald, and S. H. Vosko, Phys. Rev. A 41, 78 (1990).
[18] M. Slamet and V. Sahni, Int. J. Quant. Chem. Symp. 25, 235 (1991).
[19] M. Slamet and V. Sahni, Phys. Rev. B 44, 10921 (1991).
[20] E. Clementi and C. Roetti, Atom. Data Nucl. Data Tables 14, 177 (1974).
[21] J. C. Slater, Phys. Rev. 81, 385 (1951).

[22] L. J. Sham, in *Computational Methods in Band Theory*, P. Marcus, J. F. Janak, and A. R. Williams, Eds. (Plenum, New York, 1971).

[23] A.-R. E. Mohammed and V. Sahni, Phys. Rev. B **29**, 3687 (1984).

[24] L. Kleinman and S. Lee, Phys. Rev. B **37**, 4634 (1988); J. A. Chevary and S. H. Vosko, Phys. Rev. B **42**, 5320 (1990); E. Engel and S. H. Vosko, Phys. Rev. B **42**, 4940 (1990).

[25] V. Sahni, J. Gruenebaum, and J. P. Perdew, Phys. Rev. B **26**, 4371 (1982); V. Sahni and M. Levy, Phys. Rev. B **33**, 3869 (1986).

[26] R. T. Sharp and G. K. Horton, Phys. Rev. **90**, 3876 (1953); J. D. Talman and W. F. Shadwick, Phys. Rev. A **14**, 36 (1976).

Nonlocal Exchange and Kinetic-Energy Density Functionals for Electronic Systems

M. D. GLOSSMAN, A. RUBIO, L. C. BALBÁS, and J. A. ALONSO

Departamento de Física Teórica, Universidad de Valladolid, E-47011 Valladolid, Spain

Abstract

The nonlocal weighted density approximation (WDA) to the exchange and kinetic-energy functionals of many-electron systems proposed several years ago by Alonso and Girifalco is used to compute, within the framework of density functional theory, the ground-state electronic density and total energy of noble gas atoms and of neutral *jellium*-like sodium clusters containing up to 500 atoms. These results are compared with analogous calculations using the well known Thomas-Fermi-Weizsäcker-Dirac (TFWD) approximations for the kinetic (TFW) and exchange (D) energy density functionals. An outstanding improvement of the total and exchange energies, of the density at the nucleus and of the $\langle r^{-1} \rangle$ expectation values is obtained for atoms within the WDA scheme. For sodium clusters we notice a sizeable contribution of the nonlocal effects to the total energy and to the density profiles. In the limit of very large clusters these effects should affect the surface energy of the bulk metal. © 1992 John Wiley & Sons, Inc.

Introduction

The density-functional theory (DFT) of Hohenberg and Kohn [1] allows one to study the ground-state (g.s.) properties of electronic systems in terms of the electronic density $\rho(\vec{r})$ instead of the many-particle wave function. The basic theorem of DFT states that the total energy of a many-electron system can be written as a functional $E[\rho(\vec{r})]$ of the total electronic density, and this energy is a minimum for the exact g.s. density [1]. Consequently, the minimization of $E[\rho(\vec{r})]$ with respect to the density, subject to the charge normalization condition, leads to the g.s. density and energy of the system, which is achieved by solving the Euler equation

$$\mu = \frac{\delta E[\rho]}{\delta\rho(\vec{r})} \tag{1}$$

where μ is the chemical potential.

The functional $E[\rho]$ can be written as the sum of several terms (in a.u.) [1,2]

$$E[\rho] = \frac{1}{2} \int \int \frac{\rho(\vec{r})\rho(\vec{r}')}{|\vec{r} - \vec{r}'|} \, d\vec{r} \, d\vec{r}' + \int \rho(\vec{r}) V_i(\vec{r}) \, d\vec{r} + F[\rho]. \tag{2}$$

In this equation, the first two terms represent the Hartree energy, which includes the Coulomb interaction between independent electrons, and the interaction of the electrons with the external potential, $V_i(\vec{r})$, created by the ions. The functional

$F[\rho]$ in Eq. (2) is unknown and one must resort to some approximations. $F[\rho]$ is usually written as the sum

$$F[\rho] = T[\rho] + E_{xc}[\rho] \tag{3}$$

where $T[\rho]$ is defined as the kinetic-energy functional for a system of noninteracting electrons and $E_{xc}[\rho]$, called the exchange-correlation (xc) energy, describes the effects due to the Pauli principle (exchange energy) and to the remaining many-body effects not included in the Hartree and kinetic-energy functionals (correlation energy). One can split further $E_{xc}[\rho]$ in $E_x[\rho] + E_c[\rho]$. By neglecting the correlation energy, $E_c[\rho]$, one is constrained to the independent electron model, that is to say, one is working at the Hartree–Fock level.

The simplest approximation to $F[\rho]$ of Eq. (2) is the so-called local-density approximation (LDA) [2,3] and leads to the well-known Thomas–Fermi term $T_0[\rho]$ for the kinetic energy [4] and to the Dirac term $K_0[\rho]$ for the exchange energy [5]. The corresponding functional, known as Thomas–Fermi–Dirac (TFD) energy, although somewhat successful in computing global properties of the system, is locally inaccurate. So, the next step has been to improve the local behavior of the energy functional by expanding the kinetic and exchange energy terms in gradients of the density $\rho(\vec{r})$ [3]. Although this represents an improvement, it has serious drawbacks. The number of terms in this gradient expansion (GE) is unknown and, in practice, one is able to deal with only a small number of terms. We should mention that in order to achieve some particular results, the coefficients in front of each term in the gradient expansion have been sometimes empirically fitted [6] but, evidently, this is not a satisfactory procedure.

In order to avoid these problems, different alternatives have been developed. One of them is the nonlocal weighted-density approximation (WDA), developed independently by Alonso and Girifalco [7], and Gunnarsson, Jonson, and Lundqvist [8]. Starting from the exact expression for the exchange and correlation energy, and using a reasonable approximation for the exchange-correlation hole, the WDA scheme arrives at a nonlocal functional for the exchange-correlation energy which avoids the use of gradient expansions. Moreover, if correlation is neglected in this theory, Alonso and Girifalco have shown that a WDA approximation can also be derived for the kinetic energy, which allows for a unified nonlocal treatment of the kinetic and exchange energies [7].

In this article we present an exact (numerical) solution of the Euler equation associated with the WDA model for the kinetic and exchange energy functionals. In this way, we have calculated electron densities, total energies, and their different components for neutral noble gas atoms. A comparison has been done with the results obtained through other theoretical approximations, showing that the WDA model is quantitatively more accurate than the usual gradient expansion functionals, in addition to be free of parameters.

We have also used the WDA to calculate the g.s. total energies and densities of neutral jellium-like sodium clusters, Na$_N$, containing up to $N \leq 500$ atoms. This is a first step in order to determine the manner that the total energy per atom and other electronic properties of metallic clusters evolve, as the cluster grows, to the

corresponding properties of the bulk metal. By using the WDA method we attempt to assess, without the ambiguity of TFD(λ)W methods (λ indicates here the value of the coefficient in the gradient term of the kinetic energy), the kinetic and exchange-correlation contributions to the evolution of, for example, the ionization potential of the clusters towards the work function of the bulk metal as the cluster size increases [9–13]. In this report, however, we restrict ourselves to study the evolution of total energies and densities in comparison with other types of calculations.

Nonlocal Weighted Density Approximation

The exchange-correlation energy of a system of electrons can be written exactly in the following way [8]

$$E_{xc}[\rho] = \frac{1}{2} \int \rho(\vec{r}) \, d\vec{r} \int \frac{\rho(\vec{r}')G(\vec{r}, \vec{r}')}{|\vec{r} - \vec{r}'|} \, d\vec{r}' \tag{4}$$

where $G(\vec{r}, \vec{r}')$ is the pair correlation function. This expression can be interpreted as the Coulomb interaction between two charge distributions: the charge density $\rho(\vec{r})$ and the exchange correlation hole charge $\rho_{xc}(\vec{r}, \vec{r}') = \rho(\vec{r}')G(\vec{r}, \vec{r}')$ which surrounds an electron at $\vec{r}$. The functional derivative of $E_{xc}[\rho]$ with respect to the density, which is needed in the Euler equation (1), is called the exchange-correlation potential

$$V_{xc}(\vec{r}) = \frac{\delta E_{xc}[\rho]}{\delta\rho(\vec{r})} . \tag{5}$$

Since $G(\vec{r}, \vec{r}')$ is generally unknown, it is necessary to resort to some approximation to it. In the LDA the product $\rho(\vec{r}')G(\vec{r}, \vec{r}')$ in the second integral in Eq. (4) is replaced by $\rho(\vec{r})G_h[|\vec{r} - \vec{r}'|; \rho(\vec{r})]$, where $G_h[|\vec{r} - \vec{r}'|; \rho(\vec{r})]$ is the pair-correlation function in a homogeneous system with constant density equal to the local density $\rho(\vec{r})$. Considering only exchange effects, G_h is exactly known in analytical form,

$$G_h = -\frac{9}{2} \left(\frac{\sin y - y \cos y}{y^3} \right)^2; y = |\vec{r} - \vec{r}'|(3\pi^2\rho)^{1/3} . \tag{6}$$

this LDA approximation leading to the Dirac expression for the exchange energy $K_0[\rho]$ mentioned above. On the other hand, in the nonlocal weighted-density approximation (WDA), the correct factor $\rho(\vec{r}')$ is preserved in the second integral of Eq. (4) and $G(\vec{r}, \vec{r}')$ is approximated by $G_h[|\vec{r} - \vec{r}'|; \bar{\rho}(\vec{r})]$, where $G_h[|\vec{r} - \vec{r}'|; \bar{\rho}(\vec{r})]$ is again the pair-correlation function of a homogeneous system, but now characterized by an effective density $\bar{\rho}(\vec{r})$, evaluated at each point $\vec{r}$ by using the sum rule for the exchange-correlation hole charge:

$$\int \rho(\vec{r}')G_h[|\vec{r} - \vec{r}'|; \bar{\rho}(\vec{r})] \, d\vec{r}' = -1 . \tag{7}$$

With this ansatz, the exchange-correlation energy becomes:

$$E_x^{WDA}[\rho] = \frac{1}{2} \int \rho(\vec{r}) \, d\vec{r} \int \frac{\rho(\vec{r}')}{|\vec{r} - \vec{r}'|} \, G_{ic}[|\vec{r} - \vec{r}'|; \tilde{\rho}(\vec{r})] \, d\vec{r}', \qquad (8)$$

The WDA improves the asymptotic behavior of E_x, that is, E_x decays as $-1/2r$ at large r for a neutral atom, which differs from the exact behavior only in the constant $\frac{1}{2}$. This is an important improvement over the LDA, which shows an exponential decay. The constant $\frac{1}{2}$ is due to the fact that the WDA pair-correlation function does not fulfill the symmetry property of the exact pair-correlation function, that is, $G^{WDA}(\vec{r}, \vec{r}') \neq G^{WDA}(\vec{r}', \vec{r})$. This lack of symmetry is due to the dependence of G^{WDA} on $\tilde{\rho}(\vec{r})$.

As has been stated in the Introduction, one can also establish a WDA approximation for the kinetic energy. The key is a relation between the one and two particle density matrices in Hartree–Fock theory (see Ref. [7] for details). Although this relation is not universal, it is exact for some cases of practical interest, like systems with closed electronic shells. Using that relation and the WDA approximation for the pair-correlation function G (of course at the exchange-only, or Hartree–Fock, level) one arrives at the following approximate expression for the kinetic energy [7]

$$T^{WDA}[\rho] = \int t^{WDA}[\vec{r}; \rho] \, d\vec{r} \qquad (9)$$

where the kinetic-energy density is given by

$$t^{WDA}[\vec{r}; \rho] = C_k \rho \tilde{\rho}^{2/3} + \frac{1}{8} \frac{(\nabla \rho)^2}{\rho} - \frac{1}{4} \nabla^2 \rho \qquad (10)$$

with $C_k = (3/10)(3\pi^2)^{2/3}$. The first term is a nonlocal extension of the local Thomas–Fermi term $(C_k\rho^{5/3})$ and the second is the original Weizsäcker quantum correction [14].

It is interesting to recall that the Weizsäcker term, $T_W[\rho]$, without any other kinetic contribution, is the exact kinetic energy for one-electron systems. Also $T_W[\rho]$ should be exact for many-electron systems in the regions with very low electron density [15]. The gradient expansion of $T[\rho]$ yields $\lambda T_W[\rho]$ for the second-order gradient term, with $\lambda = 1/9$ [3]. A factor $\lambda = 1/5$ was found by Tomishima and Yonei [6] by fitting the energies of atoms to Hartree–Fock results [16].

Model and Computational Details

By considering the WDA energy functional derived above, the Euler equation becomes

$$\mu = V_r(\vec{r}) + \frac{1}{8} \frac{\nabla \rho \nabla \rho}{\rho^2} - \frac{1}{4} \frac{\nabla^2 \rho}{\rho}$$

$$+ C_k \left[\tilde{\rho}^{2/3} + \frac{2}{3} \int \rho(\vec{r}') \tilde{\rho}(\vec{r}')^{-1/3} \frac{\delta \tilde{\rho}(\vec{r}')}{\delta \rho(\vec{r})} \, d\vec{r}' \right] \qquad (11)$$

where

$$V_j(\vec{r}) = V_i(\vec{r}) + V_c(\vec{r}) + V_x(\vec{r}).\tag{12}$$

V_j is the total potential, sum of the external, electronic (Hartree) and exchange parts (notice that we have restricted ourselves to the exchange-only case, since our intention is to compare with Hartree–Fock results). Equation (11) must now be solved coupled with Poisson's equation which guarantees self-consistency between density and potential. Defining a function

$$g(\vec{r}) = \frac{3}{5}f(\vec{r}) + \frac{2}{5}\rho(\vec{r})^{-2/3}\int \rho(\vec{r}')\bar{\rho}(\vec{r}')^{-1/3}\frac{\delta\bar{\rho}(\vec{r}')}{\delta\rho(\vec{r})}d\vec{r}'\tag{13}$$

where $f(\vec{r}) = [\bar{\rho}(\vec{r})/\rho(\vec{r})]^{2/3}$, the resulting Euler equation closely resembles the form of the TFDW equation

$$\mu = V_j(\vec{r}) + \frac{1}{8}\frac{\nabla\rho\nabla\rho}{\rho^2} - \frac{1}{4}\frac{\nabla^2\rho}{\rho} + g(\vec{r})\frac{5}{3}C_k\rho^{2/3}.\tag{14}$$

In a former work by Deb and Ghosh [17], this equation was solved for noble gas atoms using a function $g(\vec{r})$ evaluated by means of Hartree–Fock densities [16] and the exchange potential $V_x(\vec{r})$ was treated in the LDA of Dirac.

In a recent work by us [18], Eq. (14) was self-consistently solved coupled with Poisson equation for several neutral atoms. However, in Ref. [18], we used the exponential approximation of Berkowitz [19] to the exact exchange pair-correlation function of Eq. (6), that is, $G_h(y) \approx -1/2e^{1/y^{1/5}}$. In the present work we have used the exact $G_h(y)$ of Eq. (6) and we have also employed a different numerical method to integrate Eq. (14). By putting $\psi(\vec{r}) = \rho^{1/2}(\vec{r})$ and

$$V_{eff}(\vec{r}) = V_j(\vec{r}) + g(\vec{r})\frac{5}{3}C_k\rho^{2/3}(\vec{r})\tag{15}$$

Eq. (14) can be viewed as a Schrödinger-like equation

$$\left[-\frac{1}{2}\nabla^2 + V_{eff}(\vec{r})\right]\psi(\vec{r}) = \mu\psi(\vec{r})\tag{16}$$

which we solve by the conventional self-consistent Kohn–Sham method for only one orbital normalized to Z electrons [20]. With the purpose of comparison we also solve in this work analogous equations corresponding to the following local TFD(λ)W functionals: $\lambda = 1/9$ (corresponding to the exact second-order gradient expansion of $T[\rho]$), $\lambda = 1/5$ (corresponding to the effective λ found by Tomishima and Yonei [6]) and $\lambda = 1$ (which contains the full Weizsäcker term like the WDA). In all these TFD(λ)W functionals the exchange energy is the original $K_0[\rho]$ Dirac term. Let us notice that our results for noble gas atoms are slightly different than the results quoted by Tomishima and Yonei [6] and by Yang [21], which used a different numerical procedure. We have used a logarithmic integration mesh up to 60 a.u. in the radial direction instead of the linear mesh in $r^{1/2}$ used in Refs. [6] and [21] and also in our previous work [18]. Because of this change, we think that

the present results (see the Results section) are more accurate than the previous ones in Refs. [6, 18, 21]: this comment affects, of course, also to the WDA results.

To solve the Euler equation corresponding to metallic clusters we have adopted a different numerical technique called the *imaginary step method* [22] with the boundary conditions $[\bar{r}\rho(\bar{r})]_{r=0} = [\bar{r}\rho(\bar{r})]_{r=\infty} = 0$.

Results

Neutral Atoms

The calculated total energies for noble gas atoms are shown in Table I together with those obtained through the TFD(λ)w model (see preceding section), and with Hartree–Fock results [16]. The results of the calculation by Engel and Dreizler [23], which included up to fourth-order gradient corrections to the kinetic energy are also shown in Table I under the entry $T_0 + T_2 + T_4$ (exchange was treated in these calculations at the local density, or K_0, level). It is clear from Table I that the WDA results are the closest ones to HF. We stress that the WDA functional is free from empirical parameters. Note also that the WDA method is exact, at the HF level, for two-electron systems like the He atom. In this case the weighted density $\bar{\rho}$ obtained from the sum rule [Eq. (7)] must be exactly zero, giving an exchange hole equal to $-1/2\rho(\bar{r}')$; the corresponding exchange energy balances in this way the electron self-interaction contained in the Hartree term. As a test of our numerical accuracy we have obtained from Eq. (7) values of $\bar{\rho}(\bar{r})$ lower than 10^{-7} a.u. for all $\bar{r}$. The WDA total energies of Table I are, to our knowledge, the most accurate ones ever obtained from direct minimization of an energy functional fully expressed in terms of the electron density. The average error with respect to HF is only 0.4 per cent.

As the virial theorem is well obeyed, the accuracy of the kinetic energies in the WDA approximation can be estimated from the accuracy of the total energies. On the other hand, exchange energies are compared in Table II. Again the WDA results show a better overall agreement with HF than the results from TFD(λ)w functionals. This can be ascribed to the better description of the WDA exchange potential compared with the local exchange potential from the Dirac term. The entry $K_0 + K_2$

TABLE I. Total ground-state energies of noble gas atoms (in a.u.) for several density functionals: WDA, TFD(λ)w, and $T_0 + T_2 + T_4$ (fourth-order gradient expansion [23]). Exact Hartree–Fock (HF) results are given as a reference.

Atom	HF	TFD(1/9)w	TFD(1/5)w	TFDw	WDA	$T_0 + T_2 + T_4$
He	-2.86	-3.22	-2.82	-1.48	-2.86	-2.96
Ne	-128.55	-139.88	-128.80	-85.73	-130.01	-133.74
Ar	-526.82	-561.80	-524.75	-374.15	-526.83	-542.12
Kr	-2752.05	-2896.93	-2744.16	-2095.43	-2754.79	-2819.12
Xe	-7232.13	-7495.22	-7208.54	-5695.87	-7261.80	-7383.55
Rn	-21866.8	—	—	-17823.32	-22099.06	-22256.3

Atom	HF	TFD(1/9)W	TFD(1/5)W	TFDW	WDA	$K_0 + K_2$
He	1.03	0.76	0.71	0.43	1.03	0.84
Ne	12.11	10.48	10.13	8.01	12.66	10.94
Ar	30.18	27.66	26.96	22.63	32.65	28.55
Kr	93.9	87.23	85.72	75.79	102.07	89.16
Xe	179.1	170.94	168.69	152.67	200.71	174.09
Rn	387.5	—	—	339.36	436.42	375.97

in Table II corresponds to a calculation by Engel and Dreizler [23] which in addition to the terms mentioned above in connection with Table I, also includes the second-order gradient term in the expansion of the exchange energy. These exchange energies become of comparable accuracy to the WDA energies for heavy atoms. Notice, however that the inclusion of K_2 slightly worsens the total energies obtained by only including K_0 [23].

A comparison of the radial electron density of the Ne atom for the different models is shown in Figure 1. As expected for these approximate models, the radial density profiles do not show the peaks that characterize shell structure as in the Hartree-Fock case (see however the WDA results for jellium-like sodium clusters below). In comparison with the TFD(λ)W models, the WDA density seems to be more compact. This statement also holds true for a comparison with the density of the TFD(1/5)W model, which is not plotted in the figure. Another test of the quality of the atomic density is provided by the calculation of its value at the site of the nucleus. The WDA results are given in Table III for different noble gas atoms together with the values obtained from Hartree-Fock and TFD(λ)W calculations. The densities obtained from TFD(λ)W functionals (λ = 1/9, λ = 1/5) drastically overestimate the HF values; this is well-known [23]. On the other hand, this behavior is greatly improved in the WDA approximation which is the only one that leads to realistic (that is, close to HF) values. Notice in this context that a kinetic functional containing the Weizsäcker term alone, Tw, reproduces the cusp at the position of nuclei [24]. The calculated WDA densities for noble gases obey the cusp condition within a factor of about 2/3, $[\rho'(0)/2Z\rho(0)]_{WDA} \sim 2/3$, whereas the TFD(λ)W functionals give too large factors. Another related test for the goodness of the atomic density is provided by the expectation value of r^{-1}. The calculated $\langle r^{-1} \rangle$ values for the WDA and TFD(λ)W functionals are compared with HF values in Table IV. We see again that the WDA method gives the best results.

Jellium-like Sodium Clusters

In the spherical jellium model [9], the ionic background in the cluster is considered as a uniform distribution of positive charge $\rho_+(\vec{r}) = \rho_+^0 \theta(r - R)$. The radius
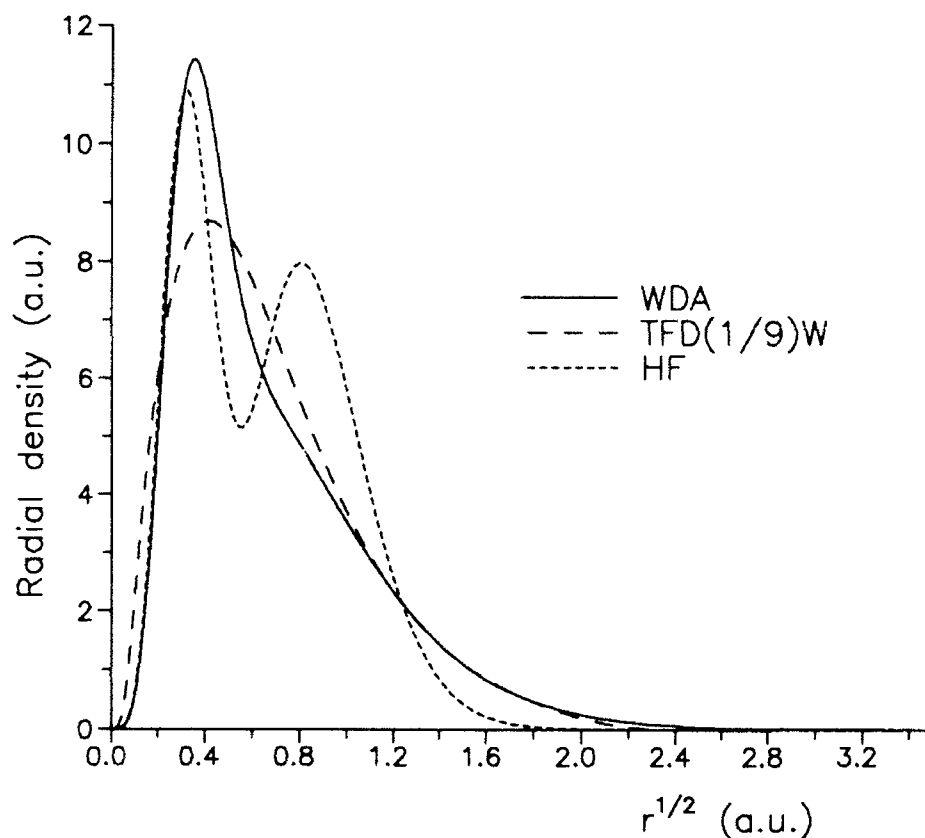
Figure 1.   Radial density $(4\pi r^2 \rho)$ of the Ne atom versus r^1 for the different models compared in this article.

R of the ionic background is linked to the number of atoms N by means of the relation $\frac{4}{3}\pi R^3 = N\Omega$, Ω being the volume per atom in the bulk metal, and ρ^0 is equal to Z/Ω, where Z is the valence ($Z = 1$ for Na, etc. . . .).

The external potential V_i created by this ionic distribution is

TABLE III.   Electron densities at the site of the nucleus for noble gas atoms $(\rho(0)/Z^3)$.

Atom	HF	TFD(1/9)W	TFD(1/5)W	TFDW	WDA
He	0.4495	6.2964	2.3976	0.1179	0.4496
Ne	0.6199	6.4374	2.5716	0.1693	0.5555
Ar	0.6584	6.4383	2.6154	0.1868	0.5769
Kr	0.6909	6.4485	2.6275	0.2042	0.5960
Xe	0.7063	6.4700	2.6334	0.2123	0.6025
Rn	0.7199	—	—	0.2197	0.6054

TABLE IV. $\langle r^{-1}\rangle$ expectation values for noble gas atoms (in a.u.) for the nonlocal WDA functional, as compared with TFD(λ)W and Hartree-Fock results [28].

Atom	HF	TFD(1/9)W	TFD(1/5)W	TFDW	WDA
He	3.37	3.65	3.23	1.75	3.38
Ne	31.11	33.00	30.70	21.38	30.84
Ar	69.72	73.79	69.57	51.72	69.60
Kr	182.85	190.26	181.63	143.76	182.56
Xe	317.88	328.44	317.60	259.18	321.30
Rn	604.39	—	—	506.22	613.28

$$V_i = -\frac{4\pi}{3} R^3 \rho_+^0 \begin{cases} \dfrac{r^2}{2R^3} - \dfrac{3}{2R} & \text{if } r \le R \\[2mm] -\dfrac{1}{r} & \text{otherwise .} \end{cases} \tag{17}$$

In our calculations for sodium clusters we include a local correlation energy functional derived by Wigner [25]

$$E_c[\rho] = -\int \frac{0.44\rho(\vec{r})}{7.8 + (4\pi\rho(\vec{r})/3)^{-1/3}} \, d\vec{r} \; . \tag{18}$$

We then solve the Euler equation 14 with $V_T(\vec{r}) = V_i(\vec{r}) + V_c(\vec{r}) + V_x(\vec{r}) + V_c(\vec{r})$, where $V_c(\vec{r})$ is given by Eq. (17) and $V_c(\vec{r}) = \delta E_c/\delta\rho$ is easily obtained from Eq. (18). Then we obtain the g.s. electronic energy $E[\rho]$ and density of the cluster. The total energy is $E_T = E[\rho] + E_{\text{ion-ion}}$, where $E_{\text{ion-ion}}$ is given by the self-energy of the positive background, which is fixed for a given metal cluster of a fixed size.

We show in Figure 2 the difference in the total energy per atom between our results using the WDA + E_c functional and the results obtained with the TFD(1/2)W + E_c functional for sodium clusters with $N \le 500$. The choice of $\lambda = 1/2$ in the TFD(1/2)W functional arises from a best fit to total energies and to $\langle r^2 \rangle^{1/2}$ values obtained by a Kohn-Sham calculation for the same clusters [26]. In the Kohn-Sham calculations the kinetic energy of independent electrons is treated exactly, the exchange energy was given by the Dirac LDA term $K_0[\rho]$ and the correlation energy by the Wigner term of Eq. (18). We can see in Figure 2 that nonlocal contributions to the kinetic and exchange energies are sizeable. In the limit of very large clusters, the nonlocal contributions affect the surface energy of the bulk metal. This point has been quantitatively studied by Tarazona and Chacón [27] although these authors used a different nonlocal kinetic-energy functional.

In Figure 3 the electronic density and the kinetic-energy density of Na$_{200}$ corresponding to the WDA and TFD(1/2)W functionals (both including local Wigner correlation) have been compared. The WDA electron density has more structure, emulating the Friedel oscillations that appear in the density profile of a metallic
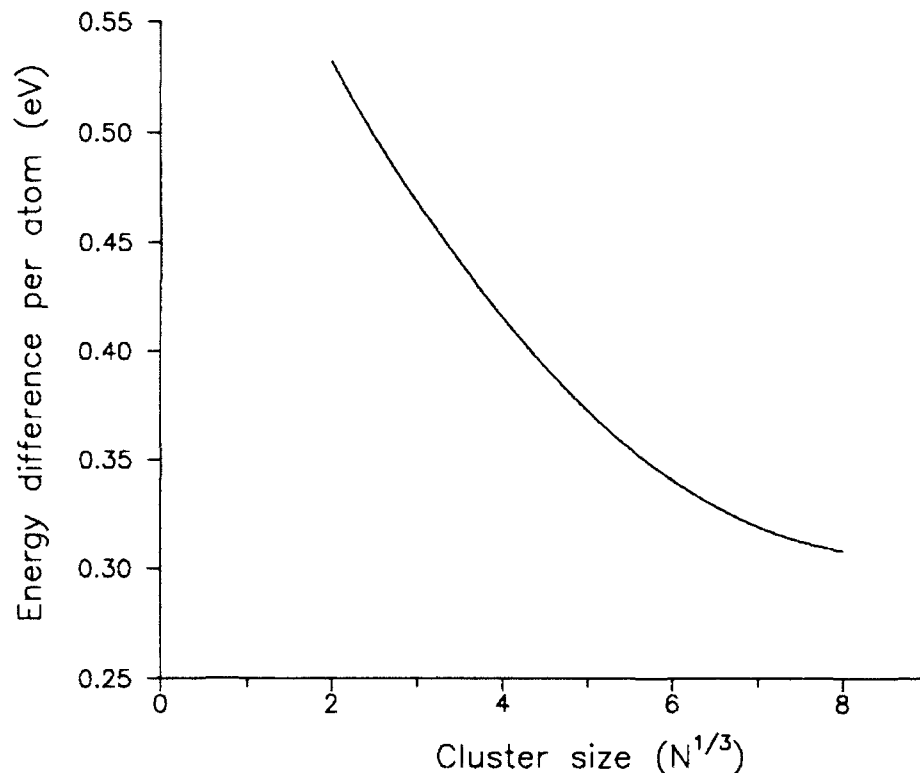
Figure 2.   Difference in the energy per atom of sodium clusters Na$_N$. between results
obtained with the WDA + E_c and TFD($1/2$)W + F_c functionals.

surface. The enhancement of the peak in the WDA density near the cluster surface is similar to the enhancement of the Kohn–Sham density for a metallic surface with respect to TFD(λ)W calculations [27].

Conclusions

In this article we have solved (for the first time in an accurate way) the Euler equation associated with the nonlocal weighted-density approximation for the exchange and kinetic energies, calculating electronic densities, total energies, and exchange energies for noble gas atoms. We have obtained improved results compared with the results from TFD(λ)W models. Also the density at the nucleus and $\langle r^{-1} \rangle$ expectation values are substantially improved. In particular, the total energies are the most accurate ever obtained from an energy functional fully expressed in terms of the density.

For jellium-like sodium clusters we find a sizeable contribution of the nonlocal effects to the total energy. The WDA densities of these clusters show much more structure (Friedel oscillations) than the corresponding TFD(λ)W densities.
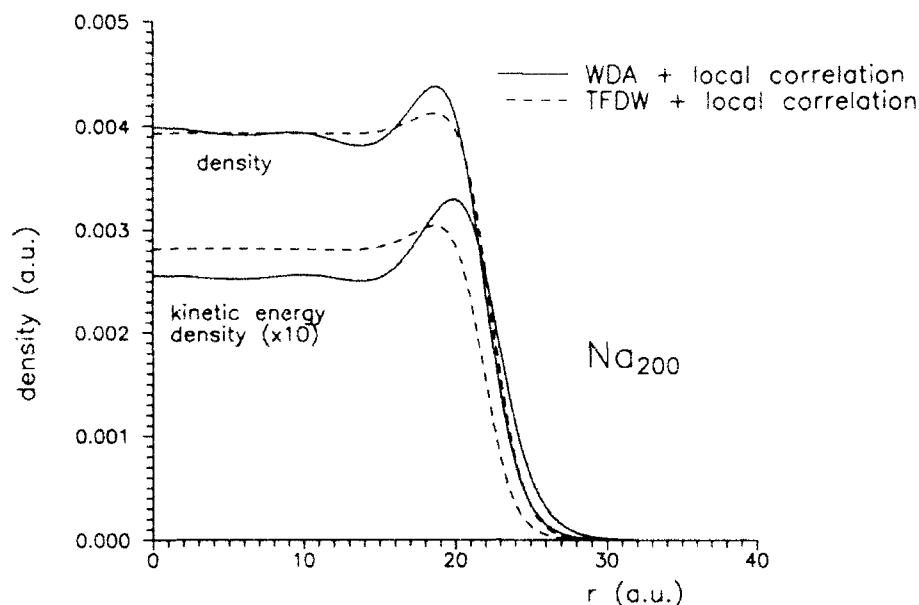
Figure 3. Electron density and kinetic-energy density of Na₂₀₀ obtained from the WDA and TFDW approximations.

Acknowledgments

Bibliography

[1] P. Hohenberg and W. Kohn. Phys. Rev. 136, B864 (1964).

[2] R. G. Parr and W. Yang. Density Functional Theory of Atoms and Molecules (Oxford University Press. New York, 1989).

[3] R. M. Dreizler and E. K. U. Gross. Density Functional Theory. An Approach to the Quantum Many-Body Problem (Springer, Heidelberg, 1990).

[4] N. H. March. Adv. Phys. 6, 1 (1957).

[5] P. A. M. Dirac. Proc. Cambridge Philos. Soc. 26, 376 (1930).

[6] Y. Tomishima and K. Yonei. J. Phys. Soc. Jpn. 20, 142 (1966).

[7] J. A. Alonso and L. A. Girifalco. Phys. Rev. B17, 3735 (1978).

[8] O. Gunnarsson, M. Jonson, and B. I. Lundqvist. Phys. Rev. B20, 3136 (1979).

[9] W. A. de Heer. W. D. Knight, M. Y. Chou, and M. L. Cohen, in Solid State Physics, H. Ehrenreich and D. Turnbull. Eds. (New York, Academic, 1987), Vol. 40.

[10] M. Seidl, K. H. Meiwes-Broer, and M. Brack. J. Chem. Phys. 95, 1295 (1991).

[11] E. Engel and J. P. Perdew. Phys. Rev. B 43, 1331 (1991).

[12] G. Makov and A. Nitzan, J. Chem. Phys. **95**, 9024 (1991).

[13] W. A. de Heer and P. Milani, Phys. Rev. Lett. **65**, 3356 (1990).

[14] C. F. Weizsäcker, Z. Phys. **96**, 431 (1935).

[15] Y. Tal and R. F. W. Bader, Int. J. Quantum Chem., Quantum Chem. Symp. **12**, 153 (1978), J. A. Alonso and N. H. March, J. Chem. Phys. **78**, 1382 (1983).

[16] E. Clementi and E. Roetti, Atomic Data and Nuclear Data Tables **14**, 177 (1974).

[17] B. M. Deb and S. K. Ghosh, Int. J. Quantum Chem. **23**, 1 (1983).

[18] M. D. Glossman, A. Rubio, L. C. Balbás, and J. A. Alonso, New Journal of Chemistry (to be published).

[19] M. Berkowitz, Chem. Phys. Lett. **129**, 486 (1986).

[20] There has been a good deal of attention given to Schrödinger-like equations for the square root of the electron density. See, for example (i) M. Levy, J. P. Perdew, and V. Sahni, Phys. Rev. A **30**, 2745 (1984); (ii) N. H. March, Phys. Lett. A **113**, 66 (1985); (iii) ibid, 476 (1986); (iv) E. N. Lassettre, J. Chem. Phys. **83**, 1709 (1985); (v) N. H. March and A. M. Murray, Proc. R. Soc. London Ser. A **256**, 400 (1960).

[21] W. Yang, Phys. Rev. A **34**, 4575 (1986).

[22] D. Dalili, J. Nemeth and C. Ngô, Z. Phys. A **321**, 335 (1985).

[23] E. Engel and R. M. Dreizler, J. Phys. B **22**, 1901 (1989).

[24] R. F. W. Bader and P. M. Bedall, J. Chem. Phys. **56**, 3320 (1972).

[25] E. P. Wigner, Phys. Rev. **46**, 1002 (1934).

[26] Ll. Serra, F. Garcías, M. Barranco, J. Navarro, L. C. Balbás, A. Rubio, and A. Mañanes, J. Phys. Condens. Matter **1**, 103911 (1989).

[27] P. Tarazona and E. Chacón, Phys. Rev. B **39**, 10366 (1989).

[28] C. F. Fischer, The Hartree-Fock Method for Atoms (Wiley, New York, 1977).

Current Density Functional Theory in a Continuum and Lattice Lagrangians: Application to Spontaneously Broken Chiral Ground States

MARK RASOLT

Solid State Division, Oak Ridge National Laboratory, Oak Ridge, Tennessee 37831

G. VIGNALE

Department of Physics, University of Missouri-Columbia, Missouri 65211

F. PERROT

Commissariat à l'Energie Atomique, Boîte Postale 27, F-94190 Villeneuve-Saint-Georges, France

Abstract

We formulate the current-density functional theory for systems in arbitrarily strong magnetic fields. A set of self-consistent equations comparable to the Kohn–Sham equations for ordinary density functional theory is derived, and proved to be gauge-invariant and to satisfy the continuity equation. These equations of Vignale and Rasolt involve the gauge field corresponding to the external magnetic field as well as a new gauge field generated *entirely* from the *many-body* interactions. We next extend this gauge theory (following Rasolt and Vignale) to a lattice Lagrangian believed to be appropriate to a tight-binding Hamiltonian in the presence of an external magnetic field. We finally examine the nature of the ground state of a strongly nonuniform electron gas in the presence of this many-body, self-induced gauge field. © 1992 John Wiley & Sons, Inc.

Introduction

Since the seminal articles by Hohenberg and Kohn [1] and Kohn and Sham [2], density functional theory (DFT) has developed into an important tool for the treatment of many-body problems in condensed matter physics. Its practical success has prompted much theoretical work aimed at extending the applicability of the theory to systems more general than those considered in the original studies [3,4].

The interest of this article is the formulation of the *current-density functional theory* for systems in the presence of an external magnetic field. Many recent exciting phenomena [5,6] involving electrons in large magnetic fields are a strong motivation for the need of such a formulation.

Magnetic fields have been incorporated in the DFT only insofar as they cause spin polarization [3,7–9]. The fact that orbital currents are also induced has long been recognized [7]. Here we incorporate this effect into the self-consistent formulation of one-particle equations which lies at the heart of a practical implementation of DFT. The basic variables are the particle density $n(\vec{r})$, and the "paramagnetic" current density, $\vec{j}_p(\vec{r})$ [see eq. (2)]. The latter must be used rather than

the physical current density [see eq. (3)] because it uniquely determines the vector potential and the ground-state wavefunction. Furthermore, since in the variational principle the external vector potential is kept constant, the minimization of the energy functional will have to be with respect to $\vec{j}_p$. Consequently, a key difficulty we had to overcome is that a one-particle equations formulation does not *a priori* satisfy the physical requirements of gauge invariance and the continuity equation.

In the following we demonstrate that both requirements can actually be satisfied because of an exact transformation property of the exchange-correlation energy functional, which we derive here. As a consequence of this transformation, the exchange-correlation energy functional $E_{xc}[n, \vec{j}_p]$, which is now a functional of *both* particle density and "paramagnetic" current density, takes the form

$$E_{xc}[n(\vec{r}), \vec{j}_p(\vec{r})] = \bar{E}_{xc}\left[n(\vec{r}), \vec{\nabla} \times \left(\frac{\vec{j}_p(\vec{r})}{n(\vec{r})}\right)\right] \tag{1}$$

($\bar{E}_{xc}$ is a functional of both $n(\vec{r})$ and $\vec{\nabla} \times (\vec{j}_p(\vec{r})/n(\vec{r}))$). This is the one of the key results of this study, and it is this which allows the formulation of single-particle equations in the presence of a magnetic field.

Current Density Functional Theory for a Continuum Lagrangian

We start with a brief discussion of the uniqueness and variational properties of the energy, now in the presence of an external magnetic field; we follow the derivation of Vignale and Rasolt [10]. The nonrelativistic Hamiltonian for a system of N electrons in external scalar and vector potentials, $V(\vec{r})$ and $\vec{A}(\vec{r})$, is

$$H = T + U + V + W.$$

The definitions for the various terms are (e is the absolute value of the charge)

$$T = \int d\vec{r}\,\psi^*(\vec{r})\left(-\frac{\hbar^2}{2m}\nabla^2\right)\psi(\vec{r}),$$

$$U = \frac{1}{2}\int d\vec{r}\int d\vec{r}'\,\psi^*(\vec{r})\psi^*(\vec{r}')u(\vec{r}, \vec{r}')\psi(\vec{r}')\psi(\vec{r}),$$

$$V = \int d\vec{r}\,V(\vec{r})n^{op}(\vec{r}),$$

$$W = \frac{e}{c}\int d\vec{r}\,\vec{j}_p^{op}(\vec{r})\cdot\vec{A}(\vec{r}) + \frac{e^2}{2mc^2}\int d\vec{r}\,n^{op}(\vec{r})A^2(\vec{r}).$$

The density operator is defined as $n^{op}(\vec{r}) \equiv \psi^*(\vec{r})\psi(\vec{r})$, and the paramagnetic current density operator is

$$\vec{j}_p^{op}(\vec{r}) = \frac{\hbar}{2mi}\{\psi^*(\vec{r})\vec{\nabla}\psi(\vec{r}) - [\vec{\nabla}\psi^*(\vec{r})]\psi(\vec{r})\} \tag{2}$$

The physical current density operator is given by

$$\vec{j}^{cr}(\vec{r}) \cdot \vec{j}_p^{cr}(\vec{r}) + \frac{e}{mc} n^{cr}(\vec{r}) \vec{A}(\vec{r}) ,\qquad (3)$$

and satisfies the continuity equation $\vec{\nabla} \cdot \vec{j}^{cr}(\vec{r}; t) + \partial n^{cr}(\vec{r}; t)/\partial t = 0$. In the above equations, we have disregarded spin in order to concentrate on the novel physical feature of the orbital currents.

We now run through the basic theorems of density functional theory in magnetic fields. Let $\vec{j}_p(\vec{r})$, $\vec{j}(\vec{r})$, and $n(\vec{r})$ denote the ground-state averages of the corresponding operators; then the potentials, $V(\vec{r})$ and $\vec{A}(\vec{r})$, and hence, the ground-state wavefunction, ψ, are uniquely determined (apart from an additive constant in the scalar potential) by the knowledge of the density distributions $n(\vec{r})$ and $\vec{j}_p(\vec{r})$ [10]. For, suppose that there are two sets of fields, $V(\vec{r})$, $\vec{A}(\vec{r})$ and $V'(\vec{r})$, $\vec{A}'(\vec{r})$, giving the same ground-state distributions $n(\vec{r})$ and $\vec{j}_p(\vec{r})$. Let $|\psi\rangle$ and $|\psi'\rangle$ be the two different ground states corresponding to the two sets of fields. Let H and H' be the two corresponding Hamiltonians and E and E' the two ground-state energies. Then, from the variational principle for the ground state of H, we obtain the inequality

$$E = \langle \psi | H | \psi \rangle < \langle \psi' | H | \psi' \rangle$$

$$= E' + \int d\vec{r}\, n(\vec{r})[V(\vec{r}) - V'(\vec{r})] + \frac{e}{c} \int d\vec{r}\, \vec{j}_p(\vec{r}) \cdot$$

$$[\vec{A}(\vec{r}) - \vec{A}'(\vec{r})] + \frac{e^2}{2mc^2} \int d\vec{r}\, n(\vec{r})[A^2(\vec{r}) - A'^2(\vec{r})] .$$

Another inequality is obtained by interchanging the primed and the unprimed variables, and summing the two inequalities we get the contradiction

$$E + E' < E + E'$$

which proves the theorem.

For the variational principle, let

$$F[n', \vec{j}_p'] \equiv \langle \psi[n', \vec{j}_p'] | T + U | \psi[n', \vec{j}_p'] \rangle \qquad (4)$$

where $\psi[n', \vec{j}_p']$ is the ground-state wavefunction corresponding to n' and $\vec{j}_p'$. Then the functional

$$E_{V,A}[n', \vec{j}_p'] = F[n', \vec{j}_p'] + \int d\vec{r}\, n'(\vec{r})V(\vec{r}) + \frac{e}{c} \int d\vec{r}\, \vec{j}_p'(\vec{r}) \cdot$$

$$\vec{A}(\vec{r}) + \frac{e^2}{2mc^2} \int d\vec{r}\, n'(\vec{r})A^2(\vec{r}) \qquad (5)$$

has a minimum when n' and $\vec{j}_p'$ take the actual values corresponding to the potentials V and $\vec{A}$. This follows from the variational principle for the ground state of H, since

$$E_{V,A}[n', \vec{j}_p'] = \langle \psi[n', \vec{j}_p'] | H | \psi[n', \vec{j}_p'] \rangle \geq$$

$$\langle \psi[n, \vec{j}_p] | H | \psi[n, \vec{j}_p] \rangle = E_{V,A}[n, \vec{j}_p]$$

which proves the theorem.

We now turn to the formulation of the one-particle equations. We first define the exchange-correlation energy functional E_{xc} as follows

$$F[n, \vec{j}_p] = T_s[n, \vec{j}_p] + \frac{1}{2} \int d\vec{r} \int d\vec{r}' n(\vec{r}) u(\vec{r}, \vec{r}') n(\vec{r}') + E_{xc}[n, \vec{j}_p], \quad (6)$$

where

$$T_s[n, \vec{j}_p] = \langle \psi_0[n, \vec{j}_p] | T | \psi_0[n, \vec{j}_p] \rangle, \quad (7)$$

and $\psi_0[n, \vec{j}_p]$ is the ground-state wavefunction corresponding to n and $\vec{j}_p$ in a noninteracting version of the system [11]. $\psi_0[n, \vec{j}_p]$ is a Slater determinant of one-electron orbitals, ψ_i, which satisfy a one-particle Schrödinger equation with some, as yet undetermined, effective potentials. The functional, T_s, is also expressed in terms of the ψ_i's. Putting this representation of T_s in eqs. (6) and (5), and carrying out the minimization of E_{xc}, $\vec{A}$, determines the effective potentials. We get the following self-consistent formulation for the ground-state density and current:

$$n(\vec{r}) = \sum_{i}^{N} |\psi_i(\vec{r})|^2,$$

$$\vec{j}_p(\vec{r}) = \frac{\hbar}{2mi} \sum_{i}^{N} \{ \psi_i^*(\vec{r}) \nabla \psi_i(\vec{r}) - [\nabla \psi_i^*(\vec{r})] \psi_i(\vec{r}) \},$$

$$\left\{ \frac{1}{2m} \left[-i\hbar \nabla + \frac{e}{c} (\vec{A}(\vec{r}) + \vec{A}_{xc}(\vec{r})) \right]^2 + \frac{e^2}{2mc^2} [\vec{A}^2(\vec{r}) - (\vec{A}(\vec{r}) + \vec{A}_{xc}(\vec{r}))^2] \right.$$

$$\left. + V(\vec{r}) + \int d\vec{r}' u(\vec{r}, \vec{r}') n(\vec{r}') + v_{xc}(\vec{r}) \right\} \psi_i(\vec{r}) = \epsilon_i \psi_i(\vec{r}), \quad (8)$$

$$v_{xc}(\vec{r}) = \frac{\delta E_{xc}[n, \vec{j}_p]}{\delta n(\vec{r})} \bigg|_{\vec{j}_p}, \quad (9)$$

$$\frac{e}{c} \vec{A}_{xc}(\vec{r}) = \frac{\delta E_{xc}[n, \vec{j}_p]}{\delta \vec{j}_p(\vec{r})} \bigg|_{n}. \quad (10)$$

The ground-state energy is given by

$$E = \sum_{i}^{N} \epsilon_i - \frac{1}{2} \int d\vec{r} \int d\vec{r}' n(\vec{r}) u(\vec{r}, \vec{r}') n(\vec{r}') - \int d\vec{r} v_{xc}(\vec{r}) n(\vec{r})$$

$$- \frac{e}{c} \int d\vec{r} \vec{j}_p(\vec{r}) \cdot \vec{A}_{xc}(\vec{r}) + E_{xc}[n, \vec{j}_p]. \quad (11)$$

Notice that the effective vector potential $\vec{A} + \vec{A}_{xc}$ enters the Schrödinger-like equation *linearly*.

We now prove the important result, eq. (1), for the form of E_{xc}. *Proof* Consider the transformation

$$\vec{j}_p(\vec{r}) \rightarrow \vec{j}_p(\vec{r}) + \frac{e}{mc} n(\vec{r})\vec{\nabla}\Lambda(\vec{r}) = \vec{j}_p'(\vec{r}) . \tag{12}$$

where $\Lambda(\vec{r})$ is an arbitrary function. Clearly, the transformation of the wavefunction is $\psi[n, \vec{j}_p'] = \psi[n, \vec{j}_p] \exp[i(e/\hbar c) \sum_i \Lambda(\vec{r}_i)]$. The transformation of F is easily obtained from the definition (4):

$$F[n, \vec{j}_p'] = F[n, \vec{j}_p] + \frac{e}{c} \int d\vec{r} \vec{j}_p(\vec{r}) \cdot \vec{\nabla}\Lambda(\vec{r}) + \frac{e^2}{2mc^2} \int d\vec{r} n(\vec{r})|\vec{\nabla}\Lambda(\vec{r})|^2 .$$

The crucial point about this equation is that the transformation depends only on n and $\vec{j}_p$, not on the wavefunction. Therefore, the same transformation applies also to $T[n, \vec{j}_p]$, defined in eq. (7). Putting these results together in eq. (6), we discover

$$E_{xc}\left[n, \vec{j}_p + \frac{e}{mc} n\vec{\nabla}\Lambda\right] = E_{xc}[n, \vec{j}_p] . \tag{13}$$

This is an *exact* property of the E_{xc} functional. Another way of expressing this property is that E_{xc} can only depend on the combination $\vec{\nu}(\vec{r}) = \vec{\nabla} \times (\vec{j}_p(\vec{r})/n(\vec{r}))$

$$E_{xc}[n, \vec{j}_p] = \bar{E}_{xc}[n, \vec{\nu}] . \tag{14}$$

We next prove that this form, in conjunction with eq. (8), implies $\vec{\nabla} \cdot \vec{j} = 0$, i.e., the static continuity equation is satisfied. *Proof:* Taking the functional derivatives of eq. (14) we find

$$\frac{e}{c} \vec{A}_{xc}(\vec{r}) = -\frac{1}{n(\vec{r})} \vec{\nabla} \times \left.\frac{\delta \bar{E}_{xc}[n, \vec{\nu}]}{\delta \vec{\nu}(\vec{r})}\right|_{n} , \tag{15}$$

$$v_{xc}(\vec{r}) = \left.\frac{\delta \bar{E}_{xc}[n, \vec{\nu}]}{\delta n(\vec{r})}\right|_{\vec{\nu}} - \frac{e}{c} \vec{A}_{xc}(\vec{r}) \cdot \frac{\vec{j}_p(\vec{r})}{n(\vec{r})} . \tag{16}$$

Eq. (15) implies that $\vec{\nabla} \cdot (n(\vec{r})\vec{A}_{xc}(\vec{r})) = 0$. Since the Schrödinger-like eq. (8) already guarantees $\vec{\nabla} \cdot \{ \vec{j}_p(\vec{r}) + (e/mc)n(\vec{r})[\vec{A}(\vec{r}) + \vec{A}_{xc}(\vec{r})] \} = 0$, it follows that $\vec{\nabla} \cdot (\vec{j}_p + (e/mc)n\vec{A}) = \vec{\nabla} \cdot \vec{j} = 0$.

Current Density Functional Theory for a Lattice Lagrangian

It was first suggested by Anderson [12] that the strong correlations of the carriers within the copper oxygen plane (CuOP) of high-T_c materials could provide a mechanism for the superconducting condensation. Following this suggestion, various spin singlet liquid flux phases [13–19] were proposed for a description of the normal state. Such phases are characterized by self-induced effective gauge field and these are almost exclusively formulated on tight-binding Hamiltonians. The extension of our results for the continuum Lagrangian of the first section to a Lagrangian on

a lattice [9] is motivated by these suggestions. We provide *exact* formulation for these gauge fields.

We start with the lattice Hamiltonian

$$\hat{H} = \sum_{\substack{ij \\ \alpha\beta\sigma_1\sigma_2}} \left\{ \frac{1}{2} F^{\alpha\beta}_{ij\sigma_1\sigma_2} \hat{C}^{\dagger}_{i\alpha\sigma_1} \hat{C}_{j\beta\sigma_2} + h.c. + \frac{1}{2} U^{\alpha\beta}_{ij\sigma_1\sigma_2} \hat{n}_{i\alpha\sigma_1} \hat{n}_{j\beta\sigma_2} \right\} \tag{17a}$$

where

$$F \equiv F^{\alpha\beta}_{ij\sigma_1\sigma_2} = [e^{iA^{\alpha\beta}_{ij\sigma_1\sigma_2}} t^{\alpha\beta}_{ij} + \varepsilon^{\alpha}\delta_{\sigma_1\sigma_2}\delta_{\alpha\beta}\delta_{ij} + V^{\alpha\beta}_{i\sigma_1\sigma_2}\delta_{ij}] \tag{17b}$$

($F, A, V \cdots$ are matrix short hand notation for all the indices). In eq. (17), $\hat{C}_{i\alpha\sigma}$ and $\hat{n}_{i\alpha\sigma}$ are the Fermion (electrons or holes) creation and spin density operators, respectively, at site i, with band index α and spin σ. $U^{\alpha\beta}_{ij\sigma_1\sigma_2}$ represent the most general configurations of the Hubbard U's. ε^{α} are the band energies, and $t^{\alpha\beta}_{ij}$ are the hopping matrix elements (where $t^{\alpha\beta}_{ij} = t^{*\beta\alpha}_{ji}$). A and V are the external vector and scalar potentials.

We now prove two basic theorems equivalent to eqs. (4) and (5) of the continuum case. (1) The quantities

$$\chi \equiv \chi^{\alpha\beta}_{ij\sigma_1\sigma_2} = \langle G | \hat{C}^{\dagger}_{i\alpha\sigma_1} \hat{C}_{j\beta\sigma_2} | G \rangle \tag{18}$$

uniquely determine A (mod(2π)) and V (to within an additive constant) and, therfore, the ground state $|G(\chi)\rangle$ and ground-state energy $E_{A,V}(\chi)$. *Proof:* Suppose there are two such fields, A, V and A', V'. Let $\hat{H}$ and $\hat{H}'$ be the two corresponding Hamiltonians with the corresponding $|G\rangle$ and $|G'\rangle$ and ground-state energies, $E_{A,V}$ and $E_{A',V'}$. Then

$$E_{A,V} \equiv \langle G | \hat{H} | G \rangle < \langle G' | \hat{H} | G' \rangle$$

and

$$E_{A',V'} \equiv \langle G' | \hat{H}' | G' \rangle < \langle G | \hat{H}' | G \rangle$$

Summing the two sides and using eqs. (17a) and (18) we get

$$\sum_{\substack{ij \\ \sigma_1\sigma_2\alpha\beta}} (F^{\alpha\beta}_{ij\sigma_1\sigma_2} + F'^{\alpha\beta}_{ij\sigma_1\sigma_2})\chi^{\alpha\beta}_{ij\sigma_1\sigma_2} < \sum_{\substack{ij \\ \sigma_1\sigma_2\alpha\beta}} (F^{\alpha\beta}_{ij\sigma_1\sigma_2} + F'^{\alpha\beta}_{ij\sigma_1\sigma_2})\chi^{\alpha\beta}_{ij\sigma_1\sigma_2}.$$

which is a contradiction and proves the theorem. (2) For fixed A and V, the ground-state energy reaches a minimum for the correct χ. *Proof:* Let a different set of χ' originate from a second Hamiltonian, $\hat{H}'$. Then

$$E_{A,V}(\chi') \equiv \langle G'(\chi') | \hat{H} | G'(\chi') \rangle > \langle G(\chi) | \hat{H} | G(\chi) \rangle \equiv E_{A,V}(\chi) \tag{19}$$

Q.E.D.

We can next write $E_{A,V}$ as

$$E_{A,V}(\chi) = \sum_{\substack{ij \\ \sigma_1\sigma_2\alpha\beta}} \left[\frac{1}{2} F^{\alpha\beta}_{ij\sigma_1\sigma_2} \chi^{\alpha\beta}_{ij\sigma_1\sigma_2} + c.c. \right] + E_{xc}(\chi) \tag{20a}$$

where

$$E_{xc}(\chi) \equiv E_{xc}(\chi_{ij\sigma_1\sigma_2}^{\alpha\beta}) = \frac{1}{2} \sum_{\substack{ij \\ \alpha\beta\sigma_1\sigma_2}} U_{ij\sigma_1\sigma_2}^{\alpha\beta} \langle G(\chi) | \hat{n}_{i\alpha\sigma_1} \hat{n}_{j\beta\sigma_2} | G(\chi) \rangle . \quad (20b)$$

According to eq. (19), we get the distribution of the χ's by minimizing eq. (20a) at fixed A and V. However, it is crucial to recognize that not all the χ's are admissible for variation since, according to eq. (18) (using the Schwartz inequality), these χ's must satisfy the constraint $|\chi_{ij\sigma_1\sigma_2}^{\alpha\beta}| < 1$. We satisfy it by introducing auxiliary orthogonal orbitals, $\phi_{i\alpha\sigma}^q$, i.e.

$$\langle \phi^{q_1} | \phi^{q_2} \rangle \equiv \sum_{i\alpha\sigma} \phi_{i\alpha\sigma}^{*q_1} \phi_{i\alpha\sigma}^{q_2} = \delta_{q_1 q_2} \quad (21a)$$

and we write

$$\chi_{ij\sigma_1\sigma_2}^{\alpha\beta} \equiv \sum_q \phi_{i\alpha\sigma_1}^{*q} \phi_{j\beta\sigma_2}^q . \quad (21b)$$

Minimizing eq. (20a), using eqs. (21a) and (21b), we get the following set of equations written in matrix form

$$(F + \tilde{F}) | \phi^q \rangle = \lambda_q | \phi^q \rangle \quad (22a)$$

where F is given in eq. (17b) and

$$\tilde{F} \equiv \frac{\partial E_{xc}}{\partial \chi_{ij\sigma_1\sigma_2}^{\alpha\beta}} (\chi_{i'j'\sigma_1'\sigma_2'}^{\alpha'\beta'}) \quad (22b)$$

and the λ_q's are Lagrange multipliers insuring the orthonormality of eq. (21a).

Eq. (22a) is then solved self-consistently for the $|\phi^q\rangle$, yielding the χ's and $E_{xc}(\chi)$ [eq. (20a)]. In solving eq. (22a) the lowest N values of λ_q's are kept (N is the number of Fermions). Provided $E_{xc}(\chi)$ is exactly known, the solution of eq. (22) gives a rigorous description for the spontaneously broken ground state properties of either chiral symmetry [13-19], spin symmetry, or both [20,21].

We can next prove that eq. (22) satisfies all the current conservations within each band, α, and any spin current component configuration. The general proof, however, involves nonabelian gauge symmetries; here we scale eq. (22) to only one band and a ferromagnetic or antiferromagnetic spin nonuniformity, therefore neglecting spin spiral configurations [20,21] (i.e., $F_{ij\sigma_1\sigma_2}^{\alpha\beta} = F_{ij\sigma\sigma}$). Now from $\hat{H}$ in eq. (17) we get at once that

$$\sum_j I_{ij\sigma\sigma} = \sum_j [F_{ij\sigma\sigma} \chi_{ij\sigma\sigma} - F_{ij\sigma\sigma}^* \chi_{ij\sigma\sigma}^*] = 0 , \quad (23a)$$

which is Kirkhoff's law. However, simple use of eq. (22) leads to

$$\sum_j [(F_{ij\sigma\sigma} + \tilde{F}_{ij\sigma\sigma}) \chi_{ij\sigma\sigma} - (F_{ij\sigma\sigma} + \tilde{F}_{ij\sigma\sigma})^* \chi_{ij\sigma\sigma}^*] = 0 \quad (23b)$$

i.e., we must prove that

$$\sum_l [\dot{F}_{ll\sigma\lambda} X_{ll\sigma\lambda} - \dot{F}^*_{ll\sigma\lambda} X^*_{ll\sigma\lambda}] = 0 .$$ (23c)

Proof: Eq. (17) is gauge invariant under $A_{ll\sigma\lambda} \to A_{ll\sigma\lambda} + (\theta^\sigma_l - \theta^\sigma_j)$ and $C_{l\sigma} \to e^{-i\theta^\sigma_l} C_{l\sigma}$. But the uniqueness theorem 1 implies that

$$E_{il}(X_{lk\sigma\lambda}) = E(X_{lk\sigma\lambda}) = E(e^{i(\theta^\sigma_l - \theta^\sigma_k)} X_{lk\sigma\lambda})$$ (24a)

and so from eq. (20a)

$$E_{xc}(X_{lk\sigma\lambda}) = E_{xc}(e^{i(\theta^\sigma_l - \theta^\sigma_k)} X_{lk\sigma\lambda}) .$$ (24b)

We next choose a special gauge transformation $\theta^\sigma_l = 0$ and $\theta^\sigma_j = \theta^\sigma$ for all $j \neq i$. Then, from eq. (24b), with $\theta^\sigma \to 0$, we get

$$E_{xc}(X_{lk\sigma\lambda}) - E(X_{lk\sigma\lambda}(1 + i(\theta^\sigma_l - \theta^\sigma_k))) = 0$$

$$= \sum_l \left[\left(\frac{\partial E_{xc}}{\partial X_{ll\sigma\lambda}} \right) X_{ll\sigma\lambda} i\theta^\sigma - \left(\frac{\partial E_{xc}}{\partial X_{ll\sigma\lambda}} \right)^* X^*_{ll\sigma\lambda} i\theta^\sigma \right]$$

which, from eq. (22b), proves eq. (23c).

We next scale down eq. (17) to a nearest neighbor hopping $t_{ll} = t_{l,l+\tau}$ (where $\tau_x = \tau_y = a$ are the nearest neighbor distances on a square lattice). The gauge symmetry (GS) now leads to

$$E_{xc}(X_{l,l+\tau\sigma\lambda}) = E_{xc}(e^{i(\theta^\sigma_{l+\tau} - \theta^\sigma_l)} X_{l,l+\tau\sigma\lambda})$$ (25a)

and similarly for $E(X)$.

We can always write

$$(X_{l,l+\tau\sigma\lambda}) \equiv |X_{l,l+\tau\sigma\lambda}| e^{i\psi_{l,l+\tau\sigma\lambda}}$$ (25b)

(ψ mod(2π)). So, GS leads to

$$E_{xc}(X_{l,l+\tau\sigma\lambda}) = E'_{xc}(|X_{l,l+\tau\sigma\lambda}|, (\psi_{l,l+\tau\sigma\lambda} + \theta^\sigma_{l+\tau} - \theta^\sigma_l)) .$$ (25c)

We can show that the most general gauge-invariant form of $E_{xc}(X)$ is given by

$$E'_{xc}(|X_{l,l+\tau\sigma\lambda}|, X_{l,l\sigma\lambda}, \psi_{l,l+\tau\sigma\lambda}) = \bar{E}_{xc}(|X_{l,l+\tau\sigma\lambda}|, X_{l,l\sigma\lambda}, \nu^\sigma_l) ,$$ (26a)

where the basic gauge-invariant unit is

$$\nu^\sigma_l = \psi_{l,l+\tau_x\sigma} + \psi_{l+\tau_x,l+\tau_x+\tau_y\sigma} + \psi_{l+\tau_x+\tau_y,l+\tau_y\sigma} + \psi_{l+\tau_y,l\sigma} ,$$ (26b)

i.e., the sum of the phases of ψ around a plaquette.

It is not difficult to see that eqs. (21), (22), (25), and (26) represent the lattice equivalent of eqs. (8), (9), (10), and (14)–(16) and that, therefore, eq. (26) maps to

$$\vec{\nu}_\sigma(\vec{r}) \to \nabla \times \left(\frac{\vec{j}_{p\sigma}(\vec{r})}{n_\sigma(\vec{r})} \right) .$$ (27)

Application and Conclusions

In this section, we apply the results of our continuum formulation of the second section to a spontaneously generated broken symmetry chiral ground state. All theoretical calculations of the ground-state properties of an interacting two-dimensional (2d) electron gas show that, at low enough densities (i.e., large r_s), the system spontaneously forms spin polarizations [22]. The issue we address in this section is whether spontaneously broken current carrying states (SBCCS) are also a realistic possibility in such an itinerant 2d system. The answer is yes, provided the system is sufficiently inhomogeneous, as we describe next.

Prejudice against such SBCCS in favor of spin-polarized ground states originate in the Landau diamagnetic response, χ_L versus the Pauli susceptibility χ_p. Although χ_L is roughly of the same magnitude [23] as χ_p, it is of opposite sign to χ_p, suggesting that the system has no desire to accommodate such a SBCCS. This is true for the weakly inhomogeneous Fermi liquid but for a strongly inhomogeneous system (and particularly in 2d) things can be quite different.

For example, *unique to 2d* the energy of noninteracting Fermions in a uniform magnetic field is *equal* to the energy in its absence, when the Landau levels are filled [24]. This is different than the 3d Landau diamagnetism discussed above and encouraging for SBCCS in 2d. The inhomogeneity further strongly enhances the 2d SBCCS as can be seen from the work of Hasagawa et al [24]. Hasagawa et al put the noninteracting electrons on a lattice. Making contact with our discussion in the third section, we take the simplest one-band noninteracting version of eq. (17). The Hamiltonian is now [24]

$$\hat{H} = -\sum_{i,j\sigma} t_{ij} C^{\dagger}_{i\sigma} C_{j\sigma} \qquad t_{ij} = t \exp\left[-i2\pi \int_i^j \vec{A} \cdot d\vec{l}\right] \tag{28}$$

with $\vec{A}(\vec{r}) = B(0, x, 0)$. Its ground-state energy for several different crystal structures is *lower* than when $B = 0$ for many appropriate ratios of electron densities and magnetic fluxes.

To calculate for the SBCCS, we use the formulation derived in the second section.

Now, from eq. (8), the transition to a SBCCS is clearly driven by a self-induced gauge field $\vec{A}_{xc}(\vec{r})$, whose origin is the exchange and correlation functional. $E_{xc}(n(\vec{r}), \nabla \times (\vec{j}_p(\vec{r})/(n(\vec{r}))))$. A realistic search for SBCCS then requires a realistic form for E_{xc}: our conclusions will crucially depend on a reasonable form (both in magnitude and structure) for E_{xc}. We derive E_{xc} from the energy of a uniform 2d two-component electron gas in arbitrary but uniform $B(\vec{r}) = B$. In the range of ν, where the Laughlin liquid state is valid, we used our results for the energy of a 2d two-component quantum plasma [25] at $\nu = \frac{1}{5}, \frac{1}{3}$ and 2. In the limit when $\nu \to \infty$ we use the Tanatar and Ceperly [26] $E^0_{xc}(n_0)$. Our Padé form is then

$$\bar{E}_{xc}(n_0, \nu) = \frac{E^0_{xc}(n_0, \nu) + a\nu^4 E^0_{xc}(n_0)}{1 + a\nu^4} \tag{29}$$

where a is chosen to closely reproduce the values of $\bar{E}_{xc}(n_0, \nu)$ at $\nu = \frac{1}{5}, \frac{1}{3}, 2$. Our form of E_{xc} is finally given by noting that for an arbitrary but uniform $\vec{B}$, $\vec{j} = \vec{j}_p(\vec{r}) - (en_0/mc)\vec{A}(\vec{r}) = 0$. So, $\nabla \times (\vec{j}_p(\vec{r})/n_0) = (e/mc)\nabla \times \vec{A}(\vec{r}) = (e/mc)\vec{B}$.

From the definition $\nu \equiv n_0 2\pi l^2 = n_0 2\pi(\hbar c / eB)$ and the usual extension [1] from $n_0 \rightarrow n(\vec{r})$ and from $\vec{j}_p(\vec{r})$ (appropriate to a uniform B) to arbitrary $\vec{j}_p(\vec{r})$, we get the corresponding local current density approximation (LCDA) form for $E_{xc}(n(\vec{r}), \nabla \times (\vec{j}_p(\vec{r})/(n(\vec{r}))))$.

Actually, here we do not solve the full set of self-consistent eqs. (8–10), rather we define a local current density functional approximation for T, in eq. (6); it is given by

$$T_s(n(\vec{r}), \vec{j}_p(\vec{r})) = T_0(n(\vec{r}))$$

$$+ \left[\frac{1}{2} \hbar |\vec{\nu}(\vec{r})| \delta n(\vec{r}) - \frac{\pi}{2} \hbar^2 (\delta n(\vec{r}))^2 + \frac{m|\vec{j}_p(\vec{r})|^2}{2n(\vec{r})} \right],$$
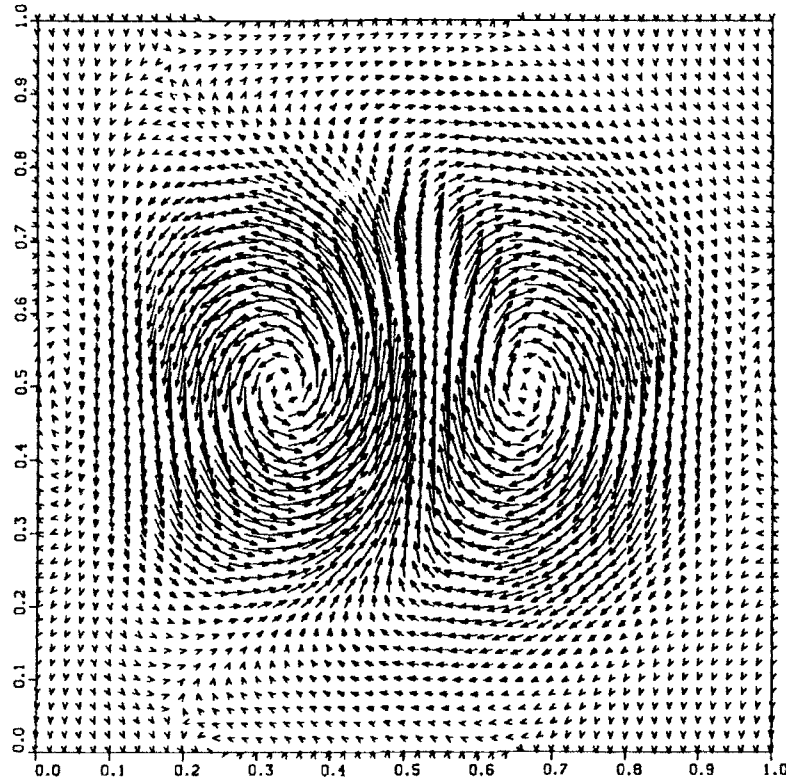
Figure 1.   The current patterns in a unit cell of a symmetry-broken, current-carrying state in a two-dimensional nonuniform interacting electron gas. The density nonuniformity corresponds to $m^*/m \approx 6.4$ (see text). The corresponding $V_{eff}(\vec{r})$ is made up of two spherical wells, one at the corner and one at the center of the squares (see text). The two spherical wells have depth $V_1 = -.2$ and $V_2 = -1$ in atomic units, and radii of $R_1 = .278a_0$ and $R_2 = .222a_0$. The square corner is located in the center of the panel. The effective dipole moments $\vec{\mu}$ per square $|\vec{\mu}| = \hbar e\alpha/2mc$, with $\alpha = m \int d^2r \vec{j}(\vec{r}) \times \vec{r}$, we get $\alpha \approx$ 2.1×10^{-3}. The dipole moments per each vertex are considerably larger.

$$\delta n(\vec{r}) = n(\vec{r}) - \frac{Nm|\vec{v}(\vec{r})|}{\pi \hbar}, \quad \text{and} \quad N \equiv \text{integ. part of } \frac{\pi \hbar}{m} \frac{n(\vec{r})}{|\vec{v}(\vec{r})|}. \quad (30)$$

$T_0(n(\vec{r}))$ is the kinetic energy of a 2d electron gas in the absence of $\vec{B}$.

For $V_{\text{eff}}(\vec{r}) \equiv V(\vec{r}) + \int d\vec{r}'u(\vec{r}, \vec{r}')n\vec{r}'$ in eq. (8), we take the following geometry. We put one spherical well potential at the four corners of a square (with sides of lengths $7a^0$; $a^0 = \hbar^2/mc^2$) and another spherical well at the center of the four sides. We fix the electron density and use a depth well with effective band structure mass of $m^*/m \approx 6.4$, and replace the m by m^* in eqs. (29) and (30).

To find the nature of the ground state, we minimize eq. (5) [using eqs. (29) and (30)] with respect to $n(\vec{r})$ and $\vec{j}_p(\vec{r})$ in the lim.$\vec{A}(\vec{r}) \to 0$. (Actually, a posteriori, $\vec{j}_p(\vec{r})$ is very small; we then do better. We solve the Kohn–Sham equations for $n(\vec{r})$ above the SBCCS [i.e., eqs. (8)–(10) with $\vec{A}_\epsilon(\vec{r}) = 0$] and insert $n(\vec{r})$ in eqs. (29), (30), and (5) to minimize with respect to $\vec{j}_p(\vec{r})$ below the SBCCS transition). To facilitate the calculation and, in particular, the $\nabla \times (\vec{j}_p(\vec{r})/n(\vec{r}))$ term, we work in a plane wave basis. The increasing inhomogeneity (i.e., m^*) then requires larger and larger basis set. The density $n(\vec{r})$ above the SBCCS transition is calculated using up to 225 plane waves of reciprocal lattice vectors $\vec{K}$. Below the SBCCS transition, the current is expanded as $\vec{j}_p(\vec{r}) = \sum_{\vec{K}} \vec{a}_{\vec{K}}(C_{\vec{K}} \cos(\vec{k} \cdot \vec{r}) + S_{\vec{K}} \sin(\vec{k} \cdot \vec{r}))$ where $\vec{K} \cdot \vec{a}_{\vec{K}} = 0$. The total energy change of eq. (30) was calculated by numerical integration of the unit cell of a 61×61 point mesh. Eq. (30) was then minimized with respect to all the $C_{\vec{K}}$ and $S_{\vec{K}}$ using a "conjugate gradients method." Other details are self-explantory in the figure captions.

In conclusion, the formulation we gave for an interacting many-Fermion system in the presence of an external magnetic field leads to a self-generated many-body gauge field, both in continuum and on a lattice. We find that the exact gauge structure of this field leads to the possibility of spontaneously broken current carrying ground states in strongly nonuniform interacting Fermi liquids (Fig. 1). The SBCCS is, however, not incompressible [12–18], as proved by Rasolt and Vignale [9] (see also ref. [27]), and therefore cannot be a chiral state of the type suggested, e.g., in ref. [17].

ACKNOWLEDGMENTS

Bibliography

[1] P. Hohenberg and W. Kohn. Phys. Rev. 136, B846 (1964).

[2] W. Kohn and L. J. Sham. Phys. Rev. 140, A1133 (1965).

[3] W. Kohn and P. Vashishta, in Theory of the Inhomogeneous Electron Gas, S. Lundqvist and N. H. March, Eds. (Plenum, New York, 1983) ch. 2.

[4] A time-dependent formulation of DFT has been recently achieved by Erich Runge and E. K. U. Gross. Phys. Rev. Lett. **52**, 997 (1984) and E. K. U. Gross and Walter Kohn. Phys. Rev. Lett. **55**, 2850 (1985).

[5] R. E. Prange and S. M. Girvin Eds. *The Quantum Hall Effect*. (Springer-Verlag, New York, 1987).

[6] B. I. Halperin, *Condensed Matter Theories* (vol. 2). P. Vashishta et al., Eds. (Plenum, New York, 1989).

[7] A. L. Rajagopal and J. Callaway. Phys. Rev. B **7**, 1912 (1973).

[8] O. Gunnarsson and B. I. Lundqvist. Phys. Rev. B **13**, 4274 (1976).

[9] G. Vignale and M. Rasolt, Phys. Rev. B **37**, 10685 (1988); M. Rasolt and G. Vignale. Phys. Rev. Lett. **65**, 1498 (1990); M. Rasolt. Phys. Rev. B **16**, 3234 (1977).

[10] We assume, as customary, that our distributions belong to the class of distributions that can be physically realized in some external fields.

[11] We are assuming here that the current and density distributions of interest are representable by some external potentials both in the interacting and in the noninteracting case.

[12] P. W. Anderson. Sciences **235**, 1196 (1987).

[13] I. Affleck and J. B. Marston, Phys. Rev. B **37**, 3774 (1987). Phys. Rev. B **39**, 11538 (1989); T. Dombre and G. Kotliar. Phys. Rev. B **39**, 855 (1989); D. P. Arovas and A. Auerbach. Phys. Rev. B **38**, 316 (1988).

[14] P. W. Anderson, B. S. Shastry, and D. Hristopulos. Phys. Rev. B **40**, 8939 (1989).

[15] V. Kalmeyer and R. B. Laughlin. Phys. Rev. Lett. **50**, 2095 (1987).

[16] R. B. Laughlin and Z. Zou. Phys. Rev. B **41**, 664 (1989).

[17] X. G. Wen, F. Wilczek. and A. Zee. Phys. Rev. B **39**, 11413 (1989).

[18] P. Lederer, D. Poilblanc, and T. M. Rice. Phys. Rev. Lett. **63**, 1519 (1989).

[19] S. Liang and N. Trivedi. Phys. Rev. Lett. **64**, 232 (1990).

[20] D. Yoshioka. J. Phys. Soc. (Japan) **58**, 3733 (1989).

[21] B. I. Shraiman and E. D. Siggia, Phys. Rev. Lett. **61**, 467 (1988).

[22] D. Ceperley. Phys. Rev. B **18**, 3126 (1978).

[23] G. Vignale, M. Rasolt, and D. J. W. Geldart. Phys. Rev. B **37**, 2502 (11988).

[24] Y. Hasegawa, P. Leterer, T. M. Rice, and P. B. Wiegmann. Phys. Rev. Lett. **63**, 907 (1989).

[25] M. Rasolt, F. Perrot, and A. H. MacDonald. Phys. Rev. Lett. **55**, 433 (1985).

[26] B. Tanatar and D. M. Ceperley. Phys. Rev. B **39**, 5005 (1964).

[27] E. T. Tomboulis Phys. Rev. Lett. **68**, 3100 (1992).

Precision in the Numerical Integration of the Thomas–Fermi–Dirac Kinetic-Energy and Exchange-Energy Functionals Using a Modeled Electron Density

P. CSAVINSZKY

Department of Physics and Astronomy, University of Maine, Orono, Maine 04469

Abstract

In the Hohenberg and Kohn formulation of density-functional theory of an electronic system, such as the nondegenerate ground state of an atom, the basic variable is the electron density. This quantity, however, is not known. For this reason, in an actual calculation of the ground-state energy, one may resort to a modeled electron density. This poses the question: what is the accuracy beyond which one cannot penetrate in the numerical evaluation of certain integrals when using the modeled electron density and an integration technique? The present work attempts to provide an answer to this question by considering the Ne atom as an example, by using the Thomas–Fermi–Dirac energy-density functional, a modeled electron density, and Simpson's (three-point) rule for the numerical integration. © 1992 John Wiley & Sons, Inc.

Introduction

In the Hohenberg and Kohn [1] formulation of DFT, the (nondegenerate) ground-state energy of an electronic system, such as an atom, is a unique functional of the respective electron density. In a previous work [2], using the Ne atom as an example, the author used the TFD energy-density functional, modeled the electron density, and carried out a variational calculation of the total atomic binding energy. In the TFD energy-density functional, the kinetic-energy functional, and the exchange-energy functional, must be evaluated by numerical integration. In the work cited [2], Simpson's (three-point) rule was applied. This raises two questions: (1) What is the precision of the numerical integration with the modeled electron density, and the integration technique selected? (2) Which integral (kinetic, or exchange) will determine the overall precision of the variational calculation of the total atomic binding energy? These questions are investigated in the present work.

The article is organized as follows: in the second section, the theoretical framework of Ref. [2] is very briefly outlined. In the third section, the error estimates of the numerical integrations based on Simpson's (three-point) rule are presented. The final section gives the conclusions.

All quantities used in the present work are expressed in atomic units (the unit of energy is the hartree, the unit of length is the bohr).

Z_1	Z_2	Z_3	$\mathcal{N}$	$\mathcal{H}$
10.828	2.832	7.186	1.7101	0.1014

Theoretical Framework

The TFD total-energy functional is [2]

$$E_t^{TFD}[\rho] = E_k^{TFD}[\rho] + E_{ne}[\rho] + E_{ee}[\rho] + E_x^{TFD}[\rho] \tag{1}$$

where $E_k^{TFD}[\rho]$ is the kinetic-energy functional, $E_{ne}[\rho]$ is the functional describing the (attractive) interaction of the electrons with the atomic nucleus. $E_{ee}[\rho]$ is the classical (or the direct) part of the (repulsive) interaction among the electrons. $E_x^{TFD}[\rho]$ is the exchange-energy functional, and ρ is the electron density. The quantities requiring numerical integrations, are

$$E_k^{TFD}[\rho] = \frac{3}{10}(3\pi^2)^{2/3} \int_0^r \rho^{5/3} 4\pi r^2 \, dr \tag{2}$$

and

$$E_x^{TFD}[\rho] = -\frac{3}{4}\left(\frac{3}{\pi}\right)^{1/3} \int_0^r \rho^{4/3} 4\pi r^2 \, dr. \tag{3}$$

In Ref. [2], the electron (number) density was so chosen that it is (1) finite at the atomic nucleus, (2) exhibits an exponential decay with the distance from the atomic nucleus, and (3) the radial electron (number) density exhibits the extrema associated with the shell structure of the Ne atom.

In Ref. [2], hydrogenlike wave functions [3] were used, and ρ was given as

$$\rho = \frac{1}{4\pi}[2R_{1s}(Z_1)^2 + 2\mathfrak{R}_{2s}(Z_1, Z_2)^2 + 6R_{2p}(Z_3)^2] \tag{4}$$

In Eq. (4). Z_1, Z_2, Z_3 are variational parameters, used to minimize Eq. (1), and

$$\mathfrak{R}_{2s}(Z_1, Z_2) = \mathcal{N}[R_{2s}^{un}(Z_2) + \mathcal{H}R_{1s}(Z_1)] \tag{5}$$

is a 2s function orthogonalized to a 1s function by the Gram–Schmidt procedure [4]. In Eq. (5), the superscript un means unnormalized, while $\mathcal{N}$ is a normalization constant, and $\mathcal{H}$ is an orthogonalization constant. Details are given elsewhere [5].

$E_t^{TFD}[\rho]$ has been minimized [2] with respect to the parameters Z_1, Z_2, and Z_3. The minimization has been carried out by numerical integration, based on Simpson's compound (or three-point rule) [6]. An integration interval from 0 bohr to 8 bohr was found [2] to be satisfactory, subdivided into $M = 2048$ equal subintervals (or panels). The minimizing values of the variational parameters Z_1, Z_2, and Z_3,

together with the (script) normalization and orthogonalization constants $\mathcal{N}$ and $\mathcal{H}$, are listed in Table I. Table II gives the values of the energy components.

At this point, it is convenient to rewrite Eqs. (2) and (3) as

$$E_x^{HD}[\rho] = \frac{3}{10}\left(\frac{3}{4}\pi\right)^{2/3} \int_{1 \cdot 0}^{H \cdot \infty} g(r)\,dr \tag{6}$$

and

$$E_x^{HD}[\rho] = -\frac{3}{4}\left(\frac{3}{4}\pi^2\right)^{1/3} \int_{1 \cdot 0}^{H \cdot \infty} h(r)\,dr. \tag{7}$$

where the integrands are given by

$$g(r) = r^2[2R_{1s}(Z_1)^2 + 2\mathcal{R}_{2s}(Z_1, Z_2)^2 + 6R_{2p}(Z_3)^2]^{5/3} \tag{8}$$

and

$$h(r) = r^2[2R_{1s}(Z_1)^2 + 2\mathcal{R}_{2s}(Z_1, Z_2)^2 + 6R_{2p}(Z_3)^2]^{4/3} \tag{9}$$

Error Estimates

The question is posed: what is the precision of the numerical integrations involving the integrals in Eqs. (6) and (7), when using Simpson's (three-point) rule? For this technique, the maximum errors are given [6] by

$$|E| \leq \frac{(B - A)^5}{180 M^4} \max|g^{(4)}(r)| \tag{10}$$

$$A \leq r \leq B$$

and

$$|F| \leq \frac{(B - A)^5}{180 M^4} \max|h^{(4)}(r)|. \tag{11}$$

$$A \leq r \leq B$$

where the superscripts indicate the fourth derivatives of $g(r)$ and $h(r)$.

To investigate the quantities denoted by $\max|g^{(4)}(r)|$, and $\max|h^{(4)}(r)|$, successively refined tabulations in r have been carried out. The results show that both $|g^{(4)}(r)|$, and $|h^{(4)}(r)|$, have several maxima, separated by minima. The maxima

TABLE II.   Values of the energy components
(in a.u.).

E_x^{HD}	E_{ne}	E_{ee}	E_x^{HD}
140.26	-336.78	67.91	11.63

TABLE III. Maxima of $|g^{(4)}(r)|$ as functions of r (in a.u.). $|E|$ is the error as defined in Eq. (10). The value of $(B - A)^5/180\ M^4$ is 1.035×10^{-11}.

r	max $\|g^{(4)}(r)\|$ $A \le r \le B$	$\|E\|$
0.0760	1.007×10^9	1.042×10^{-2}
0.1964	3.026×10^7	3.131×10^{-4}
0.6415	6.339×10^4	6.560×10^{-7}
1.0782	4.869×10^3	5.039×10^{-8}
2.4177	3.069×10^0	3.176×10^{-11}
3.2743	7.449×10^{-1}	7.709×10^{-12}

of $|g^{(4)}(r)|$, as functions of r, are tabulated in Table III, while the maxima of $|h^{(4)}(r)|$ are tabulated in Table IV.

Conclusions

The most pessimistic conclusion, from Tables III and IV are: the integral in Eq. (6) cannot be evaluated to a precision greater than 1.042×10^{-2}, and the integral in Eq. (7) cannot be evaluated to a precision greater than 4.470×10^{-4}. This conclusion pertains only to the case of $M = 2048$. A doubling of the number of subintervals, that is, using $M = 4096$, would introduce a factor of $1/16$, that would permit precisions of 6.512×10^{-4} and 2.793×10^{-5}. As to the other maxima in $|g^{(4)}(r)|$ and $|h^{(4)}(r)|$, shown in Tables III and IV, no problems arise. These maxima permit much smaller values for $|E|$ and $|F|$, even without doubling the panels.

Another conclusion may also be derived from Tables III and IV. The integral involved in the kinetic-energy expression is associated with a larger error than the integral occurring in the exchange-energy expression.

TABLE IV. Maxima of $|h^{(4)}(r)|$ as functions of r (in a.u.). $|F|$ is the error as defined in Eq. (11). The value of $(B - A)^5/180\ M^4$ is 1.035×10^{-11}.

r	max $\|h^{(4)}(r)\|$ $A \le r \le B$	$\|F\|$
0.0923	4.319×10^7	4.470×10^{-4}
0.2513	7.242×10^5	7.495×10^{-6}
0.6969	1.407×10^4	1.456×10^{-7}
1.2891	5.476×10^2	5.667×10^{-9}
2.5071	5.255×10^0	5.438×10^{-11}
3.9741	1.799×10^{-1}	1.861×10^{-12}

Finally, one has to keep in mind that other numerical integration techniques [6] would give different error estimates.

Bibliography

[1] P. Hohenberg and W. Kohn, Phys. Rev. **136**, B864 (1964).
[2] P. Csavinszky, Int. J. Quantum Chem., Quantum Chem. Symp. **19**, 559 (1986), Int. J. Quantum Chem. **32**, 407(E) (1987).
[3] L. Pauling and E. B. Wilson, *Introduction to Quantum Mechanics* (McGraw-Hill, New York, 1985).
[4] G. Arfken, *Mathematical Methods for Physicists*, 3rd ed. (Academic, New York, 1985).
[5] P. Csavinszky, Int. J. Quantum Chem., Quantum Chem. Symp. **25**, 261 (1991).
[6] Philip J. Davis and Philip Rabinowitz, *Methods of Numerical Integration*, 2nd ed. (Academic, New York, 1984).

Electron Density Theory in Extreme Homogeneous and Heterogeneous Environments and in Intense External Fields

N. H. MARCH

Theoretical Chemistry Department, University of Oxford, 5 South Parks Road, Oxford, OX1 3UB, England

Abstract

After a brief discussion of the deformation of the ground-state electron density asymptotically, in free space homonuclear diatomics by dispersion interactions, dimers in dense homogeneous plasma will be treated. Polarization interaction will be shown to lead to an R^{-4} interaction energy at large internuclear separation, R, supplementing the well-known long-range oscillatory interaction. The relevance of these interactions, when suitably modified for a heterogeneous environment, to lateral forces between CO molecules chemisorbed on a transition metal surface will then be considered, with specific reference to experiments on thermal desorption. Finally, the theory of the inhomogeneous electron liquid in intense magnetic fields will be briefly discussed, for both localized and delocalized electrons. © 1992 John Wiley & Sons, Inc.

Introduction

In this article, electron density theory will be used in essentially two areas*:

(i) To treat the long-range interactions between atoms (and also CO molecules) in unusual environments; and
(ii) To deal with atoms and, in principle at least, molecules in intense applied magnetic fields.

While a (somewhat major) modification of conventional ground-state density-functional theory can be applied to area (i), to date it has proved very helpful to tackle area (ii), for arbitrary magnetic field strengths, starting from the so-called Slater sum. Nevertheless, the aim again, in spite of this use of statistical mechanics, is to calculate the ground-state electron density.

The layout of this article is as follows. In the second section, area (i) will be motivated by briefly recalling how electron density theory can be used to calculate the nonretarded dispersion interaction between atoms in free space. Then, the binding of a homonuclear dimer, such as Na_2, K_2, Be_2, or Mg_2, will be discussed, when the dimer is embedded in a cold, dense plasma. It will be shown that the oscillatory

---

* This article was prepared specifically as part of a session on "Density Functional Theory in Extreme Circumstances."

long-range interaction arising from a sharp Fermi surface must be supplemented by a long-range polarization interaction which falls off as the inverse fourth power of internuclear distance, R, in contrast to the R^{-6} dispersion interaction in free space. The third section considers the effect of inhomogeneity of the environment on the range of both types of interaction.

Area (ii) will then be treated in the fourth section. An approximation to the Slater sum characteristic of the simplest density-functional theory, namely the Thomas–Fermi (TF) statistical method, is generalized there to treat both bound and delocalized electrons in a constant magnetic field of arbitrary strength. The final section constitutes a summary plus some proposals for future work.

Long-Range Interactions in a Homonuclear Dimer in a Homogeneous Environment

Free Space Dispersion Interaction

To motivate the following discussion via electron density of atomic and molecular long-range interactions in unusual environments, let us start from the well-known dispersion interaction in free space. Then, neglecting retardation effects, the interaction energy, $\Delta E(R)$ say, as a function of internuclear separation, R, can be expressed in the form

$$\Delta E(R) = -\frac{c_6}{R^6} : \text{large } R \text{ limit} \tag{1}$$

where the London constant, c_6, can be written precisely in terms of the frequency-dependent polarizabilities $\alpha_i(\omega)$ of the component atoms, i.

Egorov and March [1] have generalized the above result to treat the deformation of the ground-state atomic density in a homonuclear diatomic molecule due to the above dispersion interaction. To do this, these workers use a result by Koide [2], who wrote an expression for the dispersion energy ΔE in terms of wave vector (k) and frequency (ω)-dependent polarizabilities $\alpha(k, k'; \omega)$. Egorov and March show how his result can be used, in conjunction with the Hellmann–Feynman theorem [3], to construct an expression for that deformation of the atomic electron density which, when inserted in the above theorem, will yield the correct long-range dispersion force $-6c_6/R^7$, from eq. (1). No claim is made that the total atomic density can be constructed at large internuclear separation, R, in a homonuclear diatomic molecule in this way. It is only a correction to the atomic density such that, when inserted in the Hellmann–Feynman force expression, will exactly reproduce Koide's dispersion energy at sufficiently large R. Koide's result

$$\Delta E = -\frac{1}{4\pi^4} \int \frac{d\mathbf{k}}{k^2} \exp(i\mathbf{k} \cdot \mathbf{R}) \int \frac{d\mathbf{k}'}{k'^2} \exp(-i\mathbf{k}' \cdot \mathbf{R})$$

$$\times \frac{\hbar}{2\pi} \int_0^\infty du\, \alpha_a(\mathbf{k}, \mathbf{k}'; iu)\alpha_b(-\mathbf{k}, -\mathbf{k}'; iu) \tag{2}$$

can, of course, readily be converted to a force, since $d\Delta E/dR$ is simply the dispersion force referred to above.

It is next to be noted that an alternative, and quite general, expression for the force can be written in a neutral homonuclear diatomic molecule built from individual atoms with atomic number, Z, as

$$F_a = \frac{Z^2}{R^2} + \int \frac{z_{a1}}{r_{a1}^3} \rho(\mathbf{r}_1, R) \, d\mathbf{r}_1 \tag{3}$$

where z_{a1} is the z component of the distance of the point $\mathbf{r}_1$ from nucleus a for instance. For the case of two hydrogen atoms, a and b, separated by a distance R, eq. (3) holds evidently with $Z = 1$. Here F_a is the force on nucleus a in the direction of nucleus b, taken as the z axis, while $\rho(\mathbf{r}_1, R)$ is the total electronic density:

$$\rho(\mathbf{r}_1, R) = 2 \int \Psi^*(\mathbf{r}_1, \mathbf{r}_2) \Psi(\mathbf{r}_1, \mathbf{r}_2) \, d\mathbf{r}_2 \tag{4}$$

with Ψ the ground-state electronic wave function. As it stands, eq. (3) is valid for all R. However, at intermediate R at or around the equilibrium bond length, the solution of the two-center problem is essential for the determination of $\rho(\mathbf{r}_1, R)$. At large R, alternatively, the total electronic density may be represented by the superposition of two "atomic" parts, $\rho(a)$ and $\rho(b)$, each of which can be written as a sum of the unperturbed spherically symmetric density, ρ_0, and the series expansion in inverse powers of R starting with the R^{-n} term:

$$\rho(a) = \rho_0(a) + \frac{1}{R^6} \rho_6(a) + \frac{1}{R^7} \rho_7(a) + \cdots \tag{5}$$

The spherical part, $\rho_0(a)$, evidently makes zero contribution to the integral in eq. (3). The R^{-6} component of the "atomic" density, $\rho(a)$, which results in turn from the R^{-3} component of the wave function, forms a quadrupole charge distribution around nucleus a and, being symmetric with respect to coordinate z_{a1}, it does not lead to an attraction between the two nuclei [except for the R^{-10} attraction between the quadrupoles from $\rho(a)$ and $\rho(b)$]. The R^{-7} component in the vicinity of nucleus a is slightly larger in the direction of nucleus b than away from it [3]. Thus, the force on the nucleus results from its attraction to the centroid of the charge density corresponding to its associated electrons. The van der Waals force $= 6c_6/R^7$, from eq. (3), arises entirely from the R^{-7} component of the total density.

Differentiating Koide's expression (2) with respect to R, Egorov and March then use the molecular form factor for X-ray scattering, $f(\mathbf{k}, R)$ say, defined by

$$f(\mathbf{k}, R) = \int \rho(\mathbf{r}, R) \exp(i\mathbf{k} \cdot \mathbf{r}) \, d\mathbf{r}, \tag{6}$$

to derive the equivalence

$$\frac{ikz}{k^2} f(\mathbf{k}, R) - \frac{\pi^2}{2k} + F = -\frac{1}{4\pi^4 k^2} \int \frac{d\mathbf{k'}}{k'^2} i \frac{(\mathbf{k} - \mathbf{k'})_z}{2}$$

$$\times \exp\left(-\frac{i\mathbf{k'} \cdot \mathbf{R}}{2}\right)$$

$$\times \frac{\hbar}{2\pi} \int_0^\infty du\, \alpha_a(\mathbf{k}, \mathbf{k'}; iu) \alpha_b(-\mathbf{k}, -\mathbf{k'}; iu). \qquad (7)$$

In eq. (7), F designates that part which integrates to zero: since eq. (7) emerges from equating two integrands.

To summarize this free-space argument, the deformation of the ground-state density, to accord with the known form of dispersion interaction, can be reduced to a one-center purely atomic problem by the use of $\mathbf{k}$- and ω-dependent polarizabilities. We now turn to contrast this with the interaction when we embed a dimer in a cold, dense plasma; e.g., Na_2 or Mg_2 in their own liquid metal just above its freezing point. Even at such a temperature, the itinerant electrons are essentially completely degenerate.

Dimer Potential Energy Curve in Cold, Dense Plasma

Debye-Hückel-Like Interaction Between Test Charges. Alfred and March [4] considered the interaction energy of two like test-charges Ze embedded in a cold, dense plasma. The self-consistent potential, $V(\mathbf{r})$, satisfies the linearized Thomas–Fermi equation, derived from this simplest density functional theory (see also Appendix 1):

$$\nabla^2 V = q^2 V \qquad (8)$$

The inverse screening length q is given by

$$q^2 = \frac{4k_f}{\pi a_0}; \quad a_0 = \frac{\hbar^2}{me^2}, \qquad (9)$$

where the Fermi wave number, k_f, is related to the mean electron density, ρ_0, in the (originally homogeneous) plasma by

$$\rho_0 = \frac{k_f^3}{3\pi^2}. \qquad (10)$$

In Ref. 4, V was constructed from the superposition of potentials, V_1 and V_2, centered on the test charges Ze at separation R. This led to the repulsive interaction

$$\Delta E(R) = \frac{(Ze)^2}{R} \exp(-qR). \qquad (11)$$

Very recently, Perrot et al. [5] have allowed the displaced spherical charges centered on 1 and 2 at infinite separation to float off the nuclei by an amount $\delta(R)$. The displacement, δ, was then obtained variationally from the density-functional form

$$E = E_s \int \Delta \, dr + c_2 \int \Delta^2 \, dr + \text{classical potential energy terms} . \qquad (12)$$

Minimizing this energy expression with respect to Δ leads back to

$$\Delta(r) = \frac{q^2}{4\pi} V(r) . \qquad (13)$$

Combining eq. (13) with Poisson's equation yields eq. (8).

The total energy E for q as in liquid metal Cu [5] was calculated variationally from eq. (12) by allowing the spherical blobs of displaced charge to float from the test charges by the amount δ. It is then found that this Debye-Hückel-like theory is deficient in a degenerate electron gas: one must allow for diffraction of the de Broglie waves representing the itinerant electrons off the test charges, as first shown by Corless and March [6]. However, again their treatment was based on a superposition assumption. Perrot et al. [5] argue that this wave theory, again allowing "floating" blobs of displaced charge off the test charges, leads to

$$\delta \sim \frac{1}{R^2} \qquad (14)$$

at large R. The corresponding long-range interaction energy is now

$$\Delta E(R) \sim \frac{A \cos 2k_f R}{R^3} + \frac{\text{constant}}{R^4} + \cdots \qquad (15)$$

the first term on the right-hand side of eq. (15) being given by Corless and March [6], while the $1/R^4$ term is from the "polarization" interaction considered here. It must be stressed that it is essential to use the wave theory to obtain eq. (15): see the original argument for this R^4 term in ref. 5.

Long-Range Interaction in a Heterogeneous Environment

Test Charges Embedded in Electron Density at a Model Metal Surface

Below, following Flores et al. ([7: see also Lau and Kohn [8]), use will be made of the Bardeen model of a metal surface [9]. For this model, not only the unperturbed density, $\rho(r)$, but also the Dirac density matrix, $\rho(r, r')$, is known. This latter quantity allows the response function, $F(r, r')$, appearing in the relation between a perturbing potential, V, and the displaced charge, $\Delta\rho$ it creates (see also Appendix 1):

$$\Delta\rho(r) = \int F(r, r') V(r') \, dr' . \qquad (16)$$

to be found. If the perturbation, $V(r')$, is short-ranged, and in particular can be modeled by $\lambda\delta(r')$, then

$$\Delta\rho(r) \sim F(r, 0) . \qquad (17)$$

This leads to a perturbed density which oscillates, as for the bulk case. However, for test charges parallel to the planar metal surface in the (x, y) plane, the interaction energy is now shorter range: the leading term in eq. (15) being replaced, in this lateral interaction, by

$$\Delta E(R) \sim \frac{A \cos 2k_f R}{R^5} .$$ (18)

Range of Polarization Interaction. While, in eq. (15), the oscillatory interaction has range R^{-3} times an oscillatory function, which therefore, except at or very near the nodes of the $\cos 2k_f R$ factor, dominates the polarization interaction, having range R^{-4}, it is important in the future to know whether that situation also obtains in the heterogeneous environment provided by a metal surface—since, in the parallel configuration, eq. (18) shows that the range of the oscillatory term is reduced to R^{-5} times an oscillatory factor.

$2\pi^*$ *Resonance Model for CO Molecules Interacting Outside a Transition Metal Surface*

CO Chemisorbed on Pt(III). It is of interest in the present context to extend the discussion of the oscillatory long-range interaction in a heterogeneous environment to treat lateral interactions between CO molecules chemisorbed on Pt(III).

The additional ingredient required to give a realistic account of such lateral interactions on transition metal surfaces is the concept of a CO $2\pi^*$ resonance. Independent evidence in support of this resonance model comes from:

(a) The analysis of the desorption measurement of Ertl et al. [10], by Joyce et al. [11]; and

(b) The study of a variety of experimental spectroscopic features, e.g., threshold energies, level shift, and line shapes, by Gumhalter et al. [12].

Briefly, the model can be understood by reference to Figure 1, which makes specific the energy level spectrum of CO on a transition-metal surface. Both the $2\pi^*$ and the 5σ levels of the CO molecule are positioned relative to the Fermi level, E_f. To modify, for a pair of CO molecules in the configuration parallel to the planar metal surface, the asymptotic oscillatory interaction $\sim \cos(2k_f R)/R^5$ discussed above, it is important to recognize that the $2\pi^*$ level, which overlaps unoccupied energy bands, will be broadened into a virtual bound state. With reasonable assumptions about the interaction between the $2\pi^*$ orbitals on CO and the metal band wave functions, the broadening of the virtual bound state can be such that it overlaps the Fermi level. It is this effect of such a state near the Fermi level that is the dominant reason for the importance of the indirect interaction between CO molecules on some transition-metal surfaces. It turns out that the $2\pi^*$ orbital interacts predominantly [13] with the sp band of Ni, Pd, and Pt; this allows a model to be constructed based on an sp band for the metal and solely the $2\pi^*$ level of the molecule.
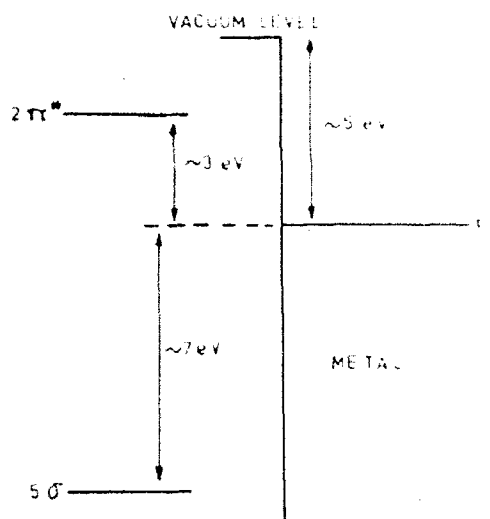
Figure 1 Shows $2\pi^*$ and 5σ levels of CO molecule placed relative to vacuum level and to metal Fermi energy. Since $2\pi^*$ overlaps unoccupied energy band states, it will be broadened to become a virtual bound state. In circumstances such that this broadened state overlaps the Fermi level, the indirect lateral interaction between a pair of chemisorbed CO molecules can be substantially enhanced.

What is relevant then in the present context is that the asymptotic oscillatory interaction is changed to

$$\Delta E(R) \sim \beta \cos(2k_f R + \phi)/R^5 . \qquad (19)$$

Major changes then occur, from the $2\pi^*$ resonance model, in the expressions for the amplitude, β, and the phase shift, ϕ. These can, in fact, be extracted by analyzing thermal desorption data as a function of coverage for CO chemisorbed on Pt [111]. One finds $\phi = 0.95$ and $\beta = 10^7$ J mol^{-1} Å^5. The $2\pi^*$ resonance model, with reasonable parameterization, yields $\phi \approx 3\pi/8$ and $\beta \sim \frac{1}{2} \times 10^7$ J mol^{-1} Å^5.

As discussed earlier, there is the possibility of incorporating asymptotically an additional polarization interaction: this has been seen to have a range of R^{-4} in a homogeneous environment [5]. One anticipates, as with the oscillatory term, a shortening of the range to R^{-n}, $n \approx 5$, but further work is required on the effect of a heterogeneous environment on the polarization interaction.

We now turn to area (ii) referred to in the Introduction: the focus again being on the use of electron density theory in extreme circumstances. In area (ii), these circumstances are afforded by the application of intense magnetic fields to atomic and molecular systems (see also Schmelcher and Cederbaum [14–16]).

Thomas-Fermi Theory in Constant Magnetic Field of Arbitrary Strength

We turn from asymptotic interactions in homogeneous and heterogeneous environments to the treatment of bound and delocalized electrons moving in a constant

magnetic field of arbitrary strength.[2] As emphasized recently by Amovilli and March [17], the ground-state electron density $\rho_H(\mathbf{r}, E)$ is then conveniently calculated via the so-called Slater sum, $Z_H(\mathbf{r}, \beta)$, with $\beta = (k_B T)^{-1}$. Though not based on the Slater sum, here it is relevant to note the work of Li and Percus [18,19] and the earlier study of Harris and Cina [20].

Zero-Field Limit

The Thomas-Fermi theory in zero magnetic field, as is clear from the studies of March and Murray [21], corresponds to the following approximation to the Slater sum $Z(\mathbf{r}, \beta)$:

$$Z(\mathbf{r}, \beta) = Z_0(\beta)\exp(-\beta V(\mathbf{r})) \tag{20}$$

where $Z_0(\beta) = (2\pi\beta)^{-3/2}$ is the partition function per unit volume for free electrons. Using the Laplace transform relation between the ground-state electron density, $\rho(\mathbf{r}, E)$, and the Slater sum, namely

$$Z(\mathbf{r}, \beta) = \beta \int_0^\infty \rho(\mathbf{r}, E)\exp(-\beta E)\, dE, \tag{21}$$

one finds the zero magnetic field density-potential relation characterizing the Thomas–Fermi theory as [4]

$$\rho(\mathbf{r}, E) = \frac{8\pi}{3h^3}(2m)^{3/2}[E - V(\mathbf{r})]^{3/2}. \tag{22}$$

Inclusion of Constant Magnetic Field H

The objective below is now to generalize the above argument, to include the modification of the electronic "orbits" by the application of a constant external magnetic field H of arbitrary strength. It should be emphasized here that everything that follows is within the framework of a one-electron Hamiltonian, $\mathscr{H}$, given by

$$\mathscr{H} = \frac{\left(\mathbf{p} - \dfrac{e\mathbf{A}}{c}\right)^2}{2m} + V(\mathbf{r}) \tag{23}$$

where the vector potential, $\mathbf{A}$, represents the constant magnetic field. As usual, the one-body potential energy $V(\mathbf{r})$ should eventually be calculated self-consistently.

One wishes therefore to generalize each of the eqs. (20), (21), and (22) to include the effect of a constant magnetic field, H. One follows the same philosophy as above, namely, to solve first the free-particle problem, corresponding to $Z_0(\beta)$

---

[2] A link between van der Waals interaction in a heterogeneous metal surface environment and diamagnetism of electrons treated in the present section is forged in Appendix 2, where Rydberg atoms in intense fields are discussed.

below eq. (20) in the limit H tends to zero, and then to introduce V(r) just as in eq. (20).

The free-electron problem has been solved by Sondheimer and Wilson [22], who obtained the Slater sum, $Z_{oH}(\beta)$, as

$$Z_{oH}(\beta) = \frac{1}{(2\pi\beta)^{3/2}} \frac{\mu H\beta}{\sinh(\mu H\beta)} \qquad (24)$$

where $\mu = eh/(4\pi mc)$ is the Bohr magneton. Eq. (24) is readily shown to reduce to the value $Z_o(\beta) = (2\pi\beta)^{-3/2}$ corresponding to eq. (20) in the limit $H \rightarrow 0$. Again, for an assumed spatial slowly varying potential, V(r), in the Hamiltonian (23), the corresponding Slater sum is approximated in the Thomas–Fermi theory by

$$Z_H(r, \beta) = Z_{oH}(\beta)\exp(-\beta V(r)) \qquad (25)$$

where Z_{oH} has the form (24). Since the Laplace transform relation (21) remains intact for arbitrary magnetic field H, one reaches the form of the ground-state electron density $\rho_H(r, E)$ as [23]:

$$\rho_H(r, E) = \mathcal{L}^{-1}[Z_H(r, \beta)/\beta]. \qquad (26)$$

Eqs. (25) and (26) constitute the desired generalization of the Thomas–Fermi relation (22) to include a constant magnetic field, H, of arbitrary strength [23].

Pfalzner and March [23] have obtained results based on eqs. (25) and (26) and sample calculations are presented in Figures 2 and 3. Figure 2 corresponds to "switching off" the self-consistent V(r); the results were obtained for selected values of H by inverting the Laplace transform occurring in eq. (26) numerically. The zero-field limit is then $\rho(E) \propto E^{3/2}$ as in eq. (22) for V = 0; the smooth dependence on energy is no longer valid for $H \neq 0$ because of the modification of the zero-field energy level spectrum by Landau level quantization. Figure 3 shows the effect of including the Thomas–Fermi (H = 0) self-consistent neutral atom potential.

Case of Extreme High Field Limit

While, as is clear from the above discussion, the intermediate magnetic field regime must currently be treated numerically, because of the difficulties of obtaining a compact closed analytical form for the inverse Laplace transform of $Z_{oH}(\beta)/\beta$ obtained from eq. (24), it turns out that, as in the zero field limit (22), the extreme high field limit, H, tends to infinity and can also be handled analytically. Then one can replace, in eq. (24) the sinh by a single exponential term, to obtain

$$\lim_{H \rightarrow \infty} Z_{oH}(\beta) \sim \frac{1}{(2\pi\beta)^{3/2}} \mu H\beta \exp(-\mu H\beta) \qquad (27)$$

The inverse Laplace transform of $Z_{oH}(\beta)/\beta$ can then be completed analytically, to yield

$$\rho_{oH}(E) = \text{constant } H(E - \mu H)^{1/2} \qquad (28)$$
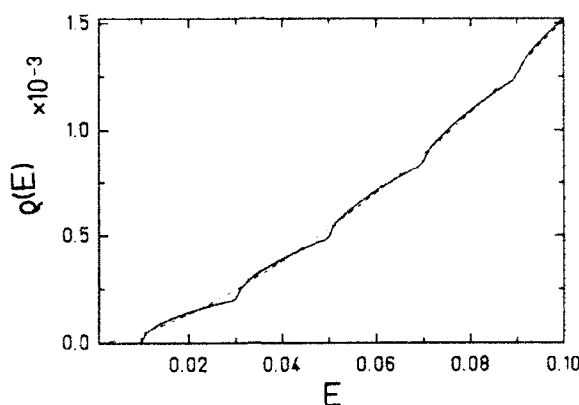
Figure 2. Depicts uniform electron density $\rho(E)$ for itinerant electrons in a constant magnetic field of strength such that $\mu H = 0.5$ atomic units. Essentially this figure represents the generalization of the high field limit [eq. (28)] to intermediate field strengths, and reveals features due to Landau-level quantization. Dashed curve represents the zero field $\rho(E)$ given in eq. (22) with $V(r)$ set equal to zero (after Pfalzner and March [23]).

and the ground-state electron density in the Thomas–Fermi limit of slowly varying $V(r)$ yields

$$\rho_{H}(r, E) = \text{constant } H(E - \mu H - V(r))^{1/2} \qquad (29)$$

In fact, this result (29) has been derived much earlier using phase-space arguments [24–28].

Summary and Proposals for Further Work

In this discussion of electron density theory in extreme circumstances, attention has first been focused on long-range interactions in homogeneous and heterogeneous environments. When one goes from a dimer in free space to a dimer in a cold, dense plasma (e.g. Na_2 or Be_2 in their own liquid metals near freezing), the non-retarded dispersion interaction of range, R^{-6}, gives way to the asymptotic form (15). The oscillatory term comes from itinerant electrons contained in k space within a sharp Fermi surface of diameter $2k_f$. The polarization interaction, of range R^{-4} in eq. (15) appears to affect the small-angle scattering from liquid Na [29], but quantitative work is not presently complete here.

Turning to the heterogeneous environment afforded by metal surfaces, for a pair of atoms, or CO molecules, chemisorbed parallel to a planar surface, the range of the oscillatory term in eq. (15) is reduced, the modified form of the oscillatory component being given in eq. (18). It remains for future work to establish the precise reduction in range of the polarization interaction contribution, αR^{-4}, in the homogeneous environment when one goes over to the highly heterogeneous situation of chemisorption on a transition-metal surface.

The second area briefly discussed, that of atomic systems in intense applied mag-
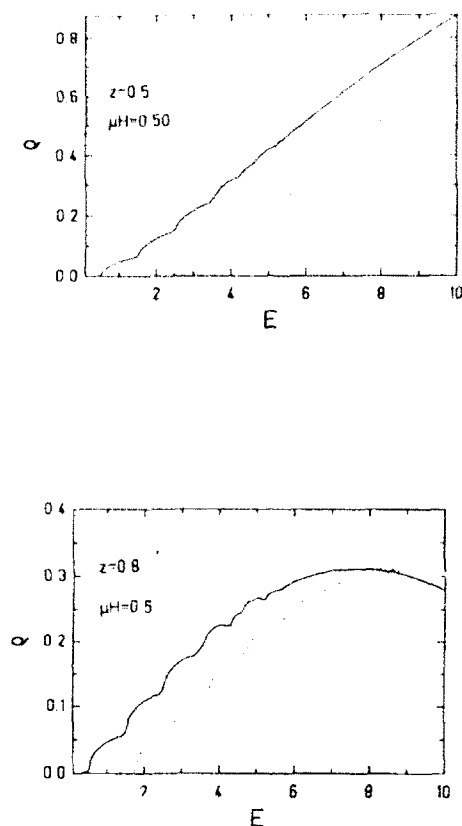
Figure 3. Modification of Figure 2 as a result of including the Thomas-Fermi ($H = 0$) self-consistent neutral atom potential $V(r)$ via eq. (25). The full line corresponds to $V(r) = 0$. The dashed curve is for the bare Coulomb potential, $V(r) = 1/r$, while the dotted curve represents the Thomas-Fermi potential. The constant magnetic field is along the z axis, and upper curve corresponds to $z = 0.5$ and lower to $z = 0.8$, again, in atomic units. In both parts of the figure, $\mu H = 0.5$ atomic units as in Figure 2. (Reproduced from work of Pfalzner and March [23])

netic fields, has been tackled via the Slater sum, which can be viewed as an electron density in classical Maxwell–Boltzmann statistics. The ground-state density can then be extracted by an inverse Laplace transform according to eq. (26), and examples have been presented [23] embracing both itinerant and bound electrons. In future work, self-consistency should, of course, be imposed, within this theoretical framework, whereas to date this has only been accomplished based on the limiting extreme high field result (29); numerical self-consistent fields then being presented for atomic ions in ref. 30. For intermediate fields, the numerical inverse Laplace transform techniques of Pfalzner and March [23] should eventually allow self-consistent calculations on both atoms and molecules [14–16,31] to be achieved.

Appendix 1

Asymptotic Displaced Charge Round Localized Perturbations in Homogeneous and Heterogeneous Metallic Environments

The purpose of this Appendix is to provide insight into the asymptotic interactions in eqs. (15) and (18). This will be done within a linear response framework. Thus, for a one-body perturbation, $V(r)$, one can write for the displaced charge $\Delta\rho(r)$ the formal result

$$\Delta\rho(\mathbf{r}) = \int F(\mathbf{r}, \mathbf{r}') V(\mathbf{r}') \, d\mathbf{r}' . \tag{A1}$$

Form of Linear Response Function F *in Homogeneous Electron Gas.* As derived by March and Murray [21] for the homogeneous electron gas, the linear response function, F, is given by

$$F_{HOMO}(\mathbf{r}, \mathbf{r}') = -\frac{k^2}{2\pi^2} \frac{j_1(2k|\mathbf{r} - \mathbf{r}'|)}{|\mathbf{r} - \mathbf{r}'|^2} . \tag{A2}$$

where k has been written for the Fermi wavenumber. Whereas the Thomas–Fermi result, $\Delta\rho(r) = (q^2/4\pi) V(\mathbf{r})$, follows from eq. (A1) if $V(\mathbf{r}')$ is so slowly varying that it can be evaluated at $\mathbf{r}' = \mathbf{r}$, and hence, brought outside the integral, let us consider a localized perturbation represented by the model potential

$$V(\mathbf{r}) = \lambda\delta(\mathbf{r}) . \tag{A3}$$

Inserting eq. (A3) into eq. (A2) and using the asymptotic large distance form of the first-order spherical Bessel function $j_1(x) = x^{-2}[\sin x - x \cos x]$, one readily finds

$$\Delta\rho(r) \sim \frac{A \cos 2kr}{r^3} ; r \text{ large} . \tag{A4}$$

These so-called Friedel oscillations in a single-center problem have the counterpart for the two-center case in the interaction energy, $\Delta E(R)$ in eq. (15), as demonstrated by Corless and March ([6], see also Ziman [32]).

Response Function F *for a Barrier Model of a Metal Surface.* For the Bardeen infinite barrier model [9] of a metal surface, Moore and March [33] have shown that the result (A2) for the homogeneous linear response function, F, is changed to read

$$F(\mathbf{r}, \mathbf{r}') = -\frac{k^2}{2\pi^2} \left(\frac{j_1(2k|\mathbf{r} - \mathbf{r}'|)}{|\mathbf{r} - \mathbf{r}'|^2} + \frac{j_1[2k(|\mathbf{r} - \mathbf{r}'|^2 + 4zz')^{1/2}]}{|\mathbf{r} - \mathbf{r}'|^2 + 4zz'} \right.$$

$$\left. - \frac{2j_1\{k[|\mathbf{r} - \mathbf{r}'| + (|\mathbf{r} - \mathbf{r}'|^2 + 4zz')^{1/2}]\}}{|\mathbf{r} - \mathbf{r}'|(|\mathbf{r} - \mathbf{r}'|^2 + 4zz')^{1/2}} \right) \text{ for } z, z' > 0$$

$$= 0 \text{ otherwise} \quad (A5)$$

and the unperturbed electron density is [9]

$$\rho(z) = \frac{k^3}{3\pi^2}\left(1 - \frac{3 j_1(2kz)}{2kz}\right), \tag{A6}$$

where the planar metal surface is evidently in the (x, y) plane. Taking again a suitable model potential, having now the form

$$V(\mathbf{r}) = V(\mathbf{X})\delta(z - a) \tag{A7}$$

where $\mathbf{X} = (x, y)$ is the component of $\mathbf{r}$ parallel to the surface, while $V(\mathbf{X})$ remains general, one can substitute eq. (A7) into eq. (A1) to find, for $2kX \gg 1$:

$$\Delta\rho(\mathbf{X}, a) \simeq A\left(\frac{\cos 2kX}{X^3} + \frac{\cos 2k(X^2 + 4a^2)^{1/2}}{(X^2 + 4a^2)^{3/2}}\right.$$
$$\left. - \frac{4\cos k[X + (X^2 + 4a^2)^{1/2}]}{X(X^2 + 4a^2)^{1/2}[X + (X^2 + 4a^2)^{1/2}]}\right) \tag{A8}$$

where the amplitude, A, depends on the Fourier transform of $V(\mathbf{X})$ at the diameter $2k$ of the Fermi sphere as well as on k itself. For $X \gg a$, one recovers from eq. (A8) an asymptotic decay as $\cos(2kX)/X^3$, which has as its counterpart in the two-center case the asymptotic form (18) for the interaction energy $\Delta E(R)$. This has a different range from that which would have been obtained by direct use of a local-density approximation in the homogeneous result (A4). Indeed, one has extreme circumstances here for density functional theory due to the marked heterogeneity induced by the metallic surface.

Appendix 2

Atoms in External Fields: A Link Between Diamagnetism and Surface Effects

The sensitivity of Rydberg atoms to perturbations, and the rich variety of experimental information than can thereby be extracted, has been important in the revival of interest in the study of atoms in external fields. In this general context, the purpose of this Appendix is two-fold: (i) To link the diamagnetism discussed in the section "Inclusion of Constant Magnetic Field, H" and the heterogeneity due to a metal surface (see "Test Charges Embedded in Electron Density at a Model Metal Surface"); and (ii) to summarize some salient points of theory worked out to date.

As to purpose (i) above, the instantaneous van der Waals (vW) potential representing the interaction between an atom and a metal surface, as studied by Lennard-Jones [34], can be expressed in the form

$$V_{vW} = -(1/16d^3)(x^2 + y^2 + 2z^2), \tag{A9}$$

while the diamagnetic potential (see, e.g., review by Kleppner et al. [35]) can be written as

$$V_{diam} = (\omega_c^2/8)(x^2 + y^2), \tag{A10}$$

with ω, the cyclotron angular frequency.

As noted by Alhassid et al. [36], and others, the potentials (A9) and (A10) are embraced by the general form

$$V = \gamma(x^2 + y^2 + \beta^2 z^2) ,$$ (A11)

This observation then prompts the study of the Hamiltonian, $\mathscr{H}$, representing a Rydberg atom, namely

$$\mathscr{H} = \frac{p^2}{2} - \frac{Z}{r} + \gamma(x^2 + y^2 + \beta^2 z^2) ,$$ (A12)

where Z is evidently equal to unity for the hydrogen atom.

With regard to purpose (ii) above, it should first be noted that, by employing Painlevé singularity analysis and Lie symmetry invariance, Ganesan and Lakshmanan [37] have shown that the system (for angular momentum $L_z = 0$) is integrable for the three choices $\beta = \frac{1}{2}$, 1, and 2 in the Hamiltonian (A12). For these special choices of β, the existence of dynamical symmetries has already been pointed out by Alhassid et al. [36].

For the case $Z = 0$ in eq. (A12), the Slater sum of eq. (21) has been studied for some cases by March and Tosi [38] and by Amovilli et al. [39]. In addition, by means of the inverse Laplace transform of the Slater sum discussed in the main text, preliminary results for the Hamiltonian (A12) for $\gamma = 0$ are already available [40].

Finally, it is relevant to note that, again, for the case $\gamma = 0$, the angular momentum and the Runge–Lenz vector are constants of the motion [41]. This well-known situation is transcended in the work of Holas and March [42]. In their study, the classical generalization of the Runge–Lenz vector is treated for non-Coulomb central fields appropriate approximately to multielectron atoms.

Bibliography

[1] S. A. Egorov and N. H. March, Phys. Lett. A 157, 57 (1991).

[2] A. Koide, J. Phys. B 9, 3173 (1976).

[3] J. O. Hirschfelder and M. A. Eliason, J. Chem. Phys. 47, 1164 (1976).

[4] L. C. R. Alfred and N. H. March, Phil. Mag. 2, 985 (1957).

[5] F. Perrot, M. Blažej, and N. H. March, work in progess.

[6] G. K. Corless and N. H. March, Phil. Mag. 6, 1285 (1961).

[7] F. Flores, N. H. March, and I. D. Moore, Surface Sci. 69, 133 (1977).

[8] K. H. Lau and W. Kohn, Surface Sci. 75, 69 (1978).

[9] J. Bardeen, Phys. Rev. 49, 653 (1936).

[10] G. Ertl, M. Neumann, and K. M. Streit, Surface Sci. 64, 393 (1977).

[11] K. Joyce, A. Martin-Rodero, F. Flores, P. J. Grout, and N. H. March, J. Phys. C 20, 3381 (1987).

[12] B. Gumhalter, K. Wandelt, and P. Avouris, Phys. Rev. B 37, 8048 (1988).

[13] B. Gumhalter, Phys. Rev. B 33, 5245 (1986).

[14] P. Schmelcher and L. S. Cederbaum, Phys. Rev. A 37, 672 (1988).

[15] P. Schmelcher and L. S. Cederbaum, Phys. Rev. A 41, 4936 (1990).

[16] P. Schmelcher and L. S. Cederbaum, Int. J. Quant. Chem. Symp. 25, 371 (1991).

[17] C. Amovilli and N. H. March, Phys. Rev. A 44, 2846 (1991).

[18] S. Li and J. K. Percus, Phys. Rev. A 41, 2344 (1990).

[19] S. Li and J. K. Percus, J. Chem. Phys. 93, 4266 (1990).
[20] R. A. Harris and J. A. Cina, J. Chem. Phys. 79, 1381 (1983).
[21] N. H. March and A. M. Murray, Phys. Rev. 120, 830 (1960).
[22] E. H. Sondheimer and A. H. Wilson, Proc. Roy. Soc. A (London) 210, 173 (1951).
[23] S. Pfalzner and N. H. March, J. Math. Phys. (to appear).
[24] B. B. Kadomtsev, Sov. Phys. JETP 31, 945 (1970).
[25] R. O. Mueller, A. R. P. Rau, and L. Spruch, Phys. Rev. Lett. 26, 1136 (1971).
[26] B. Banerjee, D. H. Constantinescu, and P. Rehak, Phys. Rev. D 10, 2384 (1974).
[27] A. R. P. Rau, R. O. Mueller, and L. Spruch, Phys. Rev. A 11, 1865 (1975).
[28] N. H. March and Y. Tomishima, Phys. Rev. D 19, 449 (1979).
[29] C. C. Matthai and N. H. March, Phys. Chem. Liquids 11, 207 (1982).
[30] S. H. Hill, P. J. Grout, and N. H. March, J. Phys. B 16, 2301 (1983); J. Phys. B 18, 4665 (1985).
[31] C. Amovilli and N. H. March, Chem. Phys. 146, 207 (1990).
[32] J. M. Ziman, Adv. Phys. 13, 89 (1964).
[33] I. D. Moore and N. H. March, Ann. Phys. 97, 136 (1976).
[34] J. E. Lennard-Jones, Trans. Faraday Soc. 28, 334 (1932).
[35] D. Kleppner, M. G. Littman, and M. L. Zimmerman, in *Rydberg State of Atoms and Molecules,*
     R. F. Stebbings and F. B. Dunning, Eds. (Cambridge University Press, New York, 1983), p. 73.
[36] Y. Alhassid, E. A. Hinds, and D. Meschede, Phys. Rev. Lett. 59, 1545 (1987).
[37] K. Ganesan and M. Lakshmanan, Phys. Rev. A 45, 1548 (1992).
[38] N. H. March and M. P. Tosi, J. Phys. A 18, L643 (1985).
[39] C. Amovilli, N. H. March, and S. Pfalzner, Phys. Chem. Liquids 24, 79 (1991).
[40] S. Pfalzner and N. H. March (unpublished work, 1992).
[41] L. D. Landau and E. M. Lifshitz, *Mechanics Course of Theoretical Physics,* vol. 1 (Pergamon,
     Oxford, 1976).
[42] A. Holas and N. H. March, J. Phys. A 23, 735 (1990).

Quintet Electronic States of MoO: Gaussian Density Functional Calculations

EWA BROCLAWIK* and DENNIS R. SALAHUB

Departement de Chimie, Université de Montréal, CP 6128, Succursale A, Montréal Québec, Canada

Abstract

Spin-polarized LSD calculations for MoO, both all-electron and model core potential, are reported and compared with the recent spectroscopic data. The properties of the $^5\Pi$ ground state and four quintet excited states are evaluated, their agreement with the experiment was found to be quite satisfactory. One of the states, $^5\Sigma$, is approached theoretically for the first time. © 1992 John Wiley & Sons, Inc.

Introduction

Transition metal oxides form a class of chemical compounds of particular interest, and have been investigated extensively for many years both experimentally and theoretically [1-6]. The nature of the bonding with oxygen in selected first- and second-row transition metal oxides has been studied theoretically both within cluster model treatments and in diatomics [1-4] in the hope that detailed knowledge about the features of the metal-oxygen diatomic bond may provide some guidance for the understanding of the interaction of oxygen with metal surfaces and within bulk oxides.

On the other hand, spectroscopic investigation of the transition metal monoxides has been a very rapidly growing field as it is an important class of unsaturated metal-ligand complexes which have interesting electronic structures and, at the same time, are relatively easy to prepare and stable at high temperatures. The ground states and many excited electronic states of the entire 3d series of transition metal oxides have been already characterized experimentally [5]. The present understanding of the 4d series of metal oxides is, however, much more limited.

Recently a thorough study of the spectra of the MoO diatomic has been published [6], providing the first conclusive gas-phase investigation of this molecule, complete with rotational analyses, isotope shift measurements, and assignments of several electronic states. Some of these states have never been approached theoretically, thus it seemed to be of particular interest to extend the available theoretical calculations for MoO.

Previously reported theoretical studies on the electronic structure of MoO have been performed by means of self-consistent field HF and multiconfiguration SCF

---

* Currently leave from the Institute of Catalysis, Polish Academy of Sciences, Cracow, Poland.

calculations, followed by single and double excitation (SDCI) calculations [1]. These computational techniques fall among the most accurate traditional quantum chemical methods, however, only at the highest degree of calculations at a large expense of computing time do they prove to approach the experimental values for transition metal oxides.

At the same time, the local-spin-density (LSD) method appeared to be a very useful tool for the description of the electronic structure of various molecules containing transition metal atoms [7]. DFT-Based methods have proven to be numerically very efficient and lead to reasonably accurate results with moderate computational effort. The introduction of the model core potential (MCP) method into the spin-polarized local-spin-density calculations extended the scope of this method to the treatment of large clusters containing transition metal atoms [8]. Thus, this method has been chosen as a tool for the study of the electronic structure of the MoO molecule.

In this study, spin-polarized LSD calculations for MoO, both all-electron and model core potential, are reported and compared with the recent spectroscopic data of Hamrick et al. [6]. The properties of the $^5\Pi$ ground state and four-quintet excited states are evaluated, and their agreement with the experiment found to be quite satisfactory. One of the states, $^5\Sigma$, is, to our best knowledge, described theoretically for the first time.

Calculational Details

The computations have been performed by means of the spin-polarized LSD method using both all electron GTF basis sets and with a MCP for molybdenum. Calculations were done using the program, deMon, developed by St-Amant and Salahub [9,10] at the Université de Montréal. A description of the theory and the technical details of the program are given in Refs. 10 and 11.

An oxygen orbital basis set with a $(621/41/1*)$ contraction pattern was used, while the all-electron basis set on molybdenum had a $(633321/5321*/531+)$ contraction pattern and the Mo MCP orbital basis was $(311111/31111/2111)$. The auxiliary basis sets, used in the fitting of charge density and exchange-correlation potential, were O $(4,3;4,3)$ and Mo $(5,5;5,5)$. The model core potential for molybdenum was the one developed by Andzelm et al. [8] for Mo $4s$, $4p$, $4d$, and $5s$ electrons treated as the valence shell. Only the local spin-density approximation was employed in the calculations for MoO, however, its validity for molybdenum compounds and the MCP scheme has been tested against nonlocal gradient-type corrections for the molybdenum atom and for Mo_2. The results indicate that these corrections should have a minor influence on the electronic properties for the near equilibrium region. Nevertheless, the detailed study of the electronic structure of MoO within the nonlocal scheme is in progress and will be published soon.

Potential energy curves for all states of MoO were evaluated by point-wise calculations over a limited number of points around the equilibrium geometry, and equilibrium distances and spectroscopic constants were calculated from simple cubic fits. We are also progressing in doing more precise potential energy curves, on which

TABLE I. Test of the frozen core approximation for the Mo atom (all entries in eV).

Level	ΔE_q	ΔE_{sf}	I	A
MCP/L	2.78	1.28	7.34	0.68
MCP/P	2.28	1.15	7.32	0.82
All/L	2.68	1.25	7.32	0.61
All/P	2.51	1.12	7.26	0.76
Exp	1.36	—	7.10	0.747

MCP, Model core potential; all, all-electron calculations; L, local; P, nonlocal (Perdew) exchange-correlation functional.

full vibrational–rotational analyses could be performed. The reported dissociation energies have been calculated for the minima of total energies with respect to atomic energies corrected for basis set superposition error.

Results and Discussion

Molybdenum Atom and Diatomic

The results of the calculations are summarized in Tables I and II for Mo and Mo$_2$, respectively. The reported computations have been performed with the all-electron basis within local (all/L) and nonlocal (all/P) approximations, and with the use of the model core potential, both local (MCP/L) and nonlocal (MCP/P) exchange-correlation functional.

In Table I, the interconfigurational energy, $\Delta E_{ic} = E(s^1 d^5) - E(s^2 d^4)$, s spin-flip energy $\Delta E_{sf} = E(s^1 d^5, ^5S) - E(s^1 d^5, ^7S)$, ionization potential, I, and electron affinity, A, are listed for the molybdenum atom. The energy of the $s^2 d^4$ configuration

TABLE II. Test of the frozen core approximation for Mo$_2$ molecule.

Level	R_e [Å]	D_e [eV]
MCP/L	2.00	4.31
MCP/P	2.05	3.39
All/L	2.00	4.54
All/P	2.04	2.95
LCAO LSD[a]	1.97	5.0
Exp[b]	1.938	4.2

See Table I for abbreviations.
[a] From Ref. 8.
[b] From Ref. 4.

was calculated for the multiplet average (spherical Mo atom). The last two entries are calculated as the difference between the total energies of the neutral atom and the appropriate ion in the lowest electronic state. From Table I, the agreement between model core potential and all electron calculations is very good. The nonlocal corrections also do not change the overall picture in a qualitative way.

The agreement of ionization potential and electron affinity with the experiment may be regarded as satisfactory. The calculations generally overshoot the value of the interconfigurational energy by about 50%, but this is consistent with other theoretical results (e.g., compare ΔE_{ii} = 2.7 eV given by Harris in Ref. 12). There are no other data available to compare the s spin-flip energy, but, it may be concluded that the value is reasonable by comparing with the value for chromium, ΔE_{si} = 1.1 eV (0.9 eV exp), computed by Harrison [13].

Similar conclusions follow from Table II regarding the Mo_2 molecule. The agreement between all-electron and MCP calculations is again very good regarding the optimum bond distance. The value of the binding energy is, in general, difficult to approach even by advanced quantum chemical methods. Here this quantity also appeared to be sensitive to the assumed computational scheme. It may seem somewhat surprising that the nonlocal corrections lead to some worsening of bond distances and underestimated binding energy—it could likely be attributed to overall difficulties in describing the Mo_2 molecule with symmetry adapted ($D_{\infty h}$) MOs [14]. Nevertheless, all discussed entries from Table II have acceptable values (compare also R_e = 1.98 A and D_e = 4.8 eV obtained from extended basis set calculations by Baykara et al. [14]).

Finally, it may be inferred that the MCP for molybdenum within the local approximation provides a reasonably accurate description of its electronic properties and bonding features and may be used in the calculations for larger systems.

MoO

Using the calculational technique described above, we have studied the electronic structure of the MoO molecule in its ground $^5\Pi$ state and the following excited states: $^5\Sigma^+$, $^5\Sigma^-$, $^5\Delta$, and B' $^5\Pi$. The dominant electronic configurations for these

TABLE III. Dominant configurations for low-lying quintet states of MoO.

State	Configuration
$^5\Pi$	$\sigma_1^2\pi_1^4 4d\delta^2 5s\sigma^1 4d\pi^1$
$^5\Delta$	$\sigma_1^2\pi_1^4 4d\delta^1 5s\sigma^1 4d\pi^2$
$^5\Sigma^+$	$\sigma_1^2\pi_1^4 4d\sigma^2 4d\pi^2$
$^5\Sigma^-$	$\sigma_1^2\pi_1^4 4d\delta^2 5s\sigma^1 4d\sigma^1$
B' $^5\Pi$	$\sigma_1^2\pi_1^4 4d\delta^1 5s\sigma^1 4d\pi^1 4d\sigma^1$

states are listed in Table III. Excited states have been optimized individually using the technique of exciting particular electrons from appropriate ground state levels followed by the levelshifting option to assure good convergence. Due to the levelshifting technique no averaging over two degenerate components could be used for the excited states of Π and Δ symmetry. Only the ground state has been calculated with half-electron occupancy on each of the π orbitals, which introduced the increase in the state energy by about 0.15 eV. All but one of the states of molybdenum oxide are the lowest states of a given symmetry where such a procedure is well justified. The only somewhat troublesome state is the B' $^5\Pi$ one, where extreme care must be taken to avoid mixing with the ground state.

The results for all quintet states are summarized in Table IV. The calculations have been performed for each state within the local approximation, using the all-electron basis or the MCP for molybdenum. The labeling of the computational level is the same as in Tables I and II. For each state, the potential energy curve was fitted by a cubic polynomial using a limited number of points. The estimates of reported spectroscopic constants have been evaluated from this simple fit. The dissociation energy was calculated with respect to the separate atom limit, corrected for basis set superposition error.

In the third column of Table IV equilibrium bond distances are given for all states under consideration, accompanied by one extra state resolved by Hamrick et al. [6], but extremely difficult to approach theoretically. As a rule theoretical bond distances are overestimated by 0.02–0.03 Å (roughly 1%). The highest discrepancy was found for the excited state of the same symmetry as the ground state, B' $^5\Pi$. Excited states of the same symmetry, as the ground state are, as a rule,

TABLE IV. Summary of calculated spectroscopic properties of MoO in quintet states.

State	Level	R_e [Å]	D_e [eV]	Δ [cm^{-1}]	ω_e [cm^{-1}]	B_e [cm^{-1}]	$k \times 10^5$ [dyn cm]	$\omega_e x_e$
$^5\Pi$	Exp	1.70	5.00	—	893	0.418	—	—
	MCP I	1.73	6.55	—	882	0.411	6.24	0.42
	All I	1.735	6.55	—	907	0.408	6.53	0.31
$^5\Sigma^-$	Exp	—	—	7350	—	—	—	—
	MCP I	1.77	5.62	7450	970	0.393	6.84	0.50
	All I	1.77	5.65	7205	927	0.391	5.94	0.43
$^5\Sigma$	Exp	—	—	13373	—	—	—	—
	MCP I	1.765	5.00	12420	941	0.395	7.15	0.39
	All I	1.77	4.94	12980	929	0.391	6.98	0.29
$^5\Delta$	Exp	1.75	—	14362	867	0.398	—	—
	MCP I	1.78	4.87	13510	944	0.389	7.20	0.47
	All I	1.78	4.86	13580	945	0.386	7.22	0.38
B' $^5\Pi$	Exp	1.73	—	21712	—	0.408	—	—
	MCP I	1.80	2.90	29370	941	0.378	7.16	0.42
	All I	1.82	2.90	29680	1021	0.373	8.42	0.35
B $^5\Pi$	Exp	1.76	—	20723	764	0.392	—	—

See Table I for abbreviations.

difficult to compute by any SCF scheme, which was also our case. We did not succeed in spotting the third state of $^5\Pi$ symmetry, labeled by experimentalists as $B\,^5\Pi$. It can be still brought under discussion if the two $B\,^5\Pi$ states are assigned in the proper order. The mutual interchange seems apparently to be true for the two $^5\Sigma$ states, where the data listed in Table IV do not agree with the assignment given in Ref. 6. Our assignment of $^5\Sigma^+$ to the lower state is fully supported by SDCI calculations. Bauschlicher et al. [2] report CASSCF and SDCI calculations on $^5\Pi$, $^5\Sigma^+$, $^7\Pi$, and $^7\Sigma$ states. Only inclusion of the extensive CI treatment led to the improved in comparison with our bond distances ($R_e = 1.71\,\text{Å}$ for the ground state). Other parameters, however, such as dissociation energies, vibrational frequencies, and relative position of septets, had less reliable values. Closer inspection of the remaining entries in Table IV shows that our conclusions regarding the good performance of the MCP for molybdenum, inferred from atomic and homonuclear calculations, are also valid for the oxide molecule. Excitation energies, vibrational frequencies, and rotational constants calculated with both computational schemes agree closely with each other and with the experiment. Again, the largest discrepancy with experimental data was found for the second Π quintet.

In the last column of Table IV the charge on the molybdenum atom is given as measured by a Mulliken population analysis. Its value may be taken as a measure of the charge transfer from the oxygen to the molybdenum atom. The model core potential gives a larger charge transfer than the all-electron calculations, still smaller, however, than HF calculations. Both schemes agree in describing the $^5\Sigma^+$ and $^5\Delta$ states as the more pronounced charge-transfer states.

Conclusions

The spectroscopy of the MoO molecule is still far from fully understood, however, good progress has been made [6]. The results presented in this study may be of considerable importance for further resolution of spectroscopic data and may also serve as independent support for available assignments. The ground state has already been definitely established as $^5\Pi$; also, the position of the excited $^5\Delta$ state seems to be certain. Recent calculations can contribute to the tentative assignment of the part of the spectrum in which the transitions $^5\Pi-^5\Sigma^+$ and $^5\Pi-^5\Sigma$ are expected.

As low-lying triplets should also contribute to the spectrum of MoO in the same region, the calculations for multiplicities other than quintet are presently in progress. At this point, it should be stressed that the accuracy of the reported results is at least comparable with other very extensive theoretical treatments which require a qualitatively larger computational effort than the local spin-density formalism. Thus, we are also attempting to obtain a more detailed description of the potential energy curves, which would allow for more complete analysis. The results of such an analysis for quintet, triplet, and septet states of MoO will hopefully be published in due course.

Acknowledgments

Bibliography

[1] C. W. Bauschlicher, Jr., C. J. Nelin, and P. S. Bagus, J. Chem. Phys. **82**, 3265 (1985).

[2] C. J. Nelin and C. W. Bauschlicher, Jr., Chem. Phys. Lett. **118**, 221 (1985).

[3] S. R. Langhoff and C. W. Bauschlicher, Jr., Ann. Rev. Phys. Chem. **39**, 181 (1988).

[4] S. R. Langhoff, C. W. Bauschlicher, Jr., and L. G. M. Pettersson, Chem. Phys. Lett. **132**, 49 (1989).

[5] A. J. Merer, Ann. Rev. Phys. Chem. **40**, 407 (1989).

[6] Y. M. Hamrick, S. Taylor, and M. D. Morse, J. Molec. Spectrosc. **146**, 274 (1991).

[7] D. R. Salahub, in *Ab Initio Methods in Quantum Chemistry—II*, K. P. Lawley, Ed. (Wiley, New York, 1978); D. R. Salahub and M. C. Zerner, ACS Symp. Ser. **394**, 128 (1989).

[8] J. Andzelm, E. Radzio, and D. R. Salahub, J. Chem. Phys. **83**, 4573 (1985).

[9] A. St-Amant and D. R. Salahub, Chem. Phys. Lett. **169**, 387 (1990).

[10] A. St-Amant, Ph.D. thesis, Université de Montréal, 1991.

[11] D. R. Salahub, R. Fournier, P. Mlynarski, I. Papai, A. St-Amant, and J. Ushio, in *Density Functional Methods in Chemistry*, J. Labanowski and J. Andzelm, Eds. (Springer, Berlin, 1991).

[12] J. Harris and R. O. Jones, J. Chem. Phys. **70**, 830 (1979).

[13] J. G. Harrison, J. Chem. Phys. **79**, 2265 (1983).

[14] N. Y. Baykara, B. N. McMaster, and D. R. Salahub, Molec. Phys. **52**, 891 (1984).

On the Intercorrelation of Topological Indices in Benzenoid Hydrocarbons*

D. HORVAT

Faculty of Food Technology and Biotechnology, University of Zagreb, Pierottijeva 6,
HR-41000 Zagreb, The Republic of Croatia

A. GRAOVAC, D. PLAVŠIĆ, and N. TRINAJSTIĆ

The Rugjer Bošković Institute, HR-41001 Zagreb, POB 1016, The Republic of Croatia

M. STRUNJE

Faculty of Technology, University of Zagreb, Pierottijeva 6,
HR-41000 Zagreb, The Republic of Croatia

Abstract

The pairwise intercorrelation between 12 topological indices is studied in benzenoid hydrocarbons with up to six rings. The functions used in the intercorrelations were linear, quadratic, cubic, power low, and logarithmic relationships. The last two relationships failed to intercorrelate the selected topological indices. The results obtained suggested that there are basically three subclasses of independent topological indices in the benzenoids studied. When contrasted with the previous findings in alkanes, our results suggest that the cyclicity leads to the stronger intercorrelation of topological indices than the branching of a molecule. © 1992 John Wiley & Sons, Inc.

Introduction

It is well-known that the chemical behavior of a compound is dependent upon the structure of its molecule. Quantitative structure–activity relationship (QSAR) studies [1] and quantitative structure–property relationship (QSPR) studies [2] are active areas of chemical research that focus on the nature of this dependency [3]. Regression analysis [2], expert system [4], and other techniques are used to model the prediction of property/activity of molecules from their structural parameters.

The structure of a molecule could be represented in a variety of ways [5]. The information on the chemical constitution of a molecule is conveniently represented by a molecular graph [2]. Usually hydrogen-suppressed graphs are used.

A number that is mathematically derived in an unambiguous manner from the molecular graph is called a *topological index*. Evidently, topological index must be graph invariant [2]. The first reported use of a topological index in chemistry was by Wiener [6] in his study of paraffin boiling points. Since then, in order to model

---

* Dedicated to the memory of the late Dr. Ioan Motoc.

various molecular properties/activities, a hundred of topological indices have been designed [2]. Such a proliferation is still going on and is becoming counterproductive [7]. Therefore, we have decided to study the *intercorrelation* between different, at the first glance unrelated topological indices. It is known for some time [2] that topological indices reflect mainly molecular size and shape, and only in a less extent they are sensitive to other structural features of molecules. Therefore, one should not be surprised to find that a plethora of topological indices could be reduced to a small number of independent, mutually orthogonal (or almost orthogonal) topological indices [8-11].

Previously we have studied [12] the intercorrelation between 12 different topological indices [13] in alkanes. Here the intercorrelation between the same set of topological indices is studied but now in benzenoid hydrocarbons. The findings are compared with those of alkanes.

Topological Indices Studied

We have studied the same set of 12 topological indices as in Refs. [12,13].

The connectivity in a hydrogen-suppressed molecule is represented by the molecular graph G. Let N and A denote the *number of atoms(vertices)* and *bonds (edges)* in a molecule (molecular graph), respectively.

The first and the simplest index studied here is A. It is also called the *total adjacency of a molecule*.

Let v_a stand for the degree (valency) of the vertex a in the graph G. The *Zagreb Group indices*, M_1 and M_2, are defined as [14]:

$$M_1 = \sum_a v_a^2 \tag{1}$$

$$M_2 = \sum_{(a,b)} v_a v_b \tag{2}$$

where the summation in Eq. (2) runs over all bonds (a,b) in G.

The following adaptation of M_2 [15]:

$$RI = \sum_{(a,b)} (v_a v_b)^{-1/2} \tag{3}$$

is called the *Randić connectivity index*, RI, and represents up to now the index which has found the widest applications in the field [1,2].

The *Platt index*, F, is defined [16] as the sum of the number of bonds adjacent to each of the bonds in a molecule and is accordingly also called the *edge total adjacency*. It could be expressed as [17]:

$$F = \sum_a v_a(v_a - 1) \tag{4}$$

The *Gordon–Scantlebury index*, S, equals the number of distinct ways in which an acyclic $C-C-C$ fragment can be superimposed on the hydrogen-suppressed molecular graph [18]. It does not represent a new index as it is easy to prove that:

$$S \quad F/2$$

The remaining topological indices considered here are based on the distances in a graph G. The distance, $d_{a,b}$, between vertices a and b in G equals the number of edges connecting a and b on the shortest path in G between them [2]. By definition:

$$d_{a,a} = 0.$$

The sum of all distances in a graph [6]:

$$W = \frac{1}{2} \sum_{a} \sum_{b} d_{a,b} \tag{5}$$

defines the *Wiener index*, W. This oldest topological index still finds its applications in chemistry [17].

A half of the number of distances of length three in G defines the *polarity number*, P [6].

Let us consider the sum of all distances originating from the vertex a:

$$v_{D,a} = \sum_{b} d_{a,b} \tag{6}$$

The sum represents an analogon of the vertex degree and is called the *distance sum*, $v_{D,a}$, of the vertex a [19].

Having the above in mind Balaban has defined, in analogy with the Randić connectivity index, the following index [20]:

$$J = \frac{A}{\mu + 1} \sum_{(a,b)} (v_{D,a} v_{D,b})^{-1/2} \tag{7}$$

where the cyclomatic number, $\mu = A - N + 1$, equals the number of cycles in G. The *Balaban index*, J, is the most discriminating topological index proposed so far.

The Wiener index W can be written as [17]:

$$W = \sum_{k=1}^{l} k W_k \tag{8}$$

where W_k is the frequency of occurrence of the distance k in a graph. L stands for the diameter (the largest distance) of G. The frequencies W_k define the distance distribution and enable a definition of the following index [17]:

$$D_v = \left[\frac{\sum_{k=1}^{l} W_k k^v}{\sum_{k=1}^{l} W_k} \right]^{1/v} \tag{9}$$

This index is related to the *s*th moment of the distance distribution and is called the *s*th *mean square distance topological index*. The indices D_1, D_2, D_3, and D_4 are considered in the present article.

Results

The intercorrelation of the 12 topological indices introduced above is studied here for benzenoid hydrocarbons having up to six rings. This set of benzenoids contains 115 structures and is taken from Ref. [21].

All topological indices considered here could be defined [13] in terms of the higher order adjacency matrices [2] of a graph.

This observation serves as the basis of the program TOPIND which has been developed by Razinger et al. [22]. Here we use the modified version [12] of this program. Although there are existing more efficient algorithms for computation of
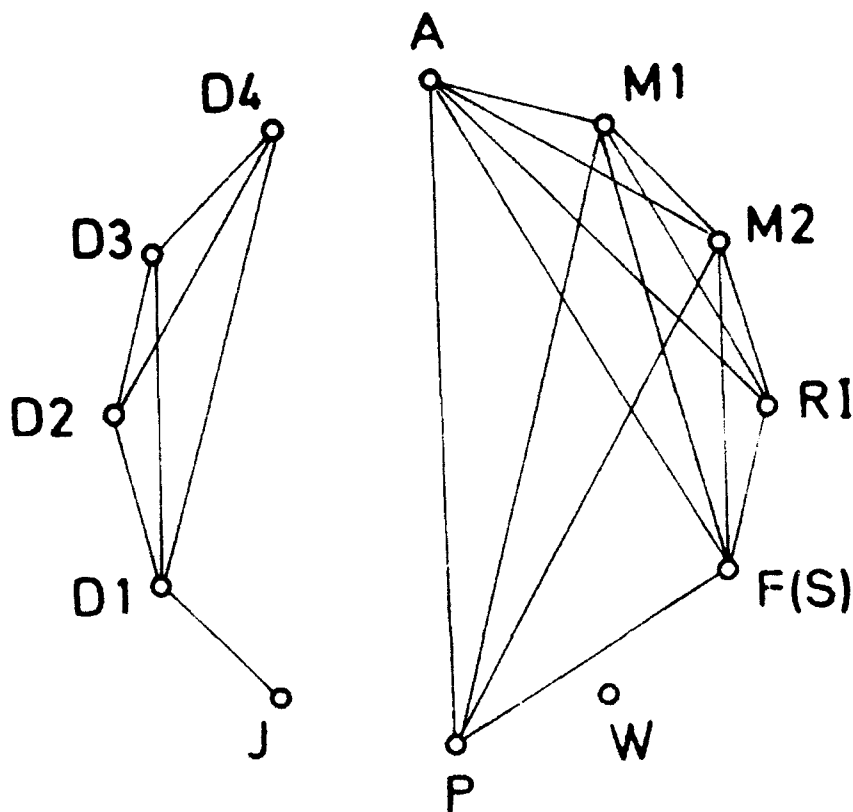
Figure 1.   Graph of strongly intercorrelated topological indices in benzenoid hydrocarbons with up to six rings. The case of linear relationship.
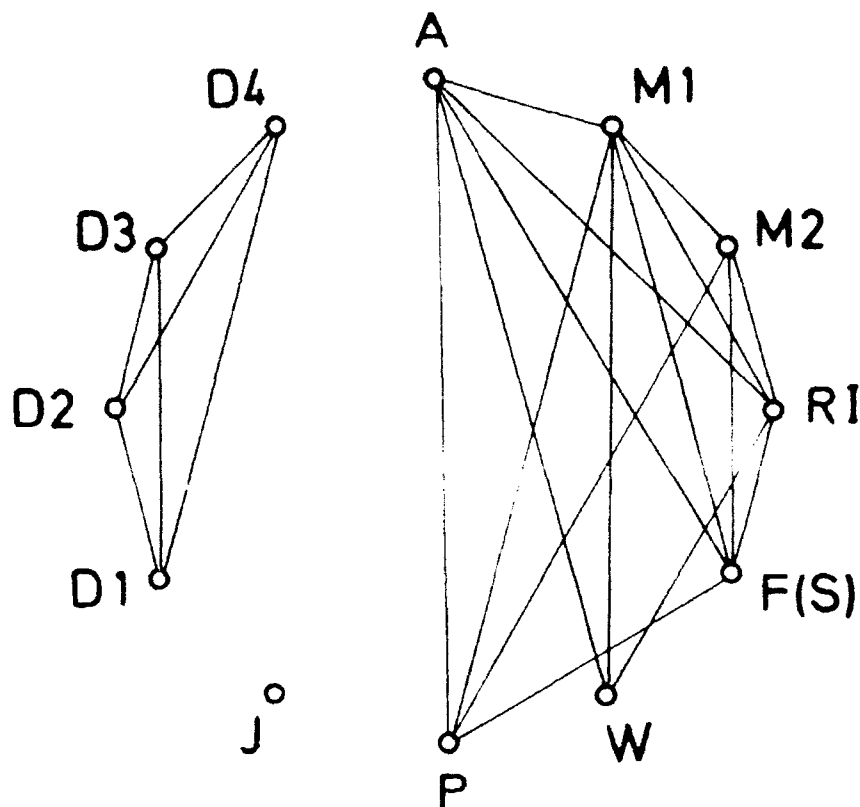
Figure 2. Graph of strongly intercorrelated topological indices in benzenoid hydrocarbons with up to six rings. The case of quadratic relationship.

particular topological indices, the higher order adjacency matrices approach has been advocated [13] as being able to point in more direct way to the similarities and differences between the topological indices.

The intercorrelation of topological indices is studied here *pairwise*, that is, we investigate the quality of the functional relationship between the topological indices T_i and T_j

$$T_i = f(T_j) \qquad (10)$$

or in other words we investigate the degree of similarity of their structural information contents. The one-parameter linear, quadratic, cubic, logarithmic, and power low relationships have been tested.

Quality of fitting these relationships between T_i and T_j is given by the corresponding correlation coefficient $r_{i,j}$. Strongly intercorrelated pairs of topological indices are those with $r_{i,j} \geq 0.98$.
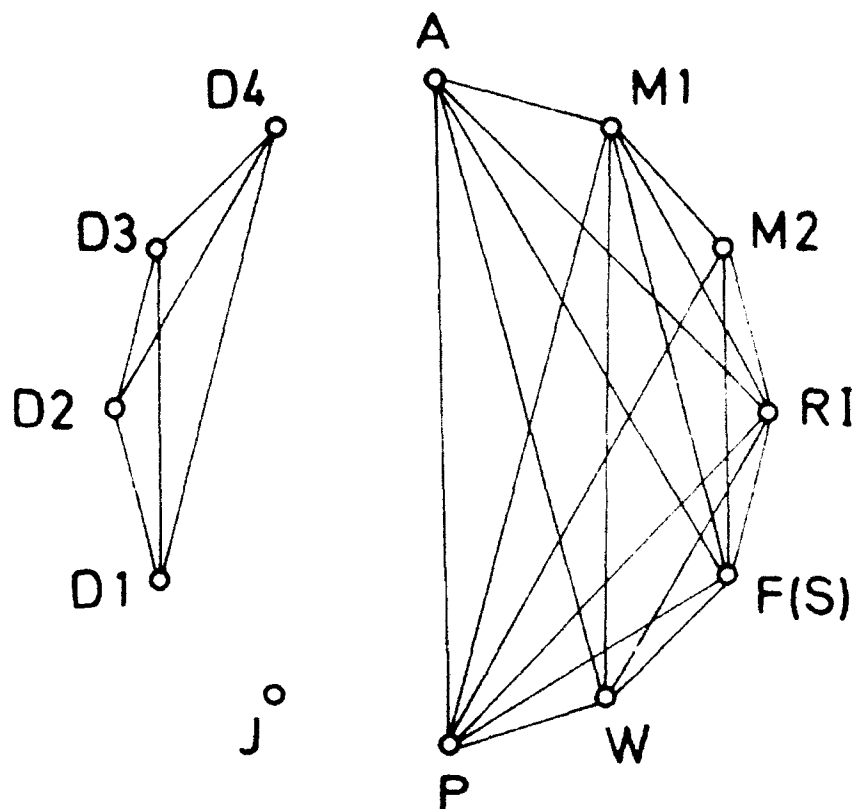
Figure 3.   Graph of strongly intercorrelated topological indices in benzenoid hydrocarbons
with up to six rings. The case of cubic relationship.

The correlation coefficients are usually presented in the form of matrices but we prefer a pictorial representation: each topological index T_i is depicted as a vertex i and an edge (i,j) is drawn between i and j only if T_i and T_j are strongly intercorrelated. Such a drawing [8–10] we call the *graph of strongly intercorrelated topological indices*.

The graphs of strongly intercorrelated topological indices for benzenoid hydrocarbons with up to six rings for the linear, quadratic, and cubic relationships are given in Figures 1, 2, and 3, respectively. The topological indices M_1, M_2, D_1, D_2, D_3, and D_4 are denoted in the figures by $M1$, $M2$, $D1$, $D2$, $D3$, and $D4$, respectively.

One notes that the indices D_1, D_2, D_3 and D_4 form a separate subclass of indices independent of all the other indices. Only in the case of the linear relationship the index D_1 is strongly intercorrelated with the Balaban index J.

Let us note that for the linear relationship the Wiener index W is independent of the other indices but for the quadratic relationship it becomes strongly correlated

with I, M_1, and RI and in addition to that it becomes further strongly correlated with F when one proceeds to the cubic relationship.

Let us further note that the Randić index RI is strongly correlated with the indices I, M_1, and M_2 for three relationships depicted. In proceeding from the linear to quadratic relationship it becomes also strongly correlated with H and in addition to that by proceeding further to the cubic relationship it starts to correlate strongly with P.

Let us further comment on the logarithmic and power low relationships whose intercorrelation graphs are not depicted here. For these relationships the indices I, M_1, M_2, RI, F, S, W, and P are independent.

The previously recognized subclass of strongly intercorrelated indices D_1, D_2, D_3, and D_4 survives also in the case of the logarithmic and power low relationships but is enlarged by the new member into the subclass: the Balaban index J.

Discussion

The above intercorrelation results suggest that there are basically three subclasses of independent topological indices in benzenoid hydrocarbons with up to six rings: the first comprises D_1, D_2, D_3, and D_4; the second contains a single index J; and the third consists of the indices I, M_1, M_2, RI, F, P, and H, where the last index could be taken as the fourth independent subclass. Therefore, we suggest that in modeling properties/activities of the molecules considered here the choice of three up to mostly four indices should suffice. The previous studies on alkanes with up to 6, 9, and 12 carbon atoms have shown [12] that an increase in the number of carbon atoms, that is, the increased participation of the *branched* species leads to drastic reduction in the intercorrelation of topological indices. Therefore, one could conclude that the *cyclicity* (as presented in benzenoids) leads to the stronger intercorrelation of indices than the branching.

Acknowledgment

Bibliography

[1] L. B. Kier and L. H. Hall, *Molecular Connectivity in Structure-Activity Indices* (Wiley, New York, 1986).
[2] N. Trinajstić, *Chemical Graph Theory*, 2nd revised ed. (CRC Press, Boca Raton, FL, 1992).
[3] S. Basak, G. J. Niemi, and G. D. Veith, J. Math. Chem. 7, 243 (1991).
[4] G. Klopman and R. V. Henderson, J. Math. Chem. 7, 187 (1991).
[5] M. Randić, J. Math. Chem. 4, 157 (1990).
[6] H. Wiener, J. Chem. Soc. 69, 17 (1947).
[7] M. Randić, Croat. Chem. Acta 64, 43 (1991).
[8] A. T. Balaban and I. Motoc, MATCH 5, 197 (1979).
[9] I. Motoc, A. T. Balaban, O. Makenyan, and D. Bonchev, MATCH 13, 369 (1982).
[10] K.-D. Gundermann, C. Tohberger, and M. Zander, Z. Naturforsch. 36a, 137 (1981).

[11] M. Randić, J. Chem. Inf. Comput. Sci. **31**, 311 (1991).

[12] K. Kovačević, D. Plavšić, N. Trinajstić, and D. Horvat, in MATH/CHEM/COMP *1988*, A. Graovac, Ed. (Elsevier, Amsterdam, 1989), p. 213.

[13] M. Barysz, D. Plavšić, and N. Trinajstić, MATCH **19**, 89 (1986).

[14] I. Gutman, B. Ruščić, N. Trinajstić, and C. F. Wilcox, Jr., J. Chem. Phys. **62**, 3339 (1975).

[15] M. Randić, J. Am. Chem. Soc. **97**, 6609 (1975).

[16] J. R. Platt, J. Chem. Phys. **15**, 419 (1947).

[17] A. T. Balaban, I. Motoc, D. Bonchev, and O. Mekenyan, Topics Curr. Chem. **114**, 21 (1984).

[18] M. Gordon, and G. R. Scantlebury, Trans. Faraday Society **60**, 604 (1964).

[19] D. Bonchev, A. T. Balaban, and O. Mekenyan, J. Chem. Inf. Comp. Sci. **20**, 106 (1980).

[20] A. T. Balaban, Chem. Phys. Lett. **89**, 399 (1982).

[21] J. V. Knop, W. R. Müller, K. Szymanski, and N. Trinajstić, *Computer Generation of Certain Classes of Molecules* (SKTH/Kem. ind., Zagreb, 1985).

[22] M. Razinger, J. R. Chretien, and J. E. Dubois, J. Chem. Inf. Comput. Sci. **25**, 23 (1985).

Correlated *Ab Initio* Geometry and Vibrational Spectra of Imidazole and its Different Forms

JOANNA SADLEJ* and W. DANIEL EDWARDS

Department of Chemistry, University of Idaho, Moscow, Idaho 83843

Abstract

The equilibrium geometry, rotational constants, and vibrational frequencies for neutral imidazole, the protonated imidazole cation, the deprotonated imidazole anion, imidazole ylide and the imidazole-Li$^+$ complex have been calculated at the second-order MP level with the 6-31G* basis set. The ylide form of imidazole is found to be 32.5 kcal/mol less stable than the neutral form. Infrared spectra predicted at this level of theory reproduce the experimental spectra sufficiently accurately to enable a reliable assignment for cationic, anionic, and ylide forms and to confirm the interpretation of the SERS spectra of imidazole adsorbed on a silver electrode. © 1992 John Wiley & Sons, Inc.

Introduction

Imidazole, a component of the amino acid histidine, plays an important role in biological systems acting as a general base catalyst, and as a ligand toward transition metal ions in a variety of biologically important molecules. For aqueous solutions (pH ≈ 7), imidazole behaves like a base and forms the imidazole-cation form (Im H$^+$). In strongly basic solutions (pH > 10), neutral imidazole undergoes deprotonation and forms the imidazole anion (Im$^-$) [1]. A tautomeric ylide form of neutral imidazole (ImY) is known to exist and has been found as a reactive species in exchange processes [1].

Recently, the adsorption of imidazole on the silver electrode has been studied by surface enhanced Raman spectroscopy (SERS) [2]. According to the authors, the spectra observed at more positive potentials cannot be interpreted in terms of the complex between the imidazole molecule and Ag$^+$ ions. Their SERS results indicated that different forms of imidazole can be observed at the Ag surface when the electrode potential is changed. Thus they discussed their SERS spectra in terms of contributions from cationic, anionic, and ylide forms. The experimental vibrational spectra for neutral imidazole in vapor, matrix, and solution phases are also known [3], as are the Na$^+$Im$^-$ (in KBr) [4] and crystalline Im$^+$Cl$^-$ [5] spectra, though the latter two are without assignments. We believe that correct interpretation of the SERS results may well depend on the proper assignment of the spectra of these various imidazole forms.

---

* Department of Chemistry, University of Warsaw, 02-093 Pasteur 1, Warsaw, Poland.

The vibrational spectrum of the imidazole was a subject of a previous *ab initio* calculation [6] and a classical normal coordinate analysis [7]; however, some of the assignments are controversial [8–11]. In Ref. [12], a 3–21G calculated spectrum of 4(5) methylimidazole is mentioned, and in Ref. [13], the results of a 4–21G calculation are presented. This latter study clearly shows that it is necessary to use a large basis set and to take electron correlation into account in order to calculate the geometry and spectra with a reasonable accuracy. We believe that more work is needed.

Computational Method

The *ab initio* calculations were carried out using the GAUSSIAN 90 program [14]. All calculations were done with the 6–31G* basis set [15], and electron correlation was included by second-order Møller–Plesset perturbation theory [16].

The optimization has been carried out under the constraint that the molecules are planar. The optimized planar geometries correspond to a minimum (not to a saddle point) on the MP2–631G* calculated potential energy hypersurface. This was confirmed by the subsequent calculations of the vibrational frequencies, which are all positive.

The optimized geometries were used as input data in the calculations of the harmonic force field. The second derivative of the energy was evaluated numerically from the gradients. The calculated Cartesian force field and transition dipole moments were transferred to a separate program for the standard potential energy distribution (PED) analysis [17]. The internal coordinates were chosen according to Ref. [18]. The convention for the atom numbering is shown in Figure 1 and the internal coordinates used in the calculations are listed in Table I.

Results and Discussion

Molecular Geometries

Table II shows the experimental geometry [17] for imidazole as well as the MP2–631G* optimized geometries, dipole moments, and energies for imidazole (Im), the imidazole cation (ImH⁺), the imidazole anion (Im⁻), the ylide (ImY) form and the ImLi⁺ complex. The experimental geometries of the ImH⁺, Im⁻, and ImY are not known.

Table II shows that, in general, the geometry predicted by the calculation is in good agreement with the experimental data. For bonds between the heavy atoms, the greatest discrepancies between the predicted and experimental values are no larger than 0.015 Å. The predicted bond angles between the heavy atoms differ from the experimental values by no more than 1 to 2°. The hydrogen substitution on N4 changes the CN bond distances by no more than 0.095 Å, and the NCN and CNC angles by 4°. Opposite changes are seen in the anionic form of imidazole. The NCN angle increases and CNC angle decreases relative to neutral imidazole. The changes caused by the simultaneous substitution of a proton on H4 and the removal of a proton from C2 are significant, especially for the NCN and CNC

Imidazole-neutral

Cation form

Anion form

Ylide form

Imidazole-Li⁺ complex
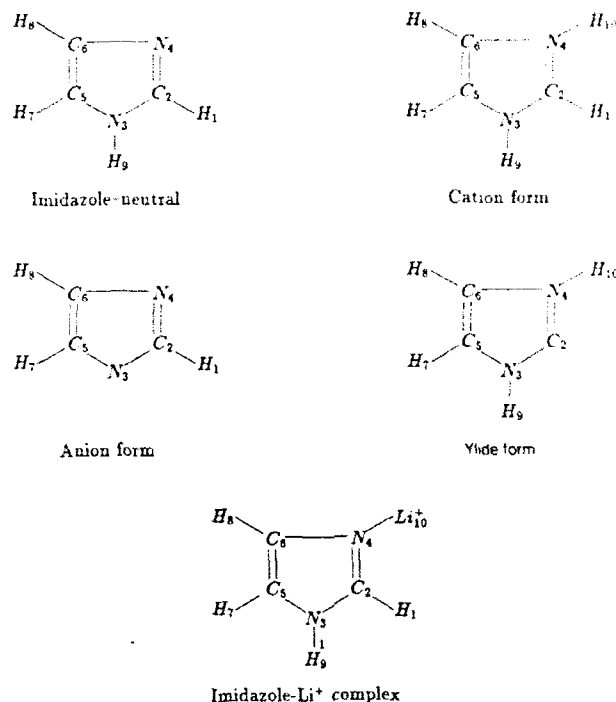
Figure 1.   Numbering scheme for the various forms of Imidazole.

angles in ylide form. The corresponding rotational constants obtained from the optimized geometries of Im and the various other forms of Im are shown in Table II. A comparison of our results for neutral imidazole with the experimentally obtained rotational constants [19] show a relative error of 0.4% and attests to the quality of the MP2 calculated geometries.

Tautomerism

The difference of the total internal energies of the tautomers at O Kelvin has been calculated as a sum Etot (MP2–631G*) + ZPE (MP2–631G*) where the ZPE is zero-point vibrational energy, calculated from the vibrational frequencies of the normal modes computed at the MP2–631G* level, without scaling factors. The large (32.5 kcal/mol) energy difference between tautomers suggests that only the neutral form of the compound should be observed at low temperature in the gas phase. However, the ylide form could be stabilized by solvent interactions and/or the potential field of the silver electrode.

Population Analysis

Table III shows the total atomic charges for all atoms in each of the various imidazole forms as calculated from the MP2–631G* density matrices. The positive

TABLE I. Definition of internal coordinates for the C_s form of cation (ImH⁺) anion (Im⁻), and ylide (ImY) of imidazole and for imidazole molecule (Im). Number pairs are bond lengths, number triplets are bond angles, number quartets are dihedrals. H out (a, b, c) refers to motion of the proton out of the plane defined by atoms a, b, c.

	ImH⁺	Im⁻	ImY	Im
q1	r(2,3) + r(2,4)	q1	q1	r(2,3)
q2	r(4,6) + r(3,5)	q2	q2	r(2,4)
q3	r(1,2)	q3		r(4,6)
q4	r(5,6)	q4	q4	r(5,6)
q5	r(6,8) + r(5,7)	q5	q5	r(3,5)
q6	r(3,9) + r(4,10)		q3	r(3,9)
q7	(4,3,2) + a((2,6,4) + (2,5,3) + b(4,5,6) + (3,6,5))ᵃ	q6	q6	r(5,7)
q8	(8,5,6) - (8,4,6) + (7,6,5) - (7,3,5)	q7	q8	r(6,8)
q9	(10,2,4) - (10,6,4) + (9,2,3) - (9,5,3)		q7	r(1,2)
q10	r(2,3) - r(2,4)	q8	q9	q7
q11	r(4,6) - r(3,5)	q9	q10	q14
q12	r(6,8) - r(5,7)	q10	q12	(9,3,2) - (9,3,5)
q13	r(3,9) - r(4,10)		q11	(7,3,5) - (7,6,5)
q14	(a - b)((2,5,3) - (2,6,4)) + (1 - a)((3,6,5) - (4,5,6))	q11	q13	(8,4,6) - (8,5,6)
q15	(1,4,2) - (1,3,2)	q12		(1,3,2) - (1,4,2)
q16	(8,5,6) - (8,4,6) - (7,6,5) + (7,3,5)	q13	q15	q22
q17	(10,2,4) - (10,6,4) - (9,2,3) + (9,5,3)		q14	q18
q18	(a - b)((2,3,5,6) - (2,4,6,5)) + (1 - a)((4,2,3,5) + (3,2,4,6))	q14	q16	q19
q19	H1 out (4,2,3)	q15		H9 out (3,2,4)
q20	H8 out (4,6,5) + H7 out (6,5,3)	q16	q18	H8 out (5,6,4)
q21	H10 out (2,4,6) + H9 out (5,3,2)		q17	H7 out (3,5,6)
q22	(3,5,6,4) + b((4,2,3,5) + (3,2,4,6) + a((2,3,5,6) + (2,4,6,5)))	q17	q19	
q23	H8 out (4,6,5) - H7 out (6,5,3)	q18	q21	
q24	H10 out (2,4,6) - H9 out (5,3,2)		q20	

ᵃ $a = -0.809$, $b = 0.309$.

charge in ImH⁺ is distributed among the heavy atoms, so C2 becomes more positive, N3 and N4 become less negative, and C5 and C6 become more positive relative to neutral imidazole. In contrast, the negative charge in Im⁻ is distributed across all atoms except C2. The ylide form has charges quite similar to the neutral form. The dipole moment determined from Stark effect measurements on Im is 3.667 ± 0.05 D [19], while the dipole moment of Im in benzene, extrapolated to infinite dilution is 3.8 D. Our calculated value of 3.95 D agrees well with these measurements.

Infrared Spectra

Our calculated IR spectra for imidazole as well as experimental results are shown in Table IV. Our results for the other forms of imidazole are presented in Tables

TABLE II Experimental [18] and MP2/6-31G* optimized geometries, total energies (Hartrees), dipole moments (Debye), ZPE (Hartrees), and rotational constants A, B, and C (Ghz) for imidazole and its different forms. Bond lengths are given in Å, bond angles are in degrees. E_{rel} is relative to the total energy of neutral imidazole (−225.541173) except for ImLi+ which is relative to infinitely separated imidazole and lithium cation (−7.235040).

Parameters	Im Expt	Im C_s	ImH(+) C_{2v}	Im(−) C_s	ImN C_s	ImLi+ C_s
R(C2H1)	1.078	1.0816	1.0800	1.0902	.	1.0808
R(C2N3)	1.364	1.3645	1.3385	1.3549	1.3713	1.3840
R(C2N4)	1.313	1.3237	1.3385	1.3549	1.3713	1.3383
R(N3C5)	1.377	1.3742	1.3748	1.3735	1.3833	1.3603
R(N4C6)	1.382	1.3753	1.3748	1.3735	1.3833	1.3841
R(C5C6)	1.364	1.3762	1.3695	1.3907	1.3628	1.3713
R(N3H9)	0.998	1.0119	1.0182	---	1.0108	1.0157
R(C5H7)	1.078	1.0813	1.0794	1.0884	1.0794	1.0807
R(C6H8)	1.077	1.0796	1.0794	1.0884	1.0794	1.0734
R(N4H10)	—	—	1.1820	---	1.0108	--
R(N4Li)	—	—	—	---	1.0108	1.9435
(H1C2N3)	122.5	122.52	126.74	121.32	---	123.47
(H9N3C5)	126.9	126.07	125.39	---	123.87	124.30
(H7C5N3)	121.9	122.29	122.58	121.22	123.78	122.10
(H8C6C5)	127.9	127.81	127.98	126.21	127.90	128.08
(N3C2N4)	112.0	111.56	106.51	117.37	99.40	110.07
(C5N3C2)	106.9	105.70	110.36	101.65	115.02	107.21
(C5C6N4)	110.7	1.00	108.91	112.20	111.78	109.66
(C6N4C2)	104.9	104.94	110.36	101.65	115.02	105.94
(H9N3C2)	126.2	126.34	124.25	--	121.10	126.79
(LiN4C2)	—	—	—	---	..	129.23
(LiN4C6)	—	—	—	—	—	124.82
ΔE_{tot}		0.000000	0.373228	+0.578518	+0.052229	0.088076
μ	3.662	3.95			2.733	
ZPE		0.071870	0.086078	0.058053	0.072212	0.074176
A	9.7253	9.7669	9.3221	10.2789	9.6327	9.6272
B	9.3740	9.2421	9.0676	9.5397	9.4005	4.3105
C	4.7719	4.7749	4.5965	4.9478	4.7576	2.9769

V–IX. In each case, there are three main regions of the spectrum: a low frequency region, 500 to 900 cm⁻¹, an intermediate frequency region, 900 to 1600 cm⁻¹, and a high frequency region 3300 to 3700 cm⁻¹. The relative error between the experimental frequencies and our calculated frequencies is the largest for the C—H and N—H stretching in the third region, though overall, the predicted vibrational spectrum of imidazole is in satisfactory agreement with the experimental data.

The first region contains the frequencies ν_1 to ν_6, which consist of NH and CH wagging modes and ring torsions (tors). Our calculations predict the NH wag mode as the lowest frequency, in agreement with the experimental data. The 4-21G calculation gives ring torsion as the lowest frequency.

TABLE III   Total atomic charges (MP2-631G*)

Atom	Im	ImH⁺	Im	ImN	ImI⁺
C2	0.1545	0.2761	0.0429	0.1012	0.3385
N3	0.5789	0.5616	0.4900	0.5939	0.7128
N4	0.4099	0.5616	0.4900	0.5939	0.7169
C5	0.0759	0.0185	0.1068	0.0292	0.0215
C6	0.0238	0.0185	0.1068	0.0292	0.0305
H1	0.1882	0.3056	0.1498	0.1960	0.2707
H7	0.1748	0.2962	0.0505	0.3765	0.2482
H8	0.1933	0.2962	0.0505	0.3765	0.2830
H9	0.3776	0.4538		0.1960	0.4494
H10		0.4538			0.8309

The second region contains the frequencies ν_7 to ν_1 which consist of in-plane deformation modes. As expected for a small ring molecule, the normal modes contain contributions from the movements of all of the atoms, and each of these modes has a large contribution from in-plane bending modes and the stretching

TABLE IV.   MP2-631G* frequencies (cm⁻¹) and IR intensities (km/mol) for imidazole.

No.	Sym.	ν	I^IR	PED^a	Approx. descrip.	Expt P/K^b
1	A″	526	87.4	q19(80),q17(22)	NH wag + tors	513/538
2	A″	641	37.2	q16(53),q17(38),q19(13)	tors(5) + NH wag	626/631
3	A″	686	1.9	q17(48),q16(40),q10(13)	tors(4)	(658)/662
4	A″	693	11.8	q20(77)	CH wag	723/725-8
5	A″	771	42.0	q18(98)	C₃H wag	809/810
6	A″	819	20.5	q21(106)	CH wag	855/850
7	A′	906	7.4	q11(87)	CNC def	890/892
8	A′	946	1.9	q10(87)	CNC def	930/900
9	A′	1106	26.8	q13(35),q5(16),q1(13)	HCCd + CNst	1055/1056
10	A′	1129	23.	q14(24),q12(23),q4(16)	HCCd + HNCd	1074/1074
11	A′	1179	2.8	q1(31),q2(18),q3(14)	CNst	1127/-
12	A′	1202	3.4	q3(53),q5(29)	CNst	(1160)/1120-30
13	A′	1303	0.9	q15(47),q14(22),q2(15)	HC₃Nd + HCCd	1260/1252
14	A′	1402	11.2	q2(25),q3(24),q14(23)	CNst + HCCd	1330/1352
15	A′	1496	20.1	q5(32),q12(27),q1(20)	CNst + HNCd	1405/1404
16	A′	1537	19.0	q2(27),q15(24),q1(17),q13(15)	CNst + HC₃Nd	1480/1480
17	A′	1570	8.6	q4(42),q2(15),q12(15)	C=Cst + CNst + HCNd	1530/1518
18	A′	3308	4.1	q8(84),q7(13)	CHst	(3060)/
19	A′	3312	0.9	q9(96)	C₃Hst	3135/-
20	A′	3336	0.9	q7(85),q8(14)	CHst	3160/
21	A′	3674	71.6	q6(99)	NHst	3518/3504

ᵃ PED's lower than 10% not included.
ᵇ P = Perchard [3] (vapor), K = King [9] (matrix).

TABLE V. MP2 6-31G* frequencies (cm⁻¹) and IR intensities (km/mol) for imidazole cation form, ImH⁺. Modes that do not appear in neutral imidazole are marked.

No	Sym	ν	I^IR	PED	Approx. descrip
1		619	0.0	q22(110)	tors(8)
2	B	639	36.0	q18(104)	tors(4)
3*		712	0.0	q24(98)	NH wag
4	B	740	23.3	q19(38),q20(37),q21(16)	CH wag + CH wag
5	B	765	302.9	q21(51),q20(40)	NH wag CH wag
6	B	829	6.6	q18(61),q21(45)	CH wag + NH wag
7		838	0.0	q23(112)	CH wag + (NH)
8	B	923	0.5	q14(90)	CNC def(4)
9		946	0.9	q7(87)	CNC def(8)
10	B	1099	32.4	q11(42),q16(24),q5(15)	CNst + HCCdef + CHst
11		1135	32.3	q8(39),q4(23),q9(15)	HCCd + C Cst + HCNd
12		1177	3.9	q2(56),q8(26),q9(16)	CNst + HCCd + HCNd
13	B	1226	0.0	q15(46),q17(26),q9(16)	HCNd + HCNd
14		1232	14.6	q15(53),q2(18),q9(13)	CNst + HNCd
15	B	1369	0.0	q16(52),q17(32)	HCCd + HNCd
16		1491	4.9	q4(27),q9(26),q2(17)	C Cst + HNCd
17*	B	1509	17.4	q11(41),q17(36)	CNst + HCNd
18	B	1606	11.4	q10(70),q15(20)	CNst + HCN
19		1639	53.2	q4(38),q9(27),q8(16)	C Cst + HNCd
20	B	3345	23.8	q1(99)	CH st
21		3349	60.4	q3(95)	C Hst
22		3360	17.9	q5(95)	CH st
23	B	3612	398.8	q13(100)	NH st
24*		3619	32.3	q6(99)	NH st

modes. Previous workers [11] have assigned the band, $\nu = 918$ cm⁻¹ (for Im in aqueous solution) as out-of-plane CH deformation. We find that $\nu = 906$ cm⁻¹ and $\nu = 946$ cm⁻¹ correspond to ring deformations, in agreement with Fan et al. [6].

The N—H deformation mode was not assigned in the vapor spectrum, so Fan et al. adopted the solution Raman value of 1160 cm⁻¹ for this fundamental. King [9] assigned this to the band at 1125 cm⁻¹ in the matrix spectrum, based on the spectrum of pyrole. Cordes and Walter [7] assigned $\nu = 1160$ cm⁻¹ as $\delta(NH)$, while Salome and Spiro [11] assigned $\nu = 1431$ cm⁻¹ as $\delta(NH)$. According to our calculations and PED analysis this mode is not characteristic. To us, it seems more reasonable to assigned $\nu_{15} = 1496$ cm⁻¹ which contains 32% of CN stretch and 27% of $\delta(NH)$ as this fundamental.

We find the C—H stretch bands, ν_{19} and ν_{20} to be the weakest fundamentals in the spectrum, in agreement with the previous calculations.

Comparison of Spectra

For the cation form, the addition of a proton gives rise to three new bands: ν_3, ν_{17}, and ν_{23}. In the lithium complex, the new bands are: ν_1, ν_2, and ν_3. In the anion

Table VI. MP2-631G* frequencies (cm^{-1}) and IR intensities (Km/mole) for imidazole-anion form. Im

No.	Sym.	ν	I^{IR}	PED^a	Approx. descrip.
1	A_2	632	0.0	q17(79),q18(21)	tors(5)
2	B_1	704	0.0	q14(103)	tors(4)
3	A_2	712	0.0	q18(79),q17(21)	CH( )wag
4	B_1	727	23.1	q16(82)	CH( )wag
5	B_1	772	21.7	q15(99)	C$_2$H wag
6	B_2	931	20.3	q11(93)	CNC def(4)
7	A_1	936	4.6	q6(80)	CNC def(5)
8	A_1	1121	0.3	q74(53),q4(38)	HCCd + C C
9	B_2	1130	29.9	q9(42),q1(29),q8(13)	CNst + HCC
10	A_1	1205	0.7	q2(52),q1(37)	CNst
11	B_2	1287	2.0	q12(54),q13(24)	HC$_2$Nd + HCCd
12	A_1	1290	11.3	q1(49),q2(41)	CNst
13	B_2	1390	2.5	q9(39),q13(29)	CNst + HCCd
14	A_1	1513	6.1	q4(59),q7(29)	C C + HCCd
15	B_2	1516	30.0	q8(47),q12(32),q13(18)	CNst + HC$_2$Nd
16	A_1	3191	114.2	q3(98)	C$_2$Hst
17	B_2	3195	50.5	q10(100)	CH(-)st
18	A_1	3224	72.0	q5(97)	CH(+)st

form, loss of a proton results in the removal of three bands as compared to the neutral imidazole spectrum. The ylide form has the same number of bands as imidazole spectrum. The ylide form has the same number of bands as imidazole.

The most important changes caused by the H-substitution is the shift of NH wag mode (in the first region) to higher frequencies for the cation, ylide, and complex forms. This is in agreement with the well-known observation that the bands due to NH are much more sensitive to changes in structure and molecular interactions than other bands in this region.

Contributions from the ring stretching vibrations, which form the ring deformations are spread over many normal modes with frequencies in the second region. Except for ν_7, ν_8 the corresponding bands are not characteristic, and these two are close to each other in the different forms.

Neutral Im has an N—H deformation mode at 1496 cm^{-1} and the protonated form, the ImH$^+$ cation has an additional N—H deformation mode at 1509 cm^{-1}. All of these vibrations have some CN stretch contributions. The deprotonated anionic form does not have this mode. In the ylide form, one of these δ(NH) frequencies is shifted to lower frequencies (ν_{13} = 1248), and the N—H in-plane bending vibration contributes significantly more to the ylide ν_{16} = 1458 cm^{-1}), than in the imidazole molecule. However, one should notice, that ring deformation modes ν_{16}, ν_{17}, and ν_{18} have lower frequencies than in imidazole molecules. Addition of a lithium cation caused only small changes in frequency in the second region.

The bands due to CH stretching modes are very weak in the imidazole, but became much stronger in other forms. They are shifted towards higher frequencies

Table VII. MP2-631G* frequencies (cm⁻¹) and IR intensities (km/mol) for imidazole-ylide form, ImY. Modes that do not appear in neutral form are marked.

No.	Sym.	ν	I^{IR}	PED^a	Approx. descrip
1	B_1	592	21.5	$q16(61),q17(37)$	tors(4)
2	A_2	593	0.0	$q19(97)$	tors(5)
3	B_1	682	20.9	$q18(90)$	CH(+) wag
4*	A_2	688	0.0	$q20(75),q19(13)$	NH(-) wag + tors
5	A_2	732	0.0	$q21(98)$	CH(-) wag
6	B_1	761	216.2	$q17(61),q16(31)$	NH(+) wag + tors
7	B_2	933	2.9	$q13(93)$	CNC(4)
8	A_1	934	4.8	$q6(83),q8(11)$	CNC(5), +HCCd
9	B_2	1083	20.2	$q10(43),q15(37)$	CNst + HCCd
10	A_1	1112	19.2	$q8(47),q1(34)$	HCCd + CNst
11	A_1	1169	8.9	$q2(66),q7(24)$	CNst + HCNd
12	A_1	1189	0.1	$q1(47),q8(25),q4(18)$	CNst + HCC
13*	B_2	1248	0.9	$q9(68),q14(22)$	CNst + HNCd
14	B_2	1406	4.7	$q15(44),q9(19),q14(30)$	HCCd + CN
15	B_2	1439	3.9	$q4(40),q10(39)$	C - Cst + CNst
16	A_1	1458	29.3	$q7(45),q2(17)$	HNCd + CN
17	A_1	1627	7.4	$q4(55),q7(20),q8(17)$	C = Cst + HNCd
18	B_2	3324	0.2	$q12(99)$	CH(-)st
19	A_1	3345	0.3	$q5(99)$	CH(+)st
20	B_2	3689	124.1	$q11(100)$	NH(-)st
21*	A_1	3690	11.7	$q3(99)$	NH(+)st

in the cation form and towards lower frequencies in the anion form. The values for ylide form are close to neutral imidazole.

In the third region there is a very strong NH stretching vibration, which is shifted by about 62 cm⁻¹ towards lower frequencies in the cation form, 32 cm⁻¹ in complex, and 15 cm⁻¹ towards higher frequencies in the ylide form. However these frequencies can only be compared with the gas phase experiments, since the H atom is involved in strong hydrogen bonding in the solution and in the solid state phase.

SERS Spectra

Our calculated spectra for the cation and anion form of imidazole are compared to available experimental results in Table IX. The experimental spectra of Im⁺Cl⁻ [5] and [(Im)⁻Fe(CN)₅]₃ [4] have been published without assignment. However, by comparing them with the published Raman spectra of imidazole, we have assigned the bands in the second region of spectrum. Table IX shows that the change in experimental spectrum as protons are added or removed matches the corresponding change in the calculated spectrum. Only the 936 cm⁻¹ (in Im⁻) and 1639 cm⁻¹ (in ImH⁺) modes seem to deviate from experimental changes. One should, however, take into account the experimental uncertainties in this data.

TABLE VIII   MP2-631G* frequencies (in cm⁻¹) and IR intensities (km/mol) for imidazole-Li⁺ complex. Modes that do not appear in neutral imidazole are marked

No.	Sym.	ν	I^IR	PED^a	Approx. descrip.
1*	A"	149	82.9	q24(85)	Li·N wag
2*	A'	175	71.2	q22(87)	Li·Nst
3*	A'	495	123.0	q23(73),q14(12)	Li·NCd
4	A"	607	36.8	q19(80),q17(20)	NH wag + tors
5	A"	659	87.8	q16(50),q17(37),q19(19)	tors(5) + NH wag
6	A"	695	17.8	q17(49),q16(35),q10(10)	tors(4)
7	A"	730	2.9	q20(79)	CH wag
8	A"	779	84.5	q18(91)	C₃H wag
9	A"	809	2.3	q21(103)	CH wag
10	A'	933	6.9	q11(80)	CNC def
11	A'	956	10.6	q10(82)	CNC def
12	A'	1103	24.7	q13(37),q5(15),q1(10)	HCCd + CNst
13	A'	1143	57.9	q14(20),q12(25),q4(10)	HCCd + HNCd
14	A'	1178	4.2	q1(38),q2(18),q3(10)	CNst
15	A'	1206	1.6	q3(50),q5(27)	CNst
16	A'	1298	5.9	q15(41),q14(20),q2(16)	HC₃Nd + HCCd
17	A'	1396	10.7	q2(23),q3(20),q14(25)	CNst + HCCd
18	A'	1474	48.1	q2(30),q15(20),q1(20)	CNst + HNCd
19	A'	1543	15.3	q5(27),q12(24),q1(12)	CNst + HC*Nd
20	A'	1590	16.9	q4(40),q2(18),q12(14)	C Cst + CNst + HCNd
21	A'	3319	2.2	q8(86),q7(12).	CHst
22	A'	3328	8.4	q9(96)	C₃Hst
23	A'	3347	6.2	q7(84),q8(14)	CHst
24	A'	3642	175.0	q6(99)	NHst

ᵃ for Im-Li⁺, q1 to q21 are the same as for Im (Table I).

$q22 = r(4,10)$.

$q23 = (10,2,4) - (10,6,4)$.

$q24 = $ H10 out (2,4,6).

The shift in frequency accompanying complexation with Li⁺ were found to be quite small, with most of the bands shifted to higher frequencies. One can compare these calculated frequencies with the data of Salome and Spiro [11], who found that coordination of imidazole with Co⁺² ions had only a subtle effect.

SERS spectra of imidazole on a silver electrode ($E = -0.7$ V) is similar to the normal Raman spectrum, with the following exceptions: The band at 1428 cm⁻¹ is shifted to 1440 cm⁻¹, a new intense band at 970 cm⁻¹ appears, and there is considerable change in intensity for all bands, especially the band at 1162 cm⁻¹ [2]. All of these changes are reproduced in our calculated spectrum of Im-Li⁺. ν_{15} of Im is shifted to higher frequency $\nu_{19} = 1543$ cm⁻¹ in the complex. ν_{10} in Im is shifted to higher frequency $\nu_{13} = 1143$ cm⁻¹ (calc) and shows a marked increase in intensity. Our calculation also shows that the ring deformation frequencies, ν_7 and ν_8 in Im are shifted to higher frequencies ν_{10} and ν_{11} after coordination with the cation.

Table IX. The comparison between experimental and calculated spectra for cationic and anionic forms of imidazole.

No fund. in Im[6]	Raman experimental			Calculated—this work		
	Im [6]	ImH⁺ [5]	Im⁻ [4]	Im	ImH⁺	Im⁻
ν_7	915	917	923	906	923	931*
ν_8	935		971	946	946	936
ν_9	1065	1060	1079	1106	1099	1121
ν_{10}	1098	1100	1106	1129	1135*	1130
ν_{11}	1135	1124	1146	1179	1177	1205
ν_{12}	1160	1183	1237	1202	1226*	1290
ν_{13}	1260	1204	1276	1303	1232	1287*
ν_{14}	1328	1322	1313	1402	1369	1390*
ν_{15}	1430	1415		1496	1497	
N		1449			1509*	
ν_{16}	1490		1459	1537	1606	1516*
ν_{17}	1535	1536	1489	1570	1539?	1513

N—New band found in protonated species.
*—Bands found in the SERS spectrum (our assignment).

According to Ref. [2], the new intense bands at 1640, 1490, 1375, 1300, and 920 cm⁻¹ which appear in the spectrum at electrode potentials more positive than −0.6 V are due to Im⁻. We concur with this interpretation, since all but the 1640 cm⁻¹ band are present in our Im⁻ calculated spectrum. The bands reported at 1130, 1215, and 1450 cm⁻¹ are present in our calculated spectrum of ImH⁺. These SERS bands which arise from ionic forms are marked by an asterisk in Table IX.

The authors [2] cite electrogenerated surface species—most likely the ylide form—as the source of the bands at 1025, 1285, and 1350 cm⁻¹. Based on our calculated ylide spectrum and recognizing that our predicted spectrum is generally too high in energy, we would tentatively assign these bands to ν_{10}, ν_{13}, and ν_{14} at 1112, 1248, and 1406 cm⁻¹.

Conclusion

We have shown that *ab initio* MP2-631G* calculations give the equilibrium geometry of the imidazole very close to the experimental results. This is supported by the close match between calculated and experimental rotational constants. The ylide form is found to be 32.75 kcal/mol less stable than imidazole-neutral form. The force field obtained at this level for imidazole and the cationic, anionic, and ylide forms reproduces the experimental frequencies. An assignment of the observed bands is proposed for cationic and anionic forms based on the comparison of experimental frequencies with those calculated theoretically. Spectra predicted at this level of theory reproduce the experimental spectra sufficiently accurately to enable a reliable assignment and to confirm the interpretation of SERS results about the adsorption of imidazole on silver electrode.

Acknowledgments

Bibliography

[1] (a) S. Kotrly and L. Sucha, *Handbook of Chemical Equilibrium in Analytical Chemistry*, Technical Literature (Prague, 1985); (b) R. J. Sundberg and R. B. Martin, Chem Rev. 74, 471, 1979.

[2] J. Bukowska, A. Kudelski, and K. Jackowska, J. Electroanal. Chem. 309, 251 (1991).

[3] C. Perchard, A. M. Bellocq, and A. Novak, J. Chim. Phys. 62, 1344 (1965).

[4] M. D. Walters and T. G. Spiro, Inorg. Chem. 22, 4014 (1982).

[5] D. Garfiukel and J. T. Edsoll, J. Am. Chem. Soc. 80, 3807 (1958).

[6] K. Fan, Y. Xie, and J. E. Boggs, J. Mol. Struct. (Theor.) 136, 339 (1986).

[7] M. Cordes and J. L. Walter, Spectrochim. Acta 24A, 237 (1968).

[8] L. Colombo, P. Bleckmann, B. Schrader, R. Schneider, and Th. Plesser, T. Chem. Phys. 61, 3270 (1974).

[9] S. T. King, J. Phys. Chem. 74, 2133 (1970).

[10] O. Siiman, R. Rivellini, and R. Patel, Inorg. Chem. 27, 3940 (1988).

[11] S. Salome and T. G. Spiro, J. Am. Chem. Soc. 100, 1105 (1978).

[12] M. Majoube, P. Derreumaux, and G. Vergoten, XII Int. Conf. of Raman Spectr. 150 (1990).

[13] J. Sadlej, A. Jaworski, and K. Miaskiewicz J. Mol. Struct. (in print).

[14] GAUSSIAN 90, M. J. Frisch, M. Head-Gordon, G. W. Trucks, J. B. Foresman, H. B. Schlegel, K. Raghavachari, M. A. Robb, J. S. Binkley, C. Gonzales, D. J. Defrees, D. J. Fox, R. A. Whiteside, R. Seeger, C. F. Melius, J. Baker, R. L. Martin, L. R. Kahn, J. J. P. Stewart, S. Topiol, and J. A. Pople, Gaussian, Inc., Pittsburgh, PA, 1990.

[15] P. C. Harriharan and J. A. Pople, Theor. Chim. Acta 28, 213 (1973).

[16] C. Møller and M. S. Plesset, Phys. Rev. 46, 618 (1934).

[17] S. Califano, *Vibrational States* (Wiley, New York, 1976).

[18] P. Pulay, G. Fogarasi, F. Pang, and J. E. Boggs, J. Am. Chem. Soc. 101, 2550 (1979).

[19] D. Christen, J. H. Griffiths, and J. Sheridan, Z. Naturforsch. 36, 1378 (1981).

Ab Initio Post-Hartree–Fock Studies on Molecular Structure and Vibrational IR Spectrum of Formaldehyde

JÓZEF S. KWIATKOWSKI* and JERZY LESZCZYŃSKI

Department of Chemistry, Jackson State University, Jackson, Mississippi 39217

Abstract

High-level *ab initio* studies using the 6-311G($3df$, $2p$) basis set with electron correlation included at the second-order Møller–Plesset perturbation theory are reported. At this level, full geometry optimization was performed, followed by calculation of the vibrational IR spectrum. Predicted molecular parameters (bond lengths, bond angles, dipole moment, rotational constants) and vibrational IR spectra (harmonic wavenumbers, absolute intensities) of formaldehyde and its deuterated species agree very well with the experimental data. © 1992 John Wiley & Sons, Inc.

Introduction

The formaldehyde molecule, CH_2O, is a parent compound for many species. Among them, a class of chemically and biologically important systems possessing a carbonyl group should be mentioned. Due to the small size of this model system, it has been used to test a reliability of different levels of theory.

The molecular properties (geometry, dipole moment, rotational constants) and vibrational IR spectrum of formaldehyde are well known, because this species has been a subject of number of both experimental and quantum-mechanical studies. A review of the theoretical studies goes beyond the scope of the present study. Instead, we will refer to the most recent *ab initio* studies, in which references to previous studies can be found.

The aim of this article is an accurate prediction of molecular structure and vibrational IR spectrum (harmonic frequencies, absolute intensities) of formaldehyde using the *ab initio* post-Hartree–Fock calculations, namely, the second-order Møller–Plesset perturbation theory (MP2) with the 6-311G($3df$, $2p$) basis set that is a triple valence basis set augmented by an extended set of polarization functions. Recently, using the same level of theory, an excellent agreement between theoretically predicted and experimentally determined molecular properties of formamide has been noticed [1].

---

* Permanent address: Instytut Fizyki, Uniwersytet M. Kopernika, 87-100 Toruń, Poland.

Computational

The geometry of the studied molecule was optimized at the electron correlation MP2 level [2,3] using the triple valence 6-311G basis set [4] augmented by three sets of d and one set of f functions on carbon and oxygen, and by two sets of p functions on hydrogens, respectively. The harmonic frequencies and absolute intensities were calculated at the optimized geometry also at the MP2/6-311G(3df, 2p) level. All quantum-mechanical calculations were performed with the GAUSS-IAN 90 program [5].

Transformation of the force constant matrix in Cartesian coordinates to the force constant matrix in internal symmetry coordinates allowed ordinary normal coordinate calculations to be performed, as described by Schachtschneider [6]. The potential energy distribution (PED) analysis to assign the modes was carried out using the PACK program [7]. This program was also used to calculate the vibrational IR spectra (harmonic frequencies, absolute intensities, PED) of deuterated species of formaldehyde using the force constant matrix from the ab initio calculations for formaldehyde itself.

Results and Discussion

Molecular Geometry

The optimized geometry of formaldehyde, its dipole moment, rotational constants, and energies are listed in Table I and compared with the available experimental data. As we can see, the calculated bond lengths and bond angle agree very well with the corresponding experimental data determined from microwave spec-

TABLE I. Calculated [MP2/6-311G(3df,2p)] and experimental molecular parameters of formaldehyde.

Quantity[a]	Calculation	Experiment	
$r(CO)$	1.2046	1.206[b]	1.2033 (10)[c]
$r(CH)$	1.0977	1.108	1.1005 (20)
$\angle HCH$	116.23	116.6	116.30 (25)
μ	2.208[d]	2.33168(1)[e]	
	(2.729)[f]		
A	287573.8716	281970.57 (24)[g]	
B	38944.1514	38836.0455 (13)	
C	34299.2411	34002.2034 (12)	
E^{SCF}	-113.90880		
E^{MP2}	-114.34658		

[a] Bond lengths (Å), bond angles (°), dipole moments (D), rotational constants (MHz), energies (SCF, MP2) (a.u.).
[b] Ref. 8; [c] Ref. 9; [d] calculated using the MP2 density; [e] Ref. 10; [f] calculated using the SCF density; [g] Ref. 11.

troscopic study of Duncan [9]. The calculated rotational constant, A, is higher than the experimental constant by 2%, while the B and C constants are predicted to be higher only by 0.3% and 0.9%, respectively, than the corresponding experimental values. The agreement between predicted (2.21 D) and experimental (2.33 D) dipole moments is also good. It is important to note that the dipole moment calculated using the SCF density is higher by 0.52 D than that calculated using the MP2 density (see Table I).

Vibrational Spectrum

The vibrational IR spectra of formaldehyde and its deuterated species have been measured by a number of groups and analyzed in several studies (for review on spectroscopy of CH_2O molecule see Ref. 12). Several levels of *ab initio* quantum-mechanical method (HF, MP2, MP3, and CI) have been recently applied by Harding and Ermler [13] to predict harmonic wavenumbers and vibrational anharmonicity constants for the studied species. Their article also provides the positions of harmonic frequencies for formaldehyde that were derived from the experimental information. It is important to note that observed frequencies of CH_2O are very strongly affected by Fermi resonances (compare the harmonic frequencies and normal mode frequencies in Table II).

Here the predicted unscaled frequencies for CH_2O agree very well with the experimental harmonic frequencies. The CH symmetric and asymmetric stretching modes are about 40 cm^{-1} higher than the experimental frequencies, while the frequencies of the remaining modes are higher only by 10–20 cm^{-1}. After scaling the calculated frequencies by a factor of 0.988, the predicted harmonic frequencies agree with the experimental values within 7 cm^{-1}.

The predicted (unscaled) harmonic frequencies are, of course, higher than the experimental frequencies of fundamental modes (the frequencies of CH-stretching modes by 200 cm^{-1} and those of the remaining modes by 30–60 cm^{-1}). Since the anharmonicity of the fundamental modes are different for stretching and bending modes, it is better to use two various scaling factors for different modes. Thus, after multiplying the frequencies of the CH-stretching modes (modes 1 and 5) by 0.933 and the frequencies of the remaining modes by 0.970, the scaled harmonic frequencies (see Table II) agree with the experimental frequencies of fundamental modes within 10 cm^{-1}. We shall note an agreement between the predicted and measured absolute intensities of vibrational modes for formaldehyde (Table II). The correct prediction of the intensities of the IR bands is not an easy task and requires high accuracy in prediction of the molecular geometry of a molecule and also its dipole moment (strictly speaking, the gradients of the dipole moment) [15]. Since the present calculations accurately predicted both the geometry and dipole moment of CH_2O, the good agreement of the predicted absolute intensities with the experimental intensities is not unexpected. We shall emphasize that for correct prediction of the IR intensities for the formaldehyde molecule it is necessary to carry out the calculation at the electron correlation level, because the SCF calculations do not correctly reproduce the experimental intensities [16,17].

TABLE II. Calculated (MP2/6-311G(3df,2p)) and experimental vibrational IR spectrum of formaldehyde.

Mode[a]	Calc. ν cm^{-1}	A[b] (km/mol)	Exp.		
			$\nu(h)$[c] (cm^{-1})	ν[d] (cm^{-1})	A[e] (km/mol)
1 CH s str	2979 (2943, 2779)[f]	64.1	2937	2783	75.5 ± 7.05
2 C=O str	1791 (1770, 1737)	58.2	1778	1746	73.99 ± 5.29
3 CH$_2$ bend	1557 (1538, 1510)	9.4	1544	1500	11.15 ± 1.02
4 oopl bend	1209 (1194, 1173)	7.0	1188	1167	6.49 ± 0.64
5 CH a str	3050 (3013, 2846)	99.7	3012	2843	87.6 ± 8.02
6 CH$_2$ rock	1283 (1268, 1245)	11.8	1269	1249	9.94 ± 0.97

[a] The modes are orderd in the standard spectroscopic ordering.
[b] Absolute intensities.
[c] Harmonic wavenumbers. see Ref. 13.
[d] Wavenumbers of fundamental modes. see Ref. 12.
[e] Ref. 14.
[f] Scaled wavenumbers are given in the parentheses: the first frequencies are scaled frequencies by single factor of 0.988 to fit the harmonic experimental frequencies; the second frequencies are scaled frequencies of CH-stretching modes (modes 1 and 5) by 0.933; and the remaining frequencies by 0.970 to fit the experimental frequencies of fundamental modes. For discussion see text.

It is important to note that the ν_2 and ν_3 bands of the CH$_2$O molecule. as well as the ν_2 band of dideuterated species, can be well separated from the other fundamental bands. and intensities of the above bands might be obtained in a straightforward manner. However, the other bands (ν_1 and ν_5 of both CH$_2$O and CD$_2$O: ν_4 and ν_6 of CH$_2$O; and ν_3, ν_4, and ν_6 of CD$_2$O) overlap each other in the corresponding spectral regions. so Nakanaga et al. [14] have estimated the individual band intensities of these regions through the simulation technique [18] using the spectroscopic parameters of both CH$_2$O and CD$_2$O species (rotational constants, Coriolis interaction parameters). The individual band intensities for formaldehyde itself—those "estimated" from the experiment—are presented in Table II. There is still, however, some uncertainty in estimate of the individual band intensities caused by "experimental simulation." To avoid this uncertainty, we have added the intensities calculated for the overlapping bands of CH$_2$O and CD$_2$O and compared these values with the total intensities measured in the corresponding regions from experiment (Table III). As we see, the calculations correctly reproduce the changes of the intensities of fundamental modes on going from CH$_2$O to CD$_2$O.

Table IV presents the comparison between predicted (both unscaled and scaled) shifts of the harmonic frequencies and experimental shifts of fundamental modes.

TABLE III. Predicted (MP2/6-311G(3df,2p)) and experimental absolute intensities (in km/mol) of vibrational IR bands of CH₂O and CD₂O.

	Calc.	Exp.[a]
CH_2O		
ν_1, ν_5	163.8	163.05 ± 5.94
ν_2	58.2	73.99 ± 2.40
ν_3	9.4	11.15 ± 0.48
ν_4, ν_6	18.8	16.41 ± 0.65
Sum	250.2	264.60
CD_2O		
ν_1, ν_5	133.1	128.69 ± 4.08
ν_2	43.9	53.09 ± 1.69
ν_3, ν_4, ν_6	14.3	12.48 ± 0.62
Sum	191.3	194.26

[a] Ref. 14.

The predicted shifts (scaled frequencies) of the modes 2, 3, 4, and 6 agree within 10 cm⁻¹ with the experimental shifts, but for modes 1 and 5 (CH-stretching modes) the predicted shifts are higher by 20–50 cm⁻¹.

In summary, the applied MP2/6-311G(3df, 2p) calculations allow for an accurate prediction of the molecular parameters and vibrational IR spectrum of formaldehyde (for an additional comparison of the calculated and experimental spectroscopic parameters of formaldehyde, including the symmetry force constants, see Ref. 19).

TABLE IV. Calculated (MP2/6-311G(3df,2p)) and experimental shifts (in cm⁻¹) of vibrational IR bands of CH₂O upon deuteration.

Mode[a]	ν_1	ν_2	ν_3	ν_4	ν_5	ν_6
$CH_2O \rightarrow CHDO$						
Cal.[b]	760	26	111	113	33	228
	(709)	(25)	(107)	(110)	(31)	(222)
Exp.[c]	662	22	100	109	12	221
$CH_2O \rightarrow CD_2O$						
Cal.[b]	810	50	420	240	772	271
	(750)	(48)	(407)	(233)	(683)	(263)
Exp.[c]	726	46	394	229	683	259

[a] For an assignment of the normal modes of CH₂O see Table II. For CHDO, with reduced symmetry, the same numbering system of the modes is used as for CH₂O.

[b] The shifts of the unscaled harmonic frequencies. The shifts of harmonic frequencies scaled by 0.933 (modes 1 and 5) or 0.970 (the remaining modes) are given in the parentheses (for details see text and Table II).

[c] The shifts of fundamental modes [12].

It has also been shown that, calculated at this level, intensities of IR vibrational bands compare well with the experimental data. Though applied level is not feasible for larger molecular systems, the revealed data could be used for evaluation of lower level theoretical predictions as applied to biological and chemically important species.

Bibliography

[1] J. S. Kwiatkowski and J. Leszczyński, J. Mol. Struct. (to appear).
[2] C. Møller and M. S. Plesset, Phys. Rev. 46, 618 (1934).
[3] W. J. Hehre, L. Radom, L. P. v. R. Schleyer, and J. A. Pople, *Ab Initio Molecular Orbital Theory* (Wiley, New York, 1986).
[4] A. D. McLean and G. S. Chandler, J. Chem. Phys. 72, 5639 (1980).
[5] M. J. Frisch, M. Head-Gordon, G. W. Trucks, J. B. Foresman, H. B. Schlegel, K. Raghavachari, M. Robb, J. S. Binkley, C. Gonzalez, D. J. Defrees, D. J. Fox, R. A. Whiteside, R. Seeger, C. F. Melius, J. Baker, R. L. Martin, L. R. Kahn, J. J. P. Stewart, S. Topiol, and J. A. Pople, GAUSSIAN 90, Revision H, Gaussian, Inc., Pittsburgh, PA (1990).
[6] J. H. Schachtschneider, Technical Report, Shell Development Co., Emeryville, CA (1969).
[7] K. KuBulat, Ph.D. Dissertation, University of Florida, 1989; W. B. Person and K. KuBulat (unpublished).
[8] K. T. Takagi and T. Oka, J. Phys. Soc. Jpn. 18, 1174 (1963); see M. D. Harmony, V. W. Laurie, R. L. Kuczkowski, R. H. Schwendeman, D. A. Ramsay, F. J. Lovas, W. J. Lafferty, and A. G. Maki, J. Phys. Chem. Ref. Data 8, 619 (1978).
[9] J. L. Duncan, Mol. Phys. 28, 1177 (1974).
[10] B. Fabricant, D. Krieger, and J. S. Mautner, J. Chem. Phys. 67, 1576 (1977).
[11] G. Winnerwisser, R. A. Cornet, F. W. Birss, R. M. Gordon, D. A. Ramsay, and S. M. Till, J. Mol. Spectrosc. 74, 327 (1979).
[12] D. J. Clouthier and D. A. Ramsay, Ann. Rev. Phys. Chem. 34, 31 (1983).
[13] L. B. Harding and W. C. Ermler, J. Comput. Chem. 6, 13 (1985).
[14] T. Nakanaga, S. Konto, and S. Saeki, J. Chem. Phys. 76, 3860 (1982).
[15] W. B. Person and G. Zerbi, Eds. *Vibrational Intensities in Infrared and Raman Spectroscopy* (Elsevier, Amsterdam, 1982).
[16] H. C. Hsieh and W. C. Ermler, J. Comput. Chem. 9, 95 (1988).
[17] J. Leszczyński, J. S. Kwiatkowski, and D. Leszczyńska (to appear).
[18] T. Nakanaga, S. Kondo, Y. Koga, and S. Saeki, J. Natl. Chem. Lab. Ind. 74, 190 (1979).
[19] J. S. Kwiatkowski and J. Leszczyński, J. Mol. Spectrosc. (to appear).

Vibrational Calculations on Water With Improved Force Fields

MING-JU HUANG

Center for Drug Discovery, College of Pharmacy, J. Hillis Miller Health Center, P.O. Box 100497,
University of Florida, Gainesville, Florida 32610

Abstract

By using the full Watson Hamiltonian and a variational technique, the lower-lying vibrational state energies ($J = 0$) of H_2O, HDO, D_2O, HTO, DTO, and T_2O are calculated from a high-level ab initio potential energy surface. The basis functions are products of one-dimensional harmonic oscillator functions. Comparison is made with experiment, and also with results obtained from different theoretical techniques. © 1992 John Wiley & Sons, Inc.

Introduction

Bartlett et al. [1] have reported an ab initio valence quartic force field for water based on the CCSDT-1 coupled-cluster approximation. This method [2] includes effects of single, double, and triple excitations. Calculations were performed with an extended STO basis set at 36 points in the vicinity of the equilibrium geometry. There have since been two variational calculations of the vibrational energies of water based on these ab initio data [3,4]. Bowman et al. [3] used the triatomic Hamiltonian in terms of mass-weighted Jacobi coordinates. The functions of the basis set correspond to products of Legendre polynomials, and the matrix elements of the Hamiltonian were obtained by Gauss–Legendre and Gauss–Hermite quadrature. Jensen [4] used the Morse Oscillator Rigid Bender Internal Dynamics (MORBID) Hamiltonian, and the eigenvalues of this Hamiltonian were obtained by diagonalizing its matrix representation in a basis of Morse oscillator functions describing the stretches, numerical bending functions obtained through the Numerov–Cooley procedure.

In the present work, the procedure of Whitehead and Handy [5] has been used. No study has been undertaken to examine if the Whitehead–Handy procedure is the optimal one for water with the new ab initio-improved force field. The valence quartic force field has been converted to a slightly different force field for the internal displacement potential and SPF potential [6]. The vibrational state energies at $J = 0$ for H_2O, HDO, D_2O, HTO, DTO, and T_2O have been calculated by using the Watson Hamiltonian and a variational technique. The basis functions are products of one-dimensional harmonic oscillator functions, one corresponding to each of the three normal coordinates; the integrals are evaluated by Gauss–Hermite numerical quadrature. The results are compared with experiment and previous theoretical work [3,4].

TABLE I. The force constants for the internal displacement coordinate fit of the *ab initio* CCSD+T potential of Bartlett et al. [1]

Term type in potential	Coefficient of term type
$(\Delta R)^2$	4.2215 md/Å
$\Delta R_i \Delta R_j$	0.1000 md/Å
$\Delta R \Delta \theta$	0.263081 md/rad
$(\Delta \theta)^2$	0.364316 md Å/(rad)^2
$(\Delta R)^3$	-9.80085 md/(Å)^2
$(\Delta R_i)^2 \Delta R_j$	-0.0396205 md/(Å)^2
$(\Delta R)^2 \Delta \theta$	-0.042 md/(Å rad)
$\Delta R_i \Delta R_j \Delta \theta$	-0.505 md/(Å rad)
$\Delta R(\Delta \theta)^2$	-0.153936 md/(rad)^2
$(\Delta \theta)^3$	-0.114708 md Å/(rad)^3
$(\Delta R)^4$	15.3282 md/(Å)^3
$(\Delta R_i)^3(\Delta R_j)$	-0.0543553 md/(Å)^3
$(\Delta R_i)^2(\Delta R_j)^2$	0.141324 md/(Å)^3
$(\Delta R)^3(\Delta \theta)$	-0.208529 md/(Å^2 rad)
$(\Delta R_i)^2(\Delta R_j)(\Delta \theta)$	0.104264 md/(Å^2 rad)
$(\Delta R)^2(\Delta \theta)^2$	-0.07 md/(Å rad^2)
$(\Delta R_i)(\Delta R_j)(\Delta \theta)^2$	0.31 md/(Å rad^2)
$\Delta R(\Delta \theta)^3$	0.103583 mg/(rad)^3
$(\Delta \theta)^4$	-0.0285161 md Å/(rad)^4

Method and Results

For $J = 0$ states, the Watson form of the Wilson–Howard Hamiltonian for the kinetic energy operator is expressed in terms of the three normal coordinates, Q_k, and has the form

$$\hat{H} = \frac{1}{2} \sum_k^{3N-6} P_k^2 + \frac{1}{2} \sum_{\alpha \beta} \mu_{\alpha \beta} \pi_\alpha \pi_\beta - \hbar^2/8 \sum_\alpha \mu_{\alpha \alpha} + V \qquad (1)$$

Here P_k refers to the momentum conjugate to the normal coordinate, Q_k, so that

$$P_k = -i\hbar(\partial/\partial Q_k) \qquad (2)$$

The $\mu_{\alpha \beta}$ refer to the inverse of the effective moment of inertia tensor, π_α is the Cartesian component of the vibrational angular momentum, subscripts α and β refer to the components of Cartesian coordinates, and V is the potential energy, which is expressed in terms of internal valence displacement coordinates.

The force field of Bartlett et al. [1] is given relative to the energy expression [7]

$$V = +\frac{1}{2} f_{RR}(\Delta_1^2 + \Delta_2^2) + \frac{1}{2} f_{\theta \theta} \Delta_3^2 + f_{RR} \cdot \Delta_1 \Delta_2 + f_{R\theta}(\Delta_1 + \Delta_2)\Delta_3 + \cdots \qquad (3)$$

where $\Delta_i = \Delta R_i = R_i - R_e$ ($i = 1, 2$) and $\Delta_3 = R_e \Delta \theta = R_e(\theta - \theta_e)$. The equilibrium geometry obtained from the calculations is $R_e = 0.9591$ Å and $\theta_e = 104.45°$, in very close agreement with experiment. The potential energy expression employed is a Taylor

TABLE II. The force constants for the SPF fit of the ab initio CCSDT-1 potential of Bartlett et al. [1]

Term type in potential	Coefficient of term type
$(\Delta \rho)^2$	3.88324 md A
$\Delta \rho_1 \Delta \rho_2$	0.0919873 md A
$\Delta \rho \Delta \rho_3$	0.252321 md A/rad
$(\Delta \rho_3)^2$	0.364316 md A/rad^2
$(\Delta \rho)^3$	0.880320 md A
$(\Delta \rho_1)^2 \Delta \rho_2$	0.126942 md A
$(\Delta \rho)^2 \Delta \rho_3$	0.213686 md A/rad
$\Delta \rho_1 \Delta \rho_2 \Delta \rho_3$	0.464836 md A/rad
$\Delta \rho (\Delta \rho_3)^2$	0.147640 md A/rad^2
$(\Delta \rho_3)^3$	0.114708 md A/rad^3
$(\Delta \rho)^4$	1.32047 md A
$(\Delta \rho_1)^3 (\Delta \rho_2)$	0.207891 md A
$(\Delta \rho_1)^2 (\Delta \rho_2)^2$	0.0423141 md A
$(\Delta \rho)^3 (\Delta \rho_3)$	0.008923 md A/rad
$(\Delta \rho_1)^2 (\Delta \rho_2)(\Delta \rho_3)$	0.372549 md A/rad
$(\Delta \rho)^2 (\Delta \rho_3)^2$	0.212031 md A/rad^2
$(\Delta \rho_1)(\Delta \rho_2)(\Delta \rho_3)^2$	0.285161 md A/rad^2
$\Delta \rho (\Delta \rho_3)^3$	0.0993465 md A/rad^3
$(\Delta \rho_3)^4$	0.0285161 md A/rad^4

expansion in the displacement ΔS_k of internal coordinates from their respective equilibrium values. The three internal coordinates are two stretches, ΔR_1, ΔR_2, and one bend, $\Delta \theta$. The potential contains up to quartic terms in the displacements

$$V = + \sum_{i \cdot j} K_{ij} \Delta S_i \Delta S_j + \sum_{i \cdot j \cdot k} K_{ijk} \Delta S_i \Delta S_j \Delta S_k + \sum_{i \cdot j \cdot k \cdot l} K_{ijkl} \Delta S_i \Delta S_j \Delta S_k \Delta S_l \quad (4)$$

where $\Delta S_1 = R_1 - R_{1e}$, $\Delta S_2 = R_2 - R_{2e}$, and $\Delta S_3 = \theta - \theta_e$. The force constants in the internal displacement coordinate fit to the ab initio data for water are given in Table I. The quartic Simons–Parr–Finlan (SPF) expansion of the potential energy is

$$V = + \sum_{i \cdot j} L_{ij} \rho_i \rho_j + \sum_{i \cdot j \cdot k} L_{ijk} \rho_i \rho_j \rho_k + \sum_{i \cdot j \cdot k \cdot l} L_{ijkl} \rho_i \rho_j \rho_k \rho_l \quad (5)$$

where $\rho_1 = (R_1 - R_{1e})/R_1$, $\rho_2 = (R_2 - R_{2e})/R_2$, and $\rho_3 = (\theta - \theta_e)$. R_1 and R_2 are the two OH stretches. R_{1e} and R_{2e} are their equilibrium values, and θ is the HOH-bond angle. The force constants for the SPF fit to the ab initio data are given in Table II.

The basis function are products of the three harmonic oscillator wave functions corresponding to the three normal coordinates of water. It was found that 204 basis functions were sufficient for the first 20 levels of the vibrational problem. These functions included all combinations of the excitation levels such that

$$n_1 + (1/2)n_2 + n_3 \leq 7 \quad (6)$$

TABLE III. Vibrational energies (cm^{-1}) in H$_2$O calculated from different potential expansions.

State	IC	SPF	Exp.
ZPE[a]	4660.5	4648.0	—
ν_2	1627.0	1624.8	1595
$2\nu_2$	3219.7	3214.7	3151
ν_1	3712.7	3656.2	3657
ν_3	3810.9	3752.2	3756
$3\nu_2$	4777.0	4769.1	4667
$\nu_1 + \nu_2$	5329.6	5266.8	5235
$\nu_2 + \nu_3$	5423.1	5358.4	5331
$4\nu_2$	6296.6	6285.2	6134
$\nu_1 + 2\nu_2$	6911.9	6840.3	6775
$2\nu_2 + \nu_3$	7002.8	6929.7	6871
$2\nu_1$	7410.1	7218.1	7201
$\nu_1 + \nu_3$	7499.3	7265.6	7250
$2\nu_3$	7601.3	7444.6	7445
$5\nu_2$	7777.0	7762.0	—
$\nu_1 + 3\nu_2$	8459.7	8380.3	8274
$3\nu_2 + \nu_3$	8549.5	8469.3	8374
$2\nu_1 + \nu_2$	9021.7	8828.2	8762
$\nu_1 + \nu_2 + \nu_3$	9108.0	8873.3	8807
$\nu_2 + 2\nu_3$	9201.9	9037.7	9000

[a] Zero point energy.

where n_1, n_2, and n_3 refer to the excitation levels of the three normal mode wave functions in the triple product of the basis functions, with subscript 2 designating the "bending" mode. The numerical evaluation of matrix elements used 2304 Gauss–Hermite points, 12 integration points along each of the "stretching" normal coordinates and 16 points along the "bending" coordinate for H$_2$O for the potential function in Eq. (4). For the SPF potential, 2880 Gauss–Hermite points, 12 integration points along each of the "stretching" normal coordinates and 20 points along the "bending" coordinate. were used for the H$_2$O, HDO, D$_2$O, HTO, DTO, and T$_2$O.

The frequency parameters of the harmonic oscillator wave functions could also be regarded as variational parameters. We took { 3832.0 cm^{-1}, 1648.9 cm^{-1}, 3942.6 cm^{-1}} for H$_2$O, {2824.0 cm^{-1}, 1445.1 cm^{-1}, 3889.8 cm^{-1}} for HDO, {2763.9 cm^{-1}, 1206.2 cm^{-1}, 2888.9 cm^{-1}} for D$_2$O, {2369.3 cm^{-1}, 1370.1 cm^{-1}, 3888.7 cm^{-1}} for HTO, {2361.9 cm^{-1}, 1114.5 cm^{-1}, 2835.3 cm^{-1}} for DTO, and {2302.3 cm^{-1}, 1014.1 cm^{-1}, 2439.3 cm^{-1}} for T$_2$O. The first number is for symmetrical stretching, the second number is for the bending, and the third number is for the asymmetrical stretching.

Discussion

The calculated energies of the lowest 20 vibrational levels of H$_2$O given by the internal coordinate (IC) and SPF representations are shown along with experimental

TABLE IV Vibrational energies (cm⁻¹) in H₂O calculated from different variational approaches

State	Bowman et al.[3]	Jensen	Ours	Expt
ν_2	1624.0	1614	1624.8	1595
$2\nu_2$	3212.7	3164	3214.7	3151
ν_1	3656.4	3656	3656.2	3657
ν_3	3751.8	3751	3752.2	3756
$3\nu_2$	4764.8	—	4769.1	4667
$\nu_1+\nu_2$	5264.9	5264	5266.8	5235
$\nu_2+\nu_3$	5355.2	5357	5358.4	5331
$4\nu_2$	6280.0	—	6285.2	6134
$\nu_1+2\nu_2$	6837.1	—	6840.3	6775
$2\nu_2+\nu_3$	6924.4	—	6929.7	6871
$2\nu_1$	7215.6	7192	7218.1	7201
$\nu_1+\nu_3$	7264.8	7235	7265.6	7250
$2\nu_3$	7441.6	7441	7444.6	7445
$5\nu_2$	7753.1	—	7762.0	—
$\nu_1+3\nu_2$	8372.5	—	8380.3	8274
$3\nu_2+\nu_3$	8459.0	—	8469.3	8374
$2\nu_1+\nu_2$	8811.0	—	8828.2	8762
$\nu_1+\nu_2+\nu_3$	8857.0	8838	8873.3	8807
$\nu_2+2\nu_3$	9188.2	—	9037.7	9000

ᵃ The results are from the unadjusted potential of Bowman et al. [3].

data [8] in Table III. The IC and SPF vibrational energies of states arising from excitation of the bending mode are very close, even for high levels of excitation, e.g., $5\nu_2$. For the stretching modes there are more significant differences, 56.5 cm⁻¹ for ν_1 and 58.7 cm⁻¹ for ν_3. Energies of all states involving excitation of streching modes are computed to have lower energies with the SPF representation than with the IC representation.

Better agreement with experiment is achieved for the SPF representation. The agreement for states arising from excitation of just stretching modes is particularly good. Both representations are less adequate at describing energies of states arising from excitation of the bending mode. The results obtained by Bowman et al. and Jensen show the same deficiency. This is discussed further below.

As noted by Bowman et al., the superiority of the SPF representation can be attributed to its more physical behavior away from the equilibrium. Thus, it has a smooth Morse-like behavior, while the IC representation may be oscillatory at comparable displacements.

In Table IV we compare our SPF results with the data of Bowman et al. and Jensen. The unadjusted data of Bowman et al. are used since it is a more valid comparison. Our data are in extremely good agreement with those of Bowman et al., differing by less than 5 cm⁻¹, except for some of the highest energy states

TABLE V.   Vibrational energies (cm^{-1}) in HDO, D$_2$O, and HTO calculated from SPF potential.

State	HDO		D$_2$O		HTO	
	Calc.	Obs.	Calc.	Obs.	Calc.	Obs.
ZPE	4031.5	—	3397.4	—	3771.4	—
ν_2	1429.4	1403	1199.8	1178	1356.7	1324
$2\nu_2$	2835.0	2779	2380.9	2340	2690.4	—
ν_1	2722.3	2727	2670.2	2668	2297.2	2300
ν_3	3704.9	3707	2784.1	2788	3716.1	3717
$3\nu_2$	4218.8	—	3543.1	—	4000.7	—
$\nu_1 + \nu_2$	4136.9	4120	3863.1	—	3635.6	—
$\nu_2 + \nu_3$	5114.2	5090	3973.8	3956	5057.7	—
$4\nu_2$	5587.5	—	4685.7	—	5287.0	—
$\nu_1 + 2\nu_2$	5514.9	—	5035.6	—	4956.4	—
$2\nu_2 + \nu_3$	6500.3	—	5144.4	—	6372.1	—
$2\nu_1$	5366.3	5364	5294.2	5292	4536.8	—
$\nu_1 + \nu_3$	6417.4	6416	5375.7	5374	7265.6	7250
$2\nu_3$	7264.5	—	5525.5	—	7444.6	7445
$5\nu_2$	6852.7	—	5809.2	—	7762.0	—
$\nu_1 + 3\nu_2$	6949.7	—	6189.8	—	8380.3	8274
$3\nu_2 + \nu_3$	7870.6	—	6297.6	—	8469.3	8374
$2\nu_1 + \nu_2$	6780.1	—	6484.7	—	8828.2	8762
$\nu_1 + \nu_2 + \nu_3$	7807.7	—	6564.1	6533	8873.3	8807
$\nu_2 + 2\nu_3$	8666.0	—	6707.3	—	9037.7	9000

considered. Our results are in excellent agreement with five of the nine energies computed by Jensen, but there are significant differences for ν_2, $2\nu_2$, $2\nu_1$, and $\nu_1 + \nu_2$. For the first three of these, Jensen achieves better agreement with experiment, but for the fourth the errors are approximately equal but of opposite sign.

The greatest difficulty experienced in this and other work is the treatment of states which involve excitation of the bending mode. This may arise from two sources. First, as mentioned by Chen et al. [9], for nonlinear triatomic molecules the Hamiltonian operator given in Eq. (1) is deficient for high excitations of the bending mode. This is because of a singularity that occurs in linear configurations [10]. One way of avoiding this problem is to use the normal coordinate Hamiltonian of a linear system, as was done by Carter and Handy [11]. Another possibility, used by Bowman et al. [3], is to treat the force constant for bending, p_3^2, as a variable, which may be adjusted slightly to fit the vibrational energies. This procedure of effectively adjusting the potential led to improved agreement with experiment [3]. A second source of error, which should not be ignored, is the incompleteness of the *ab initio* treatment. In particular, the basis set used does not contain f or g functions, which are likely to be important in the description of the bending mode. While the harmonic stretching frequencies calculated by Bartlett et al. are in excellent agreement with experiment, (deviations of 2.4 cm^{-1} for ω_1 and 3 cm^{-1} for ω_3) the bending frequency has a significantly larger error (28

TABLE VI. Vibrational energies (cm⁻¹) in DTO and T₂O calculated from SPT potential.

State	DTO		T₂O	
	Calc.	Obs.	Calc.	Obs.
ZPE	3128.9	—	2856.0	—
ν_2	1110.8	—	1013.1	995
$2\nu_2$	2203.7	—	2012.8	—
ν_1	2293.5	—	2235.7	2237
ν_3	2734.4	2735	2363.2	2367
$3\nu_2$	3280.6	—	2999.1	—
$\nu_1 + \nu_2$	3401.6	—	3244.4	—
$\nu_2 + \nu_3$	3834.6	—	3368.9	3358
$4\nu_2$	4341.4	—	3971.8	—
$\nu_1 + 2\nu_2$	4483.9	—	4238.4	—
$2\nu_2 + \nu_3$	4917.0	—	4360.8	—
$2\nu_1$	4536.4	—	4440.2	—
$\nu_1 + \nu_3$	5018.5	—	4543.6	4537
$2\nu_3$	5389.0	—	4692.0	—
$5\nu_2$	5386.0	—	4931.0	—
$\nu_1 + 3\nu_2$	5555.2	—	5219.0	—
$3\nu_2 + \nu_3$	5984.3	—	5340.1	—
$2\nu_1 + \nu_2$	5645.6	—	5447.0	—
$\nu_1 + \nu_2 + \nu_3$	6116.5	—	5548.1	—
$\nu_2 + 2\nu_3$	6483.4	—	5691.5	—

cm⁻¹). In addition, the accuracy of the CCSDT-1 method should be considered, although this error is likely to be of less importance than the basis set error.

The lowest 20 calculated vibrational state energies for the HDO, D₂O, HTO, DTO, T₂O isotopomers are shown in Tables V and VI. Available experimental data are also shown [12]. The same general trends seen in the data for H₂O are again apparent.

The results obtained in the present work and in that of Bowman et al. [3] are very similar and it is pertinent to examine the differences in the methods more closely. There are differences in the forms of the Hamiltonian and the basis functions used. We have used the Watson Hamiltonian, while Bowman et al. used a scattering Jacobi coordinate Hamiltonian in a body-fixed frame [13]. The motivation for this choice of coordinates over normal coordinates is that the Hamiltonian is well-defined over the entire range of motion, including large-amplitude motion. Our basis functions are products of harmonic oscillator functions, while those of Bowman et al. use Legendre polynomials and harmonic oscillator functions. The use of Legendre polynomials is recommended, since they are eigenfunctions of the angular part of the kinetic energy operator. However, it has been suggested [13] that it would in fact be preferable to use harmonic (or Morse) oscillator functions, leading to reduced computer time. While we have used just 204 basis functions, at least 980 functions were used by Bowman et al., although it should be mentioned that very similar results were obtained using the same method and only 308 functions [13].

Finally, we note another variational technique, the discrete variable representation-distributed Gaussian oasis (DVR-DGB) approach, developed by Bačić and Light [14]. This offers advantages over conventional variational methods for highly excited vibrational states. It has been applied to the Sorbie–Murrell semiempirical surface [15] for the water molecule [16], but not to the force field of Bartlett et al. [1].

Acknowledgments

Bibliography

[1] R. J. Bartlett, S. J. Cole, G. D. Purvis, W. C. Ermler, H. C. Hsieh, and I. Shavitt, J. Chem. Phys. 87, 6579 (1987).

[2] Y. S. Lee, S. A. Kucharski, and R. J. Bartlett, J. Chem. Phys. 81, 5906 (1984).

[3] J. M. Bowman, A. Wierzbicki, and J. Zúñiga, Chem. Phys. Lett. 150, 269 (1988).

[4] P. Jensen, J. Mol. Struc. 190, 149 (1988).

[5] R. J. Whitehead and N. C. Handy, J. Mol. Spectrosc. 55, 356 (1975).

[6] G. Simons, R. G. Parr, and J. M. Finlan, J. Chem. Phys. 59, 3229 (1973); G. Simons, J. Chem. Phys. 61, 369 (1974).

[7] B. J. Rosenberg, W. C. Ermler, and I. Shavitt, J. Chem. Phys. 65, 4072 (1976).

[8] D. F. Smith and J. Overend, Spectrochim. Acta 28A, 471 (1972); C. Camy-Peyret, J. M. Flaud, and J. P. Morillard, J. Phys. (Paris) 41, L23 (1980); J.-Y. Mandin, J.-P. Chevillard, C. Camy-Peyret, and J.-M. Flaud, J. Molec. Spectry. 116, 167 (1986); C. Camy-Peyret, J.-M. Flaud, J.-Y. Mandin, J. P. Chevillard, J. Brault, D. A. Ramsay, M. Vervloet, and J. Chauville, J. Molec. Spectrosc. 113, 208 (1985).

[9] C.-L. Chen, B. Maessen, and M. Wolfsberg, J. Chem. Phys. 83, 1795 (1985).

[10] M. N. Adamov and G. A. Natanson, Vestn. Leningr. Univ. 22, 30 (1970); R. Bartholomae, D. Martin, and B. T. Sutcliffe, J. Mol. Spectrosc. 87, 367 (1981); B. T. Sutcliffe, Molec. Phys. 48, 561 (1983).

[11] S. Carter and N. C. Handy, J. Molec. Spectrosc. 95, 9 (1982).

[12] W. S. Benedict, N. Gailar, and E. K. Plyler, J. Chem. Phys. 24, 1139 (1956); J. M. Flaud, C. Camy-Peyret, A. Mahmoudi, and G. Guelachvili, Int. J. Infrared Spectrosc. Millimeter Waves 7, 1063 (1986); N. Papineau, J.-M. Flaud, C. Camy-Peyret, and G. Guelachvili, J. Molec. Spectrosc. 87, 219 (1981); P. A. Staats, H. W. Morgan, and J. H. Goldstein, J. Chem. Phys. 24, 916 (1956); A. Fayt and G. Steenbeckeliers, C. R. Acad. Sci. Ser. B275, 459 (1972); R. A. Carpenter, N. M. Gailar, H. W. Morgan, and P. A. Staats, J. Mol. Spectrosc. 44, 197 (1972); G. Wilemski, J. Quant. Spectrosc. Radiat. Transfer 20, 291 (1978).

[13] J. M. Bowman, J. Zúñiga, and A. Wierzbicki, J. Chem. Phys. 90, 2708 (1989).

[14] Z. Bačić and J. C. Light, J. Chem. Phys. 85, 4594 (1986); J. Chem. Phys. 86, 3065 (1987).

[15] K. S. Sorbie and J. N. Murrell, Molec. Phys. 29, 1387 (1975); 31, 905 (1976).

[16] Z. Bačić, D. Watt, and J. C. Light, J. Chem. Phys. 89, 947 (1988).

Multiphoton Absorption in Anharmonic Systems

J. BROECKHOVE, B. FEYEN,* and P. VAN LEUVEN

Universitair Centrum Antwerpen (RUCA), Department of Mathematics and Computer Sciences,
Groenenborgerlaan 171, B2020 Antwerpen, Belgium

Abstract

We study the multiphoton absorption of the diatomic HF by time propagating a wave packet on the electronic potential under the action of a monochromatic laser field. We apply the pseudo-spectral split-operator method for the propagation. We use different approximations for the potential and for the dipole function. We find that the quantitative details of the absorption spectrum are sensitive to the form of the dipole function. © 1992 John Wiley & Sons. Inc.

Introduction

The behavior of molecules in intense laser fields has become of major importance in recent years. The simplest case, from the theoretical point of view, of the diatomic in a monochromatic infrared laser field has been studied by several authors [1,2]. As even the simplest mathematical model, the driven Morse oscillator, is not solvable in analytic form, theoretical studies must rely on approximations. Some authors have applied time-independent methods [3,4] while others have used a time-dependent description [5-7]. Among the latter, propagation schemes range from purely classical to various quantal techniques.

In this article we consider again the multiphoton excitation of an isolated diatomic molecule under the action of a monochromatic intense infrared laser field. We exclude electronic, rotational, and collisional degrees of freedom, such that energy can only be absorbed in the chemical bond represented by the interatomic distance, considered as one-dimensional coordinate. We specify the numerical calculations to the case of $X\,^1\Sigma^+$-state of the Hydrogen fluoride molecule.

This molecule has already received widespread attention from both theoreticians and experimentalists. Nevertheless, except for Ref. [6], all previous calculations use basis set expansions or Finite Difference schemes. For these methods, its advantageous to use functions in closed analytic form for potential energy and dipole function. We want to investigate what sort of corrections are introduced using functions in nonclosed form (e.g., cubic spline interpolations from experimental datapoints). With the more recent pseudo-spectral split-operator method, which we use, one can use straightforwardly any form of potential energy function (provided it does not contain derivatives with respect to space).

---

* Research associate IIKW, Belgium.

We consider two different models for the internuclear potential: the Morse potential and an experimentally based potential curve [8]. Because of the delocalization of the wavefunction after multiphoton absorption, we expect the form of the dipole function to be relevant. Therefore we consider different versions of the dipole: the linear approximation (effective charge), a simple analytical model [3], and an *ab initio* dipole function recently proposed in Ref. [9].

Starting from the molecule in its ground state, we perform a calculation of the time evolution over a number of field periods. In the calculations we use the split operator method combined with the Fast Fourier Transform. As the multiphoton absorption is a long-time process, the number of optical cycles is taken sufficiently large. From these time-dependent quantities we derive meaningful averages which we then consider as a function of the field frequency and intensity. In this way we obtain a consistent picture the features of which we can study in the resonant and nonresonant regimes. In this article we are particularly interested in the influence of the approximations on the potential and the dipole. We shall concentrate on the absorption spectrum.

Theory

We will follow the time evolution of a system with the Hamiltonian

$$H = H_0 + H_1 \tag{1}$$

where H_0 is the Hamiltonian of the unperturbed molecule (in units $\hbar = 1$)
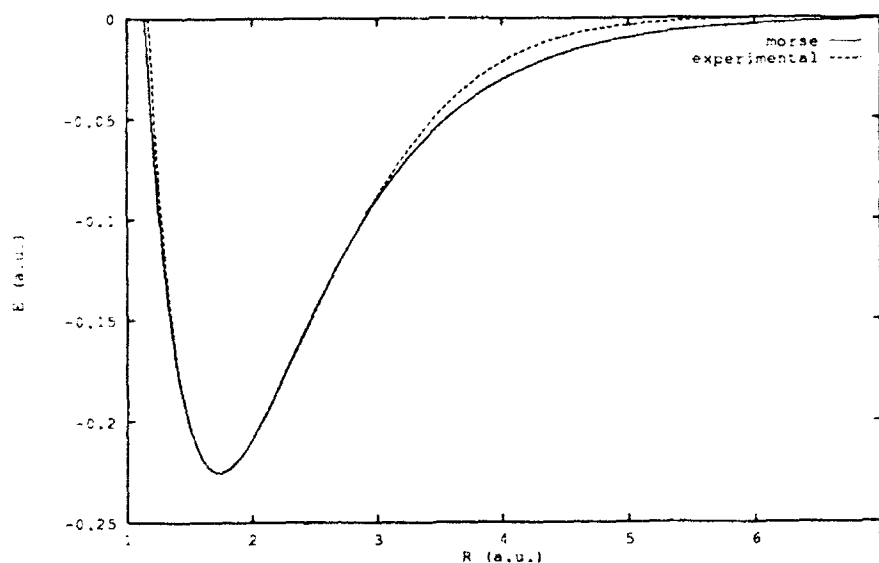
Figure 1. Potential energy curves.
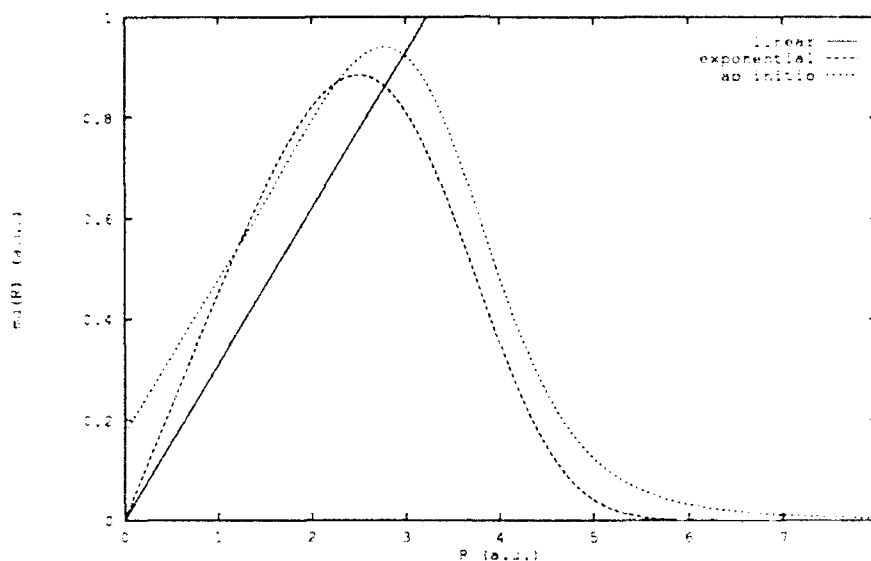
Figure 2. Dipole moment functions.

$$H_0 = -\frac{1}{2m}\frac{\partial^2}{\partial x^2} + V(x) \qquad (2)$$

Here $x = R - R_0$ where R is the interatomic distance and R_0 its equilibrium value. H_1 describes the interaction of the molecule with the external laser field in the classical dipole approximation.

$$H_1 = -\mu E \cos \Omega t. \qquad (3)$$

The reduced mass $m = 1744.843$ a.u. and the parameters of V are those corresponding to the case of HF. For the potential V we consider two models
  (a) The Morse potential

$$V_1 = D[1 - \exp(-ax)]^2 \qquad (4)$$

where $D = 0.225088$ a.u., $R_0 = 1.7329$ a.u., and $a = 1.1741$ a.u.

  (b) The potential V_2 given by Coxon and Hajigeorgiou which is defined by analytical expressions in the regions of small and large x and by tensioned cubic spline fits to numerical data given in Ref. [8] for the intermediate region.

For the dipole function μ we have compared three different approximations.
  (a) The dipole function proposed by Whaley and Light

$$\mu_1(R) = AR \exp(-BR^4). \qquad (5)$$

The values of the constants $A = 0.45414$ a.u. and $B = 0.0064$ a.u. are taken from Ref. [3].

(b) The linear approximation to (5)

$$\mu_2(R) = \frac{d\mu_1}{dR}(R_0)R \tag{6}$$

which is consistent with the value of the effective charge used in [1] and [2].

(c) The *ab initio* dipole moment function of Zemke et al. which is linear at small distances, zero for $R > 20$ a.u. and given by a tensioned cubic spline fit to numerical data given in Ref. [9] in the intermediate region.

In Figures 1 and 2 we show a graphical representation of the potentials and dipole functions. Although very similar in the neighborhood of the equilibrium distance, the discrepancy in the tail regions might influence the results because by multiphoton absorption the molecule is excited to high lying vibrational states.

The electric field strength E is considered as a constant (monochromatic field). E and the field frequency Ω are the two variable parameters of our model. We consider values of E corresponding to a field intensity of $43.7\,TW/cm^2$. This might be considered super-strong but not irrealistic in the context of our model. The values of Ω are taken in the range 0.35 eV to 0.55 eV relevant for resonance with the vibrational spectrum.

The time-dependent Schrödinger equation, in units $h = 1$, is given by

$$i\frac{\partial \Psi}{\partial t} = H\Psi \tag{7}$$
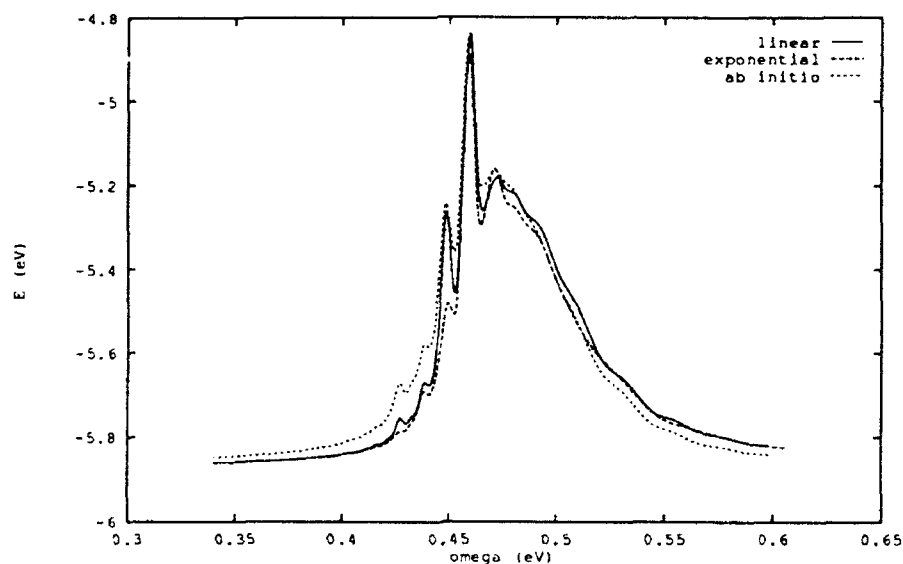
Figure 3. Time averaged energy versus driving field frequency. The electronic potential is approximated by a Morse well. The dipole moment function is approximated by a linear function (full line), an exponential model (long dashes) and an *ab initio* expression (short dashes). Intensity is $43.7\,TW/cm^2$. Energy and frequency in eV.
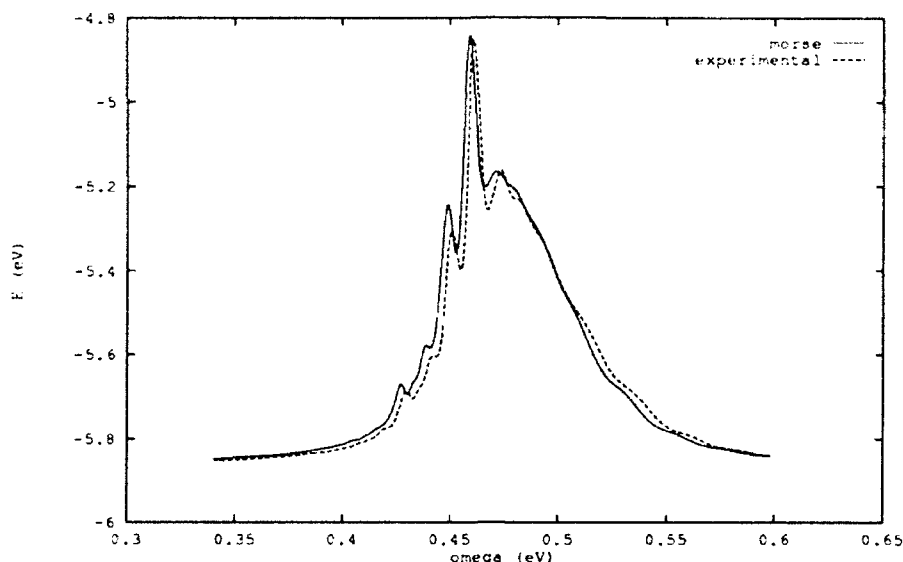
Figure 4. Time averaged energy versus driving field frequency. The electronic potential is approximated by a Morse well (full line) and a spectroscopically determined curve (dashed line). The dipole moment is an *ab initio* function. Intensity is 43.7 TW/cm². Energy and frequency in eV.

and must be solved subject to the initial condition that $\Psi(t = 0)$ is the ground state of the unperturbed Morse potential. The time evolution is generated by the propagator

$$U(t) = \mathcal{T} \exp\left(-i \int_0^t H(s)\, ds\right) \tag{8}$$

where $\mathcal{T}$ stands for the time ordering operator. The propagator is broken up into short time slices

$$U(t) = \prod_1^N U(\varepsilon), \quad t = \varepsilon N \tag{9}$$

with N large and ε small. This allows one to use an approximate short time propagator for $U(\varepsilon)$ which, in the split operator scheme, is given by

$$U(t_j, t_{j-1}) \approx \exp\left(-i \frac{\varepsilon}{2} T\right)\exp\left(-i \int_{t_{j-1}}^{t_j} ds V(s)\right)\exp\left(-i \frac{\varepsilon}{2} T\right) \tag{10}$$

and is correct up to second order in ε [10]. The power of the algorithm lies in the splitting of the V and T terms. The action of the first is evaluated while the wavefunction Ψ is in a coordinate representation, that is, defined by its values on a grid in coordinate space. For the second, one transforms the wavefunction to the mo-

mentum representation, using the discrete Fourier Transform associated with the grid. The T operator is multiplicative in that representation, so its action is easy to evaluate. Afterwards one transforms Ψ back to the coordinate representation with an inverse Fourier Transform. This is a viable approach because of the availability of FFT software that performs these transformations very efficiently.

Results

We have calculated the time evolution of the total energy $\mathcal{E}(t) = \langle \Psi(t) | H_0 | \Psi(t) \rangle$ of the molecule for field frequencies Ω between 0.3 a.u. and 0.6 a.u. The Fourier Transform was performed using an 256-point grid on the interval [0.6, 6.6] for the x-coordinate. These parameter settings ensure that there be no reflections of Fourier components off the end-points of the domain in real or reciprocal space. Under those conditions the computations are completely stable [10]. The number of time-slices we used was of the order of 2700 per optical cycle, or roughly 8 slices per atomic unit of time. This is sufficient for the split-operator formula to be applicable.

The absorption spectrum is defined by the time averaged energy

$$\bar{\mathcal{E}} = \frac{1}{T} \int_0^T \mathcal{E}(t) \, dt .$$ (11)

This converges to a stationary value if the time interval T over which the average is taken is large enough. By inspection of the time dependence of $\bar{\mathcal{E}}$ we find that in cases of resonant absorption the convergence is rather slow [11]. This implies that the calculations should be carried through over a period of at least 150 optical cycles. For a complete scan of the whole frequency domain, we have, for practical reasons, made a compromise and restricted the interval to 30 cycles (see also [1]). In Figures 3 and 4 we show the time averaged energy as a function of field frequency for different models of the molecule. These curves show a broad absorption region between 0.42 eV and 0.55 eV with superimposed peaks corresponding to the multiphoton resonance frequencies (from three to seven photons visible). The four-photon resonance is dominant.

Conclusion

In this article we have simulated the behavior of a light diatomic molecule in the presence of an intense infrared laser field by performing a numerical experiment. We have followed the time evolution of a wave packet (initially the unperturbed ground state) in a driven potential. The choice of parameter values corresponds to Hydrogen fluoride and a monochromatic field.

As an application of the split-operator technique to explicitly time-dependent Hamiltonians, it shows that this method is well-adapted and flexible because it allows an easy treatment of realistic potentials and dipole functions. This is due to the fact that no matrix elements have to be evaluated.

The general results corroborate the conclusions of earlier studies using different methods. The absorption spectrum shows a broad structure with superimposed

peaks corresponding to multiphoton resonance frequencies. The four-photon peak is dominant.

When the dipole moment function is approximated successively by a linear function, an exponential model function, and an *ab initio* expression we find that the corresponding absorption spectra do not converge systematically. In fact the linear approximation, although quite drastic, seems to reproduce better the *ab initio* result than the more sophisticated exponential model. In particular, the ratios of the five-photon and three-photon peaks to the dominant four-photon peak is affected quite strongly. The replacement of the Morse potential by a spectroscopically determined curve shows little effect.

Bibliography

[1] R. B. Walker and R. K. Preston, J. Chem. Phys. **67**, 2017 (1977).
[2] M. E. Goggin and P. W. Milonni, Phys. Rev. A **37**, 796 (1988).
[3] K. B. Whaley and J. C. Light, J. Chem. Phys. **77**, 1818 (1982).
[4] S. Chu, J. Chem. Phys. **75**, 2215 (1981).
[5] S. Chelkowski and A. D. Bandrauk, Phys. Rev. A **41**, 6480 (1990).
[6] S. Chelkowski, A. D. Bandrauk, and P. B. Corkum, Phys. Rev. Lett **65**, 2355 (1990).
[7] J. R. Stine and D. W. Noid, J. Chem. Phys. **78**, 1876 (1983).
[8] J. A. Coxon and P. G. Hajigeorgiou, J. Mol. Spec. **142**, 254 (1990).
[9] W. T. Zemke et al., J. Chem. Phys. **95**, 7846 (1991).
[10] J. A. Fleck, J. R. Norris, and M. D. Feit, Appl. Phys. **10**, 129 (1976).
[11] J. Broeckhove, B. Feyen, and P. Van Leuven, J. Mol. Structure (Theochem) (to be published).

The Photoelectron Spectra of Methyl Pseudohalides

T. PASINSZKI,[1] T. VESZPRÉMI,[1] M. FEHÉR, B. KOVAC,[2]
L. KLASINC,[3,4] and S. P. MCGLYNN[4]

[1]Department of Inorganic Chemistry, Technical University of Budapest, H1521 Budapest, Hungary,
[2]Institute of Physical Chemistry, University of Basel, CH-4056 Basel, Klingelbergstrasse 80,
Switzerland, Ruder Bošković Institute, Zagreb, Croatia, [4]Department of Chemistry,
Louisiana State University, Baton Rouge, Louisiana 70803

Abstract

The He I and He II photoelectron (PE) spectra of methyl pseudohalides (MeNCO, MeNCS, MeNCSe, MeSCN, and MeSeCN) have been recorded. Assignments are based on *ab initio* quantum chemical calculations, and their comparison with high-resolution He I spectra and He I/He II band intensity ratios. Contradictions found in previous works are largely resolved. The strikingly different spectra of the isomeric forms are interpreted using a consistent model for a methyl-distorted NCX substructure. The effects of the heavy atoms are also discussed. © 1992 John Wiley & Sons, Inc.

Introduction

Alkyl cyanates, isocyanates, and their sulphur and selenium analogs, are the most common examples of distorted linear triatomic systems—a circumstance which has given rise to the very large number of papers dealing with the electronic structure of these compounds [1–8]. In the case of the methyl derivatives, however, contradictions concerning the assignment of photoelectron spectra do exist. It is the aim of this work to use He I high-resolution spectra, He I/He II band intensity ratios, *ab initio* HF/4-31G** and MP2/4-31G** calculations in an attempt to remove these contradictions and provide more definitive assignments.

Experimental and Calculations

The ultraviolet (UV) PE spectra were recorded on a Vacuum Generators UV-G3 spectrometer [9] using a 0.5-mm slit and an analyzer energy of 5 eV. The instrumental resolution, defined at full-width-half maximum (FWHM) of Ar^{2}P$_{3/2}$, ^{2}P$_{1/2}$, was 15 meV. The spectra were calibrated by adding small amounts of Argon and Xenon to the sample flow.

Ab initio molecular orbital (MO) calculations were performed for all molecules. Ionization energies were obtained using Koopmans' theorem [10]. The geometry of each molecule was first optimized using a standard 4-31G* basis set for H, C, N, O, S and a [5s,4p,2d] contracted basis set for selenium [11]. An accurate description of the geometry of CH$_3$NCX molecules, as was pointed out earlier [12], requires consideration of the correlation energies. As a result, the geometries of the
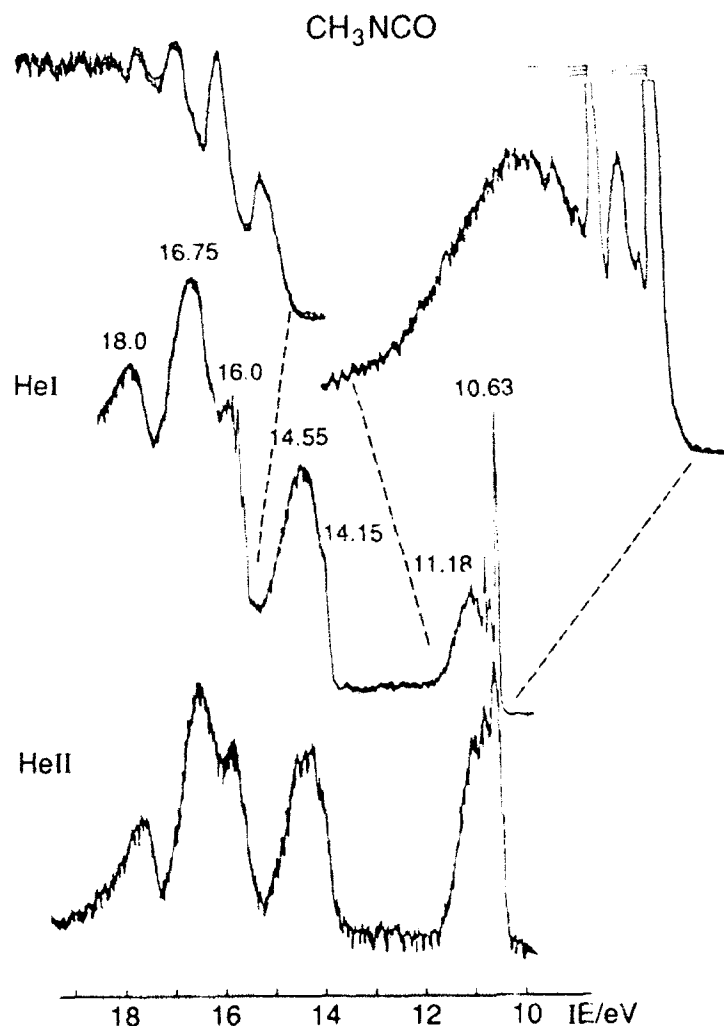
CH₃NCO

Figure 1. The He I and He II PE spectra of methyl isocyanate.

CH₃NCX molecules were optimized in conjunction with second-order Moller-Plesset (MP) perturbation theory. All calculations were performed with the CADPAC quantum chemistry package [13].

Results and Discussion

The spectrum of methyl isocyanate (CH₃NCO) is shown in Figure 1. The first two bands, 10.6–11.5 eV, are unambiguously attributable to ionizations from the nonbonding π_2 (a″,a′) orbitals of the NCO group, which concurs with the assignments of Cradock et al. [2] and Eland [3]: [π_2(a″,a′), π_1(a′,a″), 4σ,Me(a′,a″),3σ]

Table I. CH$_3$NCO

System	Relative intensity			Experimental IP (eV)	Calculated MP2 4-31G**	Assignment
	He I	He II	He II/He I			
1, 2	0.159	0.276	1.74	10.63	11.28 (a')	π
				11.18	11.77 (a)	
3, 4	0.155	0.21	1.35	14.15 sh	15.89 (a')	CH
				14.55	16.12 (a')	CH
5	0.065	0.092	1.42	16.0	17.28 (a')	
6, 7	0.146	0.19	1.30	16.75	17.79 (a')	
					18.74 (a')	
8	0.041	0.10	2.44	18.0	19.98 (a')	

and $[\pi_2(a'',a'),\pi_1(a',a''),\mathrm{Me}(a',a''),4\sigma,3\sigma]$, respectively. The highly resolved spectrum of Figure 1, however, provides considerably more vibronic detail: three vibrational modes are clearly evident (see Fig. 1, top), namely the ν(C–N), ν(NCO).
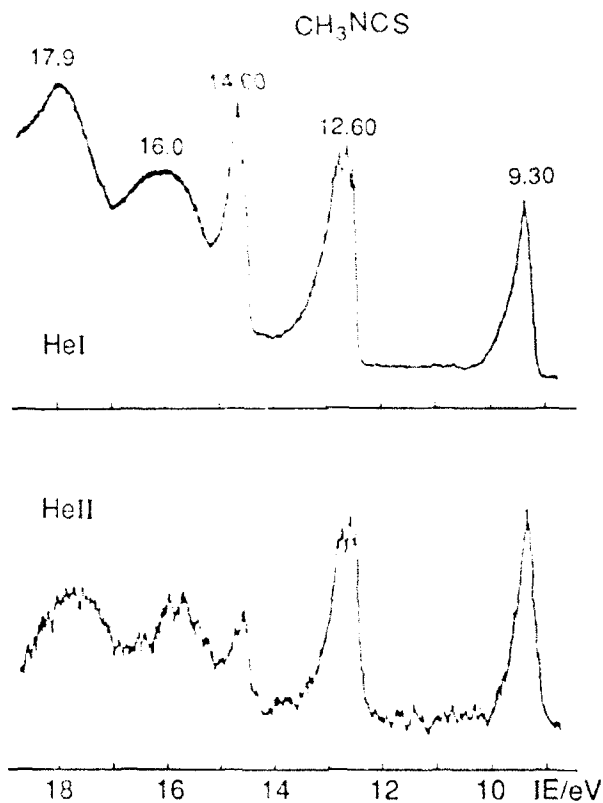
Figure 2. The He I and He II PE spectra of methyl isothiocyanate

Table II. CH₃NCS.

System	Relative intensity			Experimental IE/(eV)	Calculated MP2/4-31G**	Assignment
	He I	He II	He II/He I			
1, 2	0.284	0.336	1.18	9.30	9.35 (a")	π_2
					9.63 (a')	π_2
3, 4	0.175	0.239	1.37	12.60	14.05 (a')	π_1
					14.07 (a")	π_1
5	0.092	0.086	0.93	14.60	15.87 (a')	n_s
6, 7	0.115	0.211	1.83	16.0	17.41 (a")	CH₃
					17.47 (a')	CH₃
8	0.055	0.145	2.64	17.9	19.74 (a')	σ_{CN}

and ν_a(NCO) frequencies at 800, 1290, and 2150 cm⁻¹, respectively. (These modes occur in the ground state at 852, 1437, and 2288 cm⁻¹, respectively [14].)

Our energy assignments in the 14–17 eV region differ from those in the literature. In this region, one expects ionizations arising from orbitals which consist of a symmetry-controlled mixing of methyl group orbitals, CH₃(a",a'), with NCO group orbitals, π_1(a",a') and n_0(a'). The broad system at 14.55 eV and a shoulder at 14.15 eV, should be assigned to the two antisymmetric linear combinations of the methyl group orbitals with the π_1 orbitals, the amplitudes on the methyl group being dominant in both cases. Calculation supports these assignments. The 16.0 eV system contains an extensive vibrational progression in 800 cm⁻¹. This system is assigned to the π_1(a") bonding orbital, which has dominant amplitude on NCO group. This assignment is confirmed by both calculation (Table I) and the HNCO spectrum [3]. The π_1(a') band, again derivative of the bonding combination of π_1 and NCO group orbitals, is obscured by the 16.0 eV band and by the next band system at 16.75 eV. The 16.75 eV system, in turn, is attributed to an ionization from the n_0(a') orbital. According to calculation, the highest-energy band at 18.0 eV can be attributed to an ionization of the σ_{NCO} orbital of the pseudohalide group.

Table III. CH₃NCSe.

System	Relative intensity			Experimental IE/(eV)	Calculated MP2/4-31G**	Assignment
	He I	He II	He II/He I			
1, 2	0.236	0.293	1.24	8.90	8.90 (a")	π_2
					8.99 (a')	π_2
3, 4	0.279	0.399	1.43	12.35	14.10 (a")	π_1
					14.10 (a')	π_1
5	0.110	0.085	0.77	14.22	15.10 (a')	n_{Se}
6	0.081	0.12	1.48	15.8	17.72 (a")	CH₃
					16.5	17.76 (a')	CH₃
				18.1	20.10 (a')	σ_{CN}
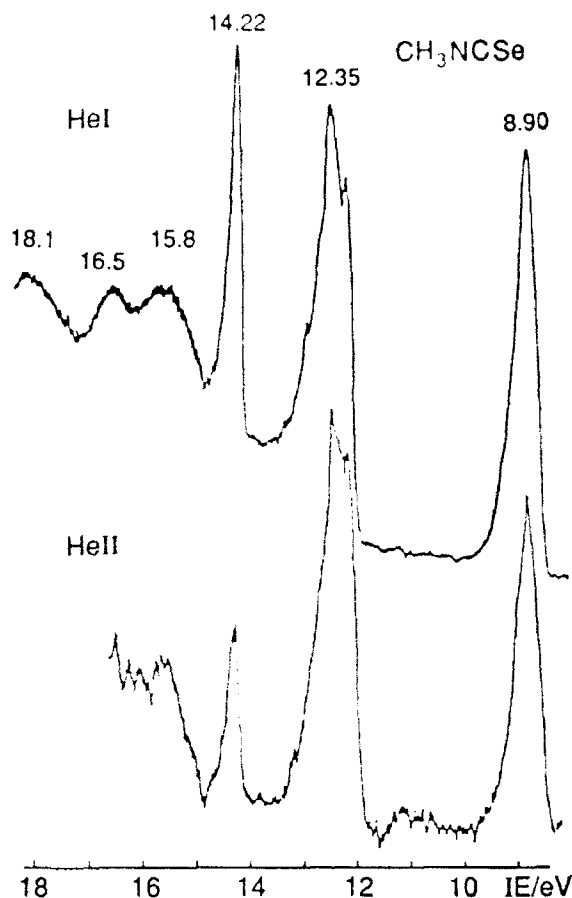
Figure 3.   The He I and He II PE spectra of methyl isoselenocyanate.

The CH_3NCS spectrum differs considerably from that for CH_3NCO (Fig. 2). The first and second band systems, at 9.30 and 12.60 eV, are attributed to ionization of the π_3 and π_1 (a' and a") orbitals of the NCS group, respectively. This assignment is supported by quantum-chemical calculations and by the He I/He II intensity ratios (Table II). The splitting of the π_2 bands is much smaller than in CH_3NCO, and is inferred from the existence of a shoulder. The intensity of the third system at 14.60 eV decreases strongly, in a relative sense, in the He II spectrum and, consequently, it can be assigned to the lone pair orbital of sulphur (n_S). The broad band at 16.0 eV corresponds to ionization of the methyl group orbitals. The band at 17.9 eV is an $I(\sigma_{CN})$ event, in agreement with calculation (Table II). These assignments are in good agreement with earlier investigations [2,3].

The PE spectrum of CH_3NCSe is shown in Figure 3. A striking resemblance to that of CH_3NCS is evident. The former spectrum is shifted to lower energies and

CH₃SCN
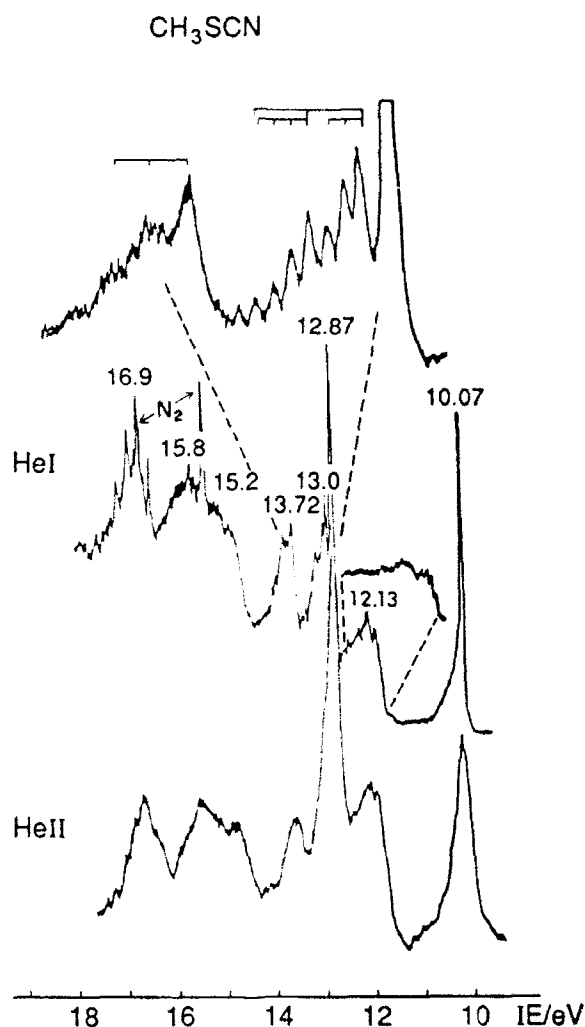
Figure 4.   The He I and He II PE spectra of methyl thiocyanate.

the π_2/π_1 splitting is greater than for CH_3NCS. The splitting of the $\pi_2(a'')/\pi_2(a')$ components is negligible and only a single symmetric band is observed. The third system corresponds to $I(n_{Se})$, initiating in an orbital that is mainly localized on selenium. Confirmation of this latter assignment is provided by the large intensity reduction of this system in the He II spectrum (Table III). The system at 16.1 eV is assigned to orbitals localized mainly on the methyl group. The system at 18.1 eV is an $I(\sigma_{CN})$ event.

The electronic structure of the isomers CH_3XCN is also of considerable interest. The PE spectrum of CH_3SCN is shown in Figure 4. This PE spectrum has been

CH₃SeCN
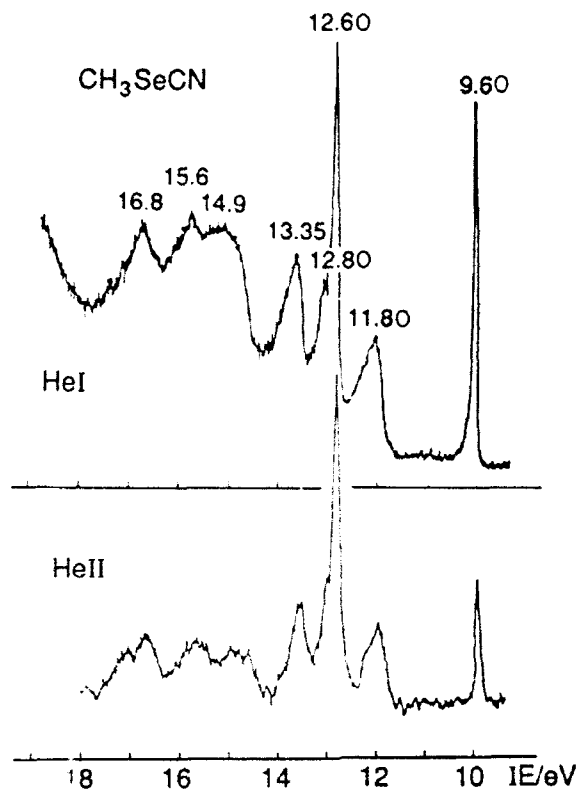
Figure 4   The He I and He II PE spectra of methyl selenocyanate.

assigned by Neijzen et al. [4] and Andreocci et al. [5]. Unfortunately, the only assignments that a e quite certain refer to ionizations from the outermost orbitals $\pi_2(a'')$ and $\pi_2(a')$ The π_2 system of a'' symmetry at 10.13 eV is very sharp and narrow. The other π_2 component, a' symmetry, occurs at 12.13 eV, is a broad band, and exhibits a 390 cm⁻¹ vibrational progression with maximum at v = 3 or 4 superposed on another progression in 1450 cm⁻¹ (an SCN bending for which the ground state value is 440 cm⁻¹ [15]) and CN stretching for which the ground state value is 2170 cm⁻¹) The system at 12.8–13.5 eV also exhibits a vibrational structure which has been referred [4] to as an "irregular vibrational progression." This vibrational structure is shown resolved at the top of Figure 4. Two clear progressions may be seen: 1850 and 560 cm⁻¹ modes which are attributable to ν_{CN} stretching (2171 cm⁻¹ in the ground state) and the ν_{CSe} stretching (ca. 700 cm⁻¹ [15] in the ground state), respectively. The separation of the very sharp structureless peaks at 12.87 and 13.0 eV is not vibrational, supporting the thesis that the former corresponds to I[$\pi_1(a'')$] and latter to I[$\pi_1(a')$] events. The fifth system at 13.72 eV, which exhibits a progression in 1200 cm⁻¹, is assigned to the n_N orbital (rather than to π_1 as in [4]) because the intensity decreases in the He II spectrum (Table

TABLE IV.   CH₃SCN.

System	Relative intensity			Experimental IE'/(eV)	Calculated HF/6-31G**	Assignment
	He I	He II	He II/He I			
1	0.099	0.141	1.41	10.07	10.33 (a")	π₂
2	0.082	0.136	1.66	12.13	12.41 (a')	π₂
3, 4	0.124	0.226	1.82	12.87	14.10 (a")	π₁
				13.0	14.39 (a')	π₁
5	0.101	0.09	0.89	13.72	15.23 (a')	nₙ
6, 7	0.177	0.212	1.2	15.2	16.54 (a')	CH₃
				15.8	17.11 (a")	CH₃
8	0.051	0.093	1.82	16.9	18.54 (a')	σₛₙ

IV). In accord with this, the calculations of Table IV predict a very small splitting of the two π_1 orbitals (0.29 eV), in good agreement with experiment.

The assignment of the PE spectrum of CH₃SeCN (Fig. 5) is very similar to that for CH₃SCN, except that the $\pi_2(a'')/\pi_2(a')$ splitting is more pronounced. (ΔE = 2.2 compared to 2.0 eV in CH₃SCN). The first (9.60 eV) and the third (12.60 eV) systems are narrow and sharp; the second (11.80 eV) and the fourth (12.80 eV) contain vibronic structure which is not as pronounced as in CH₃SCN. However, since the electronic structures are very similar, we deduce, by analogy, that the $\pi_1(a'')/\pi_1(a')$ splitting is probably about the same size, namely 0.2 eV. The fifth system at 13.35 eV is assigned to an n_N system, because of He I/He II intensity ratios and correspondence with calculations (Table V). The bands in the 15–16 eV region in both compounds can be attributed to ionizations centered on orbitals localized on the methyl groups. The band at ∼17 eV in both compounds can be assigned to ionization from σ_{SCN} and σ_{SeCN} orbitals, respectively.

The results of the quantum chemical calculations mimic the experimental trends (Fig. 6). The splitting of the π_2 bands is computed to be largest in CH₃SeCN and

TABLE V.   CH₃SeCN.

System	Relative intensity			Experimental IE'/(eV)	Calculated HF/4-31G**	Assignment
	He I	He II	He II/He I			
1	0.094	0.09	0.96	9.60	9.76 (a")	π₂
2	0.069	0.12	1.74	11.80	12.10 (a')	π₂
3, 4	0.126	0.24	1.90	12.60	13.94 (a")	π₁
				12.80	14.10 (a')	π₁
5	0.099	0.12	1.21	13.35	14.99 (a')	nₙ
6, 7	0.179	0.185	1.03	14.9	16.48 (a')	CH₃
				15.6	17.21 (a")	CH₃
8	0.057	0.111	1.95	16.8	17.94 (a')	σₛₑₙ

Calculated
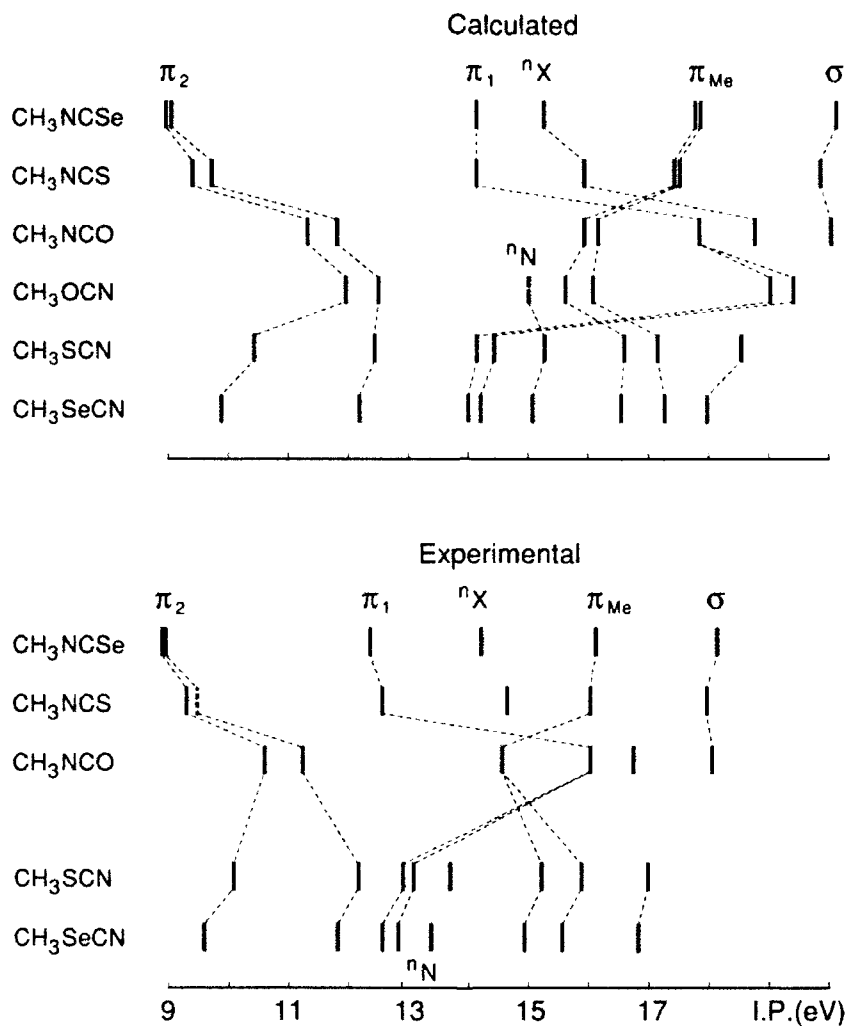
Experimental

Figure 6.   Calculated and experimental ionization energy correlation diagram of MeNCSe. MeNCS. MeNCO. MeOCN. MeSCN. and MeSeCN.

to get smaller in the series CH_3SeCN. CH_3SCN. CH_3OCN, CH_3NCO, CH_3NCS. and CH_3NCSe. which accords with experiment. Indeed. this splitting is so small in CH_3NCSe that we cannot observe it. The reason for this trend is embedded in differences of electronic structure: According to calculation, the π_2 orbitals in the $-NCO$ and $-OCN$ groups are more or less symmetric; however, as O is replaced by S or Se. this symmetric distribution distorts and the π_2 orbitals tend to localize on the sulphur atom and, to a higher degree, on the selenium atom. Therefore. the π_2 bands of compounds containing the $-NCX$ group will be less sensitive to substituent effects, and band splittings will be less sensitive to the bond angle at the
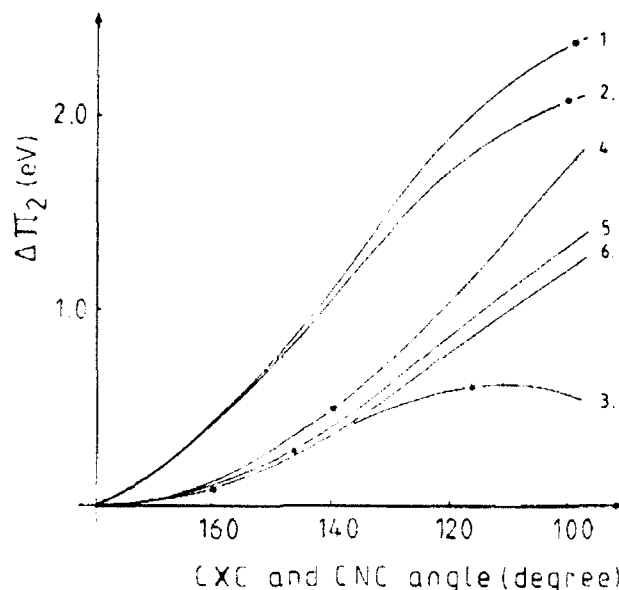
Figure 7.   Calculated splitting of π_2 orbitals as a function of CXC or CNC angle. 1. MeSeCN; 2. MeSCN; 3. MeOCN 4. MeNCO 5. MeNCS; 6. MeNCSe.

nitrogen when X = S or Se; in compounds containing the −XCN group; however, the sensitivity to substituent and the bands splitting will increase as the X-atom gets larger. The electron distribution in the π_1 orbital should be opposite to that of π_2, the orbital now being localized on the NC fragment with an amplitude which increases as the oxygen changes to S or Se. Since $I(\pi_1)$ is of high energy, π_1 usually is heavily mixed with other orbitals. Consequently, the predicted π_1 splittings contrary to the π_2 splittings are difficult to verify experimentally. Finally, the decreasing energy of the two components of the π_2 bands is, to some extent, a result of the increasing C–X–C and C–N–C angle in the series CH_3SeCN, CH_3SCN, CH_3OCN, CH_3NCO, CH_3NCS, CH_3NCSe. According to ab initio calculations, these angles are 98.7°, 99.9°, 118.8°, 139.7°, 146.1°, and 159.7°, respectively.

The splitting of the π_2 orbitals as a function of CXC or CNC angle is given in Figure 7. The calculated bond angles at the minimum energy geometry are denoted by an asterisk. It can be seen that the π_2 splitting decreases as one goes from CH_3SeCN to CH_3NCSe because the C–X–C angle is the smallest in CH_3SeCN and increases thereafter.

Bibliography

[1] T. Veszpremi, T. Pasinszki, and M. Feher. J. Chem. Soc., Faraday Trans. 87, 3805 (1991).
[2] S. Cradock. E. A. V. Ebsworth, and J. D. Murdoch. J. Chem. Soc., Faraday Trans. 2 28, 86 (1972).
[3] J. H. D. Eland. Phil. Trans. Roy. Soc. London. Ser. A268, 87 (1970).
[4] B. J. M. Neijzen and C. A. DeLange. J. Electron Spectrosc. Relat. Phenom. 18, 179 (1980).

[5] M. V. Andreocci, M. Bossa, C. Furlani, M. N. Piancastelli, C. Cauletti, and T. Tarantelli, J. Chem. Soc., Faraday Trans. 2 75, 105 (1979).

[6] G. Jonkers, N. Mooyman, and C. A. DeLange, Mol. Phys. 43, 855 (1981).

[7] D. C. Frost, C. B. MacDonald, C. A. McDowell, and N. P. C. Westwood, Chem. Phys. 47, 111 (1980).

[8] D. C. Frost, C. B. MacDonald, C. A. McDowell, and N. P. C. Westwood, J. Am. Chem. Soc. 103, 4423 (1981).

[9] L. Klasinc, B. Kovac, and D. Ruscic, Kem. Ind. (Zagreb) 23, 569 (1974).

[10] T. Koopmans, Physica 1, 104 (1934).

[11] J. M. Lehn, G. Wipff, and J. Demuynck, Helv. Chim. Acta 60, 1239 (1977).

[12] T. Pasinszki, T. Veszpremi, and M. Feher, Chem. Phys. Lett. 189, 245 (1992).

[13] R. D. Amos and J. E. Rice, The Cambridge Analytical Derivatives Package, CADPAC, 1987, Issue 4.0.

[14] R. P. Hirschmann, R. N. Kniseley, and V. A. Fassel, Spectrochim. Acta 21, 2125 (1965).

[15] J. F. Sullivan, H. L. Hensel, and J. R. Durig, J. Mol. Struct. 115, 391 (1984).

Study of the Diffuse Spectral Series
of Boron-Like Atomic Systems

C. LAVÍN, I. MARTIN, and M. J. VALLEJO

*Departamento de Química Física, Facultad de Ciencias, Universidad de Valladolid,
47005 Valladolid, Spain*

Abstract

The diffuse spectral series, $2s^2np\ ^2P-2s^2nd\ ^2D$, of the boron isoelectronic sequence has been studied through a one-particle scheme, by explicitly treating only the active electron. Oscillator strengths for various transitions ($n = 2,3$; $n' = 3-16$) have been computed with the quantum defect and relativistic quantum defect formalisms, and results comparing very satisfactorily with other theoretical data have been obtained. © 1992 John Wiley & Sons, Inc.

Introduction

Within the last few years, the description, understanding, and prediction of the physical processes that take place in the universe have been the object of increasing attention. This has been partly due to the outstanding technological development and the enormous amount of "rough" data which is awaiting careful analysis and interpretation. However, the reproduction in the laboratory of the very extreme conditions to which the constituents of the universe are subjected is, if not impossible, at least extremely difficult, time-consuming, and expensive. Quantum-mechanical calculations have, thus, become crucial in the accomplishment of these goals. However, in the estimation of some properties of astrophysical interest, the calculation of transition probabilities for a great number of lines is required. Results for 1.7 million lines have recently been reported by Kurucz [1]. In addition to their astrophysical importance, the intensities of the transitions of moderately to highly stripped ions present an enormous interest for the diagnosis of Tokamak plasmas [2], and, in general, for the development of controlled thermonuclear fusion reactors [3].

Reliable computational procedures are, thus, required. A method that has so far proven to be very accurate for predicting transition probabilities and *f*-values for transitions in moderately to highly stripped atomic ions, and in heavy atomic systems, is the multiconfigurational Dirac–Fock (DF) approach [4]. However, it is fast becoming increasingly time-consuming and costly with the number of configurations included in the calculation and with the number of transitions to be studied. Hence, it is quite convenient to develop methods which are both simple and reliable.

The usefulness of model potential methods in this type of problems has been the subject of a review by Hibbert [5], and of general comments by Crossley [6].

TABLE I. Oscillator strengths for $np\,^2P-n'd\,^2D$ ($n = 2,3$; $n' = 3-15$) transitions in Bl.[a]

Transition	QDO[b]	MCHF[c]		SOC[d]	FC[e]
		Length	Velocity		
2p-3d	0.1201	0.86 (-1)	0.102	0.197	0.125
2p-4d	0.5302 (-1)	0.40 (-1)	0.45 (-1)		
2p-5d	0.2678 (-1)	0.21 (-1)	0.23 (-1)		
2p-6d	0.1529 (-1)	0.12 (-1)	0.13 (-1)		
2p-7d	0.9531 (-2)				
2p-8d	0.6340 (-2)				
2p-9d	0.4429 (-2)				
2p-10d	0.3215 (-2)				
2p-11d	0.2408 (-2)				
2p-12d	0.1850 (-2)				
2p-13d	0.1452 (-2)				
2p-14d	0.1161 (-2)				
2p-15d	0.942 (-3)				
3p-3d	1.023	0.860	0.919		
3p-4d	0.4140 (-1)				
3p-5d	0.9374 (-2)				
3p-6d	0.7080 (-2)				
3p-7d	0.4920 (-2)				
3p-8d	0.3452 (-2)				
3p-9d	0.2490 (-2)				
3p-10d	0.1841 (-2)				
3p-11d	0.1400 (-2)				
3p-12d	0.1085 (-2)				
3p-13d	0.8612 (-3)				
3p-14d	0.6921 (-3)				
3p-15d	0.5668 (-3)				

[a] In this and the remaining tables, $A(-B)$ denotes $A \cdot 10^{-B}$.
[b] Present work.
[c] Ref. 17.
[d] Ref. 22.
[e] Ref. 23.

who considers some of them capable of achieving a good balance between computational effort and accuracy of results, as compared with more complex theoretical procedures.

For several years, we have studied the behavior of transition probabilities, oscillator strengths, and photoionization cross sections for several series of homologous atoms [7] and isoelectronic sequences [8-10] through the quantum defect orbital (QDO) method [11], which involves the analytical solution of a model Hamiltonian that contains a semiempirical parameter. Quite recently, we have formulated the relativistic version of the above procedure (RQDO), which has so far proven to be highly reliable when treating heavy atomic systems [12].

TABLE II. Oscillator strengths for $np\,^2P$-$n'd\,^2D$ (n = 2-4, n' = 3-6) transitions in CII.

Transition	QDO[a]	MCHF[b]		SOC[c]
		Length	Velocity	
$2p$-$3d$	0.2887	0.266	0.267	0.330
$2p$-$4d$	0.9728(-1)	0.95(-1)	0.92(-1)	
$2p$-$5d$	0.4450(-1)	0.44(-1)	0.42(-1)	
$2p$-$6d$	0.2413(-1)	0.24(-1)	0.23(-1)	
$3p$-$3d$	0.6339	0.577	0.620	
$3p$-$4d$	0.1165	0.103	0.96(-1)	
$3p$-$5d$	0.5554(-1)	0.47(-1)	0.45(-1)	
$3p$-$6d$	0.2985(-1)	0.25(-1)	0.23(-1)	
$4p$-$4d$	1.039	0.873	0.899	
$4p$-$5d$	0.4491(-1)	0.66(-1)	0.63(-1)	
$4p$-$6d$	0.3111(-1)	0.35(-1)	0.33(-1)	

[a] This work.
[b] Ref. 17.
[c] Ref. 22.

In this work, we report oscillator strengths for several members of the boron isoelectronic sequence, from BI to KrXXXVI, for which atomic energy data have been found in the literature. The transitions studied by us involve levels of the diffuse spectral series, $np\,^2P$-$n'd\,^2D$, including those starting from excited states, n = 2-4, and n' = 3-15 in some cases. For the lightest members of this sequence, BI to OIV, only multiplet oscillator strengths have been reported. For the heavier ions, starting at SiX, fine-structure calculations have been performed, through both QDO and RQDO procedures.

This isoelectronic sequence offers interest to us not only from a methodological point of view, as we shall mention later, but also because many of the ions belonging to it, such as OIV, MgVIII, SiX, SXII, and FeXXII, have been observed in many astrophysical objects [13]. The abundance of SiX in the solar corona has also been emphasized by Träbert et al. [14], who have measured lifetimes and report on cascading effects and other experimental difficulties. Vernazza and Mason [15] also point out the existence of boron-like ions in the solar corona.

The boron isoelectronic sequence has a ground level configuration $1s^2 2s^2 2p\,^2P$, which can be considered as a one-electron system (one electron outside a closed subshell), having a relatively simple Rydberg spectra, as El-Sherbini et al. have recently remarked [16]. Hence, it seems appropriate that the use of one-electron techniques in the treatment of these systems, in particular as the atomic number increases and the closed subshell becomes more contracted. By employing a single-configuration Hartree-Fock (HF) technique, as well as a Coulomb-approximation (CA) approach, El-Sherbini et al. [16] have obtained oscillator strengths of claimed general accuracy.

TABLE III. Oscillator strengths for $np\,^2P-n'd\,^2D$ ($n = 2,3$; $n' = 3-12$) transitions in NIII.

Transition	QDO[a]	MCHF[b]		Model[c]
		Length	Velocity	
2p–3d	0.3888	0.384	0.371	0.3..
2p–4d	0.1147	0.116	0.109	0.1084
2p–5d	0.5005 (−1)	0.51 (−1)	0.47 (−1)	0.47 (−1)
2p–6d	0.2658 (−1)	0.27 (−1)	0.25 (−1)	0.248 (−1)
2p–7d	0.1586 (−1)	0.16 (−1)	0.149 (−1)	0.148 (−1)
2p–8d	0.1025 (−1)			
2p–9d	0.7011 (−2)			
2p–10d	0.5023 (−2)			
2p–11d	0.3773 (−2)			
2p–12d	0.1938 (−2)			
3p–3d	0.4543	0.415	0.441	
3p–4d	0.2369	0.206	0.199	
3p–5d	0.7985 (−1)	0.76 (−1)	0.73 (−1)	
3p–6d	0.3898 (−1)	0.36 (−1)	0.35 (−1)	
3p–7d	0.2222 (−1)			
3p–8d	0.1396 (−1)			
3p–9d	0.9390 (−2)			
3p–10d	0.6620 (−2)			
3p–11d	0.4800 (−2)			
3p–12d	0.3469 (−2)			

[a] This work.
[b] Ref. 17.
[c] Ref. 24.

TABLE IV. Oscillator strengths for $np\,^2P-n'd\,^2D$ ($n = 2,3$; $n' = 3-6$) transitions in OIV.

Transition	QDO[a]	MCHF[b]		SOC[c]
		Length	Velocity	
2p–3d	0.4517	0.455	0.437	0.486
2p–4d	0.1222	0.124	0.116	
2p–5d	0.5171 (−1)	0.52 (−1)	0.49 (−1)	
2p–6d	0.2705 (−1)	0.27 (−1)	0.25 (−1)	
3p–3d	0.3534	0.322	0.337	0.319
3p–4d	0.2799	0.278	0.274	
3p–5d	0.9513 (−1)	0.92 (−1)	0.90 (−1)	
3p–6d	0.5453 (−1)	0.43 (−1)	0.42 (−1)	

[a] This work.
[b] Ref. 17.
[c] Ref. 22.

TABLE V. Oscillator strengths for $2p\,^2P-3d\,^2D$ fine-structure transitions in boron-like ions

Z	Ion	Transition	QDO	RQDO	Ref. 2	Ref. 25
14	SiX	$2p_{1/2}-3d_{3/2}$	0.5883	0.5857		
		$2p_{3/2}-3d_{3/2}$	0.5883(−1)	0.5874(−1)		
		$2p_{3/2}-3d_{5/2}$	0.5295	0.5284		
15	PXI	$2p_{1/2}-3d_{3/2}$	0.5977	0.5946		
		$2p_{3/2}-3d_{3/2}$	0.5977(−1)	0.5966(−1)		
		$2p_{3/2}-3d_{5/2}$	0.5379	0.5367		
16	SXII	$2p_{1/2}-3d_{3/2}$	0.6054	0.6017		
		$2p_{3/2}-3d_{3/2}$	0.6054(−1)	0.604(−1)		
		$2p_{3/2}-3d_{5/2}$	0.5449	0.5434		
17	ClXIII	$2p_{1/2}-3d_{3/2}$	0.612	0.6079		
		$2p_{3/2}-3d_{3/2}$	0.612(−1)	0.6104(−1)		
		$2p_{3/2}-3d_{5/2}$	0.5508	0.5489		
18	ArXIV	$2p_{1/2}-3d_{3/2}$	0.6178	0.613	0.6235	
		$2p_{3/2}-3d_{3/2}$	0.6178(−1)	0.6159(−1)	0.6357(−1)	
		$2p_{3/2}-3d_{5/2}$	0.5560	0.5539	0.572	
19	KXV	$2p_{1/2}-3d_{3/2}$	0.6221	0.6172		
		$2p_{3/2}-3d_{3/2}$	0.6221(−1)	0.6204(−1)		
		$2p_{3/2}-3d_{5/2}$	0.5599	0.5571		
20	CaXIV	$2p_{1/2}-3d_{3/2}$	0.6172	0.6110		
		$2p_{3/2}-3d_{3/2}$	0.6172(−1)	0.6147(−1)		
		$2p_{3/2}-3d_{5/2}$	0.5555	0.5527		
21	ScXVII	$2p_{1/2}-3d_{3/2}$	0.6299	0.6231		0.65
		$2p_{3/2}-3d_{3/2}$	0.6299(−1)	0.6271(−1)		0.64(−1)
		$2p_{3/2}-3d_{5/2}$	0.5669	0.5637		0.58
22	TiXVIII	$2p_{1/2}-3d_{3/2}$	0.6337	0.6263	0.6295	0.65
		$2p_{3/2}-3d_{3/2}$	0.6337(−1)	0.6307(−1)	0.648(−1)	0.64(−1)
		$2p_{3/2}-3d_{5/2}$	0.5703	0.5667	0.583	0.58
23	VXIX	$2p_{1/2}-3d_{3/2}$	0.6368	0.6287		0.65
		$2p_{3/2}-3d_{3/2}$	0.6368(−1)	0.6335(−1)		0.64(−1)
		$2p_{3/2}-3d_{5/2}$	0.5731	0.569		0.58
24	CrXX	$2p_{1/2}-3d_{3/2}$	0.6320	0.6226		0.65
		$2p_{3/2}-3d_{3/2}$	0.632(−1)	0.628(−1)		0.64(−1)
		$2p_{3/2}-3d_{5/2}$	0.5688	0.5645		0.58
26	FeXXII	$2p_{1/2}-3d_{3/2}$	0.6433	0.632	0.631	0.65
		$2p_{3/2}-3d_{3/2}$	0.6433(−1)	0.6382(−1)	0.658(−1)	0.65(−1)
		$2p_{3/2}-3d_{5/2}$	0.579	0.5737	0.592	0.59
28	NiXXIV	$2p_{1/2}-3d_{3/2}$	0.6406	0.6273		
		$2p_{3/2}-3d_{3/2}$	0.6406(−1)	0.6347(−1)		
		$2p_{3/2}-3d_{5/2}$	0.5765	0.5703		
30	ZnXXVI	$2p_{1/2}-3d_{3/2}$	0.6413	0.6257		
		$2p_{3/2}-3d_{3/2}$	0.6413(−1)	0.6345(−1)		
		$2p_{3/2}-3d_{5/2}$	0.5772	0.5699		
32	GeXXVIII	$2p_{1/2}-3d_{3/2}$	0.6437	0.6257	0.628	
		$2p_{3/2}-3d_{3/2}$	0.6437(−1)	0.6358(−1)	0.668(−1)	
		$2p_{3/2}-3d_{5/2}$	0.5793	0.5709	0.602	
34	SeXXX	$2p_{1/2}-3d_{3/2}$	0.6453	0.6247		
		$2p_{3/2}-3d_{3/2}$	0.6453(−1)	0.6363(−1)		
		$2p_{3/2}-3d_{5/2}$	0.5808	0.5711		
36	KrXXXII	$2p_{1/2}-3d_{3/2}$	0.646	0.6225	0.623	
		$2p_{3/2}-3d_{3/2}$	0.646(−1)	0.6358(−1)	0.675(−1)	
		$2p_{3/2}-3d_{5/2}$	0.5814	0.5705	0.607	

TABLE VI. Oscillator strengths for $3p\,^2P$–$3d\,^2D$ fine-structure transitions in boron-like ions

Z	Ion	Transition	QDO	RQDO	Ref. 2
14	SiX	$3p_{1/2}$–$3d_{3/2}$	0.8139 (-1)	0.8074 (-1)	
		$3p_{3/2}$–$3d_{3/2}$	0.8139 (-2)	0.8074 (-2)	
		$3p_{3/2}$–$3d_{5/2}$	0.7325 (-1)	0.7355 (-1)	
18	ArXIV	$3p_{1/2}$–$3d_{3/2}$	0.1062	0.1088	0.1063
		$3p_{3/2}$–$3d_{3/2}$	0.1062 (-1)	0.1028 (-1)	0.1001 (-1)
		$3p_{3/2}$–$3d_{5/2}$	0.9558 (-1)	0.9438 (-1)	0.9173 (-1)
20	CaXIV	$3p_{1/2}$–$3d_{3/2}$	0.9382 (-1)	0.9700 (-1)	
		$3p_{3/2}$–$3d_{3/2}$	0.9382 (-2)	0.8965 (-2)	
		$3p_{3/2}$–$3d_{5/2}$	0.8444 (-1)	0.8300 (-1)	
22	TiXVIII	$3p_{1/2}$–$3d_{3/2}$	0.8481 (-1)	0.8880 (-1)	0.877 (-1)
		$3p_{3/2}$–$3d_{3/2}$	0.8481 (-2)	0.7966 (-2)	0.782 (-2)
		$3p_{3/2}$–$3d_{5/2}$	0.7633 (-1)	0.7455 (-1)	0.73 (-1)
24	CrXX	$3p_{1/2}$–$3d_{3/2}$	0.7653 (-1)	0.8129 (-1)	
		$3p_{3/2}$–$3d_{3/2}$	0.7653 (-2)	0.7039 (-2)	
		$3p_{3/2}$–$3d_{5/2}$	0.6888 (-1)	0.6677 (-1)	
26	FeXXII	$3p_{1/2}$–$3d_{3/2}$	0.7244 (-1)	0.7809 (-1)	0.7765 (-1)
		$3p_{3/2}$–$3d_{3/2}$	0.7244 (-2)	0.6517 (-2)	0.6423 (-2)
		$3p_{3/2}$–$3d_{5/2}$	0.652 (-1)	0.6271 (-1)	
28	NiXXIV	$3p_{1/2}$–$3d_{3/2}$	0.6850 (-1)	0.7506 (-1)	
		$3p_{3/2}$–$3d_{3/2}$	0.6850 (-2)	0.6003 (-2)	
		$3p_{3/2}$–$3d_{5/2}$	0.6165 (-1)	0.5878 (-1)	
30	ZnXXVI	$3p_{1/2}$–$3d_{3/2}$	0.6577 (-1)	0.7344 (-1)	
		$3p_{3/2}$–$3d_{3/2}$	0.6577 (-2)	0.5587 (-2)	
		$3p_{3/2}$–$3d_{5/2}$	0.5919 (-1)	0.558 (-1)	
32	GeXXVIII	$3p_{1/2}$–$3d_{3/2}$	0.6394 (-1)	0.7271 (-1)	0.712 (-1)
		$3p_{3/2}$–$3d_{3/2}$	0.6394 (-2)	0.5256 (-2)	0.5078 (-2)
		$3p_{3/2}$–$3d_{5/2}$	0.5755 (-1)	0.5376 (-1)	0.5162 (-1)
34	SeXXX	$3p_{1/2}$–$3d_{3/2}$	0.6015 (-1)	0.7005 (-1)	
		$3p_{3/2}$–$3d_{3/2}$	0.6015 (-2)	0.4727 (-2)	
		$3p_{3/2}$–$3d_{5/2}$	0.5414 (-1)	0.4990 (-1)	
36	KrXXXII	$3p_{1/2}$–$3d_{3/2}$	0.6131 (-1)	0.7245 (-1)	0.704 (-1)
		$3p_{3/2}$–$3d_{3/2}$	0.6131 (-2)	0.4671 (-2)	0.446 (-2)
		$3p_{3/2}$–$3d_{5/2}$	0.5518 (-1)	0.5040 (-1)	0.478 (-1)

Note: QDO and RQDO from present work.

Cohen and Nahon [17] also followed frozen core (FC) and limited multiconfigurational frozen core (MCFC) procedures. In the former, all but a single valence electron are kept fixed, and only a single radial equation need be solved for each state considered. In the latter, the choice of core configurations was limited to the $1s^2 2s^2\ ^1S$ and $1s^2 2p^2\ ^1S$ complex. The resulting valence orbitals and energies were employed in calculations of electric dipole oscillator strengths in the boron sequence, obtaining what they consider to be very good results for all but a few exceptional cases [17].

Here we are also considering transitions which arise from the jump of one external electron to other levels located far out from a spectroscopically inert $1s^2 2s^2$ "core."

except for the configuration mixing and series perturbations that may take place in this "core." However, the transitions we are studying involve levels that seem to be free from such interactions and, therefore, we have treated the boron-like systems, for these purposes, with a central field model potential, within a one-particle scheme, in both QDO and RQDO procedures.

Method of Calculation

The quantum defect orbital (QDO) method [5–11] and its relativistic generalization (RQDO) [12] belong to simple and reliable methods of estimation of oscillator strengths. We shall only briefly mention their features which are relevant for the present calculations. The quantum defect orbitals are the analytical solutions of the one-particle (nonrelativistic) Schrödinger equation with a model Hamiltonian,

$$[-d^2/dr^2 + \lambda(\lambda + 1)/r^2 - 2Z_{net}/r]\Psi^{OD} = 2E^{OD}\Psi^{OD},\tag{1}$$

where atomic units are used throughout. Z_{net} is the nuclear charge acting on the valence or Rydberg electron at large r, and

$$\lambda = l - \delta + c,\tag{2}$$

where l is the angular momentum quantum number, δ is the quantum defect, and c is an integer chosen to ensure the normalizability of the quantum defect orbitals and their correct nodal structure. The eigenvalue, E^{OD}, depends only on the non-integral part of λ and, hence, it is independent of c. The quantum defect is obtained individually for each state from empirical energy data. This carries along the implicit inclusion in the model Hamiltonian of some effects not explicitly included such as core-valence polarization and relativistic effects. However, in the calculation of properties concerning highly stripped ions and heavy atoms, it is important to give explicit account of relativistic effects. The RQDO theory has recently been developed by Martin and Karwowski, and applied successfully to some heavy atomic systems [12]. In the RQDO method, the parameters appearing in eq. (1) are replaced by others, that is, λ by Λ, δ by δ', Z_{net} by Z'_{net} and E^{OD} by e, in the following manner:

$$\Lambda = \begin{cases} s - 1 - \delta' + c, & \text{if } j = l + \dfrac{1}{2} \\[2mm] -s - \delta' + c & \text{if } j = l - \dfrac{1}{2} \end{cases}\tag{3}$$

where

$$s = k(1 - \alpha^2 Z^2/k^2)^{1/2},\tag{4}$$

α being the fine structure constant, Z the atomic number, and k the quantum number, for which we adopt the original convention of Dirac [18]:

$$k = \begin{cases} j + \frac{1}{2} = l + 1, & \text{if } j = l + \frac{1}{2} \\[2ex] -j - \frac{1}{2} = -l, & \text{if } j = l - \frac{1}{2} \end{cases} \tag{5}$$

$$Z'_{net} = Z_{net}(1 + \alpha^2 E^x) \tag{6}$$

E^x being the experimental energy, and

$$\varepsilon = -(Z'^2_{net})/[2(\bar{n} - \delta')^2] = E^x(1 + \alpha^2 E^x/2)/(1 + \alpha^2 E^x)^2, \tag{7}$$

where $\bar{n}$ is the relativistic principal quantum number [19]. This reformulation of the QDO theory takes into account most of the relativistic effects and has, in our view, important advantages. On the one hand, the RQDO method does not add any complication to the QDO formal structure and, on the other, it creates a more solid background for interpreting properties of highly ionized, heavy atoms. In both procedures, the transition integrals can be written as closed-form analytical expressions, and their computation is quite straightforward and inexpensive.

Results and Discussion

Oscillator strengths for $1s^22s^2np\ ^2P-1s^22s^2n'd\ ^2D$ ($n = 2$–4, $n' = 3$–15) are displayed in Tables I–VI. For the lighter atomic systems, for which relativistic effects are not expected to be important, we have followed the QDO procedure and report multiplet oscillator strengths only. We did also perform RQDO calculations, but the f-values so obtained showed negligible differences from those computed with the QDO method for BI ($Z = 5$) to OIV ($Z = 8$). Individual tables are devoted to each of these ions, since a larger amount of energy data than for the heavier ions (SiX to KrXXXII) was available [2,20]. Dankwort and Trefftz [21], have carried out a multiconfigurational treatment of the BI sequence, and confirm that relativistic effects are unimportant for the calculation of oscillator strengths up to SiX ($Z = 14$). From this ion onward we report both QDO and RQDO f-values. However, we must be aware that relativistic corrections lose importance with increasing l, and for np–$n'd$ transitions, they cannot be expected to be very noticeable. In all calculations, the integer c of eqs. (2) and (3) was always taken equal to zero, and the dipole length formulation of the transition integral was always employed.

In Tables I–IV we show the QDO oscillator strengths, together with other theoretical results that we have found in the literature: the dipole length and dipole velocity f-values of the multiconfigurational frozen core (MCFC) calculation by Cohen and Nahon [17], the refined superposition of configuration (SOC) results by Weiss [22], and the frozen core (FC) oscillator strengths obtained by McEachran and Cohen [23]. Both MCFC and FC calculations consider the $2s^2$ subshell as part of the atomic core, as described in the Introduction. Cohen and Nahon [17] stress that for their MCFC $2p$–nd oscillator strengths, their results are in much better agreement with FC f-values [23] than for ns–$2p$ transitions. This strengthens our confidence in the adequacy of one-electron calculations for the transitions object

of the present work. Also included in some of the tables are the results of model potential length calculations by Ganas [24], and those of recent critical compilation by Martin et al. [25].

The QDO results (Tables I–IV) show a generally good agreement with the comparatively calculated *f*-values. Unfortunately, no experimental measurements seem to be available. As to the RQDO results (Tables V and VI), it can be noticed that they generally differ very little from the corresponding QDO fine-structure *f*-values (obtained by multiplying the calculated multiplet *f*-values by the appropriate angular factors) in the $2p\,^2P$–$3d\,^2D$ transitions, although the differences increase with the atomic number, as expected. The agreement with the comparative data is also very satisfactory. For the $3p\,^2P$–$3d\,^2D$ transitions, the RQDO and QDO oscillator strengths begin to differ at lower Z values than in the previous case, being that the agreement with the comparative data is appreciably better in the RQDO case.

Conclusions

It seems apparent that both QDO and RQDO procedures yield quite satisfactory oscillator strengths for various transitions in the diffuse spectral series of the boron isoelectronic sequence. The adequacy of a one-electron treatment for these atomic systems in excited states has also been proven. This may save computational time and costs, and may serve as an alternative to *ab initio* procedures which explicitly account for electron correlation in the valence, $2s^2\,2p$, shell.

Acknowledgments

Bibliography

[1] R. L. Kurucz, in *Transactions of the International Astronomical Union*, D. McNally, Ed. (Kluwer, Dordrecht, 1990), vol. 20, and references therein.

[2] A. K. Bhatia, U. Feldman, and J. F. Seely, Atom. Data Nucl. Data Tables 35, 319 (1986).

[3] F. J. De Heer, in *Atomic and Molecular Physics of Controlled Thermonuclear Fusion*, C. J. Joachain and D. E. Post, Eds. (Plenum, New York, 1983).

[4] I. P. Grant, B. J. McKenzie, P. H. Norrington, D. F. Mayers, and N. C. Pyper, Comput. Phys. Commun. 21, 207 (1980).

[5] A. Hibbert, in *Advances in Atomic and Molecular Physics*, D. R. Bates and B. Bederson, Eds. (Academic, New York, 1982), vol. 18, p. 309.

[6] R. Crossley, Phys. Scr. T8, 117 (1984).

[7] I. Martin and C. Barrientos, Can. J. Phys. 64, 867 (1987), and references therein.

[8] C. Lavin, I. Martin, and C. Barrientos, Stud. Phys. Theor. Chem. 62, 231 (1989).

[9] I. Martin, C. Barrientos, and I. Gutiez, Int. J. Quant. Chem. 37, 221 (1990); C. Barrientos and I. Martin, Phys. Rev. A42, 432 (1990); I. Martin, C. Lavin, and C. Barrientos, Can. J. Phys. 69, 1273 (1991).

[10] C. Lavin, C. Barrientos, and I. Martin, J. Quant. Spectrosc. Radiat. Transfer (to appear).

[11] G. Simons, J. Chem. Phys. 60, 645 (1974); I. Martin and G. Simons, J. Chem. Phys. 62, 4799 (1975); Mol. Phys. 32, 1017 (1976).

[12] I. Martin and J. Karwowski, J. Phys. B: Atom. Mol. Opt. Phys. **24**, 1539 (1991); I. Martin, J. Karwowski, C. Lavin, and G. H. F. Diercksen, Phys. Scr. **44**, 567 (1991).

[13] A. K. Dupree, in *Advances in Atomic and Molecular Physics*, D. R. Bates and B. Bederson, Eds. (Academic, New York, 1980), vol. 14, p. 341.

[14] E. Träbert, P. H. Heckmann, and H. V. Buttlar, Z. Phys. **A281**, 333 (1977).

[15] J. E. Vernazza and H. E. Mason, Astrophys. J. **226**, 720 (1978).

[16] Th. M. El-Sherbini, A. A. Farrag, H. M. Mansour, and A. A. Rahman, Ann. Phys. Leipzig **44**, 412 (1987).

[17] M. Cohen and J. Nahon, J. Phys. B: Atom. Mol. Phys. **13**, 4325 (1980).

[18] P. A. M. Dirac, *The Principles of Quantum Mechanics* (Clarendon, Oxford, UK, 1984).

[19] J. Karwowski and J. Kobus, Int. J. Quant. Chem. **30**, 809 (1986), and references therein.

[20] R. L. Kelly, J. Phys. Chem. Ref. Data **16**(suppl. 1), part 1 (1987).

[21] W. Dankwort and E. Trefftz, J. Phys. B: Atom. Mol. Phys. **10**, 2541 (1977).

[22] A. W. Weiss, Phys. Rev. **188**, 119 (1969).

[23] R. P. McEachran and M. Cohen, J. Quant. Spectrosc. Radiat. Transfer **11**, 1819 (1971).

[24] P. S. Ganas, J. Chem. Phys. **71**, 1981 (1979).

[25] G. A. Martin, J. R. Fuhr, and W. L. Wiese, J. Phys. Chem. Ref. Data **17**(suppl. 3) 67, 191, 295, 397 (1988); J. R. Fuhr, G. A. Martin, and W. L. Wiese, J. Phys. Chem. Ref. Data **17** (suppl 4), 257 (1988).

Fine-Structure Oscillator Strengths for Excited-State Transitions in Cu-Like Ions

I. MARTIN and C. LAVÍN

*Departamento de Química Física, Facultad de Ciencias,
Universidad de Valladolid, 47005 Valladolid, Spain*

C. BARRIENTOS

*Departamento de Química Física y Analítica, Facultad de Química,
Universidad de Oviedo, 33006 Oviedo, Spain*

Abstract

Transitions originating from excited states in copper-like ions have been studied. Fine-structure oscillator strengths obtained with both the quantum defect orbital (QDO) and its relativistic (RQDO) counterpart are reported for 4p ^{2}P – nd ^{2}D (n = 5, 6), 5p ^{2}P – nd ^{2}D (n = 5, 6), and np ^{2}P – 6s ^{2}S (n = 4, 5) absorption transitions. © 1992 John Wiley & Sons, Inc.

Introduction

Spectroscopy data on highly stripped ions are needed in fusion devices for plasma diagnosis, as well as for estimating the effect of impurity ions in high-temperature plasmas [1]. Moreover, the need for extended and improved data to match the observational development in contemporary stellar spectroscopy has been very recently remarked [2]. Reliable values of transition probabilities and oscillator strengths are needed to model stellar atmospheres, in particular to find chemical abundances and the energy transport through the star. Estimation of these and other important properties requires the knowledge of transition probabilities for a very large number of lines in many atoms, including the highly ionized ones, for which experimental data are either scarce or not available. Theoretical calculations are often the only source of information on many transitions. The multiconfiguration Dirac–Fock method [3] offers the most reliable results. However, this approach becomes very time-consuming if the number of transitions to be determined is very large. On the other hand, other, much simpler methods, are usually much less accurate. Therefore, developing procedures which combine reliability with simplicity is quite important, not only from the practical point of view, but also because of the physical implications involved [4].

In previous calculations of atomic transition probabilities and related properties, such as oscillator strengths and photoionization cross sections, we have followed two simple but rather reliable semiempirical procedures. These are the quantum

defect orbital (QDO) formalism [5-7] and the recently proposed quasirelativistic formulation (RQDO) of this method [8-11].

In this article, we report oscillator strengths for transitions arising from excited states in moderately to highly stripped copper-like ions, computed through both QDO and RQDO procedures. Results for fine structure transitions in the principal, 4s ^{2}S → 4p ^{2}P, and diffuse, 4p ^{2}P → 4d ^{2}D, spectral series, covering a large number of copper-like atomic systems (from $Z = 29$ to $Z = 92$) have been reported elsewhere [12]. For the principal and diffuse spectral series, oscillator strengths of high accuracy have been obtained, and the considerable improvement brought about by the explicit introduction of relativistic effects through the RQDO procedure has been made apparent for the moderately heavy to heavy ions. Also, correct systematic trends of the individual fine-structure f-values along the copper isoelectronic sequence, which may not be adequately described at the low $1/Z$ end if relativistic effects are not well accounted for, have been found when the RQDO f-values have been plotted vs. $1/Z$ [12].

One of the goals of the present calculations is to test the ability of the QDO and RQDO procedures in yielding oscillator strengths for transitions that involve higher-lying states. The latter have some specific usefulness within the context of the more general one remarked above. Recombination phenomena often proceed through high-lying states, making their transition probabilities important for plasma physical problems. A knowledge of higher-lying transition probabilities is also very valuable in the experimental measurement of lower level lifetimes, since usually severe cascade effects seem to occur in copper-like ions, at least in the cases examined by Younger and Wiese [13]. Common methods for establishing the cascade contributions require an extensive set of theoretical estimates of lifetimes and branching ratios [13,14].

In a very comprehensive study of the copper isoelectronic sequence through a numerical Coulomb Approximation (NCA) procedure, Lindgård et al. [15] quote Wiese and Weiss [16], and remark on the possibility of tracing isoelectronic and homologous trends in oscillator strengths using additional theoretical estimates for only a few selected ions, and, hence, saving further computations. However, they also warn about the danger of very sharp cancellation effects being likely to occur in the transition integrals of alkali-like ions, which causes the f-value for a given transition in one particular ion to be anomalously small. As a consequence, Lindgård et al. [15] consider it sensible to make independent calculations for individual ions. Given the very time-consuming task that performing many calculations with sophisticated *ab initio* methods brings about, they find a solid justification for the use of semiempirical procedures.

Lindgård et al. [15], as well as other authors who have studied these atomic systems [17-20], remark that for ions of reasonably high ionization stage, the CuI sequence is a pure alkali-like system with a single electron outside a closed 3d shell, giving rise to a simple Rydberg-type spectrum. However, for low charge states there are problems which require some caution. For instance, there exist core-excited configurations of $3d^9 4snl$ type that fall below the first ionization continuum $3d^{10}$ ^{1}S. These can mix with the Rydberg series giving rise not only to a shift in the

position of the 4s and 4p levels, but also to altering their spectroscopic character
[17]. In the neutral copper and first few ions of its sequence, rather large pertur-
bations of the ^2P Rydberg series arising from mixing with the $3d^9 4s4p$ ^2P config-
uration have been reported [15,19]. Froese–Fisher [18] found great improvement
in her calculated f-values for the resonance transition by the inclusion of the $3d^9$
$4d4s$ and $3d^9 3d4p$ configurations in the ground and first excited states, respectively.
Lindgård et al. [15] point out that the higher members of the ^2P spectral series are
not well described within the LS coupling scheme, and, hence, a single electron
picture may yield only crude estimates for the lower members of the CuI sequence.
Another problem that must be dealt with is, according to several authors
[15,17,18,20], the core-valence polarization effects, which are mainly found to
occur in the low $p_{1/2}$ and $p_{3/2}$ states, rather than in the $s_{1/2}$, $d_{3/2}$ or $d_{5/2}$ states [20].
Curtis and Theodosiou, in their accurate and extensive semi-empirical study of 4s
and 4p lifetimes and fine-structure f-values involving 4s–4p and 4p–4d transitions
for a very large number of ions in the CuI sequence ($Z = 29-92$) [17], made a
remark that we find important: core-polarization and other types of electron cor-
relation, spin-orbit coupling, and other relativistic interactions, can vary with the
degree of ionicity along the sequence. Hence, the applicability of various *ab initio*
approaches changes over the sequence. This strengthens our confidence in the con-
venience of applying reliable semiempirical approaches, such as the QDO and RQDO
methods. In particular, the latter has the advantage of being able to deal in a uniform
way with the entire isoelectronic sequence. The correct performance of the RQDO
procedure has already been proven at low and high Z-values in other isoelectronic
sequence [10]. On the other hand, the semiempirical parameters of both QDO and
RQDO methods account implicitly for core-valence polarization effects.

Computational Procedure

The QDO method has been described in detail in previous articles (see, e.g., Refs.
[5] and [6]). So has been its relativistic counterpart, the RQDO procedure [8–10].
We shall just summarize here the main features of the latter.

The relativistic quantum defect orbitals corresponding to the state characterized
by the experimental energy E are the analytical solutions to the quasirelativistic
second-order Dirac-like equation:

$$[-d^2/dr^2 + \Lambda(\Lambda + 1)/r^2 - 2Z'_{net}/r]\psi(r) = 2\epsilon\psi(r) \tag{1}$$

$$\text{where} \quad Z'_{net} = Z_{net}(1 + \alpha^2 E), \tag{2}$$

$$\epsilon = -(Z'_{net})^2/2(\tilde{n} - \delta')^2 = E(1 + \alpha^2 E/2)/(1 + \alpha^2 E)^2, \tag{3}$$

$$\Lambda = \tilde{n} - n + l - \delta + c; \tag{4}$$

α is the fine structure constant, Z_{net} is the nuclear charge acting on the valence
electron at large r, n and l are the principal and orbital angular momentum quantum
numbers, $\tilde{n}$ is the relativistic principal quantum number, δ is the quantum defect,
and c is an integer that is chosen to ensure the normalizability of the wavefunction

and its correct nodal structure. The quantum defect, δ, is obtained empirically from Eq. (3). Then Eq. (1) is solved analytically and the solutions used to calculate transition probabilities and oscillator strengths (as well as other properties, if required). The nonrelativistic QDO equation is obtained by setting $\alpha = 0$. Then E^v becomes the experimental term energy (averaged over the fine structure components).

We have carried out calculations for transitions for which recent empirical energy data were available [22–31]. Given the likely presence of configuration mixing, in particular for the lower ionization stages in the CuI sequence, as indicated in the previous section, we cannot establish whether in the atomic data used here the level classification is entirely correct. Hence, we have not attempted to perform extrapolations or interpolations for those levels for which energy data was unavailable, as other authors did [15].

Results and Discussion

In Tables I to IV we display the results of the present calculations, for some representative ions of the CuI sequence, together with some comparative data. Although the need for transition probability data concerning ions of this sequence has been accentuated by their determination of impurity concentrations in high temperature plasmas, the comparative data for the transitions studied here is rather scarce. No experimental measurements seem to be available, and only theoretical data from two sources have been found in the literature. These are, respectively, the NCA [17] and RHF [21] calculations, of which some details are given in the Introduction. None of these include explicitly core-valence polarization effects, although, by using empirical energy data in their method, Lindgård et al. [17] give some implicit account of these effects, as both our QDO and RQDO procedures do. Cheng and Kim [21] report to have found already for ions in moderate ionization stages, not to mention the very highly stripped ions, that the explicit inclusion core-valence correlation (for instance, through a polarization-corrected transition operator), has very little effect in the calculated oscillator strengths.

For the $4p\ ^2P \rightarrow nd\ ^2D$ ($n = 5, 6$) transitions, Table I, the comparative results were not expected, a priori, to show a good coincidence with our computed f-values, given the different input energy data employed in the reported procedures. This was especially so in these transitions, which involve the perturbed $4p\ ^2P$ state, regarding which we make some comments in the Introduction. However, the agreement between the RQDO and RHF f-values is fairly good for the $3/2-3/2$ and $3/2-5/2$ fine structure transitions, in particular for $n = 5$, and, overall, it is much better than the agreement of the QDO f-values with the RHF results. These features increase with Z, quite probably due to the relativistic effects becoming stronger. A much better general agreement is found among all sets of comparative data displayed in Table II for the $5p\ ^2P \rightarrow 5d\ ^2D$ fine structure transitions. We should bear in mind that the $5p\ ^2P$ state seems to be free from the configuration mixing from which the $4p\ ^2P$ state is reported to suffer. A good feature regarding the RQDO f-values is that, as Z increases along the sequence, all the three fine-structure oscillator strengths

TABLE I. Oscillator strengths for 4p ^{2}P→nd ^{2}D (n = 5, 6) fine structure transitions in copper-like ions.[a]

Z	Ion	Transition	QDO	RQDO	RHF
56	BaXXVIII	$4p_{1/2}-5d_{3/2}$	0.1136	0.8751 (-1)	
		$4p_{3/2}-5d_{3/2}$	0.1136 (-1)	0.1348 (-1)	
		$4p_{3/2}-5d_{5/2}$	0.1022	0.1112	
57	LaXXIX	$4p_{1/2}-5d_{3/2}$	0.1194	0.9133 (-1)	
		$4p_{3/2}-5d_{3/2}$	0.1194 (-1)	0.1419 (-1)	
		$4p_{3/2}-5d_{5/2}$	0.1075	0.1171	
60	NdXXXII	$4p_{1/2}-5d_{3/2}$	0.1412	0.1071	
		$4p_{3/2}-5d_{3/2}$	0.1412 (-1)	0.1688 (-1)	
		$4p_{3/2}-5d_{5/2}$	0.1271	0.1384	
62	SmXXXIV	$4p_{1/2}-5d_{3/2}$	0.1530	0.1152	0.1386
		$4p_{3/2}-5d_{3/2}$	0.1530 (-1)	0.1845 (-1)	0.2207 (-1)
		$4p_{3/2}-5d_{5/2}$	0.1377	0.1498	0.1785
64	GdXXXVI	$4p_{1/2}-5d_{3/2}$	0.1586	0.1148	
		$4p_{3/2}-5d_{3/2}$	0.1586 (-1)	0.1899 (-1)	
		$4p_{3/2}-5d_{5/2}$	0.1427	0.1577	
66	DyXXXVIII	$4p_{1/2}-5d_{3/2}$	0.1646	0.1182	0.1470
		$4p_{3/2}-5d_{3/2}$	0.1646 (-1)	0.2005 (-1)	0.2460 (-1)
		$4p_{3/2}-5d_{5/2}$	0.1481	0.1634	0.1969
70	YbXLII	$4p_{1/2}-5d_{3/2}$	0.1778	0.1232	0.1512
		$4p_{3/2}-5d_{3/2}$	0.1778 (-1)	0.2211 (-1)	0.2684 (-1)
		$4p_{3/2}-5d_{5/2}$	0.1600	0.1776	0.2123
73	TaXLV	$4p_{1/2}-5d_{3/2}$	0.1890	0.1269	
		$4p_{3/2}-5d_{3/2}$	0.1890 (-1)	0.2377 (-1)	
		$4p_{3/2}-5d_{5/2}$	0.1701	0.1901	
44	RuXVI	$4p_{1/2}-6d_{3/2}$	0.1389 (-1)	0.1127 (-1)	0.2350 (-1)
		$4p_{3/2}-6d_{3/2}$	0.1389 (-2)	0.1611 (-2)	0.3061 (-2)
		$4p_{3/2}-6d_{5/2}$	0.1250 (-1)	0.1343 (-1)	0.2594 (-1)
45	RhXVII	$4p_{1/2}-6d_{3/2}$	0.1706 (-1)	0.1378 (-1)	
		$4p_{3/2}-6d_{3/2}$	0.1706 (-2)	0.1935 (-2)	
		$4p_{3/2}-6d_{5/2}$	0.1535 (-1)	0.1657 (-1)	
47	AgXIX	$4p_{1/2}-6d_{3/2}$	0.2383 (-1)	0.1972 (-1)	
		$4p_{3/2}-6d_{3/2}$	0.2383 (-2)	0.2690 (-2)	
		$4p_{3/2}-6d_{5/2}$	0.2145 (-1)	0.2286 (-1)	
70	YbXLII	$4p_{1/2}-6d_{3/2}$	0.6203 (-1)	0.4386 (-1)	0.6010 (-1)
		$4p_{3/2}-6d_{3/2}$	0.6203 (-2)	0.6849 (-2)	0.8931 (-2)
		$4p_{3/2}-6d_{5/2}$	0.5583 (-1)	0.6164 (-1)	0.7375 (-1)

[a] In this and the remaining tables, $A(-B)$ denotes $A \cdot 10^{(-B)}$. QDO, RQDO, this work.
RHF, relativistic Hartree–Fock [21].

TABLE II. Oscillator strengths for $5p\ ^2P \to nd\ ^2D$ ($n = 5, 6$) fine structure transitions in copper-like ions.[a]

Z	Ion	Transition	QDO	RQDO	RHF	NCA
36	KrVIII	$5p_{1/2}-5d_{3/2}$	1.396	1.402	1.401	1.373
		$5p_{3/2}-5d_{3/2}$	0.1396	0.1388	0.1383	0.1353
		$5p_{1/2}-5d_{5/2}$	1.256	1.253	1.249	1.222
38	SrX	$5p_{1/2}-5d_{3/2}$	1.352	1.366	1.343	1.322
		$5p_{3/2}-5d_{3/2}$	0.1352	0.1335	0.1311	0.1290
		$5p_{3/2}-5d_{5/2}$	1.217	1.209	1.187	1.168
39	YXI	$5p_{1/2}-5d_{3/2}$	1.321	1.339	1.310	1.287
		$5p_{3/2}-5d_{3/2}$	0.1321	0.1301	0.1271	0.1249
		$5p_{3/2}-5d_{5/2}$	1.189	1.180	1.153	1.133
40	ZrXII	$5p_{1/2}-5d_{3/2}$	1.286	1.308	1.276	1.251
		$5p_{3/2}-5d_{3/2}$	0.1286	0.1263	0.1231	0.1205
		$5p_{3/2}-5d_{5/2}$	1.157	1.147	1.118	1.095
41	NbXIII	$5p_{1/2}-5d_{3/2}$	1.250	1.276	1.244	1.225
		$5p_{3/2}-5d_{3/2}$	0.1250	0.1223	0.1191	0.1172
		$5p_{3/2}-5d_{5/2}$	1.125	1.113	1.084	1.067
42	MoXIV	$5p_{1/2}-5d_{3/2}$	1.217	1.246	1.212	1.198
		$5p_{3/2}-5d_{3/2}$	0.1217	0.1187	0.1153	0.1139
		$5p_{3/2}-5d_{5/2}$	1.095	1.082	1.051	1.039
44	RuXVI	$5p_{1/2}-5d_{3/2}$	1.152	1.188	1.152	1.134
		$5p_{3/2}-5d_{3/2}$	0.1152	0.1114	0.1080	0.1060
		$5p_{3/2}-5d_{5/2}$	1.037	1.020	0.9889	0.9721
45	RhXVII	$5p_{1/2}-5d_{3/2}$	1.121	1.161		1.107
		$5p_{3/2}-5d_{3/2}$	0.1121	0.1080		0.1026
		$5p_{3/2}-5d_{5/2}$	1.009	0.9901		0.9429
46	PdXVIII	$5p_{1/2}-5d_{3/2}$	1.090	1.133	1.099	1.085
		$5p_{3/2}-5d_{3/2}$	0.1090	0.1046	0.1014	0.9991 (−1)
		$5p_{3/2}-5d_{5/2}$	0.981	0.9612	0.9322	0.9203
47	AgXIX	$5p_{1/2}-5d_{3/2}$	1.063	1.109		1.055
		$5p_{3/2}-5d_{3/2}$	0.1063	0.1014		0.9624 (−1)
		$5p_{3/2}-5d_{5/2}$	0.9567	0.9346		0.8958
48	CdXX	$5p_{1/2}-5d_{3/2}$	1.036	1.085	1.052	1.034
		$5p_{3/2}-5d_{3/2}$	0.1036	0.9838 (−1)	0.9536 (−1)	0.9349 (−1)
		$5p_{3/2}-5d_{5/2}$	0.9324	0.9086	0.8813	0.8624
49	InXXI	$5p_{1/2}-5d_{3/2}$	1.010	1.064		1.016
		$5p_{3/2}-5d_{3/2}$	0.1010	0.9549 (−1)		0.09118
		$5p_{3/2}-5d_{5/2}$	0.909	0.8844		0.8513
50	SnXXII	$5p_{1/2}-5d_{3/2}$	0.9865	1.044	1.012	
		$5p_{3/2}-5d_{3/2}$	0.9865 (−1)	0.9276 (−1)	0.8993 (−1)	
		$5p_{3/2}-5d_{5/2}$	0.8879	0.8610	0.8357	

TABLE II. (Continued)

Z	Ion	Transition	QDO	RQDO	RHF	NCA
56	BaXXVIII	$5p_{1/2}-5d_{3/2}$	0.8714	0.9487		
		$5p_{3/2}-5d_{3/2}$	0.8714 (−1)	0.7885 (−1)		
		$5p_{3/2}-5d_{5/2}$	0.7843	0.7483		
57	LaXXIX	$5p_{1/2}-5d_{3/2}$	0.8542	0.9363		
		$5p_{3/2}-5d_{3/2}$	0.8542 (−1)	0.7675 (−1)		
		$5p_{3/2}-5d_{5/2}$	0.7688	0.7304		
60	NdXXXII	$5p_{1/2}-5d_{3/2}$	0.8136	0.9056		
		$5p_{3/2}-5d_{3/2}$	0.8136 (−1)	0.7139 (−1)		
		$5p_{3/2}-5d_{5/2}$	0.7322	0.6895		
62	SmXXXIV	$5p_{1/2}-5d_{3/2}$	0.7888	0.8840	0.8683	
		$5p_{3/2}-5d_{3/2}$	0.7888 (−1)	0.6797 (−1)	0.6649 (−1)	
		$5p_{3/2}-5d_{5/2}$	0.7099	0.6659	0.6465	
64	GdXXXVI	$5p_{1/2}-5d_{3/2}$	0.7689	0.8843		
		$5p_{3/2}-5d_{3/2}$	0.7689 (−1)	0.6591 (−1)		
		$5p_{3/2}-5d_{5/2}$	0.6920	0.6369		
66	DyXXXVIII	$5p_{1/2}-5d_{3/2}$	0.7533	0.8756	0.8491	
		$5p_{3/2}-5d_{3/2}$	0.7533 (−1)	0.6277 (−1)	0.6109 (−1)	
		$5p_{3/2}-5d_{5/2}$	0.6780	0.6202	0.6063	
70	YbXLII	$5p_{1/2}-5d_{3/2}$	0.7277	0.8652	0.8406	
		$5p_{3/2}-5d_{3/2}$	0.7277 (−1)	0.581 (−1)	0.5649 (−1)	
		$5p_{3/2}-5d_{5/2}$	0.6549	0.5900	0.5737	
73	TaXLV	$5p_{1/2}-5d_{3/2}$	0.7107	0.8643		
		$5p_{3/2}-5d_{3/2}$	0.7107 (−1)	0.5481 (−1)		
		$5p_{3/2}-5d_{5/2}$	0.6396	0.5657		
45	RhXVII	$5p_{1/2}-6d_{3/2}$	0.2336 (−1)	0.1599 (−1)		
		$5p_{3/2}-6d_{3/2}$	0.2336 (−2)	0.2969 (−2)		
		$5p_{3/2}-6d_{5/2}$	0.2102 (−1)	0.2430 (−1)		
46	PdXVIII	$5p_{1/2}-6d_{3/2}$	0.3226 (−1)	0.2366 (−1)	0.3602 (−1)	
		$5p_{3/2}-6d_{3/2}$	0.3226 (−2)	0.4107 (−2)	0.5856 (−2)	
		$5p_{3/2}-6d_{5/2}$	0.2903 (−1)	0.3255 (−1)	0.4734 (−1)	
47	AgXIX	$5p_{1/2}-6d_{3/2}$	0.3963 (−1)	0.2910 (−1)		
		$5p_{3/2}-6d_{3/2}$	0.3963 (−2)	0.4922 (−2)		
		$5p_{3/2}-6d_{5/2}$	0.3567 (−1)	0.4005 (−1)		
70	YbXLII	$5p_{1/2}-6d_{3/2}$	0.1497	0.8612 (−1)	0.1254	
		$5p_{3/2}-6d_{3/2}$	0.1497 (−1)	0.1826 (−1)	0.2480 (−1)	
		$5p_{3/2}-6d_{5/2}$	0.1347	0.1643	0.1920	

[a] See the footnotes to Table I; NCA, numerical Coulomb Approximation [15].

TABLE III. Oscillator strengths for 4p ²P → 6s ²S fine structure transitions in copper-like ions.ᵃ

Z	Ion	Transition	QDO	RQDO	RHF	NCA
33	AsV	$4p_{1/2}$–$6s_{1/2}$	0.1848(-1)	0.1843(-1)	0.2076(-1)	0.1759(-1)
		$4p_{3/2}$–$6s_{1/2}$		0.1849(-1)	0.2156(-1)	0.1839(-1)
34	SeVI	$4p_{1/2}$–$6s_{1/2}$	0.1846(-1)	0.1837(-1)	0.2086(-1)	0.1794(-1)
		$4p_{3/2}$–$6s_{1/2}$		0.1848(-1)	0.2182(-1)	0.1885(-1)
37	RbIX	$4p_{1/2}$–$6s_{1/2}$	0.1830(-1)	0.1813(-1)	0.2065(-1)	0.1814(-1)
		$4p_{3/2}$–$6s_{1/2}$		0.1836(-1)	0.2205(-1)	0.1941(-1)
38	SrX	$4p_{1/2}$–$6s_{1/2}$	0.1822(-1)	0.1803(-1)	0.2051(-1)	0.1812(-1)
		$4p_{3/2}$–$6s_{1/2}$		0.1829(-1)	0.2205(-1)	0.1953(-1)
39	YXI	$4p_{1/2}$–$6s_{1/2}$	0.1814(-1)	0.1792(-1)	0.2035(-1)	0.1807(-1)
		$4p_{3/2}$–$6s_{1/2}$		0.1822(-1)	0.2203(-1)	0.1965(-1)
40	ZrXII	$4p_{1/2}$–$6s_{1/2}$	0.1809(-1)	0.1784(-1)	0.2019(-1)	0.1806(-1)
		$4p_{3/2}$–$6s_{1/2}$		0.1817(-1)	0.2201(-1)	0.1976(-1)
41	NbXIII	$4p_{1/2}$–$6s_{1/2}$	0.1805(-1)	0.1778(-1)	0.2002(-1)	0.1776(-1)
		$4p_{3/2}$–$6s_{1/2}$		0.1814(-1)	0.2198(-1)	0.1960(-1)
42	MoXIV	$4p_{1/2}$–$6s_{1/2}$	0.1797(-1)	0.1767(-1)	0.1985(-1)	0.1768(-1)
		$4p_{3/2}$–$6s_{1/2}$		0.1807(-1)	0.2196(-1)	0.1966(-1)
44	RuXVI	$4p_{1/2}$–$6s_{1/2}$	0.1785(-1)	0.1748(-1)	0.1952(-1)	
		$4p_{3/2}$–$6s_{1/2}$		0.1796(-1)	0.2192(-1)	
46	PdXVIII	$4p_{1/2}$–$6s_{1/2}$	0.1779(-1)	0.1737(-1)	0.1920(-1)	
		$4p_{3/2}$–$6s_{1/2}$		0.1791(-1)	0.2190(-1)	
47	AgXIX	$4p_{1/2}$–$6s_{1/2}$	0.1773(-1)	0.1727(-1)		
		$4p_{3/2}$–$6s_{1/2}$		0.1785(-1)		
49	InXXI	$4p_{1/2}$–$6s_{1/2}$	0.1766(-1)	0.1715(-1)		
		$4p_{3/2}$–$6s_{1/2}$		0.1780(-1)		

ᵃ See footnotes to Table II.

become more similar to those of the relativistic Hartree–Fock calculation, and depart progressively from those that not give explicit account of relativistic effects. The 4p ²P → 5s ²S QDO results (which are not to show fine-structure splitting in the LS coupling scheme for p–s transitions), as well as the RQDO ƒ-values, are in general good agreement with both RHF and NCA results. Similar comments can be made as to the 5p ²P → 6s ²S transitions, shown in Table IV. It is a common feature in many atomic systems that relativistic effects have little importance in calculated np → n's transition probabilities and oscillator strengths.

Given the lack of data for many ions in some of the transitions studied, we do not give here graphs of the fine structure ƒ-values for individual ions versus $1/Z$, which is a way to search for regularities along the isoelectronic sequence. However, by inspection of the tables, it can be noticed that all the fine-structure ƒ-values

TABLE IV. Oscillator strengths for $5p\ ^2P \rightarrow 6s\ ^2S$ fine structure transitions in copper-like ions.[a]

Z	Ion	Transition	QDO	RQDO	RHF	NCA
33	AsV	$5p_{1/2}-6s_{1/2}$	0.2459	0.2407	0.2288	0.2129
		$5p_{3/2}-6s_{1/2}$		0.2484	0.2409	0.2246
34	SeVI	$5p_{1/2}-6s_{1/2}$	0.2357	0.2298	0.2185	0.2093
		$5p_{3/2}-6s_{1/2}$		0.2385	0.2318	0.2220
37	RbIX	$5p_{1/2}-6s_{1/2}$	0.2164	0.2091	0.1956	0.1806
		$5p_{3/2}-6s_{1/2}$		0.2199	0.2123	0.1962
38	SrX	$5p_{1/2}-6s_{1/2}$	0.2114	0.2036	0.1897	0.1772
		$5p_{3/2}-6s_{1/2}$		0.2151	0.2075	0.1939
39	YXI	$5p_{1/2}-6s_{1/2}$	0.2068	0.1985	0.1844	0.1801
		$5p_{3/2}-6s_{1/2}$		0.2107	0.2023	0.1983
40	ZrXII	$5p_{1/2}-6s_{1/2}$	0.2036	0.1947	0.1796	0.1733
		$5p_{3/2}-6s_{1/2}$		0.2077	0.1995	0.1923
41	NbXIII	$5p_{1/2}-6s_{1/2}$	0.2007	0.1914	0.1752	0.1707
		$5p_{3/2}-6s_{1/2}$		0.2051	0.1962	0.1911
42	MoXIV	$5p_{1/2}-6s_{1/2}$	0.1878	0.1875	0.1711	0.1670
		$5p_{3/2}-6s_{1/2}$		0.2019	0.1933	0.1885
44	RuXVI	$5p_{1/2}-6s_{1/2}$	0.1923	0.1813	0.1640	
		$5p_{3/2}-6s_{1/2}$		0.1973	0.1885	
46	PdXVIII	$5p_{1/2}-6s_{1/2}$	0.1889	0.1768	0.1579	
		$5p_{3/2}-6s_{1/2}$		0.1944	0.1847	
47	AgXIX	$5p_{1/2}-6s_{1/2}$	0.1864	0.1738		
		$5p_{3/2}-6s_{1/2}$		0.1922		
49	InXXI	$5p_{1/2}-6s_{1/2}$	0.1833	0.1694		
		$5p_{3/2}-6s_{1/2}$		0.1895		

[a] See footnotes to Table II.

obtained with the RQDO and the RHF approaches present the same systematic trends in all of the reported transitions. This may be considered as a hint for the correctness of our results.

Concluding Remarks

As in previous studies with the QDO and RQDO procedures, the adequacy of these methods to yield good estimates of oscillator strengths seems to have become apparent for the transitions reported here. Additionally, it also seems apparent, as has been recently shown [8-10] that, when dealing with moderately heavy to heavy atomic systems, the RQDO approach is undoubtedly to be chosen. It possesses the great advantage of retaining the simplicity and lack of expensiveness of the RQDO

formalism, while at the same time it gives good account of most of the relativistic effects.

Acknowledgments

Bibliography

[1] J. M. Peacok, Phys. Scr. T8, 10 (1984).
[2] B. Gustafsson, Phys. Scr. T34, 14 (1991).
[3] I. P. Grant, B. J. McKenzie, P. H. Norrington, D. F. Mayers, and N. C. Pyper, Comput. Phys. Commun. 21, 207 (1980).
[4] H. Xinghong, L. Baiwen, C. Aiqiu, and Z. Chengxiu, J. Phys. B23, 661 (1990).
[6] I. Martin, C. Barrientos, and I. Gútiez, Int. J. Quantum Chem. 37, 221 (1990), and references therein.
[7] C. Lavín, C. Barrientos, and I. Martin, J. Quant. Spectrosc. Radiat. Transfer 47, 411 (1992).
[8] I. Martin and J. Karwowski, J. Phys. B24, 1539 (1991).
[9] J. Karwowski and I. Martin, Phys. Rev. A43, 4832 (1991).
[10] I. Martin, J. Karwowski, C. Lavin, and G. H. F. Diercksen, Phys. Scr. 44, 567 (1991).
[11] C. Lavín, I. Martin, and J. Karwowski, THEOCHEM: J. Mol. Struct. 254, 161 (1992).
[12] C. Lavín, C. Barrientos, and I. Martin, submitted for publication.
[13] S. M. Younger and W. L. Wiese, Phys. Rev. A17, 1944 (1978).
[14] L. J. Curtis and D. G. Ellis, J. Phys. B11, 1543 (1978).
[15] A. Lindgärd, L. J. Curtis, I. Martinson, and S. E. Nielsen, Phys. Scr. 21, 47 (1980).
[16] W. L. Wiese and A. W. Weiss, Phys. Rev. 175, 50 (1968).
[17] L. J. Curtis and C. E. Theodosiou, Phys. Rev. A39, 605 (1989).
[18] C. Froese Fischer, J. Phys. B10, 1241 (1977).
[19] P. Hannaford and D. C. McDonnald, J. Phys. B11, 1177 (1978).
[20] J. Migdalek and W. E. Baylis, J. Phys. B11, L497 (1978).
[21] K.-T. Cheng and Y.-K. Kim, At. Data Nuclear Data Tables 22, 547 (1978).
[22] E. H. Pinnington, J. L. Bahr, J. A. Kernahan, and D. J. G. Irwin, J. Phys. B14, 1291 (1981).
[23] Y. N. Joshi and Th. A. M. van Kleef, Physica 94C, 270 (1978).
[24] A. E. Livingston, L. J. Curtis, R. M. Schectman, and H. G. Berry, Phys. Rev. A21, 771 (1980).
[25] S. Goldsmith, J. Reader, and N. Acquista, J. Opt. Soc. Am. B1, 631 (1984).
[26] N. Acquista and J. Reader, J. Opt. Soc. Am. 71, 569 (1981).
[27] J. Reader and N. Acquista, J. Opt. Soc. Am. 69, 1285 (1979); 69, 1659 (1979); 70, 317 (1980).
[28] J. Reader, G. Luther, and N. Acquista, J. Opt. Soc. Am. 69, 144 (1979).
[29] J. Reader, N. Acquista, and D. Cooper, J. Opt. Soc. Am. 73, 1765 (1983).
[30] J. Reader and G. Luther, Phys. Scr. 24, 732 (1981).
[31] D. R. Kania, B. J. MacGowan, C. M. Brown, J. O. Ekberg, J. F. Seely, U. Feldman, and J. Reader, J. Opt. Soc. Am. B7, 1993 (1990).

On the Calculation of Oscillator Strength
for Electronic Transitions using
"Effective Core" Methods

JENWEI YU, JOHN DAVID BAKER, and MICHAEL C. ZERNER

Quantum Theory Project, Department of Chemistry, University of Florida, Gainesville, Florida 32611

Abstract

We examine the effect on calculated oscillator strengths for electronic transitions caused by reintroducing the nodes of valence orbitals in effective core methods through a simple Schmidt orthogonalization. This refinement is then tested within the Intermediate Neglect of Differential Overlap (INDO) model, a valence orbital only model, in both configuration interaction and Random-Phase Approximation (RPA) calculations. It is shown that the differences in oscillator strengths calculated using the dipole-length and dipole-velocity formulations are reduced somewhat for $\pi \rightarrow \pi^*$ transitions and significantly for $n \rightarrow \pi^*$ transitions. The oscillator strengths calculated from the dipole-length formalism by the RPA model are in best accord with experiment. © 1992 John Wiley & Sons, Inc.

Introduction

This article examines the calculation of oscillator strengths in methods that do not explicitly contain core orbitals. Semi-empirical methods, and those effective-core potential methods that do not consider the inner-shell outer-shell nodal structure are thus germane. A simple orthogonalization scheme is introduced that is shown to have minor effect on oscillator strength calculated using the dipole-length formulation, and, perhaps not surprisingly, major effect on the velocity formulation.

Spectroscopy is a plot of frequency (or wavelength) versus intensity. Most theoretical calculations estimate only frequency. But the estimate of intensity is equally important in assigning spectra, and can even be used to correct errors in calculated frequency in making assignments among close lying transitions.

Recently, the Random Phase Approximation (RPA) with the Intermediate Neglect of Differential Overlap for Spectroscopy (INDO/S) Hamiltonian has been used to calculate the electronic spectra of benzene, pyridine, diazines, large aromatic systems composed of fused benzenes [1], and free base porphin [2]. These studies show that the RPA formalism performs as well as does the singles only configuration-interaction (CIS) procedure for obtaining singlet excitation energies, but it gives a better estimate of oscillator strengths and better agreement between the values calculated from the dipole-length and the dipole-velocity formulas.

$$f_k = \frac{2}{3} E_k \left| \left\langle \psi_{HF} \left| \sum_{i=1}^{n} \vec{r}_i \right| \psi_k \right\rangle \right|^2 \tag{1}$$

$$f_k = \frac{2}{3} E_k^{-1} \left| \left\langle \psi_{HF} \left| \sum_{i=1}^{n} \vec{\nabla}_i \right| \psi_k \right\rangle \right|^2 \tag{2}$$

where f_k are oscillator strengths for the kth excitation, $\vec{r}$ and $\vec{\nabla}$ are dipole-length and velocity operators, E_k and ψ_k are the kth excitation energy and wavefunction, ψ_{HF} is the Hartree–Fock ground-state wavefunction, and the sum is over all n electrons. The improvement of agreement is quite noticeable for $\pi \rightarrow \pi^*$ transitions but not for $n \rightarrow \pi^*$ transitions. Although the RPA formalism yields the equivalence between the dipole length and velocity results in a complete Hartree–Fock basis [3,4], truncation of the basis does not ensure this. One might therefore be content with results such as those reported in Refs. [1–2,5]. One can still ask the question, however, why the RPA model does not improve the equivalence of calculated intensities of $n \rightarrow \pi^*$ transitions to the same degree as it does to $\pi \rightarrow \pi^*$ transitions.

From the forms of the above two equations, one can see that the length operator places emphasis on the long-range region of wavefunctions, whereas the velocity operator, because of taking derivatives over coordinates, places emphasis on the short-range region of wavefunctions where they change more dramatically with respect to coordinates. Thus one can expect that the valence-shell basis set used in the INDO/S method and most other effective core potential methods will not give a proper description of oscillator strength by using the velocity formula due to the nonorthogonality of valence-shell atomic orbitals to the neglected core atomic orbitals. From simple MO pictures, $\pi \rightarrow \pi^*$ transitions involve only $2p$ orbitals but $n \rightarrow \pi^*$ transitions involve $2s$ orbitals due to hybridization. The velocity formula may thus not give proper oscillator strength since the $2s$ valence orbitals, which have no nodal structure, are not orthogonal to $1s$ orbitals. One scheme [6] to orthogonalize the valence orbitals to the core is by Schmidt orthogonalization.

$$\chi'_{nl} = N'_{nl} \left\{ \chi_{nl} - \sum_{i=1}^{n-l-1} \langle \chi_{nl} | \chi'_{(n-i)l} \rangle \chi'_{(n-i)l} \right\} \tag{3}$$

$$N'_{nl} = \left(1 - \sum_{i=1}^{n-l-1} \langle \chi_{nl} | \chi'_{(n-i)l} \rangle^2 \right)^{-1/2} \tag{4}$$

where n and l are principle and angular quantum numbers. Note the recursive nature of these two equations. According to this, the orthogonalized $2s$ basis orbital becomes

$$\chi'_{2s} = N'_{2s}(\chi_{2s} - \Delta_{2s1s}\chi_{1s}) \tag{5}$$

and the normalization constant is

$$N'_{2s} = (1 - \Delta^2_{2s1s})^{-1/2} \tag{6}$$
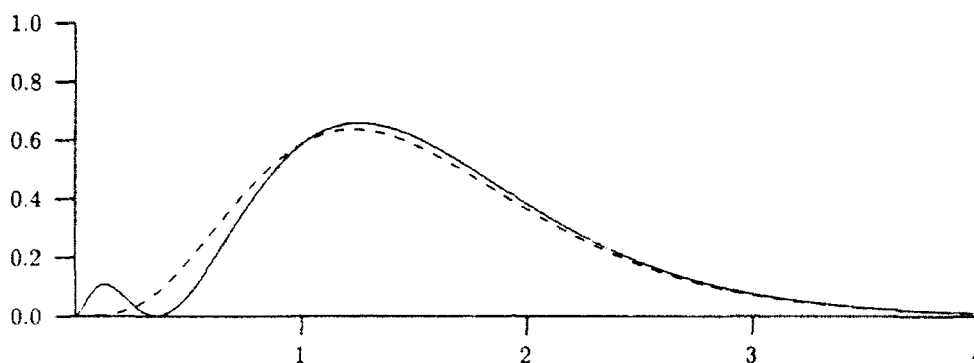
Figure 1. Plot of $4\pi r^2 \chi_{2s}^* \chi_{2s}$ (- - -) and $4\pi r^2 \chi_{2s}'^* \chi_{2s}'$ (——).

where Δ is the overlap. Transition moments in Eq. (1) and (2) can be expressed, after the solution of the spectral form of the RPA equation [7,8], as

$$\langle \psi_{HF} | \sum_{i=1}^{n} \vec{r}_i | \psi_k \rangle = \sqrt{2} \sum_{a,m} \langle \chi_a | \vec{r} | \chi_m \rangle \{ X + Y \}_{a,m,k}$$ (7)

where χ_a denotes occupied orbitals and χ_m denotes unoccupied orbitals. A more detailed description of the implementation of the RPA formalism can be found in Refs. [1] ard [2]. In this report which examines spectroscopic predictions of the INDO/S model, χ STO orbitals will be replaced by χ' orbitals. Since all one- and two-center dipole and velocity integrals are evaluated in the STO basis, we transform the integral matrix to the orthogonalized basis before multiplying with the molecular orbital coefficients obtained from the INDO/S calculations. Such transformations would not be required if only one-center integrals were evaluated, or if the molecular integrals were calculated over the original basis set, as in *ab-initio* work.

One can see how this correction will change the results of oscillator strengths by inspecting Figures 1 to 3 where representative graphs of overlap, dipole-length, and
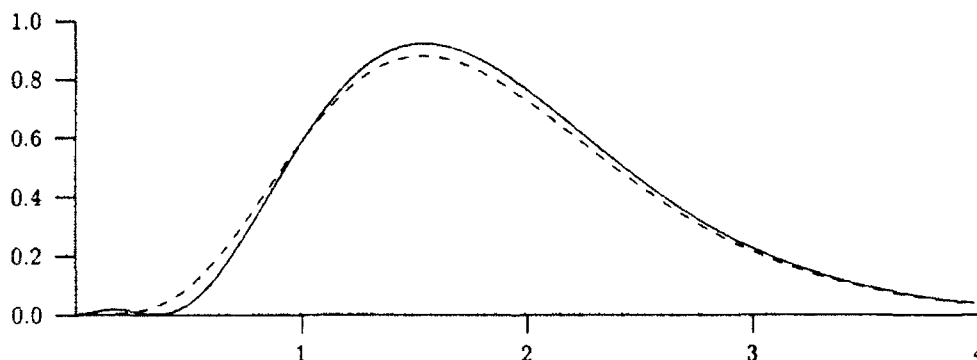
Figure 2. Plot of $4\pi r^2 \chi_{2s}^* r \chi_{2s}$ (- - -) and $4\pi r^2 \chi_{2s}'^* r \chi_{2s}'$ (——).
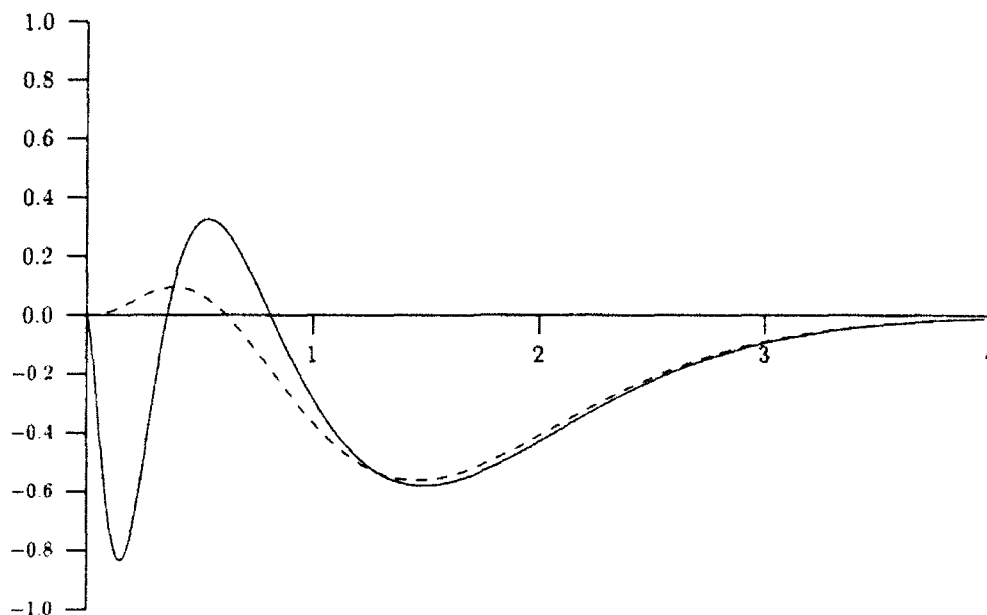
Figure 3.   Plot of $4\pi r^2 \chi_{2s}^* \frac{d}{dr} \chi_{2s}$, (– – –) and $4\pi r^2 \chi_{2s}'^* \frac{d}{dr} \chi_{2s}'$, (———).

dipole-velocity kernels over $2s$ STO orbital with carbon exponent are plotted. First we see that a spherical node is present in the χ_{2s}' orbital in Figure 1. In Figure 2 one can see that this new orbital will not change the dipole-length property integral very much, but there is a dramatic change to the dipole-velocity kernel in the 0 to 1 bohr region in Figure 3. We report here the singlet electronic excitations, calculated from RPA–INDO/S model with core orthogonalized valence-shell orbitals, of formaldehyde, benzene, pyridine, dibenzene, 1,4-benzoquinone monoimid N(para) dimethyl aniline, and Mg-porphyrin. Corrections are applied to one-center integrals and/or two-center integrals. The results and effect on timing of calculations are compared with those calculated with noncore orthogonalized valence orbitals and those from the widely used CIS–INDO/S model.

Results

The results presented in the tables are arranged in four main columns—the first column contains data without any inner-shell orbital (core) correction, the second with only one-center corrections, the third with full corrections applied to dipole length and velocity property integrals, and the last column with full corrections to all integrals, including the overlaps. From experience, we have observed that when differences exist between length and velocity predictions, length values more closely resemble experimental values. For this reason we define the % error as the difference between length and velocity values relative to the length values.

Experimentally, formaldehyde has a weak ($f = 0.00024$) $n \rightarrow \pi^*$ transition, which is forbidden in C_{2v} symmetry, with $\lambda_{onset} = 28329$ cm^{-1} and maximum at

TABLE I. Calculated spectra of CH_2O. The meanings of E_k, f^+, f^-, and the four main columns denoted as "no correction," "one center," "$1-O_P + 1.2 - r, \nabla$," "full" are as described in the text. E_k is given in 1000 cm^{-1}, time in seconds, and ratio $= f^+/f^-$.

	No correction			One center			$1-O_P$ $+1.2 - r, \nabla$			Full			
E_k	f^+	f^-	Ratio	f^+	f^-	Ratio	f^+	f^-	Ratio	f^+	f^-	Ratio	Type
	CI			CI			CI			CI			
29.2	—	—	—	—	—	—	—	—	—	—	—	—	$n \rightarrow \pi^*$
63.8	0.165	0.530	0.31	0.164	0.296	0.55	0.162	0.287	0.56	0.160	0.286	0.56	$\pi \rightarrow \pi^*$
sum	4.837	3.490		4.808	2.134		4.769	2.091		4.741	2.083		
	RPA			RPA			RPA			RPA			
29.1	—	—	—	—	—	—	—	—	—	—	—	—	$n \rightarrow \pi^*$
63.5	0.144	0.627	0.23	0.143	0.361	0.40	0.142	0.350	0.41	0.140	0.349	0.40	$\pi \rightarrow \pi^*$
sum	4.082	3.912		4.061	2.466		4.023	2.412		4.000	2.402		
Time*	1.32			1.58			2.12			2.10			

* Seconds on a SUN 4/380.

TABLE II. Calculated spectra of benzene. Energy in 1000 cm^{-1} and ratio $= f^+/f^-$.

	No correction			One center			$1-O_P$ $+1.2 - r, \nabla$			Full			
E_k	f^+	f^-	Ratio	f^+	f^-	Ratio	f^+	f^-	Ratio	f^+	f^-	Ratio	Type
	CI			CI			CI			CI			
37.8	—	—	—	—	—	—	—	—	—	—	—	—	$\pi \rightarrow \pi^*$
48.8	—	—	—	—	—	—	—	—	—	—	—	—	$\pi \rightarrow \pi^*$
54.6*	2.041	0.445	4.60	2.045	0.624	3.28	2.049	0.649	3.16	2.056	0.653	3.15	$\pi \rightarrow \pi^*$
sum	3.878	4.156		3.850	2.289		3.819	2.117		3.775	2.089		
	RPA			RPA			RPA			RPA			
37.3	—	—	—	—	—	—	—	—	—	—	—	—	$\pi \rightarrow \pi^*$
43.3	—	—	—	—	—	—	—	—	—	—	—	—	$\pi \rightarrow \pi^*$
51.6*	1.357	1.083	1.25	1.360	1.239	1.10	1.363	1.259	1.08	1.368	1.263	1.08	$\pi \rightarrow \pi^*$
sum	2.745	5.067		2.721	3.040		2.694	2.850		2.656	2.819		
Time+	8.91			8.91			14.68			14.59			

* Experimental value of the oscillator strength is 1.38. Ref. [12].
+ Seconds on a SUN 4/380.

33898 cm⁻¹, and a strong $\pi \rightarrow \pi^*$ transition with maximum at 64103 cm⁻¹ [9]. The calculated spectra for formaldehyde is shown in Table I. We see that both CIS and RPA give favorable excitation energies compared with the experimental results. After the inclusion of one-center core corrections, the ratios between the two forms of oscillator strengths are improved by about a factor of 2 for both CIS and RPA. With the inclusion of two-center corrections, the changes are only minor compared with the one-center only results. Since the $n \rightarrow \pi^*$ transition is symmetry forbidden, the oscillator strengths are all zero. The effect on the $\pi \rightarrow \pi^*$ transitions which involves principally $2p$ orbitals is indirect and is explained by the presence of $\sigma \rightarrow \sigma^*$ configurations in the total wavefunction.

The calculated spectra for benzene, pyridine, and dibenzene are collected in Table II to IV. The ratios between the dipole-length and dipole-velocity oscillator strengths are all improved. Similar to the formaldehyde findings, the full treatment of corrections does not significantly improve the results over those obtained with only one-center corrections. Pyridine is of C_{2v} symmetry and has two low lying $n \rightarrow \pi^*$ transitions. As shown in Table III, the symmetry allowed transition has

TABLE III. Calculated spectra of pyridine. Energy in 1000 cm⁻¹ and ratio = f'/f^r.

E_k	No correction			One center			1 - Or + 1.2 - r, r			Full			Type
	f'	f^r	Ratio	f'	f^r	Ratio	f'	f^r	Ratio	f'	f^r	Ratio	
	CI			CI			CI			CI			
36.0¹	8.87	0.210	0.04	9.1	0.030	0.30	8.7	0.031	0.28	8.7	0.032	0.27	n→π*
	(-3)			(-3)			(-3)			(-3)			
44.2	—	—	—	—	—	—	—	—	—	—	—	—	n→π*
38.8²	0.061	0.011	5.55	0.061	0.014	4.36	0.061	0.014	4.36	0.061	0.014	4.36	π→π*
50.0³	0.067	0.021	3.19	0.067	0.028	2.39	0.068	0.028	2.43	0.068	0.029	2.34	π→π*
56.3⁴	0.732	0.037	19.8	0.735	0.162	4.54	0.738	0.173	4.27	0.742	0.177	4.19	π→π*
56.7⁴	0.888	0.210	4.23	0.889	0.292	3.04	0.891	0.300	2.97	0.893	0.302	2.96	π→π*
sum	3.424	3.887		3.407	1.945		3.384	1.841		3.361	1.820		
	RPA			RPA			RPA			RPA			
35.8¹	8.2	0.231	0.04	8.5	0.031	0.27	8.1	0.032	0.25	8.1	0.033	0.25	n→π*
	(-3)			(-3)			(-3)			(-3)			
44.1	—	—	—	—	—	—	—	—	—	—	—	—	n→π*
38.1²	0.055	0.042	1.31	0.055	0.046	1.20	0.055	0.046	1.20	0.055	0.046	1.20	π→π*
49.2³	0.099	0.083	1.93	0.099	0.101	0.98	0.099	0.102	0.97	0.099	0.103	0.96	π→π*
54.0⁴	0.510	0.220	2.32	0.512	0.369	1.39	0.514	0.381	1.35	0.517	0.384	1.35	π→π*
54.0⁴	0.594	0.449	1.32	0.595	0.519	1.15	0.597	0.525	1.14	0.598	0.527	1.13	π→π*
sum	2.413	4.714		2.399	2.597		2.379	2.481		2.360	2.458		
Time⁵	8.99			8.76			12.90			14.50			

¹ Experimental value of the oscillator strength is 0.003. Refs. [12], [13].
² Experimental value of the oscillator strength is 0.03. Refs. [12], [13].
³ Experimental value of the oscillator strength is 0.20. Refs. [12], [13].
⁴ Experimental value of the oscillator strength for these two unresolved peaks is 1.30. Refs. [12], [13].
⁵ Seconds on a SUN 4/380.

TABLE IV. Calculated spectra of dibenzene. Energy in 1000 cm^{-1} and ratio $= I'/I^v$.

E_A	No correction			One center			$1 - Or$ $+1.2 - r, r$			Full			Type
	I'	I^v	Ratio	I'	I^v	Ratio	I'	I^v	Ratio	I'	I^v	Ratio	
	CI			CI			CI			CI			
53.5	0.284	2.2(-3)	12.9	0.286	0.032	8.94	0.288	0.039	7.38	0.291	0.040	7.28	$\pi \uparrow \pi^*$
55.6	3.354	0.479	7.00	3.363	0.845	3.98	3.376	0.899	3.76	3.392	0.911	3.72	$\pi \uparrow \pi^*$
59.2	1.5(-3)	4.0(-5)	37.5	1.5(-3)	1.8(-4)	8.33	1.5(-3)	2.2(-4)	6.82	1.5(-3)	2.2(-4)	6.82	$\pi \uparrow \pi^*$
59.6	3.1(-3)	4.6(-4)	6.7	3.1(-3)	7.4(-4)	4.19	3.1(-3)	7.8(-4)	3.97	3.1(-3)	8.0(-4)	3.88	$\pi \uparrow \pi^*$
sum	10.99	12.22		10.90	6.484		10.72	5.947		10.56	5.852		
	RPA			RPA			RPA			RPA			
50.8	0.284	0.180	1.58	0.286	0.254	1.13	0.289	0.265	1.10	0.292	0.268	1.09	$\pi \uparrow \pi^*$
52.4	2.120	1.603	1.32	2.126	1.937	1.10	2.135	1.982	1.08	2.147	1.991	1.08	$\pi \uparrow \pi^*$
59.2	3.6(-4)	1.2(-4)	3.00	3.6(-4)	2.0(-4)	1.80	3.6(-4)	2.2(-4)	1.64	3.8(-4)	2.2(-4)	1.73	$\pi \uparrow \pi^*$
59.6	6.6(-4)	3.6(-4)	1.83	6.6(-4)	4.4(-4)	1.50	6.8(-4)	4.6(-4)	1.48	6.8(-4)	4.6(-4)	1.48	$\pi \uparrow \pi^*$
sum	7.947	14.89		7.872	8.503		7.723	7.885		7.584	7.774		
Time*	35.52			35.49			56.74			61.27			

* Seconds on a SUN 4/380.
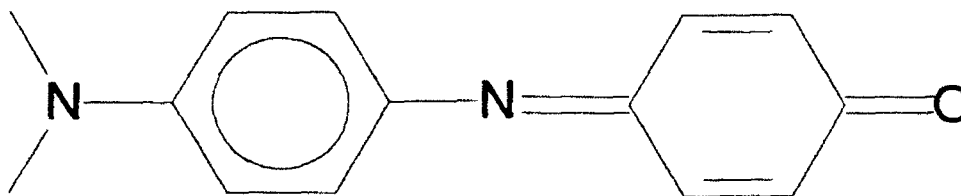
Figure 4.   The structure of 1,4-benzoquinone monoimid N(para) dimethyl aniline.

small oscillator strengths and with the one-center corrections the agreement of the two oscillator strengths improves by a factor of about 7 for both CIS and RPA. The agreement of the RPA estimated dipole-length oscillator strengths with experiment is quite good for benzene and pyridine. A more interesting molecule to be tested is 1,4-benzoquinone monoimid N(para) dimethyl aniline shown in Figure 4. It has two weakly allowed $n \to \pi^*$ transitions, one from oxygen lone pair and the other from nitrogen lone pair, and a strong $\pi \to \pi^*$ transition. The calculated spectra is reported in Table V. Similar improvement as noted in pyridine is observed. The last example is Mg-porphyrin with the structure shown in Figure 5. With a small 9×9 active space for the CI, the core corrections do not change any of the CIS and RPA results since only $\pi \to \pi^*$ configurations are included. The results of a larger 12×17 CI that includes many $\sigma \to \sigma^*$ configurations are reported in Table VI. In this case, one can see that the ratios of the RPA results are already close to 1 without any core corrections and the inclusion of corrections do not change the results very much. The changes to the CIS results are all small. The calculated dipole-length oscillator strengths for the Q and B bands are too large, but the RPA model is again in best agreement with experiment.

From the tables, one can see that inclusion of only the one-center core corrections do much more to improve the agreement of the oscillator strengths calculated by the two formulations than subsequent inclusion of two-center corrections, and the timing nearly doubles going from the one-center only treatment to the full treatment. The time spent to include the one-center corrections is almost undetectable for small molecules and only 4 s more for systems as large as Mg-porphyrin. One notes that in general the agreement of the sum rules calculated through the length and velocity formulation follows the trend of RPA(core) > RPA(nocore) and CIS(nocore) > CIS(core). It is further noted that the agreement between the sum rules for RPA(length) and RPA(velocity) are greatly improved by using orthogonalized orbitals. This would in turn suggest that this procedure would improve equivalence between different formalisms for those response properties best represented as a sum over state solution such as polarizabilities [10] and NMR shielding [11].

Conclusions

With the introduction of a simple core-valence orthogonalization procedure to valence-orbital only methods, we demonstrate a great improvement between os-

TABLE V. Calculated spectra of 1,4 benzoquinone monoimid N (para) dimethyl aniline. Energy in 1000 cm⁻¹ and ratio $= f'/f'$.

E_A	No correction			One center			1 − Ov + 1.2 − r, ∇			Full			
	f'	f'	Ratio	f'	f'	Ratio	f'	f'	Ratio	f'	f'	Ratio	Type
	CI			CI			CI			CI			
21.4	7.0(−5)	3.5(−3)	0.02	7.0(−5)	4.8(−4)	0.15	7.0(−5)	4.9(−4)	0.14	7.0(−5)	5.0(−4)	0.14	$n(O) \to \pi^*$
23.3	4.6(−3)	0.226	0.02	4.8(−3)	0.029	0.17	4.6(−3)	0.029	0.16	4.6(−3)	0.030	0.15	$n(N) \to \pi^*$
26.1	1.184	0.372	3.18	1.184	0.426	2.78	1.185	0.433	2.74	1.186	0.435	2.73	$\pi \to \pi^*$
sum	8.826	10.385		8.774	5.528		8.707	5.172		8.625	5.109		
	RPA			RPA			RPA			RPA			
21.3	8.0(−5)	5.7(−3)	0.01	8.0(−5)	7.2(−4)	0.11	8.0(−5)	7.3(−4)	0.11	8.0(−5)	7.6(−4)	0.11	$n(O) \to \pi^*$
23.1	4.4(−3)	0.264	0.02	4.5(−3)	0.032	0.14	4.4(−3)	0.033	0.13	4.4(−3)	0.034	0.13	$n(N) \to \pi^*$
25.3	0.919	0.755	1.22	0.920	0.788	1.17	0.920	0.792	1.16	0.921	0.793	1.16	$\pi \to \pi^*$
sum	6.453	12.453		6.407	7.106		6.349	6.708		6.279	6.637		
Time*	47.03			48.14			75.74			83.08			

* Seconds on a SEL 4/380.
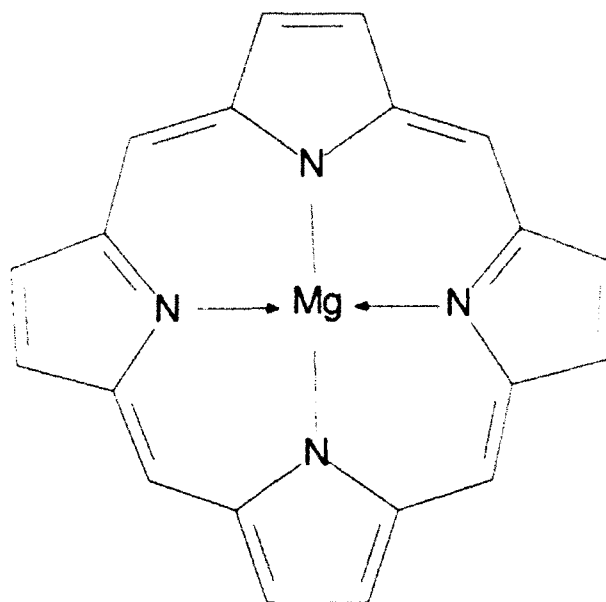
Figure 5.   The structure of Mg-porphyrin.

cillator strengths calculated with the dipole-length and dipole-velocity formulations.
The RPA model stresses this equivalence, although one certainly does not expect it
for small basis sets. Nevertheless, even with the minimal basis set representation
of the INDO/S model, the ratios of the oscillator strengths calculated from the RPA
model for $\pi \rightarrow \pi^*$ excitations are brought, generally, close to 1, while the ratios
for $n \rightarrow \pi^*$ excitations are improved by a factor of about 10.

In *ab-initio* calculations one should include all the corrections implied in the
core-orthogonalization recommended in Eq. (3), and this should involve very little
additional computer time, for this is not the time-consuming step. In fast semi-
empirical techniques, such as the INDO/S examined here, we have demonstrated
that only the one-center corrections are really needed to accomplish this improve-
ment in calculated oscillator strengths, and in this case, there is a considerable
savings in time.

From the studies reported here and others we have made, the oscillator strength
calculated from the dipole-length formalism within the RPA model agree best with
experiment, and these results are not greatly affected by the nodal structure of the
valence orbitals.

Before concluding it might be recalled that semi-empirical methods such as INDO/
S obtain their energy parameters from experiment. Because of this the actual basis
set used is not directly specified, but might be considered to be of Hartree–Fock
quality, or even better. We have here related these orbitals to simple STO's. Since
we have shown that most of the inner-shell correction is one-center it could be
argued that the atomic dipole and velocity integrals (one-center) might be calculated
from Hartree–Fock orbitals and tabulated, or even parameterized to be equivalent

TABLE VI. Calculated spectra of Mg-porphyrin. Energy in 1000 cm⁻¹ and ratio f'/f^c.

E_A	No correction			One center			Or 1–1.2 c,v			Full			
	f'	f^c	Ratio	f'	f^c	Ratio	f'	f^c	Ratio	f'	f^c	Ratio	Type
	CI			CI			CI			CI			
16.2	0.137	5.7(3)	24.0	0.137	0.010	13.7	0.137	0.011	12.5	0.137	0.011	12.5	Q
29.6	5.090	0.597	8.53	5.093	0.712	7.15	5.096	0.728	7.00	5.098	0.729	6.99	B
35.6	0.216	0.029	7.45	0.216	0.029	7.45	0.216	0.029	7.45	0.216	0.029	7.45	
40.6	0.494	0.072	6.86	0.494	0.079	6.25	0.494	0.080	6.18	0.494	0.080	6.18	
sum	13.706	8.286		13.669	5.606		13.623	5.394		13.573	5.359		
	RPA			RPA			RPA			RPA			
15.1	0.121	0.135	0.90	0.121	0.140	0.86	0.121	0.141	0.86	0.121	0.141	0.86	Q
26.0	2.700	2.467	1.10	2.702	2.846	1.06	2.703	2.855	1.06	2.706	2.856	1.06	B
35.2	0.057	0.048	1.19	0.057	0.046	1.24	0.057	0.046	1.24	0.057	0.046	1.24	
40.3	0.028	0.189	1.31	0.208	0.162	1.28	0.208	0.166	1.25	0.208	0.163	1.28	
sum	7.970	11.33		7.939	8.464		7.980	8.232		7.888	8.194		
Time	127.56			132.98			224.74			251.54			

1 Experimental value of the oscillator strength is about 0.08. Refs. [14], [18]

2 Experimental value of the oscillator strength is about 1.66–1.74. Refs. [14], [18]

3 Seconds on a SI/3/380.

at the RPA-level of theory. We have chosen not to do this, at least not yet, as the dipole-length formalism within the RPA theory gives quite satisfactory results when compared with experimental oscillator strengths. Nevertheless one cannot help but wonder what the effects of parameterizing the one-center velocity integrals, which yield somewhat less satisfactory results here, could have on other calculated properties that require these integrals.

Acknowledgment

Bibliography

[1] J. D. Baker and M. C. Zerner, J. Phys. Chem. 95, 8614 (1991).
[2] J. D. Baker and M. C. Zerner, Chem. Phys. Lett. 175, 192 (1990).
[3] A. E. Hansen and T. D. Bouman, Mol. Phys. 37, 1713 (1979).
[4] D. J. Rowe, Rev. Mod. Phys. 40, 153 (1968).
[5] It should be pointed out that the CIS formalism is not capable of achieving this equivalence even in a complete basis, thus the interest in the RPA formalism.
[6] M. C. Zerner, Mol. Phys. 23, 963 (1972).
[7] P. Jørgensen and J. Simons, Second Quantized-Based Methods in Quantum Chemistry (Academic Press, New York, 1981).
[8] J. Linderberg and N. Y. Öhrn, Propagators in Quantum Chemistry (Academic Press, London, 1973).
[9] Hiroshi Suzuki, Electronic Absorption Spectra and Geometry of Organic Molecules (Academic Press, New York, 1967), pp. 430–431.
[10] W. A. Parkinson and M. C. Zerner, J. Chem. Phys. 94, 478 (1991).
[11] J. D. Baker and M. C. Zerner, Int. J. Quantum Chem. 43, 327 (1992).
[12] J. E. Parkin and K. K. Innes, J. Mol. Spectrosc. 15, 407 (1965).
[13] K. K. Innes, J. P. Byrne, and I. G. Roos, J. Mol. Spectrosc. 22, 125 (1967).
[14] G. D. Dorough, J. R. Miller, and F. M. Huennekens, J. Am. Chem. Soc. 73, 4315 (1).
[15] C. Weiss, H. Kobayashi, and M. Gouterman, J. Mol. Spectrosc. 16, 415 (1965).

A Comparison of Dipole Polarizability Obtained From Linear and Quadratic Response Functions

WILLIAM A. PARKINSON*

Department of Chemistry, Odense University, DK-5230 Odense M, Denmark

Abstract

Elements of the frequency-dependent polarizability tensor are obtained from the quadratic response function (QRF). This is accomplished from equations of motion (EOM) which relate QRFs and the linear response function (LRF). The response functions are evaluated within the random-phase approximation (RPA), where the EOM are exact in a complete basis. Hence, the agreement between LRF and QRF polarizability provides a criterion for basis set selection when calculating second- as well as third-order properties. Numerical examples are provided for the static and dynamic polarizability of H_2O. © 1992 John Wiley & Sons, Inc.

Introduction

Propagators [1] are response functions which directly measure the effect of external perturbations upon atoms or molecules. For instance, the linear response function (LRF) [2] and quadratic response function (QRF) [3,4] are propagators describing the frequency-dependent polarizability [2] and first hyperpolarizability [5] of a system subjected to an oscillating electric field. The following spectral representations are given for the LRF [2]

$$\langle\langle A; B \rangle\rangle_{\omega_B} = \lim_{\epsilon \to 0^+} \sum_m \left\{ \frac{\langle 0|A|m\rangle\langle m|B|0\rangle}{\omega_B - \omega_m + i\epsilon} - \frac{\langle 0|B|m\rangle\langle m|A|0\rangle}{\omega_B + \omega_m + i\epsilon} \right\} \quad (1)$$

and QRF [3]

$$\langle\langle A; B, C \rangle\rangle_{\omega_B,\omega_C} = \lim_{\epsilon \to 0^+} \lim_{\eta \to 0^+}$$

$$\times \frac{1}{2} \sum_{m,n} \left\{ \frac{\langle 0|A|m\rangle\langle m|B|n\rangle\langle n|C|0\rangle}{(\omega_B + \omega_C - \omega_m + i\epsilon + i\eta)(\omega_C - \omega_n + i\eta)} \right.$$

$$+ \frac{\langle 0|A|m\rangle\langle m|C|n\rangle\langle n|B|0\rangle}{(\omega_B + \omega_C - \omega_m + i\epsilon + i\eta)(\omega_B - \omega_n + i\epsilon)}$$

$$\left. + \frac{\langle 0|C|m\rangle\langle m|B|n\rangle\langle n|A|0\rangle}{(\omega_B + \omega_C + \omega_n + i\epsilon + i\eta)(\omega_C + \omega_m + i\eta)} \right.$$

* Permanent address: Department of Chemistry and Physics, Southeastern Louisiana University, Hammond, LA 70402.

$$+ \frac{\langle 0| B|m\rangle\langle m|C|n\rangle\langle n|A|0\rangle}{(\omega_B + \omega_C + \omega_n + i\epsilon + i\eta)(\omega_B + \omega_m + i\epsilon)}$$

$$- \frac{\langle 0| B|m\rangle\langle m|A|n\rangle\langle n|C|0\rangle}{(\omega_B + \omega_m + i\epsilon)(\omega_C - i\eta)}$$

$$- \frac{\langle 0|C|m\rangle\langle m|A|n\rangle\langle n|B|0\rangle}{(\omega_C + \omega_m + i\eta)(\omega_B - \omega_m + i\epsilon)}\Bigg\} .\qquad (2)$$

Equations (1) and (2) are first- and second-order retarded propagators [1], obtained upon expanding the ω-Fourier component of expectation value $\langle A\rangle$ subjected to perturbing influences B and C [3,6]. The frequency dependence of the perturbations is related in the quantities ω_B and ω_C, with the expressions containing poles with the state vertical excitation energies ω_m or ω_n correspond to the applied frequency of ω_B in the LRF case or ω_B, ω_C, or $\omega_B + \omega_C$ in the QRF case. When electric field dipole operators are explicitly considered, the propagator residues correspond to transition moments from the reference state $|0\rangle$ to excited state $|m\rangle$ for the LRF [2], while the first residue of the QRF describes two-photon absorption [4,7] and the double residue determines the transition moment between excited states [3,8]. The QRF has been applied in frequency-dependent first hyperpolarizability calculations [5] from a single-determinantal reference theory [3] which is based on the random phase approximation (RPA) [9,10]. Multiconfigurational response theory calculations [4] have been performed for QRF first hyperpolarizability [11] and finite-field second hyperpolarizability [12].

The above spectral representation are derived from two-time Green's functions [1,13] which time-evolve according to an equation of motion (EOM). Fourier transform of the time-domain expressions then leads to the more spectroscopically interesting energy formulations given in Eqs. (1) and (2), and also to EOM in the energy domain. This form of the EOM is readily recognized for the LRF [2]

$$\omega_B\langle\langle A; B\rangle\rangle_{\omega_B} = \langle 0|[B, A]|0\rangle + \langle\langle A; [B, H]\rangle\rangle_{\omega_B}.\qquad (3)$$

The right-hand side terms of Eq. (3) both use commutators, the first averaged over the reference state wavefunction, and the second contained in a LRF involving the time-independent Hamiltonian, H.

Equation (3) may be iterated using superoperator algebra to formulate the propagator moment expansion [14], leading to approximations of the exact LRF based on Hartree–Fock, perturbative, or multiconfigurational wavefunctions [6,15]. Equation (3) is also traditionally used to obtain formally equivalent dipole length and dipole velocity expressions of various sum rules [2]. More recently this identity has been applied as a means to develop relations between ground state expectation values and LRFs [16–18]. This approach provides an interesting solution to the gauge origin problem of magnetizability [16], and is also particularly useful in perturbative propagator calculations of second-order properties involving both a ground state expectation value term along with a sum-over-states component, e.g., the shielding effect [18]. Using Eq. (3) the diamagnetic contribution to shielding, which is normally a second-order operator averaged over the reference function, is

represented as a TRF, and may then be evaluated at, for instance, the correlated second-order polarization propagator (SOPPA) level along with the paramagnetic term [18].

The present work also exploits EOM, but this time involving identities between the next rank of propagators, e.g., the following expression

$$(\omega_B + \omega_C) \quad A; B, C \quad {}_{\omega_B, \omega_C} \quad [A, H]; B, C \quad {}_{\omega_B, \omega_C}$$

$$+ \frac{1}{2} \quad [A, B]; C \quad {}_{\omega_C} + \frac{1}{2} \quad [A, C]; B \quad {}_{\omega_B} \quad (4)$$

is an energy-domain EOM for the QRF [3]. It has been shown [3] that the RPA formulation of Eq. (4) is exact, so this expression provides a direct connection between the linear and quadratic response functions computed at the RPA level. Equation (4) will here be used to equate second- and third-order properties—specifically, it will be shown in the next section that a QRF evaluated using a position, momentum, and angular momentum operator is equivalent to the TRF describing the dipole polarizability of a system. Since the formulations involve angular momentum, the QRF polarizability will be inherently dependent on choice of coordinate origin. The magnitude of this origin dependence is expressed as a function of an invariant QRF. Sample calculations are then provided for the water molecule.

Theory

QRF Polarizability

To extract QRF dipole polarizability expressions, the operators A, B, and C are specified as components of position and angular momentum in the following manner:

$$(\omega_B + \omega_C) \quad r; x, L \quad {}_{\omega_B, \omega_C} \quad [r, H]; x, L \quad {}_{\omega_B, \omega_C}$$

$$+ \frac{1}{2} \quad [r, x]; L \quad {}_{\omega_C} + \frac{1}{2} \quad [r, L]; x \quad {}_{\omega_B} \quad (5)$$

Explicit evaluation of the commutators leads to

$$x; x \quad {}_{\omega} \quad 2[\quad p; x, L \quad {}_{\omega_B, \omega_C} + i(\omega_B + \omega_C) \quad r; x, L \quad {}_{\omega_B, \omega_C}] \quad (6)$$

The left-hand side of Eq. (6) is recognized as the negative of the TRF representation for the xx component of dynamic polarizability [2]. In the static-field limit, this expression further simplifies to

$$x; x \quad {}_{\omega, 0} \quad 2 \quad p; x, L \quad {}_{\omega, \omega, 0} \quad (7)$$

All other components of the polarizability tensor may be similarly expressed. Table I summarizes the operator choices for diagonal elements of the QRF static-field polarizability tensor that are obtained as a consequence of the EOM in Eq. (4).

Since Eq. (4) is satisfied at the RPA level [3], the RPA QRF and TRF polarizabilities must be identical in the limit of complete basis. Comparison of QRF and TRF polarizability values may therefore provide a measure of balance of the chosen basis set toward its representation of both second- and third-order properties.

TABLE I. Relations between LRF and QRF static-field dipole polarizability components.[a]

LRF	QRF[b]	QRF Origin-dependence[c]
$\langle\langle x; x\rangle\rangle_{\omega_B=0}$	$-2\langle\langle p_x; x, L_z\rangle\rangle_{\omega_B=0,\omega_C=0}$	Independent
	$2\langle\langle p_z; x, L_y\rangle\rangle_{\omega_B=0,\omega_C=0}$	$2\langle\langle p_z; x, p_y\rangle\rangle_{\omega_B=0,\omega_C=0}$
$\langle\langle y; y\rangle\rangle_{\omega_B=0}$	$2\langle\langle p_x; y, L_z\rangle\rangle_{\omega_B=0,\omega_C=0}$	Independent
	$-2\langle\langle p_z; y, L_x\rangle\rangle_{\omega_B=0,\omega_C=0}$	$-2\langle\langle p_z; y, p_x\rangle\rangle_{\omega_B=0,\omega_C=0}$
$\langle\langle z; z\rangle\rangle_{\omega_B=0}$	$-2\langle\langle p_x; z, L_y\rangle\rangle_{\omega_B=0,\omega_C=0}$	$2\langle\langle p_x; z, p_y\rangle\rangle_{\omega_B=0,\omega_C=0}$
	$2\langle\langle p_y; z, L_x\rangle\rangle_{\omega_B=0,\omega_C=0}$	$-2\langle\langle p_y; z, p_x\rangle\rangle_{\omega_B=0,\omega_C=0}$

[a] Identities derived using Eq. (4).

[b] In the static field case, this and all other QRFs presented are equivalent under interchange of the operators to the right of the semicolon. For field-dependent cases, the interchange of frequencies ω_B and ω_C is also required.

[c] For a C_{2v} system (see text).

The second QRF on the right-hand side of Eq. (6) (when computed with $\omega_C = 0$) is recognized as a component of the Verdet constant [19,20], which describes optical rotation in a static magnetic field [21,22]. Rearrangement of Eq. (6) provides an expression for one contribution to the mixed-velocity Verdet constant

$$\langle\langle ip_y; x, iL_z\rangle\rangle_{\omega_B,\omega_C=0} = \omega_B\langle\langle y; x, iL_z\rangle\rangle_{\omega_B,\omega_C=0} + \tfrac{1}{2}\langle\langle x; x\rangle\rangle_{\omega_B} \quad (8)$$

Calculation of Verdet constants in length and mixed-velocity representations can hence be accomplished within the same formalism. This approach will be used in a future publication to provide a stringent test of basis set completeness when computing this property [23].

Alternative QRF Polarizability Formulations

In the static field limit, the LRF and QRF spectral representations are invariant to any permutation of the operators A, B, and C [see Eqs. (1) and (2)]. Equation (7) must therefore hold for any ordering of the QRF or LRF operators. However, the polarizability equalities arise only when the position and angular momentum operators are inserted in the specific order chosen for Eq. (5), as only then do the EOM contain the appropriate commutators. To derive the static-field limit expressions corresponding to permutation of the operators, it is necessary to employ two different forms of the QRF EOM [7,24]

$$\omega_B\langle\langle A; B, C\rangle\rangle_{\omega_B,\omega_C} = \langle\langle A; [H, B], C\rangle\rangle_{\omega_B,\omega_C}$$
$$+ \tfrac{1}{2}\langle\langle [A, B]; C\rangle\rangle_{\omega_C} + \tfrac{1}{2}\langle\langle A; [C, B]\rangle\rangle_{\omega_B+\omega_C} \quad (9)$$
$$\omega_C\langle\langle A; B, C\rangle\rangle_{\omega_B,\omega_C} = \langle\langle A; B, [H, C]\rangle\rangle_{\omega_B,\omega_C}$$
$$+ \tfrac{1}{2}\langle\langle [A, C]; B\rangle\rangle_{\omega_B} + \tfrac{1}{2}\langle\langle A; [B, C]\rangle\rangle_{\omega_B+\omega_C} \quad (10)$$

Equations (9) and (10) are particularly convenient for extracting dynamic polar-izability. The frequency-dependent components obtained from Eq. (4) involve two QRFs, whereas similar relations can be obtained from the above LOM as a function of one QRF. For instance, using Eq. (10) and the operator choices $A = x$, $B = L_z$, and $C = r$ leads to

$$\langle\langle x; x \rangle\rangle_{\omega} = 2\langle x; L_z, p_x \rangle\rangle_{\omega,\omega} \qquad (11)$$

Origin-Dependence of the QRF Polarizability

The presence of the angular momentum operator, $\vec{L} = \vec{r} \times \vec{p}$, introduces a co-ordinate dependence into the QRF expressions; for example, the expression in Eq. (11) under translation ($\vec{r}' = \vec{r} + \vec{d}$) becomes

$$\langle x; L_z, p_x \rangle\rangle_{\omega,\omega} = \langle x; L_z, p_x \rangle\rangle_{\omega,\omega}$$
$$+ d_x\langle x; p_y, p_x\rangle\rangle_{\omega,\omega} - d_y\langle x; p_x, p_x\rangle\rangle_{\omega,\omega} \qquad (12)$$

For a system of point group C_{2v} with the principal axis along the z-direction, only QRFs containing the Cartesian components xxz, yyz, or zzz (or their permutations) are nonvanishing. It follows that within the C_{2v} point group the xx polarizability is given exactly by Eq. (11), without consideration of the displacement-weighted QRF terms, because

$$\langle x; L_z, p_x \rangle\rangle_{\omega,\omega} = \langle x; L_z, p_x \rangle\rangle_{\omega,\omega} \qquad (13)$$

The same argument can be made for the C_{2v}-restricted yy component given by $\langle y; L_z, p_y \rangle\rangle_{\omega,\omega}$. However, along the principal axis, the QRF determining the zz polarizability would have the following form

$$\langle z; z \rangle\rangle_{\omega} = 2\langle z; L_z', p_x \rangle\rangle_{\omega,\omega} = 2\langle z; L_z, p_x \rangle\rangle_{\omega,\omega}$$
$$+ d_x\langle z; p_y, p_x\rangle\rangle_{\omega,\omega} - 2d_y\langle z; p_x, p_x\rangle\rangle_{\omega,\omega} \qquad (14)$$

Under C_{2v} symmetry, the zz polarizability component will hence depend on the displacement of coordinate origin as a function of the QRF $\langle z; p_x, p_x \rangle\rangle_{\omega,\omega}$. This QRF is an alternative measure on the basis set representation, as it must vanish in the limit of complete basis, where overall origin invariance is achieved. The translational properties of the QRFs listed in Table I are summarized there, assuming a system of C_{2v} point group symmetry.

Application to H₂O

To test the relationships, calculations of RPA LRF and QRF polarizability were performed for H_2O at the experimental equilibrium geometry [25] using basis sets which were described elsewhere (basis A: 62 contracted GTOs B: 80 CGTOs, C: 101 CGTOs) [5]. The molecule was oriented in the xz plane with the z-direction chosen as the principal axis. The expressions were evaluated by a QRF program [5] which is part of the polarization propagator package of the MUNICH program system [26].

TABLE II.   Comparison of the RPA LRF and QRF xx component of static polarizability for H_2O.[a]

Basis	$\langle\langle x; x \rangle\rangle_{\omega_B=0}$	$2\langle\langle p_x; x, L_z \rangle\rangle_{\omega_B=0,\omega_C=0}$	CPHF[b]	MBPT[c]	Exp.[d]
A	8.69	7.95			
B	8.89	8.49			
C	9.16	9.01	9.06	9.92	10.01 ± .09

[a] All values given in a.u.
[b] Ref. 28; [c]Ref. 29; [d]Ref. 27.

Tables II and III report the LRF xx and yy components of static dipole polarizability, along with that obtained from the QRFS $\langle\langle p_x; x, L_z \rangle\rangle_{\omega_B=0,\omega_C=0}$ and $\langle\langle p_x; y, L_z \rangle\rangle_{\omega_B=0,\omega_C=0}$, respectively. These QRF components are origin-independent by virtue of the C_{2v} symmetry of the molecule (see discussion in previous section). The RPA EOM identities are, of course, only valid in the limit of complete basis, and the computed xx tensor elements display a convergence trend as basis set size is increased. Discrepancy of the RPA results with estimated experimental values [27] are mostly attributed to the fact that RPA is only first-order in electron correlation [3], and is therefore at the same level of theory as the included coupled Hartree–Fock calculations [28]. Fourth-order MBPT results [29] are also listed, from which it is clear that the correlation correction for this system is significant.

Table IV compares the static zz component LRF and QRF polarizabilities calculated with the origin of the coordinate system located at (0, 0, 0) and (0, 0, 1.0) a.u. Also included are calculated values for the QRF $\langle\langle z; p_x, p_x \rangle\rangle_{\omega_B=0,\omega_C=0}$. As the results verify, the translation of the coordinate system is a function of this propagator.

Tables V and VI contain the xx and yy values of QRF and LRF dynamic polarizability calculated in basis set C. The QRF values are computed in two different forms, one derived from the EOM of Eq. (4) and another obtained using the EOM of Eq. (9). Although the polarizability arising from Eq. (4) is computed with two frequencies and two QRFS, the values compare favorably with the single-frequency QRF [Eq. (9)] and with LRF results. From the spectral representations [Eqs. (1) and (2)], it is obvious that a two-frequency QRF experiences three times as many possible poles as either the single-field LRF or QRF. This effect is quantified in the last three entries of Table V, where individual QRF values indicate the two-frequency

TABLE III.   Comparison of the RPA, LRF, and QRF yy component of static polarizability for H_2O.[a]

Basis	$\langle\langle y; y \rangle\rangle_{\omega_B=0}$	$2\langle\langle p_x; y, L_z \rangle\rangle_{\omega_B=0,\omega_C=0}$	CPHF[b]	MBPT[c]	Exp.[d]
A	6.96	6.87			
B	7.25	7.25			
C	7.84	7.94	7.67	9.36	9.26 ± .09

[a] All values given in a.u.
[b] Ref. 28; [c]Ref. 29; [d]Ref. 27.

TABLE IV. Comparison of H₂O static polarizability from the RPA ERF and the QRFs of Eq. (14).[a]

Basis	$\sum_i c_i / P_i$	$\sum_i c_i P_i / P_i$	Sum	
	Origin at (0, 0, 0)			
A	7.41	0.00[b]	7.41	7.72
B	7.96	0.07	7.96	8.09
C	8.45	0.24	8.45	8.45
	Origin at (0, 0, 1.0)			
A	7.41	0.00	7.41	7.72
B	8.03	0.07	7.96	8.09
C	8.69	0.24	8.45	8.45
	CPHF[c]			8.31
	MBPT4[d]			9.56
	Exp.[e]			9.62 ± .02

[a] All values are given in a.u.
[b] The zero entries are zero to three significant figures.
[c] Ref. 28; [d] Ref. 29; [e] Ref. 27

forms are indeed approaching their third resonance. It is compelling to note in these instances the inter-relation of the QRFs. In spite of their marked difference in value and their proximity to resonances, their sum compares reasonably to the other forms of the polarizability.

Conclusions

Equations of motion for quadratic response functions have been applied to develop relations between quadratic and linear response functions. These identities

TABLE V. Comparison of H₂O xx dynamic polarizability computed from the RPA ERF and QRF expressions obtained from EOM Eqs. (4) and (9).[a,b]

ω_k	Eq. (4)			Eq. (9)	
	$\sum p_i x_i l_i$	$\sum x_i x_i l_i$	Total	$\sum x_i p_i l_i$	$x_i x_i$
.00	9.54	4.22	9.01	9.01	9.16
.06	10.56	8.07	9.09	9.08	9.22
.09	11.61	11.33	9.19	9.17	9.32
.13	13.89	17.96	9.38	9.35	9.50
.23	3.79	17.94	10.12	10.28	10.44
.30	17.72	14.06	11.13	11.71	11.83
.46	123.44	256.91	25.79	22.71	26.64

[a] All values given in a.u.
[b] Calculated in basis C.
[c] Computed with $\omega_k = 0.13$ a.u.

TABLE VI. Comparison of H_2O yy dynamic polarizability computed from the RPA LRF and QRF expressions obtained from EOM Eqs. (4) and (9).[a,b]

	Eq. (4)[c]			Eq. (9)	
ω_B	$-2\langle\langle p_x; y, L_z\rangle\rangle_{\omega_B,\omega_C}$	$-2\langle\langle x; y, L_z\rangle\rangle_{\omega_B,\omega_C}$	Total	$-2\langle\langle y; p_x, L_z\rangle\rangle_{\omega_B,\omega_C=0}$	$\langle\langle y; y\rangle\rangle_{-B}$
.00	8.15	1.66	7.94	7.94	7.85
.06	8.86	4.55	8.03	8.03	7.93
.09	9.56	6.51	8.16	8.16	8.06
.13	10.77	9.42	8.41	8.41	8.31
.23	20.33	28.70	10.20	10.18	10.07
.30	125.84	235.64	24.75	24.90	24.64
.46	1526.6	2612.8	8.86	14.44	9.30

[a] All values given in a.u.
[b] Calculated in basis C.
[c] Computed with $\omega_C = 0.13$ a.u.

lead to formulas for static and frequency-dependent dipole polarizability from quadratic response. The expressions are constructed from position, momentum, and angular momentum, and have been identified as the response functions describing the Verdet constant. For C_{2v} point group symmetry, it is found that the origin-dependence of the angular momentum operator along the principal axis is a function of a translationally invariant QRF, while the other two Cartesian directions are invariant.

Under the random-phase approximation, the equations of motion are exact within a complete basis, and test calculations on H_2O show convergence of the polarizability values for extended basis sets. This provides a means to gauge the completeness of the chosen basis set toward its representation of both second- and third-order properties.

The utility of QRF methods which use the RPA EOM have been demonstrated here and in previous instances [5,7]. This work uses quadratic response to compute properties obtainable at the linear response level but, more importantly, underscores the fact that tractable relations exist between QRFs and LRFs. There yet exists the interesting possibility of applying this technique in the reverse sense; i.e., using LRFs to describe properties which would normally be associated with QRFs, providing a means to extract third-order properties at second order.

Acknowledgments

Bibliography

[1] J. Linderberg and Y. Öhrn. *Propagators in Quantum Chemistry* (Academic, London, 1973).
[2] J. Oddershede. Adv. Chem. Phys. **69**, 201 (1987).

[3] E. Dalgaard, Phys. Rev. A 26, 42 (1982).

[4] J. Olsen and P. Jørgensen, J. Chem. Phys. 82, 201 (1985).

[5] W. A. Parkinson and J. Oddershede, J. Chem. Phys. 94, 7251 (1991).

[6] P. Jørgensen, J. Oddershede, and D. L. Yeager, Comp. Phys. Rep. 2, 33 (1984).

[7] W. A. Parkinson, P. W. Sengeløv, and J. Oddershede, Int. J. Quantum Chem. Symp. 24, 487 (1990).

[8] P. W. Sengeløv and J. Oddershede, Chem. Phys. 124, 371 (1988).

[9] T. H. Dunning and V. McKoy, J. Chem. Phys. 47, 1735 (1967).

[10] T. H. Dunning and V. McKoy, J. Chem. Phys. 48, 52 (1968).

[11] H. Hettema, H. J. Aa. Jensen, P. Jørgensen, and J. Olsen, J. Chem. Phys. 97, 1174 (1992).

[12] H. J. Aa. Jensen, P. Jørgensen, H. Hettema, and J. Olsen, Chem. Phys. Lett. 187, 387 (1991).

[13] D. N. Zubarev, Sov. Phys. Usp. 3, 320 (1960).

[14] B. T. Pickup and O. Goscinski, Mol. Phys. 26, 1013 (1973).

[15] S. Eriksen, J. Geertsen, and J. Oddershede, Adv. Quantum Chem. (to appear).

[16] J. Geertsen, J. Chem. Phys. 90, 4892 (1989).

[17] J. Geertsen, F. Jensen, and G. E. Scuseria, J. Chem. Phys. 91, 364 (1989).

[18] J. Geertsen, Chem. Phys. Lett. 179, 479 (1991).

[19] R. Serber, Phys. Rev. 41, 489 (1932).

[20] D. M. Bishop and M. Cybulski, J. Chem. Phys. 93, 590 (1990).

[21] M. Faraday, Phil. Mag. 28, 294 (1846).

[22] E. M. Verdet, Ann. Chimie (3rd Ser.) 41, 370 (1854).

[23] W. A. Parkinson, J. Oddershede, S. P. A. Sauer, and D. M. Bishop, J. Chem. Phys. (to appear).

[24] In the original derivation of Ref. 13 the factor ½ was not included before the linear response function contributions. This is because the definition of the time-domain propagator for quadratic response lacked this factor. As pointed out in Ref. 3, this value is desirable so that the quadratic response function does not contain spurious poles, and also is more directly related to physical phenomena. When the factor ½ is included in quadratic response, it arises naturally in the derivation of the equations of motion.

[25] N. Gailar, W. S. Benedict, and E. K. Plyler, J. Chem. Phys. 24, 1139 (1956).

[26] G. H. F. Diercksen and W. P. Kraemer, Munich Reference Manual. Special Technical Report, Max Planck Institute for Physics and Astrophysics, Munich (1981).

[27] G. B. Bacskay, I. G. John, and N. S. Hush, Chem. Phys. 51, 49 (1980).

[28] P. Lazzeretti and R. Zanasi, J. Chem. Phys. 68, 1523 (1978).

[29] V. Kellö, G. H. F. Diercksen, and A. J. Sadlej, J. Chem. Phys. 79, 2918 (1983).

Gaussian-2 and Density Functional Studies of H₂N — NO₂ Dissociation, Inversion, and Isomerization

JORGE M. SEMINARIO and PETER POLITZER

Department of Chemistry, University of New Orleans, New Orleans, Louisiana. 70148

Abstract

Several computational approaches, including Gaussian-2 (G2) and nonlocal density functional theory (DFT-GGA), have been used to calculate the energy requirements for (a) H₂N — NO₂ dissociation (through N — N bond scission), (b) inversion of the amine group, and (c) isomerization through the nitro–nitrite rearrangement. Taking zero-point energies into account, the G2 predictions are 53.6 kcal/mole for the dissociation energy and 1.5 kcal/mole for the inversion barrier. The corresponding DFT-GGA values are 48.4 and 0.9 kcal/mole, and an activation energy of 48.7 kcal/mole for the nitro–nitrite rearrangement. The DFT-GGA results indicate that dissociation and rearrangement should be competitive for H₂N — NO₂. The same conclusion was reached earlier by Saxon and Yoshimine on the basis of MRCISD/6-31G* calculations, although their computed energy requirements differ from the present ones by approximately 8 kcal/mole. © 1992 John Wiley & Sons, Inc.

Introduction

The decomposition reactions of nitramines are of considerable interest because of the importance of these compounds as energetic materials [1,2]. Among the likely unimolecular processes that they may undergo are N — N bond scission and isomerization through the nitro–nitrite rearrangement, as shown in Eqs. (1) and (2) for the smallest nitramine, H₂N — NO₂:

$$H_2N - NO_2 \rightarrow H_2N + NO_2 \tag{1}$$

$$H_2N - NO_2 \rightarrow H_2N - ONO \tag{2}$$
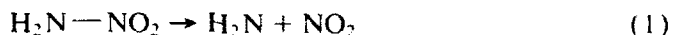
Saxon and Yoshimine have recently investigated reactions (1) and (2) computationally, at the MRCISD/6-31G*//MCSCF/4-31G level [3]. Taking zero-point energies into account, they found the N — N dissociation energy to be 40.55 kcal/mole, while the nitro–nitrite activation barrier was 40.70 kcal/mole. It was accordingly concluded that the two processes, Eqs. (1) and (2), are competitive. Melius and Binkley also studied reaction (1), using an MP4/6-31G**//HF/6-31G* procedure augmented by a bond additivity correction (BAC) [4]; they reported an N — N dissociation energy of 48.0 kcal/mole, of which more than 5 kcal/mole was the BAC contribution [3].

TABLE I. Optimized geometries (in angstroms and degrees) of the ground state of H_2N-NO_2.

	HF/6–31G*	MP2/6–31G*	DFT–LSDA DZVPP	DFT–GGA DZVPP	Expt.[a]	Expt.[b]
N—N	1.356	1.399	1.371	1.416	1.427	1.381
N—O	1.191	1.233	1.230	1.244	1.206	1.232
					(ass.)	
N—H	0.988	1.017	1.022	1.023	1.005	1.007
O—N—O	127.0	127.7	127.4	127.4	130.1	132.7
H—N—H	116.7	114.3	119.6	115.1	115.2	120.9
H—N—N—O	25.7	29.5	22.9	28.6	26.5	22.5

[a] Reference [23].
[b] Reference [24].

As part of a continuing investigation of density functional techniques [5,6], using precise *ab initio* calculations as a frame of reference, we have now examined reactions (1) and (2) by means of (a) the Gaussian-2 (G2) procedure [7], and (b) nonlocal density-functional theory (DFT), in the generalized gradient approximation (DFT–GGA) [8,9]. G2 theory is an *ab initio* method which has been shown to yield atomization energies, ionization potentials, electron affinities, and proton affinities for molecules containing first- and second-row atoms to within an average absolute deviation of less than 1.6 kcal/mole [7], relative to experimental results having an uncertainty of less than 1 kcal/mole. However G2 imposes severe demands upon computational resources, increasing with the number of basis functions as N^7, compared to N^3 for DFT.

Methods

Gaussian-2

The G2 procedure is based on Gaussian-1 (G1) [10,11], with corrections added to the energy. G1 uses MP2/6–31G* optimized geometries to compute

TABLE II. Optimized geometries (in angstroms and degrees) of the ground states of NO_2 and NH_2.

	HF/6–31G*	MP2/6–31G*	DFT–LSDA DZVPP	DFT–GGA DZVPP	Experiment[a]
NO₂					
N—O	1.165	1.216	1.209	1.225	1.197
O—N—O	136.1	133.7	133.5	132.3	133.8
NH₂					
N—H	1.012	1.028	1.041	1.043	1.024
H—N—H	104.3	103.3	102.9	101.8	103.3

[a] Reference [25].

TABLE III. Optimized geometries (in angstroms and degrees) of the planar form of H-N...NO.

	HF/6-31G*	MP2/6-31G*	DFT-LSDA/DZVPP	DFT-GGA/DZVPP
N—N	1.327	1.361	1.354	1.379
N—O	1.194	1.236	1.232	1.248
N—H	0.992	1.008	1.017	1.015
O—N—O	126.8	127.6	127.3	127.4
H—N—H	126.5	126.9	126.9	126.8

energies at the MP4/6-311G** level. These are improved through subsequent MP4/6-311 + G**, MP4/6-311G(2df,p) and QCISD(T)/6-311G** calculations; the difference between each of these and the original MP4/6-311G** energy is taken to represent, respectively, the effect of diffuse sp-functions on the heavy atoms, additional d and f polarization functions on the latter, and correlation beyond MP4. These three corrections are assumed to be additive. Finally an empirical term is added, which depends upon the numbers of valence electrons of α and β spins. The zero-point energy is computed from scaled HF/6-31G* frequencies.

TABLE IV. Optimized geometries (in angstroms and degrees) for the transition state of the nitro–nitrite rearrangement, Eq. (2).
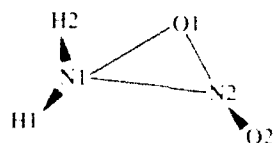
	DFT-GGA/DZVPP	MCSCF/4-31G*
N1—N2	2.831	2.845
N1—O1	3.193	3.214
N2—O1	1.229	1.212
N2—O2	1.224	1.207
N1—H	1.042	1.014
O1—N2—O1	131.7	133.1
H2—N1—H1	102.8	108.3
H2—N1—N2	95.5	96.3
H1—N1—N2	110.5	110.3
N1—N2—O1	95.5	96.4
N1—N2—O2	110.5	111.1
O2—N2—O1—N1	123.9	126.9
H1—N1—N2—O1	136.6	102.5
H2—N1—N2—O1	2.0	9.7

^a Reference [3].

TABLE V. Calculated total energies, in hartrees, for ground-state H_2N-NO_2, its dissociation products, and planar H_2N-NO_2.

	H_2N-NO_2 (ground state)	NH_2	NO_2	H_2N-NO_2 (planar)
HF/6-31G*	259.63941	55.55770	204.03149	259.63645
MP2/6-31G*	-260.35192	55.69375	204.56859	260.34700
MP4/6-311G**	260.52087	55.75310[a]	204.69102	260.51435
MP4/6-311 + G**	260.53715	55.75796[a]	204.70294	260.53108
MP4/6-311G(2df,p)	-260.66334	55.77971[a]	204.79941	260.65872
QCISD(T)/6-311G**	-260.51069	55.75444[a]	204.67501	260.50439
G1	-260.74312	55.80452[a]	204.84463	260.73917
G2	260.74628	55.80738[b]	204.84163	260.74239
DFT-LSDA/DZVPP	259.20225	55.41055	203.65776	259.20093
DFT-GGA/DZVPP	-261.39234	55.95635	205.34709	261.38945

[a] Reference [11].
[b] Reference [7].

G2 theory improves G1 by accounting for nonadditivity of the diffuse and polarization function corrections and by including a third d function on the heavy atoms and a second p on the hydrogens [7]. The empirical term is also modified. In the present study, the G2 calculations were carried out with the GAUSSIAN 90 program [12].

Density-Functional Theory

The Hohenberg–Kohn theorem [13] states that the energy of a system of electrons in an external potential $v(r)$ is a functional of the electronic density $\rho(r)$:

$$E[\rho(r)] = \int v(r)\rho(r)\, dr + F[\rho(r)] \tag{3}$$

TABLE VI. Calculated dissociation energies and inversion barriers for $H_2N—NO_2$, in kcal/mole. Zero-point corrections are not included.

	Dissociation energy	Inversion barrier
HF/6-31G*	31.5	1.9
MP2/6-31G*	56.2	3.1
MP4/6-311G**	48.2	4.1
MP4/6-311 + G**	47.8	3.8
MP4/6-311G(2df,p)	52.8	2.9
QCISD(T)/6-311G**	51.0	4.0
G1	59.0	2.5
G2	61.0	2.4
DFT-LSDA/DZVPP	84.0	0.8
DFT-GGA/DZVPP	55.8	1.8

Table VII. Gaussian-2 and nonlocal density functional results (in kcal/mole) for HN NO dissociation energy, amine group inversion barrier, and nitro-nitrite rearrangement activation energies. Zero-point corrections are included.

	Dissociation energy	Inversion barrier	Activation energy
G2	53.6	7.5	
DF-GGA	48.4	0.9	48.7

(In atomic and molecular calculations, the external potential is that due to the nuclei.) $F[\rho(r)]$ is a universal functional of the electron density. Hohenberg and Kohn also established the existence of a variational principle for $F[\rho]$. Later, Kohn and Sham [14] developed a working procedure to solve the N-electron problem, in which $F[\rho]$ was partitioned in the form,

$$F[\rho] = T_s[\rho] + \frac{1}{2}\int \frac{\rho(r)\rho(r')}{|r-r'|}\,dr\,dr' + E_{xc}[\rho] \tag{4}$$

in which $T_s[\rho]$ is the kinetic energy of a set of N noninteracting electrons having density $\rho(r)$ identical to the density in the real (interacting) system. $E_{xc}[\rho]$ is the exchange-correlation energy, whose functional form is unknown. Expressing $\rho(r)$ in terms of one-electron orbitals, and

$$\rho(r) = \sum_{i=1}^{N} |\varphi_i(r)|^2 \tag{5}$$

applying the variational principle to Eq. (3), subject to the condition of conserving the number of electrons, the N-particle problem is simplified eventually to solving a set of one-particle Schrödinger equations with the canonical form,

$$\left[-\frac{1}{2}\nabla^2 + v_{eff} \right]\varphi_i(r) = \epsilon_i\varphi_i(r) \quad i = 1, 2, \ldots, N \tag{6}$$

These are known as the Kohn–Sham equations. The effective potential v_{eff} is given by,

$$v_{eff}(r) = v(r) + \int \frac{\rho(r')\,dr'}{|r'-r|} + \frac{\delta E_{xc}[\rho]}{\delta\rho} \tag{7}$$

Once an approximation for $E_{xc}[\rho]$ has been selected, the Kohn–Sham equations can be solved in a self-consistent manner to obtain the orbitals φ_i and eigenvalues ϵ_i, and subsequently $\rho(r)$, $E[\rho]$ and other properties.

In the program deMon that was used in this work [15], $E_{xc}[\rho]$ is separated into exchange and correlation portions; for both of these, formulations in terms of the generalized gradient approximation (GGA) were selected:

$$E_{xc}[\rho] = E_x^{GGA}[\rho, \nabla\rho] + E_c^{GGA}[\rho, \nabla\rho] \qquad (8)$$

Perdew and Wang's expression was used for $E_x^{GGA}[\rho, \nabla\rho]$ [18]; when $\nabla\rho(\mathbf{r}) = 0$, this reduces to Dirac's formula for the uniform electron gas [16]. $E_c^{GGA}[\rho, \nabla\rho]$ was represented by Perdew's improved version [9] of the Langreth–Mehl functional [17]. This is made up of two terms, the first (which is the only term when $\nabla\rho = 0$) being the correlation energy of a uniform electron gas. This is expressed by the Vosco–Wilk–Nusair functional [18,19], which is based on the accurate quantum Monte Carlo calculations of Ceperley and Alder [20]. Thus our treatment of $E_{xc}[\rho]$ can be regarded as a local spin-density approximation (LSDA) plus gradient correction terms. (The LSDA assumes that $\rho(\mathbf{r})$ can be viewed as uniform locally [21].) An interesting review and comparison of nonlocal functionals implemented in deMon has been given by Mlynarski and Salahub [22].

A Gaussian basis set, the DZVPP, was used for the orbitals φ_i in the present computations; it is double-zeta for the valence electrons plus polarization functions (approximately equivalent to the 6-31G**). The program deMon also requires auxiliary basis sets for fitting the electron density and the exchange and correlation potentials; this is done to reduce the computational effort. We used the (4,3; 4,3)/ (5,1; 5,1) which includes four lone s-type and three constrained sets of s-, p-, and d-type functions on the heavy atoms, and five s-type and one set of s-, p-, and d- on the hydrogens.

Results

Tables I to IV present optimized geometries, at different computational levels, for (a) ground-state H_2N — NO_2, (b) its dissociation products in Eq. (1), (c) its planar form that is the transition state for the inversion of the amine group, and (d) the transition state for the nitro–nitrite rearrangement, Eq. (2). Experimental data are included where available; Table I shows that there are some discrepancies in the latter. There is consistently good agreement between the MP2/6-31G* and the DFT–GGA results. In optimizing the transition state for Eq. (2), we took Saxon and Yoshimine's geometry [3] as our starting point. The major changes are in some of the angles involving the hydrogens (Table IV). Saxon and Yoshimine had already noted that the 4-31G basis set does not position the hydrogens properly [3]. For ground-state and planar H_2N — NO_2, and for NH_2 and NO_2, the HF/6-31G* and MP2/6-31G* optimized geometries were confirmed to correspond to local energy minima by verifying that they have no imaginary frequencies.

Table V contains total energies, calculated at several computational levels, for ground-state H_2N — NO_2, its dissociation products in Eq. (1), and its planar form. Zero-point energies are not included. These data were used to obtain the H_2N — NO_2 dissociation energies and inversion barriers that are in Table VI. In the G1 and G2 procedures, zero-point energies are computed from scaled HF/6-31G* frequencies. These give correction terms of -7.4 kcal/mole for the dissociation energy and -0.9 kcal/mole for the inversion barrier. If we take the G2 results as our standard, then our predictions for the H_2N — NO_2 dissociation energy and inversion barrier are

53.6 and 1.5 kcal/mole, respectively (Table VII). Using the same zero-point corrections, our DFT–GGA/DZVPP values are 48.4 and 0.9 kcal/mole.

Finally, the DFT–GGA/DZVPP energy for the transition state in the nitro-nitrite rearrangement, Eq. (2), is −261.30519 hartrees. Using the zero-point correction term calculated by Saxon and Yoshimine [3], we find an activation energy of 48.7 kcal/mole (Table VII).

Discussion

The DFT–GGA/DZVPP dissociation energy for HN–NO underestimates the G2 value by 5.2 kcal/mole. This may indicate a need for a larger basis set for the DFT calculations. Nevertheless, both the dissociation energy and the inversion barrier computed by the DFT–GGA/DZVPP procedure are closer to the G2 results than are most of the correlated *ab initio* values.

As anticipated, the DFT–LSDA/DZVPP dissociation energy is much too large. It is well known that density functional theory in the local approximation overestimates dissociation energies [5,6,26–29]. This is apparently a reflection of size inconsistency in the LSDA approach: an undissociated molecule and its fragments are not treated at the same level of accuracy [29]. As can be seen in Table VI and has been shown elsewhere [26,29,30], this problem can be handled quite well by treating exchange and correlation in a nonlocal manner, as was done in this work through the gradient terms in Eq. (8). We have shown that the total energy errors in the local approximation vary in a systematic fashion with the numbers of electrons and nuclei [5,6], so that the resulting dissociation energies can also be corrected empirically. Size inconsistency is not a problem when a molecule is undergoing rearrangement rather than fragmentation; thus the DFT–LSDA inversion barrier in Table VI is reasonably close to the G2.

Our DFT–GGA calculations indicate that the energy requirements for Eqs. (1) and (2) are very similar, 48.4 and 48.7 kcal/mole, respectively (Table VII). (Both values include zero-point corrections.) Thus we reach the same conclusion as did Saxon and Yoshimine [3], that the two processes, HN–NO dissociation and its rearrangement to HN–ONO, are competitive. However we find the energies needed to be significantly larger, by about 8 kcal/mole, than did they. Our predicted dissociation energy is in fact very close to that obtained by Melius and Binkley [4], 48.0 kcal/mole, which supports their inclusion of the BAC term.

Summary

We have used the highly accurate G2 procedure to compute the N–N dissociation energy and the inversion barrier of HN–NO; our results are 53.6 and 1.5 kcal/mole, respectively. Nonlocal density functional calculations (DFT–GGA/DZVPP) yield 48.4 and 0.9 kcal/mole, both of which are closer to the G2 than are most of the results obtained by other correlated *ab initio* methods. Our DFT–GGA value for the activation barrier of the nitro-nitrite rearrangement of HN–NO is 48.7 kcal/mole, indicating that it should be competitive with scission of the N–N bond.

Acknowledgments

Bibliography

[1] T. Urbanski, *Chemistry and Technology of Explosives* (Pergamon, New York, 1984), Vol. 4, Chap. 13.

[2] R. Meyer, *Explosives* 3rd ed. (VCH, New York, 1987).

[3] R. P. Saxon and M. Yoshimine, J. Phys. Chem. **93**, 3130 (1989).

[4] C. F. Melius and J. S. Binkley, *Twenty-First Symposium International on Combustion* (Combustion Institute, Pittsburgh, 1986), p. 1953.

[5] J. M. Seminario, M. C. Concha, and P. Politzer, Int. J. Quantum Chem., Quantum Chem. Symp. **25**, 249 (1991).

[6] P. Politzer, J. M. Seminario, M. C. Concha, and J. S. Murray, Theor. Chim. Acta (in press).

[7] L. A. Curtiss, K. Raghavachari, G. W. Trucks, and J. A. Pople, J. Chem. Phys. **94**, 7221 (1991).

[8] J. P. Perdew and Y. Wang, Phys. Rev. B **33**, 8800 (1986).

[9] J. P. Perdew, Phys. Rev. B **33**, 8822 (1986).

[10] J. A. Pople, M. Head-Gordon, D. J. Fox, K. Raghavachari, and L. A. Curtiss, J. Chem. Phys. **90**, 5622 (1989).

[11] L. A. Curtiss, C. Jones, G. W. Trucks, K. Raghavachari, and J. A. Pople, J. Chem. Phys. **93**, 2537 (1990).

[12] GAUSSIAN 90, Revision F, M. J. Frisch, M. Head-Gordon, G. W. Trucks, J. B. Foresman, H. B. Schlegel, K. Raghavachari, M. Robb, J. S. Binkley, C. Gonzalez, D. J. DeFrees, D. J. Fox, R. A. Whiteside, R. Seeger, C. F. Melius, J. Baker, R. L. Martin, L. R. Kahn, J. J. P. Stewart, S. Topiol, and J. A. Pople, Gaussian, Inc., Pittsburgh, PA, 1990.

[13] P. Hohenberg and W. Kohn, Phys. Rev. B **136**, 864 (1964).

[14] W. Kohn and L. J. Sham, Phys. Rev. A **140**, 1133 (1965).

[15] D. R. Salahub, R. Fournier, P. Mlynarski, I. Papai, A. St. Amant, and J. Ushio, in *Density Functional Methods in Chemistry*, J. K. Labanowski and J. W. Andzelm, Eds. (Springer-Verlag, New York, 1991), Chap. 6.

[16] P. A. M. Dirac, Proc. Camb. Philos. Soc. **26**, 376 (1930).

[17] D. C. Langreth and M. J. Mehl, Phys. Rev. B **28**, 1809 (1983).

[18] S. J. Vosko, L. Wilk, and M. Nusair, Can. J. Phys. **58**, 1200 (1980).

[19] G. S. Painter, Phys. Rev. B **24**, 4264 (1981).

[20] D. M. Ceperley and B. J. Alder, Phys. Rev. Lett. **45**, 566 (1980).

[21] R. G. Parr and W. Yang, *Density-Functional Theory of Atoms and Molecules* (Oxford University Press, New York, 1989).

[22] P. Mlynarski and D. R. Salahub, Phys. Rev. B **43**, 1399 (1991).

[23] J. K. Tyler, J. Mol. Spectrosc. **11**, 39 (1963).

[24] N. I. Sadova, G. E. Slepnev, N. A. Tarasenko, A. A. Zenkin, L. V. Vilkov, I. F. Pankrushev, and A. Yu, Zh. Strukt. Khim. **18**, 865 (1977).

[25] M. D. Harmony, V. W. Laurie, R. L. Kuczkowski, R. H. Schwendeman, D. A. Ramsay, F. J. Lovas, W. J. Lafferty, and A. G. Maki, J. Phys. Chem. Ref. Data **8**, 619 (1979).

[26] A. D. Becke, J. Chem. Phys. **84**, 4524 (1986).

[27] M. Grodzicki, J. M. Seminario, and P. Politzer, J. Chem. Phys. **94**, 1668 (1991).

[28] E. Wimmer, in *Density Functional Methods in Chemistry*, J. K. Labanowski and J. W. Andzelm, Eds. (Springer-Verlag, New York, 1991), Chap. 2.

[29] T. Ziegler, Chem. Rev. **91**, 651 (1991).

[30] L. Fan and T. Ziegler, J. Chem. Phys. **94**, 6057 (1991).

Ab-Initio SCF Investigation of Glycolic Acid

MICHAEL A. FLOCK and MICHAEL RAMEK

*Institute for Physical and Theoretical Chemistry, Technical University Graz,
A-8010 Graz, Austria*

Abstract

The potential energy surface of glycolic acid was investigated using *ab-initio* 4-31G SCF calculations. Geometries, energies, and wavenumbers for all seven symmetry-unique local minima are reported together with all reaction paths and their energetical barriers. © 1992 John Wiley & Sons, Inc.

Introduction

The simplest of the α-hydroxy acid homologues, glycolic acid, is of some biological interest, for example as an important intermediate in the photorespiratory carbon oxidation cycle in higher plants and algae [1], as metabolite of ethylene glycol [2], or as metabolic precursor of oxalate in human beings [3]. As most of the bifunctional molecules glycolic acid is able to polymerize. Polyglycolic acid, as well as its co-polymeres with lactic acid, is biodegradable and utilized for absorbable sutures [4–6], for carriers for drug delivery systems [7,8], and for prostheses. Our interest in glycolic acid arose in the course of an *ab-initio* study of α-amino acids and related compounds [9–13]. *Ab-initio* calculations on glycolic acid were previously performed by Newton et al. [14] and by Ha et al. [15,16]. Newton et al. described four conformations, which were determined with a fixed set of bond lengths and angles with the 4–31G basis set. Ha et al. concentrated on mirror symmetrical conformations, which they optimized by gradient methods using the 4–21G and the 6–31G* basis set.

A complete investigation of the glycolic acid potential energy surface (PES) was carried out in our group as part of the *ab-initio* study mentioned above.

Local Minima

The conformations described in Ref. [16] were taken as starting points for our study. According to this study, the PES of glycolic acid consists of nine local minima. Four of them form two pairs of mirror symmetric conformers with C_1 symmetry. The remaining minima, including the global minimum, are of C_s symmetry. All energies and geometry data are given in the appendix, which also contains the structural formulae of all symmetry-unique minima.

The calculations were performed with the program GAMESS [17,18] using the standard *ab-initio* SCF (RHF) procedure [19] and the 4–31G split valence basis set [20]. All geometries are fully optimized with remaining maximum and root-mean-

square gradients less then 4×10^{-4} and 1.34×10^{-3} H bohr^{-1}. All minima (except VII) were verified to have only real frequencies and saddle points to have exactly one imaginary frequency. The frequency values were calculated using unscaled analytical second derivatives and the harmonic oscillator approximation. Conformer VII is a stationary point of inflexion. Such a point may be regarded as a special case of a local minimum, namely one without an energy barrier along one reaction path [21]. For such points the harmonic oscillator approximation is not adequate, which explains the imaginary frequency obtained for VII.

The following atom labeling is used throughout.

$$
\begin{array}{ccc}
\text{H2} & & \text{O1} \\
| & & // \\
\text{H1} - \text{O2} - \text{C2} - \text{C1} \\
| & & \backslash \\
\text{H3} & & \text{O3} - \text{H4}
\end{array}
$$
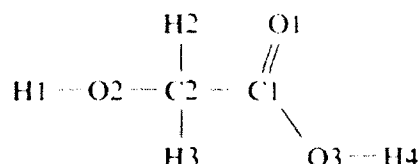
The minima of C_s symmetry compare well with the rotamers described by Ha et al. [16]. Rotamer 2 of [16] turned out to be a saddle point, which interconnects II with its mirror image II^m.

$$\text{II} \qquad\qquad \ddagger \qquad\qquad \text{II}^m$$
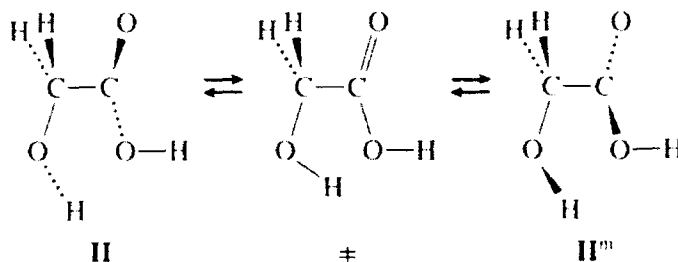
Similarly, rotamer 7 was found to be the saddle point in the reaction VII $\rightleftharpoons$ VII^m. Rotamer 8 turned out to be a second-order saddle point.

According to an analysis of the electron densities, two different intramolecular interactions can clearly be distinguished in the various minima. III, on the one hand, is stabilized by an intramolecular hydrogen bond with a H4$\cdots$O2 distance of 1.97 Å. On the other hand, the global minimum is stabilized by an electrostatic interaction with an H1$\cdots$O1 distance of 2.22 Å. The O $-$ H$\cdots$O $-$ H interactions in both II and the saddle point II $\rightleftharpoons$ II^m are also of electrostatic nature.

Reaction Paths

Reaction paths concerning the internal rotation of the O3 $-$ C1 bond (reaction paths 1 and 2), of the C1 $-$ C2 bond (reaction paths 3 and 4), and of the O2 $-$ C2 bond (reaction paths 5 and 6) were investigated in clockwise (1, 3, 5) and counterclockwise (2, 4, 6) direction. The results are collected in Table I.

Some of the reaction paths may be gathered from Figure 1, which shows a map of the potential energy as a function of the dihedral angles H1 $-$ O2 $-$ C2 $-$ C1 and O1 $-$ C1 $-$ C2 $-$ O2, with H4 $-$ O3 $-$ C1 $-$ C2 $\approx 180°$. The reaction paths in this map confirm that VII indeed has to be qualified as a local minimum, which

TABLE I   Initial and final geometries and energy barriers of the different reaction paths on the potential energy surface of glycolic acid. Reaction paths denoted with "—" cannot be realized. "TS" denotes the transition state I → II (see text)

Initial geometry	Final geometry					
	1 (O=C–C–O)	2	3 (H–O–C–C)	4	5 (H–O–C–C)	6
I	V 53.44	V 53.43	II 27.64	II 23.44	IV 27.64	IV 21.26
II	III 47.48	III 52.01	I 17.11	I 21.31	VII 18.45	II^m 1.99
III	II 44.96	II^m 40.43			V 52.48	V 57.61
IV	—		VII 8.86	VII^m 8.86	I 0.56	I 0.56
V	I 16.69	I 16.69	III 34.25	III 15.66	VI 28.04	VI 28.03
VI	—				V 0.18	V 0.18
VII	—		VII^m 3.62	IV 4.78	5.08	II

has no transition state in the reaction **VII → II** but distinct saddle points for all other reactions. This map also contains an interesting reaction, which has to be mentioned explicitly: decreasing the dihedral angle H1–O2–C2–C1 of **VII** induces a reaction, which, after passing a transition state, ends in the saddle point **I → II^m**. This reaction path is noteworthy, because there are no symmetry constraints forcing this behavior.

Basis Set Influence

Since *ab-initio* SCF results of H-bonded systems may critically depend on the basis set choice [22], the local minima described above were also optimized with the following standard basis sets: STO-3G [23], STO-6G [23], 3-21G [24], 6-31G [25], 6-31+G [25,26], 6-31++G [25,26], Dunnings 10s.5p/4s basis set [27], 6-311G [28], 6-31G* [25,29], 6-31G** [25,29], and 6-31+G** [25,26,29]. After this optimization frequencies were calculated with all basis sets. It turned out that the choice of basis set influences the relative energies and the values of most geometry parameters, but not the nature of the stationary points. As an example, Figure 2 shows the values of the bond length O2–C2 in all symmetry unique local minima with the various basis sets. These displays indicate that all basis sets except the minimal ones yield identical trends for the geometry data. Table II lists the deviations between the experimentally determined and the calculated rotational constants for the global minimum with all basis sets mentioned. These deviations are less then 1% for all split valence and double zeta basis sets, and up to 4% for basis sets with polarization functions and minimal basis sets.
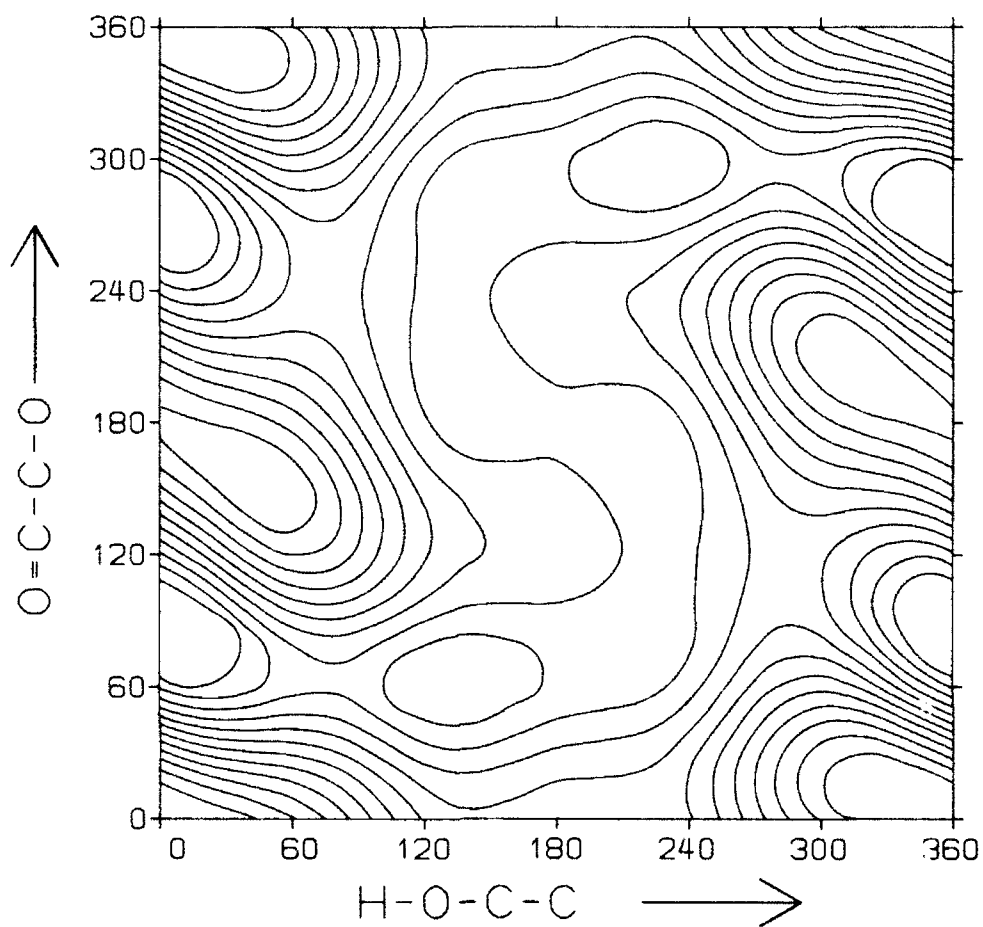
Figure 1. The potential energy as a function of the dihedral angles H1—O2—C2—C1 and O1—C1—C2—O2, with the dihedral angle H4—O3—C1—C2 = 180°. The local minima I (0°/0°), II (−40°/−150°), IV (180°/0°), and VII (−160°/−130°) are part of this map.

There is, however, another kind of basis set influence: the minimal basis sets and the basis sets with polarization functions give an additional local minimum **VIII** of C_1 symmetry, which has a very low energy barrier in the reaction **VIII** ⇌ **III**.

VIII   **III**
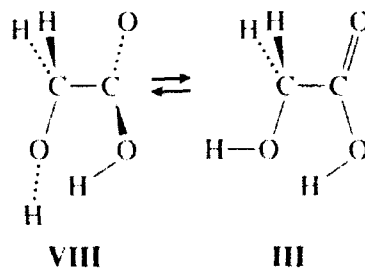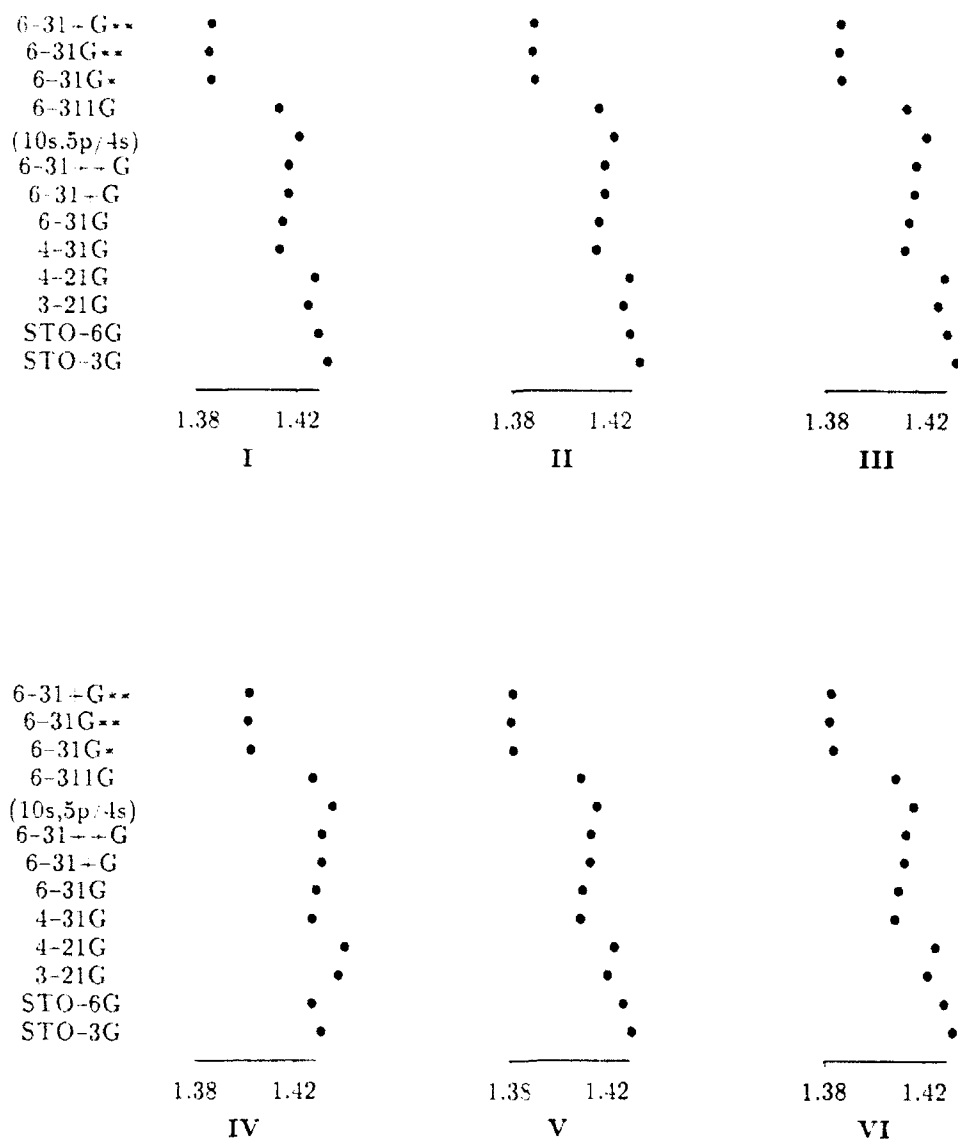
Figure 2. Basis set influence on the optimized value of the bond length O2—C2 [Å] in all local minima of the glycolic acid PES, except VII.

This barrier is 0.85 kJ/mol for the minimal basis sets, 0.33 kJ/mol for the 4–31G**, 0.30 kJ/mol for the 6–31G*, and 0.22 kJ/mol for the 6–31G** basis set. Using the 6–31+G** and the 6–31++G** basis sets VIII collapses with its saddle point to a stationary point of inflexion, which has no energy barrier to III.

Comparison with Glycine

The biological importance of hydrogen bonds makes a comparison of the O···H—O and N···H—O interactions worthwhile. The results of this study

TABLE II.   Ab-initio SCF(RHF) results for the glycolic acid conformation I obtained with various standard basis sets. The absolute energies are listed in Hartree, the rotational constants in GHz in differences from the experimental values [31] ($I_a = 10.6961$, $I_b = 4.0510$, $I_c = 2.9947$ GHz).

Basis	E_{el} [a.u.]	δI_a	δI_b	δI_c
STO-3G	-298.63524	0.1642	0.1571	0.1005
STO-6G	-301.51535	-0.1187	0.1433	0.0897
3-21G	-300.96339	0.0009	0.0145	0.0052
4-31G	-302.20754	0.0806	0.0097	0.0087
6-31G	-302.51371	0.0315	0.0114	0.0066
6-31+G	-302.52526	0.0215	0.0203	0.0121
6-31++G	-302.52575	0.0215	0.0203	0.0121
(10s, 5p/4s)	-302.57910	-0.0667	-0.0676	0.0451
6-311G	-302.59875	0.0784	0.0022	0.0041
6-31G*	-302.65697	0.2936	0.0647	0.0554
6-31G**	-302.67352	0.3044	0.0673	0.0577
6-31+G**	-302.68443	0.2888	0.0557	0.0503

and the analogous data for glycine [9,30] allow such a comparison in a straight-forward manner, since both were obtained at the same "level of theory".

The mean value of the O3 — H4 bond length in the conformations V and VI, which exhibit the same orientation of the — COOH group as III, is 0.9515 Å; the O3 — H4 length in III is 0.9572 Å, which means an increase of 0.0057 Å due to the intramolecular H-bond. The corresponding difference for glycine is 0.0082 Å, which indicates that the H-bond N · · · H — O is approximately 50% stronger than the O · · · H — O bond. A similar picture is obtained from the O3 — H4 vibration frequencies: the mean value in V and VI is 4006.9 cm^{-1}, the III value is 3924 cm^{-1}, which means a lowering of 82.9 cm^{-1}. The corresponding lowering in glycine is 142.3 cm^{-1}.

The different strength of the intramolecular H-bonds does not, however, influence the kinetic stability of these conformations: the lowest potential energy barrier is 40 kJ/mol for glycolic acid and 43 kJ/mol for glycine.

Acknowledgment

Appendix

Here the data of all local minima in the glycolic acid PES are given, which were obtained with the 4-31G [20] basis set in RHF calculations. Vibration frequencies were obtained via analytical second derivatives and have not been scaled.

The nuclear coordinates of all local minima are also available upon request from the authors by electronic mail.

Global Minimum I ($E_{el} = -302.20754$ a.u.)

Approximate geometry:
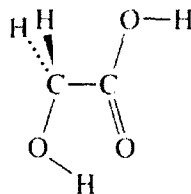
Geometry data:

Bond lengths:		Valence angles:		Dihedral angles:	
O1—C1	1.2071 Å				
C1—C2	1.4954 Å	C2—C1—O1	124.18°		
O2—C2	1.4127 Å	O2—C2—C1	111.12°	O2—C2—C1—O1	0.00°
H1—O2	0.9548 Å	H1—O2—C2	112.97°	H1—O2—C2—C1	0.00°
H2—C2	1.0800 Å	H2—C2—C1	108.84°	H2—C2—C1—O1	121.21°
H3—C2	1.0800 Å	H3—C2—C1	108.84°	H3—C2—C1—O1	-121.21°
O3—C1	1.3383 Å	O3—C1—C2	112.36°	O3—C1—C2—O2	180.00°
H4—O3	0.9554 Å	H4—O3—C2	114.73°	H4—O3—C1—C2	180.00°

Vibration frequencies:

48.910 cm^{-1}	256.09 cm^{-1}	299.53 cm^{-1}	505.99 cm^{-1}	560.87 cm^{-1}	698.17 cm^{-1}
699.55 cm^{-1}	929.63 cm^{-1}	1152.6 cm^{-1}	1160.9 cm^{-1}	1254.0 cm^{-1}	1368.0 cm^{-1}
1395.5 cm^{-1}	1466.9 cm^{-1}	1586.5 cm^{-1}	1660.4 cm^{-1}	1931.2 cm^{-1}	3234.5 cm^{-1}
3276.6 cm^{-1}	3960.5 cm^{-1}	3963.0 cm^{-1}			

Vibrational zero point energy: 187.870 kJ/mol

Rotation constants: $3.0034 \cdot 10^9$ s^{-1} $4.0607 \cdot 10^9$ s^{-1} $10.7767 \cdot 10^9$ s^{-1}

Local minimum II ($E_{el} = -302.20513$ a.u., $E_{rel} = 6.33$ kJ/mol)

Approximate geometry:
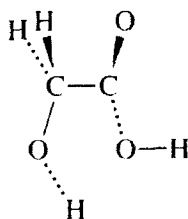
Geometry data:

Bond lengths:		Valence angles:		Dihedral angles:	
O1—C1	1.2033 Å				
C1—C2	1.4996 Å	C2—C1—O1	125.19°		
O2—C2	1.4140 Å	O2—C2—C1	113.22°	O2—C2—C1—O1	153.80°
H1—O2	0.9527 Å	H1—O2—C2	112.97°	H1—O2—C2—C1	-44.70°

H2—C2	1.0847 Å	H2—C2—C1	107.62°	H2—C2—C1—O1	82.66°
H3—C2	1.0748 Å	H3—C2—C1	108.69°	H3—C2—C1—O1	34.47°
O3—C1	1.3485 Å	O3—C1—C2	111.91°	O3—C1—C2—O2	29.28°
H4—O3	0.9552 Å	H4—O3—C2	114.56°	H4—O3—C1—C2	179.41°

Vibration frequencies:

87.836 cm⁻¹	285.80 cm⁻¹	380.44 cm⁻¹	511.17 cm⁻¹	575.67 cm⁻¹	647.63 cm⁻¹
730.08 cm⁻¹	908.1 i cm⁻¹	1116.0 cm⁻¹	1155.2 cm⁻¹	1241.0 cm⁻¹	i353.1 cm⁻¹
1458.4 cm⁻¹	1489.2 cm⁻¹	1540.0 cm⁻¹	1654.6 cm⁻¹	1950.9 cm⁻¹	3193.6 cm⁻¹
3329.5 cm⁻¹	3968.8 cm⁻¹	3995.0 cm⁻¹			

Vibrational zero point energy: 188.843 kJ/mol

Rotation constants: $3.0809 \cdot 10^9$ s⁻¹ $4.1898 \cdot 10^9$ s⁻¹ $10.0576 \cdot 10^9$ s⁻¹

Local minimum III (E_{el} = −302.20244 a.u., E_{rel} = 13.38 kJ/mol)

Approximate geometry:

Geometry data:

Bond lengths:		Valence angles:		Dihedral angles:	
O1—C1	1.2012 Å				
C1—C2	1.5102 Å	C2—C1—O1	121.37°		
O2—C2	1.4269 Å	O2—C2—C1	107.18°	O2—C2—C1—O1	180.00°
H1—O2	0.9497 Å	H1—O2—C2	115.43°	H1—O2—C2—C1	180.00°
H2—C2	1.0804 Å	H2—C2—C1	108.59°	H2—C2—C1—O1	59.24°
H3—C2	1.0804 Å	H3—C2—C1	108.59°	H3—C2—C1—O1	59.24°
O3—C1	1.3327 Å	O3—C1—C2	115.64°	O3—C1—C2—O2	0.00°
H4—O3	0.9572 Å	H4—O3—C1	113.72°	H4—O3—C1—C2	0.00°

Vibration frequencies:

106.33 cm⁻¹	267.36 cm⁻¹	349.91 cm⁻¹	558.33 cm⁻¹	634.33 cm⁻¹	669.52 cm⁻¹
722.44 cm⁻¹	920.03 cm⁻¹	1138.8 cm⁻¹	1146.1 cm⁻¹	1237.3 cm⁻¹	1371.3 cm⁻¹
1371.4 cm⁻¹	1454.0 cm⁻¹	1563.1 cm⁻¹	1657.5 cm⁻¹	1980.4 cm⁻¹	3227.2 cm⁻¹
279.2 cm⁻¹	3924.0 cm⁻¹	4036.2 cm⁻¹			

Vibrational zero point energy: 189.097 kJ/mol

Rotation constants: $3.1009 \cdot 10^9$ s⁻¹ $4.3097 \cdot 10^9$ s⁻¹ $10.3486 \cdot 10^9$ s⁻¹

Local minimum IV (E_{el} = −302.19965 a.u., E_{rel} = 20.70 kJ/mol)

Approximate geometry:
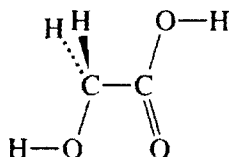
Geometry data:

Bond lengths		Valence angles		Dihedral angles	
O1—C1	1.1981 Å				
C1—C2	1.4947 Å	C2—C1—O1	128.35		
O2—C2	1.4116 Å	O2—C2—C1	108.75	O2—C2—C1—O1	0.00
H1—O2	0.9506 Å	H1—O2—C2	113.61	H1—O2—C2—C1	180.00
H2—C2	1.0827 Å	H2—C2—C1	107.76	H2—C2—C1—O1	121.91
H3—C2	1.0827 Å	H3—C2—C1	107.76	H3—C2—C1—O1	121.91
O3—C1	1.3350 Å	O3—C1—C2	108.91	O3—C1—C2—O2	180.00
H4—O3	0.9547 Å	H4—O3—C1	114.08	H4—O3—C1—C2	180.00

Vibration frequencies:

83.860 cm	191.70 cm	298.33 cm	509.20 cm	565.22 cm	629.27 cm
691.56 cm	918.37 cm	1143.5 cm	1167.8 cm	1234.3 cm	1310.1 cm
1391.0 cm	1442.7 cm	1542.9 cm	1660.3 cm	1979.6 cm	3201.7 cm
3242.2 cm	3975.2 cm	4016.3 cm			

Vibrational zero point energy: 187.288 kJ/mol

Rotation constants: 2.9619·10⁹ s⁻¹   4.3475·10⁹ s⁻¹   10.6641·10⁹ s⁻¹

Local minimum V (E₀): 302.19354 a.u., E₀ = 36.74 kJ/mol)

Approximate geometry:

Geometry data:

Bond lengths		Valence angles		Dihedral angles	
O1—C1	1.1909 Å				
C1—C2	1.5073 Å	C2—C1—O1	122.42		
O2—C2	1.4086 Å	O2—C2—C1	111.24	O2—C2—C1—O1	0.00
H1—O2	0.9560 Å	H1—O2—C2	112.50	H1—O2—C2—C1	0.00
H2—C2	1.0830 Å	H2—C2—C1	109.17	H2—C2—C1—O1	120.90
H3—C2	1.0830 Å	H3—C2—C1	109.17	H3—C2—C1—O1	120.90
O3—C1	1.3444 Å	O3—C1—C2	116.47	O3—C1—C2—O2	180.00
H4—O3	0.9518 Å	H4—O3—C2	117.84	H4—O3—C1—C2	0.00

Vibration frequencies:

86.640 cm	302.60 cm	306.76 cm	444.44 cm	504.58 cm	618.05 cm
720.03 cm	953.89 cm	1153.0 cm	1167.7 cm	1248.5 cm	1361.4 cm
1378.2 cm	1405.9 cm	1567.9 cm	1665.5 cm	1975.1 cm	3197.5 cm
3235.4 cm	3944.6 cm	4003.0 cm			

Vibrational zero point energy: 186.699 kJ/mol

Rotation constants: 2.9955·10⁹ s⁻¹   4.0640·10⁹ s⁻¹   10.6476·10⁹ s⁻¹

Local minimum VI (E_{el} = −302.18292 a.u., E_{rel} = 64.64 kJ/mol)

Approximate geometry:
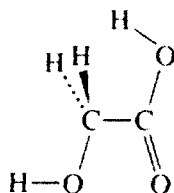
Geometry data:

Bond lengths:		Valence angles:		Dihedral angles:	
O1—C1	1.1906 Å				
C1—C2	1.5068 Å	C2—C1—O1	126.36°		
O2—C2	1.4080 Å	O2—C2—C1	109.04°	O2—C2—C1—O1	0.00°
H1—O2	0.9510 Å	H1—O2—C2	113.81°	H1—O2—C2—C1	180.00°
H2—C2	1.0859 Å	H2—C2—C1	108.12°	H2—C2—C1—O1	−121.62°
H3—C2	1.0859 Å	H3—C2—C1	108.12°	H3—C2—C1—O1	121.62°
O3—C1	1.3610 Å	O3—C1—C2	113.25°	O3—C1—C2—O2	180.00°
H4—O3	0.9512 Å	H4—O3—C2	118.03°	H4—O3—C1—C2	0.00°

Vibration frequencies:

60.630 cm⁻¹	187.97 cm⁻¹	298.42 cm⁻¹	383.72 cm⁻¹	508.24 cm⁻¹	623.80 cm⁻¹
700.67 cm⁻¹	918.45 cm⁻¹	1141.6 cm⁻¹	1175.7 cm⁻¹	1223.4 cm⁻¹	1310.2 cm⁻¹
1326.1 cm⁻¹	1399.0 cm⁻¹	1604.9 cm⁻¹	1665.9 cm⁻¹	2017.1 cm⁻¹	3162.0 cm⁻¹
3197.5 cm⁻¹	4009.6 cm⁻¹	4010.7 cm⁻¹			

Vibration frequencies:

60.630 cm^{-1}	187.97 cm^{-1}	298.42 cm^{-1}	383.72 cm^{-1}	508.24 cm^{-1}	623.80 cm^{-1}
700.67 cm^{-1}	918.45 cm^{-1}	1141.6 cm^{-1}	1175.7 cm^{-1}	1223.4 cm^{-1}	1310.2 cm^{-1}
1326.1 cm^{-1}	1399.0 cm^{-1}	1604.9 cm^{-1}	1665.9 cm^{-1}	2017.1 cm^{-1}	3162.0 cm^{-1}
3197.5 cm^{-1}	4009.6 cm^{-1}	4010.7 cm^{-1}			

Vibrational zero point energy: 184.976 kJ/mol

Rotation constants: $2.9486 \cdot 10^9$ s⁻¹ $3.9959 \cdot 10^9$ s⁻¹ $10.5211 \cdot 10^9$ s⁻¹

Local minimum VII (E_{el} = −302.19810 a.u., E_{rel} = 24.78 kJ/mol)

Approximate geometry:

Geometry data:

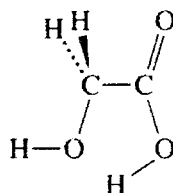| Bond lengths:		Valence angles:		Dihedral angles:	
O1—C1	1.2056 Å				
C1—C2	1.4967 Å	C2—C1—O1	124.38°		
O2—C2	1.4224 Å	O2—C2—C1	107.88°	O2—C2—C1—O1	−125.50°
H1—O2	0.9505 Å	H1—O2—C2	113.82°	H1—O2—C2—C1	−158.95°
H2—C2	1.0826 Å	H2—C2—C1	108.25°	H2—C2—C1—O1	113.56°
H3—C2	1.0777 Å	H3—C2—C1	107.90°	H3—C2—C1—O1	−5.05°
O3—C1	1.3403 Å	O3—C1—C2	112.74°	O3—C1—C2—O2	57.19°
H4—O3	0.9552 Å	H4—O3—C1	114.01°	H4—O3—C1—C2	−177.85°

Vibration frequencies:

98.490 i cm^{-1}	71.080 cm^{-1}	294.46 cm^{-1}	471.52 cm^{-1}	601.84 cm^{-1}	628.97 cm^{-1}
788.33 cm^{-1}	935.21 cm^{-1}	1107.2 cm^{-1}	1137.2 cm^{-1}	1271.8 cm^{-1}	1323.3 cm^{-1}
1389.2 cm^{-1}	1520.7 cm^{-1}	1596.6 cm^{-1}	1670.1 cm^{-1}	1945.0 cm^{-1}	3210.4 cm^{-1}
3289.4 cm^{-1}	3966.7 cm^{-1}	4016.9 cm^{-1}			

Vibrational zero point energy: 186.833 kJ/mol

Rotation constants: $3.1893 \cdot 10^9$ s^{-1} $4.1322 \cdot 10^9$ s^{-1} $9.5007 \cdot 10^9$ s^{-1}

Bibliography

[1] P. Jolivet, P. Gans, and C. Triantaphylides, Anal. Biochem. 147, 86 (1985).
[2] T. P. Hewlett, K. E. McMartin, A. J. Lauro, and F. A. Ragan, Clin. Toxicology 24, 389 (1986).
[3] M. Petrarulo, M. Marangella, and F. Linari, Clinica Chimica Acta 196, 17 (1991).
[4] E. J. Frazza and E. E. Schmitt, J. Biomed. Mater. Res. Symp. 1, 43 (1971).
[5] H. Dardik, I. Dardik, and H. Laufman, Am. J. Surg. 121, 656 (1971).
[6] C. C. Chu and N. D. Campbell, J. Biomed. Mater. Res. 16, 417 (1982).
[7] A. D. Schwope, D. L. Wise, and J. F. Howes, Life Sci. 17, 1877 (1975).
[8] D. L. Wise, G. J. McCormick, G. P. Willet, and L. C. Anderson, Life Sci. 19, 867 (1976).
[9] M. Ramek, Int. J. Quantum Chem., Quantum Biol. Symp. 17, 45 (1990).
[10] M. Ramek, J. Mol. Struct. (Theochem) 208, 301 (1990).
[11] A.-M. Kelterer, M. Flock, and M. Ramek, J. Mol. Struct. (Theochem) (accepted).
[12] A.-M. Kelterer and M. Ramek, J. Mol. Struct. (Theochem) 232, 189 (1991).
[13] M. Ramek, M. Flock, A.-M. Kelterer, and V. K. W. Cheng, J. Mol. Struct. (Theochem) (accepted).
[14] M. D. Newton and G. A. Jeffrey, J. Am. Chem. Soc. 99, 2413 (1977).
[15] T.-K. Ha, C. E. Blom, and H. H. Günthard, J. Mol. Struct. (Theochem) 85, 285 (1981).
[16] H. Hollenstein, T.-K. Ha, and H. H. Günthard, J. Mol. Struct. (Theochem) 146, 289 (1986).
[17] M. Dupuis, D. Spangler, and J. J. Wendoloski, N. R. C. C. Software Catalogue 1 Program No. QG01 (1980).
[18] M. W. Schmidt, K. K. Baldridge, J. A. Boatz, J. H. Jensen, S. Koseki, M. S. Gordon, K. A. Nguyen, T. L. Windus, and S. T. Elbert, QCPE Bulletin 10, 52 (1990).
[19] C. C. J. Roothaan, Rev. Mod. Phys. 23, 69 (1951).
[20] R. Ditchfield, W. J. Hehre, and J. A. Pople, J. Chem. Phys. 54, 724 (1971).
[21] P. G. Mezey, Potential Energy Hypersurfaces (Elsevier, Amsterdam, 1987), p. 73.
[22] M. Ramek, V. K. W. Cheng, R. F. Frey, S. Q. Newton, and L. Schäfer, J. Mol. Struct. (Theochem) 235, 1 (1991).
[23] W. J. Hehre, R. F. Stewart, and J. A. Pople, J. Chem. Phys. 51, 2657 (1969).
[24] J. S. Binkley, J. A. Pople, and W. J. Hehre, J. Am. Chem. Soc. 102, 939 (1980).
[25] W. J. Hehre, R. Ditchfield, and J. A. Pople, J. Chem. Phys. 56, 2257 (1972).
[26] T. Clark, J. Chandrasekhar, G. W. Spitznagel, and P. v. Ragué Schleyer, J. Comput. Chem. 4, 294 (1983).
[27] T. H. Dunning, Jr. and P. J. Hay, in Methods of Electronic Structure Theory, H. F. Schaefer III, Ed. (Plenum Press, New York, 1977), p. 1.
[28] R. Krishnan, J. S. Binkley, R. Seeger, and J. A. Pople, J. Chem. Phys. 72, 650 (1980).
[29] P. C. Hariharan and J. A. Pople, Theor. Chim. Acta 28, 213 (1973).
[30] M. Ramek and V. K. W. Cheng, Int. J. Quantum Chem., Quantum Biol. Symp. 19 (1992).
[31] C. E. Blom and A. Bauder, J. Am. Chem. Soc. 104, 2993 (1982).

Multireference Møller–Plesset Perturbation Treatment of Potential Energy Curve of N₂

K. HIRAO

Department of Chemistry, College of General Education, Nagoya University, Nagoya, Japan

Abstract

A multireference Møller–Plesset (MR-MP) perturbation method, at the second-order level, is applied to the potential energy curve of the ground state of N₂, for comparison with a variety of standard *ab initio* methods. In spite of the drastic simplification, the MR-MP results are very reliable. The energy errors are almost independent of geometry, allowing unbiased treatment of potential energy curves. The potential efficiency and accuracy of the MR-MP approach are emphasized. © 1992 John Wiley & Sons. Inc.

Introduction

During recent years the *ab initio* molecular orbital theory has moved from a qualitative theory to a quantitative one and being available to experimentalists. The conventional correlated theories are generally effective, at least, for medium-sized molecules in their ground state, near equilibrium geometry. Typically more than 98% of the full CI correlation energy is accounted for in a given basis set. However, the difficulty with these theories is that, as the number of electrons increases and the molecular bonds are stretched, the percentage of correlation energy recovered can decrease substantially. We are now seeing a similar evolution of techniques that are accurate for any large molecule in all nuclear configurations. At the present time reasonable accuracy can be obtained, but this is not obtained cheaply. In calculations of potential energy surfaces, it is particularly important to use an approach which provides a balanced description of the various regions of surface. In addition, the explicit determination of a wavefunction requires the calculation of the variables. Unfortunately, the number of variables is normally much too large for optimization, even though significant progress has been made in the solution of large-scale secular equations. For these reasons there has been a growing interest in multireference based perturbation methods [1–4].

In the previous article [4], we have developed a multireference Møller–Plesset (MR-MP) method. The essential feature of the theory is that the multireference technique is used as a means of recognizing nondynamical, near degeneracy, correlation effects and, as a consequence, of ensuring that a molecule correctly dissociates into its fragments. Once these state-specific correlation effects are included in a reference function, the remaining are composed mainly of dynamical, transferable pair correlations. It is really caused not by the full Coulomb repulsions but by the sum of fluctuation potentials as discussed by Sinanoğlu [5]. As a result of

TABLE I. Selected N_2 energies as a function of internuclear separation with Dzp + basis. Energies (E) are in hartree.

r (a_0)	SCI	MP2	MP4	CISD[a]	CCSD[a]
1.5	108.43726	108.70086	108.72011	108.70005	108.71269
1.8	108.90455	109.19682	109.21676	109.18794	109.20472
1.9	108.95142	109.25562	109.27558	109.24260	109.26115
2.0	108.96801	109.28553	109.30543	109.26741	109.28797
2.068	108.96662	109.29403	109.31385	109.27182	109.29388
2.5	108.83561	109.24415	109.26594	109.18054	109.21504
2.75	108.72623	109.19773	109.23075	109.09500	109.13919
3.0	108.61885	109.16547	109.23317	109.01092	109.06702
4.0	108.28943	109.24161	110.00465	108.76169	108.92926
5.0	108.10000	109.57697	115.94364	108.63123	—
6.0	107.99052	110.06605	131.76845	108.56262	—
100.	107.69824	—	—	108.42118	—

r (a_0)	MCSCI-52	MCSCF-176[a]	MR-CISD[a]	MR-CCM[a]	MR-MP2[b]
1.5	108.51797	108.52680	108.71080	108.71854	108.69087
1.8	109.01134	109.02217	109.20805	109.21663	109.18706
1.9	109.06853	109.07999	109.26634	109.27517	109.24528
2.0	109.09626	109.10832	109.29516	109.30422	109.27416
2.068	109.10290	109.11534	109.30254	109.31176	109.28163
2.5	109.03128	109.04536	109.23566	109.24590	109.21659
2.75	108.96255	108.97652	109.16931	109.18019	109.15223
3.0	108.90040	108.91310	109.10861	109.12020	109.09418
3.5	108.82035	108.82749	109.02613	109.03901	109.01648
4.0	108.79409	108.79695	108.98477	109.00561	108.98290
5.0	108.78887	108.78943	108.98040	108.99285	108.96693
6.0	108.78889	108.78903	108.97879	108.99110	108.96457
100.	108.78880	108.78880	108.97786	108.99004	108.96374

[a] Reference [9].

[b] The minimum energy is −109.28251 au at r 2.1035.

the short-range nature of the fluctuation potential, pair correlations are nearly independent. Thus, the pair correlations can be estimated, to a good approximation, by the second-order Møller–Plesset (MP) perturbation method [6] when near degeneracy is removed. To the second-order energy, the electron pairs decouple. The concept underlying our MR–MP approach is simple. That is, the independent electron pair model is effective if no near degeneracy is present. In the previous article [4], the MR–MP method was successfully applied to potential energy surface studies of chemical processes involving single bond breaking. In spite of the drastic simplification the MR–MP results were very reliable.

This study has as its main objective the testing of the effectiveness of the MR–MP approach for the description of a potential energy surface of the ground state N_2. After a brief discussion of the MR–MP theory in the next section, computational results are presented in the final section.
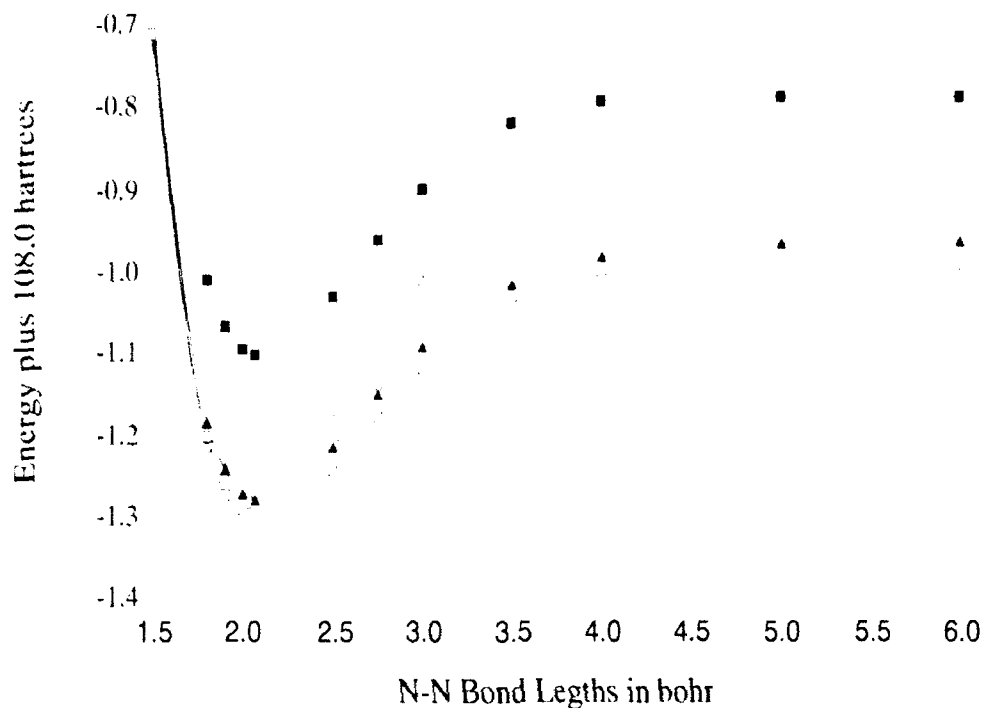
Figure 1. MCSCF-52, CISD, CCSD, MR-ICCM, and MR-MP potential curves for N_2. The various curves are identified as follows: (—■—) MCSCF-52; (—△—) CISD; (—○—) CCSD; (—□—) MR-ICCM; and (—▲—) MR-MP.

Multireference Møller–Plesset Method

We start with the MCSCF wavefunctions with energies that can be expressed as

$$ E = 2 \sum_i f_i h_{ii} + \sum_{ij} (a_{ij} J_{ij} - b_{ij} K_{ij}) \tag{1} $$

where the summation runs over orbital basis functions $\{ \varphi_i \}$ in terms of which the wavefunction is described. Here the f_i are given by

$$ 2 f_i = D_i^i \tag{2} $$

where D_i are diagonal elements of the one-electron density matrix. The a_{ij} and b_{ij} are energy coefficients and J_{ij} and K_{ij} indicate the usual Coulomb and exchange integrals, respectively. Requiring that the energy be stationary with respect to all orbital variations leads to the general variational condition

$$ \sum_i \langle \delta \varphi_i | F_i^{MCSCF} | \varphi_i \rangle = 0 \tag{3} $$

where F_i^{MCSCF} is the generalized Fock operator

TABLE II. Equilibrium bond length and
dissociation energy for N_2.

Method	r_e (Å)	D_e (eV)
SCI	1.0703	34.57
CSD[a]	1.0958	23.15
CCSD[a]	1.1037	9.93[b]
MCSCI-52	1.1087	8.560
MCSCI-176[a]	1.1098	8.903
MR-SDCI[a]	1.1120	8.857
MR-LCCM[a]	1.1128	8.778
MR-MP	1.1131	8.674
Experiment	1.0977	9.91

[a] Reference [9].
[b] The dissociation energy is computed as
the difference between the minimum and
4.0 bohr energy.

$$F_i^{MCSCI} = f_i h + \sum_j (a_{ij} J_j - b_{ij} K_j) \qquad (4)$$

Now let us consider the perturbation theory based on the MCSCF function. Many-body perturbation theory is useful only if the zeroth-order Hamiltonian H_0 is a one-electron operator. Experience shows that, for closed-shell systems, the best results are obtained with the MP partitioning, that is, with the sum of one-electron Fock operator as H_0. The possible choice of the one-electron operator for the MR case is the generalized Fock operator given by Eq. (4). However, one disadvantage of the choice is lack of the physical meaning of the operator unlike the closed-shell case. A one-electron operator which is closely analogous to the closed-shell Fock operator can be defined for MCSCF wavefunctions as

$$F = h + \sum_i f_i (2J_i - K_i) \qquad (5)$$

In order to remove the arbitrariness of the density weighting, we use the *natural orbitals*. That is, canonical MCSCF orbitals are transformed to the natural orbitals before perturbing. The complete active space (CAS) SCF wavefunction [7] is invariant to unitary transformations among the active orbitals, provided the CI coefficients are reoptimized. This definition is unique and can be extended to the virtual space. The orbital energies for the doubly occupied orbitals correspond to the Koopmans' ionization potentials and those for virtual orbitals to the Koopmans' electron affinities. The orbital energies for active orbitals are the average of ionization potentials and electron affinities. The F is not diagonal in a basis of orbitals. The one-electron operator in the sense of diagonal form can be redefined in terms of natural orbitals $\{\lambda_r\}$ as

$$\hat{F} = \sum_r |\lambda_r\rangle\langle\lambda_r| F |\lambda_r\rangle\langle\lambda_r| \qquad (6)$$

TABLE III. Energy errors $(E - E_{MR-CCSD}$ in millihartree) for N

r (a.u.)	SCF	MP2	CISD[a]	CCSD[a]
1.5	281.28	17.68	18.49	5.88
1.8	312.98	19.81	28.69	11.92
1.9	323.75	19.55	32.5	14.32
2.0	336.21	18.69	36.81	16.25
2.068	345.14	17.73	39.04	17.88
2.5	410.29	1.75	65.36	30.86
2.75	453.96	17.54	88.19	41.00
3.0	501.35	45.27	109.28	53.18
4.0	716.18	236.00	243.92	76.35
5.0	892.85	584.12	361.62	—
6.0	1000.58	1074.95	425.48	—
100.	1291.80	—	568.86	—

r (a.u.)	MCSCF-52	MCSCF-176[a]	MR-CISD[a]	MR-MP
1.5	200.57	191.74	7.74	27.67
1.8	205.29	194.46	8.58	29.57
1.9	206.64	195.18	8.83	29.89
2.0	207.96	195.90	9.06	30.06
2.068	208.86	196.42	9.22	30.13
2.5	214.62	200.54	10.20	29.31
2.75	217.64	203.67	10.88	27.96
3.0	219.80	207.10	11.59	26.15
3.5	218.66	211.52	12.88	22.53
4.0	211.52	208.66	20.84	22.71
5.0	203.98	203.42	12.45	25.92
6.0	202.21	202.07	12.31	26.83
100.	201.24	201.24	12.38	26.30

[a] Reference [9]

We then have eigenfunctions Φ_I and eigenvalues H_I of the zeroth-order Hamiltonian H_0

$$H_0\Phi_I = H_I\Phi_I \qquad (7)$$

with

$$H_0 = \sum_I |\Phi_I\rangle\langle\Phi_I| \sum_i F(i) |\Phi_I\rangle\langle\Phi_I| \qquad (8)$$

The Φ_0 is the MCSCF wavefunction with the eigenvalue

$$H_0 = 2 \sum_i \langle\lambda_i| F |\lambda_i\rangle \qquad (9)$$

The sum in Eq. (8) goes over all possible orthonormal configurations $\{\Phi_I\}$ which may be constructed from the occupied and virtual orbitals. The functions $\{\Phi_I^{(1)}\}$
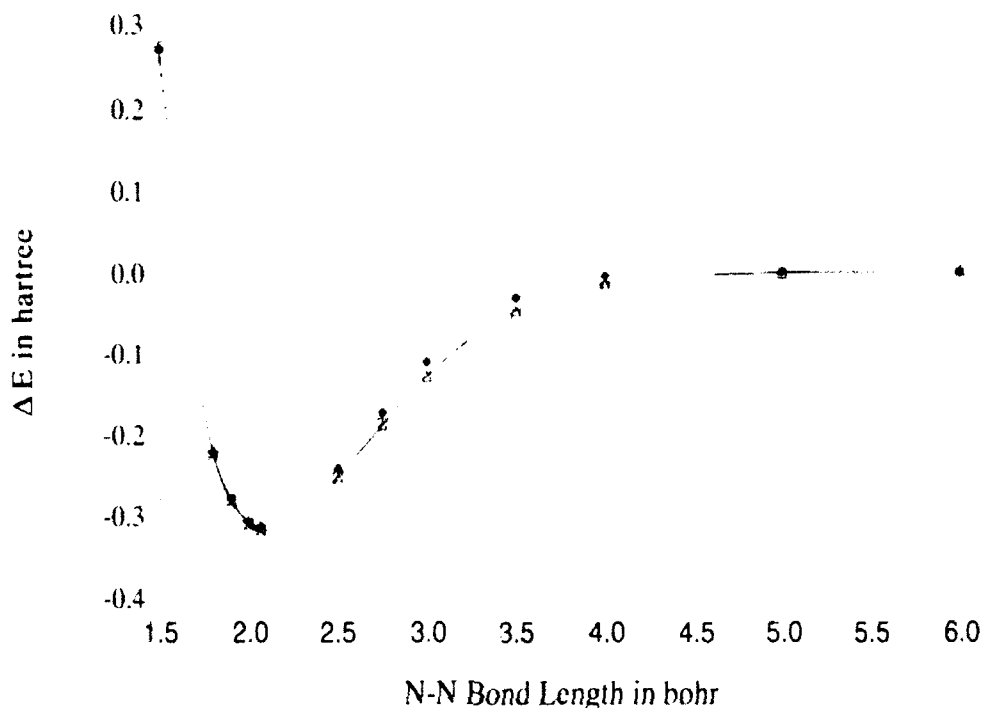
Figure 2. MCSCF-52, MR-MP, and MR-I CCM potential curves for N₂ shifted such that their respective dissociated energies are zero. The various curves are identified as follows: (—◆—) MCSCF-52; (—□—) MR-MP; and (—△—) MR-I CCM.

which span the first-order space used here are mutually orthogonal, orthogonal to all configurations in the reference. However, the first-order basis generated by double excitations of the reference wavefunction[1,3] is not orthogonal and orthogonalization step is necessary to avoid the complications of perturbation calculations in a nonorthogonal basis. The perturbation is $V = H - H_0$. This choice of H_0 in the Rayleigh–Schrödinger perturbation series guarantees size consistency if the reference function is size consistent. There is a very close parallel between the standard single reference MP theory and its MR version. The first-order wavefunction, for instance, contains only double substitutions. Singles cannot contribute due to the generalized Brillouin theorem [8]. Triples and higher substitutions are also excluded because any configurations having a nonzero matrix element with the reference function do not enter into the first-order correction to the wavefunction.

The present MR–MP method is very efficient and cost effective. Neither iteration nor diagonalization is necessary in the calculation of the first-order corrections. The importance of efficiency cannot be overestimated.

Potential Curve of N₂

The ground-state potential energy surface for N_2 has been well studied [9] by a variety of standard *ab initio* techniques such as single reference CI singles and doubles

TABLE IV. External, semi-internal, and internal contributions to the correlation energy for the ground state of N_2. Energies (E) are in hartree.

	Contributions			Total	
r (a₀)	External	Semi-internal	Internal	$E_{SRE\ MP}$	E_{MCSCF}
1.5	0.11363	0.08322	0.00605	0.17290	
1.8	0.10875	0.05951	0.00745	0.17572	
1.9	0.10723	0.06164	0.00788	0.17675	
2.0	0.10578	0.06382	0.00829	0.17789	
2.068	0.10484	0.06534	0.00855	0.17873	
2.5	0.09981	0.07575	0.00974	0.18530	
2.75	0.09796	0.08192	0.00981	0.18969	
3.0	0.09711	0.08750	0.00917	0.19378	
3.5	0.09790	0.09242	0.00581	0.19612	
4.0	0.09913	0.08697	0.00272	0.18884	
5.0	0.10094	0.07655	0.00057	0.17806	
6.0	0.10172	0.07383	0.00013	0.17568	
100.	0.10176	0.07318	0.00000	0.17494	

(CISD), finite-order MP perturbation theory, coupled cluster singles and doubles (CCSD) [10], multireference CISD (MR–CISD) and linearized MR coupled cluster method (MR–LCCM) [11]. We also apply our MR–MP approach, at the second-order level (MR–MP2), to the bond-breaking process of N_2. The basis set (DZ p+) and geometries used in the present calculations were identical to those used by Laidig, Saxe, and Bartlett [9]. The reference space for the MR–MP method was of the CAS SCF type. The CAS SCF wavefunctions were obtained by distributing six electrons among the six 2p active orbitals, corresponding to 52 reference configurations. This is the smallest active space which leads to the qualitatively correct description of the triple bond dissociation process. On the other hand, MR–CISD and MR–LCCM results by Bartlett et al. [9] were obtained based on the CAS SCF function with 176 reference functions. The MCSCF calculations will be distinguished via either a –52 or a –176 suffix. The two 1s-core orbitals were frozen.

Results obtained for the potential curves of N_2 with the DZ p+ basis set are given in Table I and Figure 1. The dissociation energies (D_e) and equilibrium distances (r_e) are listed in Table II.

The SCF potential well is over three times as deep as the experimental values of 9.91 eV and the equilibrium distance is nearly 0.03 Å shorter. The single reference based finite-order perturbation series was found to diverge beyond approximately 3.0 bohr. Even in the minimum region the series is oscillatory. The single reference CISD dissociation energy is still too high by over a factor of 2 compared to experiment. The CISD and experimental r_e values differ by only 0.002 Å. The full CI r_e in this basis is estimated around 1.113 Å [9]. If this is the case, the CISD r_e is nearly 0.02 Å too short. The CCSD, which is equivalent to our symmetry adapted cluster (SAC) theory [12], appears to give a much better estimate of r_e. Also the CCSD curve is accurate out to 4.0 bohr. However, it was reported that CCSD curve beyond 4.5
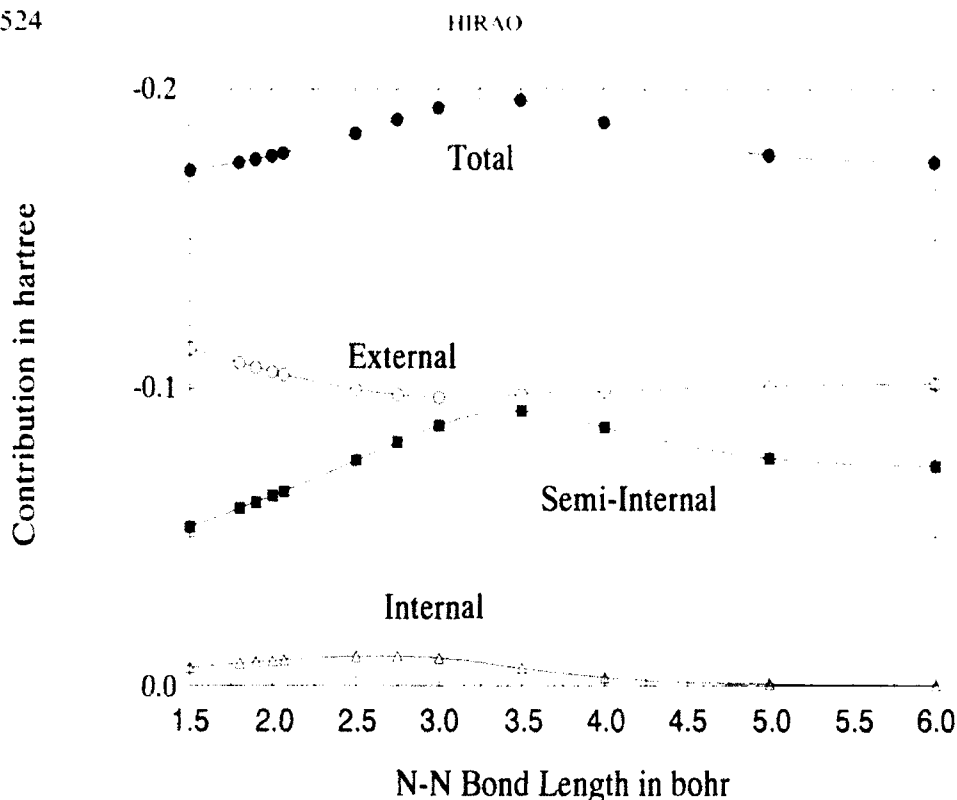
Figure 3.   External, semi-internal, and internal contributions to the total correlation energy
($E_{MR\ MP2}$ − E_{MCSCF}), in hartree, as a function of the internuclear separation.

bohr cannot be obtained due to the convergence difficulties of the CCSD equations
[9]. Thus, none of these single reference based methods can describe all regions of
the N_2 potential curve to high accuracy.

Now let us examine the energy errors along the bond lengths. Since the full CI
calculations are not available in this basis set, we defined the energy error as the
difference between the computed energy and the MR-LCCM energy. These energy
errors are displayed in Table III. In the calculation of potential energy surfaces, it
is important to keep this error as constant as possible, in order to obtain an accurate
surface. It is obvious from Table III that the single reference based methods cannot
be expected, in general, to satisfy this requirement. Appropriate multireference
based methods, on the other hand, can give a more balanced treatment and nearly
constant errors.

The dissociation energies and equilibrium geometries have been improved in the
MR based methods. The MCSCF-52 surface itself contains no substantial qualitative
defects. Like MR-CISD and MR-LCCM, the MR-MP2 energy curve dissociates correctly
and the three are nearly parallel. While the MR-MP is size consistent, the MR-CISD
is not rigorously size consistent just like any truncated CI. The present MR-MP2
gives D_e = 8.67 eV and r_e = 1.113 Å. The D_e is computed only 12% in error and
r_e is within 0.015 Å of experiment and nearly identical with the estimated full CI

r_e. In Figure 2 we draw potential curves for N_2 computed in MCSCI-52, MR-MP2, and MR-LCCM methods shifted such that their respective dissociated energies are zero. The MCSCI-52 dissociation energy of 8.56 eV is within 0.22 eV of the MR-LCCM result. However, the MCSCI-52 curve deviates most from MR-LCCM surface in the region surrounding 3.5 bohr. On the contrary, the MR-MP2 curve is quite close to the MR-LCCM curve for the entire bond lengths. This suggests that the higher order contributions are almost independent of the internuclear configuration and therefore cancel in a calculation of potential energy surfaces.

In terms of the Fermi sea determined by the reference function the first-order corrections to the wavefunction may be classified in terms of the number (0, 1, or 2) of external orbitals introduced as internal, semi-internal, and external. In Table IV and Figure 3 we showed external, semi-internal, and internal contributions to the total correlation energy, ($E_{MR MP} - E_{MCSCI}$), as a function of the bond length. The internal correlation is found to be small within 0.01 au. The semi-internal terms include significant single excitations which arise from the failure of the reference function to satisfy the Brillouin theorem. Although the semi-internal correlation is about half of the external correlation near the equilibrium distance, it increases as the bond length and becomes maximum at about 3.5 bohr and competitive to the external correlation. The external terms resemble the pair correlations of the closed-shell theory. As expected the external terms are found to be rather insensitive to the change of the bond length. Therefore, the total correlation curve is almost parallel to the semi-internal curve. This suggests that the balanced description of the potential curves cannot be obtained before the semi-internal terms are correctly taken into account.

The MR-MP method is designed to compete directly against the traditional highly correlated methods. The theory retains the attractive features of the single reference MP theory without a consequent loss of efficiency. The MR-MP results were shown to compare favorably with those of the highly correlated methods for the description of the triple bond breaking. The present approach is very powerful as a reliable method for the computation of correlation energy where errors of the order of a few percent are acceptable.

Acknowledgments

Bibliography

[1] K. Wolinski, H. L. Sellers, and P. Pulay, Chem. Phys. Lett. 140, 225 (1987).
[2] J. J. W. McDouall, K. Peasley, and M. A. Robb, Chem. Phys. Lett. 148, 183 (1988).
[3] K. Andersson, P. Malmqvist, B. O. Roos, A. J. Sadlej, and K. Wolinski, J. Phys. Chem. 94, 5483 (1990); K. Andersson, P. Malmqvist, and B. O. Roos, ibid. 96, 1218 (1992).
[4] K. Hirao, Chem. Phys. Lett. 190, 374 (1992).

[5] O. Sinanoğlu. J. Chem. Phys. **36**, 706 (1962); *ibid.* **36**, 3198 (1962); Adv. Chem. Phys. **6**, 315 (1964).

[6] C. Møller and M. S. Plesset. Phys. Rev. **46**, 618 (1934).

[7] P. E. Siegbahn, A. Heiberg, B. O. Roos, and B. Levy. Physica Scripta **21**, 323 (1980); B. Roos, P. R. Taylor, and P. E. Siegbahn, Chem. Phys. **48**, 157 (1980); B. O. Roos, Int. J. Quantum Chem. **S14**, 175 (1980).

[8] B. Levy and G. Berthier, Int. J. Quantum Chem. **2**, 307 (1968).

[9] W. D. Laidig, P. Saxe, and R. J. Bartlett, J. Chem. Phys. **86**, 887 (1987).

[10] R. J. Bartlett, Ann. Rev. Phys. Chem. **32**, 359 (1981).

[11] W. D. Laidig and R. J. Bartlett, Chem. Phys. Lett. **104**, 424 (1984).

[12] H. Nakatsuji and K. Hirao, J. Chem. Phys. **68**, 2053 (1978); K. Hirao, J. Chem. Phys. **79**, 5000 (1983).

[13] M. Dupuis, J. D. Watts, H. O. Villar, and G. J. B. Hurst, IBM Technical Report KGN-181 (1988). QCPE Program #544, University of Indiana.

Hydrogen Bonding: Methodology and Applicati
Complexes of HF and HCl with HCN and CH₃C?

JANET E. DEL BENE

Department of Chemistry, Youngstown State University, Youngstown, Ohio 44555

Abstract

A detailed investigation has been made of the methodological dependence of computed structures, binding energies, and some vibrational properties of selected hydrogen-bonded complexes. Structures and vibrational frequencies have been computed using four different levels of theory: HF/6-31G(d), HF/6-31+G(d, p), MP2/6-31G(d), and MP2/6-31+G(d, p). Correlation energy effects on computed binding energies and the basis set dependence of these energies have been evaluated using the Dunning correlation-consistent polarized valence double-, triple-, and truncated quadruple-split basis sets (cc-pVXZ, with X = D for double, T for triple, and Q for truncated quadruple), and these same basis sets augmented with diffuse functions on nonhydrogen atoms (cc-pVXZ+). The results of these studies suggest that the methodology of MBPT(4) = MP4/cc-pVTZ+ electronic energies without the counterpoise correction computed at MP2/6-31+G(d, p) geometries is an appropriate theoretical model for investigating complexes RCN···HX, with R = H or CH₃ and X = F or Cl. This model has been applied to investigate the structures, binding energies at absolute zero, binding enthalpies at room temperature, and vibrational frequencies of these complexes. Trends are noted, and comparisons are made with available experimental data. © 1992 John Wiley & Sons, Inc.

Introduction

Ab initio studies of hydrogen bonding date back about 20 years. In that time, great strides have been made, but the demands on theory have also increased. With new methodologies, improved algorithms, and supercomputers, it is incumbent upon theory to provide reliable quantitative information about hydrogen-bonded systems with an accuracy comparable to that which can be measured experimentally. Thus, a goal of modern theory is the reliable prediction of the structures of hydrogen-bonded complexes, their binding energies to about 1 kcal/mol, and their spectroscopic properties. This article reports the results of a systematic study of the dependence of some of these properties on the level of theory employed for the calculations. The computed results are evaluated by two criteria, one internal and the other external. The internal criterion refers to convergence of computed properties with respect to further extensions of the level of theory; the external is comparison with experimental data. Ideally, when the internal criterion has been satisfied, the agreement between theory and experiment should also be good. Unfortunately, there can be problems with the application of these criteria. In some cases, it is not feasible from a calculational point of view to go beyond a particular level of theory,

so the internal criterion cannot always be applied. In other cases, reliable experimental data may not be available. Despite these limitations, systematic investigations of the methodological dependence of computed properties of hydrogen-bonded complexes are essential for progress in this area. The results of such an investigation will be reported here, and will be used to identify an appropriate level of theory for investigating the structures and energies of hydrogen-bonded complexes $RCN \cdots HX$, where $R =$ H or CH_3 and $X =$ F or Cl.

Method of Calculation

The structures of the monomers HF, HCl, HCN, and CH_3CN and the complexes $CH_3CN \cdots HF$, $HCN \cdots HF$, $CH_3CN \cdots HCl$, and $HCN \cdots HCl$ have been optimized at Hartree–Fock (HF) and at second-order many-body Møller–Plesset pertubation theory [1–4] (MP2) with two different basis sets, 6-31G(d) and 6-31+G(d, p). 6-31G(d) is a split-valence basis set with d polarization functions on nonhydrogen atoms [5,6]. 6-31+G(d, p) is the same split-valence basis with first polarization functions on all atoms and diffuse functions on nonhydrogen atoms [7,8]. Harmonic vibrational frequencies have been computed for all structures to verify that they are equilibrium structures (no imaginary frequencies) on the appropriate potential surface, and to evaluate zero-point and thermal vibrational energies.

The electronic binding energy of each complex at absolute zero is defined as ΔE_e^0 (or $-D_e$) for the reaction $RCN + HX \rightarrow RCN \cdots HX$, where $R =$ H or CH_3 and $X =$ F or Cl. The binding enthalpy, ΔH^{298}, can be obtained from ΔE_e^0, the zero-point and thermal vibrational energies, and other thermal terms, with these latter terms (rotational and translational energy terms and the PV work term) evaluated classically. The nature of the zero-point energy contribution and its dependence on the calculational model will be examined in this study.

To obtain an estimate of the variation of binding energies and the basis set superposition error [9] with basis set size, calculations have been performed on a selected group of hydrogen-bonded complexes using the Dunning correlation-consistent polarized double-, triple-, and quadruple-split valence basis sets (cc-pVXZ, where $X = D$ for double, T for triple, and Q for quadruple) [10], and these basis sets augmented with diffuse s and p functions on nonhydrogen atoms (cc-pVXZ+), with exponents of 0.04, 0.06, 0.08, and 0.10 for carbon, nitrogen, oxygen, and fluorine, respectively. These basis sets were chosen because they systematically increase the valence space as the polarization space is also increased, and include a quadruple-split valence basis set. Since the GAUSSIAN 90 program [11], which was used for all calculations, cannot handle g functions, the Dunning quadruple-split basis has been truncated in the polarization space to include three sets of first polarization functions and two sets of second polarization functions on all atoms, omitting the third polarization g functions on first-row atoms, and f functions on hydrogen (cc-pVQZ' and cc-pVQZ'+). The Dunning basis sets have not been defined for chlorine, so the chlorine basis used with cc-pVTZ+ is the McLean–Chandler (12, 9) basis set contracted to (6, 5) [12] augmented with a set of diffuse

s and p functions, two sets of d functions, and a set of f functions, with exponents taken from the 6-31 + G(2df, 2pd) basis set. For reasons of computational feasibility, the basis set study has been carried out on a group of small hydrogen-bonded complexes, including (HF)$_2$, (H$_2$O)$_2$, (NH$_3$)$_2$, H$_3$N$\cdots$HF and HCN$\cdots$HF, the latter representative of the complexes RCN$\cdots$HX, with R = H or CH$_3$ and X = F or Cl. Binding energies for the complexes of HF and HCl with HCN and CH$_3$CN have also been evaluated with the triple-split 6-311 + G(2df, 2pd) basis set [13], which is the same size as cc-pVTZ +. A detailed description of the Dunning basis sets and an analysis of their performance for predicting energies of hydrocarbons and carbocations has been reported recently [14].

Correlation energies have been evaluated using many-body Møller–Plesset perturbation theory (MBPT = MP). Since the MP expansion for binding energies may be slowly convergent in particular cases [15], the appropriateness of this method for studying complexes of HF and HCl with HCN and CH$_3$CN has been investigated by comparing MP binding energies for HCN$\cdots$HF with the binding energy obtained from the infinite-order method of quadratic configuration interaction with noniterative inclusion of the effect of triple excitations [QCISD (T)] [16]. All calculations were performed on the Cray Y-MP8/864 computer at the Ohio Supercomputer Center.

Results and Discussion

Structures

The structures of the complexes CH$_3$CN$\cdots$HF, HCN$\cdots$HF, CH$_3$CN$\cdots$HCl, and HCN$\cdots$HCl have been optimized at four different levels of theory: HF/6-31G(d), HF/6-31 + G(d, p), MP2/6-31G(d), and MP2/6-31 + G(d, p). At all levels, the complexes with HCN have C$_{\infty v}$ symmetry, while those with CH$_3$CN have C$_{3v}$ symmetry. In each complex, a directed lone pair of electrons on the proton acceptor atom participates in a linear hydrogen bond. The intermolecular distances, increases in the proton-donor H—X distances in the complexes, and associated changes in the H—X stretching frequency computed at the various levels of theory, are reported in Table I. In complexes with HF as the proton donor, the computed values of these variables depend both on the method of calculation and on the basis set. At Hartree–Fock, intermolecular distances are too long and potential curves too steep. Thus, the HF/6-31G(d) intermolecular distances of 2.878 and 2.923 Å in CH$_3$CN$\cdots$HF and HCN$\cdots$HF, respectively, are reduced significantly to 2.758 and 2.808 Å, respectively, at MP2/6-31 + G(d, p). Similarly, the H—F bondlength in these two complexes lengthens significantly as the level of theory is improved from HF/6-31G(d) to MP2/6-31 + G(d, p). The increase in the H—F bondlength is accompanied by a decrease in the H—F stretching frequency in the complex. At MP2/6-31 + G(d, p) there is excellent agreement between the computed bathochromic shifts of the H—F stretching frequency and experimental data [17–19].

The intermolecular distances, changes in H—Cl bondlengths, and shifts in the H—Cl stretching frequency for CH$_3$CN$\cdots$HCl and HCN$\cdots$HCl, also reported

530

TABLE 1. Intermolecular distances (R. A). changes in H—X distances (δr. A), and changes in H—X stretching frequencies (δv, cm⁻¹).

	CH₃CN· · · ·HF			HCN· · · ·HF		
	R	δr	δv	R	δr	δv
HF/6-31G(d)	2.878	0.007	-146	2.923	0.006	106
HF/6-31+G(d, p)	2.850	0.010	234	2.900	0.008	176
MP2/6-31G(d)	2.835	0.009	-162	2.875	0.007	119
MP2/6-31+G(d, p)	2.758	0.015	343	2.808	0.012	262
Experimental			-334ᵃ			245ᵇ

	CH₃CN· · · ·HCl			HCN· · · ·HCl		
	R	δr	δv	R	δr	δv
HF/6-31G(d)	3.434	0.008	-110	3.498	0.005	-73
HF/6-31+G(d, p)	3.462	0.008	-103	3.522	0.006	-68
MP2/6-31G(d)	3.324	0.012	-173	3.380	0.009	-126
MP2/6-31+G(d, p)	3.316	0.012	-167	3.376	0.009	-113
Experimental	3.291ᶜ	0.013ᶜ	-155ᵈ	3.402ᶜ	0.011ᵉ	

ᵃ Refs. 17 and 18; ᵇRefs. 17 and 19; ᶜRef. 20; ᵈRef. 21.

in Table I, show a strong dependence on method (HF vs. MP2) but little dependence on basis set. At the highest level of theory [MP2/6-31+G(d, p)], the computed Cl—N distances of 3.316 and 3.376 Å for CH₃CN· · ·HCl and HCN· · ·HCl, respectively, are in good agreement with the experimental values of 3.291 and 3.402 Å, respectively, reported by Legon and Millen [20]. The 0.012 and 0.009 Å increases in the H—Cl bondlength in the complexes CH₃CN· · ·HCl and HCN· · ·HCl, respectively, are also in agreement with Legon and Millen's values of 0.013 and 0.011 Å, respectively [20]. The decrease of 167 cm⁻¹ in the H—Cl stretching frequency in CH₃CN· · ·HCl agrees with the experimentally determined decrease of 155 cm⁻¹ [21]. Based on these data, it would appear that the MP2/6-31+G(d, p) level of theory provides consistent structural data and spectroscopic H—X frequency shifts for these hydrogen-bonded complexes.

Electronic Binding Energies

The basis set dependence of correlated fourth-order Møller-Plesset (MP4) electronic binding energies has been investigated for selected small complexes including (NH₃)₂, (H₂O)₂, (HF)₂, H₃N· · ·HF and HCN· · ·HF, all at their equilibrium MP2/6-31+G(d, p) geometries. Binding energies were computed with the cc-pVDZ, cc-pVTZ, and cc-pVQZ' basis sets, and these same basis sets augmented with diffuse functions on nonhydrogen atoms. Graphical data for the complexes (HF)₂, (H₂O)₂, and (NH₃)₂ in Figure 1 show that the presence of diffuse functions leads to a significant decrease of MP4/cc-pVDZ hydrogen bond energies. For this series the
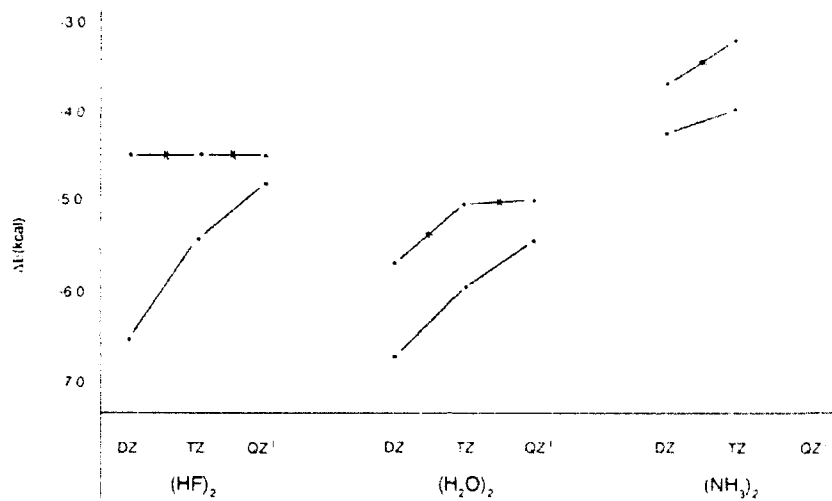
Figure 1. Computed MP4 binding energies for $(HF)_2$, $(H_2O)_2$, and $(NH_3)_2$. (—): cc-pVXZ; ( ): cc-pVXZ+.
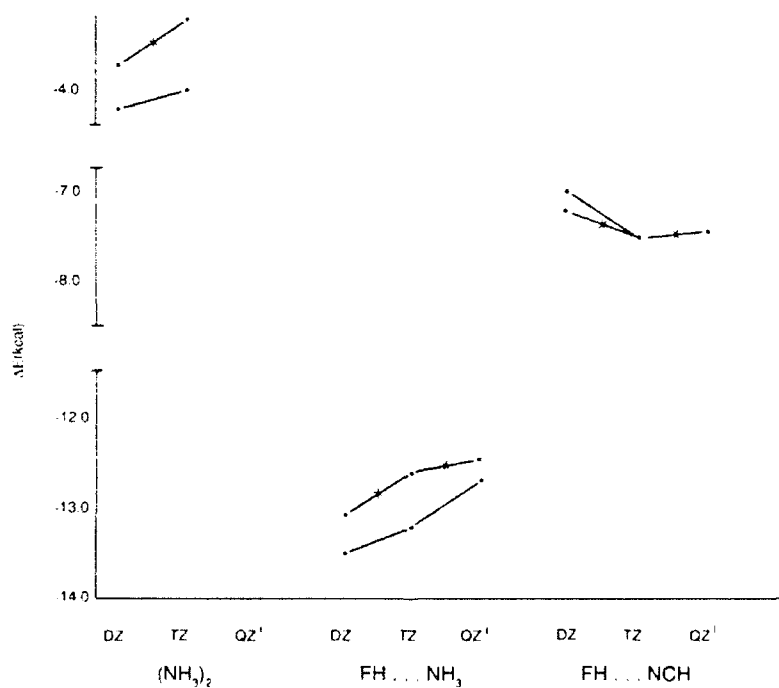
Figure 2. Computed MP4 binding energies for $(NH_3)_2$, FH···NH$_3$, and FH···NCH. (—): cc-pVXZ; ( ): cc-pVXZ+.

magnitude of this decrease is dependent on the nature of hydrogen-bonded atoms, increasing with increasing electronegativity. For $(HF)_2$, diffuse functions decrease the hydrogen-bond energy by 2.1 kcal/mol; for $(H_2O)_2$, the decrease is 1.0 kcal/mol; and for $(NH_3)_2$, 0.5 kcal/mol. Figure 2 presents similar data for the complexes $(NH_3)_2$, $H_3N\cdots HF$, and $HCN\cdots HF$, which have nitrogen as the proton acceptor. The 0.4 kcal/mol decrease of the MP4/cc-pVDZ binding energy of $H_3N\cdots HF$ by diffuse functions is similar to the decrease for $(NH_3)_2$, suggesting that the dependence is on the nature of the proton acceptor atom. Diffuse functions lead to a small increase of 0.2 kcal/mol in the MP4/cc-pVDZ binding energy of $HCN\cdots HF$.

The MP4/cc-pVTZ hydrogen bond energies of $(HF)_2$, $(H_2O)_2$, and $(NH_3)_2$ also decrease significantly by 0.9, 0.8, and 0.7 kcal/mol, respectively, when diffuse functions are added, but there is much less dependence on the nature of the proton-acceptor atom. Diffuse functions decrease the cc-pVTZ binding energies of $(NH_3)_2$ and $H_3N\cdots HF$ more than the cc-pVDZ energies, but this may be a result of some cancellation of other limitations of the cc-pVDZ basis. Diffuse functions have no effect on the binding energy of $HCN\cdots HF$.

The addition of diffuse functions has a small effect on the MP4/cc-pVQZ' hydrogen-bond energies of $(HF)_2$, $(H_2O)_2$, and $H_3N\cdots HF$, decreasing them by only 0.3 to 0.4 kcal/mol, and has no effect on the MP4/cc-pVQZ' hydrogen-bond energy of $HCN\cdots HF$. It is significant that the cc-pVTZ+ hydrogen-bond energies of $(HF)_2$, $(H_2O)_2$, and $H_3N\cdots HF$ are within 0.2 kcal/mol of the cc-pVQZ'+ binding energies, these latter ones serving as a possible benchmark of basis-set converged values. In contrast, the cc-pVTZ binding energies of these complexes are about 0.5 kcal/mol greater than cc-pVQZ' energies, and 1 kcal/mol greater than cc-pVQZ'+.

Basis Set Superposition Errors

Computed electronic stabilization energies are subject to a basis set superposition error (BSSE) [9], which results from the use of an incomplete basis set. This error artificially increases computed binding energies, but the effect should disappear as the basis set approaches completeness. The counterpoise estimate [9] of this error and its basis set dependence for $(H_2O)_2$, $(HF)_2$, and $HCN\cdots HF$ are shown graphically in Figure 3. Diffuse functions reduce the basis set superposition error dramatically. Using $HCN\cdots HF$ as an example, the counterpoise estimates of the BSSE are 1.8, 1.1, and 0.5 kcal/mol at cc-pVDZ, cc-pVTZ, and cc-pVQZ', respectively. These corrections are reduced to 1.1, 0.6, and 0.3 kcal/mol at cc-pVDZ+, cc-pVTZ+, and cc-pVQZ'+, respectively. Figure 3 clearly shows that the counterpoise correction overestimates the basis set superposition error, since the corrected binding energies increase and approach the uncorrected values as the basis set is improved. At cc-pVQZ'+, the counterpoise correction is reduced to 0.3 kcal/mol for all of the complexes investigated. Table II shows that the uncorrected cc-pVTZ+ binding energies of $(HF)_2$, $(H_2O)_2$, and $HCN\cdots HF$ are essentially identical to the uncorrected cc-pVQZ'+ energies, differing by no more than 0.1 kcal/mol.
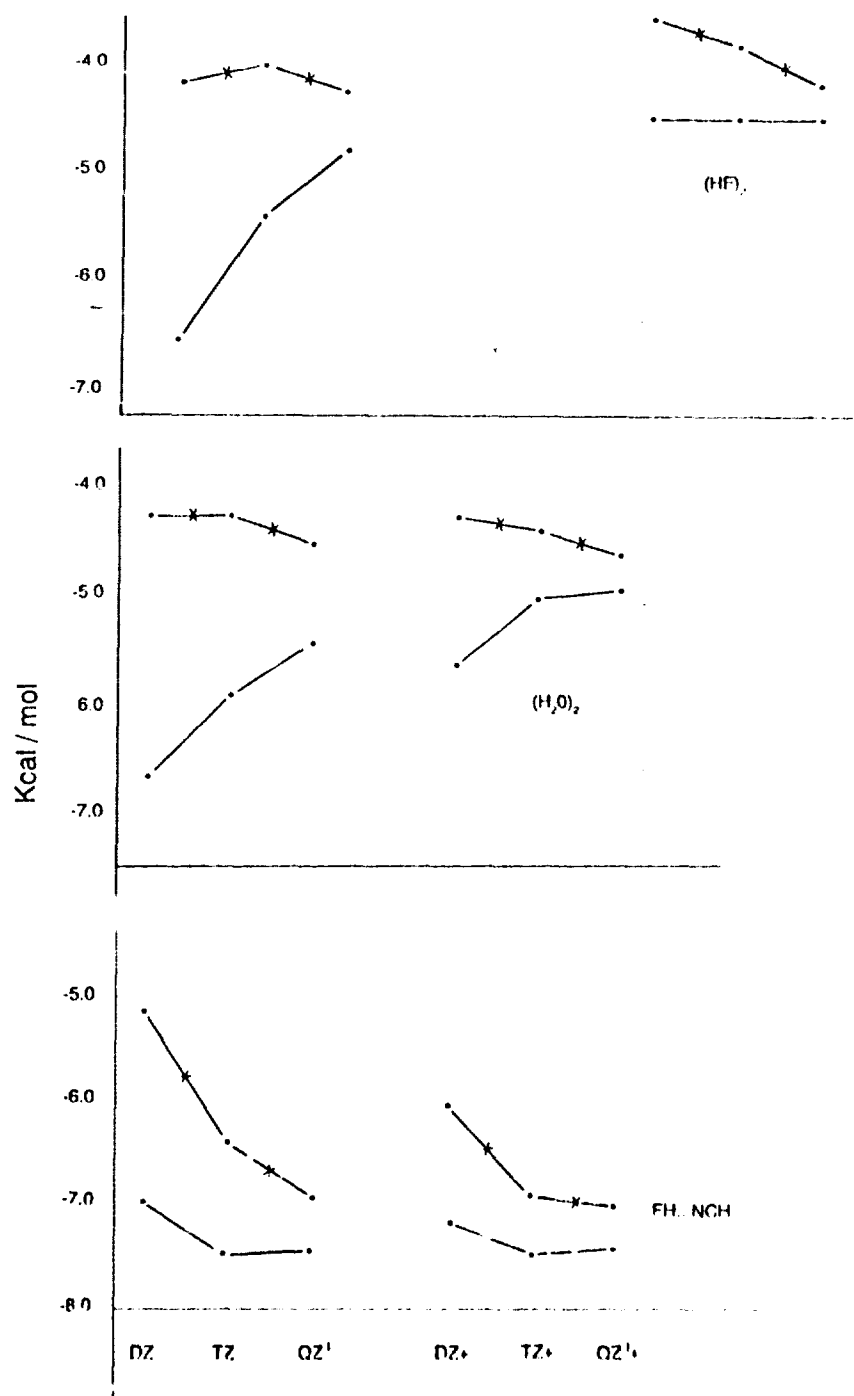
Figure 3. Computed binding energies and counterpoise-corrected binding energies for $(HF)_2$, $(H_2O)_2$, and $FH \cdots NCH$. (——): MP4 energies; (X): counterpoise-corrected binding energies.

TABLE II. MP4/cc-pVTZ+ and MP4/cc-pVQZ'+ binding energies (kcal/mol) with and without the counterpoise correction.

	cc-pVTZ+		cc-pVQZ'+	
	Corrected	Uncorrected	Corrected	Uncorrected
$(HF)_2$	-3.8	-4.5	-4.5	-4.2
$(H_2O)_2$	-4.4	-5.1	-5.0	-4.7
HCN···HF	-6.9	-7.5	-7.4	-7.1

Moreover, the counterpoise-corrected MP4/cc-pVTZ+ energies lie outside the range of the corrected and uncorrected MP4/cc-pVQZ'+ energies. These results, and those reported in the preceding section, support the use of the cc-pVTZ+ basis set without the counterpoise correction for the calculation of hydrogen bond energies at minimal computational expense.

MP4 binding energies for the complexes of HF and HCl with HCN and CH_3CN have also been computed with the 6-311 + G(2df, 2pd) basis set, which is the same size as cc-pVTZ+. The computed binding energies are −9.4, −7.7, −6.2, and −4.9 kcal/mol for CH_3CN···HF, HCN···HF, CH_3CN···HCl, and HCN···HCl, respectively. These energies are similar to but slightly greater than the MP4/cc-pVTZ+ energies of −9.1, −7.5, −5.9, and −4.7 kcal/mol, respectively. The counterpoise correction for HCN···HF at MP4/6-311 + G(2df, 2pd) is 0.8 kcal/mol, which is 0.2 kcal/mol greater than the MP4/cc-pVTZ+ correction.

MP4 Versus QCI Electronic Binding Energies for HCN···HF

It is known that in specific cases computed Møller–Plesset hydrogen-bond energies may be slowly convergent [15]. Therefore, it is appropriate to examine the variation of these energies at second- (MP2), third- (MP3), and fourth- (MP4) order, and to compare them with the infinite-order QCISD(T) binding energy. The computed cc-pVTZ+ binding energies of the model complex HCN···HF at HF, MP2, MP3, and MP4 are −6.2, −7.6, −7.3, and −7.5 kcal/mol, respectively. The QCISD(T)/cc-pVTZ+ binding energy is −7.4 kcal/mol. At both MP4 and QCISD(T), the triples contribution leads to 0.2 kcal/mol stabilization. The smooth behavior of the MP energies, and the good agreement between MP4 and QCISD(T) suggest that MP4 is an appropriate level of correlation to use for the complexes of HF and HCl with HCN and CH_3CN.

Zero-Point Energies and Vibrational Spectra

Zero-point vibrational energy contributions have a nonnegligible effect on the stabilities of hydrogen-bonded complexes, but they also show a dependence on methodology. Some insight into this dependence and the origin of the zero-point vibrational energy contribution to binding energies may be gained by examining

data from two levels of theory, HF/6-31G(d) and MP2/6-31+G(d, p). Since computed Hartree–Fock vibrational frequencies are too high relative to experimental frequencies, it has been the practice to scale these, with a scaling factor of 0.9 or 0.89 [22]. (In a recent study in this laboratory [14], and also in a study by Schaeffer et al. [23], it was noted that the scaling used to reproduce frequencies may not be the most appropriate one to use for obtaining zero-point vibrational energies, and both studies suggested that a slightly greater scaling factor would be better. For the purpose of this analysis, however, the standard 0.9 scaling of the Hartree–Fock vibrational frequencies and the energies computed from them will be used.) Since MP2 frequencies are usually closer to experimental values, these have been used without scaling.

Formation of the hydrogen-bonded complexes $CH_3CN\cdots HF$, $HCN\cdots HF$, $CH_3CN\cdots HCl$, and $HCN\cdots HCl$ gives rise to five new low-frequency vibrational modes ("dimer modes"). The normal coordinate analyses of these modes in the $HCN\cdots HF$ complex has been given by Wofford et al. [19] and are shown schematically in Figure 4. ν_α is the doubly degenerate dimer bending mode in which one monomer unit moves clockwise while the other moves in a counterclockwise direction. This is the lowest-frequency dimer vibration. ν_σ is the hydrogen-bond stretching mode, which changes the intermolecular distance. ν_β is a doubly degenerate vibration which corresponds to an excursion of the hydrogen-bonded proton away from its equilibrium position along the intermolecular F—N or Cl—N line. This is the highest-frequency dimer vibration in these complexes, which varies with hydrogen-bond strength.

The zero-point vibrational energy contribution from the new dimer modes leads to destabilization of these complexes, whereas the decrease in the H—X-stretching frequency leads to stabilization. These six modes combined account for the entire zero-point vibrational energy contribution to the binding energies of these complexes. This is evident from the data of Table III, where the sum of the energies of these six modes is compared with the zero-point vibrational energy contribution computed as the difference between the zero-point vibrational energy of the complex minus the sum of the zero-point vibrational energies of the isolated proton-donor and proton-acceptor molecules. This implies that the vibrational frequencies of the proton-acceptor molecule are essentially unchanged in the complex.
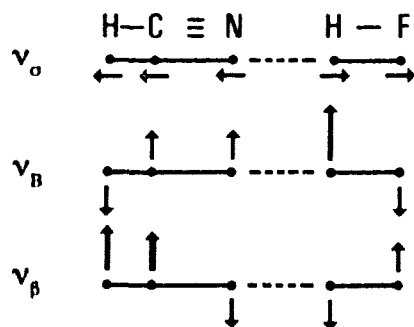
Figure 4. Dimer modes of $HCN\cdots HF$.

TABLE III.   Zero-point vibrational energy contributions (kcal/mol).

	Dimer Modes	δ(H—X)	Sum	Full Calculation
CH₃CN···HF				
0.9 × HF/6-31G(d)	1.61	0.19	1.42	1.46
MP2/6-31+G(d,p)	2.42	-0.49	1.93	2.01
HCN···HF				
0.9 × HF/6-31G(d)	1.55	0.14	1.41	1.46
MP2/6-31+G(d,p)	2.35	-0.37	1.98	2.05
CH₃CN···HCl				
0.9 × HF/6-31G(d)	1.22	0.14	1.08	1.13
MP2/6-31+G(d,p)	1.46	0.24	1.22	1.28
HCN···HCl				
0.9 × HF/6-31G(d)	1.20	0.09	1.11	1.14
MP2/6-31+G(d,p)	1.45	0.16	1.29	1.33

Table III also shows that the zero-point vibrational energy contribution for complexes with HF as the proton donor is about 0.5 kcal/mol larger when evaluated at MP2/6-31+G(d, p) than at 0.9-scaled HF/6-31G(d). This difference arises from the contribution of the dimer modes, which is 0.8 kcal/mol greater at MP2/6-31+G(d, p) than at 0.9-scaled HF/6-31G(d). This difference would be even greater except for the underestimation of the shift of the H—F-stretching frequency at HF/6-31G(d). Table IV, which lists the energy contribution from each dimer mode, shows that the difference arises primarily from v_B, the doubly degenerate mode which corresponds to the excursion of the hydrogen-bonded proton away from the hydrogen-bonding axis. This is a higher-frequency vibration at MP2/6-31+G(d, p), and the contribution from this degenerate mode to the zero-point energy of the complex is 0.7 kcal/mol greater at MP2/6-31+G(d, p) than at 0.9-scaled HF/6-

TABLE IV.   Zero-point vibrational energy contributions (kcal/mol) from dimer modes.

	CH₃CN···HF			HCN···HF		
	v_σ	v_π	v_B	v_B	v_π	v_B
0.9 × HF/6-31G(d)	0.11	0.21	1.30	0.18	0.21	1.17
MP2/6-31+G(d,p)	0.14	0.24	2.02	0.24	0.24	1.86
	CH₃CN···HCl			HCN···HCl		
	v_σ	v_π	v_B	v_B	v_π	v_B
0.9 × HF/6-31G(d)	0.09	0.14	1.01	0.14	0.14	0.92
MP2/6-31+G(d,p)	0.10	0.17	1.20	0.16	0.17	1.10

31G(d). In contrast to the complexes with HF, the zero-point vibrational energy contribution for complexes with HCl at MP2/6-31+G(d, p) and at 0.9-scaled HF/6-31G(d) differ by less than 0.2 kcal/mol. However, even this small difference arises from the difference in the energy of the degenerate mode, ν_b, at these two levels of theory.

The frequencies of the dimer modes at 0.9-scaled HF/6-31G(d) and at MP2/6-31+G(d, p) for all complexes are reported in Table V. Also given for comparison are available experimental data. It should be emphasized that the experimental frequencies are anharmonic and should therefore be less than the computed frequencies which are harmonic. The experimental value of ν_b for $CH_3CN\cdots HF$ is 620 cm^{-1} [18], which is less than the computed MP2/6-31+G(d, p) value of 709 cm^{-1}, but larger than the 0.9-scaled HF/6-31G(d) value of 453 cm^{-1}. The experimental value of ν_b for $HCN\cdots HF$ is 550 cm^{-1} [24], which is again lower than the MP2/6-31+G(d, p) value of 649 cm^{-1}, but higher than the 0.9-scaled HF/6-31G(d) value of 406 cm^{-1}. The experimental value of this mode for the complex $CH_3CN\cdots HCl$ is 350 ± 100 cm^{-1} [21], which encompasses both the MP2/6-31+G(d, p) value of 417 cm^{-1} and the 0.9-scaled HF/6-31G(d) value of 396 cm^{-1}.

Computed zero-point vibrational energy changes should be compared with experimental data. However, this comparison is complicated by two factors. First, the computed zero-point vibrational energies are derived from harmonic frequencies. The neglect of anharmonicity particularly for the low-frequency dimer modes does introduce an error. Second, the experimental determination of zero-point vibrational energies is also difficult. It is D_o, dissociation from the zero vibrational level which is measured experimentally. The zero-point vibrational energy change which leads to D_e is generally approximated from anharmonicities and empirical relationships.

TABLE V. Vibrational frequencies (cm^{-1}) of dimer modes.

	$CH_3CN\cdots HF$			$HCN\cdots HF$		
	ν_σ	ν_π	ν_b	ν_σ	ν_π	ν_b
0.9 · HF/6-31G(d)	38	144	453	64	144	406
MP2/6-31+G(d, p)	52	169	709	87	169	649
Experimental[a]	45	156	620	74	168	550

	$CH_3CN\cdots HCl$			$HCN\cdots HCl$		
	ν_σ	ν_π	ν_b	ν_σ	ν_π	ν_b
0.9 · HF/6-31G(d)	30	95	396	51	95	319
MP2/6-31+G(d, p)	35	117	417	59	122	386
Experimental[b]	40	97	350			
	(20)	(3)	(100)			

[a] Data for $CH_3CN\cdots HF$ from ref. 18; data for $HCN\cdots HF$ from ref. 24.
[b] From ref. 21. The experimental uncertainties are given in parentheses.

Wofford et al. [25] estimated a zero-point vibrational energy contribution of 1.9 kcal/mol for HCN · · · HF, in good agreement with the MP2/6-31+G(d, p) value of 2.0 kcal/mol. Legon et al. [18] estimated a zero-point vibrational contribution of only 0.7 kcal/mol for the CH₃CN · · · HF complex, which is significantly less than the MP2/6-31+G(d, p) value of 2.1 kcal/mol. If this experimental estimate is correct, the experimental electronic binding energy of CH₃CN · · · HF would be equal to the experimental electronic binding energy of HCN · · · HF as determined by Wofford et al. This does not seem likely in view of the stronger proton-accepting ability of CH₃CN, the corresponding experimental data for HCN · · · HF and the computed MP2/6-31+G(d, p) data.

Binding Energies of Complexes and Comparisons with Experimental Data

Based on the above analyses of methodology, the MP4/cc-pVTZ+ level of theory without the counterpoise correction has been used to compute the electronic binding energies of the complexes CH₃CN · · · HF, HCN · · · HF, CH₃CN · · · HCl, and HCN · · · HCl at their MP2/6-31+G(d, p) equilibrium geometries. Zero-point and thermal vibrational energies have also been evaluated from MP2/6-31+G(d, p) vibrational frequencies. Thus, the model used for these complexes is MP4/cc-pVTZ+//MP2/6-31+G(d, p).

Computed MP4/cc-pVTZ+ binding energies for CH₃CN · · · HF, HCN · · · FH, CH₃CN · · · HCl, and HCN · · · HCl are reported in Table VI. These binding energies (ΔE_e^0 or $-D_e$), measured from the minima on the MP2/6-31+G(d, p) potential energy surfaces, vary significantly from −4.7 kcal/mol for HCN · · · HCl, to −9.1 kcal/mol for CH₃CN · · · HF. This wide range results from differences in the proton-accepting ability of HCN and CH₃CN, and the proton-donating ability of HF and HCl. Substitution of methyl for hydrogen in HCN increases the electron density on the nitrogen and the polarizability of the proton-acceptor molecule. Both of these factors make CH₃CN the stronger proton acceptor for hydrogen bonding. The greater charge on the hydrogen in HF compared to HCl makes complexes with HF more stable than those with HCl, independent of the proton acceptor. The

TABLE VI.   MP4/cc-pVTZ+ stabilities (kcal/mol) of complexes of HF and HCl with HCN and CH₃CN.[a]

Complex	$-D_e$	$-D_0$	ΔH^{298}
CH₃CN · · · HF	−9.1	−7.1	−7.6
HCN · · · HF	−7.5	−5.4	−6.0
CH₃CN · · · HCl	−5.9	−4.6	−4.8
HCN · · · HCl	−4.7	−3.4	−3.6

[a] D_e is the dissociation energy measured from the minima on the potential surfaces; D_0 is the dissociation energy measured from the zero-point vibrational levels of the potential surfaces; ΔH^{298} is the binding enthalpy at 298 K.

binding energies measured from the zero-point vibrational levels of monomers and complexes ($-D_0$) are decreased relative to $-D_e$ by approximately 2 kcal/mol for complexes with HF, and by 1.3 kcal/mol for complexes with HCl. Binding enthalpies at 298 K (ΔH^{298}) reflect the trend in binding energies, $-D_e$ and $-D_0$. Changes in thermal vibrational energies destabilize these complexes at 298 K, while the remaining thermal terms and the PV term contribute -2.1 kcal/mol to their stabilization.

The binding energies computed in this work may be compared with previous theoretical calculations of binding energies and with experimental data. Most previous theoretical studies have reported binding energies at the Hartree–Fock level of theory. Among the more recent of these is the study of De Almeida and Hinchliffe [26] who reported Hartree–Fock structures and stabilization energies ($-D_e$) for HCN $\cdots$ HCl and CH$_3$CN $\cdots$ HCl computed with a small basis set without diffuse functions or polarization functions. Their Hartree–Fock binding energies are -5.4 and -6.7 kcal/mol, respectively. The HCN $\cdots$ HF complex was investigated by Somasundram et al. [27], using a large TZ basis set including two sets of polarization functions but no diffuse functions. Their Hartree–Fock binding energy is -7.0 kcal/mol. These binding energies are greater than the HF/cc-pVTZ+ binding energies computed in this work, which are -3.1, -4.1, and -6.2 kcal/mol for HCN $\cdots$ HCl, CH$_3$CN $\cdots$ HCl, and HCN $\cdots$ HF, respectively. As evident from a comparison of these numbers and the binding energies reported in Table VI, electron correlation has a significant effect, contributing more than 1 kcal/mol to the stabilization energies of these complexes. Botschwina [28] computed the binding energy ($-D_e$) of HCN $\cdots$ HF using the CPV method to evaluate the electron correlation contribution, and obtained a value of -6.8 kcal/mol. This value is 0.7 kcal/mol greater than that obtained in the present study. The most recent investigation of one of these complexes is that reported by Bacskay et al. [29], who examined the HCN $\cdots$ HCl complex at its experimental geometry with a split-valence, polarized basis set, and computed its correlated binding energy using the averaged coupled-pair functional method (ACPF). Their binding energy is -4.1 kcal/mol, which is 0.6 kcal/mol less than the MP4/cc-pVTZ+ energy.

Complexes of HCN and CH$_3$CN with HF and HCl have also been investigated experimentally. A very detailed study of the HCN $\cdots$ HF complex has been made by Wofford et al. [25] using high-resolution FTIR spectroscopy. They reported a $-D_0$ value of -5.0 kcal/mol, and estimated $-D_e$ to be -6.9 kcal/mol. These authors evaluated the thermal function ΔH^{298} using three different approximations: an anharmonic approximation, an harmonic approximation, and the observed frequencies. These different approximations resulted in ΔH^{298} values of -5.4, -5.4, and -5.3 kcal/mol, respectively. The computed values of $-D_e$, $-D_0$, and ΔH^{298} are -7.5, -5.4, and -6.0 kcal/mol, respectively. The difference between the experimental and the theoretical values of the electronic binding energy is 0.6 kcal/mol, but the zero-point and thermal vibrational energies differ by only 0.2 kcal/mol.

Legon et al. [18] have investigated the CH$_3$CN $\cdots$ HF complex using microwave spectroscopy. Their reported value of $-D_0$ is -6.2 kcal/mol, which makes this

consistent with the computed MP4/cc-pVTZ+ results. which show that $CH_3CN \cdots HF$ is 1.7 kcal/mol more stable than $HCN \cdots HF$. However, Legon et al. estimated that the zero-point vibrational energy contribution destabilizes this complex by only 0.7 kcal/mol, obtaining a $-D_c$ value of -6.9 kcal/mol. This is significantly less than the computed value of -9.1 kcal/mol. Given that the computed zero-point vibrational energy contributions to the destabilization of $HCN \cdots HF$ and $CH_3CN \cdots HF$ are 2.1 and 2.0 kcal/mol. respectively, and that the experimental estimate for the $HCN \cdots HF$ complex is 1.9 kcal/mol. it would seem that the zero-point vibrational energy change for $CH_3CN \cdots HF$ has most probably been underestimated experimentally.

In a recent article, Ballard and Henderson [21] reported a study of the hydrogen-bond energy of $CH_3CN \cdots HCl$ based on FTIR photometry of the H—Cl stretching mode in the complex. Based on their temperature dependence measurements, these authors calculated a ΔH^{298} value of -3.3 ± 0.3 kcal/mol. From this value and a series of assumptions, they estimated $-D_c$ to be -5.3 ± 0.4 kcal/mol. A recent communication [30] has discussed these assumptions, and suggested that a better estimate of $-D_c$ would be -4.0 ± 0.4 kcal/mol, although this number is still subject to some uncertainty. A more recent FTIR value of ΔH^{298} gives a room-temperature binding enthalpy of -5.7 kcal/mol [31], which compares favorably with the MP4/cc-pVTZ+ value of -4.8 kcal/mol. Mettee has also recently measured ΔH^{298} for the $HCN \cdots HCl$ complex, and obtained a value of -4.4 kcal/mol [31], in agreement with the MP4/cc-pVTZ+ value of -3.6 kcal/mol.

Acknowledgment

Bibliography

[1] J.A. Pople, J.S. Binkley, and R. Seeger, Int. J. Quantum Chem. Quantum Chem. Symp. 10, 1 (1976).

[2] R. Krishnan and J.A. Pople, Int. J. Quantum Chem. 14, 91 (1978).

[3] R.J. Bartlett and D.M. Silver, J. Chem. Phys. 62, 3258 (1975).

[4] R.J. Bartlett and G.D. Purvis, Int. J. Quantum Chem. 14, 561 (1978).

[5] P.C. Hariharan and J.A. Pople, Theor. Chim. Acta. 28, 213 (1973).

[6] J.D. Dill and J.A. Pople, J. Chem. Phys. 62, 2921 (1975).

[7] G.W. Spitznagel, T. Clark, J. Chandrasekhar, and P.v.R. Schleyer, J. Comp. Chem. 3, 3633 (1982).

[8] T. Clark, J. Chandrasekhar, G.W. Spitznagel, and P.v.R. Schleyer, J. Comp. Chem. 4, 294 (1983).

[9] S.F. Boys and F. Bernardi, Mol. Phys. 19, 553 (1970).

[10] T.H. Dunning Jr., J. Chem. Phys. 90, 1007 (1989).

[11] M.J. Frisch, M. Head-Gordon, G.W. Trucks, J.B. Foresman, H.B. Schlegel, K. Raghavachari, M.A. Robb, J.S. Binkley, C. Gonzalez, D.J. DeFrees, D.J. Fox, R.A. Whiteside, R. Seeger, C.F. Melius, J. Baker, R.L. Martin, L.R. Kahn, J.J.P. Stewart, S. Topiol, and J.A. Pople, Gaussian 90 (Gaussian, Inc., Pittsburgh, PA, 1990).

[12] A.D. McLean and G.S. Chandler, J. Chem. Phys. 72, 5639 (1980).

[13] R. Krishnan, J.S. Binkley, R. Seeger, and J.A. Pople, J. Chem. Phys. 72, 650 (1980).

[14] J.E. Del Bene, D.H. Aue, and I. Shavitt, J. Am. Chem. Soc. 114, 1631 (1992).

[15] M.J. Frisch and J.E. Del Bene, Int. J. Quantum Chem. Quantum Chem. Symp. 23, 363 (1989); J.E. Del Bene and M.J. Frisch, Int. J. Quantum Chem. Quantum Chem. Symp. 23, 371 (1989).

[16] J.A. Pople, M. Head-Gordon, and K. Raghavachari, J. Chem. Phys. 87, 5968 (1987).

[17] B.A. Wooford, J.W. Bevan, W.B. Olson, and W.J. Lafferty, Chem. Phys. Lett. 124, 579 (1986).

[18] A.C. Legon, D.J. Millen, and H.M. North, J. Chem. Phys. 86, 2530 (1987).

[19] B.A. Wofford, S.G. Lieb, J.W. Bevan, J. Chem. Phys. 87, 4478 (1987).

[20] A.C. Legon and D.J. Millen, Proc. Roy. Soc. A 417, 21 (1988).

[21] L. Ballard and G. Henderson, J. Phys. Chem. 95, 660 (1991).

[22] W.J. Hehre, L. Radom, P.v.R. Schleyer, and J.A. Pople, Ab Initio Molecular Orbital Theory (Wiley, New York, 1986).

[23] R.S. Grev, C.L. Janssen, and H.F. Schaefer, J. Chem. Phys. 95, 5128 (1991).

[24] B.A. Wofford, R.S. Ram, A. Quinonez, J.W. Bevan, W.B. Olsen, and W.J. Lafferty, Chem. Phys. Lett. 152, 299 (1988).

[25] B.A. Wooford, M.E. Eliades, S.G. Lieb, and J.W. Bevan, J. Chem. Phys. 87, 5674 (1987).

[26] W.B. De Almeida and A. Hinchliffe, Chem. Phys. 137, 143 (1989).

[27] K. Somasundram, R.D. Amos, and N.C. Handy, Theor. Chim. Acta 69, 491 (1986).

[28] P. Botschwina, Proceedings of the NATO Advanced Research Workshop, Structure and Dynamics of Weakly Bound Complexes (Maratea, Italy, September 22–26, 1986), pp. 181–190.

[29] G.B. Bacskay, D.I. Kerdraon, and N.S. Hush, Chem. Phys. 144, 53 (1990).

[30] J.E. Del Bene, H.D. Mettee, and I. Shavitt, J. Phys. Chem. 95, 5387 (1991).

[31] H.D. Mettee (private communication)

SC-MEH-CI Calculations on the $(NH_4)4CuCl_6$ (D_{2h}) Cluster in $(NH_4)_2CuCl_4$

E. A. BOUDREAUX, E. BAXTER, and K. CHIN

Department of Chemistry, University of New Orleans, New Orleans, Louisiana 70148

Abstract

Calculations of electronic structure and bonding via the SC-MEH-MO method with limited Cu $3d$, $4s$, and $4p$ configuration interaction, have been carried out on the tetragonally coordinated (D_{2h} symmetry) $CuCl_6(NH_4)_4$ structural cluster unit in crystalline $(NH_4)_2CuCl_4$. The results are compared with those of other calculations. The calculated electronic spectrum, electric field gradient (EFG), and magnetic data are compared with experiment. © 1992 John Wiley & Sons, Inc.

Introduction

While a number of articles dealing with the electronic structure of copper II chlorides have appeared over a period of years, the most recent, systematic, theoretical treatment is that of Zerner et al. [1]. This study has shown that specific effects on the energetics of the 3d levels in tetracoordinated $CuCl_4^{2-}$ and axially elongated $CuCl_6^{4-}$ complexes, are very sensitive to the positions of the axial chloride ions in these clusters. While the equatorial Cu — Cl bond lengths vary only from 2.264 to 2.332 Å, axial bond lengths range from 2.78 to 3.26 Å [2–9]. For the purpose of this investigation, the $(NH_4)_4CuCl_6$ cluster, defining the nearest neighbor interactions associated with the crystalline structure of $(NH_4)_4CuCl_4$, has been selected for study. The equatorial Cu — Cl and lengths are close to being equivalent [2.332(×2) and 2.300(×2) Å], and the axially bonded chlorides is at the relatively close distance of 2.793 Å [2]. The effective local symmetry is D_{4h} distorted toward D_{2h}. While this is only 1.3% distortion in terms of bond distances, it results in a 5% splitting of the degenerate E_g orbital in pseudo-D_{4h} symmetry.

Method of Calculation

Molecular orbital calculations were performed via the SC-MEH-MO method, as discussed in Ref. 10 and other pertinent references contained therein (i.e., Refs. 2–10 in Ref. 10). The AO basis functions were calculated from HF-SCF quasi-relativistic functions for Cl, N, and H orbitals. The MO calculations were confined to the incorporation of only the valence AOs derived from the atomic calculations. The required atom charges and respective configurations used in this calculation, are presented in Table I. Pertinent bond distances and associated angles are given in Table II.

TABLE I.   Atomic basis functions.

Atom	Configuration
Cu	$3d^{10}4s^2$; $3d^{10}4s^14p^1$; $3d^94s^24p^1$
Cu^0	$3d^{10}4s^1$; $3d^94s^2$; $3d^94s^14p^1$
Cu$^+$	$3d^{10}$; $3d^94s^1$; $3d^84s^2$; $3d^84s^14p^1$
Cu^{2+}	$3d^9$; $3d^84s^1$; $3d^74s^2$; $3d^74s^14p^1$
Cu^{3+}	$3d^8$; $3d^74s^1$; $3d^64s^2$; $3d^64s^14p^1$
Cl	$3s^23p^6$
Cl^0	$3s^23p^5$; $3s^13p^6$
Cl$^+$	$3s^23p^4$; $3s^13p^5$
N$^-$	$2s^22p^4$; $2s^12p^5$
N^0	$2s^22p^3$; $2s^12p^4$
N$^+$	$2s^22p^2$; $2s^12p^3$
H$^-$	$1s^2$
H^0	$1s^1$

As pointed out above, the $(NH_4)_4CuCl_6$ cluster consists of a planar $CuCl_4$, slightly distorted unit, plus two axially elongated Cl, completing a structure having effectively D_{2h} point group symmetry. Thus, this calculation differs from those made by Zerner et al. [1], who employed bond distances of 2.265 and 2.95 Å for equatorial and axial bonds, respectively, in D_{4h} symmetry, with counter cations omitted. The NH_4^+ groups were symmetrically dispersed between the axial and equatorial chlorides at the ionic bond distance observed in NH_4Cl.

Unlike previously reported SCMEH-MO calculations, molecular correlation was included via configuration interaction over those MOs involving Cu orbital contributions. This CI was limited to one-election promotions between the initially calculated, occupied, partially occupied, and unoccupied virtual MOs. The final eigenvalues were adjusted for spin-pairing interactions, ligand field, and spin-orbit splittings.

Electronic spectra were calculated from differences in total energies of ground and excited doublet states.

TABLE II.   Bond distances and angles for $(NH_4)_4CuCl_6$.[a]

Bond	Distance (Å)	Angles (degrees)
Cu — Cl$_{(eq)x}$	2.332	90
Cu — Cl$_{(eq)y}$	2.300	90
Cu — Cl$_{(ax)z}$	2.793	180
N — Cl	3.34–3.61 (3.48 ave.)	Nonbonding
Cl — HNH$_3$ (eq)	2.84–3.07 (2.96 ave.)	Nonbonding
Cl — HNH$_3$ (ax)	2.48–2.68 (2.58 ave.)	Nonbonding

[a] Data from Ref. 2.

Another ground state comparative calculation was made using the all-electron, DMOL 2.0 density functional program with correlation [11].

Electric field gradients at Cu were calculated from the SCMEH-CI results, which were utilized in a full molecular EFG program developed by M. Grodzicki [12].

Results and Discussion

Comparisons of orbital energies and their respective percent AO character for SCMEH (with and without CI) and DMOL 2.0 calculations, are presented in Table III. It is to be noted that the SCMEH-CI results not only raise the energies, but also alter the order of the Cu $3d$ levels. Notably, the order of $3d$ levels in the DMOL 2.0 results differs from that of the SCMEH-CI; however, both have the z^2 orbital as the highest occupied. The fact that the x^2-y^2 and z^2 levels lie slightly above the zero of energy is likely due to the incompleteness of the CI procedure, which also neglected the readjustment of electrostatic effects due to NH_4 ions.

Additional details, such as orbital populations and net atomic charges, are provided in Table IV. These data were obtained via Lowdin and Mulliken formalisms for the SCMEH-CI and DMOL 2.0, respectively. Interatomic populations were not output in the DMOL 2.0 calculations. These show data that the covalency in the equatorial Cu—Cl bonds is about 19–20%, while that of the axial bonds is the order of 15%.

Electronic Spectra

The normal assignment for the energies of the Cu $3d$ levels in D_{4h} symmetry having elongated axial ligands is: $x^2-y^2 > z^2 > xy > xz,yz$. The associated d–d

TABLE III. MO Results for $(NH_4)_2CuCl_4(D_{4h}$ symmetry).

	SCMEH (no CI)			SCMEH (with CI)			DMOL 2.0 (with CI)	
E (eV)	MO (HOMO and lower)	% AO ($3d$)	E (eV)	MO (HOMO and lower)	% AO ($3d$)	E (eV)	MO (HOMO and lower)	% AO ($3d$)
9.499	a_e	23.8 (x^2-y^2)	0.048	a_e	37.5 (z^2)	3.404	a_e	72.0 (z^2)
10.177	a_e	9.3 (z^2)	0.033	a_e	54.8 (x^2-y^2)	4.245	b_{2g}	59.4 (xz)
11.168	a_e	(Cl, p)	0.024	b_{1u}	17.0 (xy)	4.272	b_{1u}	62.5 (xy)
11.187	a_e	(Cl, p)	1.188	b_{2g}	17.9 (xz)	4.626	a_e	71.2 (x^2-y^2)
11.357	b_{2g}	(Cl, p)	1.202	b_{1u}	19.0 (xz)	5.823	b_{1u}	76.6 (xy)
11.438	b_{2g}	(Cl, p)	5.424	a_e	29.1 (4s)			
					24.2 (z^2)			
11.517	b_{1u}	(Cl, p)						
13.712	b_{2g}	13.5 (xz)						
13.731	b_{2g}	14.3 (xy)						
13.918	b_{1u}	16.1 (xy)						
15.070	a_e	12.6 (4s)						
		10.9 (z^2)						

TABLE IV.   Charges and populations for $(NH_4)_4CuCl_6$.

Atom or bond	Charge		Atomic orbital	Orbital population	
	SCMEH-CI	DMOL2.0 CI		SCMEH-CI	DMOL2.0 CI
Cu	0.97	0.97	$3d$	9.75	9.54
			$4s$	0.273	0.490
			$4p$	0.020	—
$Cl_{(eq)a}$	-0.74	-0.45	$3p$	5.74	5.45
$Cl_{(eq)b}$	-0.72	-0.43	$3p$	5.72	5.43
$Cl_{(ax)z}$	-0.87	-0.76	$3p$	5.87	5.76
(NH_4)	0.92	0.58	—	—	—
$Cu - Cl_{(eq)a}$	—	—	—	0.198	—
$Cu - Cl_{(eq)b}$	—	—	—	0.192	—
$Cu - Cl_{(ax)z}$	—	—	—	0.149	—
$Cl - H_{(eq)}$	—	—	—	0.028	—
$Cl - H_{(ax)}$	—	—	—	0.066	—
$N - H$	—	—	—	0.569	—
				-0.690	—

TABLE V.   Calculated "d-d" electronic spectra for $CuCl_6^{4-}$.

Method	Symmetry	d-Orbitals	ΔE (eV)	Reference
INDO-CI	D_{4h}	$z^2 \rightarrow x^2-y^2$	0.82	[1][a]
		$xy \rightarrow x^2-y^2$	1.09	
		$xz, yz \rightarrow x^2-y^2$	1.16	
MSXα	D_{4h}[a]	$z^2 \rightarrow x^2-y^2$	1.85	[1][a]
		$xy \rightarrow x^2-y^2$	1.51	
		$xz, yz \rightarrow x^2-y^2$	1.75	
SC-MEH-CI	D_{2h}	$x^2-y^2 \rightarrow z^2$	0.94	This work
		$xy \rightarrow z^2$	1.24	
		$xz \rightarrow z^2$	1.58	
		$yz \rightarrow z^2$	1.66	
Observed	D_{4h}	?	1.03	[7]
	(or D_{2h}?)	?	1.24	
		$\left.\begin{array}{l} xz \\ yz \end{array}\right\} \rightarrow x^2-y^2$ [b]	1.58	
			1.62	

[a] The Cu — Cl bond distances assigned by Ref. 1 are: 2.265 Å(eq) and 2.950 Å(ax).

[b] It is not possible to unequivocally assign the orbitals in D_{2h} symmetry, since both z^2 and x^2-y^2 have an a_g irreducible representation.

spectra transitions for the doublet $3d^9$ configuration of Cu(II) are: $(^2B_{1g} \rightarrow ^2A_{1g})$, $(^2B_{1g} \rightarrow ^2B_{2g}) \leqslant (^2B_{1g} \rightarrow ^2E_g)$. In D_{2c} symmetry these assignments became $(^2A_1 \rightarrow ^2A_1) < (^2A_1 \rightarrow ^2B_{1g}) < (^2A_1 \rightarrow ^2B_{2g}, ^2B_{3g})$.

The highest transition involves a removal of the D_{2c}, E_g degeneracy, by splitting into the $^2B_{2g}$ and $^2B_{3g}$ states of D_{2c} symmetry. Table V provides a comparison of $d-d$ electronic spectra calculated by different methods, for the tetragonal $CuCl_4^{2-}$ cluster. In this work, the total energies calculated for both ground and excited states were employed in deriving the spectra.

There appears to be no published report of the solid state electronic spectrum of $(NH_4)_2CuCl_4$, but there is a single crystal spectrum reported for structurally similar Cs_3CuCl_5 [3]. Although the actual structure of this latter compound is a Cl bridged trimer, the Cu—Cl bond distances are: two each at 2.350 and 2.280 Å in the equatorial plane and two at 2.780 Å in the axial (Z) direction. Thus, the equatorial bonds average to be 2.315 ± 0.035 Å, and the axial bonds at 2.78 Å, are quite comparable to those reported for $(NH_4)_2CuCl_4$ [2]. Although the closest Cu—Cu distance in the cesium salt is shorter (3.062 Å) than the comparable distance in the ammonium salt (3.42 Å), the effect is not significant, since a formal Cu—Cu metallic bond is 2.56 Å. This is apparently confirmed, as Table V reveals calculated spectra for $(NH_4)_2CuCl_4$ are in good agreement with spectra observed for Cs_3CuCl_5.

Electric Field Gradient at Cu

For any atom the electric field gradient (EFG) may be specified by $V_{ij}^A = eq_{ii}^A$ ($i = x, y, z$), in which only the diagonal elements of the field gradient tensor are nonvanishing in axial symmetry. In this latter case, an asymmetry parameter, η, is defined according to the following equation

$$\frac{V_{xx} - V_{yy}}{V_{zz}} = \eta \qquad (1)$$

In the molecular environment, the tensor for the net EFG at the nucleus of a specific atom, A, may be expressed in the LCAO-MO formalism by

$$q^A = 2e \sum_u^{occ} \sum_i \sum_j C_{ui} C_{uj} \left\langle \phi_i \left| \frac{3\cos^2\theta - 1}{r^3} \right| \phi_j \right\rangle \qquad (2)$$

(MO) (AO) (AO)

In Eq. (2) all diagonal and off-diagonal contributions evaluated over AOs ϕ_i and ϕ_j must be evaluated. This also requires the familiar Sternheimer factors, but these must be calculated with reference to the variation of the position of the electrostatic charge relative to the nucleus. This varies from the usually reported γ_∞, Sternheimer factors, where the perturbing change is at a relatively large distance from the nucleus, and is thus a constant value. These are very difficult calculations, even for isolated atoms of varying charge and configuration. All the pertinent data essential for the molecular calculation have been calculated and programmed by M. Grodzicke [12].

The quadrupole frequency at atom A, ν^A, is given by the expression

$$v^{-1} = \frac{Q^{-1}e^2 q_{zz}}{2h}(1 - \eta^2/3)^{1/2} \tag{3}$$

where Q^{-1} is the atomic nuclear quadrupole moment. Although the EFG is calculated in atomic units (a_o^{-3}), it is desirable to convert Eq. (3) to megahertz (MHz) units with the factor 117.64 MHz/a_o^{-3}.

The calculated EFG data for the (NH_4)$_4CuCl_6$ are presented in Table VI, together with magnetic data. There are no observed EFG data reported for (NH_4)$_2CuCl_4$, but there are data for the analogs methyl ammonium and ethyl ammonium salts [13].

However, Cu—Cl bond distances in these latter salts are somewhat different from those found in the ammonium salt. This is likely to effect V_{zz} in an unpredictable way. Nonetheless, the agreement between calculated and observed nuclear quadrupole frequencies is quite good (see Table VI).

Magnetic g Tensors and Moments

According to perturbation theory, the magnetic g tensor for an electron in a chemical environment varies from the free electron value, ge, according to the relation:

$$g_i(i = x, yz) = g_e + 2 \sum_n \sum_i \frac{\langle \phi_o | L_i \cdot S_i | \phi_n \rangle \langle \phi_n | L_i | \phi_o \rangle}{E_n - E_o} \tag{4}$$

where the free electron, g_e, equals 2.0023 and

TABLE VI. EFG and magnetic data.

A. EFG data for Cu in $CuCl_6(D_{2h})$ cluster

Q^{Cu} (10^{-24} cm^2)	V_{zz}^{Cu} (Ao^{-3})	η	v^{Cu} (MHz)
−0.15	−1.793	0.071	31.64 (calc.) 37.0 (obs. O[a])

B. Magnetic data for $CuCl_6(D_{2h})$ cluster

λ_{Cu} (eV)	λ_{Cl} (eV)	$C^2_{(Cu)}$	$C^2_{(Cl)}$	ΔE (eV)	g_z	g_x	g_y	g_{eff}	μ_{eff} (BM)
−0.107	−0.061	0.375	0.625	1.619	2.002	2.100	2.098	2.067 (calc.) 2.110 (obs.)[b]	1.797 (calc.) 1.80 (obs.)[c]

[a] Reported for (MeNH$_3$)$_2CuCl_4$ and (EtNH$_3$)$_2CuCl_4$ [13].
[b] For (MeNH$_3$)$_2CuCl_4$ ($D_{4h}CuCl_6$ cluster): $R(CuCl)_{ax} \approx 2.9$ Å [15].
[c] For powder sample at 290 K [16]. The reported value was corrected for diamagnetic contributions.

$$\phi_i | L_j \cdot S_j | \phi_i \quad \sum_j \lambda_j(0) | L_j | n$$

in which the effective spin-orbit coupling constant, λ, is for all j atoms involved in the ground, (0) and excited state $|n\rangle$ molecular orbitals. It is convenient to express Eq. (4) in terms of an upper limit to the second-order correction, as shown in Eq. (5), where $\Delta E_{n,0}$ is for the lowest d-d excited state

$$g_i = g_e + 2 \sum_n \sum_j \lambda_j \frac{(0) | L_j^2 | n}{\Delta E_{n,0}} \tag{5}$$

These relationships have been expanded in detail for $CuCl_4^{3-}$ and $CuCl_6^{4-}$ tetragonal clusters (D_{4h}) by Smith [14]. We have followed the same approach in deriving similar relationships for D_{2h} symmetry.

Molecular g tensors have been calculated from the SCMEH-CI orbitals. The required values of λ_j were interpolated from calculated atomic values, as a function of net atom charge and orbital configuration. Both the spatial components and the average $g_{eff} = 1/3(g_x + g_y + g_z)$ are presented in Table VI.

The effective magnetic moment, μ_{eff}, may be expressed to the first order as:

$$\mu_{eff} = [S(S+1)]^{1/2}\left[1 - \frac{3(C_m^2 \lambda_m - C_j^2 \lambda_l)}{\Delta E(a_g \leftarrow b_{2g}, b_{3g})}\right] B.M. \tag{6}$$

where S is the total spin ($\frac{1}{2}$ for the case in point); λ_m and λ_l are the effective spin-orbit coupling constants for the metal (Cu) and ligand (Cl), respectively; C_m^2 and C_j^2 are the respective orbital coefficients. The results obtained for the magnetic moment are contained in Table VI. It may be concluded that the computational data presented here are in good agreement with those observed. This also lends support for the calculated result that the unpaired electron in $(NH_4)_2CuCl_4$ is in an MO having Cu $3d_z^2$ character, rather than an x^2-y^2 orbital as is usually found for $CuCl_4^{3-}$ and $CuCl_6^{4-}$ tetragonal (D_{4h}) clusters [14].

Bibliography

[1] P. Corre de Mello, M. Hekenberger, S. Larsson, and M. Zerner, J. Am. Chem. Soc. 102, 1278 (1980).

[2] R. D. Willett, J. Chem. Phys. 41, 2243 (1964).

[3] A. W. Schuetter, R. H. Jacobson, and R. E. Rundle, Inorg. Chem. 5, 277 (1966).

[4] J. P. Steadman and R. D. Willett, Inorg. Chem. Acta 4, 367 (1970).

[5] G. L. Ferguson and B. Zaslow, Acta Crystallogr. B27, 849 (1971).

[6] G. B. Birrell and B. Zaslow, J. Inorg. Nucl. Chem. 34, 1751 (1972).

[7] R. Laiko, M. Natarajun, and M. Karra, Phys. Status Solidi A15, 311 (1973).

[8] R. L. Harlow, W. J. Wells, III, G. W. Watt, and S. H. Simonsen, Inorg. Chem. 13, 2106 (1974); Inorg. Chem. 14, 1768 (1975).

[9] B. Morosin, P. Faltou, and J. S. Valentine, Acta Crystallogr. B31, 2220 (1975).

[10] F. A. Boudreaux and F. Baxter, Int. J. Quantum Chem. 39, 699 (1991).

[11] Provided courtesy of J. Seminario, postdoctoral associate of P. Politzer (University of New Orleans Department of Chemistry).

[12] M. Grodzicki, visiting professor at University of New Orleans Department of Chemistry. Currently at Institute of Theoretical Physics, University of Hamburg, Hamburg, Germany.

[13] Landolt-Bornstein, *Numerical Data and Functional Relationships in Science and Technology*, New Series, Vol 20b K. H. Hellwage and A. M. Hellwage, Eds. (Springer-Verlag, New York, 1988), p 502.

[14] D. W. Smith, J. Chem. Soc. A18, 3108 (1970).

[15] R. D. Willett, O. L. Liles, and C. Michelson, Inorg. Chem 6, 1885 (1967).

[16] G. Foex, C. J. Görter, and L. J. Smits, *Tables De Constants Et Donnees Numeriques* (vol 7) (Masson & Cie, Paris, 1957), p. 60.

On the Electronic Structure of Barrelene-Based Rigid Organic Donor–Acceptor Systems. An INDO Model Study Including Solvent Effects

THOMAS FOX, MANFRED KOTZIAN, and NOTKER RÖSCH*

Lehrstuhl für Theoretische Chemie, Technische Universität München, W-8046 Garching, Germany

Abstract

We present an INDO-s molecular-orbital investigation of organic molecules containing a barrelene moiety that provides a rigid link between an aromatic donor and a maleic ester acceptor group. Molecules of this type have recently been synthesized and characterized spectroscopically. We discuss the ground state and various excited states both *in vacuo* and in solution. Solvent effects are incorporated by use of an electrostatic cavity model which is not restricted to a spherical cavity, but allows for a cavity shape that is adapted to the solute molecule. The calculations indicate low-lying charge-transfer (CT) excitations in the region of the first aromatic transitions, even in the gas phase. © 1992 John Wiley & Sons, Inc.

Introduction

Photoinduced intramolecular charge-transfer (CT) and electron-transfer (ET) reactions have recently been studied intensively [1–4]. Much attention is focused on understanding the various factors that influence the rate of ET reactions, for example, the nature of the thermodynamic driving force and its modification [5], the effects of the surrounding solvent [1,6,7], and the spatial relationship between donor and acceptor moieties [2,8–10]. In early experimental investigations, the donor and acceptor units were separated by a flexible spacer which exerted only a limited control over the spatial relationship between donor and acceptor groups [4,11]. Detailed investigations of orientational effects were not feasible since this type of mediating bridge allowed for a variation both in the actual donor–acceptor distance as well as their relative orientation. In recent years, new insight into the nature of the donor–acceptor interaction was gained by connecting donor and acceptor groups via a rigid bridge [12–14]. In this way, both groups are not only held at a fixed separation, but also in a definite relative orientation. These well-defined donor–acceptor systems also made it possible to study effects of the bridge that go beyond pure geometrical implications, but comprise specific ("through bond") modifications of the electronic interaction between donor and acceptor groups [1,8,15].

---

* Author to whom correspondence should be addressed.

Since most previous investigations have been carried out in a condensed medium. it was rather difficult to achieve a separation of the solvent relaxation and its influence on the ET process from the effects of intramolecular degrees of freedom. Particularly the relative importance of the intramolecular and the solvent reorganization energy. crucial variables in ET theory [2], could not be established reliably. Investigations of ET processes in the gas phase would provide an opportunity to overcome these difficulties since, under such circumstances, the reorganization energy is only caused by intramolecular rearrangements. Unfortunately. molecules exhibiting ET characteristics are normally rather large and involatile. However, recently a large family of moderately sized donor–acceptor molecules has been synthesized and characterized [16] which holds promise of providing a breakthrough in studying this problem. These molecules consist of a central barrelene unit (Fig. 1) which is substituted by annelated aromatic compounds as the donor unit and by two carboxymethylester groups forming the acceptor unit.

In this article we shall report electronic structure investigations of dibenzo-barrelene-dicarboxydimethylester (DBBD), the prototypical compound of this family (Fig. 2). We will discuss the electronic structure of DBBD by building this molecule formally from barrelene and by successively adding donor and acceptor groups. We will focus our attention on the role of the rather short barrelene "bridge" in mediating the interaction of the donor and acceptor substituents. In addition. we will employ an electrostatic cavity model [17,18] to investigate the influence of a surrounding solvent on the transition energies of the charge-transfer excitations. The results of the extensive spectroscopic investigations as well as further theoretical discussions will be published elsewhere [19].

Method

The geometry of the molecules under investigation was derived from molecular mechanics calculations [20]. Common bond distances were used for symmetry-
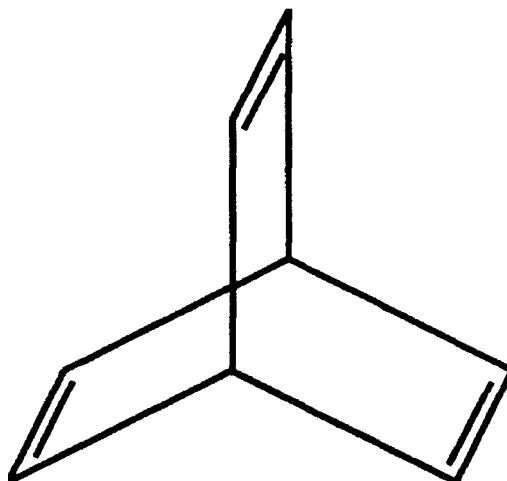
Figure 1. Sketch of bicyclo-[2.2.2]-2,5,7-octatriene (barrelene).

MeO   OMe
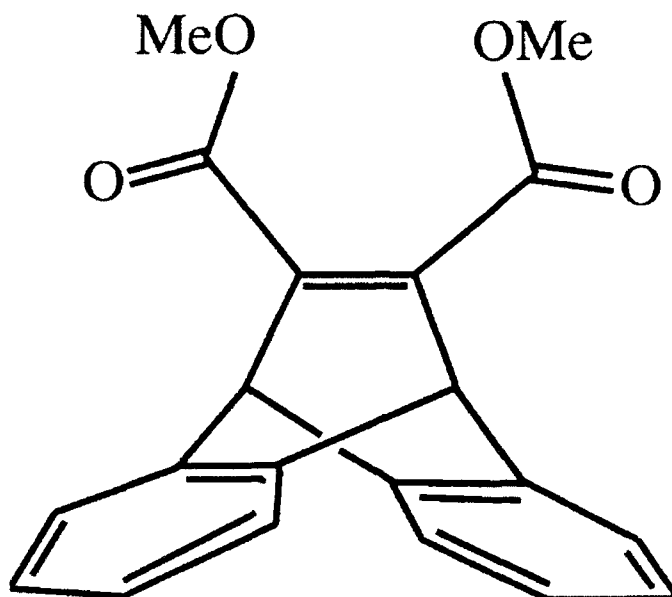
Figure 2. Sketch of dibenzo-barrelene-dicarboxymethylester (DBBD).

equivalent bonds. The carbon atoms of the carboxymethylester groups were found to lie in one plane with the carbon atoms of the ethylene moiety. Relative to this plane, the O — C — O moieties were found to be rotated about the C — C axis by an angle of about 40° with the carbonyl oxygens pointing "outward". To preserve the C_2 symmetry of the acceptor-substituted barrelene unit (see Fig. 2), in the subsequent calculations a common angle of 45° was used.

INDO/S calculations [21,22] were performed to obtain the electronic structure of the ground state and of the excited states. To incorporate solvent effects in the electronic structure we used an electrostatic cavity model with a cavity surface that is adapted to the molecular shape [18]. The model takes the polarization of a dielectric medium into account in a self-consistent fashion. Details concerning this electrostatic cavity model may be found elsewhere [17,18].

Results

The electronic structure of barrelene (bicyclo-[2.2.2]-2,5,7-octatriene, see Fig. 1) has been the subject of several studies [23–28]. The order of the frontier (π) orbitals, a textbook example for simple group theory arguments, is determined by the high symmetry (D_{3h}) of the molecule: $e' < a'_2$ (HOMO) $< e''$ (LUMO) $< a''_1$. The π molecular-orbital spectrum is displayed in the middle column of Figure 3, also depicted are sketches of these MOs as viewed along one of the three twofold axes. In the following we will use the π molecular orbitals of barrelene as a reference for the discussion of the electronic structure of various substituted compounds.

The substitution of the barrelene "bridge" by two adjacent electron withdrawing carboxymethyl groups reduces the symmetry at least to C_2 and leads to a rearrange-
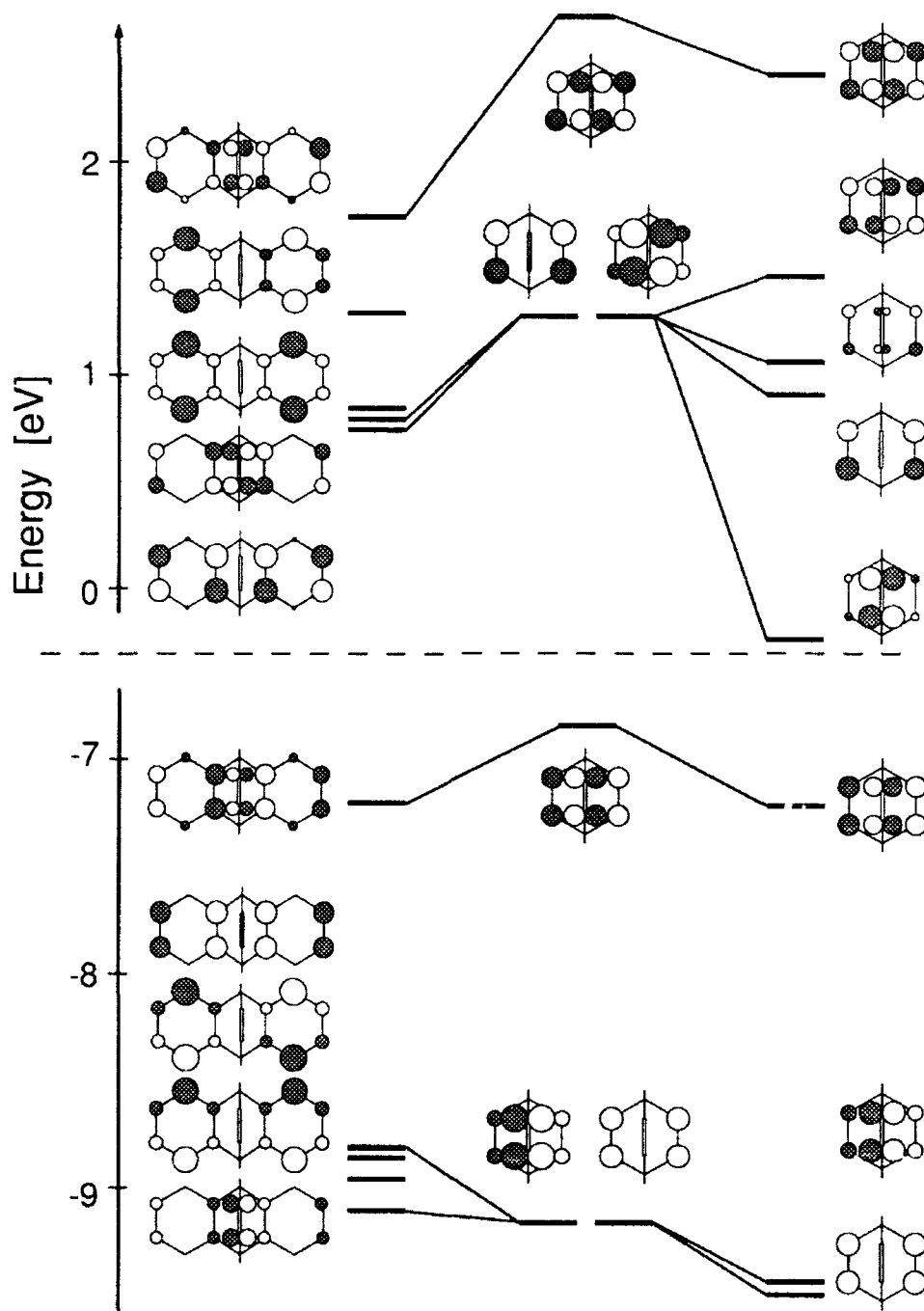
Figure 3.   Frontier orbitals of dibenzo-barrelene (D-B), barrelene (B), and barrelene-di-
carboxomethylester (B-A) as viewed from a vertical C_2 axis.

ment of the π molecular orbitals (see Fig. 3). The orbitals of this acceptor-substituted barrelene (B–A) are sketched on the right-hand side of Figure 3. In this figure the view is along the unique C_2 axis of the substituted barrelene compound (vertical in Fig. 1). However, all contributions from the substituents have been omitted for clarity. An INDO calculation finds only a small energetic relaxation of the occupied orbitals, whereas a strong interaction of the virtual π orbitals of barrelene with the electron withdrawing substituents is observed. Two acceptor-derived orbitals are found in the frontier orbital energy region of B–A, one symmetric, the other one antisymmetric with respect to the vertical plane that contains the substituted C=C double bond. (This mirror plane, although no longer a symmetry element of the substituted compound, may still be invoked to a rather good approximation.) The antisymmetric acceptor-derived virtual orbital interacts strongly with that orbital of the barrelene LUMO e'' set which has the same symmetry characteristic. The bonding combination thereof, the LUMO of B–A, is lowered in energy by about 1.5 eV. This orbital exhibits an acceptor contribution (COOMe) of 52% and a C=C π bond contribution of 40%. There is almost no π interaction with the second partner of the e'' set which originally was symmetric with respect to the nodal plane at the substituted double bond. The π orbital a_1'' interacts only weakly with the acceptor orbitals. The two further virtual orbitals of B–A drawn in Figure 3 (the second and third from the top in the right-most column) have dominant acceptor contributions. From these findings a distinct energy reduction of the HOMO–LUMO excitation is expected for the acceptor-substituted compound. This is one of the key features of the family of donor–acceptor molecules under discussion. Based on the composition of the corresponding molecular orbitals this HOMO–LUMO transition exhibits charge-transfer character as charge density is shifted "upward" from the unsubstituted "ethylene" moieties to the acceptor-substituted "ethylene" moiety and to the dicarboxymethylester units.

The orbitals of the donor-substituted compound dibenzobarrelene (D–B) may be viewed either as orbitals of a bent (9,10)-dihydroanthracene perturbed by a bridging ethylene unit or as perturbed barrelene orbitals. Using the latter scheme, one may relate three occupied (b_2, a_1, and b_2) and three virtual orbitals (a_1, a_2, and a_2) to the barrelene orbitals e', a_2', e'' and a_1'', respectively (Fig. 3). The additional orbitals of D–B in this relevant energy window, two occupied and two virtual orbitals, may be rationalized by reference to the fact that the frontier orbitals of benzene are actually comprised of degenerate pairs, e_{1g} and e_{2u}. A significant interaction of the two benzene fragments in a bent dihydroanthracene leads to a bonding and antibonding linear combination of each of these four benzene π orbitals. For symmetry reasons, the π and π^* orbitals of the bridging ethylene moiety can only mix with one orbital in each of these submanifolds, the one with proper nodal structure. Therefore, we arrive at five occupied and five virtual orbitals as sketched in Figure 3. Since the HOMO of benzene is delocalized over the ring one finds the antibonding interaction of the various C–C π units *reduced* in the HOMO of D–B compared to DBBD and, consequently, the HOMO energy is *lowered* by 0.4 eV compared to barrelene. The virtual orbitals of the benzo-substituted compound are shifted to lower energy by about 0.5 eV with respect to the e'' level of barrelene for analogous

reasons. Therefore, similar to the situation in the acceptor-substituted barrelene, but not quite to the same extent, the gap between HOMO and LUMO becomes smaller.

From these results one would expect for both derivatives of barrelene a decrease of the energy of the corresponding HOMO–LUMO transition as is indeed the case for B–A where the lowering of the HOMO–LUMO gap by about 0.6 eV with respect to the value in barrelene is accompanied by a decrease of the energy of the HOMO–LUMO transition by 6500 cm⁻¹. However, for the donor-substituted compound the simple picture of the one-electron levels fails as a guide for the transition energy. Although a small decrease of the HOMO–LUMO gap is found, the INDO–CI model yields a value for the HOMO–LUMO transition which is about 3000 cm⁻¹ larger than the corresponding value calculated for barrelene. As will be shown later, the transition energy of the donor-acceptor substituted barrelene results from a combination of both effects which leads to an overall decrease of the transition energy with respect to the unsubstituted barrelene.

The one-electron levels of DBBD, where both the benzene and the acceptor groups are attached to the central barrelene unit, are shown in Table I. The contributions from the various fragments of the molecule are listed in percent: C—H denotes the contributions of the two CH fragments connecting the two benzene rings (Benz) and the bridging ethylene unit (C—C). In accordance with the acceptor-substituted barrelene compound B–A, the LUMO (25a) of DBBD is located on the bridging ethylene and on the acceptor. It consists of 54% C—C and 34% COOMe contri-

TABLE I. Energy and Mulliken populations of pertinent molecular orbitals of DBBD (in C_2 symmetry). C—H denotes the populations of the fragments that connect the two benzene rings (Benz) and the bridging ethylene (C—C); COOMe denotes the contribution of the acceptor groups. The orbital 24a is the HOMO of DBBD.

Orbital C_2	Energy [eV]	C—H %	C—C %	COOMe %	Benz %
20b	11.55	1	1	98	1
21a	11.55	1	0	96	3
21b	10.51	2	12	81	5
22a	10.29	1	8	88	3
22b	9.17	6	42	12	40
23b	9.02	3	5	5	87
23a	8.92	1	0	0	99
24a	8.91	4	3	3	90
24b	7.37	0	24	4	72
25a	0.09	1	54	34	11
25b	0.62	1	2	1	96
26a	0.74	0	.	1	98
26b	1.16	0	0	14	86
27a	1.21	0	0	1	83
27b	1.52	0	5	81	14
28a	2.05	1	37	.	14
28b	2.77	21	43	21	15

butions. Compared to D–B, the LUMO energy is lowered by 0.9 eV through the interaction with the acceptor. The higher lying virtual orbitals are located on the aromatic systems, acceptor orbitals follow at even higher energy. None of the four highest occupied molecular orbitals carries any significant contributions from the acceptor. At lower energy one finds acceptor orbitals, essentially of oxygen lone pair character.

On the basis of the above discussion of the electronic structure of DBBD one expects several low-lying excitations of some charge transfer character from the highest occupied orbitals into the LUMO. The calculated excitation energies, the nonzero cartesian component of the state dipole as well as the corresponding oscillator strength are shown in Table II. The lowest transition at 30700 cm^{-1} results from the HOMO–LUMO excitation and is classified as a D → A transition. The amount of charge transfer is measured by the change of the Mulliken population of the acceptor moiety (C C plus COOMe; also shown in Table II). About 0.4 atomic units of charge are transferred to the acceptor during this transition. The next higher states up to about 42500 cm^{-1} are intra-aromatic transitions (D → D) that exhibit very little charge transfer. The admixture of A → A type to the state 2B is an artifact of the present INDO parameterization which places $n \rightarrow \pi^*$ transitions too low in energy [17]. The next higher transitions beyond 42600 cm^{-1} are excitations into the orbital 27b which is an almost pure acceptor orbital. These excitations may therefore be viewed as "classical" donor–acceptor transitions. The nonzero component of the state dipole also shows the largest change for these charge-transfer excitations. From these findings, it becomes clear that the goal of designing a relatively small compound that exhibits a low-lying electron transfer excitation may be within reach by using members of the barrelene based donor–acceptor complexes [19]. First experimental evidence supporting this statement has been obtained from fluorescence spectra of DBBD in various solvents [16].

TABLE II   Calculated excited states of DBBD (in C_2 symmetry) using INDO single excitations. The charge-transfer is measured by the change of the Mulliken populations of the C C and the COOMe moieties.

State	Energy [cm^{-1}]	State dipole [Debye]	Oscillator strength	Charge transfer [a.u.]	Character
1 A	0	1.551	--		
1B	30694	5.342	0.039	0.422	D → A
2 A	34062	1.175	0.014	0.018	D → D
2B	34509	1.744	0.079	0.004	D → D, A → A
3B	34727	1.015	0.033	0.045	D → D
3 A	36356	2.434	0.017	0.061	D → D
4 A	36773	4.791	0.000	0.250	D → D
4B	42516	1.197	0.133	0.054	D → D
5 A	42613	8.080	0.017	0.562	D → A
6 A	43792	8.160	0.067	0.529	D → A

However, close inspection of the theoretical results presented here makes it evident that the lowest excitation of DBBD, although of definite CT character, does not provide an example for a photoinduced electron transfer excitation. In such a photoinduced ET process, an intra-donor excitation is followed by a configurational change of molecular (and solvent) degrees of freedom which entails a stabilization of a charge-separated state that would otherwise lie too high in energy [1,2,29]. The barrelene-derived ethylene bridge in DBBD plays a dual role in that it provides a close spatial arrangement of donor and acceptor unit. But it also entails quite a strong *direct* electronic coupling of these two moieties. The ethylene bridge (C—C) contributes substantially both to the donor HOMO (24%, see Table I) and to the acceptor LUMO (54%). Therefore, the lowest excitation is no longer of pure donor–donor character from which an electron transfer process evolves, but exhibits direct CT character. This may be contrasted with the nature of some higher lying excitations of type D → A which, after suitable geometrical relaxations, could evolve into typical final states of an electron transfer process that originated from suitable D → D excitations. Examples for such "precursors" of ET final states are provided by the excited states 5A and 6A (see Table II) which may be described as a mixture of the excitations from the MO 24a into 25a and from MO 24b into 27b (see Table I). In these cases one finds the acceptor orbitals spatially well separated from the donor orbitals which allows classification of the transitions 1A → 5A and 1A → 6A as D → A CT excitations.

The different nature of the various CT transitions is also reflected in the calculated solvatochromic shifts. Typically, such shifts of CT excitations may range up to 4500 cm^{-1} in a polar solvent [30]. Calculated values for the solvent-induced shift of excitations of DBBD in an unpolar (cyclo-hexane) and in a polar solvent (water) are collected in Table III. The transition energies of the three lowest-lying excitations with significant charge transfer are shown. The HOMO–LUMO transition 1B undergoes a solvent shift of about 1000 cm^{-1}, a moderate value which reflects the rather low degree of charge separation. For the higher lying transitions with a more pronounced CT character the red shift amounts to 1600 cm^{-1}. As noted previously [17,18], the difference of the shifts in the two solvents investigated is rather small compared to the calculated shift on going from vacuum to an unpolar solvent like cyclo-hexane. Here, it is important to note that the cavity model employed only includes electrostatic contributions, but does not take dispersion interaction into account [18]. A rough estimate of the dispersion contribution [17,31] yields an

TABLE III.   Transition energies (in cm^{-1}) of the lowest-lying charge-transfer excitations of DBBD *in vacuo* and solvated in cyclo-hexane and in H$_2$O.

State	In vacuo	cyc-hexane	H$_2$O
1B	30695	29650	29565
5A	42615	40970	40855
6A	43795	42190	42180

additional red shift for all transitions of about 230 cm^{-1} in cyclo-hexane and 190 cm^{-1} in water.

It is interesting to investigate the effect of the surrounding solvent on the charge density in the ground state and in the lowest lying CT states of DBBD. We will use the total Mulliken charges on the acceptor group (A) and the donor group (D) as a rough, but informative measure for such solvent-induced changes (see Table IV). While the ground-state charge distribution remains nearly unchanged upon solvation, one finds the amount of charge separation remarkably increased in the D → A excited states, an immediate reflection of the stabilization provided by the surrounding solvent. The charge transfer from the donor to the acceptor unit increases by 30%, but again this effect is significantly larger for the proper CT states 5A and 6A compared to the first excited state 1B.

Conclusions

We have analyzed the electronic structure of dibenzo-barrelene-dicarboxydimethyl-ester (DBBD) and we have compared the donor–acceptor substituted barrelene with both the donor- and the acceptor-substituted compound. The INDO model calculations yield a first excited state with definite CT characteristics, in agreement with experiment [16]. We were able to identify the structural features which are responsible for the fact that this molecule has such a low-lying CT state, even in the gas phase. However, this transition, although accompanied by a sub-

TABLE IV. Solvent effect on the Mulliken charges of the donor (D) and the acceptor (A) unit of DBBD for the ground state (1A) and for various excited states (1B, 5A, and 6A). The following quantities are displayed: A, Mulliken population of the C—C-bridge and the COOMe groups; D, Mulliken population of the benzene rings; D → A, charge transfer from the donor to the acceptor monitored by the change in the population of the acceptor unit A.

State		Vacuum	cyc-hexane	H$_2$O
1A	A	−0.112	−0.115	−0.119
	D	−0.060	0.058	−0.057
1B	A	−0.534	−0.666	−0.678
	D	0.410	0.506	0.515
	D → A	0.422	0.551	0.559
5A	A	0.674	−0.768	−0.727
	D	0.515	0.575	0.533
	D → A	0.562	0.653	0.608
6A	A	0.641	0.713	0.741
	D	0.483	0.523	0.545
	D → A	0.529	0.598	0.622

stantial charge separation of about 0.4 a.u., does not exhibit the characteristics that are typical for a photoinduced ET process since the ethylene bridge between donor and acceptor groups contributes both to the initial and final state. Therefore it remains to be seen to what extent barrelene based compounds will be able to serve as models for the investigation of photoinduced electron transfer phenomena [19].

In addition we have applied an electrostatic cavity model to investigate the effect of a surrounding solvent on the energy of various electronic excitations and the corresponding final state charge distribution. We showed that the electrostatic interaction leads to a considerable increase of the charge separation for the CT states. Concomitantly their excitation energy is lowered, but this shift is only of moderate size due to the short distance over which the charge separation occurs.

Acknowledgment

Bibliography

[1] M. D. Newton and N. Sutin, Ann. Rev. Phys. Chem. 35, 437 (1984).
[2] R. A. Marcus and N. Sutin, Biochim. Biophys. Acta 811, 265 (1985).
[3] M. A. Fox and M. Chanon, Photoinduced Electron Transfer (Elsevier, Amsterdam, 1988).
[4] B. E. Bowler, A. L. Raphael, and H. B. Gray, Prog. Inorg. Chem.: Bioinorganic Chem. 38, 259 (1990).
[5] R. A. Marcus, Ann. Rev. Phys. Chem. 15, 155 (1964).
[6] K. Mikkelsen, E. Dalgaard, and P. Swanstrom, J. Phys. Chem. 91, 3081 (1987).
[7] H. J. Kim and J. T. Hynes, J. Phys. Chem. 94, 2736 (1990).
[8] S. Larsson and A. Volosov, J. Chem. Phys. 85, 2548 (1986).
[9] G. L. Closs and J. R. Miller, Science 240, 440 (1988).
[10] S. S. Isied, A. Vassilian, J. F. Wishart, C. Creutz, H. A. Schwarz, and N. Sutin, J. Am. Chem. Soc. 110, 635 (1988).
[11] P. Finckh, H. Heitele, M. Volk, and M. E. Michel-Beyerle, J. Phys. Chem. 92, 6584 (1988).
[12] C. A. Stein, N. A. Lewis, and G. Seitz, J. Am. Chem. Soc. 104, 2596 (1982).
[13] G. L. Closs, L. T. Calcaterra, N. J. Green, K. W. Penfield, and J. R. Miller, J. Phys. Chem. 90, 3673 (1986).
[14] H. Oevering, M. N. Padden-Row, M. Heppener, A. M. Oliver, E. Cotsaris, J. W. Verhoeven, and N. S. Hush, J. Am. Chem. Soc. 109, 3258 (1987).
[15] J. Jortner, J. Chem. Phys. 64, 4860 (1976).
[16] J. Cortes, H. Heitele, and M. E. Michel-Beyerle (in preparation).
[17] T. Fox and N. Rösch, Chem. Phys. Lett. 191, 33 (1992).
[18] T. Fox and N. Rösch, J. Mol. Struct. (THEOCHEM) (in press).
[19] J. Cortes, H. Heitele, M. E. Michel-Beyerle, T. Fox, M. Kotzian, and N. Rösch (in preparation).
[20] P. Dauber-Osguthorpe, V. A. Roberts, D. J. Osguthorpe, J. Wolff, M. Genest, and A. T. Hagler, Proteins: Structure, Function and Genetics 4, 31 (1988).
[21] J. E. Ridley and M. C. Zerner, Theor. Chim. Acta 32, 111 (1973).
[22] J. E. Ridley and M. C. Zerner, J. Mol. Spectrosc. 50, 457 (1974).
[23] H. E. Zimmerman and R. M. Paufler, J. Am. Chem. Soc. 82, 1514 (1960).
[24] R. Hoffmann, E. Heilbronner, and R. Gleiter, J. Am. Chem. Soc. 92, 706 (1970).
[25] E. Haselbach, E. Heilbronner, and G. Schröder, Helv. Chim. Acta 54, 153 (1971).
[26] F. A. Van-Catledge, J. Am. Chem. Soc. 114, 430 (1992).

[27] A. Y. Meyer and R. Pasternak, Tetrahedron **33**, 3239 (1977).

[28] A. Gedanken and A. de Meijere, J. Chem. Phys. **88**, 4153 (1988).

[29] B. S. Brunschwig, S. Ehrenson, and N. Sutin, J. Phys. Chem. **90**, 3657 (1986).

[30] C. Reichhardt, *Solvents and Solvent Effects in Organic Chemistry*, 2nd ed. (Verlag Chemie, Weinheim, 1988).

[31] W. Liptay, Z. Naturforsch. **20A**, 1441 (1965).

Attempts to Calculate the Electron Affinity of Acrylonitrile

M. MALOTEAU, D. H. MOSLEY, J. M. ANDRE, and J. DELHALLE

Laboratoire de Chimie Théorique Appliquée, Facultés Universitaires Notre-Dame de la Paix, 61, rue de Bruxelles B-5000 Namur, Belgium

B. T. PICKUP

Department of Chemistry, The University, Sheffield S3 7HF, United Kingdom

Abstract

Gas phase acrylonitrile electron affinity has recently been estimated to be in the range 0.01 to 0.02 eV. In spite of a strong theoretical prediction on the existence of stable anions for molecules having dipole moments larger than the critical 1.625 D, it has not been possible to obtain a positive electron affinity for acrylonitrile (dipole moment = 3.9 D) by *ab initio* SCF and MP2 calculations using 6-31G, 6-31G*, 6-31+G(d), 6-31++G(d,p), and 6-311++G(2d,2p) bases. © 1992 John Wiley & Sons, Inc.

Introduction

The formation of the acrylonitrile anion, AN + e → AN⁻ (AN: $CH_2=CH-C\equiv N$), has long been known to play an important role in organic electrochemistry [1]. Recently it has received renewed attention with the possibility of chemisorbing electrochemically the acrylonitrile terminal vinylic carbon on oxidizable metal surfaces and, from the resulting chemisorbed acrylonitrile anions, to grow poly(acrylonitrile) chains via an anionic mechanism [2,3]. In spite of basic differences between an electron transfer taking place from a cathode to a molecule in an electrolytic medium and the formation of an anion in gas phase, good correlations between calculated electron affinities (EA) of the isolated species and their reduction potentials are often obtained and used to assess the potential of new monomers prior to their synthesis and polymerization [4]. We ourselves have noted a satisfactory relationship between the reduction potentials and the 3-21G and 3-21+G LUMO energies (Koopmans' theorem) of neutral acrylonitrile and some of its methyl derivatives [5]. However, to be confident in such correlations one ought to understand the important differences existing between gas phase EA and reduction potentials [4,5b]. Theoretical calculations on the relative stability of the anion, both isolated and subject to the fields experienced in condensed phase, are expected to give insight on the dominant intermolecular interactions responsible for these differences [6].

A classical theorem [7,8] states that polar molecules having a permanent electric dipole moment larger than a critical value, $|p_0| > 1.625$ D, should yield a positive

electron affinity, at least in the fixed nuclei approximation. Koopmans' approximation of the vertical electron affinity (VEA) does not predict stable isolated anions for acrylonitrile and its methyl derivatives [5], in spite of having permanent dipole moments larger than the critical value (in that series: $3.69 < |p_0| < 4.50$ D, experimentally [9], and $3.92 \leq |p_0| \leq 4.62$ D theoretically (RHF-3-21G) [5b]) and contrary to the prediction of the theorem. Since Koopmans' prediction of EAs can easily be seen to be deficient [10], more rigorous treatments incorporating relaxation and correlation effects are needed to claim quantitative results.

A literature search for theoretical results on the electron affinity of acrylonitrile, the simplest in the series considered in Ref. [5], surprisingly indicates that only three works have been published over the last 20 years, all having been carried out at the semiempirical level and yielding rather different results. Houk and Munchausen [11] obtain $EA = +0.02$ eV with a frontier orbital treatment. Using the PPP method and the Koopmans' approximation, Younkin et al. [12] predict a much larger value, $EA = +1.3$ eV. From their scaled MNDO Koopmans results, Mirek and Buda [13] predict an experimental adiabatic electron affinity (AEA) of $+0.33$ eV.

Several experimental studies have been devoted to acrylonitrile [14–18], but it is only recently that the isolated acrylonitrile molecular anion has been claimed to have been observed in collisional electron transfers from high-Rydberg atoms, Kr^{**} and Ar^{**}, to AN molecules [19]. The collisional electron transfer from Kr^{**} to acrylonitrile, $AN + Kr^{**} \rightarrow AN^- + Kr^+$, indicates that the experimental AEA of AN should be larger than the ionization potential of Kr^{**}, that is, in the range 0.01 to 0.02 eV.

In view of the dispersion of the theoretical results on acrylonitrile AEA presently available, the rather low experimental value (< 0.02 eV) for a conjugated molecule exhibiting a large dipole moment due to the strong electron attracting nitrile group, and the lack of rigorous theoretical treatments, we attempt in this contribution to compute the vertical (VEA) and adiabatic (AEA) electron affinities of acrylonitrile by various ab initio procedures using several basis sets.

Computational Details

As pointed out in previous works on ab initio electron affinity calculations of isolated molecules, the quality of the wave function and therefore the basis set play a major role [10,20]. The 6-31G basis (I) [21,22] is known to yield equilibrium geometries that compare well with experiment [21] and total energies accurate enough to obtain reliable results from total energy differences. It therefore constitutes an acceptable reference basis to be gradually enriched with diffuse atomic functions needed for electron affinity calculations. The basis sets [23–25] that will be considered here are the 6-31G* (II), 6-31+G(d) (III), 6-31++G(d,p) (IV) and 6-311++G(2d,2p) (V); the exponents of the polarization and additional diffuse functions in bases (II) to (V) are listed in Table I.

Calculations have been carried out with these bases at the restricted Hartree–Fock (RHF), unrestricted Hartree–Fock (UHF) and Möller–Plesset (MP) levels with

TABLE I. Exponents of the polarization and diffuse functions added to the 6-31G basis (I). Basis set notation: (II) 6-31G*; (III) 6-31+G(d); (IV) 6-31++G(d, p); (V) 6-311++G(2d, 2p).

Basis set	(II)	(III)	(IV)	(V)
Hydrogen				
polarization				
p	—	—	1.1000	1.5000
	—	—	—	0.3750
diffuse				
s	—	—	0.0360	0.0360
Carbon				
polarization				
d	0.8000	0.8000	0.8000	1.1252
	—	—	—	0.3130
diffuse				
sp	—	0.0438	0.0438	0.0438
Nitrogen				
polarization				
d	0.8000	0.8000	0.8000	1.8260
	—	—	—	0.4565
diffuse				
sp	—	0.0639	0.0639	0.0639

the Gaussian-90 series of programs [26] running on a FPS511 computer. Standard threshold conditions have been imposed: 10^{-10} a.u. as two-electron integral cutoff, 10^{-9} for the requested convergence on the density matrices, and 5.10^{-4} hartree.bohr^{-1} as the minimum residual forces on the cartesian components.

Results

The equilibrium geometries and the charge distribution indices are presented first, followed by the computed electron affinity results.

Geometry and Charges

For each basis set, the geometry of the neutral and the anionic species have been fully optimized at the RHF, UHF, and MP2 levels, respectively. The equilibrium structures for the neutral and the anionic species are predicted to be planar. The notation for the structural parameters (bond lengths and angles) is indicated in Figure 1, and the corresponding values together with the Mulliken net atomic charges q, and the dipole moment $|p_0|$ are listed in Table II for RHF and UHF results and in Table III for MP2 calculations. In the case of UHF calculations, S^2 is also given to assess the amount of spin contamination present, as compared to the ideal 0.75 value.

With the exception of the C≡N bond length, which is generally predicted too short at the Hartree-Fock level, the geometrical parameters of acrylonitrile calculated
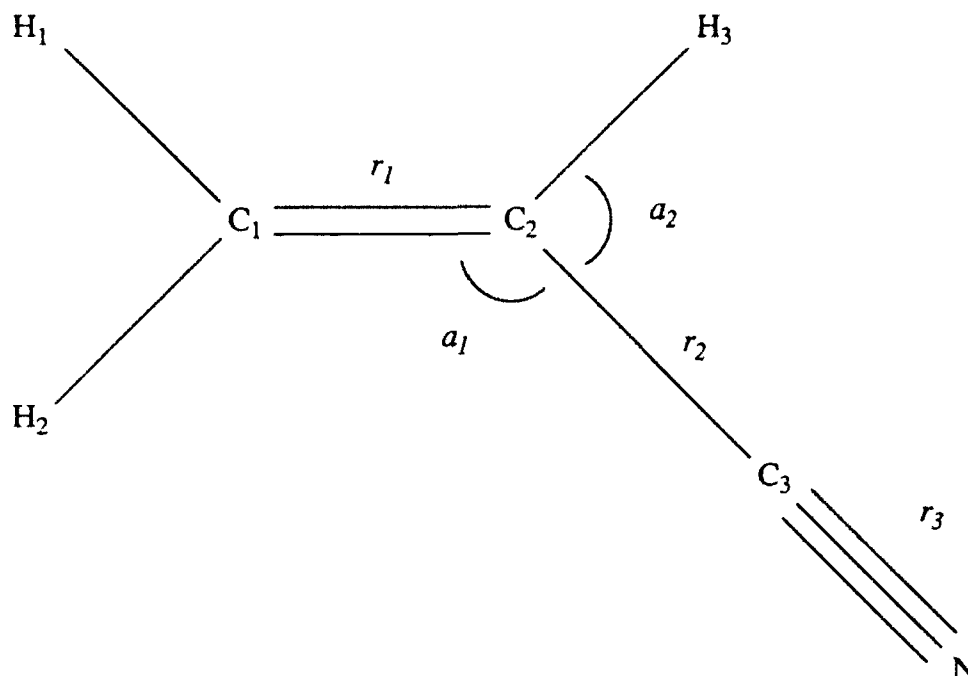
Figure 1.   Labeling convention used in Tables II and III to refer to the geometrical parameters of acrylonitrile, neutral and anion.

with all bases are in good agreement with gas phase microwave spectroscopy data [27]. The RHF calculated dipole moments range from 4.26 to 4.36 D and are also comparable with the experimental [9] gas phase value, 3.87 D, but in the average they are overestimated by about 0.5 D. In spite of a strong dependence of the Mulliken net atomic charges on the basis set, a general observation concerning the polarity of the molecule can be made. At one end of the molecule, the nitrogen atom bears a large negative charge, while at the other end the hydrogen atoms are positively charged. C_1 and C_3 are consistently negative and positive, respectively, while nothing definite can be concluded from the Mulliken charges for C_2. The results of geometry optimization at the MP2 level are slightly, but consistently better agreement with experimental data, the $C\equiv N$ bond length being the one that experiences the largest improvement. The MP2 dipole moments are in excellent agreement with the experimental value. The charge distribution is very similar to that obtained at the RHF level.

There is no experimental data on the molecular geometry of the acrylonitrile anion to compare with our calculations. Thus, we can only analyze the changes in the geometrical parameters with respect to those of the neutral molecule and their evolution with the basis set. Considering the RHF results first, the observations to consider are an increase of C—C, ca. 0.10 Å, a decrease of C—C, ca. 0.05 Å, and an increase of $C\equiv N$, ca. 0.02 Å, distances with respect to the corresponding ones in the neutral molecule. As in the case of the neutral molecule, the length of C—C,

TABLE II. Selected bond distances (r) and angles (a) of the equilibrium structure of neutral acrylonitrile and its anion calculated at the RHF and UHF levels, lengths in Å and angles in degrees. Mulliken net atomic charges (q), permanent dipole moment p, (in debye), and S^2 of UHF results. Basis set notation (I) 6-31G, (II) 6-31G*, (III) 6-31+G(d), (IV) 6-31++G(d, p), (V) 6-311++G(2d, 2p).

Basis set	(I)	(II)	(III)	(IV)	(V)	Exp
Acrylonitrile (RHF)						
r_1	1.326	1.320	1.323	1.322	1.316	1.339 [27]
r_2	1.432	1.443	1.443	1.443	1.442	1.426 [27]
r_3	1.148	1.136	1.137	1.137	1.128	1.164 [27]
a_1	123.1	122.2	122.3	122.3	122.2	122.6 [27]
a_2	115.5	115.8	115.7	115.7	115.8	115.7 [27]
q_{C1}	0.30	0.34	0.38	0.11	0.11	
q_{C2}	0.09	0.17	0.03	0.04	0.17	
q_{C3}	0.04	0.28	0.04	0.04	0.01	
q_{H1}	0.19	0.21	0.23	0.14	0.09	
q_{H2}	0.21	0.22	0.24	0.14	0.08	
q_{H3}	0.24	0.24	0.26	0.16	0.09	
q_N	0.30	0.45	0.43	0.42	0.32	
p	4.30	4.26	4.36	4.36	4.35	3.87 [9]
Acrylonitrile anion (UHF)						
r_1	1.425	1.425	1.423	1.423	1.419	
r_2	1.383	1.387	1.393	1.394	1.392	
r_3	1.179	1.164	1.163	1.162	1.153	
a_1	125.7	125.3	124.4	124.4	124.3	
a_2	115.8	115.6	115.8	115.8	115.6	
q_{C1}	0.40	0.45	0.66	0.43	0.42	
q_{C2}	0.28	0.37	0.25	0.20	0.08	
q_{C3}	0.01	0.23	0.12	0.08	0.08	
q_{H1}	0.05	0.07	0.14	0.07	0.01	
q_{H2}	0.07	0.09	0.16	0.07	0.01	
q_{H3}	0.09	0.10	0.17	0.08	0.01	
q_N	0.53	0.66	0.69	0.68	0.58	
S^2	0.806	0.790	0.789	0.789	0.789	

C—C, and C≡N bonds respectively decrease, increase, and decrease as one goes from the 6-31G (I) to the 6-311++G(2d,2p) (V) bases. Spin contamination is generally small and thus does not impair the Möller-Plesset convergence. As in the case of the neutral acrylonitrile, the MP2 results on the anion remain comparable to the UHF ones. The most significant differences are observed for the 6-31G basis, on the one hand, and a systematic increase of the C≡N bond length, on the other hand. Here also the charge pattern is very similar to that obtained at the UHF level.

Electron Affinity

In addition to RHF, UHF, and MP2 geometry optimizations, single point third- and fourth-order Möller-Plesset (MPx, x = 3 and 4) calculations based on the

TABLE III. Selected bond distances (r_i) and angles (a_i) of the equilibrium structure of neutral acrylonitrile and its anion calculated at the MP2 level, lengths in Å and angles in degrees. Mulliken net atomic charges (q_i), permanent dipole moment $|p_0|$ (in debye), and $\langle S^2 \rangle$ of UHF results. Basis set notation: (I) = 6-31G, (II) = 6-31G*, (III) = 6-31+G(d), (IV) = 6-31++G(d, p), (V) = 6-311++G(2d, 2p).

Basis set	(I)	(II)	(III)	(IV)	(V)	Exp.
Acrylonitrile (MP2)						
r_1	1.355	1.341	1.344	1.343	1.337	1.339 [27]
r_2	1.448	1.432	1.433	1.433	1.431	1.426 [27]
r_3	1.203	1.182	1.183	1.183	1.171	1.164 [27]
a_1	123.2	122.0	122.1	122.1	122.2	122.6 [27]
a_2	116.1	116.6	116.6	116.5	116.5	115.7 [27]
q_{c1}	-0.27	-0.33	-0.40	-0.16	-0.18	
q_{c2}	-0.08	-0.16	0.01	0.04	0.17	
q_{c3}	0.04	0.23	0.05	0.03	-0.03	
q_{H1}	0.16	0.19	0.22	0.14	0.10	
q_{H2}	0.17	0.20	0.23	0.14	0.10	
q_{H3}	0.20	0.22	0.25	0.16	0.11	
q_N	-0.23	-0.36	-0.36	-0.35	-0.27	
$|p_0|$	3.73	3.79	3.95	3.88	3.87	3.87 [9]
Acrylonitrile anion (MP2)						
r_1	1.447	1.425	1.419	1.418	1.416	
r_2	1.404	1.390	1.398	1.398	1.397	
r_3	1.197	1.191	1.190	1.190	1.180	
a_1	124.0	124.2	123.0	122.9	123.2	
a_2	116.9	116.3	116.8	116.6	116.2	
q_{c1}	-0.37	-0.46	-0.78	-0.56	-0.56	
q_{c2}	-0.27	-0.35	-0.21	-0.15	-0.02	
q_{c3}	-0.03	0.16	0.13	0.09	-0.01	
q_{H1}	0.03	0.06	0.15	0.08	0.04	
q_{H2}	0.05	0.07	0.17	0.09	0.04	
q_{H3}	0.06	0.08	0.17	0.09	0.03	
q_N	-0.46	-0.57	-0.64	-0.63	-0.52	

corresponding MP2 equilibrium geometries have also been carried out for 6–31G (I) and 6–31+G(d) (III) bases to assess the convergence of the correlation corrections. Total energies are listed in Table IV.

The dependence with the basis sets for predictions of VEA and AEA values calculated in different ways are compared: Koopmans, ΔSCF and ΔMPx (x = 2, 3, and 4). Koopmans vertical electron affinity (VEA) is directly obtained from the frontier orbital energies of the neutral system (VEA$_{K0}$ = $-\varepsilon^0_{LUMO}$). Another measure of the electron affinity is provided by the electron detachment energy ED$_k$: AN$^-$ → AN + e, approximated at the Koopmans level from the energy of the highest occupied orbital of AN$^-$ in its equilibrium geometry, calculated here at the UHF level. (ED$_k$ = $-\varepsilon_{HOMO}$). Total energy differences at the SCF and MPx

TABLE IV. RHF, UHF, MP2 total energies (in a.u.) for the equilibrium geometries of acrylonitrile, neutral and anion. In the case of MP3 and MP4 results, the corresponding MP2 equilibrium geometries have been used in the calculations. RHF* corresponds to total energy of the neutral molecule in the equilibrium geometry of the anion obtained at the UHF level. Basis set notation: (I) = 6-31G, (II) = 6-31G*, (III) = 6-31+G(d), (IV) = 6-31++G(d, p), (V) = 6-311++G(2d, 2p).

Basis set	(I)	(II)	(III)	(IV)	(V)
Acrylonitrile					
RHF	−169.69392	−169.76801	−169.77343	−169.77896	−169.81922
RHF*	−169.97895	−169.75196	−169.75929	−169.76492	−169.80503
MP2	−170.08303	−170.31611	−170.32698	−170.35105	−170.50218
MP3	−170.07376	—	−170.31792	—	—
MP4(DQ)	−170.08826	—	−170.32294	—	—
MP4(SDQ)	−170.09401	—	−170.33088	—	—
Acrylonitrile anion					
UHF	−169.64552	−169.71569	−169.74013	−169.74629	−169.78655
MP2	−170.01471	−170.25888	−170.29801	−170.32416	−170.48418
MP3	−170.01513	—	−170.29111	—	—
MP4(DQ)	−170.02509	—	−170.29474	—	—
MP4(SDQ)	−170.03149	—	−170.30339	—	—

levels are used to estimate the vertical (VEA: anion in the equilibrium geometry of the neutral molecule) and adiabatic (AEA: anion in its equilibrium geometry) electron affinities of acrylonitrile. These calculations are denoted by the self-explanatory notations: $VEA_{\Delta SCF}$, $VEA_{\Delta MP_i}$, $AEA_{\Delta SCF}$, and $AEA_{\Delta MP_i}$. Finally, we have considered $VEA^*_{\Delta SCF}$, the vertical electron affinity computed as the difference between UHF total energy for the anion in its equilibrium geometry and the RHF total energy of the neutral in the equilibrium geometry of the anion. The results are listed in Table V.

The energy and symmetry of the relevant frontier orbitals, the HOMO and the two unoccupied orbitals of lowest energy, $LUMO_1$ and $LUMO_2$, for acrylonitrile and its anion obtained at the RHF and UHF levels, respectively, are given in Table VI: a' corresponds to a state of σ symmetry, while a'' indicates a π symmetry.

First to note, is the fact that Koopmans approximation, VEA_{K0} in Table V, does not yield a positive vertical electron affinity. On the contrary, the electron detachment energy, ED_{K-}, eventually yields positive values as the basis sets include polarization and diffuse functions. However, these values are an order of magnitude larger than the proposed experimental value.

Total energies (Table IV) still show the anion unstable with respect to the neutral molecule, and the better theoretically grounded schemes considered in this article to compute the vertical and adiabatic electron affinity do not predict positive electron affinity values. The larger discrepancies are observed at the SCF level where $VEA_{\Delta SCF}$ and $AEA_{\Delta SCF}$ range from −1.693 to −1.225 eV, and from −1.317 to −0.889 eV, respectively. As the basis set is enriched with polarization and diffuse functions,

TABLE V. Acrylonitrile vertical (VEA), adiabatic (AEA) electron affinities and electron detachment (DEₐ) energy (in eV). Basis set notation: (I) = 6-31G, (II) = 6-31G*, (III) = 6-31+G(d), (IV) = 6-31++G(d, p), (V) = 6-311++G(2d, 2p).

Basis set	(I)	(II)	(III)	(IV)	(V)
Acrylonitrile					
VEA$_{K0}$	2.607	$-$2.802	$-$1.711	$-$0.915	0.886
DE$_K$	$-$0.005	$-$0.011	0.454	0.469	0.512
VEA$_{\Delta SCF}$	$-$1.693	$-$1.827	$-$1.238	$-$1.219	$-$1.225
VEA$^*_{\Delta SCF}$	0.918	$-$0.987	$-$0.521	$-$0.507	0.503
EA$_{\Delta SCF}$	$-$1.317	1.424	$-$0.906	$-$0.889	$-$0.889
VEA$_{\Delta MP2}$	$-$2.231	$-$2.268	$-$0.948	$-$0.891	0.658
AEA$_{\Delta MP2}$	$-$1.859	$-$1.557	$-$0.788	$-$0.732	$-$0.490
AEA$_{\Delta MP3}$	$-$1.595	—	$-$0.730	—	—
AEA$_{\Delta MP4(DQ)}$	$-$1.719	—	$-$0.767	—	—
AEA$_{\Delta MP4(SDQ)}$	$-$1.701	—	$-$0.748	—	—

VEA$_{\Delta SCF}$ and AEA$_{\Delta SCF}$ slowly tend towards less negative values (Fig. 2). As expected, the VEA$^*_{\Delta SCF}$ data are considerably less negative than the VEA$_{\Delta SCF}$ and AEA$_{\Delta SCF}$ values, but still indicate that the anion is less stable than the neutral molecule at the HF level, even at the computed equilibrium of the charged species. When adding correlation corrections at the MP2 level, the situation is improved but the results remain negative both for the adiabatic and the vertical electron affinity. The importance of diffuse functions for the consistency of the treatment can be seen from Table V where correlation corrections to the electron affinity are approximately 0.2 eV for basis (I) and reduce to 0.03 eV for basis (III) as the order in the perturbational treatment increases. This results tends to support the observation by Baker et al.

TABLE VI. RHF and UHF energies (in eV) of the HOMO and the two unoccupied orbitals of lowest energy, LUMO₁ and LUMO₂ of acrylonitrile, neutral and anion. Basis set notation: (I) = 6-31G, (II) = 6-31G*, (III) = 6-31+G(d), (IV) = 6-31++G(d, p), (V) = 6-311++G(2d, 2p).

Basis set	(I)	(II)	(III)	(IV)	(V)
Acrylonitrile (RHF)					
HOMO	$-$10.770 (a″)	$-$10.821 (a″)	$-$10.963 (a″)	$-$10.960 (a″)	$-$11.026 (a″)
LUMO₁	2.607 (a″)	2.802 (a″)	1.711 (a′)	0.915 (a′)	0.886 (a′)
LUMO₂	5.153 (a′)	5.348 (a′)	1.850 (a″)	1.459 (a′)	1.432 (a′)
Acrylonitrile anion (UHF)					
HOMO	0.005 (a″)	0.011 (a″)	$-$0.454 (a″)	$-$0.469 (a″)	$-$0.512 (a″)
LUMO₁	10.013 (a″)	10.220 (a″)	5.687 (a′)	4.286 (a′)	4.213 (a′)
LUMO₂	10.983 (a′)	11.212 (a′)	5.746 (a′)	4.308 (a′)	4.230 (a′)
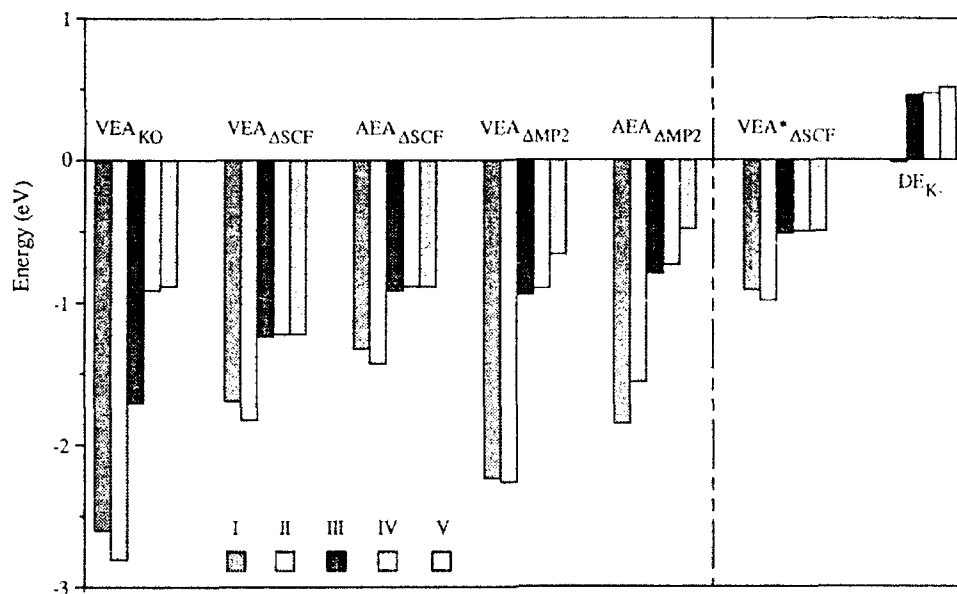
Figure 2. Evolution with the basis set of the various electron affinity estimates for acrylonitrile.

[20] that correlation corrections at the MP2 level can lead to good agreement between theory and experiment.

Discussion

The critical dipole theorem is a very strong one. It implies that any isolated molecule, in the Born–Oppenheimer approximation, should have an *infinite* number of bound anionic states provided that the leading component of a multipolar expansion of the long range part of the potential experienced by an incoming electron is dipolar, and that the critical dipole is exceeded. Details of the short-range potential (whether repulsive or attractive) are irrelevant to the existence of bound states, although they do affect their actual positions in the spectrum. Indeed, the bound states should manifest themselves in terms of negative unoccupied HF orbital energies if the conditions of the theorem are satisfied. It is rather unexpected, therefore, that a conjugated molecule such as acrylonitrile with the powerful electron withdrawing $C\equiv N$ group leading to a dipole moment larger than the critical value of 1.625 D does not readily lead to a stable isolated radical anion with the basis sets used. The situation as it stands is rather disappointing because these basis sets, which have been proposed and shown to work on more "innocent" anions [20,25], are already quite large and prevent larger molecules from being studied in this way.

Our results, combined with the analysis that leads to the critical dipole moment theorem about [7,8], suggest that the state of the acrylonitrile anion should be of σ symmetry, resembling a Rydberg state, the electron distribution of the extra elec-

tron being localized in the positively charged regions of acrylonitrile, that is, nearby the hydrogen atoms and possibly C_1, and far from the electron rich areas, that is, the nitrogen atom and the $C=C$ bond. Indication for this is provided the fact that the LUMO$_1$ in neutral acrylonitrile is of a' (or σ) symmetry for bases (III) to (V) which include diffuse functions, while bases (I) and (II) belong to a'' (or π) symmetry. However, results on the anion at the UHF and MP2 levels indicate that the additional electron charge is mainly distributed on the $C=C-C\equiv N$ backbone where, as indicated by Mulliken atomic charges, C_1, C_2, and N bear more negative charge, in agreement with the fact that the anion HOMO is of a'' (or π) symmetry.

While still so far away from a positive value, the use of more refined theories (e.g., higher orders of MP, direct methods) is not justified, and unlikely to be rewarded in leading to a more accurate (or positive) estimate of EA. Indeed, calculations with largest basis set at the MP2 level still yield an estimate for EA of -0.5 eV, a long way from being positive, indicating that something quite fundamental, possibly in the basis set, is still missing from the treatment. It is unfortunately difficult to know what extra functions might need to be included—both in terms of angular momentum and exponents. Intuition or trial and error is not desirable, not only because basis set calculations—particularly on inclusion of correlation—represent a major computational undertaking but also because there is a need to maintain balance in treatment to avoid a better representation of the anion compared to the neutral that might lead to spurious results in total energy differences.

The case of acrylonitrile serves to illustrate, once again, the difficulties encountered in calculating EA's. Yet, to get a detailed understanding of the electrochemical reduction process in condensed phase, it is essential to know about the intrinsic electron attachment capabilities of molecules, that is, gas phase electron affinity.

Acknowledgments

Bibliography

[1] M. M. Baizer and H. Lund, *Organic Electrochemistry* (Dekker, New York, 1983).

[2] (a) F. Bruno, M. C. Phan, and J. E. Dubois, J. Chim. Phys. (Pairs), 72, 490 (1975); (b) A. Desbene-Monverney and J. E. Dubois, J. Electroanal. Chem. 89, 149 (1978).

[3] (a) G. Lécayon, Y. Bouizem, C. Le Gressus, C. Reynaud, C. Boiziau, and C. Juret, Chem. Phys. Lett. 91, 506 (1982); (b) C. Boiziau and G. Lécayon, Int. J. Adhes. and Adhes. 6, 207 (1986).

[4] U. Akbulut, L. Toppare, and L. Türker, J. Polym. Sci., Polym. Chem. Ed. 23, 1631 (1985).

[5] (a) G. Hennico, J. Delhalle, E. Younang, M. Defranceschi, G. Lécayon, and C. Boiziau, Inter. J. Quantum Chem., Quantum Chem. Symp. 25, 507 (1991); (b) G. Deniau, G. Lécayon, P. Viel, G. Hennico, and J. Delhalle, Langmuir 8, 267 (1992).

[6] J. Bertran and I. G. Csizmadia, Eds. "New Theoretical Concepts for Understanding Organic Reactions," NATO ASI Series C267 (Kluwer, Dordrecht, 1989).

[7] O. H. Crawford, Mol. Phys. **20**, 585 (1971).

[8] W. R. Garrett, Chem. Phys. Lett. **62**, 325 (1979).

[9] *Handbook of Chemistry and Physics* 67th ed. (CRC Press, Bocca Raton, 1986-87), p. E-59.

[10] J. Simons and K. D. Jordan, Chem. Rev. **87**, 535 (1987).

[11] K. N. Houk and L. Munchausen, J. Am. Chem. Soc. **98**, 937 (1976).

[12] J. M. Younkin, L. J. Smith, and R. N. Compton, Theor. Chim. Acta (Berl.) **41**, 157 (1976).

[13] J. Mirek and A. Buda, Z. Naturforsch. **39a**, 386 (1984).

[14] S. Tsuda, A. Yokohata, and T. Umba, Bull. Chem. Soc. Jpn **46**, 2273 (1973).

[15] M. Heni and E. Ilenberger, Int. J. Mass. Spectrom. Ion Processes **73**, 127 (1986).

[16] J. H. J. Dawson and N. M. M. Nibbering, Int. J. Mass. Spectrom. Ion Phys. **33**, 3 (1980).

[17] C. F. Mess, J. van der Greef, and N. M. M. Nibbering, Int. J. Mass. Spectrom. Ion Phys. **34**, 259 (1980).

[18] K. D. Jordan and P. D. Burrow, Acc. Chem. Res. **11**, 341 (1978).

[19] T. Tsukuda and T. Kondow, Chem. Phys. Lett. **185**, 511 (1991).

[20] J. Baker, R. H. Nobes, and L. Radom, J. Comput. Chem. **7**, 347 (1986).

[21] W. J. Hehre, L. Radom, P. v. R. Schleyer, and J. A. Pople, *Ab Initio Molecular Orbital Theory* (Wiley, New York, 1986).

[22] W. J. Hehre, R. Ditchfield, and J. A. Pople, J. Chem. Phys. **56**, 2257 (1972).

[23] R. Krishnan, J. S. Binkley, R. Seeger, and J. A. Pople, J. Chem. Phys. **72**, 650 (1980).

[24] M. J. Frisch, J. A. Pople, and J. S. Binkley, J. Chem. Phys. **80**, 3265 (1984).

[25] T. Clark, J. Chandrasekhar, G. W. Spitznagel, and P. v. R. Schleyer, J. Comput. Chem. **4**, 294 (1983).

[26] Gaussian 90, Revision J, M. J. Frisch, M. Head-Gordon, G. W. Trucks, J. B. Foresman, H. B. Schlegel, K. Raghavachari, M. Robb, J. S. Binkley, C. Gonzalez, D. J. Defrees, D. J. Fox, R. A. Whiteside, R. Seeger, C. F. Melius, J. Baker, R. L. Martin, L. R. Kahn, J. J. P. Stewart, S. Topiol, and J. A. Pople, Gaussian, Inc., Pittsburgh PA, 1990.

[27] C. C. Costain and B. P. Stoicheff, J. Chem. Phys. **30**, 777 (1959).

Isotope Substitution Effects on Preferred Conformations of Some Hydrocarbon Radical Cations

S. LUNELL and L. A. ERIKSSON

Department of Quantum Chemistry, Uppsala University, Box 518, S-751 20 Uppsala, Sweden

Abstract

The stability of different conformational isomers of partially deuterated radical cations of ethane, butane, and cyclopropane is studied at the HF/6-31G** and MP2/6-31G** levels. It is shown that the superposition patterns of spectra corresponding to different isomers, observed in ESR spectroscopy, are accurately reproduced by Boltzmann statistics based on differences in vibrational zero-point energies (ZPE), provided that the temperature is high enough to overcome existing barriers toward internal pseudorotation in the cations. For the ethane and butane cations, the most stable conformations are, as expected, those which are deuterated in the short CH bonds, while this is found not to be the case for the cyclopropane cation. The latter result is explained by shifts in the low-frequency bending modes, which counteract the anticipated isotope effect on the C—H stretching modes. © 1992 John Wiley & Sons, Inc.

Introduction

Radical cations have recently been the subject of several experimental and theoretical investigations [1], partly because of their importance as (highly reactive) intermediates or initiators in a large number of chemical reactions. The experimental techniques used in most of these studies is low-temperature matrix isolation electron spin resonance (ESR) spectroscopy, where the test compound is mixed with a matrix substance (usually a noble gas, a halocarbon or SF_6) in low-concentration (typically 1/10,000), after which the mixture is frozen and irradiated by γ- or X-rays.

In the study of hydrocarbon radical cations, selective deuteration in combination with ESR spectroscopy makes it possible to clearly distinguish between chemically inequivalent protons, providing detailed structural information about the radical cation in question. The important difference between the proton and deuteron in this connection is, of course, their different magnetic properties. At the same time, however, the mass difference between the two isotopes will affect the vibrational properties of the radical cation. In a simple, uncoupled harmonic oscillator model, the zero-point vibrational energy (ZPE) of, e.g., a C—H stretching vibration is proportional to $\sqrt{k/m_H}$, where k is the force constant of the C—H bond, and m_H is the mass of the hydrogen atom. This implies that upon deuteration, the deuterium atoms will preferentially occupy sites with large force constants in order to lower the total ZPE. This is of special importance when chemically equivalent protons

in the neutral molecule become inequivalent in the ionized systems, as a result of Jahn–Teller or other distortions.

In the above-mentioned ESR experiments, the deuteration is performed before the radical is produced. In cases where it is possible to obtain different substitutional or rotational isomers, relating hydrogen positions which are chemically equivalent before ionization, it may be difficult to observe a unique ground state structure. At low enough temperatures, however, it may be possible to reduce the vibrational (thermal) motions of the system enough to single out a unique ground state conformation. In the case of the partially deuterated species, the bonds having the largest force constants are generally the shorter C—H bonds; these will thus be expected to be occupied by the deuterons. An illustrative case is provided by the methane radical cation where, by using doubly deuterated methane, CH_2D_2, it was shown that the Jahn–Teller active cation distorts into a structure of C_{2v} symmetry, with two elongated (C—H) and two shortened (C—D) bonds [2]. This has also been confirmed by extensive theoretical studies of the vibrational motions in this system [3,4]. In a more detailed treatment, of course, the full potential energy surface must be calculated, and the vibrational energies extracted from this by means of a normal mode analysis.

At somewhat higher temperatures, however, it may not be possible to deduce a unique ground state conformation, and a superposition of spectra corresponding to various isomers is instead observed. Let us, as an example, consider the ethane radical cation. The structure of this species is such that two of the C—H bonds (in *trans* positions) are elongated and tilted inward (cf. Fig. 1) [5]. These will be referred to as the "in-plane" protons. The four out-of-plane hydrogens with shortened C—H bonds constitute the second set of chemically inequivalent protons. The hyperfine structure is confined to the two in-plane hydrogens in the *trans* positions. For example, in the doubly deuterated ethane cation, $CH_2DCH_2D^+$, there are three possible rotational isomers that can be observed experimentally, the spectra of which differ strongly because of the different magnetic properties of the nuclei. These are formed in such a way that none (I), one (II), or both (III) of the in-plane protons are deuterated, as depicted in Figure 2. The observed spectra will be a superposition of these three isomeric types. The relative abundances of the different
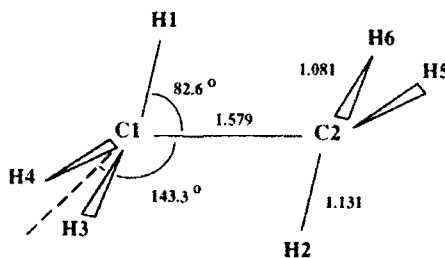
Figure 1.   The geometry of the ^2A_g electronic ground state of the ethane radical cation, optimized at the MP2/6-31G** level (from ref. 5).
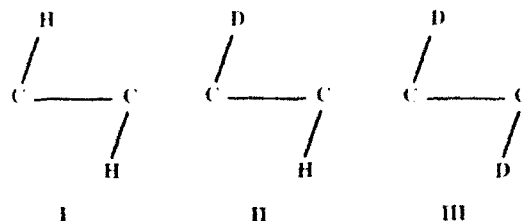
Figure 2. The three isomeric types of the partially deuterated ethane radical cation. Only the atoms in the H1–C1–C2–H2 mirror plane are shown (cf. Fig. 1).

isomers are deduced from the relative contribution of the corresponding spectra to the observed spectrum.

In this study, it is shown that the relative abundances of different substitutional isomers at a given temperature can be predicted from Boltzmann statistics based on their ZPE differences. The partially deuterated radical cations of ethane (C_2H_6), n-butane (C_4H_8), and cyclopropane (c-C_3H_6) are given as examples.

Method

Equilibrium geometries were calculated on the MP2/6-31G** level for the ethane radical cation and on the HF/6-31G** level for the n-butane and c-propane cations. At the equilibrium geometries, vibrational frequencies and ZPE were calculated for the undeuterated and partially deuterated cations, using the same levels of approximation, respectively. The program systems, GAUSSIAN 90 [6] and GAMESS [7], were used. The relative abundancies of the different substitutional isomers were calculated using Boltzmann statistics, based on the ZPE differences between the isomers.

Results

C_2H_6

The ethane radical cation is, like the methane cation, Jahn–Teller unstable. Removing an electron from the $1e_g$ orbital of the neutral molecule (D_{3d} symmetry), the system distorts in such a way that two of the hydrogens become tilted inward, as mentioned above. The cation thus attains a structure of C_{2h} symmetry, and has a ^2A_g electronic ground state. Computationally, the MP2/6-31G** level has been found to be the lowest possible level to reproduce the correct type of structure [5], and has been used throughout this study.

Considering the three types of isomers (cf. Fig. 2), it is found that, for a given stoichiometric composition, the difference in ZPE between isomeric types I and II, and between isomers II and III, is approximately 1.5 kJ/mol. Type I, where only the short, out-of-plane bonds are deuterated, is the most stable form (Table 1). At 4 K, only the isomers with the lowest ZPE (II for $CH_2DCD_3^+$ and $CHD_2CD_3^+$, I for the rest), are present. When the temperature is increased, the other isomeric forms

TABLE I. MP2/6-31G** calculated zero-point energies and degeneracy factors for the various deuterated isomers of the ethane radical cation. Isomeric type I has neither positions 1 nor 2 (cf. Fig. 1) deuterated. In type II, one of the positions, 1 or 2, is deuterated and, in type III, both H1 and H2 have been substituted for deuterons.

Deuterated position	ZPE (kJ/mol)	Degeneracy factor	Isomeric type
—	185.9422	1	I
3	177.4849	4	I
1	178.9780	2	II
3, 4	168.9627	2	I
4, 5	169.0067	2	I
3, 5	169.0173	2	I
1, 3	170.4508	4	II
1, 5	170.5081	4	II
1, 2	171.9890	1	III
3, 4, 5	160.4753	4	I
1, 3, 4	161.8616	2	II
1, 3, 6	161.9628	4	II
1, 3, 5	161.9716	4	II
2, 3, 4	161.9737	2	II
1, 2, 3	163.4505	4	III
3, 4, 5, 6	151.9250	1	I
1, 3, 4, 5	153.3654	4	II
1, 3, 5, 6	153.4202	4	II
1, 2, 3, 4	154.8504	2	III
1, 2, 3, 6	154.8964	2	III
1, 2, 3, 5	154.9036	2	III
1, 3, 4, 5, 6	144.8065	2	II
1, 2, 3, 4, 5	146.2889	4	III
1, 2, 3, 4, 5, 6	137.6673	1	III

also start to be populated. At 77 K, the calculated ratio I:II (II:III) ranges from 5: 2 ($CH D_2 CH D_2^+$) to 20:1 ($CH_2 DCD_3^+$) (Table II). These results are in qualitative agreement with the experimental findings of the ESR measurements made in SF_6 matrices at 4 and 77 K [8,9]. Analyzing the individual frequencies of the singly deuterated species, it is shown that the differences in ZPE between the isomeric forms can be accounted for by the difference in stretching frequency of one particular C — H bond before and after deuteration (cf. Fig. 3). This difference is approximately 160 cm^{-1} (1.8 kJ/mol), to be compared with the total ZPE difference of ca. 1.5 kJ/ mol. The uncoupled harmonic oscillator model thus provides a satisfactory model for the observed behavior of the partially deuterated ethane cation.

$n\text{-}C_4H_8^+$

The ESR measurements of the doubly and quadruply deuterated n-butane cations (Fig. 4) in CF_3CCl_3, at temperatures between 4 and 120 K, clearly indicate a non-

TABLE II. Boltzmann populations and abundance ratios (in %) at 4.2 K and 77 K, calculated for the different isomeric conformations in Table I.

Deuterated position	Isomeric type	exp[(E − E₀)/RT]		Abundance ratio	
		4.2 K	77 K	4.2 K	77 K
3	I	1.0	1.0	100.0	95.4
1	II	$2.7 \cdot 10^{19}$	0.097	—	4.6
3, 4	I	1.0	1.0	100.0	83.6
1, 3	II	$3.1 \cdot 10^{19}$	0.098	—	16.4
4, 5	I	1.0	1.0	57.5	45.9
3, 5	I	0.738	0.984	42.5	45.1
1, 5	II	$2.1 \cdot 10^{19}$	0.096	—	8.8
1, 2	III	$8.1 \cdot 10^{38}$	0.009	—	0.2
3, 4, 5	I	1.0	1.0	100.0	79.8
1, 3, 6	II	$3.2 \cdot 10^{19}$	0.098	—	7.8
1, 3, 5	II	$2.5 \cdot 10^{19}$	0.097	—	7.7
2, 3, 4	II	$2.3 \cdot 10^{19}$	0.096	—	3.8
1, 2, 3	III	$9.9 \cdot 10^{38}$	0.010	—	0.9
3, 4, 5, 6	I	1.0	1.0	100.0	70.2
1, 3, 5, 6	II	$2.5 \cdot 10^{19}$	0.097	—	27.2
1, 2, 3, 6	III	$1.1 \cdot 10^{37}$	0.010	—	1.4
1, 2, 3, 5	III	$9.0 \cdot 10^{?}$	0.010	—	1.2
2, 3, 4, 5	II	1.0	1.0	100.0	95.3
1, 2, 3, 4	III	$3.4 \cdot 10^{19}$	0.098	—	4.7
1, 3, 4, 5, 6	II	1.0	1.0	100.0	83.5
1, 2, 3, 4, 5	III	$3.7 \cdot 10^{19}$	0.099	—	16.5

statistical superposition pattern of the different rotational isomers possible [10,11], in analogy with the discussion made above. Defining the terminal in-plane hydrogens by the H—C—C—C(—Me) and (Me—)C—C—C—H planes, the three isomeric forms, I, II, and III, are analogous to those for the ethane radical cation (cf. Fig. 2). The statistical ratio between the three isomeric conformation types I, II, and III is for the n-butane-1,1,4,4-d_4 cation 1:4:4, and 4:4:1 for the n-butane-1,4-d_2 cation, respectively. The in-plane C—H bonds of the terminal methyl groups are the longer ones, analogously with the ethane cation. For the n-butane cation, the in-plane C—H bond lengths are 1.1095 Å, and the four methyl out-of-plane bonds are 1.0905 Å (MP2/6-31G*). Correspondingly, the ZPE for the species with the out-of-plane positions deuterated are expected to be lower than those where one or both of the in-plane protons are replaced by deuterons. This is also confirmed by the calculations (Table III).

The observed ratios for the partially deuterated 1,1,4,4-d_4 cation of n-butane at 77 K are not the statistical (degeneracy) ratios of 1:4:4, but rather 3.0:4.9:2.1. The ZPE calculations at the UHF/6-31G** level, and subsequently calculated abundance ratios, give the distribution 2.9:4.7:2.4 at 77 K [12], i.e., in excellent agreement with the experimental data (Tables III and IV).
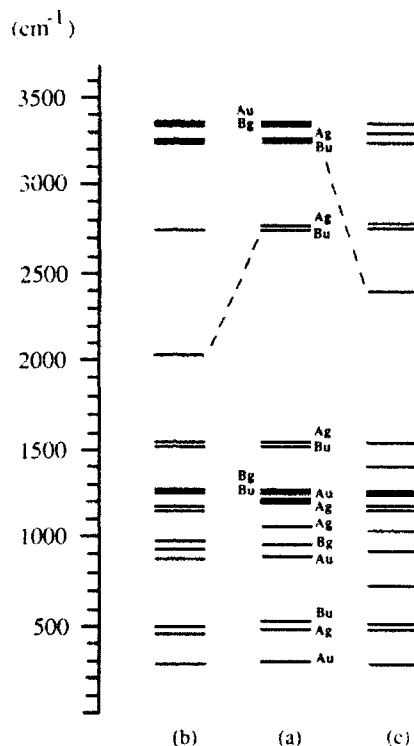
Figure 3. Vibrational frequencies of the (a) undeuterated: (b) in-plane singly deuterated. and (c) out-of-plane singly deuterated isomers of the ethane radical cation, obtained from MP2/6-31G** frequency calculations. Cases (b) and (c) belong to the isomeric types II and I of Figure 2, respectively.

For the 1,4-d_2 cations, the experimental ratio at 77 K is 6:3:(1). which is also reproduced very well by the theoretical analysis. The theoretically obtained ratio at 77 K is 6.5:3.2:0.3. At 4 K, the experimental distribution is 7:2:(0) which, from the theoretical analysis, indicates that the rotational motion of the terminal methyl groups are frozen at 40–45 K (Table V). The activation energy for the rotational
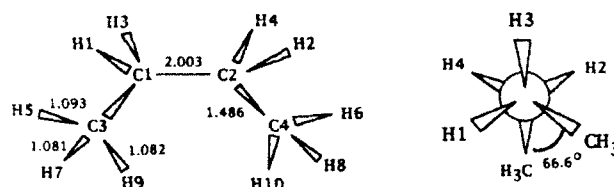
Figure 4. The HF/6-31G** optimized geometry of the gauche form of the n-butane cation [12], showing the labeling used in Tables III–V.

TABLE III. Calculated (HF/6-31G**) zero-point vibrational energies and Boltzmann populations for the different rotational isomers of the n-butane-1,1,4,4,-d_4 cation (HF/3-21G results in parentheses).

Undeuterated positions	Statistical weight	ZPE energy (kJ/mol)	exp[(E-E_o)/RT] T = 77 K	Rotational isomer
A. *Trans* conformation				
5, 6	1	320.032	1.0000	I
5, 8 [5, 10; 6, 7; 6, 9]	4	320.461	0.5116	II
7, 8 [9, 10]	2	320.981	0.2271	III
7, 10 [8, 9]	2	321.014	0.2157	III
B. *Gauche* conformation				
5, 6	1	320.190 (323.028)	1.0000 (1.0000)	I
5, 8 [6, 7]	2	320.776 (323.306)	0.4004 (0.6477)	II
5, 10 [6, 9]	2	320.744 (323.273)	0.4209 (0.6820)	II
7, 8	1	321.308 (324.103)	0.1744 (0.1865)	III
7, 10 [8, 9]	2	321.180 (323.811)	0.2130 (0.2943)	III
9, 10	1	321.145 (323.679)	0.2250 (0.3617)	III

motion has been estimated to be 9.5–10 kJ/mol, with a frequency factor of 1.8 $-3.9 \cdot 10^{11}$ s^{-1} [13]. Inserting these numbers in a rate equation of Arrhenius type, the lifetimes 1 second at 45 K, and 1 min at 40 K are obtained. Below 40 K, the rotational motions may thus be assumed to have stopped, which agrees very well with the theoretical findings.

c-$C_3H_6^+$

The cyclopropane radical cation is Jahn–Teller active, and distorts from the symmetric D_{3h} structure, to an isosceles, obtuse triangle of C_{2v} symmetry (Fig. 5). The electronic ground state is $^2A_1$. In the study of the different isomers of the doubly

TABLE IV. Calculated (HF/6-31G**) and observed abundance ratios of the rotational isomers I–III of the n-butane-1,1,4,4,-d_4 cation (HF/3-21G results in parentheses).

Rotational isomer	I	II	III
A. *Trans* conformation			
Statistical abundance ratio	1.	4	4
Calculated Boltzmann population	1.	2.0466	0.8855
Calculated abundance ratio	2.5	5.2	2.3
B. *Gauche* conformation			
Statistical abundance ratio	1	4	4
Calculated Boltzmann population	1. (1.)	1.6426 (2.6594)	0.8254 (1.1368)
Calculated abundance ratio	2.9 (2.1)	4.7 (5.5)	2.4 (2.4)
Experimental abundance ratio[a]	3.0	4.9	2.1

[a] Ref. 10; observed in CF_3CCl_3 at 77 K.

TABLE V.   Calculated (HF/6-31G**) and observed abundance ratios of the rotational isomers I–III of the gauche form of the n-butane-1,4-d_2 cation.

	Temperature (K)	Rotational isomer		
		I	II	III
Statistical abundance ratio		4	4	1
Calculated abundance ratio	77	6.5	3.2	0.3
	50	7.4	2.5	0.1
	45	7.6	2.3	0.1
	40	7.9	2.0	0.1
	30	9.4	0.6	0.0
	4	10.0	0.0	0.0
Experimental abundance ratio	77[a]	6	3	
	4[c]	7	2	(1)[b]

[a] Ref. 11; observed in CF_3CCl_3.

[b] The contribution from isomer III is only approximate, because the center lines of the spectra are affected by quartz signals [11].

[c] Ref. 11; observed in $CF_2ClCFCl_2$.

deuterated cyclopropane radical cation, the ZPE were calculated at the UHF/6-31G** level of theory, and the abundance ratios were computed as outlined above. The ESR measurements with which the computational results are compared, were performed at different temperatures between 4 and 77 K [14].

The six protons of the cyclopropane cation form two sets of chemically inequivalent atoms; the four "basal" hydrogens $(R(C-H) \simeq 1.075$ Å), and the two "top" hydrogens $(R(C-H) \simeq 1.078$ Å), respectively. From the uncoupled harmonic oscillator model, one would thus assume the deuterons to preferentially occupy the basal positions where the C-H bonds are shorter. However, the ESR measurements of the doubly deuterated isomers of the cyclopropane-1,1-d_2 radical cation show that the 1,1-substitution (i.e., deuteration at the "top" carbon) is preferred at low temperatures [14]. As can be seen from Table VI, the same result is obtained from the theoretical calculations [15].

At 4 K, the observed ratio between deuteration of the top carbon (I) and the basal carbons (II) is 2:1, instead of the statistical ratio 1:2. According to the ZPE
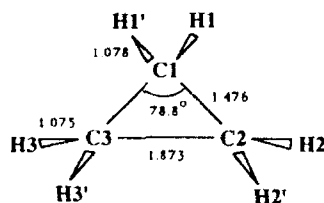
Figure 5.   The optimized structure (HF/6-31G**, ref. 15) and labeling of the cyclopropane radical cation (C_{2v} symmetry).

TABLE VI. Boltzmann distributions and, parentheses, calculated abundance ratios for the 1,1 and 2,2 (3,3) isomers of cyclopropane'—d_2.

Temperature (K)	1,1	2,2 (3,3)
100	1.0000	0.4995
	(6.7)	(3.3)
77	1.0000	0.3306
	(7.5)	(2.5)
50	1.0000	0.1248
	(8.9)	(1.1)
20	1.0000	0.0010
	(10.0)	(0.0)

analysis (Table VI), this corresponds to freezing the thermal equilibration at 100 K. This temperature agrees with the experimentally observed temperature for the onset of a dynamical averaging between isomers I and II [14].

At temperatures below 50 K, only the isomeric type I has a nonnegligible population, which agrees with the experimental result obtained after annealing the sample frozen to 4 K at slightly higher temperatures, in which only isomer I is observed.

The results from both the theoretical and experimental studies show that the uncoupled oscillator model alone cannot explain the preferred occupation sites of the doubly deuterated cyclopropane radical cation. In an analysis of the individual frequencies of the undeuterated and singly deuterated cyclopropane cations (cf. Fig. 6), it was found that the changes in the high-frequency region (>2000 cm^{-1}), corresponding to the C—H/C—D stretching vibrations, are such that the ZPE is lowered more for the isomer where one of the basal carbons is deuterated, than when a top hydrogen is replaced by a deuteron (Table VII). This is thus in accordance with the simple harmonic model. The fact that the opposite is observed in reality is, hence, a result of the strong effects on the low-frequency bending modes, which generate a lower total ZPE for deuteration at the top carbon, than for the case where a basal position is deuterated.

Conclusion

Vibrational analyses have been performed at the UHF/6-31G** and MP2/6-31G** levels on partially deuterated isomers of the ethane, n-butane, and cyclopropane radical cations. In the first two cases, it is found that deuteration preferentially occurs at the shorter binding sites, where, on account of larger force constants for C—H stretching, the largest lowering of the total ZPE is expected. In the cyclopropane cation, however, the effects on the C—H/C—D stretching vibrations are compensated by strong effects on the low-frequency bending modes, thereby
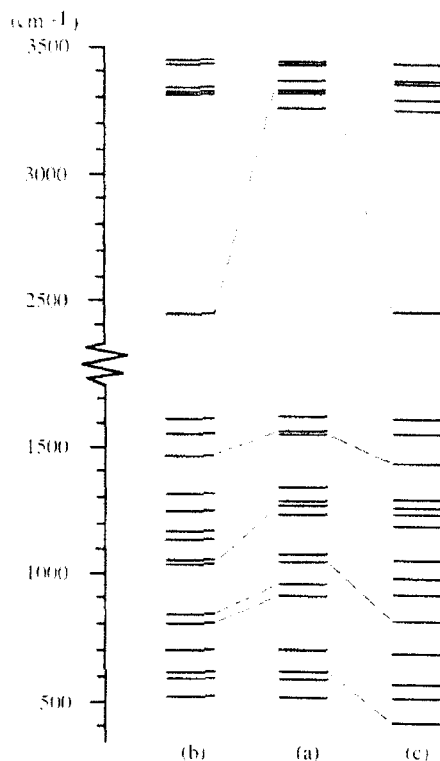
Figure 6. Frequency distributions (cm⁻¹) of the undeuterated (a) and C1 and C2 singly deuterated [(b) and (c), respectively] cyclopropane radical cations. From ref. 15.

stabilizing those isomers where the deuteration occurs at the longer binding sites (at the "top" carbon atom). For all these species, the Boltzmann populations and abundance ratios are calculated at different temperatures. These analyses fully de-

TABLE VII. Vibrational frequency components in the high- and low-frequency regions (cm⁻¹) along with the total ZPE (kJ/mol) for the undeuterated and singly deuterated isomers of the cyclopropane cation. The results are from UHF/6-31G** calculations.

| Deuterated position | Frequency range | | ZPE (kJ/mol) |
	High (2000–3500 cm⁻¹)	Low (0–2000 cm⁻¹)	
— (a)	20200.29	16454.88	219.0673
C1, apical (b)	19321.48	15753.81	209.7940
C2, basal (c)	19302.47	15868.68	210.3704

scribe the nonstatistical superposition patterns between different substitutional isomers, observed in low-temperature ESR experiments.

Acknowledgements

Bibliograph

[1] A. Lund and M. Shiotani, Eds., *Radical Ionic Systems* (Kluwer, Dordrecht, 1991).

[2] L. B. Knight, J. Steadman, D. Feller, and E. R. Davidson, J. Am. Chem. Soc. **106**, 3700 (1984).

[3] M. N. Paddon-Row, D. J. Fox, J. A. Pople, K. N. Houk, and D. W. Pratt, J. Am. Chem. Soc. **107**, 7697 (1985).

[4] R. F. Frey and E. R. Davidson, J. Chem. Phys. **88**, 1755 (1988).

[5] M.-B. Huang and S. Lunell, Chem. Phys. **147**, 85 (1990).

[6] M. J. Frisch, M. Head-Gordon, G. W. Trucks, J. B. Foresman, H. B. Schlegel, K. Raghavachari, M. A. Robb, J. S. Binkley, C. Gonzalez, D. J. Defrees, D. J. Fox, R. A. Whiteside, R. Seeger, C. F. Melius, J. Baker, R. L. Martin, L. R. Kahn, J. J. P. Stewart, S. Topiol, and J. A. Pople, GAUSSIAN 90, (Gaussian Inc., Pittsburgh, PA, 1990).

[7] M. Dupuis, D. Spangler, and J. J. Wendoloski, NRCC Software Catalogue Vol. 1, Program QG01 (GAMESS), 1980, as modified by M. W. Schmidt, K. K. Baldridge, J. A. Boatz, J. H. Jensen, S. Koseki, K. A. Nguyen, T. L. Windus, and S. T. Elbert, QCPE Bull. **10**, 52 (1990).

[8] K. Toriyama, K. Nunome, and M. Iwasaki, J. Chem. Phys. **77**, 5891 (1982).

[9] M. Iwasaki, K. Toriyama, and K. Nunome, Chem. Phys. Lett. **111**, 309 (1984).

[10] M. Lindgren, A. Lund, and G. Dolivo, Chem. Phys. **99**, 103 (1985).

[11] M. Lindgren and A. Lund, J. Chem. Soc. Faraday Trans. **83**, 1815 (1987).

[12] S. Lunell, L. A. Eriksson, and L. Worstbrock, J. Am. Chem. Soc. **113**, 7508 (1991).

[13] K. Matsuura, K. Nunome, K. Toriyama, and M. Iwasaki, J. Phys. Chem. **93**, 149 (1989).

[14] K. Matsuura, K. Nunome, M. Okazaki, K. Toriyama, and M. Iwasaki, J. Phys. Chem. **93**, 6642 (1989).

[15] L. A. Eriksson and S. Lunell, J. Am. Chem. Soc. (to appear).

Studies on CO Bonding to Rh Clusters Using an Intermediate Neglect of Differential Overlap Theory to Model Heterogeneous Catalytic Reactions

GUILLERMINA L. ESTIU and MICHAEL C. ZERNER

Quantum Theory Project, University of Florida, Gainesville, Florida 32611

Abstract

The interaction of CO with rhodium clusters of different sizes is studied by means of Intermediate Neglect of Differential Orbital (INDO) calculations. Interactions of both σ and π type are well-known to contribute to the metal—CO bond formation. The relative importance of the repulsive Rh—5σ CO interaction with the metal and the back-bonding to the π^* CO empty orbital in the stabilization of the bond is analyzed as a function of the cluster size and the coordination geometry. It is found that the shift of charge in the larger metal clusters brings about a reduction of the Rh—5σ CO repulsion, and this redistribution is important to change the optimal CO bonding geometry from *bridge* to *on top*.
© 1992 John Wiley & Sons, Inc.

Introduction

The catalytic activity of metal surfaces can be modified in order to selectively improve the performance of a given reaction. A rational modification of the metal topology, electronic and/or magnetic characteristics by means of the addition of either inhibitors or promoters, that may vary from alkali metals to foreign transition metal atoms deposited in controlled amounts, makes it possible to design the best catalyst for a given reaction [1-4].

The design of a catalyst is based on the knowledge of the effect that a given modification will have on the activity of a given surface toward a given reaction. Understanding the interactions between small molecules and transition metal atoms is, thence, a central matter for the design of electrocatalysts. Quantum chemical calculations are particularly appropriate for this objective, as they give a quantitative description of the interactions at an electronic level and a quantitative trend of their change under the effect of different perturbations.

Second- and third-row transition metal atoms are the choice in industry because of the selectivity of their reactions in normal environments. The large number of open-shell orbitals associated with them makes, on the other hand, the quantum chemical calculations of these systems a challenge for the theoretical chemist.

A great interest exists in characterizing the interaction of CO with transition metal surfaces [5-12]. Carbon monoxide provides a particularly suitable model adsorbate because of the sensitivity of its properties to the characteristics of the

bond. It has the additional significance of acting as a poison for the catalytic oxidation of small organic molecules on noble metal surfaces [13,14].

Rhodium, on the other hand, matches the requirements of being an important catalyst in the oxidation of organic fuels and in energy conversion mechanisms [15], and, as an element of the 4d block has only received cursory theoretical attention.

Although surfaces may be approached as a continuum through the definition of two-dimensional periodical properties [16], chemisorption at low coverages is usually better described, because it implies a localized interaction, by means of the interaction of adsorbates with finite clusters that model the surface and the adsorbed ensemble [17-19].

In this initial study, we analyze the interactions of a single CO molecule with Rh clusters of different sizes to study the influence of the size of the cluster in the description of the adsorption bond.

Different CO coordination geometries have been identified on both small Rh clusters [20,21] and Rh surfaces [22-24]. Whereas, according to *ab initio* calculations, two-fold (bridge) coordination is more stable for the small structures [11], experimental data indicates a slight preference for the one-fold (linear, on top) coordination on Rh(111) and Rh(100) surfaces [23].

Interactions of both σ and π type are well-known to contribute to the metal — CO bond formation [5,12]. According to *ab initio* calculations, interactions of the σ type are mainly repulsive (Pauli repulsion) [5-7]. The metal charge in σ symmetry orbitals hybridizes and polarizes away from CO to reduce the metal — 5σ CO overlap and, hence, reduces the repulsion. The interactions of the π type are, on the other hand, bonding, and are most important in the stabilization of the bond. Although this model has been frequently used to explain the interaction of CO with transition metal surfaces, it has been mainly built up using triatomic Me — CO molecules [5-7] as examples. No systematic analysis of the relative importance of both interactions for metal clusters of different sizes has been done at the self-consistent field or more accurate levels of calculation.

In this work we will apply a version of the Intermediate Neglect of Differential Overlap (INDO) [25] model at both the self-consistent field (SCF) and the configuration interaction (CI) level, using the ZINDO program [26], examining the effects of different size clusters, from one Rh atom to 15, on the bonding and structure of the CO adduct.

These calculations are our first attempt to model CO interactions with Rh metal surfaces. They also give us the opportunity to compare our results with those derived from *ab initio* [10,11] and density functional theory [12] calculations on the triatomic Rh — CO systems and to support the use of the INDO model on more extended metal systems.

Calculations

In order to better understand the localized interactions involved in the bonding of CO to Rh metal models, we start with the Rh–CO triatomic molecule, increasing then the size of the cluster up to 15 Rh atoms (Figs. 1-3).
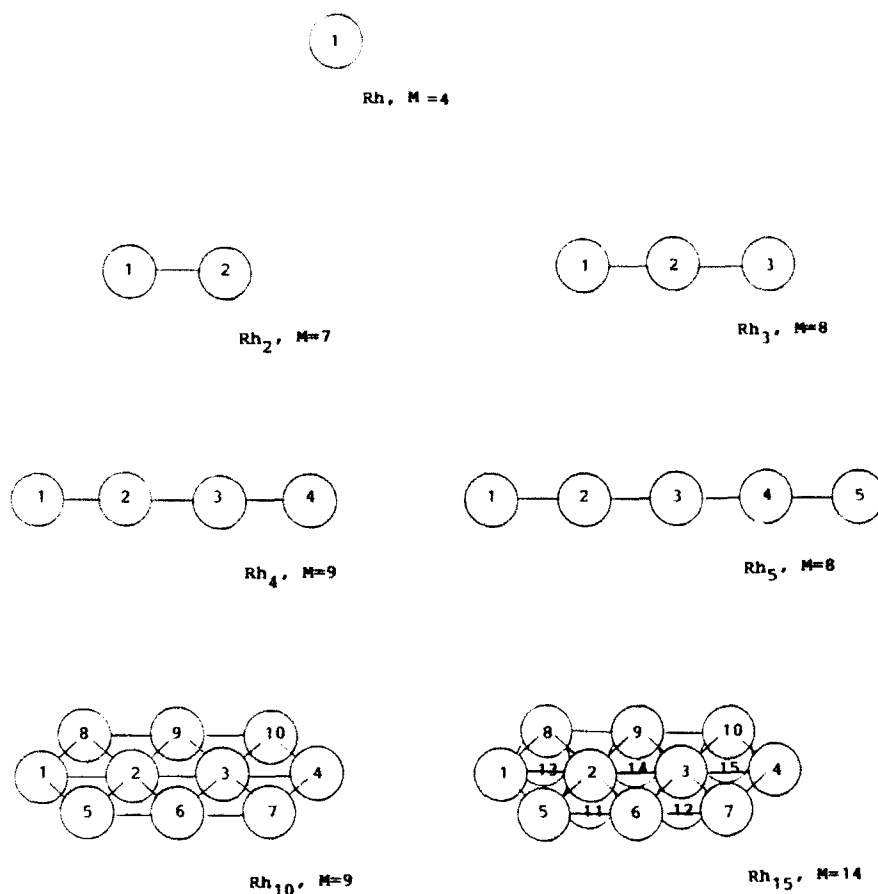
Figure 1. Different [Rh]$_n$ clusters analyzed by means of SCF–CI(NDO) calculations. M = multiplicity = $2s + 1$.

With the exception of the diatomic Rh$_2$, which is also studied for the optimized molecular geometry, the Rh — Rh interatomic distance is fixed at the bulk value (2.690 Å [27]). Linear [Rh]$_n$ clusters ($1 \le n \le 5$) are chosen as a common unit for the different metal topologies. Calculations are then extended to [Rh(111)]$_{10}$ and [Rh(111)]$_{15}$ clusters in order to study the effect of lateral metal atoms on the Rh — CO bond, when going from a one-dimensional to a two-dimensional structure, and that of the underlying metal atoms when going to a three-dimensional fcc one.

A Fock operator for the average energy of each configuration [28] is used to help overcome the state degeneracies that hinder SCF convergence caused by the large number of near-degenerate states associated with [Rh]$_n$ clusters. The average operator is defined for the nine valence electrons of each Rh atom distributed in the five 4d valence orbitals. The orbitals from the averaged operator form the reference
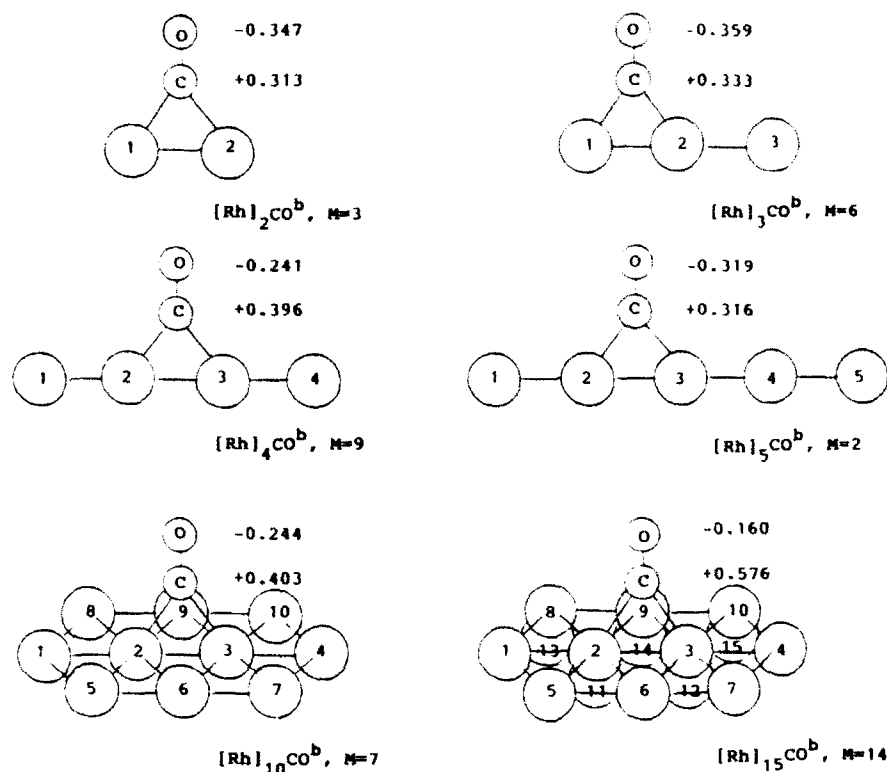
Figure 2. Local density charge on the atomic centers of the CO molecule bridge-bonded to the [Rh]ₙ clusters of different size.

for a subsequent projection over pure spin states by means of a Rumer Configuration Interaction [29].

The geometry of the adsorbed structures is optimized by means of the Head and Zerner technique [30–32], using the BFGS algorithm to update the inverse Hessian matrix. For systems of high symmetry, such as metal surfaces examined here, it becomes advantageous to use Cartesian coordinates in order to avoid possible singularities in the inversion of the metric matrix.

The INDO model that we use for these studies have been modified by choosing the resonance integrals according to formulae that take into account different electronegativities. A description of those modifications is in preparation. All other aspects of the method are as described elsewhere [25,33].

Two parameterizations of the INDO theory are used in these studies: one for geometry, which utilizes two-center coulomb integrals calculated *ab initio*; and one for spectroscopy at fixed geometries, which obtains these coulomb integrals from experiment [25,33–35].
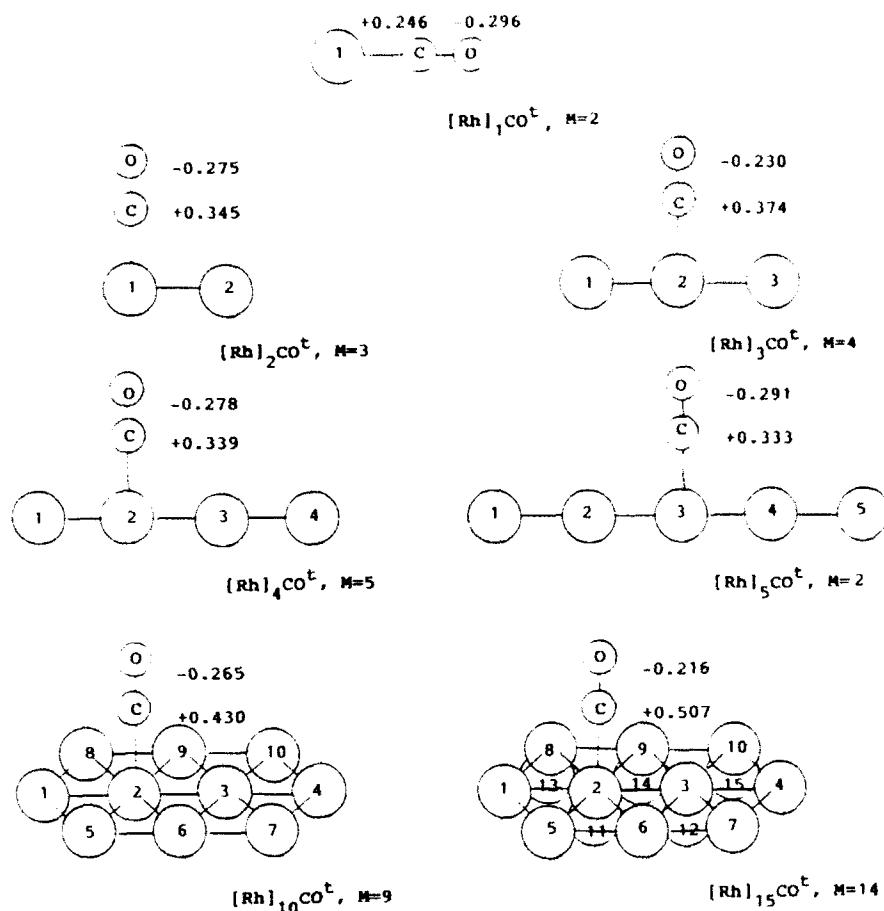
Figure 3. Local density charge on the atomic centers of the CO molecule linearly (on top), bonded to the [Rh]ₙ clusters of different size.

Geometries are optimized at the ROHF level of theory [28,36]. Spectroscopic states are examined using the orbitals obtained from the Configuration Average Hartree–Fock (CAHF) methods for a subsequent Rumer CI diagram.

Results

Multiplicity of the Clusters

By means of a Rumer CI, the average vectors belonging to the SCF calculations are projected over pure spin states for each of the different structures. In this way, the stability of different multiplicities for each structure is comparatively analyzed at the CI level. The multiplicities ($M = S(S + 1)$) of minimum energy are chosen to represent both the initial (naked metal cluster) and the final (adsorbed ensemble)

TABLE I.   Energies (a.u.) relative to the most stable state for the different multiplicities of [Rh]$_n$ clusters.

M	3	4	5	6	7	8	9	10	11	12	14
Rh$_2$	0.030	—	0.039	—	0.000	—	0.142	—			
Rh$_3$	—	0.028	—	0.022	—	0.000	—	0.049	—		
Rh$_4$		—	0.030	—	0.019	—	0.000	—	0.090		
Rh$_5$	—	0.036	—	0.034	—	0.000	—	0.041			
Rh$_{10}$				—	0.010	—	0.000	—	0.031	—	
Rh$_{15}$					—	0.037	—	0.015	—	0.004	0.000

states. Data collected in Tables I and II show that they correspond, without exception, to intermediate spin states.

For the Rh$_2$ diatomic we have examined two structures: the minimum energy structure, which we can compare with the results of others [11,37–39], and the simplest two-atom model of the surface, in which the interatomic distance is fixed at $r = 2.690$ Å.

The ground state of the Rh$_2$ diatomic is controversial, both its symmetry and its bond length. At the level of theory we utilize for the larger clusters we calculate the lowest energy state of Rh$_2$ as a $^5\Sigma_u^-(1\sigma_g^2 2\sigma_g^1 1\sigma_u^1 \delta_u^4 \delta_g^4 \pi_g^2 \pi_u^4)$, with an interatomic separation of 2.35 Å. This agrees with the UHF results of Mains and White ($r = 2.28$ Å) [11].

Balasubramanian and Liao [37], who have included spin-orbit and other relativistic effects directly into their calculations, suggest $^5\Delta_g(62\%\ 1\sigma_g^2 2\sigma_g^1 1\sigma_u^1 \delta_u^4 \delta_g^3 \pi_g^2 \pi_u^4)$, with $r = 2.28$ Å, as lowest lying. They do not report a $^5\Sigma_u$ state. On the other hand, we

TABLE II.   Energies (a.u.) relative to the most stable state for the different multiplicities of [Rh]$_n$ (CO) clusters of different geometry.

M	1	2	3	4	5	6	7	8	9	12	14
One-fold (*on top*) CO coordination [Rh]$_n$ (CO)^f											
Rh$_2$	0.009	—	0.000	—	0.013	—					
Rh$_3$	—	0.024	—	0.000	—	0.003	—	0.024	—		
Rh$_4$	0.032	—	0.022	—	0.000	—	0.008	—	0.049		
Rh$_5$	—	0.000	—	0.020	—	0.007	—	0.066	—		
Rh$_{10}$						—	0.001	—	0.000		
Rh$_{15}$							—		—	0.015	0.000
Two-fold (bridge) CO coordination [Rh]$_n$ (CO)^h											
Rh$_2$	0.053	—	0.000	—	0.025	—					
Rh$_3$	—	0.009	—	0.008	—	0.000	—	0.060	—		
Rh$_4$	0.150	—	0.129	—	0.058	—	0.028	—	0.000		
Rh$_5$	—	0.000	—	0.009	—	0.015	—	0.125	—		
Rh$_{10}$						—	0.007	—	0.000	—	0.012
Rh$_{15}$							—		—	0.007	0.000

estimate a low-lying $^3\Delta_g$ state, from CI calculations, 5890 cm^{-1} higher in energy than our $^3\Sigma_u$. Balasubramanian and Liao's $^3\Delta_g$ state is a heavy mixture of configurations, with sizeable contributions from higher energy configurations that we have not included in this CI. They estimate a binding energy of 2.1 eV to be compared with an experimental value of 2.92 ± 0.22 eV [40], whereas we obtain a value of 0.60 eV estimated from the dissociation of the lowest septet.

Illas et al. [39] found a $^3\Delta_g(68\%$ $1\sigma_g^2 2\sigma_g^2 1\sigma_u^2 \delta_g^4 \delta_u^4 \pi_u^3 \pi_g^3)(r = 2.67$ Å) as the most stable state, with a binding energy of 1.5 eV. A $^3\Sigma_u$ $(r = 2.58$ Å) is calculated to lie 725 cm^{-1} higher in energy. The $^3\Delta_g$ state $(r = 2.61$ Å) corresponding to that of Balasubramanian and Liao, is 2400 cm^{-1} higher in energy than the $^3\Sigma_u$. The interatomic distances calculated by Illas et al. are all larger than those of our work and those of Balasubramanian and Liao [37] and Mains and White [11].

Repeating our calculations utilizing the CASH method for 12 electrons in eight orbitals ($1\sigma_g^2 \pi_u^4 \delta_g^4 \delta_u^4 \pi_g^4 1\sigma_u^2 2\sigma_g^2$) at a fixed distance of 2.287 Å to generate the starting orbitals, and performing a CISD from the references $1\sigma_g^2 \pi_u^4 \delta_g^4 \delta_u^4 \pi_g^2 2\sigma_g^2 1\sigma_u^2 (^3\Sigma_u)$, $1\sigma_g^2 \pi_u^4 \delta_g^4 \delta_u^4 \pi_g^2 1\sigma_u^2 2\sigma_g^2 (^3\Delta_g)$, and $1\sigma_g^2 \pi_u^4 \delta_g^4 \delta_u^4 \pi_g^4 1\sigma_u^2 2\sigma_g^2 (^3\Delta_g)$, yields the $^3\Delta_g$ lowest. The $^3\Delta_g$ state, at this geometry, is 6300 cm^{-1} higher in energy, and the $^3\Sigma_u$ state is 12,488 cm^{-1} higher. The binding energy is estimated as 1.2 eV. This results are in best accord with those obtained by Balasubramanian and Liao.

Table I indicates that, at $r = 2.69$ Å, the septet is the lowest energy structure, when the technique described earlier to examine the larger clusters is utilized. This septet also is calculated to have a minimum at $r = 2.59$ Å and is predicted to be bound by about 0.6 eV as is the $^3\Sigma_u$. The structure corresponds to two ^4F Rh atoms brought together without spin coupling, but with some sd hybridization responsible for the weak bonding.

The number of unpaired electrons is kept almost constant, around seven and eight, for the linear [Rh]$_n$ clusters (Table I).

Although for a different (triangular) geometry, the same multiplicity as ours ($M = 8$) has been found by Mains and White [11] for Rh$_3$, which describes a ^4F Rh atom weakly bound to a Rh$_2$ structure. The Mulliken population analysis of our linear Rh$_3$ structure (discussed later) shows that it is formed from two terminal ^4F Rh atoms and one central ^2D Rh atom.

For a rhombic planar Rh$_4$ structure, Mains and White found a multiplicity equal to nine, with two ^4F and two ^2D Rh atoms at opposite vertices. In our linear structure, two terminal Rh atoms are ^2D and the two central atoms ^4F. The structure resembles, though, two Rh$_2$ molecules weakly bound.

The multiplicity of the two-dimensional [Rh]$_{10}$ structures ($M = 9$) shows that they correspond to more tightly bonded structures.

The multiplicity of the bilayers deserves further comments. The most stable multiplicity for the [Rh(111)]$_{10}$ single layers, $M = 9$, corresponds to 0.8 unpaired electrons per surface atom. If this *value per atom* is transferred to the [Rh(111)]$_{15}$ cluster, which has the same structure of the topmost layer as [Rh(111)]$_{10}$, 12 unpaired electrons might be expected for the [Rh]$_{15}$ cluster, corresponding to $M = 12$ or $M = 14$, as $M = 13$ is not compatible with this cluster size. We found the greater stability for $M = 14$ (Table I). Lower multiplicities would imply the

cancellation of the unpaired spins of the first layer with the unpaired spins of the second one, which may be seen as a partial description of a semi-infinite system, as the second layer would also interact with lower-lying metal atoms in the bulk solid. Higher multiplicities, on the other hand, may belong to unpaired spins of the second layer and the borders of the cluster which, on the same basis, may be canceled if a larger number of layers are defined. Knowing that we are dealing with an indeterminacy at this point, we choose $M = 14$ to model the bilayer cluster, on the basis that the fractional number of unpaired electrons per atom in the first metal layer is likely to be the most important concept for the definition of the number of unpaired spins on the surface.

Coordination of CO decreases the multiplicity of the linear [Rh]$_n$ structures (the particular case of two-fold coordination on Rh$_4$ will be discussed later) (Table II). The triatomic Rh—CO molecule has a lower M than atomic Rh. The decrease of the M of Rh$_2$ after bonding to CO is in agreement with UHF ab $initio$ [11] and local density functional [12] calculations. The M is, however, preserved when one CO is bonded to two- and three-dimensional structures, as the electronic spins can be relaxed through the metal—metal bonds to their most stable distribution.

A similar decrease in the local magnetic moment, not always reflected in a decrease of the global magnetic moment, has been found from LSD calculations for the adsorption of CO on Ni clusters [41]. On the basis of those calculations, the decrease in the magnetization was related to the antibonding interaction of the 5σ CO orbitals with the sd band, which destabilizes and empties the upper-level orbitals, triggering a spin-dependent rearrangement of the d electrons, which in turn, leads to the decrease in the magnetization [42]. As this is mainly a localized interaction, it has a much less pronounced effect on the magnetic moment of the metal atoms not directly involved in the bond. The local magnetization change without global magnetization change has been found [41] for several coordination geometries and cluster sizes. The lack of global magnetization change, on the other hand, was explained as a compensation effect due to the increase of the magnetic moments of the atoms not directly bonded to CO.

Both the σ and the π interactions change the number of unpaired electrons in the [Rh]$_n$CO systems and, thence, M of the cluster. The final M value will be the result of a balance of both effects. However, when the charge in the σ orbitals is polarized to the adjacent atoms of the cluster, the local change in the number of unpaired spins is only determined by the back bonding effect. This effect is not large enough to give a net change in the global magnetic moment. On the other hand, the redistribution of the electronic spins through polarization allows the system to reorganize again to the minimum energy spin distribution.

A larger decrease is found for the smaller clusters as they do not have the ability to spread the perturbation caused by the bonding. In our description, the interaction of the 5σ CO electrons with the Rh$_2$ and Rh$_3$ clusters decrease their multiplicity through the filling of empty d holes in the sd band.

Adsorption Geometries and Energies as a Function of the Cluster Size

The calculated optimized geometries of the [Rh]$_n$CO species are given in Table III, where they are compared with data derived from ab $initio$ and LDF calculations.

TABLE III. Optimized bond lengths (Å) for the different structures analyzed

Molecule	Two-fold (bridge) coordination		One-fold (on top) coordination	
	Rh—C	C—O	Rh—C	C—O
Rh—CO			1.898	1.190
			1.864[a]-1.758[c]-2.10[b]	1.142[a]-1.17[c]-1.11[b]
[Rh]₂—CO	1.910	1.205	1.881	1.190
	1.900[d]	1.092[d]		
[Rh]₃—CO	1.917	1.204	1.871	1.191
[Rh]₄—CO	1.919	1.203	1.857	1.192
[Rh]₅—CO	1.908	1.204	1.851	1.192
[Rh]₁₀—CO	1.887	1.213	1.812	1.198
[Rh]₁₃—CO	1.883	1.208	1.816	1.195

[a] MP2, MP3 [10].

[b] Density functional theory [12].

[c] Ab initio CI without correlation [11]

[d] Ref [11], not fully optimized geometry.

The equilibrium geometries were obtained through gradient optimization, keeping frozen the coordinates of the metal atoms. Bond distances and bond angles were optimized simultaneously. In order to model CO *on-top* coordination on Rh₂ and Rh₄ clusters, the translational movement of the CO molecule was restricted to the axis perpendicular to the metal atom row to avoid its evolution to the most stable bridge structure. This procedure was not necessary for model Rh₃, Rh₅, Rh₁₀, and Rh₁₃ clusters, because there are relative minima in those structures for both coordination geometries.

For all the structures analyzed, we found a coordination of CO perpendicular to the surface, through the carbon end, without angular deformation of the Rh—C—O bond.

Both the linear and the bridge coordination involve interactions of the σ and π type. σ Interactions are composed of a charge transfer from 5σ CO to empty metal orbitals along with a repulsive interaction (Pauli repulsion) between the electronic clouds centered on the 5σ CO lone pair and the adjacent metal orbitals. π Interactions, on the other hand, imply back bonding from the metal orbitals to empty π* orbitals on the CO.

For the C—O interatomic bond directed along the z-axis, the one-fold (on-top) interaction involves a 5σ CO—d_{z^2} Rh repulsion, together with charge transfer to empty p_z metal orbitals. Back bonding is completed from d_{xz}, d_{yz} Rh orbitals to the empty π* CO orbital [Fig. 4(a)]. Bridge coordination implies the interaction of the 5σ CO orbital with d_{z^2}, d_{xz} Rh orbitals, and charge transfer to empty $p_x p_z$ metal orbitals directed along the Me—Me bond. Back bonding not only involves d_{xz} and d_{yz} metal orbitals but also d_{z^2} and p_x [Fig. 4(b)], yielding a more effective back bonding interaction for this coordination geometry. Due to the antibonding

4.a-1.   4.a-2.

4.b-1.   4.b-2.
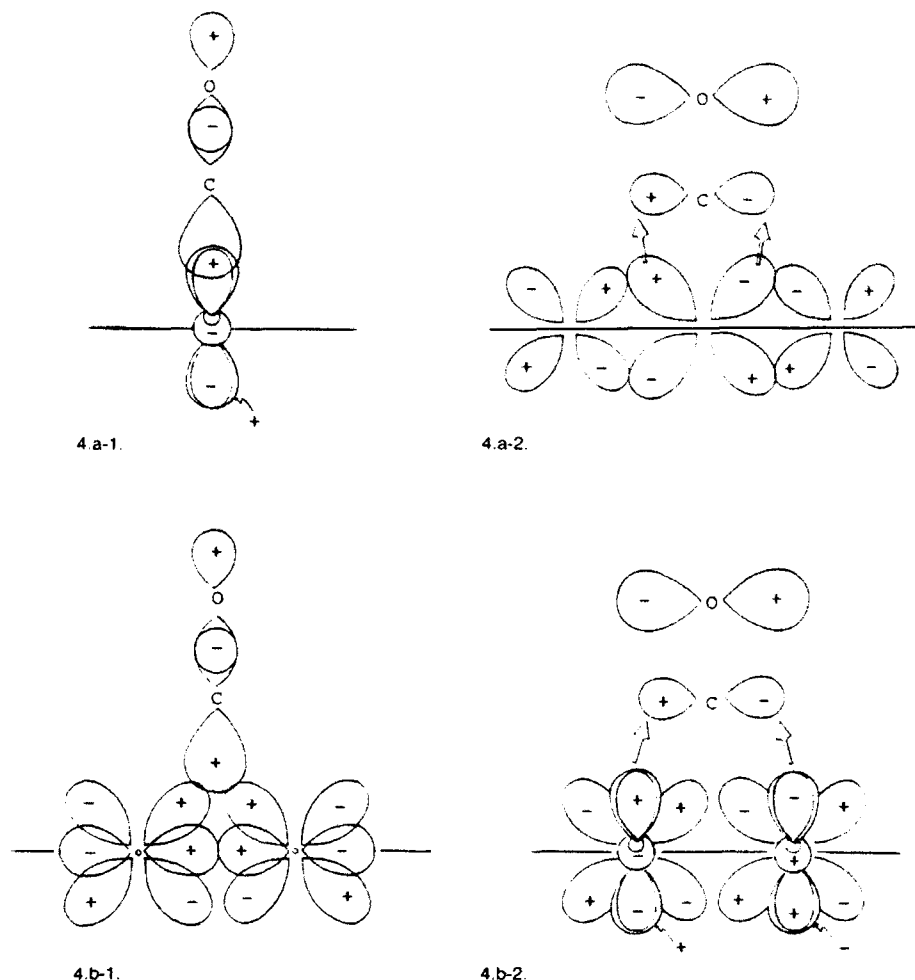
Figure 4. Molecular orbital interactions involved in the stabilization of the adsorption bond. The z-axis is directed along the adsorption bond, perpendicular to the metal surface. (a) One-fold (linear, *on top*) coordination. (a.1) 5σ CO-d_{z^2} Rh interaction. Charge transfer 5σ CO—p_z Rh. (a.2) Back bonding from d_{xz}, d_{yz} orbitals to the π^* CO. (b) Two-fold (bridge) coordination. (b.1) 5σ CO—d_{xz}, d_{yz} interaction. Charge transfer 5σ CO—p_x, p_y Rh. (b.2) Back bonding from the d_{xz}, d_{yz}, d_{z^2}, p_z Rh orbitals to the π^* CO.

character of the CO π^* bond, this more effective charge transfer results in a longer C—O bond for the bridge coordination (Table III).

Binding energy values (BE) are calculated as the difference between the total energy of the adsorbed [Rh]$_n$CO structures and the sum of the total energies of the metal cluster [Rh]$_n$ and the CO molecule, for the most stable M of each structure (Table II), evaluated, at the CI level, for the optimized geometries (Table III). Positive BE values indicate adsorption.

It is well-known that the INDO method used here overestimates bonding energies [34]. To account for this, the SCF-CI BE values derived from INDO calculations have been corrected by 2.5 eV per Rh—C bond to match the data derived from other calculation procedures (Table IV) as no BE experimental values are available. While the on-top coordination involves one Rh—C bond, the bridge coordination in the linear [Rh]$_n$ clusters implies the interaction of one C atom with two Rh atoms, for the same C—Rh distance obtained in both cases. However, in the two-dimensional [Rh(111)]$_{10}$ structures, first-nearest-neighbor and second-nearest-neighbor Rh atoms are to be considered for CO bridge adsorption. On the basis of the analysis of the atomic bond index matrix [43], a correction of a quarter the value of a Rh-first-nearest-neighbor—C bond is added for each interacting Rh-second-nearest-neighbor atom to calculate the Rh—CO BE correction. No further correction is necessary for the CO interaction with Rh bilayers as the C—second-layer-Rh-atom bond indices are negligible.

In agreement with *ab initio* calculations for the interaction of CO with [Rh]$_2$ [11], we found a higher stability of bicoordinated CO on the [Rh]$_n$(1 ≤ n ≤ 5)

TABLE IV. Binidng Energies (BE) (eV) of the CO molecules on the different structures.

	[Rh]CO	[Rh]$_2$CO	[Rh]$_3$CO	[Rh]$_4$CO	[Rh]$_5$CO	[Rh]$_{10}$CO	[Rh]$_x$CO
	4.09	*3.12*	*1.61*	*3.57*	*3.53*	*7.20*	*6.42*
One-fold (*on top*)	1.59 1.80[a] 2.40[b] 2.66[c]	0.62 Unbonded[d]	0.89	1.07	1.03	4.70	3.92
		7.54	*5.84*	*7.67*	*6.84*	*11.39*	*10.00*
Two-fold (bridge)		2.53 0.57[d]	0.84	2.67	1.84	5.14	3.76
		4.41	*4.22*	*4.10*	*3.30*	*4.18*	*3.58*
CI[e]		1.91	1.72	1.60	0.80	0.44	-0.17
		4.55	*6.36*	*3.67*	*3.46*	*4.49*	*3.84*
SCI[e]	—	2.05 0.93[d]	3.86	1.17	0.96	0.74	0.00

Raw data (*italic*) are corrected by 2.5 eV per Rh—CO bond, estimating the number of bonds from the atomic bond index matrix (see text).
[a] MP3 [10].
[b] MP2 [10].
[c] Density functional theory [12].
[d] HF *ab initio* without correlation effects.
[e] Energy difference (eV) are positive when the bridge structure is more stable than the on-top one.

linear clusters. The relative energy difference (BE_{bridge}—$BE_{on\ top}$) decreases as the cluster size increases (Table IV). This trend is also observed for the two-dimensional [Rh(111)]$_{10}$ clusters. The addition of in-plane atoms does not appear to further reduce the preference for bridge coordination over the on-top coordination. Since on-top binding is experimentally observed, monolayers of Rh atoms do not appear to yield a good model for the interaction of CO with a metal surface.

A similar BE for both geometries (Table IV) is found when the surface is modeled by the [Rh(111)]$_{13}$ bilayer structure. This fact reflects the importance of a proper modeling of the immediate environment of the metal atoms that are defining the adsorption site in order to reproduce the electronic interactions involved in the adsorption bond. In the bilayer structures, the Rh atoms bonded to CO have the same number of nearest neighbors as in the actual solid surface. We anticipate that on-top bonding will be more stable within a three-layer model, as this will be better able to distribute the σ bond repulsions.

Mulliken Population Analysis

The analysis of the metal—CO bonding in terms of σ, π interactions is usually based on population analysis results [44]. The change of the Mulliken populations on the atomic orbitals after adsorption (coordination) allows one to separate the different effects (σ charge transfer, σ polarization, and π back bonding) that are involved in the definition of the adsorption bond, and to rationalize, then, which is the more important effect for each structure (defined by the coordination geometry and cluster size). For the Mulliken population analysis, the INDO basis is assumed to be related to the Slater basis through symmetrical orthogonalization.

The corresponding orbital analysis after the INDO calculations shows that the relative importance of the σ, π interactions is highly dependent on the size of the cluster and on the coordination geometry (Tables V and VI).

There is good agreement between our analysis of the Rh—CO molecule and that obtained from *ab initio* calculations. The charge transfer from the metal to empty π^* CO orbitals is the most important bonding interaction, and leads to an increase of the population of the p orbitals centered on the C and O atoms (Table V). The 5σ CO—metal interaction is not as effective, because the charge in the σ orbital can only be distributed in the unique metal center. The overall effect leads to a negative charge density on the CO moiety.

When more than one Rh atom is considered in the model cluster, the charge is polarized to the adjacent metal atoms. This polarization causes the σ charge associated with the adsorption-site metal-atom to be directed away from CO leading to a reduction of the σ repulsion between the metal and CO.

This decrease of the repulsion in the σ bonding allows σ electrons of linearly (on-top) bonded CO to be transferred to the metal, yielding a positively charged CO. The magnitude of the charge transfer and back bonding effects do not change when the number of Rh atoms increases in the linear clusters (Table V). The local density charges on the C and O atoms, as well as the stability of the different [Rh]$_n$CO structures depends on the decrease of the Pauli repulsion in the σ-bonding

orbitals, which is accomplished by either hybridization in the Rh atom bonded to CO or polarization to adjacent atomic centers.

Due to the symmetry of the orbitals involved in the interaction (Fig. 4), π back bonding is more effective for the two-fold coordination, and the CO molecule has a negative net charge when bonded to [Rh]$_2$ and [Rh]$_3$ structures. However, since the polarization of the charge to the adjacent atoms is not only important for the linear but also for the two-fold coordination, it is important for the model that CO be bonded to *internal* atoms for both geometries. [Rh]$_4$ is therefore the smallest structure able to properly describe most of the effects involved in the interaction.

When CO is bridge-bonded to [Rh]$_4$, the decrease of the repulsion in the σ-symmetry orbitals allows a greater σ donation, which becomes even more evident than the back bonding change observed along the π-type orbitals, and the coordinated CO molecule is again characterized by a positive charge. The importance of the extra stabilization of the [Rh]$_4$CO bridge structure through polarization of the charge is reflected by its multiplicity, M (Table II). The reduction of the multiplicity of this structure from $M = 9$ to a lower value empties the HOMO orbital, which is responsible for much of the charge polarization to the terminal Rh atoms in the linear cluster (Fig. 5). The stability of the structure decreases by 0.7 eV when the multiplicity changes from 9 to 7.

When the cluster is defined by more than one row the charge is mainly polarized away from CO to adjacent rows. This more effective reduction of the σ repulsion, which is reflected in a shorter Rh—C bond length (Table III), and in a larger positive charge on the CO molecule (Figs. 2 and 3), stabilizes both coordination geometries. Although the relative energy difference decreases (Table IV), a single layer Rh cluster is not enough to reproduce the experimental results of a slightly higher stability of the on-top coordination.

In the bilayer metal clusters, there is a competition for the use of the δ and π orbitals of the adsorption site between forming a bond with CO or with other metal atoms of the second layer. The lower availability of the δ and π orbitals decreases the back bonding (the C—O bond length is shorter, Table III) and lowers the calculated stability of the CO adsorption, more markedly for the bridge structure than for the *on top* one.

The charge transfer from CO to the metal is more efficient than in a single layer metal cluster (larger positive charge on CO, Figs. 2 and 3) because the charge is also polarized to the second metal atom layer.

As the back bonding effect is more important for the bridge coordination, the decrease of this interaction, which is reflected in an increase of the negative charge on the Rh atoms bonded to CO, results in a destabilization of the two-fold vs. the one-fold coordination. Although not directly involved in the coordination, the presence of the second-layer metal atoms reverse the sign of the energy difference between two- and one-fold coordination geometries, yielding the experimentally observed result.

We might conclude, then, that bilayer [Rh(111)]$_{18}$ clusters are of the appropriate size to model the adsorptive interaction with a CO molecule.

TABLE V.   Changes in the Mulliken populations on the Rh, C, and O atomic orbitals and CO molecular orbitals through linear coordination.

	Atom	Before coordination			After coordination		
RhCO	Rh[a]	1.00 s		8 d	0.94 s	0.45 p	7.55 d
	C	1.79 s	1.99 p		1.41 s	2.30 p	
	O	1.78 s	4.42 p		1.80 s	4.50 p	
	CO	6.00 σ	4.00 π		5.60 σ	4.49 π	
Rh$_2$CO	Rh$_1$[a]	1.00 s	0.15 p	7.83 d	0.51 s	0.33 p	8.26 d
	Rh$_2$	1.00 s	0.15 p	7.83 d	0.63 s	0.15 p	8.18 d
	C	1.79 s	1.99 p		1.33 s	2.32 p	
	O	1.78 s	4.42 p		1.76 s	4.51 p	
	CO	6.00 σ	4.00 π		5.44 σ	4.46 π	
Rh$_3$CO	Rh$_1$	0.90 s	0.09 p	7.90 d	0.25 s	0.14 p	8.47 d
	Rh$_2$[a]	0.26 s	0.19 p	8.50 d	0.52 s	0.49 p	8.36 d
	C	1.79 s	1.99 p		1.31 s	2.30 p	
	O	1.78 s	4.42 p		1.76 s	4.45 p	
	CO	6.00 σ	4.00 π		5.43 σ	4.44 π	
Rh$_4$CO	Rh$_1$	0.40 s	0.12 p	8.35 d	0.22 s	0.15 p	8.30 d
	Rh$_2$[a]	0.70 s	0.28 p	8.02 d	0.60 s	0.52 p	8.28 d
	Rh$_3$	0.70 s	0.28 p	8.02 d	0.57 s	0.28 p	8.20 d
	Rh$_4$	0.40 s	0.12 p	8.35 d	0.49 s	0.15 p	8.31 d
	C	1.79 s	1.99 p		1.31 s	2.30 p	
	O	1.78 s	4.42 p		1.76 s	4.50 p	
	CO	6.00 σ	4.00 π		5.43 σ	4.47 π	
Rh$_6$CO	Rh$_1$	0.34 s	0.10 p	8.35 d	0.49 s	0.18 p	8.52 d
	Rh$_2$	0.70 s	0.26 p	8.20 d	0.07 s	0.31 p	8.18 d
	Rh$_3$[a]	0.30 s	0.27 p	8.47 d	0.65 s	0.49 p	~.39 d
	C	1.79 s	1.99 p		1.31 s	2.35 p	
	O	1.78 s	4.42 p		1.76	4.53 p	
	CO	6.00 σ	4.00 π		.44 σ	4.50 π	
Rh$_{10}$CO	Rh$_1$	0.56 s	0.40 p	7.96 d	0.53 s	0.35 p	8.05 d
	Rh$_2$[a]	0.90 s	0.78 p	7.83 d	0.35 s	1.05 p	7.83 d
	Rh$_3$	0.90 s	0.78 p	7.83 d	0.90 s	0.64 p	7.94 d
	Rh$_4$	0.56 s	0.40 p	7.96 d	0.54 s	0.33 p	8.20 d
	Rh$_5$	0.59 s	0.32 p	7.97 d	0.55 s	0.36 p	8.06 d
	Rh$_6$	0.64 s	0.49 p	7.74 d	0.61 s	0.42 p	7.88 d
	Rh$_7$	0.59 s	0.32 p	7.97 d	0.52 s	0.32 p	7.71 d
	Rh$_8$	0.59 s	0.32 p	7.97 d	0.55 s	0.36 p	8.06 d
	Rh$_9$	0.64 s	0.49 p	7.74 d	0.61 s	0.42 p	7.88 d
	Rh$_{10}$	0.59 s	0.32 p	7.97 d	0.52 s	0.32 p	7.71 d
	C	1.79 s	1.99 p		1.22 s	2.35 p	
	O	1.78 s	4.42 p		1.76 s	4.49 p	
	CO	6.00 σ	4.00 π		5.30 σ	4.53 π	

TABLE V. (Continued)

Atom		Before coordination			After coordination		
Rh$_{15}$CO	Rh$_1$	0.50 s	0.47 p	7.85 d	0.53 s	0.53 p	7.88 d
	Rh$_2^a$	0.83 s	0.98 p	7.47 d	1.11 s	1.08 p	7.27 d
	Rh$_3$	0.83 s	0.98 p	7.47 d	0.83 s	1.02 p	7.44 d
	Rh$_4$	0.50 s	0.47 p	7.85 d	0.53 s	0.49 p	7.88 d
	Rh$_5$	0.54 s	0.49 p	7.87 d	0.55 s	0.53 p	7.83 d
	Rh$_6$	0.75 s	0.76 p	7.60 d	0.82 s	0.81 p	7.58 d
	Rh$_7$	0.54 s	0.49 p	7.87 d	0.56 s	0.50 p	7.76 d
	Rh$_8$	0.55 s	0.49 p	7.84 d	0.57 s	0.54 p	7.82 d
	Rh$_9$	0.72 s	0.70 p	7.66 d	0.76 s	0.73 p	7.64 d
	Rh$_{10}$	0.55 s	0.49 p	7.84 d	0.57 s	0.51 p	7.85 d
	Rh$_{11}$	0.64 s	0.78 p	7.57 d	0.73 s	0.78 p	7.47 d
	Rh$_{12}$	0.64 s	0.78 p	7.57 d	0.66 s	0.815 p	7.49 d
	Rh$_{13}$	0.58 s	0.66 p	7.69 d	0.62 s	0.68 p	7.54 d
	Rh$_{14}$	0.74 s	0.89 p	7.56 d	0.86 s	0.89 p	7.44 d
	Rh$_{15}$	0.58 s	0.66 p	7.69 d	0.60 s	0.67 p	7.54 d
	C	1.79 s	1.99 p		1.21 s	2.28 p	
	O	1.78 s	4.42 p		1.76 s	4.48 p	
	CO	6.00 σ	4.00 π		5.29 σ	4.40 π	

^{a} Metal atom coordinated to the CO molecule.

Conclusions

We characterize the metal—CO bonding as a π donation from the metal coupled with a σ donation from CO. This latter interaction can become less repulsive by spreading charge to neighboring metal atoms in order to reduce the repulsion between the 5σ CO bond and the chelating Rh atoms.

The CO molecule must be bonded to internal surface atoms (as regarded to edges and ends) to properly model this charge transfer effect. In addition, the second metal layer is of utmost importance in modeling the metal–metal interactions, avoiding in this way an overestimation of the back bonding to the CO molecule, and correcting for the preference of bridged vs. on-top bonding.

Although a four-metal-atom cluster defines the minimum size for a good qualitative description of the interactions involved in the CO—metal bond, three-dimensional bilayer clusters are really necessary to reproduce experimental findings on a metal surface. We might extrapolate from this that large clusters cannot be modeled by fewer than the number of atoms needed to define the adsorption site environment with the same number of neighbors as in the actual metal surface.

We find that, although back bonding from the metal to the CO is the most important bonding interaction in the Rh–CO molecule, as is also found from *ab initio* and LSD calculations, charge transfer followed by polarization of the charge to the adjacent atoms is the most important effect when the interaction with larger metal clusters is considered.

TABLE VI.   Changes in the Mulliken populations on the Rh, C, and O atomic orbitals and on the CO molecular orbitals through two-fold coordination.

	Atom	Before coordination			After coordination		
Rh_2CO	Rh^a	1.00 s	0.15 p	7.83 d	0.34 s	0.29 p	8.31 d
	C	1.79 s	1.99 p		1.22 s	2.46 p	
	O	1.78 s	4.42 p		1.76 s	4.59 p	
	CO	6.00 σ	4.00 π		5.30 σ	4.72 π	
Rh_3CO	Rh_1^a	0.90 s	0.09 p	7.90 d	0.40 s	0.27 p	8.16 d
	Rh_2^a	0.26 s	0.19 p	8.50 d	0.51 s	0.48 p	8.06 d
	Rh_3	0.90 s	0.09 p	7.90 d	0.96 s	0.12 p	8.35 d
	C	1.79 s	1.99 p		1.21 s	2.46 s	
	O	1.78 s	4.42 p		1.76 s	4.56 p	
	CO	6.00 σ	4.00 π		5.30 σ	4.71 π	
Rh_4CO	Rh_1	0.40 s	0.12 p	8.35 d	0.84 s	0.11 p	7.97 d
	Rh_2^a	0.70 s	0.28 p	8.02 d	0.52 s	0.45 p	8.19 d
	C	1.79 s	1.99 p		1.21 s	2.41 p	
	O	1.78 s	4.42 p		1.76 s	4.49 p	
	CO	6.00 σ	4.00 π		5.30 σ	4.54 π	
Rh_5CO	Rh_1	0.33 s	0.10 p	8.35 d	0.09 s	0.14 p	8.72 d
	Rh_2^a	0.70 s	0.26 p	8.20 d	0.40 s	0.42 p	8.14 d
	Rh_3^a	0.30 s	0.27 p	8.47 d	0.54 s	0.30 p	8.05 d
	Rh_4	0.70 s	0.26 p	8.20 d	0.14 s	0.40 p	8.57 d
	Rh_5	0.33 s	0.10 p	8.35 d	0.02 s	0.10 p	8.65 d
	C	1.79 s	1.99 p		1.23 s	2.45 p	
	O	1.78 s	4.42 p		1.76 s	4.56 p	
	CO	6.00 σ	4.00 π		5.35 σ	4.65 π	
$Rh_{10}CO$	Rh_1	0.56 s	0.40 p	7.96 d	0.49 s	0.33 p	7.92 d
	Rh_2^a	0.90 s	0.78 p	7.83 d	0.62 s	0.93 p	7.89 d
	Rh_5	0.59 s	0.32 p	7.97 d	0.52 s	0.33 p	7.96 d
	Rh_6	0.64 s	0.49 p	7.74 d	0.51 s	0.60 p	8.08 d
	C	1.79 s	1.99 p		1.13 s	2.46 p	
	O	1.78 s	4.42 p		1.76 s	4.48 p	
	CO	6.00 σ	4.00 π		5.22 σ	4.62 π	
$Rh_{13}CO$	Rh_1	0.50 s	0.47 p	7.85 d	0.52 s	0.52 p	7.41 d
	Rh_2^a	0.83 s	0.98 p	7.47 d	0.92 s	1.03 p	7.42 d
	Rh_5	0.54 s	0.49 p	7.87 d	0.55 s	0.52 p	7.80 d
	Rh_6	0.75 s	0.76 p	7.60 d	0.84 s	0.81 p	7.56 d
	Rh_8	0.55 s	0.49 p	7.84 d	0.57 s	0.51 p	7.82 d
	Rh_9	0.71 s	0.70 p	7.66 d	0.61 s	0.75 p	7.67 d
	Rh_{11}	0.64 s	0.78 p	7.57 d	0.68 s	0.80 p	7.51 d
	Rh_{13}	0.58 s	0.66 p	7.69 d	0.59 s	0.67 p	7.59 d
	Rh_{14}	0.74 s	0.89 p	7.56 d	0.84 s	0.92 p	7.48 d
	C	1.79 s	1.99 p		1.08 s	2.34 p	
	O	1.78 s	4.42 p		1.75 s	4.40 p	
	CO	6.00 σ	4.00 π		5.24 σ	4.44 π	

[a] Metal atoms coordinated to the CO molecule. Only the populations on nonequivalent atoms are reported.
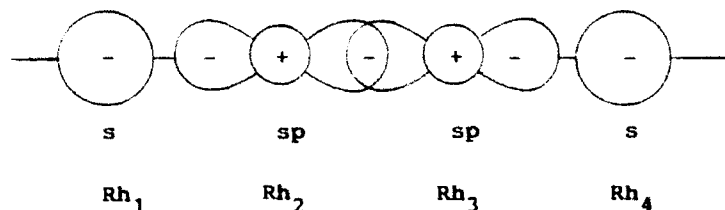
Figure 5. Atomic orbitals involved in the HOMO of the [Rh]₄CO bridge structure. The size of the orbitals reflects the relative contributions to the molecular orbital derived from the MO coefficients.

Acknowledgments

Bibliography

[1] R. R. Adzic, in *Advances in Electrochemistry and Electrochemical Engineering* (vol. 13). H. Gerischer and C. W. Tobias, Eds. (Wiley, New York, 1984).

[2] D. M. Kolb, in *Advances in Electrochemistry and Electrochemical Engineering* (vol. 11). H. Gerischer and C. W. Tobias, Eds. (Wiley, New York, 1984).

[3] J. A. Rodriguez and D. W. Goodman, J. Phys. Chem. **95**, 4196 (1991).

[4] C. T. Campbell, Ann. Rev. Phys. Chem. **41**, 775 (1990).

[5] P. S. Bagus, C. N. Nelin, and C. W. Bauschlicher, Phys. Rev. **28**, 5423 (1983).

[6] C. W. Bauschlicher, P. S. Bagus, C. N. Nelin, and B. Roos, J. Chem. Phys. **85**, 354 (1986).

[7] L. A. Barnes and C. W. Bauschlicher, J. Chem. Phys. **91**, 314 (1989).

[8] Si-Chung Chang and M. Weaver, J. Electroanal. Chem. **285**, 263 (1990).

[9] Si-Chung Chang, Lam-Wing, H. Leung, and M. Weaver, J. Phys. Chem. **90**, 7426 (1989).

[10] M. L. McKee and S. D. Worley, J. Phys. Chem. **92**, 3699 (1988).

[11] G. J. Mains and J. M. White, J. Phys. Chem. **95**, 112 (1991).

[12] I. Papai, A. Goursot, St-Amant, and D. R. Salahub, Theor. Chim. Acta (to appear).

[13] R. Parsons and T. VanderNoot, J. Electroanal. Chem. **257**, 9 (1988).

[14] B. Beden, F. Hahn, J. M. Leger, C. Lamy, C. L. Perdriel, N. R. de Tacconi, R. O. Lezna, and A. J. Arvia, J. Electroanal. Chem. **301**, 129 (1991).

[15] K. C. Canoon, S. K. Jo, and J. M. White, J. Am. Chem. Soc. **111**, 5064 (1989).

[16] J. E. Inglesfield, in *Interaction of Atoms and Molecules With Solid Surfaces*. V. Bortolani, N. H. March, and M. P. Tosi, Eds. (Plenum Press, New York, 1990).

[17] M. Matos and J. B. L. Neto, Surf. Sci. **258**, 439 (1991).

[18] H. Nakatsuji, Y. Matsuzaki, and Y. T. Yonezawa, J. Chem. Phys. **88**, 5759 (1988).

[19] P. S. Bagus and G. Pacchioni, Surf. Sci. **236**, 233 (1990).

[20] C. A. Rice, S. D. Worley, C. W. Curtis, J. A. Guin, and A. R. Tarrer, J. Chem. Phys. **74**, 4150 (1981).

[21] R. Dictor and S. Roberts, J. Phys. Chem. **93**, 5846 (1989).

[22] Shueh-Lin Yau, Xiaoping Gao, Si-Chung Chang, B. C. Schardt, and M. J. Weaver, J. Am. Chem. Soc. **113**, 6049 (1991).

[23] B. A. Gurney, L. J. Richter, J. S. Villarrubia, and W. Ho, J. Chem. Phys. **87**, 6710 (1987).

[24] H. C. Paehles, J. M. White, C. T. Campbell, Surf. Sci. **150**, 120 (1985).

[25] (a) J. A. Pople, D. L. Beveridge, and P. A. Dobosh, J. Chem. Phys. **47**, 2026 (1967); (b) J. E. Ridley and M. C. Zerner, Theor. Chim. Acta (Berl.) **42**, 223 (1976); (c) M. C. Zerner, G. H. Loew, R. F. Kirchner, and U. T. Mueller-Westerhoff, J. Am. Chem. Soc. **16**, 589 (1980); (d) A. D. Bacon and M. C. Zerner, Theor. Chim. Acta **53**, 21 (1979).

[26] M. C. Zerner, ZINDO Package, Quantum Theory Project, University of Florida, Gainesville, FL.

[27] D. R. Lide, Ed. *CRC Handbook of Chemistry and Physics* (CRC Press, Boca Raton, FL, 1990–91.

[28] (a) M. C. Zerner, Int. J. Quant. Chem. **35**, 567 (1989); (b) W. D. Edwards and M. C. Zerner, Theoret. Chim. Acta **72**, 347 (1987).

[29] R. Pauncz, *Spin Eigenfunctions* (Plenum Press, New York, 1979).

[30] J. D. Head and M. C. Zerner, Chem. Phys. Lett. **122**, 264 (1985).

[31] J. D. Head and M. C. Zerner, Chem. Phys. Lett. **131**, 359 (1986).

[32] J. D. Head, B. Weiner, and M. C. Zerner, Int. J. Quant. Chem. **33**, 177 (1988).

[33] W. P. Anderson, T. R. Cundari, and M. C. Zerner, Int. J. Quant. Chem. **34**, 31 (1991).

[34] M. C. Zerner in *Reviews in Computational Chemistry* (vol. 2), K. B. Lipkowitz and D. B. Boyd, Eds. (VCH Publishers, New York, 1990).

[35] J. P. Stewart, in *Reviews in Computational Chemistry* (vol. 1), K. B. Lipkowitz and D. B. Boyd, Eds. (VCH Publishers, New York, 1990).

[36] A. Szabo and N. S. Ostlund, *Modern Quantum Chemistry: Introduction to Advanced Electronic Structure Theory* (McGraw-Hill, New York, 1989).

[37] K. Balasubramanian and D. Liao, J. Phys. Chem. **93**, 3989 (1989).

[38] I. Shim, Mat.-Fys. Medd.—K. Dan. Vidensk. Selsk. **41**, 147 (1985).

[39] F. Illas, J. Rubio, and J. Canellas, J. Chem. Phys. **93**, 2603 (1990). Note: the leading configuration in Table IV for the $^5\Delta g$ state is inconsistent with the text just above it. We have corrected the table in presenting the leading configuration.

[40] D. L. Cocke and K. A. Gingerich, J. Chem. Phys. **60**, 1958 (1974).

[41] R. Fournier and D. R. Salahub, Surf. Sci. **238**, 330 (1990).

[42] F. Raatz and D. R. Salahub, Surf. Sci. **176**, 219 (1986).

[43] K. B. Wiberg, Tetrahedron **24**, 1083 (1968).

[44] R. S. Mulliken, J. Chem. Phys. **23**, 1833 (1955).

Revised June 8, 1992

Electronic and Magnetic Properties of Organometallic Clusters: From the Molecular to the Metallic State

LUTZ ACKERMANN and NOTKER RÖSCH

Lehrstuhl für Theoretische Chemie, Technische Universität München, 8046 Garching, Germany

BRETT I. DUNLAP

Theoretical Chemistry Section, Code 61 9, Naval Research Laboratory, Washington, DC 20375-5000

GIANFRANCO PACCHIONI*

Dipartimento di Chimica Inorganica e Metallorganica, Centro CNR, Universita' di Milano, via Venezian 21, 20133 Milano, Italy

Abstract

We have performed a linear combination of Gaussian-type orbitals, LCGTO, local density functional, LDF, calculations on a series of low- and high-nuclearity carbonylated Ni clusters and on their naked counterparts. We have found that while the bare Ni clusters do exhibit several features in common with the bulk metal, the low-nuclearity carbonylated clusters do not show any metallic behavior. Signs of a developing metallic character are found for high-nuclearity Ni cluster carbonyls where it is possible to distinguish between "surface" atoms, which are directly interacting with the ligand sphere, and "bulk" atoms, which are only interacting with other metal atoms. Through the analysis of the magnetic properties of these systems it is possible to formulate a general model which rationalizes both the metallic behavior of the free Ni clusters and the nonmetallic behavior in certain carbonylated Ni clusters. This model is based on the perturbations induced by the ligands on the electronic structure of the metal atoms in the cluster. © 1992 John Wiley & Sons, Inc.

Introduction

Molecular metal clusters constitute a relatively young field in coordination chemistry [1] which opens new perspectives for understanding the transition from the molecular to the metallic state. Molecular metal clusters can be obtained in solution, but also exist in the solid state, giving rise in several cases to crystalline structures [2]. When a crystal is obtained, it consists of an assembly of identical macromolecules, the inorganic clusters, which are composed of a core of metal atoms surrounded by a shell of ligands, which include carbonyls, phosphines, and atoms, such as Cl, S, O, etc. This ligand shell is essential for the chemical stabilization of the complex and for preventing the coalescence of the metal cores to form large

---

* Corresponding author.

metallic particles; furthermore, it provides an "insulating" phase between the metal cores. These cores are usually composed of a few (from 3 to 10–15) metal atoms but, in some cases, the size of the metallic part of the cluster can be considerably larger. Clusters containing up to about 50 metal atoms have been synthesized, crystallized, and characterized by X-ray diffraction techniques [2]. Much larger clusters, containing several hundreds of metal atoms have also been synthesized [1c]; for these "giant" clusters, which start to resemble colloidal particles, it has been impossible to obtain crystalline structures and the characterization of the stoichiometry and shape of the cluster "molecules" has been done by high-resolution electron microscopy.

These inorganic compounds, containing a frame of a few hundred metal atoms are an ideal class of materials for investigating the evolution of the properties associated with metallic behavior. A great advantage compared to other methods of producing isolated metal clusters, like the cluster beam techniques [3], is that considerable yields (of the order of a few grams) of the material can be obtained through chemical synthesis; moreover, inorganic clusters are stable under normal experimental conditions [2].

In this way it has been possible to perform a series of physical measurements on clusters of various size [4–8]. Recently, EXAFS studies [5] on $Au_{55}(PPh_3)_{12}Cl_6$, where the Au_{55} unit has a cubo-octahedral structure, have shown that the X-ray absorption edge of the cluster has several features in common with the bulk. Also the photoelectron spectra [6] of this gold cluster shows striking similarities with that of the metal. On the other hand, significant differences have been found with Mössbauer measurements [7], because the response of the "surface" Au atoms, directly interacting with the ligand shell, is different from that of the "internal" Au atoms, where the average coordination resembles that of the bulk. A similar effect, i.e., a different behavior of the "surface" with respect to the "bulk" metal atoms in high-nuclearity clusters, has been recently proposed in order to interpret the spin-lattice relaxation time and the metallic Knight shifts in ^{195}Pt NMR experiments on a $Pt_{309}Phen_{36}O_{30}$ cluster [8]. Even more interesting for the understanding of the development of a metallic behavior are the magnetic measurements performed on carbonylated clusters [4]. Interestingly, all the low-nuclearity clusters, with a metal core composed of up to about 10 atoms, are diamagnetic. Temperature-dependent magnetic susceptibility measurements on larger clusters, composed of about 40 metal atoms, exhibit a total magnetic moment per cluster of the order of 4–9 μ_B [4]. The average magnetic moment per atom in bulk Ni is 0.6 μ_B [9]; for a cluster containing 40 atoms, this should correspond to a total magnetic moment of 24 unpaired electrons, while the observed moment is much smaller [4].

All these data indicate that the ligand shell induces strong modifications in the electronic structure of the metal frame so that some of the metal-like properties are retained while others are partly or totally lost. Moreover, some of these properties change as a function of the cluster nuclearity. Clearly, the large body of data collected on these systems requires rationalization in a comprehensive theory. In this article we present a unifying theory which accounts for the different behavior of ligand-free metallic clusters, like the ones obtained in gas-phase cluster beam experiments,

and of molecular metal clusters, usually prepared by organometallic synthesis. This theory is based on electronic structure calculations performed with the linear combination of Gaussian-type orbitals (LCGTO), local density functional (LDF) method [10,12], which allows a self-consistent all-electron treatment.

We will show that the surrounding ligands stabilize the organometallic cluster, but also that they deeply modify the electronic characteristics of the metal atoms of the cluster. The perturbation of the ligand shell is strong enough so that all the "metallic" properties are lost for the "surface" metal atoms, while some "metallic" behavior is still present on the "bulk" metal atoms, provided that the cluster is large enough to allow for such distinction.

Computational Method

All the calculations have been carried out by means of the LCGTO-LDF method [10–12]. This computational technique is quite well suited for the study of the transition from molecular to metallic systems. Here we recall only the major features of the method. Further details can be found elsewhere [12].

In the LCGTO-LDF method one has to solve one-electron equations derived in the Kohn–Sham approach to density functional theory [10,11]:

$$[-\tfrac{1}{2}\nabla^2 + v(\mathbf{r})]\,\psi_i(\mathbf{r}) = \epsilon_i\psi_i(\mathbf{r})$$

where the local potential, $v(\mathbf{r})$, is composed of the nuclear-electron attraction, the classical interelectronic repulsion, and the exchange-correlation potential, $v_{xc}(\mathbf{r})$. In the present investigation, $v_{xc}(\mathbf{r})$ is taken to be the $X\alpha$ variant of the LDF approximation

$$v_{xc}(\mathbf{r}) = -3/2\,\alpha\,[(3/\pi)\rho(\mathbf{r})]^{1/3}$$

where $\rho(\mathbf{r})$ is the charge density

$$\rho(\mathbf{r}) = \Sigma n_i[\psi_i(\mathbf{r})]^2$$

and α is set to 0.7.

The LCGTO-LDF method makes use of three Gaussian-type basis sets, one for the construction of the Kohn–Sham orbitals; one to fit the charge density, $\rho(\mathbf{r})$, when calculating the interelectronic repulsion potential; and one to fit the exchange-correlation potential, $v_{xc}(\mathbf{r})$. All-electron calculations have been performed in order to determine the cluster ground state using a spin-polarized version of the method. The filling of the one-electron levels is done according to the fractional occupation number, FON, technique [12]; according to this procedure, one formally broadens each one-electron level by a Gaussian (half-width 0.3 eV) and fills the resulting density of states, DOS, by the appropriate number of electrons. Thus, a cluster Fermi energy is determined in a self-consistent way, and need not result in an occupied highest occupied molecular orbital (HOMO) that contains an integral number of electrons.

The calculations have been performed on a series of bare and carbonylated Ni clusters of various sizes: the cluster structures are taken from the corresponding X-

ray crystallographic data [2]. In some cases, the experimental structure has been idealized to take advantage of the symmetry properties of the computational program. To give an idea of the complexity of the calculations, we mention that the basis set for the largest cluster considered, [Ni$_{44}$(CO)$_{48}$]^n, consists of about 3300 contracted functions; the compound contains 140 atoms and more than 1900 electrons, depending on the net charge, n.

The accuracy of the method in predicting electronic and structural properties of carbonylated Ni clusters is shown, for instance, by the results of the partial optimization of the Ni—C distances in Ni$_3$(CO)$_8$; the optimal r(Ni—CO, terminal) = 1.76 Å and r(Ni—CO, bridge) = 1.86 Å are in excellent agreement with the average experimental bond lengths, 1.75 Å and 1.90 Å, respectively [2].

Free Ni Clusters

In the last decade, the knowledge of the physical properties of small, ligand-free, metal clusters has grown considerably thanks to the development of sophisticated experimental techniques in which gas-phase clusters are produced under controlled conditions and investigated by means of photophysical measurements [3]. In addition, accurate quantum-mechanical calculations have been performed to interpret the experiments and to predict other properties that are not easy to obtain experimentally [13].

Gas-phase Ni clusters have been studied theoretically [12,14–19] and experimentally [20]. The present LDF calculations indicate, in agreement with other theoretical investigations [14–18], that Ni clusters are highly magnetic, see Table

TABLE I. Binding energy per atom, BE/n (eV); Fermi energy, E_f (eV); total, N_f = N_{up} − N_{down}; and average, n_s = N_f/n, number of unpaired electrons in bare Ni$_n$ clusters.

Ni$_n$	from Ni$_n$(CO)$_m$	r_1, r_2[a]	BE/n[b]	E_f	N_f	n_s
Ni$_3$	from Ni$_3$(CO)$_6$	2.38	1.35	2.93	2.49	0.83
Ni$_4$	from Ni$_4$(CO)$_{12}$	2.38, 2.81	1.69	3.17	4.20	0.84
Ni$_6$	from Ni$_6$(CO)$_{12}$	2.38, 2.77	2.03	3.47	6.84	1.14
Ni$_8$[c]	from Ni$_8$C(CO)$_{16}$	2.63	2.56	3.54	7.92	0.99
Ni$_8$C[c]	from Ni$_8$C(CO)$_{16}$	2.63	3.22	3.44	4.24	0.53
Ni$_8$[d]	from Ni$_8$(CO)$_8$(PR)$_6$	2.65	2.09	3.59	7.92	0.99
Ni$_9$	from Ni$_9$(CO)$_{18}$	2.38, 2.77	2.33	3.27	8.11	0.90
Ni$_{10}$	from Ni$_{10}$Ge(CO)$_{20}$	2.55, 2.72	2.40	3.47	8.79	0.88
Ni$_{10}$Ge	From Ni$_{10}$Ge(CO)$_{20}$	2.55, 2.72	2.83	3.48	5.58	0.55
Ni$_{12}$	from Ni$_{12}$C$_6$(CO)$_{16}$	2.40, 2.46, 2.63	4.15	3.73	26.44	0.83
Ni$_{12}$C$_6$	from Ni$_{12}$C$_6$(CO)$_{16}$	2.40, 2.46, 2.63	4.95	3.77	10.13	0.32
Ni$_{44}$	from Ni$_{44}$(CO)$_{48}$	2.58	4.10	3.71	32.66	0.74

[a] The Ni—Ni distances (in Å) are fixed at the experimental values found in the carbonylated clusters.
[b] Binding energy per atom computed as $[nE(Ni) + iE(C) + jE(Ge) − E(Ni_nC_iGe_j)]/(n + i + j)$.
[c] Square antiprism.
[d] Cube.

I. The magnetic behavior of the small clusters, which is reminiscent of the ferro-magnetic ordering of the bulk metal, can be explained by the nature of the chemical bonding in these systems. The low-lying electronic states in Ni clusters arise from the interaction of Ni atoms in the $3d^9 4s^1$ configuration. While the $4s$ orbital is spatially very diffuse, the $3d$ orbitals are contracted and highly localized; therefore, when two or more Ni atoms interact to form a diatomic or a larger aggregate, the interaction involves mainly the $4s$-levels, whereas the $3d$–$3d$ overlap is weak. The bonding originates from the coupling of the $4s$ electrons via the formation of a partially occupied $4s$-manifold, while the $3d$ "band" is narrow and the unpaired $3d$ electrons are only partially coupled. This results in an average number of unpaired electrons per Ni atom close to one for small Ni molecules like Ni_2, which probably has a $^3\Sigma_g$ ground state [21], or Ni_3, for which a ^3A_u linear molecule is virtually degenerate with a $^5A_2$ equilateral triangle [17]. As the cluster grows, the number of electronic spin states grows very rapidly, forming a dense manifold immediately above the ground state. The energy separation between these states is much smaller than the thermal energy, kT, for room or even lower temperatures. For high-nuclearity gas-phase Ni clusters it becomes virtually impossible to compute all these states and to determine the electronic ground state and its spin multiplicity. In this respect, the FON technique used in this work when determining the occupation numbers of the Kohn–Sham orbitals in the LDF approximation is ideally suited because it provides an average over the several close-lying electronic configurations of a cluster.

The Ni clusters considered in this work are somewhat "special" in the sense that their geometry was taken from the corresponding structure of the metal core in carbonylated Ni clusters [2]. The Ni—Ni distances, Table I, and the geometry of the Ni_n units are thus nonoptimal for a free cluster of the same size. For this reason, the average number of unpaired electrons per atom, $n_s = 0.7$–1.1 (Table I), is considerably higher than the magnetization of bulk Ni, $0.6 \mu_B$ per atom [9]. This larger magnetization arises mainly for two reasons. First, the Ni—Ni distances in the Ni_n units considered are often larger than in the bulk, where the Ni—Ni separation is 2.49 Å; second, the average coordination of the Ni atoms in a cluster is much lower than in the bulk.

The dependence of the magnetization of these two factors, metal–metal distance and average coordination, has been analyzed by computing a Ni_{44} cluster for different values of $r(Ni—Ni)$ (see Table II). Ni_{44} is a regular octahedron constituted by an inner core of six Ni atoms surrounded by 38 "surface" Ni atoms. Thus, it is possible to distinguish in the cluster two types of atom, the "bulk" Ni atoms, Ni1 in the notation of Figure 1 and Table II, with 12 nearest neighbors (NN) and three types of "surface" Ni atoms, Ni2, Ni3, and Ni4, with 9, 7, and 4 NN, respectively. Six distances, from $r(Ni—Ni) = 2.18$ Å to $r(Ni—Ni) = 2.68$ Å have been considered (Table II). The minimum of the potential energy curve, $r_e(Ni—Ni) = 2.36$ Å is about 5% shorter than in the bulk. For this distance, the magnetization of the "bulk" Ni atoms is $\mu_B(Ni1) = 0.64$, quite close to the bulk value. The magnetization of the "surface" atoms, 0.65 (Ni2), 0.66 (Ni3), and 0.72 (Ni4) μ_B per atom, exhibits a trend opposite to the average coordination. This is due to the narrowing of the

TABLE II.   Binding energy per atom, BE/n (eV); Fermi energy, E_f (eV); ionization potential, IP (eV); total number of unpaired electrons per atom, $N_j = N_{up} - N_{down}$; and their distribution between "bulk" and "surface" atoms in Ni_{44} as function of the Ni—Ni distances (in Å).

| | | | | | Unpaired Electrons/Atom[a] | | | |
| | | | | | Bulk | Surface | | |
$r(Ni—Ni)$	BE/n	IP	E_f	N_j	Ni1	Ni2	Ni3	Ni4
2.18	3.99	—	-3.88	24.1	0.50	0.54	0.53	0.64
2.28	4.33	—	-3.84	26.9	0.58	0.60	0.60	0.68
2.38[b]	4.40	—	-3.79	29.0	0.64	0.65	0.66	0.72
2.48	4.30	4.97	-3.75	30.9	0.68	0.69	0.70	0.75
2.58	4.09	—	-3.71	32.7	0.72	0.73	0.74	0.79
2.68	3.83	—	-3.67	34.2	0.74	0.76	0.78	0.82

			Bulk Ni					
2.49[c]	4.44[d]	5.35[e]	—	—	0.60[f]	—	—	—

[a] Number of unpaired electrons per Ni atom, see Figure 1 for definitions. Ni1 has 12 nearest neighbors, NN; Ni2 has 9 NN; Ni3 has 7 NN; and Ni4 has 4 NN. N_j for bulk nickel magnetization would be $44 \times 0.6 = 26.4$

[b] Close to the equilibrium value, $r_e = 2.36$ Å.

[c] From R. G. Wickoff, *Crystal Structures* (2nd Ed.) (Interscience, New York, 1964).

[d] Heat of formation of gaseous atoms from the metal, from L. Brewer and G. M. Rosenblatt, Adv. High Temp. Chem. **2**, 1 (1969).

[e] Work function of the (111) surface; from .' Baker, E. B. Johnson, and G. I. C. Maire, Surf. Sci. **24**, 572 (1971).

[f] From ref. 9.

bands and to the concomitant promotion of electrons from minority to majority spin bands as the average coordination of the atom decreases. This effect is responsible for the $\simeq 5\%$ enhancement of the magnetic moment of the first layer of Ni(100) with respect to a bulk layer [22]. The change of the Ni—Ni distance has a pronounced effect on the cluster magnetic moment. A $\simeq 10\%$ decrease of the Ni—Ni distance corresponds to a $\simeq 20\%$ reduction of the magnetization for the high-coordinated Ni atoms and to a $\simeq 10\%$ reduction for the low-coordinated ones. A $\simeq 10\%$ increase of $r(Ni—Ni)$ results in the enhancement of the magnetic moment by $\simeq 10\%$ (Table II).

The Kohn–Sham eigenvalues are, unlike the Hartree–Fock orbital energies, not directly related to ionization potentials (IP), but only after allowing a proper relaxation as done when applying Slater's transition state approach. Of course, an alternative for determining an IP is to do a ΔSCF calculation. We find that with this technique the lowest IP of Ni_{44} at $r(Ni—Ni) = 2.58$ Å to be 5.66 eV, which is reasonably close to the bulk work function, 5.35 eV (see Table II), and to the IP of gas-phase Ni clusters of this size, about 5.7 eV [23]. Note the difference in the cluster Fermi energy, which is -3.71 eV at this distance.
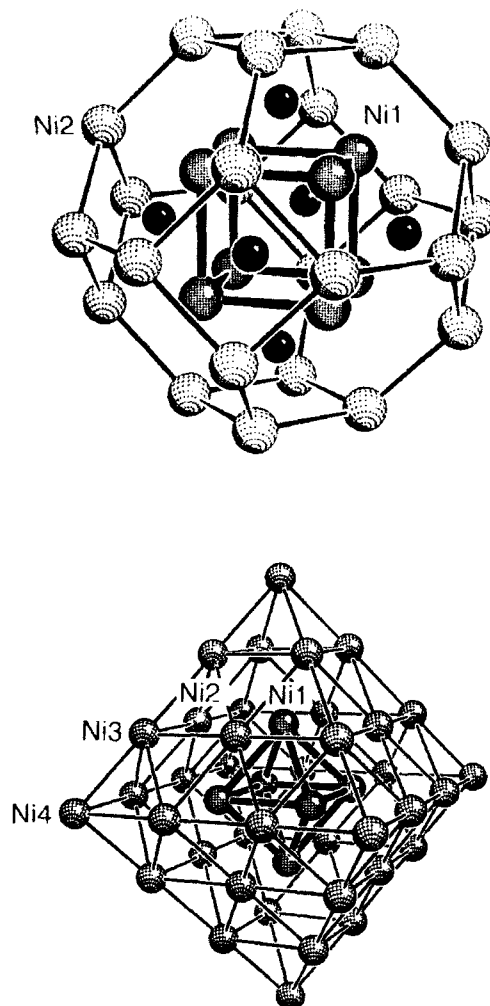
Figure 1. Geometry of the metal frame of the Ni₃₂(CO)₃₆ and of the Ni₄₄(CO)₄ₓ molecular metal clusters: the CO ligands are not shown for clarity.

In Figure 2 we present the local density of states, LDOS, for Ni₄₄. The LDOS curves have been obtained by Gaussian broadening (half width = 0.1 eV) of the one-electron energy spectrum of majority and minority spins. The contribution from the 4s orbitals has been distinguished from that of the 3d orbitals (see Fig. 2a). The most obvious characteristic of the 3d-level distribution in Ni₄₄ is that the majority-spin d levels are completely filled, while there is a tail of the minority-spin d band extending above E_F. The LDOS curve for Ni₄₄ shows a strong similarity to the DOS curves of bulk Ni [24]: two intense features are present in the spectra at the Fermi level, E_F, and $\simeq 2$ eV below it; the 3d band is $\simeq 4$ eV wide in both
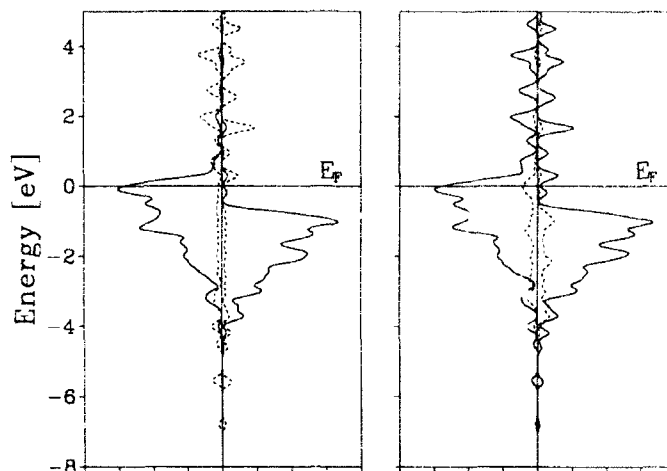
Figure 2. Ni₄₄ density of states (in arbitrary units) generated by Gaussian broadening of the one-electron energies with a Gaussian function of fixed half-width 0.1 eV. (a) (——) Ni 3d contribution; (------) Ni 4sp contribution. (b) (———) "Surface" Ni atoms contribution; (------) "bulk" Ni atoms contribution.

cluster and bulk regimes. In Ni₄₄, however, there is a characteristic low-intensity feature below the d-band which is due to the bonding combination of the 4s orbitals. This peak, at ≃5.5 eV below E_F, corresponds to the very stable totally symmetric bonding combination of Ni 4s orbitals. Topological arguments suggest that this orbital is always occupied in bare Ni clusters, thus stabilizing the structure [25,26]. The rest of the 4s band is distributed over a large range of energies, as is to be expected because of the nodal structure of the weakly bonding and nonbonding 4s-derived MOs in Ni₄₄. In Figure 2b, the contribution of the "surface" atoms to the total DOS has been separated from that of the "bulk" atoms. However, apart from the obviously different intensity which reflects the ≃6:1 ratio of "surface" versus "bulk" atoms, the two DOS curves exhibit the same shape.

Interstitial Atoms in Ni Clusters

Many of the isolated molecular metal clusters include main group atoms, i.e., C, Si, Ge, P, H, etc., in the metal cage [2]. The global effect of these internal atoms on the electronic structure of the cluster is reminiscent of that of impurity atoms in the bulk metal, at least as far as the magnetic properties are concerned. Hydrogen or carbon atoms adsorbed on a Ni surface induce a local quenching of the magnetic moment of the surface atoms [27]. The same effect occurs when carbon or germanium atoms are introduced in the bare Ni cluster (see Table I). In Ni₆C, the total number of unpaired electrons is reduced by almost 50% with respect to Ni₈. In Ni₁₀Ge, a single interstitial Ge atom reduces the number of unpaired electrons from 8.8 to 5.5 (Table I). In Ni₃₂C₆, the six C atoms, occupying the six square

antiprism cavities of the Ni$_{13}$ cluster (see Fig. 1), reduce the average magnetization from 0.88 μ_B per atom in Ni$_{13}$ to 0.32 μ_B per atom in Ni$_4$C$_2$, which represents a quenching of the original magnetic moment by about 60%.

The origin of this spin quenching is connected to the overlap between the singly occupied $n$sp hybrid orbitals on the impurity atoms and the Ni 3d orbitals. This leads to the formation of strong covalent bonds and subsequent spin pairing. Indeed, the interstitial atoms induce a considerable stabilization of the whole structure, as can be seen from the values of the atomization energy (Table 1).

The Magnetic and "Metallic" Properties of Ni Carbonyl Clusters

From the previous analysis, it is possible to conclude that small, ligand-free, Ni clusters have many features in common with the bulk metal. This does not mean that a cluster of a few tens of atoms already possesses the collective properties of the bulk, but simply that the nature of the chemical interaction between the constituting Ni atoms, hence several derived electronic properties, is similar in a finite cluster and in the extended crystal.

The situation is completely different for carbonylated metal clusters. For many years it has been assumed that the structural and spectroscopic similarities in inorganic clusters and bulk metals are due to an intrinsic similarity of the metal–metal interaction in the two regimes [28]. Only recently, physical measurements [4] and theoretical calculations [29–33] have shown that this similarity is not entirely justified. One of the most important signs of the difference between bare and ligated Ni clusters is the different magnetic behavior. We have shown in a series of previous studies [31–33] that the addition of the ligand shell to the bare Ni cluster has the effect of quenching most of the magnetization of the bare particle. The magnetic moments of the "surface" Ni atoms are completely suppressed; for clusters where all the Ni atoms are directly coordinated to the CO ligands, this results in a diamagnetic system [31–33]. The electronic mechanism behind this effect is the electron transfer from the 4s Ni orbital into the 3d shell [26,31–33]. This transfer is induced by the repulsive interaction of the diffuse 4s-derived metal MOs with the 5σ CO lone pair [34]. The 4s-derived orbitals are destabilized and pushed above the Fermi level; the 4s electrons end up in the 3d band, which is now energetically favorable. A covalent bond is then formed between the filled 3d orbitals and the 2π^* virtual orbitals of the CO ligands. Because of the back donation from the metal to CO, the final population of the 3d shell is lower than 3d^{10} [31–33].

The same mechanism causes the local quenching of the magnetic moment induced by a single CO molecule adsorbed on a Ni surface [35,36]. In particular, Raatz and Salahub found that the nearest neighbor Ni atoms are greatly affected while the second neighbors are only moderately affected, a feature of considerable importance in view of the incomplete magnetic quenching found in high-nuclearity organometallic clusters (see below).

The net result of this ligand-induced configuration change in carbonylated clusters is that the 4s-band is formally empty and the 3d-band is formally filled. Of course,

some $4s$-$3d$ mixing occurs, because it is favorable for the formation of the covalent bonds with the ligands, but the final result of this strong electronic redistribution is that the electronic structure of the metal core in the carbonylated cluster has little in common with that of the corresponding ligand-free metal cluster.

This description, which fully accounts for the observed behavior of small ligated clusters containing less than 10-20 metal atoms, remains valid also for larger aggregates, where some of the metal atoms are not coordinated to the ligand sphere. In $[Ni_{38}Pt_6(CO)_{48}]^n$ [2h] the six Pt atoms are in the "bulk" of the cluster. This cluster has been modeled in our study by a $[Ni_{44}(CO)_{48}]^n$ cluster where the Pt atoms of the core have been replaced by Ni atoms (Fig. 1). In contrast to the case for "small" carbonylated clusters, we found that this large cluster exhibits a permanent magnetic moment corresponding to about three unpaired electrons (Table III). The analysis of the spin distribution shows that the magnetic moment of the surface Ni atoms is completely suppressed, while that of the six internal Ni atoms is reduced to ≈ 0.5 μ_B per atom (see Table III) as opposite to 0.72 μ_B per atom in the bare Ni_{44}, Table II. This result provides a consistent explanation for the observed temperature dependence of the magnetic susceptibility of $[Ni_{38}Pt_6(CO)_{48}]^n$ which indicates a total magnetic moment of ≈ 4 μ_B [4]. Similar results have been obtained for the $Ni_{32}(CO)_{36}$ cluster which is composed of 8 "bulk" and 24 "surface" equivalent atoms, see Figure 1 and Table III.

The existence of a permanent magnetic moment in high-nuclearity carbonylated Ni clusters provides a solid indication that, in order to observe the beginning of a metallic behavior, the cluster must be large enough to accommodate internal metal atoms. In the next section we will show that the appearance of metallic properties depends on the structure of the DOS near the Fermi level. This, in turn, is a function of the ratio between the "bulk" and the "surface" atoms in the cluster.

Density of States Around the Fermi Level and Related Properties

Recent physical measurements on inorganic clusters [4-8] suggest that the ligand-induced perturbations on the electronic structure of the metal atoms are of short

TABLE III. Fermi energy, E_f (eV); total number of unpaired electrons per atom, N_T N_{up} N_{down}; and their distribution between "bulk" and "surface" atoms in various Ni clusters

Cluster	$r(Ni-Ni)$ (Å)	E_f	N_T	Unpaired Electrons/Atom [a]			
				Bulk	Surface		
				Ni1	Ni2	Ni3	Ni4
Ni_{32}	2.40, 2.46	-3.74	26.4	0.74	0.86	—	—
$Ni_{32}(CO)_{36}$	2.40, 2.46	-5.49	3.8	0.50	0.00	—	—
Ni_{44}	2.58	-3.71	32.7	0.72	0.73	0.74	0.79
$Ni_{44}(CO)_{48}$	2.58	-5.53	3.4	0.56	0.01	0.01	0.02

[a] Number of unpaired electrons per Ni atom, see Figure 1 for definitions.

range and involve mainly the "surface" atoms. These conclusions are based not only on NMR and magnetic susceptibility, but also on specific heat measurements on the clusters $Pt_{309}Phen_{36}O_{30}$ and $Pd_{561}Phen_{36}O_{190}$ [4–8]. These clusters are sufficiently large that a considerable fraction, about half or more, of the metal atoms is in the "bulk" of the cluster. Thus, if the appearance of metallic properties is indeed connected to the fraction of "bulk" atoms, it should be clearly observable in clusters of this size.

Two features of the NMR signal are of interest in determining whether the Pt nuclear spins are in a "metallic" or in an "insulating" environment. One is the combination of chemical shift with its associated Knight shift, the latter being a signature of metals, which is due to the Pauli spin susceptibility of the conduction electrons; the second is the nuclear-spin lattice relaxation time, T_1. In insulators, T_1 is very long while, for metals, the conduction electrons provide an efficient channel for the relaxation so that T_1 is relatively short. On the basis of the field-dependence of T_1, the ^{195}Pt NMR signal of the Pt_{309} cluster has been decomposed in two contributions, one at a resonance typical of insulators with a long T_1 and a second component at a resonance typical for metals with a short value of T_1 [8a]. This would be consistent with a contribution to the signal due to the 162 "surface" Pt atoms, and a "metallic" term due to the 147 "bulk" Pt atoms.

The presence of two kinds of metal atoms in a ligated cluster is also consistent with two other experimental observations related to the effective DOS near E_f. The magnetic susceptibility of the Pd_{561} cluster was found to be about one-third of that of bulk Pd; about the same factor was observed for the electronic contribution to the specific heat, $C = \gamma T$, of the cluster where γ is a coefficient directly proportional to the DOS around the Fermi level. The appearance of an electronic contribution to the specific heat is considered a stringent test of metallic behavior. Like the Knight shift, the observation of a linear specific heat term requires the cluster DOS at E_f to form a quasi-continuum. For Pd_{561}, γ is about one-third of the bulk value [8b]. Taking into account that in Pd_{561} there are 252 ($\simeq 50\%$) "surface" atoms, it has been possible to explain the factor one-third by assuming an almost complete elimination of the "surface" atoms contribution to the DOS near E_f and a reduction of the contribution of the next inner sphere of "bulk" atoms [8b]. Both these assumptions are fully supported by our theoretical model.

The perturbation induced by the ligands involving mainly, but not only, the "surface" atoms is consistent with the computed reduction of the magnetic moment in the carbonylated Ni_{13} and Ni_{44} clusters (Table III). While the magnetic moment of the "surface" atoms is completely suppressed, that of the "core" atoms is reduced by $\simeq 10\%$ with respect to the free cluster (compare Tables I and III). Hence, the modifications induced by the ligand sphere, although of short range, also affect the inner metal atoms to some extent.

Further support for the proposed interpretation of the experimental results comes from the analysis of the computed DOS for the $Ni_{44}(CO)_{48}$ cluster (Fig. 3). The contribution to the DOS of the "surface" Ni atoms has been separated from that of the "bulk" Ni atoms. It is apparent that, while in the "surface" component, the majority and minority DOS mirror eachother, resulting in a complete spin pairing.
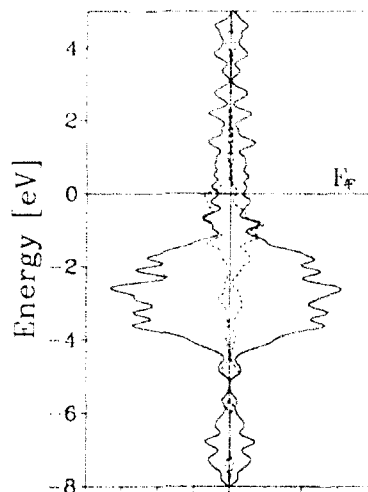
Figure 3.   Ni₄₄(CO)₄ₓ density of states (in arbitrary units) generated by Gaussian broadening of the one-electron energies with a Gaussian function of fixed half-width 0.1 eV.
(————) "Surface" Ni atoms contribution; (-----) "bulk" Ni atoms contribution.

the "bulk" component exhibits a residual magnetic moment. Moreover, the contribution of the "surface" Ni atoms to the DOS at E_f is negligible; the "surface" atoms' $3d$-band is, in fact, well below E_f as the consequence of the chemical interaction with the CO ligands and, in particular, of the charge transfer, or back donation, into the $2\pi^*$ CO MOs. Clearly, all those properties directly connected to the DOS near E_F, depend largely on the number of "bulk" atoms in the cluster.

In the clusters considered here, the ratio of the number of "bulk" atoms to the number of "surface" atoms is too small to allow the formation of a quasi-continuum around the Fermi level. This is indeed shown by the one-electron energy levels of Ni₅(CO)₁₂ (see Table IV), which has no "bulk" atoms, and of Ni₄₄(CO)₄ₓ, which starts to exhibit some "metallic" behavior. The average one-electron energy separation around E_f in Ni₅(CO)₁₂, ≃170 meV, is typically molecular, but also in the high-nuclearity Ni₄₄(CO)₄ₓ the average spacing, ≃40 meV, is still larger than kT at room temperature, ≃24 meV. In order to reach a quasi-continuum, clusters of a few hundreds of metal atoms are required as is the case for the Pd₅₆₁ cluster.

Conclusions

Molecular metal clusters stabilized by ligands represent an interesting class of materials for the study of the evolution of metallic properties as function of the cluster size. In this work we have shown that the electronic properties and the bonding nature in bare and carbonylated Ni clusters are completely different. While naked Ni clusters have several features reminiscent of the bulk metal, low-nuclearity Ni cluster carbonyls, containing about 20 metal atoms or less, have nothing in common with the solid, because the ligands induce strong modifications in the

TABLE IV. One-electron energy levels in the vicinity of the cluster Fermi energy (or cluster HOMO) in $Ni_4(CO)_{12}$ and $Ni_{44}(CO)_{48}$. The position of the HOMO and of the Fermi energy is indicated by a separating line. *Italics* are used to identify the virtual levels.

$Ni_4(CO)_{12}$, D_{3h}, $E(HOMO)$ -5.07 eV		$Ni_{44}(CO)_{48}$, O_h, E_f -5.53 eV			
7 a'₂	2.58	*24 eu*	3.51	57 t₂u	5.69
18 a'₂	4.64	*50 eg*	3.81	42 a₁g	5.74
———	———	*59 t₂u*	4.08	57 eg	5.82
33 e'	-5.07	*60 t₁g*	4.12	44 t₁g	5.96
17 e"	5.83	*20 a₂u*	4.20	56 t₂u	6.09
32 e'	5.88	*45 t₁g*	4.24	43 t₁g	6.33
29 a'₁	5.93	*58 t₂u*	4.53	78 t₁u	6.35
2 a"₁	6.16	*43 a₁g*	4.54	18 a₂g	6.36
6 a'₂	6.20	*59 t₂g*	4.68	23 eu	6.39
17 a"₂	-6.28	*81 t₁u*	4.81	56 eg	-6.43
16 e"	-6.33	58 t₂g	-5.06	55 eg	6.54
28 a'₁	-6.59	58 eg	-5.07	57 t₂g	-6.71
31 e'	-6.62	*19 a₂g*	-5.30	77 t₁u	6.72
15 e"	-6.69	*80 t₁u*	5.33	55 t₂u	6.84
30 e'	-7.03	*79 t₁u*	5.48	41 a₁g	-6.84
29 e'	-7.16			22 eu	6.87
				56 t₂g	-7.00

electronic structure of the metal atoms. In relatively small clusters, where all the metal atoms are directly interacting with the ligands or, in other words, are on the "surface" of the cluster, this results in an almost complete suppression of the "metallic" character of the bare Ni cluster. This is shown, for instance, by the diamagnetism of the carbonylated clusters, whereas the naked ones are ferromagnetic.

When the ligated cluster becomes large enough to have both "surface" and "bulk" metal atoms, some metallic character is retained. This metallic character is directly connected to the density of states at the Fermi level. In a high-nuclearity molecular metal cluster this is determined only by the number "bulk" metal atoms, because the contribution of the "surface" metal atoms is negligible.

Acknowledgments

Bibliography

[1] (a) B.F.G. Johnson, Ed., *Transition Metal Clusters* (Wiley, New York 1980); (b) M. Moskovits, Ed., *Metal Clusters* (Wiley, New York 1986); (c) G. Schmidt, Struct. Bond. (Berlin) 62, 51, (1985); (d) P. Chini, J. Organomet. Chem. 37, 200 (1980).

[2] (a) G. Longoni, P. Chini, L.D. Lower, and L.F. Dahl. J. Am. Chem. Soc. **97**, 5034 (1975); (b) J.C. Calabrese, L.F. Dahl, A. Cavalieri, P. Chini, G. Longoni, and S. Martinengo. J. Am. Chem. Soc. **96**, 2616 (1974); (c) L.D. Lower and L.F. Dahl. J. Am. Chem. Soc. **98**, 5046 (1976); (d) A. Ceriotti, G. Longoni, M. Manassero, M. Perego, and M. Sansoni. Inorg. Chem. **24**, 117 (1985); (e) D.A. Nagaki, L.D. Lower, G. Longoni, P. Chini, L.F. Dahl. Organometallics **5**, 1764 (1986); (f) A. Ceriotti, F. Demartin, B.T. Heaton, P. Ingallina, G. Longoni, M. Manassero, M. Marchionna, and N. Masciocchi. J. Chem. Soc. Chem. Commun., 786 (1989); (g) A. Ceriotti, A. Fait, G. Longoni, and G. Piro. J. Am. Chem. Soc. **108**, 8091 (1986); (h) A. Ceriotti, F. Demartin, G. Longoni, M. Manassero, M. Marchionna, G. Piva, and M. Sansoni. Angew. Chem. Int. Ed. Engl. **24**, 697 (1985).

[3] See (a) G. Benedek, T.P. Martin, and G. Pacchioni, Eds., *Elemental and Molecular Clusters* (Springer, Berlin, 1988); (b) P. Jena, B.K. Rao, and S.N. Khanna, Eds. *Physics and Chemistry of Small Clusters*, NATO ASI Series B, vol. 158 (Plenum, New York, 1986).

[4] (a) B.J. Pronk, H.B. Brom, L.J. de Jongh, G. Longoni, and A. Ceriotti. Solid State Commun. **59**, 349 (1986); (b) L.J. de Jongh, J.A.G. de Aguiar, H.B. Brom, G. Longoni, J.M. van Ruitenbeek, G. Schmid, H.H.A. Smit, M.P.J. van Staveren, and R.C. Thiel. Z. Phys. D **12**, 445 (1989); (c) S.R. Drake, P.P. Edwards, B.F.G. Johnson, J. Lewis, S.D. Obertelli, and N.C. Pyper. J. Chem. Soc. Chem. Commun., 1190 (1987); (d) S.R. Drake, P.P. Edwards, B.F.G. Johnson, J. Lewis, F.A. Marseglia, S.D. Obertelli, and N.C. Pyper. Chem. Phys. Lett. **139**, 336 (1987).

[5] M.C. Fairbanks, R.E. Benfield, R.J. Newport, and G. Schmid. Solid State Commun. **74**, 431 (1990).

[6] M. Quinten, I. Sander, P. Steiner, U. Kreibig, K. Fauth, and G. Schmid, Z. Phys. D **20**, 377 (1991).

[7] H.H.A. Smit, R.C. Thiel, L.J. de Jongh, G. Schmid, and N. Klein. Solid State Commun. **65**, 915 (1988).

[8] (a) D. van der Putten, H.B. Brom, L.J. de Jongh, and G. Schmid, in *Physics and Chemistry of Finite Systems: From Clusters to Crystals*, NATO ASI Series (Plenum, New York, to appear); (b) J. Baak, H.B. Brom, and L.J. de Jongh. NATO ASI Series.

[9] H. Darmon, R. Heer, and J.P. Meyer. J. Appl. Phys. **39**, 669 (1968).

[10] J.C. Slater. *Quantum Theory of Molecules and Solids* (McGraw-Hill, New York, 1965).

[11] R.G. Parr and W. Yang. *Density Functional Theory of Atoms and Molecules* (Oxford University Press, New York, 1989).

[12] (a) B.I. Dunlap and N. Rösch. J. Chim. Phys. Physico-Chim. Biol. **86**, 671 (1989); (b) B.I. Dunlap and N. Rösch. Adv. Quantum Chem. **21**, 317 (1990); (c) N. Rösch, P. Knappe, P. Sandl, A. Görling, and B.I. Dunlap, in *The Challenge of d and f Electrons: Theory and Computations*. ACS Symposium Series No. 394. D.R. Salahub and M.C. Zerner, Eds. (American Chemical Society, Washington DC, 1989). p. 180.

[13] J. Koutecky and P. Fantucci. Chem. Rev. **86**, 539 (1986).

[14] H. Basch, M.D. Newton, and J.W. Moskowitz. J. Chem. Phys. **73**, 4492 (1980).

[15] K. Lee, J. Callaway, K. Kwong, R. Tang, and A. Ziegler. Phys. Rev. B **31**, 1796 (1985).

[16] M. Tomonari, H. Tatewaki, and T. Nakamura. J. Chem. Phys. **85**, 2875 (1986).

[17] S.P. Walch. J. Chem. Phys. **86**, 5082 (1987).

[18] Z. Yu and J. Almlöf. J. Phys. Chem. **95**, 9167 (1991).

[19] G.M. Pastor, J. Dorantes-Davila, and K.H. Bennemann. Chem. Phys. Lett. **148**, 459 (1988).

[20] M.B. Knickelbein, S. Yang, and S. Riley. J. Chem. Phys. **93**, 94 (1990).

[21] (a) D.R. Salahub. Adv. Chem. Phys. **69**, 447 (1987); (b) M.D. Morse. Chem. Rev. **86**, 1049 (1986).

[22] (a) O. Jepsen, J. Madsen, and O.K. Andersen. Phys. Rev. B **26**, 2790 (1982); (b) H. Krakauser, A.J. Freeman, and E. Wimmer. Phys. Rev. B **28**, 610 (1983); (c) F. Liu, M.R. Press, S.N. Khanna, and P. Jena. Phys. Rev. B **38**, 5760 (1988).

[23] M.B. Knickelbein, S. Yang, and S. Riley. J. Chem. Phys. **93**, 94 (1990).

[24] V.L. Moruzzi, J.F. Janak, and A.R. Williams, *Calculated Electronic Properties of Metals* (Pergamon Press, New York, 1978).

[25] (a) A.J. Stone. Mol. Phys. **41**, 1339 (1980); (b) A.J. Stone. Inorg. Chem. **20**, 563 (1981); (c) A.J. Stone. Polyhedron **3**, 1299 (1984).

[26] G. Pacchioni, N. Rösch, and L. Ackermann Gazz. Chim. Ital., in press (1992).

[27] (a) R. Fournier, J. Andzelm, A. Goursot, N. Russo, and D.R. Salahub, J. Chem. Phys. **93**, 2919 (1990); (b) G. Chiarello, J. Andzelm, R. Fournier, N. Russo, and D.R. Salahub, Surf. Sci. **202**, 2621 (1988).

[28] E.L. Muetterties, T.N. Rhodin, E. Band, C.F. Brucker, and W.R. Pretzer, Chem. Rev. **79**, 91 (1979).

[29] G.F. Holland, D. Ellis, and W.C. Trogler, J. Chem. Phys. **83**, 3507 (1986).

[30] (a) G. Pacchioni and P. Fantucci, Chem. Phys. Lett. **134**, 407 (1987); (b) G. Pacchioni, in *Elemental and Molecular Clusters*, G. Benedek, T.P. Martin, and G. Pacchioni, Eds. (Springer, Berlin, 1988).

[31] G. Pacchioni and N. Rösch, Inorg. Chem., **29**, 2901 (1990).

[32] N. Rösch, L. Ackermann, G. Pacchioni, and B.I. Dunlap, J. Chem. Phys. **95**, 7004 (1991).

[33] N. Rösch, L. Ackermann, and G. Pacchioni, J. Am. Chem. Soc. **114**, 3550 (1992).

[34] P.S. Bagus, C.J. Nelin, and C.W. Bauschlicher, Phys. Rev. B **28**, 5423 (1983).

[35] F. Raatz and D.R. Salahub, Surf. Sci. **176**, 219 (1986).

[36] C.W. Bauschlicher and C.J. Nelin, Chem. Phys. **108**, 275 (1986).

Orientational Ordering of Adsorbed Monolayers

E. E. MOLA and J. L. VICENTE

*Instituto de Investigaciones Fisicoquímicas Teóricas y Aplicadas, División Química Teórica,
Sucursal 4, CC 16, La Plata 1900, Argentina*

L. BLUM

*Department of Physics, P.O. Box 23343, University of Puerto Rico,
Río Piedras, Puerto Rico 00931-3343*

Abstract

We set up a model for the adsorption energy for a closed-packed hexagonal monolayer deposited on a substrate surface of the same structure, but different lattice constant, as a function of the epitaxy angle between the principal axis. The surface substrate potential is expressed in the form of a periodic potential with symmetry and periodicity of the substrate surface. The particular case of lead underpotentially deposited on Ag(111) is examined.

Introduction

Recent in situ grazing x-ray diffraction experiments on the under-potentially deposited (UPD) monolayer of Pb deposited onto Ag(111) [1] have shown that Pb monolayer is compressed 1.2% from bulk lead. The first order diffraction peak was 0.037-Å wide in the radial and azimuthal directions, indicating that, even in an aqueous environment, the lead monolayer forms a well-ordered two-dimensional (2D) solid. A rotational epitaxy angle (the angle between the adsorbate Pb and substrate Ag lattices) of $4.4°$ was observed.

The aim of the present article is to set-up a model to determine the relationship between the substrate periodic potential and the rotational epitaxy angle.

The Model

Since the effect of the substrate atoms can be expressed in the form of a periodic potential with the symmetry and periodicity of the substrate surface, we expand the potential energy per surface atom in a Fourier series of the form,

$$V(\vec{R}) = \sum_{\vec{G}} V_{\vec{G}} e^{i\vec{G}\cdot\vec{R}}, \tag{1}$$

where the $\vec{G}$'s are the 2D reciprocal lattice vectors of the substrate surface and $\vec{R} = (x,y)$ is the position of an atom on the top layer. The coordinate axes (x,y) in real space form an angle of $(2/3)\pi$. The lattice constant of the 2D hexagonal lattice is a. Eq. (1) can also be written in the following manner:

$$V(\vec{R}) = \sum_{(h,k)} [a_{h,k} \cos(\vec{G} \cdot \vec{R}) + b_{h,k} \sin(\vec{G} \cdot \vec{R})] \tag{2}$$

If we truncate eq. (2) after the second surface Brillouin zone of $\vec{G}$, we obtain

$$V(\vec{R}) = v_{00} + \alpha[\cos(2\pi x) + \cos(2\pi y) + \cos 2\pi(x - y)]$$
$$+ \beta[\cos 2\pi(x + y) + \cos 2\pi(2x - y) + \cos 2\pi(2y - x)] \tag{3}$$

where $a_{00} = v_{00}$, $a_{h,k} = \alpha$ if

$$[(h,k)] = [(1,0), (0,1), (-1,0), (0,-1), (1,-1), (-1,1)] \tag{4}$$

and $a_{h,k} = \beta$ if

$$[(h,k)] = [(1,1), (-2,1), (1,-2), (-1,-1), (2,-1), (-1,2)] \tag{5}$$

The summation over $\sin(\vec{G} \cdot \vec{R})$ is identically zero because the sine is an odd function. The coefficients of the cosine in every surface Brillouin zone are equal to each other. It is possible to write down the coefficients of eq. (3) as a function of the substrate potential in a small set of characteristic points of the substrate unit cell (see Fig. 1).

Let us call V_A the potential value at the hollow site A, V_B is the potential at the bridge site B, and the zero of the potential energy is taken at the top site T. After some algebra eq. (3) can be written as follows:

$$V(\vec{R}) = (3/4)V_B - (2/9)V_A[\cos(2\pi x) + \cos(2\pi y) + \cos 2\pi(x - y)]$$
$$- [(1/4)V_B - (2/9)V_A][\cos 2\pi(x + y)$$
$$+ \cos 2\pi(2x - y) + \cos 2\pi(2y - x)], \tag{6}$$

since

$$v_{00} = (3/4)V_B, \qquad \alpha = -(2/9)V_A, \qquad \beta = -(1/4)V_B + (2/9)V_A. \tag{7}$$

Using eq. (3) we define the function $\phi(x,y)$.
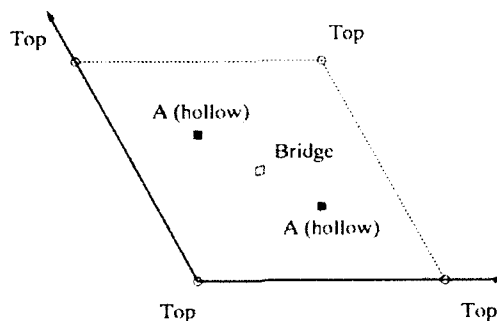
Figure 1.   Schematic top view of the (111) face of Ag. (A): Hollow site; (B): bridge site, and T indicates the top site.

$$\phi(x,y) = \frac{V(\vec{R}) - v_{(x)}}{3(|\alpha| + |\beta|)} \qquad (8)$$

which is bounded by $|\phi(x,y)| \le 1$; this function can also be written in the following way,

$$\phi(x,y) = \frac{x_1}{3} [\cos(2\pi x) + \cos(2\pi y) + \cos 2\pi(x - y)]$$

$$+ \frac{x_2}{3} [\cos 2\pi(x + y) + \cos 2\pi(2x - y) + \cos 2\pi(2y - x)] \qquad (9)$$

with

$$x_1 = \frac{\alpha}{|\alpha| + |\beta|}, \qquad x_2 = \frac{\beta}{|\alpha| + |\beta|} \qquad (10)$$

The relationship between the coefficients of eq. (6) and eq. (9) is

$$V_B = (8/9)\frac{x_1 + x_2}{x_1} V_A. \qquad (x_1 \neq 0) \qquad (11)$$

In Figure 2a and b we show a three-dimensional (3D) and a contour plot of $3\phi(x,y)$ in orthogonal Cartesian coordinates.

Let us now consider the closed packed hexagonal monolayer of lead with lattice constant A, underpotentially deposited on Ag(111). Figure 3 shows this particular situation when the epitaxy angle is θ. Open circles represent the adlayer of Pb, and full circles represent those of the Ag(111) substrate.

Consider now the Hamiltonian for the interaction between the adlayer and the substrate surface plane,

$$\mathscr{H} = \sum_i V(\vec{R}_i), \qquad (12)$$

where $\vec{R}_i$ is the position of the ith adatom. This Hamiltonian is the potential seen by the Pb atoms due to the substrate, and it is described by eq. (6). We note that $V(x,y)$ in eq. (6) does not describe the total interaction potential energy of the top Pb layer with the substrate, but rather the relative energy change as the atoms in the top layer change from one site to another. We are mainly interested in knowing the angular orientational energy per adatom (AOEA) imposed by the underlying substrate potential. We know that, in general, there are two competing interactions:

• the adatom–adatom longitudinal interactions; and
• the adatom–substrate transversal interactions that pin the surface atoms to their "in registry" positions, as is established by the 2D Frenkel–Kontorowa (FK) model [2,3].

In the present article we study the limiting case in which the two interactions are decoupled. We study the AOEA for a given fixed constant adsorbate lattice parameter.
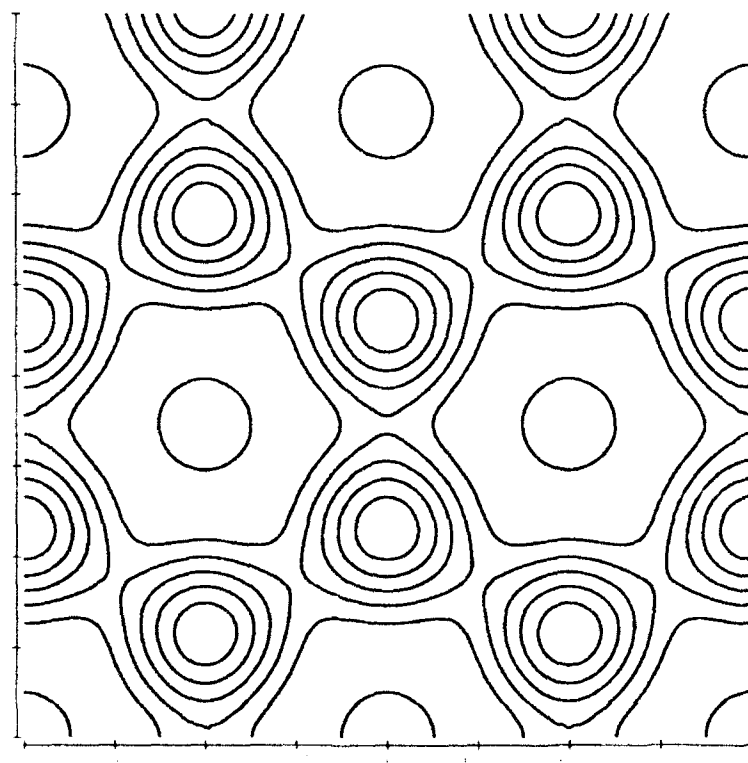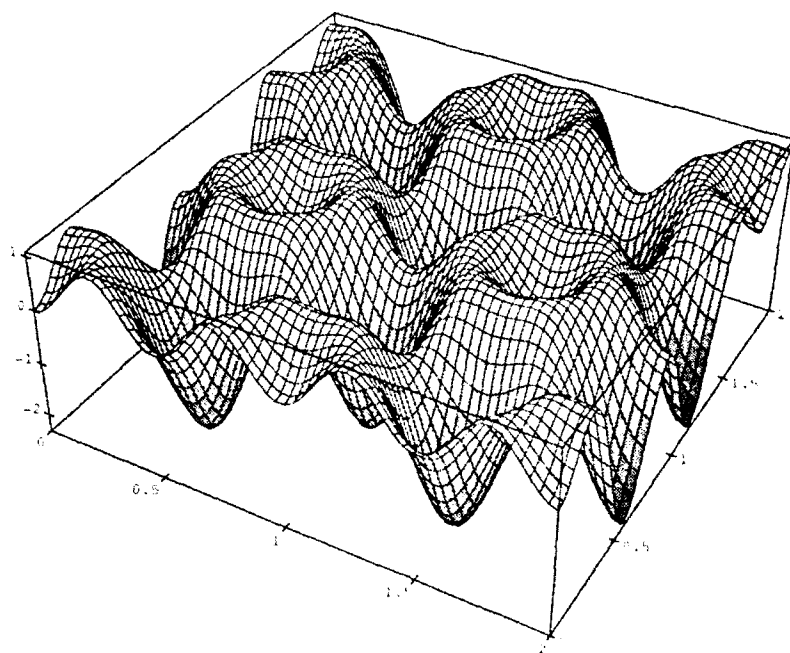
Figure 2. (a) Three-dimensional plot of $3\phi(x,y) = F(\hat{R}) = t_{00}/t(o) + (\beta)$, eqs (8) and (9), using $v_1 = 0.5$ and $v_2 = 0.5$. (b) Contour plot of $3\phi(x,y) = F(\hat{R}) = t_{00}/t(o) + (\beta)$, eqs (8) and (9), using $v_1 = 0.5$ and $v_2 = 0.5$.
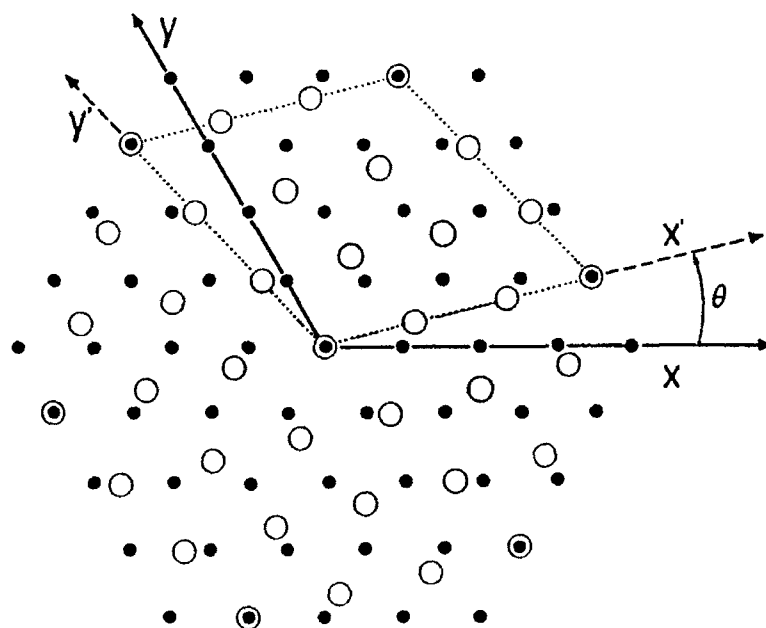
Figure 3. An example of commensurate lattices: Full black circles are substrate atoms, empty circles are adsorbate atoms. The dotted lines indicate a $(N + 1)(N + 1)$ commensurate unit cell: in this case, $N = 3$ and the lattice parameter ratio $A/a = \sqrt{13}/3$.

Angular Orientational Energy

To evaluate the binding energy per adatom, $S(\theta)$, over a cell of adatoms with $(N + 1)(N + 1)$ sites, we form the summation

$$S(\theta) = v_{00} + \frac{1}{N^2} \sum_{m=0}^{N} \sum_{n=0}^{N} V(\vec{R}_{mn}) . \tag{13}$$

where the second term is the AOEA. From eqs. (2) and (12)

$$S(\theta) = v_{00} + \frac{1}{N^2} \sum_{(h,k)}' a_{h,k} \left[\sum_{m=0}^{N} \sum_{n=0}^{N} \cos(\vec{G}_{h,k} \cdot \vec{R}_{mn}) \right] . \tag{14}$$

The symbol $\sum'$ means that we have excluded from the summation the term $(h,k) = (0,0)$. It should be noted that every term $V(\vec{R}_{mn})$ in eq. (13) should be weighted by factors $1, \frac{1}{2}$ or $\frac{1}{4}$, depending on the location of the adatom in the cell, inner, edge, or corner, respectively.

We performed summations over the set (h,k) specified by eqs. (4) and (5). $\vec{R}_{mn}$ represents the location of a Pb atom on the adlayer in the adlayer reference system, x', y' (see Fig. 3).

$$\vec{R}_{mn} = m\vec{e}_1 + n\vec{e}_2 . \tag{15}$$

$(\vec{e}_1, \vec{e}_2)$ are vectors of modulus A, the lattice adlayer constant. For an epitaxy angle. θ, the coordinates of the (m,n)th Pb atom in the substrate reference system (x,y) are

$$\mathbf{X} = A\mathbf{T}(\theta)\mathbf{R} \tag{16}$$

$$\mathbf{X} = \begin{pmatrix} x \\ y \end{pmatrix}$$

$$\mathbf{R} = \begin{pmatrix} m \\ n \end{pmatrix}. \tag{17}$$

$\mathbf{T}(\theta)$ is

$$\mathbf{T}(\theta) = \frac{2\sqrt{3}}{3} \begin{pmatrix} \sin(\pi/3 + \theta) & -\sin\theta \\ \sin\theta & \sin(\pi/3 - \theta) \end{pmatrix} \tag{18}$$

Therefore, the (m,n)th Pb atom will have the following coordinates in the substrate reference system, $\vec{R}_{xy}$

$$x = mt_{11}(\theta) + nt_{12}(\theta) \tag{19}$$

$$y = mt_{21}(\theta) + nt_{22}(\theta) \tag{20}$$

The dot product, $\vec{G}_{hk}\vec{R}_{xy}$, of eq. (14) is then

$$\vec{G}_{hk}\vec{R}_{xy} = \frac{2\pi A}{a} [(t_{11}h + t_{21}k)m + (t_{12}h + t_{22}k)n] = m\mu_{hk}(\theta) + n\nu_{hk}(\theta) \tag{21}$$

The summations in the brackets in eq. (14) can be divided into three different groups, depending on the location of the (m,n)th Pb atom in the surface unit cell (inner, edge, corner). It is important to note that the AOEA is due to the summations in brackets of eq. (14) because the coefficients a_{hk} do not depend on the angle θ.

After some algebra we get

$$u_{hk}(\theta) = \sum_{(m,n)}^{\text{inner}} \cos(\vec{G}_{h,k} \cdot \vec{R}_{x,y}) = \cos\left[N\left(\frac{\mu_{hk}(\theta) + \nu_{hk}(\theta)}{2}\right)\right]$$
$$\times \frac{\sin[(N-1)\mu_{hk}(\theta)/2]}{\sin[\mu_{hk}(\theta)/2]} \frac{\sin[(N-1)\nu_{hk}(\theta)/2]}{\sin[\nu_{hk}(\theta)/2]} \tag{22}$$

$$s_{hk}(\theta) = \sum_{(m,n)}^{\text{edge}} \cos(\vec{G}_{h,k} \cdot \vec{R}_{x,y}) = \left[\cos\left[N\left(\frac{\mu_{hk}(\theta)}{2}\right)\right] + \cos\left[N\left(\frac{\mu_{hk}(\theta)}{2} + \nu_{hk}(\theta)\right)\right]\right]$$
$$\times \frac{\sin[(N-1)\mu_{hk}(\theta)/2]}{\sin[\mu_{hk}(\theta)/2]} + \left[\cos\left[N\left(\frac{\nu_{hk}(\theta)}{2}\right)\right] + \cos\left[N\left(\frac{\nu_{hk}(\theta)}{2} + \mu_{hk}(\theta)\right)\right]\right]$$
$$\times \frac{\sin[(N-1)\nu_{hk}(\theta)/2]}{\sin[\nu_{hk}(\theta)/2]} \tag{23}$$

$$w_{hk}(\theta) = \sum_{(m,n)}^{\text{corner}} \cos(\vec{G}_{h,k} \cdot \vec{R}_{x,y})$$
$$= 1 + \cos[N(\mu_{hk}(\theta))] + \cos[N(\nu_{hk}(\theta))]$$
$$+ \cos[N(\mu_{hk}(\theta) + \nu_{hk}(\theta))] \tag{24}$$

TABLE I. Set of the lowest values of N and
lattice constant ratios A/a for commensurate
adlayers, compatible with eq. (27).

N	A/a
3	$\sqrt{13}/3 \simeq 1.2018$
5	$6/5 = 1.2$
13	$9\sqrt{3}/13 \simeq 1.1991$
28	$\sqrt{1129}/28 \simeq 1.2000$

Therefore, eq. (14) now becomes

$$S(\theta) = v_{00} + \frac{1}{N^2} \sum_{(h,k)}' a_{h,k}[u_{hk}(\theta) + (1/2)s_{hk}(\theta) + (1/4)w_{hk}(\theta)] , \quad (25)$$

Using eqs. (4) and (5) and the coefficient $a_{hk} = (\alpha \text{ or } \beta)$,

$$S(\theta) = v_{00} + \frac{1}{N^2}\left[\alpha \sum_{(h,k)_1} (u_{hk}(\theta) + (1/2)s_{hk}(\theta) + (1/4)w_{hk}(\theta)) \right.$$

$$\left. + \beta \sum_{(h,k)_2} (u_{hk}(\theta) + (1/2)s_{hk}(\theta) + (1/4)w_{hk}(\theta)) \right] . \quad (26)$$

where the sets $(h,k)_i$ in the summations are over the first and second Brillouin zone as done in eqs. (4) and (5).
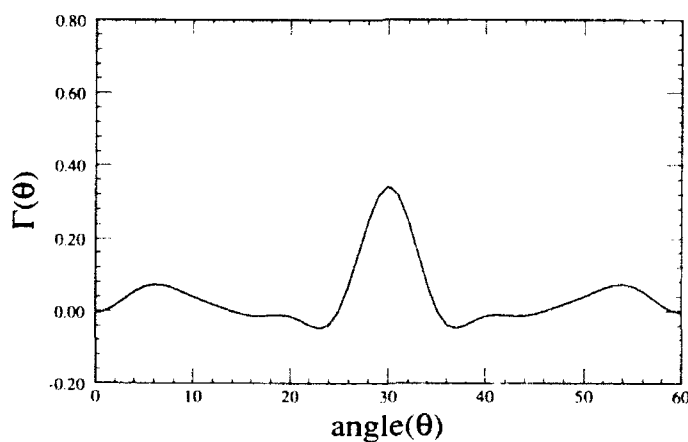
Figure 4. Plot of $\Gamma(\theta)$, eq. (28), the normalized angular orientational energy per adatom, AOEA, on the substrate potential shown in Figure 2a, with the commensurability ratio of Figure 3.

TABLE II. (A) and (B) show the dependence of $\Gamma(\theta)$ on the relative weight of the first harmonic, x_1, and the second harmonic, x_2, for a cell with $N = 3$ and $A/a = \sqrt{13}/3$.

(A)						(B)					
$N = 3$		$A/a = \sqrt{13}/3$				$N = 3$		$A/a = \sqrt{13}/3$			
x_1	x_2	$\Gamma(\theta_m)$	$\Gamma(\theta_M)$	θ_m	θ_M	x_1	x_2	$\Gamma(\theta_m)$	$\Gamma(\theta_M)$	θ_m	θ_M
0.0	1.0	-0.6839	0.1083	30	23	0.0	1.0	0.1083	0.6839	23	30
0.1	0.9	-0.6154	0.0986	30	23	0.1	0.9	-0.0986	0.6154	23	30
0.2	0.8	-0.5468	0.0889	30	23	0.2	0.8	0.0889	0.5468	23	30
0.3	0.7	-0.4783	0.0792	30	23	0.3	0.7	-0.0792	0.4783	23	30
0.4	0.6	-0.4098	0.0695	30	23	0.4	0.6	-0.0695	0.4098	23	30
0.5	0.5	-0.3413	0.0598	30	23	0.5	0.5	0.0598	0.3413	23	30
0.6	0.4	-0.2728	0.0663	30	8	0.6	0.4	0.0663	0.2728	8	30
0.7	0.3	-0.2042	0.0787	30	8	0.7	0.3	0.0787	0.2042	8	30
0.8	0.2	0.1357	0.0912	30	8	0.8	-0.2	0.0912	0.1357	8	30
0.9	0.1	-0.0672	0.1039	30	7	0.9	0.1	0.1039	0.0672	?	30
1.0	0.0	-0.0277	0.1181	17	7	1.0	0.0	0.1181	0.0277	7	17
0.9	0.1	-0.0251	0.1086	17	7	0.9	0.1	-0.1086	0.0251	7	17
0.8	-0.2	-0.0225	0.1378	17	30	0.8	0.2	-0.1378	0.0225	30	17
0.7	-0.3	0.0244	0.2060	23	30	0.7	0.3	-0.2060	0.0244	30	23
0.6	0.4	0.0364	0.2743	23	30	0.6	0.4	-0.2743	0.0364	30	23
0.5	0.5	0.0484	0.3426	23	30	0.5	0.5	0.3426	0.0484	30	23
0.4	0.6	-0.0604	0.4108	23	30	0.4	0.6	0.4108	0.0604	30	23
0.3	-0.7	0.0723	0.4791	23	30	0.3	0.7	-0.4791	0.0723	30	23
0.2	-0.8	-0.0843	0.5474	23	30	-0.2	0.8	-0.5474	0.0843	30	23
0.1	-0.9	-0.0963	0.6156	23	30	-0.1	0.9	0.6156	0.0963	30	23
0.0	-1.0	-0.1083	0.6839	23	30	0.0	1.0	-0.6839	0.1083	30	23

It is important to note that the size $(N + 1)(N + 1)$ of the unit cell is determined by the ratio A/a, which, in our case, must be such that the adsorbate is in some way commensurate with the substrate, albeit with an arbitrary (large) cell size.

In a previous work [4] two of the authors had studied the requirements on the potential when the lattice constants A and a between an adlayer of UPD Pb and the Ag(111) substrate was determined with an accuracy of

$$\left| \frac{A}{a} - 1.2 \right| < 2.10^{-3},$$ (27)

Although there are an infinite set of numbers in that small interval, there is only a small set of values that allows both lattices to be commensurate, for low values of N. Figure 3 shows an example when $A/a = \sqrt{13}/3 = 1.2018$ and $N = 3$. In Table I we quote the small unit cell sizes and their corresponding lattice constant ratios.

From eq. (26) we define the function

TABLE III. (A) and (B) show the dependence of $\Gamma(\theta)$ on the relative weight of the first harmonic, x_1, and the second harmonic, x_2, for a cell with $N = 5$ and $A/a = 6/5$.

(A)						(B)					
$N = 5$		$A/a = 6/5$				$N = 5$		$A/a = 6/5$			
x_1	x_2	$\Gamma(\theta_m)$	$\Gamma(\theta_M)$	θ_m	θ_M	x_1	x_2	$\Gamma(\theta_m)$	$\Gamma(\theta_M)$	θ_m	θ_M
0.0	1.0	-0.3533	0.0979	30	26	0.0	-1.0	-0.0979	0.3533	26	30
0.1	0.9	-0.3173	0.0882	30	26	-0.1	0.9	-0.0882	0.3173	26	30
0.2	0.8	-0.2813	0.0785	30	26	-0.2	-0.8	-0.0785	0.2813	26	30
0.3	0.7	-0.2454	0.0688	30	26	-0.3	0.7	-0.0688	0.2454	26	30
0.4	0.6	-0.2094	0.0591	30	26	-0.4	0.6	-0.0591	0.2094	26	30
0.5	0.5	-0.1735	0.0493	30	26	-0.5	-0.5	-0.0493	0.1735	26	30
0.6	0.4	-0.1375	0.0396	30	26	-0.6	-0.4	-0.0396	0.1375	26	30
0.7	0.3	-0.1015	0.0299	30	26	-0.7	-0.3	-0.0299	0.1015	26	30
0.8	0.2	-0.0656	0.0275	30	15	-0.8	-0.2	-0.0275	0.0656	15	30
0.9	0.1	-0.0356	0.0301	9	15	-0.9	-0.1	-0.0301	0.0356	15	9
1.0	0.0	-0.0396	0.0328	9	15	-1.0	0.0	-0.0328	0.0396	15	9
0.9	-0.1	-0.0356	0.0410	9	30	-0.9	0.1	-0.0410	0.0356	30	9
0.8	-0.2	-0.0316	0.0757	9	30	-0.8	0.2	-0.0757	0.0316	30	9
0.7	-0.3	-0.0288	0.1104	26	30	-0.7	0.3	-0.1104	0.0288	30	26
0.6	-0.4	-0.0386	0.1451	26	30	-0.6	0.4	-0.1451	0.0386	30	26
0.5	-0.5	-0.0485	0.1798	26	30	-0.5	0.5	-0.1798	0.0485	30	26
0.4	-0.6	-0.0584	0.2145	26	30	-0.4	0.6	-0.2145	0.0584	30	26
0.3	-0.7	-0.0683	0.2492	26	30	-0.3	0.7	-0.2492	0.0683	30	26
0.2	-0.8	-0.0782	0.2839	26	30	-0.2	0.8	-0.2839	0.0782	30	26
0.1	-0.9	-0.0880	0.3186	26	30	-0.1	0.9	-0.3186	0.0880	30	26
0.0	-1.0	-0.0979	0.3533	26	30	0.0	1.0	-0.3533	0.0979	30	26

$$\Gamma(\theta) = \frac{S(\theta) - v_{00}}{3(|\alpha| + |\beta|)} = \frac{1}{3N^2}$$

$$\times \left[x_1 \sum_{(h,k)_1} (u_{hk}(\theta) + (1/2)s_{hk}(\theta) + (1/4)w_{hk}(\theta)) \right.$$

$$\left. + x_2 \sum_{(h,k)_2} (u_{hk}(\theta) + (1/2)s_{hk}(\theta) + (1/4)w_{hk}(\theta)) \right] \qquad (28)$$

where x_1 and x_2 have been defined by eq. (10). We notice that $|\Gamma(\theta)| \leq 1$. In Figure 4, we show a plot of $\Gamma(\theta)$ for the parameters

$$A/a = \sqrt{13}/3, \qquad N = 3, \qquad x_1 = 1/2, \qquad x_2 = -1/2$$

The period of the function is $\pi/3$, as required by the lattice's symmetry.

In Tables II and III we display the dependence of $\Gamma(\theta)$ on the relative weights of the first and second harmonics, as well as the maxima and minima of this function. We learn from these tables that for a larger unit cell the values of $\Gamma(\theta)$ decrease.
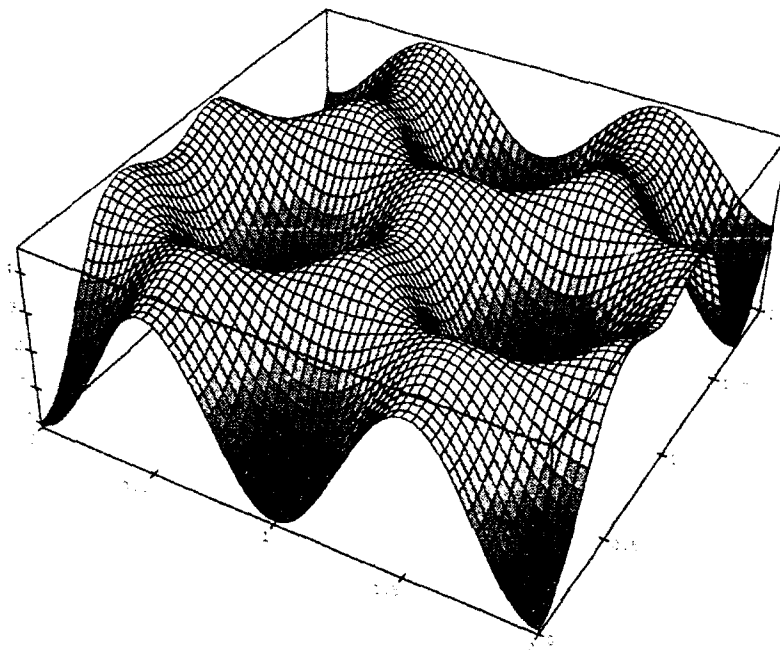
Figure 5.   Plot of $\Gamma(\vec{R})$, eq. (31), in arbitrary units, potential energy seen by an adatom
as a function of position.

since a bigger number of locations of the substrate potential are sampled. In fact,
the asymptotic limit of $\Gamma(\theta)$ for $N \rightarrow \infty$ is zero.

Another interesting property of $\Gamma(\theta)$ is that the locus of their extrema does not
change continuously as the weights of the first and second harmonics are changed.
There is a small and discrete set of epitaxy angles, θ, for which $\Gamma(\theta)$ has maxima
and minima, and the transitions from one regime to another are abrupt.

Discussion of Results

We are particularly interested in establishing the set of values (Γ_A, Γ_B) (see Fig.
1) that will enable the Hamiltonian described by eq. (12) to predict a low epitaxy
angle (4.4°) as is experimentally found [1] in the UPD of Pb on Ag(111).

From Tables II and III we learn that the lowest angle values for which $\Gamma(\theta)$ shows
a minimum are $\theta = 7°$ and $\theta = 9°$, which are obtained using

$$A/a = \sqrt{13}/3, \quad N = 3, \quad x_1 = -1, \quad x_2 = 0, \quad \theta_m = 7°, \quad \Gamma(\theta_m) = -0.1181$$

and

$$A/a = 6/5, \quad N = 5, \quad x_1 = 1, \quad x_2 = 0, \quad \theta_m = 9°, \quad \Gamma(\theta_m) = -0.0396$$

In every case, the coefficient of the second harmonic is zero, but they represent
mutually exclusive alternatives as Γ_1 cannot be positive and negative at the same
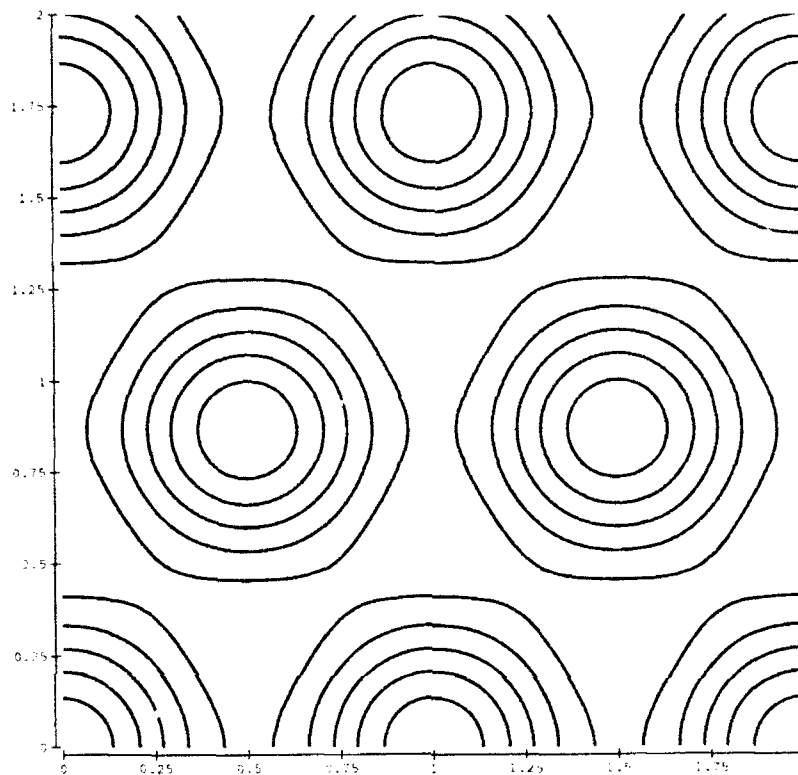
Figure 6.   Contour plot of $\Gamma(\vec{R})$, eq. (31).
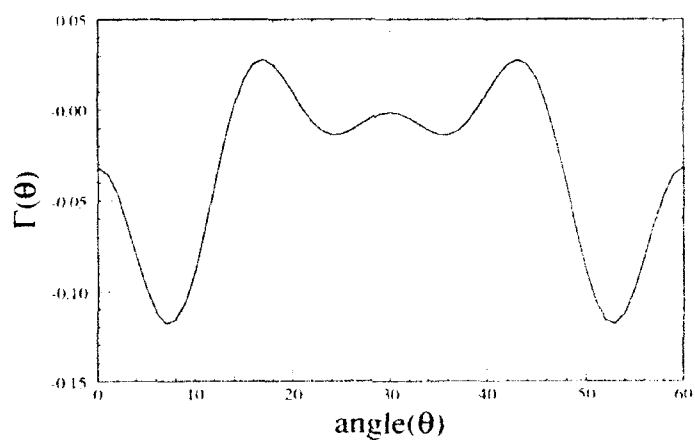
Figure 7.   Plot of $\Gamma(\theta)$, eq. (28), the normalized angular orientational energy per adatom, AOEA, on the substrate potential shown in Figure 5, with the commensurability ratio of Figure 3.

time. We should remember from eq. (7) and (10) that the signs of x_1 and V_1 are different. Therefore, we are going to select the first set of values because they provide the epitaxy angle that is closest to experiment, and has the highest AOEA.

From eq. (28) and, using the fact that for $x_2 = 0$ we have $\beta = 0$, we obtain the AOEA

$$S(\theta_m) - v_{00} = 3|\alpha|\Gamma(\theta_m) \tag{29}$$

or from eq. (7)

$$S(\theta_m) - (2/3)V_1 = (2/3)|V_1|\Gamma(\theta_m) \tag{30}$$

Therefore, the AOEA for $x_2 = 0$ is $(2/3)|V_1|\Gamma(\theta_m)$. The substrate potential that yields an epitaxy angle of $\theta_m = 7°$ when the ratio of the lattice constants is $A/a = \sqrt{13}/3$ is

$$V(\vec{R}) = (2/3)V_1 - (2/9)V_1[\cos(2\pi x) + \cos(2\pi y) + \cos 2\pi(x - y)],$$

$$V_1 > 0 \tag{31}$$

A 3D plot of this potential is shown in Figure 5. The corresponding contour plot is shown in Figure 6. Figure 7 displays $V(\theta)$ as a function of θ for this set or parameters. A well-defined minimum for $\theta = 7°$ is observed. For reasons of symmetry there is another minimum at $\theta = 53°$, which is equivalent to the one at $\theta = -7°$. We should mention that in the Pb/Ag(111) UPD, in addition to the peak with $\theta = 4.4°$, a similar peak at $\theta = -4.4°$ is observed [1]. There is a small difference in intensity however, presumably caused by anisotropies in the sample.

Finally we can fix the sign and the relative potential values at the bridge and hollow sites using eq. (7).

$$V_B = (8/9)V_1 \quad \text{and} \quad V_1 > 0 \tag{32}$$

Acknowledgment

Bibliography

[1] M. G. Samant, M. F. Toney, G. L. Borges. L. Blum, and O. R. Melroy, Surface Sci. Lett. 193, L29–L36 (1988).
[2] J. Frenkel and T. Kontorowa, Phys. Z. Sowjetunion 13, 1 (1938).
[3] N. Takeuchi, C. T. Chan, and K. M. Ho, Phys. Rev. B43, 13899 (1991); Phys. Rev. Lett. 63, 1273 (1989).
[4] E. E. Mola and L. Blum, Int. J. Quantum Chem. 23, 687 (1989).

Calculations of Thickness Dependencies in the Properties of Ultra-Thin Films

J. C. BOETTGER

Theoretical Division, Los Alamos National Laboratory, Los Alamos, New Mexico, USA

Abstract

The linear combinations of Gaussian type orbitals-fitting function (LCGTO-FF) technique has been used over the past eight years, to study a number of ultra-thin film (UTF) systems. Unlike most first principles work in this field, this ongoing investigation focussed on the ground-state properties of UTFs at their equilibrium geometries, as opposed to simply using the UTFs to model some macroscopic system. A summary of the status of LCGTO-FF UTF work is presented with emphasis on the variation of properties as a function of film thickness. One of the more important findings is that the interplanar separation and binding of Li has not converged for a 5-layer UTF. This result calls into question all surface relaxation calculations in which only the outer one or two layers are allowed to relax. © 1992 John Wiley & Sons, Inc.

Introduction

It has been more than 15 years since it was demonstrated that the work function of an ultra-thin (atomic scale) jellium film exhibits quantum oscillations as a function of the film thickness [1,2]. Since that time, a number of theoretical investigations have addressed this quantum size effect (QSE), with emphasis on the question of whether or not QSE will be evident in the work functions of real ultra-thin films (UTFs) [3–9]. All but two [3,9] of these investigations were conducted with the lattice parameters fixed at bulk values.

A much larger body of theoretical work (too much to fully reference) has been directed toward using first principles UTF calculations as a tool for modeling the one-electron properties of surfaces or interfaces [e.g., Refs. 10–12]. Once again, the UTF lattice parameters generally have been constrained to match bulk lattice parameters; although, in a few cases, the interplanar spacings of the outermost layers have been allowed to relax [e.g., Ref. 12].

To date, only a handful of first principles studies [3,9,13–20] have focussed on the properties of the UTFs themselves (beyond the monolayer level) at their own equilibrium lattice parameters. This relative scarcity of geometry-optimized UTF calculations is understandable since they are quite demanding computationally. However, even the few results published so far have revealed a number of interesting (and often counterintuitive) thickness dependencies in the properties of UTFs.

The results of a number of geometry-optimized UTF calculations performed with the linear combination of Gaussian type orbitals-fitting function (LCGTO-FF)

technique are examined [9,21,22]. Two fundamental questions will be emphasized. (1) Do the lattice parameters and electronic properties other than ϕ exhibit a QSE? (2) How rapidly, as a function of film thickness, do the properties of a UTF become bulk-like?

In the next section, the LCGTO-FF method is described. Geometry-optimized LCGTO-FF calculations are discussed for a number of monolayer and dilayer systems, and for Li n-layers ($n = 1 \rightarrow 5$). Some conclusions are given in the final section.

Methodology

The results presented here were obtained within the context of density functional theory (DFT), using the Hedin-Lundqvist [23] local density approximation (LDA) for the exchange-correlation terms in the total energy and the potential. The solutions to the LDA one-electron equations were obtained via the LCGTO-FF technique as embodied in the computer program FILMS [9,21,22]. This method is an all-electrons, full-potential, electronic band structure technique which is characterized by its use of three independent Gaussian basis sets to expand the one-electron orbitals, the charge density, and the exchange-correlation energy density and potential.

The purpose of the charge fit is to reduce the number of coulomb integrals required by ensuring that only 3-center integrals appear in the total energy and one-electron equations, instead of the usual 4-center integrals. In FILMS, the expansion coefficients for the charge density are obtained by variational minimization of the error in the coulomb energy due to the fit [21]. Once the necessary coulomb integrals have been evaluated analytically, the variational fit can be accomplished by solving a simple linear matrix equation.

The exchange-correlation fitting technique acts as a rather sophisticated numerical quadrature scheme which allows an accurate evaluation of the exchange-correlation integrals on a relatively sparce integration mesh. The expansion coefficients of the fitting functions are obtained from a weighted least-squares fit to the exact exchange-correlation energy density or potential on the mesh. This fitting procedure can be reduced to solving another linear matrix equation whose elements are obtained via numerical integration. The fitted energy density and potential can then be used to analytically calculate the matrix elements of the secular equation (and total energy) to a much higher level of precision than that of the numerical integration. In FILMS, the exchange-correlation fit procedure differs from that used in Ref. 21 in that the "exact" exchange-correlation functions are determined from the fitted charge density instead of the orbitals. This change substantially reduces the time required for the SCF cycle by obviating the need to generate the exact density on the numerical integration mesh.

Although the above description of the LCGTO-FF technique is valid for all of the results discussed here, the program FILMS has evolved rapidly during the 8 years spanned by those results. Fortunately, comparison of the results produced by different versions of FILMS (and diverse basis sets) reveal no substantive changes. For example, the predicted value of the Li monolayer lattice constant has varied by less than 1%.

TABLE I. Monolayer lattice constants and binding energies compared with theoretical and experimental bulk values

	a_0 (a.u.)			E (eV)	
	1-layer[a] theory	Bulk[b] theory	Bulk[c] exp.	1-layer[a] theory	Bulk[b] theory
Li	5.78	5.55 (5.65)[d]	5.71	1.11	1.65
Na	6.64	6.67	6.92	0.81	1.12
K	8.28	8.30	8.56	0.65	0.90
Rb	8.92	8.90	9.15	0.61	0.65
Be	3.99	4.19	4.33	3.27	3.97
Mg	5.68	5.94	6.07	1.02	1.69
Ca	7.01	7.08	7.46	1.31	2.24
Sr	7.91	7.69	8.12	0.99	1.89
C(g)	4.64[e]	4.65[f]	4.65[g]	8.57[e]	8.83[c]

[a] Ref. 22.
[b] Ref. 24 (AM in bcc structure, AFM in fcc structure).
[c] Ref. 27.
[d] Ref. 25 (hcp struc.).
[e] Ref. 19.
[f] Ref. 26.
[g] Ref. 28.

Results

Before examining the results of geometry-optimized UTF calculations, it is useful to consider the intuitive coordination number model (CNM) for the layer by layer growth of a UTF [9,17]. The CNM is based on the assumption that the nearest neighbor separation of a system will increase with its coordination number. Thus, one would anticipate that for a given element at zero pressure, the nearest neighbor distance of the bcc structure (coordination number 8) will be less than that of the fcc structure (coordination number 12), as is generally the case. Similarly, if one were able to simply remove some of the neighbor atoms in a system, the bond length would be expected to contract due to the improved screening of the remaining neighbors.

Applying the CNM to the layer by layer growth of a UTF produces a very simple intuitive picture. For a monolayer, the reduced coordination number relative to the bulk should result in a nearest neighbor distance a which is substantially reduced. When a second layer is brought in to form a dilayer, the intraplanar nearest neighbor distance a should be intermediate between the monolayer and the bulk. As additional layers are added, a should rapidly converge to the bulk value. Similarly, for a dilayer, the interplanar separation d should be smaller than that of the bulk. For a sufficiently thick film, the interplanar spacing should steadily increase as a function of the depth inside of the film and should rapidly converge to the bulk value. Although it would be unrealistic to expect the CNM to hold for all real materials, it does provide a useful reference for assessing UTF geometry optimization results.

In all of the calculations discussed here, it is assumed that the UTFs are in the hexagonal close-packed (hcp) phase; except for graphite. This is consistent with the fact that most of the elements considered here crystallize into a close-packed structure at $T = 0$ and $P = 0$. Due to length considerations, only the alkali metals (AMs), alkaline-earth metals (AEMs), and graphite are considered here.

Monolayers

Table I compares calculated monolayer lattice constants a_0 and binding energies E_b for the AMs [22], the AEMs [22] and graphite [19] with theoretical [24–26] and experimental [27,28] bulk values. Note that Ref. 24 assumes that the AM structure is body centered cubic (bcc), unlike the monolayer calculations. For Li, Table I also includes a theoretical bulk value of a_0 for the hcp structure [25]. As expected from the CNM, the bcc value of a_0 is smaller than the hcp value. Similar results could be expected for the other AMs.

Three trends are immediately apparent from Table I. (1) For all of the monolayers, E_b is sensibly smaller than the corresponding bulk value. (2) The theoretical bulk nearest neighbor distances exhibit the usual LDA underestimate of lattice parameters (LDA value $\leq$ experimental value), emphasizing the importance of comparing theory with theory in this analysis. (3) Given that use of the bcc structure produces an underestimate of the theoretical bulk a_0 for the AMs, it is apparent that the CNM is followed for 7 of the 9 entries in Table I. The lattice expansion exhibited by the Li and Sr monolayers relative to the bulk is a significant anomaly which, in the case of Li, persists even when the comparison is with the larger hcp lattice constant.

Analysis of the predicted one-electron properties of the monolayers also reveals interesting trends. Figure 1 shows the electronic band structure and density of states (DOS) for an AM monolayer [17]. Although this particular band structure is for Li, it is qualitatively similar to the band structure of any other AM. The horizontal dashed line in Figure 1 indicates the energy at which one additional electron state per atom would be occupied. Thus, Figure 1 would look like the band structure of an AEM if the Fermi level were taken to be the horizontal dashed line. The most important qualitative difference between the band structures of AM and AEM monolayers is the partial occupation of the p_z-derived band around Γ and the corresponding peak in the occupied density of states for an AEM. There is evidence that for the AEMs, this band is a precursor to a partially occupied (0001) surface state [14].

In Table II, the work functions (ϕ) and densities of states at the Fermi level ($n(-\phi)$) of the AM and AEM monolayers [22] are compared with experimental values [29] of ϕ and theoretical bulk values [24] of $n(-\phi)$. For both the AMs and the AEMs, the monolayer work functions are larger than the corresponding bulk values. This suggests that the electron density of the outermost layer of the semi-infinite solid is drawn into the surface, thereby reducing the surface dipole barrier. The AMs and AEMs exhibit distinctly different trends in $n(-\phi)$, with the AM monolayer values being less than or roughly equal to the bulk values and the AEM
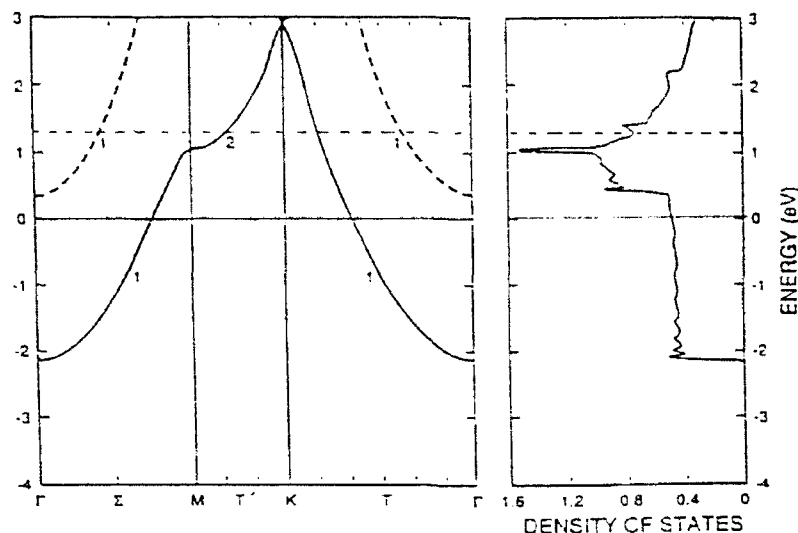
Figure 1. The electronic band structure (eV) and density of states (states/eV) for a Li monolayer are shown, with energies given relative to the Fermi energy (solid horizontal line). The horizontal dashed line indicates the energy at which one additional electron per atom would be occupied.

monolayer values generally being larger than the bulk values (except for Ca). The enhancement of $n(-\phi)$ for the AEM monolayers is due to the surface state in Figure 1, with the most dramatic example being Be for which the bulk is a poor conductor and the monolayer is a good conductor.

TABLE II. Monolayer work function (ϕ) and density of states at the Fermi level $(n(-\phi))$[a] compared to experimental values of ϕ[b] and theoretical bulk values of $n(-\phi)$.[c]

System	ϕ(eV)		$n(-\phi)$(states/eV)	
	1-Layer theory	Bulk exp.	1-Layer theory	Bulk theory
Li	3.58	2.90	0.52	0.48
Na	3.16	2.75	0.44	0.45
K	2.67	2.30	0.68	0.73
Rb	2.55	2.16	0.73	0.90
Be	5.39	5.10	0.34	0.054
Mg	3.99	3.66	0.60	0.45
Ca	3.15	2.87	1.53	1.56
Sr	2.92	2.59	1.31	0.31

[a] Ref. 22.
[b] Ref. 29.
[c] Ref. 24.

Dilayers

For three of the elements in Table I (Li, Be, and C), dilayer calculations have been performed. Table III compares the calculated [13,17,19] monolayer and dilayer lattice parameters with theoretical [25,26,30] and experimental [27,28,31] values obtained for the close packed crystal structure. The most interesting feature in Table III is the fact that each of the systems behaves differently.

For graphite, the difference between the monolayer, dilayer, and bulk lattice parameters is negligible, as one would expect for a loosely bound layer compound. Given the sensitivity of the lattice parameter calculation for graphite due to its exceptionally weak binding, this result is quite reassuring.

For Be, the CNM is followed for the intraplanar spacing a (i.e., monolayer value < dilayer value < bulk value). However, the interplanar spacing d shows an anomalous 2.4% expansion compared with the theoretical bulk value. Since the initial publication of this result in 1985 [13], there has been a measurement of the relaxation of the outermost layer of the Be (0001) surface which reveals an anomalous 5.8% expansion [32], in qualitative agreement with tne dilayer calculation.

The behavior of Li is opposite to that of Be, with d following the CNM and a exhibiting anomalous behavior. In fact, the value of a is diverging from the bulk value (i.e., dilayer value > monolayer value > bulk value) [17]. This curious behavior motivated a careful study [9] of Li n-layers with $n = 1 \rightarrow 5$.

Li n-layers

In Table IV, calculated n-layer lattice parameters for Li ($n = 1 \rightarrow 5$) [9] are compared with theoretical [25] and experimental [31] bulk values. The value of

TABLE III.   Monolayer and dilayer lattice parameters (a = intraplanar parameter, d = interplanar spacing) compared to theoretical and experimental bulk values (au).

	Li		Be		C (g)	
	a	d	a	d	a	d
1L	5.74[a]	—	3.99[b]	—	4.64[c]	—
2L	5.81[a]	4.25	4.10[b]	3.46	4.64[c]	6.49
Bulk	5.65[d]	4.64	4.25[e]	3.38	4.65[f]	6.45
exp.	5.88[g]	4.81	4.33[h]	3.39	4.65[i]	6.34

[a] Ref. 17.
[b] Ref. 13.
[c] Ref. 19.
[d] Ref. 25.
[e] Ref. 30.
[f] Ref. 26.
[g] Ref. 31.
[h] Ref. 27.
[i] Ref. 28.

TABLE IV. Li n-layer lattice parameters (a intraplanar separation, d interplanar separation, i interior, e exterior) from Ref. 9 are compared with theoretical (Ref. 25) and experimental (Ref. 31) bulk values.

System	a(au)	d_i(au)	d_e(au)
1L	5.73	--	—
2L	5.76	—	4.27
3L	5.75	—	4.39
4L	5.69	4.38	4.32
5L	5.67	4.37	4.41
bulk theory	5.65	4.64	4.64
bulk exp.	5.88	4.81	4.81

the intraplanar spacing has a maximum for the dilayer and then rapidly converges on the bulk value. It was noted in Ref. 9 that, for the dilayer and the trilayer, the energy shows a long nearly flat minimum in the range $5.70 \leq a \leq 5.80$ au. For the 4- and 5-layer films, the minimum becomes well-localized near the bulk value of a. This behavior may be attributed to the existence of a true interior for the 4- and 5-layer films. In contrast, the interplanar spacings for the n-layers have not begun to converge on the bulk value by $n = 5$, a disheartening result for those who would calculate surface relaxations by only varying the positions of the outermost one or two layers.

In Table V, the binding energies per atom (E_b), interplanar binding energies (E_i; defined as the binding energy of the n-layer minus the binding energy of the monolayer), and the ratio of E_i to its corresponding bulk value are compared for the n-layers [9] and the theoretical bulk crystal [25]. Although the n-layer values are behaving sensibly (i.e. monotonically converging on the bulk, the rate of convergence is very slow). In Ref. 9, it was noted that the ratio $R = E_i(n)/E_i(\infty)$ could be fitted by the expression

TABLE V. Calculated equilibrium cohesive energies E_b(eV/atom), interplanar binding energies E_i(eV/atom), and the ratio of E_i to its crystalline value $E_i(\infty)$ for Li n-layers (Ref. 9) compared with theoretical bulk values (Ref. 25).

System	E_b	$-E_i$	$E_i/E_i(\infty)$
1L	1.10	0.00	0.00
2L	1.39	0.29	0.46
3L	1.48	0.38	0.60
4L	1.51	0.41	0.65
5L	1.53	0.43	0.68
Bulk	1.73	0.63	1.00

$$R(n) \simeq [\arctan[0.12(n - 1)]/\arctan(x)]^{0.29}. \qquad (1)$$

This implies that reaching 90% of the crystalline interplanar binding energy would require $n = 17$ while 95% would require $n = 33$; another indication that modeling a macroscopic sample may require a very thick film.

Some of the one-electron properties of the Li n-layers [9] are shown in Table VI together with experimental [29] and theoretical [24] bulk values. It has been noted [9] that the experimental work function for Li is in disagreement with all theoretical calculations and may be unreliable. If the experimental value of ϕ is ignored, it becomes clear that the one-electron properties are rapidly convergent. It also is apparent that the QSE in the work function of Li is minimal.

In contrast to the weak QSE in ϕ, the density of states itself shows a rather interesting form of layer dependence. The densities of states for the 5 Li n-layers are shown in Figure 2. Since the density of states for a two-dimensional parabolic band is a step function, and the occupied band structure of Li can be represented as a series of parabolic bands (one for each layer), the density of states for a given Li n-layer has a stair-like form, with one step for each layer. Thus, $n(\epsilon)$ exhibits a quantized behavior which has a one-to-one correspondence with the number of atomic layers.

Conclusions

It is evident that UTF properties are in many cases distinctly different from those of the corresponding bulk systems. For example, all AM and AEM monolayers have larger work functions than the bulk. In addition, the AEM monolayers tend to have an enhanced density of states at the Fermi energy due to a p_z-derived surface state.

The structural parameters of several of the UTFs considered here exhibit anomalous behavior relative to the CNM. At the monolayer level, Li and Sr both manifest an expansion relative to the bulk. Among the dilayers, Be shows an anomalous

Table VI. Calculated work function (ϕ), density of states per atom at the Fermi level ($n(-\phi)$), and occupied bandwidth (W) for the Li n-layers (Ref. 9) compared to theoretical (Ref. 24) and experimental (Ref. 29) bulk values.

System	ϕ(eV)	$n(-\phi)$ (states/eV)	W(eV)
1L	3.56	0.49	2.2
2L	3.63	0.55	3.1
3L	3.60	0.58	3.4
4L	3.61	0.46	3.5
5L	3.56	0.47	3.6
theory	—	0.48	3.6
expt.	2.90	—	—

IS-12/91-2255
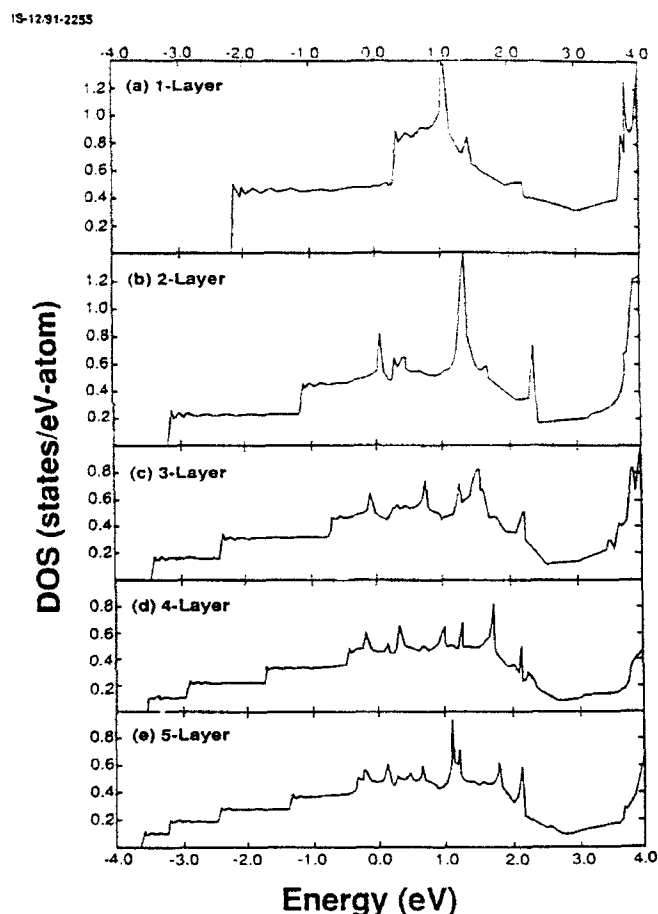
Figure 2. The density of states per atom (states/eV) is shown as a function of one-electron energy (relative to the Fermi level, eV) for the Li n-layer films; (a) 1-layer; (b) 2-layer; (c) 3-layer; (d) 4-layer; (e) 5-layer.

expansion of the interplanar spacing compared with the bulk value (a result which is supported by recent experimental data) [32], while all of the Li n-layers exhibit an anomalous expansion of the intraplanar separation.

The study of Li n-layers ($n = 1 \rightarrow 5$) reveals that the rate at which a UTF evolves into a bulk depends upon what property is being considered. The work function, density of states at the Fermi level, occupied band width, and intraplanar spacing are all rapidly convergent to bulk values. In contrast, the interplanar spacing and binding energy are very slowly converging quantities and may require tens of layers to adequately model the bulk. This result calls into question any surface relaxation calculations which only allow the outermost one or two layers of a film to relax.

Finally, the densities of states for the Li n-layers exhibit a stair structure with the number of steps being equal to the number of layers. Whether or not the size of this QSE is large enough to be measurable remains to be determined.

Acknowledgments

Bibliography

[1] F. K. Schulte. Surf. Sci. 55, 427 (1976).
[2] E. E. Mola and J. L. Vicente. J. Chem. Phys. 84, 2876 (1986).
[3] P. Feibelman. Phys. Rev. B27, 1991 (1983).
[4] P. Feibelman and D. R. Hamann. Phys. Rev. B29, 6463 (1984).
[5] K. M. Ho and K. P. Bohnen. Phys. Rev. B32, 3446 (1985).
[6] S. Ciraci and I. P. Batra. Phys. Rev. B33, 4294 (1986).
[7] I. P. Batra, S. Ciraci, G. P. Srivastava, J. S. Nelson, and C. Y. Feng. Phys. Rev. B34, 8246 (1986).
[8] J. L. Vicente, A. Paola, A. Razzitte, E. E. Mola, and S. B. Trickey, Phys. Status Solidi B155, K93 (1989).
[9] J. C. Boettger and S. B. Trickey, Phys. Rev. B45, 1363 (1992).
[10] R. C. Albers, A. M. Boring, and J. C. Boettger, Adv. Quantum Chem. 21, 365 (1990); and references therein.
[11] Y. G. Hao, O. Eriksson, G. W. Fernando, and B. R. Cooper, Phys. Rev. B43, 9467 (1991).
[12] C. Li and A. J. Freeman, Phys. Rev. B43, 780 (1991).
[13] J. C. Boettger and S. B. Trickey, Phys. Rev. B32, 1356 (1985).
[14] J. C. Boettger and S. B. Trickey, Phys. Rev. B34, 3604 (1986).
[15] J. Z. Wu, J. R. Sabin, S. B. Trickey, and J. C. Boettger, Int. J. Quantum Chem. Symp. 24, 873 (1990).
[16] J. Z. Wu, S. B. Trickey, J. R. Sabin, and J. C. Boettger, Phys. Rev. B45, 8610 (1992).
[17] J. C. Boettger, S. B. Trickey, F. Mueller-Plathe, and G. H. F. Diercksen, J. Phys. Condensed Matter 2, 9589 (1990).
[18] S. B. Trickey, G. H. F. Diercksen, and F. Mueller-Plathe, Astrophys. J. 336, 137 (1989).
[19] S. B. Trickey, F. Mueller-Plathe, G. H. F. Diercksen, and J. C. Boettger, Phys. Rev. B45, 4460 (1992).
[20] J. C. Boettger, Int. J. Quantum Chem. Symp. 25, 629 (1991).
[21] J. W. Mintmire, J. R. Sabin, and S. B. Trickey, Phys. Rev. B26, 1743 (1982).
[22] J. C. Boettger and S. B. Trickey, J. Phys. Condensed Matter 1, 4323 (1989).
[23] L. Hedin and B. I. Lundqvist, J. Phys. C4, 2064 (1971).
[24] V. L. Moruzzi, J. F. Janak, and A. R. Williams, Calculated Electronic Properties of Elemental Solids (Pergamon, New York, 1978).
[25] J. A. Nobel, S. B. Trickey, P. Blaha, and K. Schwarz (unpublished).
[26] H. J. F. Jansen and A. J. Freeman, Phys. Rev. B35, 8207 (1987).
[27] N. W. Ashcroft and N. D. Mermin, Solid State Physics (Holt, Rinehart, and Winston, 1976).
[28] J. Donohue, The Structures of the Elements (Krieger, Malabar FL, 1982) p. 256.
[29] H. B. Michaelson, J. Appl. Phys. 48, 4729 (1977).
[30] P. Blaha and K. Schwarz, J. Phys. F: Met. Phys. 17, 899 (1987).
[31] C. S. Barrett, Acta Crystallogr. 9, 671 (1956).
[32] H. L. Davis, J. B. Hannon, K. B. Ray, and E. W. Plummer (unpublished results), quoted by S. P. Chen (unpublished preprint).

Received April 8, 1992

Application of Thin Films Method in the Study of Alkali–Semiconductor Interaction

INDER P. BATRA

*IBM Research Division, Almaden Research Center K62/802,
650 Harry Road, San Jose, California 95120*

Abstract

The computation of atomic structure from first principles is a challenging theoretical endeavor. The complexity grows substantially when dealing with films and surfaces, because one can no longer exploit the three-dimensional periodicity. Here we expound upon the self-consistent field pseudopotential slab method with local density approximation to study thin films and ordered overlayers on surfaces. Plane wave basis sets are used because they are free from linear dependency problems due to their orthonormal properties. The results are illustrated by investigating the atomic structure of metal overlayers on the Si(001)-2 × 1 surface at initial coverages. Major emphasis is on alkali metals, but Al is included for comparative purposes. The nature of the interaction and the role of Peierls distortions in metal–semiconductor energetics are presented. © 1992 John Wiley & Sons, Inc

Introduction

Professor Löwdin graciously reminded us by quoting P. Debye that we should use brain power before using computer power in solving problems. Clearly, this advice is easy to follow if one is gifted with the Löwdin brain. Unfortunately, many of us working in the area of surfaces and interfaces are not so blessed. Most of us use the computer as an extension to our brain power. Supplementing brain power with computer power is often a necessity. Working for the IBM Corporation, I am glad it is so! This paradigm is certainly valid in resolving some issues connected with metal interactions with Si(001)-2 × 1, the subject matter of the present study.

The computation of atomic arrangement is challenging considering that the atomic reconstruction of various clean Si surfaces have involved efforts extending over several decades. Even in the current year it is not uncommon to encounter publications on this very subject. The complexity arises from the fact that, when dealing with films and surfaces, one can no longer exploit the three-dimensional periodicity. The adsorption of metals on Si can lead to further complications.

In this article, we primarily study the interaction of alkali metals (AM) with Si(001)-2 × 1 surface at initial coverages. A brief description of simple metals like Al is only included at the end for elucidating certain aspects of AM–Si interactions by comparison. Understanding of the atomic and electronic structure of metals adsorbed on semiconductors is important for fundamental and a variety of application areas [1].

Numerous investigations [1-4] carried out recently for the interaction of AM with the Si(001)-2 × 1 substrate are due to the fact that Si(001) is among one of the few surfaces [5,6] which can be driven into a negative electron affinity (NEA) state. An NEA state is achieved when the vacuum level falls below the conduction band edge of the semiconductor. The carriers excited across the band gap can then escape without any additional energy cost, thus making for efficient emitters. It is worth noting that the deposition of AM alone on Si(001) is not sufficient to drive it into an NEA state. The AM must be supplemented by oxygen to achieve the ultimate lowering of the work function. A large number of calculations [7-16] have attempted to predict the optimum AM overlayer registry pattern. Since that itself has generated so much debate we have strayed somewhat from our main goal.

The nature of AM–Si bond continues to draw substantial attention to explain the work function reduction. Extreme views have been expressed [11-18], ranging from the weakly covalent to the strongly ionic. Alkali metals adsorbed on other metals have been characterized by Langmuir [19], Gurney [20] and, more recently, Lang [21], as having an ionic to metallic transition with increase in coverage. Muscat and Batra [22] further developed these models. Based on the *ab initio* results of Batra and Ciraci [23] bond length relaxation was introduced as a companion to the transition. This enabled one to obtain quantitative agreement with the change in the work function data [22]. Bond length relaxation has recently been confirmed experimentally [24].

At low coverages, the AM atoms are believed to be mostly ionized. The AM overlayer turns metallic at higher coverages. This intuitively plausible picture of ionic to metallic transition is being questioned [25]. Values of charge transfer (ΔQ) from AM to Si have been obtained in the range $0 < \Delta Q < 1$. In this study, we argue persuasively in favor of an ionic-bonding picture. Our conclusions are based on self-consistent field pseudopotential calculations and physical arguments. We describe briefly the pseudopotential slab model with plane wave basis sets for investigating electronic properties of surfaces and interfaces. Other methods have been discussed by Trickey et al. [26].

Pseudopotential Method for Surfaces

Surface electronic structure calculations are complicated due to the loss of translational invariance in the direction normal to the surface. By now, a number of theoretical models have been developed to overcome this difficulty. We employ a slab model in which the three-dimensional periodicity is artificially imposed. The slab has the correct two-dimensional crystal periodicity, but the third dimension (z) is terminated after a finite number of layers. To study clean and adsorbate-covered surfaces, empty space is introduced between slabs and the entire assembly periodically repeated along the z-direction. The empty space serves to isolate the slabs of atoms and, hence, a solid vacuum interface is simulated. Since the new geometry has three-dimensional periodicity, most of the standard methods for band structure calculations can be adopted to treat this model. The price that is paid is that one has to deal with a large unit cell. The band structure technique used in

our examples is the self-consistent field (SCF) pseudopotential method in the momentum space representation [27].

The main idea behind the pseudopotential method can be best illustrated by an example. The Si atom has the electronic configuration of $1s^2 2s^2 2p^6 3s^2 3p^2$. The core electrons, $1s$, $2s$, and $2p$, are tightly bound to the nucleus and are essentially undisturbed when bulk solid is formed. Thus, unless one is specifically interested in core states energies, these states can be lumped with the nucleus. The wave functions for the valence electrons are quite smooth away from the core region, and can be well represented by plane waves. The difficulty arises from the fact that valence wave functions inside the core region oscillate rapidly to maintain orthogonality with the core states. The number of nodes in the wave function (n-ℓ-1) is equal to the number of core states with the same angular momentum. To represent their oscillations in the core regions is not too different from expanding the core states in the plane wave basis set. This is clearly hopeless, and some further approximation is still needed.

To alleviate this problem the pseudopotential method not only combines the tightly bound core electrons and the nucleus into one inert entity (ion-core) but it is further required that the pseudo-wavefunctions must be nodeless. This implies that the pseudopotential, V_{ps}, must not support any bound (core) states at energies below the valence state energies. Since the valence electrons interact with the inert ion-core through a highly reduced potential (V_{ps}), the pseudo-wavefunctions are smooth and nodeless. Pseudopotential and wavefunctions for Si are shown in Figure
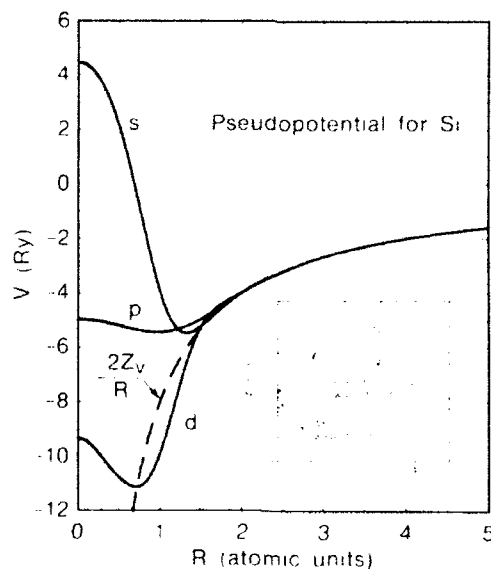
Figure 1. Nonlocal ionic pseudopotential for Si proposed by Bachelet et al. (see Ref. 28). The inset shows the pseudo-wavefunction and the true atomic wavefunction for Si (3s) orbital.

1. The pseudo-wavefunction is smooth inside the core region and matches the all-electron wavefunction outside the core region. The decoupling of the valence electrons from the ion-core has insured that the valence wavefunctions will be smooth and easily represented with a small number of plane waves.

One method by which *ab initio* ion-core pseudopotentials can be obtained from atomic calculations has been given by Bachelet et al. [28]. The basic idea is to generate a potential by inverting the Schrödinger equation. The angular momentum-dependent, all-electron atomic potentials, V^l, are screened to produce the atomic pseudopotentials, V^l_{ps}. The atomic pseudopotential, V^l_{ps}, must produce the same eigenvalue for the valence electron as the all-electron potential. The final bare ion-core pseudopotential, V^l_{ps}, is obtained from the neutral pseudopotential V^l_{ps} by subtracting the coulomb, exchange, and correlation potential from the pseudo-valence charge density. This scheme guarantees the maximum transferability of the ion-core pseudopotentials.

Once the *ab initio* pseudopotentials have been determined, the Schrödinger equation is solved self-consistently in the plane wave basis set. Being orthonormal, such basis sets do not have any linear dependence problems [29]. One can also study convergence systematically by altering the energy range of the plane waves. The plane wave basis sets are efficient for describing semiconductors and alkali metals.

Structural Results for Alkali Metals—Si(001)-2 × 1

Atoms in the surface layer of clean Si(001) have two dangling bonds each for an ideal bulk truncated structure. The 2 × 1 structure is obtained when these atoms dimerize along the x-direction (generating a σ-bond) resulting in rows of dimers along the y [110] direction. Each surface atom nominally has a single dangling bond. Since there are two Si atoms per surface unit cell, one gets two bands (π and π^*) in the gap region, which are only partially occupied. The AM atoms interact with these dangling bond orbitals located near the Fermi level. Six probable adsorption sites labeled by the letters H, B, C, D, T, and Y are shown in Figure 2. At ½ a ML coverage there is one AM atom per 2 × 1 cell (3.39×10^{14} atoms/cm^2) in one of the above-mentioned sites.

In 1973, Levine [30] proposed, for Cs adsorption on Si(001) that, at low coverages, this metal occupied a quasi-hexagonal hollow site (H) above the rows of dimers. The H-site occupancy offered a simple explanation for negative electron affinity (NEA) because it left the long bridge (B)-sites, where the adatom connects two dimers in adjacent rows, unoccupied. The coadsorption permits the oxygen atoms to submerge under the B-sites to cause additional (beyond that produced by AM) lowering of the work function required to achieve NEA. The C-site has adsorbates above the third layer of Si and, due to reconstruction, this is a more open site than H. Others have called [12,13] the C-site a "valley bridge site" (T3), and the B-site a "cave site" (T4). The dimer bridge site, D, locates the adsorbate above the midpoint of the Si dimer. In the top site, T adsorbate is above one of the dimer forming Si atoms. The Y-site is an off-centered site between the H- and the C-sites.
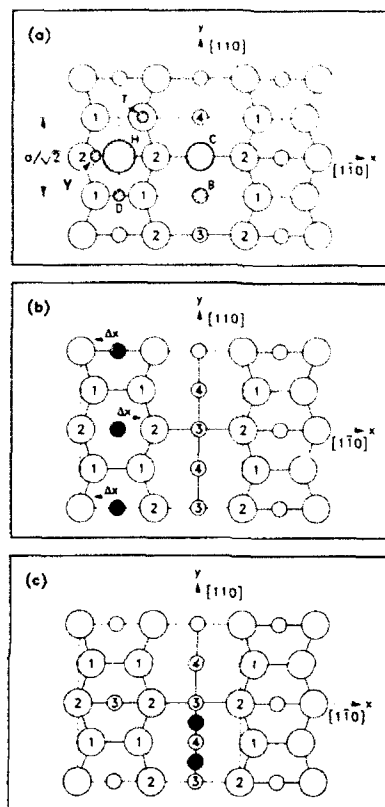
Figure 2. Top views describing the positions of metals on Si(001)-2 × 1. Filled and empty circles denote metal and Si atoms, respectively. Numerals in the circles indicate Si atomic layers. (a) H-, B-, Y-, C-, D-, and T-sites have been labeled in the 2 × 1 unit cell shown by dotted lines. At 1/2 a ML coverage, only one of these sites is occupied by metal atoms per unit cell. (b) The 2 × 2 unit cell shown by dotted lines used to study Δx Peierls' distorted structure of metals at 1/2 a ML. (c) The 2 × 2 unit cell shown by dotted lines used to study dimerization of metal atoms (Δy distortion) at 1/2 a ML.

Scanning tunneling microscopy (STM) work [31-35] on alkali metals at low coverages is responsible for revealing the Y-site [34].

STM experiments [31-35] have provided valuable information about the geometrical arrangement for AM on Si(001)-2 × 1. By carefully monitoring the density of bright spots and deposition time the adsorbed AM atoms have been identified. Hashizume et al. [31], from their STM data, earlier suggested that at low coverages, Li, K atoms are adsorbed on the top (T)-site above one of the dimer-forming Si atoms. This data has been reinterpreted [32] in terms of the Y-site adsorption.

Our total energy calculations for the adsorption of Na on Si(001)-2 × 1 at ½ a ML coverage have been reported earlier. The symmetric dimer model given by Abraham and Batra [36] was employed. The energy-ordered sequence we found

for the Na/Si system in the order of decreasing stability is E(H) ≈ E(B) < E(Y) < E(C). The D- and T-sites were found [10] to be much less stable. The computed bond length of 2.6 Å was smaller by about 0.3 Å from the value obtained in a LEED study [37].

Without numerically intensive computer calculations one could not have guessed that the H-, B-, Y-, and C-sites are competitive adsorption sites at ½ a ML coverage. Given this input one can now put forward physical arguments to wrap a story around it. This is what we eluded to in the Introduction about supplementing brain power with computer power. Clearly, a computed potential energy surface is desired for complete understanding. As a prelude to that we present a calculated potential energy line passing through the likely adsorption sites, as shown in Figure 3. Since full-relaxation calculations were not performed one should view the results shown in Figure 3 for qualitative or semiquantitative purposes only. A general conclusion to be drawn from Figure 3 is that, at ½ a ML coverage, no single site has a clear monopoly.

The above assertions are consistent with the conclusions drawn from the STM data. At ~0.2 ML coverage, the coexistence of adsorption in several sites has been reported [35]. At ½ a ML coverage the well-known, one-dimensional linear chains parallel to the Si dimer rows have been confirmed [35] for K on Si(001)-2 × 1. Although they were unable to deduce a definitive adsorption site, the H-site is fully compatible with this STM data [35].

A cluster model calculation [13] has suggested that an AM adsorbate in an H-site may be unstable toward a Peierls type of distortion. It was noted [13] that a
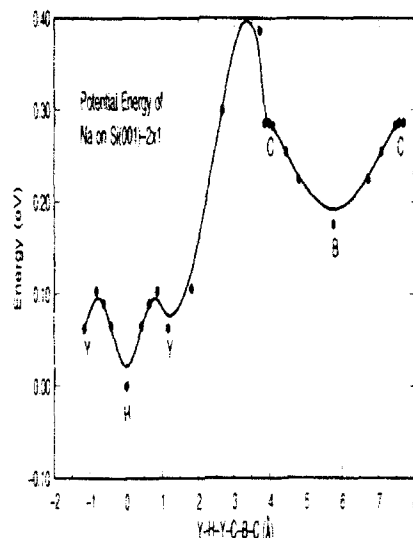
Figure 3. Total energy of Na–Si(001)-2 × 1 (referenced with respect to the H-site) at 1/2 a ML coverage along a line passing through various competitive sites. Positive energies correspond to less stable structures.

zig-zag chain, obtained by moving alkali metal atoms away from the H-site by equal and opposite amounts (Δx) along the x-direction, as shown in Figure 2(b), can have lower energy. We discuss this in the next section.

A note of caution is appropriate at this time. In all our considerations we had thought all along that results for all alkali metals are expected to be similar. We expressed our conclusions often using Na and K interchangeably. It has become clear from some recent work [38] that such a position may not be defendable. It has been pointed out that K and Cs on Si(111) do show results which depend on the AM under consideration. For example, Cs leads to removal of the π-bonded reconstruction on Si(111), whereas K does not.

There are some hints in the calculations which suggest AM-specific results. For example, the cluster calculation by Freeman et al. [15] pointed out that the B-site is a more favorable adsorption site that the H-site when K is considered. In our calculations [8,10], the H-site was favored. The revised cluster model calculations by Freeman et al. [15] (including full relaxation) have found that, for K-Si, the binding energies at the H-site (2.39 eV) and at the B-site (2.38) are comparable. It is therefore now stated [15] that either of the two sites can serve as a possible chemisorption site for K atoms. The major effect of surface relaxation was demonstrated by Batra [10] earlier. This is now being corroborated by the cluster model calculation by Freeman et al. [15]. Their computed value of charge transfer of $\sim0.6e$ at the H-site clearly rules out the suggestion [17] that the bonding is covalent. A bonding energy of ~2.4 eV also argues against the proposal [17] of a weak bond. A strong ionic picture is also supported by a cluster model calculation [11] based on the *ab initio* Hartree-Fock method. The strong bonding picture is also consistent with the recent band structure calculations by Morikawa et al. [39], as well as the thermal desorption results of Tanaka et al. [40].

The C-site is preferred (over H- or B-sites) by some recent pseudopotential calculations [14] for K on Si(001)-2 $\times$ 1 at $\frac{1}{2}$ a ML coverage. All these calculations clearly suggest that the potential energy surface is rather flat. This, incidentally, should be the case when ionic bonding is predominant. Covalent bonds, being directional in nature, tend to have potential energy surfaces [41] with well-defined peaks and valleys.

The structural results can now be summarized for AM adsorption on Si(001)-2 $\times$ 1 at $\frac{1}{2}$ a ML coverage. For Na, the H-site is a preferred site. For K, the H-, B-, C-, and Y-sites all seem to offer themselves as potential adsorption sites with the H-site still holding a bit of an edge over the other sites. The substrate relaxation plays a crucial role in arriving at these conclusions. The AM–Si bond is decidedly strong (~2 eV per alkali metal atom) with a bond length [42,43] in the range of 2.6–3.3 Å.

Peierls Distortion at 1/2 a ML Coverage

An objection to the adsorption at the H-sites was raised from the results obtained by a cluster model calculation [13] for the K–Si system. According to these calculations the total energy of the AM chain continued to decrease upon introducing

zig-zag distortions of various amounts Δx shown in Figure 2(b). These findings were rationalized by appealing to Peierls theorem [44]. according to which a mono-atomic chain can always lower its total energy by lattice distortions. The cost of lattice distortion is offset by the electronic energy benefit up to a certain critical distortion. It was thus argued that the AM chain is inherently unstable and should undergo some sort of Peierls distortion. Realizing that dimerization of alkali metal atoms by longitudinal distortions is not likely due to steric hindrance at the surface, the authors [13] settled on the zig-zag distortion.

Our calculations done for the Na–Si system did not show any energy lowering due to the zig-zag distortion. This was obviously of some concern because, apparently, our numerical calculations seem to be violating the fundamental Peierls theorem. The latter demands an energy lowering in a one-dimensional chain due to reduction in the translational symmetry which opens a gap at the new zone edge. Eventually, we realized that, although zig-zag transverse distortions lead to an apparent reduction in the translational symmetry, they do not lead to any gap opening at the zone edge. We chose to call such distortions as leading to gapless Peierls transitions [45]. This does not contradict the well-known Peierls theorem which is valid only for longitudinal displacements. For completeness, we give an elementary proof based on tight binding arguments.

In a one-dimensional chain oriented along the y-direction, $\pm \Delta x$ distortions along the x-direction double the apparent size of the unit cell. The new primitive translation vector becomes $2a\hat{y}$ and the corresponding reciprocal cell is reduced to $-\pi/2a \leq k_y < \pi/2a$ as in the standard Peierls case. But we now show that, unlike the standard Peierls case, these transverse distortions are not able to lift the degeneracy at the zone edge, $\pm \pi/2c$.

For simplicity, we consider one orbital ϕ per atom and construct the system wave function as a linear combination of Bloch functions, χ_j, localized on atomic sites j ($=1,2$) in the unit cell

$$\psi_{n\vec{k}}(\vec{r}) = C_{1n\chi 1}(\vec{r}, \vec{k}) + C_{2n\chi 2}(\vec{r}, \vec{k}). \tag{1}$$

The Hamiltonian matrix $H_{ij}(\vec{k}) = \langle \chi_i | H | \chi_j \rangle$, can be written in the form,

$$H_{ij}(\vec{k}) = \sum_{\vec{R}_v} e^{i\vec{k} \cdot (\vec{r}_i - \vec{r}_j - \vec{R}_v)} \int \phi(\vec{r}) H \phi(\vec{r} + \vec{r}_i - \vec{r}_j - \vec{R}_v) d\vec{r} . \tag{2}$$

Denoting the diagonal elements (which are obviously identical) E_0 and the off-diagonal terms by u and u^*, the 2×2 matrix at the zone edge is

$$H\left(\frac{\pi}{2a}\hat{y}\right) = \begin{vmatrix} E_0 & u \\ u^* & E_0 \end{vmatrix}, \tag{3}$$

where u can be expressed in the form,

$$u = \sum_{\vec{R}_v} \exp\left[-\frac{i\pi}{2a}\hat{y} \cdot (\vec{r}_1 - \vec{r}_2 - \vec{R}_v)\right] \int \phi(\vec{r}) H \phi(\vec{r} + \vec{r}_1 - \vec{r}_2 - \vec{R}_v) d\vec{r} . \tag{4}$$

In the nearest neighbor approximation, the structure factor in the above equation reduces to $\cos \pi/2$, leading to $u = 0$. In fact, u vanishes identically even when all distant neighbor interactions are included. Thus, the band at the zone edge is doubly degenerate, with $\lambda_{1,2} = E_0$. For the half-filled band under consideration, the Fermi level passes through this degeneracy point and the system is metallic.

Thus, unlike the well-known Peierls case with longitudinal distortions, the transverse displacements do not open a gap at the zone edge. Total energy may or may not be lowered upon zig-zag distortions, depending upon materials-specific interactions, however. For AM adsorbed on Si(001)-2 × 1 at the H-sites, there is no energy lowering due to the zig-zag distortions. A small energy lowering due to longitudinal displacements cannot be ruled out. But these displacements have to be rather small, because any sensible reduction in AM–AM distance leads to a large repulsive barrier due to ion–ion repulsion energy. Hence, we conclude that Peierls instability considerations do not preclude AM adsorption at the H-sites.

Nature of Alkali Metal–Si Bonding

There have been some suggestions [17,18] in the literature that the interaction between AM and Si is weak at $\frac{1}{2}$ a ML coverage. It is difficult to reconcile this with STM data where AM atoms have been shown to form one-dimensional chains parallel to the substrate Si dimer row directions. In the proposed geometry, for say, K on Si(001)-2 × 1, the nearest neighbor K — K interatomic distance of 3.8 Å is considerably shorter than the bulk equilibrium distance of 4.6 Å. For Cs, the deviation from the bulk bond length (5.2 Å) is even greater. This suggests that AM atoms are being forced to locate on the repulsive part (≥ 0.5 eV) of the potential energy surface in the AM–AM coordinate. From thermal desorption experiments [40], binding energies of 1.6 and 1.9 eV have been obtained, depending on the adsorption site. The overall stabilization of the structure must then arise from AM–Si interactions. This interaction has to be substantial and, in fact, most theoretical calculations [8–15] estimate this number to be in the 2-eV range. The origin of the stabilization energy must lie in the image interaction between the alkali ion and the Si surface.

The predominantly covalent AM–Si interaction proposal [17] is also not being supported by the STM data. At intermediate coverages (~ 0.2 ML) the AM atoms have been shown [35] to occupy a variety of adsorption sites. Covalent bonds are usually highly directional [41] in nature and tend to be site-specific. Several total energy calculations [10,14,15], and the Na potential energy line shown in Figure 3, support multiple adsorption sites in agreement with the STM data. Thus, both the data and the current calculations argue against a purely covalent bond. Multiple sites can be consistent with a weakly interacting metallic overlayer on Si(001)-2 × 1 surface. However, we have noted above that the bond energy is ~ 2 eV, which is certainly not weak. Hence, the overall interactions must have a strong ionic contribution. This conclusion is also supported by cluster calculations [11,13].

The precise quantitative value of the charge transfer, ΔQ, from AM to Si, lacks consensus. All values ranging between 0 and 1 have been quoted in the literature.

This is not too surprising since there is no unique definition for ΔQ. The computed charge transfer value depends on the model used. The spatial and spectral distribution clearly suggest that the bond is substantially ionic. We believe that the STM observations are consistent with the Langmuir–Gurney picture of ionic interaction at low coverages.

The magnitude of surface core level shifts upon AM adsorption in photoemission experiments have been used as a measure of charge transfer. Recent work by Riffe et al. [46] for K on W(110) and Si(001) is prototypical. Based on small observed binding energy shifts, it was concluded that there is little or no charge transfer. The complication associated with relating the core shift to charge transfer arises from the fact that the net core shift [47] arises from two contributions of opposite sign. The charge transfer from AM to Si shifts the Si core level toward the vacuum level (lower binding energy). But the extra-atomic Madelung contribution, of opposite sign, cancels the greater part of this effect. Thus, the net core level shift may well be negligible even when ΔQ is significant. Only the intra-atomic contributions of the core level shift is related to ΔQ. This quantity is not directly observable and must be supplemented by either theoretical calculations or by other empirical data.

Bagus and Pacchioni [48] have also illustrated this by going to the extreme of representing K with a point charge of +1 on Cu(100). The calculated shifts in binding energies of Cu surface atoms in the range of 0.1 eV are clearly much smaller than the shift expected due to the large electrostatic potential. The substrate charge polarizes to offset the shift due to the point charge. The conclusion being that small binding energy shifts can be fully consistent with ionic interaction.

In summary, we can state that AM–Si interaction is strong, with a substantial ionic component. Perhaps a consensus on the precise value of the charge transfer from AM to Si is not necessary. We believe that the Langmuir–Gurney picture of ionic to metallic transition only supplemented by our distance relaxation concept is valid. The H-site at $\frac{1}{2}$ a ML coverage is somewhat favored. In conformity with the concept of the ionic bond, several other sites should, and do, lie close in energy.

The Aluminum–Si System

We summarize our findings for the interactions of Al with the Si(001)-2 × 1 surface to contrast with alkali metals. Lander and Morrison [49] first reported that, at room temperature, Al deposition on Si(001) leads to a disordered phase at low (≤ 0.5 ML) coverages. It is only recently that Ide et al. [50] reported a number of ordered surface structures determined by LEED and AES for Al–Si(001) up to 1 ML. Different structures appeared, depending on the coverage and substrate temperature. Nogami et al. [51] have produced STM images of Al on Si(001) revealing metallic dimers that run perpendicular to the underlying Si dimers rows below 0.5 ML, as shown in Figure 2(c).

Thus, experimentally, Al, unlike K or Na, is capable of producing metal dimers [50–52]. The unit cell here is 2 × 2 Si(001) as opposed to 2 × 1 for alkali metal adsorption. STM Experiments [51] show clear evidence of dimers up to 0.5 ML. Our total energy calculations [53] support the formation of metal dimers. At $\frac{1}{2}$ a

ML, the structure shown in Figure 1(c), where Al dimers are formed near the B-sites on the reconstructed surface, is stable. The stability of the structure has its origin in the fact that Al and substrate bonds are fully saturated at this coverage. Our calculation shows that, near 1 ML, the surface reconstruction is lifted. We now have ideal 1 × 1 substrate but Al dimers are present in a 1 × 2 structure. Once again, all bonds are saturated. The origin of the dimers is explained in terms of standard (longitudinal) Peierls [44] distortion of a nearly one-dimensional metallic system. Unlike the AM-Si case, the substrate reconstruction is lifted at about 0.5 ML coverage of Al. The Al-Si bonds are primarily covalent.

Conclusion

We have provided the atomic and electronic structure of ordered metallic layers on the Si(001)-2 × 1 surface using theoretical techniques suited for current computational machinery. The interaction of AM with Si is primarily ionic, but for Al it is covalent. Peierls distortions can explain the Al-Si structures. The basic 2 × 2 unit cell seen by LEED arises because Peierls distortions lead to significant energy benefit for Al-Si(001). No such benefit arises in the AM-Si system. Our results help explain the dramatic work function reduction and support the proposal for NEA by Levine [30].

Acknowledgments

This article is based on the plenary talk delivered at the Sanibel Symposium in St. Augustine, Florida, March 1992. The other speakers in this session were Jack Gay (a former graduate student of Prof. P.-O. Löwdin) and the giant of a man, Professor Löwdin himself. The opportunity accorded to me to speak in this session by Professor S. Trickey is nothing short of granting Nirvana. For this I am forever indebted to him. That Professor Löwdin sat through my entire talk is a tribute to his greatness.

Bibliography

[1] I. P. Batra, Ed. For a number of comprehensive articles see *Metallization and Metal-Semiconductor Interfaces*, (NATO ASI series B, Vol. 195) (Plenum, New York, 1989).

[2] I. P. Batra, Prog. Surf. Sci. **25**, 175 (1987); I. P. Batra, J. Chim. Phys. **86**, 689 (1989).

[3] H. P. Bonzel, A. M. Bradshaw, and G. Ertl, Eds. *Physics and Chemistry of Alkali Metal Adsorption*, (Elsevier, New York, 1989).

[4] I. P. Batra, E. Tekman, and S. Ciraci, Prog. Surf. Sci. **36**, 289 (1991).

[5] R. U. Martinelli, Appl. Phys. Lett. **16**, 261 (1970); R. U. Martinelli and D. G. Fisher, Proc. IEEE **62**, 1339 (1974).

[6] I. Abukawa, Y. Enta, T. Kashiwakura, S. Suzuki, and S. Kono, J. Vac. Sci. Technol. **A8**, 3205 (1990).

[7] M. Tsukada, H. Ishida, and N. Shima, Phys. Rev. Lett. **53**, 376 (1984); H. Ishida, N. Shima, and M. Tsukada, Phys. Rev. B **32**, 6236 (1985); also, see Ref. 1.

[8] S. Ciraci and I. P. Batra, Phys. Rev. Lett. **56**, 877 (1986); Phys. Rev. B **37**, 2955 (1988); also, see Ref. 1.

[9] R. Ramirez, Phys. Rev. B **40**, 3962 (1989); C. K. Ong, J. Phys. Condens. Matt. **2**, 6731 (1989).

[10] I. P. Batra, Phys. Rev. B **43**, 12322 (1991); J. Vac. Sci. Technol. **A8**, 3425 (1990); Phys. Rev. B **39**, 3919 (1989).

[11] P. S. Bagus and I. P. Batra, Surf. Sci. 206, L895 (1988); I. P. Batra and P. S. Bagus, J. Vac. Sci. Technol. A6, 600 (1988).

[12] H. Ishida and K. Terakura, Phys. Rev. B 40, 11519 (1989); K. Kobayashi, S. Blügel, H. Ishida, and K. Terakura, Surf. Sci. 242, 349 (1991).

[13] Y. Ling, A. J. Freeman, and B. Delley, Phys. Rev. B 39, 10144 (1989).

[14] B. L. Zhang, C. T. Chan, and K. M. Ho, Phys. Rev. B 44, 8210 (1991).

[15] A. J. Freeman, S. Tang, S. H. Chou, Y. Ling, and B. Delley, Density Functional Methods in Chemistry (Springer, New York, 1991).

[16] R. V. Kasowski and M. H. Tsai, Phys. Rev. Lett. 60, 546 (1988); see response to this comment by S. Ciraci and I. P. Batra, Phys. Rev. Lett. 60, 547 (1988).

[17] P. Soukiassian, M. H. Bakshi, Z. Hurych, and T. M. Gentle, Surf. Sci. 221, L759 (1989).

[18] E. M. Oellig and R. Miranda, Surf. Sci. 177, L947 (1986); E. M. Oellig, E. G. Michel, M. C. Asensio, R. Miranda, J. C. Duran, A. Munoz, and F. Flores, Europhys. Lett. 5, 727 (1988); J. E. Ortega, E. M. Oellig, J. Ferron, and R. Miranda, Phys. Rev. B 36, 6213 (1987); also see Ref. 1.

[19] I. Langmuir, Phys. Rev. 23, 112 (1924).

[20] R. W. Gurney, Phys. Rev. 47, 479 (1935).

[21] N. D. Lang, Phys. Rev. B 4, 4234 (1971).

[22] J. P. Muscat and I. P. Batra, Phys. Rev. B 34, 2889 (1986); also see P. A. Serena, J. M. Soler, N. Garcia, and I. P. Batra, Phys. Rev. B 36, 3452 (1987).

[23] I. P. Batra and S. Ciraci, Phys. Rev. B 33, 4313 (1986).

[24] G. M. Lamble, R. S. Brooks, and D. A. King, and D. Norman, Phys. Rev. Lett. 61, 1112 (1988).

[25] E. Wimmer, A. J. Freeman, J. R. Hiskes, and A. M. Karo, Phys. Rev. B 28, 3074 (1983); H. Ishida and K. Terakura, Phys. Rev. B 38, 5752 (1988).

[26] J. C. Boettger and S. B. Trickey, Phys. Rev. B 45, 1363 (1992).

[27] M. Schlüter, J. R. Chelikowsky, S. G. Louie, and M. L. Cohen, Phys. Rev. B 12, 4200 (1975); J. Ihm, A. Zunger, and M. L. Cohen, J. Phys. C 12, 4409 (1979); M. T. Yin and M. L. Cohen, Phys. Rev. Lett. 45, 1004 (1980); K. C. Pandey, Phys. Rev. Lett. 49, 223 (1982); I. P. Batra and S. Ciraci, Phys. Rev. B B33, 4313 (1986).

[28] G. B. Bachelet, D. R. Hamann, and M. Schlüter, Phys. Rev. B 26, 4199 (1982).

[29] P.-O. Löwdin, Adv. Phys. 5, 1 (1956); also see G. Aissing and H. J. Monkhorst, Int. J. Quant. Chem. (to appear).

[30] J. D. Levine, Surf. Sci. 34, 90 (1973).

[31] T. Hashizume, Y. Hasegawa, I. Kamiya, T. Ide, I. Sumita, S. Hyodo, H. Tochihara, M. Kumota, and Y. Murata, J. Vac. Sci. Technol. A8, 233 (1990).

[32] Y. Hasegawa, I. Kamiya, T. Hashizume, T. Sakurai, H. Tochihara, M. Kubota, and Y. Murata, Phys. Rev. B 41, 9688 (1990).

[33] T. Sakurai, T. Hashizume, I. Kamiya, Y. Hasegawa, N. Sano, H. W. Pickering, and A. Sakai, Prog. Surf. Sci. 33, 3 (1990).

[34] T. Hashizume, K. Motai, Y. Hasegawa, I. Sumita, H. Tanaka, S. Amano, S. Hydo, and T. Sakurai, J. Vac. Sci. Technol. B9, 745 (1991); T. Hashizume, Y. Hasegawa, and T. Sakurai, Appl. Surf. Sci. 48/49, 119 (1991).

[35] J. Kubby, W. J. Greene, and P. Soukiassian, J. Vac. Sci. Technol. B9, 739 (1991).

[36] F. F. Abraham and I. P. Batra, Surf. Sci. 163, L752 (1985); I. P. Batra, Phys. Rev. B 41, 5048 (1990).

[37] C. H. Wei, H. Huang, S. Y. Tong, G. S. Glander, and M. B. Webb, Phys. Rev. B 42, 11284 (1990).

[38] B. Reihl and K. O. Magnusson, Phys. Rev. B 42, 11839 (1990); also, see I. P. Batra and S. Ciraci, Phys. Rev. B 37, 8432 (1988).

[39] Y. Morikawa, K. Kobayashi, K. Terakura, and S. Blügel, Phys. Rev. B 44, 3459 (1991).

[40] S. Tanaka, N. Takagi, N. Minami, and M. Nishijima, Phys. Rev. B 42, 1868 (1990).

[41] G. Brocks, P. J. Kelly, and R. Car, Phys. Rev. Lett. 66, 1729 (1991).

[42] E. G. Michel, M. C. Asensio, and R. Miranda, see Ref. 1, 381 (1989).

[43] T. Kendelewicz, P. Soukiassian, R. S. List, J. C. Woicik, P. Pianetta, I. Lindau, and W. E. Spicer, Phys. Rev. B 37, 7115 (1988).

[44] R. E. Peierls, Quantum Theory of Solids (1st ed) (Oxford University Press, Oxford, UK, 1955).

[45] I. P. Batra. Phys. Rev. B **42**, 9162 (1990); I. P. Batra. Surf. Sci. **242**, 354 (1991).

[46] D. M. Riffe, G. K. Wertheim, and P. H. Citrin. Phys. Rev. Lett. **64**, 571 (1990); D. M. Riffe, G. K. Wertheim, J. E. Rowe, and P. H. Citrin, (to appear).

[47] S. Ossicini, C. Arcangeli, and O. Bisi. Phys. Rev. B **42**, 7671 (1990).

[48] P. S. Bagus and G. Pacchioni, (to appear).

[49] J. J. Lander and J. Morrison. Surf. Sci. **2**, 553 (1964).

[50] T. Ide, T. Nishimori, and T. Ichinokawa. Surf. Sci. **209**, 335 (1989).

[51] J. Nogami, A. A. Baski, and C. F. Quate. Phys. Rev. B (to appear).

[52] T. Sakamoto and H. Kawanami. Surf. Sci. **111**, 177 (1981); J. Knall, J.-E. Sundgren, G. V. Hansson, and J. E. Greene, Surf. Sci. **166**, 513 (1986).

[53] I. P. Batra. Phys. Rev. Lett. **63**, 1704 (1989).

Extreme Sensitivity of Corrugation Strength on Diffraction Resonance Line-Shapes for the Gas–Surface System He(21 meV)/Cu(115)

ERIK ENGDAHL*

Department of Physical Chemistry and The Fritz Haber Research Center for Molecular Dynamics, The Hebrew University, Jerusalem 91904, Israel

Abstract

An example of an isolated resonance with highly non-Lorentzian line-shape has been found for the gas–surface diffraction system He(21 meV)/Cu(115). When the corrugation strength parameter for the surface is very slightly varied, the signature of the narrow resonance structure shifts. © 1992 John Wiley & Sons, Inc.

Introduction

In previous works [1,2], a good agreement between calculations and experiments over the whole incident angular range for the gas–surface diffraction system, He(21 meV)/Cu(115), was obtained. The agreement concerned both the off-resonance elastic relative intensities in between the selective adsorptive resonances and the line-shape signatures of the narrow resonance structures. This kind of resonance, called selective adsorptive resonance, is associated with a temporary vibrational trapping of the scattered atom at the surface. A very simple phenomenological model potential was used. It contained only two parameters, the lattice constant and a corrugation strength parameter.

The system is effectively two-dimensional and for a chosen incident angle, γ, the parallel and perpendicular momenta of the incoming particle are given by

$$\begin{cases} p_x = p_0 \sin \gamma \\ p_z = -p_0 \cos \gamma = -(p_0^2 - p_x^2)^{1/2} \end{cases} \tag{1}$$

where $1/(2M)p_0^2$ is the kinetic energy of the incoming Helium atom ($\hbar = 1$ in this article). The coordinate system is chosen such that x is the parallel coordinate and z is the reaction coordinate with positive direction pointing from the surface.

As the corrugation is periodic with period a, the parallel momentum may change by an integer multiple of the shortest reciprocal lattice vector. This gives rise to a discrete set of diffracted beams with diffraction angles $\{\gamma^{(r)}\}$ as function of the

---

* Currently on leave from the Department of Quantum Chemistry, Uppsala University, P.O. Box 518, S-751 20 Uppsala, Sweden.

incident angle γ (see Fig. 1). In the diffracted beam labeled ν, the momenta are given by

$$\begin{cases} p_x^{(\nu)} = p_0 \sin \gamma^{(\nu)} = p_x + \dfrac{2\pi}{a} \nu \\[2mm] p_z^{(\nu)} = p_0 \cos \gamma^{(\nu)} = (p_0^2 - (p_x^{(\nu)})^2)^{1/2} \end{cases} \tag{2}$$

where ν runs over those integers such that $p_z^{(\nu)}$ is real. $\nu = 0$ Gives the specularly diffracted beam with $\gamma^{(0)} = \gamma$.

If the integer. n, is such that $p_z^{(n)}$ defined in Eq. (2) is imaginary, n labels a closed channel. The asymptotic energy in the perpendicular motion $1/(2M)(p_z^{(n)})^2 = 1/(2M)(p_0^2 - (p_x + n2\pi/a)^2)$ is then negative and it may match the mth vibrational bound state energy $E_m^{(0)}$ of the surface averaged potential, $V_0(z) = 1/a \int_{-a/2}^{a/2} V(x, z) dx$. Put another way, the total energy $1/(2M)p_0^2$ may match the mth vibrational bound state of the diagonal potential

$$\frac{1}{2M}\left(p_x + \frac{2\pi}{a} n\right)^2 + V_0(x) \tag{3}$$

for channel n. This state is labeled by $\binom{n}{m}$. When the corrugation-induced coupling is included, it becomes a Feshbach resonance carrying the same label. Its resonance energy becomes $E_{res} = E_r - i\Gamma/2$ with lifetime $\tau = \hbar/\Gamma = 1/\Gamma$.

The relative intensities of the diffracted beams and in particular the line-shapes of the selective adsorptive resonances can be calculated by means of the on-shell T matrix elements for the system. $t(\mathbf{p}' \leftarrow \mathbf{p}) = \langle \mathbf{p}' | T(E_p + i0) | \mathbf{p} \rangle$, where $T = V + VG_E^+V$, V is the potential for the system, and G_E^+ is the outgoing Green's
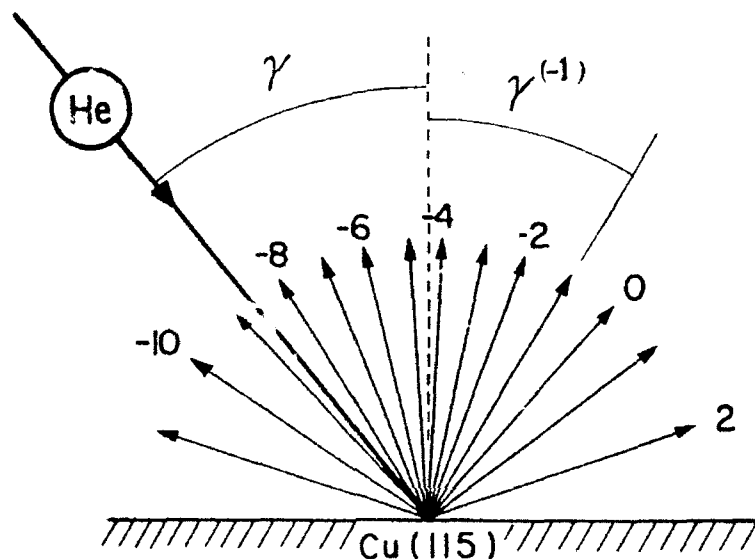
Figure 1.   The graph shows the set of diffraction angles, $\{\gamma^{(\nu)}\}$, for a specific choice of γ according to Eqs. (1)-(2). The numbers at some of the arrow heads give their ν label.

function. If the Green's function is expressed by its spectral resolution, the heavy part of the computation is the summation over discrete states and integration over the continua, symbolically

$$t' = \sum_{i}^{\text{bound\&res}} \frac{R_i}{E_{\text{beam}} - E_i} + \sum_{n} \int_{n\text{th continua}} dE \, \frac{R_{I,E}}{E_{\text{beam}} + i0 - E} \quad (4)$$

In the present, as well as previous works [1,2], the dependence of the wave functions on the perpendicular coordinate was expanded in a basis set. As a consequence, the integrations in Eq. (4) were replaced by summations over the discretized continua. In order to regularize the energy denominators, the integration contours were rotated down on higher-order Riemann energy sheets by using the complex coordinate method. To achieve this, the perpendicular coordinate that was identified as the reaction coordinate was scaled by multiplication by a complex phase factor in accordance with the Balslev–Combes theorem. The resonances that were uncovered by the rotated continua became square integrable and joined the first sum in Eq. (4).

In the experiments on the present gas–surface system performed by, for instance, Perreau and Lapujoulade [3], the beam energy E_{beam} is kept fixed and the incident angle, γ, is varied. As a consequence, it is the continuum and resonance energies in Eq. (4) that vary as a function of γ. When, in resonance with a particular resonance labeled $i = $ res, E_{beam} equals the real part of the selected resonance with complex energy $E_{\text{res}}(\gamma_{\text{res}}) = E_r(\gamma_{\text{res}}) - i\Gamma_r(\gamma_{\text{res}})/2$. The term

$$\frac{R_{\text{res}}(\gamma)}{E_{\text{beam}} - E_{\text{res}}(\gamma)} \quad (5)$$

in Eq. (4) then has a fast variation as γ is varied around γ_{res}.

In addition to the resonant term fulfilling $\text{Re} E_{\text{res}} = E_{\text{beam}}$, there is a background contribution to the scattering amplitude. The background contains contributions from all continua as well as all resonant and bound states that are not in resonance with E_{beam}. The background also contains the contribution from the direct scattering term $\langle p'|T|p \rangle$.

In order to obtain a Lorentzian line-shape or its tilted relatives for a resonance structure, there are two conditions that should be satisfied. First, the resonance should be *isolated*. Second, the background contribution to the scattering amplitude should *vary slowly* over the range of the resonance structure. It is, in principle, possible to obtain a Lorentzian line-shape whose origin is non-Lorentzian in the sense that many resonances and continua cooperate to build up a Lorentzian line-shape. Such an esoteric situation is not considered in this article.

In this study the resonance labeled $\binom{10}{0}$ is studied. It is isolated, but its narrow structure is highly non-Lorentzian due to a fast varying background. It is found that when the corrugation strength parameter is varied in a very narrow interval, the resonance line-shape changes its signature.

Results

The same computational scheme and the same physical and technical parameters were used as in Ref. 2, except for the corrugation strength parameter, h, that was varied. h is one of the two parameters in the corrugation function

$$\phi(x) = ah \cos\left(\frac{2r}{a} x\right) \tag{6}$$

that describes the shape of the surface. This corrugation function is used to modulate a Morse potential such that the interaction between the gas atom and the static copper surface is modeled by the corrugated Morse potential

$$V(x, z) = D\left[\frac{1}{v_\phi} e^{-2b[z - \phi(x)]} - 2e^{-bz}\right] \tag{7}$$

The number, $v_\phi = 1/a \int_{-a/2}^{a/2} e^{2b\phi(x)}$, is defined such that the surface average of the potential equals the uncorrugated Morse potential. For the copper surface, $D = 6.5$ meV and $b = 1.05$ Å^{-1}. The lattice constant for Cu(115) is $a = 12.5$ Bohr.

As a consequence of the corrugation, there is coupling between the parallel and the perpendicular motion. Since the corrugation is periodic, to each incident angle γ there is a set of outgoing angles $\{\gamma^{(v)}\}$, that is determined by the modulus of wave vector of the incident particle, p_0, and the lattice constant, a. $\gamma^{(0)} = \gamma$ Gives the direction of the specular beam and $\gamma^{(-1)}$ gives the direction of the particular nonspecular beam that is especially studied in this article. The latter is determined by the condition $p_0 \sin \gamma^{(-1)} = p_0 \sin \gamma - 2\pi/a$.

In Ref. 2, it was found that the choice $h = 0.027$ lead to reproduction of experimental specular as well as nonspecular intensities. In this work, this parameter is varied and the line-shape of the selective adsorptive resonance labeled ($^{10}_0$) is studied.

Figure 2a shows the specular intensity versus incident angle for a set of corrugation parameters in a wide range. When the corrugation strength increases, the peak intensity, the level shift, as well as the width of the resonance change in a monotonous fashion. Also, the off-resonance intensity decreases monotonously.

The intensity for the nonspecular beam labeled $v = -1$ as function of the incident angle is displayed in Figure 2b. Also, the off-resonance intensity decreases monotonously when the corrugation is increased. This is in agreement with the general tendency that when the corrugation increases there is an increased probability of big changes of parallel momenta in the diffraction scattering process. Comparison of the intensity pattern for the corrugations $h = 0.030$ and $h = 0.035$ might lead to the false conclusion of a nonmonotonous change of the level shift for the resonance. Comparison with Figure 2a reveals that this is an artifact. The underlying reason is that the background scattering amplitude does not vary slowly within the range of the resonance width. The true resonance position is exactly the same for all scattered beams although a fast varying background may induce displacements of the apparent positions.

However, the most important feature of Figure 2b is that the resonance minimum for the nonspecular beam, $v = -1$, turns into a maximum when the corrugation is increased. As shown in Figures 3 and 4, this change of resonance signature happens very fast. In fact, the signature change happens in the very narrow interval $0.0315 \leq h \leq 0.0325$. For the intermediate value, $h = 0.320$, of the corrugation strength parameter, the resonances appear neither as a minimum nor as a maximum. Instead, the resonance structure resembles a "leaning arcus tangent" curve. If the background

Specular beam

Non-specular beam v=-1
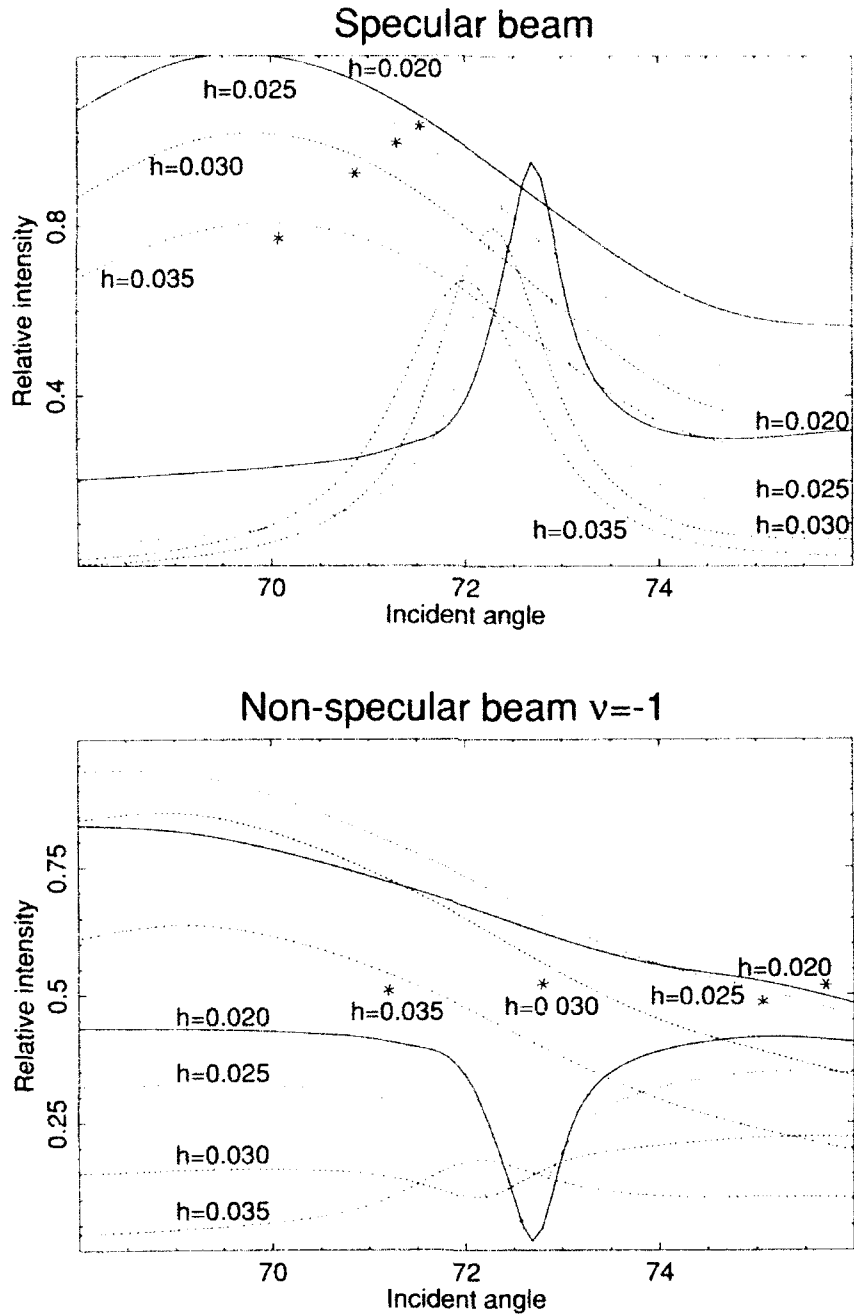
Figure 2. Branching ratios or relative intensities, $p_\nu(\gamma) = I^{(\nu)}(\gamma)/I_{flat}^{(0)}$, versus incident angle γ for four different values of the corrugation strength parameter in the wide interval $0.020 < h < 0.035$. The adjoint starred set of curves shows the corresponding background intensities defined as the square modulus of $I_{backgr}^{(\nu)}$ occurring in Eq. (8). (a) Specular relative intensity, $\nu = 0$. (b) Nonspecular relative intensity, $\nu = -1$.

Non-specular beam v=-1
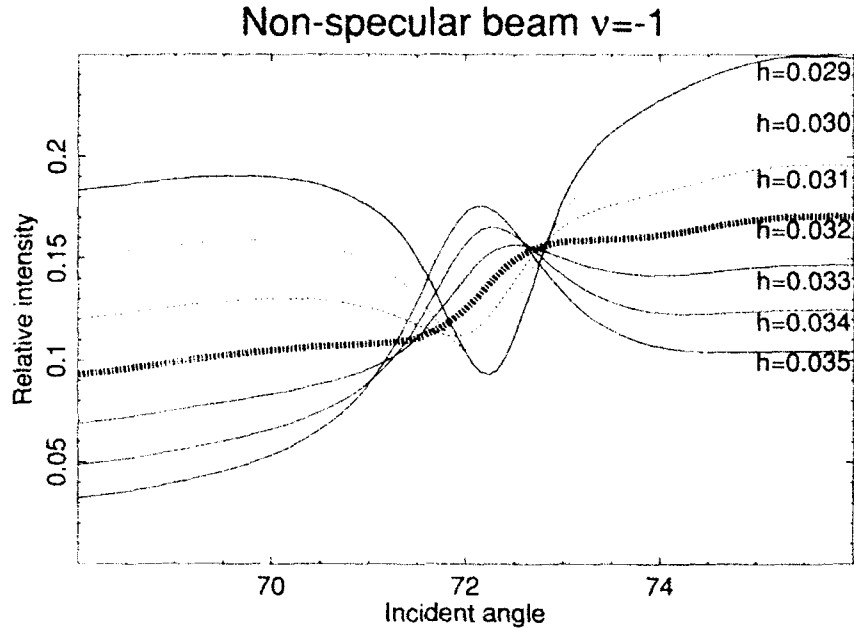
Figure 3. Nonspecular relative intensities. $v = -1$, as in Figure 2b, but with seven corrugation strengths in the smaller interval $0.029 < h < 0.035$. The dashed line displays the "leaning arcus tangent" line shape obtained for $h = 0.032$.

would have been slowly varying, one would probably get a tilted Lorentzian line-shape.

From Figures 2a and b one might guess that the effect of the resonance term in Eq. (4) is to simply add something that "rides" on the background. However, there is a very strong phase interference. This could be seen from the starred set of curves in the same figures which shows the background diffraction obtained when the resonant term is simply omitted in Eq. (4). This background diffraction does not show the slightest similarity with the apparent off-resonance "background."

A phasor diagram will be used here in order to display the interference between contributions from the background and the resonance term. The phasors are defined as $f^{(v)}_{\text{total}} = f^{(v)}_{\text{backgr}} + f^{(v)}_{\text{res}}$, where

$$f^{(v)}_{\text{total}} = \frac{\sqrt{p_z/p_z^{(v)}}}{|t_{\text{flat}}(\mathbf{p} \leftarrow \mathbf{p})|} t(\mathbf{p}^{(v)} \leftarrow \mathbf{p})$$

$$f^{(v)}_{\text{res}} = \frac{\sqrt{p_z/p_z^{(v)}}}{|t_{\text{flat}}(\mathbf{p} \leftarrow \mathbf{p})|} \frac{R^{(v)}_{\text{res}}}{E_{\text{beam}} - E_{\text{res}}}$$

$$f^{(v)}_{\text{backgr}} = \frac{\sqrt{p_z/p_z^{(v)}}}{|t_{\text{flat}}(\mathbf{p} \leftarrow \mathbf{p})|} \left(t(\mathbf{p}^{(v)} \leftarrow \mathbf{p}) - \frac{R^{(v)}_{\text{res}}}{E_{\text{beam}} - E_{\text{res}}} \right) \tag{8}$$

where the subindex "res" denotes the particular resonance under study, in this work the one labeled ($^{10}_{0}$). The reader is reminded that the E_{beam} is kept fixed, whereas

Non-specular beam v=-1

h=0.031
h=0.031
h=0.032
h=0.032
h=0.033
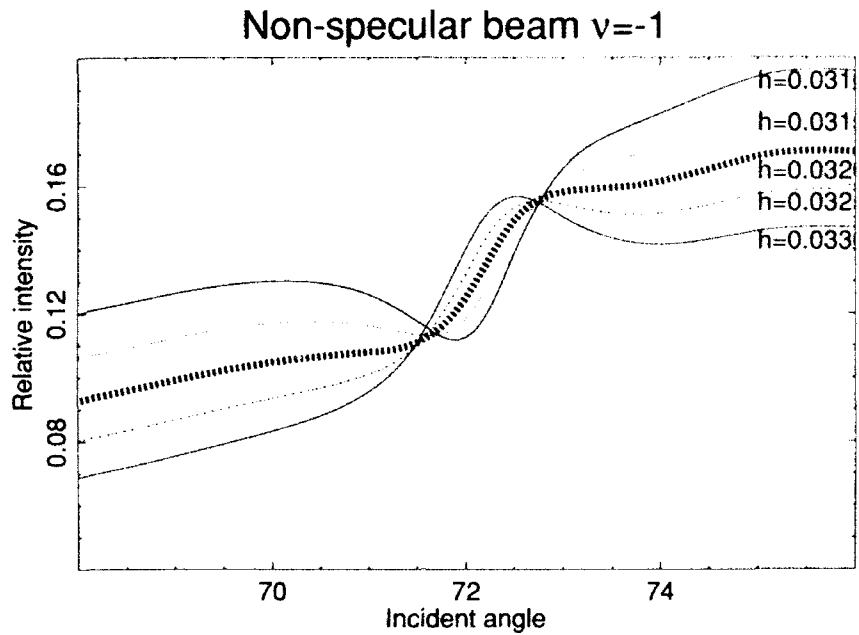
Figure 4. Nonspecular relative intensities, *v* = -1, as in Figures 2b and 3, but with five corrugation strengths in the very narrow interval 0.031 ≤ *h* ≤ 0.033. The dashed line displays the "leaning arcus tangent" line shape obtained for *h* = 0.032.

Phasors, non-specular beam v=-1
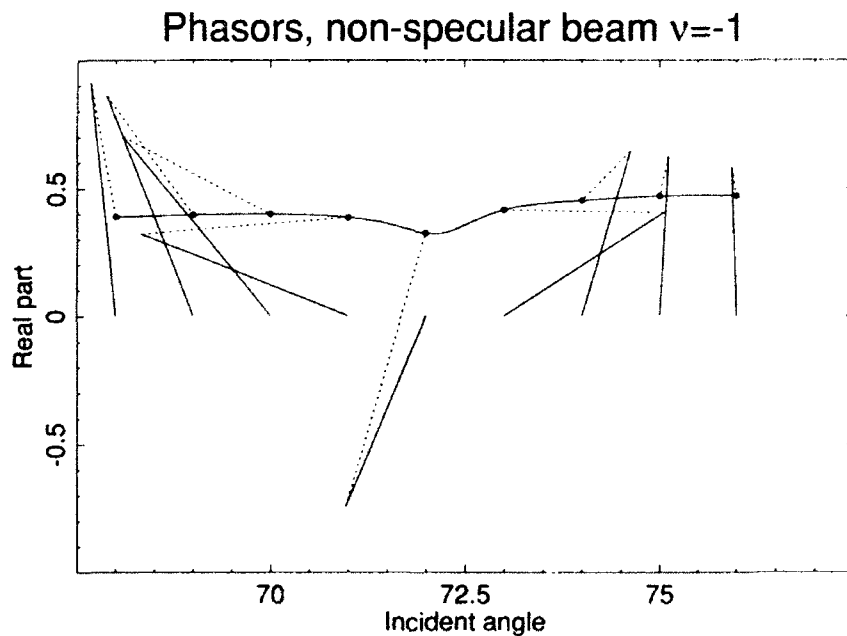
Figure 5. Phasor diagrams versus incident angles corresponding to *h* = 0.030 in Figure 2b. The total phasor for each incident angle has been rotated such that they point upward. The background phasors are displayed by straight solid lines and the resonance contribution by dotted lines. Each total phasor ends in a dot on the line that represents the square root of the corresponding intensity in Figure 2b.

all the other quantities depend on the incident angle γ. The resonance term stems from the term in the first sum of Eq. (4) whose $\mathrm{Re} E_{res} \approx E_{beam}$. For the other symbols, see Ref. 2. The relative intensities or the branching ratios for the various outgoing beams (labeled by ν) are given directly by the square modulus of the total phasors. The peculiar square roots of the ratio between the perpendicular components of the initial and final wave vectors enters in Eq. (8) due to the particular geometry of the scattering situation.

Figure 5 displays the phasors corresponding to $h = 0.030$ in Figure 2b. The absolute phase of the sum of the background phasor and the resonance phasor is irrelevant. For each incident angle the total phasor has been rotated such that it is real and positive. The dependence on the incident angle is displayed by translating the origins of the phasors along the horizontal axis.

Non-specular beam ν=-1
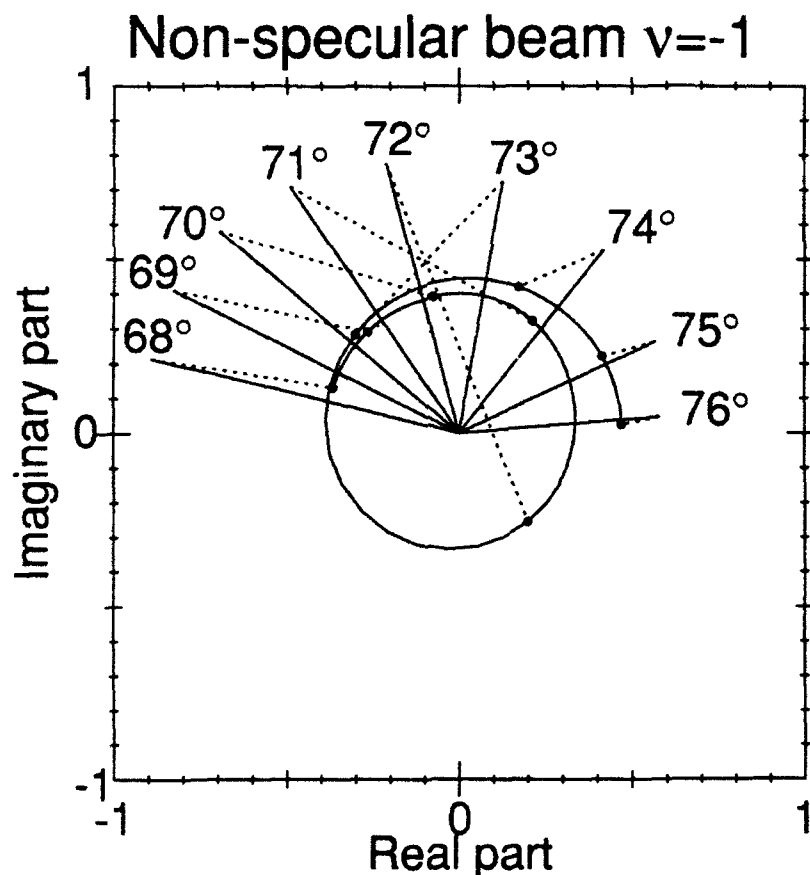
Figure 6. Phasor diagrams versus incident angles corresponding to $h = 0.030$ in Figure 2b. They are the same phasors as in Figure 5, but with a common origin. Each individual phasor has here instead been rotated such that the residues $R_{res}^{\nu}(\gamma)$ of the resonance term in Eq. (8) is real and positive.

Figure 6 shows the same phasors but in a traditional phasor diagram with all phasors beginning at the same point. Here each total phasor has been rotated such that the residue R_{res} in the resonance term in Eq. (8) is real and positive. The purpose with this kind of rotation of the phasors is to make the phasor diagram to resemble those with *fixed* residue and resonance energy but with varying total energy. Note that when increasing the incident angle from $\gamma = 68°$ to $\gamma = 76°$, the resonance phasor decreases its phase by about 180°.

Concluding Remarks

For kinetic energy, 21 meV of a He atom impinging on the Cu(115) surface the physical value of the corrugation parameter is $h = 0.027$, as was determined in Ref. 2. This value lead to reproduction of experimental specular as well as nonspecular intensities. In this work, this parameter was varied and around the increased value of $h = 0.320$ it was found that the resonance pattern displayed a dramatic sensitivity on the corrugation strength.

Although this extreme sensitivity was demonstrated for a nonphysical value of the corrugation strength, it may be possible to find a similar effect in experiments. Salanon et al. [4] has determined the energy dependence of the corrugation strength parameter for the system He/Cu(110). It was found that the corrugation strength increased monotonously with increasing He energy. Hence, it is plausible that it is possible to find a He energy for the system He/Cu(115) such that a slight variation of this energy would cause a dramatic change in the resonance pattern.

Acknowledgments

Bibliography

[1] E. Engdahl, T. Maniv, and N. Moiseyev, J. Chem. Phys. 94, 6330 (1991).
[2] E. Engdahl, N. Moiseyev, and T. Maniv, J. Chem. Phys. 94, 1636 (1991).
[3] J. Perreau and J. Lapujoulade, Surf. Sci. 122, 341 (1982).
[4] B. Salanon, G. Armand, J. Perreau, and J. Lapujoulade, Surf. Sci. 127, 135 (1983).

Electronic and Structural Properties of N and N_2 in Type-IV Semiconductors

A. FAZZIO and C. R. MARTINS DA CUNHA

Instituto de Física da Universidade de São Paulo, C P 20516, 01498 São Paulo, S P, Brazil

S. CANUTO

Departamento de Física da Universidade Federal de Pernambuco, 50000, Recife, PE, Brazil

Abstract

The electronic and structural properties of the single N and the pair N_2 complex substitutional impurity systems in type-IV semiconductors (C, Si, and Ge) are investigated through an *ab initio* LCAO cluster model. We find that the stable position for N atoms (N and N_2) is off-center with dislocation in a 111 direction to form sp³ bonds with the host atoms. Particularly for ionized complex N_2 there is a symmetry break lowering the point group symmetry of the system from D_{3d} to C_{3v}. We present also the results for hyperfine interactions over the impurity and its nearest neighbor which for isotropic terms are in fair agreement with the experiment. © 1992 John Wiley & Sons, Inc.

Introduction

The aim of this work is to investigate the behavior of the N and N_2 impurity systems in group-IV semiconductors like diamond (C), silicon (Si), and germanium (Ge) which are of considerable technological interest. In spite of the large number of theoretical studies of N in diamond [1,2] and silicon [3,4] and recently in germanium [5], this is the first calculation of the N_2 complex in these semiconductor materials. From the experimental point of view N in diamond and silicon is well-known: electron paramagnetic resonance (EPR) [6,7] data indicate that in both cases the center is distorted from T_d symmetry, the impurity being displaced along a $\langle 111 \rangle$ direction. Using an *ab initio* cluster model we predict the general role played by N atoms in type-IV semiconductors. Also, we present the total energy surface for ionized N_2, where we obtain a symmetry break (C_{3v}) different from the neutral system which is (D_{3d}). The magnetic hyperfine interactions, isotropic and anisotropic, are calculated and compared with experimental results.

We use two types of clusters to represent a small piece of a semiconductor crystal: the NX_4H_{12} cluster (X = C, Si, or Ge) to study the single N impurity centers, where the N atom is surrounded by X atoms as in the crystal (without distortions); and the $N_2X_6H_{18}$ cluster (X = C, Si, or Ge) for studying the impurity pair N_2 complexes, where each N is surrounded by 3X atoms and a N atom (as they are in the nearest-neighbor substitutional sites). The role played by the H atom is to tie up the crystal atoms valences on the surface of the cluster in sp³ bonds. Initially all geometrical

parameters are assumed as in the pure crystal, and in all calculations the H atoms are fixed at the crystalline positions.

The electronic structure is obtained using an all-electron *ab initio* (SCO) procedure. The molecular orbital expansion is over the contracted gaussian basis sets, and all one-electron, two-electron, and overlap integrals are fully calculated. We have used basis sets proposed by Dunning and Hay [8]: 4s contracted to 2s for H; 9s5p contracted to 3s, 2p for C; and 12s, 5p contracted to 6s, 4p for Si. For Ge we used the "Husinaga-MIDI" basis set [9]. The calculations were performed using the program GAMESS [10] in both restricted Hartree–Fock (RHF) and unrestricted Hartree–Fock (UHF) schemes.

Results and Discussion

Single N Impurity

Using the procedure described in the last section we analyzed the orbital structure and total-energy surfaces for a large number of positions of the N-impurity coupled with displacement of one of the nearest neighbors in the clusters. In all three semiconductors (C, Si, and Ge) the substitutional N impurity introduces an a_1 antibonding orbital in the energy gap region and, a higher energy t_2 state, leading to a nondegenerate $^2A_1$ ground state in T_d symmetry. It is important to note that no pure Jahn–Teller distortion is expected.

For the three doped semiconductors we find that the systems distort to a C_{3v} symmetry. In Figure 1 we show the total energy surface obtained from our calculations for a grid of 68 coupled displacements between N and X —bulk atom in the (111) direction. The arrow in the figure indicates the T_d initial configuration. As we can observe the N is unstable in T_d symmetry in all three semiconductors, moving to C_{3v} symmetry. We must stress that, in diamond and silicon, if we displace only the N atom keeping the first neighbors fixed, no off-center energy minimum is found: In order for this to happen, it is essential that the C or Si atom is allowed to move in the (111) direction away from the n impurity. These results are in agreement with Schultz and Messmer [3], for N in silicon. The atomic displacements obtained from our calculation of the minima in the energy surface are: for the N-atom, in a (111) direction away from the T_d substitutional site, 0.23Å in diamond, 0.47Å in Si, and 0.49Å in Ge: for the ligand atom in the C_{3v} axis in (111) direction away from the impurity, 0.36Å in diamond, 0.47Å in Si, and 0.48Å in Ge. For these coupled displacements, the gain in (cluster) total energy is 1.01 eV diamond, 0.72 eV in Si, and 0.63 eV in Ge.

As we said in the introduction, there are EPR [6,7,11] results for N in Si and Ge which provide a detailed picture of the centers. In Table I we compare our results, for the isotropic (A) and anisotropic (B) terms of the hyperfine interaction, with experimental data. We obtain an overall agreement, with the exception of the values for anisotropic term in Si (although present the observed trend) which is very small and not easy to calculate with a small cluster.

Finally, we find, for the minimum-energy a C_{3v} configuration, for all three systems. It is important to observe that the energy level in the energy gap (a^*) is not predominant from N; this energy level is concentrated in the host atom located in
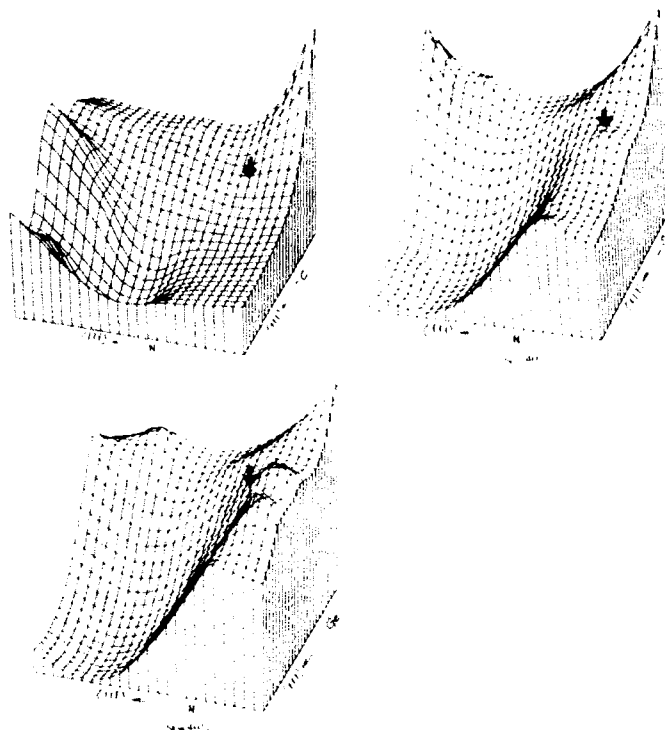
Figure 1.   Total energy surface for coupled displacement of N in diamond, silicon, and germanium. The arrow indicates the T_d initial configuration.

the (111) direction. The N atom introduces a resonant level very close to the top of the valence band with a strong p_z-character (lone-pair).

Impurity N_2 Pair

In Figure 2 we show a schematic representation for the orbitals of a N_2 substitutional pair in a D_{3d} field, together with those for the free N atom. The levels in

TABLE 1.   Isotropic and anisotropic hyperfine terms for the N impurity in diamond and silicon; all entries in units of 10^{-4} cm^{-1}, obtained using values for the isotopes ^{14}N, ^{13}C, and ^{29}Si.

	Diamond				Silicon			
	C(111)		N		Si(111)		N	
	A	B	A	B	A	B	A	B
Expt.	68.95	22.17	30.37	3.63	95.7	18.4	13.10	1.00
This work	63.7	12.5	16.1	3.9	114.1	5.3	3.7	0.3
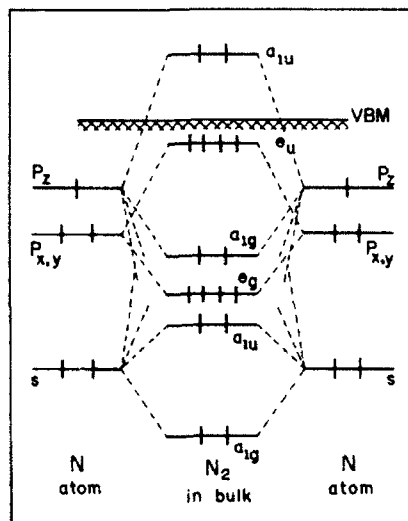
Figure 2. Schematic orbital representation of a substitutional N_2 pair in a type-IV semi-conductor (see text). VBM indicates the top of the valence band.

the N_2 pair were occupied taking into account the six dangling bonds coming from the ligands in the crystal, each one occupied by one electron. In all semiconductors studied we obtained an a_{1u}-orbital above the valence band maximum (VBM), with a strong p_z-character coming from the N atoms, which is fully occupied, leading to a nondegenerate $^1A_1$ ground state. Here also we analyzed the total-energy surface for a large number of positions for both N atoms displaced in the $\langle 111 \rangle$ direction. For all three systems in the neutral-charge state (a_{1u}^2) the symmetry remains D_{3d}, that is, the lowest total-energy configuration corresponds to a symmetrical dislo-cation of the two nitrogens, in the $\langle 111 \rangle$ direction, moving away from each other. Each N atom will use three valence electrons to bond with its ligands in the crystal, leaving two electrons to form a_{1g}-bonding and a_{1u}-antibonding orbitals, which are fully occupied. These orbitals come from the symmetrical and antisymmetrical combinations of the "lone-pair" p_z. Although, at the minimal energy, the $N-N$ distance is higher compared to the undistorted bulk, the electrons in a_{1g} ($N - p_z$) prefer to be equally distributed between the N atoms, but locally each one looks like a lone pair. In other words, each N atom becomes threefold coordinated, going to a planar-like geometry. In Figure 3 we show our results for the impurity N_2 pair in (a) carbon, (b) silicon, and (c) germanium. The displacements, in percents, plotted in the figure are relative to half of the initial $N-N$ bond length. From Figure 3 we observe that the displacement increases from diamond ($d = 0.38$ Å). to germanium ($d = 0.85$ Å). These results were expected since the covalent radius of N is small which can move more in a type-IV semiconductor with higher lattice parameter.

We also have investigated the total energy surface for the ionized system, $Si:N_2^+$. When the complex defect is positively charged it undergoes a distortion
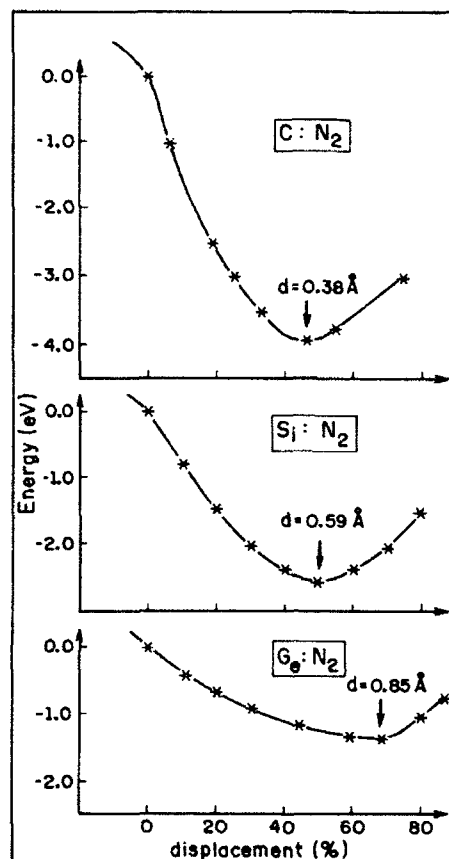
Figure 3. Total Energy curve for N₂ in diamond, silicon, and germanium. The displacements are in the (111) direction. The percentage represents the dislocation relative to the half crystal bond-distance. d represents the value of the displacement.

from the D_{3d} to the C_{3v} symmetry, differently from the neutral system. Now one of the nitrogens (N^1) stays almost at the same position as in the neutral case, and the other nitrogen atom (N^2) displaces from the initial substitutional position only 37% ($d = 0.42$ Å) in the (111) direction. Therefore, there is no inversion symmetry in the system. The gap orbital $a_1(a_{1u})$, which is now occupied by one-electron, has a very strong p_z-character from N^1, and the resonant state $a_1(a_{1g})$ has predominantly a p_z-character from the N^2 atom; each one behaves as a long pair occupied by two "unbonded" electrons in N^2 and one electron in N^1. In Figure 4 we show a contour plot of the total-energy surface, the contour spacing is 0.1 eV.

In conclusion we obtained for the N and N₂ systems in type-IV semiconductors large lattice distortions, where the role played by the N-atoms is to form a three-fold coordinated system going to a planar-like geometry and forming a sp^2 hybridization with the host atoms. Particularly for the N_2^+ in silicon we obtained a break in the symmetry with atomic rearrangement to the C_{3v} configuration.
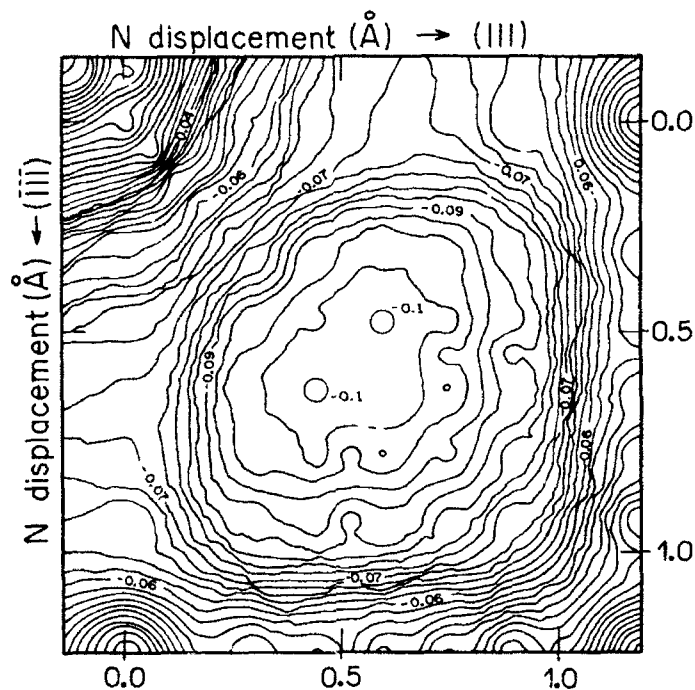
Figure 4.   Contour plot of the total energy surface for coupled displacement of N_2, in positively charged system, in the (111) direction. The contour spacing is 0.004 hartree.

Acknowledgments

Bibliography

[1] R. P. Messner and G. D. Watkins, Phys. Rev. B7, 2568 (1973).
[2] S. A. Kajihara, A. Antonelli, J. Bernholc, and R. Car, Phys. Rev. Lett. 66, 2010 (1991).
[3] P. A. Schultz and R. P. Messmer, Phys. Rev. B34, 2532 (1986).
[4] H. P. Hjalmarson, D. R. Jennison, and J. S. Binkley, Mater. Res. Soc. Symp. Proc. 59, 553 (1986).
[5] A. Fazzio, C. R. Martins da Cunha, and S. Canuto, Mater. Sci. Forum 83, 463 (1992).
[6] J. H. N. Loubser and L. Du Preez, Br. J. Appl. Phys. 16, 457 (1965).
[7] K. L. Brower, Phys. Rev. B26, 6040 (1982).
[8] T. H. Dunning, Jr., and P. J. Hay, in Modern Theoretical Chemistry Methods of Electronic Structure Theory, H. F. Schaefer III, Ed. (Plenum, New York, 1977), Vol. 3, p. 1.
[9] S. Huzinaga, J. Chem. Phys. 42, 1293 (1965).
[10] M. Dupuis, D. Splangler, and J. J. Wendowski: NRCC Software Catalog, Vol. 1 Program GG01 (GAMESS), 1980.
[11] R. J. Cook and D. H. Whiffen, Proc. R. Soc. London A295, 99 (1986).

Ab Initio SCF Calculations on Mn-Related Defects in CaF$_2$

A. C. LEWANDOWSKI and T. M. WILSON

*Computational Solid State Research Laboratory, Physics Department,
Oklahoma State University, Stillwater, Oklahoma, 74078*

Abstract

We report on the progress in a study to determine the structure of radiation-induced Mn defect complexes in CaF$_2$. The purpose of this study is to correlate the calculated transition energies with those measured experimentally and to determine what effect the inclusion of the external lattice field has on these transitions. Unrestricted open shell Hartree–Fock Self-Consistent Field (UHF) calculations were performed on the unperturbed F-center [Ca$_4$F$_6$Vac]$^{1+}$ S = 1/2, the unperturbed Mn^{2+} center [MnF$_8$]^6 S = 5/2, S = 3/2 and the Mn^{2+} perturbed F-center [Mn$_2$Ca$_3$F$_6$Vac]$^{1+}$ S = 11/2, S = 9/2 defect clusters. A method by which the effects of the external lattice field may be incorporated in the SCF procedure is developed and used in these calculations. Several transition energies are calculated and Mulliken population results for these clusters are presented and discussed. © 1992 John Wiley & Sons, Inc.

Introduction

CaF$_2$:Mn has long been the subject of intense study because of its importance in the field of thermoluminescence (TL) dosimetry [1–5]. While this material has been used in radiation dosimetry [6], the fundamental absorption and emission processes involved in the production of TL have only recently been understood to a limited degree [7–10]. One of the main questions remaining, however, is the exact nature of the various Mn-related defects and the mechanisms by which these defects control the dosimetric and absorption properties (see, for instance, Refs. [7], [8], and [11]).

Over the last two decades, a considerable amount of experimental data has become available. Optical absorption [3–5,8,9], photoluminescence [12], TL [1,2,7,10,11], and optical dichroism [13] measurements have led to a wealth of experimental data from which different models and energy level assignments have been put forward. Of particular interest is the work of McKeever et al. [8] in which they describe a series of studies of Mn absorption in CaF$_2$:Mn using a variety of methods, for samples with varying levels of Mn dopant, and over wide temperature ranges. While the experimental details are reported elsewhere [8], it is worthwhile to briefly outline their conclusions.

As a result of the experimental studies, a plausible explanation for the observed absorption spectra for irradiated samples seems to be that the Mn^{2+} ions enter the lattice substitutionally and are associated with radiation-induced defects such as *F*-

centers. This idea is further enhanced by the observed thermal quenching of the absorption bands and the appearance of an intense TL signal at 495 nm during heating following irradiation. This model envisions several types of Mn-defect complex each differing as to the location of the radiation-induced defect with respect to the Mn^{2+} ion, the type of the radiation-induced defect, and the number of Mn^{2+} ions within the complex [8]. However, a remaining question is whether the observed spectra are due to internal Mn^{2+} transitions or whether the transitions actually take place within the F-center.

According to the internal transition model, the association of the Mn^{2+} ion with the F-center gives rise to a spin exchange coupling which in turn increases the oscillator strength of the Mn^{2+} transitions by a factor of 10^3. Since the ground state of the $3d^5$ electrons in Mn^{2+} is a spin sextet the excited state transitions all require a spin reversal and hence are highly forbidden. This and parity considerations lead to excited state lifetimes greater than 10^{-3} s and oscillator strengths of the order $10^{-6} - 10^{-7}$. Thus this theory relies on the perturbation of the neighboring defect to increase the oscillator strengths so that the internal Mn^{2+} transitions become visible and give measurable absorption peaks.

The alternative model to explain the observed spectra and its annealing behavior does not rely on the enhancement of the oscillator strengths as such. This model stems mainly from the observation that a 564 nm absorption band quenches at the same temperature as the lower wavelength bands leading to the conclusion that the 564 nm band is due to the same defect as the lower wavelength Mn-related absorption bands. Since the quenching of the Mn-related bands is accompanied by a TL emission at 495 nm, and since this emission has already been confirmed as being due to the first excited state to ground-state transition in Mn^{2+} (Ref. [8]), it follows that the 564 nm band is not due to Mn^{2+} transitions. Therefore, the lower wavelength absorption bands are also not due to internal Mn^{2+} transitions. A model that could explain this behavior is that the transitions actually occur within an F-center perturbed by one or more Mn^{2+} ions.

The above two models notwithstanding, optical dichroism measurements [13] indicate that the optically active defect possess C_{2v} symmetry with an alignment along the $\langle 100 \rangle$-direction. While several defect structures could possess this symmetry [14] (such as M-centers or Mn/H-centers), this alignment indicates that the center could consist of an F-center perturbed by two Mn^{2+} ions.

In this article we discuss the results of ab $initio$ self-consistent field molecular orbital calculations performed on the unperturbed F-center $[Ca_4F_6Vac]^{1+}$ $S = 1/2$, the unperturbed Mn^{2+} center $[MnF_8]^{6-}$ $S = 5/2$, $S = 3/2$, and the Mn-perturbed F-center $[Mn_2Ca_2F_6Vac]^{1+}$ $S = 11/2$, $S = 9/2$ defect structures. The main purpose of this investigation is to verify or exclude one of the above models by determining which one produces energy levels which correspond most closely with the observed spectra.

The calculations were performed using the set of programs GAUSSIAN 90 (Ref. [15]). A new feature recently added to these programs is the SOLVENT option which allows the placement of charges outside the cluster. In this way one may place either external point charges or points about which a spherical distribution

of charge may be placed. This improved option allows the possibility that one may construct an external field that would model an infinite lattice both in symmetry and in electrostatic variation within the SCF cluster. As a result, it has recently become possible within these programs to determine the effects an external field has on the transition energies.

The Calculations

Cluster Geometry and Basis Set

The $[MnF_8]^{6-}$ cluster consists of a Mn^{2+} ion surrounded by eight F^- ions arranged in O_h symmetry. With the Mn^{2+} at the origin the F^- ions are located at $(\pm\frac{a}{2}, \pm\frac{a}{2}, \pm\frac{a}{2})$, where a is the F—F distance, taken to be 2.7314 Å (ref. [14]). Figure 1(a) shows the geometry of this cluster. The $[Ca_4F_6Vac]^{1+}$ cluster was constructed so that the vacancy site is at the origin surrounded by the four nearest-neighbor Ca^{2+} ions arranged in T_d symmetry at $(\frac{a}{2}, \frac{a}{2}, \frac{a}{2})$, $(-\frac{a}{2}, \frac{a}{2}, -\frac{a}{2})$, $(\frac{a}{2}, -\frac{a}{2}, -\frac{a}{2})$, $(-\frac{a}{2}, -\frac{a}{2}, \frac{a}{2})$, and the six next nearest-neighbor F^- ions at $(\pm a,0,0), (0,\pm a,0), (0,0,\pm a)$. Figure 1(b) shows this cluster. The $[Mn_2Ca_2F_6Vac]^{1+}$ cluster has the same geometry
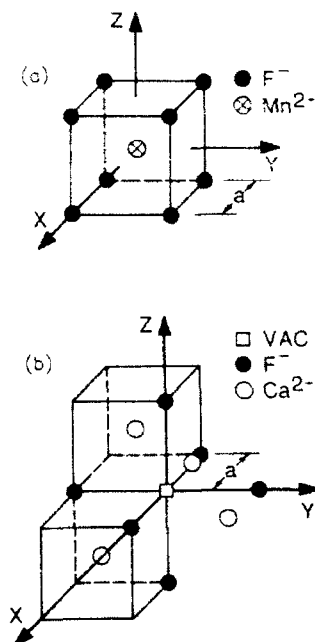
Figure 1. (a) Mn-impurity, $[MnF_8]^{6-}$, and (b) unperturbed F-center, $[Ca_4F_6Vac]^{1+}$ clusters used for the present calculations. This figure also shows the geometry of the Mn-perturbed F-center, $[Mn_2Ca_2F_6Vac]^{1+}$ cluster if two of the Ca^{2+} ions are replaced by two Mn^{2+} ions.

TABLE I. The exponents (Bohr⁻²) and the coefficients of the Gaussian functions used as the variational basis set in the present study. The contraction coefficients multiply the single normalized Gaussians. The notation $x(\pm a)$ means $x \times 10^{\pm a}$.

Shell type	Calcium		Fluorine		Manganese	
	Exp.	Coeff.	Exp.	Coeff.	Exp.	Coeff.
s	8.876 (+3)	1.754 (−2)	1.041 (+3)	1.923 (−2)	8.876 (+3)	1.754 (−2)
	1.339 (+3)	1.226 (−1)	1.567 (+2)	1.333 (−1)	1.339 (+3)	1.226 (−1)
	3.037 (+2)	4.422 (−1)	3.512 (+1)	4.610 (−1)	3.037 (+2)	4.422 (−1)
	8.164 (+1)	5.516 (−1)	9.293	5.267 (−1)	8.164 (+1)	5.516 (−1)
s	1.225 (+2)	−1.060 (−1)	1.399 (+1)	−7.975 (−2)	1.225 (+2)	1.060 (−1)
	1.327 (+1)	6.361 (−1)	1.162	5.839 (−1)	1.327 (+1)	6.361 (−1)
	5.458	4.354 (−1)	3.232 (−1)	5.076 (−1)	5.458	4.354 (−1)
s	9.586	−2.256 (−1)	8.407 (−2)	7.169 (−1)	9.586	2.256 (−1)
	1.535	7.285 (−1)	3.277 (−2)	3.161 (−1)	1.535	7.285 (−1)
	6.139 (−1)	4.029 (−1)			6.139 (−1)	4.029 (−1)
s	1.016 (−1)	6.976 (−1)			1.016 (−1)	6.976 (−1)
	3.574 (−2)	3.442 (−1)			3.574 (−2)	3.442 (−1)
p	3.498 (+2)	2.956 (−2)	1.911 (+1)	5.236 (−2)	3.498 (+2)	2.956 (−2)
	8.161 (+1)	1.871 (−1)	4.146	2.585 (−1)	8.161 (+1)	1.871 (−1)
	2.497 (+1)	5.076 (−1)	1.072	5.083 (−1)	2.497 (+1)	5.076 (−1)
	8.359	4.518 (−1)	2.398 (−1)	4.634 (−1)	8.359	4.517 (−1)
p	4.973 (−1)	2.291 (−1)	1.004	2.738 (−1)	4.973 (−1)	2.291 (−1)
	3.526	3.258 (−1)	9.598 (−2)	3.580 (−1)	3.526	3.258 (−1)
	1.334	5.647 (−1)	3.360 (−1)	5.439 (−1)	1.332	5.647 (−1)
p	8.152 (−2)	8.148 (−1)			8.152 (−2)	8.148 (−1)
	2.963 (−1)	2.654 (−1)			2.963 (−1)	2.654 (−1)
d					2.096 (+1)	6.373 (−2)
					5.516	2.822 (−1)
					1.668	5.196 (−1)
					4.628 (−1)	4.433 (−1)
d					5.499	1.560 (−1)
					1.311	4.892 (−1)
					3.098 (−1)	6.272 (−2)

as shown in Figure 1(b) except that two of the Ca^{2+} ions are replaced by Mn^{2+} ions. It should be further noted that for these calculations the lattice constant a in all the clusters was taken to be the equilibrium F—F distance for the perfect lattice and that no relaxation effects were considered.

The choice of the variational basis set is perhaps the most important consideration when attempting to perform accurate SCF calculations for many electron systems. Basis set related errors have been reviewed extensively in the literature [16]. Of particular interest in these calculations is the correct modeling of the Mn 3d orbitals which are believed to be the ones primarily responsible for the observed transitions. As always in calculations of this type, one attempts to choose a basis that is both flexible enough so as not to unduly bias the results and limited enough for practical use. The general strategy adopted here was to construct the core orbitals mainly from standard basis functions used for atomic calculations of the F⁻ ions and Ca

and Mn atoms from Huzinaga [17]. These were then augmented by the addition of more diffuse s, p, and d Gaussian-type functions.

The basis set adopted for the present study is shown in Table 1. Nine atomic basis functions were used for fluorine, 13 for calcium and 23 for manganese. Each atomic basis function consists of a linear combination (contraction) of Gaussian-type functions which are the product of a radial Gaussian and a real spherical harmonic function. For the F-center clusters, the vacancy was represented by two s-type atomic basis functions (not shown in Table 1) each consisting of a single normalized Gaussian with exponents 8.0 and 0.5, respectively. The average radii of these Gaussians were 0.282 and 1.128 Bohr, respectively. GAUSSIAN 90 allows the option by which one may designate nonatomic centers ("ghost atoms") about which basis functions may be placed. While this option allows for the modeling of the F-center vacancy, the program's symmetry determination routines are deactivated in the presence of ghost atoms. As a consequence, this limits the symmetry identification of the Mn-perturbed F-center states.

The External Field

The deficiency of isolated cluster calculations has been pointed out by several authors [18]. Preliminary F-center calculations have shown that cluster calculations can give quite reasonable results for localized states of defects, like the ground state, but fail to adequately describe diffuse states, like the excited states of the F-center, where the neglect of the rest of the lattice becomes very important [19]. It therefore becomes important to approach the studies of Mn/F-center complexes within the framework of a model which takes into account the interactions of the defect/impurity cluster with the surrounding lattice.

GAUSSIAN 90 allows the placement outside the cluster of a distribution of either point ions or points about which a spherical distribution of charge may be located. Given this flexibility, it is possible to construct external fields that vary greatly in symmetry and electrostatic variation within the cluster. However, one must still determine the criteria to be satisfied when an accurate model of the external lattice is achieved. For the present calculations the criterion chosen was that a proper arrangement of point ions and/or spherical charge densities will be such that it produces the variation in field intensities that correspond to those predicted from calculations of the Madelung potential at F and Ca sites for the perfect lattice. For instance, for the perturbed and unperturbed F-center clusters it was necessary to choose an appropriate external arrangement so the electrostatic field thus produced would be the same at the vacancy site as at one of the next nearest-neighbor F sites excluding the contributions to the field from the ions of the SCF cluster. This arrangement must also simultaneously produce a variation in the external field from a F-site to a Ca-site that would be predicted from the calculated Madelung potentials for the perfect lattice-again, excluding the contributions from the SCF cluster.

Figure 2 shows the variation in the ratio of the potential at the Mn site to the potential at a F site due to the external lattice as a function of external lattice size
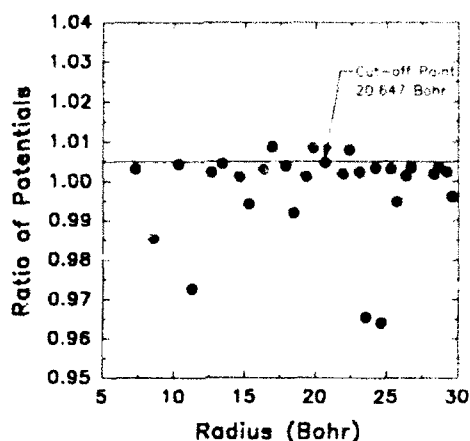
Figure 2. The variation in the ratio of the potential at the Mn²⁺ site to the potential at a F site due to the external lattice as a function of lattice size about the [MnF₈]⁶ cluster. The cut-off point at 20.647 Bohr best satisfies the Madelung ratio condition of 1.005.

about the [MnF₈]⁶⁻ cluster. The external lattice consisted of +2 and −1 point charges arranged in the fluorite structure representing the Ca²⁺ and F ions, respectively. The Madelung potentials at the Mn²⁺ and F sites are −19.95 v and 10.73 v, respectively [14]. After subtracting the electrostatic contributions to these Madelung potentials by the SCF cluster ions, the Mn-site to F-site Madelung ratio was found to be 1.005. From Figure 2 it can seen that an external lattice extending out to approximately 20.647 Bohr produces a ratio of about 1.004 which compares well to the desired ratio. Hence, for the [MnF₈]⁶ calculations the external field was modeled by placing outside the cluster point charges arranged in a fluorite structure out to a radius of 20.647 Bohr. In total, this consisted of 412 point charges of which 140 had charge +2 while the remaining 272 had charge −1.

For the F-center clusters a slightly more involved approach was required. Figure 3 shows an overlay of the ratio of the potential at a Ca²⁺ site to the potential at a F⁻ site (●), and the ratio of the potential at the vacancy to the potential at a F site (O) as a function of external lattice size about either the [Ca₄F₆Vac]¹⁺ or the [Mn₂Ca₂F₆Vac]¹⁺ cluster. The external lattice for this figure consists of +2 and −1 point charges arranged in the fluorite structure. After subtracting the electrostatic contributions to the Ca²⁺ and F site Madelung potentials from the SCF cluster, the Ca-site to F-site Madelung ratio was found to be 2.399. The problem is then to find an optimum external lattice size that will produce this desired Ca-site to F-site ratio and simultaneously produce a vacancy-site to F-site Madelung ratio of 1.000. While Figure 3 shows more variation than Figure 2, nowhere are these two conditions simultaneously satisfied. As a consequence, it was necessary to choose a lattice size that best approximates the desired conditions then vary the charges and/or the radial distribution of the charges on the point ions so as to produce a field that would satisfy the above Madelung ratio conditions.
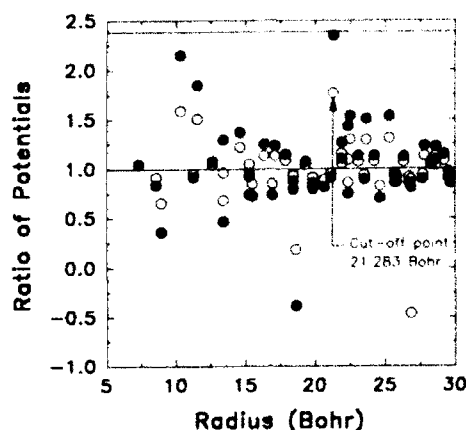
Figure 3. The variation in the ratio of the potential at a Ca^{2+} site to the potential at a F$^-$ site (●), and the ratio of the potential at the vacancy to the potential at a F site (○) as a function of external lattice size about either the [Ca$_4$F$_6$Vac]$^{1+}$ or the [Mn$_2$Ca$_2$F$_6$Vac]$^{1+}$ cluster. The cut-off point at 21.283 Bohr best satisfies the condition. $V(r_{Ca})/V(r_f) = 2.399$.

From Figure 3 it is seen that the desired conditions come close to being satisfied for a point ion arrangement out to a distance of 21.283 Bohr. This arrangement contains a total of 446 point ions of which 298 have -1 charge and the remaining 148 have $+2$ charge.

The optimization scheme adopted for the present study envisions the SCF cluster surrounded first by an *active shell* in which both the charges of the ions and the Gaussian exponents of the point ion charge distributions are varied. Surrounding this shell the remaining point ions have only their charges varied. This will be known as the *point ion shell*. For the present study, the active shell was taken to extend from just outside the SCF cluster to a radius of 11.3 Bohr containing a total of 50 ions of which 26 will have an initial charge of -1 and 24 will have an initial charge of $+2$. The point ion shell was then taken to extend from just outside the active shell out to a radius of 21.283 Bohr containing a total of 396 point ions of which 272 will have an initial charge of -1 and 124 will have an initial charge of $+2$.

To calculate the field due to an arrangement of N ions each having a spherical charge density described by a normalized s-type Gaussian, we consider an external charge density of the form,

$$\rho(\mathbf{r}') = \sum_{i=1}^{N} q_i \left(\frac{\xi_i}{\pi}\right)^{3/2} e^{-\xi_i |\mathbf{r}'-\mathbf{R}_i|^2}, \tag{1}$$

where q_i is the total charge of ion i at location $\mathbf{R}_i$ with Gaussian exponent ξ_i. The potential $V(\mathbf{r})$ is then,

$$V(\mathbf{r}) = \sum_{i=1}^{N} q_i \left(\frac{\xi_i}{\pi}\right)^{3/2} \int \frac{e^{-\xi_i |\mathbf{r}'-\mathbf{R}_i|^2}}{|\mathbf{r}' - \mathbf{r}|} d\mathbf{r}'. \tag{2}$$

Integrating over all space, the expression for the potential then becomes,

$$V(r) = \sum_i q_i \frac{\text{erf}[\xi_i^{1/2} |R_i - r|]}{|R_i - r|},\tag{3}$$

where here the error function is defined, $\text{erf}(x) = 2/\sqrt{\pi} \int_0^x e^{-u^2} du$. The final expression for the potential including both the active and point ion shells becomes,

$$V(r) = q_F^a \sum_{i=1}^{N_F^a} \frac{\text{erf}[\xi_F^{1/2} |R_i^F - r|]}{|R_i^F - r|} + q_{Ca}^a \sum_{i=1}^{N_{Ca}^a} \frac{\text{erf}[\xi_{Ca}^{1/2} |R_i^{Ca} - r|]}{|R_i^{Ca} - r|}$$

$$+ q_F^p \sum_{i=1}^{N_F^p} \frac{1}{|R_i^F - r|} + q_{Ca}^p \sum_{i=1}^{N_{Ca}^p} \frac{1}{|R_i^{Ca} - r|}.\tag{4}$$

where, for instance the notation, $\sum_{i=1}^{N_F^a}$ means that the sum is to consist of all F ions in the active shell only. The terms, q_F^a, ξ_F, q_{Ca}^a, ξ_{Ca}, q_F^p, q_{Ca}^p become variational parameters to be adjusted so that $V(r_{Ca})/V(r_F) = 2.399$ and $V(r_{Ca})/V(r_F) = 1.000$.

It should be noted that the above procedure is not a fit but merely an optimization since the number of "data points" is two whereas the number of adjustable parameters is six. This leads to a large "degeneracy of fit" meaning that a large number of different parameter combinations satisfy the fit criteria. This problem could be responsible for physically unreasonable optimized parameters. For instance. if ξ_{Ca} and ξ_F are set to 2000 Bohr^{-2} to form tight Gaussians. the charges of the both the active and point ion shells take on very large positive and negative values. Since. from the initial selection of the lattice size the Madelung ratios only vary slightly from the desired ones. one would expect that the charges in both the active and point ion shells would also vary slightly from their initial values. Hence. it was found necessary to allow ξ_{Ca} and/or ξ_F to vary as well.

In a series of optimizations. in which different initial parameter sets were experimented with. it was generally found that. upon optimization. the value of ξ_F only slightly effected the outcome of the value of ξ_{Ca} when ξ_F was chosen to form tight Gaussians about the F ions. When ξ_F was varied so as to allow a more diffuse charge. the value of ξ_{Ca} also varied to produce a more diffuse charge about the Ca ions. Since F ions form the shell just outside the cluster. it was considered desirable to model them as tight Gaussians ($\xi_F \sim 2000$ Bohr^{-2}) and allow ξ_{Ca} and the charges in and outside the active shell to vary.

The parameters chosen to produce the external field in the present study were: $q_F^a = -0.9818$. $\xi_F = 2000.0$. $q_{Ca}^a = 2.0186$. $\xi_{Ca} = 0.06164$. $q_F^p = -0.9977$. $q_{Ca}^p = 2.0052$. These parameters gave an essentially exact agreement to the desired Madelung ratios. Figure 4(a) shows the variation in the potential from the Vacancy site to a Ca-site in the F-center cluster and Figure 4(b) shows the variation from the Vacancy to a F-site for the same cluster. From these figures it can be seen that the desired variations are achieved with the above parameters. The potential profiles are as expected. and the deviations from the initial charges are small which is also expected. The charge on the Ca ions within the active shell is more diffuse than
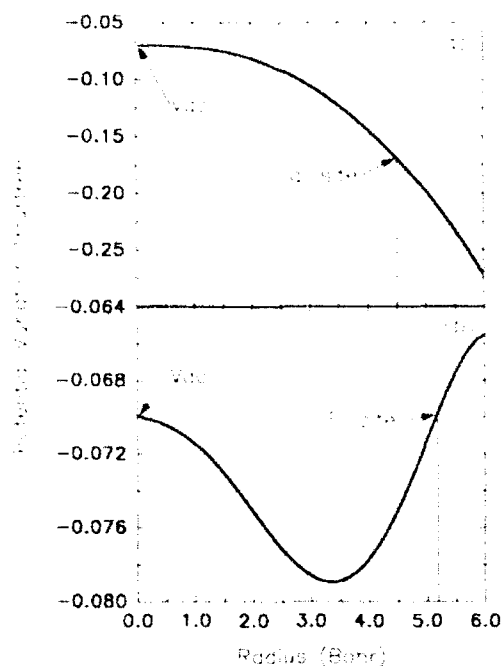
Figure 4. The variation in the potential from: (a) the vacancy to a Ca site and, (b) the vacancy to a F site as determined from optimizing the external lattice parameters to match the Madelung ratio conditions for either the unperturbed or Mn-perturbed F-center cluster.

expected; however, we believe that this is merely an artifact of approximating an infinite lattice with a finite arrangement of ions and does not represent a serious intrusion upon the bonding characteristics within the SCF cluster. It has been suggested that in addition to satisfying the above Madelung ratio conditions, one may reduce the degeneracy of fit problem by imposing the additional condition that the *variation* of the potential (that is, $V(r_{ca}) - V(r_f) = 4.9164$ v and $V(r_{ca}) - V(r_f) = 0.0000$ v) within the cluster be satisfied [20]. While this suggestion represents a refinement in the way in which the external field is modeled, the method chosen for this study still provides for a good first approximation. It has been found that when this additional constraint is imposed, the potential due to the external field at a Ca-site within the cluster is further reduced by approximately 2.00 v with respect to the vacancy.

Results and Discussion

The main purpose of this study is to identify the radiation-induced Mn/defect complex in CaF and to correlate the calculated transition energies with those measured experimentally and to determine what effect (if any) the external lattice has on these transitions. Unrestricted open shell Hartree–Fock SCF (UHF) calculations were performed on the [MnF₆] cluster for the ground-state spin configuration

$S = 5/2$ both with and without the external field contributions. The same UHF calculations were performed on the first excited spin configuration, $S = 3/2$, also with and without the external field. In addition to the ground state of the $S = 3/2$ spin configuration, an additional excited state of this spin was calculated with the aid of the method of singly-excited configuration interaction (CIS). The CIS method enables one to calculate states that exist in the space spanned by single substitutions of the reference state. It is a useful tool in identifying excited configurations that are reachable by a single particle interchange. Thus, it is sometimes possible from a CIS calculation to determine the initial guess that would be necessary to coax the UHF procedure into convergence for an excited configuration. In this regard, excited state multiconfigurational self-consistent field (MCSCF) calculations [21,22] will be helpful both in terms of correcting the presently calculated transitions and elucidating transitions not presented here.

At present, within the context of UHF calculations we have identified with certainty two transitions within the $[MnF_8]^{6-}$ complex. The ground state to first excited state transition ($^6A_{1g} \rightarrow {}^4T_{1g}({}^4G)$ [$(t_{2g})_a^2(e_g)_a^2(t_{2g})_d^1$]) has a UHF energy of 3.44 eV. This differs from the experimental value for this transition of 2.81 eV (Ref. [8]) by 0.63 eV. Errors of this magnitude for d-to-d transitions in Mn-related defects in other hosts have been reported in the literature [23]. For instance, Richardson et al. [23] report a UHF error of 1.6 eV for the ground state to first excited state transition for Mn defects in ZnS. Table II shows a summary of Mulliken population analysis for the clusters and states considered in this study. The table shows the results obtained both with and without the external field for the Mn defect and F-center clusters. For the Mn defect cluster, this analysis shows that the effect of the external field tends to localize the electron charge density slightly more about the fluorines while reducing it about the central Mn. This appears to be true for both the ground and excited states. However, the effect of the external field on the ground to first excited transition energy is minimal. That is, it does not change the UHF calculated transition energy until well past the number of significant figures reported here. This observation is consistent with studies of Mn centers in other hosts [23]. The excited configuration $(t_{2g})_a^2(e_g)_a^2(e_g)_d^1$ was found to have a UHF energy 4.23 eV above the ground state. The state appears to be either the $^4T_{2g}({}^4G)$ or $^4E_g({}^4G)$. A firm state designation will not be possible until the MCSCF calculations are complete. Nevertheless, this would place this state approximately 1.09 eV above its experimental value.

UHF results for the unperturbed F-center, $[Ca_4F_6Vac]^{1+}$ cluster show transitions that correspond to excitations from the $^2A_1$ ground state to the triply degenerate $^2T_2$ state in T_d symmetry. The UHF energies for these transitions are 4.66 eV and 4.14 eV with and without the external field, respectively. These are spin-allowed transitions. The oscillator strength for the isolated F-center cluster was calculated to be 0.055. In the presence of the external field this value reduced to 0.042. Table II shows the total atomic charges from a Mulliken population analysis for the ground state both with and without the presence of the external field. This result shows that the effect of the field is to localize more charge in the vacancy and slightly more on the fluorines while reducing the charge on the calciums.

TABLE II. Summary of Mulliken population analysis for the Mn defect ([MnF₈]⁶⁻), the F-center. ([Ca₄F₆Vac]¹⁺), and the Mn-perturbed F-center, ([Mn₂Ca₂F₆Vac]¹⁺) clusters obtained from LIH calculations both with and without an external field. The charges are in atomic units.

Cluster and state	Atomic site	Isolated cluster	Cluster with external field
[MnF₈]⁶⁻ ⁶A₁ᵧ	Mn	1.8495	1.8879
	F	-0.9812	-0.9860
⁴T₁ᵧ(⁴G)	Mn	1.8473	1.8853
	Fᵃ	-0.9810	-0.9858
		-0.9808	-0.9855
⁴T₂ᵧ(⁴G) or ⁴Eᵧ(⁴G)	Mn	1.8371	1.8750
	Fᵃ	-0.9814	-0.9862
		-0.9778	-0.9826
[Ca₄F₆Vac]¹⁺ ²A₁	Vac.	-0.5004	-0.6001
	Ca	0.8409	0.8689
	F	-0.3106	-0.3126
[Mn₂Ca₂F₆Vac]¹⁺ ¹²A₁	Vac	—	-0.0672
	Mn	—	1.3921
	Ca	—	0.9299
	F(1)ᵇ	—	-0.2986
	F(2)	—	-0.8492
	F(3→6)	—	-0.6072
¹⁰?	Vac.	—	-0.0980
	Mn	—	1.4252
	Ca	—	0.9265
	F(1)ᵇ	—	-0.2989
	F(2)	—	-0.8672
	F(3→6)	—	-0.6098

ᵃ In both of these states F atoms lying in a plane passing diagonally through the center of the cube in Figure 1(a) have identical charges.

ᵇ In this cluster F(1) is the F atom lying between Ca atoms. F(2) lies between the Mn atoms, and F(3→6) signify the remaining F atoms in Figure 1(b).

Theories of the F-center in the fluorite structure have essentially relied on point ion models [14]. To date, there has been very little work that approaches the theory of the F-center in the alkaline earth fluorides from an *ab initio* standpoint. Past theoretical work has mainly consisted of various pseudo-potential formulations which differ mainly in the degree by which the anisotropy of the potential is taken into account [14] or semi-empirical multiple scattering Xα methods [24,25]. Both of these methods are semi-empirical in nature and as a consequence provide transition energies that agree well with experiment. In the alkaline earth fluorides, the F-center has T_d symmetry and the anisotropy is expected to be more important than in the alkali halides. Bartram et al. [26], for instance, emphasize the importance of this anisotropy to account for the observed discrepancy in energies from pseudo-potential calculations and the observed F-band in CaF₂. In their calculations they expand the point ion potential up to $L = 6$ but argue that better agreement would be achieved if polarization, distortion, and ion size effects were taken into account.

While these considerations are quite important, it must be emphasized that in the *ab initio* approach the form of the potential must be modeled independently of the SCF variational scheme. It is therefore quite conceivable that the discrepancy in the *F*-center transition energies as compared with the experimental value of 3.30 eV (Ref. [14]) could be due to an inaccurate modeling of the external potential as well as the obvious need for including correlation effects. In addition, we have not considered the effects of allowing the nearest-neighbor calciums to relax. This would certainly have a significant effect on the calculated transition energy [18]. Improvements in this regard should include higher-order terms beyond the Madelung constant in the point ion potential expansion and a greater number of points within the cluster upon which to optimize. This could be of crucial importance in *F*-center calculations where even the first excited state wavefunctions are expected to be much more diffuse than the localized ground state. The solution is to perform configuration interaction calculations up to triply or even higher-order substitutions or to perform multiconfigurational SCF calculations. Both options are currently under investigation. However, it is presently unclear how polarization effects could be incorporated in an *ab initio* SCF formalism without greatly increasing the size of the SCF cluster.

UHF calculations for the Mn-perturbed *F*-center, [Mn$_2$Ca$_2$F$_6$Vac]$^{1+}$, cluster could only be performed in the presence of an external field. Without the external field self-consistent results could not be achieved with this basis. However, since we feel that we are using a sufficiently flexible basis, this convergence problem must indicate that the correct modeling of the field is of crucial importance in the analysis of this cluster. This cluster has C$_2$, symmetry so it is assumed (though not proven here) that these transitions represent excitations from a ^{12}A$_1$ state to various excited states of spin multiplicity ten. The first excited state of this multiplicity has been identified 0.48 eV above the ground state. This cluster has been proposed as a possible model that would describe the experimentally observed transitions [8]. This model envisions a Mn-perturbed *F*-center in which the observed transitions take place. From Table II, however, the results of a Mulliken population analysis show that compared to the unperturbed *F*-center, the electron in the Mn-perturbed *F*-center does not stay in the vacancy but becomes localized on the fluorines that neighbor the manganese atoms both in the ground state and in the first excited state. These calculations seem to indicate that an electron in the vacancy is not a stable configuration for this cluster. As a consequence, no *F*-center is actually formed and therefore no absorption bands can be attributable to transitions "within" the *F*-center. As further evidence, the 0.48 eV energy associated with a spin flip of the "*F*-center" electron is too small to account for any of the observed spectra. This result further supports the alternative model that the observed spectra is due to d-to-d transitions within the Mn ions perturbed by a vacancy.

A model of this type could also explain the thermal quenching behavior observed in the absorption bands [8]. In particular, this model would need to explain the presence and behavior of the 564 nm band. It has been shown experimentally that this band quenches along with and at the same rate as the other lower wavelength bands [8]. The quenching of these bands is related to the production of Tl at 495

nm which has been shown to be due to the first excited state to ground state transition in Mn^{2+} for unirradiated samples. Optical bleaching of this band would also need to be explained by this model. The experimental results [13] show that bleaching at 560 nm causes this and the lower wavelength bands to decay at the same rate with no associated luminescence. Taken together, this evidence strongly indicates that the 564 nm band is due to the same defect as the lower wavelength bands. Any model must, therefore, explain both its presence and behavior. The results presented in this article tend to favor the internal-transition model, and until a more comprehensive series of calculations is completed, the question as to whether this model explains the presence and behavior of the 564 nm band is still open.

Acknowledgments

Bibliography

[1] R. J. Ginther and R. D. Kirk, J. Electrochem. Soc. **104**, 365 (1957).

[2] P. J. Alonso and R. Alcalá, J. Lumin. **21**, 147 (1980).

[3] P. J. Alonso and R. Alcalá, J. Lumin. **22**, 321 (1981).

[4] R. Alcalá, P. J. Alonso, G. Lalinde, and A. Carretero, Phys. Status Solidi B**98**, 315 (1980).

[5] P. J. Alonso, V. M. Orera, and R. Alcalá, Phys. Status Solidi B**99**, 585 (1980).

[6] S. W. S. McKeever, *Thermoluminescence of Solids* (Cambridge University Press, Cambridge, 1985).

[7] J. F. Rhodes, R. J. Abbundi, D. W. Cooke, V. K. Mathur, and M. D. Brown, Phys. Rev. B**31** (8), 5393 (1985).

[8] S. W. S. McKeever, B. Jassemnejad, J. F. Landreth, and M. D. Brown, J. Appl. Phys. **60** (3), 1124 (1986).

[9] D. W. McMasters, B. Jassemnejad, and S. W. S. McKeever, J. Phys. D **20**, 1182 (1987).

[10] B. Jassemnejad, R. J. Abbundi, M. D. Brown, and S. W. S. McKeever, Phys. Status Solidi A**108**, 753 (1988).

[11] S. W. S. McKeever, *Thermoluminescence Processes in Manganese-doped CaF$_2$*, Naval Surface Weapons Center Reports, Oklahoma State University, Stillwater, April 1985 to June 1987 (unpublished).

[12] S. W. S. McKeever, *Photoluminescence Measurements in CaF$_2$:Mn*, Naval Surface Weapons Center Reports, Oklahoma State University, Stillwater, January 1989 (unpublished).

[13] S. W. S. McKeever, *Optical Dichroism in Calcium Fluoride Doped with Manganese*, Naval Surface Weapons Center Reports, Oklahoma State University, Stillwater, January 1988 (unpublished).

[14] W. Hayes, Ed., *Crystals with the Fluorite Structure* (Oxford University Press, Oxford, 1974).

[15] M. J. Frisch, M. Head-Gordon, G. W. Trucks, J. B. Foresman, H. B. Schlegel, K. Raghavachari, M. A. Robb, J. S. Binkley, C. Gonzalez, D. J. Defrees, D. J. Fox, R. A. Whiteside, R. Seeger, C. F. Melius, J. Baker, R. L. Martin, L. R. Kahn, J. J. P. Stewart, S. Topiol, and J. A. Pople, GAUSSIAN 90 (Gaussian Inc., Pittsburgh, PA, 1990).

[16] S. Wilson, in *Advances in Chemical Physics*, K. P. Lawley, Ed. (Wiley, New York, 1987), Vol. 67(1), pp. 439–500.

[17] S. Huzinaga, J. Andzelm, M. Klobukowski, E. Radzio-andzelm, Y. Sakai, and H. Tatewaki, *Gaussian Basis Sets for Molecular Calculations* (Elsevier, Amsterdam, 1984).

[18] R. F. Wood and T. M. Wilson, *Defects in Insulating Solids*, V. M. Tuchkevich and K. K. Shvarts, Eds. (Springer-Verlag, Berlin, 1981), pp. 186–206.

[19] S. W. S. McKeever and T. M. Wilson, Naval Surface Weapons Center Reports, Oklahoma State University, Stillwater, June 1988 (unpublished).

[20] Willem Nieuwpoort (private communication).

[21] H.-J. Werner, *Advances in Chemical Physics*, K. P. Lawley, Ed. (Wiley, New York, 1987), Vol. 67(2), pp. 1–62.

[22] R. Shepard, *Advances in Chemical Physics*, K. P. Lawley, Ed. (Wiley, New York, 1987), Vol. 67(2), pp. 63–200.

[23] J. W. Richardsen and G. J. M. Janssen, Phys. Rev. B39 (8), 4958 (1989).

[24] C. E. Bielschowsky and B. Maffeo, Phys. Stat. Sol. B110, 263 (1982).

[25] O. E. Taurian and A. H. Tang Kai, J. Phys. Chem. Solids 47 (1), 65 (1986).

[26] R. H. Bartram, A. L. Harmer, and W. Hayes, J. Phys. C4, 1665 (1971).

Ab Initio Factorized LCAO Calculations of the Electronic Band Structure of ZnSe, ZnS, and the (ZnSe)₁(ZnS)₁ Strained-Layer Superlattice

T. S. MARSHALL and T. M. WILSON

Computational Solid State Research Laboratory, Department of Physics, Oklahoma State University, Stillwater, Oklahoma 74078

Abstract

We report on the results of electronic band structure calculations of bulk ZnSe, bulk ZnS, and the (ZnSe)₁(ZnS)₁ strained-layer superlattice (SLS) using the *ab initio* factorized linear combination of atomic orbitals method. The bulk calculations were done using the standard primitive nonrectangular 2-atom zincblende unit cell, while the SLS calculation was done using a primitive tetragonal 4-atom unit cell modeled from the CuAu I structure. The analytic fit to the SLS crystalline potential was determined by using the nonlinear coefficients from the bulk fits. The CPU time saved by factorizing the energy matrix integrals and using a rectangular unit cell is discussed. © 1992 John Wiley & Sons, Inc.

Introduction

Recent advancements in crystal growth techniques have allowed for the growth of high quality (ZnSe)ₘ(ZnS)ₙ strained-layer superlattices (SLS's) with clean interfaces and precise control over the monolayer thickness (i.e., the set of $\{m,n\}$ values). The elastic strain is introduced into the superlattice through the 4.5% mismatch between the lattice constants of ZnSe (5.66 Å) and ZnS (5.41 Å). Because of this strain, desirable electronic properties are found in these SLS's that are not present in either of the constituent bulk materials. The strain has been found to depend on the monolayer thickness and should this thickness exceed the critical value (ca. 200 Å), then the strain is broken and dislocations are formed at the interfaces [1]. Photoluminescence measurements on long-period ZnSe—ZnS SLS's (20–100 Å monolayer thickness for each constituent material) grown on GaAs substrates by metalorganic vapor phase epitaxy (MOVPE), metalorganic molecular beam epitaxy (MOMBE), and metalorganic chemical-vapor deposition (MOCVD) showed an intense, sharp blue emission from the ZnSe quantum wells. The peaks were observed to shift towards higher energies as the thickness of the ZnSe quantum well layer was decreased [2–4]. This has led to a recent interest in ZnSe—ZnS heterostructures as prime candidates in the development of a blue-emitting semiconductor laser diode and the need to achieve a good understanding of the electronic properties as a function of monolayer thickness.

Ab initio LCAO electronic band structure calculations of the (ZnSe)ₘ(ZnS)ₙ SLS's are presented with three difficulties. Every increase in the monolayer thickness

requires (i) the determination of a new stable lattice structure, (ii) a redetermination of the crystalline potential or crystalline charge density, and (iii) a larger number of atoms per unit cell. The impact of varying the monolayer thickness is more severe for the short-period SLS's ($m, n < 7$) than for the long-period SLS's. However, for the latter case, the massive number of multicentered integrals that need to be evaluated and stored present the most imposing problem. Stable structures for the SLS's can be determined using the valence force field (VFF) or Keating model, in which the stable SLS is found by minimizing the deformation energy [5–7]. We show that it is possible to effectively reduce the second difficulty by using the non-linear coefficients from the analytic fits to the bulk crystalline potentials, described in the next section, in the fit of the SLS crystalline potential. In this way, the fit to the SLS crystalline potential requires only a linear least-squares fit, which converges quite rapidly.

To handle the burden of the numerous multicenter integrals, we use the *ab initio* factorized linear combination of atomic orbitals (FLCAO) or tight-binding method of Lafon [8]. The strength of the FLCAO method is that for a unit cell with rectangular symmetry, the factorization of the energy matrix integrals into x-, y-, and z-components effectively reduces a N^3 problem down to a $3N$ problem, where N represents the number of equivalent lattice sites which need to be summed over to reach the required convergence of the integrals. Furthermore, only the integrals involving unique equivalent lattice sites need to be evaluated and stored. Inside a sphere of radius R, the number of equivalent lattice sites is proportional to R^3. However, the number of such unique sites is typically only proportional to R. As a result, the amount of CPU time needed for the evaluation of the integrals and disk space for their storage can be significantly reduced. To date, the FLCAO method has been used to determine the electronic band structure of bulk copper (1-atom/unit cell) and a (100) copper surface (33-atoms/unit cell) [8]; alpha quartz (9- and 18-atoms/unit cell) and quartz with an oxygen vacancy (72-atoms/unit cell) [9]; berlinite (18-atoms/unit cell) [10]; and bulk ZnSe (2-atoms/unit cell), bulk ZnS (2-atoms/unit cell), and the $(ZnSe)_1(ZnS)_1$ SLS (4-atoms/unit cell) [this work].

Method and Approach

Crystalline Potential

In this work, it was assumed that the exchange correlation interactions can be adequately described by the local density functional approximation (LDA) as formulated by Slater [11]. The crystalline potential, which exhibits the periodicity of the lattice, is numerically calculated for a specified grid within the unit cell from the superposition of self-consistent spherically-symmetric atomic charge densities. The atomic charge densities were calculated using a modified Herman–Skillman code [12], where it was assumed that the Zn atom was in the first excited state while the Se and S atoms were in the ground states. This numeric crystalline potential is then fitted into the following analytic expression

$$V(r) = \sum_r \sum_i (V_i^s(r - [R_r + t_i]) + V_i^c(r - [R_r + t_i])) + V^A(r).$$

where

$$V^I(r) = \frac{Z_i \exp[-\beta_0 r^2]}{r},$$

$$V^s(r) = \sum_i \sigma_i \exp[-\beta_i r^2],$$

and

$$V^F(r) = \sum_\mu U_\mu(C) \exp[i\mathbf{K}_\mu \cdot (\mathbf{r} - C)].$$

The vector C connects the origin to some arbitrary point in the lattice about which the Fourier series is expanded. The $V^s(r)$ term is an expansion of s-like Gaussian-type orbitals (GTO's), which were chosen to ease the burden of the multicenter integrals and are certainly amenable to factorization. In its present form, on the other hand, integrals involving the $V^I(r)$ term cannot be factorized. However, since the purpose of this term is to reproduce the Coulombic singularity, β_0 can be chosen to be large so that the following fit can be made

$$\frac{\exp[-\beta_0 r^2]}{r} \cong \sum_n a_n \exp[-\lambda_n r^2].$$

This factorizable form of $V^I(r)$ was not used in this article as the unit cells used were small enough that the CPU time saved would have been less than the time needed to calculate the fit. Together, the $V^I(r)$ and $V^s(r)$ terms can viewed as an analytic atomic-centered potential (ACP), displaying much the same behavior as an atomic potential in the region close to the nucleus. The σ's and β's of the ACP's are calculated by means of a nonlinear least-squares fit and are not unique. Generally, these coefficients are determined so that only the $\mathbf{K}_\mu = 0$ term of the Fourier contribution needs to be considered and often even this term can be ignored in nonself-consistent calculations. Table I lists the coefficients we calculated for the ACP's of bulk ZnSe and ZnS. The rms errors were 5.675×10^{-3} a.u. for ZnSe and 5.610×10^{-3} a.u. for ZnS. The lone Fourier contribution was determined to be -0.10 a.u. for ZnSe and -0.40 a.u. for ZnS and had an negligible effect on the RMS errors.

For the ZnSe — ZnS SLS's, every increase in monolayer thickness requires a new fit to the crystalline potential. From a CPU time aspect, it would be impractical to generate a new fitted crystalline potential for each SLS. For the short-period SLS's, a set of coefficients for the ACP's would have to be determined for each monolayer and this can quickly add up to an imposing nonlinear least-squares fit. Just for the $(ZnSe)_2(ZnS)_2$ SLS, coefficients would be needed for each ACP at the sites of Se, S, Zn at the interfaces, Zn between Se layers, and Zn between S layers. To reduce the CPU time, we feel that an effective approximation to the fit of the SLS crystalline potential would be to freeze the nonlinear coefficients from the bulk fits and allow

TABLE I. The nonlinear and linear coefficients for the analytic atomic-centered potentials of ZnSe and ZnS. The rms errors for the fitted crystalline potentials were 5.675×10^{-3} a.u. for ZnSe and 5.610×10^{-3} a.u. for ZnS.

ZnSe

Zinc ACP		Selenium ACP	
$\beta_0 = 2685.0700$		$\beta_0 = 2707.5200$	
$\beta_1 = 0.0805989$	$\sigma_1 = -0.2616660$	$\beta_1 = 0.0635699$	$\sigma_1 = 0.0536461$
$\beta_2 = 0.2644960$	$\sigma_2 = -0.7784020$	$\beta_2 = 0.2151610$	$\sigma_2 = 1.1188600$
$\beta_3 = 0.8679790$	$\sigma_3 = -3.9147400$	$\beta_3 = 0.7282400$	$\sigma_3 = 3.7851600$
$\beta_4 = 2.8483900$	$\sigma_4 = -15.647500$	$\beta_4 = 2.4648300$	$\sigma_4 = 14.095900$
$\beta_5 = 9.3473700$	$\sigma_5 = -45.246800$	$\beta_5 = 8.3425300$	$\sigma_5 = 46.472300$
$\beta_6 = 30.674600$	$\sigma_6 = 91.883300$	$\beta_6 = 28.236400$	$\sigma_6 = 102.03800$
$\beta_7 = 100.66300$	$\sigma_7 = -193.01000$	$\beta_7 = 95.569800$	$\sigma_7 = 214.65900$
$\beta_8 = 330.33900$	$\sigma_8 = -347.56800$	$\beta_8 = 32.346900$	$\sigma_8 = 402.86000$
$\beta_9 = 1084.5000$	$\sigma_9 = -679.26600$	$\beta_9 = 1094.8200$	$\sigma_9 = 768.09100$
$\beta_{10} = 3557.4500$	$\sigma_{10} = 930.48400$	$\beta_{10} = 3705.5700$	$\sigma_{10} = 1075.9200$

ZnS

Zinc ACP		Sulfur ACP	
$\beta_0 = 2638.4100$		$\beta_0 = 2162.7500$	
$\beta_1 = 0.0939085$	$\sigma_1 = -0.2921120$	$\beta_1 = 0.0613623$	$\sigma_1 = 0.2643280$
$\beta_2 = 0.3026590$	$\sigma_2 = -0.8512680$	$\beta_2 = 0.2023960$	$\sigma_2 = -0.8859110$
$\beta_3 = 0.9754470$	$\sigma_3 = -4.6016300$	$\beta_3 = 0.6675780$	$\sigma_3 = -3.0402900$
$\beta_4 = 3.1437800$	$\sigma_4 = -16.957600$	$\beta_4 = 2.2019200$	$\sigma_4 = -7.4765600$
$\beta_5 = 10.132200$	$\sigma_5 = -47.231700$	$\beta_5 = 7.2627800$	$\sigma_5 = -22.307300$
$\beta_6 = 32.655100$	$\sigma_6 = -93.792000$	$\beta_6 = 23.955400$	$\sigma_6 = -43.721700$
$\beta_7 = 105.24500$	$\sigma_7 = -195.10700$	$\beta_7 = 79.013800$	$\sigma_7 = -95.690700$
$\beta_8 = 339.19500$	$\sigma_8 = -347.04600$	$\beta_8 = 260.61700$	$\sigma_8 = -166.66100$
$\beta_9 = 1093.2000$	$\sigma_9 = -667.30400$	$\beta_9 = 859.61400$	$\sigma_9 = -327.90600$
$\beta_{10} = 3523.2900$	$\sigma_{10} = 940.24700$	$\beta_{10} = 2835.3300$	$\sigma_{10} = 437.73900$

the linear coefficients to be adjusted to describe the change in potential brought about by the interfaces. In this way, only a linear least-squares fit would be needed and considerable CPU time savings should result. We calculated two potential fits for the $(ZnSe)_1(ZnS)_1$ SLS: one in which the set of nonlinear coefficients from the ACP's for the Zn from ZnS were used and the other using the set of nonlinear coefficients from the ACP's for the Zn from ZnSe. The latter gave a slightly better rms error $(6.316 \times 10^{-3}$ a.u.), so we opted for that fit. Table II lists the adjusted bulk linear coefficients for this fit. We have determined that approximately only 3.0×10^{-4} a.u. accuracy is lost by using this approximation and not generating both new nonlinear and linear coefficients for the $(ZnSe)_1(ZnS)_1$ SLS. Furthermore, our studies suggest that as the monolayer thickness is increased significantly (i.e., long-period SLS's), the accuracy lost by using this approximation will become negligible.

TABLE II   The adjusted bulk linear coefficients for the analytic atomic-centered potentials of the $(ZnSe)_1(ZnS)_1$ SLs. The rms error for the fitted crystalline potential was $6.316 \cdot 10^{-3}$ a.u.

	Zinc ACP		Selenium ACP		Sulfur ACP
σ_1	0.334430	σ_1	0.0071650	σ_1	0.0462053
σ_2	0.7216690	σ_2	1.0512100	σ_2	0.7873360
σ_3	3.9561800	σ_3	3.9062600	σ_3	3.1684000
σ_4	15.620200	σ_4	13.873800	σ_4	7.2926100
σ_5	45.270300	σ_5	46.791200	σ_5	22.592100
σ_6	91.853900	σ_6	101.53600	σ_6	43.260000
σ_7	193.05400	σ_7	215.54500	σ_7	96.446700
σ_8	347.49700	σ_8	401.38800	σ_8	165.41300
σ_9	679.37100	σ_9	770.33800	σ_9	329.76800
σ_{10}	930.59500	σ_{10}	1078.3800	σ_{10}	439.67800

Basis

For these calculations, uncontracted atomic Gaussian basis sets constructed for use in *ab initio* molecular calculations were used for Zn [13], Se [14], and S [15]. Because the ACP's behave much like the atomic potentials in the region close to the nucleus, the core states of the bulk materials are expected to be very similar to the atomic core states of Zn, Se, and S. Contractions can then be performed on the *s*- and *p*-GTO's of Zn and Se to construct the atomic-like Zn and Se $1s$, $2s$, $2p$, $3s$, and $3p$ core basis functions of ZnSe. Similarly, contractions can be performed on the *s*- and *p*-GTO's of Zn and S to construct the atomic-like Zn and S $1s$, $2s$, $2p$, and $3s$ core basis functions and the Zn $3p$ core basis function of ZnS. The contraction procedure we use is straightforward. Each Bloch function consists of a lattice sum involving a single atomic GTO

$$b^i_{n l m}(\mathbf{k}, \mathbf{r}) = N^{-1/2} \sum_\nu \exp\{i\mathbf{k} \cdot \mathbf{R}_\nu\} x^n y^l z^m \exp\{-\alpha^i_j |\mathbf{r} - [\mathbf{R}_\nu + \mathbf{t}_j]|^2\},$$

so that the single electron wavefunction becomes a lattice sum involving those uncontracted GTO's

$$\psi(\mathbf{k}, \mathbf{r}) = N^{-1/2} \sum_j \sum_i \sum_{n l m} \sum_\nu C^{n l m}_{i,j} \exp\{i\mathbf{k} \cdot \mathbf{R}_\nu\} x^n y^l z^m$$

$$\times \exp\{-\alpha^i_j |\mathbf{r} - [\mathbf{R}_\nu + \mathbf{t}_j]|^2\}.$$

The wavefunction associated with the Γ-point core state of, say Zn $1s$ in ZnSe, will then only have nonnegligible $C^{n l m}_{i,j}$'s involving the Zn *s*-GTO's. The normalized atomic-like core basis functions constructed using the $C^{n l m}_{i,j}$'s as weighting factors will have the following form

$$\Phi^i_{n l m}(\mathbf{k}, \mathbf{r}) = \sum_i d^{n l m}_{i,j} x^n y^l z^m \exp\{-\alpha^i_j |\mathbf{r} - [\mathbf{R}_\nu + \mathbf{t}_j]|^2\}.$$

TABLE III.   The calculated energies for ZnSe at high symmetry points in the Brillouin zone. All values are in electron volts and measured with respect to the top of the valence band at the Γ-point. The results are from: HLCAO using the full Slater exchange correlation [this work], OLCAO using an adjustable Slater exchange correlation to match the experimental band gap [21], self-consistent LCGO using the semi-relativistic Wigner exchange correlation [23], self-consistent PVMB using the Ceperley–Alder exchange correlation [22], self-consistent OPW using the full Slater exchange correlation [24], and experimental measurements.

	HLCAO	OLCAO	LCGO	PVMB	OPW	Expt.
Γ_{1v}	12.83	-12.37	12.67	12.86	11.82	15.2(6)[a]
Γ_{15c}	8.76		6.7	7.86	12.6	
Γ_{12c}	8.48		6.7	-7.50		
Γ_{15v}	0.00	0.00	0.00	0.00	0.00	
Γ_{1c}	2.41	2.83	1.83	1.45	2.94	2.82[b]
Γ_{15c}	7.81	7.38	5.86	5.77	6.66	7.80[c,d]
Γ_{1c}	11.93			9.79		
X_{1v}	12.08	10.94	11.55	11.79	10.48	12.5(4)[a]
X_{3v}	4.05	4.38	4.69	4.82	4.31	5.6(3)[a] or 5.3(3)[e]
X_{5v}	1.61	1.79	2.16	2.20	1.65	2.1(3)[a]
X_{1c}	5.17	4.42	3.18	2.88	4.19	
X_{3c}	5.54	6.10	3.64	3.47	4.49	
X_{1c}	12.28		10.85	10.58		
L_{1v}	12.26	11.31	11.83	12.06	10.84	13.1(3)[a]
L_{1v}	4.21	4.67	5.15	-5.21	4.40	
L_{3v}	0.62	0.66	0.85	0.87	-0.64	1.3(3)[a] or 0.7(2)[e]
L_{1c}	4.16	4.23	2.91	2.63	3.79	
L_{3c}	8.88	8.72	6.70	6.36	7.31	
$L_{3v} \rightarrow L_{1c}$	4.78	4.89	3.76	3.50	4.43	4.91[b]
$X_{5v} \rightarrow X_{1c}$	6.78	6.21	5.34	5.08	5.84	6.00[e]

[a] Reference [16].
[b] Reference [20].
[c] Reference [18].
[d] Reference [19].
[e] Reference [17].

No orthogonality conditions are placed on these contractions. The valence states of the bulk materials can then represented by these atomic-like basis functions augmented by several uncontracted diffuse GTO's from the atomic bases. For the ZnSe—ZnS SLS's, the bulk core basis functions can be directly transferred over. The justification for doing this is straightforward. First, the bond lengths in going from the bulk materials to the SLS's change only slightly (less than 1%) so that there will not be any new significant overlap contributions from nearby orbitals. Secondly, the primary terms of the fitted bulk crystalline potentials involved in the construction of these basis functions are the $V_i^c(r)$'s, and innermost gaussians in $V_j^a(r)$, which change very little in going over to the SLS's. These basis functions can

then be augmented with the same uncontracted diffuse GTO's used in the bulk calculations.

Results

ZnSe and ZnS

Bulk ZnSe and ZnS have been studied extensively by both experimental and theoretical methods. Interband transition energies at high symmetry points have been determined by photoemission [16,17] and reflectivity [18–20] measurements. Theoretical calculations of the electronic band structure of both bulk materials have been made using the semi-*ab initio* orthogonalized LCAO (OLCAO) method by Huang and Ching [21]; the self-consistent potential-variation mixed-basis (PVMB) method by Bernard and Zunger [22]; the self-consistent linear combination of Gaussian orbitals (LCGO) method by Wang and Klein [23]; the self-consistent orthogonalized plane wave (OPW) method by Stukel and et al. [24]; the self-consistent tight-binding method of Bertho and et al. [25]; the semi-empirical tight-binding method by Vogl and et al. [26]; and the pseudopotential method of Cohen and Bergstresser [27]. This information provides us with the means to (i) determine the effectiveness of the LCAO method and (ii) determine the effect basis size has on the conduction and valence bands. For these calculations, the standard 2-atom nonrectangular zincblende unit cell was used. The primitive lattice vectors are

$$\mathbf{a}_1 = \frac{a}{2}(1, 1, 0), \; \mathbf{a}_2 = \frac{a}{2}(1, 0, 1), \text{ and } \mathbf{a}_3 = \frac{a}{2}(0, 1, 1).$$

where the Zn atom is positioned at

$$t = (0, 0, 0)$$

and the Se or S atom is positioned at

$$t = \frac{a}{4}(1, 1, 1).$$

The notation a represents the lattice constant for either ZnSe or ZnS. The LCAO method is most effective when the cell has rectangular symmetry. For these bulk calculations, we could have attained this symmetry by simply choosing a larger nonprimitive 4-atom unit cell. This was not done so we could compare the needed CPU time for these calculations with that of the (ZnSe),(ZnS):SI S, which does have a primitive rectangular unit cell. These CPU time comparisons will be presented in the next section.

An approximation often used to reduce the complexity and CPU time of the calculation is to remove the more diffuse GTO's from the basis. To see what effect this would have on the band structure, we removed the most diffuse s-GTO (0.051142) from the Zn basis. The resulting band structure showed a good representation of the valence states and band gaps (2.56 eV for ZnSe and 3.69 eV for ZnS). Excluding the Zn 4s band, however, overall accuracy was lost with the con-

duction bands as their resulting energies were several eV too high. Returning the diffuse Zn s-GTO to the basis, the calculations were repeated. The resulting band structure showed that the valence states deviated from the previous results by only a few hundredths of an eV. The conduction bands showed improvement, though the energies were still a few eV higher than expected. As a result of the conduction bands being lowered, the values of both band gaps decreased.

To improve the representation of the conduction bands, we augmented the Zn basis with a diffuse p-GTO (0.15000). Contractions were performed according to the procedure outlined in the previous section. The resulting basis functions were then augmented with uncontracted diffuse GTO's (including the additional Zn p-GTO) to bring the basis size to 102 basis functions for ZnSe and 72 basis functions for ZnS. The resulting electronic band structures are shown in Figures 1 and 2. Tables III and IV list the calculated energies at high symmetry points in the Brillouin zone. Also included in these tables are experimental results and theoretical results from the semi-*ab initio* OLCAO method, LCGO method, PVMB method, and OPW method. A consequence of using the additional Zn p-GTO can be seen in Figure 2, where the L_{1c} state for ZnS is ca. 0.2 eV lower than the L_{3c} state. Our results are very similar to those obtained by Huang and Ching using the OLCAO method, but significant differences are present in comparison to the LCGO, PVMB, and OPW methods. In general, our upper valence bands and conduction bands lie higher by a few tenths of an eV to a few eV than the corresponding bands from the other three methods. This is a result of our calculations being nonself-consistent, while

ZnSe (2-atom unit cell)
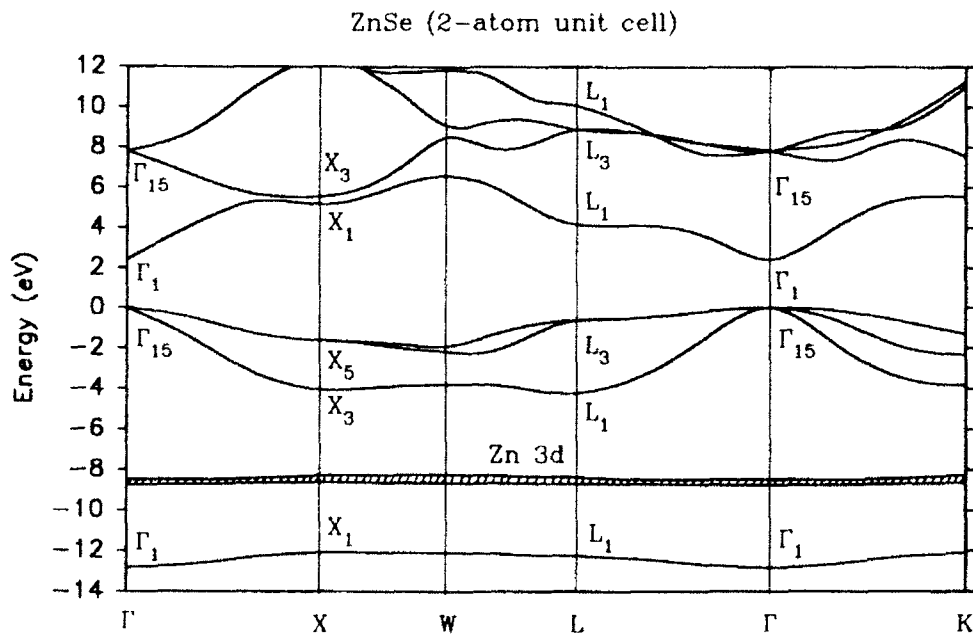
Figure 1.   The energy band structure of bulk ZnSe (2-atoms/unit cell). The resulting band gap is direct.
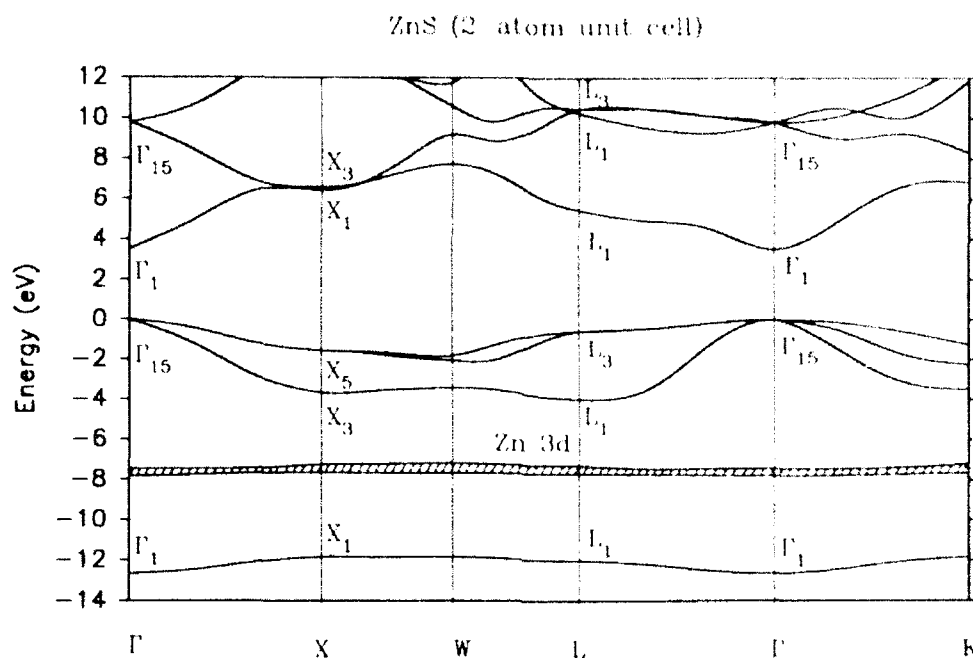
ZnS (2 atom unit cell)

Figure 2. The energy band structure of bulk ZnS (2-atoms unit cell). The resulting band gap is direct.

the LCGO, PVMB, and OPW calculations are self-consistent. Self-consistent calculations using the LDA are known to underestimate the excited states [22–24]. It is interesting to note that some disparity also exists in the experimental data. Photoemission spectroscopy measurements on ZnSe [16,17], for example, differ by 0.6 eV for the L_3 state.

The (ZnSe)₁(ZnS)₁ SLS

Interest in the ZnSe—ZnS SLS's has occurred rather recently and, to the best our knowledge, there have been only two electronic band structure studies on the short-period SLS's: a self-consistent pseudopotential calculation by Nakayama [28] and a self-consistent PVMB calculation by Bernard and Zunger [22]. The latter calculation was done on the ordered pseudobinary alloy Zn₂SeS, which in the crystal limit goes to the (ZnSe)₁(ZnS)₁ SLS. These results represent the first *ab initio* LCAO calculation on the band structure of the (ZnSe)₁(ZnS)₁ SLS. There have also been two electronic structure calculations: a semi-empirical tight-binding calculation to determine the energy band gaps by Wu et al. [29] and a self-consistent linear muffin-tin orbital calculation to determine the valence band offsets (not considered in this article) by Gorczyca and Christensen [30].

The (ZnSe)₁(ZnS)₁ SLS can be modeled using the CuAu-I structure (shown in Fig. 3), where the SLS is assumed to be free-standing so that the effects of the substrate can be ignored. The effects of the elastic strain on the lattice can be

696

MARSHALL AND WILSON

TABLE IV. The calculated energies for ZnS at high symmetry points in the Brillouin zone. All values are in electron volts and measured with respect to the top of the valence band at the Γ-point. The results are from: FLCAO using the full Slater exchange correlation [this work], OLCAO using an adjustable Slater exchange correlation to match the experimental band gap [21], self-consistent LCGO using the semi-relativistic Wigner exchange correlation [23], self-consistent PVMB using the Ceperley–Alder exchange correlation [22], self-consistent OPW using the full Slater exchange correlation [24], and experimental measurements.

	FLCAO	OLCAO	LCGO	PVMB	OPW	Expt.
Γ_1	-12.66	-12.27	12.89	13.06	-11.77	13.5 (4)[a]
Γ_{15}	-7.82		6.4	7.65	-14.1	
Γ_{15}	7.45		-6.4	-7.27		
Γ_{15}	0.00	0.00	0.00	0.00	0.00	
Γ_1	3.51	3.81	2.26	1.96	3.77	3.85[b]
Γ_{15}	9.79	9.22	7.04	6.45	7.99	
Γ_1	14.35			11.59		
X_1	11.84	10.80	11.67	-11.88	10.29	12.0 (3)[a]
X_3	3.67	-3.95	-4.49	7.61	3.93	5.5 (2)[a]
X_5	-1.56	-1.57	2.19	-2.30	-1.61	2.5 (3)[a]
X_1	6.44	5.76	3.61	3.18	5.01	
X_3	6.58	7.61	4.58	4.08	5.95	
X_1	12.33		10.92	10.70		
L_1	-12.04	-11.18	11.97	-12.17	10.66	12.4 (3)[a]
L_1	-4.00	-4.25	-5.20	-5.38	4.20	
L_3	-0.59	0.56	0.84	0.94	-0.61	1.4 (4)[a]
L_1	5.44	5.64	3.65	3.24	4.96	
L_3	10.47	10.60	7.51	6.96	8.62	
$L_{3v} \rightarrow L_{1c}$	6.03	6.20	4.49	4.18	5.57	5.81[b]
$X_{5v} \rightarrow X_{1c}$	8.00	7.33	5.80	5.48	6.62	6.6[b]

[a] Reference [16].
[b] Reference [20].

determined using the VFF model, as was done in the works of Bernard and Zunger and of Nakayama. A primitive tetragonal 4-atom unit cell was used with the following lattice vectors

$$\mathbf{a}_1 = a_{xy}(1/2, -1/2, 0), \ \mathbf{a}_2 = a_{xy}(1/2, 1/2, 0), \text{ and } \mathbf{a}_3 = a_z(0, 0, 1),$$

where a_{xy} and a_z are the lattice constants which are, respectively, parallel and perpendicular to the interface. Furthermore, a_z can be expressed as $2d_{Zn\text{-}Se} + 2d_{Zn\text{-}S}$, where the d's represent the interatomic distances along the z-direction. The positions of the atoms are: for Zn

$$\mathbf{t}_1 = (0, 0, 0) \text{ and } \mathbf{t}_2 = (a_{xy}/2, 0, 2d_{Zn\text{-}Se}),$$

for Se

TABLE V. The calculated energies for the (ZnSe)$_1$(ZnS)$_1$ SLS at the Γ-point in the CuAu I Brillouin zone. All values are measured in electron volts and measured with respect to the top of the valence band maximum. The results are from LCAO [this work], self-consistent PVMB [20], and self-consistent psuedopotential [28]. For Ref. [28], values were taken from the graphs and are only approximate. Where degeneracies are broken, the representation in the zincblende structure is given followed by the new representation in the CuAu I structure. The values inside the parentheses indicate the degeneracies.

	LCAO	PVMB	SCP
Se 4s/S 3s bands			
Γ_{1r} (1)	13.10	13.01	11.6
X_{1t} (1)	12.09	11.85	10.3
Zn 3d bands			
$\Gamma_{15c} \rightarrow \Gamma_{4c}''$ (1)	8.57	7.78	
$\Gamma_{15c} \rightarrow \Gamma_{5c}''$ (2)	8.56	7.78	
X_{3c} (1)	8.38	7.65	
X_{5c} (2)	8.38	7.53	
$\Gamma_{12c} \rightarrow \Gamma_{1c}''$ (1)	8.23	7.40	
$\Gamma_{12c} \rightarrow \Gamma_{3c}''$ (1)	8.23	7.40	
X_{4c} (1)	8.23	7.33	
X_{1c} (1)	8.02	7.12	
Upper valence bands			
X_{3v} (1)	4.14	4.84	3.8
X_{5v} (2)	1.99	2.33	1.8
$\Gamma_{15v} \rightarrow \Gamma_{4v}''$ (1)	0.24	0.06	0.15
$\Gamma_{15v} \rightarrow \Gamma_{5v}''$ (2)	0.00	0.00	0.0
Conduction bands			
Γ_{1c} (1)	2.63	1.61	2.5
X_{1c} (1)	5.62	3.06	3.4
X_{3c} (1)	5.72	3.70	4.1
$\Gamma_{15c} \rightarrow \Gamma_{4c}''$ (1)	8.47	6.08	6.6
$\Gamma_{15c} \rightarrow \Gamma_{5c}''$ (2)	8.50	6.07	6.6

$$t_3 = (a_{xy}/4, a_{xy}/4, d_{Zn\ Se}).$$

and for S

$$t_4 = (a_{xy}/4, -a_{xy}/4, [2d_{Zn\ Se} + d_{Zn\ S}]).$$

The values we used for these lattice constants and interatomic distances were taken from the results of Nakayama's VFF calculations [28].

At high symmetry points, the following approximate correspondence relations exist between the SLS (denoted by the prime symbol) and the bulk materials
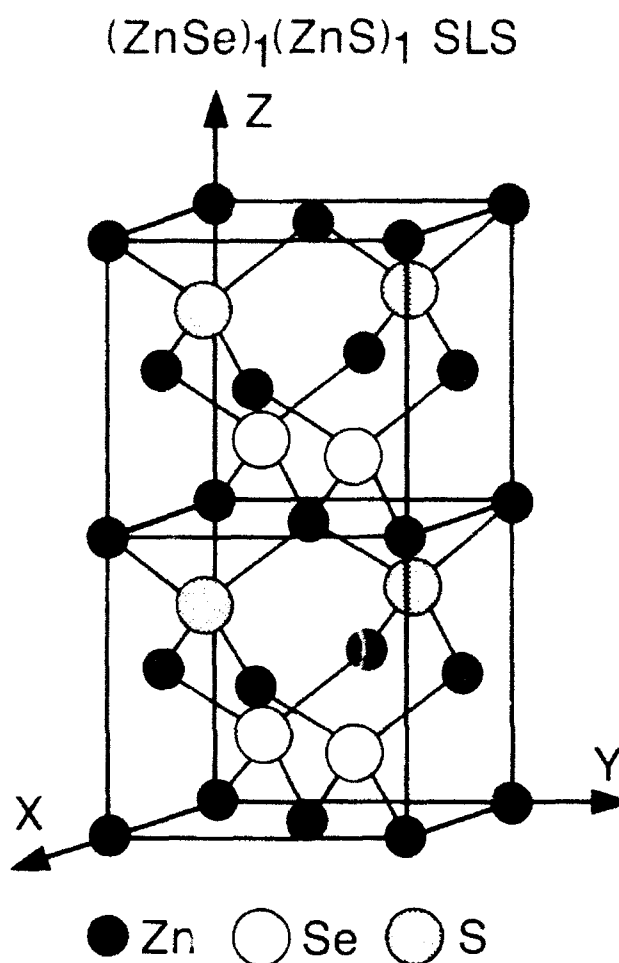
(ZnSe)₁(ZnS)₁ SLS

Figure 3.   The (ZnSe)₁(ZnS)₁ strained-layer superlattice.

$$\Gamma' \leftrightarrow \Gamma + X_Z,$$

$$M' \leftrightarrow X_X + X_Y,$$

and

$$A' \leftrightarrow W + W.$$

The relations are approximate as the expected degeneracies from such foldings are removed due to (i) the anions now consist of both Se and S and (ii) a_{xx} is not equal to a_z [22]. The resulting band structure is shown in Figure 4. Table V lists our calculated energies at the Γ'-point in the CuAu I Brillouin zone along with the results of Bernard and Zunger and those of Nakayama. As was the case with the bulk materials, our upper valence bands and conduction bands lie higher than the

(ZnSe)₁(ZnS)₁ SLS (4-atom unit cell)
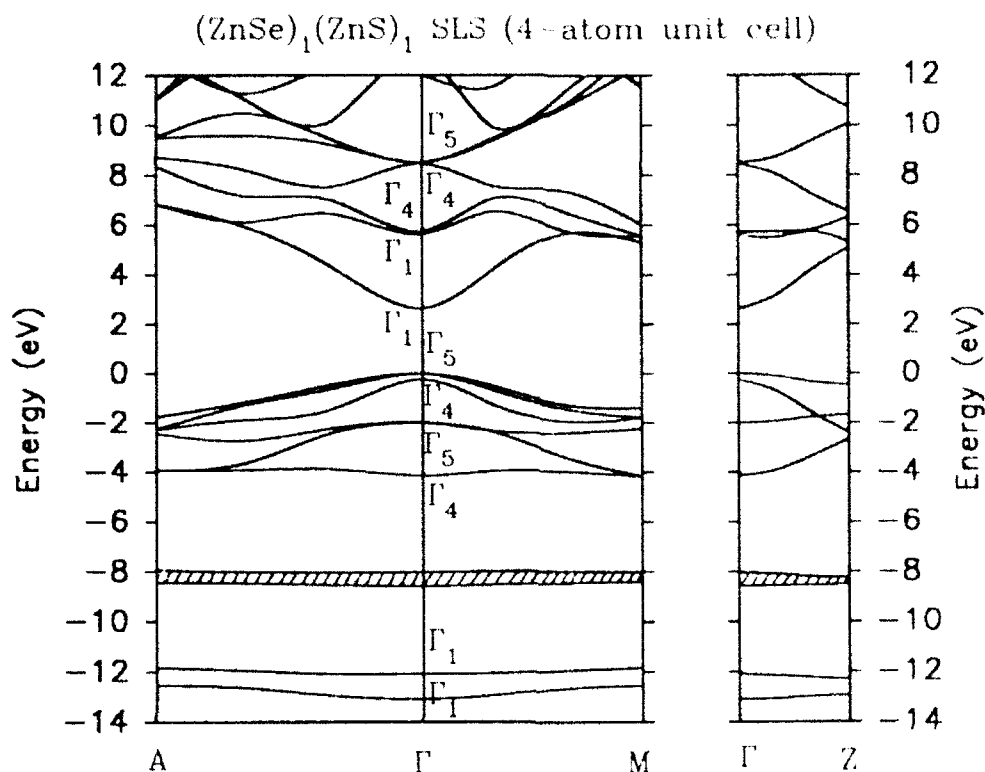
Figure 4. The energy band structure of the (ZnSe)₁(ZnS)₁ strained-layer superlattice (4-atoms unit cell). The resulting band gap is direct.

corresponding bands from the two self-consistent methods. The experimental work being done on these ZnSe—ZnS SLS's are in the areas of perfecting growth techniques and measurements on the long-period SLS's [1-3,31], so that no comparison of experimental results to our calculations is possible.

A Mulliken population analysis of our results at the Γ-point shows the following. For the two Γ_1 states of the lower valence bands, the bottom is localized in ZnS and the top is localized in ZnSe. The heavy-hole Γ_5 state is localized in the ZnSe layer, while the light-hole Γ_4 state is a mix between the ZnSe (ca. 50%) and ZnS (ca. 42%) layers. The Γ_{1c} state (i.e., the conduction band minimum) was found to be dominant Zn, while the $\Gamma_{4c}(X_{1c})$ and $\Gamma_{5c}(X_3)$ states showed small amounts of s and p mixing with the Se and S anions. Presently, we have calculations in progress to determine if, as the monolayer thickness is increased, (i) the localization of the heavy- and light-hole states in the ZnSe layers becomes more distinct and (ii) the Γ_{1c} state will also become localized in the ZnSe layers. The results of Nakayama's work on the (ZnSe)ₘ(ZnS)ₙ SLS's, for $m \leq 4$, showed that the localization of the heavy- and light-hole states in the ZnSe layers did become more distinct with increased monolayer thickness. However, his results did not show the same distinct localization for the Γ_{1c} state.

Summary

All of the calculations for this article were done on the OSU IBM 3090-200S computer. For scalar code, the IBM will run at the equivalent speed of a Cray X-MP. For vectorized code, which should give a significant reduction in CPU time over the scalar version, the IBM is approximately 20% slower than the Cray. Presently, work is under way to vectorize the LCAO code. For the bulk 2-atom unit cells, the energy matrix integrals (excluding those involving the $V(r)$ terms) were factorized. However, since the cells were nonrectangular, a reduction from an N^4 problem could not be made. The CPU times needed for their evaluation and construction of the energy matrix was ca. 20 1/2 min for ZnSe and ca. 26 min for ZnS. The tetragonal 4-atom unit cell used for the $(ZnSe)_1(ZnS)_1$ SLS allowed the reduction to a 3N problem for the factorizable integrals. For this case, only ca. 7 1/2 CPU min were needed for the evaluation of the integrals and construction of the energy matrix. Although the size of the unit cell is double that of the zincblende unit cell, only a third of the CPU time was required due to the rectangular symmetry.

The CPU time needed for the diagonalization of the energy matrix is roughly proportional to the number of basis functions cubed. For each k point, the CPU time required to diagonalize the energy matrix and solve for the eigenvectors was: ca. 2 s for ZnS, ca. 41 s for ZnSe, and ca. 3 minutes for the $(ZnSe)_1(ZnS)_1$. To demonstrate how drastically these times rise with larger bases, we calculated energies of the $(ZnSe)_2(ZnS)_2$ SLS at a few high symmetry points using a rectangular 16-atom unit cell. The evaluation of the integrals and construction of the energy matrix needed ca. 1/2 CPU h, which was the expected factor of four increase in time from the 4-atom unit cell. However, each k point needed ca. 2 1/2 h of CPU time for the diagonalization of the matrix and solution of the eigenvectors. For the long-period SLS's, this large time demand will be the prime difficulty for band structure calculations. Vectorizing the code will certainly help reduce this time, as would freezing the core. However, improved techniques for the diagonalization of the energy matrix need to be considered as well [32].

The experimental studies reporting the blue emissions and peak shifts were working with long-period SLS's. So before we can make any definitive conclusions regarding the prospects of using ZnSe—ZnS SLS's in the development of a blue-emitting semiconductor laser diode, further calculations (in progress) of these SLS's for increasing monolayer thicknesses are required. The purpose of this article was to establish the LCAO method as an effective technique for studying the long-period SLS's. We believe we have done this by showing that (i) for a unit cell with rectangular symmetry, factorization of the integrals greatly reduces the amount of CPU time needed for their evaluation and (ii) the results of our bulk ZnSe, bulk ZnS, and the $(ZnSe)_1(ZnS)_1$ SLS calculations compared well to the results of other self-consistent methods.

Acknowledgments

Bibliography

[1] Y. Kawakami, T. Taguchi, M. Satou, and A. Hiraki, Nucl. Instrum. Methods B **33**, 603 (1988).
[2] T. Yokogawa, M. Ogura, and T. Kajiwara, Appl. Phys. Lett. **49**, 1702 (1986).
[3] N. Teraguchi, Y. Takemura, R. Kimura, M. Konagai, and K. Takahashi, J. Cryst. Growth **93**, 720 (1988).
[4] Y. Kawakami, T. Taguchi, and A. Hiraki, J. Cryst. Growth **93**, 714 (1988).
[5] P. N. Keating, Phys. Rev **145**, 637 (1966).
[6] R. M. Martin, Phys. Rev. B **1**, 4005 (1970).
[7] J. L. Martins and A. Zunger, Phys. Rev. B **30**, 6217 (1984).
[8] E. E. Lafon, J. Comp. Phys. **83**, 185 (1989).
[9] T. M. Wilson and E. E. Lafon (elsewhere in this issue).
[10] T. M. Wilson, E. E. Lafon, and L. Merican (unpublished).
[11] J. C. Slater, Phys. Rev. **81**, 385 (1951).
[12] F. Herman and S. Skillman, *Atomic Structure Calculations* (Prentice-Hall, Englewood Cliffs, NJ, 1963).
[13] A. J. H. Wachters, J. Chem. Phys. **52**, 1033 (1970).
[14] R. Poirier, R. Kari, and I. G. Csizmadia, *Handbook of Gaussian Basis Sets* (Elsevier, New York, 1985).
[15] A. D. McLean and G. S. Chandler, J. Chem. Phys. **72**, 5639 (1980).
[16] L. Ley, R. A. Pollak, F. R. McFeely, S. P. Kowalczyk, and D. A. Shirley, Phys. Rev B **9**, 600 (1974).
[17] D. E. Eastman, W. D. Grobman, J. L. Freeouf, and M. Erbudak, Phys. Rev. B **9**, 3473 (1974).
[18] Y. Petroff, M. Balkanski, J. P. Walter, and M. L. Cohen, Solid State Commun. **7**, 459 (1969).
[19] J. Walter, M. L. Cohen, Y. Petroff, and M. Balkanski, Phys. Rev. B **1**, 2661 (1970).
[20] D. Theis, Phys. Status Solidi B **79**, 125 (1977).
[21] M. Huang and W. Y. Ching, J. Phys. Chem. Solids **46**, 977 (1985).
[22] J. E. Bernard and A. Zunger, Phys. Rev. B **36**, 3199 (1987).
[23] C. S. Wang and B. M. Klein, Phys. Rev. B **24**, 3393 (1981).
[24] D. J. Stukel, R. N. Euwema, T. C. Collins, F. Herman, and R. L. Kortum, Phys. Rev. **179**, 740 (1969).
[25] D. Bertho, D. Boiron, A. Simon, C. Jouanin, and C. Priester, Phys. Rev. B **44**, 6118 (1991).
[26] P. Vogl, H. P. Hjalmarson, and J. D. Dow, J. Phys. Chem. Solids **44**, 365 (1983).
[27] M. L. Cohen and T. K. Bergstresser, Phys. Rev. **141**, 789 (1966).
[28] T. Nakayama, J. Phys. Soc. Jpn. **59**, 1029 (1990).
[29] Y. Wu, S. Fujita, and S. Fujita, J. Appl. Phys. **67**, 908 (1990).
[30] I. Gorczyca and N. E. Christensen, Solid State Commun. **72**, 785 (1989).
[31] The J. Cryst. Growth **117** (1992) contains the *Proceedings of the Fifth International Conference on II-VI Compounds*, which offers several articles on recent experimental work done on the long-period ZnSe–ZnS sl s's.
[32] One such method, the Sturm sequences, was discussed by F. Harris during his presentation at the *1992 Sanibel Symposia*.

Ab Initio Factorized LCAO Calculation of the Electronic Structure of α-SiO₂

T. M. WILSON and E. E. LAFON*

Computational Solid State Research Laboratory, Physics Department, Oklahoma State University, Stillwater, Oklahoma 74078

Abstract

We report on the results of calculations of the electronic structure of α-quartz that were made using the first principles, factorized linear combination of atomic orbitals method. Results were obtained for the primitive 9-atom, and orthorhombic 18- and 72-atom unit cells. Application of this method to the calculation of the electronic structure of the neutral oxygen vacancy in α-quartz is discussed and results obtained using a 72-atom unit cell are given. ⓒ 1992 John Wiley & Sons, Inc.

Introduction

The *ab initio* linear combination of atomic orbitals (LCAO) or tight binding method has been shown capable of accurately predicting the electronic band structure and associated bulk properties of insulating, semiconducting, and metallic solids [1-5]. Recently, the method has been extended to the study of surface states, complex crystals, and amorphous materials that require large numbers of atoms within the unit cell [6-10]. These extensions are made possible by the fact that the tight binding method requires an extremely small number of basis functions per atom to accurately describe the electronic structure of a solid. Nevertheless, as the number of atoms within the unit cell becomes large, the CPU time needed to calculate and disk space needed for storage of the enormous number of multicenter integrals required for an accurate determination of the electronic structure place practical limits on the size of the problems that can be treated by this approach.

A recent mathematical reformulation of the *ab initio* LCAO method, the Factorized LCAO (FLCAO) method, has greatly increased the size of the problems that can be studied using this approach [8]. Within the framework of this formulation it is shown that, for those crystals which have cubic, tetragonal or orthorhombic symmetry or can be "forced" to assume such symmetry by simply choosing a larger nonprimitive unit cell, (i) the number of multicenter integrals to be evaluated can be reduced from an N^3 problem to a $3N$ one, where N denotes the number of equivalent sites within a radius R about a given center in the unit cell, and (ii) the multicenter integrals, per se, need not be directly calculated. We report in this article on the results of a study of the electronic band structure of α-quartz and of

---

* Deceased.

the neutral oxygen vacancy in α-quartz, and in an accompanying article our results for ZnS, ZnSe, and the $(ZnS)_i/(ZnSe)_i$ heterostructure [11] that were obtained using the FLCAO method.

Factorized LCAO Method and Approach

In this section we briefly summarize the relevant features of the FLCAO method as it applies to this calculation and refer the interested reader to Ref. [8] for further details. As with all band theoretical methods, we are interested in obtaining the single particle states of electrons in a solid. We assume that the electron–electron interactions can be adequately described by a local crystalline potential that exhibits the periodicity of the chosen unit cell. The exchange/correlation interactions were described using the form of the local density functional approximation to the exchange first suggested by Slater [12]. This appears to work quite well for nonself-consistent calculations such as the ones that are reported on in this article. A numerical crystalline potential is calculated for a predetermined grid of points from a charge density that is obtained from a linear superposition of free atom atomic charge densities. It is further assumed that the crystalline potential can be written in the form

$$V(\mathbf{r}) = V^c(\mathbf{r}) + V^x(\mathbf{r}) + V^k(\mathbf{r}),$$ (1)

where

$$V^c(\mathbf{r}) \cong \sum_i \sum_j (-Z_j/r_{ej}) \exp[-\beta_{ij}(r_{ej})^2].$$

$$V^x(\mathbf{r}) \cong \sum_v \sum_j \sum_t \sigma_{tj} \exp[-\beta_{tj}(r_{ej})^2].$$

$$V^k(\mathbf{r}) \cong \sum_\mu U_\mu^k(\mathbf{C}) \exp[i\mathbf{K}_\mu \cdot (\mathbf{r} - \mathbf{C})].$$

and where $r_{ej} = |\mathbf{r} - (\mathbf{R}_e - \mathbf{t}_j)|$ and $\mathbf{C}$ is some point in the lattice about which the Fourier series is expanded. Since the decomposition of $V(\mathbf{r})$ is not unique, the $V^c(\mathbf{r})$ and $V^x(\mathbf{r})$ contributions are chosen in such a manner as to make the Fourier contributions from $V^k(\mathbf{r})$ negligible. In this study we found it sufficient to retain only the $\mathbf{K}_1 = 0$ term. This decomposition greatly simplifies the evaluation of the multicenter integrals when the variational wave functions for a point $\mathbf{k}$ in the Brillouin zone are expressed as an expansion of Bloch functions formed from Gaussian orbitals.

Many crystals have either cubic, tetragonal or orthorhombic symmetry, and many others can be forced to assume such rectangular symmetry by simply choosing a larger unit cell than the primitive cell. For example, the Bravais lattice of α-quartz is hexagonal where the primitive lattice vectors are given by

$$\mathbf{a}_1 = a(3^{1/2}, -1.0)/2, \qquad \mathbf{a}_2 = a(0,1,0), \qquad \mathbf{a}_3 = c(0,0,1),$$ (2)

and contains nine atoms, three silicons, and six oxygens. For this primitive unit cell, the primitive vectors of the reciprocal lattice are

$$\mathbf{b}_1 \quad (4\pi/3^{1/2}a)(1,0,0), \quad \mathbf{b}_2 \quad (2\pi/3^{1/2}a)(1,3^{1/2},0), \quad \mathbf{b}_3 \quad (2\pi/c)(0,0,1). \quad (3)$$

The crystal can be "forced" to have orthorhombic symmetry by choosing a new unit cell that is twice as large with "primitive" lattice vectors

$$\mathbf{A}_1 \quad 2\mathbf{a}_1 + \mathbf{a}_2 \quad 3^{1/2}a(1,0,0), \quad \mathbf{A}_2 \quad \mathbf{a}_2 \quad a(0,1,0), \quad \mathbf{A}_3 \quad \mathbf{a}_3 \quad c(0,0,1), \quad (4)$$

and reciprocal lattice vectors given by

$$\mathbf{B}_1 \quad (2\pi/3^{1/2}a)(1,0,0), \quad \mathbf{B}_2 \quad (2\pi/a)(0,1,0), \quad \mathbf{B}_3 \quad (2\pi/c)(0,0,1). \quad (5)$$

By a similar transformation, it is possible to choose a unit cell for the zinc blende structure that is tetragonal and twice the size of the primitive cell or cubic and four times the size of the primitive cell [11]. More importantly, it is almost always possible to choose a rectangular "supercell" for use in calculations of surface states, amorphous materials, or defects in solids. The presence of such symmetry greatly simplifies tight binding calculations.

Where rectangular symmetry exists or can be forced, the lattice vectors can be written as

$$\mathbf{R}_i \quad r_{i1}d_1\hat{\mathbf{x}} + r_{i2}d_2\hat{\mathbf{y}} + r_{i3}d_3\hat{\mathbf{z}}.$$

In such a case, it is shown in Ref. [8] that the multicenter integrals are factorizable. The primitive Gaussians are written as

$$\chi_\mathbf{n}(\alpha,\mathbf{r}) \quad x^n y^l z^m \exp\{-\alpha r^2\}, \quad \text{where } \mathbf{n} \quad (n,l,m).$$

Then, following the notation used in Ref. [8], a potential energy matrix element of Γ^{xc}, evaluated at a point $\mathbf{k}$ in the Brillouin zone, can be written in factorized form as

$$\sum_i \exp(i\mathbf{k}\cdot\mathbf{R}_i)X_{n_1 n_2 n_3}(\alpha_1, \alpha_2, \beta, \mathbf{A}, \mathbf{B} \quad \mathbf{R}_i, \mathbf{C})$$

$$\left[\sum_{i_1} \exp(ik_x r_{i1}d_1)H_{n_1 n_2 n_3}(\alpha_1, \alpha_2, \beta, A_x, B_x \quad r_{i1}d_1, C_x) \right]$$

$$\cdot \left[\sum_{i_2} \exp(ik_y r_{i2}d_2)H_{n_1 n_2 n_3}(\alpha_1, \alpha_2, \beta, A_y, B_y \quad r_{i2}d_2, C_y) \right]$$

$$\cdot \left[\sum_{i_3} \exp(ik_z r_{i3}d_3)H_{n_1 n_2 n_3}(\alpha_1, \alpha_2, \beta, A_z, B_z \quad r_{i3}d_3, C_z) \right]. \quad (6)$$

where the elements of the H matrices are given by

$$H_{n_1 n_2 n_3}(\alpha_1, \alpha_2, \beta, A_x, B_x, C_x) \quad \sum_{i_1} U_{n_1 n_2 n_3}(\alpha_1, \alpha_2, \beta, A_x, B_x, C_x \quad r_{i1}d_1).$$

The U's are, in general, simply 3-center, 3-gaussian integrals. This shows that (i) the lattice sum over N^3 terms that must normally be done in conventional LCAO calculations reduces to three summations of only N terms each and (ii) the individual

multicenter integrals need not be evaluated and that only the H'-matrices need to be calculated and stored on disk. These two features not only lead to a significant increase in the speed of computation, but also leads to a significant reduction in the amount of disk storage. Vectorized computer codes are in the process of being developed for the IBM 3090-200S that utilize these features of the FLCAO method, although the scalar versions were used to calculate the electronic structure of α-quartz that will be reported in the next section of this article, and of ZnS, ZnSe, and the 1-1 heterostructure in an accompanying article [11].

Energy Band Structure of α-SiO$_2$

Review

In this section we present the results of our calculation of the electronic band structure of α-SiO$_2$. Among the oxides, quartz is a rather unique material. It is extremely stable and can be grown with high quality. Due to its piezoelectric nature, it is widely used as the key element in precision frequency control [13]. Because of its high technological importance, its crystal and electronic structures have been intensively studied both experimentally and theoretically for several decades. Alpha-quartz, also known as low quartz, is stable at room temperature. It exists in both right- and left-handed forms, corresponding to the enantiomorphous space groups $D_3^6 = P3_221$ and $D_3^4 = P3_121$, respectively. Here, we only consider the right-handed form, although both forms often exist in real crystals. The unit cell contains nine atoms and was discussed in the previous section. At 293 K, the primitive lattice constants are $a = 4.9134$ A and $c = 5.4052$ A [14]. In addition to the 9- and 18-atom unit cells, energy bands were also calculated for the 72-atom orthorhombic unit cell where, the lattice parameters were chosen to be (in terms of those for the 18-atom cell) $A_1' = A_1$, $A_2' = 2A_2$, and $A_3' = 2A_3$.

There have been several recent band structure calculations reported for alpha quartz [7,15-19]. Chelikowski and Schluter [15] made a self-consistent pseudopotential calculation of the valence band structure that gives good agreement with experimental data for the band gap, optical spectrum, and photoemission spectrum. The calculations of Calabrese and Fowler [16] were made using the mixed-basis function method for a crystalline potential that was constructed by superimposing atomic Hartree–Fock–Slater potentials obtained from the Herman–Skillman codes [20]. The results reported in Refs. [7], [17-18] were obtained from nonself-consistent tight-binding calculations that differ in the way the exchange was treated, the choice of basis, and the method used for decomposing the crystalline potential. The calculations of Li and Ching [18] are noteworthy in that they report the energy bands and densities of states for all the polycrystalline forms of SiO$_2$. The calculation of Dovesi et al. was made using the periodic Hartree–Fock method [21] with a minimal STO-3G basis. They compare their SCF results with those obtained from SCF Hartree–Fock calculations for the molecular cluster Si$_2$O$_7$H$_6$ and find very good agreement between the two sets of results.

Results

The crystalline potential used in this calculation was constructed by superimposing atomic charge densities that were calculated using modified Herman–Skillman codes [20]. The atomic configuration of the Si was assumed to be $3s^1 3p^3$, and the Slater form of the exchange [12] used throughout. The crystalline charge density was determined along nonequivalent directions about the oxygen and silicon sites in the lattice, and used to calculate the crystalline potential. This numerical potential was the deconvoluted into a superposition of atomic centered analytic potentials as described by Eq. (1). The linear and nonlinear parameters appearing in these expressions were determined by a least squares fitting process, and the results are given in Table I. For this set of potential parameters, $V^A(r) \cong V_{A,0} = -0.15$ a.u. and gives a fit potential having a rms error of 7.88×10^{-3} a.u. with respect to the numerical crystalline potential. For our basis, we chose the atomic Gaussian sets of Veillard [22] for the silicons and the (10/6) basis of Huzinaga [23] for the oxygens. None of the Gaussians were omitted from either basis as is often done in order to reduce the computational burden. Several methods were studied for contracting the basis, including those contained in the articles cited, through calculations of the states at selected **k** points in the first Brillouin zone for the 18-atom unit cell. These had little to no effect upon the valence band states, but some showed significant effects on the conduction band states. The method of contraction which we have found most appealing, and was employed in our II–VI studies [11], goes as follows. A calculation was made for the 18-atom unit cell at the Γ point using the fully uncontracted basis. For this basis, this gives rise to 570 Bloch functions. The coefficients of the Bloch functions for the core states can be readily identified as being predominantly due to symmetrized combinations of atomic-like orbitals that can be expressed as a linear combination of the basis of one type of atom. These coefficients are renormalized and used to describe the core orbitals in subsequent calculations. From the results for the valence and conduction band states, it is possible to determine which of the uncontracted Gaussians can be omitted from the remainder of the basis. In this case, a 342-member contracted basis was constructed

TABLE I. Coefficients and exponential parameters of the analytic fit potentials V^O and V^S.

i	σ_O	β_O	σ_S	β_S
0	8.0	2002.65	14.0	2002.65
1	0.536899	0.197593	1.62780	0.317549
2	3.88680	1.16285	4.44274	1.35059
3	8.41624	4.10013	11.7732	4.01768
4	18.4726	14.2877	29.8739	13.6113
5	34.8756	45.1368	60.3810	46.0991
6	71.4705	154.882	122.423	155.198
7	145.591	570.433	254.028	570.838
8	222.912	4262.91	1390.828	4280.00
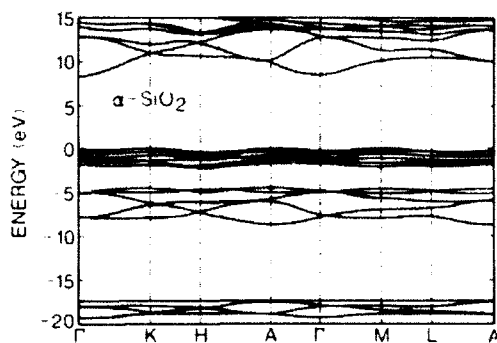
Figure 1.   Band structure of α-quartz.

which had negligible effect on the calculated bands. We calculated an indirect band
gap energy for α-quartz using the 570 uncontracted Gaussian basis of 8.39 eV and
8.47 eV using the 342 contracted basis. In Figures 1 to 8 we show the results of
our calculations of the energy band structure and densities of states (DOS) for α-
quartz. For purposes of comparison with earlier calculations by other methods,
and due to the difficulty in displaying twice as many states in a figure of this size,
we only show a detailed plot of the band structure for the 9-atom primitive cell.
The DOS's, shown in Figures 2 to 5 are for the 18-atom unit cell results, although
we could detect no discernable differences between the DOS's obtained for the two
cases, which is as it should be. It should be noted that in going from the 9- to the
18-atom unit cell, the volume doubles and the number of occupied states per reduced
k-vector also doubles. The Γ point for the 18-atom cell contains both the Γ and M
points of the 9-atom cell. A good picture of the bands for the 18-atom cell along
this direction can be seen from Figure 1 by recognizing that M folds over onto Γ,
L onto A, where the "fold" is made at ½ M. A similar folding over of bands occurs
in going from the 18- to the 72-atom unit cell. This results in there being 96 occupied
states   per   k-vector   in   the   72-atom   unit   cell's   oxygen   nonbonding
"2p" band.
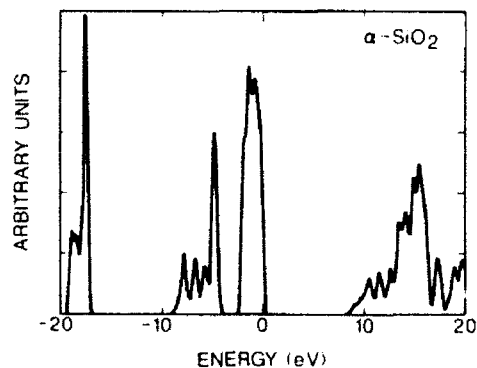
Figure 2.   Calculated density of states for α-quartz.
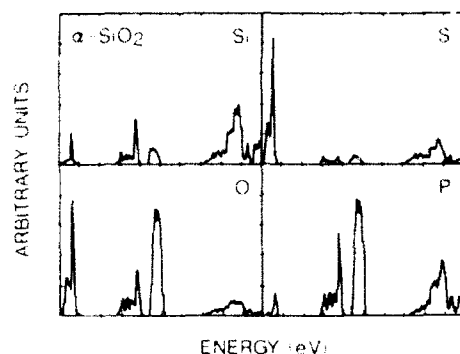
Figure 3. Partial densities of states for α-quartz

Discussion

In Figure 4 we show the calculated valence band DOS and have also plotted the experimentally measured x-ray and ultraviolet photoemission spectra for α-quartz for comparison [24,25]. The agreement should be considered to be quite good since the theoretical DOS does not contain any corrections for instrumental line broadening effects nor for the different optical-absorption cross section for electrons of different quantum numbers [26]. The four-peaked structure in the calculated DOS, which from the partial DOS results shown in Figure 3 we attribute to the O (2p) — Si (3p) bonding band between −4 and −9 eV, is in agreement with the XPS data [27]. In Figure 5 we compare our calculated DOS for the states near the bottom of the conduction band with effective photoionization cross section data [28]. The data suggests that there is a conduction band density of states peak at about 1 eV above the bottom of the conduction band. The calculated DOS shows a shoulder in that range but the first peak occurs ca.1 eV higher and may reflect
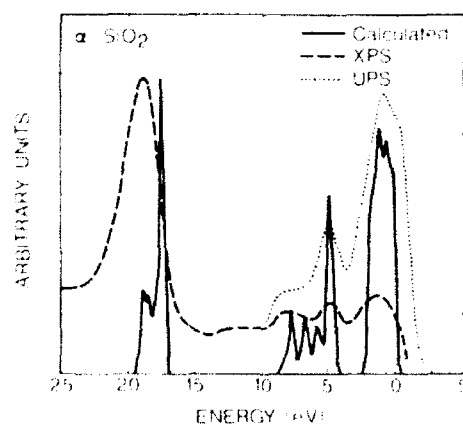
Figure 4. Comparison of the calculated valence band density of states with x-ray (XPS) and ultraviolet (UPS) photoemission spectra for α-quartz
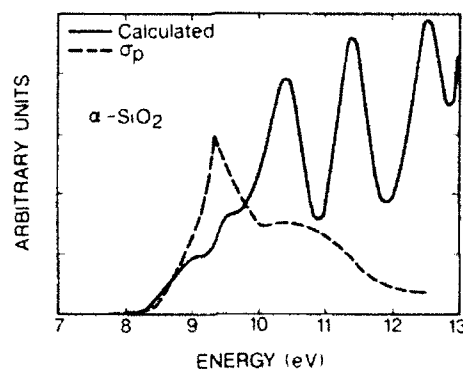
Figure 5.   Comparison of the calculated conduction band density of states with the effective photoionization cross section σ_p for α-quartz.

the fact that this calculation is not self-consistent. Our calculations using the contracted basis give an indirect band gap of 8.47 eV from $K \rightarrow \Gamma_c$, although the $M \rightarrow \Gamma_c$ transition is only 0.01 eV above this. The experimental gap energy, E_g, as determined from photoconductivity measurements is 8.9 eV [29]. The difference between the value for E_g obtained from our calculations and the experimental value can be attributed in part to our use of the Slater exchange and to the fact that the calculations are not self-consistent. This value is somewhat smaller than those obtained by (i) Heggie et al. (8.61 eV) [7], who used the Wigner interpolational formula for the exchange and correlation, (ii) Li and Ching (8.8 eV) [18], that was obtained from an OLCAO calculation where they used a value for the exchange parameter of $\alpha = 0.8$ and a minimal basis, and is larger than that calculated by Batra (7.6 eV), who used the extended tight binding method with the Kohn–Sham exchange [17]. Nevertheless, aside from the calculated values for the gap energy, the calculated valence band widths and positions are in generally good agreement with experiment, and with previous LCAO calculations, in spite of the fact that all
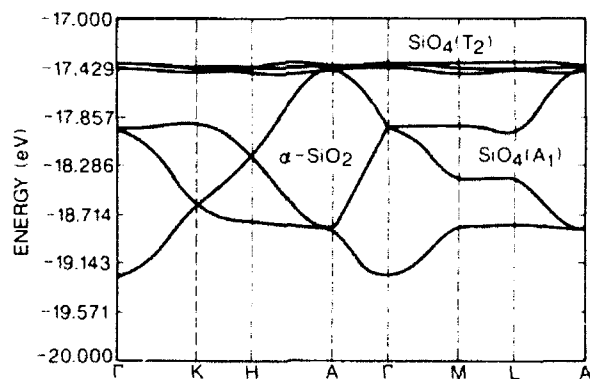
Figure 6.   Oxygen "2s" valence bands for α-quartz.
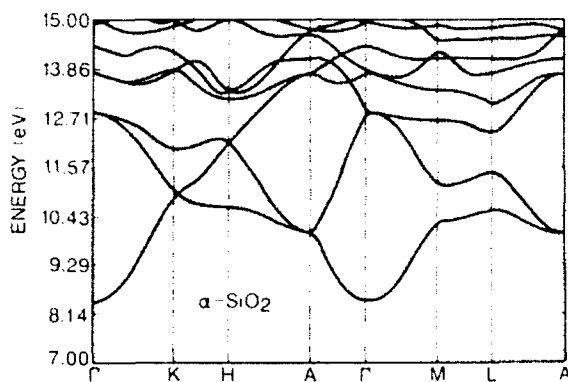
Figure 7.   Low lying conduction bands for α-quartz.

were made using highly contracted basis sets. It should be noted that the contracted basis used in this work is three times larger than the minimal basis (114 for the 18-atom unit cell).

In Figure 3 and Table II we show our results for the partial densities of states and Mulliken population analysis of the valence bands and of the states near the bottom of the conduction band. They clearly show that the major contributions to the valence band states are from the oxygen s- and p-orbitals, with only small, but as we shall see important, contributions from the silicons. The contributions to the low lying states of the conduction band arising from the oxygens and silicons are comparable, whereas the silicon p-orbital contributions dominate the higher conduction band states. The six bands shown in Figure 6, (from bottom to top we label these 1 → 6), comprise the lowest of the valence bands of α-SiO₂ that the population analysis shows to be predominantly oxygen "2s" in origin. From the results of this analysis and that of the coefficients of the LCAO Bloch functions, it was possible for us to develop a simple model for describing the origin and ordering of the states of this band. We begin by placing a silicon at the center of a tetrahedron
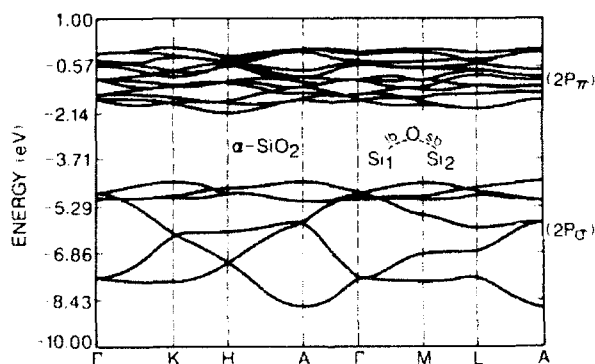
Figure 8.   Oxygen "2p" bonding and nonbonding valence bands for α-quartz.

formed by four oxygens. The silicon can form sp^3 hybrid bonds with the "2s"
orbitals on all four oxygens. These bonds are strong and help hold the tetrahedron
together. They give rise to a low-lying A_1 bonding state, where the silicon p-orbitals
have no role for a perfect tetrahedron, and a higher 3-fold degenerate T_2 state,
where the silicon s-orbital similarly has no role. In α-quartz, the SiO_4 tetrahedra
are not perfect as there are two Si — O long bonds (1.612 A) and two Si — O short
bonds (1.607 A), and the angles between them are not those of a perfect tetrahedron.
Therefore, these cancellations are not exact. We now bring together these SiO_4
"molecules," or fragments, to form α-quartz and assume that the resultant wave-
functions can be represented by linear combinations of the bonding MO's. (LCBMO)
[30]. This results in a twelve MO basis from which 12 Bloch functions can be
constructed, only 6 of which are linearly independent. From this procedure we find
that the three lower bands arise from the A_1 states of the constituent SiO_4 fragments.
The oxygens are strongly bound to the central silicon with large overlapping charge
and is why they are shifted to such low energies. Band 1 produces the most bonding
charge, where every overlap between the A_1 MO's is positive. Bands 2 and 3 are
again made up of the totally bonded A_1 MO's, but combine out of phase in order
to maintain orthogonality to the band 1 state. In this way, all the possible in- and
out-of phase combinations of the SiO_4 A_1 MO's are used up. Thus, bands 4, 5, and
6 have no other choice but to form Bloch functions from the higher energy T_2 SiO_4
states. The bonding between the silicon p's with the oxygen 2s's in these bands is
not as favorable as that of the silicon s's with the oxygen 2s's in bands 1 → 3. In
fact, in band 1 there is 11% Si (s) but in band 6 there is 0% Si (s) and only 5% Si
(p). As a result, in bands 4 → 6 the oxygens are more or less on their own and,
due to the small overlap, there is little dispersion. This analysis carries over to that
of the six lowest bands of the conduction bands shown in Figure 7, and accounts
for their striking resemblance to the oxygen "2s" bands shown in Figure 6.

However, an extension of this analysis to the oxygen $2p_\sigma$ bonding and $2p_\pi$ non-
bonding bands (see Table II), shown in Figure 8, fails to provide any clear insight
into the nature of the bonding. Instead, we find that the $2p_\sigma$ and $2p_\pi$ band states
can best be described in terms of LCMO's formed from Si_2O MO's, where each of
the Si_2O fragments involves one long- and one short-bond, that is, we picture α-
SiO_2 as a network of Si_2O fragments. In the p_σ bonding band, the p-orbitals on the
central oxygens "point" in a direction parallel to a vector that lies in the Si — O — Si
plane and from the long-bond silicon to the short-bond silicon for half of the oxygens,
and anti-parallel for the remaining half. Similarly, the analysis of the p_π nonbonding

TABLE II. Analysis of the oxygen "2s" and "2p" valence bands in α-SiO_2.

Band	% Si(s)	% Si(p)	% O(s)	% O(p)	Width (eV)
"2s"	3.34	3.02	91.92	1.72	1.85
"$2p_\sigma$"	6.01	8.43	0.68	84.88	4.9
"$2p_\pi$"	0.44	3.92	0.88	94.76	2.2

band states correspond to the oxygen's p-orbital being ⊥ to the Si—O—Si plane, where the O—O π-interactions dominate the Bloch functions with weak O—Si interactions. These are precisely the orientations predicted by this simple picture and the LCAO results.

This analysis of the LCAO state functions for the valence bands helps to explain the long known fact that experimental peaks in the valence band density of states (from UPS or XPS) can best be interpreted in terms of MO calculations by using Si₂O results to describe the upper (O—2p) two valence bands, and SiO₄ results for describing the lower (O—2s) valence band [31]. It also helps to account for the incredible success of SCF calculations on "minimal" clusters involving two (SiO₄) fragments in modeling the oxygen-vacancy related defects in SiO₂ [32,33].

Electronic Structure of the Neutral Oxygen Vacancy in α-SiO₂

In this section we summarize the principle results of a LCAO calculation of the electronic structure of the ground state of the neutral oxygen vacancy, or E'₁ center, in α-quartz. The E'₁ center, an oxygen vacancy containing two spin-paired electrons, is widely believed to be the precursor of many of the defects in SiO₂. Since EPR has been the primary tool used to characterize defects in quartz, there is little direct experimental information on this diamagnetic defect. Recent optical-absorption studies of high-purity SiO₂ glass suggest that the observed 5.0 and 7.6 eV absorption bands are associated with this defect [34]. Several recent SCF MO molecular cluster calculations show that (i) the two electrons are localized on the Si—sp³ orbitals that "point" into the vacancy, and (ii) the silicons "relax" inward by ca. 0.2 Å [35,36] or by ca. 0.5 Å [37,38] if the nnn oxygens are also allowed to "relax" from their perfect lattice positions. An earlier nonself-consistent LCAO, minimal basis calculation, employing a 72-atom unit cell, was made on this center which gave a filled vacancy level 2.9 eV below the conduction band edge [39]. Lattice relaxation effects were not included, thus these results are not considered very realistic.

A series of SCF MO cluster and LCAO band structure calculations have been carried out in order to determine the ground and excited states of the E'₁ center in α-SiO₂. The LCAO band structure was calculated in the same fashion as described above where one of the oxygens was removed from the unit cell. The bands were calculated for both an 18-atom and a 72-atom unit cell using the 18-atom α-SiO₂ contracted basis described above. Lattice relaxation effects were included by determining the nn silicon and nnn oxygen "relaxed" positions from SCF MO cluster calculations [38]. The results for "vacancy" band obtained from the 18-atom unit cell calculation displayed ca. 0.2 eV dispersion showing that there was not enough separation between the defects to adequately describe an isolated vacancy state. The results from the 72-atom calculation gave only ca. 0.01 eV dispersion in this "band" and the results for the Γ 1/2 M direction are shown along with the 72-atom perfect crystal bands in Figure 9. 1/2 M is the edge of the 72-atom BZ in the (1,0,0) direction. These results give the "vacancy" level, or band, to lie 3.7 eV above the valence band and a band gap of ca. 8.4 eV. An analysis of the "vacancy" band Bloch functions shows that the two electrons are localized on the nn silicons
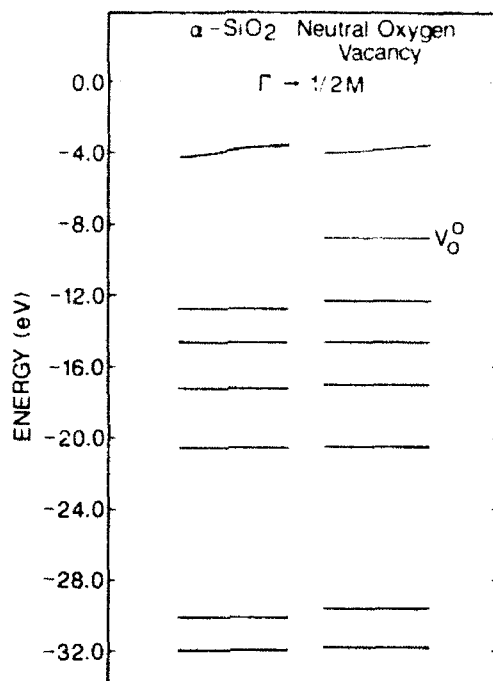
Figure 9. Electronic structure of α-quartz and the neutral oxygen vacancy (V_O^0) center
in α-quartz calculated by the FLCAO method employing a 72-atom supercell.

and the nnn oxygens. There is a second, well defined "vacancy" band ca. 0.5 eV *above* the bottom of the conduction band, which gives rise to a calculated value of 5.2 eV for the observed 5.0 eV (V_O^0) absorption band [34]. Rudra and Fowler [39] calculated this splitting to be 6.6 eV using the MINDO/3 technique. However, although our calculations include lattice relaxation effects, since they (i) are not self-consistent, and (ii) involve no corrections to the LDA for treating the exchange, the good agreement of our results with experiment may justifiably be regarded as fortuitous.

Summary and Conclusions

In this article, we have reported the results of our application of the recent reformulation of the LCAO method to the calculation of the electronic structure of α-SiO$_2$ and of the neutral oxygen vacancy defect in this material. Although the calculations are not self-consistent, they represent the most comprehensive study yet made of the electronic structure of, and the nature of the bonding in, α-quartz. These calculations, along with those for a 33-atom thick (100) copper thin film [8], and for the 1–1 ZnS/ZnSe strained-layer superlattice [11], clearly establish the FLCAO method as a powerful and practical technique for determining the electronic structure of surfaces, amorphous materials, strained-layer superlattices, or defects, where large numbers of atoms must be included in the unit cell, and a

rectangular "supercell" can almost always be employed. This makes possible the factorization of the multicenter integrals that results in a considerable reduction of computational complexity and CPU time, thereby making this technique competitive with LAPW and LMTO methods [40] that are frequently employed in such studies.

The deconvolution of the crystalline potential shown in Eq. (1) differs in an important way from the one that has been used with considerable success in the study of thin films using the LCAO method [10]. There, the crystalline charge density and exchange potential are separately fit to a linear combination of gaussians. This method results in a significant reduction in the complexity of evaluating matrix elements involving $\rho^{1/3}$, but it does not yield expressions for the multicenter potential energy integrals that are factorizable. In the reformulation described here and in Ref. [8], the only matrix element that does not factorize involves V^c. Since the sole purpose of this term is to reproduce the coulombic singularity, the exponent β_0 is chosen to be quite large (see Table I). It has been shown that good results can be achieved by simply fitting V^c to a sum of Gaussians [8,41], thereby making all the matrix elements factorizable. The LCAO method is ideally suited to vectorization and work is underway to vectorize and make the programs self-consistent.

Acknowledgments

Bibliography

[1] E. E. Lafon and C. C. Lin, Phys. Rev. 152, 579 (1966).

[2] D. W. Bullett, Solid State Physics, Advances in Research and Applications, F. Seitz and D. Turnbull, Eds. (Academic, New York, 1980), Vol. 35, p. 129.

[3] W. Y. Ching and J. Callaway, Phys. Rev. B9, 5115 (1974).

[4] R. Heaton and E. E. Lafon, Phys. Rev. B17, 1958 (1978).

[5] J. E. Simmons, C. C. Lin, D. F. Fouquet, E. E. Lafon, and R. C. Chaney, J. Phys. C8, 1549 (1975).

[6] M. Mehta-Ajmani, I. P. Batra, E. E. Lafon, and C. S. Fadley, J. Phys. C13, 2807 (1980).

[7] M. M. Heggie, R. Jones, and M. Nylen, Phil. Mag. B51, 573 (1985).

[8] E. E. Lafon, J. Comput. Phys. 83, 185 (1989).

[9] W. Y. Ching and C. C. Lin, Phys. Rev. B12, 5536 (1975); 16, 2989 (1977).

[10] J. W. Mintmire, J. R. Sabin, and S. B. Trickey, Phys. Rev. B26, 1743 (1982).

[11] I. S. Marshall and J. M. Wilson (elsewhere in this issue).

[12] J. C. Slater, Phys. Rev. 81, 385 (1951).

[13] E. A. Gerber and A. Ballato, Precision Frequency Control, (Academic, New York, 1985).

[14] Y. Le Page and G. Donnay, Acta Crystallogr. Sec. B32, 2456 (1976).

[15] J. R. Chelikowsky and M. Schluter, Phys. Rev. B15, 4020 (1977).

[16] F. Calabrese and W. B. Fowler, Phys. Rev. B18, 2888 (1978).

[17] I. P. Batra, The Physics of SiO₂ and its Interfaces, S. T. Pantelides, Ed. (Pergamon, New York, 1978), p. 65.

[18] Y. P. Li and W. Y. Ching, Phys. Rev. B31, 2172 (1985).

[19] R. Dovesi, C. Pisani, C. Roetti, and B. Silvi, J. Chem. Phys. **86**, 6967 (1987).

[20] F. Herman and S. Skillman, *Atomic Structure Calculations* (Prentice-Hall, Englewood Cliffs, NJ, 1963).

[21] C. Pisani and R. Dovesi, Int. J. Quantum Chem. **17**, 501 (1980).

[22] A. Veillard, Chim. Acta (Berlin) **12**, 405 (1968).

[23] S. Huzinaga, J. Chem. Phys. **42**, 1293 (1965).

[24] H. Ibach and J. E. Rowe, Phys. Rev. **B10**, 710 (1974).

[25] T. H. DiStefano and D. E. Eastman, Phys. Rev. Lett. **27**, 1560 (1971).

[26] J. H. Scofield, J. Electron Spectrosc. Relat. Phenom. **8**, 129 (1976).

[27] B. Fischer, R. A. Pollak, T. H. DiStefano, and W. D. Grobman, Phys. Rev. **B15**, 3193 (1976).

[28] D. D. Rathman, F. J. Feigl, and S. R. Butler, *Insulating Films on Semiconductors 1979*, G. G. Roberts and M. J. Morant, Eds. (Institute of Physics, London, 1980), p. 48; and unpublished

[29] T. H. DiStefano and D. E. Eastman, Solid State Commun. **9**, 2259 (1971).

[30] P. W. Kervin and E. E. Lafon, J. Chem. Phys. **58**, 1535 (1973).

[31] D. L. Griscom, J. Non-Cryst. Solids **24**, 155 (1977).

[32] J. K. Rudra, W. B. Fowler, and F. J. Feigl, Phys. Rev. Lett. **55**, 2614 (1985).

[33] T. M. Wilson, L. E. Halliburton, M. G. Jani, and J. J. Martin, *Proceedings of the Fortieth Annual Symposium on Frequency Control* (1986), p. 26.

[34] R. Tohmon, H. Mizuno, Y. Ohki, K. Sasagane, K. Nagasawa, and Y. Hama, Phys. Rev. **B39**, 1337 (1989).

[35] A. H. Edwards and W. B. Fowler, J. Phys. Chem. Solids **46**, 841 (1985).

[36] F. Sim, C. R. A. Catlow, M. Dupuis, and J. D. Watts, J. Chem. Phys. **95**, 4215 (1991).

[37] J. K. Rudra and W. B. Fowler, Phys. Rev. **35**, 8223 (1987).

[38] T. M. Wilson (unpublished results used in these calculations).

[39] M. Nylen, J. Phys. C**19**, 2403 (1986).

[40] O. K. Anderson, Phys. Rev. **B12**, 3060 (1975).

[41] R. N. Euwema (private communication).

Finite Elements and Partial Waves
in Scattering Calculations

JAN LINDERBERG

Department of Chemistry, Aarhus University, DK-8000 Aarhus C, Denmark

Abstract

The conventional use of pure angular momentum state representations in the algorithms for reactive scattering is discussed and the merits of alternative formulations in a finite element framework are considered with respect to possible numerical effectiveness. Four- and seven-dimensional hyperspheres are discretized as means of describing three- and six-dimensional scattering problems. © 1992 John Wiley & Sons, Inc.

Motivation

Pure angular momentum states are the preferred choice in quantum mechanical analyses of rotationally invariant systems. Their application in the theory of atom-diatom scattering, the partial wave analysis leads to slowly converging series for scattering cross sections since the heavy particles have relatively large momenta and rotational energy levels have a high density. The use of the Born approximation and its extensions, which are adequate in elastic and some inelastic processes, gets to be quite involved for reactive processes. All algorithms for reactive scattering are computationally demanding and the search is going on for simplifications and more general methods that can be efficiently implemented on more varied computer systems.

This note will not attempt to review the status of reactive scattering theory; Launay and Miller represent two major lines of development as witnessed at this Sanibel Symposium. The purpose is to point towards some possibilities for general and formally simple treatments by means of a finite element method implementation of the hyperspherical formulation. As initiated by Gronwall and Bartlett [1] the hyperspherical approach was presented in Kemble's book [2] and was later used frequently in atomic physics. It is now also established as a useful representation in reactive scattering as we have learned from Launay's lecture. Finite element methods are also gaining recognition as effective tools of the trade. They appeal to quantum chemists through the familiar basis set expansions and the variational origin. The numerical advantage arises from the sparse matrix structures and the possibilities to apply the full machinery of efficient linear algebra routines. Huge matrix problems do appear, but Löwdin's teachings has provided us with a rich arsenal of partitioning tools, inner projections, and perturbation schemes with which we may attack formidable tasks.

After this preamble follows a section on the particular difficulties with the partial wave expansion and preliminaries are given on the finite element alternative. A previously reported pilot calculation on the free rotor is referred to in the third part and a mapping from the rotor to the potential scattering problem is given in the fourth. Generalizations to the three-particle problem are discussed in terms of discretized hyperspheres in six- and seven-dimensions in the fifth section, which is followed by a few speculative remarks.

Partial Waves

Schrödinger's equation in the time independent case, and the associated boundary conditions, derive from the condition of stationarity of the functional

$$J(\Psi,\Phi) = \int_{\Omega} dx \{ [E - W(x)] |\Psi(x)|^2 - |\nabla\Psi(x)|^2 \}$$

$$+ \int_{\Gamma} dx [\Psi(x)^*\Phi(x) + \Phi(x)^*\Psi(x)]$$

$$- \int_{\Gamma} dx \Phi(x)^* \int_{\Gamma} dy R(x,y)\Phi(y) \tag{1}$$

The wave function $\Psi(x)$ is defined on a domain Ω, with the boundary Γ, in R^n. An auxiliary function $\Phi(x)$ is defined on Γ and equals the normal derivative of $\Psi(x)$ there. The integral kernel $R(x,y)$ provides the boundary condition

$$\Psi(x) = \int_{\Gamma} dy R(x,y)\Phi(y) \tag{2}$$

Mass weighted coordinates are implied and units are chosen so that E is the total energy of the system and $W(x)$ is the potential. A more detailed account is given elsewhere [3].

It is assumed that the boundary Γ and the potential $W(x)$ are invariant under the operations of a group G. This is formulated in terms of a function, $S(x)$, with the properties

$$S(x) = 0, \qquad x \in \Gamma \tag{3}$$

and

$$gS(x) = S(g^{-1}x) = 0, \qquad g \in G, \qquad x \in \Gamma \tag{4}$$

Similarly it holds that

$$gW(x) = W(g^{-1}x) = W(x), \qquad g \in G, \qquad x \in \Omega \tag{5}$$

for the potential. It is then conventional to expand the wave function in terms of the irreducible representations of the group:

$$\Psi(x) = \sum_{jmm'} \psi_{jmm'}(g^{-1}x) D^j_{mm'}(g)^* \tag{6}$$

Continuous groups, in particular the three-dimensional rotation group, offer parameterizations with variables which serve as coordinates in conjunction with the internal ones.

Scattering problems lead to wave functions with finite amplitude and normal derivative at the boundary Γ for arbitrarily large domains. The boundary conditions are specified in terms of free waves of the form

$$\Psi(x) \sim \exp(i k \cdot x) \quad \sum (2\lambda + 1)(i)^\lambda j_\lambda(k \cdot x)(2\lambda + 1) P_\lambda\left(\frac{k \cdot x}{k \cdot x} \right) \quad (7)$$

where the spherical Bessel functions are the amplitudes of the partial waves on a sphere in R^3. An illustration of their magnitude is given in Figure 1. The oscillatory behavior with increasing amplitude until the order of the expansion exceeds the argument of the Bessel function is indicative of the problem. Our lightest system with three hydrogen atoms requires, at the relative collision energy of 1 eV, an argument of at least 60 to ensure the asymptotic form.

It is realized that an expansion such as (6) decouples the components of the wave function belonging to different irreducible representations and that a multicomponent system of the degree of the dimension of the representation remains for each. The general case of rotational symmetry gives the estimate that a calculation which has a cost $A(0)$ for zero total angular momentum will have a price tag of

$$A(J + 1) \quad A(0) \sum (2\lambda + 1)^3 \quad A(0) J^3 (2J + 1) \quad (8)$$
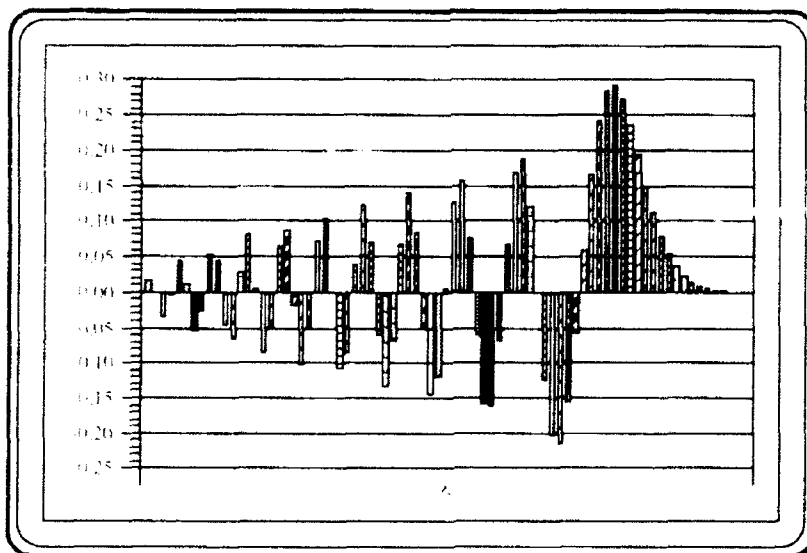
Figure 1.   Amplitudes of partial wave coefficients $(2\lambda + 1) j_\lambda (64.4)$.

in the case that J partial waves are included. The estimate would indicate that it will be 26 million times more expensive to do the full calculation for H_2 than the $I = 0$ case. Experience, as reported at this meeting, shows that the structure of the matrices in the angular momentum eigenstate form admits a scaling where the matrices require work proportional to the first power of the dimension and the total effort runs as the second power of the largest eigenvalue. Efficient alternatives have a market.

Discrete variable representations [4] utilize orthogonal basis functions associated with a lattice determined from the projection kernel for a given function space [5]. The relevant kernel for the rotation group.

$$\sum_{m,m',J} \frac{(2J+1)}{2\pi^2} D^{J*}_{mm'}(g) D^{J}_{mm'}(g') \quad \frac{U'_{2J+1}(t)}{4\pi^2} \tag{9}$$

is expressed in terms of the derivative of a Chebyshev polynomial of the second kind in the variable t, which gives a measure of the magnitude of the composite rotation $g^{-1}g'$. It provides no automatic way to find a suitable lattice, such as the discrete Fourier transform and, in a single dimension, the Gaussian integration rules do. The rank of the kernel is $(J+1)(2J+1)(2J+3)/3$ and the discretization would correspond to the construction of a subset of this order with "distances" between elements such that the kernel would be diagonal.

Were it possible to generate a set of suitably distributed elements of the rotation group, the associated, localized basis functions would have a global character with an oscillatory behavior as given by the form (9). This will necessitate the inclusion of matrix elements between distant neighbors and there will be no particular sparseness pattern. In contrast, the finite element method offers a regular way of discretizing diverse spaces and involves a basis of strictly localized, albeit nonorthogonal, functions. The matrix patterns are reflections of the connectivity in the discretized structure and indicate ways to handle the large matrices by partitioning methods, outer and inner projections [6], and Lanczos techniques [7]. An equal number of points in the finite element method and the discrete variable representation will give an equivalent resolution in terms of "distances" between group elements. The finite element approach will not be as accurate for the high angular momentum components included in the discrete variable formulation, but does include higher components. One might expect that the finite element method basis should cover the relevant function space equally efficient as the partial wave expansion, and that the associated computational effort should be less.

Rigid Rotor

A pilot study of the rigid rotor has been performed [8] in order to examine some particular discretization procedures. The Euler–Rodrigues parameters [9] for the group $SU(2)$ were used to obtain approximate representation matrices for $SO(3)$. Thus we have that the relevant domain Ω is closed and consists of the three-dimensional, unit hypersphere in R^4. Boundary terms disappear from the functional

(1) and the transformations from a many-particle problem to the rigid rotor lead to the following representation of the components of the angular momentum in the system defined by the principal moments of inertia (I_1, I_2, I_3):

$$P_1 \Psi = \frac{i}{2} \left(\alpha_1 \frac{\partial \Psi}{\partial \alpha_0} - \alpha_0 \frac{\partial \Psi}{\partial \alpha_1} - \alpha_3 \frac{\partial \Psi}{\partial \alpha_2} + \alpha_2 \frac{\partial \Psi}{\partial \alpha_3} \right)$$

$$P_2 \Psi = \frac{i}{2} \left(\alpha_2 \frac{\partial \Psi}{\partial \alpha_0} + \alpha_3 \frac{\partial \Psi}{\partial \alpha_1} - \alpha_0 \frac{\partial \Psi}{\partial \alpha_2} - \alpha_1 \frac{\partial \Psi}{\partial \alpha_3} \right)$$

$$P_3 \Psi = \frac{i}{2} \left(\alpha_3 \frac{\partial \Psi}{\partial \alpha_0} - \alpha_2 \frac{\partial \Psi}{\partial \alpha_1} + \alpha_1 \frac{\partial \Psi}{\partial \alpha_2} - \alpha_0 \frac{\partial \Psi}{\partial \alpha_3} \right) \qquad (10)$$

The variational functional is

$$J_K(\Psi) = \int_\Omega d\alpha \left\{ \lambda |\Psi(\alpha)|^2 - \frac{1}{I_1} |P_1 \Psi(\alpha)|^2 \right.$$

$$\left. - \frac{1}{I_2} |P_2 \Psi(\alpha)|^2 - \frac{1}{I_3} |P_3 \Psi(\alpha)|^2 \right\} \qquad (11)$$

with stationary value zero for eigenvalues λ. The domain

$$\Omega: \{ \alpha = (\alpha_0, \alpha_1, \alpha_2, \alpha_3); \ |\alpha| = 1 \} \qquad (12)$$

is curved and we chose to employ isoparametric finite elements with third-degree polynomials.

The hypersphere was partitioned into 384 equivalent simplexes, each one generated from a primitive one.

$$\Omega_0: \{ \alpha \in \Omega; \ 1 \geq \alpha_0 \geq \alpha_1 \geq \alpha_2 \geq \alpha_3 \geq 0 \} \qquad (13)$$

by means of permutations and sign changes of the coordinates. The set of 384 operations form a group known as a Coxeter reflection group [10]. It is generated by a set of reflections, similarly as the elements of the rotation group may be composed of two reflections [7]. There are 768 faces, 464 edges, 80 vertices, and 1776 nodes in an isoparametric finite element approximation, where the curved simplex is mapped on a straight one through third-degree polynomials in standard baricentric coordinates [11]. The Coxeter group is the symmetry group of the functional (11) when all the moments of inertia are equal, that is for the spherical rotor. It has 20 irreducible representations. A general rotor admits a lower symmetry group with 32 elements and 17 irreducible representations. One of these is four dimensional while the remaining ones are of the first degree and are admissible for $SO(3)$. This group has been used to block diagonalize the matrix into one block of dimension 69, six of dimension 51, and nine of dimension 57. Calculations for the spherical rotor demonstrate that this simple approximation gives angular momentum eigenvalues of reasonable accuracy, the 49 states corresponding to the manifold for $J = 3$ occur in the range $[12.23, 12.60]$.

The Euler–Rodrigues parameterization of the rotation group is readily transformed into the axis–angle parameterization in terms of the direction of the axis of rotation in R^3 and the magnitude of the angle. These parameters are defined on a solid sphere domain in R^3. Conversely, one may convert a solid sphere domain to a part of the unit hypersphere in R^4 and use the tesselation of this as a means of generating a suitable set of simplexes and nodes for a standard scattering problem in R^3. Thus we may put

$$x = (x_1, x_2, x_3) = (\alpha_1, \alpha_2, \alpha_3); \qquad \alpha_0 > 0; \qquad \alpha \in \Omega \qquad (14)$$

for the interior of the unit sphere in R^3 and

$$x = (x_1, x_2, x_3) = (\alpha_1, \alpha_2, \alpha_3); \qquad \alpha_0 = 0; \qquad \alpha \in \Omega \qquad (15)$$

for its boundary. The tesselation of the sphere with the previously offered set of simplexes will give a structure with octahedral symmetry since the subgroup of the Coxeter group which leaves one component of a four-vector invariant is isomorphic to the octahedral group O_h. There will be 48 spherical triangles, 72 edges, 26 vertices, and 218 nodes on the boundary. A similar resolution will be accomplished with an expansion in spherical harmonics including angular momentum terms of order 14. The interior of the sphere will have 779 nodes and the resulting network will be made up of tetrahedra of very similar volume.

Intricate networks can be constructed for the hypersphere in four dimensions [10]. They arise from the great variety of regular polytopes which exists in this particular case. The five Platonic solids in three dimensions do not generalize in higher spaces, only the tetrahedron, the octahedron, and the cube possess higher dimensional analogues [10] and for three-particle quantum mechanics in the center-of-mass system we expect that only the regular polytope corresponding to the octahedron will be relevant.

General Hyperspheres

Atom–diatom scattering problems lead, in the Born–Oppenheimer approximation, to a six-dimensional problem. A finite element application will necessarily involve a considerable number of nodes and we will give a preliminary account of the consequences of the kind of tesselation which was used previously. Thus we consider a hypersphere in seven dimensions:

$$\Omega: \{ \alpha = (\alpha_0, \alpha_1, \alpha_2, \alpha_3, \alpha_4, \alpha_5, \alpha_6);$$
$$\alpha_0^2 + \alpha_1^2 + \alpha_2^2 + \alpha_3^2 + \alpha_4^2 + \alpha_5^2 + \alpha_6^2 = 1 \} \qquad (16)$$

It will then be possible to generate $7!2^7 = 645.120$ simplexes from the basic one:

$$\Omega_1: \left\{ \alpha; \quad 1 \geq \alpha_0 \geq \alpha_1 \geq \alpha_2 \geq \alpha_3 \geq \alpha_4 \geq \alpha_5 \geq \alpha_6 \geq \frac{1}{\sqrt{7}}, \quad \alpha \in \Omega \right\} \qquad (17)$$

by means of the appropriate Coxeter group [10]. A third-degree version requires 745.418 nodes, which may be partitioned so that 102.024 nodes have $\alpha_0 = 0$ and

321.697 have $\omega_i > 0$. Formally, this would result in a matrix problem of order 423.721. Rotational symmetry is reduced to octahedral and we may construct an adapted basis which will cause a block form with cubic symmetry labels and dimensions about $\frac{1}{4}$ of the original. The tessellation supports particle permutation symmetry when two are equal, but does not automatically include the operations for three identical atoms.

The Coxeter group [10] corresponding to the tessellation in six dimensions has 46,080 elements and can be structured as the 48-element octahedral group and 959 cosets [8]. There is thus a basic domain in the tessellation consisting of the union of the basic simplex Ω and 959 others formed by the coset generators. Only half of these are necessary when there is particle label symmetry. It is awkward to imagine the connectivity in the six-dimensional simplex structure, but the calculation of a suitable numbering of the nodes, the symmetry analysis, and the actual evaluation of nonzero matrix elements are quite direct. Progress is being made in the construction of computer codes.

It is not anticipated that the 400,000 nodes which are distributed over the interior and boundary of the six-dimensional hypersphere will give a satisfactory description of an atom–diatom scattering problem. One will need a denser mesh in certain parts of the space. This can also be accomplished rather automatically by subdivisions of the previous design. It will then be quite obvious that many of the new nodes will be unimportant and the finite element literature provides many schemes for the elimination of insignificant detail. Several of these methods correspond to the well-known quantum chemical methods for the contraction of large basis sets to smaller ones. There remains in the finite element method the possibility of retaining strict locality.

Speculations

It is advocated in this article that the finite element representation for the quantum mechanical variational problem is feasible. The use of accurate angular momentum eigenfunctions is not obviously the most efficient. Scattering problems do not require a very high angular resolution, particularly when no differential cross sections are sought, and may be dealt with in terms of a discretization of the directions in space. Only few data are available to support the present view, while a multitude of calculations have demonstrated the poor performance of the partial wave expansion.

Acknowledgment

Bibliography

[1] T. H. Gronwall and J. H. Bartlett, Phys. Rev. 51, 655, 661 (1937).
[2] E. C. Kemble, *The Fundamental Principles of Quantum Mechanics with Elementary Applications* reprinted ed. (Dover, New York, 1958), p. 210.

[3] J. Linderberg, Int. J. Quant. Chem. **35**, 801 (1989).

[4] J. C. Light, I. P. Hamilton, and J. V. Lill, J. Chem. Phys. **82**, 1400 (1985).

[5] J. Linderberg, Y. Öhrn, and S. B. Padkjaer, J. Chem. Phys. **91**, 4793 (1989).

[6] P. O. Löwdin and O. Goscinski, Int. J. Quant. Chem. **S5**, 685 (1971) and references therein.

[7] See, for example, T. Ericsson and A. Ruhe, Math. of Comp. **35**, 1251 (1980).

[8] J. Linderberg and Y. Öhrn, "Isoparametric Finite Elements on Hyperspheres," in *Advances in Molecular Vibrations and Collision Dynamics*, J. M. Bowman, Ed. (JAI Press, Inc., Greenwich, CT, 1992).

[9] L. C. Biedenharn and J. D. Louck, *Angular Momentum in Quantum Physics* (Addison-Wesley, Reading, MA, 1980), p. 19.

[10] H. S. M. Coxeter, *Regular Polytopes* 2nd ed. (Macmillan, London, 1963).

[11] P. G. Ciarlet, *The Finite Element Method for Elliptic Problems* (North-Holland, Amsterdam, 1978), p. 224.

Theoretical Model Studies for Surface-Molecule Interacting Systems

HIROSHI NAKATSUJI

Department of Synthetic Chemistry, Faculty of Engineering, Kyoto University, Kyoto 606, Japan and
Institute for Fundamental Chemistry, Nishi Hiraki-cho, Kyoto 606, Japan

Abstract

Surface-molecule interactions and reactions are important elementary steps of catalytic reactions. Since they involve interactions between infinite and finite systems, modelings are necessary for theoretical investigations of catalytic reactions on a surface. The cluster model (CM) is most frequently used for quantum chemical calculations but neglects the effect of the bulk solid. For including such effect, (1) embedding the cluster onto a surface (actually into a larger cluster) is a method proposed by Grimley and Pisani, and (2) dipping the adcluster (admolecule + cluster) onto the electron bath of the solid and letting the system be at equilibrium for electron and spin exchanges is another model proposed by Nakatsuji. We show some applications of the embedding cluster model (ECM) and the dipped adcluster model (DAM). We will also report in the lecture on the study of the photochemical decomposition reaction of MnO_4 into $MnO_2 + O_2$. © 1992 John Wiley & Sons, Inc.

Introduction

Chemistry and physics of surface-molecule interaction and reaction systems are of much interest from both purely scientific and industrial standpoints. Since these interactions involve finite and infinite systems, modelings are necessary for theoretical investigations of these systems. Since the results of the investigations are largely dependent upon the nature and the quality of the model adopted, we have to carefully examine the models for surface-molecule interactions and reactions.

Electron correlations are very important since we are mostly interested in the system involving transition metals. Since surface has many dangling bonds, it usually has several lower excited states and further the catalytically active state is not necessarily the ground state, so that our theory should be able to deal with both ground and excited states in a same accuracy. Moreover, electron transfer is sometimes of crucial importance for surface electronic processes and therefore should be described accurately.

Cluster model (CM) has been most frequently used by quantum chemists for investigating chemisorptions and catalytic reactions on metal and semiconductor surfaces. It also has a direct implication in the field of cluster chemistry growing up very rapidly in recent years. However, as a model of surface reactions, this model has a defect that it neglects the effect of bulk metal. For including such effect, Grimley, Pisani, and others proposed the embedded cluster model [1-3] and Nakatsuji the dipped adcluster model [4,5].

How do we model a surface ?

Cluster model
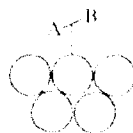
Embedded cluster model

Dipped adcluster model

electron "bath"
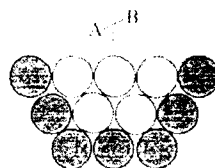
Figure 1.   Conceptual sketch of the cluster model (CM), embedded cluster model (ECM), and dipped adcluster model (DAM).

Figure 1 is a sketch of the concepts of the embedded cluster model (ECM) and the dipped adcluster model (DAM) in comparison with the CM. We define the combined system of admolecule plus cluster in the CM as *adcluster*. Then, the CM is a free adcluster model. In the ECM, the cluster part of the adcluster is "embedded" onto the shaded cluster of atoms which are thought to represent the bulk. The direct interaction between the admolecule and the shaded part is neglected but its effect is taken into account effectively, using the Green's function formalism, in the calculation of the adcluster. On the other hand in the DAM, the adcluster is dipped onto the electron bath of the solid and is let to be in equilibrium for the electron exchange between the adcluster and the solid. This equilibrium is governed by the chemical potentials of the adcluster and the solid.
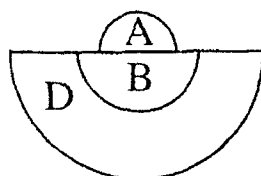
Figure 2.   Schematic representation of the embedded cluster model. A is the adsorbate, B the cluster, and D represents the solid.

Figure 3   H₂ and H... clusters interacting with H₂ and H₂ embedded onto Li... and interacting with H₂.

In this lecture, a brief account of our studies on the ECM and the DAM is given. More details will be published somewhere in the literature [5–9].

We also give in this lecture some results of the theoretical study for the photochemical decomposition reaction of permanganate ion [10,11].

Embedded Cluster Model Applied to H₂ Chemisorption on a Lithium Surface

We use here the moderately large embedded cluster (MELC) model of Pisani, Ravenek, and others [2,3]. Figure 2 illustrates the definition of the model. A is an adsorbate, B is the cluster directly interacting with A, and D represents the solid.

In the closed-shell Hartree–Fock–Roothaan approximation,

$$FC = SC\varepsilon \tag{1}$$

the Green's function G and the matrix Q are defined by

$$Q(z)G(z) = 1 \tag{2}$$

$$Q(z) = zS - F \tag{3}$$

where S and F are, respectively, the overlap and Fock matrices. The Green's function G is further written as

$$G(z) = (zS - F)^{-1} \tag{4}$$

$$G_{\lambda\sigma}(z) = \sum_i \frac{C_{\lambda i}C_{\sigma i}}{z - \varepsilon_i} \tag{5}$$

where λ and σ stand for the basis in the LCAO approximation and $C_{\lambda i}$ is the MO coefficient of the orbital φ_i with the orbital energy ε_i. The essential steps of the ECM may be summarized as follows.

(1) Neglect the direct interaction between A and D

$$\begin{pmatrix} Q_{AA} & Q_{AB} & 0 \\ Q_{BA} & Q_{BB} & Q_{BD} \\ 0 & Q_{DB} & Q_{DD} \end{pmatrix} \begin{pmatrix} G_{AA} & G_{AB} & 0 \\ G_{BA} & G_{BB} & G_{BD} \\ 0 & G_{DB} & G_{DD} \end{pmatrix} = \begin{pmatrix} 1 & 0 & 0 \\ 0 & 1 & 0 \\ 0 & 0 & 1 \end{pmatrix} \tag{6}$$

(2) Calculate the free $B + D$ system without A
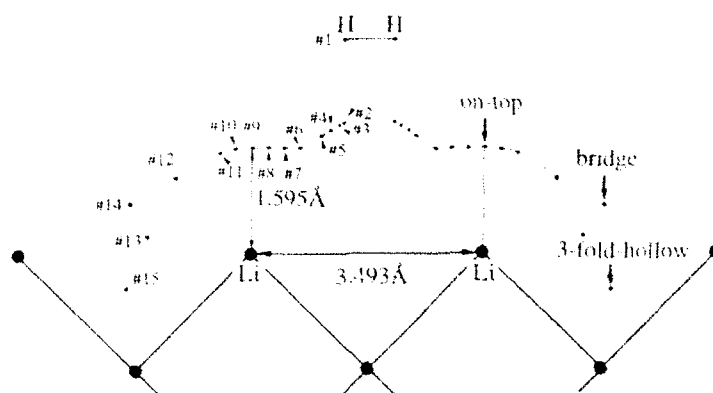
Figure 4. Reaction path for the H_2 adsorption on a Li surface. This reaction path keeps the C_{2v} symmetry and is the same for all of the five different cluster and embedded cluster calculations except that some Li atoms are missing in some models. Points 13, 14, and 15 are the most stable structures for the Li_4H_2, $Li_{14}H_2$, and $Li_{10}H_2$ clusters, respectively.

$$\begin{pmatrix} Q'_{BB} & Q'_{BD} \\ Q'_{DB} & Q'_{DD} \end{pmatrix}\begin{pmatrix} G'_{BB} & G'_{BD} \\ G'_{DB} & G'_{DD} \end{pmatrix} = \begin{pmatrix} 1 & 0 \\ 0 & 1 \end{pmatrix} \tag{7}$$

(3) Calculate only the $A + B$ system using the equation derived from Eq. (6) and approximate the interaction between B and D to be a constant which is given from the second step above.

$$\begin{pmatrix} Q_{AA} & Q_{AB} \\ Q_{BA} & Q_{BB} \end{pmatrix}\begin{pmatrix} G_{AA} & G_{AB} \\ G_{BA} & G_{BB} \end{pmatrix} = \begin{pmatrix} 1 & 0 \\ 0 & 1 - Q'_{BD}G'_{DB} \end{pmatrix} \tag{8}$$

We have adopted basically the calculational scheme given by Ravenek and Geurts, but added some modifications for improving convergence in the Green function calculation. Details are described elsewhere [6].

We have applied the embedded cluster model to an H_2 adsorption on a Li(100) surface. The calculated model systems are as follows:

(1) Li_{14} cluster interacting with H_2
(2) Li_{10} cluster interacting with H_2
(3) Li_4 cluster interacting with H_2
(4) Li_4 embedded onto Li_{10} interacting with H_2
(5) Li_4 embedded onto Li_6 interacting with H_2

Figure 3 illustrates the systems. The Li clusters are taken out from the Li(100) surface with the lattice constant fixed at 3.52 Å. The shaded Li_4 is the smallest cluster in the CM or the embedded cluster in the ECM. The gaussian basis is double-zeta (31) set for hydrogen and STO 3G plus diffuse s function ($\zeta = 0.076$) for lithium.

The assumed reaction pathway is displayed in Figure 4. The ECM is applicable only to the region from position 1 to position 10, since there the direct interaction between H_2 and the region D may be neglected. In this region the ECM calculations for the systems (4) and (5) above should simulate respectively the full-cluster cal-
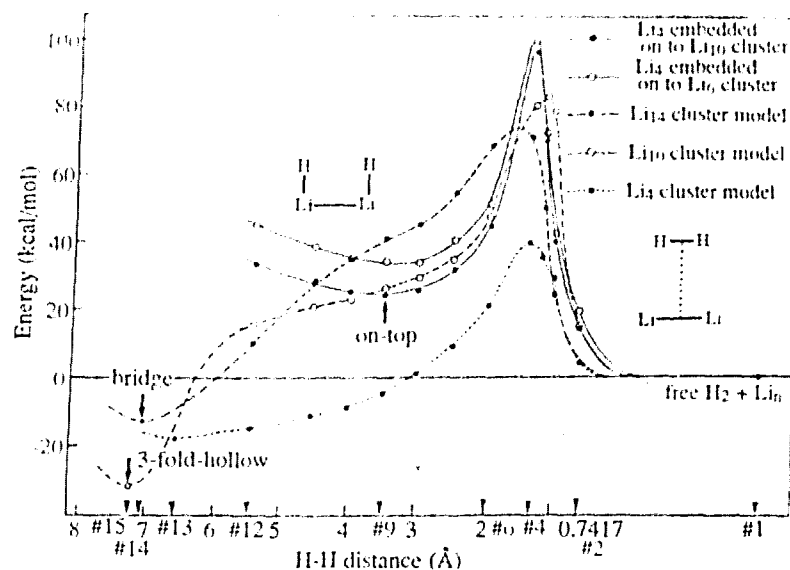
Figure 5. Potential curves for the H_2 adsorption on lithium.

culations for (1) and (2). As a cluster model calculation, we further perform calculations up to the positions 13 to 15.

Figure 5 shows the potential curves obtained by the CM and ECM. The minimum geometries and the corresponding energies are summarized in Table I. The following results may be deduced.

(1) Embedding the Li_4 cluster onto the larger cluster, the curve for the Li_4 cluster model is shifted up to those for the Li_4 embedded cluster models. This is reasonable in comparison with the curves obtained by the full-cluster model calculations.

(2) The value and the position of the barrier calculated by the CM is dependent on the cluster size, but those of the ECM is less dependent on the size of the region D. The barrier of the ECM is higher than that of the full cluster model, since the approximation of the fixed electronic effect of D on B can not fully describe the relaxation of the system.

TABLE I. Adsorption site, adsorption barrier, adsorption energy, and atomic population on H at the most stable adsorption geometry calculated by the cluster and embedded cluster models.

Cluster	Adsorption site	Adsorption barrier (kcal/mol)	Adsorption energy (kcal/mol)	Atomic population on H
Li_4 cluster	on-top	40.0	18.9	1.25
Li_{10} cluster	3-fold-hollow	84.8	31.2	1.23
Li_{14} cluster	bridge	72.3	14.2	1.22
Li_4 embedded onto Li_{10}	on-top	98.2	24.7	1.29
Li_4 embedded onto Li_6	on-top	100.8	34.9	1.28
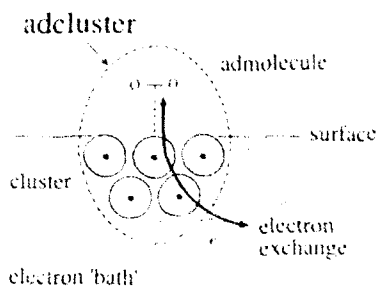
(3) The ECM gives a minimum at the on-top geometry. though it is less stable than the separated system. The corresponding full cluster model does not have such a minimum. This minimum may be artificial because the present ECM is too small for the regions of the points 9 to 12; the direct interaction between H_2 and the D region is not negligible there.

(4) In the CM calculations. the most stable geometries are the bridge site (position 14) for Li_{14}. the three-fold-hollow site (position 15) for Li_{10}, and the on-top site (position 13) for Li_4. The stabilization energies are summarized in Table I.

(5) The atomic charges of the adsorbed hydrogens are given in Table I and are between −0.2 and −0.3.
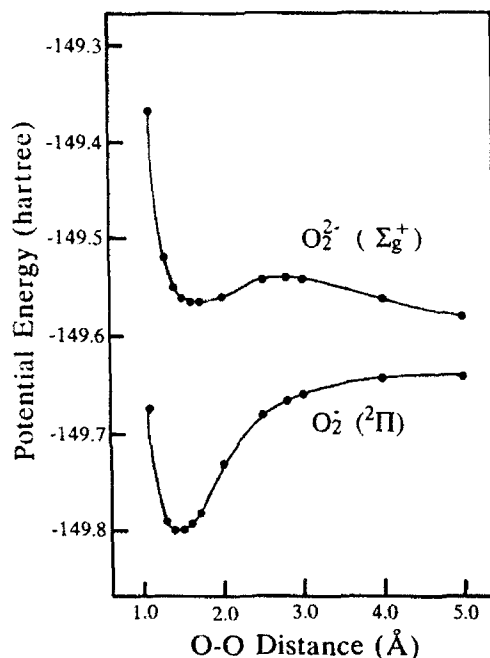
Figure 7.   Potential energy curves for the ground states of dioxygen anion species. O_2^- and O_2^{2-}. calculated by the SAC/SAC−CI method.

The criticism of the present result is rather difficult. If the results of the embedded cluster model should reproduce those of the full-cluster model, the results shown in Figure 9 are by no means favorable to the embedded cluster model. On the other hand, if the D region of the embedded cluster model should be considered as representing a boundary of the bulk metal instead of an outer part of the larger cluster, the present result shown in Figure 9 is difficult to evaluate since there are no experimental estimations on the potential surface for the dissociative adsorption of H_2 on a Li surface, especially between #1 and #9.

For doing FCM calculations, we have to calculate the $B + D$ cluster, which is Li_{10} or Li_{14} in the present calculations. For studying catalytic activity of a metal surface, we have to deal with transition metals, and doing *ab initio* calculations for even this size of cluster is still a hard job. Further, accounts of electron correlations are very important for dealing with such systems. Therefore, satisfactory applications of the FCM to transition metal surfaces are rather difficult at present.

Dipped Adcluster Model

For surface-molecule interacting systems in which electron transfer between surface and admolecule is important, the CM and the FCM are insufficient as far as the cluster size is not large enough. However, there are many cases in which the electron transfer seems to be very important: oxygen and halogen chemisorptions on a metal surface, the roles of alkali metals and halogens as *promoters*, and the *activity of electropositive metals* for dissociative adsorptions of CO, N_2, and so forth. The dipped adcluster model (DAM) [4,5] has been proposed for dealing with such systems. Since this model has been published 5 years ago, the accounts are given only briefly for being pertinent to the following applications.

Figure 6 illustrates the concept of the DAM. The adcluster is a combined system of an admolecule and a cluster and it is dipped onto the electron "bath" of the bulk metal. Then, electron and spin exchanges occur between the adcluster and the solid until the equilibrium is established for the exchange. The equilibrium would be established when the chemical potential of the adcluster becomes equal to the chemical potential of the surface.

$$\frac{\partial E(n)}{\partial n} = \mu \qquad (9)$$

or more generally when the following condition is satisfied,

$$\min(E(n)) \text{ in the range } \frac{\partial E(n)}{\partial n} = \mu \qquad (10)$$

where $E(n)$ is the energy of the adcluster as a function of n, the number of electrons transferred into the adcluster and μ the chemical potential of the surface. We note that n may be a noninteger since we are dealing with a partial system. In this model, the cluster atoms need not to supply all the electrons transferred into the adcluster; some are supplied from the electron bath of the solid.

Previously, we explained several general behaviors of the $E(n)$ curves and their implications [4]. Depending on the shape of the $E(n)$ curve, either a partial electron

transfer or one or two (integral) electron transfer may occur. We have proposed the molecular orbital model of the dipped adcluster [4]. We have assumed that only the active MO of the adcluster, like HOMO, LUMO, or SOMO, is partially filled in the electron-transfer process. There are two extreme ways of spin occupation in the active MO. One is the highest spin coupling in which α spin electron is first occupied and after the occupation reaches unity, the β spin electron is then added. The other is the paired spin coupling in which equal number of α and β spin electrons occupy the active MO. The former model is locally paramagnetic and the latter always diamagnetic. Energetically, the former is more stable than the latter.

When an electron is transferred from a surface to an admolecule, the electrostatic interaction between them would become important. For a metal surface, the so-called image force would occur and its inclusion was described in Ref. [5]. For a semiconductor surface, the interaction should be more localized and such treatment was described in Ref. [4].

Potential Curves of Dioxygen Anion Species

In the next section, we study O_2 chemisorption on an Ag surface. On a metal surface, oxygen is adsorbed in molecular and dissociative states and they are negatively charged as superoxide, O_2^-, peroxide O_2^{2-}, and atomic anions O^- and O^{2-}. Here, we investigate the bondings and the potential curves of the dioxygen anion species O_2^- and O_2^{2-} in their isolated free states for giving a comparative basis [12].

The gaussian basis is the Huzinaga–Dunning (9s5p)/[4s2p] set [13] plus diffuse s,p functions ($\alpha = 0.059$) and polarization d functions ($\alpha = 0.30$), which gives the electron affinity of oxygen atom as 0.97 eV, after electron correlation is included, in comparison with the experimental value of 1.31 eV.

We calculate the potential curves of O_2^- and O_2^{2-} by the SAC (symmetry adapted cluster)/SAC–CI method [14–16]: O_2^{2-} is calculated by the SAC method, since it is a closed-shell molecule, and O_2^- is calculated by the SAC–CI method as a cation produced from O_2^{2-}. Figure 7 shows the result. Table II gives a summary of the spectroscopic constants. The superoxide O_2^- is a stable molecule with the dissociation

TABLE II. The bond length R_e, vibrational frequency ω_e, dissociation energy D_0, electron affinity EA, and gross charge of the O_2 and O_2^- molecules in a gas phase and of the superoxide O_2^- and peroxide O_2^{2-} species on a silver surface.

Species	Method	R_e (Å)	ω_e (cm⁻¹)	D_0 (eV)	EA (eV)	Gross charge (per O_2)
O_2	SAC–CI	1.44	1010	4.00	6.24	1
	exptl.	1.35	1090	4.09		1
O_2^-	SAC	1.67	545	2.94 (0.70)ᵃ		2
O_2 on Ag surface	SAC–CI, DAM	1.47	974, 1055			0.54, 0.65
	exptl.		1053			
O_2^- on Ag surface	SAC–CI, DAM	1.66	689			1.4
	exptl.	1.47 ± 0.05	628, ca. 697			

ᵃ Hump height

energy of 4.00 eV (experimental value is 4.09 eV). The calculated equilibrium length and the vibrational frequency are 1.44 Å and 1010 cm^{-1} in reasonable agreement with the experimental values 1.35 Å and 1090 cm^{-1}. On the other hand, the peroxide O_2^- is only a transient species though it has a minimum at R_{0-0} 1.67 Å with the hump height of 0.703 eV. The repulsive tail in the longer region is shown to be entirely due to the electrostatic repulsion between the negatively charged oxygen atoms [12].

Dipped Adcluster Model Applied to O_2 Chemisorption on an Ag Surface

O_2 chemisorption on an Ag surface is of interest to many investigators because this system shows very efficient catalytic activity for partial oxydation of ethylene giving ethylene oxide [17]. Several theoretical studies have been published using CM with inclusion of electron correlations [18-20]. Though they could describe the geometry and the vibrational frequency of the adsorbed O_2 in good agreement with experiment, they failed to reproduce the adsorption energy and the dissociatively adsorbed states. Actually, most calculated adsorption energies were negative.

We think that the reason of the failure lies in its model, that is, the CM. The effect of the electron transfer from the bulk metal to the adcluster and the electrostatic image force interaction between O_2 and an Ag surface, which are included in the DAM but not in the CM, are expected to be important for this system.

We first take Ag_2O_2 as an adcluster and consider side-on bridge form interaction. The Ag–Ag distance is fixed at 2.8894 Å, which is the equilibrium distance in the solid. The gaussian basis set for Ag is (3s3p4d)/[3s3p2d] set with the effective core potential for Kr core [21]. For oxygen, the basis set is the same as that used in the preceding section.

Before doing electron correlation calculations, we have applied the molecular orbital model of the dipped adcluster using the highest spin coupling model. The resultant $E(n)$ curve has shown the occurrence of one electron transfer from the bulk Ag solid to the adcluster. We have therefore performed electron-correlation calculations for the Ag_2O_2 anion as the adcluster using the SAC/SAC–CI method [14-16], which is applicable to the ground and excited states of both neutral and electron transferred states. We have included all the valence electrons, together with the d-electrons of Ag, into electron correlation calculations.

Figure 8 is a display of the potential curves for the process of O_2 approach onto Ag_2 dipped onto the metal bulk. The broken lines are the results without the electron transfer ($n = 0$) and the solid one with the electron transfer ($n = 1$). Without the electron transfer, the potential curve, denoted by $^3B_2$ ($n = 0$), is repulsive so that the chemisorption does not occur. Another broken line, denoted by $^3A_2$ ($n = 0$), corresponds to the electron transferred state within the adcluster from Ag_2 to O_2. Though this state is attractive, the minimum is less stable than the separated system which is $^3B_2$. Though these curves include the image force corrections, they essentially correspond to the CM calculations and do not explain the occurrence of the O_2 chemisorption. On the other hand, the potential given by the solid line, which is for the electron transferred state of the DAM, stabilizes as O_2 approaches Ag_2. The asterisk at about 2.5 Å is obtained by the optimization of the O–O distance
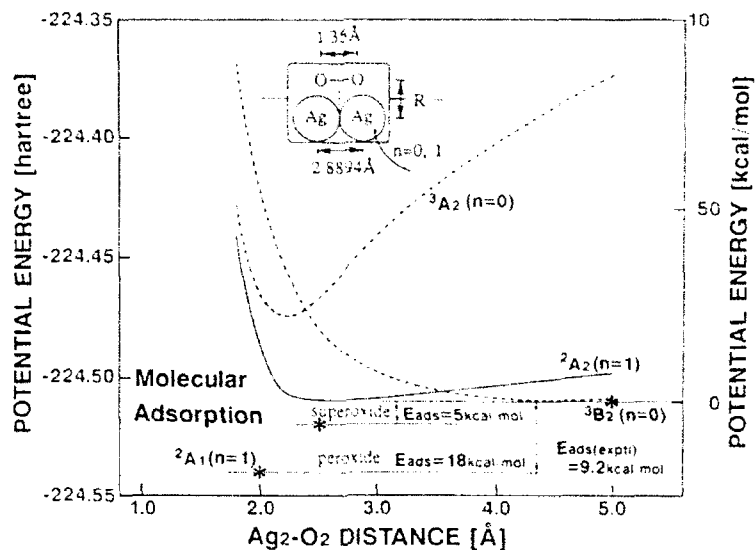
Figure 8.   Potential energy curves for the approach of O_2 onto Ag_2 in the Ag_2O_2 adcluster.
   n denotes the number of electrons transferred from the bulk metal to the adcluster.

and corresponds to the superoxide state. The calculated adsorption energy is 3 kcal/
mol. Near 2.0 Å, there are another minimum corresponding to the peroxide state
and the adsorption energy is 16 kcal/mol. The experimental molecular adsorption
energy is 9.2 kcal/mol [22]. Thus, the adsorption energy calculated by the DAM
is positive and agrees well with the experimental value.
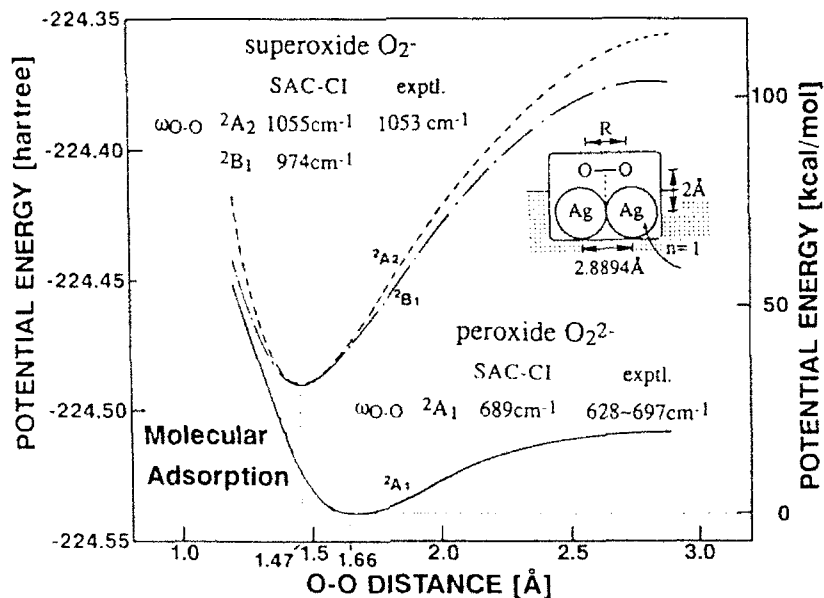
Figure 9.   Potential energy curves for the O—O stretching in the Ag_2O_2 adcluster.

We next study the potential curve for the O-O stretching on a silver surface using again the Ag₃O₂ adcluster. Figure 9 and Table II show the results. The lowest solid curve is for the peroxide and the upper two curves for the superoxides. As shown in the figure, the calculated vibrational frequencies agree quite well with the experimental values [23], showing that the molecular adsorption states expressed by the DAM correspond well to the actual systems observed experimentally. The equilibrium O-O distance is 1.47 Å for the superoxide and 1.66 Å for the peroxide. In comparison with the spectroscopic values of O₂ and O₂⁻ in their free states, the peroxide state on an Ag surface has very similar vibrational frequency, through the charge on O₂ is only -0.54 ca. 0.65. The peroxide on an Ag surface has a larger vibrational frequency than that in a gas phase, because the former is a stable species in contrast to the transient nature of the latter.

In Figure 9, a point of dissapointment at a first glance is a lack of the dissociatively adsorbed state. Up to the O-O distance of 2.8874 Å, which is the distance of the Ag lattice, the potential monotonously increases. However, at this distance, we found that the gross charge on oxygen is -0.72, so that the electrostatic repulsion between the two oxygens amounts as large as 60 kcal/mol. Therefore, we expect that if we further elongate the O-O distance, we should get a stabilization which might lead to the second minimum corresponding to the dissociatively adsorbed state. For this purpose, we undertake the DAM calculation for O₂ on the linear Ag₃.

The results for the Ag₃-O₂ adcluster are displayed in Figure 10. We certainly get two different potential minima. The minima at around 1.5 to 1.7 Å correspond to the molecular adsorption states (superoxide and peroxide) and another minimum at about 6 to 7 Å corresponds to the dissociatively adsorbed state. The dissociative state is obtained from the peroxide molecular adsorption state. After the optimization of the O-O and Ag-O distances, the dissociated state is calculated at the asterisk
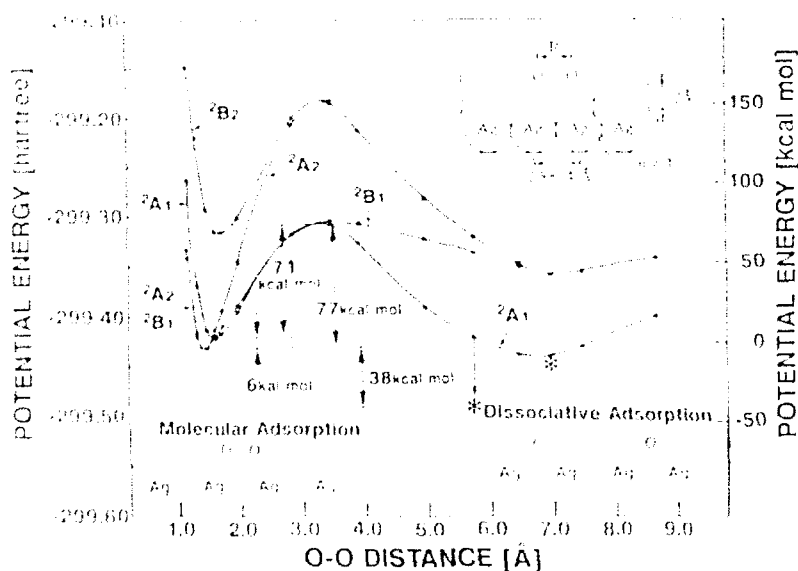
Figure 10   Potential energy vs. the O-O distance in the Ag₃O₂ adcluster

at the O–O distance of 5.78 Å. The dissociative state is calculated to be more stable than the molecular adsorption state by about 40 kcal/mol; the corresponding experimental value is 31 to 33 kcal/mol [22].

Thus, using the DAM and the SAC–CI method, we could successfully describe the O_2 chemisorption on an Ag surface. The inclusions of the electron transfer from the bulk Ag metal to the adcluster and the electrostatic image force correction described by the DAM, and the electron correlations for several lower surface states described by the SAC–CI method are the reason of the success of the present study.

Acknowledgment

Bibliography

[1]   T. B. Grimley and C. Pisani, J. Phys. C7, 2831 (1974); T. B. Grimley and E. E. Mola, ibid. C9, 3437 (1976).
[2]   C. Pisani, Phys. Rev. B17, 3143 (1978).
[3]   W. Ravenek and F. M. M. Geurts, J. Chem. Phys. 84, 1613 (1986).
[4]   H. Nakatsuji, J. Chem. Phys. 87, 4995 (1987).
[5]   H. Nakatsuji, H. Nakai, and Y. Fukunishi, J. Chem. Phys. 95, 640 (1991).
[6]   Y. Fukunishi and H. Nakatsuji, J. Chem. Phys. (in press).
[7]   H. Nakatsuji and H. Nakai, Chem. Phys. Lett. 174, 283 (1990).
[8]   H. Nakatsuji and H. Nakai, Can. J. Chem. (in press).
[9]   H. Nakatsuji and H. Nakai, J. Chem. Phys. (in press).
[10] H. Nakai, Y. Ohmori, and H. Nakatsuji, J. Chem. Phys. 95, 8287 (1991).
[11] H. Nakatsuji, H. Nakai, and Y. Ohmori (submitted for publication).
[12] H. Nakatsuji and H. Nakai, Chem. Phys. Lett. (in press).
[13] S. Huzinaga, J. Chem. Phys. 42, 1293 (1965); T. H. Dunning, Jr., ibid. 53, 2823 (1970).
[14] H. Nakatsuji, Chem. Phys. Lett. 67, 329 (1978).
[15] H. Nakatsuji, Theor. Chim. Acta 71, 201 (1987).
[16] H. Nakatsuji, Acta Chimica Hungarica (in press).
[17] A. Ayame and H. Kanoh, Shokubai 20, 381 (1978) (in Japanese).
[18] A. Selmani, J. Andzelm, and D. Salahub, Int. J. Quantum Chem. 29, 829 (1986).
[19] T. H. Upton, P. Stevens, and P. J. Madix, J. Chem. Phys. 88, 3988 (1988).
[20] E. A. Carter and W. A. Goddard III, Surf. Sci. 209, 243 (1989).
[21] P. J. Hay and W. R. Wadt, J. Chem. Phys. 82, 270 (1985).
[22] C. T. Campbell, Surf. Sci. 157, 43 (1985).
[23] C. Pettenkofer, I. Pockrand, and A. Otto, Surf. Sci. 135, 52 (1983); C. Pettenkofer, J. Hickmans, U. Erturk, and A. Otto, ibid. 151, 9 (1985).

An Adiabatic State Approach to Electronically Nonadiabatic Wave Packet Dynamics

G. PARLANT* and D. R. YARKONY

Department of Chemistry, The Johns Hopkins University, Baltimore, Maryland 21218

Abstract

In the present study we introduce a time-dependent wave packet method to treat electronically non-adiabatic processes explicitly in the coupled adiabatic state representation. The method is applied to the predissociation of the MgClÃ(A $^2\Pi$) state and is shown to be easy to implement, with the computational effort being comparable to the corresponding calculation in the diabatic basis. © 1992 John Wiley & Sons, Inc.

Introduction

The adiabatic representation [1,2] is a fundamental concept in quantum chemistry. In this representation, the electronic states are calculated with the nuclei fixed in space, and subsequently, the evolution of the nuclei on the associated potential energy surfaces is studied. If these surfaces are well separated, it is generally a good approximation to restrict the nuclear motion to a single electronic state (Born–Oppenheimer approximation [3,4]). When two or more surfaces intersect or come close together, this is no longer the case since the nuclear kinetic energy produces derivative couplings [see eq. (4) in the next section] that can induce nonadiabatic transitions between these states. Frequently, multiple potential energy surface collision dynamics are treated not in the adiabatic representation, but in the so-called *diabatic* representation [2,5–11]. In this representation, the derivative coupling is "transferred" into the potential part of the Hamiltonian. This approach is useful when a sharp avoided crossing is encountered or at high collision energy [11] and has been used very successfully, particularly in atom–atom collisions [12].

Although the diabatic representation is constructed explicitly to facilitate dynamics calculations, the approximations involved in the construction of diabatic states and their implications for the accuracy of dynamics calculations are rarely addressed. Only the adiabatic representation has a unique definition: adiabatic states diagonalize the electronic Hamiltonian. On the other hand, *diabatic* is sometimes loosely defined as *not adiabatic*, and an infinite number of diabatic representations can be defined. As discussed by Garrett and Truhlar [2], two broad classes of diabatic representations can be distinguished. One is obtained by effecting a transformation from

an adiabatic basis to a new basis for which the first derivative coupling vanishes. F. T. Smith provided the first formal definition for this type of diabatic states in diatomic molecules [7,13]. This definition was later extended to atom–diatom systems by Baer [8]. Recently, this problem was also examined by Mead and Truhlar [9], who separated the derivative coupling vector into a longitudinal part and a transverse part. They were able to show that while the longitudinal part can always be transformed away, in general, the transverse part cannot. Only diatomic systems constitute an exception to this rule. In this latter case, *strictly diabatic*—according to Smith's definition—and adiabatic representations, are perfectly equivalent. For more than two atom systems, it is in general *not* possible to build a strictly diabatic representation. However, Mead and Truhlar showed that *approximately* diabatic states can be built if, for example, the transverse part of the coupling is negligible. The second class of diabatic representation, in the terminology of Garrett and Truhlar, does not use a mathematical transformation but, instead, is based on physical arguments. These states are only approximately diabatic. For example, nearly diabatic states have been defined as states that preserve a particular molecular property [14–16], or in terms of a particular set of atom-like orbitals [17]. Patcher et al. have considered the use of block diagonal matrices to define approximate diabatic states [18].

To summarize, most of the diabatic bases used in the literature are only approximately diabatic—in the sense of Smith—either because the system under study contains more than one internal degree of freedom, or because they have been deliberately built on an intuitive basis. The use of approximate diabatic bases involves approximations which are largely uncontrollable (see next section), and have not been studied quantitatively. It is important to understand the limitations involved in the use of such states in dynamics calculations. One of the goals of this investigation is to present a dynamical method that will allow such studies.

Previously, only a limited number of time-independent quantum dynamics calculations have been performed in the adiabatic representation [19] (see also references in Garrett and Truhlar [2], Baer [20], and Sidis [11]). A principal reason for this is that the derivative operator can lead to difficulties in the nuclear dynamics calculations when a sharp avoided crossing is encountered or at high collision energy [11]. Another reason appears to be the complexity of solving the time-independent Schrödinger equation when the first derivative operator appears. In this article we use a time-dependent wave packet method to overcome this difficulty. A particularly appealing aspect of time-dependent methods when compared with conventional stationary close-coupling techniques [2,21–23], is that it requires only minor modifications to be utilized with an adiabatic basis instead of a diabatic one. The extra derivative coupling terms are easily computed by means of Fourier transforms [24], routinely used in wave packet propagations. Perhaps surprisingly, there do not appear to have been any previous calculations using a time-dependent adiabatic state formalism. Time-dependent wave packet treatments in approximate diabatic bases have been reported [25–29]. These approaches, in general, neglect all derivative couplings, an approximation which may not be justified in practice [see discussion of eqs. (16)–(18)].

Another factor contributing to the limited use of the coupled adiabatic state representation appears to be the computational expense required to determine the requisite derivative couplings. However, this limitation has been removed. It has recently been shown [30], that analytic gradient techniques can be used to obtain derivative couplings with little computational effort beyond that required to obtain the requisite potential energy surfaces. Related techniques permit efficient location of the regions of avoided or real crossings between surfaces [30], where nonadiabatic transitions are more probable. The methodology espoused in this work is designed to exploit these advances in computational electronic structure theory.

It has been suggested that, in some cases, time-dependent wave packet treatments in the adiabatic basis would not be cost effective when compared with equivalent treatments in the diabatic basis [31]. In this work we show that the propagation in the adiabatic basis presents no extra difficulty relative to the propagation in a diabatic basis and that both methods require comparable computational effort.

The adiabatic state representation is expected to be particularly well-suited to systems in which electronically nonadiabatic effects are preeminent in the region of avoided crossing seams [30]. Examples of this class of systems include the frequently studied $M(^2P) + HX \rightarrow MX + H(^2S)$ reactions [32–35] where M is an alkali atom and X a halogen. Alternatively, the diabatic states approach is advantageous in instances when sharp spikes exist in the derivative coupling matrix elements. An example is the ArH_2 system where the two diabatic charge transfer states present an intersection seam which runs parallel to the $Ar-H_2$ distance and extends to infinity [36]. At large distances the charge exchange probability is zero and, accordingly, the derivative coupling between the two adiabatic states is infinitely sharp. In this region, a transformation to a diabatic representation would facilitate the accurate propagation of the wave packet.

The adiabatic state wave packet method espoused herein has the usual advantages attributed to time-dependent methods. In one single calculation a wave packet gives results over a whole range of energies. Another attractive feature of the wave packet technique is that it permits the straightforward treatment of collision-induced dissociation. This process is hard to describe in a time-independent formalism because of the difficulty of representing the continuum of vibrational basis functions [37]. Although multidimensional quantum scattering calculations, in general, require significant amounts of computer time [38–40], wave packet methods scale better with the number of states and the number of degrees of freedom than time-independent methods [41]. It is quite reasonable to consider the use of the present method for polyatomic systems for which rigorous diabatic bases do not exist. This implementation is currently in progress in our group [42].

As a first application, the method is used here to calculate resonance energies and lifetimes of the predissociated state $A^2\Pi$ of MgCl by considering the long-time evolution of a wave packet. We have previously studied the MgCl system by means of a close-coupling method [43]. Propagating a wave packet in order to obtain the $t \rightarrow \infty$ limit is not the optimal procedure for obtaining the lifetime of a long-lived state. Alternative wave packet procedures have been developed recently to deal with very long lifetimes [40,44]. However, we chose to apply our method to a

predissociation problem because it constitutes a stringent test of the algorithm. The resonance lifetimes are derived from Smith's collision-lifetime matrix [43,45,46], which is expressed in terms of the S-matrix for the system. In this case, a very accurate propagation of the wave packet is required so that the moduli as well as the phases of the S-matrix elements are obtained with negligible errors over a substantial range of energies [46].

The formulation in terms of adiabatic states also gives us the opportunity to study the influence of the adiabatic correction (see eq. (18b) in the next section), also called the Born-Oppenheimer (BO) diagonal correction, on the dynamics of the system. This term is generally considered as negligibly small. However, some studies [19,47,48] have shown that the adiabatic correction can play a significant role in predissociations.

Next we present the time-dependent coupled electronic state Schrödinger equation and outline its solution using wave packets. The results of the MgCl($A^2\Pi$) lifetime calculations are presented and discussed in Results and Discussion, and the final section gives a brief summary and conclusion.

Theoretical Approach

Time-Dependent Schrödinger Equation and Coupled Electronic State Expansion

For an electronically nonadiabatic process, the time-dependent Schrödinger equation is given by (we use atomic units throughout):

$$H(\mathbf{r},\mathbf{R})\Psi(\mathbf{r},\mathbf{R},t) = i\frac{\partial}{\partial t}\Psi(\mathbf{r},\mathbf{R},t),\tag{1}$$

where $\mathbf{r}$ and $\mathbf{R}$ represent the electronic and nuclear coordinates, respectively, and H is the total Hamiltonian in the space-fixed coordinate frame:

$$H(\mathbf{r},\mathbf{R}) = \sum_{a}\frac{-1}{2m_a}\frac{\partial^2}{\partial R_a^2} + H^{el}(\mathbf{r},\mathbf{R}) \equiv T^N + H^{el}(\mathbf{r},\mathbf{R}).\tag{2}$$

In eq. (2), T^N is the nuclear kinetic energy operator and H^{el} is the nonrelativistic BO electronic Hamiltonian. The total wave function, Ψ, is expanded in a complete real orthonormal electronic basis set $\{\psi_k\}$:

$$\Psi(\mathbf{r},\mathbf{R},t) = \sum_k \chi_k(\mathbf{R},t)\psi_k(\mathbf{r};\mathbf{R}).\tag{3}$$

Projecting eq. (1) onto the ψ_k gives the following system of equations for the time-dependent coefficients (wave packets) χ_k:

$$T^N\chi_j(\mathbf{R},t) + \sum_k \mathcal{H}_{jk}(\mathbf{R})\chi_k(\mathbf{R},t) - \sum_{a,k}\frac{1}{m_a}f_a^{jk}(\mathbf{R})\frac{\partial}{\partial R_a}\chi_k(\mathbf{R},t) = i\frac{\partial}{\partial t}\chi_j(\mathbf{R},t),\tag{4}$$

with

$$\omega_a(\mathbf{R}) \quad H_a(\mathbf{R}) \quad \sum \frac{1}{2m_a} h_{aa}(\mathbf{R}) . \tag{5}$$

$$H_{ij}(\mathbf{R}) \quad \psi_i(\mathbf{r};\mathbf{R}) H^{el}(\mathbf{r},\mathbf{R}) \psi_j(\mathbf{r};\mathbf{R}) , \tag{6}$$

$$h_{ij}(\mathbf{R}) \quad \left\langle \psi_i(\mathbf{r};\mathbf{R}) \left| \frac{\partial^2}{\partial R_a \partial R_a} \psi_j(\mathbf{r};\mathbf{R}) \right\rangle_\mathbf{r} . \tag{7}$$

$$f_{ij}^a(\mathbf{R}) \quad \left\langle \psi_i(\mathbf{r};\mathbf{R}) \left| \frac{\partial}{\partial R_a} \psi_j(\mathbf{r};\mathbf{R}) \right\rangle_\mathbf{r} . \tag{8}$$

Because our electronic basis functions are real and orthonormal, the derivative matrix, f_{ij}, is antisymmetric and the elements of f and h satisfy

$$h_{ij}^a(\mathbf{R}) \quad \frac{\partial}{\partial R_a} f_{ij}^a(\mathbf{R}) + \sum_k f_{ik}^a(\mathbf{R}) f_{kj}^a(\mathbf{R}) . \tag{9}$$

which is valid only for a complete basis.

At this point, we have the choice of working in different electronic representations. In the adiabatic representation, denoted $|\psi_i^a|$, the basis functions are eigenfunctions of H^{el}:

$$\left\langle \psi_i^a(\mathbf{r};\mathbf{R}) | H^{el}(\mathbf{r},\mathbf{R}) | \psi_j^a(\mathbf{r};\mathbf{R}) \right\rangle_\mathbf{r} = E_i^a(\mathbf{R}) \delta_{ij} . \tag{10}$$

while in a rigorously diabatic basis, denoted $|\psi_i^d|$, the matrix elements of $\partial/\partial R_a$ should vanish [7]:

$$f_{ij}^{d,a}(R) \equiv \left\langle \psi_i^d(\mathbf{r};\mathbf{R}) \left| \frac{\partial}{\partial R_a} \psi_j^d(\mathbf{r};\mathbf{R}) \right\rangle_\mathbf{r} = 0 . \tag{11}$$

To see the implications of eq. (11) it is convenient to make the assumption that the process under study can be described using only two of the infinity of electronic states. In this case, the states in question are connected by the following transformation, which depends on a function $\theta(\mathbf{R})$, to be determined:

$$\begin{pmatrix} \psi_1^d(\mathbf{r};\mathbf{R}) \\ \psi_2^d(\mathbf{r};\mathbf{R}) \end{pmatrix} = \begin{pmatrix} \cos\theta(\mathbf{R}) & -\sin\theta(\mathbf{R}) \\ \sin\theta(\mathbf{R}) & \cos\theta(\mathbf{R}) \end{pmatrix} \begin{pmatrix} \psi_1^a(\mathbf{r};\mathbf{R}) \\ \psi_2^a(\mathbf{r};\mathbf{R}) \end{pmatrix} . \tag{12}$$

Inserting eq. (12) into the requirement eq. (11) gives the system of equations

$$\frac{\partial}{\partial R_a} \theta(\mathbf{R}) = -f_{12}^{a}(\mathbf{R}) . \tag{13}$$

where $f_{12}^{a}(\mathbf{R})$ is given by eq. (8), using adiabatic wave functions. Eq. (13) is solved by partial integration. In order for $\theta(\mathbf{R})$ to be uniquely defined the condition for an exact derivative must hold:

$$\left(\frac{\partial^2}{\partial R_a \partial R_b} - \frac{\partial^2}{\partial R_b \partial R_a} \right) \theta(\mathbf{R}) = 0 . \tag{14}$$

Combining eqs. (13) and (14), and using eq. (9), yields the following condition [9]:

$$\sum_{k \geq 2} f_{ij}^{2k,a} f_{ji}^{k1,a} - f_{ij}^{2k,a} f_{ji}^{k1,a} = 0 . \qquad (15)$$

In general, this equation cannot be satisfied, except by the trivial solution made of constant (independent of **R**) wave functions [9]. Thus, f_{ij}^{12} cannot be rigorously excluded from eq. (4) [see eq. (17) below]. However, since this term is difficult to evaluate, it is common practice to omit it. Finally, note that for a diatomic systems for which there is only one internal degree of freedom eq. (14) becomes trivial.

For two electronic states the time-dependent coupled equations (4) for the adiabatic and diabatic cases, respectively, can be written

$$T^\Lambda \begin{pmatrix} \chi_1^a \\ \chi_2^a \end{pmatrix} + \begin{bmatrix} E_1^a - \sum_a \dfrac{1}{2m_a} h_{aa}^{11,a} & -\sum_a \dfrac{1}{2m_a}\left(h_{aa}^{12,a} + 2 f_a^{12,a} \dfrac{\partial}{\partial R_a} \right) \\[2ex] -\sum_a \dfrac{1}{2m_a}\left(h_{aa}^{21,a} + 2 f_a^{21,a} \dfrac{\partial}{\partial R_a} \right) & E_2^a - \sum_a \dfrac{1}{2m_a} h_{aa}^{22,a} \end{bmatrix} \begin{pmatrix} \chi_1^a \\ \chi_2^a \end{pmatrix} = i \frac{\partial}{\partial t}\begin{pmatrix} \chi_1^a \\ \chi_2^a \end{pmatrix}. \qquad (16)$$

and

$$T^\Lambda \begin{pmatrix} \chi_1^d \\ \chi_2^d \end{pmatrix} + \begin{bmatrix} E_1^d - \sum_a \dfrac{1}{2m_a} h_{aa}^{11,d} & H_{12}^d - \sum_a \dfrac{1}{2m_a} h_{aa}^{12,d} \\[2ex] H_{21}^d - \sum_a \dfrac{1}{2m_a} h_{aa}^{21,d} & E_2^d - \sum_a \dfrac{1}{2m_a} h_{aa}^{22,d} \end{bmatrix} \begin{pmatrix} \chi_1^d \\ \chi_2^d \end{pmatrix} = i \frac{\partial}{\partial t}\begin{pmatrix} \chi_1^d \\ \chi_2^d \end{pmatrix},$$

$$(17)$$

with obvious notations, and where the variable **R** has been omitted for simplicity. In eq. (16), it appears clearly that the derivative operator is responsible for the so-called adiabatic correction $h_{aa}^{11,a}(\mathbf{R})$. Note that this correction appears also in the diabatic eqs. (17); it vanishes rigorously only if the two-state basis is assumed complete [see eq. (9)].

If the two-state basis approximation is used, the matrix elements of h_{aa}^{a} and h_{aa}^{d} satisfy the relations

$$h_{aa}^{12,a}(\mathbf{R}) = -h_{aa}^{21,a}(\mathbf{R}) = \frac{\partial}{\partial R_a} f_a^{12,a}(\mathbf{R}), \qquad (18a)$$

$$h_{aa}^{11,a}(\mathbf{R}) = h_{aa}^{22,a}(\mathbf{R}) = -[f_a^{12,a}(\mathbf{R})]^2 , \qquad (18b)$$

and

$$h_{aa}^{a,d}(\mathbf{R}) = 0 . \qquad (18c)$$

Under the approximations (18a–c) the adiabatic and diabatic bases are equivalent.

Wave Packet Propagation

The propagation in time and space of the coupled wave packets χ_1 and χ_2—in the following we will often refer to "the wave packet" although two coupled wave packets are actually propagated—is carried out by means of a grid method [49] using an expansion of the evolution operator over Chebychev polynomials [50] and using fast Fourier transforms [51,52] (FFT) to calculate the action of the derivative operator on the wave packet [53]. In a recent comparison of several algorithms, this combination was found to be one of the fastest available for systems with a time-independent Hamiltonian [54]. The method will be described only briefly here since wave packet techniques have been extensively reviewed [49,55,56].

The time-evolution operator corresponding to the time-dependent Schrödinger equation (1) can be expanded as [41,57]:

$$\exp(-iH\Delta t) = \exp(-i\bar{E}\Delta t) \sum_{n=0}^{N} c_n T_n(H_{scal}) ,$$

(19)

where Δt is the time step and the $T_n(x)$ are Chebychev polynomials [24], defined over the interval $[-1,+1]$, that obey the recurrence relations:

$$T_{n+1}(x) = 2xT_n(x) - T_{n-1}(x) ,$$

(20a)

$$T_0(x) = 1 ,$$

(20b)

$$T_1(x) = x .$$

(20c)

The coefficients. c_n, are given by:

$$c_n = (2 - \delta_{n0})(-i)^n J_n(\Delta E \Delta t)$$

(21)

where the J_n are Bessel functions of the first kind.

The Hamiltonian is scaled so that the eigenvalues of H_{scal} are limited to the interval $[-1,+1]$:

$$H_{scal} = \frac{H - \bar{E}}{\Delta E} .$$

(22a)

$$\Delta E = (E_{max} - E_{min})/2 ,$$

(22b)

$$\bar{E} = (E_{max} + E_{min})/2 .$$

(22c)

E_{min} and E_{max} are the minimum and maximum eigenvalues of H, respectively. Following Mowrey and Kouri [46] we determine E_{min} as the lowest potential matrix element and E_{max} as the sum of the highest potential matrix element and the largest kinetic energy that can be described on the grid. that is, $\pi^2/(2m\Delta R^2)$ where ΔR is the R stepsize.

To follow a predissociation process, the propagation of the wave packet must be pursued for a duration at least equal to the lifetime of the levels under study. that is generally several picoseconds or more. To avoid the reflection of the wave packet on the boundaries of the grid, a negative imaginary potential is used to absorb the

wave packet [41,58,59]. As established by Neuhauser et al. [41], in this case the energy domain, ΔE has to be extended by approximately 5% to compensate for the fact that Chebychev polynomials with a complex argument are not bounded.

The action of the Hamiltonian on the wave packet is calculated by discretizing the coordinate R on a uniform grid. The action of the electronic coupling is obtained by a simple matrix multiplication for each grid point, since the potential energy operator is diagonal in the coordinate representation. To evaluate the action of the derivative operator we make use of the fact that this operator is diagonal in the momentum representation. The wave packet is successively Fourier-transformed to the momentum representation, multiplied by the appropriate momentum on the momentum grid, and back Fourier-transformed to the coordinate representation. Both the kinetic energy term and (in the adiabatic representation) the derivative coupling are computed by means of FFT.

In the particular case of the predissociative system studied here, we consider ψ_1^d to be a metastable bound ground state and ψ_2^d to be a bound excited state (see Fig. 1) such that the diabatic states, ψ_1^d and ψ_2^d, represent the purely bound and dissociative states, respectively [43]. Asymptotically, the wave packet for the open channel can be expanded in terms of incoming and outgoing plane waves:

$$\psi(R, t) \xrightarrow[R,t \to \infty]{} \frac{1}{\sqrt{2\pi}} \int g(k)[e^{-ikR} - S_{nn}e^{+ikR}]e^{-i\omega t} dk \ . \tag{23}$$

In this equation, k is the wave number, $\omega = k^2/2m$; $g(k)$ is chosen as a Gaussian distribution; and $S_{nn}(n = 1, 2$ in the adiabatic, diabatic formulation, respectively) represents the only open–open S-matrix element. Using stationary phase arguments, it can be shown that, after the collision ($R \to \infty$ and $t \to \infty$), only the outgoing wave contributes to the asymptotic form [4]. By examination of eq. (23) it is seen
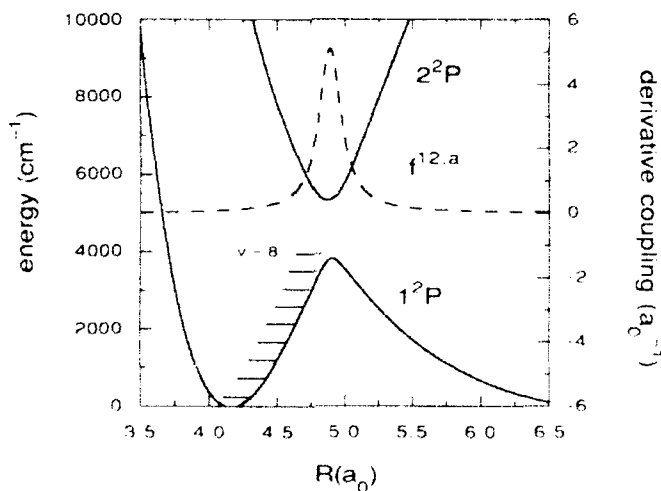
Figure 1.   Potential energy curves and derivative coupling, $f^{1,2,a}(R)$, for the 1,2$^2\Pi$ adiabatic states of MgCl. The vibrational level of the diabatic 1$^2\Pi$ state up to $v = 8$ are also indicated.

that the S-matrix element can be extracted from the wave packet as a Fourier transform *either* over the distance R *or* over the time t [41]. Here we choose the second alternative and express S_{nn} as

$$S_{nn} = \frac{k}{m} \frac{e^{ikR_\infty}}{g(k)} \frac{1}{\sqrt{2\pi}} \int \psi(R_\infty, t) e^{+i\omega_k t} \, dt \,. \tag{24}$$

where R_∞ is some fixed asymptotically large distance. In practice, we "watch" the wave packet as it crosses R_∞, and then use a FFT to evaluate eq. (24). Monitoring the modulus of S_{nn}, which should equal one over the energy domain of interest, can be used to ensure that the propagation was continued until only a negligible part of the wave packet remained in the interaction region [46].

Finally, for any wave number k, Smith's collision delay-time [45] is given by:

$$\tau = -iS_{nn}^* \frac{\partial S_{nn}}{\partial \omega_k} \,. \tag{25}$$

where the derivative of S_{nn} was computed by means of a FFT. By plotting τ as a function of the energy it is thus possible in a single propagation to localize the resonances and determine their lifetimes.

Application to MgCl ($A^2\Pi$) Predissociation

The $1,2^2\Pi$ adiabatic electronic states of MgCl (Fig. 1) were computed in ref. 43 where a set of rigorously diabatic states were deduced by a unitary transformation chosen to satisfy eq. (11). The relativistic effects included in ref. 43 have been neglected here in order to simplify the analysis. The $1,2^2\Pi$ diabatic states were fit, respectively, to a Morse curve

$$E_1^d \equiv E(1^2\Pi) = V_1 + D_1[1 - \exp(-\beta_1(R - R_1))]^2 \,. \tag{26}$$

where $V_1 = 0.0$, $D_1 = 26581.05$ cm^{-1}, $\beta_1 = 0.718643$ a$_0^{-1}$, and $R_1 = 4.159150$ a$_0$, and a decaying exponential

$$E_2^d \equiv E(2^2\Pi) = V_2 + D_2 \exp(-\beta_2 R) \,. \tag{27}$$

where $V_2 = -530.09$ cm^{-1}, $D_2 = 2,760,693.25$ cm^{-1} and $\beta_2 = 1.290188$ a$_0^{-1}$. The diabatic coupling interaction was fit to a Gaussian function

$$H_{12}^d \equiv \langle \psi_{1^2\Pi} | H^d | \psi_{2^2\Pi} \rangle = D_3 \exp(-\beta_3(R - R_3)^2) \,. \tag{28}$$

where $D_3 = 769.62$ cm^{-1}, $\beta_3 = 0.618122$ a$_0^{-1}$, and $r_3 = 4.890010$ a$_0$.

In order to facilitate a precise comparison of the adiabatic and diabatic treatments, the adiabatic potential energy curves and derivative couplings used in the present calculations were derived from the diabatic fit through the transformation

$$E_{1,2}^a = \frac{E_1^d + E_2^d \pm \sqrt{(E_1^d - E_2^d)^2 + 4H_{12}^{d2}}}{2} \,. \tag{29}$$

$$f^{12,a} = \frac{(E_1^d - E_2^d)\partial H_{12}^d/\partial R - H_{12}^d \partial(E_1^d - E_2^d)/\partial R}{(E_1^d - E_2^d)^2 + 4H_{12}^{d2}} \,. \tag{30}$$

rather than through a direct fit to the *ab initio* points. In the anticipated applications of this method, the adiabatic potential energy surfaces and derivative couplings would be obtained directly from the *ab initio* data, without any reference to diabatic states.

Results and Discussion

We chose to illustrate the method on the $v = 8$ vibrational level of MgCl ($1^2\Pi$) (see Fig. 1), whose lifetime is approximately 0.3 ps. No attempt to calculate longer lifetimes was made, although, in view of the stability of the integrator, this is perfectly feasible. The energy profile of the collision delay-time (Fig. 2) was obtained after propagating a Gaussian wave packet of width 0.25 a_0 centered on $v = 8$. The calculation was carried out with the maximum accuracy available in double precision over 8192 steps of 10^{-15} s on a grid of 2048 points between 3 and 30 a_0. The wave packet was analyzed at $R = 21 a_0$ and absorbed by an imaginary potential linearly decreasing from 0 at 22.5 a_0 to -500 cm^{-1} at 30 a_0; the reflected part was approximately 10^{-9} of the primary wave packet. After the propagation, the modulus of the open–open S-matrix element was equal to one within 0.08%. The CPU time on an IBM RISC 6000/550 workstation was approximately 3.5 s and 4.5 s per step for the calculations in the diabatic and adiabatic representations, respectively.

Figure 2 presents the results of four different calculations. The resonance energy profile obtained from the wave packet calculation in the diabatic representation is compared to a time-independent close-coupling calculation using a log-derivative propagator [43]. These results are in excellent agreement, as expected. The reso-
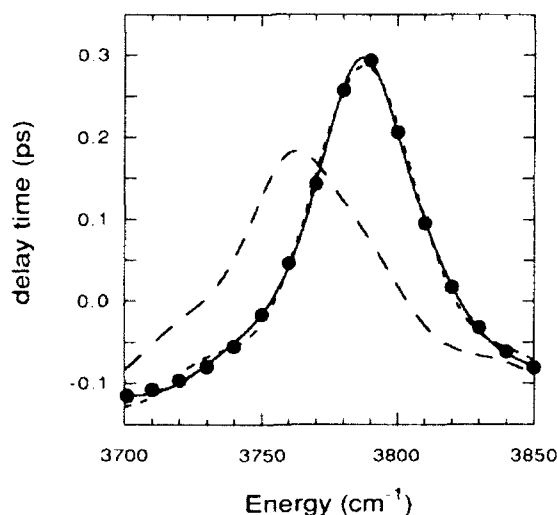
Figure 2. Resonance profile of the collision delay-time. The wave packet calculation in the diabatic representation (solid line) is compared with the calculation in the adiabatic representation, with the adiabatic correction $h^{kk,a}(R)$ included (dashed line) or neglected (broken line). The result of a time-independent calculation (full circles) is also presented.

nance curve represented by a broken line was obtained by propagating the wave packet in the adiabatic representation where the adiabatic correction $h^{**}(R)$ (k = 1, 2) was arbitrarily set to zero. This has the effect of changing significantly the resonance shift (-176.3 instead of -152.2 cm^{-1}) as well as the lifetime (0.18 instead of 0.29 ps). Although this phenomenon has also been noticed by other authors [19,47,48], the adiabatic correction is very often assumed negligible in predissociation calculations.

Summary and Conclusion

The wave packet method developed here permits dynamics calculations to be carried out explicitly in the coupled adiabatic state representation. This methodology is introduced to exploit recent advances in computational electronic structure theory which permit efficient evaluation of derivative couplings between adiabatic states. This approach will also enable the study of the implications of using diabatic representations in the treatment of nonadiabatic processes. Relative to procedures involving diabatic bases, this procedure is straightforward to implement, requiring only one extra FFT evaluation, and the computational effort is comparable. Note, however, that for vibronic problems of large dimensions, it has been reported that the propagation in the adiabatic basis was much more costly than in the diabatic basis [31]. The method is currently being extended to higher dimensions in order to study electronic quenching processes, including $H_2(B^1\Sigma_u^+)$ by He [42].

Acknowledgments

Bibliography

[1] H. Köppel, W. Domcke, and L. S. Cederbaum. Adv. Chem. Phys. 57, 59 (1984), and references therein.
[2] B. C. Garrett and D. G. Truhlar, Theor. Chem. Adv. Perspect. 6A, 215 (1981), and references therein.
[3] M. Born and R. Oppenheimer. Ann. Phys. 84, 457 (1927).
[4] A. Messiah. Quantum Mechanics (Wiley, New York, 1962).
[5] W. Lichten. Phys. Rev. 131, 229 (1963).
[6] W. Lichten. Phys. Rev. 164, 131 (1967).
[7] F. T. Smith. Phys. Rev. 179, 111 (1969).
[8] M. Baer. Chem. Phys. 15, 49 (1976).

[9] C. A. Mead and D. G. Truhlar, J. Chem. Phys. 77, 6090 (1982), and references therein.

[10] T. F. O'Malley, Adv. Atom. Mol. Phys. 7, 223 (1971).

[11] V. Sidis in *State Selected and State-to-State Ion-Molecule Reaction Dynamics. Advanced Chemical Physics*, M. Baer and C. Y. Ng, Eds. (Wiley, New York, 1991), vol. 82, part 2, p. 73.

[12] J. B. Delos, Rev. Mod. Phys. 53, 287 (1981).

[13] For an historical background, see reference 11.

[14] H. J. Werner and W. Meyer, J. Chem. Phys. 74, 5802 (1981).

[15] C. W. Bauschlicher and S. R. Langhoff, J. Chem. Phys. 89, 4246 (1988).

[16] L. R. Kahn, P. J. Hay, and I. Shavitt, J. Chem. Phys. 61, 3530 (1974).

[17] P. Archirel and B. Levy, Chem. Phys. 106, 51 (1986).

[18] T. Pacher, L. S. Cederbaum, and H. Köppel, J. Chem. Phys. 89, 7367 (1988).

[19] E. F. van Dishoeck, M. C. van Hemert, A. C. Allison, and A. Dalgarno, J. Chem. Phys. 81, 5709 (1984).

[20] M. Baer, G. Drolshagen, and J. P. Toennis, J. Chem. Phys. 73, 1690 (1980).

[21] A. C. Allison, Adv. Atom. Mol. Phys. 25, 323 (1988).

[22] F. Mrugala and D. Secrest, J. Chem. Phys. 78, 5954 (1983).

[23] F. Mrugala and D. Secrest, J. Chem. Phys. 79, 5960 (1983).

[24] W. H. Press, B. P. Flannery, S. A. Teukolsky, and W. T. Vetterling, *Numerical Recipes The Art of Scientific Computing* (Cambridge University Press, New York, 1986).

[25] J. Alvarellos and H. Metiu, J. Chem. Phys. 88, 4957 (1988).

[26] J. Broeckhove, B. Feyen, L. Lathouwers, F. Arickx, and P. van Leuven, Chem. Phys. Lett. 174, 504 (1990).

[27] D. J. Kouri and R. C. Mowrey, J. Chem. Phys. 86, 2087 (1987).

[28] P. Pernot, R. M. Grimes, W. A. Lester, and C. Cerjan, Chem. Phys. Lett. 163, 297 (1989).

[29] S. E. Choi and J. C. Light, J. Chem. Phys. 90, 2593 (1989).

[30] B. H. Lengsfield, III and D. R. Yarkony, in *State Selected and State-to-State Ion-Molecule Reaction Dynamics, Advanced Chemical Physics*, M. Baer and C. Y. Ng, Eds. (Wiley, New York, 1991), vol. 82, part 2, p. 1.

[31] U. Manthe and H. Köppel, J. Chem. Phys. 93, 345 (1990).

[32] C. Eaker, J. Chem. Phys. 93, 8073 (1990).

[33] J. M. C. Plane, B. Rajasekhar, and L. Bartolotti, J. Chem. Phys. 91, 6177 (1989).

[34] M. F. Vernon, H. Schmidt, P. S. Weiss, M. H. Covinsky, and Y. T. Lee, J. Chem. Phys. 84, 5580 (1986).

[35] P. S. Weiss, J. M. Mestdagh, M. H. Covinsky, B. A. Balko, and Y. T. Lee, Chem. Phys. 93, 126 (1988).

[36] P. J. Kuntz and A. C. Roach, J. Chem. Soc. Faraday II. 68, 259 (1972).

[37] D. J. Diestler, in *Atom-Molecule Collisions Theory: A Guide for the Experimentalist*, R. B. Bernstein, Ed. (Plenum, New York, 1979), p. 655.

[38] U. Manthe, H. Köppel, and L. S. Cederbaum, J. Chem. Phys. 95, 1708 (1991).

[39] C. J. Williams, J. Qian, and D. J. Tannor, J. Chem. Phys. 95, 1721 (1991).

[40] S. K. Gray and C. E. Wozny, J. Chem. Phys. 91, 7671 (1989).

[41] (a) G. G. Balint-Kurti, R. N. Dixon, and C. C. Marlston, J. Chem. Soc. Farad. Trans. 86, 1741 (1990); (b) G. G. Balint-Kurti, R. N. Dixon, C. C. Marlston, and A. J. Mulholland, Comp. Phys. Comm. 63, 126 (1991); (c) D. Neuhauser, M. Baer, R. S. Judson, and D. J. Kouri, Comp. Phys. Comm. 63, 460 (1991).

[42] G. Parlant and D. R. Yarkony, (work in progress).

[43] G. Parlant, J. Rostas, G. Taieb, and D. R. Yarkony, J. Chem. Phys. 93, 6403 (1990).

[44] P. Villarreal, S. Miret-Artés, O. Roncero, G. Delgado-Barrio, J. A. Beswick, N. Halberstadt, and R. D. Coalson, J. Chem. Phys. 94, 4230 (1991).

[45] F. T. Smith, Phys. Rev. 118, 349 (1960).

[46] R. C. Mowrey and D. J. Kouri, J. Chem. Phys. 86, 6140 (1987).

[47] M. C. van Hemert, D. Dohman, and S. D. Peyerimhoff, Chem. Phys. 55, 110 (1986).

[48] M. C. van Hemert and S. D. Peyerimhoff, J. Chem. Phys. 94, 4369 (1991).

[49] R. Kosloff, J. Phys. Chem. 92, 2087 (1988).

[50] H. Tal-Ezer and R. Kosloff, J. Chem. Phys. **81**, 3967 (1984).

[51] J. W. Cooley and J. W. Tucker, Math. Comput. **19**, 297 (1965).

[52] C. Temperton, J. Comput. Phys **52**, 1 (1983).

[53] D. Kosloff and R. Kosloff, J. Comput. Phys. **52**, 35 (1983).

[54] C. Leforestier, R. H. Bisseling, C. Cerjan, M. D. Feit, R. Friesner, A. Guldberg, A. Hammerich, G. Jolicard, W. Karrlein, H. D. Meyer, N. Lipkin, O. Roncero, and R. Kosloff, J. Comput. Phys. **94**, 59 (1991).

[55] R. B. Gerber, R. Kosloff, and M. Berman, Comput. Phys. Rep. **5**, 59 (1986)

[56] V. Mohan and N. Sathyamurthy, Comp. Phys. Rep. **7**, 213 (1988).

[57] R. C. Mowrey and D. J. Kouri, Comp. Phys. Comm. **63**, 100 (1991).

[58] R. Kosloff and D. Kosloff, J. Chem. Phys. **63**, 363 (1986).

[59] D. Neuhauser and M. Baer, J. Chem. Phys. **90**, 4351 (1989).

Introduction of External Field Effects in the Frontier Molecular Orbital Theory of Chemical Reactivity

FERNANDO MENDIZABAL and RENATO R. CONTRERAS

Departamento de Química, Facultad de Ciencias, Universidad de Chile, Casilla 653-Santiago, Chile

ARIE J. AIZMAN

Departamento de Química, Facultad de Ciencias, Universidad Técnica F. Santa María, Casilla 110-V, Valparaíso, Chile

Abstract

External field effects are introduced in both charge and orbital control terms of Klopman–Salem formalism for the study of chemical reactivity in condensed phase. An analytical expression is derived for the change of the interaction energy between a nucleophile and an electrophile from gas to solution phase. The resulting simple expression contains the effect of the external field, in terms of the variation of the electrophilic superdelocalizability index associated with the highest occupied molecular orbital (HOMO) of the nucleophile. Two classical reactions are analyzed to illustrate the usefulness and reliability of the proposed formalism. © 1992 John Wiley & Sons, Inc.

Introduction

The language of frontier molecular orbital (FMO) theory has been incorporated for many years into the discussion of chemical reactivity. The widespread usage of terms like HOMO and LUMO is a measure of the success that this kind of approach has accomplished in the different fields of modern chemistry.

The current application of FMO theory is usually based in gas phase molecular orbital calculations which provide the basic variables to be used in the FMO analysis, namely, atomic charges, monoelectronic energies, and coefficients of the LCAO expansion associated with those relevant orbitals which are supposed to directly determine the reactivity pattern of the system under study.

On the other hand, most of the chemical processes occur in the presence of a liquid environment. It is also well known that the medium often participates in these processes in a nontrivial way [1–3]. Therefore, the modeling of a reacting system in solution via a gas phase molecular orbital study leaves a lot of information, concerning the relevant substrate–medium interactions, out of the analysis.

Klopman [4,5] suggested a simple formula to account for the interaction energy between the reacting systems that partially included electrostatic interactions with the medium. Within this approach, only the charge-control term was modified to include electrostatic interactions with the medium using a model compatible with the Born formula [6]. Since the orbital-control term was derived in the framework of perturbation theory, both the coefficients and the monoelectronic orbital energies

were represented by using the unperturbed wavefunction of the isolated system (i.e., in the absence of the polarizable medium).

In other words, within the Klopman–Salem formalism, the influence of the solvent on the chemical reactivity pattern is introduced in an unbalanced way that modifies the charge-control term, but it leaves the orbital-control term invariant to the influence of the polarized environment. This approximation is equivalent to consider that the MO energies move in a constant amount, equal to the solvation energy of the whole system, when passing from the gas to solution phase.

Sanchez et al. [7] have discussed the electrostatic interactions as a factor in the determination of the HOMOs of a number of benzene derivatives in liquid solutions. Significant variations in the MO sequence, involving changes in the HOMO nature, were observed. A formal treatment for the MO shifting under the influence of an external field was presented recently [8]. A very simple formula was obtained within a variation–perturbation treatment of the problem which expresses the MO shifting from gas to solution phase in terms of a solute electronic polarization contribution and an electron–solvent interaction term [8].

Based on this last approach, we propose in this work an extension of the Klopman–Salem formalism in order to include external field effects on the orbital-control contribution. The resulting formalism will be applied to the study of two well-known systems: the alpha effect observed in the OH and OOH nucleophilic reactivity pattern and the internal return rearrangement of F and CH_3 on the allylic substrate.

Theory

The main objective of the FMO analysis of chemical reactivity is to predict the reactivity pattern that is to be expected from an analysis of the weak interaction of the reacting system. In other words, the slope of the interaction potential at low values of the reaction coordinate is used to qualitatively obtain the relative location of unspecified transition states for the reaction under study. A natural approach to represent this process is a perturbation theory method.

Klopman [4] and Salem [9] proposed a simple scheme based on the interaction of the molecular orbitals of the reacting subsystems. The following expression was derived:

$$\delta E = \sum_{ab} [q_a + q_b] \beta_{ab} S_{ab} + \sum_{k} \sum_{l} \frac{Q_k Q_l}{\varepsilon R_{kl}} + \sum_{m} \sum_{n} \sum_{ab} \frac{2[c_a^m c_b^n \beta_{ab}]^2}{e_m - e_n} \qquad (1)$$

where q_a and q_b denote the electron densities associated with atomic orbitals a and b, β_{ab} and S_{ab} are the resonance and overlap integrals between atomic orbitals a and b. Q_k, Q_l denote the net atomic charges on atoms k and l, and R_{kl} is the interatomic distance. c_a^m and c_b^n are the coefficients of the LCAO expansion, e_m, e_n represent molecular orbital energies, and ε is the dielectric constant of the medium.

Klopman showed that Eq. (1) may be reasonably reduced if the ansatz that only frontier molecular orbitals account for the major part of the reactivity pattern is accepted [4]. The simplified expression becomes:

$$\Delta E \quad \frac{Q_{Nu}Q_{H}}{\varepsilon R} + \sum_{m}^{occ}\sum_{n}^{vir}\frac{2[c_{Nu}^m c_{El}^n \beta]^2}{e_H - e_l} \tag{2}$$

where Q_{Nu} and Q_{El} represent the net charges of the active sites of the nucleophile and electrophile, respectively. According to Klopman's approach [4], reduction of Eq. (1) to Eq. (2) follows essentially from the consideration in energy of the highest occupied molecular orbital of the nucleophile, e_H, and the lowest virtual molecular orbital of the electrophile, e_l.

We may immediately see that the effect of the polarizable environment is partially introduced into this formalism, because it affects the first (charge control) term of Eq. (2). Substraction of the corresponding energy variation in vacuum gives:

$$\delta \Delta E_{1 \to r} = -[1 - 1/\varepsilon]\frac{Q_{Nu}Q_{El}}{R} \tag{3}$$

Equation (3) tells us that the change in reactivity when passing from gas to solution phase is given by the electrostatic solute–solvent interaction energy (i.e., twice the Born's solvation energy contribution of the solvated active sites of the nucleophile and electrophile, respectively). We immediately see that such an approach does not include information concerning the variation of the electronic structure of the reacting system from gas to solution phase. We propose then to introduce electrostatic solvent effects in both charge and orbital control contributions.

Let us write Eq. (2) for the same system in vacuum and in the presence of the solvent:

$$E(1) = \frac{Q_{Nu}^0 Q_{El}^0}{R} + \sum_{m}^{occ}\sum_{n}^{vir}\frac{2[c_{Nu}^m(1)c_{El}^n(1)\beta]^2}{e_H(1) - e_l(1)} \tag{4}$$

and

$$E(\varepsilon) \quad \frac{Q_{Nu}(\varepsilon)Q_{El}(\varepsilon)}{\varepsilon R} + \sum_{m}^{occ}\sum_{n}^{vir}\frac{2[c_{Nu}^m(\varepsilon)c_{El}^n(\varepsilon)\beta]^2}{e_H(\varepsilon) - e_l(\varepsilon)} \tag{5}$$

respectively.

Substraction of Eqs. (5) and (4) gives, for the variation of the interaction energy from gas to solution phase:

$$\delta \Delta E_{1 \to r} \quad [1 - 1/\varepsilon]\frac{Q_{Nu}^0 Q_{El}^0}{R} + \frac{\delta[Q_{Nu}^0 Q_{El}^0]}{\varepsilon R}$$
$$+ 2\sum_{m}^{occ}\sum_{r}^{vir}\left[\frac{[c_{Nu}^m(\varepsilon)c_{El}^n(\varepsilon)\beta]^2}{e_H(\varepsilon) - e_l(\varepsilon)} - \frac{[c_{Nu}^m(1)c_{El}^n(1)\beta]^2}{e_H(1) - e_l(1)}\right] \tag{6}$$

In deriving Eq. (6), a first order variation in the net charge

$$Q_k(\varepsilon) \quad Q_k^0 + \delta Q_k^0 \tag{7}$$

has been assumed with Q_k^0 the net charge on atom k in vacuum; higher terms have been neglected.

Equation (6) expresses the variation of the interaction energy between an electrophile and a nucleophile from gas to solution phase in terms of three contributions: the first one corresponds to a Born-like solute–solvent electrostatic interaction energy; whereas the second accounts for the charge polarization contribution. The third term contains, in a complex way, the effect of the polarizable medium on the orbital control contribution.

This last term may be further simplified if we express the molecular orbital energy shifting induced by electrostatic external effects according to the model proposed by Contreras and Aizman [8]:

$$\delta e_i \atop {i \to c} = \delta e_i^{pol} + n(i)\langle V_R(\varepsilon)\rangle_c. \tag{8}$$

where the first term of Eq. (8) is the electronic polarization contribution of the MO Φ_i [8]:

$$\delta e_i^{pol} = \langle \Phi_i^c \mid F(1, P(\varepsilon)) - F(1, P(1)) \mid \Phi_i^c \rangle \tag{9}$$

whereas the second contribution represents the electron–solvent interaction, expressed in terms of the occupation number of the unperturbed MO Φ_i^c, $n(i)$, and the average reaction field potential.

Based on Eq. (6) and using the convention that the gas phase LUMO energy, $e_l(1)$, is a reference state (i.e., $e_l(1) = 0$), we may write:

$$\delta e_l \atop {i \to c} = \delta e_l^{pol} = e_l(\varepsilon). \tag{10}$$

because the occupation number of the LUMO is zero by definition.

From Eq. (8), the energy shifting of the LUMO of the electrophile is expected to be negligible as compared to the corresponding variation of the HOMO of the nucleophile [the second right hand term in Eq. (8) vanishes for the electrophile]. This approximation is valid for soft electrophiles and also for intermediate cases. In those cases, the approximation $\delta e_l^{pol} \approx 0$ may be used to get the approximate expression:

$$2\beta^2 \sum_m^{occ} \sum_n^{vir} \left[\frac{[c_{Xn}^m(\varepsilon)c_{Ll}^n(\varepsilon)]^2}{e_H(\varepsilon) - e_l(\varepsilon)} - \frac{[c_{Xn}^m(1)c_{Ll}^n(1)]^2}{e_H(1) - e_l(1)} \right]$$

$$\approx 2\beta^2 \sum_m^{occ} \sum_n^{vir} \left[\frac{[c_{Xn}^m(\varepsilon)c_{Ll}^n(\varepsilon)]^2}{e_H(\varepsilon)} - \frac{[c_{Xn}^m(1)c_{Ll}^n(1)]^2}{e_H(1)} \right] \tag{11}$$

Next, we introduce the orbital electrophilic superdelocalizability index:

$$S_l^H(\varepsilon) = 2 \sum_m^{occ} \frac{(c_H^m(\varepsilon))^2}{e_H(\varepsilon)} \tag{12}$$

to get the approximate expression for the orbital-control contribution

$$\beta^2 \sum_n [S_E^{H}(\varepsilon)(c_{Ei}^{n}(\varepsilon))^2 - S_E^{H}(1)(c_{Ei}^{n}(1))^2] \tag{13}$$

where $S_E^{H}(1)$ and $S_E^{H}(\varepsilon)$ are the electrophilic superdelocalizability of the HOMO of the nucleophile in gas and solution phase, respectively.

Substitution of expression (13) into Eq. (6) gives the desired final result

$$\delta \Delta E_{1 \to e} = -[1 - 1/\varepsilon]\frac{Q_{Nu}^{a}Q_{Ei}^{a}}{R} + \frac{\delta[Q_{Nu}^{a}Q_{Ei}^{a}]}{\varepsilon R}$$

$$+ \beta^2 \sum_n^{vir} [S_E^{H}(\varepsilon)(c_{Ei}^{n}(\varepsilon))^2 - S_E^{H}(1)(c_{Ei}^{n}(1))^2] \tag{14}$$

Equation (14) expresses, in a rather simple way, the variation of the interaction energy between an electrophile and a nucleophile from gas to solution phase.

Results and Discussion

In order to test the usefulness and reliability of the formulation presented above, two classical reactions in solution will be discussed here, with the method implemented at CNDO/2 level:
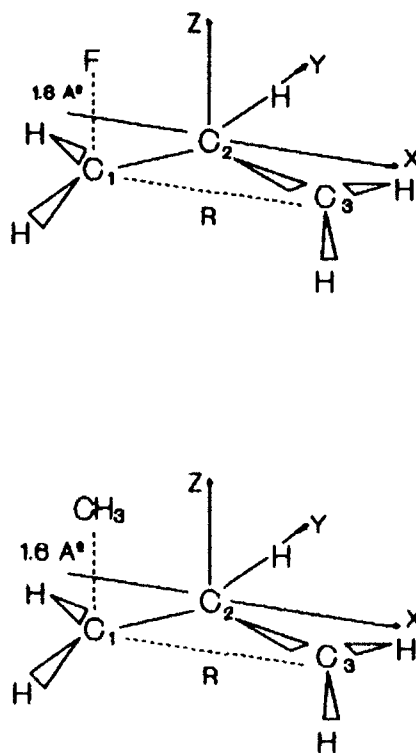
Figure 1. Molecular modeling for the 1,3 internal return rearrangement of F and CH₃ on the allyl⁺ substrate.

1.3 Internal Return Allylic Rearrangement

The model for the migration of F and CH_3 on the allyl[+] frame is shown in Figure 1. Barriers for the rearrangement were calculated in vacuum and in the presence of a highly polarizable medium ($\varepsilon = 80$). In the case of CH_3, local geometry optimization was included to account for inversion of configuration. In both cases, gas phase calculations reveal a barrier for the 1,3 migration with a common transition state consisting in an ion pair. This structure corresponds to the symmetrical form of the complex (i.e., with the nucleophile located midpoint between the imaginary C_1—C_3 axis). The unsymmetrical form, with the nucleophile associated to the C_1 or C_3 ends, present substantial covalent character.

For the allyl[+]/F^{−} system, the electrostatic solvation entails a reduction of the barrier of about 50% (see Fig. 2). The overlap population analysis (see Table 1) reveals that the ion pair degree increases with the strength of the reaction field. As a result, a strong electrostatic solute–solvent interaction accounts for the reduction of the barrier by a strong stabilization of the transition state. This analysis reinforces the previous results reported on this sytem [10], where the hypothesis of acid catalysis was completely discarded [11].

In the case of the allyl[+]/CH_3 system, electrostatic solvation effects produce a
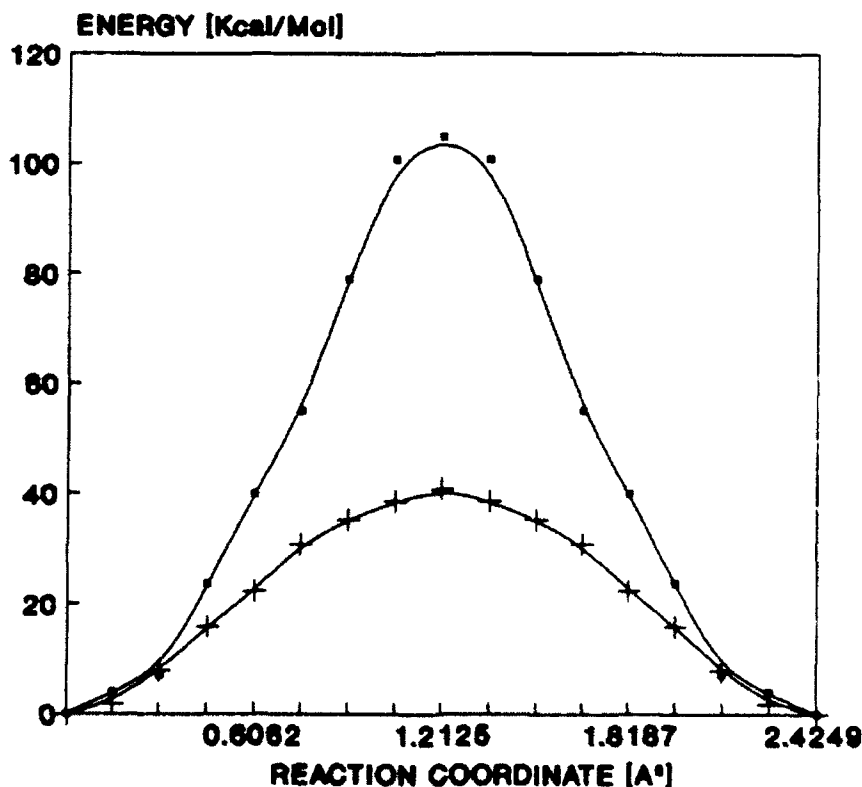
Figure 2. Barriers for F^{−} migration in vacuum (■) and solution (- + -) phase.

Table 1 Population analysis for the F/allyl and CH₃/allyl systems in vacuum and solution phases

System/bond	Gas phase		Solution phase	
	Bond order	Overlap pop	Bond order	Overlap pop
F/allyl (symmet.)				
C1—F	0.0552	0.0030	0.0207	0.0010
C2—F	0.1128	0.0100	0.0283	0.0030
C3—F	0.0552	0.0030	0.0207	0.0010
F/allyl (unsymmet.)				
C1—F	0.8328	0.0900	0.3916	0.0440
C2—F	0.0198	0.0000	0.0614	0.0030
C2—F	0.3682	0.0100	0.1646	0.0010
CH₃/allyl (symmet.)				
C1—C	0.6839	0.1290	0.5984	0.1130
C2—C	0.0000	0.0000	0.0900	0.0000
C3—C	0.6839	0.1290	0.5984	0.1130
CH₃/allyl (unsymmet.)				
C1—C	0.8138	0.1380	0.2672	0.0453
C2—C	0.1528	0.0340	0.288	0.0507
C3—C	0.1912	0.0100	0.1650	0.0086

barrier reduction of about 10% (see Fig. 3): in this case, the overlap population analysis shows that a significant covalent character in the transition state is present, and no significant variations are observed with respect to the change of phase (see Table 1). As a result, a weaker electrostatic solute–solvent interaction is operative in this system. We may then postulate, on the basis of the population analysis, that the internal return rearrangement in the allyl/F system is charge controlled, whereas for the allyl/CH₃ system, it is orbitally controlled. We will show that the same conclusion may be obtained through a formal FMO analysis based on Eq. (14).

The study of the internal return rearrangement barrier entails the comparison of total energies of the reacting system from gas to solution phase. Equation (14) gives only the interaction energy variation contribution to the barrier for this process. A standard energy partition procedure is needed to correctly identify all the contributing terms to the total energy variation from gas to solution phase. This can be seen from the following argument. Let the total energy of the reacting A and B systems in gas and solution phases be written as[1]:

$$E_f(1) = E_A(1) + E_B(1) + E_{AB}(1) \tag{15}$$

and

$$E_f(\varepsilon) = E_A(\varepsilon) + E_B(\varepsilon) + E_{AB}(\varepsilon) \tag{16}$$

---

[1] We thank a referee for suggesting this relevant point.
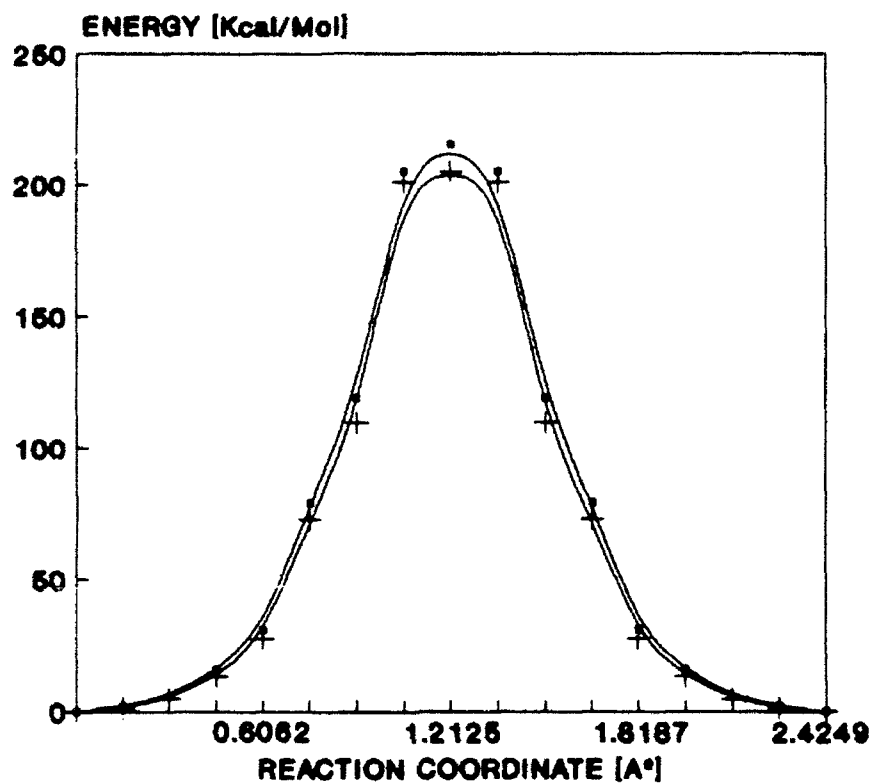
Figure 3.　Barriers for CH_3 migration in vacuum (-■-) and solution (- + -) phase.

Substraction of Eqs. (15) and (16) gives the total interaction energy variation from gas to solution phase:

$$\Delta E_{1 \to t} = E_{solv}(A) + E_{solv}(B) + \delta \Delta E_{1 \to t} \tag{17}$$

TABLE II.　Contribution to the total interaction energy for (a) the internal return rearrangement on allyl⁻ and (b) the alpha effect in the nucleophilic attack of OOH⁻ and OH⁻ on p-nitrophenyl acetate in solution.

Substrate	Nucleophile	Charge control[a] contribution	Orbital control[b] contribution
Allyl⁻	F⁻	-4.93	$0.32\beta^2$
	CH_3^-	0.10	$0.63\beta^2$
p-Nitrophenyl acetate	OH⁻	2.89	$0.16\beta^2$
	OOH⁻	-1.45	$0.07\beta^2$

[a] This contribution is the sum of first and second terms of Eq. (17), and first and second terms of Eq. (14), in electron volts.

[b] This contribution represents the third term of Eq. (14), in units of β^2.

where the third term of Eq. (17) is the interaction energy variation given by Eq. (14).

After the calculations using Eq. (17), it was found that the contribution from the FMO coefficients of the electrophile was 1.00 in both phases for the allyl⁻/F and allyl⁻/CH₃ systems. This result indicates that, for these processes, the orbital control contribution uniquely depends on the variation of the HOMO electrophilic superdelocalizability. In Table II we report the results obtained using the partition of the interaction energy variations from gas to solution phase for both systems. It may be seen that the charge control contribution is the leading term governing the internal return rearrangement for the F case. In the CH₃ situation the charge control contribution plays against the process, whereas the orbital control contribution appears as the driving force for the rearrangement. It is also worth mentioning that a global total energy variation of about 10 kcal/mol is obtained with Eq. (17), in a close agreement with the complete calculation summarized in Figure 3.

This result is reinforced by the fact that, in general, δ_{r} > $\delta_{r'}$.

The Alpha Effect

The enhanced nucleophilic reactivity of OOH⁻ with respect to OH⁻ in solution has been the object of some research [12,13]. Klopman and Frierson persuasively argued in favor of a synergistic solvent and orbital effect to explain the inversion of reactivity between these two nucleophiles with respect to their reactions with p-nitrophenyl acetate [13]. These authors proposed a FMO analysis based on gas phase calculations together with Eq. (1). This conclusion was confirmed later by Contreras and Aizman [8], who used a formalism accounting for the MO energy shifting induced by electrostatic solvation. However, this last approach was not a formal FMO analysis of this chemical process. We decided then to revisit this system to make a FMO analysis based on Eq. (17). The results are displayed in Table II. It may be seen that the total interaction energy variation from gas to solution phase is lower in OOH⁻ than it is for OH⁻, accounting for the enhanced reactivity of OOH⁻ as compared with OH⁻ in solution.

Concluding Remarks

Using a previous theoretical result giving the MO energy shifting induced by electrostatic external effects, a FMO formalism for the chemical reactivity in solution has been developed. The resulting simple expression introduces a charge polarization contribution in the charge control term. The orbital control contribution is also modified by the presence of a polarizable medium, and it is expressed in terms of the variation of an orbital electrophilic superdelocalizability index.

Two well-known chemical reactions have been analyzed. The internal return rearrangement of F and CH₃ on the allyl⁻ substrate in solution is shown to occur by charge control in the former and orbital control in the later case. The analysis of the reactivity pattern of the nucleophilic attack of OOH⁻ and OH⁻ towards a

p-nitrophenyl acetate substrate in solution is in agreement with experimental data and also in agreement with the accepted explanation of the solution alpha effect observed in this system.

Acknowledgments

Bibliography

[1] G. Klopman, *Chemical Reactivity and Reaction Paths* (Wiley, New York, 1974), p. 55.
[2] I. Fleming, *Frontier Orbitals and Chemical Reaction Paths* (Wiley, New York, 1974).
[3] R. C. Dougherty, Tetrahedron Lett. **11**, 385 (1975).
[4] G. Klopman, J. Am Chem. Soc. **90**, 223 (1968).
[5] G. Klopman and P. Andreozzi, Theoret. Chim. Acta **55**, 77 (1980).
[6] G. Klopman, Chem. Phys. Lett. **1**, 200 (1967).
[7] E. Sanchez, J. Maraver, M. Ruiz, and J. Bertran, Can J. Chem. **64**, 2353 (1986).
[8] R. Contreras and A. Aizman, Int. J. Quantum Chem. S **24**, 89 (1990).
[9] L. Salem, J. Am. Chem. Soc. **90**, 223 (1968).
[10] Fates, J. Am. Chem. Soc. **97**, 1334 (1975).
[11] L. Padilla, R. Contreras, and A. Aizman, Int. J. Quantum Chem. S **23**, 483 (1989).
[12] S. Wolfe, D. J. Mitchell, H. B. Schegal, C. Minot, and E. Eiseinstein, Tetrahedron Lett. **23**, 615 (1982).
[13] G. Klopman and M. Frierson, Croat. Chim. Acta **57**, 1411 (1984).

A Fibered Space Approach to Chemical Reaction Mechanisms

GLORIA E. MOYANO and JOSÉ L. VILLAVECES*

Grupo de Química Teórica, Departamento de Química, Universidad Nacional de Colombia, Santa Fe de Bogotá, Colombia

Abstract

In this article we generalize the necessary conditions for a topological definition of the concept of molecular structure, showing that it may be independent of the particular criterion chosen, as long as it fulfills some general conditions and may give rise to the concept of a category of stable chemical structures. We proceed to introduce a local metric in the objects of this category by using the properties of metric space bundles, and this allows us to propose a general system of reaction mechanisms within this framework of the theory of categories. We conclude by proposing a single diagram that encompasses the whole theory of stable structures and reaction mechanisms. © 1992 John Wiley & Sons, Inc.

Introduction

Theories of chemical structure are among the foundations of modern chemistry. They originated in the second half of last century with attempts to establish spatial organization for atoms within molecules in order to explain the existence of isomers. It then became possible to explain the differences between chemical or physical properties of molecules constituted by the same atoms in the same number as originating in differences between geometrical arrangements of their atoms and to explain chemical reactions as rearrangements, or modifications, of these geometries. The development of quantum mechanics lead to the combination of these structural models with quantum methods, transforming the search of configurations of minimum energy and the study of paths joining them within the potential energy hypersurface in central problems of chemistry.

However, there is one main shortcoming: these treatments are semiclassical. They properly treat electrons as quantum particles, but treat nuclei as classical entities. Thus they lack essential consistency in spite of their proven utility for the theoretical study of chemical reactions. For this reason, in recent years, several efforts have been made to overcome this problem by constructing topological (more than geometrical) definitions of the fundamental concepts of chemical structure and reaction mechanism.

Several proposals have been made in this respect [1-4], some of them based on partitions over the nuclear configuration space [5], taking advantage of some prop-

---

* To whom correspondence should be addressed.

erties of molecular systems such as electronic energy or electronic density, computed within the Born–Oppenheimer approximation. More recently, some steps toward a general definition of chemical structure, independent of the somewhat arbitrary choice of particular criteria, have been given [6].

The interest of chemists in a general theory of structure lies in the hope that this may be useful in explaining molecular properties, particularly, reactivity. Some authors [7,8] have stressed the need to refer, even in topological models, to the metric properties of the space, M, of nuclear configurations, in order to carry on local analysis related to spectroscopic properties and to establish the frontiers of sets representing chemical structures when reaction mechanisms are defined.

As we already have a general definition of stable chemical structures [6], from which the particular one based on energy stable catchment regions[1] or molecular graphs may be obtained, we wish to generalize this definition, by adding to it the metric characteristics permitting us to carry on local analysis and to put forward a general scheme of reaction mechanisms [9]. More specifically, we will use fibered spaces with metrical properties [10] to define the model of stable chemical structures, and we will try and establish the characteristics required in metric models of stable chemical structures in order to construct an abstract model of reaction mechanisms.

The Metric Model of Stable Chemical Structures

Let μ be a molecular system of N atomic nuclei and n electrons. For a given electronic state of μ, the Born–Oppenheimer energy functional, $E(K)$, is well defined over the reduced space of nuclear configurations,[2] M.

In order to construct the metric model of stable chemical structures, let us consider the set $\{K^{(0,i)}\}$ whose elements $K \in M$ are such that

$$\nabla_R E(K) = 0 \qquad \text{and} \qquad \mathbb{H}_R E(K) > 0 \qquad\qquad (1)$$

where ∇_R and $\mathbb{H}_R$ are the gradient and the Hessian matrix operators in a system of nuclear coordinates of M. We consider that each one of these equilibrium configurations is representative of a configuration set corresponding to a stable chemical structure.

---

[1] General definition of stable chemical structure given in Ref. [6] is based on proper partitions of the nuclear configuration space. Different partitions must lead to classes, each of them containing points which are equivalent to one energy minimum. Classes corresponding to the same minimum must be equipotent in order to obtain topologically equivalent definitions [1,5,6] of stable chemical structure with the possible partitions. Stable catchment region topology is presented as a case fulfilling the above conditions. Since stable catchment regions are associated with energy minima, they lead to a topological definition of molecular structure [6] different to the one proposed by Mezey [1], who uses, for this purpose, the catchment regions associated with all critical points of the hypersurface.

[2] The reduced space of nuclear configurations is well known by chemists. This space is loosely defined as the (3N-6)-dimensional space remaining after elimination of the rotational and translational degrees of freedom from the 3N-dimensional space of the nuclear coordinates of a molecule containing N nuclei. A more rigorous definition has been given by Mezey as the space where the elements are classes K of points of ^{3N}R corresponding to rotations and translations of a particular nuclear geometry. It is, in general, a non-Euclidean space [7].

Following Mezey [1], we call D_{ext} the set containing the elements $K \in M$ for which $E(K)$ is not well defined, because the hypersurface is a bad approximation to the expected value of electronic energy, i.e., where the Born–Oppenheimer approximation is not a good one, and hence, the first and second derivatives of $E(K)$ are not well defined.

Let us define:

(M-1): $T = \{ K^{(0,i)}, i \in I, \text{ and } K_{ext} \}$ a set with the discrete topology (K_{ext} being a representative element of D_{ext}).

(M-2): $G = \{ K \}$. G and M are the same set, but we will use different topologies for each one of them.

(M-3): equivalence relations in M, $\sim_j$, $j \in J$. For a given equivalence relation, we define a function, p, such that:

$$p : G \to T$$

$$K \to K^{(0,i)}, \qquad \text{if } K \sim K^{(0,i)}$$

$$K \to K_{ext}, \qquad \text{if } K \sim K_{ext} \tag{2}$$

The idea is that if a nuclear configuration of minimum energy is representative of a particular chemical structure, configurations corresponding to small geometry deformations will represent the same chemical structure (they will be equivalent), whereas large enough deformation will give rise to different chemical structures or even to geometrical arrays of nuclei not corresponding to any stable chemical structure. Relationship (2) formalizes this intuitive chemical notion of equivalence.

Several different criteria may be used to define equivalence relations; for example, two points may be equivalent if the steepest descent paths from them lead to the same minimum [1,6], or they may be equivalent if they have the same molecular shape graphs [2] or if they have the same molecular graph obtained from their charge density [4,6].

(M-4): Σ is the set of all functions, $\alpha : U \to G$, $\forall U \subset T$, such that $p \circ \alpha = \text{id} \, U$. As T is a discrete topological space, every function $\alpha \in \Sigma$ is continuous. Then, function α maps each minimum on all its equivalent configurations.

(M-5): a metric $d : G \times G \to [0, +\infty]$, such that:

$$\forall K_i, K_j \in G \begin{cases} d(K_i, K_j) = +\infty & \text{if } p(K_i) \neq p(K_j) \\ d(K_i, K_j) = q(K_i, K_j) & \text{if } p(K_i) = p(K_j) \end{cases} \tag{3}$$

where function q is defined by

$$q(K, K') = \min \{ \rho(x, x') : x \in K, x' \in K' \} \tag{4}$$

and, as has been shown [7,11], it has all the properties of a metric on M. In this definition, ρ represents the metric of the Euclidean $3N$-dimensional space from which M has been obtained [12] (see footnote 2). In this way, a couple of points corresponding to different chemical structures will be an infinite distance, whereas

for equivalent points we retain the usual metric properties of nuclear configuration space.

A bundle of metric spaces may be built with objects (M-1) to (M-5), because they satisfy the existence theorem for metric space bundles (see Appendix). In the usual language of the theory of metric space bundles [10,13], the topological space, T, is commonly called the basis space, and G is called the fibered space. For each $t \in T$, the set $p^{-1}(t)$ is known as the fiber on t.

In other words, T is a discrete point set having as many points as stable chemical structures may be obtained with the given set of nuclei. G is the nuclear configuration space with subsets of the equivalent nuclear geometries corresponding to each chemical structure. Each of these subsets is the fiber corresponding to the representative point of the structure.

With metric d and the α functions we define the ε-tubes around each α as the sets of points of G, whose distance from a point of the image of α is less than a given $\varepsilon > 0$. The ε-tubes are closely analogous to the open spheres of radius ε, which can be obtained in any metric space.

In the above-defined structure (G, p, T), G is the set of all nuclear geometries. The topology generated by the ε-tubes on G is equivalent to that obtained by the disjoint union of subspaces $p^{-1}(t)$ of M.

In this context, subspaces

$$A^{(t)} = p^{-1}(t), \forall t = K^{(0,t)} \in T \tag{5}$$

represent stable chemical structures, because $p^{-1}(t)$ is the set of configurations of M, chemically equivalents to one of the $t = K^{(0,t)}$, according to the particular criterion chosen.

To a better understanding of the topology of G, we may remember that for each fiber, $p^{-1}(t)$, $t \in T$, the metric, d, is a restriction of the global metric, q [7], of M. The "local metric," d, allows the retrieval of the characteristics of differentiability of E(K) within each stable structure, i.e., within each $A^{(t)}$.

This is an important step, because the derivatives of the "potential" electronic energy, E(K), allow local analysis in the chemically equivalent neighborhood of each minimum.

We call d "local" because it provides a metric for each separated chemical structure. For different chemical structures, the distance is infinity and they may not be compared with this criterion. This has the advantage over a global metric. In a global metric, two different points in M located at a distance, r, may or may not correspond to the same chemical structure. and thus, one does not have a good criterion to define a chemical structure. The particular criterion that may be used to build these metric models of chemical structure should lead to topologically equivalent definitions; i.e., they should lead to the construction of a set of objects (G, p, T) having in common the same space T and a set of isomorphisms.[3]

$$u: (G, p, T) \rightarrow (G', p', T) \tag{6}$$

---

[3] The morphisms between objects (G, p, T) are continuous functions. It is said that u is a T-isomorphism if and only if it exists a morphism $u^{-1}: (G', p', T) \rightarrow (G, p, T)$ with $u^{-1} u = id_G$ (the identity over G).

such that the diagram

$$u: G \longrightarrow G'$$
$$p \searrow \quad \swarrow p'$$
$$T$$

commutes.

G is the reduced space of nuclear configurations endowed with some structure according to the particular criterion chosen for the definition of equivalent points. Let us say. for example. equivalent points corresponding to the same chemical structure are all those having steepest descent paths that lead to the same minimum in the potential energy hypersurface [1,6]: p is the projection function that maps all these equivalent points on the minimum. $K^{m,o}$. and T is the point set containing one point for each chemical structure.

G' is analogous to G but with a different criterion. e.g.. in G' those points having the same molecular graph are equivalent. and p' is the corresponding projector [3,4,6].

What the commutability of D1 means for any criterion of equivalence chosen fulfills the given conditions is that all these criteria give rise to equivalent formal results. and the concept of chemical structure contains that which is common to all of them.

The set of objects and morphisms mentioned in the former lines conforms a mathematical structure called a category [13]. and thus. we have defined the *category of stable chemical structures*.

The existence of isomorphisms between two models (G. p. T) is possible for a discrete T only if the restrictions $\xi|_l$ and $\eta|_l$ are l'-isomorphic. Here. $\xi = (G. p. T)$ and $\eta = (G'. p'. T)$ and $l' \subseteq T$. That is. from local isomorphisms representing the same chemical structure. we obtain. quite naturally. global isomorphisms between all possible structures for a given molecular system and. hence. an equivalence between all definitions of stable chemical structures.

Toward a General System of Reaction Mechanisms

A subject of major importance in chemistry is the study of reaction mechanisms. From a topological point of view it has been treated in several ways. One way has been to propose a formal definition of a reaction mechanism: either as a homotopy class of paths on M [1,14]. i.e.. as sets of continuous paths that can be transformed continuously into each other; or. in catastrophe theory context. as structural discontinuous changes produced in response to smooth changes in certain parameters (control parameters) governing the system behavior [15].

On the other hand. efforts have been made to establish. for a given chemical system. all possible reaction mechanisms. based on formal definitions. and to analyze the mathematical structure (e.g.. the group structure [14]) of the complete set of reaction mechanisms.

Our proposal is in the latter sense. We take for this purpose an approach based on Mezey's definition of a regular reaction mechanism [1]. Nevertheless, we try to apply it to sets obtained from general criteria, of which the one based in steepest descent paths on the energy hypersurface is just a particular one.

For any partitioning scheme of M, the procedure to find possible reaction mechanisms consists in determining the frontiers, with respect to the global metric of the nuclear configurations space, of every set representing a chemical structure, and to determine, for each pair of such sets, if the intersection of their closures in the global metric topology is nonempty [1,4], which implies the possibility of connecting such a pair by means of a reaction mechanism.

Mezey defines, for the particular case of energy catchment regions, a neighborhood relationship, N, allowing one to study a reaction mechanism algebraically [1,14] in a similar way that is done with an interrupting circuit: i.e., assigning the values 1 and 0 to the possibility or impossibility, respectively, of connecting the two structures by means of a reaction mechanism. The purpose of this section is to generalize the neighborhood relationship, N, by allowing it to be applied to any model of chemical structures belonging to the same category, in order to obtain equivalent networks of reaction mechanisms.

The expression that we shall use to define the general neighborhood relationship, N, is:

$$N^{(A^{(i)},A^{(j)})} = \begin{cases} 1 \text{ if } \overline{A^{(i)}} \cap \overline{A^{(j)}} \neq 0 \\ \\ 0 \text{ in every other case} \end{cases} \tag{7}$$

where $\overline{A^{(i)}}$ is the closure of $A^{(i)}$ in the global metric. The most current situation, and perhaps the most important one from a chemical point of view, arrives when mechanisms in which two sets associated with two different energy minima are neighbors, i.e., when the intersection of the closures of the pair of sets with respect to the global metric of M is not empty. In this case, one talks about a regular mechanism [1]. We can visualize the difference set, $(A^{(i)} - A^{(i)})$, the frontier of $A^{(i)}$ (in the global metric), as that containing the unstable intermediate structures of the reaction mechanisms.

We will try and obtain the conditions for relationship (7) to give equivalent reaction mechanisms, when applied to equivalent models of structure. This is not an arbitrary restriction, but an essential one in order to have a coherent general model of chemical structure and reaction mechanisms. That is, if in a particular realization of the general model, we can establish a reaction mechanism involving a given couple of chemical structures, we must reach the same conclusion by working with any other particular realization of the model. In the following, we try to determine the implications brought by the mentioned restriction for objects and morphisms in the category of stable chemical structures.

The metric of model (G, p, T) of stable chemical structure does not possess the global characteristics that would allow immediate application in G of neighborhood relations, N. Nevertheless, it is possible to characterize the metric models of structure leading to the equivalent reaction mechanism, by relating G and M by means of

the identity application id: $G \to M$. Clearly, id: $p^{-1}(t) \to G$, is continuous and each $p^{-1}(t)$, $t \in T$ is both open and closed in the topology of G. Accordingly, the topology of G is finer than that of M, and hence, the function id: $G \to M$ is continuous. The possibility of building equivalent networks of regular reaction mechanisms implies, on the first hand, the necessary existence of morphisms, m, between each pair of objects (G, p, T) and (G', p', T) such that if A and B are the closures with respect to the global metric q of any pair of sets representing stable chemical structures, then:

$$A, B \subset G$$

$$\text{if } A \cap B \neq \varnothing \to m(A) \cap m(B) \neq \varnothing,$$

$$\text{and if } A \cap B = \varnothing \to m(A) \cap m(B) = \varnothing$$

Every isomorphism, $u: (G, p, T) \to (G', p', T)$, of the stable chemical structures category satisfy the former condition, due to the fact that for every function f: $Y \to Z$, if f is one-to-one and onto and $(X_i)_{i \in I}$ is an arbitrary family of subsets belonging to Y, then [16]

$$f\left(\bigcap_{i \in I} X_i\right) = \bigcap_{i \in I} f(X_i) \tag{9}$$

implying that, for any pair, A, B, whenever $A, B \subset G$, if $A \cap B \neq \varnothing$, then $u(A \cap B) = u(A) \cap u(B) \neq \varnothing$, because u is one-to-one and onto, and if $A \cap B = \varnothing$, then $u(A \cap B) = u(A) \cap u(B) = \varnothing$.

As a consequence of this result, if we can guarantee in some way that the isomorphism, u, relates each set of G corresponding to a stable structure plus its frontier, $\overline{A_G^{(i)}}$, with the set corresponding in G' to the same stable structure plus its frontier, $A_G^{(i)}$, then all reaction mechanisms between every pair of sets of G will also be reaction mechanisms for the corresponding sets of G'. The isomorphisms of the category of stable chemical structures relate each structure $A_G^{(i)}$ in G with $A_G^{(i)}$, in G', but it is then necessary to extend the relationship to one between each pair $A_G^{(i)}$, $A_G^{(i)}$. That is, it is necessary that the same isomorphisms, u, relate the closures, with respect to the global metric of M, of sets representing stable chemical structures in model (G, p, T) to the closures of the corresponding stable structures in (G', p', T), with respect to M'.[4] That is, there should exist isomorphisms u: $G \to G'$, that may be extended to homeomorphisms u': $M \to M'$ such that the following diagram commutes:

$$\tag{D2}$$

---

[4] M' is the same as M, but for clarity we designate it with a prime.

This is a condition satisfied by every isomorphism $u: (G, p, T) \to (G', p', T)$ for which u and u^{-1} are uniformly continuous, because id: $G \to M$ and id': $G' \to M'$ are uniformly continuous as well (see Appendix), and if we define subset R of M (and G)

$$R = \bigcup_{i \in I} A^{(i)} \cup \text{int}_M(A_{\text{excl}}) \tag{10}$$

where the $A^{(i)}$, $i \in I$, represent the $p^{-1}(K^{(0,i)})$ for each $K^{(0,i)} \in T$ and $\text{int}_M(A_{\text{excl}})$ represent the interior of A_{excl}, i.e., of $p^{-1}(K_{\text{excl}})$ in the topology of M (the one associated to the global metric). This means that each $A^{(i)}$ is the set corresponding to a stable chemical structure in G. The $A^{(i)}$ are disjoint, open sets in M (see Appendix) and M is connected; accordingly, A_{excl} is closed because of

$$M = \bigcup_{i \in I} A^{(i)} \cup A_{\text{excl}} \tag{11}$$

R is dense in M, due to the fact that

$$\bar{R} = \overline{\bigcup_{i \in I} A^{(i)} \cup \text{int}_M (A_{\text{excl}})} = \bigcup_{i \in I} \overline{A^{(i)}} \cup A_{\text{excl}} \tag{12}$$

then

$$\bigcup_{i \in I} \overline{A^{(i)}} \cup A_{\text{excl}} = \bigcup_{i \in I} A^{(i)} \cup A_{\text{excl}} = M \tag{13}$$

Let us consider that R has the topology induced by that of M, i.e., R is a subspace of M. R is also a subspace of G because G is the disjoint union of $A^{(i)}$ and the A_{excl}, each one of them with the topology induced by that of M.

The restriction of $u: G \to G'$ to R is uniformly continuous [16], and the function $k = \text{id} \circ u: G \to G' \to M'$ is uniformly continuous, being the composite of two uniformly continuous functions. Then, the restriction, $k|_R: R \to M'$, is uniformly continuous. Every function, $k|_{R'}$, uniformly continuous, defined in a dense subspace, R, of a uniform space M, taking its values in a uniform and complete Hausdorff space, M', may be extended [16] to a unique function, $\bar{k}$, uniformly continuous, of M in M', $\bar{k}: M \to M'$.

Isomorphisms $u: G \to G'$ are also isomorphisms at the fiber level, meaning that the restriction of u to $A_{\text{excl}} \subset G$ is an isomorphism between A_{excl} and A'_{excl}, where $A'_{\text{excl}} \subset G'$.

The restrictions

$$\bar{k}|_{A_{\text{excl}}}: A_{\text{excl}} \to M' \wedge k|_{A_{\text{excl}}}: A_{\text{excl}} \to M' \tag{14}$$

are uniformly continuous.

Let us remember that they both coincide in the interior with respect to M of A_{excl}, and also that $\text{int}_M (A_{\text{excl}})$ is a dense subset of A_{excl} (in the subspaces topology of M). Accordingly, if the extension of $k|_R$ is unique, then $k|_{A_{\text{excl}}}$ and $\bar{k}|_{A_{\text{excl}}}$ are identical. This implies that $\bar{k}: M \to M'$ is one-to-one, onto, and uniformly continuous. One may apply the same arguments to u^{-1} in order to conclude that $(\bar{k})^{-1}$ is one-to-one, onto, and uniformly continuous, i.e., $\bar{k}$ is a homeomorphism.

Summarizing, this result may be expressed as follows: the uniformly continuous isomorphisms of the categories here defined relate sets corresponding to the same stable chemical structure plus its frontier. By different definitions we can build equivalent systems of chemical structure in the sense that they belong to the same category and hence, these isomorphisms guarantee equivalence in reaction mechanisms.

Conclusion

The characteristics of the metric model of chemical structure and reactivity presented herein may be expressed by means of the following commuting diagram:

$$
\begin{array}{ccc}
u': M & \longrightarrow & M' \\
\uparrow \text{id} & & \uparrow \text{id}' \\
u: G & \longrightarrow & G' \\
\quad p \searrow & & \swarrow p' \\
& T &
\end{array}
\qquad (D3)
$$

which, in the inferior, triangular, part expresses the equivalence condition in the particular realizations of the concept of structure, and in the superior, square, part expresses the equivalence in algebraic systems of reactivity associated to each one of the particular criteria of structure discussed.

Acknowledgment

Appendix

Metric Spaces Bundle

Definitions:

(a) G and T are topological spaces
(b) $p: G \to T$ is a continuous and onto function
(c) d is a metric $d: G \times G \to [0, +\infty]$ for p, satisfying:

$$(c\text{-}1) \ \forall u, v \in G, p(u) \neq p(v) \leftrightarrow d(u, v) = +\infty$$

$$(c\text{-}2) \ \forall u, v \in G, d(u, v) = 0 \leftrightarrow u = v$$

$$(c\text{-}3) \ \forall u, v \in G, d(v, u) = d(u, v)$$

$$(c\text{-}4) \ \forall u, v, w \in G, d(u, v) \leq d(u, w) + d(w, v)$$

(d) α: U → G, where U is open in T, is a continuous function, called local section, such that p∘α = id U (the identity in U)

(e) Tε(α) = $\{$u ∈ G: p(u) ∈ U = dom α, ∧, d(u, α(p(u))) < $\varepsilon\}$ (where dom α is the domain of α) is a set known as the ε-tube around α.

The triple of (G, p, T) is called a bundle of metric spaces, if ∀u ∈ G and ∀ε > 0, $\exists\alpha$: u ∈ T$_\varepsilon$(α), and if the collection of the T$_\varepsilon$(α), ε > 0, ∀α form a basis for the topology of G [10].

Theorem of Existence of Metric Space Bundles

(a) T a topological space
(b) p: G → T an onto function
(c) Σ a set of functions α: U → G (U an open of T), such that ∀α, p∘α = id U
(d) d a metric for p.

If the following conditions are satisfied [10]:
(E-1) ∀u ∈ G ∧ ∀ε > 0, $\exists\alpha$ ∈ Σ: u ∈ T$_\varepsilon$(α), and
(E-2) ∀ε > 0 ∧ ∀(α, β) ∈ Σ × Σ, the set $\{$t ∈ T: d(α(t), β(t)) < $\varepsilon\}$ is open in T.

then G may be given a topology τ, such that:
(T-1) τ has a basis spanned by the T$_\varepsilon$(α), where ε > 0 and $\alpha|_U$ is the restriction to an open U ⊂ dom α, of a function α ∈ Σ.
(T-2) Each α ∈ Σ is continuous, and
(T-3) (G, p, T) is a bundle of metric spaces.

For objects (M-1) to (M-5):
Given any u ∈ G, the function α(p(u)) = u belongs to Σ, because p(u) is a subset of T and p∘α(p(u)) = id (p(u)). Then u ∈ T$_\varepsilon$(α), where

$$T_\varepsilon(\alpha) = \{x \in G: p(x) \in \text{dom } \alpha, \wedge, d(x, \alpha(p(x))) < \varepsilon, \forall\varepsilon > 0\},$$

because p(u) belongs to dom α and d(u, α(p(u))) = 0. In this way, (E-1) and (E-2) is satisfied, because, given any couple (α, β) ∈ Σ × Σ, α: U$_1$ → G, β: U$_2$ → G y U$_1$, U$_2$ ⊂ T, then subset $\{$t ∈ T: d(α(t), β(t)) < ε ∀ε > 0$\}$ is a part U$_3$ of T and, as T has the discrete topology, it is an open set of T.

In order to show that isomorphisms u: (G, p, T) → (G′, p′, T), such that u y u^{-1} are uniformly continuous, may be extended to homeomorphisms in such a way that Diagram (D2) commutes, it is necessary to remember that:

(a) M and G are Hausdorff spaces because they are metric spaces.

(b) M and G are metric spaces and then they are uniforms, with a uniformity U, where U is the collection of sets $U_r = \{$(x, y) ∈ X × X, δ(x, y) < ε ∀ε > 0$\}$, where X is the metric space and δ is its metric [16].

(c) From (b) it follows that the uniformity of G is finer than that of M, which is a condition [16] for function id: G → M to be uniformly continuous.

(d) We consider that the catchment region $A^{(0,J)}$ of a minimum is an open set in the metric topology of the reduced nuclear configuration space.

(e) ^{3N}R is connected, because it is the 3N-dimensional Euclidean space. Hence, M, which is a quotient space of ^{3N}R, is also connected [16].

(f) ^{33}R is complete, and M is obtained by taking the quotient of ^{33}R with respect to equivalence classes K, closed [17] in the topology of ^{33}R. And, as M does not have isolated points, it follows that M is complete.

Bibliography

[1] P. G. Mezey, Theor. Chim. Acta 62, 133 (1982).
[2] G. A. Arteca and P. G. Mezey, J. Chem. Phys. 87, 4161 (1987); Phys. Rev. A 35, 4044 (1987); Int. J. Quant. Chem., Quant. Biol. Symp. 14, 133 (1987); J. Chem. Phys. 93, 4746 (1989).
[3] R. F. W. Bader, T. T. Nguyen-Dang, and Y. Tal. Rep. Prog. Phys. 44, 894 (1981).
[4] Y. Tal, R. F. W. Bader, T. T. Nguyen-Dang, M. Ojha, and S. G. Anderson, J. Chem. Phys. 74, 5162 (1981).
[5] P. G. Mezey, J. Chem. Phys. 78, 6182 (1983).
[6] J. L. Villaveces and E. E. Daza, Int. J. Quant. Chem. Quant. Chem. Symp. 24, 97 (1990).
[7] P. G. Mezey, Int. J. Quant. Chem. Quant. Chem. Symp. 17, 137 (1983).
[8] P. G. Mezey, Int. J. Quant. Chem. Quant. Biol. Symp. 8, 185 (1981).
[9] G. E. Moyano, Graduation Work in Chemistry. National University of Colombia, (1991).
[10] G. Rodriguez, M.Sc. Thesis, National University of Colombia, (1983).
[11] P. G. Mezey, Int. J. Quant. Chem. 26, 983 (1984).
[12] P. G. Mezey, Theor. Chim. Acta 63, 9 (1983).
[13] D. Husemoller, Fibre Bundles, McGraw-Hill, New York, (1966).
[14] P. G. Mezey, Theor. Chim. Acta 60, 409 (1982); Theor. Chim. Acta 67, 43 (1985); Theor. Chim. Acta 67, 91 (1985); (d) Int. J. Quant. Chem. Quant. Chem. Symp. 19, 93 (1986); J. Mol. Struct. (THEOCHEM) 149, 57 (1987).
[15] R. F. W. Bader, T. T. Nguyen-Dang, and Y. Tal, J. Chem. Phys. 70, 4316 (1979).
[16] N. Bourbaki, Elements of Mathematics. Volume I, Theory of Sets. Volume III, General Topology (Hermann, Addison-Wesley, France, 1966).
[17] P. G. Mezey, Int. J. Quant. Chem. Quant. Chem. Symp. 21, 191 (1987).

On the Additivity and Interference of Interactions

I. MAYER

*Central Research Institute for Chemistry of the Hungarian Academy of Sciences,
H-1525 Budapest, P.O. Box 17, Hungary*

Abstract

There is a very simple criterion showing whether two (or more) Hamiltonians describe strictly additive effects. Based on this criterion, an attempt is made to develop techniques that would permit treatment of different not strictly additive interactions by separating out their components, which can be considered strictly additive, and describing the nonadditive (interference) effects as some perturbation. As a first result, a promising scheme has been developed for estimating matrix eigenvalues by an $\sim N^3$ procedure. © 1992 John Wiley & Sons, Inc.

Introduction

Considering different physical and chemical problems, one often encounters a situation in which some almost additive effects can be recognized. Nevertheless, such quasi-additivity usually is not utilized explicitly in the quantum chemical theories, owing to the absence of a proper formalism. (Implicitly, of course, all theories utilize some additivity assumptions.) We have started, therefore, to develop special techniques for treating quasi-additive interactions, hoping that this will lead to results which are useful both in understanding chemical phenomena and in facilitating their treatment in the framework of *ab initio* quantum chemical theory.

Criterion of Additivity

Let $\hat{H}^A$ and $\hat{H}^B$ be two Hamiltonians describing strictly additive interactions. This means that each eigenstate of the system can be characterized by a pair of indices i and j such that the energy is equal to $E_i^A + E_j^B$. If these Hamiltonians are defined over finite basis sets of dimensions m_A and m_B, then the total Hamiltonian $\hat{H} = \hat{H}_A + \hat{H}_B$ should be defined over a space of dimension $m_A \times m_B$, spanned by a basis obtained as (properly antisymmetrized) products of the two basis sets. The matrix elements of the Hamiltonians can then be characterized by two pairs of indices (e.g., $H_{(ij)(kl)}$). It is easily seen that the Hamiltonian matrix $\mathbf{H}$ will describe strictly additive interactions $\hat{H}^A$ and $\hat{H}^B$ if its matrix elements can be given as (or can be transformed to)

$$H_{(ij)(kl)} = H_{ik}^A \delta_{jl} + \delta_{ik} H_{jl}^B, \tag{1}$$

or, in matrix form:

$$\mathbf{H} = \mathbf{H}^A \otimes \mathbf{I}^B + \mathbf{I}^B \otimes \mathbf{H}^A \tag{2}$$

where $\mathbf{I}^A$ and $\mathbf{I}^B$ are the $m_A \times m_A$ and $m_B \times m_B$ unit matrices, respectively. In the strictly additive case, the eigenvector c of the secular equation $\mathbf{H}c = Ec$ will also represent direct products of the eigenvectors [1] obtained for the individual problems $\mathbf{H}^A c_i^A = E_i^A c_i^A$ and $\mathbf{H}^B c_j^B = E_j^B c_j^B$, respectively: $c_{ij} = c_i^A \otimes c_j^B$. So, the additive eigenvalue equation becomes

$$(\mathbf{H}^A \otimes \mathbf{I}^B + \mathbf{I}^A \otimes \mathbf{H}^B)(c_i^A \otimes c_j^B) = (E_i^A + E_j^B)(c_i^A \otimes c_j^B). \tag{3}$$

Any nonadditivity can be characterized as a deviation from this equation. Two types of effects can cause such deviations. There may be terms of the Hamiltonian which are not exactly equal to the values predicted by the strictly additive scheme. We may call them direct nonadditive interaction terms. Another type of effect is connected with the differences in the dimensions of the actual eigenvalue problem and that of the strictly additive model, due, for example, to the Pauli exclusion principle. This causes nonadditivity which may be called interference of interactions. It appears that effects of this type should be responsible for some characteristic chemical phenomena.

Some Generalizations

Generalization to the case of three or more Hamiltonians can trivially be done by induction. So the Hamiltonian matrix in the case of three strictly additive interactions $\hat{H}^A$, $\hat{H}^B$, and $\hat{H}^C$ has the form

$$\mathbf{H} = \mathbf{H}^A \otimes \mathbf{I}^B \otimes \mathbf{I}^C + \mathbf{I}^A \otimes \mathbf{H}^B \otimes \mathbf{I}^C + \mathbf{I}^A \otimes \mathbf{I}^B \otimes \mathbf{H}^C. \tag{4}$$

The eigenvectors in the strictly additive case are $c_{ijk} = c_i^A \otimes c_j^B \otimes c_k^C$, the eigenvalues $E_{ijk} = E_i^A + E_j^B + E_k^C$.

Generalization to the overlapping basis sets can also be done easily. If matrices $\mathbf{H}^A$ and $\mathbf{H}^B$ are referred to nonorthogonal basis sets with the overlap matrices $\mathbf{S}^A$ and $\mathbf{S}^B$, respectively, then the strictly additive composite eigenvalue equation becomes

$$(\mathbf{H}^A \otimes \mathbf{S}^B + \mathbf{S}^A \otimes \mathbf{H}^B)(c_i^A \otimes c_j^B) = (E_i^A + E_j^B)(\mathbf{S}^A \otimes \mathbf{S}^B)(c_i^A \otimes c_j^B). \tag{5}$$
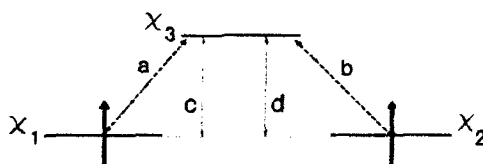
Figure 1. The simple two-electron model discussed in the text.

$$\begin{pmatrix} 0 & 0.4 & 0.2 & -0.3 & 0.4 & 0.5 \\ 0.4 & 2.0 & 0.2 & -0.2 & 0.12 & 0.2 \\ 0.2 & 0.2 & 3.0 & 0.3 & -0.3 & -0.2 \\ -0.3 & -0.2 & 0.3 & 1.0 & 0.2 & 0.1 \\ 0.4 & 0.12 & -0.3 & 0.2 & 2.0 & -0.12 \\ 0.5 & 0.2 & -0.2 & 0.1 & -0.12 & 1.8 \end{pmatrix}$$
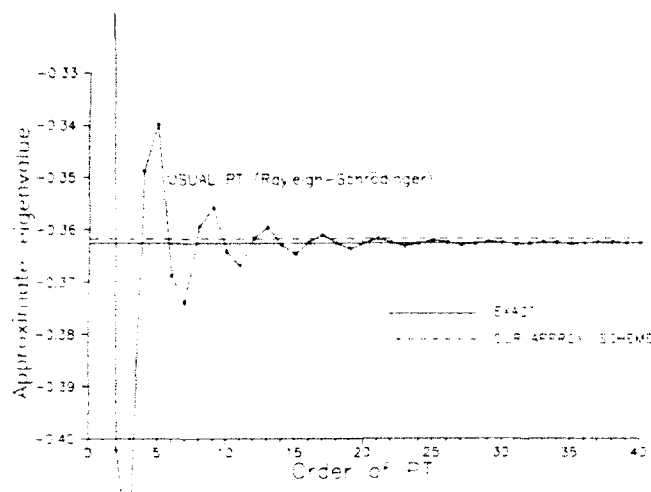
Figure 2. A 6 × 6 matrix and the performance of our scheme as compared with that of the standard PT in approximating its lowest eigenvalue. (The horizontal full and dashed lines represent the exact solution and the result of our approximation, respectively.)

Nonadditivity as a Perturbation

If the Hamiltonian matrix H describes a quasi-additive situation in which one can recognize the almost (but not strictly) additive interactions described by the Hamiltonians $\hat{H}^A$ and $\hat{H}^B$, with known solutions, then the strictly additive Hamiltonian $H^O = H^A \otimes I^B + I^A \otimes H^B$ can be introduced as an unperturbed Hamiltonian and the difference $V = H - H^O$ as a perturbation. The secular equation becomes

$$(H^O + V)(c_i^A \otimes c_j^B + \Delta c_{ij}) = (E_i^A + E_j^B + \Delta E_{ij})(c_i^A \otimes c_j^B + \Delta c_{ij}) , \quad (6)$$

and can be treated by usual perturbation theory.

Usual second-order PT often gives additive contributions, but none of the interactions is treated exactly. Our scheme permits exact treatment of individual interactions, and only the deviations from the additivity are treated by PT.

In the overlapping case, H^O is given as

$$H^O = H^A \otimes S^B + S^A \otimes H^B ,$$

$$
\begin{bmatrix}
0.0 & 0.4 & 0.2 & -0.3 & 0.4 & 0.5 & 0.5 & 0.3 & -0.3 & -0.3 \\
0.4 & 2.0 & 0.2 & -0.2 & 0.12 & 0.2 & 0.3 & -0.3 & 0.53 & 0.12 \\
0.2 & 0.2 & 3.0 & 0.3 & -0.3 & -0.2 & -0.4 & 0.4 & 0.4 & 0.4 \\
-0.3 & -0.2 & 0.3 & 1.0 & 0.2 & 0.1 & 0.1 & 0.21 & -0.2 & -0.2 \\
0.4 & 0.12 & -0.3 & 0.2 & 2.0 & -0.12 & -0.2 & -0.2 & -0.4 & 0.3 \\
0.5 & 0.2 & -0.2 & 0.1 & -0.12 & 1.8 & 0.3 & -0.3 & -0.3 & -0.3 \\
0.5 & 0.3 & -0.4 & 0.1 & -0.2 & 0.3 & 2.3 & 0.3 & 0.3 & 0.23 \\
0.3 & -0.3 & 0.4 & 0.21 & -0.2 & -0.3 & 0.3 & 1.3 & 0.3 & 0.2 \\
-0.3 & 0.53 & 0.4 & -0.2 & -0.4 & -0.3 & 0.3 & 0.3 & 2.0 & -0.3 \\
-0.3 & 0.12 & 0.4 & -0.2 & 0.3 & -0.3 & 0.23 & 0.2 & -0.3 & 1.92
\end{bmatrix}
$$
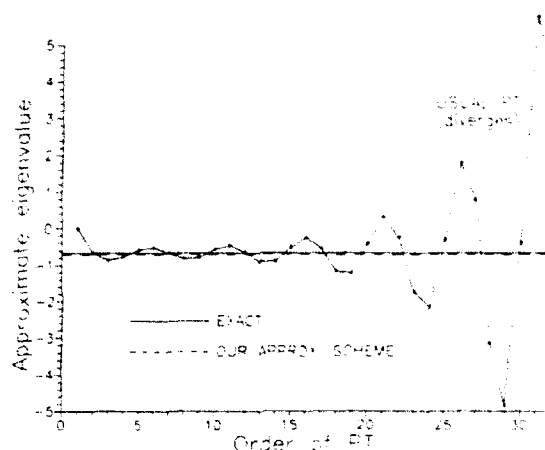
Figure 3. A 10 × 10 matrix and the performance of our scheme as compared with that of the standard PT in approximating its lowest eigenvalue. (The notations are the same as on Fig. 2.)

and one has to introduce also the deviation (if any) of the overlap matrix as $\Delta S = S - S^A \otimes S^B$. One then obtains a nonlinear perturbational equation

$$(H^O + V - E\Delta S)(c_i^A \otimes c_j^B + \Delta c_{ij})$$

$$= (E_i^A + E_j^B + \Delta E_{ij})(S^A \otimes S^B)(c_i^A \otimes c_j^B + \Delta c_{ij}) \quad (7)$$

which is to be treated in an iterative manner. (On the left-hand side $E = E_i^A + E_j^B + \Delta E_{ij}$, of course.)

In the cases of interferences caused by the exclusion principle, the Hamiltonian H is defined over a linear space of a dimension $m < m_A \times m_B$. In such a case one has to extend the space by introducing $m_A \times m_B - m$ additional abstract (nonphysical) states, requiring that they should not interact with the physical ones. (The off-diagonal elements of the H-matrix should be zero.) Under these conditions the

$$
\begin{pmatrix}
0.0 & 0.5 & 0.2 & -0.3 & -0.4 & 0.4 \\
0.5 & 1.2 & 0.2 & -0.3 & 0.32 & -0.11 \\
0.2 & 0.2 & 1.0 & 0.2 & -0.4 & 0.3 \\
-0.3 & -0.3 & 0.2 & 2.5 & 0.25 & 0.23 \\
-0.4 & 0.32 & -0.4 & 0.25 & 2.0 & -0.3 \\
0.4 & -0.11 & 0.3 & 0.23 & -0.3 & 1.5
\end{pmatrix}
$$
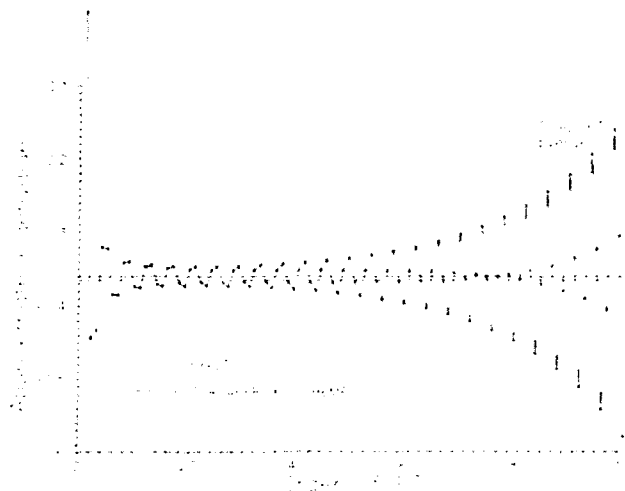
Figure 4. A 6 × 6 matrix and the performance of our scheme as compared with that of the standard PT in approximating its lowest eigenvalue. (The notations are the same as on Fig. 2.)

inclusion of the nonphysical states will not influence the physical solutions, but will only lead to some nonphysical solutions of the secular equation, which should be simply discarded. At the same time, the introduction of these nonphysical states may be important for separating out the strictly additive components of the interactions.

The Simplest Physical Model

Two electrons of the same spin occupy mainly orbitals x_1 and x_2 but can also undergo some delocalizations to a third orbital x_3. Situations of this type occur, for example, within any electron-correlation problem; the absence of a full additivity of the pair correlation energies should be partly connected with the impossibility of excitations in which both pairs utilize the same virtual orbital (Fig. 1).

The excitations $x_1 \rightarrow x_3$ and $x_2 \rightarrow x_3$ give an additive energy correction in the second-order PT, but do not represent truly additive effects, mainly because the Pauli principle does not permit a state with both electrons excited to x_3. The Hamiltonian matrix is (taking the energy of the state $|x_1^+ x_2^+ \rangle$ as zero):

$$H = \begin{pmatrix} 0 & a & b \\ a & c & e \\ b & e & d \end{pmatrix}$$

We define the extended eigenvalue problem having the same physical solutions (and also an unimportant nonphysical one) with the Hamiltonian matrix

$$H' = \begin{pmatrix} 0 & a & b & 0 \\ a & c & e & 0 \\ b & e & d & 0 \\ 0 & 0 & 0 & c+d \end{pmatrix}$$

This matrix can be considered as the sum of the unperturbed additive Hamiltonian (direct product) describing the two delocalizations as they were independent, and a perturbation: $H' = H^O + V$, where

$$H^O = \begin{pmatrix} 0 & a & b & 0 \\ a & c & 0 & b \\ b & 0 & d & a \\ 0 & b & a & c+d \end{pmatrix} \qquad V = \begin{pmatrix} 0 & 0 & 0 & 0 \\ 0 & 0 & e & -b \\ 0 & e & 0 & -a \\ 0 & -b & -a & 0 \end{pmatrix}$$

One can transform V to the basis of eigenvectors of the auxiliary strictly additive problem as $V \rightarrow (U^A \otimes U^B)^\dagger V(U^A \otimes U^B)$, and then standard PT can be used to account for nonadditivity.

Estimating Matrix Eigenvalues

We need a method for estimating how much the lowest eigenvalue differs from the corresponding diagonal matrix element H_{00}. We first make an additive estimation based on the exact solution of all 2×2 eigenvalue problems of the matrices

$$\begin{pmatrix} 0 & H_{0i} \\ H_{i0} & H_{ii}-H_{00} \end{pmatrix}$$

i.e., sum the "energy lowerings" predicted by all such subproblems [3]. Nonadditivity corrections then are calculated for each pair $i < j$ of "excitations," i.e., for the 3×3 matrices

$$\begin{pmatrix} 0 & H_{0i} & H_{0j} \\ H_{i0} & H_{ii}-H_{00} & H_{ij} \\ H_{j0} & H_{ji} & H_{jj}-H_{00} \end{pmatrix}.$$

This is performed by using second-order PT following the scheme described for the previous simple model. (Exact solution for the 3×3 matrices may also be done.) Our experience is that this method always gives reliable estimations, even if the off-diagonal matrix elements are large and standard PT is badly divergent.

Examples

Figures 2 to 4 show examples of small matrices for which the off-diagonal matrix elements are large enough to make the usual Rayleigh-Schrödinger PT either con-

verge rather slowly or be divergent. At the same time our scheme of estimating the lowest eigenvalue in all cases gives very good approximations to the exact eigenvalues. Of course, in the cases when standard PT convergence is rapid, the new scheme does not fail either: in practical examples it always gave results better than fourth-order PT, although it is easily seen that our scheme is only a $\sim N^2$ procedure.

Discussion

The primary aim of this work has been not to develop a new scheme of estimating matrix eigenvalues (although it may be useful as well), but rather to illustrate that the idea of introducing auxiliary *strictly additive* problems and then treat *nonadditivity as a perturbation* is a promising one: it does work in the simplest cases and even in models which exhibit considerable deviations from the strictly additive limit. This success will motivate us to apply the approach in different actual problems of quantum chemical theory.

Acknowledgment

Bibliography

[1] This direct product is not related to the direct product representation of wave functions used in Ref. 2.
[2] E. R. Davidson and L. L. Jones, J. Chem. Phys. 37, 1616 (1962).
[3] Buenker and Peyerimhoff have used the energy lowering given by a given state to select the important configurations for a limited CI procedure [4,5].
[4] S. D. Peyerimhoff and R. J. Buenker, Chem. Phys. Letters 16, 235 (1972).
[5] R. J. Buenker and S. D. Peyerimhoff, Theor. Chim. Acta 35, 33 (1974); ibid. 39, 217 (1975).

Theoretical Study of the Interaction of Ga, Ga$^+$, and Ga^{2+} with the Hydrogen Molecule

J. M. MARTÍNEZ-MAGADÁN* and A. RAMÍREZ-SOLÍS

SGLI. Instituto Mexicano del Petróleo, Eje Central Lázaro Cárdenas 152,
A.P. 14-805, 07730 México, D.F. México

O. NOVARO

Instituto de Física, UNAM, A.P. 20-364, México 01000 D.F., México

Abstract

The C$_{2v}$ potential energy curves for the interaction of Ga, Ga$^+$, and Ga^{2+} with the hydrogen molecule were calculated using the pseudopotential method of Durand et al. and triple-ζ gaussian basis sets. Electronic correlation has been taken into account by MRCI + MP2 calculations. We studied the ^{2}B$_2$(4p), ^{2}A$_1$(4p), ^{2}A$_1$(5s), and ^{2}B$_2$(5p) surfaces for the Ga + H$_2$, the ^{1}A$_1$, ^{3}B$_2$, and ^{1}B$_2$ surfaces for Ga$^+$ + H$_2$ and the ^{2}A$_1$(4s), ^{2}B$_2$, and ^{2}A$_1$(5s) surfaces for the Ga^{2+} + H$_2$ reaction. We first analyzed the unrelaxed H$_2$ approach to the metallic center, followed by the angle relaxation. The reactivity in all the interactions studied are analyzed with a model mechanism, previously proposed by us. © 1992 John Wiley & Sons, Inc.

Introduction

Experimental and theoretical studies of group (III), (IV), and (V)-hydrides have recently been increasing in number [1–3, and references therein]. Many of these hydrides are sources for the corresponding elements to generate semiconductor layers comprising these elements in chemical vapor deposition (CVD). Therefore, the bond energies, ionization potentials, and appearance potentials of such hydrides have been the topic of several studies. Theoretical calculations may be quite valuable for the elucidation of the low-lying electronic states and the computation of bond energies and adiabatic ionization potentials [3].

On the other hand, the quantum chemical study of AH$_2$ (where A is a p-block element) systems and their ions helps to understand the nature of bonding and reactivity trends in p-block elements. Also, these systems serve like models for chemisorption and catalysis studies. Especially, gallium is used to substitute aluminum in zeolitic materials [4]. Gallium-containing zeolites for light paraffin aromatization have received considerable attention and have been suggested an intermediate Brönsted acid strength with respect to the boron- and aluminium-containing forms [5].

---

* Also at FES-Cuautitlán, UNAM, México.

Balasubramanian has investigated the geometries and the bond energies of GaH$_n$ and GaH$_n^+$ (n = 1–3) complexes, through CASSCF/SOCI calculations using pseudopotentials [2]. For GaH$_2$ the ground state was found to be a $^2A_1$ bent state (r_e = 1.58 Å, ϑ = 120.3°) while the ground state of GaH$_2^+$ is a $^1\Sigma_g^+$ linear closed-shell state. The configuration for the $^2A_1$ ground state of GaH$_2$ was missing in that report but it is mentioned to have a coefficient of 0.97, both at the saddle point and at the bent minimum on the calculated potential energy surface. The Mulliken population analyses exhibit Ga(2.87), H(1.03), and Ga(2.17), H(0.92) gross valence populations for the ground states of GaH$_2$ and GaH$_2^+$, respectively.

Armentrout has reported preliminary experimental work of the Ga$^+$ + D$_2$, reaction using guided ion-beam tandem spectrometry [6]. He has found a similar behavior to that for Al$^+$ + D$_2$; there is an apparent threshold of about 9 eV but the relation with electronic states is not mentioned.

Mitchell et al. have encountered an extremely low cross section for quenching Ga (^{2}S excited state) atoms by H$_2$ in gas phase experiments, in contrast with the case of methane [7]. From this and from a similar study for Al using the matrix isolation technique, Parnis and Ozin have concluded that the occupation of a valence p orbital is not always an essential factor in these reactions, particularly when an insertion mechanism is involved [8].

In this work we report the potential energy surfaces for Ga, Ga$^+$, and Ga^{2+} interacting with the H$_2$ molecule. We studied the ground state and some excited states for each reaction. First, we approach H$_2$ to the metal atom keeping the H — H bond unrelaxed, and then we relax it with the M — H distance fixed for the Ga + H$_2$ and Ga$^+$ + H$_2$ reactions. For the Ga^{2+} + H$_2$ reaction we just present the unrelaxed curves. Once the minima have been localized we proceed to fully optimize these points.

Also we analyzed the results in the light of our model proposed for the Zn, Zn$^+$ and Zn^{2+} + H$_2$ interactions [9], based on the conclusion [1,10–12] that the reactivity of the M$^+$ + H$_2$ reactions is controlled by the electronic configuration of M$^+$, whether it corresponds to the ground or to an excited state, and not simply by the multiplicity or the total angular momentum or the relative energetic position of the electronic state under consideration.

Computational Details

Self-consistent field (SCF) and Multiconfiguration SCF for the excited states followed by Multireference configuration interaction (MRCI) + second-order Möller–Plesset (MP2) perturbative calculations were performed for the lowest electronic states of Ga + H$_2$, Ga$^+$ + H$_2$, and Ga^{2+} + H$_2$.

The SCF calculations were made with the PSHF code, a modified version of the HONDO program which uses the pseudopotential method of Durand et al. [13]. We are thus left with an [Ar]3d^{10} core and 3 valence electrons (4s^{2}4p^1) for the gallium atom. The pseudopotential parameters can be found in Ref. [14]. The gallium gaussian basis set with contraction is of triple-ζ quality for the 4s, 4p shells and a d-type polarization function. The s and p exponents and coefficients were taken

from Ref. [15]. This s and p basis was augmented with the two diffuse s and p orbitals and the d-type polarization function of Kim and Balasubramanian [16], since we were interested in studying excited states which differ in a unit on the principal quantum number from the ground state.

The calculated energy differences for the lower part of the atomic spectrum for Ga [17] are in good agreement with experimental results and can be seen as asymptotes to the right in Figure 1.

The MCSCF algorithm [18] was used to determine the optimal molecular orbital (MO) set to be used in the MRCI treatment. For the open-shell states we first make a restricted-SCF calculation and then we improve the molecular orbitals doing a MCSCF calculation using only the configuration of interest. In the closed-shell cases we use directly in the MRCI treatment the RSCF optimal molecular orbitals.

The variational and perturbational (second-order Möller–Plesset) MRCI calculations were carried out using the CIPSI algorithm [19] in its three class version [20]. Firstly, a reference space S containing NCF determinants is diagonalized and used to generate the perturbational space P. Then, a much larger space ($S + M$) is used to obtain a better variational energy but it does not generate any more determinants in the already fixed space P. Finally, one must substract the contribution of M from the overall perturbational energy originally calculated in P. This means that M (a subset of P) is composed of the determinants in P having the largest MP2 coefficients. In the present calculations, S, M, and P contain approximately 20, 2000, and 200 000 determinants, respectively.

In practice, the size of the reference space S is determined by the norm (using the intermediate normalization) of the resulting perturbational part of the wave function. The ratio norm(M)/norm(P) is closely related to the ratio variational/ (perturbational + variational) contributions to the total energy and it was used as a measure of the relative quality of the description of all the studied states.

Results and Discussion

In Figure 1 we present the C_{2v} potential energy surfaces corresponding to the Ga + H$_2$ reactions. Figure 1(a) shows the curves for the unrelaxed approach of H$_2$ (at its equilibrium geometry of 1.4 a.u.) to Ga in four of the lowest states, $^2B_2(4p)$, $^2A_1(4p)$, $^2A_1(5s)$, and $^2B_2(5p)$ which are diabatically related to the ($^2P;4s^24p_x^1$), ($^2P;4s^24p_z^1$), ($^2S;4s^25s^1$), and ($^2P;4s^25p_y^1$) atomic states of gallium, respectively. All these curves are totally repulsive.

In order to see if these curves would go down when one allows the hydrogen molecule to break, we followed the well-known strategy of opening the H — Ga — H angle while keeping the Ga — H distance fixed. Now, if any of the unrelaxed approach surfaces presents a well we can use the equilibrium distance of that minimum to keep it fixed while allowing the angle relaxation. Nevertheless, since we lacked any criterion to tell us what Ga — H distance would be suitable for our purpose, we decided to work with the Ga — H distance which results from considering the arbitrarily chosen Ga — H$_2$ distance of 2 Å (3.84 a.u.).

Figure 1(b) shows the surfaces corresponding to the relaxation of the H — H distance, keeping now the Ga — H distance at 3.84 a.u. The 1^2B_2 and 2^2B_2 curves
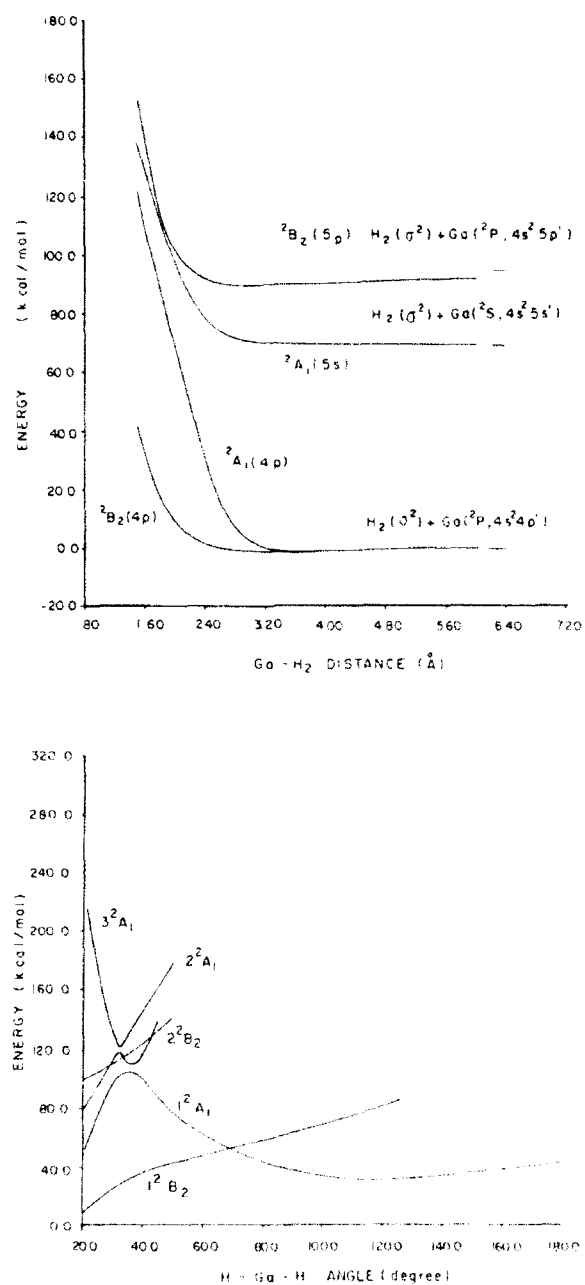
Figure 1. (a) C_{2v} potential energy surfaces for four of the lowest electronic states of GaH_2 as a function of the Ga — H_2 distance. Keeping H_2 at its equilibrium distance of 1.41 a.u.: (b) C_{2v} potential energy surfaces for four of the lowest electronic states of GaH_2 as a function of the H — Ga — H angle (in degrees). Ga — H distance for each state was kept constant at 2 Å.

are both totally repulsive; we only show these states up to $\theta = 120°$ and $45°$, respectively, because we were unable to obtain a good description of them at larger angles. In addition we report the 3^1A_1 surface originated from the Ga⁺(^{1}S;4s²4p⁰) + H₂ fragments which suffers an avoided crossing with the 2^1A_1 coming from the Ga⁺(^{1}S;4s⁰5s²) + H₂ fragments. The 2^1A_1 curve suffers afterwards an avoided crossing with the 1^1A_1 state coming from the Ga⁺(^{3}P;4s²4p¹) + H₂ separate fragments.

The 1^1A_1 curve has a barrier of 105 kcal/mol at $\theta = 37°$ that has to be surmounted to attain a bent structure at 114° that lies 31.4 kcal/mol higher than the Ga⁺(^{3}P) + H₂ ground state separate fragments level. The dominant configuration of this minimum is $1a^2 2a^1 1b^2$ (with a 0.95 coefficient) and in the saddle point this configuration is mixed with the $1a^2 2a^1 3a^1$ one. The fully-optimized minimum is located at $\theta = 120°$ and 7.2 kcal/mol higher than the Ga⁺(^{3}P) + H₂ fragments with a Ga—H distance of 3.04 a.u. This surface corresponds to the $^3A_1$ state reported by Balasubramanian [2] with the barrier at $\theta = 40°$ and 85.8 kcal/mol high whose bent minimum ($\theta = 120°$) lies only around 1 kcal/mol higher than the separate fragments. The difference between our results and those of Balasubramanian could be due to the fact that he uses a larger basis set and a different strategy to take into account the correlation energy.

In Figure 2 we present the C_{2v} surfaces corresponding to the Ga⁺ + H₂ reaction. Figure 2(a) shows the curves for the unrelaxed approach of H₂ (at its equilibrium geometry of 1.4 a.u.) to Ga⁺ in the three lowest states $^1A_1$ (ground state), $^3B_2$ and $^1B_2$ that are diabatically related with the (^{1}S;4s²), (^{3}P;4s²4p¹), and (^{1}P;4s²4p¹) atomic states of Ga⁺, respectively.

The ground state shows a totally repulsive curve. The $^3B_2$ state has a well at a distance of 3.31 a.u. while the $^1B_2$ state has it at 3.21 a.u. These wells, when we correct the error for the dissociated fragments, have energy minima with depths equal to 32.4 and 49.0 kcal/mol, respectively. The optimal Ga⁺—H distance is 3.38 a.u. for the $^3B_2$ state and 3.28 a.u. for the $^1B_2$ state, the H—H distance being kept at 1.41 a.u.

Figure 2(b) shows the curves corresponding to the relaxation of the H—H distance, this time keeping the optimal Ga⁺—H distances reported above. The $^3B_2$ surface has a minimum at 71° that lies 44.1 kcal/mol below the Ga⁺(^{3}P) + H₂ separate fragments. The $^1B_2$ surface has its minimum at $\theta = 65.0°$, which lies 74.1 kcal/mol below the Ga⁺(^{3}P) + H₂ fragments. After the full optimization of these minima, the $^3B_2$ stable bent structure is located at $\theta = 70°$ and 44.2 kcal/mol below the Ga⁺(^{3}P) + H₂ separate fragments with a Ga⁺—H distance of 3.38 a.u.; and the $^1B_2$ stable bent structure is found at $\theta = 64.5°$ and 76.9 kcal/mol below the Ga⁺(^{3}P) + H₂ fragments with a Ga⁺—H distance of 3.18 a.u. Additionally we present the 2^1A_1 curve coming from the Ga⁺(^{1}S;4s²) + H₂(σ^{*2}) fragments which suffers an avoided crossing with the 1^1A_1 surface arising from the Ga⁺(^{1}S;4s²) + H₂($\sigma²$) fragments. It should be noticed that now an excited state of H₂ leads to a stable (GaH₂)⁺ complex.

The 1^1A_1 surface has a barrier of approximately 125 kcal/mol before the complex reaches its linear closed-shell structure that lies 41 kcal/mol higher than the Ga⁺(^{1}S) + H₂($\sigma²$) ground-state fragments. The fully-optimized stable linear structure
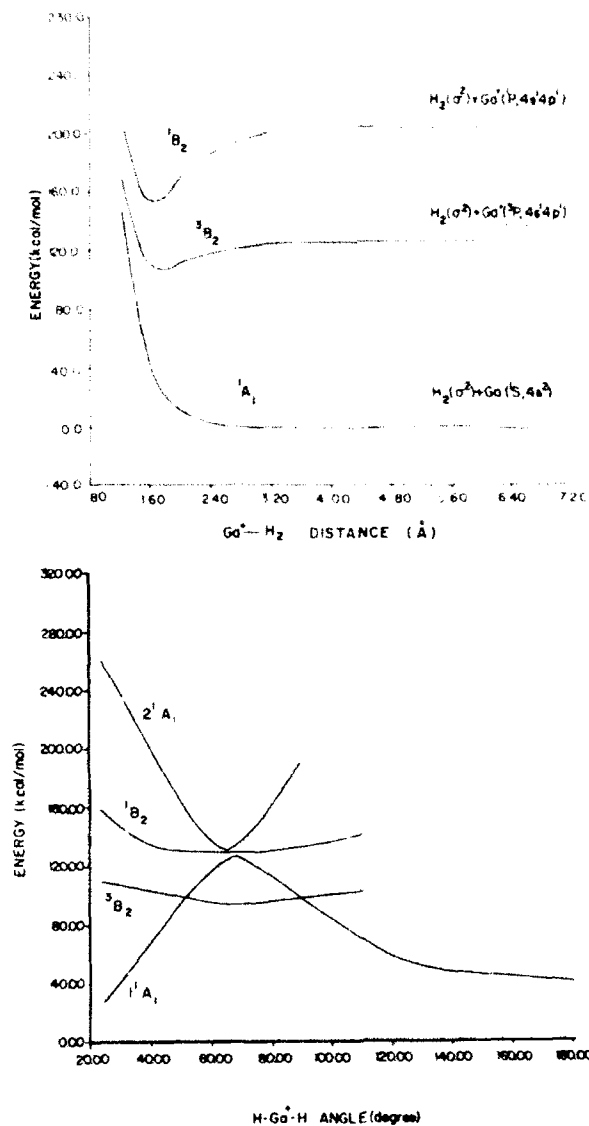
Figure 2. (a) C_{2v} potential energy surfaces for the three lowest electronic states of GaH$_2^+$ as a function of the Ga$^+$—H$_2$ distance; (b) C_{2v} potential energy surfaces for the three lowest electronic states of GaH$_2^+$ as a function of the H—Ga$^+$—H angle (in degrees). Optimal Ga$^+$—H distance for each state was kept constant. See text.

is located 26.4 kcal/mol higher than the Ga$^+$ (^1S) + H$_2(\sigma^2)$ fragments with a Ga$^+$—H distance of 2.92 a.u. In the saddle point the mixed configurations are $1a_1 2a_1$ and $2a_1 1b_2$ while for the linear complex the dominant configuration is $2a_1 1b_2$ (with a

0.97 coefficient). This linear structure corresponds to the $^1\Sigma_g^+$ state reported by Balasubramanian [2] for the ground state of GaH$_2^+$, which is found 25.49 kcal/mol higher than the Ga⁺ (^{1}S) + H$_2(\sigma^2)$ fragments with a Ga⁺—H distance of 2.87 a.u.

In Figure 3 we show the surfaces corresponding to the unrelaxed approach of H$_2$ to Ga²⁺ leading to the 1^{2}A$_1$ (ground state), 1^{2}B$_2$, 2^{2}A$_1$, 2^{2}B$_2$, 3^{2}A$_1$, and 4^{2}A$_1$ states, adiabatically correlated with the Ga²⁺(^{2}S;4s^1) + H$_2(\sigma^2)$, Ga⁺(^{1}P;4s^{1}4p^1_z) + H$_2(\sigma^2)$, Ga²⁺(^{2}P;4p^1_y) + H$_2(\sigma^2)$, Ga²⁺(^{2}P;4p^1_x) + H$_2(\sigma^2)$, Ga²⁺(^{2}S;4s^{1}5s^1) + H$_2(\sigma^2)$, and Ga²⁺(^{2}S;5s^1) + H$_2(\sigma^2)$ fragments, respectively.

The ground state has a well at a distance of 3.50 a.u. which lies 30.6 kcal/mol below the Ga²⁺(^{2}S;4s^1) + H$_2$ fragments. The 1^{2}B$_2$ and the 2^{2}B$_2$ surfaces show an avoided crossing at a distance of 6.24 a.u. The 1^{2}B$_2$ state then, has a well at 3.21 a.u. and 96.9 kcal/mol deep with respect to the diabatically correlated Ga²⁺(^{2}P) + H$_2$ fragments (we recall that all the well depths are corrected for the error at the dissociated fragments). The 2^{2}A$_1$ surface has a well in the region of the avoided crossing of the ^{2}B$_2$ curves. This minimum lies 47.0 kcal/mol below the Ga²⁺(^{2}P) + H$_2$ fragments at a distance of 5.57 a.u.

The 3^{2}A$_1$ and 4^{2}A$_1$ states also present an avoided crossing at a distance of 6.24 a.u. This produces a well 82.9 kcal/mol deep at a distance of 3.31 a.u. for the 3^{2}A$_1$ state with respect to the Ga²⁺(^{2}S;5s^1) + H$_2$ fragments.
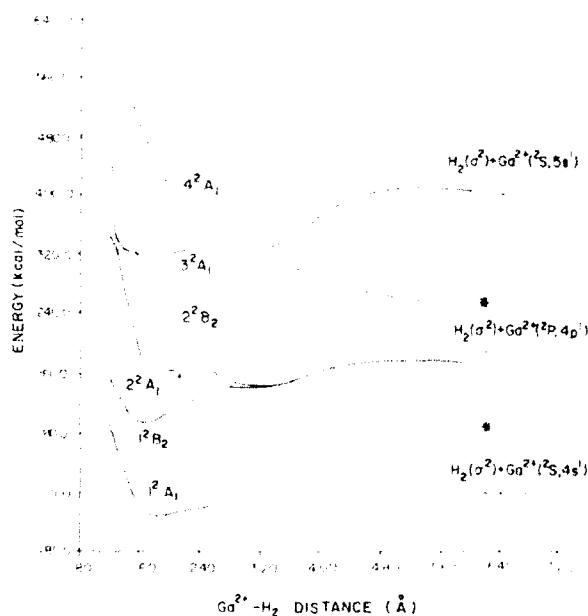
Figure 3. C$_{2v}$ potential energy surfaces for four of the lowest states of GaH$_2^{2+}$ as a function of the Ga²⁺—H$_2$ distance. (*) These curves have as asymptotical levels the H$_2$ + Ga⁺(^{1}P;4s^{1}4p^1) and H$_2$ + Ga⁺(^{1}S;4s^{1}5s^1) fragments for 1^{2}B$_2$ and 3^{2}A$_1$ molecular states.

The total valence SCF Mulliken populations for the ground states of GaH_2, GaH_2^-, and GaH_2^+ are (Ga:2.97, H:1.015), (Ga:2.12, H:0.94) and (Ga:1.33, H: 0.84), respectively, with Ga — H_2 at 2Å and keeping the H — H distance unrelaxed.

Now using the first interaction mechanism of our proposed model for the similar Zn reactions [9], let us discuss each one of the studied reactions. We briefly recall this mechanism that leads to attractive interactions:

(a) a charge transfer from the hydrogen-bonding σ orbital towards the empty or half-filled s subshell of the center A and

(b) a charge transfer from the p_i orbital of the center A to the antibonding σ^* orbital of H_2.

In order to identify each of the studied reactions we have labeled them according to the electronic configurations of the separate interacting fragments.

$Ga + H_2$

(1) $1^2B_2(4p):4s^24p_y^1 + \sigma^2$. This reaction leads to a repulsive interaction because the 4s orbital is doubly occupied. Condition (a) of the mechanism is not satisfied. As the angle is increased this situation is not changed and the resulting curve is still repulsive. The charge transfer from the $4p_y$ orbital towards the σ^* MO is not a sufficient condition for the interaction to be attractive.

(2) $1^2A_1(4p):4s^24p_z^1 + \sigma^2$. This interaction is repulsive because the 4s orbital of Ga is doubly occupied; thus no charge transfer from the σ orbital is possible, that is, condition (a) is not met. As the H — H distance is relaxed, the repulsive character is maintained until the appearance of the avoided crossing where the original configuration $1a_1^22a_1^23a_1^1$ is changed to $1a_1^22a_1^11b_2^2$ which, as we have said, is originated from the $Ga(^2S;4s^14p^2) + H_2$ fragments. Then the two conditions of the mechanism are fulfilled and a bent stable structure is formed as expected. The $1a_1^22a_1^11b_2^2$ configuration of the bent complex ($\vartheta = 114°$) is related to the second term ($^2S_{1/2}$) of the even series arising from the atomic $4s^14p^2$ configuration that resonates with the continuum states of the even P series generated from the $4s^24p^1$ atomic configuration [17].

(3) $2^2A_1:4s^25s^1 + \sigma^2$. In this case, condition (b) is not met because there is no longer any p_y orbital from which it were possible a charge transfer to the σ^* orbital of H_2, thus leading to a repulsive interaction. The charge transfer to the 5s orbital from the σ orbital of H_2 is not a sufficient condition for an attractive interaction. The avoided crossing of this 2^2A_1 curve with the 3^2A_1 surface produces a small attractive region which is not however important for this state because very soon it suffers another avoided crossing, now with the 1^2A_1 state after of which the 2^2A_1 state is repulsive again.

(4) $2^2B_2(5p):4s^25p_y^1 + \sigma^2$. Here we have again a p_y orbital capable of charge transfer to the σ^* of H_2 but we obtained a repulsive potential energy surface. This is a similar situation to that found in case (1) but only with a p_y orbital of greater spatial extension; again, since the 4s orbital is fully occupied, not even the condition (a) of the mechanism is fulfilled here. On the other hand, one could consider that the

5s empty orbital could accept charge from the σ orbital. Nevertheless, our calculations show this 5s orbital coupled to the σ^* orbital which leads to a repulsive interaction. This can be explained by the fact that a change from $n = 4$ to $n = 5$ was made in the principal quantum number, thus producing a greater destabilization of the 5s virtual orbital than that found for the 4s virtual orbital in the Zn ($^3P;3d^{10}4p^1$) + H_2 reaction.

Ga⁺ + H_2

In the case of Ga⁺ we have qualitatively a similar behavior to that of the Zn + H_2 reactions [9]. The three curves reported here can be explained by the same arguments used in Zn reactions. Except for the presence of the 3d orbitals in the valence shell of Zn (the 3d shell is taken into account in the pseudopotential for Ga), which we have found do not play a major role in the interaction mechanism, Ga⁺ has the same electronic configuration as Zn.

(5) $^1A_1;4s^2 + \sigma^2$. Here a repulsive interaction occurs for the unrelaxed approach because the 4s orbital of Ga⁺ is doubly occupied, and there is no occupied p_z orbital from which charge could be transferred to H_2. Neither condition is met. However, the H–H distance relaxation modifies the repulsive character of the curve since this state suffers an avoided crossing with the 2^1A_1 state arising from the Ga⁺(4s²) + $H_2(\sigma^{*2})$ fragments, which leads to a $^1\Sigma_g^+$ linear complex composed of a completely broken H_2 molecule with a Ga⁺ ion in-between. This linear complex lies above the fragments because there is no charge transfer, nor from the 4p$_z$ to the σ^* orbital, nor from the σ to the 4s orbital. In order to satisfy both conditions, this reaction would have to come from the Ga⁺(4p$_z^2$) + $H_2(\sigma^2)$ fragments, but the gallium ion in this electronic state does not exist.

(6, 7) $^{3,1}B_2;4s^14p_z^1 + \sigma^2$. These potential energy surfaces show an absolute minimum and both conditions of the interaction mechanism are fulfilled. The difference between these reactions with the same configuration is on the greater loss of exchange energy of the triplet when the bond with H_2 is formed; this fact is responsible for a smaller energy gain as compared with the singlet state, according with the arguments of Carter and Goddard [21].

As in the case of Zn, the optimal bent structures after H–H relaxation are explained if one thinks that the overlap between the 4s and σ orbitals reaches a maximum at a certain Ga⁺–H$_2$ distance, beyond which repulsion takes over, while the overlap of the 4p$_z$ and σ^* orbitals increases with the H–Ga–H angle because of the orientation of the 4p$_z$ orbital.

Ga⁺⁺ + H_2

(8) $^2A_1;4s^1 + \sigma^2$. Here condition (b) is not met because there is no p$_z$ orbital from which a charge transfer towards the σ^* could take place. One would therefore expect a repulsive curve. However, a possible explanation is that an admixture of the covalent and electrostatic interactions produces the observed attractive surface. This electrostatic versus covalent behavior has already been studied by Bauschlicher et al. [22] for the Nb⁺-alkene interaction. If the metal atom were not doubly charged,

the fulfillment of condition (a) alone would not allow an attractive curve to be produced; however the electrostatic attraction produced by the Ga^{2+} ion replaces condition (b) of the proposed interaction mechanism and the overall result is a relatively shallow well at short distance (3.50 a.u.). The fact that the well is found at such a short distance can be explained by noticing that the charge transfer from the σ MO of H_2 to the singly occupied 4s orbital of gallium can only take place in the region where the overlap between these orbitals is not negligible.

(9) $2^2B_2{:}4p_x^1 + \sigma^2$. In this reaction the two conditions of the mechanism are satisfied. The electron in the p_x orbital can transfer charge to the σ^* orbital of H_2 and the σ orbital can transfer charge to the empty 4s orbital of Ga^{2+}. Moreover, there is also the attractive effect on H_2 of a strongly electron-defficient species which results in a deep well as it has been shown.

The resulting attractive curve of $Ga^{2+}(^2P)$ with H_2 suffers an avoided crossing with the purely repulsive curve arising from the $Ga^+(^1P{:}4s^14p_x^1) + H_2^+$ fragments. The stable complex (recall that H — H distance is fixed at its equilibrium value) is formed following the $2^2B_2(Ga^{2+}(^2P) + H_2)$ surface and passing through a nonadiabatic transition to the $1^2B_2(Ga^+(^1P) + H_2^+)$curve to reach the absolute minimum.

(10) $4^2A_1{:}5s^1 + \sigma^2$. For this reaction, a similar situation arises to that found in reaction (8) with a single electron on an s orbital but with a larger radial extension. Since the condition (a) of the mechanism is met, the incoming σ orbital can go nearer into Ga^{2+} [the well is found at 3.31 a.u. instead of 3.50 a.u. for reaction (8)] thus producing a deeper well for this case than that in reaction (8).

Also, as in reaction (9), an avoided crossing with the purely repulsive curve arising from the $Ga^+(^1S{:}4s^15s^1) + H_2^+(\sigma^1)$ leads to a stable structure on the 3^2A_1 surface after a nonadiabatic transition coming from the $Ga^{2+}(^2S{:}5s^1) + H_2$ fragments.

Conclusion

We would like to point out the important role played by the resonant $^2S(4s^14p_z^1)$ atomic state of gallium which is responsible for the formation of the stable $^2A_1$ bent complex in the $Ga(^2P{:}4s^24p_z) + H_2$ reaction.

Another new feature observed is the fact that for the $Ga^+(^1S{:}4s^2) + H_2$ reaction, the electronic configuration of the linear complex is diabatically related to an excited state of H_2, that is, to the $Ga^+(^1S{:}4s^2) + H_2(^1\Sigma_u^+{:}\sigma^{*2})$ fragments.

For the $Ga^{2+} + H_2$ reactions we found that most of the excited stable complexes were obtained as a result of avoided crossings with the $Ga^+ + H_2^+$ reactions. This situation is new since these crossings for the $Zn^{2+} + H_2$ reactions take place at much longer intermolecular distances [9]. Finally, we also found that the electrostatic interactions play a key role since for the isoelectronic $Cu(^2S{:}3d^{10}4s^1) + H_2$ [23] and $Zn^+(^2S{:}3d^{10}4s^1) + H_2$ [9] reactions, the unrelaxed approach was totally repulsive. Therefore the enhanced electronegativity of Ga^{2+} became important in this case and leads to the admixture of covalent and electrostatic interactions.

Acknowledgments

Jean-Pierre Daudey at the Laboratoire de Physique Quantique de Toulouse. JMMM would like to acknowledge encouraging discussions and computational help from Dr. Enrique Poulain, Sidonio Castillo, and Mardonio Sánchez, colleagues at IMP.

Bibliography

[1] K. Balasubramanian, Chem. Phys. Lett. **127**, 585 (1986).

[2] K. Balasubramanian, Chem. Phys. Lett. **164**, 231 (1989).

[3] K. Balasubramanian and J. X. Tao, J. Chem. Phys. **94**, 3000 (1991).

[4] N. S. Gnep, J. Y. Doyemet, A. M. Seco, F. Ramoa Ribeiro, and M. Guisnet, Appl. Catalysis **43**, 155 (1988); A. Y. Khodakov, L. M. Kustov, T. N. Bondarenko, A. A. Dergachev, V. B. Kazansky, Kh. M. Minachev, G. Borhély, and H. K. Beyer, Zeolites **10**, 603 (1990); G. L. Price and V. Kanazirev, J. Catalysis **126**, 267 (1990).

[5] R. Challoner, R. K. Harris, S. A. I. Barri, and M. J. Taylor, Zeolites **11**, 827 (1991).

[6] P. B. Armentrout, Int. Revs. Phys. Chem. **9**, 115 (1990).

[7] S. A. Mitchell, P. A. Hackett, D. M. Rayner, and M. Flood, J. Chem. Phys. **86**, 6852 (1987).

[8] J. M. Parnis and G. A. Ozin, J. Phys. Chem. **93**, 1220 (1989).

[9] J. M. Martinez-Magadán, A. Ramirez-Solis, and O. Novaro, Chem. Phys. Lett. **186**, 107 (1991).

[10] J. Anglada, P. J. Bruna, and F. Grein, J. Chem. Phys. **92**, 6732 (1990).

[11] J. L. Elkind and P. B. Armentrout, J. Phys. Chem. **89**, 5626 (1985).

[12] P. B. Armentrout, Science **251**, 175 (1991).

[13] Ph. Durand and J. C. Barthelat, Theor. Chim. Acta **38**, 283 (1975); J. C. Barthelat, Ph. Durand, and A. Serafini, Mol. Phys. **33**, 179 (1977); J. C. Barthelat and Ph. Durand, Gazz. Chim. Ital. **108**, 255 (1978); M. Pélissier and Ph. Durand., Theor. Chim. Acta **55**, 43 (1980); PSHF program available upon request from Professor J. P. Daudey, Laboratoire de Physique Quantique de Toulouse, Université Paul Sabatier, France.

[14] Y. Bouteiller, C. Mijoule, M. Nizam, J. C. Barthelat, J. P. Daudey, M. Pélissier, and B. Silvi, Mol. Phys. **65**, 295 (1988).

[15] M. M. Hurley, L. Fernández Pacios, P. A. Christiansen, R. B. Ross, and W. C. Ermler, J. Chem. Phys. **84**, 6840 (1986).

[16] G. B. Kim and K. Balasubramanian, J. Mol. Spectrosc. **134**, 412 (1989).

[17] C. Moore, Atomic Energy Levels, NBS circular 467, 1971, Washington DC, U.S. Government Printing Office.

[18] This program was written by R. Carbó, M. Pélissier, J. Rubio, and J. P. Daudey. It is based on the Elementary Jacobi Rotation Algorithm.

[19] B. Huron, P. Rancurel, and J. P. Malrieu, J. Chem. Phys. **58**, 5745 (1973).

[20] S. Evangelisti, J. P. Daudey, and J. P. Malrieu, Chem. Phys. **75**, 91 (1983).

[21] E. A. Carter and W. A. Goddard, III, Phys. Chem. **92**, 5679 (1988).

[22] C. W. Bauschlicher, Jr., S. R. Langhoff, and H. Partridge, J. Phys. Chem. **95**, 6191 (1991).

[23] J. Garcia-Prieto, M. E. Ruíz, E. Poulain, O. A. Ozin, and O. Novaro, J. Chem. Phys. **81**, 5920 (1984).

The Activation and Elimination of H_2 by Zr Complexes

THOMAS R. CUNDARI*

Department of Chemistry, Memphis State University, Memphis, Tennessee 38152

Abstract

An *ab initio* analysis of the reaction of molecular hydrogen with the Zr-imido complex $(NH_2)_2Zr=NH$ is reported. Several interesting points are noted. The calculated stretching frequency of the $Zr=N$ bond in $(NH_2)_2Zr=NH$ is 860 cm^{-1} when properly scaled to account for electron correlation effects. The value supports the assignment of an infrared (IR) band at 865 cm^{-1} to the $Zr=N$ stretch of a tetra-hydrofuran (THF) adduct of the putative reactive intermediate $(NHSi')_2Zr=NSi'$. Although a weakly bound, H_2 complex is found, the interaction is small (1.3 kcal mol^{-1}) compared with experimentally characterized H_2 complexes. Variations in bond lengths and intrinsic stretching frequencies demonstrate that π-bonding for amido (NH_2) ligands can be substantial in a coordinatively saturated complex. H_2 activation by the *bis*(amido)imido reactive intermediate is calculated to be significantly more favorable by the 1,2-addition of H_2 across the $Zr=N$ bond to form the *tris*(amido)hydride than a sigma-bond metathesis pathway. The transition state (TS) for the addition of H_2 across the $Zr=N$ bond of the *bis*(amido)imido complex is 9.8 kcal mol^{-1} above the charge transfer (CT) complex, $(NH_2)_2Zr=NH \cdot H_2$ at the MP2 level; the reverse process, extrusion of H_2 from the *tris*(amido)hydride has a 28.2 kcal mol^{-1} barrier. The geometry of the four-center TS is of interest, deviating markedly from that of a square and being more "kite" shaped (i.e., one obtuse and three acute angles). Mulliken Bond Overlap Populations suggest that there is some interaction between the Zr and the H atom being transferred (H_t) in the various TSs studied. It is suggested that the interaction plays an important role in the ability of the Zr-imido complexes, and indeed other high-valent, multiply bonded complexes, to activate $X=H$ ($X = H$, C, Si, N, and H) bonds. The design of materials and catalysis precursors which enhance the metal-hydrogen interaction in the TS could conceivably lead to lower chemical vapor deposition (CVD) processing temperatures and higher catalytic activities. © 1992 John Wiley & Sons, Inc.

Introduction

Multiply bonded transition metal complexes ($L_{n-1}M=ER_{m-1}$) have attracted considerable experimental interest [1–5] for the selective functionalization of hydrocarbons, particularly alkanes. The elimination of small molecules (LR) from organometallic precursors ($L_nM\text{-}ER_m$) is of interest in the synthesis of solid-state materials, $[ME]_x$, by chemical vapor deposition (CVD). Many CVD processes are thought to involve coordinatively unsaturated, multiply bonded intermediates which eventually polymerize to form a solid-state material [6,7]. Thus, in some sense many catalytic processes can be considered as being the reverse of reactions of interest in CVD [Eq. (1)].

---

* E-mail: cundarit@memstvx1.memst.edu

$$\text{CATALYSIS} \xleftarrow{\qquad}$$

$$xL_nM\!-\!ER_m \underset{}{\overset{-LR}{\rightleftharpoons}} xL_{n-1}M =\!ER_{m-1} \overset{-LR}{\rightleftharpoons\rightleftharpoons\rightleftharpoons} [ME]_x \qquad (1)$$

$$\xrightarrow{\qquad}\ \text{CVD}$$

Cummins et al. have proposed that an $(NHSi')_2Zr\!=\!NSi'$ intermediate, $Si' = Si(t\text{-bu})_3$, is capable of activating the $C\!-\!H$ bonds of benzene and methane, and H_2 [1]. Walsh et al. have demonstrated that zirconocene-imido complexes, $Cp_2Zr\!=\!NR$, are capable of activating the $C\!-\!H$ bond of benzene; the presence of a Zr-imido intermediate was confirmed by x-ray crystallography [2]. Ti-imido complexes similar to the *bis*(amido)imido Zr complex show distinctly different reactivity (i.e., they do not activate $C\!-\!H$ bonds) [3]. Rothwell and co-workers have characterized a Ti-imido complex and studied its reactivity; when $(Ar''O)_2(py')Ti\!=\!N\text{-Ph}$ is refluxed in benzene for several hours no $C\!-\!H$ activation products are observed [4]. However, Doxsee et al. have demonstrated the utility of vinyl imido complexes of Ti [5] in organic synthesis.

Cummins et al. [1] discovered that various *tris*(amido)alkyl complexes of Zr, $(NHSi')_3Zr\text{-R}$ ($R = CH_3$, Ph, cyclo-C_6H_{11}), when reacted with 3 atm of molecular hydrogen in a cyclohexane solvent yield the corresponding hydride, $(NHSi')_3Zr\text{-}H$. Furthermore, reaction of the *tris*(amido)methyl complex with D_2 resulted in the formation of $(NHSi')_2(NDSi')Zr\text{-}D$ and methane. Coupled with analogous studies of the reactions of Zr tris(amido)alkyl species with methane and benzene, the data suggest a *bis*(amido)imido reactive intermediate, $(NHSi')_2Zr\!=\!NSi'$, formed by the elimination of one equivalent of alkane. The *bis*(amido)imido then reacts with H_2 (or R–H) to yield the final product, $(NHSi')_3Zr\text{-}H$ (or $(NHSi')_3Zr\text{-}R$) [2]. Two pathways can be envisioned for the conversion of the *bis*(amido)imido to the tris(amido)hydride. The first route is the addition of H–H across the $Zr\!=\!N$ bond of the *bis*(amido)imido intermediate to form the tris(amido)hydride, which is supported by the reactivity of the related $Cp_2Zr\!=\!NR$ complexes [1]. Another path is the addition of H_2 across the Zr-amido bond of $(NHSi')_2Zr\!=\!NSi'$, resulting in $(NHSi')(NH_2S')(H)Zr\!=\!NSi'$, which then undergoes rapid H-transfer from the amino $(NSi'H_2)$ to the imido (NSi') ligand to yield the tris(amido)hydride. The latter pathway, sigma-bond metathesis, is lent credence by the reactivity of the related Ti complexes [3], the fact that facile H-transfer in nitrogen-containing ligands is known in other high-valent, transition metal systems [8], and the realization that sigma-bond metathesis represents a viable alternative in many organometallic reactions when compared to traditional mechanisms [9].

Imido complexes of the early transition metals have been envisaged by many workers as intermediates and precursors in CVD processes leading to solid state transition metal nitrides [6,7]. Titanium tetrachloride has long been known to interact with organic amines to form Lewis base adducts and in some cases polymeric materials formed by the extrusion of volatiles such as HCl. In many cases, imido complexes are proposed as plausible intermediates along the pathway to the solid state material [10]. Recently, Winter et al. have reported a mechanistic study of the formation of thin films of TiN from $TiCl_4$ and t-butylamine [6]. When $TiCl_4$

and *t*-butylamine are mixed in methylene chloride in a 1:6 ratio at −78 °C and then allowed to warm to room temperature, a substance with the formula [TiCl₃(NH-*t*-bu)(NH₂*t*-bu)], is obtained; the material yields a thin film of TiN when heated to 500 °C at atmospheric pressure. When the polymeric material is refluxed in a methylene chloride solution of Ph₃PO the imido complex [TiCl₃(Ph₃PO)₃(N-*t*-bu)] results, as confirmed by x-ray analysis [6]. Mass spectral analysis of [TiCl₃(NH-*t*-bu)(NH₂*t*-bu)], supports the formation of imido species during decomposition.

For the present work the transition metal of interest is (M = Zr) and the main group element of interest is nitrogen (E = N). Given our continuing focus on the electronic structure and reactivity of multiply bonded, transition metal complexes [12–15], a computational study of the activation of small molecules by imido complexes was initiated. Herein, we report the results for one of the more interesting of these reactions: the activation of molecular hydrogen by a *bis*(amido)imido complex of Zr, (NH₂)₂Zr=NH. The relative favorability of the H₂ addition pathways (and their microscopically reverse reactions), as well as the stability of the various isomeric intermediates, is considered. Implications of these results for catalysis and CVD processes are presented throughout.

Computational Methods

The calculations described herein employ the *ab initio* quantum chemistry program GAMESS [16]. Effective core potentials (ECPs) replace the chemically less important core orbitals and thus make calculations feasible for all rows of the transition series. The ECPs and valence basis sets of Stevens, Basch, Krauss and Jasien (SBKJ) [17] are used for heavy atoms while Hs are described with the −31G basis set. Basis sets for heavy, main-group elements are augmented with a *d* polarization function [18]. Geometry optimizations employ the method of Baker [19] and unless stated otherwise are done at the restricted Hartree-Fock (RHF) level for closed-shell singlets. The present combination of ECPs, basis sets and level of theory has been thoroughly tested for a large number of transition metal complexes, and performed admirably [12–15]. The energy hessian is calculated at stationary points in order to identify them as minima or transition states. Plotting the imaginary frequency of transition states and perturbing along the mode (in the forward or reverse direction) followed by reoptimization is used to assess which transition state (TS) connects which two minima; in some cases, the intrinsic reaction coordinate (IRC) is followed from the TS toward reactants and products. Intrinsic stretching frequencies are calculated using the methods of Boatz and Gordon [20].

Previous work [11–13,21] clearly demonstrated that Zr complexes similar to those studied here are well described at the single-determinant level; thus, geometric parameters are accurately predicted as long as a suitably flexible basis set is used [11–13,21]. Important bond lengths and bond angles for calculated stationary points are collected in Figure 1. Calculated energetics will usually be poor if electron correlation is ignored. For species described well at the single-determinant level of theory, the correlation contribution can be treated as a perturbation to the single-
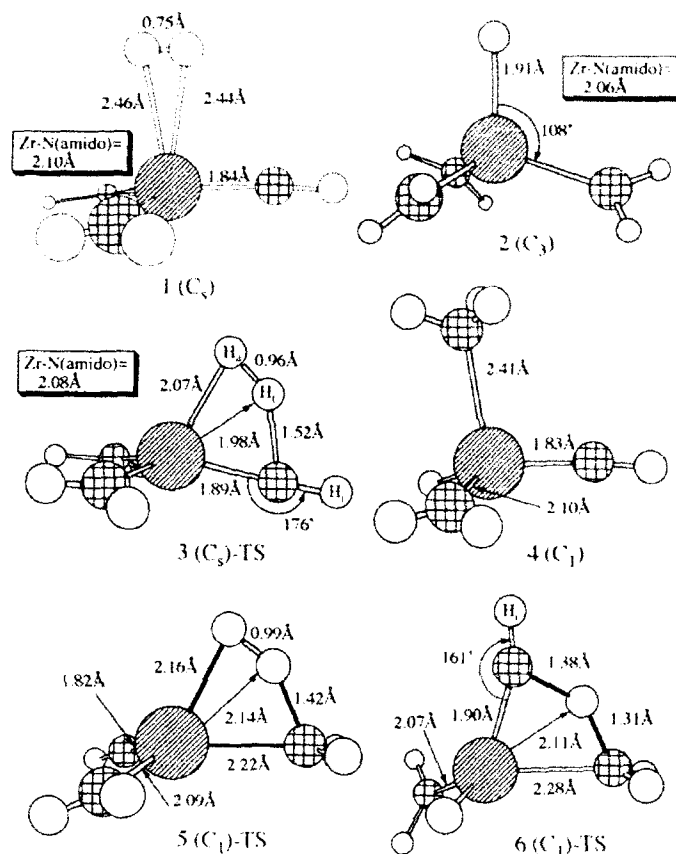
Figure 1. Calculated structural data for important minima and transition states on the PES for the reaction of H_2 and $(NH_2)_2Zr$ NH. Zr atoms are represented by circles with diagonal lines, N by crossed lines, and H by open circles.

determinant energy [18]. For this reason, the correlation energy is calculated using second-order Moller-Plesset (MP2) theory [22]. The core electrons are not included in the MP2-active space. All quoted energies are determined at MP2 level of theory using the RHF-optimized geometries with the zero-point energy (ZPE) correction included.

Results and Discussion

Initial Interaction of H_2 and the Bis(Amido) Imido Complex

The imido reactant, $(NH_2)_2Zr$ NH, has a C_s minimum which is nearly planar [21]. The geometry about the Zr and amido N atoms is roughly trigonal planar while the Zr N-H angle is nearly linear (179°), as expected. The Zr-imido (i.e.,

Zr-NH$_2$) and Zr-amido (i.e., Zr $=$ NH) bond lengths are calculated to be 1.83 and 2.10 Å, respectively, in good agreement with values for experimental models. Characterized Zr $=$ N bonds are 1.868(3) Å for Zr(NHAr)$_2$(py')$_2$(NAr) and 1.826(4) Å for Cp$_2$Zr($=$ N-t-bu)(THF) [2,23] the Zr-amido bond lengths in the former complex are roughly 2.13 Å [23]. The calculated Zr $=$ N stretching frequency is 955 cm^{-1}; it is important to note that this is not an intrinsic stretching frequency [20]. Vibrational frequencies at the RHF level are usually scaled by 0.9 [24] to account for electron correlation effects ($\nu_{Zr \cdot N}$(scaled) $=$ 860 cm^{-1}). An infrared (IR) band at 865 cm^{-1} was assigned to the Zr $=$ N stretch of the THF adduct of (NHSi')$_2$Zr $=$ NSi' [1]. Our calculated $\nu_{Zr \cdot N}$ is in agreement with the assignment of the IR band to a Zr $=$ N stretch and thus lends support to a bis(amido)imido intermediate [1] in the experimental system.

A weakly bonded complex, (NH$_2$)$_2$Zr $=$ NH $\cdot$ H$_2$, was isolated as a minimum, 1 [25]. The complex has a C$_s$ geometry and the reactant fragments are little changed from their separated geometries. The H atoms of the H$_2$ fragment are nearly symmetrically disposed with respect to the Zr atom, one ZrH distance is 2.46 Å while the other is 2.44 Å. The binding energy of the H$_2$ is only 1.3 kcal mol^{-1}. Upon "coordination" of the H$_2$, the ZrN bonds stretch by less than 0.01 Å from their values in (NH$_2$)$_2$Zr $=$ NH. The largest change is in the H–H bond, stretching by 0.02 Å. Subtle changes in the electronic structure can be measured by calculating the intrinsic stretching frequencies [20] and comparing to values for isolated molecules. The Zr-amido and Zr-imido $intrinsic$ stretching frequencies for 1 are 624 and 970 cm^{-1}, respectively, or 9 and 2% lower as compared with (NH$_2$)$_2$Zr $=$ NH. Thus, some weakening of these bonds is taking place when hydrogen coordinates, presumably by donation of electron density from the σ_{HH} into metal–nitrogen antibonding molecular orbitals (MOs). The H$_2$ intrinsic stretching frequency goes from 4646 cm^{-1} in "free" H$_2$ to 4469 cm^{-1} (−4%) in "complexed" H$_2$. There is a small amount of charge transfer from the H$_2$ to the imido, 0.13 electrons as determined from a Mulliken Population Analysis.

Addition of H_2 Across the Zr $=$ N Double Bond of (NH$_2$)$_2$Zr $=$ NH

The 1,2-addition of H$_2$ across the Zr $=$ N double bond of the bis(amido)imido leads to the $tris$(amido)hydride, (NH$_2$)$_3$Zr-H, 2. The complex has a C$_3$ minimum, with Zr–N bond lengths of 2.06 Å. Interestingly, the Zr-amido bond length is 0.03 Å longer than that calculated for the simple amido complex, H$_3$Zr-NH$_2$ indicating that π-bonding in the formally singly bonded amido ligands can be important. Another indication of the strength of the π-bonding of the amido ligands is provided by their competition with the imido ligand for the $d\pi$ AOs. The Zr-imido intrinsic stretching frequency in the parent molecule, (H)$_2$Zr $=$ NH, is 29 cm^{-1} higher than in (NH$_2$)$_2$Zr $=$ NH; the Zr-imido bond is 0.03 Å shorter in the former compared with the latter. The importance of π-bonding in early transition metal imido complexes has been the subject of much discussion by experimentalists [26]. Kapellos et al. have studied the phenomenon for the coordinatively unsaturated case, M' – NH$_2$ [27], and the present results demonstrate that π-bonding for amido ligands can be substantial in coordinatively saturated complexes.

The 1.2 addition of H_2 across a Zr—N double bond ($1 \rightarrow 2$) immediately suggests a four-center transition state, where H–H and Zr—N bonds are being stretched while Zr–H and N–H bonds are being formed. Indeed, a transition state fitting this description is found. 3 [28]. The TS for the addition of H_2 across the Zr=N bond of the *bis*(amido)imido complex is 9.8 kcal mol^{-1}, above the charge transfer (CT) complex, 1. The product, $(NH_2)_3$Zr-H, 2, is 18.4 kcal mol^{-1} stable than the CT complex. Thus, the reverse process, extrusion of H_2 from the *tris*(amido)hydride has a 28.2 kcal mol^{-1} barrier. The activation enthalpy for the elimination of methane from (NHSi')$_3$Zr-CH$_3$ is 25.9 (4) kcal mol^{-1}. As Steigerwald and Goddard [29,30] found for the addition of H_2 across metal-carbon single bonds, the TS deviates markedly from that of a square and is more "kite" shaped, with one obtuse and three acute angles. The ZrN$_i$ bond in the TS is 1.89, 0.06 Å (3%) longer the Zr-imido bond in (NH$_2$)$_2$Zr=NH, while the Zr $\cdots$ H$_a$ bond is 2.07 Å, 8% (0.16 Å) longer than that in (NH$_2$)$_3$Zr-H. The H-H and N-H bonds in 3 are stretched much more significantly: 0.22 Å (30% vs. H$_2$) and 0.51 Å (50% compared with (NH$_2$)$_3$Zr-H), respectively. The Zr—N$_i$-H$_i$ angle in TS 3 is nearly linear (176°). The data suggest a late TS when the reaction is viewed as (NH$_2$)$_3$ZrH (3) $\rightarrow$ (NH$_2$)$_2$Zr=NH $\cdot$ H$_2$. The kinetic data for (NHSi')$_3$Zr-CH$_3$ [1] has been interpreted as supporting a TS with "substantial Zr—C bond breaking ($\Delta H^{\ddagger}$ = 25.9 (4) kcal/mol) in a relatively constrained transition state ($\Delta S^{\ddagger}$ = 7(1) eu)." These calculations seem to be in qualitative agreement with the experimental results.

The most interesting point about transition state 3 is the short Zr $\cdots$ H_t transannular distance, 1.98 Å, which is only 0.07 Å (4%) longer than the Zr-terminal hydride distance in the tris(amido)hydride, and 0.09 Å (5%) shorter than the Zr $\cdots$ H$_a$ distance in 3. It is reasonable to expect that low energy $4d$ A Os on the high-valent Zr are available to stabilize the H being transferred (as well as the H_a and N$_i$H$_i$ fragments) in the TS. H_t, thus lowering the TS versus a system without vacant, lower energy d orbitals (e.g., a main group element or a late, low valent metal) and facilitating the reaction. As a rough measure of the strength of the interaction between the Zr and the various hydrogens, the Mulliken Bond Overlap Population (BOP) was calculated for the various ZrH interactions and compared to a "normal" terminally bonded hydride ligand. The ZrH BOPs were calculated to be 0.16 (H_t) and 0.38 (H_a) which compares with a value of 0.70 for the terminally bonded H in (NH$_2$)$_3$Zr-H.

Sigma-Bond Metathesis

The sigma-bond metathesis pathway ($1 \rightarrow 5 \rightarrow 4$) leads to an interesting product, Zr(NH)(NH$_2$)(NH$_3$)H, possessing a Zr-imido, Zr-imido, and Zr-amino (i.e., Zr, -NH$_3$) bond in the same complex. Thus, there is a formally double (imido), single (amido), and dative (amino) ZrN bond in 4, which should provide a good challenge for the computational methods. The various ZrN bond lengths are calculated to be 1.83 Å (imido), 2.10 Å (amido) and 2.41 Å (amino) in the C$_1$ minimum, 4. Rothwell et al. [23] have characterized the complex Zr(py')$_2$(NHAr)$_2$(=N-Ph), which has Zr-amido bond lengths of 2.13 Å and 2.14 Å, Zr-amino bond lengths of

2.36 Å and 2.38 Å, and a Zr-imido bond length of 1.87 Å. The calculated values differ from the experimental model by ≤2% which is excellent despite the differences in coordination number and steric congestion.

In the sigma bond metathesis pathway, as in the previous mechanism, the most obvious choice of TS geometry is a four-center one. The calculated barrier to addition of H₂ across the Zr-amido bond is 17.9 kcal mol⁻¹, nearly twice that for the addition of H₂ across the Zr-imido bond. The high barrier to addition of H₂ across the Zr-amido bond is consistent with a much lower driving force for the reaction; the amino(amido)imido complex is only 1.0 kcal mol⁻¹ more stable than the CT complex (1). TS 5 can also be described as kite-shaped. As before, there is a short Zr · · · H transannular distance, 2.14 Å, 0.16 Å longer than for the previous TS. The longer ZrH₁ distance in 5 vs. 3 suggests less interaction between Zr and H_t in the sigma-bond metathesis TS. However, the calculated ZrH₁ Mulliken Bond Overlap Population in 5 is similar, 0.18, to that calculated for 3.

Conversion of Zr(NH₂)₃H to Zr(NH)(NH₂)(NH₃)

The conversion of 2 to 4 (by way of TS 6) entails H-transfer from one amido group to another. A similar process has been implicated in the formation of (NHSi')(Cl)(THF)Ti = NSi' from (NHSi')₃Ti-Cl by elimination of NH₂Si' [3] and in bis(amido) complexes. The geometries of the products and reactants (2 and 4) have been discussed and compared to available experimental data above. The removal of NH₃ from Zr(NH)(NH₂)(NH₃)H is calculated to be quite endothermic, 36.3 kcal mol⁻¹. Our calculations indicate that a H-transfer process for Zr model complexes (2 → 4 or the reverse) has a high barrier. The TS for the reaction 4 → 2 is 23.8 kcal mol⁻¹ above the Zr(NH)(NH₂)(NH₃)H minimum. Complex 4 is 17.4 kcal mol⁻¹ less stable than the tris(amido)hydride.

Several things distinguish TS 6 from the related transition state for the addition of H–H across the Zr = N bond of (NH₂)₂Zr = NH. The most noticeable difference is the significantly smaller M-N-H angle of the erstwhile imido ligand (161° vs. 176°) in 6. The small M-N-H angle suggests that the transition state is early if the reaction is viewed as Zr(NH₂)₃H → Zr(NH)(NH₂)(NH₃)H. The transannular Zr · · · H_t distance of 2.11 Å (vs. 1.98 Å) is similar to that found for the sigma-bond metathesis TS, 5; however, the calculated Mulliken Bond Overlap Population for Zr · · · H_t is three times smaller for 6 (0.06) than 5 (0.18). If the reaction is viewed as the addition of the N–H bond of ammonia across the Zr = N double bond of Zr(NH₂)(H)(= NH), then the greater electronegativity of N will make the H being transferred more acidic and thus less likely to be stabilized by the high valent metal. The lower degree of stabilization of the H being transferred in TS 6 correlates with the higher activation energy for (4 → 6 → 2) versus (1 → 3 → 2) despite the comparable driving force for each reaction (17.4 kcal mol⁻¹ for the former; 18.4 kcal mol⁻¹ for the latter).

Intrinsic Reaction Coordinate from CT Complex, 1, to Tris(Amido)Hydride, 3

The intrinsic reaction coordinate (IRC) [31] for the conversion of the CT complex, 1, to the tris(amido)hydride, 2, by way of transition state 3 was studied in order

to understand the dynamics of the H_2 activation/extrusion process [32]. A plot of the changes in the pertinent bond lengths and bond angles along the IRC is shown in Figure 2. The mass-weighted distance along the reaction coordinate is denoted S_{total}; the TS is set to $S_{total} = 0$ bohr*amu$^{1/2}$. Proceeding from TS **3** to the CI complex, S_{total} becomes more negative. From TS **3** to the *tris*(amido)hydride, **2**, S_{total} becomes more positive. Not surprisingly, the two internal coordinates showing
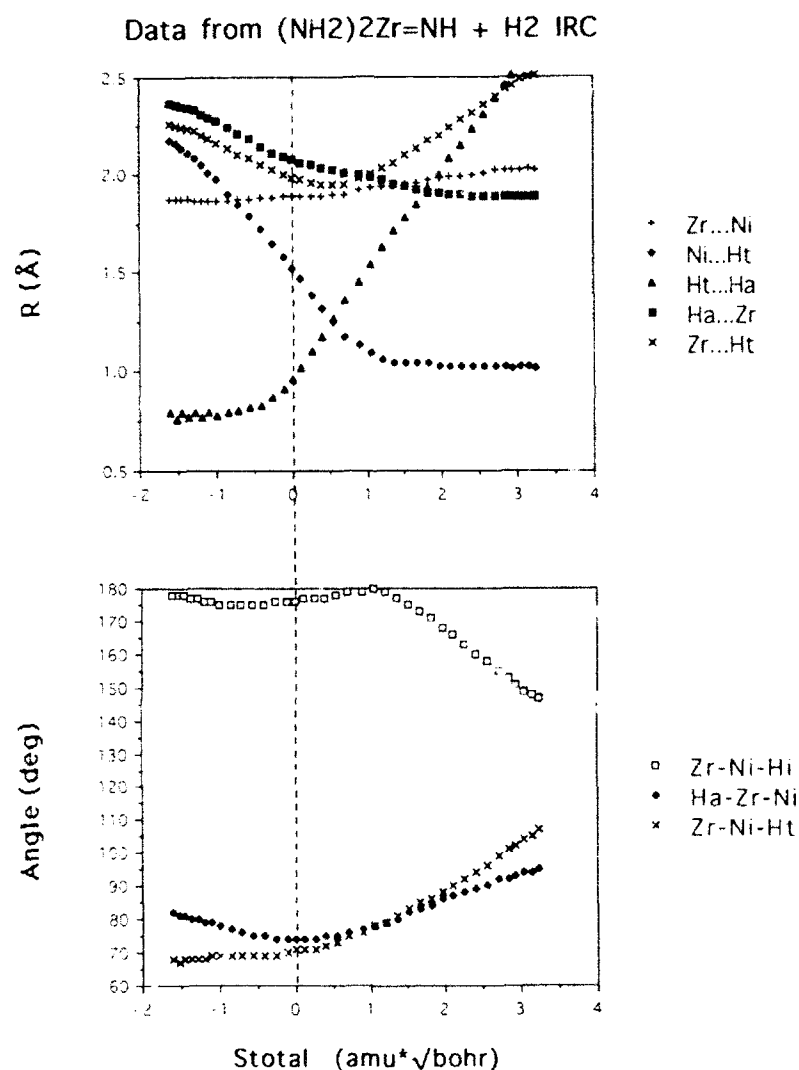
Data from (NH2)2Zr=NH + H2 IRC

Figure 2. Plots of important parameters (top: bond lengths; bottom: bond angles) along the IRC from **1** → **3** → **2**. TS **3** is set to $S = 0$, the positive direction leads to the *tris*(amido)hydride, **2**, the negative direction leads to the CI complex, **1**.

the most dramatic changes along the IRC are the H_a—H_b bond of the H_2 being activated (eliminated in the reverse reaction) and the N_j—H_b bond which is being formed (broken). There are two "breaking" points where the slopes change significantly (Fig. 2a). For the H_a—H_b bond, this is roughly at S_{total} —0.41 bohr∗amu$^{1/2}$. After S_{total} —0.41 bohr∗amu$^{1/2}$ the H_a—H_b bond, which up to this point is essentially unchanged from the CT complex, undergoes rapid elongation. H_b is in the process of being transferred to N_j, forming the third amide ligand. Note that the point is associated with a change in the direction of H_a-Zr-N_j angle (Fig. 2b); the angle which was decreasing begins to increase once again. A little consideration reveals that this is to be expected. As the H_2 fragment of 1 cants toward N_j, to form the N_j—H_b bond, the N_j-Zr-H_b angle must decrease. Concomitant with formation of the N_j—H_b bond, Zr—H_a bond formation is taking place. Eventually, in the *tris*(amido)hydride, a nearly tetrahedral H_a-Zr-N_j angle will result so that the angle must increase to roughly 109.5° as the IRC indicates. The second "break" point at S 1.21 bohr∗amu$^{1/2}$ is more illuminating (Fig. 2); the slope of the N_j-H_b line changes abruptly, from negative to near zero. At this point the N_j—H_b bond is essentially formed, N_j—H_b 1.05 Å (vs. 1.02 Å in the *tris*(amido)hydride). As before, the motion is correlated with a change in one of the angles, Zr-N_j-H_b. After S 1.21 bohr∗amu$^{1/2}$, the Zr-N_j-H_b angle starts to decrease, as the ligand fulfills its eventual destiny of transforming from an imido (linear coordination) to an amido (triagonal planar coordination).

Discussion

A schematic representation of the reaction coordinate for the various intermediates and transition states studied is shown in Figure 3. Several interesting points were noted above which are now discussed in greater detail.

A weakly bound, H_2 complex, **1**, was isolated for the initial interaction of (NH₂)₃Zr—NH and H_2. Recent experimental evidence by Bergman et al. [33] and Burkey et al. [34] suggests that metal-alkane complexes can have significant binding energies (10–12 kcal mol^{-1}), and thus play an important role in the catalytic activation of C—H bonds. Preliminary studies suggest that alkanes have greater binding energies for the initial interaction than H_2, e.g. [(H)₃Zr—NH··CH₄] is ≈ 8 kcal mol^{-1} below separated fragments. Molecular hydrogen complexes have elicited a good deal of interest since the isolation of the first examples by Kubas et al. [35], W(CO)₃(PR₃)₂, R—cyclo-C₆H₁₁, and i-Pr. Hay has calculated a substantial binding energy for the H_2 ligand, 19.1 kcal mol^{-1} [36]. Burkey and Nayak have recently measured a binding energy of 17 ± 3 kcal mol^{-1} for Cr(CO)₅(H₂) [37]. In contrast, complex **1** is weakly bound, only 1.3 kcal mol^{-1} below the isolated molecules. Calculations [36] indicate the importance of backbonding from the occupied metal d orbitals to the σ^*_{HH}. Since the metal is formally d^0 and highly electrophilic, back donation into the σ^*_{HH} is expected to be negligible. It seems unlikely that in the present case there are an appreciable concentration of these H_2 complexes in solution or that they have a long lifetime if formed.

Perhaps the most interesting feature with respect to the electronic structure of **1** is the polarity in the H_2 fragment, despite the nearly equivalent ZrH distances. The
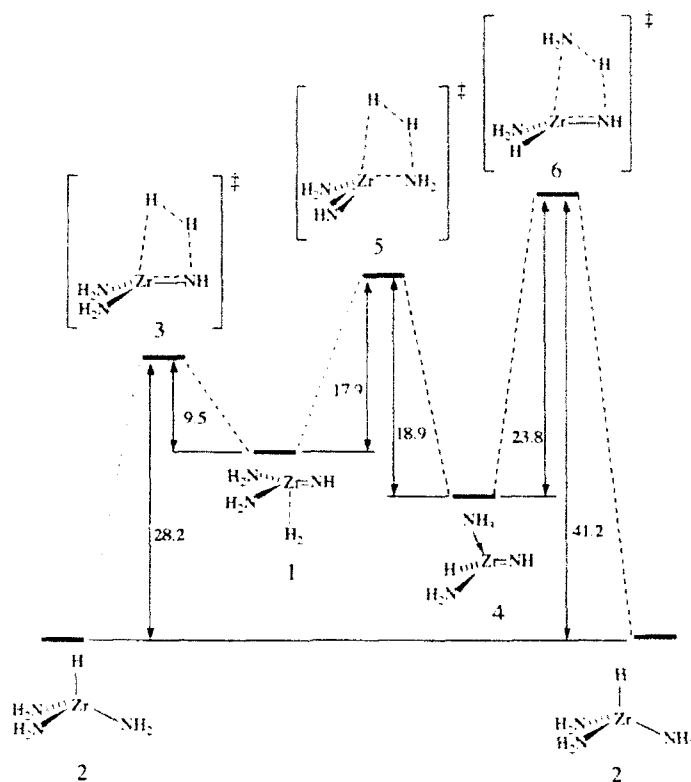
Figure 3. Schematic representation of the relative energies for the minima and transition states in this study. The energies are reported in kcal mol⁻¹, computational details are given in the text. The numbering scheme coincides with that in Figure 1 and the text.

calculated charge on the H which is slightly farther from Zr is +0.02 while that which is 2.44 Å away from the Zr (i.e., closer to the imido N) has a calculated atomic charge of +0.11. Wolczanski et al. [1] have postulated that the great polarity in the Zr $=$ N bond ($Zr^{+1.46} = N^{-0.88}$, by a Mulliken Population Analysis) induces a polarization of the C $-$ H bond which assists in its activation. The present computational results support the contention.

The calculated activation energy for the addition of H_2 across the Zr $-$ N bond of one of the amido ligands (1 → 5 → 4) is roughly twice as high as for the addition of H_2 across the Zr $=$ N bond (1 → 3 → 2). Furthermore, even if the amino(amido)imido complex (4) is formed, the high barrier to form the observed product, a tris(amido) complex, is so high as to make the second H-transfer step (4 → 6 → 2) even more unfavorable. One small point of interest is the much larger calculated dipole moment for the sigma metathesis TS (5) versus the 1,2 addition TS (3), 3.16D and 1.61D. Perhaps in a sufficiently polar solvent, the two processes may become more competitive, although there is still the high barrier for the second

H-transfer process to contend with. The experiments of Wolczanski et al. [1] were run in benzene. Our results indicate that the H, activation process by a bis(amido)imido reactive intermediate is significantly more favorable by the 1,2-addition of H, across the Zr N bond (1 → 3 → 2) to form the tris(amido)hydride than a sigma-bond metathesis pathway (1 → 5 → 4). Given the similarity of H–H and C–H activation processes, it seems reasonable to assume that a similar conclusion is valid for the activation of hydrocarbons by these complexes.

The most interesting point from the IRC is that compression of the Zr N -H angle takes place after the H (H) is essentially transferred to the imido N to form the third amido ligand of the tris(amido)hydride, 2. At S_{total} 1.21 bohr*amu$^{1/2}$ on the reaction coordinate for the H, activation/elimination process (Fig. 2), the Zr complex bears a striking resemblance to the isoelectronic (in terms of valence electrons) Ta C–H fragment in electron-deficient alkylidenes, L_nM C(R)R'. These complexes have Ta C–H angles close to 90° as revealed by neutron diffraction [38]. The fact that π-bonding in amides is significant (vide supra) makes the analogy more complete. The distorted Ta C–H angles suggest incipient C–H bond breaking, which is supported by longer than normal C–H bond lengths [38], in the alkylidene (C(H)R) to eventually yield an alkylidyne (≡CR), i.e., analogous to the process 1 → 3 → 2 followed along the IRC. Experimentally, Schrock has shown that distorted Ta-alkylidene complexes can be pushed even further by increasing steric congestion [e.g., by addition of phosphine ligands [38], Eq. (2)] to eliminate toluene. Taking the experimental data for the related Ta complexes and combining them with the computational results for Zr suggests two possible extensions for future computational

Cp*Ta(Cl)(CH₂Ph)(C(H)Ph) + 2PMe₃ →

$$Cp*Ta(Cl)(PMe_3)_2(≡CPh) + Ph-CH_3 \quad (2)$$
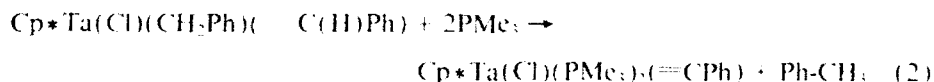
and experimental work. First, analogous complexes of the form L_nZr-N(H)R and L_nTa C(H)R may show the same interesting distortion [39]. Second, increased steric congestion in CVD precursors of the type Zr(NR)₂R by the coordination of Lewis bases may lower the barrier for extrusion of volatiles, and thus allow for lower CVD processing temperatures [40].

Although one should avoid putting too much faith in quantitative comparisons based on an arbitrary partitioning of the total electron density, the Mulliken Bond Overlap Populations suggest that there is an appreciable interaction, between the Zr and the transannular H (H,) in the TS for 1,2-addition across the Zr N bond of (NH₂)₂Zr NH, 3. The interaction may have an important role to play in the ability of the Zr-imido complexes, and indeed other multiply bonded complexes with early, high-valent metals, to activate X–H (X H, C, Si, N, and H) bonds. More activity is expected from catalysts which are designed to yield reactive intermediates in which the interaction is enhanced. Simple considerations would lead one to predict that the transannular interaction should be enhanced by a more electrophilic metal and nucleophilic transannular hydrogen. The hypothesis is supported by the greater reactivity of Zr-imido complexes [1,2] when compared to Ti

analogues [3,4]. $Zr(X_{Zr} = 1.33)$ is significantly more electropositive than $Ti(X_{Ti} = 1.54)$, and thus the Ti in Ti-imido complexes will be less electrophilic when compared with a Zr analog; Mulliken charges for the parent metal-imido complexes, $(H)_2M = NH$, are $Ti^{0.67} = N^{0.62}$ and $Zr^{1.06} = N^{0.83}$. Similarly, the synthesis of materials precursors which enhance the metal-hydrogen interaction in the TS for elimination of volatiles could allow for lower processing temperatures in CVD. For example, the relative electronegativity of Si versus C leads one to predict, based on the present results, that silyl-substituted complexes may have a greater degree of stabilization of the H in the TS for elimination of silanes, and may be preferable as low-temperature CVD precursors. Studies are underway to test these hypotheses and their effects on the mechanism of X — H bond activation and the reverse process, extrusion of X — H-bonded molecules.

Acknowledgments

Bibliography

[1] C. C. Cummins, S. M. Baxter, and P. T. Wolczanski, J. Am. Chem. Soc. 110, 8731 (1988).

[2] P. J. Walsh, F. J. Hollander, and R. G. Bergman, J. Am. Chem. Soc. 110, 8729 (1988); Walsh et al. have just recently published further details of the reactivity of Zr imido complexes, R. J. Walsh, Am. M. Baranger, and R. G. Bergman, J. Am. Chem. Soc. 114, 1708 (1992).

[3] C. C. Cummins, C. P. Schaller, G. D. Van Duyne, P. T. Wolczanski, A. W. F. Chan, and R. Hoffmann, J. Am. Chem. Soc. 113, 2985 (1991).

[4] J. E. Hill, R. D. Profilet, P. E. Fanwick, and I. P. Rothwell, Angew. Chem., Int. Ed. Engl. 29, 664 (1990).

[5] (a) K. M. Doxsee and J. B. Farahi, J. Chem. Soc. Chem. Comm. 1452 (1990); (b) K. M. Doxsee, J. B. Farahi, and H. Hope, J. Am. Chem. Soc. 113, 8889 (1991).

[6] C. W. Winter, P. H. Sheridan, T. S. Lewkebandara, M. J. Heeg, and J. W. Proscia, J. Am. Chem. Soc. 114, 1095 (1992).

[7] (a) H. T. Chiu and W. P. Chang, American Chemical Society, Inorganic Chemistry Abstracts, 4th Chemical Congress of North America, paper INOR74, New York City, 1991; (b) P. T. Wolczanski, American Chemical Society, Inorganic Chemistry Abstracts, 4th Chemical Congress of North America, paper INOR103, New York City, 1991.

[8] (a) D. S. Edwards and R. R. Schrock, J. Am. Chem. Soc. 104, 6806 (1982); (b) S. M. Rocklage, R. R. Schrock, M. R. Churchill, and H. Wasserman, Organometallics 1, 1332 (1982).

[9] For example, Tilley and co-workers have recently presented evidence in favor of a sigma-bond metathesis route for the polymerization of silanes by Group IVB catalysts in preference to the older silylene mechanism. H. G. Woo and T. D. Tilley, J. Am. Chem. Soc. 111, 8043 (1989).

[10] (a) Y. Saeki, R. Matsuzaki, A. Yajima, and M. Akiyama, Bull. Chem. Soc. Jpn. 55, 3193 (1982); (b) L. Maya, Inorg. Chem. 25, 4213 (1986).

[11] T. R. Cundari and M. S. Gordon, J. Am. Chem. Soc. **113**, 5231 (1991).

[12] T. R. Cundari and M. S. Gordon, Organometallics **11**, 55 (1992).

[13] T. R. Cundari and M. S. Gordon, J. Am. Chem. Soc. **114**, 539 (1992).

[14] T. R. Cundari and M. S. Gordon, J. Phys. Chem. **96**, 631 (1992).

[15] T. R. Cundari and M. S. Gordon, Organometallics (to be published).

[16] GAMESS (General Atomic and Molecular Electronic Structure System): M. W. Schmidt, K. K. Baldridge, J. A. Boatz, J. H. Jensen, S. Koseki, M. S. Gordon, K. A. Nguyen, T. L. Windus, and S. T. Elbert, QCPE Bull. **10**, 52 (1990).

[17] M. Krauss, W. J. Stevens, H. Basch, and P. G. Jasien, Can. J. Chem. (in press).

[18] J. A. Pople, W. J. Hehre, L. Radom, and P. v. R. Schleyer, *Ab Initio Molecular Orbital Theory* (Wiley: New York, 1986), Section 4.3.

[19] J. Baker, J. Comp. Chem. **7**, 385 (1986).

[20] J. A. Boatz and M. S. Gordon, J. Phys. Chem. **93**, 1819 (1989).

[21] T. R. Cundari, J. Am. Chem. Soc. (to be published).

[22] (a) C. Moller and M. S. Plesset, Phys. Rev. **46**, 618 (1934); (b) P. Carsky, B. A. Hess, and L. J. Schaad, J. Comput. Chem. **5**, 280 (1984).

[23] R. D. Profilet, C. H. Zambrano, P. E. Fanwick, J. J. Nash, and I. P. Rothwell, Inorg. Chem. **29**, 4364 (1990).

[24] (a) J. A. Pople, H. B. Schlegel, R. Krishnan, D. J. DeFrees, J. S. Binkley, M. J. Frisch, R. Whiteside, R. F. Hout, and W. J. Hehre, Int. J. Quant. Chem., Proc. Sanibel Symp. **15**, 269 (1981); (b) The effects of coordinating additional Lewis bases on the metal-imido stretching frequency must also be considered. Work with various Ti and Zr-imido complexes [21] shows that coordination of model bases such as water and ammonia lower the intrinsic stretching frequency of the metal-imido bond by only 10–30 cm⁻¹, depending on the metal and base.

[25] (a) These loosely bound complexes are expected to be quite sensitive to basis set size and the wavefunction employed. Test calculations on the smaller (H₂)Zr=NH·H model with polarization functions added to the H atoms and diffuse functions added to all main-group elements (including H) yields only small changes in the geometry and binding energy. Inclusion of electron correlation at the MCSCF level (correlating the metal-imido and H–H bonds) for the model system, also changes the geometry and binding energy very little; (b) Following the suggestion of a referee, it was decided to search for a stationary point in which the H–H and Zr—N bond vectors are roughly perpendicular since a CI complex with this geometry should be more appropriate to the sigma-bond metathesis TS (**1** → **5** → **4** in Fig. 3). A stationary point with this geometry was isolated, but found to have an imaginary frequency corresponding to rotation of the H₂ fragment to yield **1**. As expected, these stationary points are close in energy (ΔE ≈ 0.5 kcal mol⁻¹ at the RHF level).

[26] (a) H. E. Bryndza and W. Tam, Chem. Rev. **88**, 1163 (1988); (b) M. F. Lappert, P. P. Power, A. R. Sangerand, and R. C. Srivasta, *Metal and Metalloid Amides* (Ellis Horwood: Chichester, 1980).

[27] S. Kapellos, A. Mavridis, and J. F. Harrison, J. Phys. Chem. **95**, 6860 (1991).

[28] As for the other stationary points in this study, simple models of the TSs were calculated at various levels of theory in order to assess the importance of electron correlation and basis set size on their bonding and structure. As before, these effects were small enough to obviate the additional expense of going to a more demanding approach.

[29] M. L. Steigerwald and W. A. Goddard, J. Am. Chem. Soc. **106**, 308 (1984).

[30] For a particularly lucid discussion of the sigma-bond metathesis pathway for C–H activation by early transition metal alkyls see M. E. Thompson, S. M. Baxter, A. R. Bulls, B. J. Burger, M. C. Nolan, B. D. Santarsiero, W. P. Schaefer, and J. E. Bercaw, J. Am. Chem. Soc. **109**, 203 (1987).

[31] (a) D. G. Truhlar, R. Steckler, and M. S. Gordon, Chem. Rev. **87**, 217 (1987); (b) D. G. Truhlar and M. S. Gordon, Science **249**, 491 (1990).

[32] A preliminary investigation of the analogous reaction path at the MCSCF level for the parent molecule, (H)₂Zr=NH + H₂ → H₂Zr-NH₂, reveals that a single determinant description is valid for all points along the IRC sampled to date.

[33] E. P. Wasserman, C. B. Moore, and R. G. Bergman, Science **255**, 315 (1992).

[34] J. M. Morse, G. M. Parker, and T. J. Burkey, Organometallics **8**, 2471 (1989).

[35] (a) G. J. Kubas, Acc. Chem. Res. **21**, 120 (1988); (b) Calorimetric works by Hoff et al. have also
      been published on molecular hydrogen complexes. K. Zhang, A. A. Gonzalez, S. I. Mukerjee, S.
      J. Chou, C. D. Hoff, K. A. Kubat-Martin, D. Barnhart, and G. J. Kubas, J. Am. Chem. Soc. **113**,
      9170 (1991); (c) J. M. Millar, R. V. Kastrup, M. T. Melchior, I. T. Horvath, C. D. Hoff, and
      R. H. Crabtree, J. Am. Chem. Soc. **112**, 9643 (1990).

[36] P. J. Hay, J. Am. Chem. Soc. **107**, 705 (1987).

[37] T. J. Burkey and S. Nayak (unpublished results).

[38] R. R. Schrock, Acc. Chem. Res. **12**, 98 (1979).

[39] An Extended Huckel analysis of Ta-alkylidenes and their geometric distortion is reported in R. J.
      Goddard, R. Hoffmann, and E. D. Jemmis, J. Am. Chem. Soc. **102**, 7667 (1980).

[40] An interesting observation in connection with this prediction is found in the work of Rothwell and
      co-workers [41]. A Ti *bis*(amide) complex, $(OAr)_2Ti(NHPh)_2$ is stable until a neutral, Lewis
      base, py', is added. Upon addition of py', aniline $(PhNH_2)$ is eliminated to yield the complex,
      $(OAr)_2Ti$ $NPh)_2(py')_2$. Similar results have been obtained for Zr analogs [23].

[41] (a) D. M. T. Chan, W. C. Fultz, W. A. Nugent, D. C. Roe, and T. H. Tulip, J. Am. Chem. Soc.
      107, 251 (1985); (b) J. E. Hill, R. D. Profilet, P. E. Fanwick, and I. P. Rothwell, Angew. Chem.,
      Int. Ed. Engl. **29**, 664 (1990).

Solvation Effect on the Tunneling Rates of Proton Transfer

J. L. ESQUIVEL and D. BALMACEDA

School of Physics, University of Costa Rica, San José, Costa Rica

J. F. MATA-SEGREDA

School of Chemistry, University of Costa Rica, 2060, Costa Rica

Abstract

Solvation effect on the tunneling rates in the case of coupled motion of two protons along the reaction coordinate was semiempirically, CNDO/2, computed. The following molecular transition-state complexes (TSC) were studied: $A H \cdots B H \cdots A$, where A was either NH_3 or H_2O and BH was HI. Solvation was modeled with water molecules attached to each side of the perpendicular axis, through the bridge HI at different distances F/O, FN and FO (on-line) distances were also varied. Lower and narrower barriers were observed with the close positioning of the solvating molecules. This effect is reflected in higher tunneling probabilities. Thus, solvation favors the tunnel phenomenon in proton-transfer processes.
© 1992 John Wiley & Sons, Inc.

Introduction

The problem of environmental effects upon the proton transfer processes by considering solvent effects has been, in different ways, attacked [1-10]. The transition state theory of chemical reactions is the basic paradigm of current chemical and biochemical thought [11]. The account of macromolecular catalysis, such as enzyme catalysis, dictates that the primary function of the catalyst is the stabilization of the activated complex [12]. A macroscopic approach to the general idea of catalysis can be stated as follows:

$$Reactant + Catalyst = [Reactant.Catalyst]$$

$$[Reactant.Catalyst] = [Activated complex.Catalyst] = Product + Catalyst$$
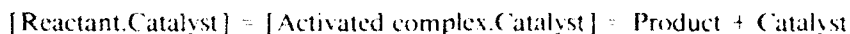
The close interaction between catalyst molecules and activated complexes result in the lowering of the free-energy barrier which separates the initial reactant state and the final product state. The function of the catalyst is to produce the necessary molecular distortion in the reactant molecules, in order to generate the configurations proper of the transition state. This process is endergonic. Compensatory binding interactions to the catalyst must give rise to the activated complex stabilization, thus leading to the observed rate accelerations over the uncatalyzed process. Some enzyme may have evolved in such a way that part of their catalytic power is derived from their ability of altering the height of energy barriers but also their
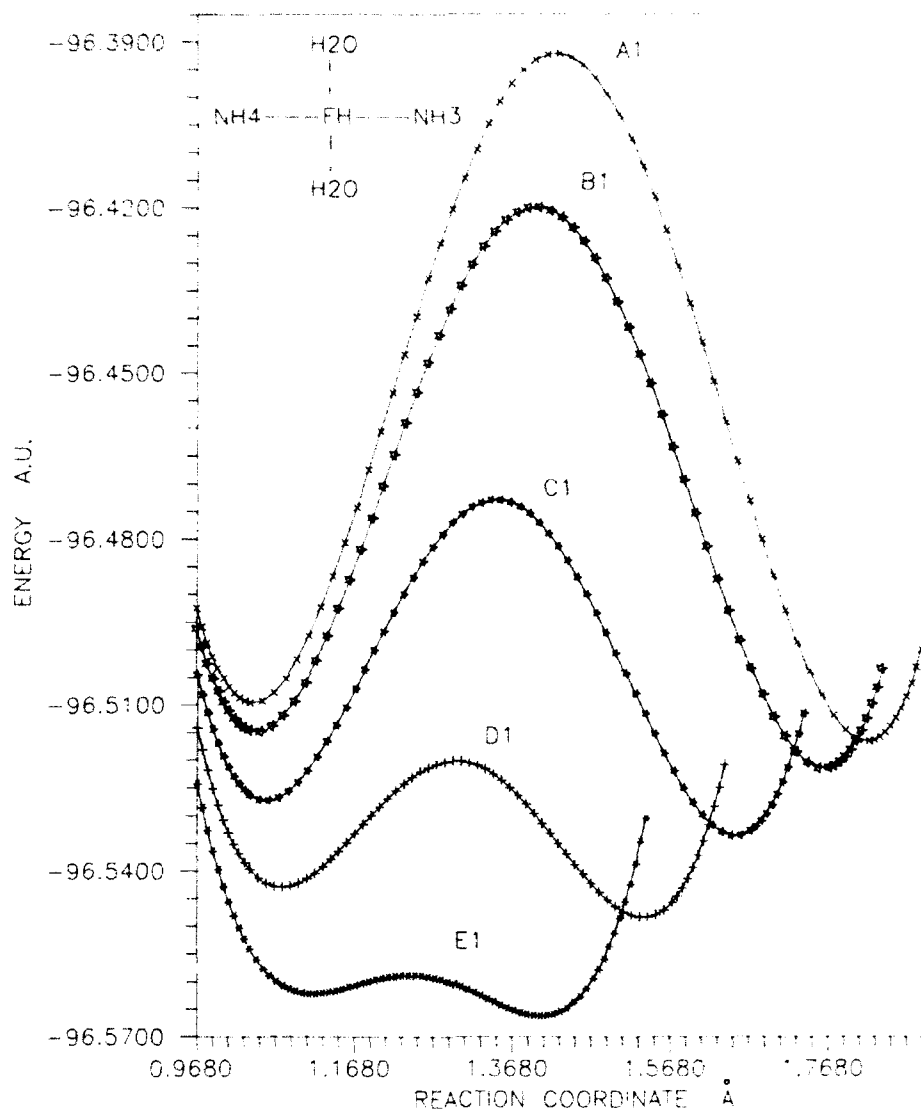
Figure 1. Energy profiles A1, B1, C1, D1, E1, when F/O = 2.90 Å while FN = A is 2.90, 2.85, 2.75, 2.65 and 2.55 respectively.

shapes. The induction of lower and narrower energy barriers increases the contribution of tunneling in chemical catalysis. In a previous article [13], we found that solvation of proton-transfer bridges led to increased contributions to the magnitude of tunneling. We present here a more complete study of the stereochemical features of solvation to the amount of tunnel effect in proton-transfer arrays.
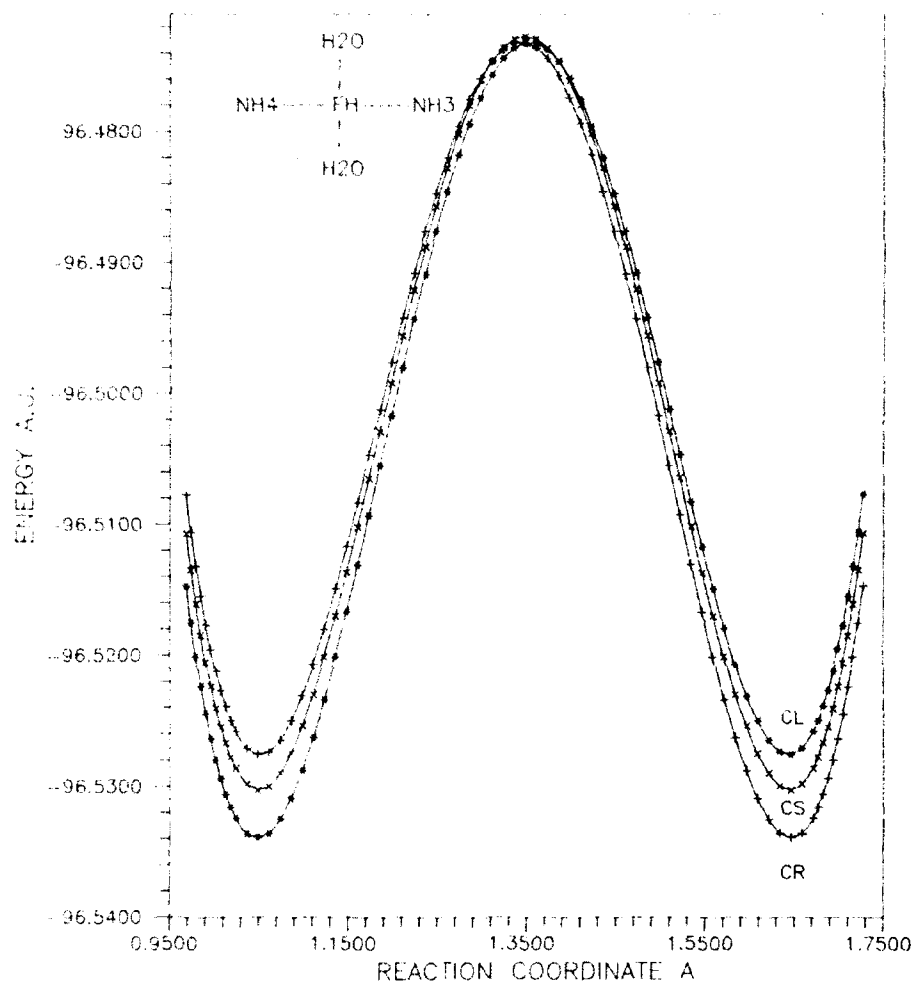
Figure 2   Energy profiles for FN = 2.75 A, F/O = 2.75 A and different solvating molecules orientations.

Acid-base catalysis is a common molecular mode of enzyme catalysis. The molecular machinery which performs these processes have become a most refined feature in biomolecular systems. The attempt to model a large array of solvent molecules seems to be successful although extrapolations of the results to the cases of supermolecules is rather difficult.

Method

Energy profiles with respect to the reaction coordinate and the respective tunneling rates were semiempirically, CNDO/2, computed in the cases of coupled motion of

TABLE I.   Catalytic acceleration and relative increment of
tunneling probability for different distances.

$F N$ Á	F/O Á	ΔE_{act} KJMol^{-1} ca		C_c/C_i
2.90	2.90	—	—	—
2.90	2.75	-0.669	0.76	1.0015
2.90	2.45	-3.527	0.24	1.0081
2.75	2.90	—	—	—
2.75	2.75	-0.650	0.77	1.0013
2.75	2.45	-3.419	0.25	1.0069
2.55	2.90	—	—	—
2.55	2.75	-0.616	0.78	1.0006
2.55	2.45	-3.240	0.27	1.0036

two protons along the reaction coordinate. The following H-bonded systems were studied:

Coupled motion of two protons along the reaction coordinate in the case of:

(1)
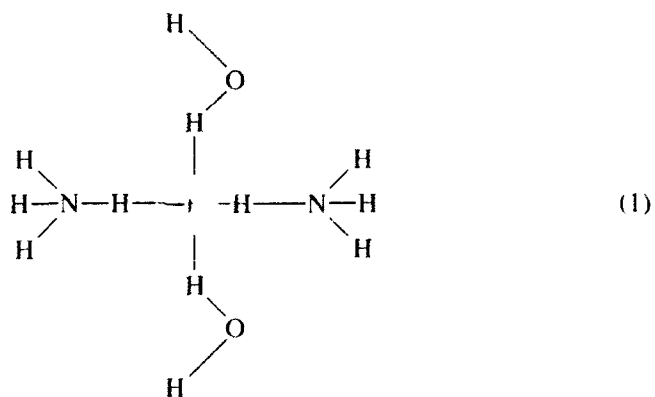
and coupled motion of two protons along the reaction coordinate in the case of:

(2)
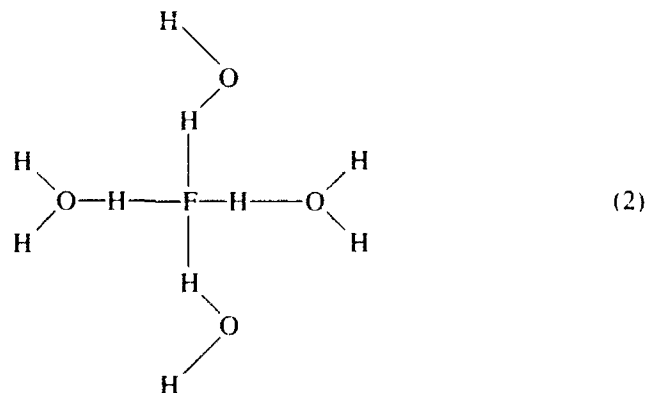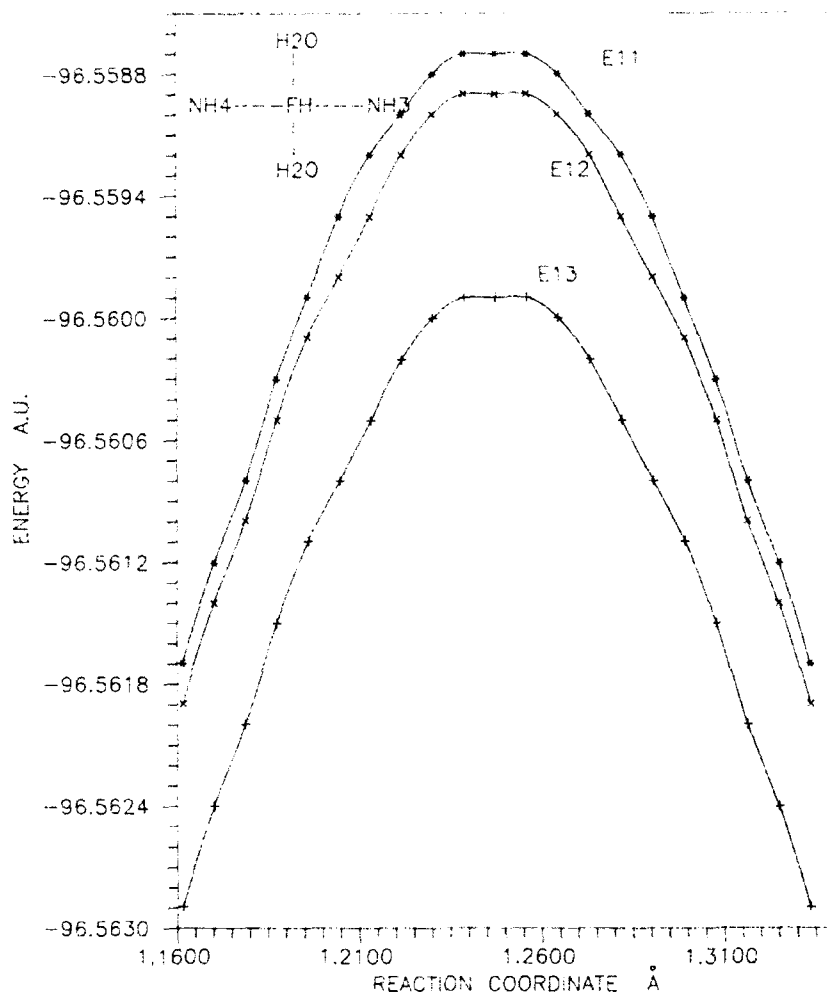
Figure 3   Top of the energy barriers for FN = 2.55 Å, F/O + 2.90 Å curve E11, F/O +
2.75 Å E12 and F/O + 2.45 Å curve E13.

In order to search about the behavior of these cases for large and short distances
FN and FO (on-line) they were made to take the values: 2.95 − 0.05n Å with n =
1 . . . . 10 meanwhile the water solvation molecules were attached perpendicularly
to the bridge FH at different distances F/O = 2.95 − 0.05n Å with n = 1 . . . . 10.
In both cases the water molecules hydrates the TSC at different orientations around
the vertical axes, but the angle F — H — O is 150°.

For the case of the proton transfer reaction (1) the energy profiles look like curves
A1, B1, C1, D1, E1 in Figure 1 for FN = 2.90 Å, 2.85 Å, 2.75 Å, 2.65 Å, and 2.55
Å, respectively, while F/O = 2.90 Å (off-line).

TABLE II. Catalytic acceleration and relative increment of tunneling probability for different distances

i_O Å	$i_{H O}$ Å	ΔE_{act} KJMol^{-1}	ea	C/C_i
2.90	2.90	—	—	—
2.90	2.75	0.545	0.80	1.0007
2.90	2.45	3.096	0.29	1.0047
2.75	2.90	—	—	—
2.75	2.75	0.530	0.81	1.0005
2.75	2.45	2.999	0.30	1.0031
2.55	2.90	—	—	—
2.55	2.75	0.496	0.82	1.0003
2.55	2.45	2.709	0.34	1.0025

In the case of the proton transfer reaction (2), similar variations were made and the energy profiles resemble a similar form, but the coordinates were calculated considering not only the translation of the protons but the simultaneous variation of the angle θ: H—O—H from 117.9 to 104.0 when going from H_3O to H_2O or vice versa. As in a previous article [13] the following functions were used:

$$\theta = 117.9 - 2.0\gamma \quad \text{or} \quad \theta = 104.0 + 2.0\gamma, \tag{3}$$

with

$$\gamma = 6.95(1.0 - \exp(-nu/0.3))/(1.0 - \exp(-d/0.3)), \tag{4}$$

where d is the total proton translation, u is the size of each step, and n goes from zero to the total number of steps.

Using cubic spline fitting, the energy profiles as functions of the reaction coordinate were adjusted and the tunneling rates were calculated for both cases near the activated state when the profile is approximated by the parabolic form:

$$V(x) = V_0(x/x_0)(2.0 - x/x_0), \tag{5}$$

where x_0 is the distance of any point along the reaction coordinate respect to the position of the activated state and V_0 is the corresponding height barrier.

According to the JWKB method, the barrier penetration factor K is:

$$K = \hbar \int_0^{2x_0} \sqrt{2.0m(V(x) - E)}\, dx. \tag{6}$$

where $E = V_0 - \sigma V_0$ with $\sigma = 0.0$ in the top and $\sigma = 1.0$ at the bottom of the tunneling barrier.

For E at the bottom, one obtains from Eq. (6)

$$K = (x_0/2\hbar)\sqrt{2mV_0}. \tag{7}$$

The transmission coefficient for the case of incoming protons from the left-hand side is:

$$g = \exp(-2K)/(1 + 1/4\exp(-2K)) \sim \exp(-2K) \qquad (8)$$

In atomic units.

$$g = \exp(-\pi x_0 \sqrt{2mI_0}) \qquad (9)$$

which can be expressed as:

$$g = \exp(-69.050 x_0 \sqrt{I_0}). \qquad (10)$$

when x_0 is in Å and I_0 in eV.

Taking the center of the wave packet as representing the proton at the left-hand well which hit the barrier in the fundamental state with a frequency:

$$v = h/2m\pi b^2 = (1.003/b^2)10^{12} \qquad (11)$$

where $2b$ is the distance in Å between the turning points in the left-hand side well.

If the full particle hits the barrier with that frequency and with the transmission coefficient given by Eq. (11) then the fraction of the particle that at a given energy is going to tunnel per second is the tunneling rate:

$$CI = vg \qquad (12)$$

$$\log CI = 13 - 29.988 x_0 \sqrt{I_0} \qquad (13)$$

Hydrogen-bond distances used were 1.046 Å in H_2O, 1.035 Å in FH, and 1.079 Å in NH_3.

As in the previous work [13] there is good agreement with the infrared spectroscopy data [14].

Discussion

The energy profiles obtained in both cases, for different distances between the donor and the acceptor were similar to those of Figure 1, showing that for short distances there was not a double potential well but a single one. The asymmetry in that figure is because the water solvating molecule is oriented in such a way that the oxygen is in the right-hand side in the plane with angle FHO of 150°. Having those water molecules in the perpendicular plane to the horizontal axes one obtains symmetric profiles as in the case of curve CS in Figure 2. That figure shows three orientations of the solvating molecules since curve CL correspond to the oxygen in the left-hand side and curve CR to the oxygen of the water solvating molecule in the right-hand side.

In the cases of double potential wells the Schrödinger equation was solved using the potential function which is obtained by cubic spline fitting. The energy eigenvalue for which convergency was reached was lower in the right-hand well than in the left-hand well. The reaction velocity v, as Arrhenius, 1889, showed it must be proportional to the exponential function [15] of the activation energy E_{act}:

$$v = e^{-E_{act}/kT}. \qquad (14)$$

then there is a kind of catalytic acceleration:

$$ca \quad \frac{\Gamma_2}{\Gamma_1} \quad e^{(I_1 - I_2) + I} \tag{15}$$

In the case of reaction Eq. (1), Table I contains data for large, intermediate, and short donor–acceptor distances, and one can see the difference in E_{act} in KJ/mol between the curves in Figure 3 with respect to the corresponding one for the larger solvation distance, F/O, and also the catalytic acceleration at 300° K, which can be compared, at the same temperature, to those when the solvating water molecules approach. On the other hand in the case of the reaction Eq. (2), Table II contains the data for large, intermediate, and short donor–acceptor distances and one can also compare, at the same temperature, the difference in ΔE_{act}, the catalytic acceleration with respect to the corresponding one to the situation in which the solvating water molecules are farther away.

Lower and narrower barriers were obtained with the close positioning of the solvating molecules as can be seen in Figure 3.

On the other hand, in the last column in Tables I and II the relative increment C_j/C_i on the tunneling rates probabilities are reported near the top of the barrier, as an example at 3/4th of the barrier height, in those energy profiles corresponding to a closer positioning of the water solvating molecules, with respect to the case of large solvating distance. It can be seen that to a closer positioning of the water solvating molecules, it corresponds to lower barriers and higher log C, which accounts for bigger barrier penetration probabilities before the proton reaches the top of the barrier. This indicates also that tunneling occurs at a frequency of 10^{13} reciprocal s. The effect is significant but it is expected that a larger effect could be obtained upon the addition of more solvating water molecules.

Catalysis is a concept that assumes situations which account for lower and narrower activation barriers and tunneling of proton transfer is probably an essential mechanism which accounts for the extreme efficiency of biocatalysis. Therefore the correct positioning of solvating amino acid residues in enzyme active sites seems a most plausible reason to explain the high catalytic accelerations observed in enzyme-catalyzed processes.

Acknowledgments

Bibliography

[1] E. D. Hughes and C. K. Ingold. Chem. Soc. 244 (1935).
[2] C. G. Swain, D. A. Kuhn, and R. L. Schowen. J. Am. Chem. Soc. 87, 1553 (1965).
[3] R. L. Schowen. In *Progress in Physical Organic Chemistry*. A. Streitwieser, Jr., and R. W. Taft, Eds., Wiley, New York, 1972, Vol. 9, pp. 275–332.
[4] O. Tapia, F. Sussman, and E. Poulain, J. Theor. Biol. 71, 49 (1978).
[5] C. Tanford, *The Hydrophobic Effect. Formation of Micelles and Biological Membranes*, 2nd ed. (Wiley, New York, 1980).
[6] S. Scheiner. Acc. Chem. Res. 18, 174 (1985).

[7] S. Sheiner, P. Redfern, and M. M. Szczesniak, J. Phys. Chem. **89**, 262 (1985).

[8] Y. Taniguchi and F. J. Mata-Segreda, Chem. Express (Japan) **1**, 535 (1986).

[9] L. J. Kurnig and S. Scheiner, Int. J. Quantum Chem., Quantum Biol. Symp. **13**, 71 (1986); S. Scheiner and T. Das, Int. J. Quantum Chem., **15**, 137 (1988).

[10] J. F. Mata-Segreda, J. Am. Chem. Soc. **110**, 6224 (1988).

[11] K. J. Laider, *Chemical Kinetics*, 3rd ed. (McGraw-Hill, New York, 1987).

[12] A. R. Fersht, *Enzyme Structure and Mechanism*, 2nd ed. (Freeman, San Francisco, 1985).

[13] J. L. Esquivel and J. F. Mata-Segreda, Int. J. Quantum Chem. **38**, 521 (1990), and references therein.

[14] P. O. Löwdin, Adv. Quantum Chem. **2**, 276 (1965).

[15] G. M. Barrow, *Química Física*, Ed. Reverté, Barcelona, 1964.

Calculation of Barriers to Proton Transfer Using a Variety of Electron Correlation Methods

KARL LUTH and STEVE SCHEINER

Department of Chemistry and Biochemistry, Southern Illinois University, Carbondale, Illinois 62901

Abstract

The usefulness of various combinations of MCSCF and CI methods in computing correlated proton transfer potentials is investigated for the systems, HF_2^-, $H_5N_2^+$, $H_5O_2^+$, and $H_3O_2^-$. MCSCF calculations can accurately determine proton transfer barriers, provided the correlation is limited to the proton transfer process. The proper correlated space can be obtained more easily if the canonical occupied MOs are first subjected to a localization. Various means are tested of including additional electron correlation into the MCSCF methods. CIS and CISD calculations are performed following MCSCF expansion of the wave function using various different MCSCF reference wave functions. The MCSCF + CISD results are excellent, being fairly independent of choice of virtual MOs, although it is important that the occupied orbitals be balanced between the donor and acceptor. Localizing the occupied MOs prior to the MCSCF part of the calculation again results in a further improvement. These results are compared to CI computations using the canonical orbitals (and which are not preceded by MCSCF preparation of the wave function) and to Møller–Plesset results. © 1992 John Wiley & Sons, Inc.

Introduction

Because of its fundamental nature and its prevalence in various important chemical and biological reactions, the proton transfer process has been the focus of increasing attention [1–5]. A number of *ab initio* quantum chemical calculations have been addressed to evaluation of the potential energy surface for the transfer of a proton from one molecule to another across a preexisting hydrogen bond. Past work has indicated that electron correlation introduces significant perturbations into the Hartree–Fock (HF) potentials [6–16]. The majority of correlated studies of proton transfers have utilized the Møller–Plesset (MP) perturbation technique [6–11]; other methods investigated have included coupled cluster and configuration interaction [12–16]. Common to all of these approaches is the assumption that a single electron configuration can serve as an adequate reference state. While such an approach may not be wise if the proton were required to transfer a long distance, it is considered quite satisfactory for H-bonded complexes, wherein the two subsystems are within 3 Å or so of one another, an assumption which has been verified for a number of systems [17–19].

The central objective of this communication is an analysis of the possibility of using multiconfiguration SCF methods to calculate proton transfer potentials, including electron correlation, in an efficient and accurate manner [20]. A prime drawback of MCSCF is the necessity to make an arbitrary choice as to which molecular

orbitals to include in the expansion. Hence, this work includes an examination of the effects upon the correlated wavefunction of including various combinations of orbitals in the MCSCF expansion. The proton transfer barrier will then be determined using the combinations which best represent correlating the proton transfer. A multiconfiguration method yields a certain fraction of the total correlation energy; the remainder may be recovered by a configuration interaction approach. Therefore, singles and singles + doubles configuration interaction calculations, taking as a reference point the multiple determinant solution obtained by the MCSCF method, are tested as well. In addition, the differences between using multiconfiguration and single configuration reference wave functions are explored by comparison with the results of a single reference CI study.

A standard HF calculation yields canonical molecular orbitals which are delocalized over the entire complex. These MOs can be transformed by a localization procedure into a set of orbitals which are much more concentrated in one region or another of the system. The concentrated nature of these orbitals should allow a more complete treatment of interactions deemed important with a minimum number of orbitals in the expansion. Another question considered is whether such a localization does in fact offer a superior framework for the MCSCF machinery, for both the situation when a subsequent CI calculation is performed and when one is not. For example, can the MCSCF procedure be accomplished more efficiently using the localized MOs representing the A — H bond and the Y lone pair, as compared to a larger number of delocalized MOs?

The final question that this communication addresses is the effect of increasing the proton transfer distance. What is the maximum H-bond length, beyond which each type of method yields unreliable results?

Computational Details

Most of the calculations discussed here were performed using the General Atomic and Molecular Electronic Structure System (GAMESS) [21]. All calculations were performed using the split valence 4-31G basis [22]. The primary focus of this work concerns the multi-configuration self-consistent-field (MCSCF) [23] and configuration interaction (CI) methods [24], as implemented in GAMESS. The full optimized reaction space (FORS) approach is used for the MCSCF portion of the calculations. FORS includes all possible combinations of electron excitations from the chosen occupied orbitals to the chosen virtual orbitals. As a result, the number of configurations included in the calculation rises dramatically with increase in the number of orbitals chosen. Our version and implementation of GAMESS allows approximately 10 orbitals to be included in the reaction space.

MCSCF FORS wave functions are computed and used as beginning wave functions for CI expansions, which involve all virtual orbitals that are not included in the MCSCF active space. The CI portion represents a complete active space (CAS) calculation [24]. The CI calculations include all single and single + double excitations, CIS and CISD, respectively, from the MCSCF reference wave function into the remaining virtual orbitals. The CAS CI calculations add a large number of configu-

rations to the already extensive MCSCF calculations, thus the maximum size of the MCSCF-active space is reduced to four or possibly six orbitals depending upon the particular system.

Localizations were carried out using the Boys criteria [25], as implemented in the program. The occupied LMOs were then substituted for the canonical orbitals in the MCSCF-FORS calculation. GAUSSIAN-88 [26] was used to carry out the Møller–Plesset (MP) calculations.

The energy barrier for proton transfer is investigated for four symmetrical H-bonded complexes, HF_2^-, $H_7N_2^+$, $H_3O_2^-$, and $H_5O_2^+$. The transfer barrier is evaluated as the difference in energy between the midpoint of the transfer and the starting or ending point (equivalent due to the symmetry). The rigid molecule approximation is applied so that only the central hydrogen atom is allowed to move during the transfer. All other bond angles and lengths remain constant throughout the transfer. Previous studies have indicated that this is a reasonable approximation for these systems [27–29]. The midpoint structure is that in which the central hydrogen atom is placed halfway along the F — F, O — O, or N — N vector. For the endpoint structure, the distance of the bridging hydrogen from the donor atom, along the same axis, is determined by a SCF/6-311G** optimization. H_c is used to designate the central hydrogen undergoing the transfer while the terminal hydrogens are denoted H_t.

The following geometrical parameters were used to construct the complexes. For HF_2^-, the F — F distance was set equal to the observed value of 2.28 Å [30], resulting in a midpoint F — H_c distance of 1.14 Å. The optimized endpoint structure is somewhat arbitrary for this complex, since the potential contains only a single and symmetric minimum. The optimized hydrogen position for the starting point was arbitrarily set slightly closer to one of the fluorines, at a distance of 1.113 Å (the transfer potential is extremely flat for longer distances). The midpoint structure has $D_{\infty h}$ symmetry, while that of the endpoint is $C_{\infty v}$.

The geometry around each nitrogen atom of $H_7N_2^+$ is tetrahedral with $r(NH)$ equal to 1.00 Å. The two tetrahedra are staggered with $R(N — N) = 2.95$ Å. The N — H_c distances are 1.475 Å and 1.043 Å in the mid- and endpoint structures, respectively. The symmetry of the midpoint is D_{3d} and the endpoint is C_{3v}.

The length of the bond between the oxygen and each terminal hydrogen (H_t) in $H_3O_2^-$ is 0.957 Å, and each O — H_t bond makes an angle of 104.5° with the O — O axis; the two terminal hydrogens are in a *trans* arrangement with respect to the O — O axis. The oxygen atoms are separated by 2.74 Å, with $r(OH)$ equal to 0.997 Å in the endpoint structure. Even though the midpoint structure is formally of C_{2h} symmetry, the calculations were limited to C_s. The endpoint structure has C_s symmetry.

In each OH_2 subunit of $H_5O_2^+$, the O — H_t distances are 0.957 Å and the H_tOH_t angle 104.5°. The HOH bisectors are disposed 120° from the O — O axis, *trans* to one another. The O — O distance is again 2.74 Å. The distance from the nearest oxygen to the central hydrogen is 1.012 Å in the starting structure. The symmetries are C_{2h} and C_s for the mid- and endpoint structures, respectively. As with $H_3O_2^-$, only C_s symmetry is explicitly used in the calculations.

SCF and MP Calculations

The 4-31G basis set was used for all calculations. Of course, the results with this basis set cannot be taken as definitive values of the transfer barriers, but the spirit of this study is directed more along the lines of examining the merit of each individual computational method rather than determination of a precise barrier of experimental quality. In that vein, the specific basis set choice is less critical than the consistency and reproducibility of the calculated barriers. As a yardstick of the accuracy of a given calculation, comparisons can be made of the calculated barriers with those found using other methods. Table I reports the barriers computed for each system at the SCF level with the 4-31G basis set as well as the results at various levels of MP perturbation theory. The negative barriers listed for FHF refer to the greater stability of the midpoint than of the somewhat arbitrary endpoint, since the transfer potential of this system contains a single symmetric well. The trend observed in each case is that MP2 lowers the barrier quite substantially relative to SCF. It is raised a bit by MP3 but lowered again at the MP4 level, all in accord with trends noted previously [16,18,19]. The data using the larger 6-311G** basis set are included to indicate how changing the size of the basis affects the calculated proton transfer barrier at various levels of correlation. In the following, we will consider the MP4/4-31G results as a sort of benchmark by which to judge the accuracy of the various calculations, also based on 4-31G.

Before discussing the various methods investigated, the SCF orbitals will be summarized. The systems investigated here are isoelectronic, each having 10 occupied orbitals. The MOs in the midpoint geometry represent either symmetric or antisymmetric combinations of the two subunits, with equal weight. The MOs are considerably more localized in the endpoint configurations, where each orbital pair consists of two similar orbitals, one located primarily on each subunit. The first two MOs are composed of the $1s$ orbitals on the first-row atoms, leaving eight valence orbitals. The third and fourth MOs are similar in character except they involve the $2s$ rather than $1s$ functions of F, O, or N, and the terminal hydrogens. The symmetric MO of this pair also contains a certain contribution from the central hydrogen. The next six MOs incorporate primarily the p orbitals of the first-row atoms and terminal hydrogens where symmetry-allowed.

TABLE I.   SCF And Møller–Plesset proton transfer barriers (kcal/mol).

	Basic set	SCF	MP2	MP3	MP4
HF$_2$	4-31G	−0.059	−0.105	−0.092	−0.077
H$_2$N$_2$	4-31G	11.15	5.61	6.94	5.96
H$_3$O$_2$	4-31G	6.71	0.54	2.42	1.16
H$_5$O$_2$	4-31G	6.24	0.94	2.57	1.52
H$_5$O$_2$	6-311G**	10.00	4.45	6.10	4.33

MCSCF Calculations

A prime issue with the MCSCF approach is proper selection of a small number of orbitals to include in the expansion. A straightforward initial approach is to include the bonding and corresponding antibonding orbitals of what are deemed the most important interactions. Since it is the motion of the bridging hydrogen which is under study, the orbitals' importance will be analyzed in terms of their interaction with this center. The situation is complicated in that one desires to ensure that the orbitals used for the end and midpoint geometries are comparable, if not identical. If this is not achieved, the energy of one structure will be artificially lowered with respect to the other.

One might reasonably suppose that only orbitals which contain a significant contribution from orbitals of the central hydrogen (i.e., "interact" with H) need be included in a MCSCF evaluation of the transfer barrier. This assertion was tested by performing three types of calculations. A first group of orbitals to include in the excitation procedure is a partial set of those which cannot interact with H. A second choice involves a more complete set of noninteracting orbitals, viz., all of the noninteracting occupied orbitals and their corresponding virtual MOs. A third choice builds on the second in that, in addition to a complete sample of noninteracting orbitals, one includes occupied or virtual orbitals that may interact.

Since the basis of the central hydrogen consists entirely of s orbitals within the context of the 4-31G basis set, H can participate (in the midpoint geometry) only in MOs which are symmetric with respect to a plane perpendicular to the H-bond axis. Additional orbitals are able to interact in the case of the endpoint due to its lower symmetry. As both HF and H-N contain an axis of symmetry coincident with the N-H-N axis, only the molecular orbitals consisting primarily of the atomic F and N 2s and 2p orbitals, of σ or a-type symmetry, are able to interact with the central hydrogen. The orbitals containing the F and N $2p_x$ and $2p_y$ atomic orbitals are orthogonal to this axis and belong to the π or e-symmetry designations and, hence, cannot interact with the central hydrogen. In contrast, the O——H——O axis of H_2O and H_2O is not a proper rotation axis. There is, however, a symmetry plane which contains the O——H——O line as well as the terminal hydrogens in H_2O; it bisects the H——O——H angles in H_2O. The six 2s, $2p_x$, and $2p_y$ orbitals contained in this plane can interact with the central hydrogen, while the two $2p_z$ orbitals perpendicular to this plane cannot. In these systems, it is the a'' orbitals which are prohibited from interacting with the central hydrogen while interaction with a' is allowed.

The results of a series of MCSCF calculations involving noninteracting orbitals are listed in Table II. For both HF and H-N, when one of the two occupied π (or e) pairs of orbitals is included along with one of the virtual pairs (the first row for each complex), the barriers are quite high, well above the SCF value. This result reflects a strong imbalance, especially for HF, since the SCF data indicate a single symmetric minimum in which a central position of the proton is favored. That is, the barrier computed as the energy difference between the two proton positions should yield a negative barrier, a result confirmed by Table I. The second rows

TABLE II. Calculated proton transfer barriers (kcal/mol) using MCSCF.

	Occupied orbitals[a]	Virtual orbitals[a]	E
HF$_2$	$1\pi_{u}1\pi_{u}$	$2\pi_{u}2\pi_{u}$	18.46
	$1\pi_{u}1\pi_{u}1\pi_{g}1\pi_{g}$	$2\pi_{u}2\pi_{u}2\pi_{g}2\pi_{g}$	0.06
	$1\pi_{u}1\pi_{u}1\pi_{g}1\pi_{g}3\sigma_{g}3\sigma_{u}$	$2\pi_{u}2\pi_{u}2\pi_{g}2\pi_{g}$	0.06
H$_2$N$_2$	$1e_{u}1e_{u}$	$2e_{u}2e_{u}$	26.93
	$1e_{u}1e_{u}1e_{g}1e_{g}$	$2e_{u}2e_{u}2e_{g}2e_{g}$	11.04
	$1e_{u}1e_{u}1e_{g}1e_{g}$	$2e_{u}2e_{u}2e_{g}2e_{g}4a_{2u}4a_{1g}$	11.05
H$_3$O$_2$	$1a''2a''$	$3a''$	10.46
	$1a''2a''$	$3a''4a''$	6.67
	$1a''2a''$	$9a''10a''11a''12a''13a''14a''$	6.82
H$_5$O$_2$	$1a''2a''$	$3a''$	11.52
	$1a''2a''$	$3a''4a''$	6.17
	$1a''2a''$	$3a''4a''9a''10a''$	6.16

[a] Symmetry designations correspond to the midpoint structure.

illustrate the effects of adding another pair of occupied and virtual π or e MOs to the set, resulting in a complete treatment of the noninteracting orbitals. The results are barriers within 0.1 kcal/mol of the SCF value. The third rows reveal that the addition of either occupied or virtual σ or a-type MOs, which can interact with the central hydrogen, have no further effect on the calculated proton transfer barrier.

The situation for the oxygen-containing systems is somewhat different in that there are only two occupied a'' MOs prohibited by their symmetry from interacting with the central hydrogen. Taking these two and adding one a'' virtual produces a rather high barrier, as in the first calculations for H$_3$O$_2$ and H$_5$O$_2$. Adding a second vacant a'' reduces the barrier to within 0.1 kcal/mol of the SCF value in either case. This barrier undergoes very little change thereafter, whether more vacant a'' MOs are added or if the vacant list includes a' MOs.

The high barriers for the first calculation on each system can be attributed to a preferential stabilization by the MCSCF procedure of the endpoint of the transfer in comparison to the midpoint. This preference may be associated with the change in character of the individual MOs as the proton is transferred. For instance, the $1\pi_{u}$ and $1\pi_{u}$ MOs of HF$_2$ distribute themselves evenly among all four atomic p_x and p_y orbitals in the midpoint structure, while in the endpoint structure they are concentrated on the p orbitals of the proton donor atom. Excitation from these MOs will therefore be similarly concentrated on the donor atom in the endpoint structure in comparison to the midpoint. However, the $(1\pi_{gx}, 1\pi_{gy})$ pair undergoes a reverse polarization in which density accumulates on the acceptor rather than the donor. Combination of the latter pair with $(1\pi_{ux}, 1\pi_{uy})$ can offer a more balanced framework. Indeed, use of both pairs in the excitation list, along with the four corresponding virtual MOs, does result in much lower barriers, near the SCF value. The same situation applies to H$_2$N$_2$ where the $(1e_{ux}, 1e_{uy})$ pair must be combined

with ($1 e_{xx}$, $1 e_{ya}$) to achieve the necessary balance. Similar conclusions are reached for H_3O_2 and H_5O_2 where balance requires $1a''$ and $2a''$ as occupied MOs (coupled with appropriate virtual pairs).

In total then, when a complete treatment of orbitals that are not symmetrically disposed to interact with the transferring hydrogen is utilized, the single-configuration SCF barrier is obtained, indicating that the hydrogen position does not affect the amount of correlation resulting from these orbitals and does not aid in incorporation of electron correlation into the proton transfer barriers. As a result, they need not be included in the allowed excitations of these calculations. However, if an incomplete treatment is used, one obtains rather erratic results. The barriers are considerably higher than better-correlated calculations would indicate and even higher than the uncorrelated SCF results. Thus, these interactions must be either completely included or completely excluded from the correlated space.

We now shift our attention to those orbitals which may interact directly with the central hydrogen. Initially, it should be noted that previous results indicate that the occupied orbitals included in the MCSCF active space must be balanced with respect to the donor and acceptor atoms to achieve reasonable results, especially for interacting orbitals [20]. As a result, only orbital combinations previously found to be balanced will be included in this study. In principle, the MCSCF results will depend only on the number of occupied and virtual orbitals of each symmetry that are included in the active space. Since only orbitals that can interact with the transferring hydrogen need be considered, the remaining procedure seems straightforward; i.e., to merely include the desired number of these orbitals. Unfortunately, that is not the case for these systems. Even though the remaining orbitals have the proper symmetry, it is not certain that they will lead to the desired correlated space. In actuality, several different correlated spaces, many containing lone pair or H_t contributions, can result. Each different correlated space represents a different local minimum. The desired minimum contains the maximum amount of proton transfer correlation with a minimal interaction with the terminal hydrogens and lone pairs. It should be stressed that the desired correlated space is not the lowest in energy because while including correlation from the other interactions may lower the calculated energy substantially, those interactions are not relevant to the proton transfer process.

The interactions that are included in the correlated space can be determined by investigation of the multiconfigurational Hartree–Fock (MCHF) natural orbitals that result from the MCSCF procedure. Terminal hydrogen incorporation is determined by inspection of the coefficients of the MCHF natural orbitals, particularly those with small occupations. The H_t interaction is considered significant if any H_t atomic orbital coefficient in these orbitals is greater than 0.1. It is more difficult to ascertain the extent of lone pair correlation. Each situation must be evaluated independently; however, the simplest method of assuring exclusion of lone pair correlation is to minimize the lone pair character of the occupied orbitals that are included in the MCSCF active space. For each of the complexes studied, the energies and resulting proton transfer barriers from the best MCSCF calculations, using the above criteria for isolating the proton transfer correlation, are listed for a variety

of active space sizes in Table III. The particular combinations of orbitals that need to be included in the MCSCF active space to produce the desired correlated space is discussed in detail in a separate communication [20].

Considering HF₂, the reader should first be reminded that since the transfer potential is of the symmetric single well type, the true barrier calculated in this way should be negative. However, only when two occupied and four virtual orbitals are included in the MCSCF active space is a negative barrier produced. Overall, the barriers calculated for HF₂ are exceptionally erratic. The difficulty in producing a consistent barrier for this complex is not surprising, since each fluorine contains three lone pairs and the symmetric combination of each fluorine's lone pairs is of the proper symmetry to interact with H_s. At the SCF level, the F-H interaction and the symmetric lone pair combination mix to form four occupied orbitals, effectively preventing the separation of the occupied interactions into lone pair and H_s, and resulting in an unsuccessful MCSCF treatment of the proton transfer correlation.

One might envision that MCSCF calculations on H_3N_2 would have problems similar to those for HF₂, because each lone pair can be considered to be replaced by a terminal hydrogen, allowing the symmetric combination to again interact with the proton transfer correlation. The results shown in Table III indicate otherwise. The calculated barriers are reasonable, being consistently midway between the SCF and MP values. Also, the barrier decreases when the correlated space is increased by addition of a third virtual orbital. A subsequent addition has only a small effect because the interaction is sufficiently handled with three virtuals. The barrier calculated using the four appropriate occupied orbitals is somewhat larger due to slight H_t correlation. The results for these complexes differ, because for H_3N_2 the terminal hydrogen interaction can be eliminated by carefully including in the active space only virtual orbitals which have no terminal hydrogen character, thus preventing

TABLE III. Calculated energies (Hartree) and proton transfer barriers (kcal/mol) using MCSCF.

	No. of occupied	No. of virtual	Midpoint energy	Endpoint energy	E^*
HF₂	2	2	199.2566214	199.2695203	8.09
	2	3	199.2569203	199.2720789	9.51
	2	4	199.2726318	199.2725029	0.07
	4	2	199.2625744	199.2694236	4.30
	4	3	199.2655946	199.2863384	13.02
	4	4	199.2880622	199.3026639	9.16
H_3N_2	2	2	112.6253642	112.6390208	8.57
	2	3	112.6285535	112.6415028	8.13
	2	4	112.6289239	112.6419400	8.17
	4	2	112.6256970	112.6397848	8.84
H_3O_2	2	2	151.2247169	151.2310205	3.96
H_5O_2	2	2	152.1658668	152.1724891	4.16
	2	4	152.1686901	152.1747244	3.79

any correlation of this type. On the other hand, this prescription is not feasible for HF$_2^-$, because the lone pair character cannot be effectively eliminated from either the occupied or virtual orbitals.

For the oxygen-containing complexes the decisions concerning which orbitals to include are slightly more complicated. It is not sufficient to simply choose virtuals that do not have terminal hydrogen character; one must also examine the relative proportion of O$_\sigma$ and O$_n$ in the orbitals. Since the proton transfer occurs along the y-axis, the O$_n$ orbitals are central to the transfer. However, the terminal hydrogens interact with the oxygen via a hybridization of the O$_\sigma$ and O$_n$ orbitals. As a result, significant virtual O$_n$ character will yield unproductive correlation even without any direct H$_t$ contribution to the virtual orbital.

For H$_3$O$_2^-$ there are only three appropriate virtual orbitals. If all three are included in the active space, substantial H$_t$ correlation results. Also, slight H$_t$ correlation is introduced when only two of the virtuals are included. Fortunately, the amount of H$_t$ correlation incorporated is equivalent in both structures, based on the H$_t$ coefficients (largest is 0.14) and occupancy (0.0073) of the natural orbital. The barrier calculated in this case is 3.96 kcal/mol, which is again between the SCF and MP results. For H$_5$O$_2^+$ more appropriate virtuals are available and either two or four virtual orbitals can be included in the active space without incorporating significant O$_n$ and H$_t$ character. The barriers calculated are 4.16 and 3.79 kcal/mol for two and four virtuals, respectively. These values are satisfactory, being slightly larger than those for H$_3$O$_2^-$, as seen for the MP results as well. In addition, as with H$_3$N$_2^+$ the barrier decreases by approximately 0.4 kcal/mol when flexibility is added by increasing the size of the active space.

Overall, the correlated space, and thus the quality, of an MCSCF calculation is highly sensitive to the choice of orbitals that are included in the active space. When the correlation is limited to the proton transfer process, consistent results are obtained, provided there is a proper balance between the donor and acceptor. Otherwise, the barriers are inconsistent and unreliable. Our results indicate that only orbitals which are allowed by symmetry to interact with the transferring hydrogen need be included in the MCSCF active space. However, not all orbitals with the proper symmetry lead to the correct correlated space. Care must be taken to exclude those orbitals, either occupied or virtual, that can introduce interactions other than those pertaining directly to the proton transfer. Using virtual orbitals in addition to one appropriate antibonding counterpart of each occupied orbital lowers the barrier by allowing more correlation to occur without introducing new types of correlation. Finally, it should be noted that it can be extremely difficult to determine whether a given set of orbitals will generate the desired correlated space without performing the calculation. This observation limits the general usefulness of this approach because additional calculations must be performed to guarantee the quality of the results.

Localized MCSCF

The localization procedure changes the character of the occupied orbitals such that each MO corresponds to a distinct bonding or lone pair orbital. For both the end and midpoint geometries of HF$_2^-$, localization produces a core orbital, one

F—H bonding orbital and three lone pairs for each F atom. The four F-centered orbitals are arranged tetrahedrally, relative to the F—H bond lying along the F—H—F axis. The localized oxygen and nitrogen orbitals in the other complexes adopt the same spatial arrangement. The localized orbitals no longer belong to irreducible representations of the point group of the complex, preventing symmetry from being used in the calculation. Although the loss of symmetry may seem to create a problem in choosing the orbitals to include, it does not. Only the occupied orbitals which consist of the O, N, or F interaction with the transferring hydrogen need be included. For the virtuals, the decision process, as described for the canonical occupied orbitals, must still be used to choose the best combinations.

The data pertaining to the desired correlated space obtained using localized molecular orbitals in the MCSCF active space are listed in Table IV. It is immediately evident that localization produces a dramatic improvement for HF_2. Whereas the canonical MOs failed to yield consistent barriers since only one combination gave the correct sign, quite good results are obtained using occupied LMOs. With two vacant orbitals a barrier of -0.07 kcal/mol is obtained. Each additional virtual MO included in the active space raises the barrier very slightly. The values are in excellent agreement with the MP barriers in Table I. These results confirm that the difficulty in producing acceptable values with the canonical orbitals is due to the contribution of the fluorine lone pairs in the occupied orbitals.

The results for $H-N_2$ computed using the two N—H$_t$ orbitals are virtually identical to those obtained with the canonical orbitals. The only difference is in the case with two occupied and four virtual orbitals where the barrier changes from 8.17 to 8.13 kcal/mol. This difference is due to a very slight decrease in the H$_t$ contribution to the correlation. For both H_3O_2 and H_5O_2 only the two O—H$_t$ localized orbitals were included in the MCSCF active space. In each case, the results are again nearly identical to those obtained using the canonical orbitals. The one exception is that reasonable natural orbitals can be obtained using four virtuals for H_3O_2 as compared

TABLE IV. Calculated energies (Hartree) and proton transfer barriers (kcal/mol) using MCSCF and localized occupied orbitals.

	No. of occupied	No. of virtual	Midpoint energy	Endpoint energy	$E^\ddagger$
HF_2	2	2	199.2696379	199.2695203	0.0738
	2	3	199.2722054	199.2720789	0.0794
	2	4	199.2726318	199.2725035	0.0805
	2	6	199.2733423	199.2732119	0.0818
$H-N_2$	2	2	112.6253642	112.6390208	8.57
	2	3	112.6285535	112.6415038	8.13
	2	4	112.6289767	112.6419410	8.13
H_3O_2	2	2	151.2247169	151.2310205	3.96
	2	4	151.2283470	151.2338450	3.45
H_5O_2	2	2	152.1658668	152.1724891	4.16
	2	4	152.1686901	152.1747249	3.79

to a maximum of two with the canonical orbitals. There remains some H interaction, but it is still equivalent for both structures and thus does not affect the calculated barrier. The trend of reducing the calculated barrier for H-N and H-O by approximately 0.4 kcal/mol by increasing the size of the active space holds true for this complex as well.

Overall, the MCSCF results using localized occupied MOs are encouraging. In principle, the correlated space should not depend on the actual characteristics of the occupied orbitals included in the active space, but should be identical whether they are localized or not. The barriers calculated using localized orbitals are indeed virtually identical to those obtained from the canonical MCSCF calculations, indicating that the canonical calculations did effectively eliminate any lone pair or terminal hydrogen interaction, except for HF. There is an additional advantage created by localizing the occupied orbitals; the character of the virtual orbitals is not as crucial, thus there can be slight contributions from the lone pairs or terminal hydrogens without creating the additional correlation, because those elements do not exist in the occupied orbitals. This also enables calculations to be successfully performed using extra virtual orbitals, which increases the amount of the desired correlation and lowers the calculated barrier.

CI Method

Table V presents the results of CI calculations of the transfer barrier using a single configuration reference. The first two rows of Table V show that when all orbitals of HF are included, a barrier of 0.09 kcal/mol is calculated at either the double or triple excitation level. Removing the core orbitals has no effect on the calculated barriers while eliminating the occupied π orbitals, which are unable to interact directly with the transferring hydrogen, has virtually no effect either. In fact, the only result that differs appreciably is that obtained when only the $(3\sigma, 3\sigma_u)$ pair, composed largely of the $2p_z$ atomic orbitals, is used with double excitations, but this 0.4-kcal difference vanishes when triples are added. The last row demonstrates that including quadruple excitations has no further effect on the energy difference between the end- and midpoints of HF. The CI barriers for HF agree nicely with the correlated values obtained by the alternate Moller–Plesset approach and listed in Table I.

The first few rows for H-N in Table V suggest a barrier of 7.5 kcal/mol, again unchanged by deletion of the core orbitals. This result is some 1.5-kcal higher than the MP4 value, but quite close to MP3. Removing the occupied π (e) orbitals raises the calculated barrier to 7.8 kcal (7.6 for triple excitations). The $2a_{1g}$ and $2a_{2u}$ orbitals are composed primarily of the $2s$ atomic orbitals while the $2p$ orbitals contribute to $3a_{1g}$ and $3a_{2u}$ extensively. Excitation from the latter pair only provides a similar barrier, virtually unaffected by the level of correlation considered. In summary, consistent and accurate barriers may be obtained with even a small number of occupied MOs, provided some care is exercised in their choice.

For H_3O, a doubles calculation using all orbitals, both occupied and virtual, yields a barrier of 2.74 kcal/mol, a result which is again unaffected by neglect of

TABLE V.   Calculated proton transfer barriers (kcal/mol) using CI.

	Occupied orbitals[a]	Virtual orbitals[b]	Ex[c]	E
HF$_2^-$	$1,2,3\sigma_g 1,2,3\sigma_u 1\pi_g 1\pi_g 1\pi_u 1\pi_u$	11–20	2	0.093
	$1,2,3\sigma_g 1,2,3\sigma_u 1\pi_g 1\pi_g 1\pi_u 1\pi_u$	11–20	3	0.093
	$2,3\sigma_g 2,3\sigma_u 1\pi_g 1\pi_g 1\pi_u 1\pi_u$	11–20	2	0.091
	$2,3\sigma_g 2,3\sigma_u 1\pi_g 1\pi_g 1\pi_u 1\pi_u$	11–20	3	0.093
	$2\sigma_g 3\sigma_g 2\sigma_u 3\sigma_u$	11–20	2	0.084
	$2\sigma_g 3\sigma_g 2\sigma_u 3\sigma_u$	11–20	3	0.085
	$3\sigma_g 3\sigma_u$	11–20	2	0.460
	$3\sigma_g 3\sigma_u$	11–20	3	0.084
	$3\sigma_g 3\sigma_u$	11–20	4	0.084
H-N$_2^-$	$1,2,3a_{1g} 1,2,3a_{2u} 1e_g 1e_g 1e_u 1e_u$	11–32	2	7.46
	$2,3a_{1g} 2,3a_{2u} 1e_g 1e_g 1e_u 1e_u$	11–32	2	7.45
	$2a_{1g} 3a_{1g} 2a_{2u} 3a_{2u}$	11–32	2	7.79
	$2a_{1g} 3a_{1g} 2a_{2u} 3a_{2u}$	11–32	3	7.58
	$3a_{1g} 3a_{2u}$	11–32	2	7.83
	$3a_{1g} 3a_{2u}$	11–32	3	7.73
	$3a_{1g} 3a_{2u}$	11–32	4	7.71
H$_3$O$_2^-$	$1,2,3,4,5,6,7,8a' 1,2a''$	11–24	2	2.74
	$3,4,5,6,7,8a' 1,2a''$	11–24	2	2.74
	$5,6,7,8a' 1,2a''$	11–24	2	2.69
	$5,6,7,8a' 1,2a''$	11–24	3	2.32
	$5,6,7,8a'$	11–24	2	2.80
	$5,6,7,8a'$	11–24	3	2.46
H$_3$O$_2^-$	$1,2,3,4,5,6,7,8a' 1,2a''$	11–28	2	2.84
	$3,4,5,6,7,8a' 1,2a''$	11–28	2	2.84
	$5,6,7,8a' 1,2a''$	11–28	2	2.98
	$5,6,7,8a'$	11–28	2	2.88
	$5,6,7,8a'$	11–28	3	2.67
	$5,6a' 1,2a''$	11–28	2	9.90
	$5,6a' 1,2a''$	11–28	3	9.86

[a] Symmetry designations correspond to the midpoint structure.

[b] Virtual orbitals are numbered from lowest energy (11) to highest energy (20, 24, 28, and 32 for HF$_2^-$, H$_3$O$_2^-$, H$_3$O$_2^-$, and H-N$_2^-$, respectively).

[c] Maximum allowed excitation level in the CI expansion.

the core orbitals. The barrier is lowered slightly by removal of the two $2s$ orbitals, but the corresponding triples calculation yields a barrier 0.4 kcal lower. The MP3 barrier for this system is 2.4 kcal/mol, quite close to the 2.3 obtained here with triple excitations in the CI expansion. The occupied a'' orbitals have only a small influence since, when they are removed both the doubles and triples barriers, increase by only 0.1 kcal.

A barrier of 2.84 kcal/mol is calculated for H$_3$O$_2^-$ when all orbitals are included. (Again, the $1s$ core orbitals may be ignored.) Limiting excitations to a' orbitals changes the barrier by only 0.1. The two $2s$-based or the a'' orbitals can also be eliminated at little cost in accuracy and raising the level to triples has minimal

impact as well. The last two rows reveal that unbalanced occupied sets produce overly high barriers, as in all previous studies.

In summary, the CI results reported here are in good coincidence with Moller–Plesset computations with the same basis set, especially MP3. Core orbitals need not be included as the results suffer little deterioration in their absence. However, orbitals of more than one symmetry are often necessary; their importance can be determined in each case by performing a few sample calculations. Increasing the excitation level from two to three lowers the calculated barriers by roughly 0.1–0.3 kcal/mol. An additional but smaller reduction results from inclusion of quadruple excitations. Therefore, calculations limited to doubles can provide an excellent upper bound to the barrier.

MCSCF + CI

In this section, the multiconfigurational wave function obtained from a given collection of occupied and virtual MOs is used as a starting point for a configuration interaction calculation. The important occupied orbitals should be included in the MCSCF active space for maximal flexibility. Therefore, the combinations that were found to be successful in the prior MCSCF calculations will be used here as well. Different combinations are investigated to determine how dependent the MCSCF + CI results are on the quality of the MCSCF reference wave function. The same combinations of occupied and virtual orbitals are used, whenever possible, for both the CIS and CISD calculations so that the effects of changing the excitation level can be evaluated explicitly.

Table VI contains the MCSCF + CI results for HF_2 using two fairly well balanced occupied sets, along with two balanced and one unbalanced virtual set. The $(3\sigma_g, 3\sigma_u)$ set contains the two F $2p_z$ orbitals, and the larger occupied group adds the two F $2s$ orbitals. The negative barriers listed for all six combinations indicate correctly that the midpoint geometry is slightly favored. The values agree nicely with the CI calculations in Table V, indicating that the multiconfigurational nature of the wave function does not perturb the character of the potential. There seems to be little sensitivity to choice of occupied and virtual sets as all barriers are approximately -0.08 kcal/mol. The only exceptions are CIS computations that use an unbalanced set of the virtuals; the barriers here are still negative but probably overly so.

In the case of $H_7N_2^+$, the two occupied combinations are first the two $2p_z$ orbitals and then the four $2s$ and $2p_z$ orbitals. With the $2p_z$ orbitals and the lowest two or three virtual orbitals, the CIS barrier is fairly high but is reduced after including an additional virtual. Similar results are obtained with the $2s$ and $2p_z$ orbitals, except the values are lower. CISD calculations using the $2p_z$ orbitals and either virtual combination yields a barrier of 8 kcal. (The corresponding calculations using the second occupied pair were too large to be performed.) These results indicate good consistency at the CISD level, as compared to much greater sensitivity of barriers to orbital choice for CIS. The CISD barrier of 8 kcal/mol is in accord with the best CI result of some 7.5 in Table V.

The first two sets of occupied orbitals of $H_3O_2^-$ listed are unbalanced. The con-

TABLE VI. Calculated proton transfer barriers (kcal/mol) using CI and a MCSCF reference wavefunction.

	Occupied orbitals[a]	Virtual orbitals[a]	CIS	CISD
HF_2^-	$3\sigma_g 3\sigma_u$	$4\sigma_g 5\sigma_g$	0.0848	0.0817
	$3\sigma_g 3\sigma_u$	$4\sigma_g 5\sigma_g 6\sigma_g$	0.2018	0.0822
	$3\sigma_g 3\sigma_u$	$4\sigma_g 5\sigma_g 6\sigma_g 4\sigma_u$	0.0834	0.0817
	$2\sigma_g 3\sigma_g 2\sigma_u 3\sigma_u$	$4\sigma_g 5\sigma_g$	0.0898	0.0853
	$2\sigma_g 3\sigma_g 2\sigma_u 3\sigma_u$	$4\sigma_g 5\sigma_g 6\sigma_g$	0.6880	0.0852
	$2\sigma_g 3\sigma_g 2\sigma_u 3\sigma_u$	$4\sigma_g 5\sigma_g 6\sigma_g 4\sigma_u$	0.0872	0.0846
$H_3N_2^-$	$3a_{1g} 3a_{2u}$	$4a_{1g} 4a_{2u}$	10.74	8.07
	$3a_{1g} 3a_{2u}$	$4a_{1g} 4a_{2u} 5a_{1g}$	5.74	7.98
	$2a_{1g} 2a_{2u} 3a_{1g} 3a_{2u}$	$4a_{1g} 4a_{2u}$	7.87	
	$2a_{1g} 2a_{2u} 3a_{1g} 3a_{2u}$	$4a_{1g} 4a_{2u} 5a_{1g}$	5.06	
$H_3O_2^-$	$5a'7a'$	$11a'12a'$	13.98	25.81
	$6a'8a'$	$13a'14a'$	10.57	18.77
	$5a'6a'7a'8a'$	$9a'10a'$	3.65	2.21
	$5a'6a'7a'8a'$	$11a'12a'$	0.80	1.86
	$5a'6a'7a'8a'$	$13a'14a'$	3.88	2.11
	$5a'6a'7a'8a'$	$14a'15a'$	4.36	2.39
	$5a'6a'7a'8a'$	$13a'15a'$	10.93	2.54
$H_5O_2^+$	$7a'8a'$	$9a'10a'$	6.12	11.94
	$7a'8a'$	$14a'15a'$	8.19	11.92
	$5a'6a'7a'8a'$	$9a'10a'$	2.23	2.65
	$5a'6a'7a'8a'$	$11a'12a'$	1.64	2.59
	$5a'6a'7a'8a'$	$14a'15a'$	2.90	
	$5a'6a'7a'8a'1a''2a''$	$9a'10a'$	1.74	
	$5a'6a'7a'8a'1a''2a''$	$11a'12a'$	1.01	
	$5a'6a'7a'8a'1a''2a''$	$14a'15a'$	7.16	

[a] Symmetry designations correspond to the midpoint structure.

sequent transfer barriers are quite large. as with all previous unbalanced occupied groups. particularly at the CISD level. Much more reasonable results are obtained for the balanced ($5a'6a'7a'8a'$) quartet of occupied orbitals. Although the CIS barriers are somewhat erratic with respect to choice of virtuals. the data are much more consistent at the singles + doubles level. with barriers all right around 2 kcal/mol. Unlike the CIS case. even the unbalanced ($13a'$, $15a'$) virtual pair produces a value similar to the others. indicating that raising the order of correlation to the doubles can overcome an unbalanced set of virtuals. These CISD barriers following MCSCF are quite similar to the single configuration CI results in Table V. reconfirming that a single configuration is sufficient as a starting point for CI.

The first group of occupied orbitals for $H_5O_2^+$ is not balanced. The second combination of occupied orbitals. which includes all those that can interact directly with the central hydrogen. was not sufficiently balanced for the MCSCF calculations. The third combination adds the oxygen lone pairs. which help balance the orbitals. Three different pairs of virtual orbitals are tested. Two of these pairs ($9a'10a'$) and ($11a'12a'$) are balanced; the third, ($14a'15a'$), is not. At the CIS level. the unbalanced

($7a'8a'$) pair leads to fairly high barriers, which are further elevated using CISD. The imbalance prevents the CISD computations from relieving the problem, similar to $H_3O_2^-$. Results are improved when ($5a'6a'$) are added to the occupied MOs, with barriers calculated in the 2–3 kcal/mol range at either level and with any of the virtual combinations. (The CISD calculation using ($14a'15a'$) would not converge because of the imbalance of the virtual orbitals.) Addition of the $1a''2a''$ oxygen lone pairs reduces the barriers somewhat (although in this case, a high barrier occurs with the unbalanced virtual set). The best quality CISD barriers again are in accord with the CI barrier in Table V, wherein all MOs are included.

Overall, the MCSCF + CI results are quite successful. CIS Results are fairly consistent although, in a couple of instances, the barrier is unreliable because the MCSCF active space is too small for a CI singles calculation to include all of the necessary virtual orbital interactions. The CISD results are excellent. In all cases, the values are nearly independent of the virtual orbitals included, and are comparable to those found using other correlation methods. The method's success is due to the extra configuration interaction compensating for any omission of important orbitals from the MCSCF active space, largely negating the need for balanced virtual orbitals. However, the occupied orbitals must still be balanced or the resulting barriers are unreliable and excessively large. A prior MCSCF does not appear to produce any significant perturbations upon these correlated potentials. In addition, the quality of the MCSCF reference wave function is not especially important in the determination of the transfer barrier.

Localized MCSCF + CI

Localization simplifies the choice of which orbitals to include in the MCSCF expansion and reduces the number necessary. CI makes much less critical the choice of virtuals. Therefore, it was deemed worthwhile to investigate the efficacy of employing both methods simultaneously; the results are reported in Table VII.

Following localization of HF_2^-, the two F—H orbitals were used in the MCSCF expansion. The data suggest very low sensitivity to choice of virtuals. All barriers are correctly negative. Indeed, there is minimal dependence for CIS and no dependence at all for CISD where all values are –0.08 kcal, comparable to the previous results. The CIS results obtained for $H_3O_2^-$ are rather poor, exhibiting a 13-kcal range of barrier relative to choice of virtuals. However, the CISD data are in excellent coincidence, all around 3.2–3.3 kcal/mol. The results for $H_5O_2^+$ and $H_7N_2^+$ are nearly identical to $H_3O_2^-$. CIS yields inconsistent barriers, which are improved by including doubles as well, with barriers of 3.6–3.7 and 8.0–8.1 kcal/mol, respectively. Overall, application of CISD, following localization, provides results that are superior to those obtained by CISD from the canonical MCSCF or by MCSCF from a localized set of occupied MOs.

Distance Dependence

The calculations reported above have each corresponded to a particular fixed H-bond length. It is important to consider also the range of length over which a given

TABLE VII.   Calculated proton transfer barriers (kcal/mol) using CI and a MCSCF reference wavefunction with localized occupied orbitals

	Occupied orbitals	Virtual orbitals[a]	CIS	CISD
HF₂	2 F—H	$4\sigma_g5\sigma_g$	0.085	0.082
	2 F—H	$6\sigma_g4\sigma_u$	0.066	0.081
	2 F—H	$7\sigma_g5\sigma_u$	0.061	0.081
	2 F—H	$4\sigma_g5\sigma_g6\sigma_g4\sigma_u$	0.083	0.082
	2 F—H	$4\sigma_g5\sigma_g7\sigma_g5\sigma_u$	0.081	0.082
	2 F—H	$6\sigma_g7\sigma_g4\sigma_u5\sigma_u$	0.065	0.082
	2 F—H	$2\pi_u2\pi_u2\pi_g2\pi_g$	0.016	0.081
H₂N₂	2 N—H	$4a_{1g}4a_{2u}$	10.99	8.07
	2 N—H	$6a_{1g}5a_{2u}$	9.81	7.98
	2 N—H	$4a_{1g}5cf2a_{1g}4a_{2u}$	5.74	7.98
	2 N—H	$5a_{1g}6a_{1g}5a_{2u}$	7.10	7.97
	2 N—H	$5a_{1g}7a_{1g}6a_{2u}$	8.75	8.03
	2 N—H	$4a_{1g}6a_{1g}4a_{2u}5a_{2u}$	6.80	7.97
	2 N—H	$4a_{1g}7a_{1g}4a_{2u}6a_{2u}$	10.68	8.07
	2 N—H	$4a_{1g}4a_{2u}5a_{2u}6a_{2u}$	12.35	8.05
H₃O₂	2 O—H	$9a'10a'$	6.95	3.28
	2 O—H	$11a'12a'$	0.73	3.17
	2 O—H	$13a'14a'$	6.23	3.34
	2 O—H	$15a'16a'$	5.46	3.29
	2 O—H	$14a'15a'$	6.69	3.31
	2 O—H	$13a'15a'$	12.65	3.34
	2 O—H	$9a'10a'11a'12a'$	3.25	3.15
	2 O—H	$9a'10a'13a'14a'$	-0.60	3.30
	2 O—H	$11a'12a'13a'14a'$	3.39	3.20
H₅O₂	2 O—H	$9a'10a'$	6.12	3.68
	2 O—H	$11a'12a'$	4.06	3.65
	2 O—H	$15a'16a'$	8.91	—
	2 O—H	$9a'10a'11a'12a'$	2.37	3.62
	2 O—H	$9a'10a'15a'16a'$	5.94	3.74

[a] Symmetry designations correspond to the midpoint structure.

theoretical method will be reliable. For example, it is clear that a single determinant would represent a poor starting point for a correlation calculation when the proton is midway between two groups very far apart. In order to investigate this question, a series of calculations on $H_7N_2^+$ is detailed, varying the internuclear N—N distance between 2.95 and 4.5 Å. In the midpoint geometry, H_c was placed equidistant from the two N atoms, as before. The $r(N—H_c)$ distances in all endpoints were taken as 1.043 Å, consistent with the shorter H-bonds above.

The calculations without localization utilized the ($3a_{1g}$, $3a_{2u}$) pair of occupied orbitals. After localization, the two N—H$_c$ orbitals were used. For each of the MCSCF methods, two combinations of virtual orbitals were investigated. The first included the lowest energy pair, and the second added $5a_{1g}$. The CI method included either all doubles or all double and triples. The results are displayed in Table VIII.

TABLE VIII. Calculated proton transfer barriers (kcal/mol) for $H_7N_2^+$ varying N—N distance.

	Occupied[a]	Virtual[a]	2.95	3.25	3.50	3.75	4.00	4.25	4.50
SCF			11.15	25.75	40.10	55.36	70.70	85.55	99.57
MCSCF	$3a_{1g}3a_{2u}$	$4a_{1u}4a_{2u}$	8.57	21.00	33.47	46.95	61.07	74.85	88.00
	$3a_{1g}3a_{2u}$	$4.5a_{1u}4a_{2u}$	8.13		31.41	46.17	58.76	72.89	84.85
Localized MCSCF	2 N—H	$4a_{1u}4a_{2u}$	8.57	21.00	33.47	46.95	60.74	81.70	88.00
	2 N—H	$4.5a_{1u}4a_{2u}$	8.13	20.50	32.85	46.17	59.70	72.89	85.38
MCSCF CISD	$3a_{1g}3a_{2u}$	$4a_{1u}4a_{2u}$	8.07	20.43	32.75	46.07	59.62	72.84	85.36
	$3a_{1g}3a_{2u}$	$4.5a_{1u}4a_{2u}$	7.98	20.38	32.75	46.07	59.62	72.84	85.36
Localized MCSCF CISD	2 N—H	$4a_{1u}4a_{2u}$	8.07	20.43	32.75	46.07	59.62	72.84	85.36
	2 N—H	$4.5a_{1u}4a_{2u}$	7.98	20.38	32.75	46.07	59.62	72.84	85.36
CI	$3a_{1g}3a_{2u}$	Doubles	7.83	20.17	32.50	45.80	59.33	72.58	85.21
	$3a_{1g}3a_{2u}$	Triples	7.73	20.03	32.33	45.58	59.07	72.26	84.80

[a] Symmetry designations correspond to the midpoint structure.

For each R(N—N) distance considered, the SCF barrier is appreciably higher than correlated values, as expected. All of the methods show an extremely similar dependence of the barrier to the transfer distance. For every 0.25-Å increase in the N—N distance, the barrier rises by roughly 12–15 kcal/mol. Most surprising is the insensitivity of the correlated barriers to the particular method employed. Barriers differ very little, regardless of whether calculated by the simple MCSCF scheme, with or without prior localization, whether a standard CI or one using the MCSCF wave function as a starting point.

Conclusions

Although the MCSCF calculations are usually able to calculate consistent proton transfer barriers, results are improved by including combinations of the other methods investigated. Localization of the SCF-occupied orbitals prior to the MCSCF calculation relieves some of the difficulties of choosing the proper orbitals to include in the calculations and allows additional virtuals to be included. The additional virtual orbitals result in more correlation and better barriers. When using Boys-localized orbitals, the calculated barriers are similar to those of other correlation methods. The barriers are approximately −0.80 kcal/mol for HF_2^-, 8.1 for $H_7N_2^+$, 3.4 kcal/mol for $H_5O_2^+$, and 3.8 for $H_3O_2^-$.

More dramatic results are observed when following the MCSCF calculation with CI. When a single electron is allowed to be excited from the MCSCF reference (CIS), the results are improved regardless of the quality of the reference MCSCF calculation, but they are still not completely reliable. Excellent and consistent barriers are obtained when two electrons are allowed to be excited (CISD) from any of the MCSCF reference wave functions studied.

Although both variations offer improved results, they take advantage of different aspects of the MCSCF procedure. The MCSCF + CI calculations alleviate the difficulty in choosing the virtual orbitals needed to produce the desired correlated space by allowing all of the virtuals to interact in some way. However, the overall quality is still extremely sensitive to the occupied orbitals chosen; they must have equal contributions from the donor and acceptor in both end- and midpoint structures. In contrast, the localized MCSCF eliminates some of the uncertainty in choosing occupied orbitals. Only the orbitals involving the transferring hydrogen, usually two of them, need to be included in the MCSCF active space. Therefore, additional virtual orbitals can be included, making it easier to include all important interactions.

Combining the methods resulted in easier choices for both sets of orbitals. The localized MCSCF + CIS results are not a significant improvement over the other methods, but the localized MCSCF + CISD results are comparable or better than either method by itself in terms of both consistency and accuracy of the calculated barriers. The best values obtained in this way are -0.08, 8.02, 3.26, and 3.68 kcal/mol for HF_2^-, $H_7N_2^+$, $H_3O_2^-$, and $H_5O_2^+$, respectively.

The disadvantage of the CISD calculations from an MCSCF reference, either localized or canonical, is that they take significantly more computer time, especially when compared to the single reference CI or MP calculations. For example, a CISD calculation on $H_7N_2^+$ can require an order of magnitude more computer time in comparison to the others. On the other hand, it requires a smaller group of orbitals to achieve consistent results, economizing on computer resources in that way. In addition, the CISD calculation gives a great deal of useful information pertaining to orbital interactions and the contributions of individual configurations that are not available from the Møller–Plesset perturbation data.

One may then conclude that the CISD method, using localized orbitals, is a reliable and cost-effective choice, particularly if analysis in terms of orbital interactions is desirable. MP3 or MP4 calculations are cheaper and may be run on a tighter budget. MCSCF using localized orbitals can be accurate, providing proper care is taken. On the other hand, MCSCF calculations are not the best choice if neither prior localization nor subsequent CI is attempted. MCSCF, followed by CIS, is not recommended either, since much more consistent results can be achieved by increasing the CI to singles and doubles at only a moderate additional effort.

The distance dependence of the proton transfer is handled consistently by all methods. In each case, the calculated proton transfer barrier increases approximately 12–15 kcal/mol for every 0.25-Å increase in the N—N distance, indicating that a single reference wave function can represent a long distance transfer.

Acknowledgment

Bibliography

[1] E. F. Caldin and V. Gold, *Proton Transfer Reactions* (Halsted, New York, 1975).
[2] R. Stewart, *The Proton: Applications to Organic Chemistry* (Academic, Orlando, FL, 1985).

[3] J. A. Dodd, S. Baer, C. R. Moylan, and J. I. Brauman, J. Am. Chem. Soc. 113, 5942 (1991).

[4] M. Meot-Ner, S. C. Smith, J. Am. Chem. Soc. 113, 862 (1991).

[5] D. W. Firth, K. Beyer, M. A. Dvorak, S. W. Reeve, A. Grushow, and K. R. Leopold, J. Chem. Phys. 94, 1812 (1991).

[6] L. Jaroszewski, B. Lesyng, J. J. Tanner, and J. A. McCammon, Chem. Phys. Lett. 175, 282 (1990)

[7] T. N. Truong and J. A. McCammon, J. Am. Chem. Soc. 113, 7504 (1991).

[8] S. P. Gejji, O. E. Taurian, and S. Lunell, J. Phys. Chem. 94, 4449 (1990).

[9] H. Basch and W. J. Stevens, J. Am. Chem. Soc. 113, 95 (1991).

[10] E. Bosch, J. M. Lluch, and J. Bertran, J. Am. Chem. Soc. 112, 3868 (1990).

[11] M. J. Frisch, A. C. Scheiner, H. F. Schaefer, III, and J. S. Binkley, J. Chem. Phys. 82, 4194 (1985).

[12] W. Meyer, W. Jakubetz, and P. Schuster, Chem. Phys. Lett. 21, 97 (1973).

[13] A. Stogård, A. Strich, J. Almlöf, and B. Roos, Chem. Phys. 8, 405 (1975).

[14] B. O. Roos, W. P. Kraemer, and G. H. F. Diercksen, Theor. Chim. Acta 42, 77 (1976).

[15] G. Karlstrom, B. Jönsson, B. Roos, and H. Wennerström, J. Am. Chem. Soc. 98, 6851 (1976).

[16] Z. Latajka and S. Scheiner, J. Mol. Struct. (Theochem) 234, 373 (1991).

[17] S. Scheiner and L. B. Harding, J. Phys. Chem. 87, 1145 (1983).

[18] S. Scheiner, M. M. Szczesniak, and L. D. Bigham, Int. J. Quant. Chem 23, 739 (1983).

[19] M. M. Szczesniak and S. Scheiner, J. Chem. Phys. 77, 4586 (1982).

[20] K. Luth and S. Scheiner, J. Chem. Phys. 97, (in press) (1992).

[21] M. Dupuis, D. Spangler, and J. J. Wendoloski, General Atomic and Molecular Electronic Structure System (National Resource for Computational Chemistry, Lawrence Berkeley Laboratory, Berkeley, CA, 1980) (as modified by M. W. Schmidt, North Dakota State University and S. T. Elbert, Iowa State University).

[22] R. Ditchfield, W. J. Hehre, and J. A. Pople, J. Chem. Phys. 54, 724 (1971); W. J. Hehre, R. Ditchfield, and J. A. Pople, J. Chem. Phys. 56, 2257 (1972); J. B. Collins, P. V. R. Schleyer, J. S. Binkley, and J. A. Pople, J. Phys. Chem. 86, 1529 (1982).

[23] B. O. Roos, in Methods in Computational Molecular Physics, G. H. F. Diercksen and S. Wilson Eds. (D. Reidel Publishing, Dordrecht, The Netherlands, 1983, p. 161; J. Olsen, D. L. Yeager, P. Jorgensen, in Advances in Chemical Physics, I, Prigogine and S. A. Rice, Eds. Wiley Interscience, New York 1983, p. 1; H. -J. Werner and R. Shepard, in Advances in Chemical Physics, K. P. Lawley, Ed. (Wiley Interscience, New York, 1987), pps. 1, 63.

[24] B. Brooks and H. F. Schaefer, J. Chem. Phys. 70, 5092 (1979); B. Brooks, W. Laidig, P. Saxe, N. Handy, and H. F. Schaefer, Physica Scripta 21, 312 (1980).

[25] S. F. Boys, Rev. Mod. Phys. 32, 296 (1960).

[26] M. J. Frisch, M. Head-Gordon, H. B. Schlegel, K. Raghavachari, J. S. Binkley, C. Gonzalez, D. J. Defrees, D. J. Fox, R. A. Whiteside, R. Seeger, C. F. Melius, J. Baker, R. Martin, L. R. Kahn, J. J. P. Stewart, E. M. Fluder, S. Topiol, and J. A. Pople, Gaussian, Inc., Pittsburgh, PA, 1988.

[27] S. Scheiner, Acc. Chem. Res. 18, 174 (1985).

[28] S. Scheiner, J. Am. Chem. Soc. 103, 315 (1981).

[29] S. Scheiner, J. Phys. Chem. 86, 376 (1982).

[30] K. Kawaguchi and E. Hirota, J. Chem. Phys. 84, 2953 (1986); and references therein.

Towards a First-Principles Implementation of Density-Functional Theory at a Metal Surface

A. G. EGUILUZ and J. J. DEISZ

Department of Physics, Montana State University, Bozeman, Montana 59717

M. HEINRICHSMEIER, A. FLESZAR, and W. HANKE

Physikalisches Institut, Universität Würzburg, 8700 Würzburg, Germany

Abstract

The implementation of the density-functional scheme requires the knowledge of the exchange and correlation potential, V_{xc}, as a functional of the electron density. In the local-density approximation (LDA) this potential becomes a function of the local value of the density. This *ansatz* breaks down qualitatively at a surface because of its neglect of long-range electron–electron correlations in the presence of strong charge inhomogeneity. This breakdown is of relevance in the context of various surface spectroscopies. We outline a scheme for going beyond the LDA without invoking gradient expansions. This scheme is based on establishing an interrelation between density-functional theory and many-body perturbation theory. In this scheme V_{xc} is obtainable from the knowledge of the electron self-energy Σ_{xc}. We solve an exact integral equation relating these two quantities for the electron-gas surface with use of the GW approximation for the self-energy. We establish a "nonlocal" relation between V_{xc} and the electron density which allows us to carry out nonlocal density-functional calculations with the same ease as LDA-based calculations. We present results of the first application of our method for the case of Al and Pd surfaces. In addition, we report on work in progress devoted to a detailed comparison of the density-functional and quasiparticle pictures of electronic excitations at a metal surface. © 1992 John Wiley & Sons, Inc.

Introduction

Most first-principles calculations of electronic properties of solids are based on the use of density-functional theory [1,2]. This formulation of the many-body problem provides a universal scheme for treating the effects of Coulomb correlations via the introduction of an exchange and correlation energy functional and associated exchange and correlation potential.

In a solid the electrons are embedded in a periodic ionic background, which makes the system inhomogeneous. The presence of a surface adds a new source of inhomogeneity on a microscopic scale. However, in the implementation of the density-functional scheme, the vast majority of papers have resorted to the use of the local-density approximation (LDA) [1], in which both sources of inhomogeneity are simply ignored in the treatment of the crucial electron–electron interactions. The crudeness of this approximation notwithstanding, it has proved capable of yielding, when used in conjunction with either all-electron schemes or norm-conserving pseudopotentials, accurate values [2] for cohesive energies, lattice param-

eters, and bulk moduli (which are typically obtained to within a few percent of their experimental values).

Because of its neglect of long-range correlations, the LDA gives rise to a surface barrier with a qualitatively incorrect asymptotic behavior, i.e., exponential decay, rather than the expected inverse power law. Until recently this failure of the LDA at a surface was perhaps academic. However, probes such as inverse photoemission [3–6], two-photon photoemission [7–9], the scanning-tunneling microscope [10–15], etc., have recently produced a wealth of data on observables such as binding energies and lifetimes of image potential-bound surface states [3–6,16–23], tunneling currents in the scanning-tunneling microscope [10–15], resonant-tunneling rates for ion-surface collisions [24], etc., whose values are affected by the details of the surface barrier, in particular, by the presence of its image tail.

The physics behind this *qualitative breakdown* of the LDA at a surface is easy to visualize. In a many-electron system a given electron is surrounded by an exchange-correlation hole, which arises by virtue of both Coulomb correlations and the antisymmetry of the many-body states. In the LDA the exchange-correlation hole is spherical, the electron being at its center. This is a good approximation in the bulk (indeed the exchange-correlation hole is spherical for the homogeneous electron gas). Now, as the electron moves outward through the surface, the exchange-correlation hole must progressively distort and lag behind the electron (since the hole must remain in the solid). However, in the LDA the exchange-correlation hole remains spherical, and centered at the position of the electron, as the latter moves out into the vacuum. Hence the LDA entirely misses the key features of the long-range correlation effects which are the origin of the image effects. (It is well known that the LDA yields accurate values for "global" ground state quantities, such as work functions, which are not affected significantly by the presence of the image tail of the surface barrier [2].)

Thus, in the study of various surface phenomena [3–24] the LDA must be superceded by a theory which properly accounts for long-range Coulomb correlation effects and their interplay with the extreme inhomogeneity of the surface environment. The theoretical challenge involved in this endeavor is significant. In particular, the phenomena of interest cannot be addressed by treating the inhomogeneity of the electron system perturbatively (i.e., gradient expansions do not suffice). What is required is an approach in which the basic features of long-range Coulomb correlations and strong charge inhomogeneity are treated from first principles within a consistent diagrammatic approach.

In this article we outline a method which incorporates these physical requirements. The same is based on defining the exchange and correlation potential of density-functional theory, V_{xc}, in terms of the electron self-energy of diagrammatic perturbation theory, Σ_{xc}. An integral equation relating these two quantities is solved exactly for the electron gas–vacuum interface with use of the GW approximation for the self-energy.

From the solution of that integral equation for $V_{xc}(\bar{x})$ we establish a "nonlocal" relation between V_{xc} and the electron density which allows us to perform *nonlocal* density functional calculations with the same relative simplicity as LDA-based cal-

culations. This scheme has been tested so far in calculations of the electronic struc-
ture of low-index surfaces of Al and Pd. Because our method properly accounts
for long-range Coulomb correlations, a Rydberg series of image surface states lying
near the vacuum level is obtained on the same footing with the conventional crystal-
termination surface states. The binding energies of the image states and the associated
effective masses compare favorably with experiment. The image states, and the
physics behind them, are beyond the LDA.

Finally, we present preliminary results of a comparison of the density-functional
and quasiparticle pictures of electronic excitations at metal surfaces. This comparison
is based on a joint analysis of V_{xc} and Σ_{xc}, and of density-functional and quasiparticle
wave functions. We find that once the main effects of the long-range electron
correlations are incorporated into V_{xc}, this local potential becomes a fair approx-
imation to the real part of the electron self-energy for low frequencies. On the other
hand, the imaginary part of the self-energy, which is related to the damping of the
quasiparticle states, has no counterpart in density-functional theory. We show that
Im Σ_{xc} is highly nonlocal in the surface region. This intrinsic feature of electron
propagation near a surface has yet to be implemented into the optical potentials
used in state-of-the art multiple scattering calculations [25].

Evaluation of the Exchange and Correlation Potential at a Metal Surface From the Knowledge of the Electron Self-Energy

Density-functional theory [1,2] provides a formally exact procedure for calculating
the ground state electron density and the total ground state energy of an interacting
many-electron system. In essence this method establishes a rigorous mapping be-
tween the intractable system of 10^{23} interacting electrons and a much simpler system
of noninteracting electrons moving in an appropriate effective potential.

The mathematical framework for this mapping is embodied by the Kohn–Sham
(KS) equation [1]

$$\left[-\frac{\hbar^2}{2m}\nabla^2 + V_{eff}(\vec{x}) \right]\Psi_i(\vec{x}) = E_i\Psi_i(\vec{x}) , \tag{1}$$

where the effective one-electron potential $V_{eff}(\vec{x})$ is defined by the equation

$$V_{eff}(\vec{x}) = V_{es}(\vec{x}) + V_{xc}(\vec{x}) , \tag{2}$$

where $V_{es}(\vec{x})$ is the usual electrostatic potential. All many-body effects enter
Eq. (1) through the exchange and correlation potential $V_{xc}(\vec{x})$, defined by the
equation

$$V_{xc}(\vec{x}) = \frac{\delta E_{xc}[n]}{\delta n(\vec{x})} , \tag{3}$$

where $E_{xc}[n]$ is the exchange and correlation energy functional. Equations (1)–
(3) are to be solved self-consistently with the following one-electron-like equation
for the electron density

$$n(\vec{x}) = \sum_i f_i |\Psi_i(\vec{x})|^2 .$$ (4)

The exact form of the energy functional $E_{xc}[n]$ is unknown. Thus, approximations must be introduced in the treatment of the electron–electron interactions. In the LDA the exchange and correlation energy density at each point of the solid is assumed to be given by that appropriate for a homogeneous electron gas (jellium model) with the local value of the density [1]. This approximation yields a V_{xc} which is a *function of the local value of the density*. Now, from basic quantum-mechanical considerations we know that the electron density decays exponentially outside the surface (tunneling). It then follows immediately that the LDA surface barrier also decays exponentially into the vacuum [26], unlike the expected image-like behavior of the correct surface potential.

As noted in the Introduction, there is significant interest in the study of various electronic processes at surfaces influenced by the presence of the image tail of the actual surface barrier [3–24]. Several models for $E_{xc}[n]$ have been proposed in the literature in order to enforce the presence of an image tail in an *ad hoc* way [27,28]. In our work we take a more fundamental approach, geared towards a first-principles investigation of the joint effects of long-range Coulomb correlations and the rapid rate of change of the electron density at the surface.

Since a suitable functional $E_{xc}[n]$ is not available [29], we do not base our method on the definition of $V_{xc}(\vec{x})$ given by Eq. (3). Rather, we proceed by making use of an interrelation between density-functional theory and many-body perturbation theory which was first established [30] and applied [31] in the context of the band-gap problem in bulk semiconductors, and in the construction of a V_{xc} for the insulating state of matter [32].

Of course, if one had at hand an accurate implementation of diagrammatic perturbation theory for real solids, in particular, near a surface, one could in principle bypass the density-functional scheme altogether (which, as originally formulated, applies for ground-state properties only). However, given the well-established power of this method, which is traced to the relative simplicity of its implementation in terms of a *local* effective potential, it is of interest to obtain a V_{xc} which incorporates long-range correlation effects.

The exact one-electron Green's function of many-body perturbation theory, $g(\vec{x},\vec{x}'|E)$, satisfies the equation [33]

$$[E - h(\vec{x})]g(\vec{x},\vec{x}'|E) - \int d^3x'' \Sigma_{xc}(\vec{x},\vec{x}''|E)g(\vec{x}'',\vec{x}'|E) = \delta(\vec{x} - \vec{x}') .$$ (5)

where $h(\vec{x})$ is the Hartree Hamiltonian

$$h(\vec{x}) = -\frac{\hbar^2}{2m}\nabla^2 + V_{es}(\vec{x}) ,$$ (6)

and $\Sigma_{xc}(\vec{x},\vec{x}'|E)$ is the nonlocal, energy-dependent electron self-energy. The self-energy can be thought of as the true "potential" in which a quasiparticle propagates

(via g), and to which it contributes self-consistently via the exchange-correlation process.

Similarly, we introduce a Green's function for the KS Hamiltonian. $g_0(\vec{x},\vec{x}'|E)$, which corresponds to propagation of what in this article we will refer to as a KS electron [i.e., an "electron" described by a density-functional wave function] in the presence of a local potential, whose many-body part is V_{xc}. The density-functional Green's function obeys the differential equation

$$[E - h(\vec{x}) - V_{xc}(\vec{x})]g_0(\vec{x},\vec{x}'|E) = \delta(\vec{x} - \vec{x}') ,\qquad (7)$$

and is related to the quasiparticle Green's function by the Dyson-like equation (which we write down symbolically)

$$g = g_0 + g_0(\Sigma_{xc} - V_{xc})g.\qquad (8)$$

From Eq. (8) and the requirement that both Green's functions yield the same exact ground-state density, i.e.,

$$n(\vec{x}) = -ig(\vec{x},t|\vec{x},t + 0^+)$$
$$= -ig_0(\vec{x},t|\vec{x},t + 0^+) ,\qquad (9)$$

we are readily led to the following exact integral equation relating V_{xc} and Σ_{xc} [30–32]:

$$\int d^3x_1 V_{xc}(\vec{x}_1) \int dE g_0(\vec{x},\vec{x}_1 | E)g(\vec{x}_1,\vec{x}| E)$$

$$= \int d^3x_1 \int d^3x_2 \int dE g_0(\vec{x},\vec{x}_1 | E)\Sigma_{xc}(\vec{x}_1,\vec{x}_2 | E)g(\vec{x}_2,\vec{x}| E) .\qquad (10)$$

Our approach consists in viewing Eq. (10) as defining V_{xc} in terms of the self-energy Σ_{xc}. By including the effects of long-range Coulomb correlation and the rapid density variation at the surface into the self-energy, these effects find their way into V_{xc} in a fundamental way.

The state-of-the-art in the computation of the electron self-energy in solids [31,34–36] is the GW approximation due to Hedin [33],

$$\Sigma_{xc}(\vec{x}_1,\vec{x}_2 | E) = \frac{i}{2\pi} \int dE' e^{iE'\eta} g(\vec{x}_1,\vec{x}_2 | E + E')W(\vec{x}_1,\vec{x}_2 | E') ,\qquad (11)$$

which is the first term in an expansion of the self-energy in powers of the dynamically screened electron–electron interaction W, defined by the equation (which we write symbolically) [33]

$$W = v + vX_\tau v ,\qquad (12)$$

where v is the bare Coulomb interaction, and X_τ is the time-ordered density-response function. The response function satisfies its own integral equation [37]

$$X_I = \tilde{X} + \tilde{X} v X_I ,$$ (13)

where $\tilde{X}$ is the irreducible polarizability. The physics behind Eq. (12) is the screening of the Coulomb interaction between a pair of electrons embedded in a many-electron system. Similarly, Eq. (13) reflects the self-consistent screening of charge fluctuations induced in an interacting electron system.

In the present work we have set $\tilde{X} = X^0$, where X^0 is the electron-hole pair bubble (i.e., the random-phase approximation for the polarizability). Thus, we ignore, e.g., excitonic effects such as are contained in ladder diagrams [38].

First-Principles Solution for V_{xc} for the Electron Gas-Vacuum Interface

We have solved Eq. (10) for the electron gas-vacuum interface with use of Eq. (11) for the electron self-energy [39]. Our calculations are performed for a slab which is thick enough [four or more Fermi wavelengths] that we have a good representation of the V_{xc} for a semi-infinite medium. The time-ordered response function X_I is expressed in terms of its retarded counterpart X_R via a Lehmann representation [33]. Following standard practice [31], we have set $g_0 = g$ throughout.

It should be noted that Eq. (10) is homogeneous, which makes it very unstable from the numerical viewpoint [40]. Furthermore, its kernel is singular, a reflection of the fact that the electron density drops to zero in the vacuum outside the surface. In addition, we would like to emphasize that:

- Since g_0 depends on the function we seek, i.e., V_{xc}, Eq. (10) poses a self-consistency problem, which we solved by iteration. Wave functions and energy eigenvalues for the computation of updated Σ_{xc} and g_0 are obtained by feeding the solution of Eq. (10) into Eq. (1). Fortunately, one or two iterations suffice.

- X_R is computed self-consistently for a jellium slab; *we do not impose any restrictions on the rate of spatial change of the electron density at the surface* [37].

- The full energy dependence of X_R is kept. We do not introduce a plasmon-pole approximation because the lack of translational invariance in the direction normal to the surface renders Landau damping important even for small wave vectors.

It should be noted that the solution of Eq. (10) for the *homogeneous* electron gas is given by [41]

$$V_{xc} = \Sigma_{xc}(k = k_F; E = E_F) ,$$ (14)

i.e., V_{xc} in the bulk equals the self-energy evaluated at the Fermi surface (where it is real). Equation (14) defines the LDA within the self-energy formalism. The LDA results we compare with below were generated from this (exact) result with use of the bulk GW self-energy [42]; we will refer to this potential as the LDA-GW V_{xc}.

In Figure 1 we show the solution of Eq. (10) for $r_s = 1.5$ [this value of the electron-gas parameter will be of interest below, when we discuss the calculation we have performed for Pd]. The solution to Eq. (10) is compared with the corresponding LDA-GW potential, and with the image potential

$$V_{im}(z) = - \frac{e^2}{4(z - z_0)} ,$$ (15)

SURFACE BARRIER
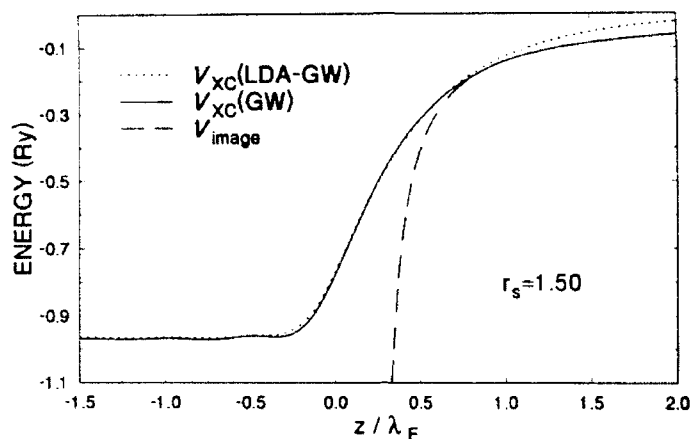## *From GW approximation for the Self-Energy*

Figure 1. V_{xc} at a simple metal surface for $r_s = 1.5$. The solid curve is the solution of Eq. (10) obtained with use of the GW approximation for the self-energy. The dotted curve is the corresponding LDA potential, and the dashed curve is the classical image potential given by Eq. (14).

where z is the coordinate normal to the surface and z_0 is the position of the effective image plane [39,43].

From Figure 1 it is clear that our solution for $V_{xc}(z)$ becomes image-like outside the surface. This is an important improvement over the LDA in the context of experiments which probe various electronic processes whose interpretation is related to the presence of the image tail of the surface barrier [3–24].

The physics of the many-body surface barrier experienced by a KS electron [the solution of Eq. (10)] is quite interesting. As noted elsewhere [39], the classical-image limit of the barrier, $V_{xc}(z) \rightarrow -e^2/4z$ for $z \geq 2\pi/k_F$, is established by virtue of the Coulomb correlation effect present in Σ_{xc}. Thus, this limit is "universal": it is the same for a KS electron and for a classical, distinguishable, test charge.

Our conclusion that the classical-image limit of the surface barrier for a KS electron is a Coulomb-correlation effect confirms by actual computation previous statements by Almbladh and von Barth [44] and Sham [45], but it disagrees with recent conclusions by Harbola and Sahni [46]. [Since the method of the latter authors is formally quite different from ours, the reason for this difference is not entirely apparent.]

In addition, we have also shown [39] that the numerical value of the effective image plane z_0 includes a significant contribution from the exchange process. It is then clear that the image-plane position that governs the surface barrier that self-binds a KS electron necessarily differs from its counterpart for a test charge. In other words, the z_0 for a KS electron is not obtainable via the well-known Lang–Kohn linear-response result [26] which equates the image plane position appropriate

for a test charge with the centroid of the charge induced at the surface by an external, uniform electric field.

The above conclusion (which is of definite importance in surface physics) is corroborated quantitatively by the following example. For $r_s = 2.07$ (corresponding to Al) the image-plane position extracted from the image tail of V_{xc} is $z_0 = 0.72 \pm 0.1$ a.u. (measured from the jellium edge—the origin of coordinates in Fig. 1), while from linear response in LDA-GW we obtain $z_0 = 1.49$ a.u. By comparison, the phenomenological V_{xc} of Ossicini et al. [28] yields $z_0 = 0.85$ a.u. for $r_s = 2.0$, which is rather close to our value. The LDA linear-response value obtained by Lang and Kohn [26], also for $r_s = 2.0$, is $z_0 = 1.60$ a.u.

A Scheme for Performing Nonlocal Density-Functional Calculations for Real Metals

With the solution of Eq. (10) for $V_{xc}(z)$ at hand, we have developed a scheme for performing nonlocal density functional calculations in which long-range electron–electron correlation effects are included from first principles.

Starting from the position of the first Friedel peak of the density, and moving out into the vacuum, we have constructed, by a point-by-point "tabulation" of the solution of Eq. (10) and the electron density n self-consistent with it, a one-to-one relation between V_{xc} and n to be symbolized as $V_{xc}(r_s; n^{1/3})$. [We note that we start from the first Friedel peak in order to make the relation one-to-one.] This relation (illustrated in Fig. 2 for $r_s = 2.07$), derives implicitly from a functional $E_{xc}[n]$ containing the physics of the nonlocal self-energy.

While the ultimate theoretical significance of a relation such as the one represented in Figure 2 remains to be elucidated [this may require the actual determination of
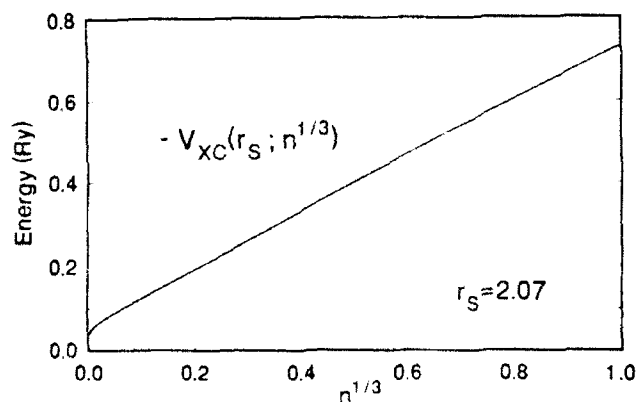

Figure 2. "Nonlocal" relation V_{xc} vs $n^{1/3}$ constructed from the solution of Eq. (10), obtained with use of the GW approximation for the self-energy. The electron number density is normalized to its value at the first Friedel peak inside the jellium: $n = 0$ corresponds to the vacuum. [This relation has been parameterized by the functional form given in Eq. (16).]

the functional $E_{xc}[n]$], the spirit of such a relation is clear: The same $V_{xc}(z)$ shown in Figure 1 [obtained by explicit solution of the integral equation (10)] can now be obtained directly from the self-consistent solution of the KS equation [Eq. (1)] in the presence of our $V_{xc}(r_s; n^{1/3})$ relation, matched to LDA-GW in the vicinity of the first Friedel peak of the density. This represents a major simplification relative to solving Eq. (10). *Thus the integral equation for V_{xc} has in effect been solved once and for all for each value of r_s.* [As Fig. 1 suggests, the precise point where the matching just alluded to is done is not important, since the nonlocal and local potentials are quite close numerically over an appreciable interval.]

A preliminary parameterization of our $V_{xc}(r_s; n^{1/3})$ relation in terms of a simple analytical form is as follows:

$$V_{xc}(r_s; n^{1/3}) = ax^\alpha + bx^\beta, \tag{16}$$

where $x = n^{1/3}$. Interestingly, in the cases we have considered so far [$r_s = 1.5, 2.07,$ and 3.93] the exponent α turns out to be very close to unity, while the other exponent is substantially smaller ($\beta \leq 0.1$). Thus, we interpret Eq. (16) as consisting of an LDA-like term (the first one), with a surface correction (the second term) giving rise to a V_{xc} which "decays" much more slowly than the density.

We would like to stress that while the form given by Eq. (16) has worked very well in the few cases for which it has been tested so far (see below), the same cannot be taken as final at this early stage in the development of our method. It is presented in these Proceedings in the spirit of a report of work in progress; other forms are still being tried, and a larger database over the metallic range of densities must yet be collected and analyzed.

The next step in our program, *which amounts to implementing a recipe à la LDA while incorporating the effects of strong charge inhomogeneity at the surface,* is to use our electron-gas $V_{xc}(r_s; n^{1/3})$ relation for a real metal surface. We turn to discussing that question next.

Image States in Al

The first application of the above method [39] was a nonlocal density-functional calculation of the electronic structure of Al(100), performed by making use of Eq. (16) in the Kohn–Sham scheme defined by Eqs. (1), (2), and (4). In the self-consistency procedure for this three-dimensional calculation, the "nonlocal" V_{xc} is matched to V_{xc} in LDA-GW in the vicinity of the nominal jellium edge. As noted above, the precise point where the matching is done does not affect our results.

Now in the implementation of our scheme an effective value of r_s must be defined. We have adopted the following criterion: We average V_{xc} over the unit cell, and extract a value of r_s from the LDA-GW V_{xc} versus n relation. The three-dimensional surface barrier determined with this criterion joins smoothly with the bulk V_{xc} potential. In the present case we obtain $r_s = 2.07$. [We note that we obtain the same r_s value using other versions of the LDA, such as Ceperley–Alder [42].]

The calculation is performed in a periodic-slab geometry, with use of a plane-wave basis set, and *ab initio* norm-conserving pseudopotentials [47]. Since the

new physics included in our method is related to the existence of image states whose wavefunctions are localized many atomic units outside the surface, a large vacuum gap between consecutive slabs must be utilized. Moreover, in order to separate the members of the Rydberg series of image states, the physical slab must be at least 25 atomic layers thick. Both requirements lead to the use of a very large unit cell.

In Figure 3 we show a weighted density of states (DOS) near the vacuum level, for both nonlocal and LDA calculations. The DOS is defined by the equation

$$\rho(E, k_\parallel) = \sum_i \Omega_i \delta(E - E_i(k_\parallel)), \tag{17}$$

where the weights Ω_i are defined as the ratio of the charge density contained in an appropriate volume of the vacuum gap (chosen such that it encompasses the state under consideration) and the charge density in the whole supercell. Both local and nonlocal calculations give the same results for the conventional crystal-termination surface states. In particular, the energy position of an occupied surface state obtained at $\bar{\Gamma}$ [39] agrees very well with the photoemission data of Levinson et al. [48]. *However, the LDA entirely misses the Rydberg series of image states, as illustrated in Figure 3.*

We note that in Al there is no gap in the projected bulk band structure near the vacuum level. The nonlocal density-functional calculation yields image-like eigenstates over a finite energy range, which accounts for the broad bumps observed in the DOS. These image states correspond to resonances.

Finally, we note that the binding energy of the $n = 1$ resonance compares favorably with the location of the image-state peak (ca. 0.45 eV) in the inverse photoemission data of Heskett et al. for Al(111).
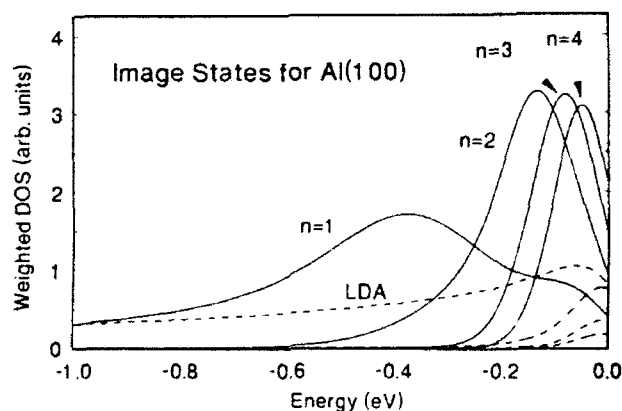

Figure 3.   Weighted density of states near the vacuum level for Al(100), at $\bar{\Gamma}$. The solid curves correspond to the image-state resonances. The dashed curves are the corresponding LDA results. Energies are measured from the vacuum level.

Image States in Pd

A similar calculation has been performed for Pd(111). The main technical difference in relation to the previous case is the use of a mixed basis consisting of plane waves and localized Gaussians. The latter are introduced in order to account for the presence of d-electrons in this transition metal.

The criterion put forth above to define an effective value of r_s yields in this case $r_s = 1.5$. A measure of the reasonableness of this choice is found in the fact that the crystal-termination surface states obtained from our procedure agree very well with those we obtained via a conventional LDA calculation [performed with use of the Ceperley-Alder [42] result for the exchange-correlation energy]. This agreement refers to energies measured from the Fermi level [42].

In Figure 4 we show the surface-projected bulk band structure. The solid lines indicate the surface states which we have identified by inspecting their energy location, appropriate DOS, and the decay of the associated wave functions into the bulk. Both nonlocal and LDA-GW calculations give the same results for the crystal-termination surface states. This is a consequence of the fact that these states are localized enough to the immediate surface region that they do not probe the image tail of the "nonlocal" surface barrier.

In addition, the nonlocal calculation produces a Rydberg series of image states inside the gap spanning the vacuum level. The presence of this gap renders these states true surface states, and not surface resonances, as was the case for Al. For the range of values of the vacuum gap that we have used we have been able to
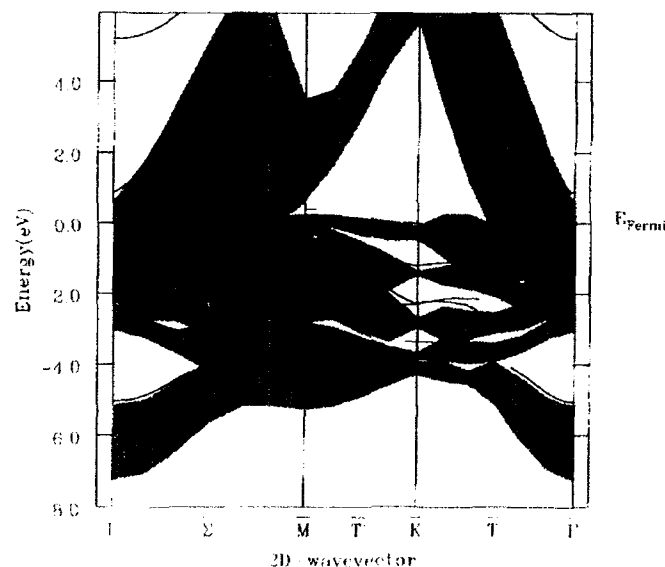

Figure 4. Surface-projected bulk band structure for Pd(111). The solid curves show the surface states. Note, in particular, the $n = 1$ image state in the gap at the vacuum level. Energies are measured from the Fermi level.

separate the $n = 1$ and $n = 2$ members of the Rydberg series; only the $n = 1$ branch is shown in Figure 4. The calculated binding energy at Γ for this state is 0.72 eV, its dispersion with wave vector is free-electron like, with an effective mass of 1.03. For the $n = 2$ state the corresponding binding energy is 0.17 eV, and the effective mass is 1.01.

We are aware of three experimental investigations of the image states of Pd(111) [49,50,51]. The experimental results are summarized in Table I, together with our theoretical results. It is apparent that the binding energy and effective mass for the $n = 1$ state compare quite well with two of the experimental observations [49,50].

Density-Functional and Quasiparticle Pictures of Electron Propagation at a Metal Surface

As noted in the second section, a quasiparticle propagates in the presence of a complex, nonlocal, energy-dependent "potential", the electron self-energy Σ_{xc}. A KS electron, on the other hand, propagates in the presence of V_{xc}, which by definition is a real, local, energy-independent potential. It is of considerable importance to assess the extent to which the simpler density-functional picture can approximate the more accurate quasiparticle picture of electronic excitations near a metal surface.

We close this article by discussing a few preliminary results which shed some light on this issue. In Figures 5 and 6 we show representative results for the real and imaginary parts of $\Sigma_{xc}(q_\parallel, \omega | zz')$ [the two-dimensional Fourier transform of the GW self-energy given by Eq. (10)] for particular values of the two-dimensional wave vector $q_\parallel$ and of the frequency ω. In Figure 5 we have placed z' at the position of the jellium edge; in Figure 6, z' is about a Fermi wavelength into the vacuum.

The contrast between both sets of results is striking: While the main feature of both real and imaginary parts of Σ_{xc} in Figure 5 is the "local" spike occurring at $z = z'$, and the same applies for $Re\ \Sigma_{xc}$ in Figure 6, in the latter figure the spike in $Im\ \Sigma_{xc}$ as function of z occurs markedly away from $z = z'$. Figure 6 leaves no doubt that the imaginary part of the self-energy becomes extremely nonlocal as the electron moves into the vacuum.

The above finding highlights an important feature of the propagation and damping of a "real" electron near a metal surface. This feature should be part of a realistic many-body description of various electron-surface scattering probes.

TABLE I. Comparison of calculated and measured binding energy and effective mass for the $n = 1$ image state of Pd(111). The corresponding theoretical numbers are also given for the $n = 2$ state. Binding energies are in eV.

		Present theory	Ref. [49] (Expt.)	Ref. [50] (Expt.)	Ref. [51] (Expt.)
$n = 1$	Binding energy	0.72	0.65 ± 0.1	0.75	0.5
	Effective mass	1.03	1.0	1.0	1.0
$n = 2$	Binding energy	0.17			
	Effective mass	1.01			

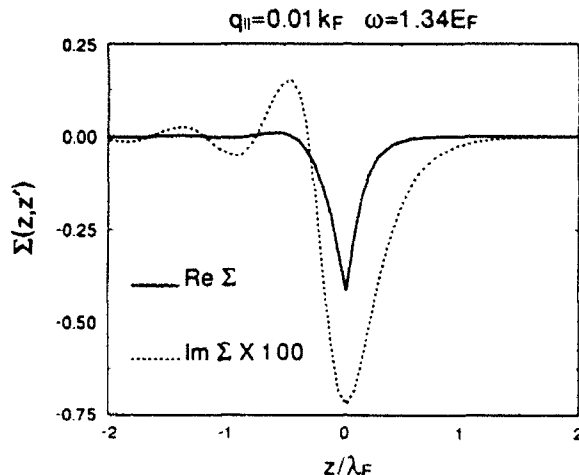$$q_\parallel = 0.01 k_F \quad \omega = 1.34 E_F$$

Figure 5. Real (solid curve) and imaginary (dotted curve) parts of the GW self-energy. [See text.] z' has been set at the jellium edge. The vacuum lies for $z > 0$.

We emphasize that the scale of the nonlocality of $Im\ \Sigma_{xc}$ is the Fermi wavelength, and this is the same scale of length over which the electron density decays to zero at the surface! We conclude that the present problem must be addressed via an approach such as the one employed in the present work, *that is, Coulomb correlation effects must be treated on the same footing with the strong inhomogeneity of the electron charge density at the surface.*

A direct study of the difference between the quasiparticle and density-functional pictures can be carried out by solving the quasiparticle equation
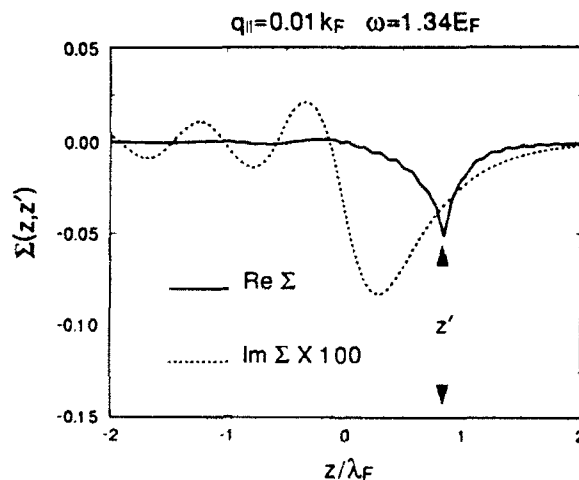
$$q_\parallel = 0.01 k_F \quad \omega = 1.34 E_F$$

Figure 6. Same as Figure 5, but for z' ca. λ_F ($= 2\pi/k_F$).

$$\left[-\frac{h^2}{2m}\nabla^2 + V_{xc}(\vec{x}) \right]\Psi_{qp}(\vec{x}) + \int d^3x_1 \Sigma_{xc}(\vec{x},\vec{x}_1 | E)\Psi_{qp}(\vec{x}_1) = E_{qp}\Psi_{qp}(\vec{x}) \quad (18)$$

self-consistently, and comparing quasiparticle wave functions and energies with their density-functional counterparts, obtained from Eqs. (1)–(4).

As an illustration, let us assume that $\Psi_{qp} = \Psi_{DFT}$. Subtracting Eq. (1) from Eq. (18), and dividing by the either wave function [which we will call Ψ] yields the equation

$$\frac{1}{\Psi(\vec{x})}\int d^3x_1 \Sigma_{xc}(\vec{x},\vec{x}_1 | E)\Psi(\vec{x}_1) - V_{xc}(\vec{x}) = E_{qp} - E_{DFT}. \quad (19)$$

whose first term on the left-hand side can serve as an approximate effective local quasiparticle potential [we will refer to it as U_{eff}] that can compared with V_{xc}.

This comparison is made in Figure 7, in which we use the wave function Ψ whose DFT eigenvalue equals $1.34\,E_f$, which is the energy at which the self-energy is evaluated. The qualitative behavior of V_{xc} and U_{eff} is indeed similar. Note that if the difference between both potentials plotted in Figure 7 were z-independent, the quasiparticle wave function would be identical to the DFT wave function. The relatively small z-dependence observed in Figure 7 suggests that both wavefunctions are indeed quite similar in the surface region.

We conclude that once the long-range correlation effects are included into the density-functional picture, the DFT wave functions, and associated surface barrier, become a fair approximation to the quasiparticle wave functions, and the real part of the self energy, respectively. A more complete analysis will be presented elsewhere.
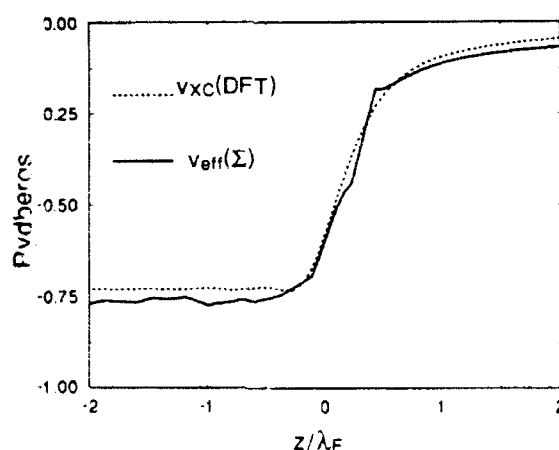

Figure 7. Comparison of a local effective potential constructed from the quasiparticle picture [first term on the left-hand side of Eq. (19)] and the exchange-correlation potential of density-functional theory.

Acknowledgments

Bibliography

[1] P. Hohenberg and W. Kohn, Phys. Rev. 136, B864 (1964); W. Kohn and L. J. Sham, ibid 140, A1133 (1965).

[2] For recent developments in density-functional theory see, for example, Density Functional Theory of Many-Fermion Systems, S. B. Trickey, Ed. (Academic, New York, 1990), and R. M. Dreizler and E. K. U. Gross, Density Functional Theory. An Approach to the Quantum Many-Body Problem (Springer-Verlag, Berlin, 1990).

[3] V. Dose, Surf. Sci. Rep. 5, 337 (1985); M. Donath, V. Dose, K. Ertl, and U. Kolac, Phys. Rev. B41, 5509 (1990); G. Borstel and G. Thörner, Surf. Sci. Rep. 8, 1 (1987).

[4] F. J. Himpsel, Comments Condens. Mat. Phys. 12, 199 (1986); Phys. Rev. B43, 13394 (1991).

[5] N. V. Smith, Rep. Prog. Phys. 51, 1227 (1988); Phys. Rev. B32, 3549 (1985).

[6] S. Yang, K. Garrison, and R. A. Bartynski, Phys. Rev. B 2025 (1991).

[7] K. Giesen, F. Hage, F. J. Himpsel, H. J. Riess, and W. Steinemann, Phys. Rev. Lett. 55, 300 (1985).

[8] R. W. Schoenlein, J. G. Fujimoto, G. L. Eesley, and T. W. Capehart, Phys. Rev. Lett. 61, 2596 (1988); Phys. Rev. B41, 5436 (1990).

[9] N. Fischer, S. Schuppler, Th. Fauster, and W. Steinmann, Phys. Rev. B42, 9717 (1990).

[10] G. Binnig and H. Rohrer, IBM J. Res. Develop. 30, 355 (1986); G. Binnig, N. Garcia, H. Rohrer, J. M. Soler, and F. Flores, Phys. Rev. B33, 4816, (1984); P. M. de Andrés, F. Flores, P. M. Echenique, and R. H. Ritchie, Europhys. Lett. 3, 101 (1987).

[11] G. Doyen, E. Koetter, J. P. Vigneron, and M. Scheffler, Appl. Phys. A51, 281 (1990).

[12] B. N. J. Persson and A. Baratoff, Phys. Rev. B38, 9616 (1988).

[13] A. A. Lucas, H. Morawitz, G. R. Henry, J. P. Vigneron, Ph. Lambin, P. H. Cutler, and T. E. Feuchtang, Phys. Rev. B37, 10708 (1988).

[14] P. M. Echenique, A. Grass Marti, J. R. Manson, and R. H. Ritchie, Phys. Rev. B35, 7357 (1987).

[15] N. D. Lang, Comments Condens. Mat. Phys. 14, 253 (1989); Phys. Rev. B37, 10395 (1988).

[16] P. M. Echenique and J. B. Pendry, J. Phys. C11, 2065 (1978); Prog. Surf. Sci. 32, 11 (1990).

[17] S. L. Hulbert, P. D. Johnson, M. Weinert, and R. F. Garret, Phys. Rev. B33, 760 (1986).

[18] L. Jurczyszyn, Surf. Sci. 247, 158 (1991); A. Kiedjna, Phys. Rev. B43, 14695 (1991).

[19] W. L. Schaich and J. T. Lee, Phys. Rev. B44, 5973 (1991).

[20] S. A. Lindgren and L. Walldén, Phys. Rev. B38, 10044 (1988); ibid 40, 11546 (1989).

[21] L.-A. Salmi and M. Persson, Phys. Rev. B39, 6249 (1989); S. Papadia, M. Persson, and L.-A. Salmi, ibid 41, 10237 (1990).

[22] W. S. Fann, R. Storz, and J. Bokor, Phys. Rev. B44, 10980 (1991).

[23] P. L. de Andrés, P. M. Echenique, and F. Flores, Phys. Rev. B39, 10356 (1989).

[24] P. Nordlander and J. C. Tully, Surf. Sci. 211/212, 207 (1989); P. D. Johnson, A. J. Viescas, P. Nordlander, and J. C. Tully, Phys. Rev. Lett. 64, 942 (1990).

[25] D. L. Mills and S. Y. Tong, Philos. Trans. R. Soc. London A318, 179 (1986).

[26] N. D. Lang and W. Kohn, Phys. Rev. B7, 3541 (1973).

[27] O. Gunnarsson and R. O. Jones, Phys. Scr. 21, 394 (1980).

[28] S. Ossicini, C. M. Bertoni, and P. Gies, Europhys. Lett. 1, 661 (1986).

[29] The functional proposed by Langreth and Mehl accounts approximately for the "bulk" electronic many-body effects brought about by the presence of the ion cores. On the other hand, it does not

852   EGUILUZ ET AL.

produce a surface barrier with an image tail. D. C. Langreth and M. J. Mehl. Phys. Rev. Lett. **47**, 446 (1981).

[30] L. J. Sham and M. Schlüter. Phys. Rev. Lett. **56**, 2415 (1983).

[31] R. W. Godby, M. Schlüter, and L. J. Sham. Phys. Rev. Lett. **56**, 2415 (1986); Phys. Rev. **B37**, 10159 (1988).

[32] W. Hanke and L. J. Sham. Phys. Rev. **B38**, 13361 (1988).

[33] L. Hedin and S. Lundqvist, in *Solid State Physics*, H. Ehrenreich, F. Seitz, and D. Turnbull, Eds. (Academic, New York, 1969), Vol. 23, p. 1.

[34] G. Strinati, H. J. Mattausch, and W. Hanke. Phys. Rev. **B25**, 2867 (1982).

[35] M. S. Hybertsen, and S. G. Louie. Phys. Rev. **B38**, 4033 (1988).

[36] J. E. Northrup, M. S. Hybertsen, and S. G. Louie. Phys. Rev. Lett. **66**, 500 (1991).

[37] A. G. Eguiluz. Phys. Rev. Lett. **51**, 1907 (1983); Phys. Rev. **B31**, 3305 (1985); Phys. Scr. **36**, 651 (1987).

[38] W. Hanke and L. J. Sham. Phys. Rev. **B21**, 4656 (1980).

[39] A. G. Eguiluz, M. Heinrichsmeier, A. Fleszar, and W. Hanke. Phys. Rev. Lett. **68**, 1359 (1992).

[40] W. H. Press et al., *Numerical Recipes* (Cambridge University Press, Cambridge, 1986).

[41] L. J. Sham and W. Kohn. Phys. Rev. **145**, 561 (1966).

[42] The GW approximation for the self-energy yields a V_{xc} which in the bulk differs from the Ceperley and Alder Monte Carlo calculation [Phys. Rev. Lett. **45**, 566 (1980)] by about 5% for small r_s.

[43] A. G. Eguiluz and W. Hanke. Phys. Rev. **B39**, 10433 (1989).

[44] C. O. Almbladh and U. von Barth. Phys. Rev. **B31**, 3231 (1985).

[45] L. J. Sham. Phys. Rev. **B32**, 3876 (1985).

[46] M. K. Harbola and V. Sahni. Phys. Rev. **B39**, 10437 (1989).

[47] G. B. Bachelet, D. R. Hamann, and M. Schlüter. Phys. Rev. **B26**, 4199 (1982).

[48] H. J. Levinson, F. Greuter, and E. W. Plummer. Phys. Rev. **B27**, 727 (1983).

[49] G. D. Kubiak. J. Vac. Sci. Technol. **A5**, 731 (1987).

[50] Conrad et al. J. Electron Spectrosc. Relat. Phenom. **38**, 289 (1986).

[51] S. L. Hulbert, P. D. Johnson, and M. Weinert. Phys. Rev. **B34**, 3670 (1986).

Neural Network Studies. 4. An Extended Study of the Aqueous Solubility of Organic Compounds

NICHOLAS BODOR,* MING-JU HUANG, and ALAN HARGET

Center for Drug Discovery, College of Pharmacy, J. H. M. Health Center, University of Florida, Gainesville, Florida 32610

Abstract

A study has been made of the effect of using different numbers of hidden units in a neural network modeling of the aqueous solubility of a wide range of organic compounds. A training set of 331 compounds was used and the trained neural network was tested on a prediction set of 19 compounds. Between two and five hidden units were used with varying numbers of iterations. Comparisons are made with the results obtained from our previous studies, one which used a neural network with 18 hidden units and another based on regression analysis. By using a smaller number of hidden units in this study, better performance has been obtained than either of the previous studies. © 1992 John Wiley & Sons. Inc.

Introduction

We have recently shown that solubilities (aqueous solubility) and distribution between solvents (partition coefficients) that depend on solute-solvent interactions are well described by equations that include linear combinations of the calculated values of selected molecular properties [1,2]. In drug design, a theoretical method which could reliably predict drug delivery, transport, distribution, and biological activity information such as aqueous solubility and partition coefficients would be extremely valuable. Although aqueous solubility is generally easy to determine experimentally, this is not always appropriate and is clearly impossible to achieve until a compound has been synthesized. A theoretical approach which provides a reliable measure of a drug's aqueous solubility could be used by the drug designer to eliminate some of the large number of candidates for a drug from synthesis and experimentation. The consequent saving in time and resources could then be directed to the better candidates.

In earlier articles of this series [3], we have pointed out that the neural network approach would seem to have great potential for determining quantitative structure-activity relationships and be a valuable tool for the medicinal chemist. The basic idea of the neural network goes back to the 1940s [4], the same era as that of the von Neumann-type digital computer [5]. It was not until the 1980s, however, when Hopfield [6] published a clear description of a neural computing system whose interconnected elements seek an energy minimum, that interest in neural networks

---

* To whom correspondence should be addressed.

was revived. Neural networks have only recently been applied to chemical problems, such as using artificial neural systems to predict protein structure from amino acid sequence information [7,8] and applying neural networks to spectral identification programs [9], nucleic acid sequence analysis [10], and QSAR problems [11,12].

In this study, we have used neural network with different numbers of hidden units to study aqueous solubilities with the same training set, prediction set, and molecular descriptors as before [1,3a]. Comparison is made with the results obtained from previous studies using either the neural network [3a] or regression analysis techniques [1].

Theory of Neural Networks

A neural network model consist of layers of brain-like neurons with feedforward and feedback interconnections. We have used the back propagation algorithm [13]. Topologically, the network consists of input, hidden, and output layers of neurons or nodes connected by bonds. A three-layer neural network was used in our study and is shown in Figure 1.

Each neuron in the input layer, s_i, is rescaled to a value region between 0 and 1 by the following equation,

$$s_i = (V_i - V_{i,min})/(V_{i,max} - V_{i,min}) \tag{1}$$

where V_i is the value of the ith independent variable, $V_{i,min}$ and $V_{i,max}$ are the minimum and maximum values of the ith independent variable. Each neuron in the hidden layer, S_i, is connected with each neuron in the input layer by the squashing function

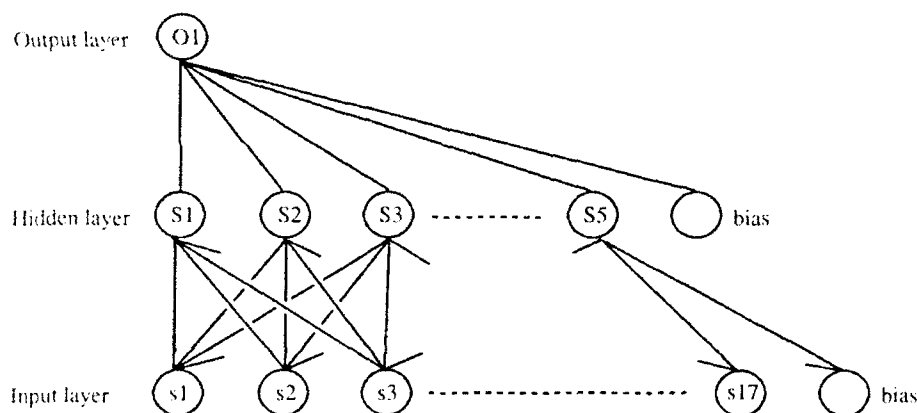$$S_i(y_i) = (1 + \exp(-y_i))^{-1} \tag{2}$$

where

Figure 1.   The neural network topology used in our studies. The network consists of 17 input neurons, one output neuron and a variable number of hidden neurons.

$$y_j = \sum_i w_{ji} s_i + \theta_j \qquad (3)$$

where w_{ji} is the weight that connects the hidden unit j with the input unit i: θ_j is the weight that connects the hidden unit j with the input layer bias unit or a characteristic value for neuron j. Again, each neuron in the output layer, O_m, is connected with each neuron in the hidden layer by the same type of the squashing function

$$O_m(y_m) = (1 + \exp(-y_m))^{-1} \qquad (4)$$

where

$$y_m = \sum_j W'_{mj} S_j + \theta_m \qquad (5)$$

where W'_{mj} is the weight that connects the output unit m with the hidden unit j: θ_m is the weight that connects the output unit m with the hidden layer bias unit.

Training of the neural network is achieved by minimizing an error function E with respect to the weights $\{w_{ji}, W'_{mj}\}$

$$E = \sum_p E_p = \tfrac{1}{2} \sum_p \sum_m (a_{pm} - O_{pm})^2 \qquad (6)$$

where E_p is the error of the pth training pattern. a_{pm} is the experimentally measured value, which has also been scaled in the same way as in Eq. (1), and O_{pm} is the calculated output of the net.

The training is carried out according to the following equations.

$$W'^{n+1}_{mj} = W'^n_{mj} + \eta \delta_j O_m \qquad (7)$$

$$w^{n+1}_{ji} = w^n_{ji} + \eta \delta_i S_j \qquad (8)$$

where η is the learning rate with values typically much less than 1 (we use 0.25), n and $n + 1$ superscripts designate consecutive iterations in the sequence. δ_j is given by

$$\delta_j = (a_{pm} - O_{pm})O_{pm}(1 - O_{pm}) \qquad (9)$$

and δ_i is given by

$$\delta_i = \sum_m (a_{pm} - O_{pm})O_{pm}(1 - O_{pm})W'_{mj}S_{pj}(1 - S_{pj}) = \sum_m \delta_j W'_{mj}S_{pj}(1 - S_{pj}) \qquad (10)$$

Similar equations are used for the θ_j and θ_m. The training continues until the error function E is converged, that is, the sum of the squared errors falls below a threshold value.

We also added the momentum term to the weight adjustment in order to enhance the stability of the learning process and decrease the training time.

$$\Delta W'^{n+1}_{mj} = W'^{n+1}_{mj} - W'^n_{mj} = \eta \delta_j O_m + \alpha \Delta W'^n_{mj} \qquad (11)$$

where α is the momentum coefficient, assigned as 0.9. The momentum term was also added in the same way as Eq. (11) to w_{ji}, θ_j, and θ_m.

Methods

The methods used are essentially the same as our previous work on octanol-water partition coefficients [2] (log P) and aqueous solubilities [1] (log W), where more details are given. First, the molecule is sketched on our IBM PC/AT computer terminal with the ChemCAD software, which generates a starting geometry. After converting the coordinate data file to the format of AMPAC [14] input files, geometry optimization is performed by the semi-empirical AM1 method [14]. From the AM1 optimum geometry and the atomic van der Waals radii, the molecular volume, surface area, and ovality are calculated by numerical integration techniques [1,2].

In our regression analysis of log W [1], we derived a 17-parameter function to describe the solvation phenomena. The 17 parameters represent the most important subset of the possible 56 descriptors. Our previous neural network approach [3a] and this study are based on the same subset of 17 parameters used in the regression analysis.

Results and Discussion

The same training set of 331 organic compounds [1,3a], was used in the present study. A wide range of organic molecules were included, such as hydrocarbons, halohydrocarbons, multiply substituted benzenes, polynuclear aromatics, ethers, alcohols, aldehydes, ketones, esters, nitrile, and nitro compounds. The experimental aqueous solubilities were taken from the compilations of Hansch et al. [15], Hine and Mookerjee [16], Mackay et al. [17], and Kamlet et al. [18], with additional results from 21 other sources [19–39]. The values of the solubilities are for atmospheric pressure and 25 °C.

The same 17 descriptors based on calculated molecular properties have been retained for this study, as previously, as listed and described in Table I. A three-layer neural network was used comprising 17 input neurons and one output neuron with the number of hidden units varied in order to determine the optimum architecture. The 17 input data and the experimental log W values for each compound were rescaled to a range between 0 and 1, as described in Eq. (1). In order to decrease the training time of the back-propagation algorithm, we used the method of Rumelhart et al. [40] and added a momentum term to the weight adjustment of the previous weight change. The learning rate was improved by enhancing the stability of the process.

The performance of a neural network depends on many variables, including the number of training examples, the number of hidden units, and the degree of homology between the training and testing sets. Few hidden units may be insufficient to extract all the pertinent features of the data, while too many units will cause the network to "memorize" the dataset.

In Table II, we show the effect of various hidden units with different starting weight ranges on neural net training and prediction. Two to five hidden units with different starting weight range and iterations gave standard deviations between 0.269 to 0.480. By comparing with the last study [3a], in which we used

TABLE I.   Selected properties of the organic compounds.

Parameter	Definition
S	Molecular surface
Ialkane	The indicator variable for alkanes
D	The calculated dipole moment
Qn	The square root of the sum of the squared charges on nitrogen atoms
Qo	The square root of the sum of the squared charges on oxygen atoms
Qn2	The square of Qn
Qo2	The square of Qo
Qn4	The square of Qn2
Qo4	The square of Qo2
V	The molecular volume
S2	The square of the molecular surface
C	The constant
O	The ovality of the molecule
O2	The square of the ovality
ABSHQ	The sum of the absolute values of atomic charges on hydrogen atoms
ABSCQ	The sum of the absolute values of atomic charges on carbon atoms
AMINE	The indicator variable for aliphatic amines
NH	The number of N — H single bonds in the molecule

18 hidden units and obtained standard deviation for the training set of 0.229 and 0.43 for the prediction set. respectively. we found that by using a smaller number of the hidden units the standard deviation of the training set was increased. but that of the prediction set was decreased. High accuracy for a training set can be obtained by using a large number of hidden units. which may overtrain the system and lead to a net with poor predictive power. Having this in mind, the best results were obtained with five hidden units. and 10 000 iterations with starting weights in the range −1 to 1. The results obtained for the training set are given in the Appendix. The standard deviation (0.269) is better than that obtained from the regression analysis. 0.299 [1]. The results of the prediction set are given in Table III. Importantly, the standard deviation for the same prediction set from this five hidden units neural network is better than both previous studies. the neural network with 18 hidden units (0.43). and the regression analysis (0.36).

In conclusion. it has been shown that correlating aqueous solubilities with structure within a neural networks with a relatively small number of hidden units give a better performance than either a neural network with 18 hidden units or a regression analysis.

TABLE II. Effect of various hidden units and starting weight range on neural net training and prediction.

The starting weight factors are in range of -2 to -1 and 1 to 2.

No. of iterations	Hidden units	Training set	Prediction set
10 000	2	0.362	0.38
20 000	2	0.356	0.37
10 000	3	0.337	0.36
20 000	3	0.338	0.37
10 000	4	0.307	0.33
15 000	4	0.302	0.34
20 000	4	0.303	0.34
10 000	5	0.371	0.43

The starting weight factors are in the range of -1 to 1.

10 000	4	0.321	0.43
20 000	4	0.291	0.38
10 000	5	0.269	0.34
20 000	5	0.252	0.36

TABLE III. Predicted results for log W using neural networks.

	Expt.	Est (NN)	Est (RA)[1]	Est (NN)[3a]	Ref.
1. 4-heptanol	-1.40	-1.33	-1.61	-1.40	[18]
2. menthone	-2.35	-2.24	-2.03	-2.72	[25]
3. 1,1-diphenylethylene	-4.52	-5.15	-5.28	-5.23	[25]
4. P-cresol	0.81	-0.79	-0.44	-0.53	[32]
5. testosterone	-4.08	-3.74	-4.49	-4.66	[29]
6. 2,4,4'-PCB	-6.24	-6.04	-5.66	-5.96	[33]
7. Dexamethasone	-3.59	-3.48	-3.58	-3.47	[29]
8. 4-chloro..robenzene	-2.85	-2.50	-2.66	-1.83	[18]
9. 2,5-PCB	-5.06	-5.75	-5.45	-5.75	[34]
10. 2,6-PCB	-5.21	-5.68	-5.35	-5.52	[34]
11. 2,4,6-PCB	-6.06	-6.12	-5.88	-6.24	[34]
12. fluorene	-4.92	-4.56	-4.78	-4.43	[17]
13. pyrene	-6.17	-5.67	-6.39	-6.04	[17]
14. indan	-3.04	-3.17	-3.2	-3.10	[17]
15. 3-methylpyridine	0.04	0.23	-0.17	-0.01	[18]
16. isoquinoline	-1.45	-1.71	-1.24	-1.11	[18]
17. tetrahydrofuran	0.48	0.33	0.74	0.59	[18]
18. cortisone	-3.27	-3.33	-3.55	-2.95	[32]
19. 2-naphthol	-2.25	-1.90	-1.61	-2.08	[32]

The standard deviation is 0.34.

Appendix: The experimental and estimated log W using neural networks (W in moles/L).

Case	Expt.	Est (NN)	Est (RA)[1]	Est (NN)[3a]	Ref.
1 1-octene	-4.62	-3.85	-4.27	-4.02	[16]
2 1,2,4-trimethylbenzene	-3.32	-3.67	-3.63	-3.50	[16]
3 1,4-pentadiene	-2.09	-1.97	-2.07	-2.08	[16]
4 1,5-hexadiene	-2.69	-2.64	-2.91	-2.86	[16]
5 1,6-heptadiene	-3.34	-3.11	-3.36	-3.21	[15]
6 1-hexene	-3.23	-2.87	-3.12	-3.02	[16]
7 1-hexen-3-ol	-0.59	-0.32	-0.69	-0.33	[15]
8 1-pentene	-2.68	-2.23	-2.44	-2.38	[16]
9 1-penten-3-ol	0.02	0.05	-0.23	0.01	[15]
10 2,2,3-trimethyl-3-pentanol	-1.27	-1.10	-1.71	-1.26	[15]
11 2,2-dimethyl-3-pentanol	-1.15	-0.89	-1.06	-0.78	[15]
12 2,2-dimethylpentane	-4.36	-4.32	-4.34	-4.06	[28]
13 2,2-dimethylpropanol	-0.39	-0.34	-0.34	-0.32	[15]
14 2,3-dimethyl-2-butanol	-0.41	-0.40	-0.69	-0.31	[29]
15 2,3-dimethyl-2-pentanol	-0.91	-0.62	-1.11	-0.59	[29]
16 2,3-dimethyl-3-pentanol	-0.86	-0.76	-1.17	-0.67	[29]
17 2,4-dimethyl-2-pentanol	-0.96	-0.88	-1.24	-0.79	[29]
18 2,4-dimethyl-3-pentanol	-1.23	-1.00	-1.17	-0.88	[29]
19 2,4-dimethyl-3-pentanone	-1.30	-1.19	-1.20	-1.14	[15]
20 2,4-dimethylpentane	-4.39	-4.30	-4.39	-4.10	[15]
21 2-heptene	-3.82	-3.45	-3.75	-3.58	[15]
22 2-hexanol	-0.87	-0.66	-1.00	-0.71	[15]
23 2-heptanone	-1.42	-1.23	-1.51	-1.30	[15]
24 2-hexen-4-ol	-0.40	-0.36	-0.68	-0.34	[15]
25 2-methyl-1-propanol	0.10	0.23	0.26	0.30	[15]
26 2-methyl-2-butanol	0.09	-0.08	-0.34	-0.07	[18]
27 2-methyl-2-hexanol	-1.07	-0.89	-1.30	-0.85	[15]
28 2-methyl-2-pentanol	-0.49	-0.41	-0.72	-0.34	[16]
29 2-methyl-3-pentanol	-0.70	-0.53	-0.65	-0.41	[16]
30 2-methyl-4-penten-3-ol	-0.50	-0.30	-0.64	-0.29	[15]
31 2-methylpentane	-3.79	-3.78	-3.89	-3.62	[16]
32 2-pentanone	-0.18	-0.07	-0.24	0.04	[18]
33 2-pentene	-2.54	-2.24	-2.46	-2.36	[15]
34 3,3-dimethyl-1-butanol	-0.50	-0.85	-0.81	-0.75	[29]
35 3,3-dimethyl-2-butanol	-0.64	-0.50	-0.58	-0.37	[29]
36 3-ethyl-3-pentanol	-0.87	-0.71	-1.18	-0.65	[29]
37 3-hexanol	-0.80	-0.62	-0.87	-0.59	[16]
38 3-hexanone	-0.83	-0.64	-0.79	-0.57	[15]
39 3-methyl-1-butanol	-0.51	-0.31	-0.43	-0.35	[15]
40 3-methyl-2-butanol	-0.21	-0.15	-0.17	-0.05	[30]
41 3-methyl-2-butanone	-0.12	-0.03	0.03	0.09	[15]
42 3-methyl-2-pentanol	-0.71	-0.55	-0.64	-0.43	[15]
43 3-methyl-2-pentanone	-0.67	-0.55	-0.56	-0.52	[15]

Case	Expt.	Est (NN)	Est (RA)[1]	Est (NN)[3a]	Ref.
44 3-methyl-3-hexanol	−1.00	−0.93	−1.33	−0.88	[29]
45 3-methyl-3-pentanol	−0.39	−0.42	−0.73	−0.34	[29]
46 3-methylpentane	−3.83	−3.80	−3.81	−3.54	[16]
47 3-pentanol	−0.21	−0.18	−0.29	−0.14	[15]
48 3-pentanone	−0.23	−0.09	−0.23	0.00	[15]
49 3-penten-2-ol	0.06	0.02	−0.36	−0.10	[15]
50 4-heptanone	−1.44	−1.21	−1.41	−1.21	[15]
51 4-methyl-1-pentene	−3.24	−2.83	−3.00	−2.95	[16]
52 4-methyl-2-pentanol	−0.79	−0.64	−0.92	−0.65	[16]
53 4-methyl-2-pentanone	−0.71	−0.57	−0.69	−0.54	[15]
54 4-methyl-3-pentanone	−0.81	−0.65	−0.70	−0.56	[15]
55 4-penten-1-ol	−0.15	−0.03	−0.16	0.00	[15]
56 5-nonanone	−2.58	−2.57	−2.30	−2.20	[15]
57 anthracene	−5.39	−5.08	−5.34	−5.28	[34]
58 benzyl alcohol	−0.45	−0.40	−0.21	−0.30	[15]
59 butyl acetate	−1.37	−1.42	−1.55	−1.21	[16]
60 cycloheptane	−3.52	−3.05	−3.15	−3.09	[20]
61 cycloheptene	−3.16	−2.83	−2.89	−2.84	[15]
62 cyclooctane	−4.15	−3.56	−3.71	−3.55	[20]
63 cyclopentane	−2.65	−2.04	−2.18	−1.96	[16]
64 cyclopentene	−2.10	−1.83	−1.91	−1.76	[16]
65 ethyl butyrate	−1.27	−1.50	−1.65	−1.29	[15]
66 ethyl decanoate	−4.10	−3.97	−3.81	−3.80	[15]
67 ethyl formate	0.08	0.15	0.23	0.22	[16]
68 ethyl heptanoate	−2.74	−3.01	−3.08	−2.47	[16]
69 ethyl hexanoate	−2.36	−2.56	−2.62	−2.07	[15]
70 ethyl isopropyl ether	−0.55	−0.56	−0.50	−0.51	[15]
71 ethyl nonanoate	−3.80	−3.61	−3.74	−3.49	[15]
72 ethyl octanoate	−3.39	−3.38	−3.43	−2.98	[15]
73 ethyl propyl ether	−0.69	−0.61	−0.46	−0.51	[16]
74 ethyl valerate	−1.77	−2.07	−2.16	−1.69	[15]
75 1-heptanol	−1.80	−1.43	−1.56	−1.45	[16]
76 heptane	−4.53	−4.34	−4.73	−4.44	[16]
77 hexane	−3.96	−3.78	−3.97	−3.71	[16]
78 isopropylbenzene	−3.38	−3.40	−3.57	−3.28	[16]
79 isopropyl acetate	−0.54	−0.59	−0.92	−0.50	[16]
80 methyl butyrate	−0.78	−0.86	−0.99	−0.82	[15]
81 methyl butyl ether	−0.99	−0.72	−0.66	−0.80	[15]
82 methyl isobutyl ether	−0.90	−0.72	−0.58	−0.73	[15]
83 methyl isopropyl ether	−0.03	0.10	0.15	0.13	[15]
84 2-methylnaphthalene	−3.84	−3.96	−4.08	−3.77	[33]
85 methyl propionate	−0.15	−0.24	−0.40	−0.21	[16]
86 methyl propyl ether	−0.38	0.04	0.03	−0.04	[16]
87 methyl sec-butyl ether	−0.73	−0.56	−0.35	−0.39	[15]

Case	Expt.	Est (NN)	Est (RA)[1]	Est (NN)[3a]	Ref.
88 methyl t-butyl ether	-0.21	-0.51	-0.45	-0.40	[15]
89 m-nitrotoluene	-2.44	-2.64	-2.18	-2.45	[15]
90 m-xylene	-2.86	-3.11	-3.10	-3.05	[21]
91 N-methylaniline	-1.28	-1.11	-1.11	-1.09	[19]
92 N,N-dimethylaniline	-2.04	-1.64	-1.59	-2.03	[19]
93 octane	-5.24	-4.82	-5.33	-4.99	[16]
94 o-toluidine	-0.82	-0.73	-1.04	-0.68	[19]
95 o-xylene	-2.79	-3.01	-3.02	-2.95	[21]
96 propyl butyrate	-1.92	-2.09	-2.20	-1.68	[16]
97 propyl isopropyl ether	-1.33	-1.31	-1.13	-1.21	[15]
98 propyl acetate	-0.73	-0.80	-1.03	-0.73	[15]
99 p-xylene	-2.83	-3.16	-3.17	-3.15	[21]
100 styrene	-2.57	-2.80	-2.96	-2.87	[33]
101 t-butylbenzene	-3.60	-3.95	-4.10	-3.73	[19]
102 1,3,5-trimethylbenzene	-3.40	-3.79	-3.76	-3.76	[21]
103 aniline	-0.41	-0.53	-0.33	-0.46	[15]
104 m-toluidine	-0.85	-1.14	-0.80	-0.98	[19]
105 toluene	-2.29	-2.48	-2.52	-2.47	[20]
106 benzoic acid	-0.78	-1.21	-0.45	-0.83	[19]
107 phenylacetic acid	-0.91	-1.60	-1.13	-1.23	[17]
108 nitrobenzene	-1.80	-2.32	-1.66	-2.07	[16]
109 ethylbenzene	-2.91	-2.95	-3.04	-2.93	[28]
110 n-propylbenzene	-3.30	-3.47	-3.56	-3.33	[20]
111 biphenyl	-4.33	-4.23	-4.55	-4.25	[33]
112 naphthalene	-3.62	-3.36	-3.70	-3.50	[33]
113 pentane	-3.27	-3.21	-3.55	-3.26	[16]
114 cyclohexane	-3.07	-2.59	-2.65	-2.60	[30]
115 methylcyclopentane	-3.30	-2.64	-2.71	-2.67	[16]
116 methylcyclohexane	-3.79	-3.08	-3.16	-3.12	[28]
117 isopentane	-3.18	-3.23	-3.34	-3.04	[15]
118 cyclohexene	-2.59	-2.32	-2.37	-2.33	[16]
119 dipropyl ether	-1.44	-1.42	-1.11	-1.24	[18]
120 diethyl ether	-0.13	0.09	-0.11	-0.09	[18]
121 ethyl acetate	-0.06	-0.24	-0.37	-0.11	[30]
122 methyl acetate	0.46	0.29	0.17	0.49	[18]
123 propyl formate	-0.51	-0.41	-0.34	-0.32	[16]
124 2-hexanone	-0.78	-0.64	-0.90	-0.62	[15]
125 2-butanone	0.49	0.45	0.36	0.58	[18]
126 cyclohexanol	-0.42	-0.30	-0.26	-0.18	[16]
127 1-octanol	-2.34	-2.13	-1.85	-1.91	[16]
128 1-hexanol	-1.21	-0.81	-0.97	-0.78	[16]
129 1-pentanol	-0.59	-0.23	-0.19	-0.10	[15]
130 2-butanol	0.29	0.29	0.12	0.27	[15]
131 1-butanol	0.03	0.25	0.04	0.19	[15]

Case	Expt.	Est (NN)	Est (RA)[1]	Est (NN)[3a]	Ref.
132 benzene	-1.68	-1.94	-2.13	-1.80	[33]
133 methane	-2.82	-2.51	-2.46	-2.38	[16]
134 ethane	-2.70	-2.29	-2.27	-2.45	[16]
135 propane	-2.85	-2.39	-2.49	-2.34	[16]
136 butane	-2.97	-2.72	-3.01	-2.68	[16]
137 2-methylpropane	-3.07	-2.74	-2.92	-2.56	[16]
138 2,2-dimethylpropane	-3.34	-3.28	-3.36	-3.04	[16]
139 2,2-dimethylbutane	-3.67	-3.82	-3.75	-3.45	[16]
140 2,2,4-trimethylpentane	-4.67	-4.71	-4.75	-4.40	[16]
141 cis-1,2-dimethylcyclohexane	-4.27	-3.55	-3.69	-3.53	[16]
142 ethylene	-2.33	-1.44	-1.51	-1.96	[16]
143 propylene	-2.03	-1.31	-1.56	-1.71	[25]
144 1-butene	-2.40	-1.66	-1.99	-1.87	[16]
145 2-methylpropene	-2.33	-1.64	-1.91	-1.79	[16]
146 trans-2-pentene	-2.54	-2.29	-2.69	-2.46	[16]
147 2-methyl-2-butene	-2.56	-2.24	-2.45	-2.29	[16]
148 3-methyl-1-butene	-2.73	-2.20	-2.33	-2.28	[16]
149 trans-2-heptene	-3.82	-3.51	-3.93	-3.79	[16]
150 1,3-butadiene	-1.87	-1.52	-1.80	-1.64	[16]
151 2-methyl-1,3-butadiene	-2.03	-2.00	-2.16	-2.05	[16]
152 2,3-dimethyl-1,3-butadiene	-2.40	-2.61	-2.71	-2.68	[16]
153 butylbenzene	-3.94	-4.06	-4.13	-3.91	[16]
154 2,3-dimethylbutanol	-0.37	-0.64	-0.60	-0.49	[16]
155 nitroethane	-0.24	-0.31	-0.25	-0.13	[16]
156 1-nitropropane	-0.80	-1.04	-0.82	-0.78	[30]
157 2-nitropropane	-0.73	-1.03	-0.67	-0.52	[16]
158 2-nitrotoluene	-2.32	-2.39	-2.27	-2.20	[16]
159 1-methylcyclohexene	-3.27	-2.94	-2.96	-2.95	[16]
160 2-methyl-1-butanol	-0.46	-0.31	-0.37	-0.30	[15]
161 2-pentanol	-0.28	-0.17	-0.46	-0.19	[15]
162 diphenylmethane	-4.70	-4.79	-4.85	-4.70	[23]
163 phenanthrene	-5.21	-5.01	-5.55	-5.31	[33]
164 isobutyl acetate	-1.28	-1.37	-1.52	-1.20	[16]
165 2-butylbenzene	-3.67	-4.02	-4.10	-3.82	[16]
166 pentamethylbenzene	-3.99	-4.74	-4.67	-4.51	[18]
167 1,2,4,5-tetramethylbenzene	-4.34	-4.30	-4.23	-4.22	[33]
168 trans-1,2-diphenylethylene	-5.79	-5.17	-5.24	-5.27	[33]
169 3,3-dimethyl-2-butanone	-0.72	-0.51	-0.43	-0.54	[25]
170 isopropyl formate	-0.63	-0.29	-0.23	-0.25	[16]
171 isobutyl formate	-1.00	-1.04	-0.77	-0.90	[16]
172 isopentyl formate	-1.52	-1.63	-1.41	-1.43	[25]
173 methyl benzoate	-1.53	-1.82	-1.21	-1.75	[16]
174 ethyl benzoate	-2.22	-2.20	-1.77	-2.05	[18]
175 ethyl cinnamate	-3.00	-3.07	-2.23	-3.00	[30]

Case	Expt.	Est (NN)	Est (RA)[1]	Est (NN)[3a]	Ref.
176 *t*-amylbenzene	−4.15	−4.46	−4.58	−4.21	[16]
177 2,2,5-trimethylhexane	−5.05	−5.09	−5.34	−5.07	[20]
178 1,3-dimethylnaphthalene	−4.30	−4.58	−4.59	−4.36	[17]
179 1,4-dimethylnaphthalene	−4.16	−4.63	−4.73	−4.64	[17]
180 2,3-dimethylnaphthalene	−4.70	−4.50	−4.50	−4.21	[17]
181 2,6-dimethylnaphthalene	−4.89	−4.71	−4.63	−4.64	[17]
182 1-ethylnaphthalene	−4.20	−4.44	−4.61	−4.24	[33]
183 benzaldehyde	−1.21	−1.66	−0.83	−0.96	[16]
184 acetophenone	−1.34	−1.41	−0.98	−1.36	[16]
185 2-ethyl-2-hexenal	−2.46	−2.19	−2.21	−2.37	[25]
186 butanal	−0.28	−0.78	−0.17	−0.28	[25]
187 hexanal	−1.30	−1.22	−1.19	−1.08	[25]
188 2-ethylbutanal	−1.52	−1.40	−0.86	−1.31	[25]
189 2-ethylhexanal	−2.13	−2.13	−1.68	−1.98	[25]
190 acetone	0.88	0.84	0.90	1.02	[18]
191 nitromethane	0.20	0.34	−0.10	0.33	[18]
192 methanol	1.56	1.24	0.96	1.55	[18]
193 ethanol	1.10	1.06	0.91	1.25	[18]
194 1-propanol	0.62	0.73	0.54	0.75	[18]
195 cyclohexanone	0.01	−0.19	0.07	−0.23	[18]
196 *N,N*-dimethyl acetamide	2.11	1.56	1.22	2.00	[18]
197 quinoline	−1.30	−1.84	−1.39	−1.24	[18]
198 furan	−0.83	−0.59	−0.15	−0.81	[30]
199 pyridine	0.47	0.45	0.27	0.58	[18]
200 benzonitrile	−1.65	−1.58	−1.06	−1.65	[18]
201 1,4-dinitrobenzene	−3.33	−3.40	−3.37	−3.25	[18]
202 acetonitrile	0.53	0.47	0.12	0.56	[18]
203 propionitrile	0.33	0.25	−0.09	0.26	[18]
204 butyronitrile	−0.33	−0.30	−0.57	−0.22	[18]
205 prednisolone	−3.18	−3.69	−3.11	−3.22	[29]
206 hydrocortisone	−2.97	−3.24	−3.59	−3.03	[29]
207 phenol	−0.08	−0.20	0.07	−0.12	[32]
208 *O*-cresol	−0.65	−0.74	−0.55	−0.83	[32]
209 *M*-cresol	−0.71	−0.74	−0.51	−0.66	[32]
210 1,3-dibromopropane	−2.08	−2.70	−2.43	−2.55	[15]
211 1,3-dichloropropane	−1.62	−1.98	−2.00	−1.98	[16]
212 2,2′-PCB	−5.35	−5.50	−5.05	−5.41	[33]
213 2-bromopropane	−1.59	−1.79	−1.67	−1.62	[16]
214 2-chloropropane	−1.41	−1.48	−1.48	−1.35	[16]
215 diiodomethane	−2.34	−2.03	−2.54	−1.92	[15]
216 hexachlorobenzene	−6.78	−6.13	−6.12	−6.51	[39]
217 bromobenzene	−2.55	−2.62	−2.58	−2.61	[33]
218 1-bromobutane	−2.36	−2.52	−2.31	−2.34	[16]
219 bromoethane	−1.08	−1.26	−1.28	−1.12	[16]

Case	Expt.	Est (NN)	Est (RA)[1]	Est (NN)[3a]	Ref.
220 1-bromopropane	−1.70	−1.81	−1.74	−1.71	[16]
221 chlorobenzene	−2.35	−2.34	−2.24	−2.31	[33]
222 chlorobutane	−2.14	−2.19	−2.11	−2.10	[16]
223 chloropropane	−1.46	−1.50	−1.54	−1.45	[16]
224 fluorobenzene	−1.87	−1.97	−1.83	−1.90	[25]
225 iodobenzene	−2.78	−2.92	−3.00	−2.94	[19]
226 iodobutane	−2.94	−2.81	−2.57	−2.63	[16]
227 iodoethane	−1.60	−1.52	−1.56	−1.41	[16]
228 iodomethane	−1.00	−1.27	−1.35	−1.08	[16]
229 iodopropane	−2.20	−2.13	−2.03	−2.05	[16]
230 isoamyl bromide	−2.88	−3.12	−2.80	−2.77	[16]
231 isobutyl bromide	−2.44	−2.48	−2.23	−2.27	[16]
232 isobutyl chloride	−2.00	−2.18	−2.05	−2.09	[15]
233 m-chloroaniline	−1.37	−1.45	−1.20	−1.43	[19]
234 m-dichlorobenzene	−3.08	−2.99	−2.83	−2.85	[16]
235 o-chloroaniline	−1.53	−1.50	−1.00	−1.38	[19]
236 o-dichlorobenzene	−2.98	−2.85	−2.64	−2.70	[19]
237 p-dichlorobenzene	−3.28	−3.26	−3.22	−3.00	[16]
238 1,2,4-trichlorobenzene	−3.57	−3.83	−3.55	−3.52	[19]
239 chloroform	−1.21	−1.36	−1.69	−1.29	[16]
240 chloroethane	−0.93	−1.06	−1.15	−0.99	[16]
241 trifluoromethane	−1.98	−2.10	−1.28	−1.80	[16]
242 1,1-dichloroethane	−1.29	−1.26	−1.40	−1.05	[16]
243 1,2-dichloroethane	−1.05	−1.22	−1.23	−0.78	[18]
244 1,2-dibromoethane	−1.67	−1.87	−1.74	−1.60	[16]
245 1-chloro-2-bromoethane	−1.32	−1.53	−1.44	−1.16	[16]
246 1,1,1-trichloroethane	−2.00	−1.73	−1.97	−1.66	[18]
247 1,1,2-trichloroethane	−1.46	−1.59	−1.64	−1.18	[16]
248 1,1,2,2-tetrachloroethane	−2.77	−2.22	−2.41	−2.26	[25]
249 p-dibromobenzene	−4.01	−4.14	−4.03	−4.06	[33]
250 cis-1,2-dichloroethylene	−1.44	−1.29	−1.42	−1.17	[25]
251 trans-1,2-dichloroethylene	−1.19	−1.54	−1.93	−1.58	[16]
252 2-iodopropane	−2.09	−2.11	−1.99	−2.00	[16]
253 1,2-dichloropropane	−1.61	−1.89	−1.65	−1.34	[16]
254 1,2-dibromopropane	−2.14	−2.57	−2.16	−2.17	[16]
255 1,1-dichlorobutane	−2.40	−2.74	−2.45	−2.50	[16]
256 1-chloropentane	−2.73	−2.86	−2.62	−2.55	[16]
257 2-chloropentane	−2.63	−2.87	−2.66	−2.56	[16]
258 3-chloropentane	−2.63	−2.82	−2.49	−2.52	[16]
259 chloroethylene	−1.75	−1.16	−1.20	−1.27	[16]
260 trichloroethylene	−2.12	−1.85	−2.23	−1.72	[25]
261 tetrachloroethylene	−2.62	−2.89	−3.14	−2.57	[17]
262 1-bromo-2-ethylbenzene	−3.67	−3.75	−3.69	−3.64	[16]
263 bromomethane	−0.81	−1.13	−1.10	−0.95	[16]

Case	Expt.	Est (NN)	Est (RA)[1]	Est (NN)[3a]	Ref.
264 dibromomethane	−1.18	−1.44	−1.70	−1.28	[16]
265 tribromomethane	−1.91	−2.28	−2.80	−2.03	[16]
266 chlorofluoromethane	−0.82	−1.06	−1.02	−0.72	[16]
267 chlorodifluoromethane	−1.45	−1.67	−1.34	−1.56	[26]
268 dichlorodifluoromethane	−2.53	−2.82	−2.26	−2.61	[27]
269 bromotrifluoromethane	−2.70	−2.64	−2.01	−2.55	[16]
270 1,1-difluoroethane	−1.31	−1.19	−1.18	−1.30	[16]
271 pentachloroethane	−2.64	−3.20	−3.30	−2.97	[25]
272 hexachloroethane	−4.47	−4.66	−4.37	−4.71	[38]
273 1,1,2,2-tetrachlorodifluoroethane	−3.19	−3.49	−3.63	−3.14	[16]
274 1,1,2-trichlorotrifluoroethane	−3.04	−3.20	−3.32	−2.90	[16]
275 1,1-dichlorotetrafluoroethane	−3.23	−3.32	−3.14	−3.13	[16]
276 1,2-dichlorotetrafluoroethane	−3.09	−3.36	−3.18	−3.08	[16]
277 chloropentafluoroethane	−3.49	−3.78	−3.08	−3.64	[16]
278 methyl fluoride	−1.23	−1.39	−1.19	−1.13	[16]
279 methyl chloride	−1.00	−1.13	−1.05	−1.03	[16]
280 dichloromethane	−0.81	−1.07	−1.18	−0.95	[37]
281 tetrachloromethane	−2.30	−2.33	−2.69	−2.05	[25]
282 3-PCB	−4.73	−4.75	−4.60	−4.69	[31]
283 2-PCB	−4.84	−4.85	−4.69	−4.66	[33]
284 2,4′-PCB	−5.07	−5.34	−4.87	−5.49	[31]
285 3-chloropropene	−1.28	−1.34	−1.35	−1.28	[16]
286 o-bromocumene	−4.19	−4.34	−4.16	−4.14	[16]
287 1,1,1,2-tetrachloroethane	−2.18	−2.30	−2.56	−2.29	[25]
288 1,2-difluorobenzene	−2.00	−2.01	−1.69	−1.89	[29]
289 1,2-dibromobenzene	−3.50	−3.51	−3.46	−3.51	[29]
290 1,2-diiodobenzene	−4.29	−4.16	−4.49	−4.35	[33]
291 1,3-difluorobenzene	−2.00	−2.20	−2.17	−2.14	[29]
292 1,3-dibromobenzene	−3.38	−3.75	−3.60	−3.57	[29]
293 1,3-diiodobenzene	−4.55	−4.49	−4.49	−4.33	[33]
294 1,4-difluorobenzene	−1.97	−2.36	−2.57	−2.11	[29]
295 1,4-diiodobenzene	−5.25	−4.92	−4.92	−5.07	[29]
296 1,2,3-trichlorobenzene	−3.76	−3.56	−3.28	−3.47	[29]
297 1,2,4-tribromobenzene	−4.50	−5.08	−4.82	−4.77	[29]
298 1,3,5-trichlorobenzene	−4.44	−4.14	−3.84	−3.97	[29]
299 1,3,5-tribromobenzene	−5.60	−5.42	−5.04	−5.56	[29]
300 1,2,3,4-tetrachlorobenzene	−4.25	−4.56	−4.11	−4.35	[34]
301 1,2,3,5-tetrafluorobenzene	−2.31	−2.66	−2.77	−2.65	[35]
302 1,2,3,5-tetrachlorobenzene	−4.77	−4.81	−4.30	−4.42	[33]
303 1,2,4,5-tetrafluorobenzene	−2.38	−2.88	−3.16	−2.63	[35]

Case	Expt.	Est (NN)	Est (RA)[1]	Est (NN)[3a]	Ref.
304 1,2,4,5-tetrachlorobenzene	−4.96	−5.08	−4.56	−5.11	[34]
305 pentachlorobenzene	−5.28	−5.60	−5.07	−5.34	[36]
306 1-fluoro-4-iodobenzene	−3.13	−3.52	−3.68	−3.34	[35]
307 1-chloro-2-fluorobenzene	−2.42	−2.43	−2.20	−2.20	[35]
308 1-chloro-3-fluorobenzene	−2.35	−2.54	−2.47	−2.46	[35]
309 1-bromo-2-fluorobenzene	−2.70	−2.75	−2.59	−2.61	[35]
310 1-bromo-3-fluorobenzene	−2.67	−2.88	−2.83	−2.79	[35]
311 1-bromo-2-chlorobenzene	−3.19	−3.19	−3.04	−3.11	[29]
312 1-bromo-3-chlorobenzene	−3.21	−3.37	−3.21	−3.20	[29]
313 1-bromo-4-chlorobenzene	−3.63	−3.65	−3.57	−3.40	[29]
314 1-bromo-4-iodobenzene	−4.56	−4.54	−4.47	−4.55	[29]
315 1-chloro-2-iodobenzene	−3.54	−3.52	−3.48	−3.51	[29]
316 1-chloro-3-iodobenzene	−3.55	−3.74	−3.63	−3.55	[29]
317 1-chloro-4-iodobenzene	−4.03	−4.07	−3.99	−3.91	[29]
318 betamethasone	−3.77	−3.58	−3.57	−3.82	[29]
319 progesterone	−4.42	−4.63	−4.32	−4.51	[29]
320 butylamine	0.96	0.88	0.80	1.02	[18]
321 propylamine	1.52	1.37	1.42	1.61	[18]
322 pentylamine	0.27	0.22	0.19	0.31	[18]
323 diethylamine	1.03	1.17	0.96	0.94	[18]
324 ethylamine	2.06	1.68	2.05	1.91	[18]
325 hexylamine	−0.25	−0.41	−0.43	−0.33	[18]
326 heptylamine	−0.90	−0.96	−1.04	−0.85	[18]
327 octylamine	−1.46	−1.42	−1.54	−1.41	[18]
328 trimethylamine	1.32	1.34	1.62	1.40	[18]
329 triethylamine	−0.26	−0.36	0.09	−0.32	[18]
330 dipropylamine	−0.54	−0.35	−0.39	−0.47	[18]
331 dibutylamine	−1.44	−1.61	−1.43	−1.51	[18]

Bibliography

[1] N. Bodor and M.-J. Huang, J. Pharm. Sci. (in press).

[2] (a) N. Bodor, Z. Gabanyi, and C.-K. Wong, J. Am. Chem. Soc. 111, 3783 (1989); (b) N. Bodor and M.-J. Huang, J. Pharm. Sci. 81, 272 (1992).

[3] (a) N. Bodor, A. Harget, and M.-J. Huang, J. Am. Chem. Soc. 113, 9480 (1991); (b) M. E. Brewster, M.-J. Huang, A. Harget, and N. Bodor, Tetrahedron 48 (17), 3463 (1992); (c) N. Bodor, A. Harget, and M.-J. Huang, J. Pharm. Sci. (submitted for publication).

[4] W. S. McCulloch and W. Pitts, Bull. Math. Biophysics 5, 115 (1943).

[5] J. Von Neumann, First Draft of a Report on the EDVAC, Contract No. W-670-Ord-4926 (Univ. of Pennsylvania, Philadelphia, 1945).

[6] J. J. Hopfield, Proc. Natl. Acad. Sci. U.S.A. 79, 2554 (1982).

[7] N. Qian and T. Sejnowski, J. Mol. Biol. 202, 865 (1988).

[8] L. Holley and M. Karplus, Proc. Natl. Acad. Sci. U.S.A. 86, 152 (1989).

[9] B. Curry and D. Rumelhart, Tetrahedron Comput. Method 3, 213 (1990).

[10] A. Lukashin, V. Anshelevich, B. Amirikyan, A. Gragerov, and M. Frank-Kamenetskii, J. Biomol. Struct. Dyn. 6, 1123 (1989).

[11] (a) T. Aoyama, Y. Suzuki, and H. Ichikawa, Chem. Pharm. Bull. 37, 2558 (1989); (b) T. Aoyama and H. Ichikawa, ibid 39, 358 (1991); (c) T. Aoyama and H. Ichikawa ibid 39, 372 (1991); (d)

T. Aoyama and H. Ichikawa, *ibid.* **39**, 1222 (1991); (e) T. Aoyama, Y. Suzuki, and H. Ichikawa, J. Med. Chem. **33**, 905 (1990); (f) T. Aoyama, Y. Suzuki, and H. Ichikawa, *ibid.* **33**, 2583 (1990).

[12] T. Andrew and H. Kalayeh, J. Med. Chem. **34**, 2824 (1991).

[13] D. E. Rumelhart and J. L. McClelland, *Parallel Distributed Processing: Explorations in the Microstructure of Cognition* (Bradford Books, MIT, Cambridge, MA, 1986).

[14] M. J. S. Dewar, E. G. Zoebisch, E. F. Healy, and J. J. P. Stewart, J. Am. Chem. Soc. **107**, 3902 (1985).

[15] C. Hansch, J. E. Quinlan, and G. L. Lawrence, J. Org. Chem. **33**, 347 (1968).

[16] J. Hine and P. K. Mookerjee, J. Org. Chem. **40**, 292 (1975).

[17] D. Mackay, A. Bobra, W. Y. Shiu, and S. H. Yalkowsky, Chemosphere **9**, 701 (1980).

[18] M. J. Kamlet, R. M. Doherty, M. H. Abraham, P. W. Carr, R. F. Doherty, and R. W. Taft, J. Phys. Chem. **91**, 1996 (1987).

[19] (a) C. T. Chiou, D. W. Schmedding, and M. Manes, Environ. Sci. Technol. **16**, 4 (1982); (b) C. T. Chiou, P. E. Porter, and D. W. Schmedding, *ibid.* **17**, 227 (1983); (c) C. T. Chiou and J. H. Block, In *Partition Coefficient Determination and Estimation*, W. J. Dunn, III, J. H. Block, and R. S. Pearlman, Eds. (Pergamon Press, New York, 1986), pp. 37–58.

[20] R. B. Hermann, J. Phys. Chem. **76**, 2754 (1972).

[21] C. Sutton and J. A. Calder, J. Chem. Eng. Data **20**, 320 (1975).

[22] S. Banerjee, S. H. Yalkowsky, and S. C. Valvani, Environ. Sci. Technol. **14**, 1227 (1980).

[23] H. H. Hollifield, Bull. Environ. Contam. Toxicol. **23**, 579 (1979).

[24] W. E. May, S. P. Wasik, and D. H. Freeman, Anal. Chem. **50**, 997 (1978).

[25] N. C. Deno and H. E. Berkheimer, J. Chem. Eng. Data **1**, 1 (1960).

[26] H. M. Parmelee, Refrigerating Engng. **61**, 1341 (1953).

[27] T. Park, T. R. Rettich, R. Battino, D. Peterson, and E. Wilhelm, J. Chem. Eng. Data **27**, 324 (1982).

[28] L. C. Price, Am. Assoc. Petrol Geol. Bull. **60**, 213 (1976).

[29] S. H. Yalkowsky and S. C. Valvani, J. Pharm. Sci. **69**, 912 (1980).

[30] S. C. Valvani, S. H. Yalkowsky, and T. J. Roseman, J. Pharm. Sci. **70**, 502 (1981).

[31] O. Hutzinger, S. Safe, and V. Zitko, *The Chemistry of PCB's* (CRC: Cleveland, OH, 1974); P. R. Wallnofer, M. Koniger, and O. Hutzinger, Analabs Res. Notes **13**, 14 (1973).

[32] S. C. Valvani and S. H. Yalkowsky, In *Solubility and Partitioning in Drug Design, Physical Chemical Properties of Drug*, S. H. Yalkowsky, A. A. Sinkula, and S. C. Valvani, Eds. (Marcel Dekker, New York and Basel, 1980), pp. 201–229.

[33] S. H. Yalkowski, S. C. Valvani, and D. Mackay, Residue Rev. **85**, 43–55 (1983).

[34] M. M. Miller, S. P. Wasik, G.-L. Huang, W.-Y. Shiu, and D. Mackay, Environ. Sci. Technol. **19**, 522 (1985).

[35] R. J. Baker, B. J. Donelan, L. J. Peterson, W. E. Acree, Jr., and C.-C. Tsai, Phys. Chem. Liq. **16**, 279 (1987).

[36] C. T. Garten, Jr. and J. R. Trabalka, Environ. Sci. Technol. **17**, 590 (1983).

[37] G. McConnell, D. M. Ferguson, and C. R. Pearson, Endeavour **34**, 13 (1975).

[38] D. Mackay and W. Y. Shiu, J. Phys. Chem. Ref. Data **10**, 1175 (1981).

[39] M. M. Miller, S. Ghodbane, S. P. Wasik, Y. B. Tewari, and D. E. Martire, J. Chem. Eng. Data **29**, 184 (1984).

[40] D. Rumelhart, G. Hinton, and R. Williams, Nature **323**, 533 (1986).

On the Stability of H⁻ in Plasmas*

ZHENGMING WANG,† YONG YAN,† HONGBIN ZHAN,†
JOHN C. MORRISON,‡ and PETER WINKLER†

†*Department of Physics, University of Nevada, Reno, Nevada, and ‡Department of Physics, University of Louisville, Kentucky*

Abstract

The ground-state energy of the negative hydrogen ion in a variety of plasma model environments has been calculated using a new pair function code which takes screening into account. The models that have been studied range from simple Debye screening to more realistic electron–ion potentials derived from density-functional theory. © 1992 John Wiley & Sons, Inc.

Introduction

The potential between electrons and ions plays a key role in plasma studies as well as in studies of atomic processes in plasmas. The ultimate goal of an *ab initio* description of plasmas is still a formidable task of many-body theory. In particular for nonideal plasmas in which the kinetic energy average is much smaller than the potential energy the difficulties are compounded by the existence of bound states of the constituents (atoms and ions) states. This requires an accurate treatment of both the global and local properties of the plasma. In spite of considerable progress made in the formulation of a fundamental theory of nonideal hydrogen plasmas [1] and reports on applications to helium [2] a comprehensive *ab initio* treatment of general plasmas is still a development of the future.

The study of atomic processes in plasmas on the other hand is one of the most active areas in conjunction with plasma diagnostics for the fusion energy program as well as for astrophysical research. It is well-known that the accuracy required for a meaningful evaluation of atomic processes is quite high. Atomic processes are sensitive to local plasma environments. Quite frequently these are either totally neglected in the corresponding calculations or roughly approximated by merely introducing a finite correlation sphere or application of simple Debye screening. These approaches reflect essentially the fact that we know much less about local properties in plasmas than their global aspects. With the appearance of increasingly detailed computer models of the plasma, however, there is hope that the potentials required for atomic calculations including the environment can be refined. It appears appropriate and timely to study alternative approaches for the extraction of realistic electron–ion potentials from detailed plasma calculations and to develop new

methods to dynamically couple the plasma electrons to the atomic electrons. The present study is our first step in this direction.

At present the majority of plasma calculations are based on the one component plasma model (OCP) which takes the electron component as a background providing a uniform charge density throughout all space mainly to ensure charge neutrality. While this approach may be adequate for high-energy plasmas it is inadequate for our purposes because the artificial immobility of the electron background introduces stronger spatial fluctuations of the calculated ion densities and the associated potentials than are to be expected in reality. Fortunately there are calculations in the two-component plasma model (TCP) available [3] the results of which have enabled us to design strategies for the refinement of potential functions to be used in future calculations of atomic processes in various plasma environments. Unfortunately such TCP computations are still all too rare and the existing ones do not directly cover the region of interest for the study atomic processes. Density-functional theory is our choice to obtain the required information about the plasma environment. Alternative approaches are Monte Carlo methods or Molecular Dynamics calculations which will not be discussed here any further, however.

Another current topic of increasing interest and full of surprises is the research on highly charged ions stimulated by the availability of efficient ion sources and experimentally restricted so far mostly to studies in the vacuum but always with the declared direction toward applications in plasmas, in particular, the study of impurities. There is a considerable need for theoretical extrapolation of the vacuum results to plasma environments. Although our studies are presently focused on hydrogen plasmas, in particular, the study of negative hydrogen ions, the methods can be applied directly to the study of highly charged positive ions as long as a nonrelativistic theory is feasible and, with moderate modifications, to heavier ions. The step to more complicated plasmas is planned for the future.

In the next section we summarize the framework of density-functional theory as applied to hydrogen plasmas. In the third section we will discuss the one "realistic" potential we have extracted so far. The fourth and fifth sections are reserved for a brief explanation of the pair function approach and the discussion of our results for various plasma models. A more general discussion of our findings and possible plasma conditions for which our calculations may be appropriate follows in the final section.

Density-Functional Approach

Here we summarize the main relations from density-functional theory applied to hydrogen plasmas [3]. The equations for the electron subsystem are given by

$$[-\tfrac{1}{2}\nabla^2 + V_c(r)]\Phi_\nu(r) = \varepsilon_\nu \Phi_\nu(r) \tag{1}$$

where v designates a quantum state (v, l, m) if ε is negative and (k, l, m) if $\varepsilon = \tfrac{1}{2}k^2$ referring to a scattering state.

$$V_c(r) = -[1/r + V_p(r)] + V_i^e(r) - V_i^e(R) \tag{2}$$

where

$$V_P(r) = \int \frac{\rho(r') - n(r')}{|\mathbf{r} - \mathbf{r}'|} d\mathbf{r}' \tag{3}$$

and the exchange potentials are taken in local density approximation. The key quantity here is the distribution function for an ion–electron pair

$$g_{ie}(r) = n(r)/n_{av} \tag{4}$$

which is related to the bound, free and average electron densities

$$n(r) = n^b(r) + \Delta n^f(r) + n_{av} \tag{5}$$

with

$$n^b(r) = \sum_{\nu,l} (2l + 1)|\Phi_{\nu,l}|^2 f(\nu, \bar{\mu}_e) \tag{6}$$

$$\Delta n^f(r) = \pi^{-2} \int_0^\infty k^2 \, dk \{ f(k, \mu_e) \sum_l (2l + 1)[R_{kl}^2(r) - j_l^2(rk)] \} \tag{7}$$

$$f(\nu, \bar{\mu}_e) = 1/[1 + \exp(\varepsilon_\nu - \bar{\mu}_e)\beta] \quad (\beta = 1/k_B T) . \tag{8}$$

For the ion subsystem the most relevant relations are the pair function equation

$$g_{ii}(r) = \exp[-\beta V_i(r)] \tag{9}$$

with

$$V_i(r) = [1/r + V_r(r)] + V_i^c(r) \tag{10}$$

where the average correlation potential is given by

$$V_i^c(r) = -(1/\beta)\rho_{av} \int [h(r') + \beta V_i(r')]h(|\mathbf{r} - \mathbf{r}'|) d\mathbf{r}' . \tag{11}$$

Finally we define

$$\ln g(r) = -\beta[1/r + V_P(r)] + \rho_{av} \int [h(r') - \ln g(r')]h(|\mathbf{r} - \mathbf{r}'|) d\mathbf{r}' \tag{12}$$

with $h(r) = g(r) - 1$.

Realistic Potentials

Once the distribution functions g_{ie} and g_{ii} have been obtained by iteration we use the densities $n(r) = n_{av}g_{ie}(r)$ and $\rho(r) = \rho_{av}g_{ii}(r)$ in Poisson's equation $\nabla^2 V(r) = -4\pi(\rho(r) - n(r))$ for the evaluation of a "realistic" potential. This term is used here to express the fact that important features of the plasma environment have been included albeit in an approximate and averaged way. Subsequent computations can be considerably accelerated if we use analytic potential functions

which are fitted to the realistic potentials. In Figure 1 we present a fit employing the analytical form of a Debye–Laughton potential

$$V_{DL}(r) = A\exp(-r/D)[1/r - Br^\mu \exp(-Cr/D)].$$ (13)

This form reproduces the potential curve obtained from one of the few existing TCP calculations [3] so well that in the graph the curves cannot be distinguished in the displayed region. We have used potentials of this form in resonance calculations previously in a study of shape resonances in the s-wave channel [4]. The plasma conditions of this particular calculation support only one bound state of the neutral atom at an energy of −0.140148 a.u. For the pair function calculations reported next we have therefore to change the parameters of the Debye–Laughton potential so that the model supports several bound states and in particular also a bound state of the negative ion. Model calculations of plasmas under corresponding conditions are well under way but not completed.

The Atomic Pair Function

Numerical pair functions [5] have become an important tool in the study of atomic structure. For helium-like systems they offer a rather convenient way to
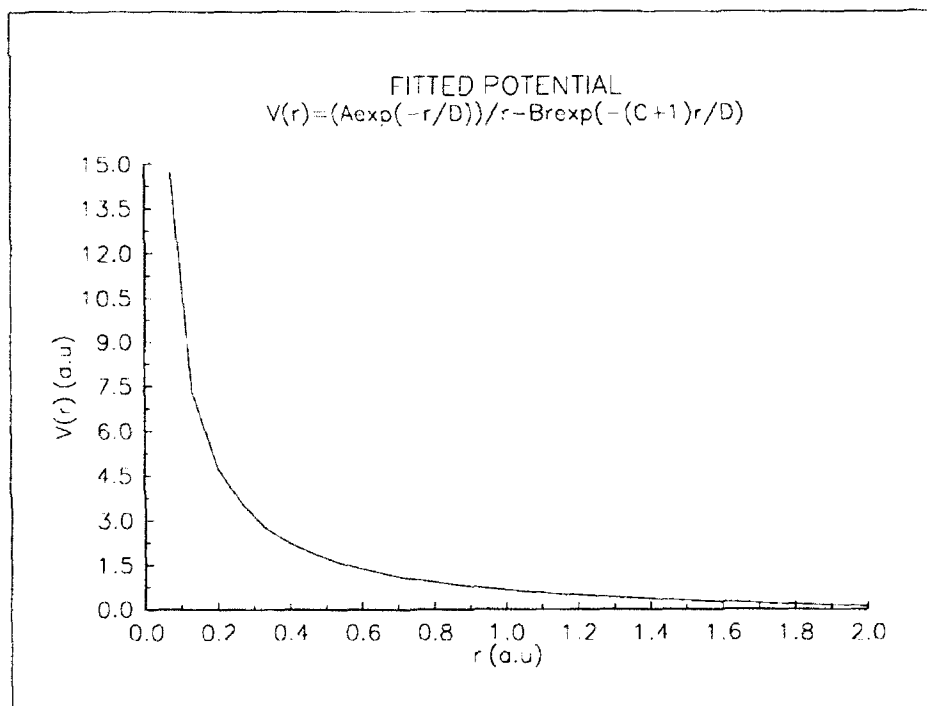

FITTED POTENTIAL
V(r)=(Aexp(-r/D))/r-Brexp(-(C+1)r/D)

Figure 1.   Fit of an analytic function to a realistic potential for hydrogen plasma (T = 10). The radius of the correlation sphere is 2 a.u. The parameters of the Debye–Laughton potential [Eq. (13)] are $A = 1, B = .223, C = .596, D = 4.737, \mu = 1$.

obtain accurate, numerical bound-state wave functions. For larger systems the construction of pair functions is a feasible alternative to the correlation of single particle functions, in particular, the infinite summation of ladder diagrams [6] and [7]. The calculation of pair functions with screened Coulomb potentials is new and requires some justification.

The theory of atomic pair functions will be outlined only briefly. Relevant details can be found in a pioneering publication by Mårtensson [8]. Although we use a code of own provenance because of the modifications required by the inclusion of plasma screening the description of the finite difference techniques provided there can serve as a guide also here.

For two-electron systems the equation for the pair function ρ_{ab} (shown in figure 2) is given by

$$[\varepsilon_a + \varepsilon_b - h_0(1) - h_0(2)]|\rho_{ab}\rangle = \sum_{rs \notin P} |rs\rangle\langle rs|V|ab + \rho_{ab}\rangle$$

$$- \sum_{cd \in P} \rho_{cd}\langle cd|V|ab + \rho_{ab}\rangle \qquad (14)$$
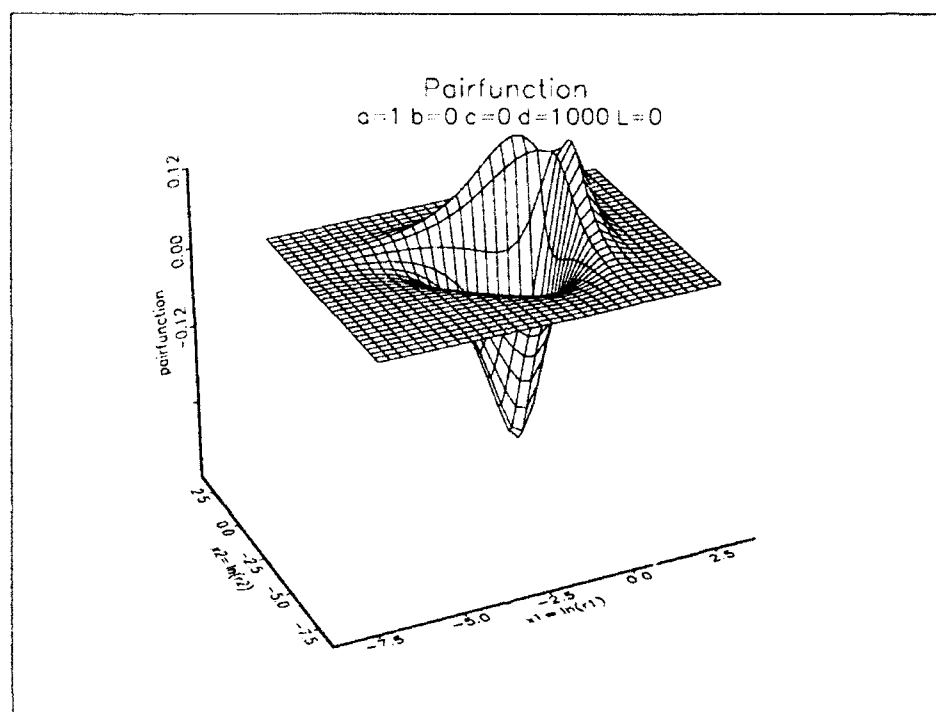

Figure 2. Plot of a pair function. Only the s-contribution is displayed. The variables x_1 and x_2 are the radial variables of the two electrons given here in terms of mesh points. The choice of the parameters corresponds to simple Debye screening with $D = 1000$ which is very similar to the unscreened Coulomb potential. A logarithmic grid $r = \exp(x)$ has been used. The parameters of the Debye–Laughton potential are $A = 1$, $B = C = 0$, $D = 1000$, $\mu = 0$.

Here P is the model space spanned by a subset of eigenfunctions of an approximate Hamiltonian consisting of a sum of single-particle operators $h_0(i)$. We notice that the pair function ρ_{ab} complements the product functions $|ab\rangle$. The right-hand side is a functional of ρ but—starting with an educated guess—we use the function obtained in the $(n - 1)$st step as right-hand side for the nth iteration until convergence has been obtained within a preset tolerance. The one-electron problem connected with h_0 has to be solved first:

$$h_0(i) = -\nabla_i^2/2 - Z/r_i + V. \tag{15}$$

In order to include, for example, Debye screening the matrix elements of V are chosen as

$$V_{ij} = \langle i|- Z[\exp(-r/D) - 1]/r|j\rangle$$

$$+ \sum_c^{core} \{\langle ic|\exp(-r/D)/r|jc\rangle - \langle ic|\exp(-r/D)/r|cj\rangle\}. \tag{16}$$

More realistic choices for V have been studied also.

Results

In Table I we present results of the present calculation for increasing Debye screening (decreasing values of D) and compare the ground-state energy of the negative hydrogen ion to the binding energy for the neutral atom in the same plasma environment. Both values decrease with increasing screening. As long, however, as the value in the last column is more negative than the corresponding entry

TABLE I. The gound-state energy of the H⁻-ion (last column) for some values of the Debye parameter D (column 1) is compared to the ground-state energy of the neutral atom (column 2). Columns 3 and 4 show the results of the present pair function calculation obtained on a grid of 45 × 45 points and the values of the Richardson extrapolation, respectively. In the pair function results s, p, and d partial waves have been consistently included.

D	H-atom	H⁻-ion ($N = 45$)	H⁻-ion (extrapolated)	H⁻-ion (GCM)
∞	-0.500000	-0.527613	-0.527322	-0.527750
1000	-0.499001	-0.525871	-0.525696	-0.525754
200	-0.495019	-0.517935	-0.517883	-0.517818
100	-0.490074	-0.508135	-0.508118	-0.508018
50	-0.480296	-0.488846	-0.488662	-0.488808
35	-0.472049	-0.472854	-0.472540	-0.472745
34.25	-0.471430	-0.471702	-0.471535	-0.471588
34	-0.471225	-0.471305	-0.471249	-0.471191
33.5	-0.470848	-0.470543	-0.470343	-0.470343
32	-0.469668	-0.468149	-0.467981	-0.468699
20	-0.451816	-0.434280	-0.434033	-0.442189

in column 2 the negative ion is bound. We notice that at values of D about 34 or less the two-electron system ceases to be bound.

What happens when we go beyond the bound regime? Does the system emit the second electron immediately into the continuum or do features of the combined and predominantly localized system persist even though the energy coexists with the one-electron continuum? Our studies are not yet at the stage to provide a quantitative answer to this question.

The fact that even beyond the bound region our calculations yield states with distinct energies and electron densities not much different from the bound systems may be an artifact of the chosen computational approach. We do not believe in this explanation, however, because in similar circumstances for heavily screened one-electron systems we were able to explicitly show the resonance character of the corresponding solutions [4]. But more studies are required here. The comparison data in the last column have been obtained from correlated wavefunctions in the generator coordinate representation described elsewhere [9] and have been included here only to assess the accuracy of the present calculations given in columns 3 and 4.

One further point is worth mentioning: While the results in the last column are obtained from a variational calculation, the same is not true for the numerical pair function results which may happen to lie below the true energy values. In view of the demonstrated accuracy of the results this distinction is of little relevance for all practical purposes and so we have abandoned this control in the following investigations.

In Tables II, III, and IV we have extended the study of the stability of the negative hydrogen ion to other screening environments. We proceed from the simple Debye screening model to more realistic potentials which in principle should be obtained from pair distribution functions of two-component plasma simulations as above but are at this time only represented by sequences of analytic potential functions which may or may not have any resemblance to realizable situations. Future efforts will show if any (or all!) of these potentials can be associated with real plasma conditions.

TABLE II. The energy of the H^--ion for several values of the parameter B, with $A = 1$, $C = 0$, $D = 1000$, $\mu = 0$.

B	H-atom	H^--ion ($N = 35$)	H^--ion ($N = 45$)	H^--ion (extrapolated)
.002	−0.497004	−0.522039	−0.521889	−0.521685
.005	−0.494008	−0.516056	−0.515915	−0.515699
.010	−0.489016	−0.506083	−0.505943	−0.505729
.0138	−0.485221	−0.498489	−0.498339	−0.498109
.020	−0.479031	−0.486122	−0.485973	−0.485745
.030	−0.469046	−0.466191	−0.466050	−0.465834
.040	−0.459061	−0.446143	−0.446104	−0.446044

TABLE III.   The energy of the H -ion for several values of the parameter B, with 1 - 1. C - 0. D - 100. μ - 0.

B	H-atom	H -ion (N 35)	H -ion (N 45)	H -ion (extrapolated)
.002	0.488104	0.504401	0.504286	0.504110
.005	0.485149	0.498561	0.498446	0.498270
.010	0.480223	0.488828	0.488713	0.488537
.0138	0.476479	0.481414	0.481261	0.481027
.020	0.470372	0.469346	0.469101	0.468726
.030	0.460520	0.449781	0.449689	0.449548
.040	0.450689	0.430314	0.430325	0.430342

Discussion

Although our foremost motivation for investigating the negative hydrogen ion at this time was dictated by the need to assess both the accuracy and efficiency of our newly developed code the problem fits well into the overall scope of our research program on atomic processes in various plasma environments and the question arises whether there are plasmas for which our results are meaningful or whether they are just of computational interest. It is well-known that the negative hydrogen ion is very weakly bound even in the vacuum and obviously in a screening environment the binding decreases. However, it has been established that H in the solar chromosphere is (together with neutral hydrogen and the positive ions of calcium and magnesium) one of the four major contributors to the absorption of radiation from the sun. This affects the opacity of the sun chromosphere substantially [10]. Obviously there is a favorable plasma environment. The corresponding temperature is assumed at 4400 K but even at much higher electron temperatures between 11 000 K and 15 000 K where negative hydrogen ions are merely temporarily formed in collision processes their contribution to the overall continuum radiation is not negligible as collisional–radiative models have established [11].

TABLE IV.   The energy of the H -ion for several values of the parameter B, with 1 - 1. C - 0. D - 50. μ - 0.

B	H-atom	H -ion (N - 35)	H -ion (N - 45)	H -ion (extrapolated)
.002	-0.478355	-0.485223	-0.485150	0.485023
.005	-0.475443	-0.479546	-0.479463	-0.479336
.010	-0.470590	-0.470069	-0.469988	-0.469864
.0138	-0.466902	-0.462917	-0.462711	-0.462396
.020	-0.460885	-0.451171	-0.451041	-0.450842
.030	-0.451179	-0.432175	-0.432100	-0.431985
.040	-0.441738	0.413540	-0.413470	-0.413363

If we finally ask the question, under which equilibrium conditions the population of negative hydrogen ions is of approximately the same order as the population of the neutral system we have to go to much lower temperature ranges and the result will critically depend on the electron density. Let us assume for a moment the validity of the simple Debye screening model. In this model the binding energy of the second electron at a screening value of $D = 40$ corresponds to approximately 0.1 eV and at $D = 35$ to 0.014 eV. From the Saha–Boltzmann population distribution (see, e.g., Hutchinson [12]) this translates into detachment (ionization) temperatures of $T = 77$ K and $T = 11$ K, respectively, for an electron density of $n_e = 10^{15}$ cm^3. For a lower electron density value of 10^4 cm^3 the corresponding numbers are $T = 28$ K and $T = 4$ K, respectively. A very important feature of this analysis is the strong dependence of the population on the binding energy and this quantity itself depends critically on the adopted model for the screening.

In the future we plan to include screening also for the electron–electron repulsion which here is still taken as the bare Coulomb interaction. It is expected that binding increases slightly when the repulsion is screened. So far, however, we have neither developed a convincing screening model of the simplicity of the Debye–Hückel type nor calculated the electron-electron distribution function from which the screened interaction can be deduced.

Bibliography

[1] H. Lehmann and W. Ebeling, Z. Naturforsch. **46a**, 583 (1991).

[2] A. Förster, T. Kahlbaum, and W. Ebeling, 1991, in *Proc XX Int. Conference on Phenomena in Ionized Gases* (in press).

[3] M. W. C. Dharma-wardana and F. Perrot, Phys. Rev. A26, 2096 (1982).

[4] Z. Wang, P. Winkler, B. T. Pickup, and N. Elander, Chem. Phys. **135**, 247 (1989).

[5] I. Lindgren and J. C. Morrison, *Atomic Many-Body Theory*, 2nd ed. (Springer-Verlag, Heidelberg, 1986).

[6] J. C. Morrison, J. Phys. B. **6**, 2205 (1973).

[7] P. Winkler, Int. J. Quantum Chem. S19, 201 (1986).

[8] A.-M. Martensson, J. Phys. B. **12**, 3995 (1979).

[9] P. Winkler and R. N. Porter, J. Chem. Phys. **62**, 2038 (1974).

[10] R. W. Noyes and E. H. Avrett, in *Spectroscopy of Astrophysical Plasmas* A. Dalgarno and D. Layzer, Eds. (Cambridge University Press, Cambridge, England, 1987).

[11] W. H. Soon and J. A. Kunc, Phys. Fluids B2, 2833 (1990).

[12] I. H. Hutchinson, *Principles of Plasma Diagnostics* (Cambridge University Press, Cambridge, England, 1990).

The ACES II Program System

JOHN F. STANTON, JÜRGEN GAUSS,* JOHN D. WATTS,
WALTER J. LAUDERDALE,† and RODNEY J. BARTLETT

*Quantum Theory Project, Departments of Chemistry and Physics, University of Florida,
Gainesville, Florida 32611*

Abstract

ACES II, a new program system for *ab initio* electronic structure calculations is described. The strengths of ACES II involve the use of many-body perturbation theory (MBPT) and coupled-cluster (CC) theory for calculating the energy, geometry, spectra, and properties of small- to medium-sized molecules. This paper gives a brief overview of the ACES II project, describes many features of the program system, and documents a number of benchmark calculations. © 1992 John Wiley & Sons, Inc.

Introduction

Since the early part of 1990, a new program system for quantum chemical calculations has been under development at the University of Florida. This suite of programs, known as ACES II [1], is ideally suited for users who are interested in performing highly accurate calculations on small to medium-sized molecules (up to 5–10 nonhydrogen atoms, depending upon the symmetry of the molecule). The program system largely reflects the research interests of its authors, and specializes in the treatment of electron correlation effects using the techniques of quantum many-body theory, namely many-body perturbation theory (MBPT) [2] and coupled-cluster (CC) [3] theory. In addition to the standard many-body approaches found in some other program systems, ACES II has many additional capabilities. In particular, the program includes a number of powerful treatments for open-shell molecules, and allows the calculation of energy gradients at almost all levels of theory where the energy is available. Additional features include analytic calculation of the second derivatives of the energy at selected levels of theory, evaluation of NMR shielding constants at both SCF and MBPT levels, and direct calculation of ionization potentials, electron affinities, and excitation energies. As such, it provides a unique tool for the study of molecular potential energy surfaces and spectroscopic properties (particularly for open-shell systems) at very high levels of theory. In addition, the program makes efficient use of molecular symmetry. The CPU time

---

* Current address: Lehrstuhl für Theoretische Chemie, Institut für Physikalische Chemie, Universität Karlsruhe, D-7500 Karlsruhe, Germany.

† Current address: Frank J. Seiler Research Laboratory, USAF Academy, Colorado Springs, CO 80840.

required for the most costly steps of correlated energy and gradient calculations scales inversely with the square of the order of the largest Abelian subgroup of the full molecular point group [4], with the result that CC calculations carried out in the D_{2h} subgroup with approximately 250 basis functions can routinely be carried out on a Cray-YMP in less than 1 hour of CPU time.

With the exception of the modules for calculation of molecular integrals and their derivatives [5], every line of ACES II has been written in the last 2 years. Consequently, it has been possible to specifically target the programs for modern hardware architectures and computing environments. Because most scientists now have access to a wide variety of computing options, a great deal of effort has been expended to make ACES II as portable as possible. The amount of machine-dependent code has been kept to an absolute minimum; routines which are intrinsically machine-dependent (such as those for obtaining timing information, allocation of memory, etc.) are kept in a special library directory. The program has been developed mostly on the Cray-YMP at the Ohio Supercomputing Center (with extensive applications carried out at the Florida Supercomputing Center), and has also been ported to other machines available to us locally (FPS-500, IBM RISC workstations, Sun SPARC, Silicon Graphics). Porting to other architectures is generally a trivial task and can easily be accomplished in a few hours. In addition, arithmetic operations have been written to exploit the features of vector computers as much as possible. Indeed, in the modules which solve for the MBPT and CC energies, all operator products are carried out with BLAS matrix multiplication routines, which are available in machine-optimized form from most vendors. On vector computers such as the Cray-YMP, very high sustained execution rates (in excess of 250 million floating point operations per second, or MFLOPS, running in single processor mode) can be achieved for larger (or less symmetric) systems where matrix sizes can be very large. Finally, to exploit the larger core memories available with modern computers, special in-core options are available which reduce the amount of disk input/output (I/O) to a minimum. The result is a set of programs which can produce answers to chemical problems with a very reasonable amount of CPU time.

In the following, we briefly describe the ACES II program system and describe many of its features. After this, we present results and timings of a variety of benchmark calculations carried out at the Ohio and Florida State Supercomputer Centers. These applications have been chosen to illustrate the variety of computational options available in ACES II as well as the performance of the program on a modern supercomputer. Additional benchmark timings may be found in refs. 4 and 6. Finally, we summarize and discuss some other aspects of the ACES II project.

Overview of Program Architecture

Currently, the ACES II program system consists of approximately 20 principal executable programs, or modules. The level of modularity is perhaps best illustrated by listing the execution sequence for a CC singles and doubles (CCSD) energy calculation and describing the actions of each module. The first executable, which serves a number of purposes, reads the input, determines the molecular symmetry,

principal axis system and rotational constants, generates the 3×3 (reducible) Cartesian representation matrices and permutation vectors for all group symmetry operations in both the full and Abelian subgroups, determines all internuclear distances and bond angles, and calculates transformation matrices relating the input coordinates (either Cartesian or Z-matrix internal coordinates) and the principal axis Cartesian frame. The second program calculates the one- and two-electron molecular integrals, using either generally contracted or segmented Gaussian basis sets. A third program determines a number of transformation matrices which are required to manipulate the basis set, such as those relating the basis set in Cartesian and spherical harmonic representations, symmetry-adapted to "bare" atomic orbitals, etc. The next program in the sequence solves the self-consistent field (SCF) problem using either restricted or unrestricted Hartree–Fock (RHF and UHF, respectively), or restricted open-shell Hartree–Fock (ROHF) methods. In addition, it checks the symmetry of the one-particle density matrix, and determines the irreducible representations of all molecular orbitals. After this, the fifth program in the sequence transforms the two-electron integrals from the atomic orbital (AO) to the molecular orbital (MO) basis. Another program processes these integrals and writes them to a direct-access file, ordered to facilitate post-SCF calculations. This program also performs the trivial task of evaluating the second-order MBPT [MBPT(2)] correlation energy. Finally, the CC/MBPT program is called and the CCSD energy and wavefunction are evaluated. The complete execution sequence is determined and subsequently controlled by a single FORTRAN program.

Due to the high level of modularity present in ACES II, the programs need to communicate with one another. This is carried out via word-addressable direct access files. Large dimension quantities such as two-electron integrals, density matrix elements, etc. are stored on "lists" in an order which is optimal for CC/MBPT calculations, an idea carried over from the ACES program system [7], written mainly by Bartlett and Purvis in the 1970s and 1980s. Other quantities such as SCF eigenvalues, information regarding the molecular geometry or symmetry, etc., are stored on the "JOBARC" file, and addressed via simple character string labels such as SCFEVECA for the α SCF eigenvectors. Two sets of two subroutines (one each for reading and writing) control all I/O to the data files. One is used for the "lists" and the other for the JOBARC file. When permitted by the amount of available machine memory, many or all of the "lists" [a series of logical records] can be read off disk at the beginning of execution and held in core throughout the calculation, resulting in significantly reduced I/O loads. In addition, all I/O to the list files is carried out by reasonably sophisticated routines that maintain a buffer cache which often contains the requested information and, therefore, does not require a physical disk read.

At the beginning of execution, each program calls a special subroutine which loads all common blocks with information, allocates the memory required for the calculation and initializes the I/O channels to the JOBARC and list files. In some sense, this routine serves to bring the executable "up-to-date" with regard to the previous steps carried out in the calculation. At the end of execution, each module calls another special routine which updates the files with information from the

calculation, purges the I/O caches, and closes the I/O channels. A great benefit of this strategy is that program interfacing is an extremely easy thing to do in ACES II. One only needs to define a few common blocks in a standard way and call the special routines at the beginning and termination of execution. All code in between these calls has easy access to all of the information accumulated by the calculation up to that point.

Features

The ACES II program system has a great number of capabilities for performing electronic structure calculations. As a result, it is not possible to give an exhaustive list of the available options here. Instead, we present a representative selection of some of the important features below, and include a brief description of the methods and algorithms used. In the following, we have not tried to provide an exhaustive list of original literature references. Rather, we list explicit citations only for some newly developed methods in ACES II and frequently refer to review articles otherwise. These articles should contain most of the original literature references. In addition, an extensive compilation of literature references is collected in the bibliography of the ACES II Program Manual, which is available upon request. The manual also contains significantly more information about the computational methodology included in the ACES II program.

- Simple input of molecular geometries via a Z-matrix or in terms of Cartesian coordinates: At present, geometry optimizations and transition state searches must be performed with Z-matrix input, but all other calculation types support both forms of input. Calculation options are specified via approximately 90 keywords, all of which have sensible default values. As a result, a geometry specification and a handful of keywords are all that is required to run a calculation. As an example, an input deck to run a CCSD(T) harmonic frequency calculation for ammonia is given below.

```
Ammonia frequency calculation
X
N 1 RX
H 2 RNH 1 A
H 2 RNH 1 A 3 T
H 2 RNH 1 A 4 T
RX=1.0
RNH=1.011269
A=112.6960417
T=120.

*ACES2(CALC=CCSD[T], BASIS=TZ2P, SPHERICAL=ON, VIB=FINDIF)
```

The keywords chosen specify the calculation level [CCSD(T)], the basis set (TZ2P), whether spherical harmonic or Cartesian basis functions are used (Cartesians are the default, necessitating use of the keyword), and the specific

type of calculation, which is a finite-difference harmonic frequency calculation. Note that all matters relating to molecular symmetry are handled internally by the program and are transparent to the user. The symbol "X" is used to denote a dummy atom, which often facilitates the construction of Z-matrices.

- Analysis of Z-matrix input for both subtle and obvious problems: Examples of this might include inequivalent coordinates given the same name, optimization of coordinates which regard to which the energy is stationary, optimization of too many degrees of freedom (more than the number of totally symmetric degrees of freedom for the molecule under study), etc. The problems are identified and described in the output, often with suggestions regarding possible improvements in the Z-matrix coordinates.

- Use of internally stored basis sets, which can be selected by keywords: The programs support the recent correlation consistent PVDZ, PVTZ, and PVQZ basis sets of Dunning [8], the basis sets used by the GAUSSIAN program system (STO-3G, 4-31G, 6-31G*, etc.) [9], Dunning's DZ and TZ basis sets [10] with and without polarization functions which have been optimized by our group [11], basis sets developed by Sadlej for the determination of molecular properties [12], and the generally contracted basis sets of Widmark et al. [13].

- Evaluation of the energy at the SCF and a number of correlated MBPT and CC levels, including MBPT through fourth-order [MBPT(4)] and CC through the CCSD + T(CCSD), CCSD(T) and CCSDT-n (n = 1-3) approximations [2,3]: Also included are CC methods based on a unitary ansatz [UCC, in particular UCCSD(4) and CCSDT(4)] and so-called quadratic configuration interaction methods [QCISD and QCISD(T)], which can be considered as approximate CC approaches. In addition to RHF and UHF reference functions, any single Slater determinant can be used in these calculations. Although this is somewhat trivial for CC methods by virtue of their invariance with respect to the partitioning of the electronic Hamiltonian, special techniques have been developed for MBPT [14,15] to allow completely general spin-orbital reference functions. While MBPT applied to an arbitrary reference function is likely to converge slowly and to be less useful for application to chemical problems, a particularly important special case of this approach is the use of ROHF reference functions in MBPT calculations. This ROHF-MBPT method has been shown to be preferable (more rapidly convergent) to UHF-MBPT in cases where the latter suffers from appreciable spin contamination [14,15].

- Analytic evaluation of the energy gradient for closed- and open-shell references (RHF and UHF) at the SCF, MBPT(2), MBPT(3), SDQ-MBPT(4), MBPT(4), CCD, QCISD, QCISD(T), UCCSD(4), UCCSDT(4), CCSD, CCSD + T(CCSD), and CCSD(T) levels [16]: Other than ACES II, no program system which is generally available at this writing has gradient capabilities beyond MBPT(2), other than a few which have either QCI or CC gradients, limited to closed-shell RHF references. In addition, ROHF-MBPT(2) [15] and ROHF-CCSD [17] gradient methods have been developed and implemented in the past 2 years, as well as those based on quasirestricted Hartree–Fock (QRHF) references [18] at the CCSD level [19]. In the latter approach, an RHF calculation is first carried out for

the molecule in a different electronic state which usually has a different number of electrons. Electrons are then either added to, removed from, or redistributed among the resulting RHF orbitals and the resulting set of occupation numbers is used in the CC calculation. The QRHF-CCSD approach benefits from the insensitivity with respect to orbital choice characteristic of CC methods which include single excitations [20], and has recently enjoyed success in the solution of problems where the more traditional reference functions exhibit pathological behavior. These include symmetry-breaking problems [21] and ionization potentials dominated by lower-lying occupied orbitals [18].

- Analytic evaluation of second derivatives of the energy at the SCF and MBPT(2) levels using RHF [22], UHF [23], and ROHF [24] reference functions: At present, symmetry has not been fully exploited in the processing of the derivative two-electron integrals, but this is a target for improvement in the near future. ACES II is the first program which can perform analytic open-shell (UHF and ROHF) second derivative calculations at the MBPT(2) level.

- Analytic evaluation of one-electron properties at all levels where gradients are available: Properties include dipole, quadrupole and octopole moments, electric field gradients, Darwin and mass-velocity relativistic corrections, and one-electron densities in the (diagonal) coordinate representation [25].

- Analytic calculation of NMR chemical shift tensors at the SCF [26] and MBPT(2) [27] levels, using the gauge-including atomic orbital method (GIAO) [28]: ACES II is the only available program with the capability to calculate GIAO-based NMR shifts at the correlated level. It has recently been shown [27] that the correlation contribution to NMR shift tensors can be appreciable, so the GIAO-MBPT(2) method is likely to be heavily used in future applications in this area.

- Stability analysis of RHF and UHF wavefunctions: The program calculates the second-order variation of the energy with respect to rotations of the orbitals and reports all instabilities (which correspond to negative eigenvalues in the orbital rotation Hessian). The eigenvectors corresponding to the instability are classified according to symmetry and type (internal RHF instability, internal UHF instability, RHF → UHF instability), and may be used to "push" the SCF eigenvectors toward the right solution. SCF Calculations restarted with these modified eigenvectors generally converge to the lower solution.

- Direct calculation of ionization potentials, electron affinities, and excitation energies using both Fock-space (FS-CC) [29] and equation of motion (EOM-CC) [30] coupled-cluster methods: Calculations can be based on either closed- or open-shell reference states. Again, these methods are unique to ACES II.

- Optimization of molecular geometries using quasi-Newton, full Newton–Raphson, rational function approximation [31] and Morse-adjusted Newton–Raphson [32] methods: Transition state location can also be performed using the eigenvector following technique [33].

- Calculation of open-shell singlet states at the CC level can be carried out using a generalization of recently developed Hilbert space multireference coupled-cluster techniques [34]. This is an additional unique feature of ACES II, and

expands the range of molecules amenable to high-level CC methods. In particular, it allows the study of many excited electronic states.

- Automated calculation of harmonic vibrational frequencies and infrared intensities by numerical differentiation of gradients and dipole moments, or via numerical differentiation of the energy. These calculations can be based on one of two algorithms. In the first, symmetry-adapted, mass-weighted Cartesian coordinates are constructed for the molecule (these have the distinct advantage of having a unit metric, or "G-matrix") and translational and (optionally) rotational components are removed by projection. These coordinates are then used as a basis for constructing the force constant matrices. A second algorithm is available which exploits the intrinsic redundancy in the Cartesian force constant matrix in an optimal way [35], resulting in the absolute minimum number of points required in the calculation. However, these must often be carried out in very low (or no) symmetry. Due to exploitation of symmetry in ACES II, however, the first method is usually preferred. These features, which are always required to calculate vibrational frequencies at high level of theory [beyond MBPT(2)] are the most sophisticated numerical differentiation procedures available today.

- Identification of the irreducible representations for normal modes, molecular orbitals and electronic states. Unlike many programs, the assignments can be made in all possible point groups. In addition, the irreducible representations in the Abelian subgroup are given as well. This is an extremely useful feature for constructing correlation diagrams, analyzing orbital interactions, etc.

- Through its use of the MOLECULE integral program and the ABACUS integral derivative program [5], ACES II allows the use of generally contracted basis sets in all energy, gradient, and Hessian calculations.

Benchmark Calculations

Although ACES II was only begun a relatively short time ago and is under continual development, it has already been used in a large number and wide variety of studies (see for example refs. 21,27,36–38). Topics include investigation of symmetry breaking phenomena, accurate calculations of properties and potential energy surfaces of small molecules, and heats of formation of azacubanes. While the varying sizes of the systems have necessitated the use of varying qualities of basis sets, in virtually all of these studies CC methods [most commonly CCSD and CCSD(T)] have been used to treat electron correlation. This is testimony to the particular efficiency of these parts of the program, which is a consequence of the philosophy on which the program was based. That is, the principal goal has been to extend the range of systems which are amenable to CC treatments.

We now describe some recent applications of ACES II. The first application we shall consider is some of our own work on isomers of the C_4 molecule [37]. This molecule has been of particular interest since it was suggested that a closed-shell cyclic isomer was comparable in energy with the open-shell cumulenic linear isomer, a suggestion contrary to chemical intuition and to early calculations on carbon

STANTON ET AL

clusters. Many calculations have since confirmed that the two isomers are indeed close in energy. We recently began a further study of these two isomers which was intended to go beyond previous work and provide a reasonably definitive study. To this end geometries of both isomers were optimized using MBPT(2), CCSD, and CCSD(T) methods and the PVTZ basis set. Harmonic vibrational frequencies and some one-electron properties were computed at the CCSD(T)/PVTZ level using analytical gradient techniques. Cartesian polarization functions were used, leading to a total of 140 basis functions. Refined estimates of the energy difference were computed using these methods and the larger PVQZ basis set $(5s4p3d2f1g)$. For this basis, spherical harmonic polarization functions were used, leading to a total of 220 basis functions. In these calculations, a closed-shell RHF reference function was used for the rhombic isomer and an open-shell UHF reference function was used for the linear isomer. Timing data are shown in Tables I and II. Table I shows times for the various modules needed in gradient calculations, and Table II shows the times for the large basis set energy calculations.

TABLE I. Timing data (in seconds) for modules of the ACES II program system for CCSD(T)/PVTZ gradient calculations on linear $(^3\Sigma_g^-)$ and rhombic (^1A_g) C_4 (140 basis functions, all electrons correlated). Data are presented for gradient calculations at the equilibrium geometries (computational symmetry is D_{2h}) and for geometries displaced along symmetry lowering modes (computational symmetry is C_{2v}).

	Linear C_4		Rhombic C_4	
	D_{2h}	C_{2v}	D_{2h}	C_{2v}
xvmol	143	277	119	220
xvscf	89	96	20	36
xftran	84	197	23	64
xintprc	104	210	41	82
xvcc (i)[a]	803			
xvcc (ii)[a]	543			
xvcc (iii)[a]	1183			
xvcc (total)[a]	2529	6642	1309	2990
xlambda	626	1835	291	761
xdens	95	263	37	104
xanti	35	49	11	57
xbcktrn	85	183	29	53
xvdint	957	1574	589	1231

[a] In these calculations the xvcc module performs three tasks: (i) solves the CCSD equations; (ii) evaluates the triples amplitudes and energies; (iii) evaluates the contribution of triples amplitudes to one- and two-particle density matrices and lambda equations. For linear C_4 in D_{2h} symmetry we have given times for all three steps, while for the other calculations just the total time is available.

	Linear C_4	Rhombic C_4
xvmol	1472	1239
xvscf	106	39
xftran	392	160
xintprc	549	167
xvcc	1362	642

The functions of the modules which are used in the benchmarks presented here are as follows.

xvmol: Evaluates one- and two-electron integrals.

xvscf: Solves the SCF equations.

xftran: Performs the two-electron integral transformation.

xintprc: Sorts transformed two-electron integrals and prepares lists for correlated calculations.

xvcc: Solves the CC equations, evaluates MBPT and CC energies. In gradient calculations involving triple excitations it also evaluates contributions of triples to one- and two-particle density matrices and lambda equations.

xlambda: Solves the Λ equations for the response of the CC amplitudes to the perturbation, and calculates certain elements of the canonically transformed Hamiltonian $\bar{H} = \exp(-T) \mathcal{H} \exp(T)$. Only the latter function is carried out for FS-CC and EOM-CC calculations.

xfsip: Calculates ionization potentials using the FS-CC method.

xdens: Evaluates one- and two-particle density matrices.

xanti: Resorts the two-particle density matrix in preparation for **xbcktrn.**

xbcktrn: Transforms the two-particle density matrices from the MO to the AO basis.

xvdint: Evaluates one- and two-electron integral derivatives.

The timings clearly show the suitability of ACES II for large-scale CC calculations. Indeed, in the large basis set calculations, the one- and two-electron evaluation time is larger than the time for the CC calculation! Also, a recurring feature of large-scale calculations with ACES II is that disk space limitations occur before CPU limitations, especially for open-shell systems. Certain of these times will be improved in the near future. For example, it may be seen that CC calculations with RHF reference functions take about half of the time of UHF reference functions, even though a higher ratio should certainly be possible. At present, beyond restriction

TABLE III. Harmonic vibrational frequencies and infrared intensities of linear and rhombic C_4 calculated at the CCSD(T)/PVTZ level. Units are cm^{-1} and km mol^{-1}.

Linear C_4			Rhombic C_4		
Symmetry	Frequency	Intensity	Symmetry	Frequency	Intensity
σ_g	2156	0	a_g	1279	0
σ_g	936	0	a_g	956	0
σ_u	1600	316	b_{1g}	1050	0
π_g	474	0	b_{1u}	306	47
π_u	203	46	b_{2u}	532	50
			b_{3u}	1405	260

to just two of the four possible triple-excitation spin cases, our triple-excitation routines take little advantage of the simplifications possible with a closed-shell RHF reference function.

The principal results of this study are shown in Tables III and IV. Table III shows the calculated harmonic vibrational frequencies and infrared intensities of the two isomers, while Table IV shows calculated isomer energy differences. One particular conclusion apparent from this work is that previous calculations on linear C_4, done at the SCF or MBPT(2) level with *spd* basis sets, do not describe the infrared intensity of the asymmetric stretching frequency of linear C_4 well. As for Table IV, these results indicate strongly that once a certain level of basis set quality has been achieved, further extension favors the rhombus. For further discussion and more data, the reader is referred to a forthcoming full study on this subject [37].

To illustrate the application of methods for the *direct* calculation of ionization potentials, electron affinities, and excitation energies which are included in ACES II, we present results and computational timings for a calculation of the ionization potentials of the nitrogen molecule. These results were obtained with the Fock-space CC model truncated to single and double excitations (FS-CCSD) using the generally contracted basis set of Widmark et al. [13]. In this calculation, which was performed at the experimental equilibrium geometry of N_2, the PVQZ basis of Dun-

TABLE IV. Absolute and relative energies of linear and rhombic C_4. Absolute energies are in Hatrees and relative energies are in kcal mol^{-1}.

Basis	Method	Rhombic C_4	Linear C_4	ΔE
PVTZ	UHF-MBPT(2)	-151.809967	-151.790495	12.22
PVTZ	UHF-CCSD	-151.819119	-151.827996	-5.57
PVTZ	UHF-CCSD(T)	-151.858459	-151.862829	-2.74
PVQZ	UHF-CCSD	-151.788859	-151.790875	-1.27
PVQZ	UHF-CCSD + T(CCSD)	-151.831014	-151.829326	1.06
PVQZ	UHF-CCSD(T)	-151.829918	-151.827295	1.65

ning [8] was used and all Cartesian components of the polarization functions were included, resulting in a basis set of 140 contracted GAUSSIAN functions. As seen from the results in Table V, the ionization potentials obtained with the FS-CCSD approach are in good agreement with well-established experimental results. It should be stressed that the theoretical values were obtained in a single calculation, underscoring the power of direct approaches for determining this type of property. An additional advantage of the FS-CC method is that the final state wavefunctions (the states of N_2^+) are rigorously spin-adapted when the reference state (the N_2 ground state in the present example) is a closed-shell system. As a result, spin-adaptation can be used to simplify the calculation and significantly reduce computational cost. Nevertheless, evaluation of the reference state CCSD wavefunction and energy represents the majority of the cost of a FS-CC ionization potential calculation. This feature is reflected in the timings presented in Table VI, where the ionization potential calculation (**xfsip**) represents only 2% of the total CPU time required for the job. The overall execution time (265 seconds) should be contrasted with the amount of time which would be required for a ΔCCSD evaluation of the ionization potentials. In addition to the reference state RHF-CCSD calculation on N_2 (which is also required in the FS-CCSD approach), such a state-by-state solution would also require open-shell CCSD calculations (using UHF, ROHF, or QRHF reference functions), each of which would require roughly three times the resources and computer time of a single RHF-CCSD calculation. Hence, one would be trading the negligible cost of a FS-CCSD calculation for additional steps which would require an order of magnitude more time than the reference CCSD calculation itself. Clearly, the FS-CCSD approach represents a cost-effective means for calculating the photoelectron spectra of molecules. For open-shell reference states, of course, the spin-adapted feature and corresponding computational simplifications are lost. Nevertheless, the FS-CCSD step is still much cheaper than the open-shell reference CCSD calculation and the attractive features of the direct computational approach are retained. Our implementation is the first to generalize the FS-CC method to arbitrary single-de-

TABLE V. Valence ionization potentials of the N_2 molecule, evaluated with the FS-CCSD method using the PVQZ basis of Ref. 8. The experimental bond length (1.097 Å) was used in these calculations. The calculated results represent vertical ionization potentials, while the experimental results are adiabatic values from Ref. 41.

Final state	Ionization potential (eV)	
	FS-CCSD	Expt.
$^2\Sigma_g^+$	15.73	15.5
$^2\Pi_u$	17.33	16.8
$^2\Sigma_u^+$	18.97	18.6

Module	CPU time (s)
xvmol	112
xvscf	13
xftran	24
xintprc	34
xvcc	58
xlambda	18
xfsip	6
Total time	265

terminant (restricted and unrestricted with respect to spin) reference functions [40] and initial calculations using this open-shell reference FS-CC method have provided encouraging results.

Another recent application is a study of spiropentadiene (C_5H_4) by Shavitt et al. [36]. This molecule is the smallest member of a class of highly strained organic molecules, and was recently synthesized by Billups and Haley [39]. Since experimental characterization is not yet possible. Shavitt et al. undertook a theoretical study to compute key structural, spectroscopic, and thermodynamic data for this molecule. In order to obtain a heat of formation, it was desired to perform a MBPT(4) calculation with the correlation-consistent polarized triple-zeta valence plus polarization (PVTZ) basis set of Dunning [8]. For C, this basis set is $4s3p2d1f$ and for H it is $3s2p1d$, leading to a total of 206 basis functions for C_5H_4. This demanding calculation could only be done with ACES II and not with any other packages to which Shavitt et al. had access. As a result of the efficient use of symmetry and vectorized algorithms, the calculation was straightforwardly completed with ACES II in roughly 2 hours of CPU time. Moreover, the calculation was performed slightly more than 1 year ago (July 1991), and there have since been improvements in the programs which would reduce this time somewhat.

As a final example of the performance of the ACES II program, we present computational timings for a CCSD calculation carried out on the $Al_2B_4H_{18}$ molecule. This molecule belongs to the D_{2h} point group, and the calculations were performed using 238 basis functions. As seen from Table VII. the entire calculation required *less than 1 hour* on a Cray-YMP. The most expensive stage of the calculation was the evaluation of the CCSD energy, requiring slightly more than 20 minutes of CPU time. It should also be pointed out that this phase of the calculation achieved a *sustained* execution rate of 254 MFLOPS, clearly demonstrating the highly vectorized nature of ACES II and its suitability for modern vector computers such as

TABLE VII. Timing data (in seconds) for
modules of the ACES II program system for
a CCSD energy calculation on Al₂B₄H₁₆ using
238 basis functions. Computational
symmetry is D₂ₕ.

Module	CPU time (s)
xvmol	630
xvscf	77
xftran	402
xintprc	561
xvcc	1303
Total time	2973

the Cray-YMP. It also serves to illustrate that the initial development of the ACES II system has made promising advances toward the goal stated early in this section— to extend the range of systems which can be addressed with high-level CC/MBPT methods.

Summary

In this study, we have presented an overview of the new ACES II program system. Although the program is relatively new, it has unrivaled capabilities for performing very accurate calculations on relatively small systems, particularly for open-shell molecules. As such, the program system should be very useful for detailed interpretations of molecular spectroscopy and reactivity. Its availability within our group has led to a tremendous growth in the scope of chemical problems that we are able to address with high-level CC/MBPT methods, and its straightforward input has greatly simplified the process of running production calculations. In addition to its value as a research tool for chemical applications, the streamlined design of ACES II has also facilitated implementation of new theoretical methods by our group. Anyone who has ever worked in the field of quantum chemistry program development knows that interfacing new programs can be one of the most difficult tasks which must be performed. In ACES II, the interfacing process consists of beginning and ending each module with specific subroutine calls and following a few simple rules. The rapid rate at which new theoretical methods have been incorporated into ACES II in the past 2 years attests to the overall design of the program system.

At this point, it is appropriate to describe what ACES II is *not*. As discussed in the Introduction, the program system reflects the research interests of its authors, all of whom are or have been members of the Bartlett group at the University of Florida's Quantum Theory Project. Our focus has been in the development and implementation of correlated CC/MBPT energy and gradient methods, and we have tried very hard to make these programs as efficient and flexible as possible. Calculations carried out in the course of our research are almost always performed at levels which go beyond the SCF approximation, and usually beyond MBPT(2). All

such methods have a computational dependence which scales at least as steeply as the *sixth* power of the number of basis functions. As a result, we have paid somewhat less attention to stages of the calculation which, for the studies we commonly pursue, are significantly less expensive than the rate-limiting steps of the calculation. As a result, we do not claim that ACES II is the program for everyone. Indeed, it is certainly not the best program to use for the very common task of performing energy calculations and geometry optimizations at the SCF level, nor have we made efforts to date toward implementing direct methods for SCF and MBPT(2) calculations, an area where great progress has recently been made by other groups. In addition, ACES II does not have the capability to perform multiconfigurational SCF calculations, although it does have limited multireference CC capabilities. Nevertheless, ACES II is an extremely efficient computer program for the calculation of energies and gradients at correlated levels. Although we have chosen not to compare the timings presented in the previous section with those of other programs, enough information has been supplied regarding the calculations so that curious readers can easily make their own comparisons.

ACES II is under extremely rapid development and is expected to continually improve both in the scope of its functionality and in its performance for existing methods each year. One of the most important areas in the latter category involves improvement of algorithms for carrying out relatively low-level calculations for very large or nonsymmetric molecules. In developing the program system, we have concentrated mainly upon developing and implementing methods so that the calculations which we commonly carry out can be performed with a reasonable amount of computer resources. Indeed, the evolution of algorithms in ACES II generally has gone from a full in-core implementation to more sophisticated out-of-core methods as they have been needed by the jobs run in our research group. At present, the memory and disk space requirements of ACES II are such that essentially all of the jobs run by our group can be carried out in 8 megawords of computer memory and 1 gigabyte of disk storage. However, other users might run into memory or disk space limitations for very large jobs, and we are acutely aware of this shortcoming of the program system. Indeed, our collaboration with the Ohio Supercomputing Center and its collection of quantum chemistry users has led to a few incidents of this type, and we have resolved the problems. In the few months previous to this writing, a number of improvements have been made to ACES II to improve memory and disk requirements at the MBPT(2) level. These have been sufficient to assure that essentially any calculation type (gradient, second derivative, NMR shift, etc.) carried out at this level can be performed in only a few megawords of memory. In the future, we will direct some of our efforts toward eliminating remaining memory and disk space bottlenecks. Nevertheless, the rather small group of ACES II authors are actively involved in developing theoretical methods as well, so implementation of these ideas will continue to be the primary focus of the ACES II project. Those who are interested in doing very accurate work on the spectroscopy and potential energy surfaces of small- to medium-sized molecules may greatly benefit from the use of the ACES II program system. Interested readers can receive information

about obtaining the program by sending an electronic mail message to "aces2@qtp.ufl.edu."

Acknowledgments

Bibliography

[1] ACES II, a program system for *ab initio* electronic structure calculations, authored by J. F. Stanton, J. Gauss, J. D. Watts, W. J. Lauderdale, and R. J. Bartlett, Quantum Theory Project, University of Florida, 1992.

[2] R. J. Bartlett, Ann. Rev. Phys. Chem. **32**, 359 (1981).

[3] R. J. Bartlett, J. Phys. Chem. **93**, 1697 (1989).

[4] J. F. Stanton, J. Gauss, and R. J. Bartlett, J. Chem. Phys. **94**, 4334 (1991).

[5] ACES II uses modified versions of the MOLECULE vectorized GAUSSIAN integral program and the ABACUS program for evaluation of integral derivatives. The authors of these programs are: J. Almlof and P. R. Taylor (MOLECULE); T. Helgaker, P. Jørgensen, H. J. A. Jensen, and P. R. Taylor (ABACUS).

[6] J. Gauss, J. F. Stanton, and R. J. Bartlett, J. Chem. Phys. **95**, 2623 (1991).

[7] ACES, a program system for *ab initio* electronic structure calculations, authored by R. J. Bartlett, G. D. Purvis III, D. E. Bernholdt, S. J. Cole, G. B. Fitzgerald, R. J. Harrison, W. D. Laidig, Y. S. Lee, D. H. Magers, L. Meissner, M. Rittby, E. A. Salter, H. Sekino, C. Sosa, J. F. Stanton, G. W. Trucks, and J. D. Watts.

[8] T. H. Dunning, J. Chem. Phys. **90**, 1007 (1989).

[9] W. J. Hehre, L. Radom, P. v. R. Schleyer and J. A. Pople *Ab Initio Molecular Orbital Theory* (Wiley, New York, 1986).

[10] T. H. Dunning, J. Chem. Phys. **58**, 2823 (1970).

[11] L. T. Redmon, G. D. Purvis, and R. J. Bartlett, J. Am. Chem. Soc. **101**, 2856 (1979) (DZP); J. F. Stanton, W. N. Lipscomb, D. H. Magers, and R. J. Bartlett, J. Chem. Phys. **90**, 3241 (1989) (DZP); J. Gauss, J. F. Stanton, and R. J. Bartlett, unpublished (TZP).

[12] A. J. Sadlej and M. Urban, J. Mol. Struct. **234**, 147 (1991), and references therein.

[13] P. O. Widmark, P. Å. Malmqvist, and B. O. Roos, Theoret. Chim Acta **77**, 291 (1990).

[14] W. J. Lauderdale, J. F. Stanton, J. Gauss, J. D. Watts, and R. J. Bartlett, Chem. Phys. Lett. **187**, 21 (1991).

[15] W. J. Lauderdale, J. F. Stanton, J. Gauss, J. D. Watts, and R. J. Bartlett, J. Chem Phys. (to appear).

[16] The literature on analytic gradients in MBPT/CC methods is far too extensive to list here. The implementation of these methods in ACES II mostly follows the general MBPT/CC gradient formalism presented by E. A. Salter, G. W. Trucks, and R. J. Bartlett, J. Chem. Phys. **90**, 1752 (1989). The detailed spin-orbital equations used in the implementation as well as the computational strategy

are described in Ref. [6]. These articles also give the original literature references for most of the methods which are implemented in ACES II. Exceptions are as follows: G. Scuseria, J. Chem. Phys. **94**, 442 (1991); T. J. Lee and A. Rendell, J. Chem. Phys. **94**, 6229 (1991) [CCSD(T)]; J. D. Watts, J. Gauss, and R. J. Bartlett, to appear [open shell QCISD(T), CCSD(T), and CCSD + T(CCSD)].

[17] J. Gauss, W. J. Lauderdale, J. F. Stanton, J. D. Watts, and R. J. Bartlett, Chem. Phys. Lett. **182**, 207 (1991).

[18] M. Rittby and R. J. Bartlett, J. Phys. Chem. **92**, 3033 (1988).

[19] J. Gauss, J. F. Stanton, and R. J. Bartlett, J. Chem. Phys. **95**, 2639 (1991).

[20] E. A. Salter, H. Sekino, and R. J. Bartlett, J. Chem. Phys. **87**, 502 (1987).

[21] J. F. Stanton, J. Gauss, and R. J. Bartlett, J. Chem. Phys. **94**, 4084 (1991); J. D. Watts, J. F. Stanton, J. Gauss, and R. J. Bartlett, J. Chem. Phys. **94**, 4320 (1991); J. F. Stanton, J. Gauss, and R. J. Bartlett, J. Chem. Phys. (to appear).

[22] N. C. Handy, R. D. Amos, J. F. Gaw, J. E. Rice, E. D. Simandiras, T. J. Lee, R. J. Harrison, W. D. Laidig, G. B. Fitzgerald, and R. J. Bartlett, in *Geometrical Derivatives of Energy Surfaces and Molecular Properties*, P. Jørgensen and J. Simons, Eds. (Reidel: Dordrecht, 1986) p. 179; N. C. Handy, R. D. Amos, J. F. Gaw, J. E. Rice, E. D. Simandiras, Chem. Phys. Lett. **120**, 151 (1985); R. J. Harrison, G. B. Fitzgerald, W. D. Laidig, and R. J. Bartlett, Chem. Phys. Lett. **124**, 291 (1986).

[23] J. F. Stanton, J. Gauss, and R. J. Bartlett, Chem. Phys. Lett. **195**, 194 (1992).

[24] J. Gauss, J. F. Stanton, and R. J. Bartlett, J. Chem. Phys. (to appear).

[25] Property calculations utilize the PROPS integral program, which was originally part of the POLYATOM program. The version used in ACES II is a slightly modified version of PROPS which has been interfaced to the MOLECULE-SWEDEN package by P. R. Taylor.

[26] K. Wolinski, J. F. Hinton, and P. Pulay, J. Am. Chem. Soc. **112**, 8251 (1990).

[27] J. Gauss, Chem. Phys. Lett. **191**, 614 (1992).

[28] R. Ditchfield, Mol. Phys. **27**, 789 (1974).

[29] M. Rittby, S. Pal, and R. J. Bartlett, J. Chem. Phys. **90**, 3214 (1992). Excellent reviews of the Fock-space coupled-cluster method may be found in Theoret. Chim. Acta. **6**(4) (1992).

[30] J. Geertsen, M. Rittby, and R. J. Bartlett, Chem. Phys. Lett. **164**, 57 (1989); H. Koch, H. J. A. Jensen, P. Jørgensen, and T. Helgaker, J. Chem. Phys. **93**, 3345 (1990). The method is also known as the coupled-cluster linear response method.

[31] J. Simons, P. Jørgensen, H. Taylor, and J. Ozment, J. Phys. Chem. **87**, 2745 (1983).

[32] J. F. Stanton and D. E. Bernholdt, J. Comp. Chem. **11**, 58 (1990).

[33] C. J. Cerjan and W. H. Miller, J. Chem. Phys. **75**, 2800 (1981); J. Simons, P. Jørgensen, H. Taylor, and J. Ozment, J. Phys. Chem. **87**, 2745 (1983).

[34] A. Balkova, and R. J. Bartlett, Chem. Phys. Lett. **193**, 364 (1992).

[35] J. F. Stanton, Int. J. Quant. Chem. **29**, 19 (1991).

[36] I. Shavitt, D. W. Ewing, and J. E. DelBene, J. Am. Chem. Soc. **113**, 9389 (1991).

[37] J. D. Watts, J. Gauss, J. F. Stanton, and R. J. Bartlett (to appear).

[38] J. D. Watts and R. J. Bartlett, J. Chem. Phys. **95**, 6652 (1991) (F$_2$, F$_2^-$); J. Chem. Phys. **96**, 6073 (1992) (C$_2$, C$_2^-$, C$_2^+$); Chem. Phys. Lett. **190**, 19 (1992) (C$_{10}$); Y. M. Hamrick, R. J. Van Zee, W. Weltner, W. J. Lauderdale, J. F. Stanton, and R. J. Bartlett, J. Phys. Chem. **95**, 2840 (1991) (BCO); J. F. Stanton, J. Gauss, R. J. Bartlett, T. Helgaker, P. Jørgensen, H. J. Aa. Jensen, and P. R. Taylor, J. Chem. Phys. **97**, 1211 (1992) (B$_3$H$_4$); P. G. Szalay, J. F. Stanton, and R. J. Bartlett, Chem. Phys. Lett. **193**, 573 (1992) (HC$_2$O).

[39] W. E. Billups and M. M. Haley, J. Am. Chem. Soc. **113**, 5084 (1991).

[40] J. F. Stanton and R. J. Bartlett, J. Chem. Phys. (to appear).

[41] K. Siegbahn, C. Nordling, G. Johansson, J. Hedman, P. F. Heden, K. Hamrin, U. Gelius, T. Bergmark, L. O. Werme, R. Manne, Y. Baer, *ESCA Applied to Free Molecules* (North-Holland, Amsterdam, 1971).

Author Index

Published Symposia of the
International Journal of Quantum Chemistry

1967   QUANTUM CHEMISTRY SYMPOSIUM NO. 1
        (Proceedings of the International Symposium on Atomic. Molecular, and Solid-State Theory)

1968   QUANTUM CHEMISTRY SYMPOSIUM NO. 2
        (Proceedings of the International Symposium on Atomic. Molecular, and Solid-State Theory and Quantum Biology)

1969   QUANTUM CHEMISTRY SYMPOSIUM NO. 3 PART 1
        (Proceedings of the International Symposium on Atomic, Molecular, and Solid-State Theory and Quantum Biology)

1970   QUANTUM CHEMISTRY SYMPOSIUM NO. 3 PART 2
        (Proceedings of the International Symposium on Atomic. Molecular, and Solid-State Theory and Quantum Biology)

1971   QUANTUM CHEMISTRY SYMPOSIUM NO. 4
        (Proceedings of the International Symposium on Atomic. Molecular, and Solid-State Theory and Quantum Biology)

1971   QUANTUM CHEMISTRY SYMPOSIUM NO. 5
        (Proceedings of the International Symposium on Atomic. Molecular, and Solid-State Theory and Quantum Biology)

1972   QUANTUM CHEMISTRY SYMPOSIUM NO. 6
        (Proceedings of the International Symposium on Atomic. Molecular, and Solid-State Theory and Quantum Biology)

1973   QUANTUM CHEMISTRY SYMPOSIUM NO. 7
        (Proceedings of the International Symposium on Atomic. Molecular, and Solid-State Theory and Quantum Biology)

1974   QUANTUM CHEMISTRY SYMPOSIUM NO. 8
        (Proceedings of the International Symposium on Atomic. Molecular, and Solid-State Theory and Quantum Statistics)
        QUANTUM BIOLOGY SYMPOSIUM NO. 1
        (Proceedings of the International Symposium on Quantum Biology and Quantum Pharmacology)

1975   QUANTUM CHEMISTRY SYMPOSIUM NO. 9
        (Proceedings of the International Symposium on Atomic. Molecular, and Solid-State Theory and Quantum Statistics)
        QUANTUM BIOLOGY SYMPOSIUM NO. 2
        (Proceedings of the International Symposium on Quantum Biology and Quantum Pharmacology)

1976   QUANTUM CHEMISTRY SYMPOSIUM NO. 10
        (Proceedings of the International Symposium on Atomic, Molecular, and Solid-State
        Theory and Quantum Statistics)
        QUANTUM BIOLOGY SYMPOSIUM NO. 3
        (Proceedings of the International Symposium on Quantum Biology and Quantum Phar-
        macology)

1977   QUANTUM CHEMISTRY SYMPOSIUM NO. 11
        (Proceedings of the International Symposium on Atomic, Molecular, and Solid-State
        Theory, Collision Phenomena, and Computational Methods)
        QUANTUM BIOLOGY SYMPOSIUM NO. 4
        (Proceedings of the International Symposium on Quantum Biology and Quantum Phar-
        macology)

1978   QUANTUM CHEMISTRY SYMPOSIUM NO. 12
        (Proceedings of the International Symposium on Atomic, Molecular, and Solid-State
        Theory, Collision Phenomena, and Computational Methods)
        QUANTUM BIOLOGY SYMPOSIUM NO. 5
        (Proceedings of the international Symposium on Quantum Biology and Quantum Phar-
        macology)

1979   QUANTUM CHEMISTRY SYMPOSIUM NO. 13
        (Proceedings of the International Symposium on Atomic, Molecular, and Solid-State
        Theory, Collision Phenomena, Quantum Statistics, and Computational Methods)
        QUANTUM BIOLOGY SYMPOSIUM NO. 6
        (Proceedings of the International Symposium on Quantum Biology and Quant im Phar-
        macology)

1980   QUANTUM CHEMISTRY SYMPOSIUM NO. 14
        (Proceedings of the International Symposium on Atomic, Molecular, and Solid-State
        Theory, Collision Phenomena, Quantum Statistics, and Computational Methods)
        QUANTUM BIOLOGY SYMPOSIUM NO. 7
        (Proceedings of the International Symposium on Quantum Biology and Quantum Phar-
        macology)

1981   QUANTUM CHEMISTRY SYMPOSIUM NO. 15
        (Proceedings of the International Symposium on Atomic, Molecular, and Solid-State
        Theory, Collision Phenomena, and Computational Quantum Chemistry)
        QUANTUM BIOLOGY SYMPOSIUM NO. 8
        (Proceedings of the International Symposium on Quantum Biology and Quantum Phar-
        macology)

1982   QUANTUM CHEMISTRY SYMPOSIUM NO. 16
        (Proceedings of the International Symposium on Quantum Chemistry, Theory of Con-
        densed Matter, and Propagator Methods in the Quantum Theory of Matter)
        QUANTUM BIOLOGY SYMPOSIUM NO. 9
        (Proceedings of the International Symposium on Quantum Biology and Quantum Phar-
        macology)

1983   QUANTUM CHEMISTRY SYMPOSIUM NO. 17
        (Proceedings of the International Symposium on Atomic, Molecular, and Solid-State
        Theory, Collision Phenomena, and Computational Quantum Chemistry)

QUANTUM BIOLOGY SYMPOSIUM NO. 10
(Proceedings of the International Symposium on Quantum Biology and Quantum Pharmacology)

1984 QUANTUM CHEMISTRY SYMPOSIUM NO. 18
(Proceedings of the International Symposium on Atomic, Molecular, and Solid-State Theory, and Computational Quantum Chemistry)
QUANTUM BIOLOGY SYMPOSIUM NO. 11
(Proceedings of the International Symposium on Quantum Biology and Quantum Pharmacology)

1985 QUANTUM CHEMISTRY SYMPOSIUM NO. 19
(Proceedings of the International Symposium on Atomic, Molecular, and Solid-State Theory, Scattering Problems, Many Body Phenomena, and Computational Quantum Chemistry)
QUANTUM BIOLOGY SYMPOSIUM NO. 12
(Proceedings of the International Symposium on Quantum Biology and Quantum Pharmacology)

1986 QUANTUM CHEMISTRY SYMPOSIUM NO. 20
(Proceedings of the International Symposium on Atomic, Molecular, and Solid-State Theory, Scattering Problems, Many Body Phenomena, and Computational Quantum Chemistry)
QUANTUM BIOLOGY SYMPOSIUM NO. 13
(Proceedings of the International Symposium on Quantum Biology and Quantum Pharmacology)

1987 QUANTUM CHEMISTRY SYMPOSIUM NO. 21
(Proceedings of the International Symposium on Quantum Chemistry, Solid-State Theory, and Computational Methods)
QUANTUM BIOLOGY SYMPOSIUM NO. 14
(Proceedings of the International Symposium on Quantum Biology and Quantum Pharmacology)

1988 QUANTUM CHEMISTRY SYMPOSIUM NO. 22
(Proceedings of the International Symposium on Quantum Chemistry, Solid-State Theory, and Computational Methods)
QUANTUM BIOLOGY SYMPOSIUM NO. 15
(Proceedings of the International Symposium on Quantum Biology and Quantum Pharmacology)

1989 QUANTUM CHEMISTRY SYMPOSIUM NO. 23
(Proceedings of the International Symposium on Quantum Chemistry, Solid-State Theory, and Molecular Dynamics)
QUANTUM BIOLOGY SYMPOSIUM NO. 16
(Proceedings of the International Symposium on Quantum Biology and Quantum Pharmacology)

1990 QUANTUM CHEMISTRY SYMPOSIUM NO. 24
(Proceedings of the International Symposium on Quantum Chemistry, Solid State Theory, and Computational Methods)
QUANTUM BIOLOGY SYMPOSIUM NO. 17
(Proceedings of the International Symposium on Quantum Biology and Quantum Pharmacology)

1991   QUANTUM CHEMISTRY SYMPOSIUM NO. 25
(Proceedings of the International Symposium on Quantum Chemistry, Solid State
Theory, and Computational Methods)
QUANTUM BIOLOGY SYMPOSIUM NO. 18
(Proceedings of the International Symposium on Quantum Biology and Quantum
Pharmacology)

1992   QUANTUM CHEMISTRY SYMPOSIUM NO. 26
(Proceedings of the International Symposium on Atomic, Molecular, and Condensed
Matter Theory and Computational Methods
QUANTUM BIOLOGY SYMPOSIUM NO. 19
(Proceedings of the International Symposium on the Application of Fundamental Theory
to Problems of Biology and Pharmacology)

All of the above symposia can be individually purchased from the Subscription Department, John
Wiley & Sons.